

DTIC FILE COPY

(2)

DNA EM-1  
PART I

DEFENSE NUCLEAR AGENCY EFFECTS MANUAL NUMBER 1

CAPABILITIES  
OF  
NUCLEAR WEAPONS

Document released under the  
Freedom of Information Act,  
DNA Case No. SI-142

AD-A955 403

1 JULY 1972



HEADQUARTERS  
Defense Nuclear Agency  
Washington, D.C. 20305

DTIC  
ELECTE  
S D  
1989  
E

This document has been approved  
for public release and makes its  
distribution unlimited.

89 2 00 029

DNA EM-1  
PART I  
1 JULY 1972

DEFENSE NUCLEAR AGENCY EFFECTS MANUAL NUMBER 1

# CAPABILITIES OF NUCLEAR WEAPONS

## PART I PHENOMENOLOGY

HEADQUARTERS  
Defense Nuclear Agency  
Washington, D.C. 20305

EDITOR  
PHILIP J. DOLAN  
STANFORD RESEARCH INSTITUTE

UNANNOUNCED

Accession No.	
NTIS GEN&I	
DTIC TAB	
Unannounced	
Justification <i>PLS</i>	
By _____	
Distribution/ _____	
Availability Codes	
Dist	Avail and/or Special

A-1



DNA EM-1  
PART I  
CHANGE 1  
1 JULY 1978

DEFENSE NUCLEAR AGENCY EFFECTS MANUAL NUMBER 1

# CAPABILITIES OF NUCLEAR WEAPONS

## PART I PHENOMENOLOGY

HEADQUARTERS  
Defense Nuclear Agency  
Washington, D.C. 20305

EDITOR  
PHILIP J. DOLAN  
SRI INTERNATIONAL

DNA EM-1  
PART I  
CHANGE 2  
1 AUGUST 1981

DEFENSE NUCLEAR AGENCY EFFECTS MANUAL NUMBER 1

# CAPABILITIES OF NUCLEAR WEAPONS

PART I  
PHENOMENOLOGY

HEADQUARTERS  
Defense Nuclear Agency  
Washington, D.C. 20305

EDITOR  
PHILIP J. DOLAN  
SRI INTERNATIONAL

[REDACTED]

DNA EM-1

HEADQUARTERS  
DEFENSE NUCLEAR AGENCY  
WASHINGTON, D.C. 20305

1 July 1972

EFFECTS MANUAL NUMBER 1  
CAPABILITIES OF NUCLEAR WEAPONS

The Revised Edition January 1968, *Capabilities of Nuclear Weapons*, [REDACTED] DASA EM-1 is hereby superseded and canceled.

With the concurrence of the Military Services, this document was redesignated DASA Effects Manual Number 1 (DASA EM-1) by action of the Joint Chiefs of Staff on 8 July 1966. With the change of the Defense Atomic Support Agency to the Defense Nuclear Agency on 1 July 1971, this document was redesignated the DNA Effects Manual Number 1 (DNA EM-1). Publication and initial distribution of future changes and revisions of this document will be effected by the Defense Nuclear Agency.

FOR THE DIRECTOR:



JOHN A. NORTHROP  
Deputy Director (Science & Technology)

## FOREWORD

This edition of the *Capabilities of Nuclear Weapons* represents the continuing efforts by the Defense Nuclear Agency to correlate and make available nuclear weapons effects information obtained from nuclear weapons testing, small-scale experiments, laboratory effort and theoretical analysis. This document presents the phenomena and effects of a nuclear detonation and relates weapons effects manifestations in terms of damage to targets of military interest. It provides the source material and references needed for the preparation of operational and employment manuals by the Military Services.

The *Capabilities of Nuclear Weapons* is not intended to be used as an employment or design manual by itself, since more complete descriptions of phenomenological details should be obtained from the noted references. Every effort has been made to include the most current reliable data available on 31 December 1971 in order to assist the Armed Forces in meeting their particular requirements for operational and target analysis purposes.

Comments concerning this manual are invited and should be addressed:

Director  
Defense Nuclear Agency  
ATTN: STAP  
Washington, D. C. 20305



C. H. DUNN  
Lt General, USA  
Director

AD-A955 385

DTIC TRUE COPY

(2)

DNA EM-1  
PART II

DEFENSE NUCLEAR AGENCY EFFECTS MANUAL NUMBER 1

# CAPABILITIES OF NUCLEAR WEAPONS

1 JULY 1972

Document released under the  
Freedom of Information Act  
DNA Case No. 86-143



HEADQUARTERS  
Defense Nuclear Agency  
Washington, D.C. 20305

DTIC  
ELECTED  
S E D  
2 MAR 1989

This document has been approved  
for public release and sale by  
the Defense Nuclear Agency.

89 3 02 026

DNA EM-1  
PART II  
1 JULY 1972

DEFENSE NUCLEAR AGENCY EFFECTS MANUAL NUMBER 1

# CAPABILITIES OF NUCLEAR WEAPONS

## PART II DAMAGE CRITERIA

HEADQUARTERS  
Defense Nuclear Agency  
Washington, D.C. 20305

EDITOR  
PHILIP J. DOLAN  
STANFORD RESEARCH INSTITUTE



UNANNOUNCED

Accession For	
NTIS GRA&I <input checked="" type="checkbox"/>	
DTIC TAB <input type="checkbox"/>	
Unannounced <input type="checkbox"/>	
Justification <i>PLA</i>	
By _____	
Distribution/ _____	
Availability Codes	
Dist	Avail and/or Special
A-1	

DNA EM-1  
PART II  
CHANGE 1  
1 JULY 1978

DEFENSE NUCLEAR AGENCY EFFECTS MANUAL NUMBER 1

# CAPABILITIES OF NUCLEAR WEAPONS

PART II  
DAMAGE CRITERIA

HEADQUARTERS  
Defense Nuclear Agency  
Washington, D.C. 20305

EDITOR  
PHILIP J. DOLAN  
SRI INTERNATIONAL

---

---

## TABLE OF CONTENTS

### PART I PHENOMENOLOGY

#### CHAPTER 1 INTRODUCTION

	<i>Page</i>
PURPOSE .....	1-1
CHARACTERISTICS OF NUCLEAR EXPLOSIONS .....	1-1
AIR BURST .....	1-7
THE SURFACE BURST .....	1-12
THE TRANSITION ZONE BETWEEN AN AIR BURST AND A SURFACE BURST .....	1-14
THE HIGH-ALTITUDE BURST .....	1-15
THE UNDERGROUND BURST .....	1-20
THE UNDERWATER BURST .....	1-23

#### CHAPTER 2 BLAST AND SHOCK PHENOMENA

INTRODUCTION .....	2-1
SECTION I AIR BLAST PHENOMENA .....	2-1
RELIABILITY .....	2-2
BLAST-WAVE CALCULATIONS IN FREE AIR .....	2-4
RELATIONS BETWEEN SHOCK FRONT PARAMETERS .....	2-21
BLAST-WAVE PHENOMENA AT THE SURFACE .....	2-38
BLAST-WAVE CALCULATIONS AT THE SURFACE .....	2-45
THE BLAST WAVE AT HIGH ALTITUDES .....	2-125
WEAPONS WITH ENHANCED OUTPUTS .....	2-138
SECTION II CRATERING PHENOMENA .....	2-147
PREDICTION OF CRATER DIMENSIONS .....	2-152
EJECTA .....	2-168
CHARGE STEMMING .....	2-173
EFFECTS OF GEOLOGICAL FACTORS .....	2-174
MULTIPLE BURST GEOMETRIES .....	2-174
SECTION III GROUND SHOCK PHENOMENA .....	2-176

## TABLE OF CONTENTS (Continued)

### CHAPTER 2 BLAST AND SHOCK PHENOMENA [REDACTED] (Continued)

	<i>Page</i>
SECTION IV UNDERWATER EXPLOSION PHENOMENA .....	2-193
WATER SHOCK WAVE AND OTHER PRESSURE PULSES .....	2-197
SURFACE EFFECTS OTHER THAN WAVES .....	2-203
WATER SURFACE WAVES .....	2-216
UNDERWATER CRATERING .....	2-223

### CHAPTER 3 THERMAL RADIATION PHENOMENA [REDACTED]

RADIANT EXPOSURE .....	3-1
TRANSMITTANCE .....	3-5
APPROXIMATE CALCULATIONS OF RADIANT EXPOSURE .....	3-37
SURFACE AND SUBSURFACE BURSTS .....	3-42
THE THERMAL PULSE .....	3-46
FIREBALL BRIGHTNESS .....	3-55
THE THERMAL PULSE FROM SPECIAL WEAPONS .....	3-56
HIGH ALTITUDE THERMAL PHENOMENA .....	3-63
RELIABILITY OF THERMAL SOURCE DATA .....	3-72
RELATION OF RADIANT EXPOSURE TO PEAK OVERPRESSURE .....	3-74
PHYSICS OF FIREBALL DEVELOPMENT .....	3-104

### CHAPTER 4 X-RAY RADIATION PHENOMENA [REDACTED]

INTRODUCTION .....	4-1
SECTION I NUCLEAR WEAPONS AS X-RAY SOURCES .....	4-9
SECTION II X-RAY ENVIRONMENTS PRODUCED BY NUCLEAR WEAPONS ..	4-25

### CHAPTER 5 NUCLEAR RADIATION PHENOMENA [REDACTED]

INTRODUCTION .....	5-1
SECTION I INITIAL NUCLEAR RADIATION .....	5-1

## **TABLE OF CONTENTS (Continued)**

<b>CHAPTER 5 NUCLEAR RADIATION PHENOMENA</b>	<b>(Continued)</b>	<i>Page</i>
NEUTRONS .....		5-2
GAMMA RAYS .....		5-17
INITIAL RADIATION DOSE TO PERSONNEL .....		5-24
SECTION II NEUTRON-INDUCED ACTIVITY IN SOILS .....		5-52
SECTION III RESIDUAL RADIATION .....		5-65
FALLOUT .....		5-65
RESIDUAL RADIATION FROM WATER SURFACE AND UNDERWATER BURSTS .....		5-104
DOSE RECEIVED WHILE FLYING THROUGH A NUCLEAR CLOUD .....		5-139
PRECIPITATION EFFECTS .....		5-145
<b>CHAPTER 6 TRANSIENT RADIATION EFFECTS ON ELECTRONICS (TREE) PHENOMENA</b>		
INTRODUCTION .....		6-1
ENVIRONMENT .....		6-3
INTERACTIONS BASIC TO TREE .....		6-6
MANIFESTATIONS OF TREE IN MATERIALS .....		6-10
<b>CHAPTER 7 ELECTROMAGNETIC PULSE (EMP) PHENOMENA</b>		
ENVIRONMENT - GENERAL DESCRIPTION .....		7-1
ELECTROMAGNETIC FIELD GENERATION .....		7-5
INTERNAL EMP .....		7-15
COMPUTER CODE DESCRIPTIONS .....		7-17
SYSTEMS EFFECTS .....		7-18
<b>CHAPTER 8 PHENOMENA AFFECTING ELECTROMAGNETIC WAVE PROPAGATION</b>		
INTRODUCTION .....		8-1

## TABLE OF CONTENTS (Continued)

CHAPTER 8 PHENOMENA AFFECTING ELECTROMAGNETIC WAVE PROPAGATION		(Continued)	Page
SECTION I	PHENOMENA AFFECTING RADIO FREQUENCIES .....		8-2
	IONIZATION AND DEIONIZATION .....		8-2
	TRAVELING DISTURBANCES IN E AND F REGIONS OF IONOSPHERE .....		8-15
	ELECTROMAGNETIC RADIATIONS.....		8-16
	ABSORPTION .....		8-16
	PHASE CHANGES .....		8-20
SECTION II	METHODS FOR CALCULATING ABSORPTION OF RADIO FREQUENCIES .....		8-23

## PART II DAMAGE CRITERIA

### CHAPTER 9 INTRODUCTION TO DAMAGE CRITERIA

SECTION I	CONTENT AND LIMITATIONS OF PART II .....	9-1
9-1	Introduction to Chapter 9 .....	9-1
9-2	Organization of Part II .....	9-1
9-3	Limitations in Part II .....	9-2
SECTION II	BLAST AND SHOCK DAMAGE .....	9-2
LOADING .....		9-3
9-4	Air Blast Loading in the Mach Reflection Region .....	9-3
9-5	Qualitative Examples of Net Loading .....	9-4
9-6	Regular and Mach Reflection .....	9-10
9-7	Target Motion .....	9-10
9-8	Nonideal Waveforms .....	9-10
9-9	Underwater Shock Wave Loading .....	9-10
9-10	Ground Shock Loading .....	9-11
RESPONSE AND DAMAGE .....		9-11
9-11	Surface Structures .....	9-11
9-12	Shielded Structures .....	9-13
9-13	Aircraft .....	9-13
SECTION III	THERMAL RADIATION DAMAGE .....	9-13
INTRODUCTION .....		9-13
9-14	Radiant Exposure .....	9-14
9-15	Thermal Pulse Duration .....	9-14

## TABLE OF CONTENTS (Continued)

CHAPTER 9 INTRODUCTION TO DAMAGE CRITERIA	(Continued)	Page
9-16 Target Response .....		9-14
9-17 Target Orientation .....		9-15
9-18 Shielding .....		9-15
<b>THERMAL RESPONSE OF MATERIALS</b> .....		9-15
9-19 Thickness Effects .....		9-16
9-20 Color .....		9-22
9-21 Transparency .....		9-23
9-22 Effect of Humidity .....		9-23
9-23 Response of Metal Sheets .....		9-25
9-24 Thermal Damage to Various Materials .....		9-25
<b>SURVIVAL IN FIRE AREAS</b> .....		9-28
9-25 Causes of Death .....		9-28
9-26 Shelters .....		9-29
9-27 Escape from the Fire Areas .....		9-30
9-28 Safe Areas Within the Fire .....		9-31
<b>SECTION IV THERMAL RADIATION DEGRADATION OF STRUCTURAL RESISTANCE TO AIR BLAST</b> .....		9-31
<b>THERMAL ENERGY ABSORBED</b> .....		9-32
9-29 Absorption .....		9-32
9-30 Energy Losses .....		9-35
<b>CHANGES IN MATERIAL STATE AND MATERIALS PROPERTIES</b> .....		9-38
9-31 Changes in Material State .....		9-38
9-32 Change in Materials Properties .....		9-46
<b>RESISTANCE TO LOAD</b> .....		9-63
<b>SECTION V X-RAY DAMAGE EFFECTS</b> .....		9-67
<b>INTRODUCTION</b> .....		9-67
<b>X-RAY ENERGY DEPOSITION CALCULATIONS</b> .....		9-68
9-33 X-ray Cross Sections .....		9-68
9-34 X-ray Energy Deposition and Shine Through Fluences .....		9-69
9-35 X-ray Energy Deposition Summary .....		9-93
<b>INITIAL PRESSURIZATION OF MATERIALS DUE TO X-RAY DEPOSITION</b> .....		9-93
9-36 Phase Changes Induced by X-ray Heating .....		9-93
9-37 The Gruneisen Parameter and the Equation of State .....		9-101
<b>SHOCK WAVE PROPAGATION AND DAMAGE PREDICTIONS</b> .....		9-103
9-38 Through-the-Thickness Elastic-Plastic Shock Propagation .....		9-105

## TABLE OF CONTENTS (Continued)

CHAPTER 9 INTRODUCTION TO DAMAGE CRITERIA	(Continued)	Page
9-39 Through-the-Thickness Material Response .....		9-107
<b>IMPULSE AND STRUCTURAL RESPONSE ANALYSIS</b> .....		9-107
9-40 Impulse Calculations .....		9-107
9-41 Structural Response Analysis .....		9-115
<b>REENTRY VEHICLE HARDENING</b> .....		9-115
9-42 Balanced Hardening with Respect to Neutrons and X-rays .....		9-116
9-43 X-ray Hardening Concepts .....		9-116
<b>SECTION VI NUCLEAR RADIATION SHIELDING</b> .....		9-118
<b>SECTION VII TREE - COMPONENT PART AND CIRCUIT RESPONSE</b> .....		9-121
<b>SEMICONDUCTOR COMPONENT PARTS</b> .....		9-122
9-44 Transient Effects .....		9-122
9-45 Permanent Effects .....		9-132
9-46 Heating and Thermomechanical Damage .....		9-140
<b>OTHER ELECTRONIC COMPONENT PARTS</b> .....		9-147
9-47 Electron Tubes .....		9-147
9-48 Capacitors .....		9-149
9-49 Resistors .....		9-151
9-50 Batteries and Cables .....		9-151
9-51 Quartz Crystals .....		9-153
9-52 Solder Joints .....		9-154
9-53 Infrared Detectors .....		9-154
<b>ELECTRONIC CIRCUITS</b> .....		9-155
9-54 Radiation Response of Discrete-Component-Part Circuits .....		9-155
9-55 Radiation Response of Integrated Circuits .....		9-158
<b>SECTION VIII ELECTROMAGNETIC PULSE (EMP) DAMAGE MECHANISMS</b> .....		9-170
<b>ENERGY COUPLING</b> .....		9-170
9-56 Basic Coupling Modes .....		9-170
9-57 Resonant Configurations .....		9-171
<b>COMPONENT DAMAGE</b> .....		9-172
9-58 Types of Damage .....		9-172
9-59 Damage Levels .....		9-173
<b>EMP HARDENING</b> .....		9-175
9-60 System Analysis .....		9-175
9-61 Recommended Practices .....		9-176
<b>TESTING</b> .....		9-178

## TABLE OF CONTENTS (Continued)

CHAPTER 9 INTRODUCTION TO DAMAGE CRITERIA	(Continued)	Page
9-62 Importance of Testing .....		9-178
9-63 Simulation Facilities .....		9-179
BIBLIOGRAPHY .....		9-183
CHAPTER 10 PERSONNEL CASUALTIES		
INTRODUCTION .....		10-1
SECTION I AIR BLAST .....		10-1
MECHANISMS AND CRITERIA FOR INJURY .....		10-1
10-1 Direct Overpressure Effects .....		10-1
10-2 Translational Forces and Impact .....		10-2
10-3 Blast-Energized Debris .....		10-3
10-4 Miscellaneous Effects .....		10-3
CASUALTY PREDICTION .....		10-4
10-5 Personnel in the Open .....		10-4
10-6 Personnel in a Forest .....		10-4
10-7 Personnel in Structures .....		10-5
10-8 Personnel in Vehicles .....		10-5
SECTION II THERMAL RADIATION .....		10-10
SKIN BURNS .....		10-10
CLASSIFICATION OF BURNS .....		10-10
10-9 First Degree Burns .....		10-10
10-10 Second Degree Burns .....		10-10
10-11 Third Degree Burns .....		10-10
10-12 Reduction in Effectiveness by Burns .....		10-11
BURN INJURY ENERGIES AND RANGES .....		10-11
10-13 Personnel Parameters .....		10-11
10-14 Burn Exposures for Unprotected Skin .....		10-12
10-15 Burns Under Clothing .....		10-12
10-16 Body Areas Involved .....		10-12
10-17 Incapacitation from Burns .....		10-15
10-18 Modification of Injury .....		10-15
EFFECTS OF THERMAL RADIATION ON THE EYES .....		10-15
10-19 Flashblindness .....		10-15
10-20 Retinal Burns .....		10-15

## TABLE OF CONTENTS (Continued)

CHAPTER 10 PERSONNEL CASUALTIES		(Continued)	
			Page
10-21	Modification of Thermal Effects on the Eye .....		10-17
10-22	Safe Separation Distance Curves .....		10-17
SECTION III NUCLEAR RADIATION .....			10-23
	INITIAL RADIATION .....		10-23
10-23	Radiation Sickness .....		10-23
10-24	Incapacitation .....		10-24
10-25	Modification of Injury .....		10-25
10-26	Military Assumptions .....		10-25
	RESIDUAL RADIATION .....		10-25
10-27	External Hazards .....		10-25
10-28	Internal Hazards .....		10-31
10-29	Modification of Injury .....		10-31
SECTION IV COMBINED INJURY .....			10-31
10-30	Radiation and Thermal Injuries .....		10-32
10-31	Mechanical and Radiation Injuries .....		10-33
10-32	Thermal and Mechanical Injuries .....		10-33
	CASUALTY CRITERIA .....		10-33
	PERSONNEL IN THE OPEN .....		10-33
	PERSONNEL IN STRUCTURES .....		10-35
	TREATMENT .....		10-35
	BIBLIOGRAPHY .....		10-36

## CHAPTER 11 DAMAGE TO STRUCTURES

INTRODUCTION .....	11-1
SECTION I DAMAGE TO ABOVEGROUND STRUCTURES .....	11-1
AIR BLAST EFFECTS .....	11-2
11-1 Nature of Loading .....	11-2
11-2 Nature of Damage .....	11-3
11-3 Structural Characteristics .....	11-3
11-4 Isodamage Curves .....	11-9

## TABLE OF CONTENTS (Continued)

CHAPTER 11 DAMAGE TO STRUCTURES	(Continued)	Page
11-5 Shallow Underground Bursts .....	11-12	
11-6 Ground Shock and Cratering .....	11-12	
<b>SECTION II DAMAGE TO BELOWGROUND STRUCTURES .....</b>		<b>11-40</b>
<b>STRUCTURES BURIED IN SOIL .....</b>		<b>11-40</b>
11-7 Definition of Burial Conditions .....	11-40	
11-8 Deeply Buried Structures .....	11-41	
11-9 Structures Buried at Shallow Depths .....	11-48	
11-10 Intermediate Depths of Burial .....	11-49	
<b>LINED AND UNLINED OPENINGS IN ROCK .....</b>		<b>11-49</b>
11-11 Definition of Damage to Openings in Rock .....	11-50	
11-12 Types of Tunnel Linings .....	11-51	
11-13 Procedures for Tunnel Vulnerability Evaluation .....	11-52	
11-14 Vulnerability Evaluation of Surface Silos in Rock .....	11-55	
<b>SECTION III SHOCK VULNERABILITY OF EQUIPMENT AND PERSONNEL .....</b>		<b>11-97</b>
11-15 Shock Mounting .....	11-97	
11-16 Nature of Elastic Systems Comprised of Mounted Equipment .....	11-99	
11-17 Design of Mounted Equipment to Resist Shock .....	11-99	
11-18 Vulnerability Analysis .....	11-100	
<b>SECTION IV DAMS AND HARBOR INSTALLATIONS .....</b>		<b>11-109</b>
<b>AIR BLAST .....</b>		<b>11-109</b>
11-19 Concrete Gravity Dams .....	11-109	
11-20 Harbor Installations .....	11-109	
<b>WATER SHOCK .....</b>		<b>11-109</b>
11-21 Concrete Dams and Water Locks .....	11-109	
<b>CRATERING .....</b>		<b>11-109</b>
11-22 Cratering Earth Dams and Causeways .....	11-109	
<b>WATER WAVES .....</b>		<b>11-110</b>
11-23 Impact and Hydrostatic Pressure .....	11-110	
11-24 Drag Forces .....	11-110	
11-25 Inundation .....	11-110	
<b>THERMAL-RADIATION DAMAGE .....</b>		<b>11-110</b>
<b>SECTION V PETROLEUM, OIL, AND LUBRICANT (POL) STORAGE TANKS .....</b>		<b>11-110</b>
11-26 Damage Criteria .....	11-110	
11-27 Loading and Response .....	11-111	
11-28 Damage .....	11-111	

## TABLE OF CONTENTS (Continued)

CHAPTER 11 DAMAGE TO STRUCTURES	(Continued)	Page
SECTION VI FIELD FORTIFICATIONS .....		11-118
11-29 Air Blast Damage .....		11-118
11-30 Protection of Fortifications from Air Blast Damage .....		11-118
11-31 Thermal Radiation Damage .....		11-121
SECTION VII FIRE IN URBAN AREAS .....		11-127
INTRODUCTION .....		11-127
EVOLUTION OF MASS FIRES .....		11-127
11-32 Ignition Points .....		11-127
11-33 Room Flashover .....		11-128
11-34 Active Burning of a Structure .....		11-128
11-35 Fire Spread Between Structures .....		11-128
11-36 Mass Fires .....		11-129
ESTIMATION AND CONTROL OF THERMAL DAMAGE .....		11-130
11-37 Radiant Exposure Thresholds .....		11-130
11-38 Fire Radii .....		11-134
11-39 The San Jose Study .....		11-134
11-40 The New Orleans Study .....		11-136
11-41 Effects of Clouds .....		11-138
11-42 Firestorm Criteria .....		11-143
11-43 Conflagrations .....		11-144
11-44 Fire Control .....		11-144
BIBLIOGRAPHY .....		11-146

## CHAPTER 12 MECHANICAL DAMAGE DISTANCES FOR SURFACE SHIPS AND SUBMARINES SUBJECTED TO NUCLEAR EXPLOSIONS

INTRODUCTION .....	12-1
12-1 Damage Mechanisms .....	12-1
12-2 Damage Classification .....	12-1
12-3 Seaworthiness Impairment .....	12-1
12-4 Mobility Impairment .....	12-2
12-5 Weapon Delivery Impairment .....	12-2
SECTION I DAMAGE TO SURFACE SHIPS FROM AIR BURSTS .....	12-2
BLAST DAMAGE .....	12-2
12-6 General .....	12-2

## TABLE OF CONTENTS (Continued)

CHAPTER 12 MECHANICAL DAMAGE DISTANCES FOR SURFACE SHIPS AND SUBMARINES SUBJECTED TO NUCLEAR EXPLOSIONS		(Continued)	Page
12-7	Damage Criteria .....		12-3
12-8	Damage Distances .....		12-3
12-9	Capsizing from Blast .....		12-6
DAMAGE FROM OTHER AIR BURST PHENOMENA .....			12-6
12-10	Thermal Radiation .....		12-6
12-11	Damage from Nuclear Radiation and Electromagnetic Pulse .....		12-8
12-12	(Omitted)		
SECTION II SURFACE SHIP DAMAGE FROM UNDERWATER BURSTS .....			12-8
DAMAGE FROM THE SHOCK WAVE IN THE WATER .....			12-8
12-13	Damage Criteria .....		12-8
12-14	Damage Distances .....		12-9
12-15	Effect of Ocean Environment on Damage Ranges .....		12-9
DAMAGE FROM OTHER UNDERWATER BURST PHENOMENA .....			12-17
SECTION III SUBMARINE DAMAGE FROM UNDERWATER BURSTS .....			12-17
DAMAGE FROM THE SHOCK WAVE IN THE WATER .....			12-17
12-16	Damage Criteria .....		12-17
12-17	Damage Distances .....		12-18
12-18	Effect of Ocean Environment on Damage Ranges .....		12-18
DAMAGE FROM OTHER UNDERWATER BURST PHENOMENA .....			12-19
BIBLIOGRAPHY .....			12-30

## CHAPTER 13 DAMAGE TO AIRCRAFT

INTRODUCTION .....		13-1
SECTION I BLAST AND THERMAL EFFECTS ON AIRCRAFT .....		13-1
13-1	Sure-Safe and Sure-Kill Envelopes .....	13-2
NUCLEAR WEAPON EFFECTS ANALYSIS .....		13-4
13-2	Gust Effects .....	13-4
13-3	Overpressure Effects .....	13-7
13-4	Thermal Radiation Effects .....	13-7
13-5	Combined Effects .....	13-9
SECTION II AIRCRAFT RESPONSE TO BLAST AND THERMAL EFFECTS .....		13-10
AIRCRAFT RESPONSE TO GUST EFFECTS .....		13-10
13-6	Aerodynamic Coefficients for Aircraft .....	13-10

## TABLE OF CONTENTS (Continued)

### CHAPTER 13 DAMAGE TO AIRCRAFT (Continued)

	<i>Page</i>
13-7 Gust Effects on In-Flight Aircraft .....	13-27
13-8 Gust Effects on Parked Aircraft .....	13-27
AIRCRAFT RESPONSE TO OVERPRESSURE EFFECTS .....	13-50
13-9 Overpressure Effects on In-Flight and Parked Aircraft .....	13-50
AIRCRAFT RESPONSE TO THERMAL RADIATION EFFECTS .....	13-59
13-10 Thermal Effects on In-Flight and Parked Aircraft .....	13-59
BURST-TIME ENVELOPES .....	13-67
13-11 Requirement for Burst-Time Envelopes .....	13-67
BIBLIOGRAPHY .....	13-86

### CHAPTER 14 DAMAGE TO MILITARY FIELD EQUIPMENT

INTRODUCTION .....	14-1
SECTION I AIR BLAST DAMAGE .....	14-1
14-1 Damage Mechanisms .....	14-1
14-2 Air Blast Environment .....	14-2
14-3 Target Characteristics .....	14-4
14-4 Target Exposure .....	14-6
14-5 Effects of Ground Surface Conditions .....	14-12
14-6 Vehicle Status .....	14-14
SECTION II DAMAGE PREDICTIONS .....	14-17
14-7 Definitions of Damage Categories .....	14-17
14-8 Prediction Techniques .....	14-18
14-9 Untested Equipment .....	14-52
SECTION III DAMAGE FROM CAUSES OTHER THAN BLAST AND NUCLEAR RADIATION .....	14-57
14-10 Fire Damage .....	14-57
14-11 Obscuration of Optical Devices .....	14-58
14-12 Damage by Missiles .....	14-58
14-13 The Effects of Time .....	14-59
SECTION IV TREE DAMAGE CRITERIA .....	14-59
SYSTEMS ANALYSIS .....	14-60
14-14 Types of Systems Analysis Used in TREE .....	14-60

## TABLE OF CONTENTS (Continued)

CHAPTER 14 DAMAGE TO MILITARY FIELD EQUIPMENT	(Continued)	Page
14-15 The Complexity of Performing System Analysis for TREE .....	14-60	
14-16 Characteristics of the Analysis Used in This Section .....	14-61	
REVIEW OF ELECTRONIC SUSCEPTIBILITY TO NUCLEAR RADIATION .....	14-62	
14-17 Component Part Vulnerability .....	14-62	
14-18 Subsystem Vulnerability .....	14-64	
TREE-DAMAGE ESTIMATES .....	14-64	
14-19 Ground Equipment .....	14-65	
14-20 An Example of Ground Equipment Survivability Estimation .....	14-65	
14-21 Aircraft Systems .....	14-67	
14-22 An Example of Aircraft Survivability Estimation .....	14-67	
14-23 Missile Systems .....	14-70	
BIBLIOGRAPHY .....	14-72	

## CHAPTER 15 DAMAGE TO FOREST STANDS

INTRODUCTION .....	15-1
SECTION I AIR BLAST .....	15-1
15-1 Forest Stand Types .....	15-1
15-2 Damage-Distance Relations .....	15-3
SECTION II TROOP AND VEHICLE MOVEMENT .....	15-41
15-3 Blowdown Debris Characteristics .....	15-42
15-4 Vehicle Movement .....	15-44
15-5 Troop Movement .....	15-46
15-6 Predicting Effects on Movement .....	15-49
SECTION III THERMAL RADIATION .....	15-52
15-7 Ignitions .....	15-52
15-8 Kindling Fuels .....	15-52
15-9 Thermal Radiation on Forests .....	15-56
15-10 Forest Fire Ignition and Spread .....	15-58
BIBLIOGRAPHY .....	15-64

## CHAPTER 16 DAMAGE TO MISSILES

SECTION I BLAST DAMAGE TO TACTICAL MISSILE SYSTEMS .....	16-1
--	------

## TABLE OF CONTENTS (Continued)

### CHAPTER 16 DAMAGE TO MISSILES (Continued)

*Page*

SERGEANT WEAPON SYSTEM .....	16-3
16-1 Description of the SERGEANT Weapon System .....	16-3
16-2 Vulnerability Levels of the SERGEANT Missile System .....	16-7
16-3 Reliability of SERGEANT Vulnerability Estimates .....	16-10
LANCE WEAPON SYSTEM .....	16-12
16-4 Description of the LANCE Weapon System .....	16-12
16-5 Vulnerability Levels for the LANCE Missile System .....	16-12
16-6 Reliability of LANCE Vulnerability Estimates .....	16-17
HAWK WEAPON SYSTEM .....	16-19
16-7 Description of the HAWK Weapon System .....	16-19
16-8 Vulnerability Levels for the HAWK Missile System .....	16-23
16-9 Reliability of HAWK Vulnerability Estimates .....	16-24
SAMPLE PROBLEM: AIR BLAST DAMAGE TO A TACTICAL MISSILE SYSTEM .....	16-26
16-10 Description of the HONEST JOHN System .....	16-26
16-11 Vulnerability Levels for HONEST JOHN Missile System .....	16-31
SECTION II BLAST AND THERMAL VULNERABILITY OF IN-FLIGHT STRATEGIC SYSTEMS .....	16-34
INTRODUCTION .....	16-34
16-12 Sources of Data .....	16-38
16-13 Limitations in Application of the Data .....	16-38
BLAST LOADING ON REENTRY (RV) SYSTEMS .....	16-39
16-14 Environment Scaling .....	16-39
16-15 General Intercept Loads and Load Duration .....	16-47
16-16 Intercept Load Duration .....	16-51
16-17 Fireball Traversal Time .....	16-51
16-18 Total Traversal Time .....	16-52
16-19 Exit Loads .....	16-57
16-20 Blast Data Generalization .....	16-57
16-21 Typical RV Aerodynamics .....	16-57
16-22 Initial Interaction of Vehicle Flow-Field and Blast Wave (Shock-Shock) ..	16-58
16-23 Damage Envelopes .....	16-58
RESULTS OF SOME RV BLAST AND THERMAL LOAD AND VULNERABILITY CALCULATIONS .....	16-66
16-24 Blast Loads on the RV .....	16-66
16-25 Thermal Radiation Loads on the RV .....	16-70

## TABLE OF CONTENTS (Continued)

CHAPTER 16 DAMAGE TO MISSILES [REDACTED] (Continued)		Page
16-26	Description of a Blast/Thermal Vulnerability Determination .....	16-75
16-27	Results of the RV Vulnerability Determination .....	16-77
16-28	Summary and Conclusions Concerning RV Vulnerability Calculations .....	16-81
ANTIMISSILE (ABM) SYSTEMS .....		16-81
16-29	Shell Breathing Response .....	16-86
16-30	Vehicle Bending Response .....	16-87
16-31	Thermal Radiation Effects .....	16-87
16-32	ABM Blast/Thermal Vulnerability Envelopes .....	16-90
16-33	Conclusions .....	16-91
BLAST AND THERMAL LETHALITY .....		16-96
16-34	Blast and Thermal Free Field Environments .....	16-96
16-35	ABM Blast Loads on Threat Vehicles (Point Mass) .....	16-96
16-36	Blast Loads on the RV Threat Vehicle .....	16-101
16-37	ABM Blast Kill Radii .....	16-106
16-38	Fireball Thermal Effects on Threat RV's .....	16-109
BIBLIOGRAPHY .....		16-116
CHAPTER 17 RADIO FREQUENCY SIGNAL DEGRADATION RELEVANT TO COMMUNICATIONS AND RADAR SYSTEMS [REDACTED]		
INTRODUCTION .....		17-1
SECTION I DEGRADATION MECHANISMS .....		17-2
ATTENUATION .....		17-2
17-1	Fireball Absorption .....	17-2
17-2	Absorption in the Region Around the Fireball .....	17-2
17-3	D-Region Absorption .....	17-4
17-4	Absorption of Noise .....	17-4
17-5	Attenuation by Scattering and Beam Spreading .....	17-4
17-6	Effects of Reflection .....	17-6
INTERFERENCE .....		17-6
17-7	Noise .....	17-6
17-8	Reflection, Refraction, and Scatter .....	17-6
SIGNAL DISTORTION .....		17-6
SECTION II SYSTEM CHARACTERISTICS AND EFFECTS .....		17-7
VLF AND LF SYSTEMS .....		17-7

## TABLE OF CONTENTS (Continued)

### CHAPTER 17 RADIO FREQUENCY SIGNAL DEGRADATION RELEVANT TO COMMUNICATIONS AND RADAR SYSTEMS [REDACTED] (Continued)

	<i>Page</i>
17-9 VLF and LF Propagation .....	17-7
17-10 Effects of Nuclear Bursts on VLF and LF Systems .....	17-7
17-11 Spread-Debris Environment .....	17-9
17-12 Effect of a [REDACTED] 6300-km Burst .....	17-9
17-13 Effect of Detonations Below About 300 km .....	17-13
<b>HF SYSTEMS .....</b>	<b>17-13</b>
17-14 HF Propagation .....	17-13
17-15 Effect of Nuclear Bursts on HF Systems .....	17-13
17-16 Effect of Surface or Near-Surface Bursts .....	17-16
17-17 Effect of a [REDACTED] 30-km Burst .....	17-16
17-18 Effects of a [REDACTED] 50-km Burst .....	17-17
17-19 Effect of Multiple Multimegaton 150-km Bursts .....	17-17
17-20 Effect of a 1-Mt, 250-km Burst .....	17-18
17-21 Effect of a [REDACTED] 1000-km Burst .....	17-19
<b>SATELLITE COMMUNICATION SYSTEMS .....</b>	<b>17-19</b>
17-22 Effects of Nuclear Bursts on Satellite Systems .....	17-19
17-23 Nuclear Effects on Two Typical Satellite Systems .....	17-20
<b>TROPOSCATTER COMMUNICATION SYSTEMS .....</b>	<b>17-22</b>
17-24 Effects of Nuclear Bursts on Troposcatter Systems .....	17-22
17-25 Nuclear Effects on Three Typical Troposcatter Systems .....	17-26
<b>IONOSCATTER COMMUNICATION SYSTEMS .....</b>	<b>17-26</b>
17-26 Effects of Nuclear Bursts on Ionoscatteer Systems .....	17-27
17-27 Nuclear Effects on Typical Ionoscatteer Systems .....	17-28
<b>RADAR SYSTEMS .....</b>	<b>17-30</b>
17-28 Ballistic Missile Defense Systems .....	17-32
17-29 Nuclear Effects on Area Defense Systems .....	17-32
17-30 Nuclear Effects on Hardsite Defense Systems .....	17-36
<b>BIBLIOGRAPHY .....</b>	<b>17-40</b>

### APPENDIX A SUPPLEMENTARY BLAST DATA [REDACTED]

<b>SECTION I MATHEMATICAL DESCRIPTION OF THE SHOCK FRONT .....</b>	<b>A-1</b>
A-1 The Rankine-Hugoniot Equations .....	A-1
A-2 Equation of State of an Ideal Gas .....	A-3
A-3 Shock Wave Equations for an Ideal Gas .....	A-3
A-4 Units, Constants, and Conversion Factors .....	A-5

## TABLE OF CONTENTS (Continued)

APPENDIX A SUPPLEMENTARY BLAST DATA		(Continued)	Page
A-5	Equation of State of Air .....		A-5
A-6	Equations for Strong Shock Waves in Air .....		A-5
SECTION II	PHYSICAL DESCRIPTION OF SHOCK WAVE BEHAVIOR .....		A-8
A-7	Step Function Shock Wave .....		A-8
A-8	Shock-Front Formation .....		A-9
A-9	Pressure-Momentum Interaction at a Shock Front .....		A-9
A-10	Normal Reflection at a Solid Barrier .....		A-10
A-11	Pressures on Simple Shapes .....		A-12
A-12	The Rankine-Hugoniot Equations (Alternate Analysis) .....		A-14
A-13	Dynamic Pressure .....		A-16
APPENDIX B USEFUL RELATIONSHIPS			
B-1	General Equivalents .....		B-1
B-2	Constants .....		B-1
B-3	Standard Sea Level Atmosphere .....		B-1
B-4	Conversions .....		B-2
B-5	Fractional Power and Dimension Scaling .....		B-4
APPENDIX C PROBABILITY CONSIDERATIONS			
C-1	Protective Design and Weapon Selection .....		C-1
SECTION I	DAMAGE PROBABILITIES .....		C-2
DAMAGE CAUSED BY MOTION INPUT .....			C-2
C-2	Description of Charts for Damage Caused by Motion Input .....		C-2
C-3	Instructions for Motion Input Analyses .....		C-3
C-4	Illustrative Examples for Motion Inputs .....		C-3
DAMAGE CAUSED BY PRESSURE .....			C-7
C-5	Description of Charts for Damage to Surface Structures Caused by Pressure Input .....		C-7
C-6	Description of Charts for Damage to Underground Structures Caused by Pressure Input .....		C-8
C-7	Instructions for Pressure Input Analyses .....		C-8
C-8	Illustrative Examples for Pressure Inputs .....		C-8
C-9	System Consideration .....		C-9
SECTION II	DERIVATION OF EQUATIONS USED IN SECTION I .....		C-14
C-10	Properties of Lognormal Variates .....		C-14
C-11	Probability of Failure or Survival .....		C-14

## **TABLE OF CONTENTS (Continued)**

	<i>Page</i>
<b>APPENDIX D ABSTRACTS OF DNA HANDBOOKS .....</b>	<b>D-1</b>
<b>APPENDIX E GLOSSARY .....</b>	<b>E-1</b>
<b>APPENDIX F LIST OF SYMBOLS .....</b>	<b>F-1</b>

AD-A955 404

Accession For	
NTIS GRA&I	
DTIC TAB	
Unannounced	
Justification <i>None</i>	
By	
Distribution/	
Availability Codes	
Dist	Avail and/or Special
A-1	

DTIC FITF MDV

(2)

PART I  
PHENOMENOLOGY  
Chapter 1  
INTRODUCTION



UNANNOUNCED

PURPOSE

This manual presents a summary of the capabilities of nuclear weapons. Quantitative treatments are presented graphically in most cases. The manual is divided into two parts. Part I, Phenomenology, treats the basic phenomena of blast and shock, thermal radiation, X-ray radiation, nuclear radiation, transient radiation effects on electronics, electromagnetic pulse phenomena, and phenomena affecting electromagnetic propagation. Part II, Damage Criteria, discusses the mechanisms of casualty production and damage to military targets, and describes the response of these targets by correlating the basic physical phenomena with various defined degrees of damage.\*

The data presented here are interpretations of complex results of the nuclear weapons effects research and test programs of the Department of Defense. A constant effort is made to deduce theoretical models and scaling laws for the various weapons effects that permit a quantitative prediction of the extent of a given effect from a weapon of one yield related to weapons of other yields. Since the initiation of the limited nuclear test ban treaty, a large amount of effort has been devoted to the development of complex computer codes to predict the environments created by the various phenomena resulting from nuclear explosions and the interactions of these environments with personnel and military systems. A large number of the scaling laws

presented herein were derived from the results of calculations performed with these codes.

An estimate of the degree of reliability accompanies most of the data presented herein. Statements of the reliability of damage data only pertain to the basic effects data, which, for the target analyst represent the "radius of effect." They should not be confused with the terms variability and probability of damage, which pertain to target response; nor do these estimates include operational considerations such as linear, circular, or spherical aiming and fuzing errors, yield variations, and target intelligence.

CHARACTERISTICS OF NUCLEAR EXPLOSIONS

An explosion, in general, results from the very rapid release of a large amount of energy within a limited space. This is true for a conventional "high explosive," such as TNT, as well as for a nuclear explosion. The sudden liberation of energy causes a considerable increase of temperature and pressure, so that all the materials present are converted into hot compressed gases. Detonation of high explosives results from chemical reactions, and the energy manifests primarily as blast energy, regardless of environmental conditions. For a given amount

The unclassified publication "The Effects of Nuclear Weapons," which contains a more detailed qualitative discussion of these basic phenomena, supplements this manual.

1-1

This document has been approved  
for public release and  
distribution is unlimited.

② DTIC ELECTED  
S 2 MAR 1989 D  
E

89 3 02 028

of energy. the mass of a nuclear explosive would be much less than that of a conventional high explosive. Consequently, there is a much smaller amount of material in the weapon itself to be converted into the hot, compressed gases mentioned above in the former than in the latter case. Also, the temperatures reached in a nuclear explosion are much higher than in a conventional explosion. In a nuclear explosion the energy manifests itself in the form of blast, thermal radiation, nuclear radiation, and other electromagnetic phenomena that will be discussed in succeeding paragraphs. The energy released from a nuclear explosion is released essentially from a point source, whereas a comparable amount of energy released from a detonation of high explosives would require an enormous volume of explosive. Additionally, the energy released in a nuclear explosion results from a fission process, a fusion process, or a combination of the two, each of which involve the formation of different atomic nuclei and the release of large quantities of energy for each reaction. As mentioned previously, the energy derived from the detonation of high explosives arises from chemical reactions; these involve the rearrangement among the atoms, e.g., of hydrogen, carbon, oxygen, and nitrogen present in the high explosive material. The forces between the protons and neutrons within atomic nuclei are tremendously greater than those between atoms; consequently, nuclear energy is of a much higher order of magnitude than conventional (or chemical) energy when equal masses are considered.

### 1-1 Fission Energy and the Chain Reaction

The materials used to produce nuclear explosions by fission are certain isotopes of uranium and plutonium. Natural uranium consists mainly of two isotopes, uranium-235 (about 0.7 percent), and uranium-238 (about 99.3 percent). Uranium-235 is the much less abundant of these isotopes, but is the readily fissionable species

that is commonly used in nuclear weapons. Another isotope, uranium-233, does not occur naturally, but it is readily fissionable and it can be made artificially starting with thorium-232. Since the element plutonium has no natural isotopes, the fissionable isotope used in nuclear weapons, plutonium-239, is made artificially from uranium-238.

When a free (or unattached) neutron enters the nucleus of a fissionable atom, it can cause the nucleus to split into two smaller parts. This is the fission process, which is accompanied by the release of a large amount of energy. The smaller (or lighter) nuclei which result are called the "fission products." The complete fission of 1 pound of uranium or of plutonium releases as much explosive energy as does the explosion of about 8,000 (short) tons of TNT.

The significant point about the fission of a uranium (or plutonium) nucleus by means of a neutron, in addition to the release of a large quantity of energy, is that the process is accompanied by the instantaneous emission of two or more neutrons; thus,



The neutrons liberated in this manner are able to induce fission of additional uranium (or plutonium) nuclei, each such process resulting in the emission of more neutrons which can produce further fission, and so on. Thus, in principle, a single neutron could start off a chain of nuclear fissions, the number of nuclei involved, and the energy liberated, increasing at a tremendous rate.

There are many different ways in which the nuclei of a given fissionable species can split up into two fission fragments, but the total amount of energy liberated per fission does not vary greatly. A satisfactory average value of this energy is 200 million electron volts. The million

electron volt (or 1 MeV) unit has been found convenient for expressing the energy released in nuclear reactions; it is equivalent to  $1.6 \times 10^{-6}$  erg or  $1.6 \times 10^{-13}$  joule. The manner in which this energy is distributed among the fission fragments and the various radiations associated with fission is shown in Table 1-1.

Table 1-1. Distribution of Fission Energy

	MeV
Kinetic energy of fission fragments	$165 \pm 5$
Instantaneous gamma-ray energy	$7 \pm 1$
Kinetic energy of fission neutrons	$5 \pm 0.5$
Beta particles from fission products	$7 \pm 1$
Gamma rays from fission products	$6 \pm 1$
Neutrinos from fission products	<u>10</u>
Total energy per fission	$200 \pm 8.5$

The results in the table may be taken as being applicable to either uranium-233, uranium-235, or plutonium-239. These are the only three known substances, which are reasonably stable so that they can be stored without appreciable decay, that are capable of undergoing fission by neutrons of all energies. Hence, they are the only materials that can be used to sustain a fission chain. Uranium-238, the most abundant isotope in natural uranium, and thorium-232 will suffer fission by neutrons of high energy only, but not by those of lower energy. For this reason these substances cannot sustain a chain reaction. However, when fission does occur in these elements, the energy distribution is quite similar to that shown in the table.

Only part of the fission energy is immediately available in a nuclear explosion; this includes the kinetic energy of the fission frag-

ments, most of the energy of the instantaneous gamma rays, which is converted into other forms of energy within the exploding weapon, and also most of the neutron kinetic energy, but only a small fraction of the decay energy of the fission products. There is some compensation from energy released in reactions in which neutrons are captured by the weapon debris, and so it is usually accepted that about 180 MeV of energy are available per fission. There are  $6.02 \times 10^{23}$  nuclei in 235 grams of uranium-235 (or 239 grams of plutonium-239), and by making use of familiar conversion factors (Appendix B) the results quoted in Table 1-2 may be obtained for the energy (and other) equivalents of 1 kiloton of TNT. The calculations are based on an accepted, although somewhat arbitrary, figure of  $10^{12}$  calories as the energy released in the explosion of this amount of TNT.\*

Table 1-2. Equivalents of 1 Kiloton of TNT

Complete fission of 0.057 kg (57 grams or 2 ounces) fissionable material
Fission of $1.45 \times 10^{23}$ nuclei
$10^{12}$ calories
$2.6 \times 10^{25}$ million electron volts
$4.18 \times 10^{19}$ ergs
$1.16 \times 10^6$ kilowatt-hours
$3.97 \times 10^9$ British thermal units

\* The majority of the experimental and theoretical values of the explosive energy released by TNT range from 900 to 1,100 calories per gram. At one time, there was some uncertainty as to whether the term "kiloton" of TNT referred to a short kiloton ( $2 \times 10^6$  pounds), a metric kiloton ( $2.205 \times 10^6$  pounds), or a long kiloton ( $2.24 \times 10^6$  pounds). In order to avoid ambiguity, it was agreed that the term "kiloton" would refer to the release of  $10^{12}$  calories of explosive energy. This is equivalent to 1 short kiloton of TNT if the energy release is 1,102 calories per gram.

## 1-2 Fusion (Thermonuclear) Reactions

In nuclear fusion, a pair of light nuclei unite (or fuse) together, to form a nucleus of a heavier atom. An example is the fusion of the hydrogen isotope known as deuterium or "heavy hydrogen." Under suitable conditions, two deuterium nuclei may combine to form the nucleus of a heavier element, helium, with the release of energy.

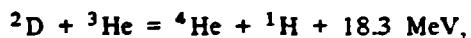
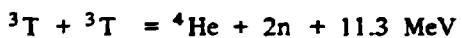
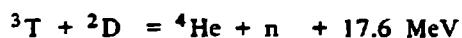
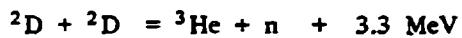
Nuclear fusion reactions can be brought about by means of very high temperatures, and they are then referred to as "thermonuclear processes." The actual quantity of energy liberated, for a given mass of material, depends on the particular isotope (or isotopes) involved in the nuclear fusion reaction. As an example, the fusion of all the nuclei present in 1 pound of the hydrogen isotope deuterium would release roughly the same amount of energy as the explosion of 26,000 tons of TNT.

Energy production in the sun and stars is undoubtedly due to fusion reactions involving the nuclei of various light (low atomic weight) atoms. From experiments made in laboratories with charged-particle accelerators, it was concluded that the fusion of isotopes of hydrogen was possible. This element is known to exist in three isotopic forms, in which the nuclei have mass numbers of 1, 2, and 3, respectively. These are generally referred to as hydrogen ( $^1\text{H}$ ), deuterium ( $^2\text{H}$  or  $^2\text{D}$ ), and tritium ( $^3\text{H}$  or  $^3\text{T}$ ). All the nuclei carry a single positive charge, i.e., they all contain one proton, but they differ in the number of neutrons. The lightest ( $^1\text{H}$ ) nuclei (or protons) contain no neutrons; the deuterium ( $^2\text{H}$ ) nuclei contain one neutron, and tritium ( $^3\text{H}$ ) nuclei contain two neutrons.

Several different fusion reactions have been observed between the nuclei of the three hydrogen isotopes, involving either two similar or two different nuclei. In order to make these reactions occur to an appreciable extent, the nuclei must have high energies. One way in which

this energy can be supplied is by means of an accelerator, such as a cyclotron. Another possibility is to raise the temperature to very high levels. In this last circumstance the fusion processes are referred to as "thermonuclear reactions," as mentioned previously.

Five thermonuclear fusion reactions appear to be of interest for the production of energy because they are expected to occur sufficiently rapidly at realizable temperatures; these are

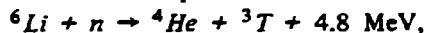


where He is the symbol for helium and n (mass = 1) represents a neutron. The energy liberated in each case is given in million electron volt (MeV) units. The first two of these reactions occur with almost equal probability at the temperatures associated with nuclear explosions (several tens of million degrees Kelvin), whereas the third reaction has a much higher probability and the fourth and fifth a much lower probability. Thus, a valid comparison of the energy released in fusion reactions with that produced in fission can be made by noting that, as a result of the first three reactions given above, five deuterium nuclei, with a total mass of 10 units, will liberate 24.8 MeV upon fusion. On the other hand, in the fission process, e.g., of uranium-235, a mass of 235 units will produce a total of about 200 MeV of energy (paragraph 1-1). Weight for weight, therefore, the fusion of deuterium nuclei would produce nearly three times as much energy as the fission of uranium or plutonium.

In order to make the nuclear fusion reactions take place at an appreciable rate, tempera-

tures of the order of several tens of million degrees are necessary. The only practical way at present in which such temperatures can be obtained on earth is by means of a fission explosion. Consequently, by combining a quantity of deuterium (or a mixture of deuterium and tritium) with a fission device, it should be possible to initiate one or more of the thermonuclear fusion reactions given above. If these reactions accompanied by energy evolution, can be propagated rapidly through a volume of the hydrogen isotope (or isotopes) a thermonuclear explosion may be realized.

Another reaction of interest in thermonuclear weapons is



where  $^6\text{Li}$  is the symbol for the lithium-6 isotope, which makes up about 7.4 percent of natural lithium. Other reactions can occur between both lithium-6 and the more abundant isotope lithium-7 and various particles that are present within the weapon. However, the reaction shown above is of most interest for two reasons: (1) it has a high probability of occurrence; (2) if the lithium is placed in the weapon in the form of lithium-deuteride, the tritium that results from the reaction has a high probability of reacting with the deuterium to produce large amounts of energy as well as additional neutrons (see the third of the previously listed fusion reactions).

As discussed above, several of the fusion processes between nuclei of hydrogen isotopes produce high energy neutrons. These can cause fission in uranium-238, the most abundant isotope in natural uranium, as well as in uranium-235 and plutonium-239. Consequently, association of the appropriate fusion reactions with fissile materials can result in an extensive utilization of the latter for the release of energy.

Fission weapon yield also may be enhanced by a process known as boosting. In this process thermonuclear reactions are used to produce fast neutrons. While some energy gain is realized as a result of the thermonuclear reactions that occur, the primary increase in the yield is due to the additional fissions produced by the interaction of the fast neutrons with the fissionable materials.

### 1-3 Weapon Yield Ratings

The "yield" of a nuclear weapon is a measure of the amount of explosive energy it can produce. It is the usual practice to state the yield in terms of the quantity of TNT that would generate the same amount of energy when it explodes. Thus, a 1-kiloton nuclear weapon is one which produces the same amount of energy in an explosion as does 1 kiloton (or 1,000 tons) of TNT. As discussed in paragraph 1-1, this quantity of energy has been somewhat arbitrarily established at  $10^{12}$  calories (see footnote on page 1-3). Similarly, a 1-megaton weapon would have the energy equivalent of 1 million tons (1,000 kilotons) of TNT, or  $10^{15}$  calories. Since about 10 percent of the total fission energy is released in the form of residual nuclear radiation some time after the detonation (Table 1-1), this is not included when the energy yield of a nuclear explosion is stated, e.g., in terms of a TNT equivalent. Hence, in a pure fission weapon the explosion energy is about 90 percent of the total fission energy. In a thermonuclear device, the explosion energy is less than the total energy by about 10 percent of the fission contribution, e.g., if the total energy is equally divided between the fission and fusion processes, the explosion energy would be about 95 percent of the total energy of the fission and fusion reactions. This common convention will be adhered to in subsequent chapters. For example, when the yield of a nuclear weapon is quoted or used in equations, figures, etc., it will represent that por-

tion of the energy delivered within a minute or so, and will exclude the contribution of the residual nuclear radiation.

[REDACTED] Another method used in comparing nuclear explosion yields with conventional explosives, and one that is often confused with the rating of energy in terms of TNT energy equivalents, is the rating of effects in terms of TNT effect equivalence, i.e., the effect of a particular phenomenon of a nuclear detonation expressed in terms of the amount of TNT that would produce the same effect. An example of TNT effect equivalence is the expression of the crater radius of a nuclear surface burst in terms of the amount of TNT that would be required to produce the same radius.

[REDACTED] A "nominal" weapon is one whose yield is 20 kt. The use of this term arose from the approximately 20-kt yields at Hiroshima, Nagasaki, and the Bikini (Crossroads) tests. In some reports nuclear weapons effects data are based on the nominal weapon.

[REDACTED] For simplicity and convenience, most physical phenomena data and much of the damage data are presented as a function of the range from a 1-kt explosion, from which the phenomena or damage for other yields may be obtained readily, by the appropriate scaling procedures given wherever their use is required.

#### 1-4 Effects of Environment and Time

[REDACTED] The effects of nuclear weapons of a particular design and yield are determined by the environment in which the weapon is burst, and the time frame under consideration. The initial physical phenomena from nuclear detonations are grossly the same during the first microsecond after initiation. Several minutes after detonation, the remaining effects will be only those of residual radiation, e.g., fallout, atmospheric ionization and associated phenomena. Since the density, composition, physical state, and pressure of the medium surrounding the detonation primari-

ly determine the resulting effects after the first microsecond, an early time history of a nuclear detonation is given in the following paragraph. This description is carried to the point when the energy released in the explosion begins to interact with its environment. Succeeding paragraphs provide brief descriptions of the phenomena that occur in different burst regimes. More complete descriptions of each phenomenon are provided in Chapters 2 through 8.

#### 1-5 Early Time History

[REDACTED] When a nuclear weapon is detonated, the actual duration of the process varies considerably, depending on the design of the weapon. It is sufficient, however, to assume that the energy is released during the first microsecond. In this period all prompt nuclear radiation (neutrons, gammas, and X-rays) has been emitted and has departed from the immediate environment of the weapon disintegration, leaving behind the energetic reaction and weapon products. These products are at high temperatures and behave as an efficient thermal radiator (see Sections I and II, Chapter 4). Although reaction products from fission will continue to decay radioactively and will emit additional gamma radiation and beta particles, they are considered as secondary effects in this time frame.

[REDACTED] The high temperature results in tremendous internal pressures. Under the influence of these pressures, the hot debris expands at a very high velocity. Because it is radiating energy rapidly and is being cooled by expansion, the residual weapon debris cools rapidly. Within about the first microsecond for most weapons, 70 to 80 percent of the explosion energy is emitted as thermal energy, most of which consists of X-rays. At the end of this period, most of the remaining weapon energy is kinetic energy. At this time, when all important detonation processes have taken place, the weapon debris has begun to react with its environment.

## AIR BURST

An air burst is defined as the explosion of a nuclear weapon at such a height that the weapon phenomenon of interest is not significantly modified by the earth's surface. (Also see description of high altitude burst in paragraph 1-26 to 1-29.) For example, when considering blast this height is such that the reflected wave passing through the fireball does not overtake the incident wave above the fireball (heights greater than about  $160 W^{0.35}$  ft  $\pm$  15 percent, where  $W$  is the weapon yield in kilotons). For thermal radiation, an air burst occurs at such heights above the surface that the apparent thermal yield viewed from the ground is not affected by surface phenomena, such as heat transfer to the surface, distortion of the fireball by the reflected shock wave, thermal reflection from the surface (heights above the surface greater than about  $180 W^{0.4}$  ft  $\pm$  20 percent for yields of 10 kt to 100 kt, and  $\pm$  30 percent for other yields). When considering fallout, an air burst occurs at such heights that militarily significant local fallout does not result (a minimum height of burst has generally been set at 100  $W^{0.35}$  feet, but for yields above 100 kt, 180  $W^{0.35}$  feet is recommended for a conservative estimate). For certain other phenomena of interest, e.g., neutron-induced activity, the height of burst at which the earth's surface fails to produce an effect is difficult or impossible to distinguish.

### 1-6 Development

The first interaction between weapon output and the surrounding atmosphere comes from the initial gamma rays emitted during the weapon detonation. These initial gammas arise both from the fission gammas and from gammas produced by inelastic neutron scattering in the weapon mass. These gamma rays interact mainly by Compton collisions with the electrons of the air molecules, resulting in ionization of the air and degradation of the gamma ray energy. The

results of such interactions are described in Chapters 5 through 8.

Another important interaction between the weapon output and the atmosphere comes from the neutrons produced during the fission and fusion reactions. Inelastic scattering of high-energy neutrons by nuclei of the air and the ground, and capture of slow neutrons by nitrogen in the air and by various elements in the ground provide sources of secondary gamma rays. The relative importance of the inelastic and capture gamma rays depends strongly upon the neutron spectrum of the source.

As a result of X-ray and debris interactions, a very hot plasma remains in the vicinity of the explosion. This plasma consists of electrons and stripped nuclei of the fission and fusion products, of the elements of the weapon case and components, and of any other elements in the immediate vicinity, such as nitrogen and oxygen in the air. The radiating temperature depends on the weapon design and the total yield, but it may range from a few million to many tens of millions of degrees Kelvin. D. See Introduction and Section 1, Chapter 4).

Although the spectrum of the emissions from this plasma is not exactly that of a black body, particularly because the temperature is by no means uniform, it often does approximate a black body spectrum. D. See Section 1, Chapter 4).

Plasmas at these temperatures emit electromagnetic radiation that is primarily in the X-ray region of the spectrum (see Introduction, Chapter 4). If the burst occurs in the lower part of the atmosphere, the radiated energy is absorbed by the air in a sphere that initially may be only a few yards larger than the weapon. Since this sphere itself is at a high temperature, it again radiates X-rays (although at a lower temperature). The process of absorption and re-radiation continues until the energy radiated by the weapon may occupy a sphere of air

[REDACTED]  
[REDACTED]  
of several tens of yards in diameter. The emission of this additional electromagnetic radiation covers a wide range of frequencies from about 1 cycle per second through radio, infrared, and visible to the soft X-rays.

[REDACTED] The photon mean free paths in the hot fireball are of the order of (or longer than) the fireball diameter, and as a result the energy distribution and temperature are fairly uniform throughout the volume of hot gas. During this phase of growth, the fireball is consequently referred to as the "isothermal sphere." This name is something of a misnomer, since temperature gradients do exist, particularly near the advancing radiation front. As the fireball cools, the growth by re-radiation of energy continues at a progressively slower rate because the mean free path of the photons becomes smaller than the fireball dimensions. The decreasing velocity of the fireball front causes the pressure of the heated air behind the front to increase, and a shock wave begins to form. This is referred to as the "outer" shock wave.

[REDACTED] During the isothermal sphere phase, the initially hot, high-pressure mass of weapon residues begins to expand outward as a pressure relief mechanism. Within a few microseconds, the material forms a thin, high-density shell, the hydrodynamic front, moving at high velocity. When this shell reaches the hot air outside the weapon, it begins to "snowplow" air ahead of it, and thereby transfers hydrodynamic energy into the air. The air is consequently heated further, and the additional radiation from the heated air contributes to fireball growth by radiation. Within a very short time, the hydrodynamic front becomes a strong shock wave, called the "inner" shock wave, propagating away from the burst point, but still within the fireball. All the phenomena described so far occur in the first few hundred microseconds after the explosion. During this period, fireball growth is dominated by radiation transport, with hydrodynamic

energy dissipation playing a relatively minor role in the interior.

[REDACTED] Since the transfer of energy by radiation becomes less rapid as the fireball cools, the inner shock front begins to advance faster than the radiation front and soon the two coincide. The inner shock front continues to advance more rapidly than the radiation front and moves ahead of it at the time when the temperature of the isothermal sphere has fallen to about 300,000°C (540,000°F). This phenomenon is called "hydrodynamic separation." For a 20-kiloton explosion it occurs at about 0.1 milliseconds ( $10^{-4}$  second) after the burst time when the fireball radius is roughly 40 feet. The partition of energy between blast and thermal at the time of hydrodynamic separation is determined by the relationship between photon mean free paths, fireball radius, and time after burst. The detonation conditions determine these quantities. The final character of the environment at some distance from the burst is not determined, however, until the time at which the inner shock wave overtakes the outer one that was formed at the radiation front. At low and moderate altitudes, the inner shock front appears to catch up with the outer at hydrodynamic separation. (At higher altitudes, the inner and outer fronts do not coincide at hydrodynamic separation, and the inner shock wave does not catch up until some later time, determined by the burst conditions.)

[REDACTED] As the (combined) shock front from a normal air burst moves ahead of the isothermal sphere it causes a tremendous compression of the ambient air and the temperature is thereby increased to an extent sufficient to render the air incandescent. The luminous shell thus formed constitutes the advancing visible fireball during this "hydrodynamic phase" of fireball growth. The fireball now consists of two concentric regions. The inner (hotter) region is the isothermal sphere of uniform temperature, and

[REDACTED]

it is surrounded by a layer of luminous, shock-heated air at a somewhat lower, but still high, temperature. The surface of separation between the very hot core and the somewhat cooler outer layer is the radiation front. The development of an air burst described in these and subsequent paragraphs is shown in Figure 1-1.

### 1-7 Thermal Radiation [REDACTED]

[REDACTED] The relatively large amount of thermal radiation emitted by a nuclear explosion is one of its most striking characteristics. This radiant energy may amount to from one-third to one-half of the total energy released by an air burst weapon (see Chapter 3).

[REDACTED] During the early stages of expansion of the incandescent shock front, the emitted radiant power increases as the luminous sphere increases in size, even though expansion causes a temperature decrease, until a maximum (the first maximum) is reached. At this point, the effect of the rapid rate of decrease in temperature overrides the enhancement of radiant power resulting from the increasing area of the luminous sphere.

[REDACTED] Subsequently, further expansion causes a reduction in the radiant power. Eventually the shock front temperature is reduced to a point where the shock front is no longer incandescent, at which time the rate of emission of radiation from the shock front will be negligible. In effect, the shock front has become transparent, and the hotter incandescent inner core would be expected to be observable. Initially, however, the radiation emitted from the inner core is absorbed by compounds formed in the shock-heated air, and the radiant power reaches a minimum. As these compounds break down, the radiant power emitted from the inner core begins to pass through, and the inner core becomes the visible source of radiation. Thus, the radiant power increases again. This change in boundary of the observable luminous sphere from the shock front to the

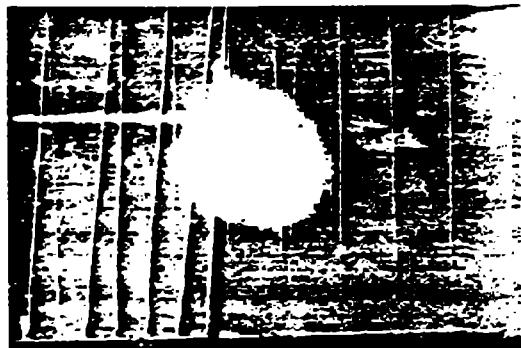
incandescent inner core gives rise to the term "breakaway."

[REDACTED] As the opacity of the shock-heated air decreases, the apparent temperature as measured from a distance approaches that of the hot gases of the inner core, and the emitted radiant power approaches a second maximum. Further expansion and radiative cooling of the hot gases, however, give rise to a slow decrease in the radiant power. This decrease is so slow, relative to the previous rise and decline, that a large percentage of the total radiant energy emitted is delivered during this period. Finally, the rate of delivery of radiant energy drops to a low value.

[REDACTED] The subsequent characteristics of the shock, or blast, wave are discussed in paragraph 1-8 below and Chapter 2. The effects of the thermal pulse are discussed in Chapter 3.

### 1-8 The Blast Wave [REDACTED]

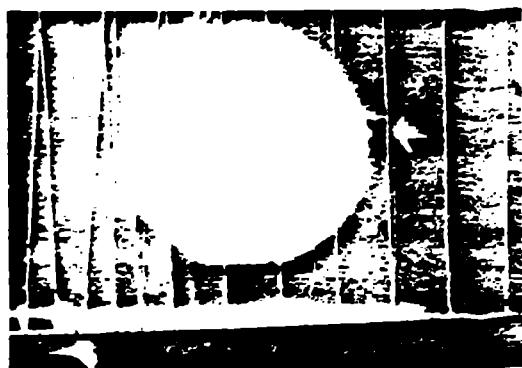
[REDACTED] A blast wave is characterized by a sharp rise in pressure, temperature, and density at its shock front. Thus, upon the arrival of a blast wave at a given location from the burst point, the sequence of events is a sudden increase in pressure, temperature, and density, followed by a subsequent decrease in pressure, temperature, and density to values below ambient, and a more gradual return to ambient conditions with the temperatures going slightly above ambient. The overall characteristics of the blast wave are preserved over long distances from the burst point, but vary in magnitude with distance. With increase in distance, for example, the maximum pressure in the shock wave decreases, and the length of time over which the blast pressure is above ambient, the "positive phase," increases. Also, under conditions of high relative humidity (50 percent or higher), the drop in air pressure below ambient lowers the temperature sufficiently to cause condensation of atmospheric moisture to form a large cloud called the Wilson Cloud. When the air pressure again becomes nor-



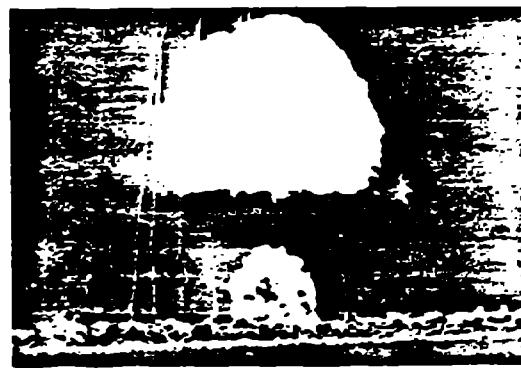
(a)



(b)



(c)



(d)

Figure 1-1. Development of an Air Burst

mal, in a matter of seconds, the cloud disappears. Although the Wilson Cloud is spectacular, because it always occurs too far behind the shock front to modify the blast effects, and too late to reduce the thermal effects appreciably, it has no military significance.

The motion of the air away from the burst point during the positive phase and toward the burst point during the negative phase, is also characteristic of a blast wave. The pattern of the air motion or air velocity is the same as for the other characteristics, with maximum velocity occurring just behind the shock front and decreasing with distance from the burst point. At 300 yards from the burst point of a 1-kt weapon, the peak wind velocity is about 240 miles per hour.

#### 1-9 Nuclear Radiation

A unique feature of a nuclear explosion is the nuclear radiation released. This consists of, but is not limited to, gamma rays, neutrons, alpha particles, and beta particles. About a third of this energy is emitted within the first second after detonation, the remainder being released from radioactive fission products and unfissioned bomb materials over long periods of time after the burst. The effects of radiation can be increased during the first few seconds as a result of the disturbance of the atmosphere by the blast wave. Such enhancement of the effects compared to the effects in an undisturbed atmosphere is called hydrodynamic enhancement. The primary direct effect of nuclear radiation is an anti-personnel effect, with the penetrating radiations (gamma rays and neutrons) being the most dangerous. Residual nuclear radiation, due either to fallout or to neutron-induced gamma activity, can under certain conditions deny entry in a bombed area for some period of time after a detonation. Direct nuclear radiation effects on materials and equipment are of less significance, except for sensitive detector materials and cer-

tain electronic components. However, nuclear radiation produces indirect effects, such as EMP and blackout, which are discussed in Chapter 7 and 8, respectively. The nuclear radiation environment and the effects on personnel are discussed in Chapter 5. The effects of nuclear radiation on electronic components are discussed in Chapter 6.

#### 1-10 Electromagnetic Pulse

The electrons that are separated from the atoms of the air by the gamma rays (paragraph 1-6) lose energy to surrounding air molecules. The energy lost in these collisions is used to free additional electrons, i.e., further ionization. The net result is a flow of negatively charged electrons radially outward from the explosion, while the heavier ions remain behind. If the explosion occurs in a homogeneous (constant density) atmosphere, two shells of charge are created: an inner positive ion shell, and an outer negative electron shell. A large local electric field is created in the radial direction; however, under such conditions, no electromagnetic field is radiated away. In practice, various asymmetries will occur that will result in electromagnetic fields being radiated from the source region. The potential importance of these fields will depend strongly on the circumstances of each individual burst. These effects are discussed in more detail in Chapter 7.

#### 1-11 Electromagnetic Wave Propagation

Air burst effects on electromagnetic wave propagation are essentially associated with the fireball region. While relatively small, this region can be highly ionized for a few tens of seconds, and may have seriously degrading effects on the propagation of radio and radar signals. The effects of nuclear explosions on the propagation of electromagnetic signals are discussed in Chapter 8.

### **1-12 The Cloud**

Because of its relatively low density compared to ambient conditions, the mass of hot gases making up the fireball rises. The rate of rise may reach several hundred feet per second, after which it decreases rapidly. As the gases rise, they expand, cool, and condense forming a radioactive cloud that consists largely of water vapor and metallic oxides from the weapon. As the fireball cools, the color changes gradually from red to a reddish brown, and ultimately water vapor from the air condenses sufficiently to produce a white color. As the heated mass of air in the fireball rises, cool air is pulled in from the sides and below, which may cause a doughnut-shaped ring to form around the column of hot air. This part of the cloud rolls violently as it rises. The cloud from a 1-kt detonation may reach a height of 5,000 to 10,000 ft above the burst point, after which it moves and diffuses according to the prevailing meteorological conditions.

### **THE SURFACE BURST**

A surface burst is defined as the explosion of a nuclear weapon at the earth's surface. (Figure 1-2 shows the development of a surface burst.) When a nuclear weapon is burst at the surface of the earth the sequence of events in the development of the fireball and the formation of the blast wave is the same as that for an air burst, except that the fireball boundary and the shock front are roughly hemispherical. Since the earth's surface is an almost perfect reflector for the blast wave, the resulting blast effects are almost the same as for a burst of twice the yield in free air.

### **1-13 Ground Shock**

When a burst takes place on the ground surface, part of the energy is directly transmitted to the earth in the form of ground shock. Also, the air blast wave induces a ground shock

wave that, at shallow depths, has essentially the same magnitude as the air blast wave at the same distance from the burst. The directly transmitted ground shock, although of higher magnitude initially, attenuates radially faster than the air blast induced shock. These effects are discussed in greater detail in Chapter 2.

### **1-14 The Crater**

A land surface explosion of a nuclear weapon exerts initial shock pressures of hundreds of thousands pounds per square inch on the surface of the earth. The pressures result in displacement of material as well as downward compression of the soil to form a crater. In addition to the material that is thrown out, some earth will be vaporized by the intense heat. As will be discussed in Section II, Chapter 2, the size of the crater will depend upon the type of soil on which the explosion occurs. A crater of approximately 120 feet in diameter and 28 feet in depth is formed by a 1 kt weapon burst on a dry soil surface.

### **1-15 Thermal Radiation**

As a result of the heat transfer to the surface, the hemispherical shape of the fireball, and the partial obscuration of the fireball by earth or water, the radiant exposure received by surface targets from a nuclear weapon burst on the surface is somewhat less than would be delivered by an air burst nuclear weapon of the same yield.

### **1-16 Initial Nuclear Radiation**

In view of the absorption by the earth, initial nuclear radiation generally is less at the same distance from a surface burst than from an air burst; however, the hydrodynamic enhancement for high yield weapons may result in an increase in the initial gamma radiation. Each case should be examined separately by the methods described in Chapter 5 to determine the total initial nuclear radiation dose for a given situation.

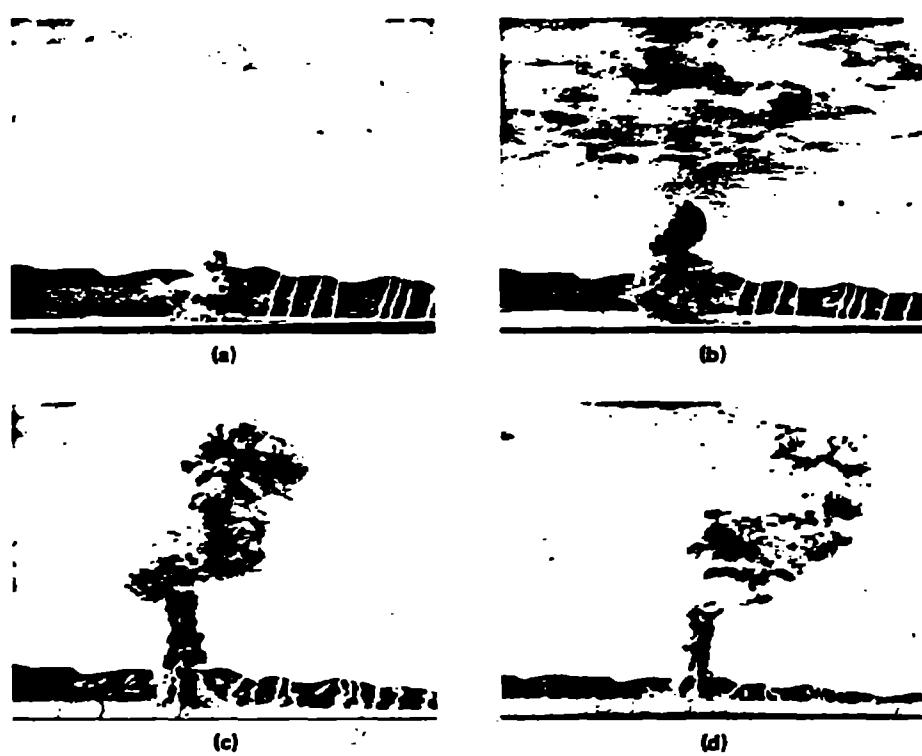


Figure 1-2. Development of a Surface Burst

### **1-17 Residual Nuclear Radiation**

The contamination effects of residual nuclear radiation from a surface burst are greater than for an air burst, and hazardous radiological effects are produced over greater areas than those seriously affected by blast or by thermal radiation. Roughly half the available radioactivity resulting from a nuclear explosion on land, for example, can be expected to fall out in the general vicinity of the burst point. Dose rate contours near the burst point as great as 10,000 r/hr at H + 1 hr have been observed at tests, regardless of yield.

### **1-18 Electromagnetic Pulse (EMP) Radiation**

If the detonation occurs at or near the surface of the earth, the EMP phenomenon mentioned in paragraph 1-11 produces intense electric and magnetic fields that may extend to distances of several thousand yards, depending on the weapon yield. The affected region is highly ionized and large electric currents flow in the air and the ground. Beyond this ionized region, the pulse strength drops fairly sharply, eventually as the inverse of the distance from the explosion. The strong fields may damage electrical and electronic equipment at distances exceeding those at which significant air blast damage may occur (see Chapter 7).

### **1-19 Electromagnetic Wave Propagation**

Surface burst effects on electromagnetic wave propagation are essentially associated with the fireball region (see paragraph 1-11). Surface material drawn up with the fireball can cause attenuation by scattering of incident radar signals and obscuration or scintillation of optical radiation.

### **1-20 The Cloud**

A great quantity of material is thrown out from the point of explosion of a nuclear

weapon that bursts on the surface. As the fireball rises, some material is drawn up under the fireball, forming a stem and sometimes forming a second cloud below the one that develops from the fireball. The stem and cloud(s) continue to rise and follow the course described for air burst.

### **1-21 Water Surface Bursts**

In general, the phenomena as outlined in paragraph 1-13 through 1-20 will occur for a surface burst on water. Also, the expanding sphere of hot gases depresses the water, causing the formation of a surface wave train and the transmission of a directly coupled shock wave into the water. The expanding air blast wave induces a shock wave in the water, which at shallow depths has essentially the same magnitude as the air blast wave at the same distance from the burst. Although the directly coupled water shock is of higher magnitude initially, it attenuates faster than the air blast induced water shock. As the height of burst increases from zero, depression, surface waves, and directly coupled water shock become smaller in magnitude. The formation of a crater on the bottom as the result of a surface burst in shallow water will depend on the depth of the water, yield of the weapon, and other factors. A 1 kt weapon, for example, burst on the surface of water 40 feet deep with a soft rock bottom, will form a crater 60 feet in diameter and 2 feet deep.

### **THE TRANSITION ZONE BETWEEN AN AIR BURST AND A SURFACE BURST**

There is a sizable zone above the earth's surface where, for weapons burst in the zone, the presence of the earth's surface modifies one or more of the basic weapon phenomena significantly. As the height of burst is successively lowered in this transition zone, the earth's surface plays an increasingly important role in modify-

ing weapon phenomena; there is a gradual transition from the characteristics of an air burst to those of a surface burst. The upper boundary of the transition zone varies depending upon the phenomenon being considered, because the effect of the earth's surface ceases to be of importance at different scaled heights of burst for different phenomena. These variations are described in detail for each phenomena in Chapters 2 through 8.

## THE HIGH-ALTITUDE BURST

### 1-22 Description

As the detonation altitude increases, the interaction of weapon energy with the atmosphere changes markedly and is affected by weapon design and atmospheric conditions (pressure, density, and composition). There are several rather broadly defined altitude regions in which the formation and subsequent motion of the fireball differ. The term high-altitude bursts as used in this document refers to these regions collectively and includes air bursts in the lowest region.

### 1-23 Development

For detonations below about 350,000 feet, a large fraction of the X-ray energy is deposited near the burst point, heating the air to incandescence. As the detonation altitude increases above sea level, the air density decreases and the X-ray mean-free path increases. The principal mechanism for the initial fireball growth gradually changes from hydrodynamic motion (shock heating) to radiation heating. After the fireball reaches the initial size where growth by the heating of surrounding air ceases, it expands and rises in a manner related to the atmospheric scale height. The atmospheric scale height is the altitude separation where the density (or pressure) differs by a factor of e (2.7); the scale height varies from 15,000 to 25,000 feet below an altitude of 350,000 feet.

If the initial fireball radius is smaller than the atmospheric scale height, the fireball expands to pressure equilibrium with the atmosphere. The subsequent fireball motion is similar to that described for air bursts; that is, the fireball rises principally due to buoyant forces. For yield-altitude combinations where the initial fireball radius is comparable to or exceeds an atmospheric scale height, large vertical pressure gradients are produced that cause an upward force on the fireball, giving it a boost or ballistic impulse upward. The fireball can be carried to altitudes far above the detonation point before expanding to pressure equilibrium with the surrounding atmosphere. As a result of the rapid decrease in atmospheric density with increasing altitude, the fireball density may become greater than the surrounding atmosphere. After reaching maximum altitude, the fireball then falls ballistically until encountering air of comparable density. This late-time fireball behavior will be modified if the fireball density at the maximum altitude is low enough that the ionized component of the fireball gas is trapped by the geomagnetic field.

For detonations below about 200,000 feet, the fireball region forms a toroid. The time required appears to depend on weapon yield and detonation altitude.

For low-altitude bursts, large temperature and pressure gradients at the boundary of the radiation fireball produce a strong shock wave (see paragraph 1-6). As the detonation altitude increases and the radiation (X-ray) fireball becomes large, the gradients at the boundary become weaker; the principal shock wave is then produced by the initial radial expansion of the debris within the X-ray fireball.

The fireball starts as a highly ionized plasma. As it expands, it pushes the geomagnetic field out ahead of it. For detonations above about 250,000 feet, the magnetic pressure caused by the deformation of the field eventual-

[REDACTED]  
ly slows the expansion across the field while the expansion along the field continues. The fireball gradually becomes cylindrical in shape. After the expansion across the magnetic field has slowed, the magnetic field reenters the fireball turbulent-  
ly, causing the local ionized fireball gas to become striated along the direction of the field.

[REDACTED] For detonations above about 350,000 feet, X-rays have a large mean-free path, deposit their energy over a large distance, and do not produce a localized fireball. However, below about 900,000 feet a fireball can be formed by deposition of the debris kinetic energy. Hydro-  
magnetic coupling between the debris and the ionized air around the burst point results in the deposition of most of the debris kinetic energy (roughly one-fourth of the total weapon energy) near the burst point, producing a local fireball.

[REDACTED] The geomagnetic field plays an increasingly important role in fireball formation as the detonation altitude increases. The hydromagnetic coupling is actually quite complex. Instabilities in the interface between the expanding debris and the magnetic field can cause jetting of debris across field lines. Debris initially directed downward is stopped by the denser air below the burst point, while upward-directed debris travels to large distances. If in being stopped by the atmosphere, the downward-directed debris heats and ionizes the air, the heated region will subsequently rise and expand. Some upward-  
directed ionized debris will follow geomagnetic field lines across the geomagnetic equator before being deposited in the atmosphere.

[REDACTED] For large-yield bursts detonated above about 350,000 feet, X-ray energy, while not producing a localized fireball, will heat the atmosphere below the burst sufficiently to cause upward motion, changing the atmospheric density and composition at higher altitudes. This phenomenon is primarily important in the analysis of sequential bursts, where changes in atmospheric properties caused by one burst affect the

deposition of energy (and thus the phenomenology) of succeeding bursts.

[REDACTED] As the fireball rises, most of the weapon debris is carried with it. After altitude stabiliza-  
tion takes place, the debris continues to be dis-  
persed by diffusion and atmospheric winds. Both expansion and horizontal displacement of the debris center occur; the specific rates depend on prevailing wind motion and eddy diffusion at the debris stabilization altitudes, but they gen-  
erally increase with increasing stabilization altitude. For detonations above about 200,000 feet, where the geomagnetic field acts to confine the debris, much of the debris may be trapped above several hundred thousand feet where the air den-  
sity is low and wind motion negligible. However, after a period of minutes to perhaps several hours, most of the debris will have diffused or settled down the field lines to altitudes where wind motion can spread the debris over large areas. The detailed debris distribution during the early fireball growth and rise, and within the toroid at later times, is poorly known at present; however, many electromagnetic propagation ef-  
fects are dependent only on the gross debris distribution.

[REDACTED] The differing regions of phenome-  
nology are illustrated in the altitude-yield map shown in Figure 1-3. Figure 1-4 shows photo-  
graphs taken after BLUE GILL [REDACTED], TEAK [REDACTED] (250 kilofeet), and  
CHECK MATE [REDACTED]. The forma-  
tion of a toroid, characteristic of detonations in  
the buoyant rise region, is illustrated in Figure  
1-4a.

DIA  
(L)(3)

[REDACTED] The photograph of TEAK at 100 sec-  
onds illustrates the difficulty in defining simple  
geometrical boundaries for fireball and debris  
regions. The innermost region is mostly weapon  
debris and heated air; the horizontal and vertical  
dimensions are about 450 kilofeet and 800 kilo-

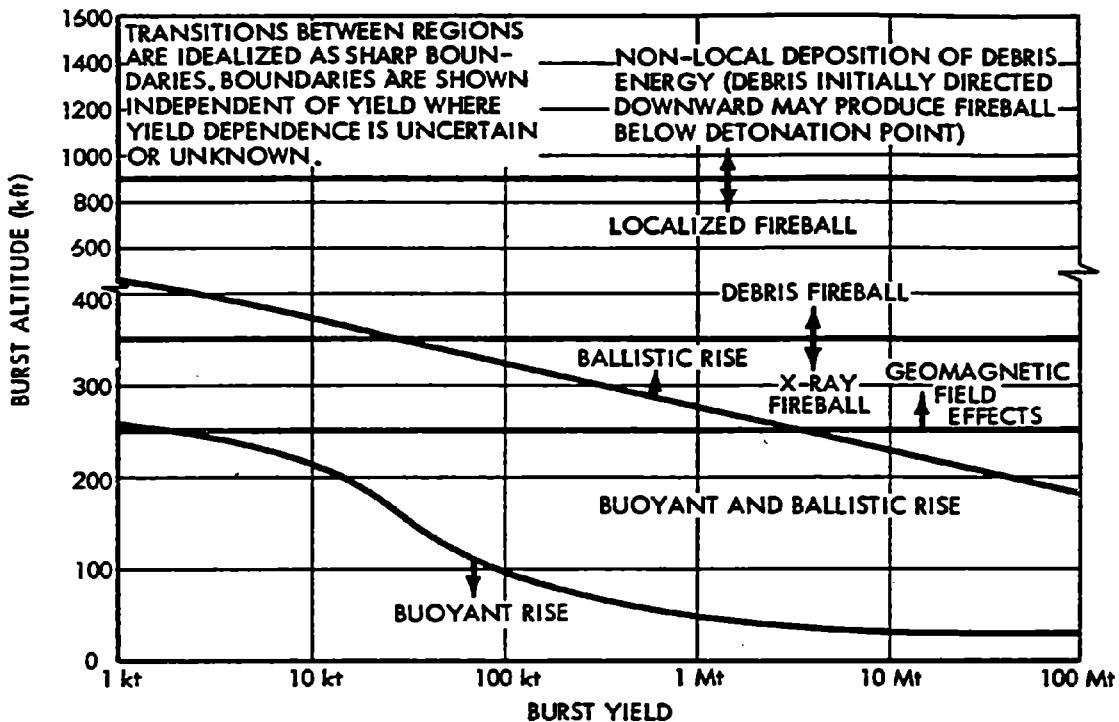


Figure 1-3. Altitude-Yield Map Showing Differing Regions of Phenomenology

feet, respectively. Most of the weapon debris appears to be concentrated near the bottom of the region. Some of the material near the top of the region is beginning to be affected by the geomagnetic field. The outer edge of the luminous region is a shock wave moving about 10,000 feet per second. While not defined as a fireball, there is still significant modification of the natural air chemistry within the region.

The influence of the geomagnetic field on fireball formation and growth is clearly evident in Figure 1-4c. The overall fireball diameter is about 300 kilofeet, and the length along the geomagnetic field is about 1,000 kilofeet. The heated air within the fireball is highly ionized,

with many striations oriented along the geometric field. (The dark spots within the fireball are rocket trails.)

#### 1-24 The Blast Wave

As the burst height is raised, the X-rays are absorbed at longer distances from the burst as a result of their greater penetrating ability in the less dense air. The blast wave develops more slowly at higher altitudes, and at about 100,000 feet burst altitude the effective blast yield begins to decrease, until at a burst altitude of about 150,000 feet the effective blast yield is only 20 to 40 percent of what it would be at sea level for the same total energy yield.



(a) Blue Gill Taken From Burst Locale



(b) Teak Taken From Maui  
(1300 km Away)



(c) Check Mate Taken From Burst Locale

Figure 1-4. [REDACTED] Photographs of High Altitude Bursts,  $t = 100$  sec [REDACTED]

### **1-25 Thermal Radiation**

Two factors affect the thermal partition of energy at high altitudes. First, as mentioned in paragraph 1-24, shock waves form much less readily in the thinner air; consequently the fireball is able to radiate thermal energy that would, at lower altitude, have been transformed to hydrodynamic energy of the blast wave. Second, the thinner air allows energy from the nuclear source to travel much farther than is possible at sea level. Some of this energy travels so far from the source that it makes no contribution to the energy contained in the fireball. In general, the first of these factors becomes effective between about 100,000 and 140,000 feet, and the thermal efficiency rises. Above about 140,000 feet the second factor becomes more important, and the thermal efficiency drops. For burst altitudes between about 290,000 feet and 350,000 feet, a layer of incandescent air may be formed below the local fireball that was described in paragraph 1-23. This layer will be on the order of 45,000 feet thick and may be centered between about 250,000 feet and 270,000 feet, depending on the effective X-ray temperature of the weapon. This heated air will reradiate at longer wavelengths that will reach the ground and will be the primary source of thermal damage at the surface of the earth; however, the thermal radiation from the local fireball (radiation of the weapon debris and nearby air) is a potential source of eye damage, i.e., retinal burns and/or flashblindness (see Chapter 10).

### **1-26 Nuclear Radiation**

Nuclear radiation also extends over large regions from high altitude bursts as a result of the thinner air. This radiation may be damaging to electronic equipment in missiles in flight (see Chapter 6 and Section VII, Chapter 9). The radiation will also produce ionization over regions large in comparison to the size of the fireball region. The extent of the ionization depends on

the mean-free path of the radiation, which differs for the several nuclear radiations, and on the detonation altitude. Since the fission debris is one source for gamma rays and beta-particles, the location of the fission debris as a function of time after burst is required to determine the extent of the ionization. Energy deposition in the atmosphere from nuclear radiation also results in radiation in the optical band of the electromagnetic spectrum.

### **1-27 Electromagnetic Pulse**

Detonations above about 130,000 feet produce EMP effects on the ground over areas that may encompass thousands of square miles. Although the strengths of these fields are less than half those in the highly ionized region surrounding a surface burst, they are of sufficient magnitude to damage electrical and electronic equipment. The mechanisms of formation of EMP are treated in Chapter 7.

### **1-28 Electromagnetic-Wave Propagation**

A phenomenological effect of considerable interest for high detonation altitudes is persistent ionization of the atmosphere. Electromagnetic waves propagating through the ionized atmosphere can incur amplitude and phase changes, and radar and communication systems dependent on electromagnetic propagation through the atmosphere can be affected. Electromagnetic radiation emitted by the burst or by disturbed regions in the atmosphere can reduce the signal-to-noise ratio by increasing the noise background.

For detonations below about 50,000 feet, the principal region affecting electromagnetic propagation is the fireball. While relatively small, it can be intensely ionized for a few tens of seconds. For detonations above 50,000 feet, the fireball can remain intensely ionized for tens to hundreds of seconds. A significant fraction of the primary products of the weapon can escape

[REDACTED]  
to great distances, and the attendant ionization (in the atmosphere) can persist for minutes to hours.

## THE UNDERGROUND BURST

### 1-29 Development

[REDACTED] An underground burst is defined as the explosion of a nuclear weapon in which the center of the detonation lies at any point beneath the surface of the ground. Figure 1-5 shows the development of a shallow underground burst. When a nuclear weapon is detonated at a sufficient depth underground, the ball of fire formed is composed primarily of vaporized materials from the bomb and vaporized earth. At shallow depths, light from the fireball generally may be seen from the time it breaks through the surface until it is obscured by dust and vapor clouds, a matter of a few milliseconds. The characteristics of the explosion and their related effects depend upon the depth, yield, and soil type. As the depth below the surface is increased, the characteristics depart gradually from those of a surface burst and finally, at depths of the order of 20 feet for a 1 kt detonation, the explosion exhibits the phenomena commonly associated with underground explosions. It is emphasized that the transition from the observed characteristics of a surface burst to those of an underground burst is not sudden, but that the characteristics change gradually.

### 1-30 Air Blast

[REDACTED] Bursts at depths shallow enough to permit significant venting will produce air blast waves similar to those of air or surface bursts. As the depth of burst increases, the magnitude of the air blast will decrease.

### 1-31 Column, Cloud, and Base Surge

[REDACTED] The first physical manifestation of an underground explosion at shallow depths is an

incandescence at the ground surface directly above the point of detonation. This is almost immediately followed by large quantities of material being thrown vertically as a consequence of the direct ground shock reflection along the ground surface. Concurrently, large quantities of gas are released. These gases entrain additional quantities of material and carry them high into the air in the form of a cylindrical column. As the column rises it fans out and forms a dense cloud. Some of the particles thrown vertically, together with the entrained particles behave like an aerosol with a density considerably greater than the surrounding air. This aerosol subsequently falls in the immediate vicinity of ground zero, and the finer soil particles spread out radially along the ground to form a low dust cloud called the base surge. For a 1 kt weapon burst at a depth of 20 ft, it is estimated that the column will reach a height of approximately 420 ft and a diameter of 660 ft, the base surge will be 4,400 ft in diameter and the upper cloud will be 5,000 ft in height. Dimensions of the base surge are discussed in Section II, Chapter 2. For shallower depths of burst, the column tends to assume the shape of an inverted cone rather than a cylindrical column and has a more pronounced radial throwout. Shallower depths of burst also become less favorable for the formation of a base surge, approaching the conditions of a surface burst where no base surge is expected.

### 1-32 Ground Shock

[REDACTED] As a burst is moved deeper and deeper into the ground, the directly transmitted ground shock increases in importance and the air induced ground shock becomes less important.

### 1-33 Crater

[REDACTED] Formation of the crater from an underground burst is essentially the same as for a surface burst, except that at shallow depths more material is thrown vertically. Subsequently,

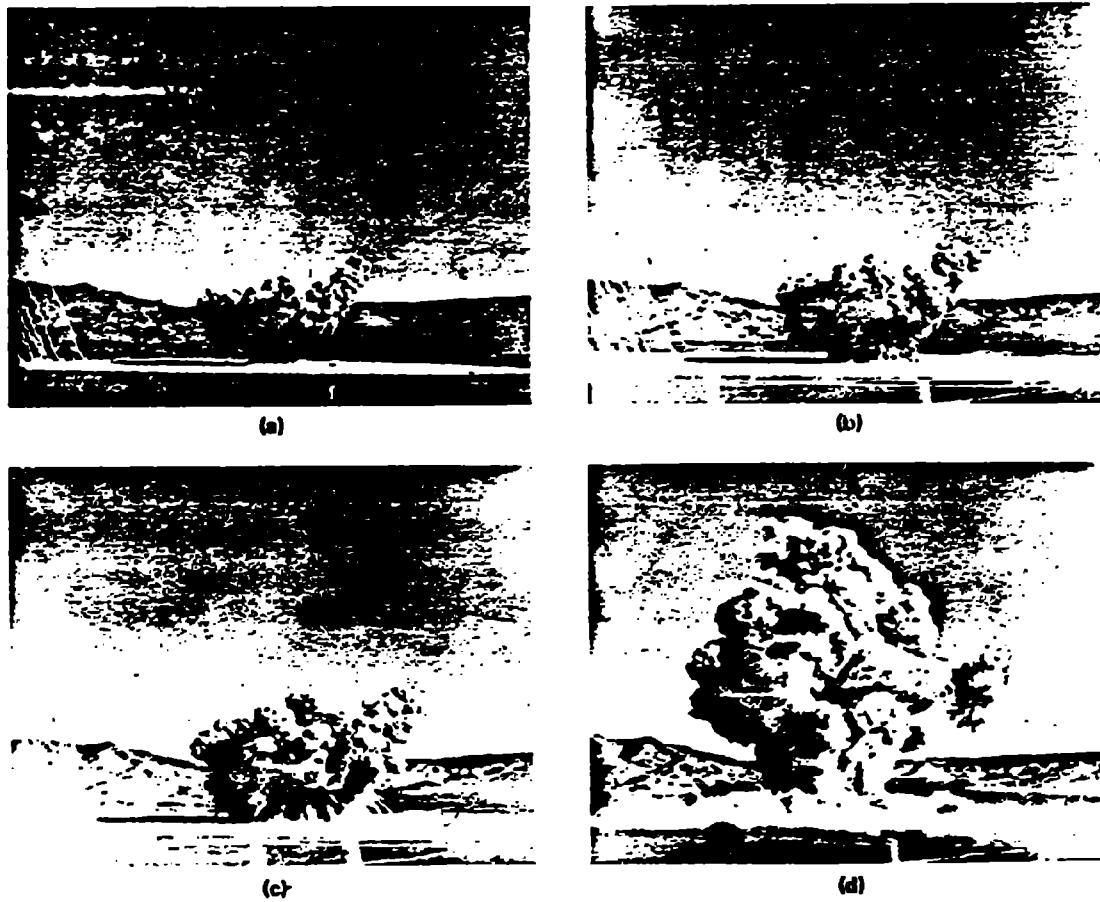
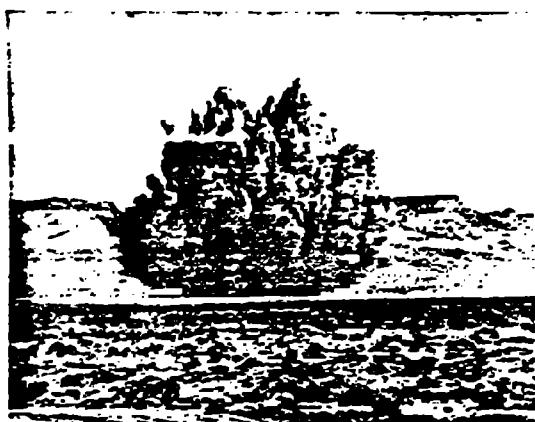


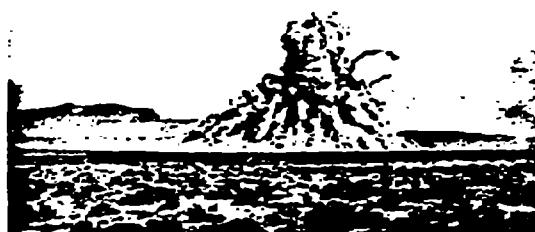
Figure 1-5. [REDACTED] Development of a Shallow Underground Burst [REDACTED]



(a)



(b)



(c)



(d)

Figure 1-6. Development of a Deep Underground Burst

[REDACTED]

much of the ejected material collapses and falls back, partly into the newly formed crater and partly onto the surrounding "lip." The general term "fallback" is used to describe the material that immediately falls back into the crater. The term "ejecta" describes material which has fallen onto the crater lip. The size of the remaining (or "apparent") crater depends on the energy yield of the detonation and on the nature of the excavated medium. In general, for equivalent conditions, the volume of the crater is roughly proportional to the yield of the explosion.

[REDACTED] The size of the apparent crater increases with increasing depth until a certain optimum depth is reached. The scaled optimum depth is different for the crater radius than for the crater depth and also varies markedly for different media. At depths below the optimum for the particular medium surrounding the burst, the crater dimensions decrease with increasing depth. At sufficiently deep depths the explosion will not vent to the surface and a cavity (camouflet) will be formed. There may or may not be disturbances at the surface, depending on the depth of the detonation and the material comprising the ground.

#### 1-34 Thermal and Nuclear Radiation

[REDACTED] As a general rule, the thermal radiation will be almost completely absorbed by the ground material, so that it does not represent a significant hazard. Most of the neutrons and early gamma rays will also be removed, although the capture of the neutrons may cause a considerable amount of induced radioactivity in various materials present in the soil. This will constitute a small part of the residual nuclear radiation, of importance only in the close vicinity of the point of burst. The remainder of the residual radiation will be due to the contaminated base surge and fallout. For shallow depths of burst, the fallout effects are similar to those of a surface burst. As the depth of burst increases how-

ever, more and more of the contaminant is deposited in the immediate vicinity of the detonation, until for the case of no surface venting, all of the contaminant is contained in the volume of the ruptured earth surrounding the point of detonation.

#### 1-35 Electromagnetic Pulse

[REDACTED] For shallow depth of burst, the electromagnetic pulse should be similar to, but of lesser magnitude than, that for a surface burst of the same size. As depth of burst increases, the extent and magnitude of the pulse will diminish. In general, the electromagnetic pulse from such bursts should be a much less significant damage mechanism than ground shock. Adequate test data for prediction are, however, lacking.

### THE UNDERWATER BURST

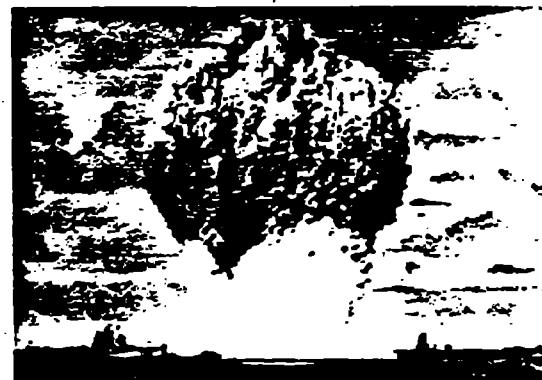
#### 1-36 Development

[REDACTED] An underwater burst is defined as the explosion of a nuclear weapon in which the center of the detonation lies at any point beneath the surface of the water. (Figure 1-7 shows development of a shallow underwater burst; Figure 1-8 shows development of a deep underwater burst.) An underwater nuclear explosion releases large amounts of thermal and nuclear radiation, essentially all of which is absorbed by the surrounding water within several feet of the explosion. (Some radiation within the visible spectrum can be radiated to greater distances depending on the transparency of the water.)

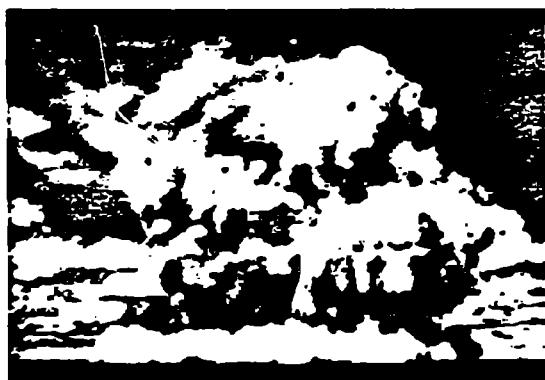
[REDACTED] During the early stages of the explosion, the bomb materials attain a very high temperature (on the order of millions of degrees) and a very high pressure (on the order of millions of atmospheres). Energy acquired by these materials is transferred to the layer of water closest to the bomb, which is heated and compressed and which, then, heats and compresses the next



(a)



(b)



(c)



(d)

Figure 1-7. Development of a Shallow Underwater Burst

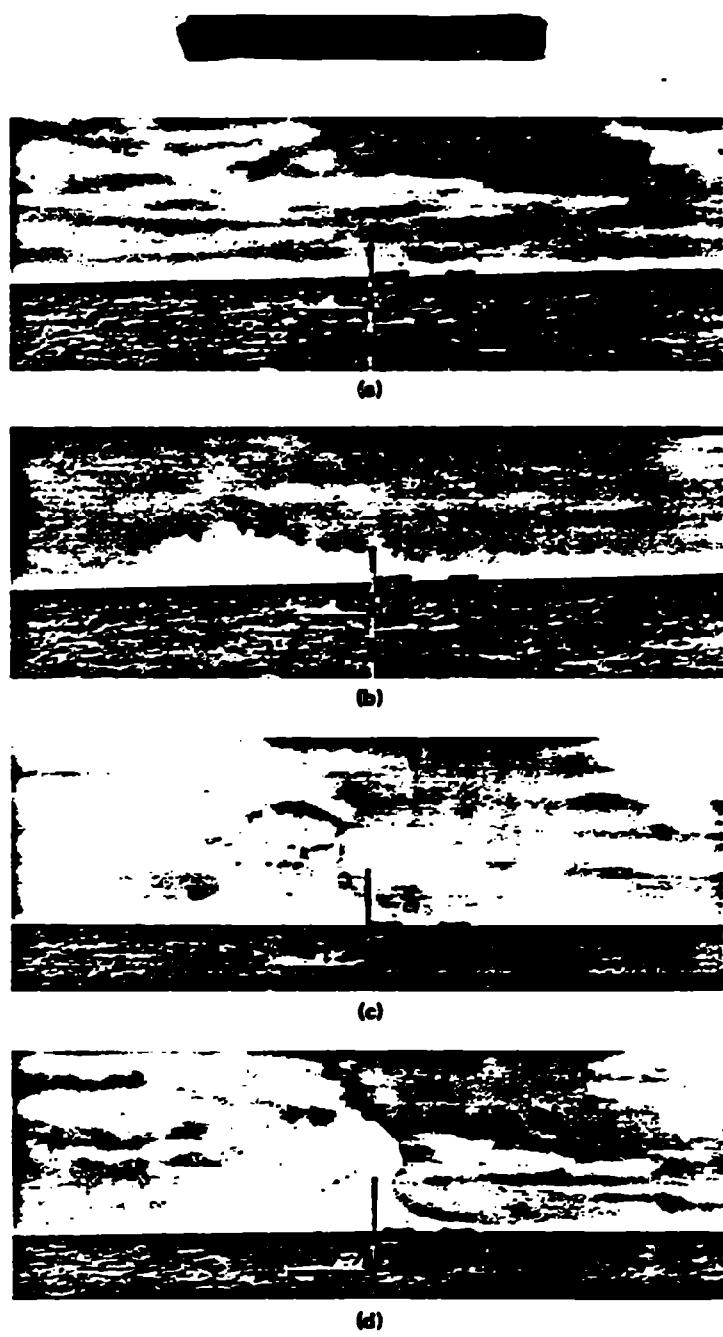


Figure 1-8. Development of a Deep Underwater Burst

outward layer. By this mechanism, a wave of compression (the hydrodynamic or shock front) is formed and moves outward from the bomb. This front moves faster than the material it engulfs, which also moves outward but at a slower rate.

As the shock front moves away from the point of explosion, energy is dissipated in the form of heat, which raises the temperature of the water passed over by the front. The largest temperature increase occurs near the center of the explosion, where it is great enough that the water is not only vaporized, but dissociated as well. At somewhat greater distances, the water is vaporized and turned to steam; at still greater distances, the water is heated, but not to its boiling point.

Thus, shortly after an underwater burst, an expanding bubble is formed. This bubble is composed largely of vaporized water with radioactive debris at its center, surrounded by heated water. Continued expansion of this bubble results in a pressure reduction within it. As the bubble pressure falls below the vapor pressure of the heated water, vaporization of additional water occurs at the interface of the bubble and the water.

In a deep underwater explosion, the bubble continues to expand at a decreasing rate until a maximum size is reached. If not too near the surface or the bottom, the bubble remains roughly spherical to this point. As a result of the inertia of the water set in motion by the early expansion of the bubble it actually overexpands, i.e., when it does attain its maximum size, its contents are at a pressure well below the ambient water pressure.

The higher pressure around the bubble causes it to contract, with a resultant increase in internal bubble pressure, and condensation of some of the bubble contents. Because the hydrostatic pressure at the bubble bottom is larger than at the top, the bubble does not remain

spherical during the contracting phase. Its bottom moves inward faster than its top (which may remain stationary or even rise slightly), contacts the top (forming a doughnut-shaped bubble viewed from above), and causes turbulence and mixing of the bubble contents with the surrounding water.

The inertia of the water set in motion by contraction of the bubble causes it to overcontract, and its internal pressure once more becomes higher than the ambient water pressure. A second compression (shock) wave in the water commences after the bubble reaches its minimum volume. This compression wave has a lower peak overpressure but a longer duration than the initial shock wave in the water. A second cycle of bubble expansion and contraction then begins.

During the initial expansion cycle, the bubble is relatively stationary, but upon contracting begins to migrate upward under the action of buoyant forces. The rate of upward migration is greatest at times of bubble minimum size, and is almost zero at times of maximum size, when the bubble is again almost spherical.

If the explosion occurs far enough from the surface, the bubble continues to pulsate and rise, though after three complete cycles enough condensation of steam has taken place to make it unlikely that additional pulsations will occur. During pulsation and upward migration, however, the water in the vicinity of the bubble acquires considerable upward momentum, and eventually breaks through the surface with some violence.

For shallow bursts, the bubble may break through the surface during one of the early pulsations or even before completion of a single pulsation cycle. If such a breakthrough occurs during the portion of the cycle at which bubble pressure is higher than ambient pressure (as with a very shallow explosion), a phenomenon known as a blowout occurs. If breakthrough

[REDACTED]

occurs when bubble pressure is below ambient pressure, the reverse phenomenon, blow-in, occurs. The character of the surface effects differs for the two phenomena. (See paragraph 1-39.)

[REDACTED] If a burst occurs near the sea (or harbor) bottom, the general bubble behavior is as described above. A pulsating bubble, however, is drawn toward the bottom and, therefore, bubble migration toward the surface is slowed.

### 1-37 Water Shock Waves and Other Pressure Pulses [REDACTED]

[REDACTED] The primary shock wave that moves out from the explosion center is characterized by an extremely rapid increase in pressure (virtually instantaneous) to a very high initial or peak pressure, and then an almost exponential decrease to a value less than the hydrostatic pressure at the explosion point. Though a water shock wave resembles an air blast wave superficially, its peak pressures are generally much higher, and durations much shorter. In the absence of nearby boundaries, the shock wave proceeds outward radially at a very high initial velocity, which soon decreases to nearly the velocity of sound in water (about 5,000 ft/sec). Shock wave velocity depends on water temperature, density, and salinity; and therefore, a shock wave may be bent (refracted) as it moves through regions of differing characteristics.

[REDACTED] Shock wave reflections from the surface and bottom affect the shock and pressure field at a point distant from the explosion. Since reflection from the surface is in the form of a negative, or tension wave, it can cause a shortening of the pressure pulse (cutoff), and, when the shock wave encounters the surface at a small enough angle, reflection can even reduce the magnitude of the primary pressure pulse. Reflection from the bottom generates a second compression wave in the water that can be effective in damaging ships.

[REDACTED] Additional shock and pressure waves,

generally of lesser importance than the primary shock wave or the bottom reflected shock waves, can be generated by shock wave energy that has been transmitted to bottom material or to the air and retransmitted to the water, by the collapse of a cavitation region near the surface, and by re-reflections of any of these.

[REDACTED] Shock or compression waves from subsequent bubble pulses generally behave in the same manner as the initial shock wave and undergo reflection and refraction of the same character.

### 1-38 Air Blast [REDACTED]

[REDACTED] As in the case of an underground burst, air blast waves are formed by an underwater burst. Their propagation depends upon the depth of burst. The first air blast wave from an underwater burst is that formed by the transfer of the shock front across the water-air interface. This front appears as a flat dome. The second air blast wave is transmitted by the venting bubble. This front will propagate essentially hemispherically. For shallow burst depths, the air blast wave resulting from venting is more intense than the shock wave transmitted across the water-air interface. For deep bursts, on the other hand, the shock wave transmitted across the water-air interface yields the higher pressures.

### 1-39 Surface Effects [REDACTED]

[REDACTED] The first surface effect of an underwater burst is caused by the intersection of the primary shock wave and the surface. Viewed from above, the effect appears to be a rapidly expanding ring of darkened water (often called the "slick"). Following closely behind the darkened region is a white circular patch (the "crack") probably caused by underwater cavitation produced by the reflected rarefaction wave. Shortly after appearance of the crack, the water above the explosion rises vertically and forms a white mound of spray (the "spray dome"). This dome

is caused by the velocity imparted to the water near the surface by the reflection of the shock wave and to the subsequent breakup of the surface layer into drops of spray. The initial upward velocity of the water is proportional to the pressure of the direct shock wave, and so it is greatest directly above the detonation point. Consequently, the water in the center rises more rapidly (and for a longer time) than water farther away. As a result, the sides of the spray dome become steeper as the water rises. The upward motion is terminated by the downward pull of gravity and the resistance of the air. The total time of rise and the maximum height depend upon the energy of the explosion, and upon its depth below the water surface. Additional slick, crack, and spray-dome phenomena may result if the shock wave reflected from the water bottom and compression waves produced by the gas bubble reach the surface with sufficient intensity.

For shallow bursts, the spray dome appears to be rapidly converted to a column formed by the upward and outward acceleration of the water surrounding the explosion. If blowout occurs, the upper part of the column is likely to be marked by a crown of explosion products. If blow-in occurs, the crown is likely to be absent. In its later stages, the column may break up into plumes (relatively broad jets or spouts of water that disintegrate into spray as they travel through the air).

For bursts deep enough that blowout does not occur, but not so deep that bubble pulsation has ceased, plumes will be formed.

If an explosion takes place deep enough for bubble pulsations to have ceased before the bubble reaches the surface, plumes caused by the upwelling of the water (and any uncondensed vapor or gas) may occur.

Upon subsidence of the column and plumes from an underwater explosion, a misty, generally highly radioactive, "doughnut-shaped

"ring" or series of rings, the "base surge" may be formed. In the few instances in which base surge formation has been observed over water, the visible configuration has been quite irregular. Nevertheless, to a good approximation, the base surge can be represented as a hollow cylinder with the inner diameter about two-thirds of the outer diameter. The heights of the visible base surge clouds have generally ranged between 1,000 and 2,000 feet.

The necessary conditions for the formation of a base surge have not been definitely established, although it is reasonably certain that no base surge would accompany bursts at great depths. The underwater test shots upon which the present analysis is based have all created both a visible and an invisible (see below) base surge. The only marked difference between the phenomena at the various tests is that at Bikini BAKER there was an airborne cloud, evidently composed of fission debris and steam. The other shots, which were at somewhat greater depths, produced no such cloud. The whole of the plume fell back into the surface of the water where the low-lying base surge cloud was formed.

From the weapons effects standpoint, the importance of the base surge lies in the fact that it is likely to be highly radioactive because of the fission (and other) residues present either at its inception, or dropped into it from the radioactive cloud. Because of its radioactivity, it may represent a serious hazard for a distance of several miles, especially in the downwind direction. The fission debris is suspended in the form of very small particles that occupy the same volume as the visible base surge at early times, that is, within the first 3 or 4 minutes. However, when the small water droplets which make the base surge visible evaporate and disappear, the radioactive particles and gases remain in the air and continue to move outwards as an invisible radioactive base surge. There may well be some fallout or rainout on the surface of the water (or

[REDACTED]  
[REDACTED]  
ship or shore station) from the radioactive base surge, but in many cases it is expected to pass over without depositing any debris. Thus, according to circumstances, there may or may not be radioactive contamination on the surfaces of objects in the vicinity of an underwater nuclear burst.

[REDACTED] The radioactive base surge continues to expand in the same manner as would have been expected had it remained visible. It drifts downwind either as an invisible, doughnut-shaped cloud, or as several such possibly concentric clouds that approximate a low-lying disc with no hole in the center. The latter shape is more probable for deeper bursts. The length of time this base surge remains radioactive will depend on the energy yield of the explosion, the burst depth, and the nearness of the sea bottom to the point of burst. In addition, weather conditions will control depletion of debris due to rainout and diffusion by atmospheric winds. As a general rule, it is expected that there will be a considerable hazard from the radioactive base surge within the first 5 to 10 minutes after an underwater explosion and a decreasing hazard for half an hour or more.

[REDACTED] After dissipation of the visible base

surge, the water surface around the explosion is seen to be white. This area (the "foam patch") results from the upward motion of the water and uncondensed explosion products in the vicinity of the bubble, their spreading over the surface of the patch, and their downward motion at the edge of the patch. In its later stages, this area is marked mainly by a ring of foam and debris that shows where downward circulation has taken place.

#### 1-40 Thermal and Nuclear Radiation [REDACTED]

[REDACTED] Thermal radiation and initial nuclear radiation effects are considered to be insignificant for underwater bursts, except for the radioactivity accompanying the base surge (paragraph 1-39). Residual nuclear radiation effects (fall-out) will approximate those of a ground surface burst if the explosion occurs in shallow water.

#### 1-41 Electromagnetic Pulse [REDACTED]

[REDACTED] The degree to which an electromagnetic pulse is generated by an underwater burst is not known, but it is expected to be insignificant except for very shallow bursts. In such cases, it is believed that a diminishing effect above the surface, approximating that described for a shallow underground burst, will result.

## BIBLIOGRAPHY\*

Bethe, H. A., et al, *Blast Wave*, LA 2000, Los Alamos Scientific Laboratory, Los Alamos, New Mexico, March 27, 1958 [REDACTED]

Brode, H. L., *Review of Nuclear Weapons Effects*, Annual Review of Nuclear Science, 18, 153, 1968 [REDACTED]

*Engineering with Nuclear Explosives: Proceedings of the Third Plowshare Symposium*, TID 7695, U.S. Atomic Energy Commission, April 1964 [REDACTED]

Glasstone, S., *Public Safety and Underground Nuclear Detonations*, TID 25708, U.S. Atomic Energy Commission, June 1971 [REDACTED]

Johnson, G. W., and C. E. Violet, *Phenomenology of Contained Nuclear Explosions*, UCRL 5124 Rev. 1, University of California, Lawrence Radiation Laboratory, Livermore, California, December 1958 [REDACTED]

Johnson, G. W., et al, *Underground Nuclear Detonations*, UCRL 5626, University of California, Lawrence Radiation Laboratory, Livermore, California, July 8, 1959 [REDACTED]

[REDACTED]

*Symposium on Engineering with Nuclear Explosives, January 14-16, 1970, Las Vegas, Nevada. Proceedings*, CONF-700101, Vols. 1 and 2, May 1970 [REDACTED]

*Proceedings for the Symposium on Public Health Aspects of Peaceful Uses of Nuclear Explosives*, Las Vegas, Nevada, April 1969, U.S. Department of Health, Education and Welfare, Public Health Service, SWRHL-82 [REDACTED]

*Proceedings of the Special Session on Nuclear Excavation, Nuclear Applications and Technology*, 7, 188-327, 1969 [REDACTED]

Snay H. G., and R. C. Tipton, *Charts for the Parameters of Migrating Explosion Bubbles*, NOLTR 62-184, U.S. Naval Ordnance Laboratory, 15 October, 1962 [REDACTED]

Steiger, W. R., and S. Matsushita, *Photographs of the High Altitude Nuclear Explosion TEAK*, Journal of Geophysical Research, 65, 545, 1960 [REDACTED]

Strange, J. N., and L. Miller, *Blast Phenomena from Explosions and an Air-Water Interface*. Report 1, Misc. Paper No. 1-814, U.S. Army Engineer Waterways Experiment Station, Vicksburg, Miss., June 1966 [REDACTED]

Taylor, G. I., *The Instability of Liquid Surfaces When Accelerated in a Direction Perpendicular to Their Planes. Part I*, Proceedings of the Royal Society, London, A 201, 192, 1950 [REDACTED]

Teller, E., et al., *The Constructive Uses of Nuclear Explosives*, McGraw-Hill Book Company, 1968 [REDACTED]

\*Additional reference material concerning the subject matter of this chapter may be found in the handbooks described in Appendix D and in the more specific bibliographies of Chapters 2 through 8.

## Chapter 2

### BLAST AND SHOCK PHENOMENA

#### INTRODUCTION

Most of the physical damage to material that is caused by nuclear explosions near the earth's surface results from the blast and shock phenomena or from the thermal radiation phenomena associated with such explosions. This chapter describes the blast and shock phenomena, while the thermal radiation phenomena are described in Chapter 3.

Damage to structures or materiel from blast and shock depends upon the location of the explosion (air burst, surface burst, subsurface burst), and the location of the structure or materiel (in the air, on or under the surface of the earth, or on or under a water surface). Accordingly, this chapter is divided into four sections. Section I describes the air blast phenomena from air and surface bursts. Section II deals with cratering phenomena and the associated problems of ejecta. Section III describes ground shock phenomena from near surface and subsurface (ground) explosions. Section IV describes the phenomena associated with underwater explosions.

#### SECTION I AIR BLAST PHENOMENA

The shock wave that propagates through air as a consequence of a nuclear explosion is commonly referred to as a blast wave. The destructive effects of a blast wave are produced by its overpressure and its dynamic pressure, both expressed in pounds per square inch (psi). Overpressure,  $\Delta p$ , is the amount by which the static pressure in the blast wave exceeds the ambient

pressure. Dynamic pressure,  $q$ , is associated with the mass motion of air in the blast wave. It is approximately equal to the pressure that this strong wind develops when it hits a stationary object. Dynamic pressure is defined more completely in paragraph 2-8.

When an ideal blast wave passes a given point, the first disturbance that is felt coincides with the arrival of the shock front, a discontinuity at which both overpressure and dynamic pressure rise abruptly to their peak values, as illustrated at point B in Figure 2-1. The over-

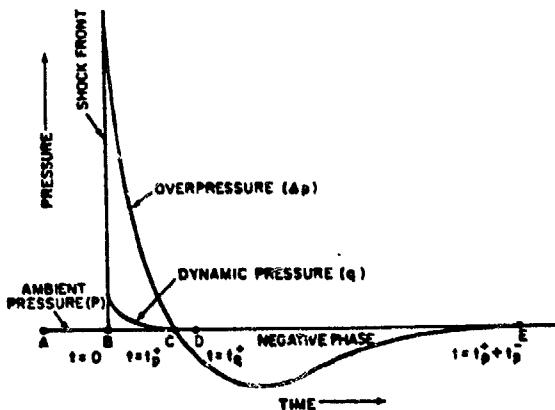


Figure 2-1. Ideal Pressure-Time Relationships for a Blast Wave in the Low Pressure Region (below 5 psi)

pressure then follows an approximately exponential decline to a negative value, i.e., to a pressure below ambient, and gradually returns to zero. The phase that is above ambient pressure (between points B and C) is termed the positive phase; the phase that is below ambient pressure

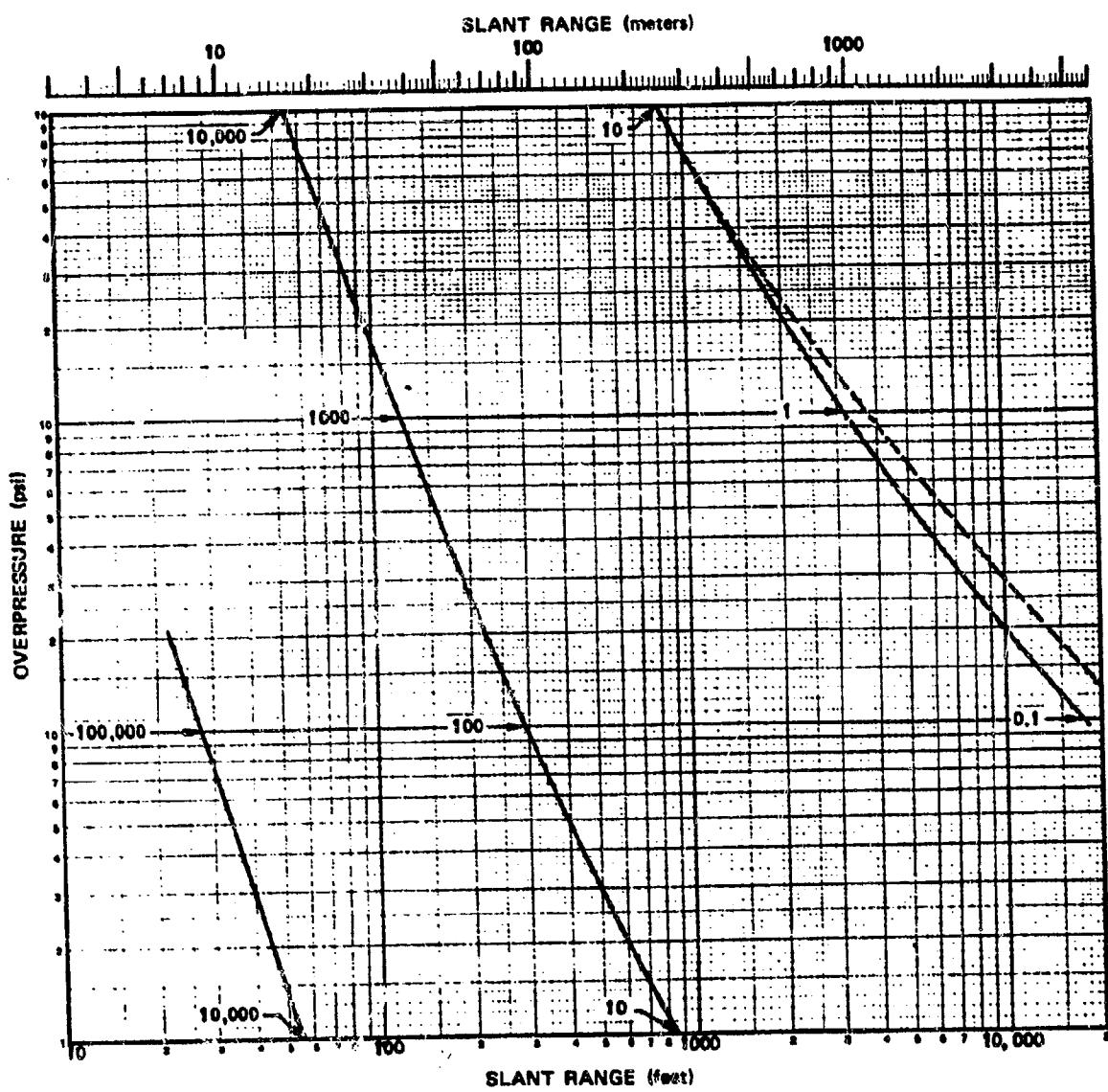


Figure 2-2. Peak Overpressure from a 1 kt Free Air Burst  
in a Standard Sea Level Atmosphere

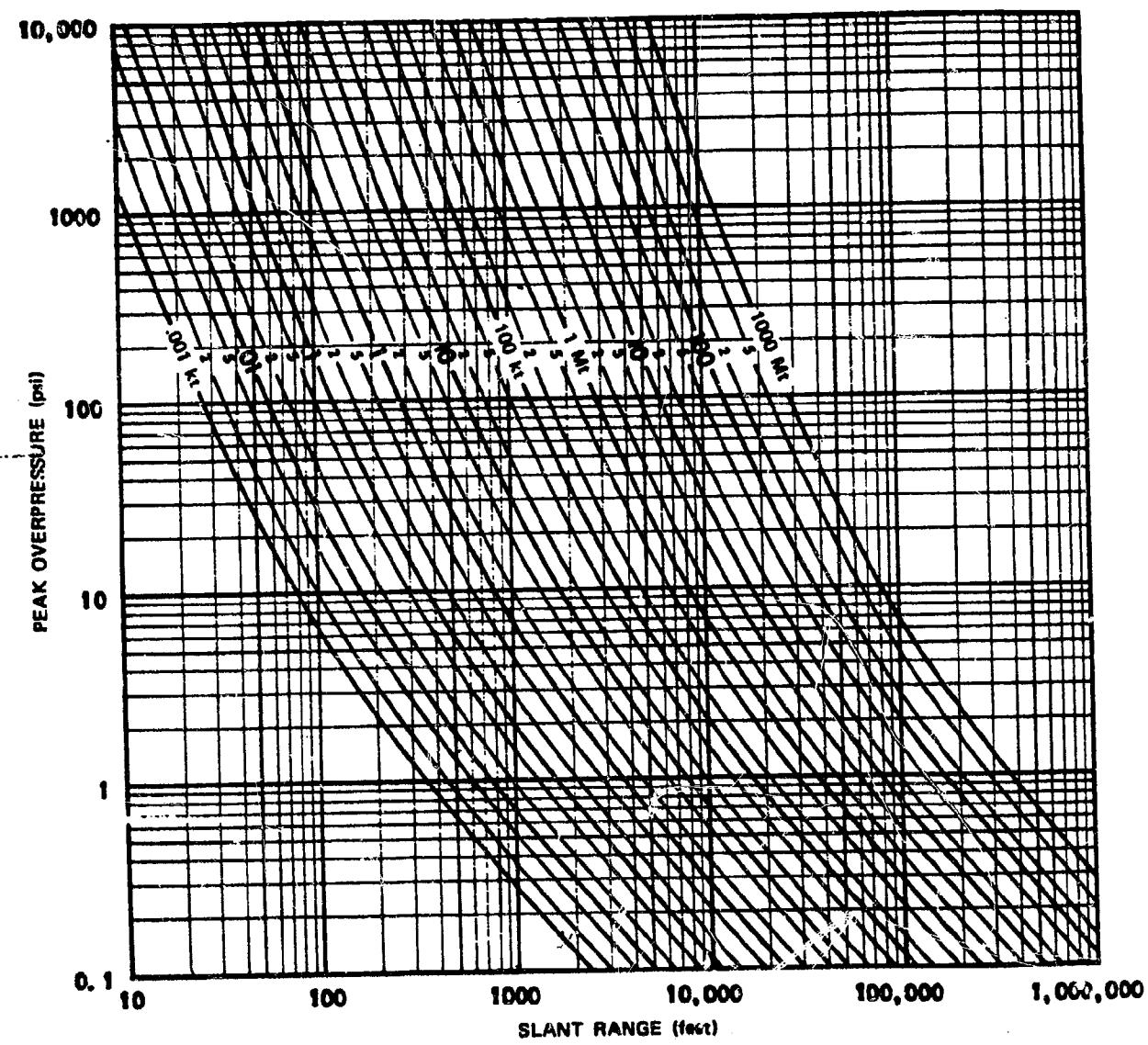


Figure 2-3. Peak Overpressure in Free Air as a Function of Yield and Slant Range

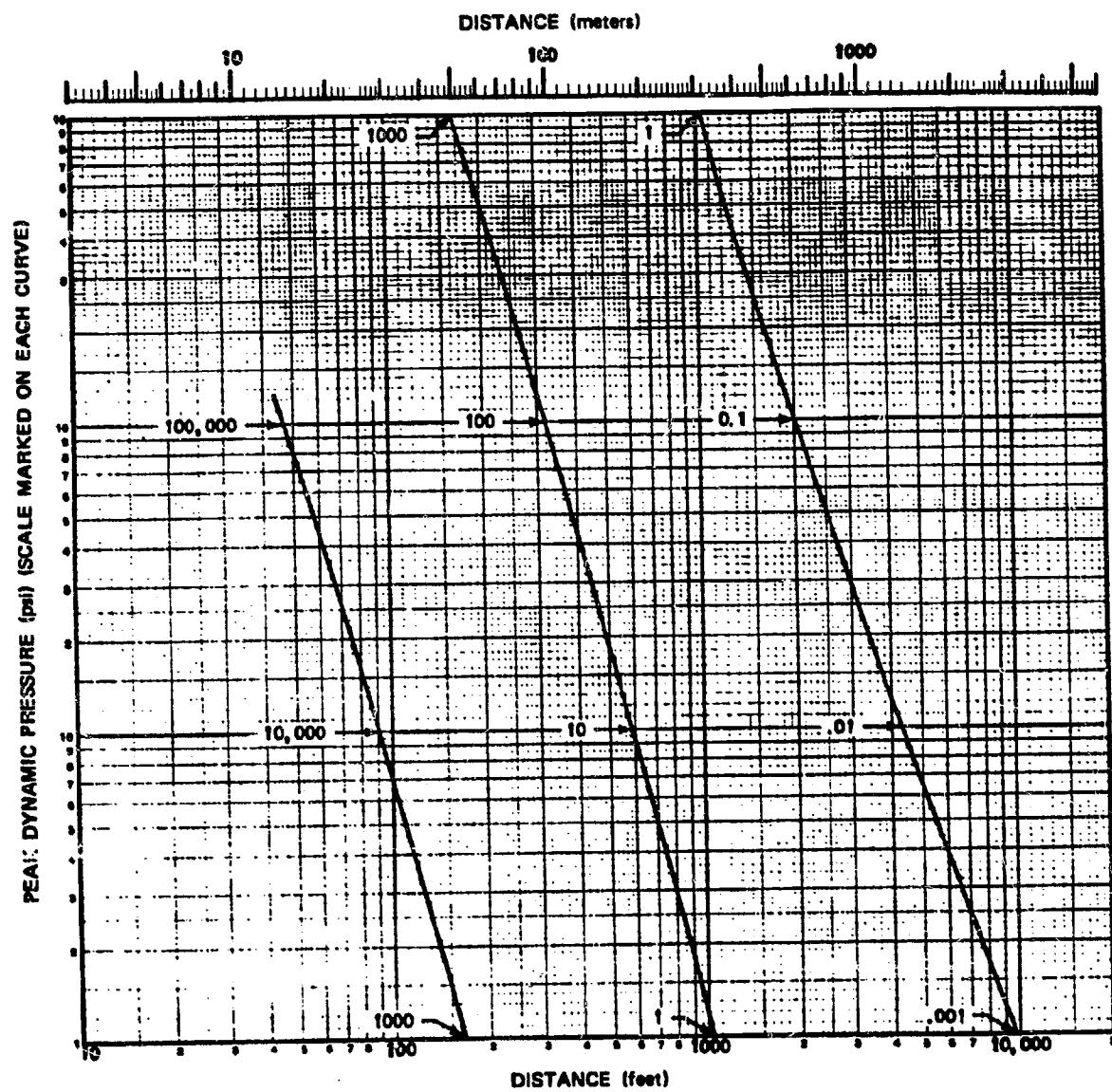


Figure 2-4. Peak Dynamic Pressure from a 1 kt Free Air Burst  
in a Standard Sea Level Atmosphere

### Problem 2-3. Calculation of Time of Arrival of the Shock Front from a Free Air Burst

Figure 2-5 shows the time of arrival of the shock front from a 1 kt free air burst in a standard sea level atmosphere as a function of distance from the burst. Figure 2-5 applies to bursts at altitudes up to 5,000 feet.

**Scaling.** For yields other than 1 kt, scale as follows:

$$\frac{t}{t_1} = W^{1/3} = \frac{d}{d_1}$$

where  $t_1$  is the time of arrival of the shock front at a distance  $d_1$  from a 1 kt explosion, and  $t$  is the corresponding time at a distance  $d$  from a yield of  $W$  kt. At scaled distances greater than 1,500 feet ( $d_1 > 1,500$  feet), the blast wave travels only slightly faster than the speed of sound, and the time of arrival may be approximated by

$$t = \frac{d - 600 W^{1/3}}{1,116} \text{ sec.}$$

where  $d$  is the distance of interest, in feet, from an explosion of yield  $W$  kt, and  $t$  is the time of arrival of the shock front at that distance. The constant 1,116 is the speed of sound in air at a temperature of 59°F (15°C). The term 600  $W^{1/3}$  is a measure of the scaled distance from the burst beyond which the shock wave travels at approximately the speed of sound. The approximation may be extended by noting that the speed of sound increases by about 1 percent for each 10°F rise from the standard 59°F (1.8 percent for each 10°C rise from 15°C) and decreases by the same percentage for corresponding temperature decreases below standard.

#### Example

**Given:** A 100 kt explosion in free air in a sea level atmosphere.

**Find:** The time of arrival of the shock front at a point 40,000 feet from the explosion.

**Solution:** The corresponding distance from a 1 kt explosion is

$$d_1 = \frac{d}{W^{1/3}} = \frac{40,000}{(100)^{1/3}} = 8,600 \text{ feet.}$$

From Figure 2-5, the time of arrival of the shock front at a point 8,600 feet from a 1 kt explosion is 7.2 seconds.

**Answer:** The corresponding time of arrival at a distance of 40,000 feet from a 100 kt explosion is

$$t = t_1 W^{1/3} = 7.2 \times (100)^{1/3} = 33.4 \text{ sec.}$$

Since  $d_1$  is greater than 1,500 feet, an alternate method for obtaining the time of arrival would be to use the equation presented above:

$$t = \frac{d - 600 W^{1/3}}{1,116} = \frac{40,000 - (600)(100)^{1/3}}{1,116}$$
$$= 33.3 \text{ sec.}$$

**Reliability:** The times of arrival obtained from Figure 2-5 are estimated to be within  $\pm 15$  percent of the true value for yields between 1 kt and 20 Mt. The curve may be used with less confidence outside this range of yields.

**Related Material:** See paragraph 2-9. See also paragraph 2-14 for scaling of times of arrival for burst altitudes above 5,000 feet. See paragraph 2-26 for time of arrival of the shock front at points on the surface.

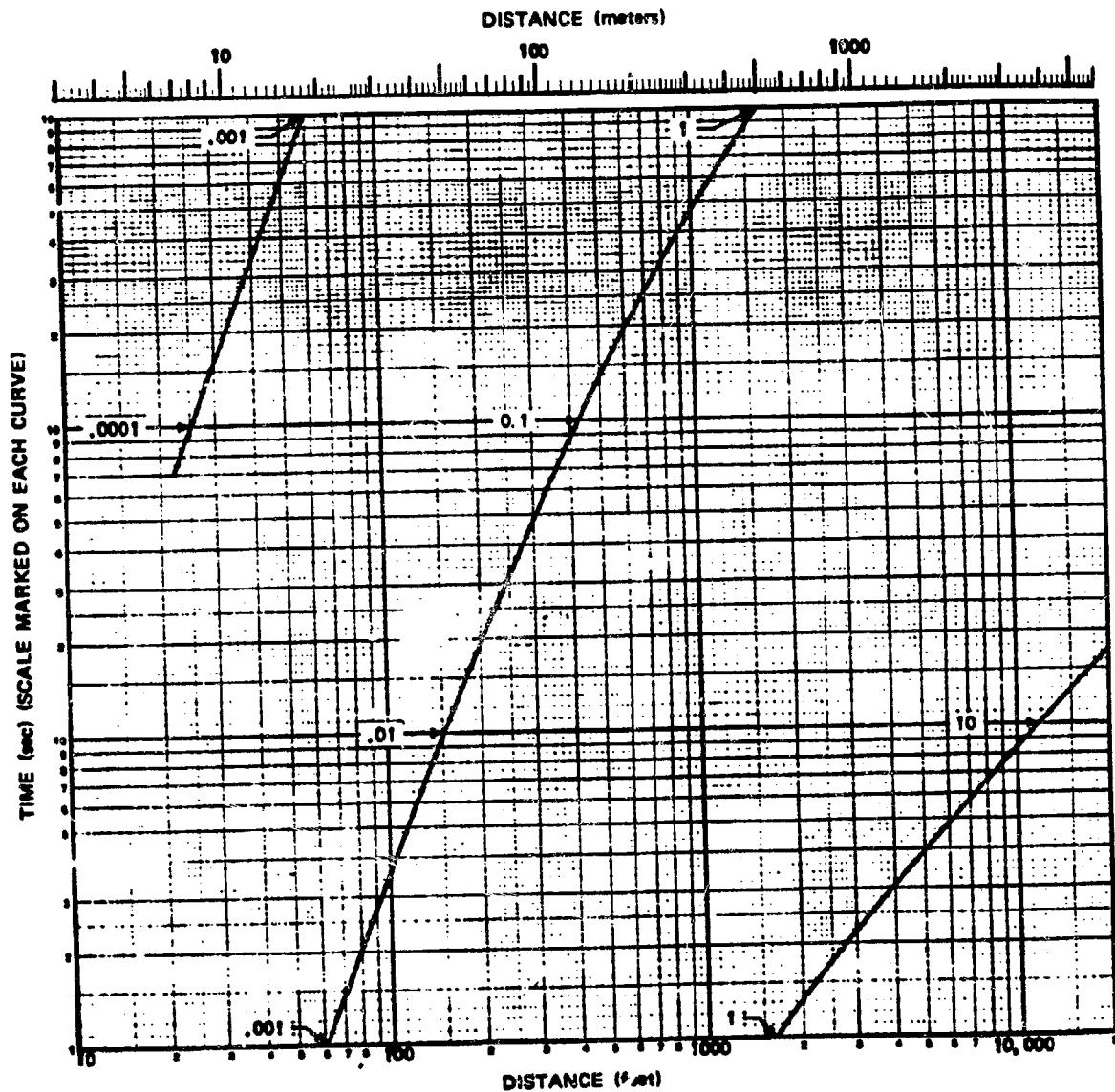


Figure 2-5. Time of Arrival of the Shock Front from a 1 kt Free Air Burst  
in a Standard Sea Level Atmosphere

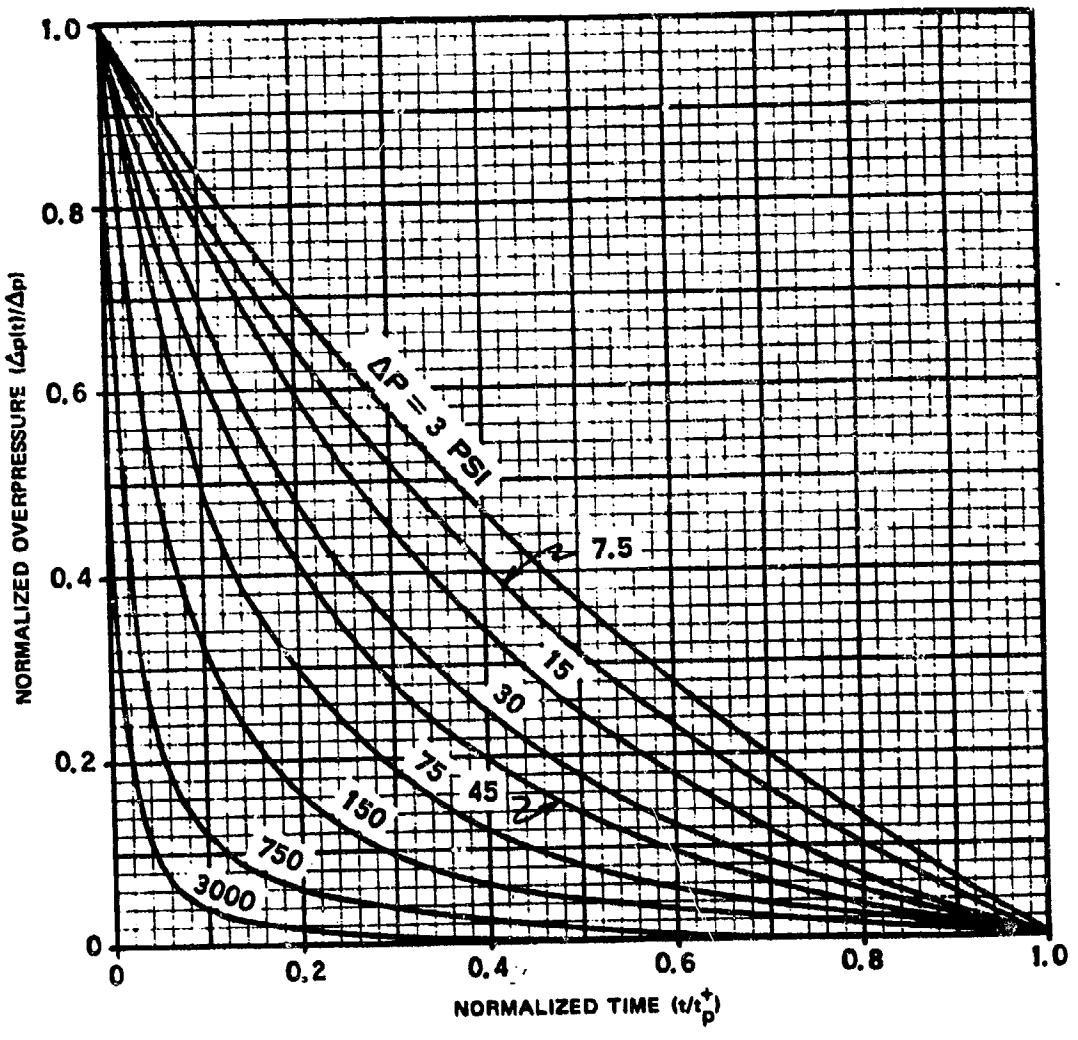


Figure 2-8. Positive Overpressure Waveforms for an Ideal Shock Wave  
in a Standard Sea Level Atmosphere

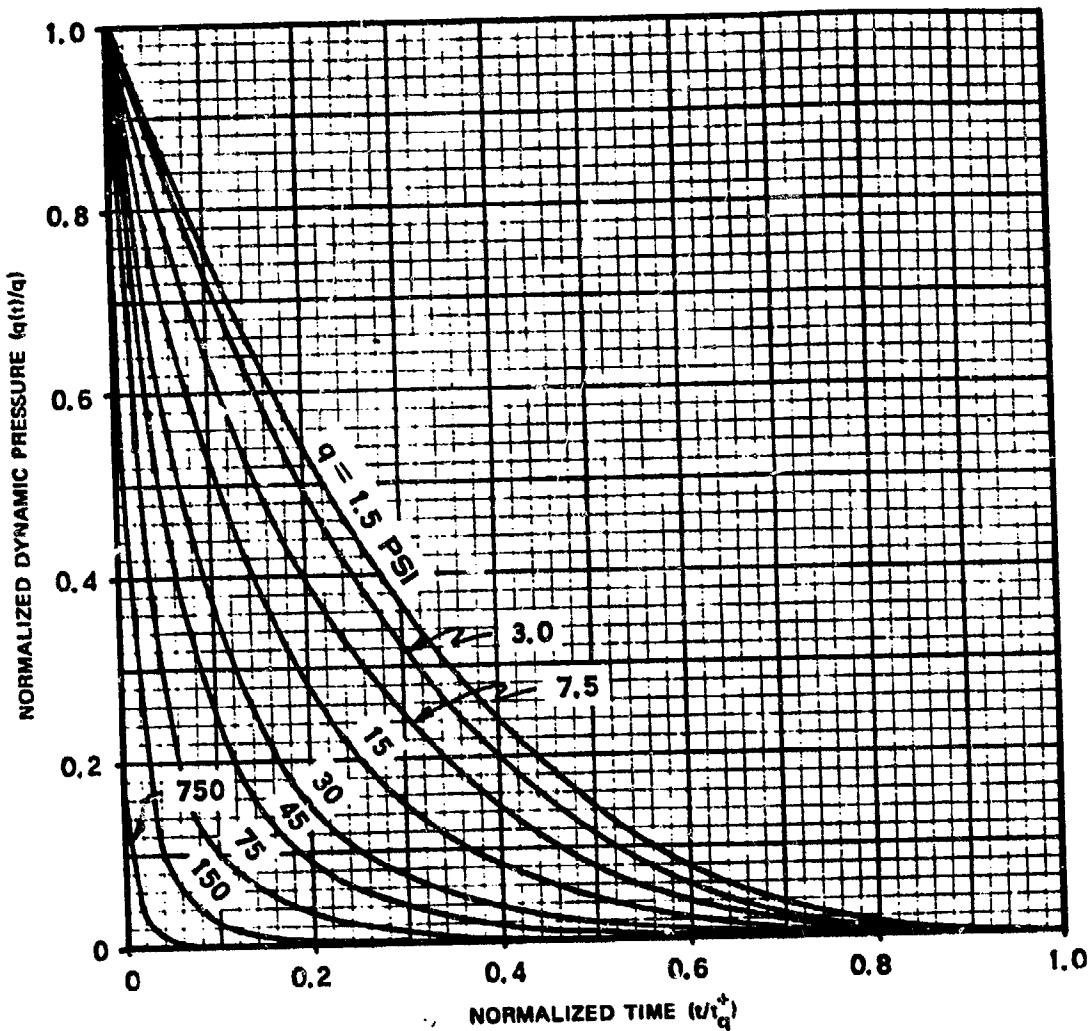


Figure 2-9. Positive Dynamic Pressure Waveforms for an Ideal Shock Wave in a Standard Sea Level Atmosphere

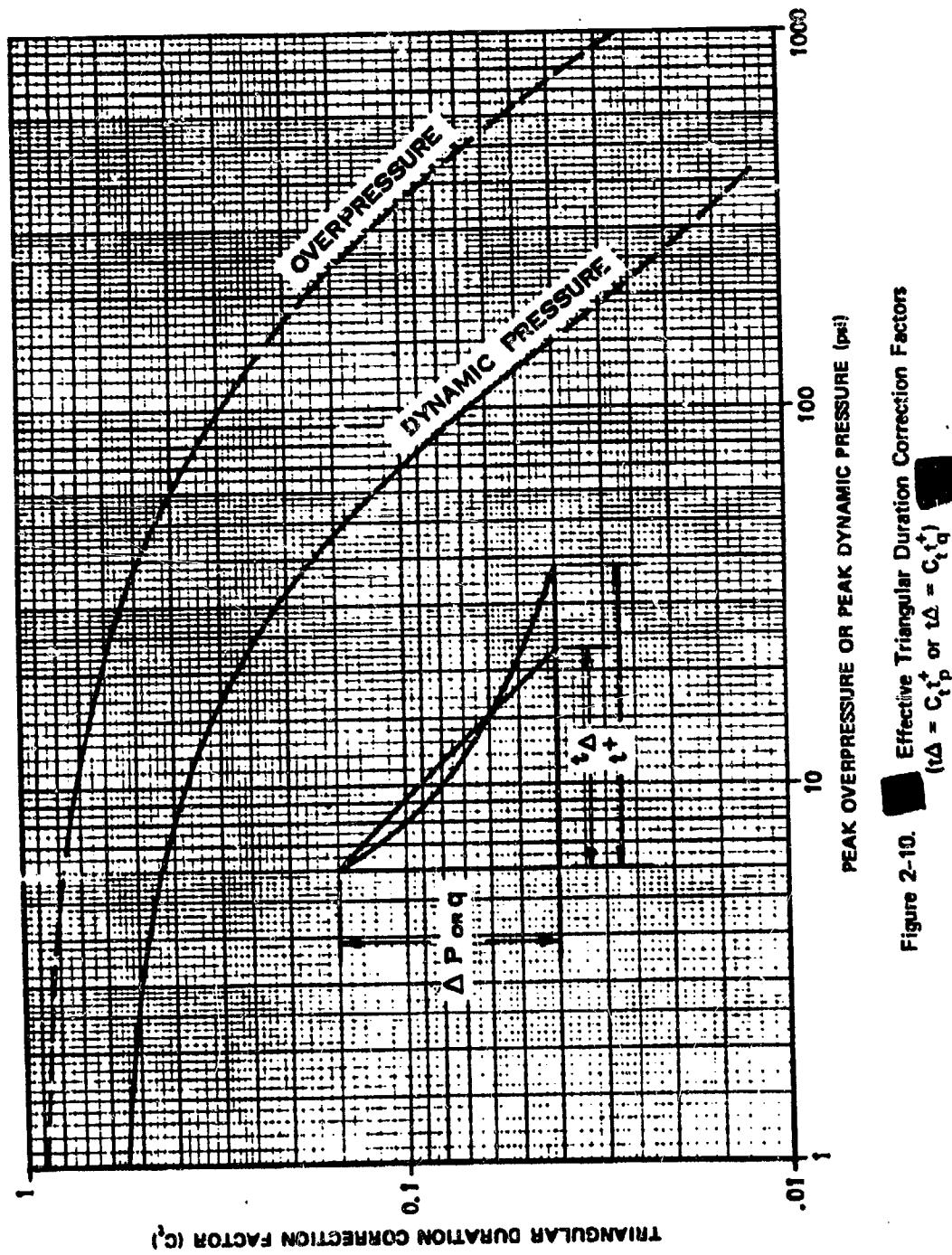


Figure 2-10. Effective Triangular Duration Correction Factors  
 $(t_\Delta = C_t t_p^+ \text{ or } t_\Delta = C_t t_q^+)$

The time duration of the equivalent waveform is called the effective triangular duration of the pressure pulse,  $t_{\Delta}$ , where

$$t_{\Delta} = C_{tp} t_p^+ \quad \text{or} \quad t_{\Delta} = C_{tq} t_q^+$$

for overpressure and dynamic pressure, respectively.

The curves shown in Figures 2-8 and 2-9 are based on theory, and specific estimates of the amount by which actual blast waveforms can be expected to deviate from these curves cannot be made. The effective triangular waveform obtained by use of the triangular duration correction factors shown in Figure 2-10 are simplified representations of the actual waveforms. These triangular waveforms do not represent structural loading functions. The latter are described in Section II, Chapter 9, and specific loading functions used in some of the structural damage analyses for this manual are shown in Figure 11-1.

## RELATIONS BETWEEN SHOCK FRONT PARAMETERS

### 2-13 Generalized Scaling

The concept of scaling various blast wave parameters was introduced in the preceding subsection with reference to the corresponding parameter from a 1 kt explosion in a standard sea level atmosphere. The various curves were presented in terms of absolute values of distance, time, or impulse from a 1 kt explosion in free air in a standard sea level atmosphere. This convention of presenting the data in terms of a 1 kt explosion with scaling laws to relate the parameters to other yields will be adhered to in subsequent sections of this chapter as well as in succeeding chapters; however, the scaling laws are not necessarily limited to scaling from 1 kt. The "Sachs" scaling laws, which pertain to scaling of blast parameters, depend only on the rela-

tive yields of two weapons being considered. Thus, the distance scaling law given in Problems 2-1 and 2-2 could be written

$$\frac{d_2}{d_1} = \left( \frac{W_2}{W_1} \right)^{1/3},$$

where  $d_2$  is the slant range (distance from the point of burst) from an explosion of  $W_2$  kilotons and  $d_1$  is the corresponding distance from an explosion of  $W_1$  kilotons. Likewise, the time and impulse scaling laws given in Problems 2-3 through 2-5 could be written

$$\frac{t_2}{t_1} = \left( \frac{W_2}{W_1} \right)^{1/3}$$

$$\frac{t_{p2}^+}{t_{p1}^+} = \frac{t_{q2}^+}{t_{q1}^+} = \left( \frac{W_2}{W_1} \right)^{1/3},$$

and

$$\frac{I_2}{I_1} = \left( \frac{W_2}{W_1} \right)^{1/3},$$

where, in each case the subscript 2 refers to the value of the parameter for yield  $W_2$  kt, and the subscript 1 refers to the value of the same parameter for a yield of  $W_1$  kt. As mentioned above,  $W_1$  will generally be taken to equal 1 kt as a matter of convenience in this manual.

The scaling laws are derived from the assumption that, at corresponding stages of development, the fireballs from two different nuclear explosions have the same energy per unit mass of air at points that are the same scaled distance from the point of burst. It is also assumed that, as the blast waves propagate outward from the fireballs, they maintain this property of equal energy densities at equal scaled

radii. The blast waves produced by two different nuclear explosions are thus assumed to be similar in all respects except for those relating to differences in size. Since, at a particular stage of development, the average energy densities throughout the two fireballs are equal, fireball volume is directly proportional to the amount of energy required to produce it; therefore, fireball radius is proportional to the cube root of the nuclear yield. Other pertinent distances, such as shock front radius, also follow this cube root scaling law.

#### 2-14 Altitude Scaling

At higher altitudes, where air density is less than at sea level, the reasoning described above still applies. At equal scaled distances and corresponding times, equal masses of air contain equal amounts of energy. Therefore, the volume of a sphere needed to contain a given amount of energy in this manner is larger at higher altitudes where the air is thinner. Specifically, this volume is inversely proportional to air density; and corresponding radii are inversely proportional to the cube root of air density. However, better results are obtained by scaling distance with the cube root of the ambient pressure (up to altitudes of 40,000 feet).\* The altitude scaling for distance is

$$\frac{d_2}{d_1} = \left( \frac{W_2}{W_1} \right)^{1/3} \left( \frac{P_0}{P} \right)^{1/3},$$

where  $P_0$  is the sea level ambient pressure,  $P$  is the ambient pressure at the altitude of interest, and the other quantities are as previously defined.

No pressure scaling factor is required for explosions in a standard sea level atmosphere since the effect of yield is taken into account by distance scaling, and, under similar ambient conditions, the pressures generated by explosions of different yields are equal at scaled distances.

When altitude must be considered, equal "shock strengths" occur at equal scaled distances. The term shock strength means the ratio of the absolute pressure behind the front to the ambient pressure, i.e., the shock strength,  $\xi$ , is,

$$\xi = \frac{\Delta p + P}{P} = \frac{\Delta p}{P} + 1,$$

which is a dimensionless quantity. At equal scaled distances,

$$\xi = \xi_0,$$

where  $\xi$  is the shock strength at the altitude of interest and  $\xi_0$  is the shock strength at the same scaled distance at sea level. This may be written

$$\frac{\Delta p}{P} + 1 = \frac{\Delta p_0}{P_0} + 1,$$

which leads to

$$\frac{\Delta p}{P} = \frac{\Delta p_0}{P_0},$$

The reasons for dismissing density in favor of pressure as a basis for calculating the altitude scaling factor for distance may be described as follows. In the early fireball region, where energy absorbed from the weapon completely overshadows any effect of initial air temperature, it would be expected that the only important question is the number of air atoms present. In this region, density scaling is appropriate. Examples of equations that are based on density scaling are given in paragraph 2-44; however, the situation is different over most of the range through which the blast wave propagates. Shock-front parameters correspond more directly to the pressure ratio across the shock front than to the density ratio. After the shock front reaches air not directly heated by the nuclear source, pressure ratio provides the better basis for scaling. The corresponding energy model for Sach's scaling laws is that two free air blast waves are equivalent when the ratio:

$$\frac{\text{energy enclosed by the shock front}}{\text{ambient internal energy of the air enclosed by the front}}$$

is the same for both blast waves. This model may be derived by noting that the pressure of an ideal gas is proportional to internal energy per unit volume.

and the altitude scaling for pressure is

$$\frac{\Delta p}{\Delta p_0} = \frac{P}{P_0},$$

where  $\Delta p$  is the overpressure at the altitude of interest,  $\Delta p_0$  is the overpressure at the same scaled distance at sea level, and  $P$  and  $P_0$  are the corresponding ambient pressures. This same relation holds for other characteristic pressures, such as the total pressure behind the shock front and the dynamic pressure.

Two factors influence time of arrival: the speed of the blast wave and the distance that it must travel. Under standard sea level conditions, the speed of the blast wave depends on overpressure, which, in turn, depends only on scaled distance from the burst. When the scaling problem is not limited to the case of a sea level atmosphere, the assumed relation between shock speed and overpressure must be stated in more general terms: for a given shock strength (and hence for a given scaled distance), the Mach number of the shock front is always the same. As altitude is increased, the time required for the shock to reach a given scaled distance increases because (1) the actual distance is farther and (2) at the lower temperatures generally associated with higher altitudes, sound speed is slower (therefore, a given Mach number corresponds to a slower shock front speed). The altitude scaling for time is

$$\frac{t_2}{t_1} = \left( \frac{W_2}{W_1} \right)^{1/3} \left( \frac{P_0}{P} \right)^{1/3} \left( \frac{T_0}{T} \right)^{1/2},$$

where  $T_0$  is the absolute temperature at sea level and  $T$  is the absolute temperature at the altitude of interest. The factor  $T_0^{1/2}/T^{1/2}$  appears in this expression because sound speed is proportional to the square root of absolute temperature. The factors involving yield and pressure are those in scaling distance. The same scaling rela-

tionships may be used for scaling the positive duration of the overpressure.

The altitude scaling for impulse may be obtained by multiplying the scaling equation for time by the scaling equation for pressure, i.e.,

$$\frac{I_2}{I_1} = \left( \frac{W_2}{W_1} \right)^{1/3} \left( \frac{P}{P_0} \right)^{2/3} \left( \frac{T_0}{T} \right)^{1/2}.$$

In the foregoing scaling relations, the subscript 0 was defined to represent ambient conditions (pressure or absolute temperature) at sea level. Strictly speaking this is not necessary, since the ratios of the values are the important quantities. However, since these equations are for use with the curves presented in the previous subsection, which are all shown for standard sea level conditions, it is convenient to scale from those conditions. In order to facilitate calculations based on the preceding equations, the following factors have been defined and are tabulated in Tables 2-1 and 2-2:

$$S_d = \left( \frac{P_0}{P} \right)^{1/3}$$

$$S_p = \frac{P}{P_0}$$

$$S_t = \left( \frac{P_0}{P} \right)^{1/3} \left( \frac{T_0}{T} \right)^{1/2},$$

so that if, as usual,  $W_1$  is taken to be 1 kt, the equations may be shown in an abbreviated form as follows:

$$d = d_1 W^{1/3} S_d$$

$$\Delta p = \Delta p_0 S_p$$

$$q = q_0 S_p$$

$$t = t_1 W^{1/3} S_t$$

$$I = I_1 W^{1/3} S_p S_t.$$

Table 2-1. Data Based on U.S. Standard Atmosphere,  
1962 English Units

Altitude feet	Temperature °F	Pressure psi	Altitude Scaling Factors			Density Ratio* $\rho/\rho_0$	Temperature Ratio $T/T_0$	Sound Speed ft/sec
			$S_d$	$S_p$	$S_t$			
0	59.0	14.696	1.000	1.0000	1.000	1.0000	1.000	1116
1 000	-55.4	14.17	1.012	.9644	1.016	.9711	.993	1113
2 000	51.9	13.66	1.025	.9298	1.032	.9428	.986	1109
3 000	48.3	13.17	1.037	.8963	1.048	.9151	.979	1105
4 000	44.7	12.69	1.050	.8637	1.065	.8881	.973	1101
5 000	41.2	12.23	1.063	.8321	1.082	.8617	.965	1097
10 000	23.4	10.11	1.133	.6878	1.174	.7386	.931	1077
15 000	5.5	8.297	1.210	.5646	1.278	.6295	.897	1057
20 000	-12.3	6.759	1.295	.4599	1.395	.5332	.863	1037
25 000	-30.0	5.461	1.391	.3716	1.528	.4486	.828	1016
30 000	-47.8	4.373	1.498	.2975	1.681	.3747	.794	995
35 000	-65.6	3.468	1.618	.2360	1.857	.3106	.740	973
40 000	-69.7	2.730	1.753	.1858	2.021	.2471	.722	968
45 000	-69.7	2.149	1.898	.1462	2.189	.1945	.752	968
50 000	-69.7	1.692	2.056	.1151	2.371	.1531	.752	968
55 000	-69.7	1.332	2.226	.09063	2.567	.1206	.752	968
60 000	-69.7	1.049	2.411	.07137	2.780	.09492	.752	968
65 000	-69.7	.826	2.611	.05620	3.011	.07475	.752	968
70 000	-67.4	.651	2.826	.04429	3.250	.05857	.756	971
75 000	-64.7	.514	3.058	.03496	3.504	.04591	.762	974
80 000	-62.0	.406	3.307	.02765	3.777	.03606	.767	978
85 000	-59.3	.322	3.574	.02190	4.068	.02837	.772	981
90 000	-56.5	.255	3.861	.01738	4.379	.02236	.777	984
95 000	-53.8	.203	4.168	.01381	4.711	.01765	.782	988
100 000	-51.1	.162	4.497	.01100	5.067	.01396	.788	991
110 000	-41.3	.103	5.225	7.011-3	5.817	8.692-3	.807	1003
120 000	-26.1	.0667	6.040	4.537	6.607	5.428	.836	1021
130 000	-10.9	.0438	6.948	2.982	7.470	3.446	.865	1038
140 000	4.3	.0292	7.953	1.988	8.410	2.222	.894	1056
150 000	19.4	.0197	9.064	1.343	9.431	1.634	.924	1073
160 000	27.5	.0135	10.29	9.176-4	10.62	9.770-4	.939	1082
170 000	27.5	9.23-3	11.68	6.283	12.05	6.690	.939	1082
180 000	18.9	6.31	13.26	4.292	13.80	4.552	.923	1072
190 000	8.1	4.27	15.09	2.908	15.89	3.225	.902	1060
200 000	-2.7	2.87	17.23	1.954	18.36	2.217	.881	1048

NOTE: 7.011-3 means  $7.011 \times 10^{-3}$

$$\rho_0 = 2.38 \times 10^{-3} \text{ slugs/ft}^3$$

$$= 7.65 \times 10^{-2} \text{ lbm/ft}^3$$

Table 2-2. Data Based on U.S. Standard Atmosphere,  
1962 Metric Units

Altitude km	Temperature °C	Pressure		Altitude Scaling Factors			Density Ratio* $\rho/\rho_0$	Temperature Ratio $T/T_0$	Sound Speed m/sec
		millibars	psi	$S_d$	$S_p$	$S_t$			
0	15.0	1013.25	14.696	1.000	1.0000	1.000	1.000	1.000	340.3
.5	11.8	954.61	13.845	1.020	.9421	1.026	.953	.989	338.4
1.0	8.5	898.76	13.035	1.041	.8870	1.053	.907	.977	336.4
1.5	5.3	845.60	12.264	1.062	.8345	1.081	.864	.966	334.5
2.0	2.0	795.01	11.531	1.084	.7846	1.110	.822	.955	332.5
3.0	-4.5	701.21	10.170	1.131	.6920	1.171	.742	.932	328.6
4.0	-11.0	616.60	8.943	1.180	.6085	1.237	.669	.910	324.6
5.0	-17.5	540.48	7.839	1.233	.5334	1.309	.601	.887	320.5
6.0	-24.0	472.18	6.848	1.290	.4660	1.387	.539	.865	316.5
7.0	-30.4	411.05	5.962	1.351	.4057	1.472	.482	.842	312.3
8.0	-36.9	356.52	5.171	1.416	.3519	1.564	.429	.820	308.1
9.0	-43.4	308.01	4.467	1.487	.3040	1.666	.381	.797	303.8
10	-49.9	265.00	3.843	1.564	.2615	1.777	.338	.775	299.5
12	-56.5	193.99	2.814	1.735	.1915	2.001	.255	.752	295.1
14	-63.5	141.70	2.055	1.927	.1399	2.222	.186	.752	295.1
16	-56.5	103.53	1.502	2.139	.1022	2.467	.136	.752	295.1
18	-56.5	75.65	1.097	2.375	.07466	2.739	.0993	.752	295.1
20	-56.5	55.29	.802	2.636	.05457	3.040	.0726	.752	295.1
22	-54.6	40.47	.587	2.925	.03995	3.359	.0527	.759	296.4
24	-52.6	29.72	.431	3.243	.02933	3.706	.0383	.765	297.7
26	-50.6	21.88	.317	3.591	.02160	4.086	.0280	.772	299.1
28	-48.6	16.16	.234	3.973	.01595	4.500	.0205	.779	300.4
30	-46.6	11.97	.174	4.391	.01181	4.952	.0150	.786	301.7
32	-44.7	8.89	.129	4.848	8.774-3	5.445	.0111	.793	303.0
34	-39.4	6.63	.0962	5.345	6.547	5.935	8.07-3	.811	306.5
36	-33.9	4.99	.0723	5.880	4.920	6.452	5.92	.830	310.1
38	-28.3	3.77	.0547	6.453	3.722	7.000	4.38	.850	313.7
40	-22.8	2.87	.0416	7.067	2.834-3	7.581	3.26-3	.869	317.2
42	-17.3	2.20	.0319	7.723	2.171	8.196	2.44	.888	320.7
44	-11.7	1.69	.0246	8.424	1.673	8.844	1.84	.907	324.1
46	-6.2	1.31	.0190	9.171	1.296	9.529	1.40	.926	327.5
48	-2.5	1.02	.0148	9.968	1.010	10.29	1.07	.939	329.8
50	-2.5	.798	.0116	10.83	7.874-4	11.17	8.38-4	.939	329.8
52	-2.5	.622	.00903	11.76	6.141	12.14	6.54	.939	329.8
54	-5.6	.485	.00703	12.78	4.786	13.27	5.15	.929	327.9
56	-9.5	.377	.00546	13.91	3.716	14.54	4.06	.915	325.5
58	-13.5	.291	.00423	15.15	2.876	15.96	3.19	.901	323.1
60	-17.4	.225	.00326	16.52	2.217-4	17.54	2.50-4	.888	320.6

NOTE:  $8.774-3$  means  $8.774 \times 10^{-3}$

\* $\rho_0 = 1.225 \times 10^{-3} \text{ gm/cm}^3 = 1.225 \text{ kg/m}^3$ .

## 2-15 Velocity and Density

For most blast-wave calculations, peak overpressure and peak dynamic pressure provide a satisfactory description of the shock front; but in a few situations a more detailed description is required. An example is the problem of dynamic pressure acting on a moving target. For this problem, the dynamic pressure data presented in paragraph 2-8 and Problem 2-2 cannot be used; instead, the dynamic pressure must be calculated from its defined value,

$$q = \frac{1}{2} \rho_s u^2,$$

where  $u$  is peak wind velocity with respect to the target. To calculate this velocity, the peak wind velocity with respect to the ambient air must be evaluated first. This velocity may be calculated from the equation

$$u = \frac{c \Delta p}{\gamma P} \left( 1 + \frac{\gamma + 1}{2\gamma} \cdot \frac{\Delta p}{P} \right)^{-1/2}$$

where  $c$  is the ambient speed of sound in air,  $\gamma$  is the ratio of the specific heat of air at constant pressure to the specific heat of air at constant volume, and the other quantities have been defined. The value of  $\gamma$  for air at moderate temperatures and pressures is 1.4. Using this value, the peak wind velocity becomes

$$u = \frac{5 \Delta p}{7P} \cdot \frac{c}{\sqrt{1 + 6 \Delta p / 7P}}$$

The value of the density,  $\rho_s$ , of the air behind the shock front is related to the ambient density,  $\rho$ , by

$$\frac{\rho_s}{\rho} = \frac{2\gamma P + (\gamma + 1)\Delta p}{2\gamma P + (\gamma - 1)\Delta p}$$

which becomes

$$\frac{\rho_s}{\rho} = \frac{7 + 6 \Delta p / P}{7 + \Delta p / P}$$

for  $\gamma = 1.4$ . A third equation of interest is that for the shock velocity,  $U$ , which is

$$U = c \left( 1 + \frac{\gamma + 1}{2\gamma} \cdot \frac{\Delta p}{P} \right)^{1/2},$$

which becomes

$$U = c \left( 1 + \frac{6 \Delta p}{7P} \right)^{1/2}$$

for  $\gamma = 1.4$ . These are three of the Rankine-Hugoniot equations, which are described in more detail in Appendix A.

A consistent set of units must be used in the equations presented above; however, since the pressures always appear as a ratio, if consistent units are used for the specific heats to obtain  $\gamma$ , as was done in obtaining a value of 1.4 for moderate temperatures and pressures, the only precaution necessary is to express  $\Delta p$  and  $P$  in the same units. Then  $u$  and  $U$  will be in the same units as  $c$ , and  $\rho_s$  will be in the same units as  $\rho$ . Appendix B provides conversion factors for the various units. As mentioned previously, these equations and others are discussed in more detail in Appendix A. For convenience, a normalized set of values of these shock front parameters is shown in Figure 2-12. Since all quantities are normalized with respect to local (ambient) atmospheric conditions in Figure 2-12, neither yield nor altitude scaling is necessary. The constants to which the values of the various parameters are normalized may be obtained from Tables 2-1 or 2-2.

It is frequently convenient to relate the peak dynamic pressure and the reflected overpressure to the incident overpressure. Figure 2-13 shows such a relationship. The data in Figure 2-13 may be obtained from other figures and

[REDACTED]  
depends on the peak overpressure,  $\Delta p$ , and the peak dynamic pressure,  $q$ , of the incident blast wave. An approximate equation for peak reflected overpressure (valid for shock strengths up to 6 or 7, i.e., or overpressures of about 75 to 90 at sea level) is

$$\Delta p_r = 2\Delta p + (\gamma + 1)q,$$

where  $\Delta p_r$  is the peak reflected overpressure, and the other quantities have been defined. If  $\gamma$  is taken to be 1.4 (see paragraph 2-15),

$$\Delta p_r = 2\Delta p + 2.4 q.$$

Using the defined value of  $q$ ,

$$q = \frac{1}{2} \rho_i u^2,$$

and the Rankine-Hugoniot equations introduced in paragraph 2-15 leads to the relation

$$q = \frac{\Delta p^2}{2\gamma P + (\gamma + 1)\Delta p},$$

and, if  $\gamma = 1.4$ , this becomes

$$q = \frac{5}{2} \cdot \frac{\Delta p^2}{7P + \Delta p}.$$

Inserting this value of  $q$  into the equation for the reflected overpressure gives

$$\Delta p_r = 2\Delta p \left( \frac{1 + 4\Delta p/P}{1 + \Delta p/P} \right)$$

[REDACTED] This equation shows that, in the limiting case of low overpressures (at overpressures sufficiently low that dynamic pressure is negligible), the peak reflected overpressure is simply twice the peak overpressure of the reflected

wave. This relation is a general one that is valid for any angle of incidence. It is valid because at low overpressures the reflected shock wave has the same strength as the incident shock wave, and the peak reflected overpressure is the sum of the overpressures of the incident and reflected waves.

[REDACTED] As  $\Delta p$  becomes very large the equation given above indicates that the peak reflected overpressure rises to eight times the incident

[REDACTED] No derivation of this expression for  $q$  will be provided, but one numerical example will be shown below to establish its validity. The values for  $\rho_i$  and  $u$  shown in paragraph 2-15 for  $\gamma = 1.4$  are

$$\rho_i = \rho \left( \frac{7P + 6\Delta p}{7P + \Delta p} \right)$$

$$u = \frac{5\Delta p}{7P} \cdot \frac{c}{\sqrt{\frac{7P + 6\Delta p}{7P}}}$$

$$u^2 = \frac{25\Delta p^2}{7P} \cdot \frac{c^2}{7P + 6\Delta p}$$

$$q = \frac{1}{2} \left[ \rho \left( \frac{7P + 6\Delta p}{7P + \Delta p} \right) \right] \left[ \frac{25\Delta p^2}{7P} \cdot \frac{c^2}{7P + 6\Delta p} \right]$$

Rearranging terms in this expression leads to

$$q = \left[ \frac{5}{2} \cdot \frac{\Delta p^2}{7P + \Delta p} \right] \left[ \frac{5}{7} \cdot \frac{\rho c^2}{P} \right].$$

It will be noted that the first term in brackets corresponds to the expression previously given for  $q$ . It should also be noted that the second term in brackets is dimensionless since both the numerator and denominator are in units of force per unit area. The sea level values of the parameters in the second term are

$$\rho = 2.38 \times 10^{-3} \text{ slugs/ft}^3$$

$$c = 1,116 \text{ ft/sec}$$

$$P = 2,117 \text{ pounds/ft}^2$$

Inserting these values into the second term gives

$$\left( \frac{5}{7} \right) \frac{(2.38 \times 10^{-3})(1,116)^2}{2,117} = 1.$$

overpressure. However, this equation fails at these high overpressures. It is based on the assumption that  $\gamma$  has a constant value, but  $\gamma$  drops to values below 1.4 in strongly shocked air. More accurate calculations for the high shock strengths show higher reflected overpressures than this equation predicts.

Users of this manual will not use the equation for reflected overpressure very frequently; they will use it principally as an aid in understanding the reflection process. The numerical results that ordinarily are needed already have been calculated and have been incorporated in the various figures in this chapter.

### 2-18 Regular and Mach Reflection

The interaction between a blast wave and the surface of the earth is shown schematically in Figure 2-15. The reflected wave near the surface travels through a region that is heated and made denser than the ambient atmosphere by the incident shock front as it passes. Since shock front velocity is greater in heated air, a portion of the reflected shock can, under

appropriate conditions, overtake and merge with the incident shock. This forms a single shock front, called the Mach stem, which produces higher peak overpressures and peak dynamic pressures at or near the surface than would be produced at the same distance in free air. The characteristics of the blast wave at or near the surface depend on yield, height of burst, and properties of the reflecting surface. The region where the incident and reflected shocks have not merged to form a Mach stem is referred to as the region of regular reflection; the region where they have merged is referred to as the region of Mach reflection. As the Mach stem travels along the surface, the triple point (the point of intersection of the incident wave, the reflected wave, and the Mach stem) rises.

### 2-19 Blast Phenomena for Bursts in the Transition Zone

When the height of a burst is less than about  $160W^{1/3}$  feet, additional phenomena affect the blast wave. If the burst is very close to the surface, within about  $5W^{0.3}$  feet, fusion of the incident and reflected waves is complete, and the blast wave has a single, approximately hemispherical shock front. A burst this close to the surface is called a contact surface burst. The single shock front of a contact surface burst may be considered a special case of Mach stem formation in which the stem extends over the entire shock front.

If a warhead is detonated above  $5W^{0.3}$  feet but below about  $160W^{1/3}$  feet, the portion of the reflected shock front that passes through the central region of the fireball moves fast enough to overtake the incident wave and fuse with it. The blast wave thus forms a single shock front above the fireball, a double shock front between this area of fusion and the triple point (or the ground if the Mach stem is absent), and a single shock front below the triple point. The strength of the fused wave above the fireball

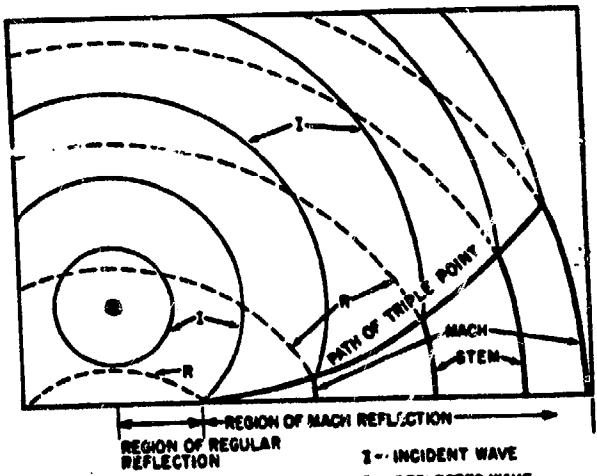


Figure 2-15. Growth of the Mach Stem (Idealized)

[REDACTED]  
varies with burst height. Unless the burst is considerably closer to the surface than  $160W^{1/3}$ , the reflected wave only makes a weak contribution to this portion of the blast wave. One reason for this weak contribution is that the reflected shock front is strongly attenuated by spherical divergence (produced by the lens-like action of the fireball). Another factor may be the attenuation resulting from the dissipation of energy when the shock front passes through heated air. The region between about  $5W^{0.3}$  feet and  $160W^{1/3}$  feet is called the transition zone, and a burst within this region is a surface burst for purposes of air blast phenomena.

[REDACTED] If a burst is above the transition zone, fusion of the incident and reflected shock fronts is confined to the Mach stem region, and the burst is called an air burst. An air burst that only produces weak reflection effects at the surface is called a free air burst. The properties of such explosions were discussed in paragraphs 2-7 through 2-12. A low air burst is sometimes called a near surface burst. As described in Chapter 1, the limits of the scaled heights of burst as well as the scaling laws for defining the various zones are different for the various phenomena. The definitions given above for the heights of a contact surface burst, a surface burst, the transition zone, and a free air burst only apply to air blast phenomena.

## 2-20 Near-Ideal and Nonideal Surface Conditions

[REDACTED] An ideal surface is defined as a perfectly flat surface that reflects all of the energy, both thermal and blast, that strikes it. No part of the surface of the earth is ideal in this sense, but a few surfaces act essentially as ideal. These surfaces are classified as near-ideal. A near-ideal surface is one that provides blast wave phenomena that are essentially free of the mechanical and thermal effects that are described in succeeding paragraphs. Some of the surfaces considered

most nearly ideal are reasonably flat and consist of ice, hard-packed snow, frozen tundra, and water.

[REDACTED] The phenomena that are characteristic of a mechanically nonideal surface are illustrated best by examples. When a blast wave that is traveling along a flat plain suddenly encounters a rising slope, a stronger overpressure impulse is produced than if the surface had remained flat. Buildings can decrease overpressure in certain areas by providing shielding from the blast; they also can increase overpressure in other areas by reflecting the blast wave. A very thick layer of snow will absorb a large amount of the blast energy that strikes it, which will produce a lower reflected overpressure than a near-ideal reflecting surface.

[REDACTED] In most cases, blast wave calculations over mechanically nonideal surfaces are performed by first finding the desired blast parameters over a near-ideal surface. The results thus obtained then are corrected to account for the changes in blast wave properties produced by the mechanically nonideal features of the surface.

[REDACTED] The phenomena produced by a thermally nonideal surface can distort overpressure and dynamic pressure waveforms of the blast wave at the surface. Whether or not the distortions are significant depends on height of burst and yield as well as the properties of the surface. Severe thermal effects are accompanied by the formation of a precursor, which alters several blast parameters severely. Precursors are described in the following paragraph.

[REDACTED] Thermally nonideal surfaces may be defined loosely as those that absorb heat; thermally near-ideal surfaces reflect thermal energy incident upon them. Radiation from the fireball incident on thermally nonideal surfaces produces a layer of heated air that interacts with the blast wave, and which may form a precursor. This type of surface is sufficiently common that nearly all blast wave data at the surface are pre-

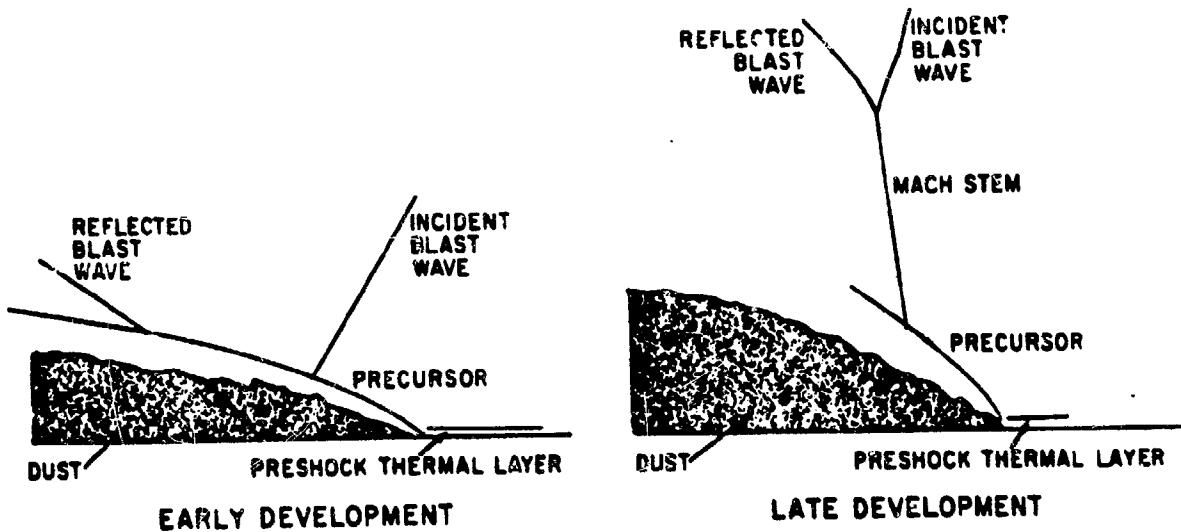


Figure 2-16. Precursor Characteristics

sented as two sets of charts: one set for near-ideal surfaces, and one set for thermally non-ideal surfaces. Methods of classifying surfaces with respect to thermal properties are discussed in paragraph 2-22.

## 2-21 Precursor Formation

Thermal radiation from the fireball of a surface or near-surface burst can cause the surface or the earth in the vicinity of ground zero to reach a temperature of several thousand degrees in a short time. "Popcorning" may then occur, wherein volatile substances vaporize explosively, throwing hot particles into the air. This (or similar heat transfer processes) produces a layer of heated air just above the surface almost instantly. When the height of burst is less than  $650W^{1/3}$  feet, and when the earth is dusty and dark in color, the thermal layer usually is intense enough to disturb the blast wave near the ground surface seriously.

Under ideal conditions, none of the energy in a blast wave can propagate faster than

the shock front itself; thus, the shock front forms an envelope within which the blast energy is confined. The thermal layer, however, provides a way for this energy to penetrate the confining surface. The energy in a blast wave propagates faster through hotter air, and the thermal layer allows energy to move ahead of the main shock front, which produces shock wave patterns such as those shown in Figure 2-16. The auxiliary blast wave that moves ahead of the main shock wave is called a precursor.

Although the details of precursor formation are not well understood, its general patterns of pressure and flow have been observed and can be described. After the precursor forms, the main shock front no longer extends to the ground; if it does, the lower portion is so weakened and distorted that it is not easily recognized. Between the ground and the bottom edge of the main shock wave is a gap, probably not sharply defined, through which the energy that feeds the precursor may flow. Wind speed in this gap is higher than the wind speed behind the

main shock front.\* Overpressure in the gap is lower than that behind the main shock front, and it is this overpressure difference which produces the higher than ideal wind velocities in the gap.

Ahead of the main shock front, the blast energy in the precursor is free not only to follow the rapidly moving shock front in the thermal layer, but also to propagate upward into the undisturbed air ahead of the main shock front. A near-equilibrium condition exists, because the energy continually fed into the precursor from the main blast wave tends to strengthen the precursor shock front, and the diverging flow pattern within the precursor itself tends to weaken it.

This description of what happens within a precursor explains some of the precursor characteristics shown in Figure 2-16. Only that portion of the precursor shock front remaining in the thermal layer travels faster than the main shock front; the energy diverging upward, out of this layer loses some of its forward speed, and the intersection of the precursor and main shock fronts indicates that the main shock is continually overtaking this upward-traveling energy. Dust, typically billowing to heights of more than 100 feet, shows the upward flow of air in the precursor. At later times, the lower edge of the main shock front is distorted by the action of the precursor.

Overpressure and dynamic pressure waveforms add information to that supplied by blast wave photographs. Typically, the waveform of a fully developed precursor shows a rounded leading edge and a slow rise to its peak amplitude. In severely disturbed waveforms, the pressure jump at the leading edge may be completely absent. These characteristics indicate that the precursor shock front is strongly attenuated and that, at least close to the ground, the precursor does not always have a true shock

front of significant amplitude. These results are consistent with the diverging flow pattern described above. Dynamic pressure waveforms often have high frequency oscillations that indicate severe turbulence. The long time durations seen in both overpressure and dynamic pressure waveforms indicate two effects: the early arrival of the initial pressure disturbance, and the sustaining effects of the strong winds developed within the precursor.

Peak amplitudes of the precursor waveforms show that overpressure has a lower peak value and dynamic pressure has a higher peak value than would appear over a surface that did not permit a precursor to form.<sup>†</sup> The drop in peak overpressure indicates the energy expended in producing the higher than ideal wind velocities. The higher dynamic pressure is partly due to the higher wind speeds, but dust loading, the increase in effective air density resulting from particulate matter carried by the wind, is believed to be a more important factor.

Additional information on precursors, particularly a description of typical precursor overpressure and dynamic pressure waveforms, is given in paragraphs 2-31 and 2-32.

\* It is tempting to think of the wind in the gap as moving faster than the main shock front. However, two velocities characterize a shock wave: wind velocity and shock front velocity. The velocity of the main shock front is the velocity of propagation of the energy in the main shock. It should be compared not to the wind speed in the gap but to the velocity with which hydrodynamic energy propagates through the gap.

† In an ideal blast wave, this relative variation of peak values would be impossible. Peak overpressure and peak dynamic pressure have a fixed relation to one another, specified by the Rankine-Hugoniot equations (paragraph 2-17 and Appendix A). However, these equations only hold at the shock front. In an ideal blast wave, shock-front amplitudes are also peak amplitudes, but in a precursor the peak values do not occur at the shock front. Thus the relation between them is not limited by these equations.

## 2-22 Identification of Thermally Near-Ideal and Nonideal Surfaces

To predict blast-wave parameters accurately, the reaction of the surface to thermal radiation from the fireball should be known. Nuclear tests have shown that a few specific types of surface act essentially as thermally ideal surfaces and a few others tend to produce a significant thermal layer. Unfortunately, a theoretical model that quantitatively explains the phenomena of surface reaction and precursor formation has not yet been developed. Without such a model, the response of untested surfaces cannot be predicted with assurance.

Despite this uncertainty, predictions have been made. Surfaces are classified as either thermally near-ideal (unlikely to produce significant precursor effects) or thermally nonideal (expected to produce a precursor for suitable combinations of burst height and ground distance). No other categories are used, i.e., no attempt is made to subdivide surface classifica-

tions according to the strength of the precursor that can form.

Examples of surfaces that are considered thermally near-ideal and thermally nonideal are shown in Table 2-3. Items in the table that are confirmed by experiment are marked with an asterisk.

Dark surfaces tend to be thermally nonideal, because they absorb thermal radiation from the fireball. Light (reflecting) surfaces tend to be near-ideal. Asphalt is the strongest precursor-forming surface for which test results are known.

The effect of moisture has not been established definitely. Since any specified amount of absorbed energy can raise the temperature of a dry surface more than the same absorbed energy would raise the temperature of a wet surface, moisture is expected to inhibit the formation of a thermal layer. This should be particularly true when the moisture is in the form of ice. Nuclear tests show that the dry, sandy

Table 2-3. Examples of Thermally Near-Ideal and Thermally Nonideal Surfaces

Thermally Near-Ideal (precursor unlikely)	Thermally Nonideal (precursor may occur for low air bursts)
*Water	*Desert sand
*Ground covered by white smoke layer	*Coral
Heat reflecting concrete	*Asphalt
Frozen tundra	*Surfaces with low, thick vegetation
Ice	*Surfaces covered by a dark smoke layer
Packed snow	Dark colored rock
Moist soil with sparse vegetation	Most agricultural areas; Residential areas in cities
Commercial and industrial areas	Dry soil with sparse vegetation

soil of the Nevada Test Site is thermally non-ideal, and that water is a near-ideal surface (however, a blast wave over rough seas may fill the air with spray and produce a dynamic pressure effect similar to the dust loading encountered over desert surfaces). Untested surfaces classed as thermally near-ideal are listed in Table 2-3 in the order of increasing uncertainty.

Sparse vegetation probably should be ignored. Leaves or thick vegetation shield the ground, prevent popcorning, and minimize dust loading, but they also generate a heat-absorbing cloud of dark smoke when they absorb radiation from the fireball. The gases driven from the leaves have high sonic velocities. As a result, they create a thicker, and probably cooler, thermal layer than that formed over desert sand or asphalt. Taller vegetation is expected to produce a thicker thermal layer and a stronger precursor. The REDWING-Inca shot, over a surface covered by low grass and vines dominated by broad-leaved shrubs about 10 feet high, produced a precursor, but the characteristic precursor waveforms were apparently suppressed to some extent because higher-than-ideal blast-wave velocities near the surface were eliminated by the vegetation.

Tests at the Nevada Test Site show weakened precursor action over areas covered by dark smoke (the surface was desert sand which forms a strong precursor). Presumably the smoke absorbs enough heat to form a thermal layer, but it shields the ground to prevent popcorning and dust loading of the air.

Variable conditions occur in cities. Commercial and crowded industrial areas are expected to act as thermally near-ideal surfaces. Although these areas contain many surfaces that are favorable to precursor formation (e.g., asphalt-coated roofs), a continuous thermal layer would not be expected. The tendency to form a precursor would be offset by its difficulty in propagating through a heavily built up

area. In typical residential areas, where the buildings are neither as close nor as tall as those in commercial areas, the surface is considered thermally nonideal.

The preceding descriptive information does not always provide clear guidelines for classifying surfaces. For example, the rules that might be applied to black, moist soil are conflicting. In such cases, blast-wave properties should be calculated for both near-ideal and thermally nonideal surface conditions in order to bracket the blast effects that can actually be expected.

## BLAST-WAVE CALCULATIONS AT THE SURFACE

Height of burst (HOB) curves provide most of the data required to calculate blast-wave properties at the surface. The HOB charts in this subsection each show the distance from ground zero as a function of height of burst for several values of the various air blast parameters that would be expected to occur along the surface as a result of a 1 kt explosion.\* For instance, any point on a curve for specified overpressure (see for instance Figure 2-17) shows a combination of burst height and ground distance at which a 1 kt explosion will produce that overpressure at the surface of the earth. Alternately, if a 1 kt burst occurs at a location corresponding to some point on a given overpressure curve, a target at the origin will receive that overpressure.

Separate families of curves are provided for near-ideal and thermally nonideal surface

\* As described in paragraph 2-13, the heights of burst and distances from ground zero could be expressed in terms of scaled distances, e.g.,  $k_t/W^{1/3}$ , with  $W$  being the yield in kt. However, since other scaling laws apply to other phenomena, the convention of expressing absolute distances from a 1 kt explosion will be maintained throughout the remainder of this chapter and throughout the manual. When "scaled distances" are employed, e.g., Section I, Chapter 11, the exceptions will be indicated clearly.

conditions. Guidelines for classifying surfaces with respect to thermal properties are provided in paragraph 2-22. The effects of mechanically nonideal surfaces (paragraph 2-20) are discussed in paragraphs 2-37 through 2-41.

Many of the HOB curves show whether a given point on the surface is in the region of regular reflection or the Mach stem region (paragraph 2-18). This information is helpful if the target is some distance above the surface, because it indicates how closely blast-wave data at the surface correspond to blast-wave data at the target. The effect of target height on blast-wave parameters is discussed in paragraph 2-29.

The data for overpressure and dynamic pressure are peak values, regardless of where these peaks occur in the blast waveform. In an undisturbed blast waveform, these peak values occur at the shock front. If a precursor is present, they usually occur later in the waveform. Precursor overpressure and dynamic pressure waveforms are described in paragraphs 2-31 and 2-32.

Whenever ambient atmospheric conditions are different from standard sea level conditions (14.7 psi, 59°F), calculations of blast-wave parameters at the surface are more accurate if the altitude scaling factors described in paragraph 2-14 are applied. These factors may be used even if the departure from standard conditions is not caused by an altitude change.

### 2-23 Reliability

Blast-wave data at the surface are subject to the uncertainties described in paragraphs 2-1 through 2-6. As mentioned in paragraph 2-5, additional uncertainties arise because the earth is not a perfect reflector. Consequently, the blast wave at the surface is inherently less predictable than the blast wave in free air. Added to this problem is the difficulty of obtaining sufficient experimental data to cover all combinations of conditions. A blast parameter in free air may be

represented by a single curve; at the surface, the available data must be scattered to cover a family of curves. Moreover, variable surface conditions require that more than one family be plotted. Consequently, a limited number of nuclear tests cannot document blast-wave data at the surface as completely as in free air. The usual reliability statements are supplemented in this section by showing portions of the curves as dashed lines. The solid lines are based upon experimental data from full-scale nuclear tests; the dashed portions are based upon theory and high-explosive experiments. In some cases, data for the dashed portions of curves are based on the assumption that for certain combinations of ground range and burst height the data for thermally nonideal surfaces should agree with data taken over near-ideal surfaces. In general, the reliability statements apply to the dotted as well as the solid portion of the HOB curves; however, the reliability of the dotted portions is purely an estimate, while the reliability stated for the solid portions is based on experimental data.

Uncertainties in the data presented in the HOB charts usually are expressed in terms of ground distance rather than in terms of blast parameters. This is an important distinction. For example, a  $\pm 10$  percent uncertainty in ground distance corresponds to an uncertainty in peak overpressure that may be as high as  $\pm 30$  percent. The curves become nearly horizontal close to ground zero, and a variation in ground distance produces very little change in blast parameters. For these portions of the HOB charts, the uncertainty should be applied to burst height rather than to ground distance. When a precursor forms, the air blast waveforms are distorted severely, and prediction of blast parameters becomes highly uncertain. As mentioned in paragraph 2-2, the scaling of most blast-wave parameters is reasonably dependable in the yield range of 1 kt to 20 Mt; however, scaling becomes questionable for yields over 50 kt at thermally non-

ideal surfaces as a result of the difficulty in predicting the criteria for precursor formation.

The scaling of subkiloton explosions at scaled heights of burst between 150 and 1,000 feet have shown large errors that correspond to discrepancies as high as factors of 2 or 3 in effective yield.

Additional uncertainties appear in the measured data for contact surface bursts as a result of less dependable experimental determination of yield. This is caused in part by the difficulties added to radiochemical yield determination as a result of the large amount of crater material in the cloud and to the uncertainty introduced into yield determination by fireball size that result from uncertainties in the amount of energy absorbed by the earth.

#### 2.24 Peak Overpressure

Figures 2-17 through 2-22 show the peak overpressure at the surface of the earth as a function of height of burst and distance from ground zero from a 1 kt explosion. Figure 2-23 shows peak overpressure as a function of distance from ground zero from a 1 kt contact surface burst. The same data could be obtained in less convenient form along the abscissas of Figures 2-17 through 2-20.

These figures show that the same ground range for a given peak overpressure is produced by a burst either at the surface or some short distance above the surface. At low overpressures, the greatest distance from ground zero occurs for an explosion at some higher distance above the surface. This effect is prominent at overpressures of 15 psi and less, and contours for these overpressures show a pronounced "knee" (the knee is defined as the extreme right projection of a contour line).

Figures 2-17 through 2-20 apply to near-ideal surface conditions; Figures 2-21 and 2-22

apply to thermally nonideal surfaces (suggestions for classifying various types of surfaces are given in paragraph 2-22). Figure 2-23 applies to near-ideal surfaces, but since the 1 kt reference burst detonated in contact with the surface is not expected to form a precursor, the curve also applies approximately to thermally nonideal surfaces.

The shaded areas in Figure 2-20 reflect the uncertainty in the prediction of very low overpressures. The shaded areas in Figures 2-21 and 2-22 correspond to the ground distances at which precursor cleanup occurs. In this phenomenon, the hydrodynamic energy of the blast wave collects behind a single, well-defined shock front, forming a nearly ideal blast wave. As this occurs, the peak overpressure usually rises instead of undergoing the normal amount of attenuation with increasing ground range. Uncertainty in the ground range at which cleanup occurs is reflected in the HOB curves as additional uncertainty in peak overpressure data at this range. This is indicated by shading of the 10 psi contour and a portion of the 15 psi contour.

#### 2.25 Peak Dynamic Pressure

Figures 2-24 through 2-26 show peak dynamic pressure at the surface as a function of scaled height of burst and ground distance from a 1 kt explosion. These curves show conditions after the blast wave has been reflected from the surface; therefore, these charts do not represent the dynamic pressure of the incident wave. At ground zero the wind in the incident blast wave is completely stopped by the ground surface, and all of the incident dynamic pressure is transformed to static overpressure. Therefore, the height of burst curves show that the peak dynamic pressure is zero at ground zero. At other locations, reflection of the incident blast wave produces winds that, at the surface, must

blow parallel to the surface.\* The dynamic pressures associated with these winds tend to produce horizontal forces; however, the direction of wind forces on a target surface depend not only on wind direction but also on surface orientation.

The thermal properties of the surface are less significant for prediction of dynamic pressure than for most blast parameters. Dynamic pressure only appears to be strongly enhanced by dust loading (or, in the case of a water surface, spray loading) of the air, whether or not a precursor is formed. The dynamic pressure height of burst curves are therefore classed as ideal, "light dust," and "heavy dust" surface conditions. Light dust conditions usually may be taken to be equivalent to near-ideal surfaces, and heavy dust equivalent to thermally nonideal, but there are exceptions. For example, a surface covered by thick vegetation is expected to produce a precursor but little dust. Conversely, the interaction of a blast wave with very rough seas is expected to produce heavy spray loading but no precursor.

Figure 2-24 shows peak dynamic pressure at an ideal surface in the very high pressure region. It is based almost entirely on theory, and does not include dust loading effects (it should be noted that the 200-psi contour of Figure 2-23 does not agree with that in either Figure 2-25 or 2-26). Figure 2-25 shows peak dynamic pressure for light dust conditions, and Figure 2-26 shows peak dynamic pressure for heavy dust conditions. Since the latter is based on limited data, height of burst curves can be drawn only for scaled burst heights up to 300 feet. As a guide to the way in which the heavy dust curves might be extrapolated, portions of the light dust curves are shown for 1 kt burst heights between 330 feet and 600 feet. These latter curves do not represent heavy dust conditions. They should be used only as a guide to obtain rough estimates.

Figure 2-27 is presented to aid in the

explanation of the effects of dust on peak dynamic pressure. The curves are drawn from data from Figures 2-25 and 2-26, and theoretical data for an ideal reflector. At a scaled distance of about 400 feet, the contribution of light dust to dynamic pressure is about twice that of heavy dust. This suggests that the inertia of heavy dust limits its velocity initially and probably also limits the velocity of the air in the blast wave by the drag force it exerts. After these inertial forces are overcome, heavy dust contributes strongly to dynamic pressure. At a scaled range of 900 feet, heavy dust exhibits its maximum effect, but the effect of light dust has diminished considerably. This also suggests an inertial effect acting to sustain the momentum of the air in the blast wave.

The explanation that has been given is only one of several possible explanations of Figure 2-27 and represents an oversimplification. For example, the explanation does not include the varying amount of dust that a given surface adds to the blast wave as a function of range. More detail may be found in DASA 1200 (see bibliography).

A large scatter exists in dynamic pressure data under heavy dust conditions. This is due to the nature and the varying amounts of particulate matter in the air. Fine grains of sand are readily carried by the air stream, flow with it as a part of a continuous fluid, and present a relatively small measurement problem. Larger

\* This statement ignores the turbulence that is often associated with dynamic pressure. It is uncertain whether or not vertical components of air velocity contribute to dynamic pressure significantly. Gages used to measure dynamic pressure are usually mounted so as to be sensitive only to the horizontal force produced by dynamic pressure. For this reason curves such as those in Figures 2-24 through 2-26 are often labeled "horizontal component of dynamic pressure." It is desirable to avoid this phrase, because it tends to imply, incorrectly, that the forces produced by dynamic pressure may be resolved into components that can be treated by the ordinary rules of vector algebra.

particles tend to plug gage openings, and their effect is difficult to measure. Large objects picked up by the blast wave and thrown through the air can be very destructive, but they cannot be measured as part of a continuous pressure record. Arbitrarily, dynamic pressure has been defined as representing the effects of only those particles that are small enough to behave essentially as air particles. Dynamic pressure as thus idealized cannot fully account for the destructive effects of blast momentum.

### 2-26 Time of Arrival

Figures 2-28 through 2-32 show the time of arrival of the blast wave from a 1 kt explosion in a standard, homogeneous, sea level atmosphere as a function of height of burst and distance from ground zero.

### 2-27 Duration of the Positive Phase of Overpressure and Dynamic Pressure

Figures 2-33 and 2-34 present families of curves that show values of the positive phase overpressure duration ( $t_p^+$ ) at points along the surface as a function of height of burst and ground distance from a 1 kt explosion in a sea level atmosphere.

Because of limited data, similar curves cannot be drawn for dynamic pressure; however, the data suggest that, as in the case of free air (paragraph 2-10 and Problem 2-4), the ratio of these two durations is a function of pressure level. Duration of dynamic pressure  $t_q^+$  may be estimated by using the curves for positive overpressure duration and the relations shown in Table 2-4. If surface conditions are such that heavy dust (or spray) loading is predicted, the longer times found in Figure 2-34 probably provide a better basis for determining  $t_q^+$  even if the surface is considered thermally near-ideal and Figure 2-33 is used to determine  $t_p^+$ .

Table 2-4. Relations Between the Positive Duration of the Overpressure Blast Wave ( $t_p^+$ ) and the Positive Duration of the Dynamic Pressure ( $t_q^+$ ) for a 1 kt Explosion

$t_p^+$ (sec)	$t_q^+$ (sec)
0.1	0.25
.15	.33
.2	.34
.25	.35
.3	.39
.35	.43
.4	.49

### 2-28 Overpressure Impulse

Figures 2-35 and 2-36 show the positive overpressure impulse (paragraph 2-11) at the surface as a function of height of burst and ground distance from a 1 kt explosion in a sea level atmosphere.

Formation of a Mach stem changes the shape of the overpressure waveform by increasing the amplitude of the shock front without changing the area under the waveform appreciably. Consequently, the HOB curves for overpressure impulse differ from the HOB curves for peak overpressure in that the impulse curves do not show a characteristic change where they cross the boundary separating the region of regular reflection from the region of Mach reflection. Overpressure impulse at the surface appears to be primarily a function of slant range; it only fluctuates strongly as a function of reflecting angle for low heights of burst.

Dynamic pressure impulse is another important blast-wave parameter, particularly under thermally nonideal conditions. Unfortun-

arely, it is a difficult parameter to measure, and there are not enough dependable data to allow HOB curves to be constructed.

## 2-29 Mach Stem Heights

The changes that occur in a blast wave as the incident and reflected waves fuse to form a Mach stem are among the changes associated with reflection from a surface. A target above the triple point, the top of the Mach stem (see paragraph 2-18), receives two shocks that correspond to the arrival of the incident and the reflected waves. A target at or below the triple point receives a single shock. As mentioned in paragraph 2-25, the reflection process transforms part of the incident dynamic pressure into overpressure. Thus, a target below the triple point is subjected to a higher overpressure impulse and a lower dynamic pressure impulse than a target above the triple point. Since a typical airborne target is more sensitive to dynamic pressure than to overpressure, such a target is usually safer below the triple point.

The height of the Mach stem height affects tall structures on the ground. The nature of the response depends on whether the structure is more sensitive to overpressure or to dynamic pressure. The relative effects of a two shock front waveform and a single, nearly vertical shock wave also depend on the mechanical response properties of the target.

Above the triple point, the strength of the first (or incident) shock wave may be found from free air data, and the time interval between the two shocks depends on the height of the target above the triple point. Below the triple point, shock parameters may be approximated best by data from the HOB charts, i.e., from

data which, strictly speaking, apply only to targets at the surface. When the scaled height (that corresponding to a 1 kt burst) of the Mach stem is 50 feet or less, blast-wave properties anywhere on the stem are essentially the same as those at the surface. For taller Mach stems, the shock-front becomes curved. This modifies blast-wave properties along the stem. Pressure values decrease and arrival times increase with height above the surface. These variations have not been studied as thoroughly as blast-wave conditions at the surface have been, and data to describe them quantitatively are not presented here.

The guidelines presented above must be applied with caution if a precursor is present. The two disturbing influences, dust and the thermal layer, are confined to a layer that is close to the ground. Above the region that is affected by the precursor, the near-ideal HOB curves are a better representation of the blast wave. The height above which the near-ideal curves apply is not known, but it is estimated to be between 50 and 300 feet (physical, not scaled height) under typical conditions.

Although there are indications that the height of the Mach stem is affected by thermal effects and by surface hardness, these effects are not large, and the curves may be applied to both near-ideal and thermally nonideal surfaces. Both thermal effects and surface roughness will, however, make the position of the triple point less predictable.

Figures 2-37 and 2-38 show the height of the Mach stem as a function of height of burst and ground distance from a 1 kt explosion in a sea level atmosphere.

### Problem 2-9. Calculation of Peak Overpressure at the Surface

Figures 2-17 through 2-22 show the peak overpressure as a function of height of burst and horizontal distance from ground zero for a 1 kt explosion in a sea level atmosphere. Figures 2-17 through 2-19 provide data for thermally near-ideal surfaces, while Figures 2-20 through 2-22 provide the same data for thermally nonideal surfaces. Figure 2-23 shows the peak overpressure as a function of horizontal distance from a contact surface burst. The data contained in the curves of Figure 2-23 could be obtained from points along the abscissas of Figures 2-17 through 2-19; however, for some applications, Figure 2-23 may be more convenient to use.

**Scaling.** For yields other than 1 kt, the ground distance and height of burst for any specific overpressure scale as follows:

$$\frac{d}{d_1} = \frac{h}{h_1} = W^{1/3},$$

where  $d_1$  and  $h_1$  are the distance from ground zero and height of burst, respectively, for 1 kt, and  $d$  and  $h$  are the corresponding distance and height of burst for a yield of  $W$  kt.

#### Example 1

**Given:** An 80 kt explosion 2,580 feet above a thermally nonideal surface.

**Find:** The horizontal distance from ground zero beyond which the peak overpressure will not exceed 3 psi.

**Solution:** The corresponding height of burst for 1 kt is

$$h_1 = \frac{h}{W^{1/3}} = \frac{2,580}{(80)^{1/3}} = 600 \text{ feet.}$$

From Figure 2-22, a peak overpressure of 3 psi extends to a distance of 2,900 feet from a 1 kt explosion at a height of burst of 600 feet.

**Answer:** The corresponding distance for an 80 kt weapon at 2,500 feet height of burst is

$$d = d_1 W^{1/3} = (2,900)(80)^{1/3} = 12,500 \text{ feet.}$$

As a result of the  $\pm 15$  percent uncertainty in this distance (see "Reliability" below), the range beyond which the peak overpressure will not exceed 3 psi is

$$12,500 + (0.15)(12,500) = 14,400 \text{ feet.}$$

#### Example 2

**Given:** A 100 kt explosion at a height of 2,320 feet above a near-ideal surface.

**Find:** The peak overpressure at a distance of 1,860 feet from ground zero.

**Solution:** The corresponding distance and ground zero and height of burst for a 1 kt weapon are

$$d_1 = \frac{d}{W^{1/3}} = \frac{1,860}{(100)^{1/3}} = 400 \text{ feet,}$$

$$h_1 = \frac{h}{W^{1/3}} = \frac{2,320}{(100)^{1/3}} = 500 \text{ feet.}$$

**Answer:** From Figure 2-18, the peak overpressure at a ground distance of 400 feet and a height of burst of 500 feet is 50 psi.

#### Reliability

Ground distances obtained from Figures 2-18, 2-19, and 2-22 are estimated to be reliable within  $\pm 15$  percent of the indicated ground range (or HOB for points close to ground

- zero — see paragraph 2-23). Figure 2-17 is based on theory, confirmed by only a few data points; it is estimated to be reliable within  $\pm 20$  percent.
- Figure 2-20 is reliable within  $\pm 15$  percent of the indicated ground range, but the  $1/2 \sim 1/4$  psi curves are subject to the additional uncertainty indicated by the shaded areas. Figure 2-21 is based on data subject to considerable scatter from thermal effects; it is estimated to be reliable within  $\pm 20$  percent.

For near-ideal surface conditions,

these reliability estimates apply to yields between 1 kt and 20 Mt; for thermally nonideal surface conditions, the estimates apply to yields between 1 kt and 50 kt. Outside this range of yields, these curves may be used with somewhat less confidence.

*Related Material:* See paragraphs 2-13, 2-14, 2-17 through 2-20, and 2-22 through 2-24. See also Tables 2-1 and 2-2 for surface conditions that differ from standard sea level atmospheric conditions.

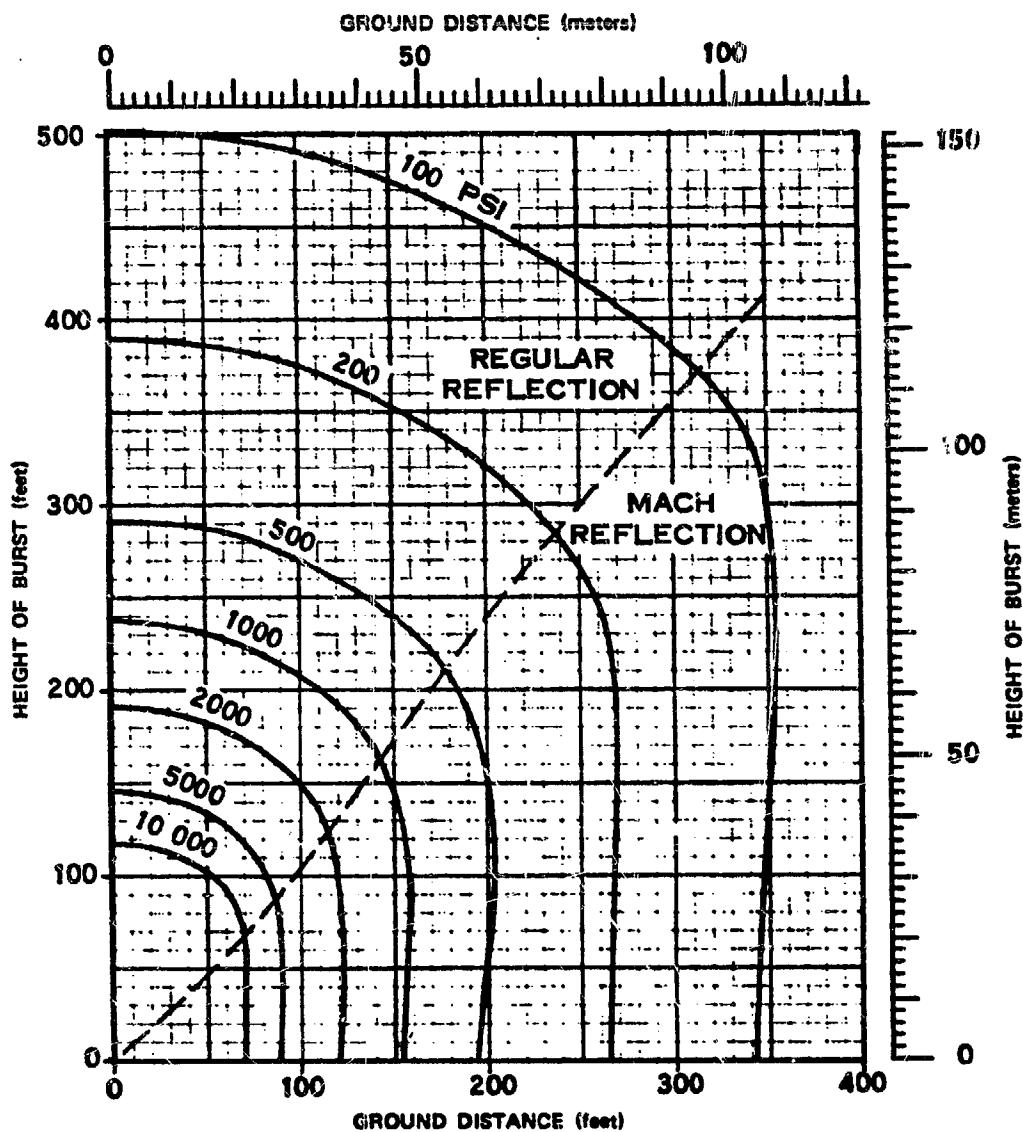


Figure 2-17. Peak Overpressures at the Surface for a 1 kt Burst Over a Near-Ideal Surface, Very High Overpressure Region

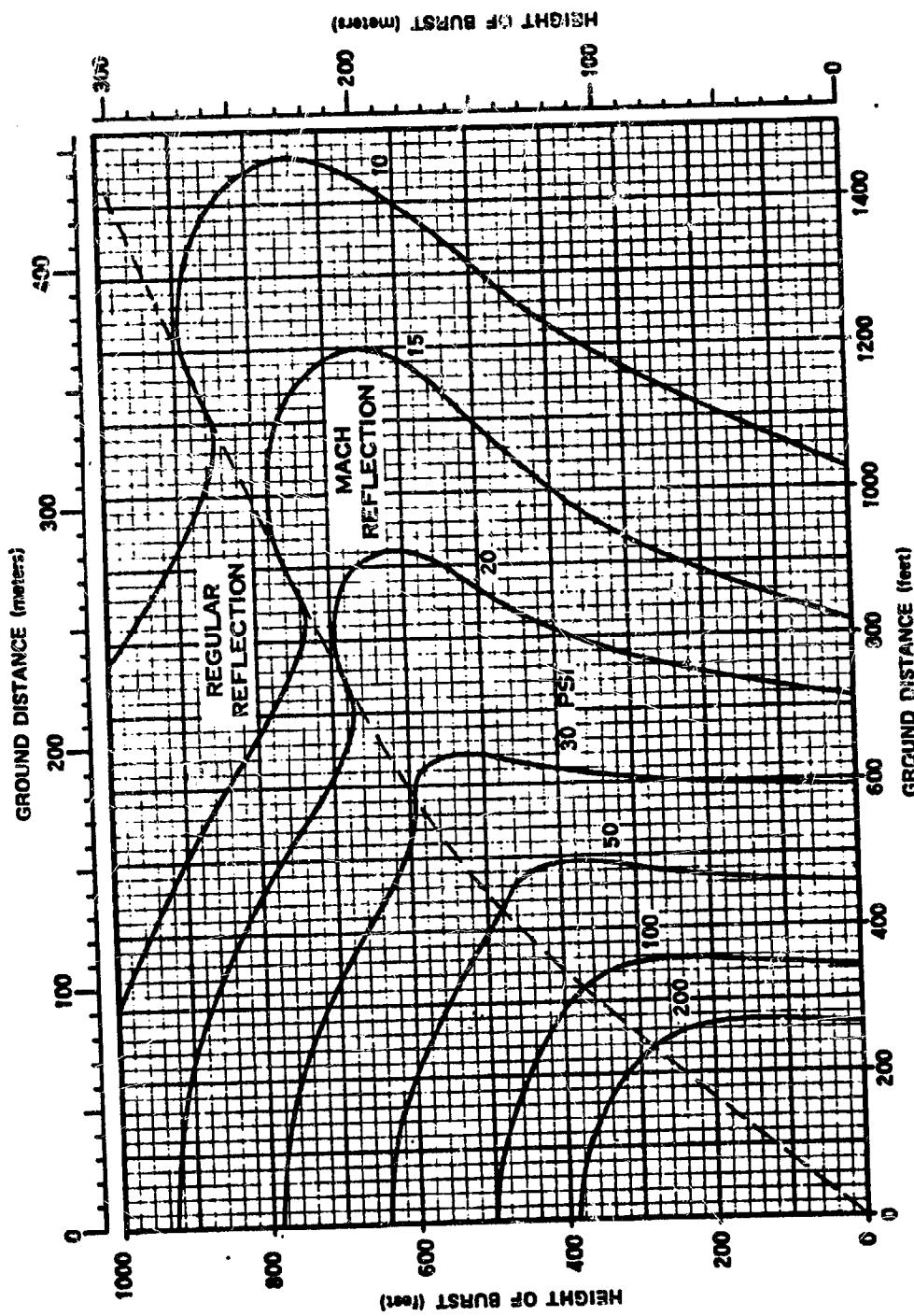
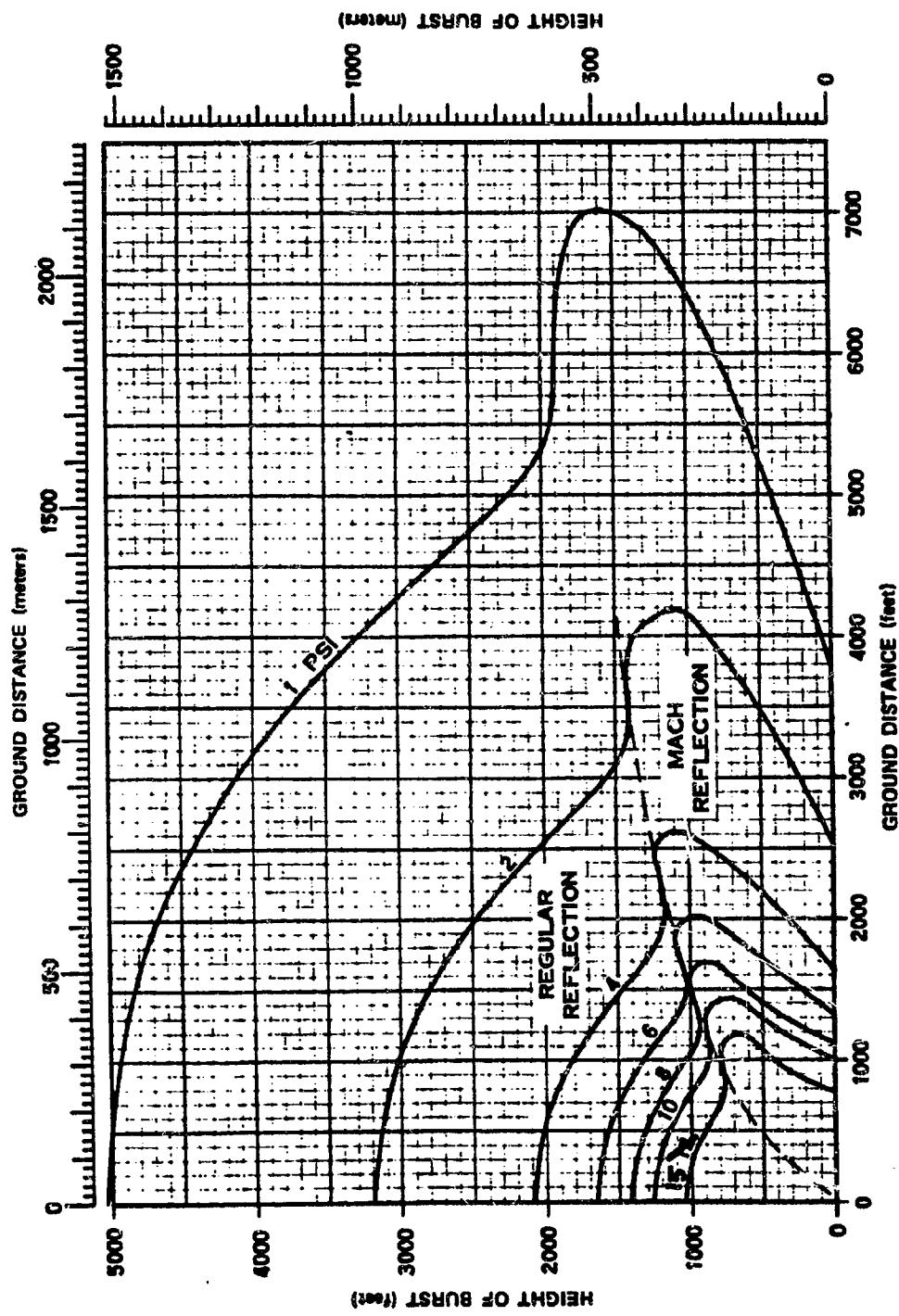


Figure 2-18. Peak Overpressures at the Surface for a 1 kt Burst Over a Near-Ideal Surface, High Overpressure Region



**Figure 2-19.** Peak Overpressures at the Surface for a 1 kt Burst Over a Near-Ideal Surface, Low Overpressure Region

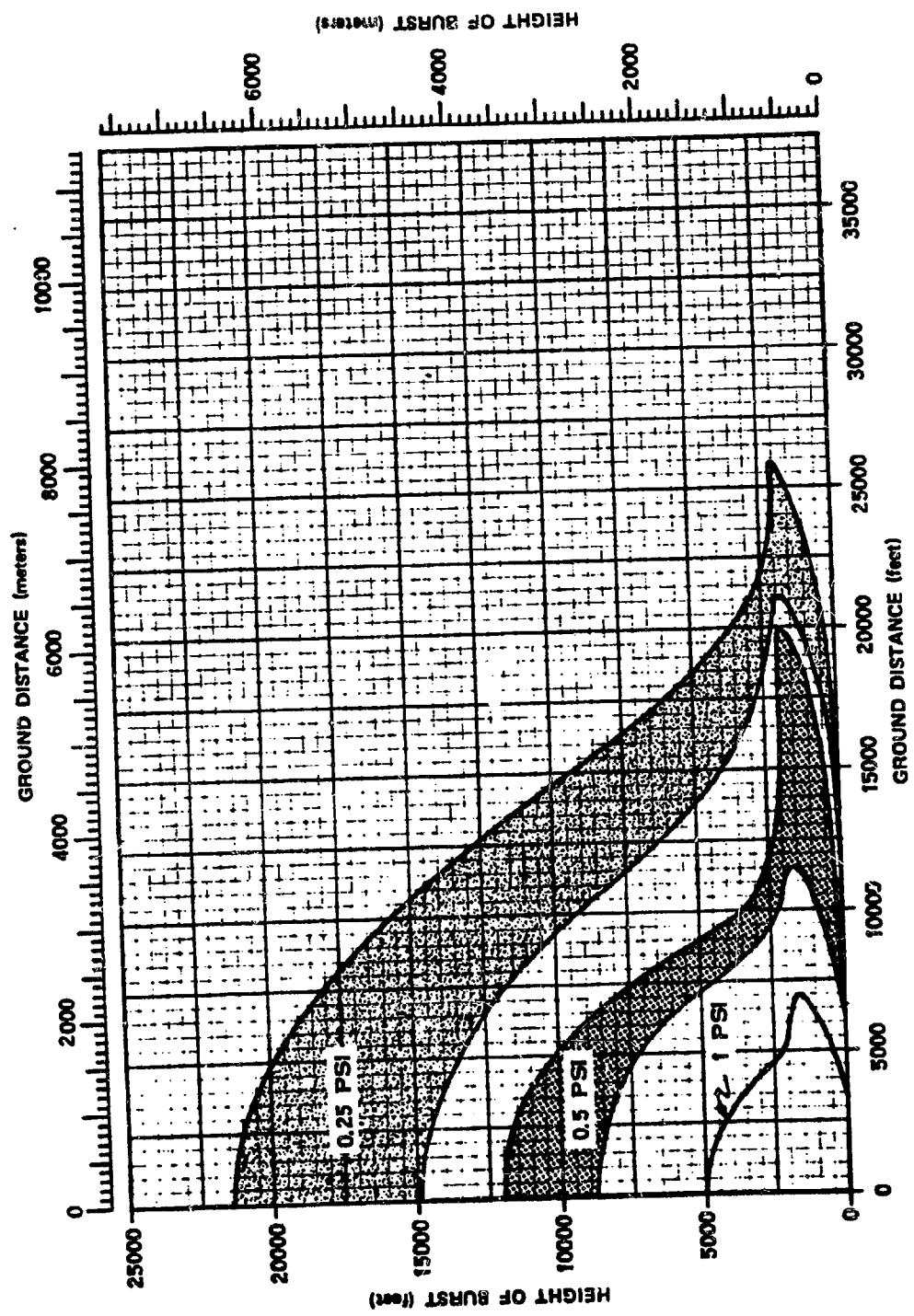


Figure 2-20. Peak Overpressures at the Surface for a 1 kt Burst Over a Near-Ideal or Thermally Nonideal Surface, Very Low Overpressure Region

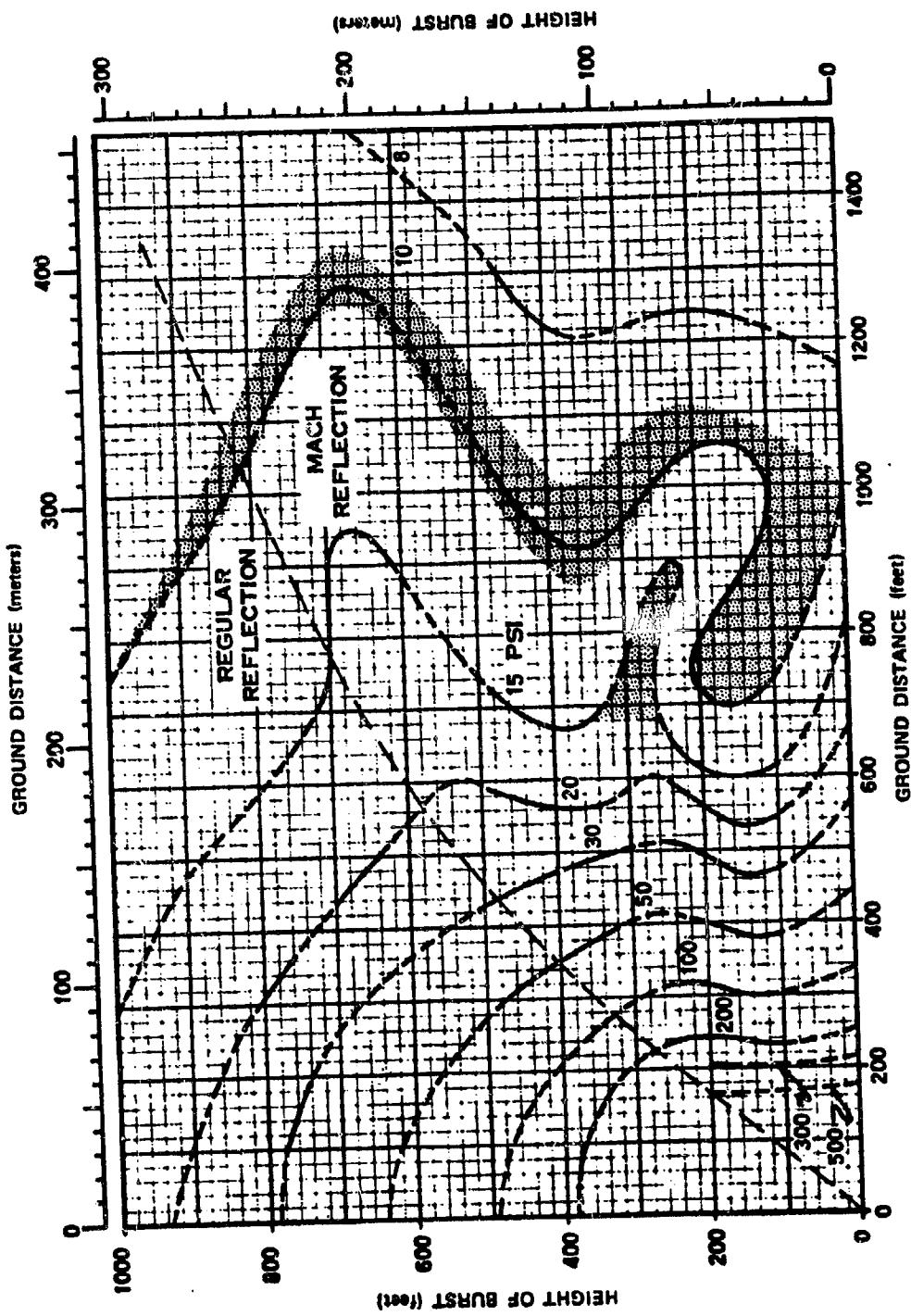
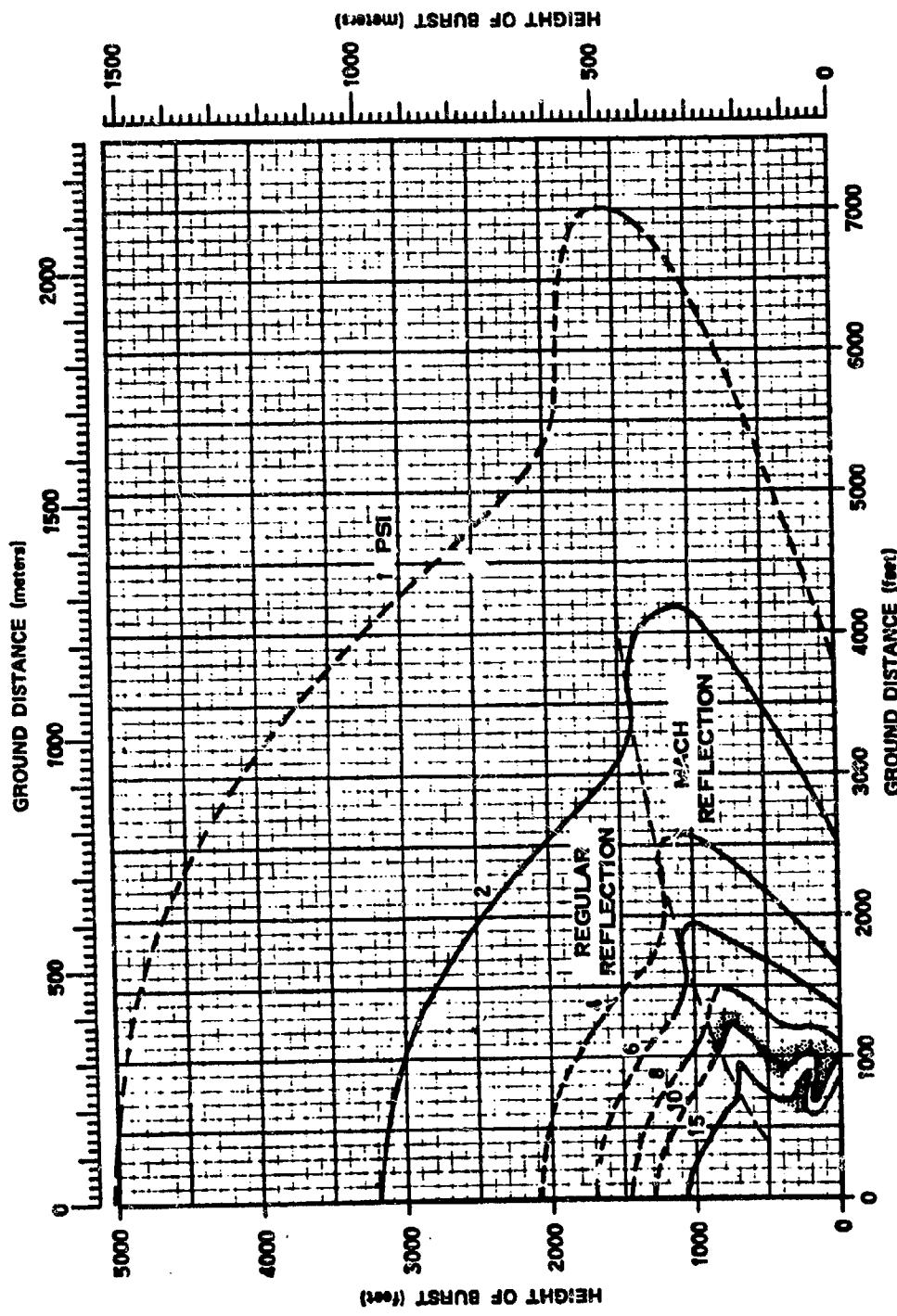


Figure 2-21. Peak Overpressures at the Surface for a 1 kt Burst Over a Thermally Nonideal Surface, High Overpressure Region



**Figure 2-22.** Peak Overpressures at the Surface for a 1 kt Burst Over a Thermally Nonideal Surface, Low Overpressure Region

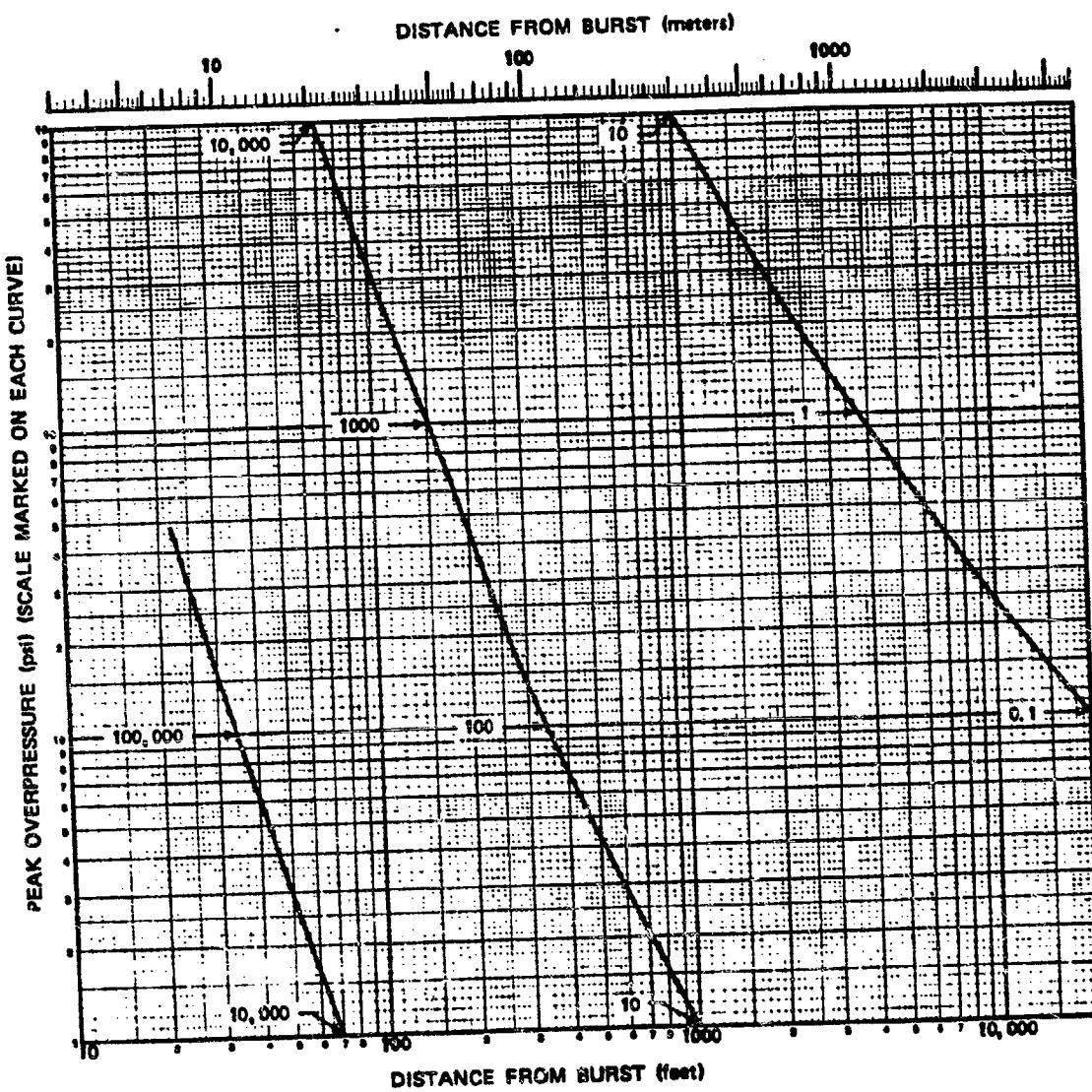


Figure 2-23. Peak Overpressure from a Contact Surface Burst

### Problem 2-10. Calculation of Peak Dynamic Pressure at the Surface

Figures 2-24 through 2-26 show peak dynamic pressure at the surface as a function of height of burst and horizontal distance from ground zero for a 1 kt explosion in a sea level atmosphere. Figure 2-24 is based almost entirely on theory and applies to peak dynamic pressure in the very high overpressure region at an ideal surface. Dust loading effects are not included in the curves of Figure 2-24. Figure 2-25 shows the peak dynamic pressure at the surface under light dust conditions, while Figure 2-26 shows similar data under heavy dust conditions. Figure 2-27 shows a comparison of the data from Figures 2-24 through 2-26 for a 1 kt explosion at a height of burst of 200 feet. A discussion of the comparisons is given in paragraph 2-25.

**Scaling.** For yields other than 1 kt, the ground distance and height of burst for any specific peak dynamic pressure scale as follows:

$$\frac{d}{d_1} = \frac{h}{h_1} = W^{1/3},$$

where  $d_1$  and  $h_1$  are the distance from ground zero and height of burst, respectively, for 1 kt, and  $d$  and  $h$  are the corresponding distance and height of burst for a yield of  $W$  kt. If the surface is above 5,000 feet, or if the surface atmospheric conditions differ from standard, the altitude scaling procedures given in paragraph 2-14 should be used.

#### Example

**Given:** A 160 kt explosion 3,000 feet above a light dust surface.

**Find:** The peak dynamic pressure at a distance of 6,000 feet from ground zero.

**Solution:** The corresponding height of burst and ground distance from a 1 kt explosion are

$$h_1 = \frac{h}{W^{1/3}} = \frac{3,000}{(160)^{1/3}} = 550 \text{ feet},$$

$$d_1 = \frac{d}{W^{1/3}} = \frac{6,000}{(160)^{1/3}} = 1,100 \text{ feet}.$$

**Answer:** From Figure 2-25, the peak dynamic pressure corresponding to a height of burst of 550 feet and a distance of 1,100 feet is about 3 psi. Since this value of peak dynamic pressure is below 6 psi, the actual value (see "Reliability" below) may be between that shown for ground distances of  $1,100 \pm 25$  percent (1,375 and 825 feet) or between about 1.5 and 7 psi; however, since the reliability estimates do not extend to yields above 50 kt, the precise limits cannot be stated.

**Reliability:** Distances for peak dynamic pressures below 6 psi are estimated to be reliable within  $\pm 25$  percent. For dynamic pressures above 6 psi, the distances in Figure 2-25 (light dust) are estimated to be correct within  $\pm 50$  percent; and distances in Figure 2-26 (heavy dust), to within  $+100$  percent, or  $-50$  percent. The reliability of Figure 2-24 has not been estimated. These reliability figures apply to yields between 1 and 50 kt. Outside this range of yields, scaling may introduce additional error.

**Related Material:** See paragraphs 2-13 through 2-15, 2-17 through 2-23 and 2-25. See also Tables 2-1 and 2-2 when atmospheric conditions at the surface differ from standard sea level conditions.

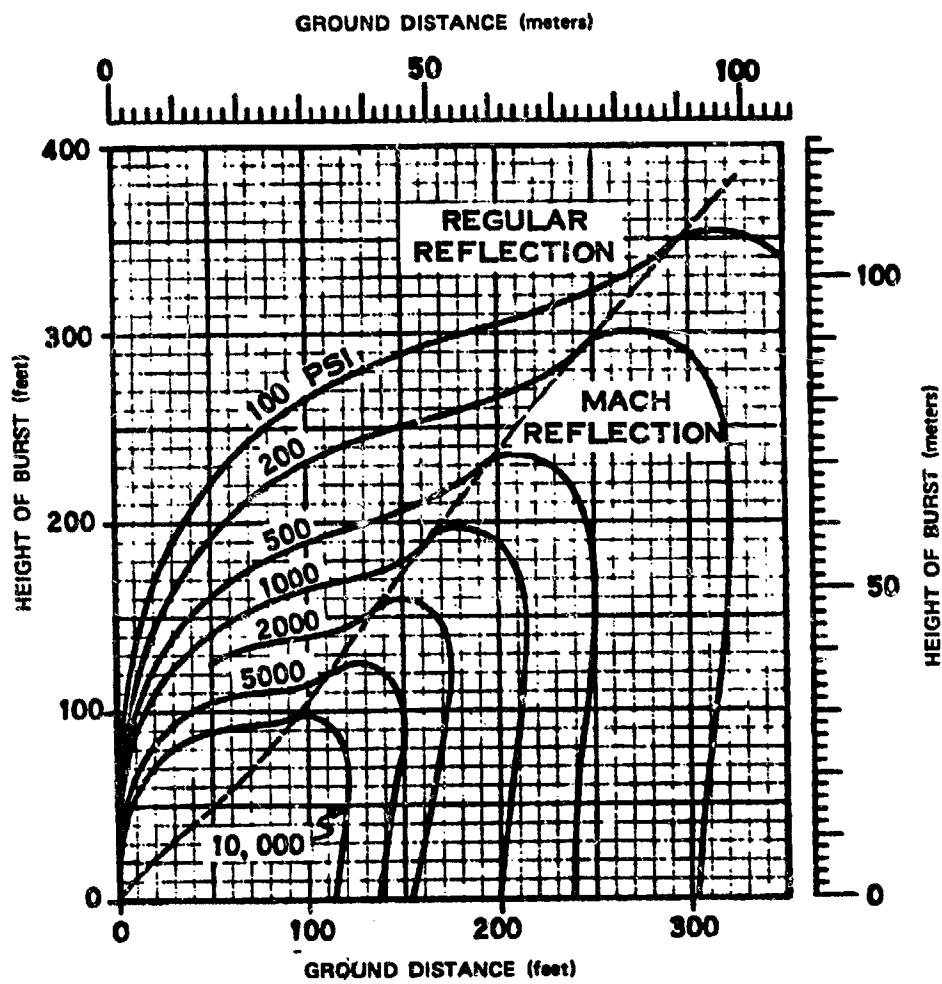


Figure 2-24. Peak Dynamic Pressure at the Surface from a 1 kt Explosion Over an Ideal Surface

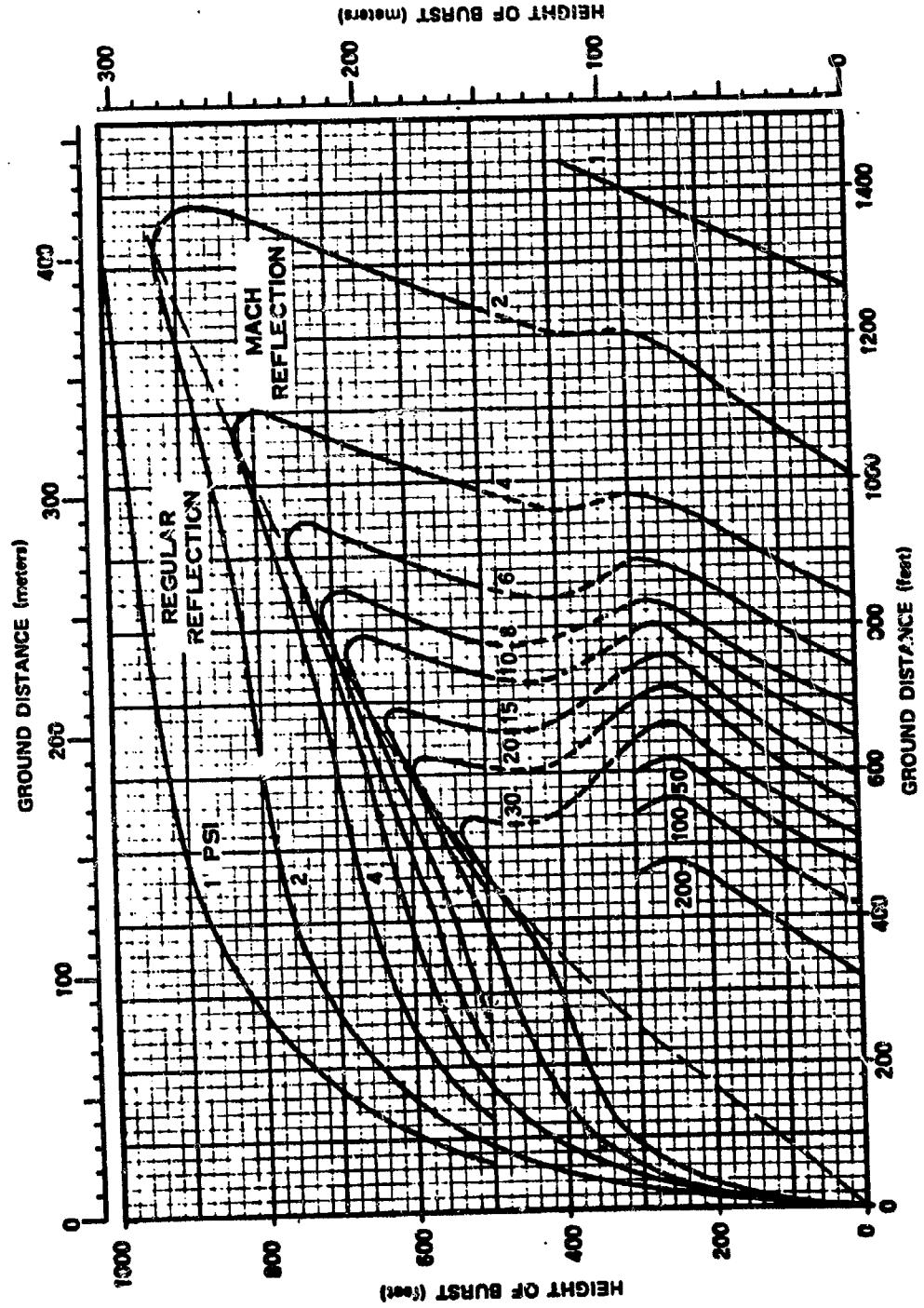


Figure 2-25. Peak Dynamic Pressure at the Surface from a 1 kt Explosion over a Surface with Light Dust Conditions

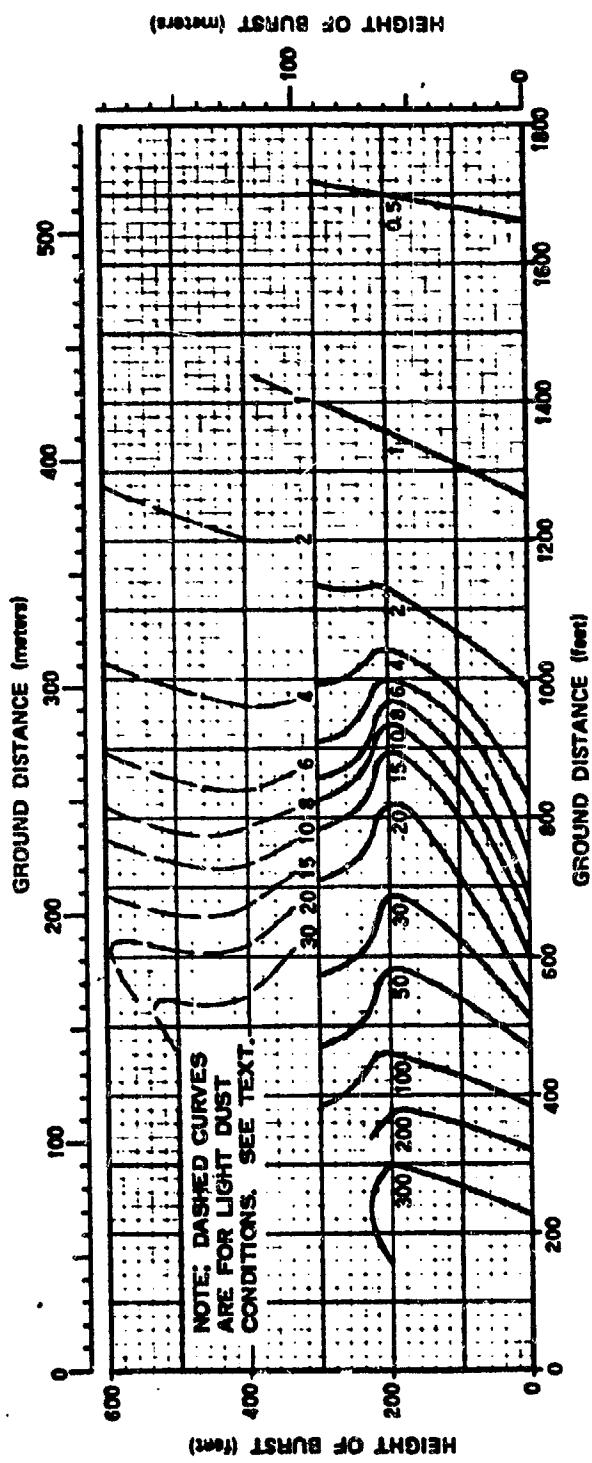


Figure 2-28. Peak Dynamic Pressure at the Surface from a 1 kt Explosion  
Over a Surface with Heavy Dust Conditions

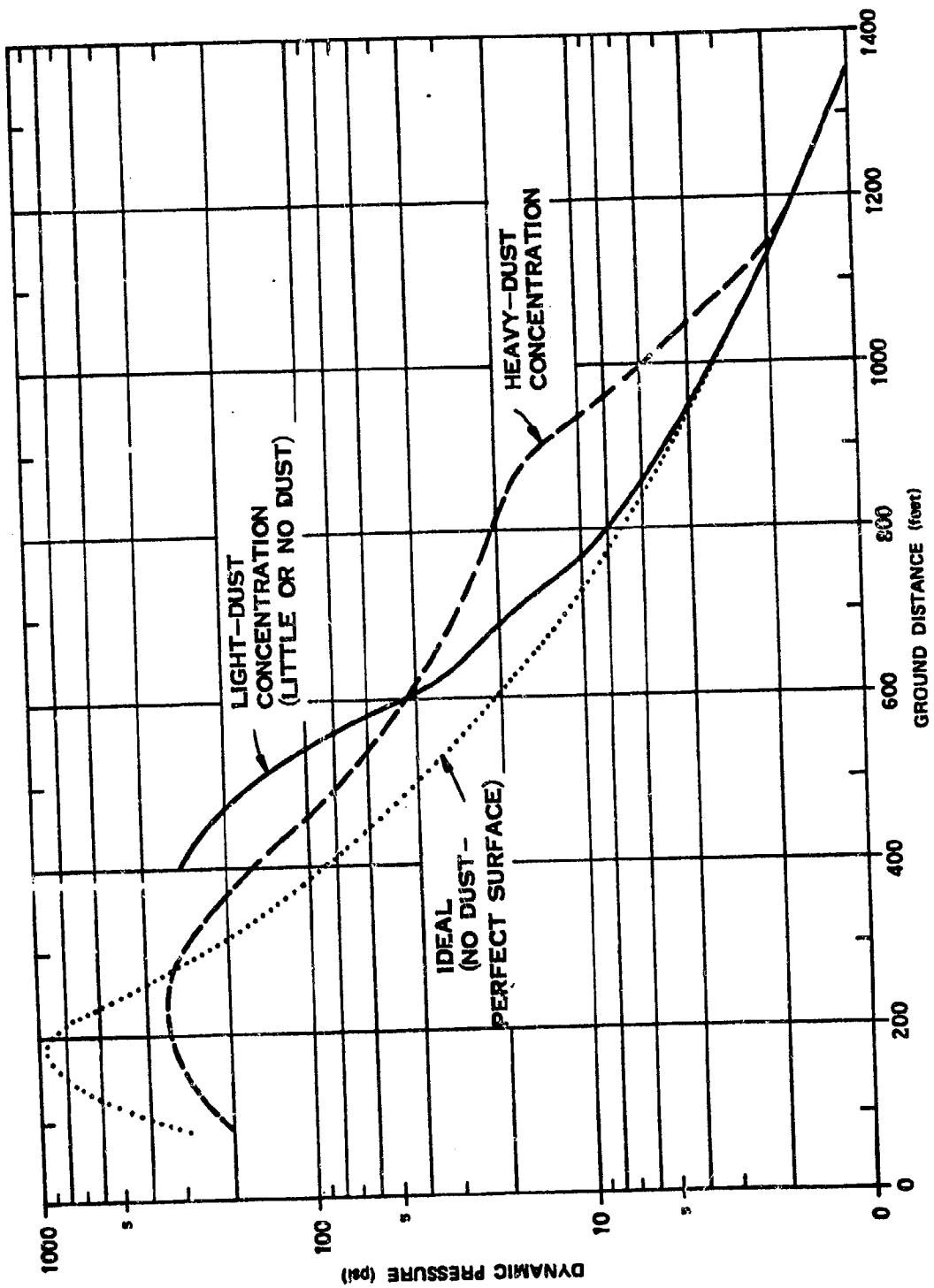


Figure 2-27. Comparison of Predicted Ideal, Light-Dust, and Heavy-Dust Dynamic Pressures for a 1 kt Explosion at a Height of 200 feet in a Sea Level Atmosphere

**Problem 2-11. Calculation of the Time of Arrival of  
a Blast Wave at the Surface**

**Figures 2-28 through 2-32** show the time of arrival of a blast wave as a function of height of burst and horizontal distance from a 1 kt explosion in a sea level atmosphere. Figures 2-28 and 2-29 apply to bursts over thermally near-ideal surfaces while Figures 2-30 through 2-32 apply to bursts over thermally nonideal surfaces.

**Scaling.** For yields other than 1 kt, the time of arrival, ground distance, and height of burst scale as follows:

$$\frac{t}{t_1} = \frac{d}{d_1} = \frac{h}{h_1} = W^{1/3},$$

where  $t_1$ ,  $d_1$ , and  $h_1$  are the time of arrival, ground distance and height of burst, respectively for 1 kt and  $t$ ,  $d$ , and  $h$  are the corresponding time and distances for a yield of  $W$  kt. If the surface is above 5,000 feet, or if the surface atmospheric conditions differ from standard, the altitude scaling procedures given in paragraph 2-14 should be used.

**Example**

**Given:** An 8 kt explosion 400 feet above a thermally nonideal surface.

**Find:** The time of arrival of the blast wave at a horizontal distance of 1,200 feet from ground zero.

**Solution:** The corresponding height of burst and ground distance for a 1 kt explosion are

$$h_1 = \frac{h}{W^{1/3}} = \frac{400}{(8)^{1/3}} = 200 \text{ feet.}$$

$$d_1 = \frac{d}{W^{1/3}} = \frac{1,200}{(8)^{1/3}} = 600 \text{ feet.}$$

From Figure 2-31, the time of arrival of a blast wave at a ground distance of 600 feet from a 1 kt explosion 200 feet above a thermally nonideal surface is 0.15 seconds.

**Answer:** The corresponding time of arrival for an 8 kt explosion is

$$t = t_1 W^{1/3} = (0.15)(8)^{1/3} = 0.30 \text{ sec.}$$

Under the specified conditions the ground range is reliable to within  $\pm 15$  percent (see "Reliability" below), or the 1 kt ground distance could vary between 510 and 690 feet, providing arrival times from a 1 kt explosion of 0.12 and 0.19 seconds. The time of arrival from the 8 kt explosion may therefore be expected to fall between

$$t = t_1 W^{1/3} = (0.12)(8)^{1/3} = 0.24 \text{ sec, and}$$

$$t = t_1 W^{1/3} = (0.19)(8)^{1/3} = 0.38 \text{ sec,}$$

with an expected value of 0.30 seconds as previously calculated.

**Reliability:** Over near-ideal surfaces, the ground distance for a given arrival time is estimated to be reliable within  $\pm 10$  percent. Over nonideal surfaces, two reliability estimates have been made: in the region of Mach reflection and for times less than about 0.8 sec per kt, the ground distances are estimated to be reliable within  $\pm 15$  percent; at later times or in the region of regular reflection, the values are about  $\pm 10$  percent. These reliability estimates apply to yields between 1 kt and 1 Mt. Outside this range of yields, the curves may be used with somewhat less confidence.

**Related Material:** See paragraphs 2-13 through 2-15 and paragraph 2-26. See also Tables 2-1 and 2-2.

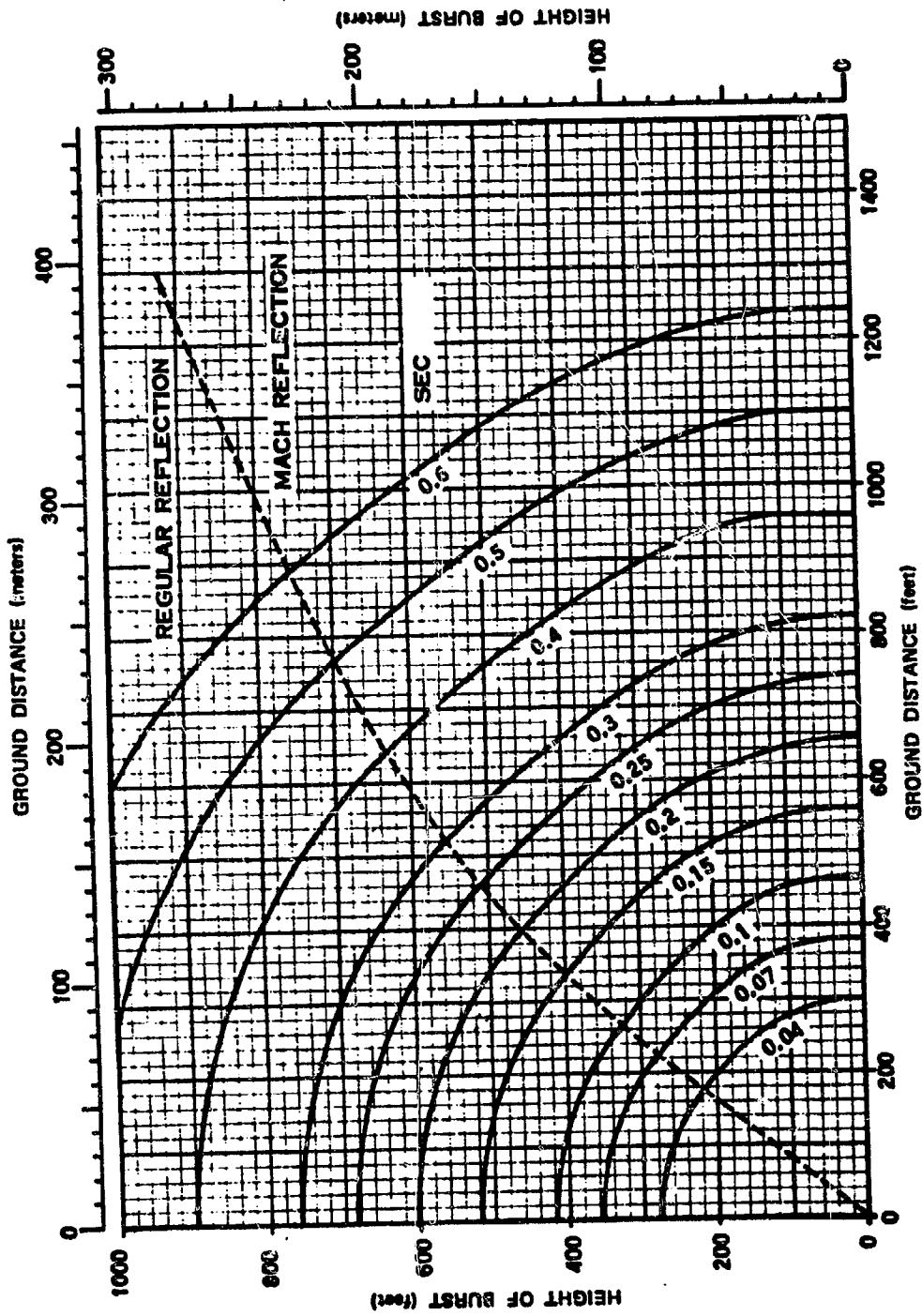


Figure 2-28. Time of Arrival of the Blast Wave Along the Surface from a 1 kt Explosion Over a Near-ideal Surface, High Overpressure Region.

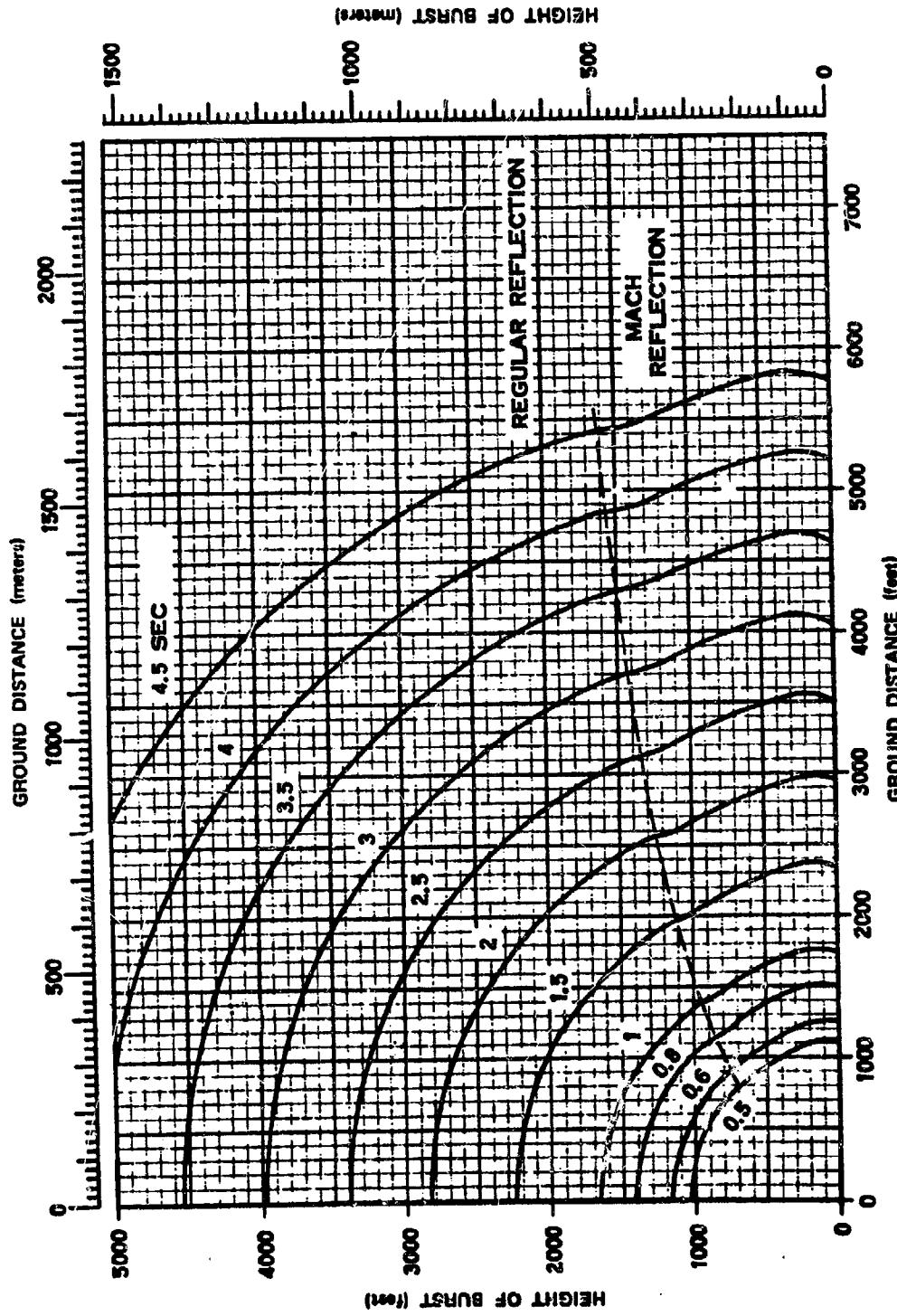


Figure 2-29. Time of Arrival of the Blast Wave Along the Surface from a 1 kt Explosion Over a Near-Ideal Surface, Low Overpressure Region

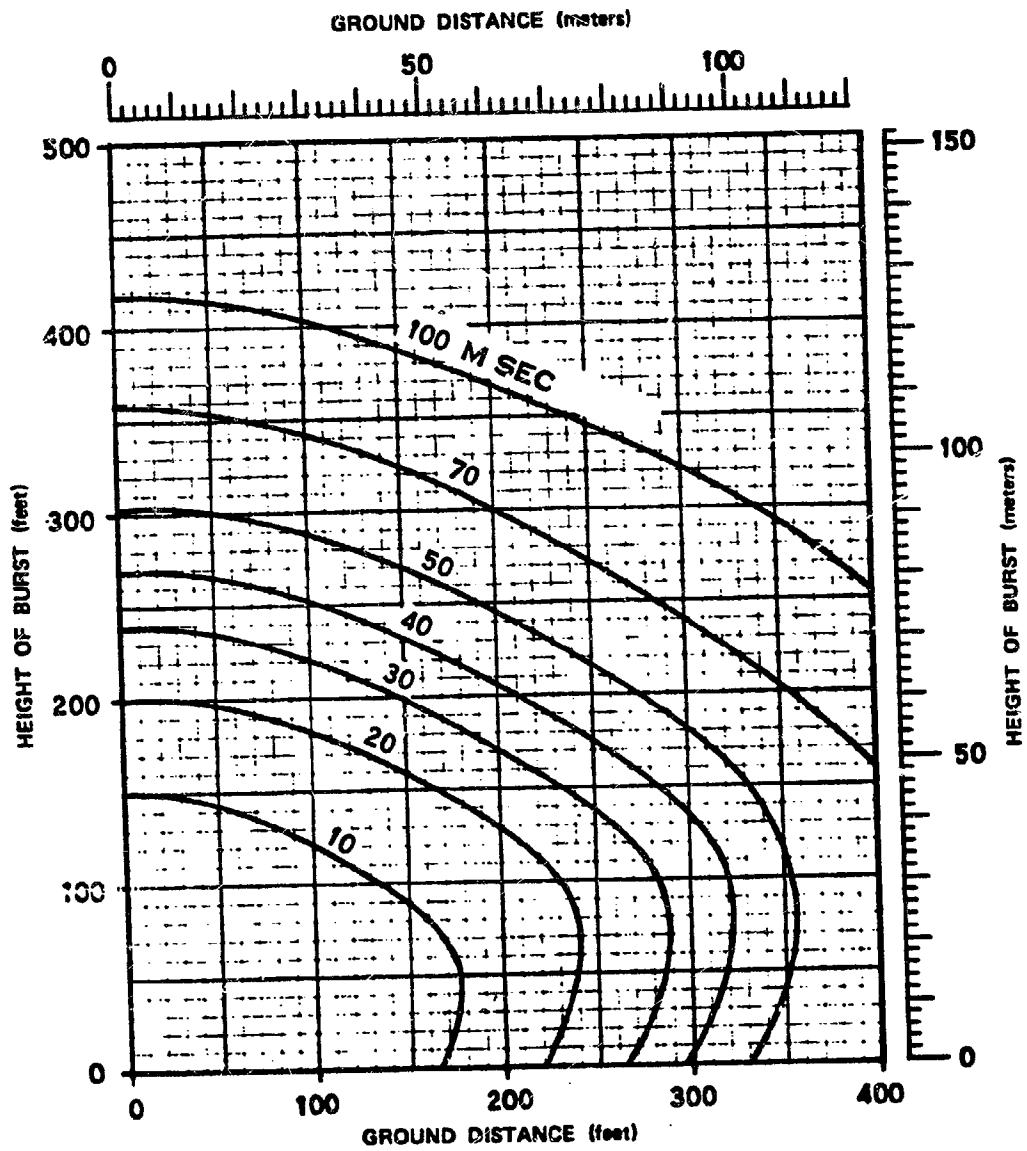


Figure 2-30. Time of Arrival of the Blast Wave Along the Surface from a 1 kt Explosion Over a Thermally Nonideal Surface, Very High Overpressure Region

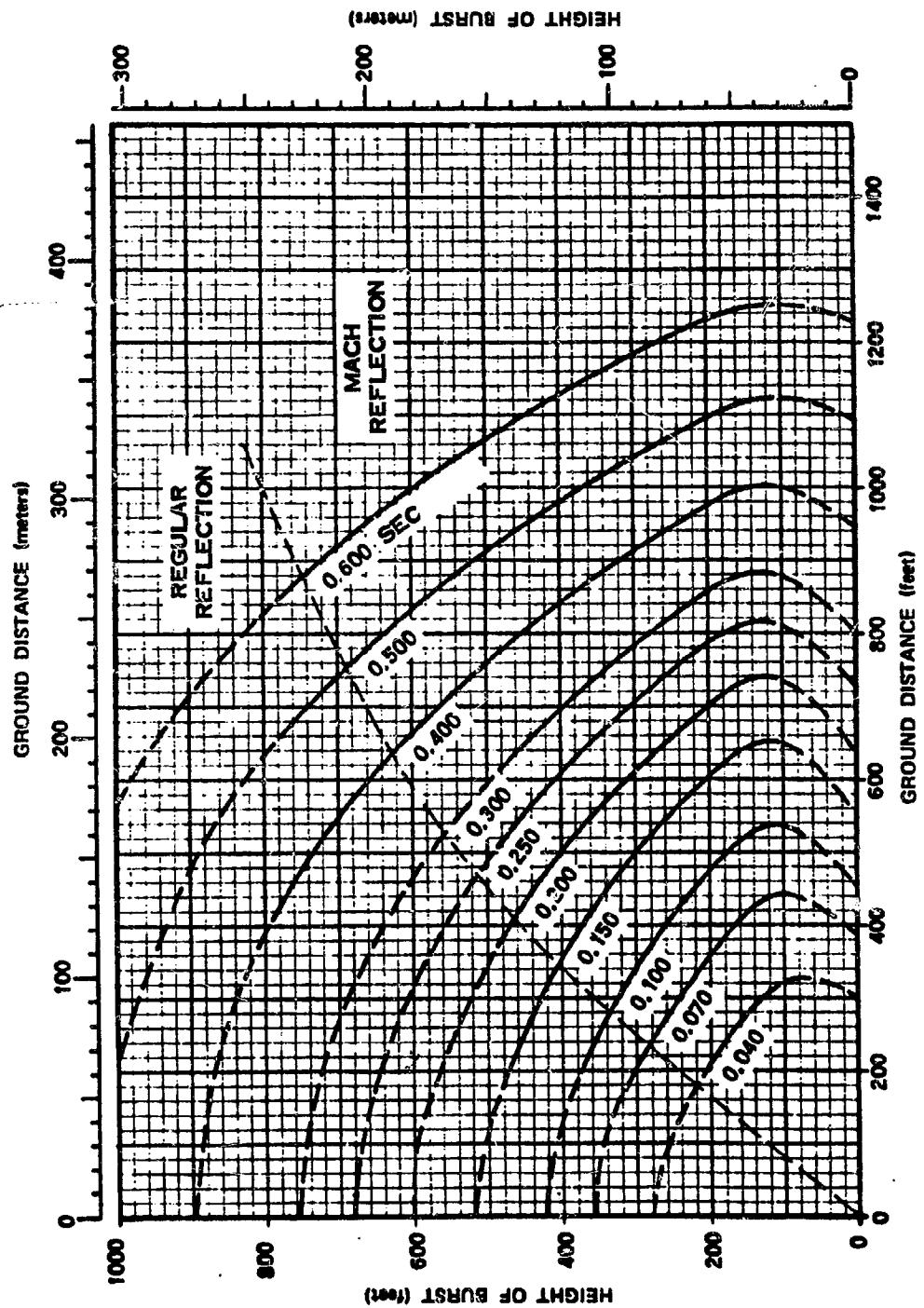


Figure 2-31. Time of Arrival of the Blast Wave Along the Surface from a 1 kt Explosion Over a Thermally Nonideal Surface, High Overpressure Region

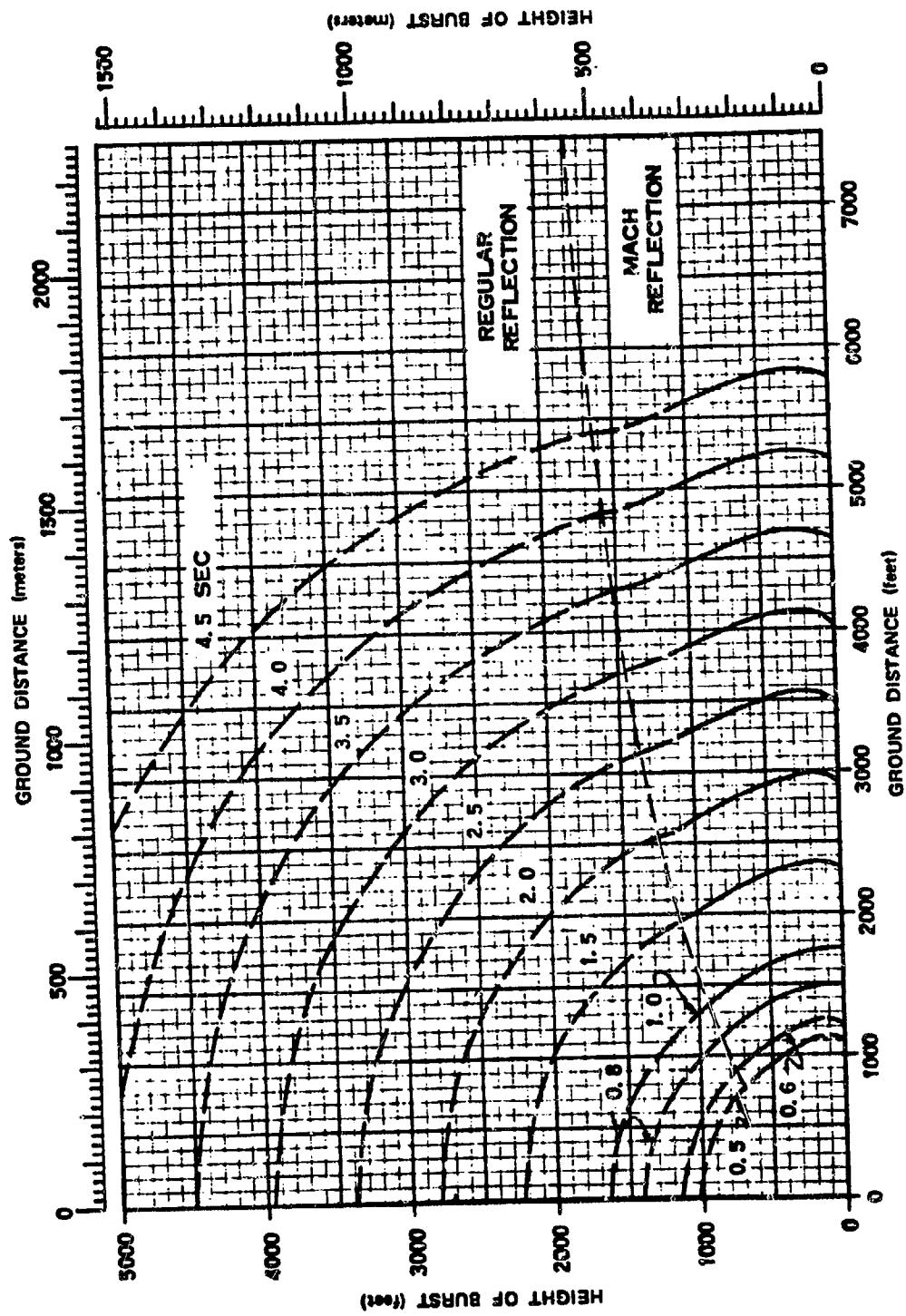


Figure 2-32. Time of Arrival of the Blast Wave Along the Surface from a 1 kt Explosion Over a Thermally Nonideal Surface, Low Overpressure Region

**Problem 2-12. Calculation of Positive Phase Duration  
of the Blast Wave at the Surface**

**Figures 2-33 and 2-34** show the duration of the positive phase of the overpressure pulse at the surface as a function of height of burst and horizontal distance from ground zero for a 1 kt explosion in a sea level atmosphere. The two figures are for near-ideal and thermally nonideal surface conditions, respectively. Positive phase duration of the dynamic pressure pulse may be estimated from data obtained from Figures 2-33 and 2-34, and Table 2-4.

**Scaling.** For yields other than 1 kt, the duration of the positive overpressure, height of burst, and distance from ground zero scale as follows:

$$\frac{t_p^+}{t_{p1}^+} = \frac{h}{h_1} = \frac{d}{d_1} = W^{1/3},$$

where  $t_{p1}^+$ ,  $h_1$ , and  $d_1$  are the positive overpressure duration, height of burst, and ground distance for a 1 kt explosion, and  $t_p^+$ ,  $h$ , and  $d$  are the corresponding time and distances for a yield of  $W$  kt. If the surface is above 5,000 feet, or if the atmospheric conditions at the surface differ from standard conditions, the altitude scaling procedures given in paragraph 2-14 should be used.

**Example**

**Given:** A 160 kt explosion 2,700 feet above a thermally nonideal surface.

**Find:** The positive overpressure and dynamic pressure durations at the surface 9,000 feet from ground zero.

**Solution:** The corresponding height of burst and ground distance for a 1 kt explosion are

$$h_1 = \frac{h}{W^{1/3}} = \frac{2,700}{(160)^{1/3}} = 500 \text{ feet},$$

$$d_1 = \frac{d}{W^{1/3}} = \frac{9,000}{(160)^{1/3}} = 1,660 \text{ feet}.$$

From Figure 2-34, the positive overpressure duration corresponding to a height of burst of 500 feet and a ground distance of 1,660 feet is about 0.3 seconds for a 1 kt explosion. From Table 2-4, the corresponding duration of the positive dynamic pressure is 0.39 seconds.

**Answer:** The corresponding positive overpressure and dynamic pressure durations for a 160 kt explosion are

$$t_p^+ = t_{p1}^+ W^{1/3} = (0.3)(160)^{1/3} = 1.6 \text{ seconds},$$

$$t_q^+ = t_{q1}^+ W^{1/3} = (0.39)(160)^{1/3} = 2.1 \text{ seconds}.$$

These are expected values. The range of possible values for the positive phase durations could be obtained by applying the uncertainties in ground distance given below in "Reliability" by methods similar to those illustrated for time of arrival in Problem 2-11. Since the uncertainties in  $t_q^+$  are greater than for  $t_p^+$ , the smaller value of  $t_q^+$  may be less than the smaller value of  $t_p^+$ . In this case, the smaller value of  $t_p^+$  should be used as the lower limit for  $t_q^+$  since the dynamic pressure positive phase is expected to last longer than the overpressure positive phase.

**Reliability:** Figures 2-33 and 2-34 were constructed entirely from experimental data. Since overpressure usually is changing slowly

when it passes through zero, the exact time marking the end of the positive overpressure phase is difficult to determine experimentally, and the uncertainty of the curves, in terms of ground distance, is large. Ground distance for  $t_p^+$  obtained from these curves is estimated to be reliable within  $\pm 25$  percent for durations of 300 msec or less and within  $\pm 50$  percent for longer durations. Use of Table 2-4 to obtain values for  $t_p^+$  gives ground distances estimated to be within  $\pm 50$  percent for durations of 390 msec or less and within  $\pm 100$  percent for longer durations. *The positive dynamic pressure phase is expected to last longer than the positive overpressure*

phase. Therefore, the lower limit for  $t_p^+$  should be no smaller than the lower limit calculated for  $t_p^+$ . For near-ideal surface conditions, these estimates apply to a yield range between 1 kt and 20 Mt; for nonideal surface conditions, the estimates apply to a yield range between 1 kt and 50 kt. The curves may be used outside this range of yields with somewhat less confidence.

**Related Material:** See paragraphs 2-13 through 2-15, 2-17 through 2-23 and 2-27. See also Tables 2-1 and 2-2 when atmospheric conditions at the surface differ from standard sea level conditions.

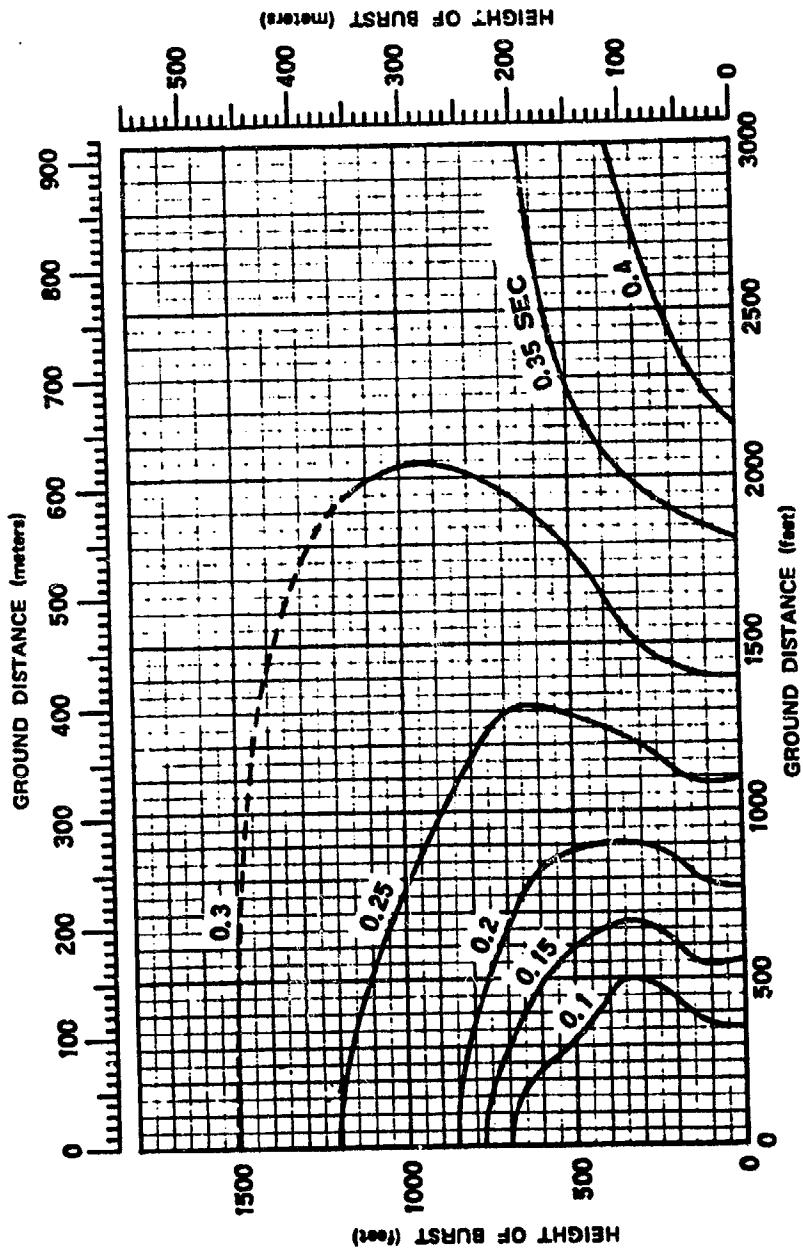


Figure 2-33. Duration of Positive Overpressure at the Surface from a 1 kt Explosion Over a Near-Ideal Surface

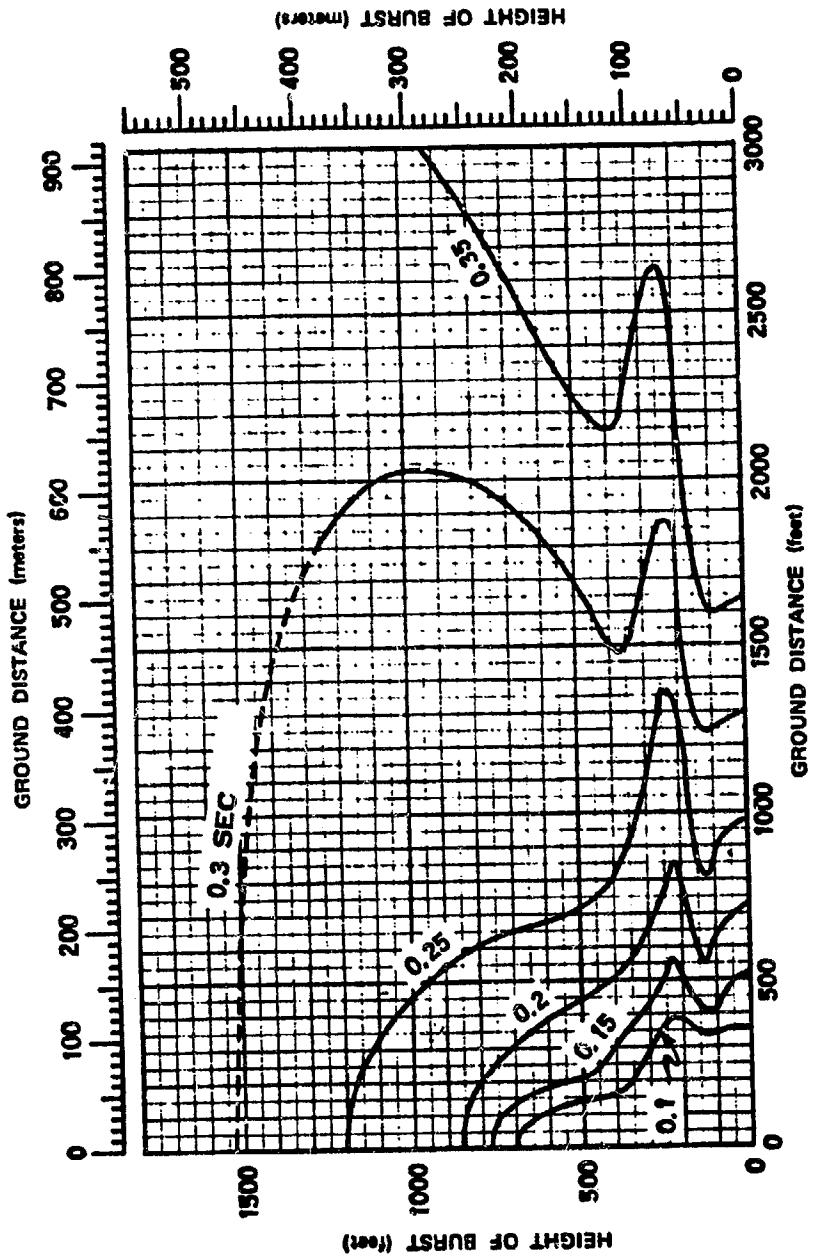


Figure 2-34. Duration of Positive Overpressure at the Surface from a 1 kt Explosion Over a Thermally Nonideal Surface

**Problem 2-13. Calculation of Positive Overpressure Impulse at the Surface**

**Figures 2-35 and 2-36 show the positive overpressure impulse at the surface as a function of height of burst and the horizontal distance from ground zero for a 1 kt explosion in a sea level atmosphere. The two figures apply to near-ideal and thermally nonideal surface conditions, respectively.**

**Scaling.** For yields other than 1 kt, the positive overpressure impulse, height of burst, and distance from ground zero scale as follows:

$$\frac{I}{I_1} = \frac{h}{h_1} = \frac{d}{d_1} = W^{1/3},$$

where  $I_1$ ,  $h_1$ , and  $d_1$  are the positive phase impulse at the surface, height of burst, and distance from ground zero, respectively, for a 1 kt explosion, and  $I$ ,  $h$ , and  $d$  are the corresponding impulse and distances from a yield of  $W$  kt. If the surface is above 5,000 feet, or if the atmospheric conditions at the surface differ from standard conditions, the altitude scaling procedures given in paragraph 2-14 should be used.

**Example**

**Given:** A 30 kt explosion 1,000 feet above a thermally nonideal surface.

**Find:** The overpressure positive phase impulse along the surface 6,000 feet from ground zero.

**Solution:** The corresponding height of burst and ground distance for a 1 kt explosion are

$$h_1 = \frac{h}{W^{1/3}} = \frac{1,000}{(30)^{1/3}} = 320 \text{ feet},$$

$$d_1 = \frac{d}{W^{1/3}} = \frac{6,000}{(30)^{1/3}} = 1,930 \text{ feet.}$$

From Figure 2-36, the overpressure impulse 1,930 feet from ground zero of 1 kt explosion at 320 feet is 0.55 psi-sec. To account for unpredictable variations in overpressure impulse, the 1 kt ground distance should be taken to be 1,930  $\pm$  20 percent (see "Reliability" below), i.e., 1,540 to 2,320 feet. From Figure 2-36, the overpressure impulses at these distances are 0.70 and 0.45 psi-sec, respectively.

**Answer:** The overpressure positive phase impulse from the 30 kt explosion will be between

$$I = I_1 W^{1/3} = (0.70)(30)^{1/3} = 2.2 \text{ psi-sec,}$$

and

$$W^{1/3} = (0.45)(30)^{1/3} = 1.4 \text{ psi-sec,}$$

with an expected value of

$$I = I_1 W^{1/3} = (0.55)(30)^{1/3} = 1.7 \text{ psi-sec.}$$

**Reliability:** The overpressure impulse contours in Figures 2-35 and 2-36 are estimated to be reliable within  $\pm$  20 percent of the indicated ground distance. For near-ideal surface conditions, this reliability estimate applies to yields between 1 kt and 20 Mt and burst heights for 1 kt below 1,000 feet; for nonideal surfaces, the estimates apply to yields between 1 kt and 50 kt and burst heights for 1 kt below 1,000 feet. Outside this range of yields and burst heights, these curves may be used with somewhat less confidence.

**Related Material:** See paragraphs 2-13 through 2-15, 2-17 through 2-23 and 2-28. See also Tables 2-1 and 2-2 when atmospheric conditions at the surface differ from standard sea level conditions.

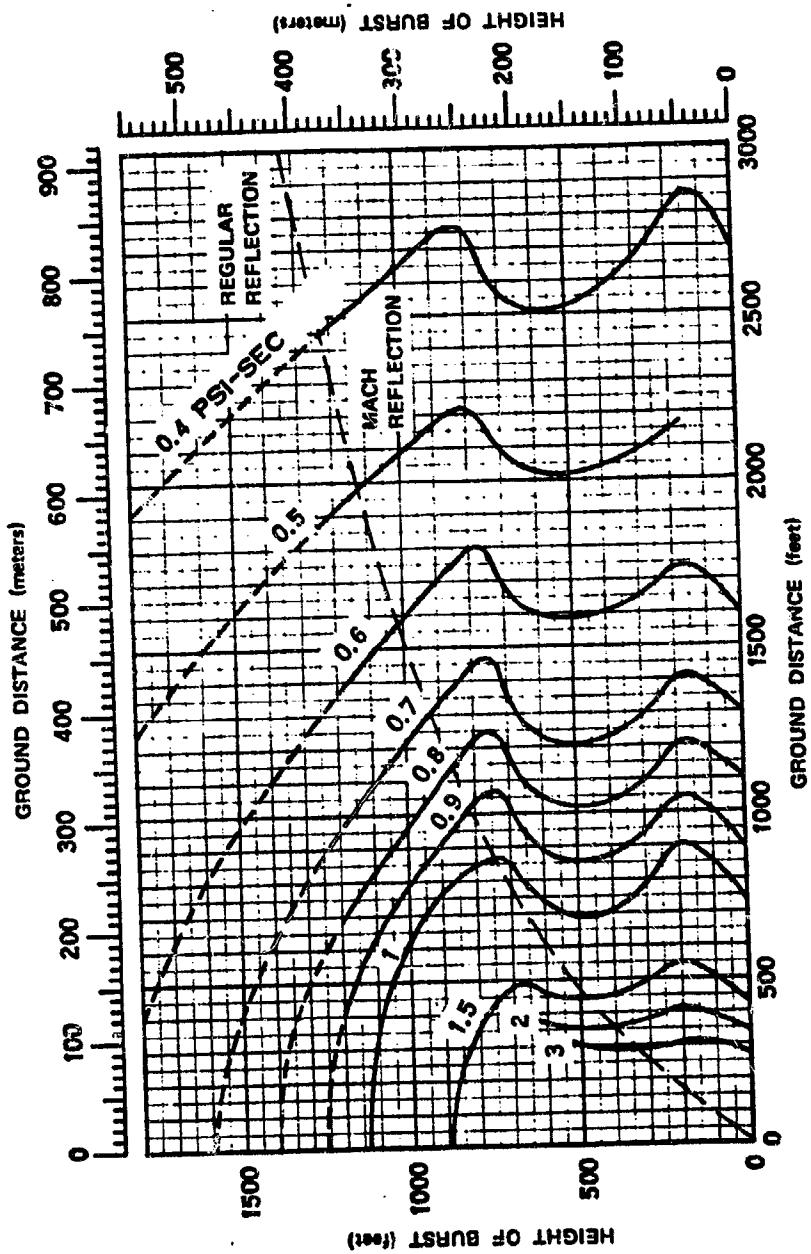


Figure 2-35. Positive Overpressure Impulse at the Surface from a 1 kt Explosion Over a Near-Ideal Surface

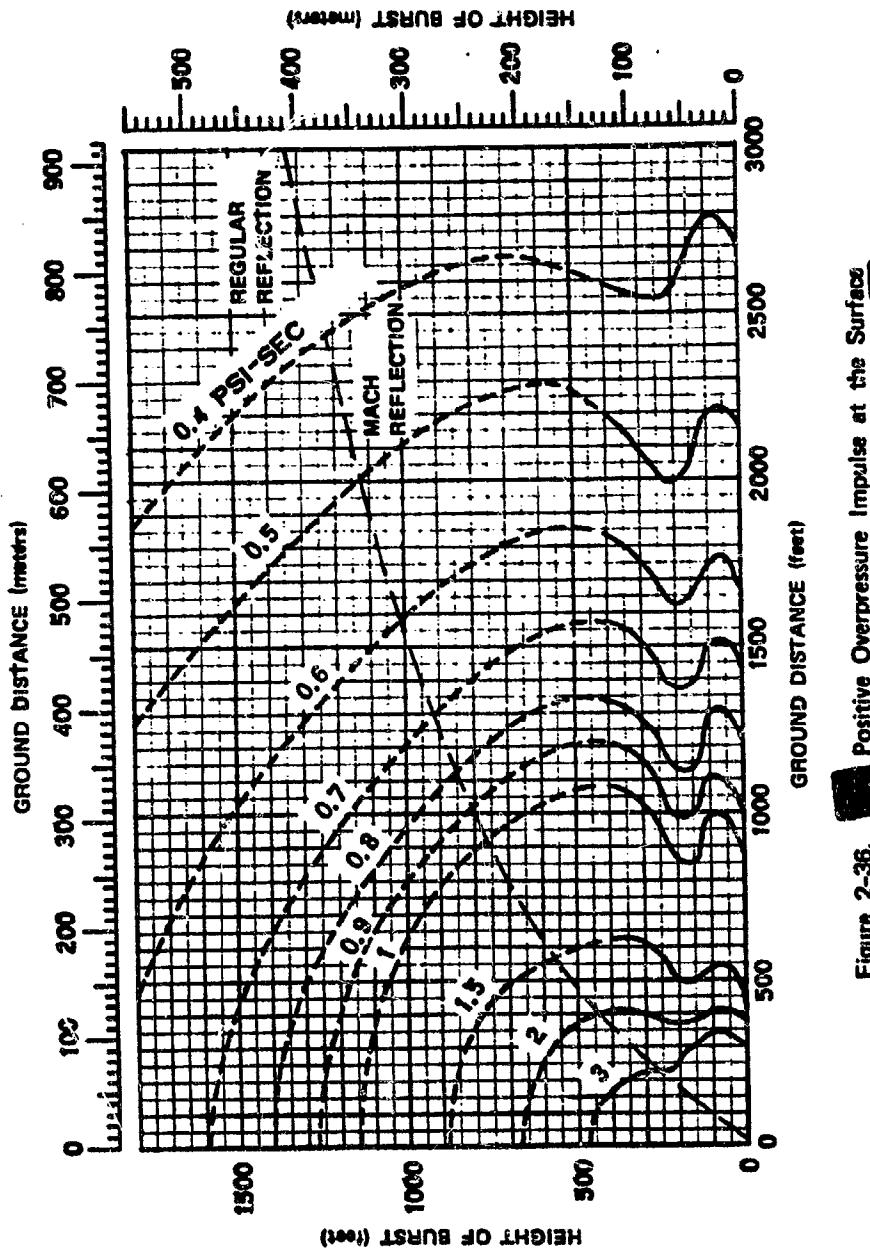


Figure 2-36. Positive Overpressure Impulse at the Surface from a 1 kt Explosion Over a Thermally Nonideal Surface

### Problem 2-14. Calculation of Mach Stem Height

Figures 2-37 and 2-38 show the height of the Mach stem as a function of horizontal distance from ground zero for several heights of burst for a 1 kt explosion in a sea level atmosphere. These curves, in effect, show the trajectory of the triple point (paragraph 2-18 and 2-29).

**Scaling.** For yields other than 1 kt, the Mach stem height, height of burst, and ground distance scale as follows:

$$\frac{H}{H_1} = \frac{h}{h_1} = \frac{d}{d_1} = W^{1/3},$$

where  $H_1$ ,  $h_1$ , and  $d_1$  are the height of the Mach stem, the height of burst, and the distance from ground zero, respectively, for a 1 kt explosion, and  $H$ ,  $h$ , and  $d$  are the corresponding distances for a yield of  $W$  kt. If the surface is above 5,000 feet, or if the atmospheric conditions at the surface differ from standard conditions, the altitude scaling procedures given in paragraph 2-14 should be used.

**Example**

**Given:** A 55 kt explosion 1,000 feet above the surface.

**Find:** The ground distance beyond which an aircraft flying 500 feet above the surface will be in the Mach reflection region.

**Solution:** The corresponding height of burst and Mach stem height for a 1 kt explosion are

$$h_1 = \frac{h}{W^{1/3}} = \frac{1,000}{(55)^{1/3}} = 260 \text{ feet},$$

$$H_1 = \frac{H}{W^{1/3}} = \frac{500}{(55)^{1/3}} = 130 \text{ feet.}$$

Interpolation between the curves of Figure 2-37 shows that a 1 kt explosion burst at 260 feet will have a Mach stem height of 130 feet when the triple point is at a ground distance of about 750 feet.

**Answer:** The corresponding ground distance for a 55 kt explosion is

$$d = d_1 W^{1/3} = (750)(55)^{1/3} = 2,850 \text{ feet.}$$

Since this yield is close to the upper limit at which a  $\pm 10$  percent tolerance applies (see "Reliability" below), the distance may reasonably be expected to be within about  $\pm 15$  percent ( $\pm$  about 430 feet). Therefore the Mach stem height may reasonably be expected to exceed 500 feet at a ground range beyond about 3,300 feet.

**Reliability:** The range at which a given Mach stem height is shown to occur in Figures 2-37 and 2-38 is considered reliable within  $\pm 10$  percent for yields between 1 kt and 50 kt and within  $\pm 25$  percent for yields up to 20 Mt. This decrease in confidence with increasing yield results from the lack of knowledge concerning the effect of atmospheric nonhomogeneity on the triple-point trajectory. It is suggested that no correction be made for *burst* altitude; however, when the data are applied to high-yield air bursts, the results should be treated with somewhat less confidence.

**Related Material:** See paragraphs 2-13 through 2-15, 2-17 through 2-23, and 2-29. See also Tables 2-1 and 2-2 when atmospheric conditions at the surface differ from standard sea level conditions.

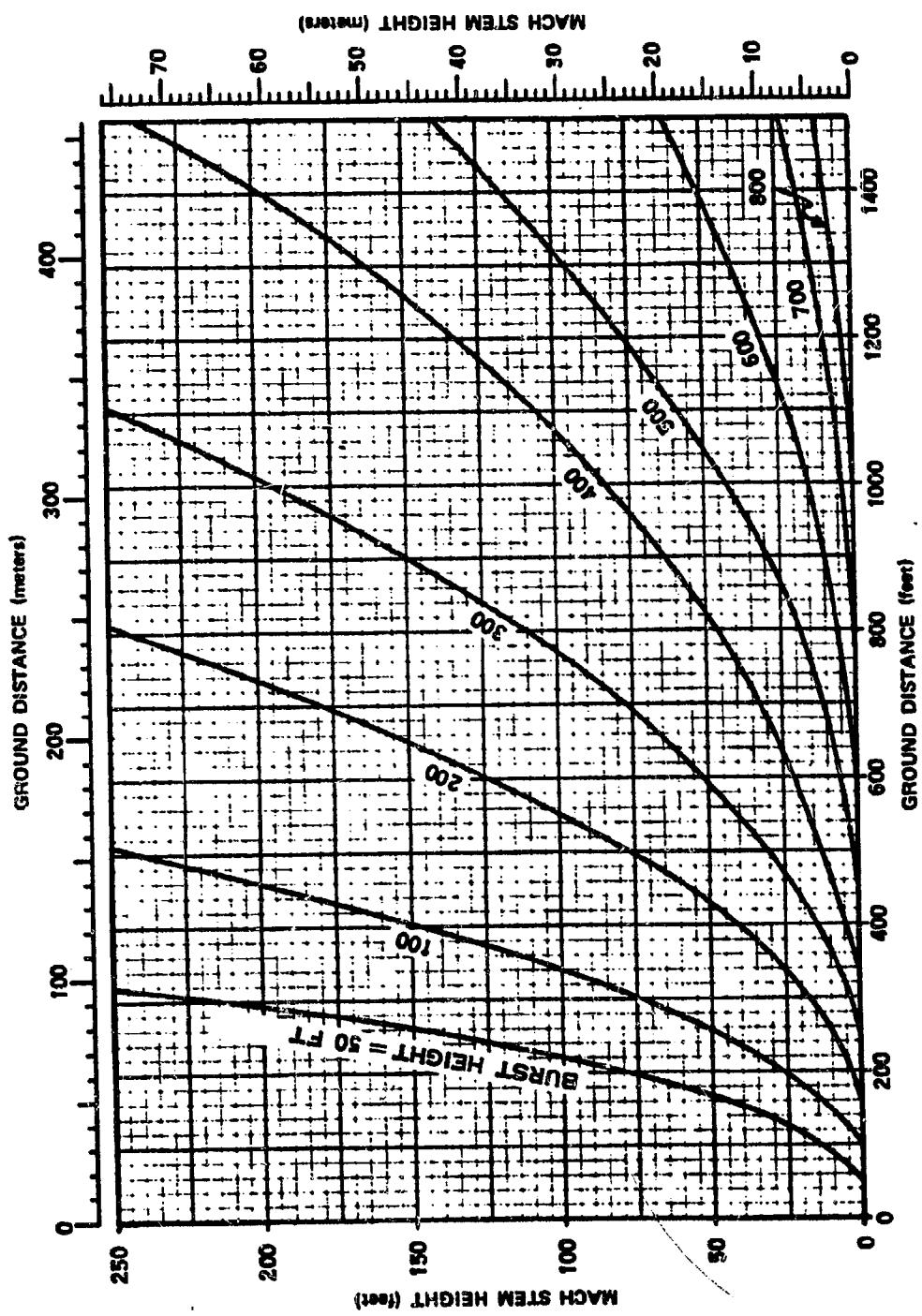


Figure 2-37. Mach Stem Height for a 1 kt Explosion.  
High Overpressure Region

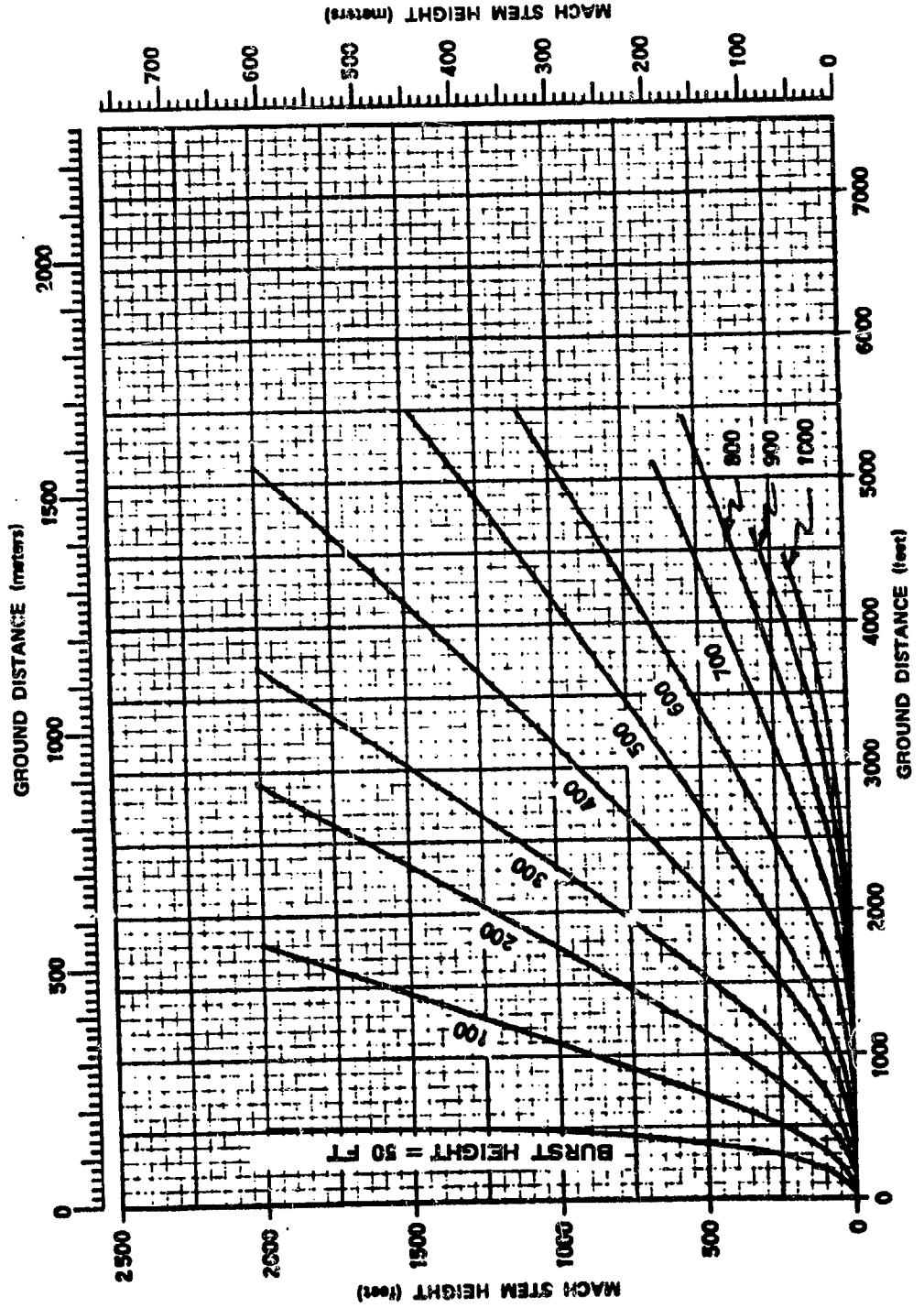


Figure 2-38. Mach Stem Height for a 1 kt Explosion.  
 Low Overpressure Region

### 2-30 Criteria for Precursor Formation

Figure 2-39 shows heights of burst at which an explosion over a thermally nonideal surface is likely to produce a precursor. As indicated in Figure 2-39, bursts higher than  $800 W^{1/3}$  feet are not expected to form a precursor. This is the maximum height that will produce a precursor over asphalt, a surface that produces a precursor more readily than any other that has been tested. A burst below  $650 W^{1/3}$  feet will produce a precursor over desert sand. Since desert sand is considered a more typical nonideal surface than asphalt, it provides the basis for predicting precursors over most thermally nonideal surfaces.

Figure 2-39 also shows that a burst may be too low to produce a precursor as well as too high. At the ranges where a precursor might form, a contact surface burst of less than 30 kt is not expected to heat the surface sufficiently to produce a strong thermal layer; higher yields may create precursors over thermally nonideal surfaces.

Theories suggest that precursor formation depends not only on the amount of thermal energy absorbed by the surface, but also upon the time that is available for the thermal layer to form before the blast wave arrives. When time as well as thermal energy density is considered, theory indicates that the thermal layer and its influence on the blast wave might scale approximately as  $W^{1/3}$ , as indicated in Figure 2-39; however, no theory has yet been developed that explains the criteria for precursor formation in a completely satisfactory manner. For this reason, these criteria must be based on experimental data. Precursors have been observed from yields as high as 15 Mt; however, the yields that have been detonated between about  $650 W^{1/3}$  and  $800 W^{1/3}$  feet above the surface, and therefore the yields that are of value in confirming these criteria for precursor formation, are limited to the range of about 1 to 50 kt. Over this range of

yields, the precursor seems to follow the cube root scaling; however, this may only result from the range of yields for which data are available being inadequate to reveal deviations. No reliability tolerances can be assigned to Figure 2-30, but if the surface is similar to desert sand, precursors may be predicted with reasonable accuracy for yields between 1 and 50 kt.

### 2-31 Overpressure Waveforms

The classical free air overpressure waveform (paragraph 2-12) is seldom found along the surface at overpressure levels above 6 psi. At higher overpressures, such waveforms approach the ideal for special surface conditions such as snow, ice, and water (where thermal effects are normally at a minimum). Even for these surfaces, minor mechanical effects may be present. For example, the rise time over water may not be instantaneous, and there may be a slight rounding of the peak of the overpressure waveform. When these near-ideal conditions exist, overpressure waveforms may be approximated by those for free air, shown in Figure 2-8.

In the simple case of ideal waveforms in free air, all of the properties of the blast wave, and therefore its damage potential, may be determined by specifying the ambient atmospheric conditions plus two blast parameters (for example, peak overpressure and positive overpressure impulse). When the blast wave loses its ideal characteristics, two other properties of the overpressure waveform become important: (1) for most overpressure-sensitive targets, a gradual rise to a given overpressure is less destructive than the abrupt rise of an ideal pulse; (2) as a result of the sustained overpressures often found in nonideal waveforms, a given peak overpressure may be associated with a much larger positive impulse than if overpressure pulse shape were ideal. Additional effects caused by changes in the dynamic pressure waveform are discussed in succeeding paragraphs.

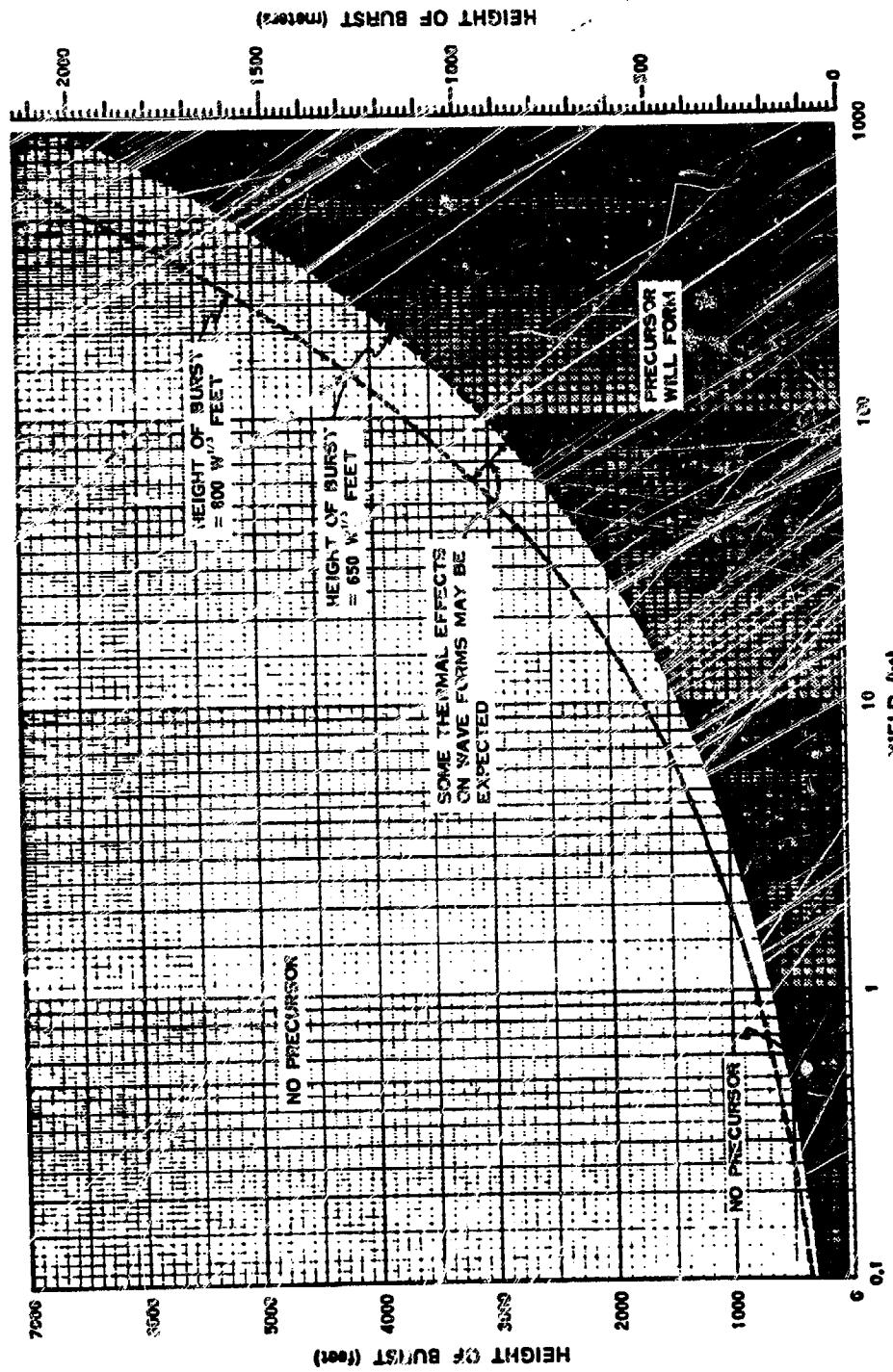


Figure 2-39. Criteria for Precursor Formation

A series of eleven waveforms characteristic of the blast wave over a thermally nonideal surface is shown in time sequence in Figure 2-40. Although the evolution of a precursor is a continuous process, the waveforms may be classified loosely into five types, according to the state of development of the precursor:

- Type I: Waveform before precursor forms (a)
- Type II: Development of the precursor (b, c, d)
- Type III: Evolution of fully developed precursor (e, f, g)
- Type IV: Decline of precursor (h, i, j)
- Type V: Return to nearly ideal waveform (k)

The overpressure waveforms generated under any particular set of conditions depend strongly on the degree to which nonideal surface effects interact with the blast wave. In general, the more nonideal the surface conditions, the more nonideal will be waveforms near the surface. The waveforms shown in Figure 2-40 are typical for scaled heights of burst between 100 and 400 feet over flat desert surfaces. Characteristics of these waveforms are discussed below.

- Type I — Just before the precursor forms, the waveform *a* is relatively ideal.
- Type II — As the precursor starts to develop, a separate shock front forms in the thermal layer and moves out ahead of the main shock. In waveform *b* these two shock fronts are nearly ideal but, as the precursor develops, its diverging flow pattern weakens its own shock front. At the same time, the growing precursor interferes more strongly with the main blast wave, which apparently loses any semblance of a true shock front at the surface. Separation of the two peaks indicates the forward growth of the precursor; however, the second peak in waveforms *c* and *d* no longer marks the exact position of the main blast wave. Typical changes in Type

II waveforms at early times are a rapid attenuation of the first peak and a rounding of the second peak. At later times, the second peak is attenuated more rapidly than the first, and the first loses its shock-like rise. The slow decay after the first peak in waveforms *c* and *d* is sometimes replaced by a plateau.

- Type III — As the distance from ground zero increases, the peaks and valleys become poorly defined. At close distances, the waveform *e* has a large rounded maximum followed by a slow decay, and a later and smaller second peak. At longer distances, the first peak is attenuated more rapidly than the second, and the two peaks become comparable in magnitude (*f*). The rise times also become longer. The second peak disappears at longer distances, leaving a low, rounded, flat-topped waveform *g* with a long initial rise and slow decay, during which there is considerable turbulence. This waveform is typical of strong precursor action.
- Type IV — Farther from ground zero, the thermal layer becomes less intense, and the precursor begins to weaken and lose forward speed. The second peak reappears, and both peaks become sharper. The rounded plateau in waveform *h* and the step-like appearance of *i* are typical. As the main shock overtakes the precursor, the waveform assumes an almost classical form *j* with a sharp rise to a more or less level plateau, followed by an essentially regular decay. This waveform is typical of the "clean-up" portion of the precursor cycle.
- Type V — After the precursor has disappeared, the pressure pulse again approaches a classical waveform *k*. This waveform is longer than it would be if a precursor had never formed.

Methods for determining ground dis-

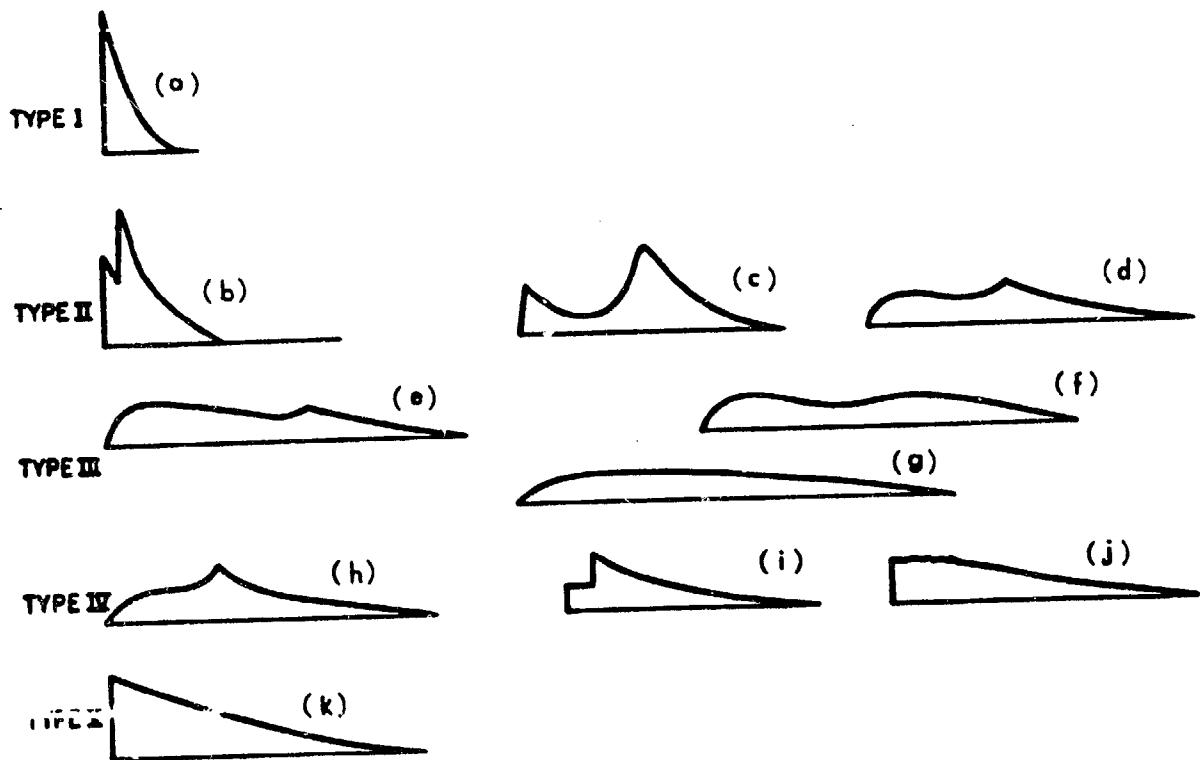


Figure 2-40. [REDACTED] Typical Sequence of Overpressure Waveforms  
Over Thermally Nonideal Surfaces [REDACTED]

tances at which the waveforms described above will occur are described in Problem 2-15.

### 2-32 Dynamic Pressure Waveforms

Dynamic pressure waveforms at the surface approach the classical shape shown in Figure 2-9 when the surface conditions are near-ideal. The conditions under which this occurs are more restricted than those for overpressure waveform. Differences result from surface conditions that do not lead to precursor formation but do lead to dust or spray loading of the air. Such surfaces are expected to modify the dynamic pressure waveform without changing the overpressure waveform to any great extent.

Dynamic pressure waveforms that appear over thermally nonideal surfaces are more difficult to measure than overpressure waveforms, and the measurements are subject to wider variations. For these reasons it is not possible at this time to provide a figure that shows zones in which various waveforms can be expected. However, representative waveforms have been constructed (Figure 2-41), and tentatively have been classified into five categories: A, B, C, D, and E (letters rather than Roman numerals are used with dynamic pressure waveforms to emphasize that the various types cannot be directly correlated with the waveform types used to classify overpressure waveforms). These waveforms are discussed below.

- Type A — Before the precursor forms, the waveform is relatively ideal (1).
- Type B — As the precursor starts to develop, the waveform shows two distinct

peaks. The first, corresponding to the precursor, has a shock type rise in most cases. The second is larger than the first at close distances (waveforms 2 and 3), but at longer distances (waveform 4) it becomes comparable in magnitude to the first.

- Type C — As the precursor becomes fully developed, the waveform retains its double peak but loses its rapid initial rise time. Actual record traces have a very turbulent appearance. The second peak is smaller than the first (5) and tends to become indefinite with increasing distance (6).
- Type D — As the precursor becomes weaker, the waveform assumes an essentially single peaked form, characterized at close distances (waveform 7) by a low-amplitude plateau with a slow rise. Actual traces have a very turbulent appearance. As the distance from ground zero increases (waveform 8), the turbulence lessens, and the plateau develops a shock rise with either a flat top or a slow steady increase to a second shock rise, followed by a smooth decay. The second shock eventually overtakes the first (waveform 9), leaving a smooth, clean trace with a slight rounding after the initial shock type rise.
- Type E — After precursor cleanup, the waveform (10) resumes its approximately classical shape. Positive phase duration is longer than it would be at this distance if a precursor had not formed. This longer duration is more marked for dynamic pressure than for overpressure.

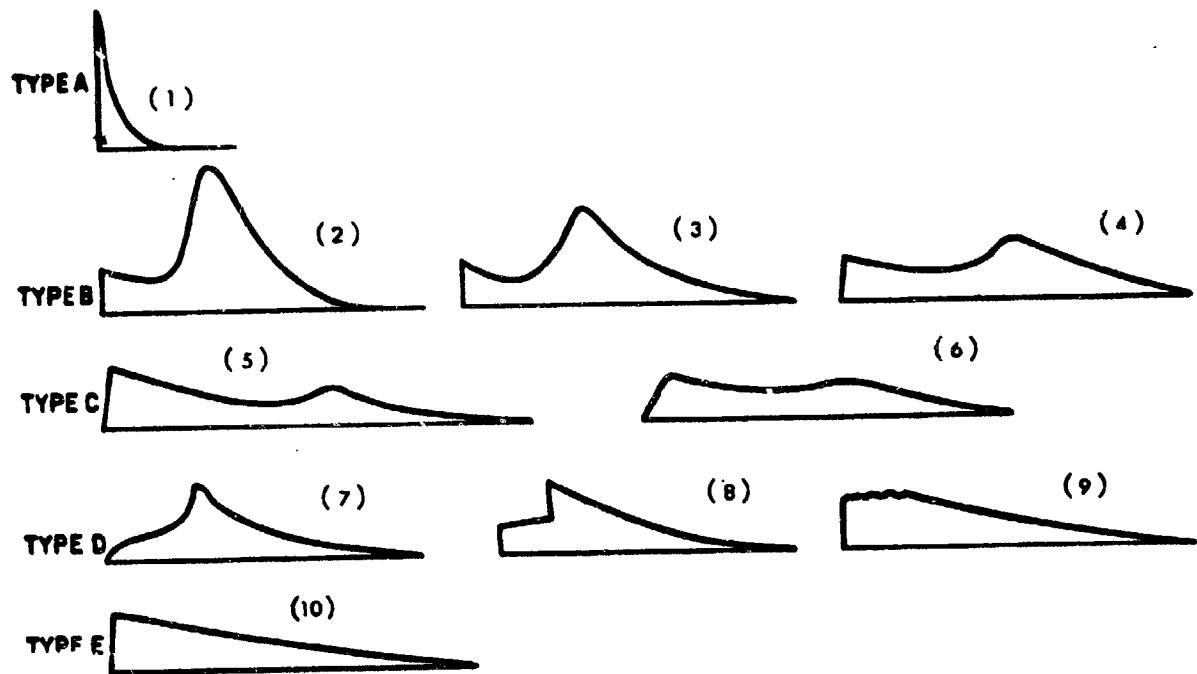


Figure 2-41. [REDACTED] Typical Sequence of Dynamic Pressure Waveforms  
Over Thermally Nonideal Surfaces [REDACTED]

**Problem 2-15. Calculation of Distances for Overpressure Waveforms in the Precursor Region**

Figure 2-42 shows zones, defined by height of burst and distance from ground zero, wherein overpressure waveforms depicted in Figure 2-40 might be expected to occur from a 1 kt explosion over a thermally nonideal surface. Neither the waveforms nor the ranges at which they occur can be predicted reliably for all conditions. The waveforms will be modified as height of burst changes; if the scaled height of burst is above 400 or below 100 feet, the waveforms may differ significantly from those shown in Figure 2-40. Any other surface effect that modifies the precursor also will modify the waveforms. For example, distortion of the overpressure waveform will be less severe if trees or shrubs decrease the velocity of the surface winds required for precursor formation (other surface interactions are discussed in paragraphs 2-20 through 2-22). Moderate thermal effects may produce disturbed waveforms that are neither ideal nor as extreme as those shown in Figure 2-40. Information from Figures 2-40 and 2-42 should be considered a useful guide, not an infallible prediction.

**Scaling.** For yields other than 1 kt, scale as follows:

$$\frac{h}{h_1} = \frac{d}{d_1} = W^{1/3},$$

where  $h_1$  and  $d_1$  are the height of burst and the ground distance for 1 kt, and  $h$  and  $d$  are the corresponding distances for a yield of  $W$  kt. If the surface is above 5,000 feet, or if atmospheric conditions at the surface differ from standard sea level conditions, the altitude scaling procedures described in paragraph 2-14 should be used.

**Example**

**Given:** A 100 kt explosion 600 feet above a thermally nonideal surface.

**Find:**

- The ground distance to which a precursor may be expected to extend.
- The waveform to be expected at the surface 1,800 feet from ground zero.

**Solution:** The corresponding height of burst for 1 kt is

$$h_1 = \frac{h}{W^{1/3}} = \frac{600}{(100)^{1/3}} = 130 \text{ feet.}$$

a. From Figure 2-42, the precursor zone extends to approximately 1,130 feet for a 1 kt explosion at a height of 130 feet (the zone indicating a Type V waveform shows the region where precursor characteristics disappear and the waveform approaches the classical shape (Figure 2-40)).

b. The ground distance for a 1 kt explosion corresponding to a distance of 1,800 feet for 100 kt is

$$d_1 = \frac{d}{W^{1/3}} = \frac{1,800}{(100)^{1/3}} = 390 \text{ feet.}$$

**Answer:**

a. The distance to which a precursor may be expected to extend from ground zero of a 100 kt explosion at a height of 600 feet is

$$d = d_1 W^{1/3} = (1,130)(100)^{1/3} = 5,240 \text{ feet.}$$

b. From Figure 2-42, a distance of 390 feet from ground zero of a 1 kt explosion at a

height of 130 feet falls within the zone corresponding to waveform II. This same waveform would be expected at a distance of 1,800 feet from a 100 kt burst at a height of 600 feet.

**Reliability:** Specific reliability figures have not been set on the boundary positions in Figure 2-42. The zone boundaries are derived primarily from full scale tests over desert surfaces. Overpressure waveforms over other sur-

faces are subject to the variations noted above. Yield scaling is uncertain outside the range of 1 kt to 50 kt, but should be used in the absence of confirming experimental data. Altitude scaling is also a questionable procedure, but it should provide reasonable results for surface altitudes below 10,000 feet.

**Related Material:** See paragraphs 2-12, 2-20 through 2-22, and 2-31.

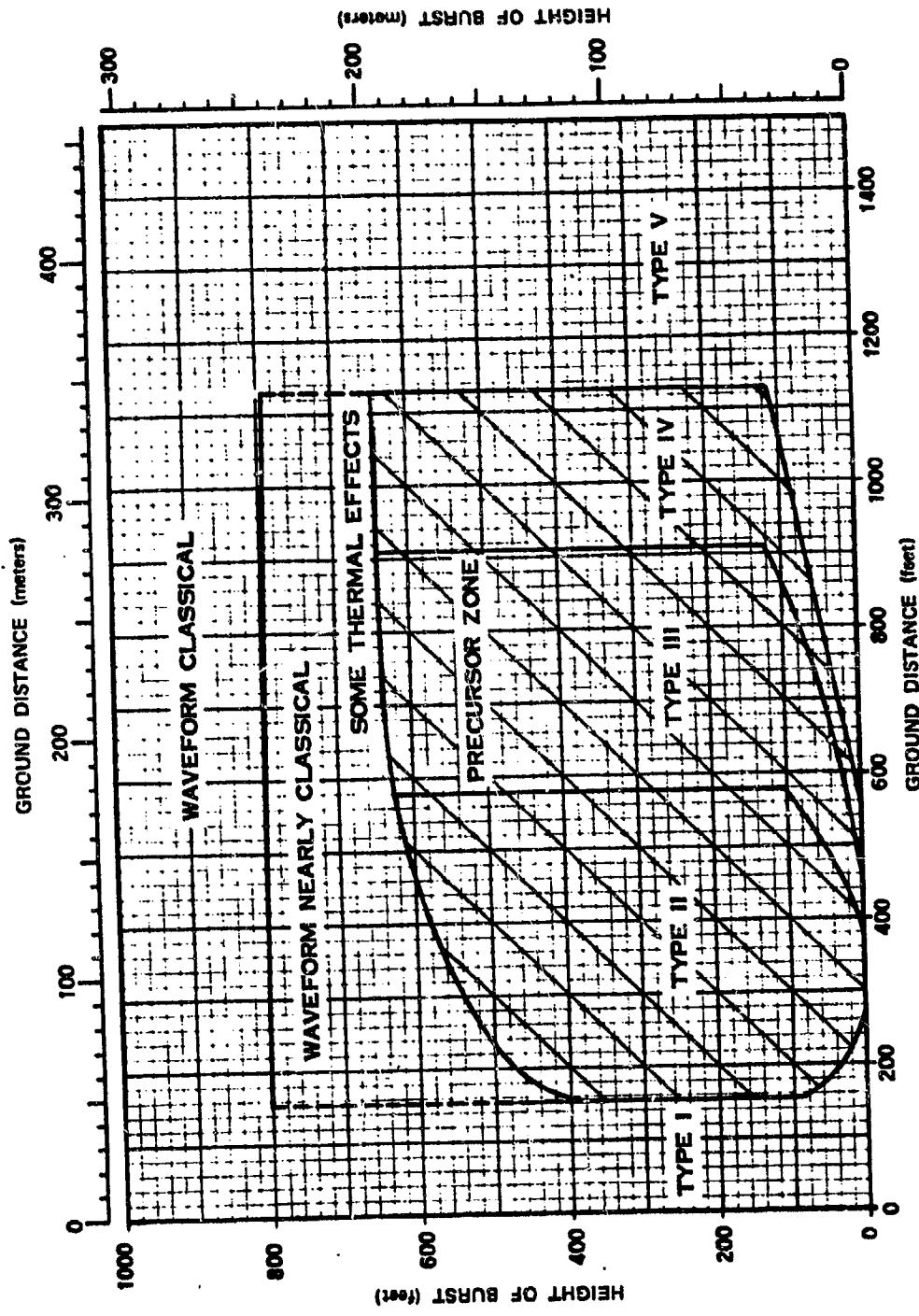


Figure 2-42. Variation of Overpressure Waveform from a 1 kt Explosion Over a Thermally Nonideal Surface

### 2-33 Effect of Rain and Fog on Overpressure

The effects of atmospheric moisture on blast propagation are not well known; however, theoretical studies agree qualitatively with the small amount of experimental data. As a strong blast wave propagates through air containing water droplets it vaporizes some or all of the water. Vaporization of the water absorbs energy that otherwise would be available for the blast wave to propagate through the air.\* As a result, the blast wave is attenuated more rapidly in air that contains water droplets than in air that does not.

The effect of water droplets on peak overpressure may be calculated in terms of effective yield. This procedure is used to obtain lower calculated overpressures at some distance from the burst. Rain or fog has a negligible effect on the amount of available energy close to the nuclear source. The energy density within the fireball is orders of magnitude higher than the energy required to vaporize whatever water may be present, and the amount by which the suspended liquid increases effective air density, even under the extreme conditions within clouds producing severe thunderstorms, is not likely to exceed 2 percent.

Figure 2-43 shows the effective yield for three yields and two conditions of moisture content. Examination of these curves reveals several trends:

- The attenuation produced by heavy rain is greater than the attenuation produced by light rain or fog.
- Effective yield decreases as overpressure decreases, i.e., it decreases as distance (and, therefore, the amount of rain through which the blast wave must propagate) increases.
- At any overpressure level, the blast wave from a 1 kt burst is attenuated less than

the blast wave from the two other yields. This difference results from the shorter distances for the 1 kt blast wave. Light rain or fog attenuates the blast wave from a 1 kt explosion to such a small extent that the curve is not included in Figure 2-43.

- At a given overpressure level, the blast wave from a 1 Mt burst is attenuated less than the blast wave from a 125 kt burst. This effect, opposite to that described above, probably results from the relatively large amount of hydrodynamic energy carried by the long-duration blast wave from a 1 Mt source.

The curves shown in Figure 2-43 are based on the assumption of uniform water content between the source and the target. In an actual rainstorm, this assumption is artificial. Typically, water content is several times as high within a rain cloud as it is below the cloud, but without such an assumption the analysis of rain effects would be unduly complex. Actual water distribution patterns are complex, different for different rainstorms, and generally unpredictable. The water densities used in the calculations correspond roughly to precipitation rates of 0.1 and 0.5 inches per hour.

As a blast wave propagates through air, it continuously expends hydrodynamic energy at the shock front to compress and accelerate the air entering the blast wave. At the same time, the air behind the front expands and decelerates, thereby returning energy to the blast wave. The flow of energy in a weak shock wave resembles that in a sound wave. The expanding air returns nearly all of the energy that it received when it entered the shock front. Consequently, the attenuation of weak blast waves is due principally to spherical divergence. On the other hand, strong shock waves lose appreciable energy, because the sudden compression at the shock front is partially irreversible. Thus, the expanding air beyond the strong shock front returns less energy than was required to compress it, and the corresponding energy loss contributes to the attenuation of the blast wave. If the air contains water droplets, the energy extracted from the blast wave when the water evaporates is returned to the surrounding air when the water condenses; however, condensation occurs too slowly to contribute appreciable energy to the blast wave.

Rain or fog effects should be evaluated only when the optimization of blast against soft targets is important, and then only if the rain or fog extends throughout a volume that includes both the target and the burst. HOB curves for thermally near-ideal surface conditions should be used with Figure 2-43 since thermal energy is attenuated by rain or fog and a wet surface is not expected to form a strong thermal layer.

The effects of atmospheric moisture on

other blast parameters, such as time of arrival, positive-phase duration, and dynamic pressure are not well known; however, theoretical considerations indicate that arrival times will remain essentially unchanged, positive-phase durations will be slightly reduced, and dynamic pressures will be slightly increased. Calculations for these other parameters should be made in the normal manner, without applying the yield correction factor obtained from Figure 2-43.

### Problem 2-16. Calculation of Overpressure During a Rainstorm

Figure 2-43 shows the reduced yield in percentage of actual yield, that should be used for overpressure calculations under conditions of rain and fog. This figure should be used together with Figures 2-17 through 2-19 to obtain overpressure values under conditions of rain or fog.

**Scaling.** Interpolation between the curves of Figure 2-43 provides the only yield scaling available. After obtaining an effective yield from Figure 2-43, the scaling procedures described in Problem 2-9 are applicable.

**Example**

**Given:** A 50 kt explosion at a height of burst of 3,000 feet during a heavy rainstorm.

**Find:** The peak overpressure 4,000 feet from ground zero.

**Solution:** The corresponding height of burst and ground distance for a 1 kt explosion yield are

$$h_1 = \frac{h}{W^{1/3}} = \frac{3,000}{(50)^{1/3}} = 815 \text{ feet},$$

$$d_1 = \frac{d}{W^{1/3}} = \frac{4,000}{(50)^{1/3}} = 1,090 \text{ feet.}$$

From Figure 2-18, the peak overpressure expected in clear air is about 13 psi. At this peak overpressure, Figure 2-43 indicates that the effective yield during heavy rain is about 84 percent for 1 kt, 73 percent for a 125 kt burst. A probable effective yield for 50 kt should be between these values and may be about 77 percent. Uncertainty in the degree of attenuation produced by

a rainstorm would cause the effective yield to vary according to the reliability estimates given below. This calculation will determine the most probable value of the peak overpressure rather than the upper and lower limits. The effective yield for further calculations is

$$50 \times 0.77 = 39 \text{ kt.}$$

The corresponding height of burst and ground distance for a 1 kt explosion are

$$h_1 = \frac{h}{W^{1/3}} = \frac{3,000}{(39)^{1/3}} = 885 \text{ feet},$$

$$d_1 = \frac{d}{W^{1/3}} = \frac{4,000}{(39)^{1/3}} = 1,180 \text{ feet.}$$

**Answer:** From Figure 2-18, the most probable peak overpressure is 10 psi.

**Reliability:** Figure 2-43 is based on theoretical calculations and a limited amount of data from small scale field tests and laboratory experiments. Thus, a high reliability cannot be assigned to the curves of Figure 2-43. The upper limit of the effective yield is 100 percent of the actual yield, while the lower limit is estimated to be 60 percent of the value obtained from Figure 2-43. If the burst is below or close to the cloud base in fairly uniform rainfall, somewhat greater reliability might be expected.

**Related Material:** See paragraphs 2-24 and 2-33. See also Problem 2-9.

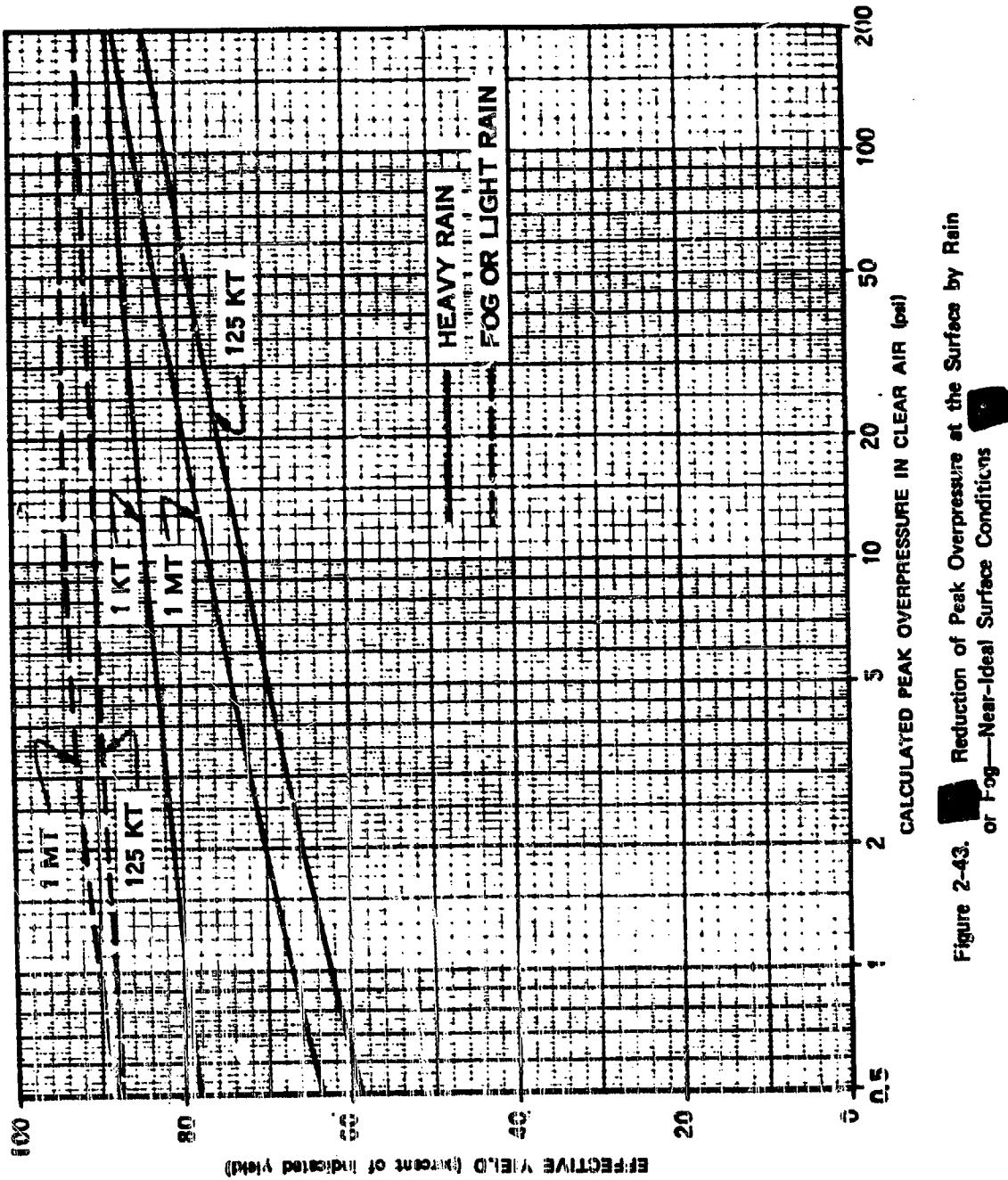


Figure 2-43. Reduction of Peak Overpressure at the Surface by Rain or Fog—Near-Ideal Surface Conditions

## 2.34 Peak Overpressure at the Surface of Deep Snow

When a shock front enters a layer of snow it is attenuated strongly. Drag forces on the snow crystals dissipate energy contained in the wind behind the shock front. The energy transmitted to the snow crystals is then consumed in compacting the snow layer.

Reflection occurs at the top surface of a deep snow layer just as it does at a ground surface. Momentum is conserved in the interaction, and, in the case of a ground surface, the process is analogous to a light, elastic object striking a heavy one. The light object bounces away, retaining most of the energy that it had before the collision. The heavy object receives a small amount of energy. A blast wave striking the earth transmits only a small fraction of its energy as ground shock; consequently, the earth's surface approximates an ideal reflector. A blast wave striking a snow surface is analogous to a ball bouncing from a heavy rug. The reflecting surface has a cushioning effect that makes it a poorer reflector.

In the case of a thin layer of snow, the cushioning effect ceases when the pressure wave penetrates the snow layer, reflects from the ground surface, and propagates back to the snow surface. At this time, the snow layer is supported by an internal pressure as high as the pressure produced by the blast wave reflecting from the surface; the reflecting qualities of the snow layer then approach the near-ideal reflecting qualities of the underlying surface.

Neither theoretical nor experimental data are available on the effects of thin snow layers on a blast wave, however, a rough calculation is enlightening. If a shock front in snow moves with a speed comparable to that of sound in air, a layer of snow one foot thick, struck by a normally incident blast wave, will absorb energy from the blast wave for about 2 milliseconds and will have the properties of a near-ideal re-

flecting surface after that time. This 2-millisecond interval is appreciably long only when compared with relatively sharp blast waves. For example, it might alter a 750 psi blast wave from a 1 kt source significantly. The overpressure pulse of this blast wave has an effective triangular duration (see Figure 2-10) of about 20 milliseconds. At lower overpressures, the pulse becomes broader. For a given overpressure, larger yields than 1 kt also produce broader pulses. This comparison indicates the following:

- If a blast wave with a very narrow pressure pulse strikes a thin layer of snow, the snow may alter the leading edge of the pressure pulse enough to reduce peak reflected overpressure.
- In a more typical situation, i.e., one for lower overpressures and yields greater than 1 kt, a thin snow cover affects such a small portion of the overpressure pulse that peak reflected overpressure is essentially the same as at a near-ideal surface.

Presently available experimental data on the properties of blast waves over deep snow surfaces are based on high-explosive (HE) experiments. In all of the tests, the snow layers were sufficiently thick to react as though they were infinitely thick. The thinnest snow layers tested (7 inches) correspond to snow layers about  $60 W^{1/3}$  feet thick ( $W$  in kt). For an 8 kt burst, this thickness is about 120 feet. Since snow layers thicker than about 120 feet compress to form glacial ice, the 7 inch snow layers have no real scaled counterpart for nuclear bursts larger than about 8 kt.

The available data for the effects of snow on the blast wave, when scaled for calculations of the blast wave from bursts larger than 1 kt may be applied with confidence only to regions such as the arctic, where large areas are covered by very thick snow layers.

Scaling HE data over snow to the blast wave from a nuclear burst involves considerable uncertainty. Predictions of peak overpressure over a deep snow surface, are based on the following reasoning: (1) the HE studies show that snow reduces the ground distance to which a given peak overpressure extends by about 10 percent (this figure is never smaller than 0 percent or greater than 20 percent); (2) HE data over snow are not available at points near ground zero, and thus, the experimental data fail to show how much burst height should be changed for a given peak overpressure.

Figures 2-18 and 2-19 may be used to predict peak overpressures over deep snow by reducing all ground distances by 10 percent.

One significant effect of snow cover is that it forms a thermally near-ideal surface. Clean snow reflects most of the thermal radiation that strikes it. Dirty snow absorbs more energy than clean snow but it absorbs it in a way that is unlikely to produce a thermal layer. An experimental study indicates that thermal radiation from a nuclear burst will melt a negligible amount of a clean snow surface and that the water formed will be absorbed quickly by the remaining snow.

An important unknown is the degree to which propagation through snow lengthens the rise time of the overpressure pulse. Even when snow cover is not thick enough to reduce peak reflected overpressure significantly, a layer of snow covering overpressure-sensitive targets may offer protection by reducing the sharpness of the overpressure pulse. This effect may be particularly important in evaluation of ground-shock damage to buried targets.

In the absence of confirming data from nuclear tests over snow, use of the curves in Figures 2-18 and 2-19 must be regarded as tentative. Ground distances obtained from the curves are estimated to be reliable within  $\pm 25$  percent for yields between 1 kt and 10 kt when used to

predict peak overpressures over snow. Outside this range of yields, the curves may be used with somewhat less confidence.

### 2-35 Peak Overpressure at an Infinite Reflecting Surface

Curves showing peak reflected overpressure may apply to finite surfaces, such as the side of a building, or they may apply to the earth's surface, which is effectively infinite in extent. The two types of curves resemble one another except at angles of incidence close to  $90^\circ$ , i.e., at grazing incidence (see footnote to paragraph 2-17 for a summary of the conventions used in specifying the angular orientation of reflecting surfaces). At this grazing angle of incidence, a finite area produces no enhancement of the incident overpressure, the incident overpressure is sometimes called the "side-on" overpressure.

A reflecting surface that is infinite in extent affects the blast wave differently. Figure 2-44 shows that the reflection coefficient  $\Delta p_r / \Delta p_i$  of such a surface at grazing incidence is greater than 1. A blast wave having an angle of incidence of exactly  $90^\circ$  with a flat, infinite surface is, by definition, a contact surface burst. The surface of the earth confines the blast wave from a contact surface burst to half of the volume it would occupy in free air. As a result, peak overpressure is higher than it would be in free air; this fact is indicated by a reflection coefficient greater than 1.

Figure 2-44 has two parts, corresponding to the regions of regular reflection and of Mach reflection. A peak occurs near the boundary between the two regions; at the lower incident overpressures, this peak shows a higher reflected overpressure than that produced by a blast wave striking a surface head-on. The same phenomenon appears in the height-of-burst charts as the knee of an overpressure curve.

At incident overpressures greater than

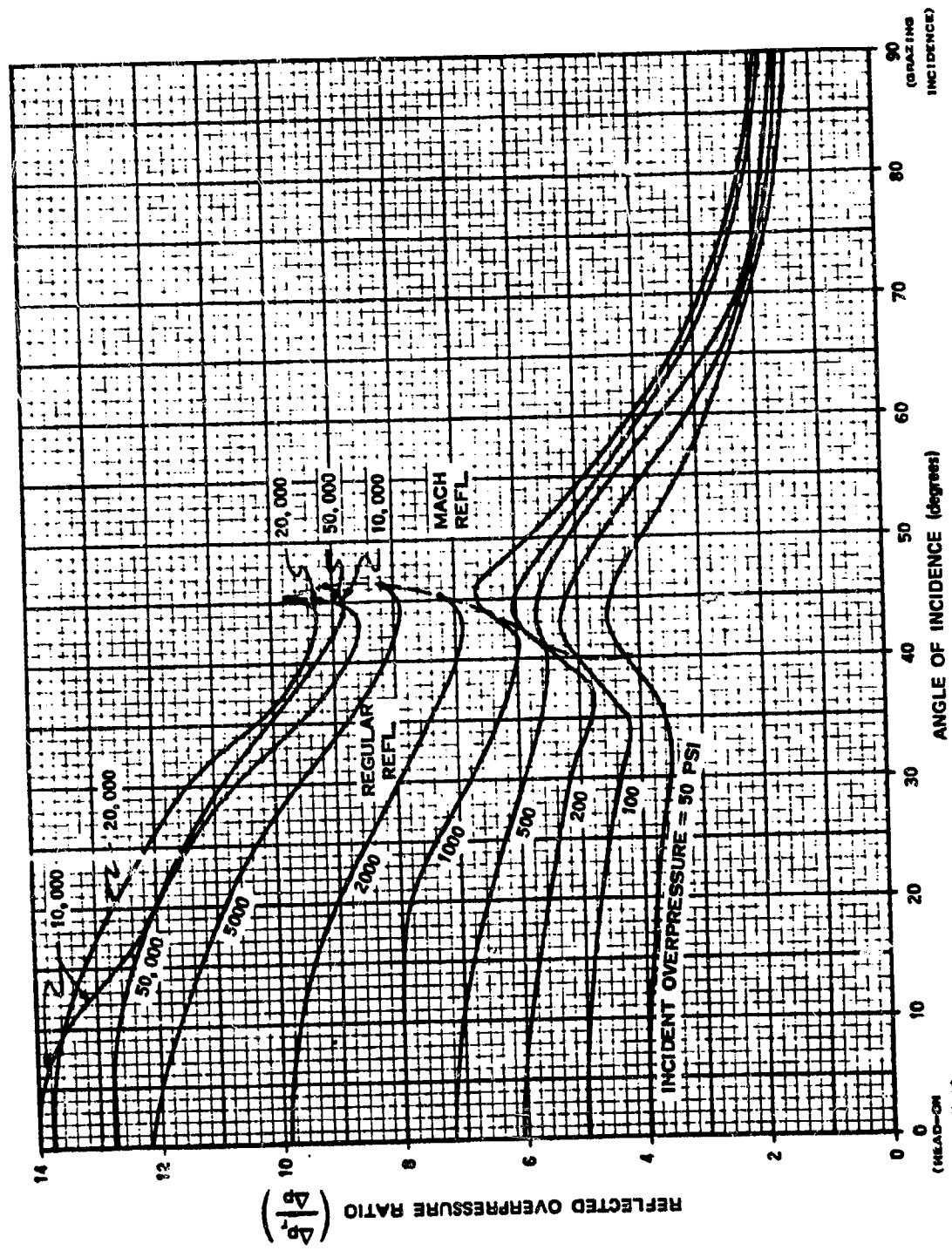


Figure 2-44. Reflection Properties of Strong Shock Waves at an Infinite Surface

5,000 psi, the curves in Figure 2-44 deviate from the regular pattern seen at lower incident overpressures. These deviations result from the high temperatures produced at the shock front, which cause dissociation and ionization of the air atoms to absorb energy that would otherwise increase the pressure of the gas.

The data in Figure 2-44 may be replotted to prepare a height of burst graph. An intermediate plot, consisting of a family of curves, each for a given angle of incidence should be plotted first. Figure 2-45 shows, as an example, the curve for an angle of incidence of 30°. Slant ranges for this intermediate plot are found as a function of incident overpressure from Figure 2-2, the overpressure-distance curve for free air. The data from the intermediate plot may be transferred to the HOB chart by plotting slant range and angle of incidence as shown in the inset of Figure 2-45.

Such a transformation should lead to the HOB chart shown in Figure 2-17; however, certain discrepancies exist between that HOB chart and the data in Figure 2-44. The principal difference is that the peaks shown at angles near 45° in Figure 2-44 have been rounded off in the HOB chart since it is uncertain how well the data in Figure 2-44 describe the actual reflecting properties of the surface of the earth for reasons described below. Although the peaks shown in Figure 2-44 probably occur, the angle at which they occur may be different from that indicated. Therefore, a transformation of every detail of the curves in Figure 2-44 to the HOB chart implies a more detailed knowledge of the shapes of the HOB curves than actually exists.

Uncertainty of the data in Figure 2-44 arises from the way in which these data had to be obtained. The Mach reflection portions of the curves in Figure 2-44 were obtained theoretically, using the shock-wave equations and the air equation of state given in Appendix A. The calculation is complex, involving successive ap-

proximations that are most appropriately handled on a computer.

A large portion of the regular reflection regions of the curves were obtained experimentally. Many data points from nuclear tests document the low pressure curves at angles close to 90°, and theory plus a few data points were used to extrapolate the data to smaller angles and to the highest overpressures shown.

Accuracy of the Mach reflection data is limited because the calculations for these data were based on an ideal reflecting surface. When the burst height is low, errors may result from the resiliency of the earth's surface (or, in the extreme case, cratering), and from thermal energy extracted from the fireball by absorption at the surface. Dirt thrown into the air may alter blast wave properties. Accuracy of the regular reflection data is limited by the difficulty of obtaining a large number of accurate blast wave data points at very high overpressures. These uncertainties are the reasons for smoothing the overpressure contours in Figure 2-17. They are also the reasons for omitting, as unrealistic, curves for peak reflected overpressures higher than 10,000 psi.

### 2-36 Peak Overpressure at a Finite Reflecting Surface

Since a finite surface may cause either regular or Mach reflection, the curves showing reflected overpressure at a finite surface resemble those showing reflected overpressure at an infinite surface.

Figure 2-46 shows curves of reflected overpressure as a function of peak incident overpressure. These curves apply directly to the reflection that occurs at flat surfaces (e.g., sides of buildings) when they are struck by the nearly vertical shock front which characterizes the Mach stem. Although the curves also may be used to determine peak reflected overpressure from the incident free air blast wave when regu-

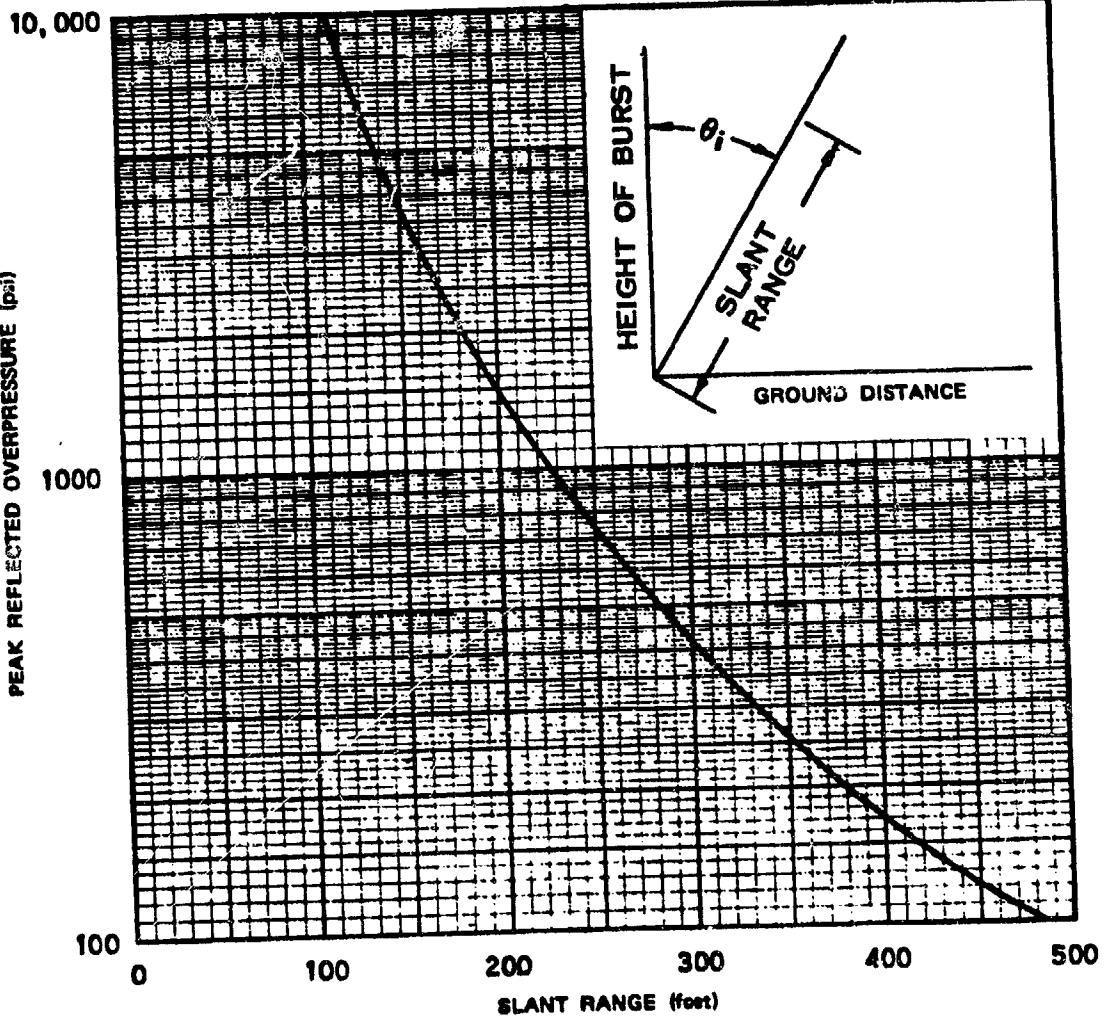


Figure 2-45. Peak Reflected Overpressure Versus Slant Range  
for an Angle of Incidence  $\theta_i$  of 30°

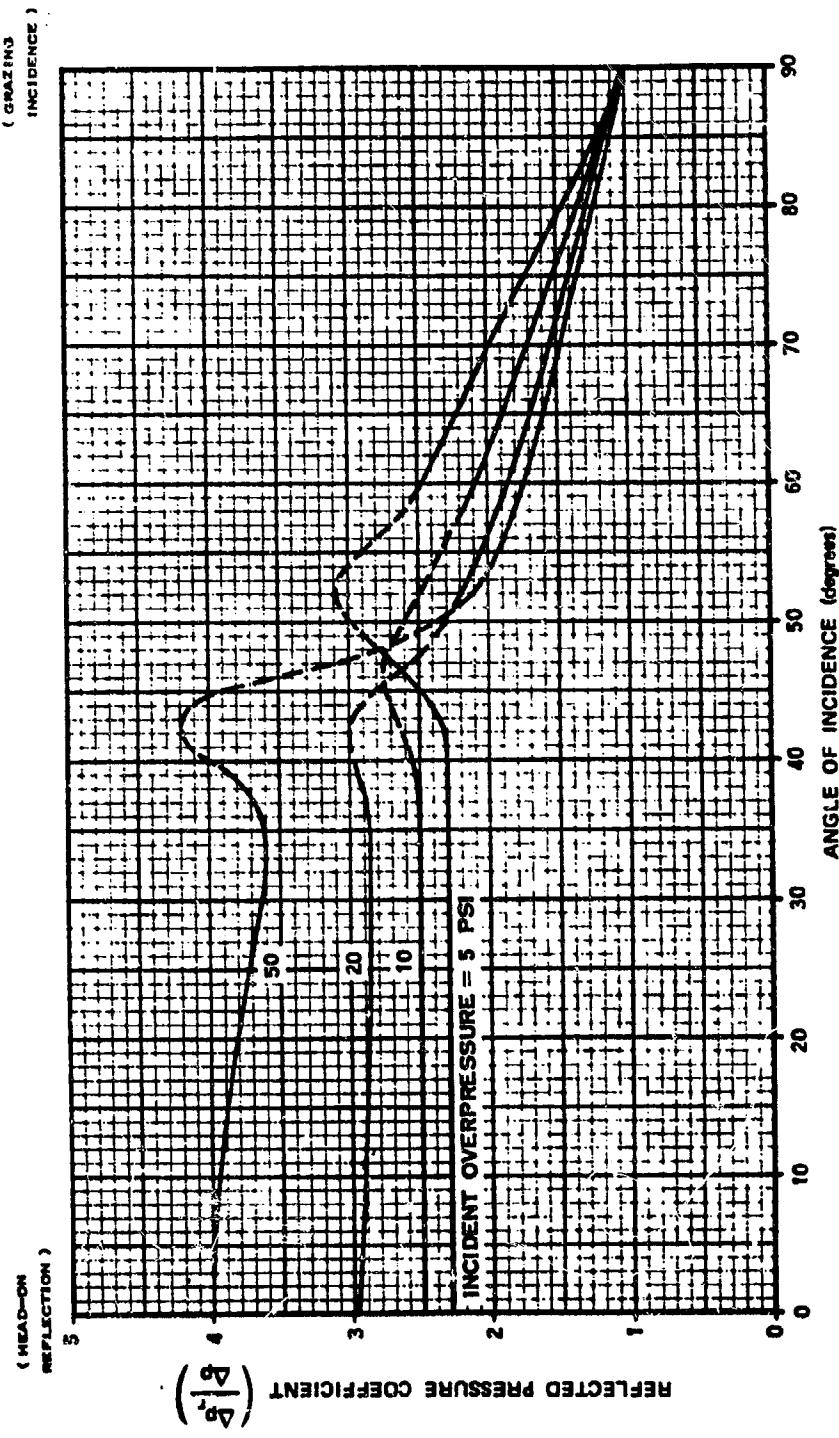


Figure 2-46. Reflection Properties of Shock Waves at a Finite Surface

lar reflection is occurring at the surface of the earth, they do not represent the total effect of multiple reflections that occur when this direct wave strikes the angle formed by the earth and a vertical surface.

These curves only predict the peak overpressure produced when the shock front arrives. In many problems, the total waveform produced by the blast-target interaction also is important; however, the latter is a function of target dimensions as well as blast wave properties as discussed in Section II of Chapter 9 and Section I of Chapter 11.

### 2-37 Peak Overpressure at Rising and Falling Slopes (U)

If a shock wave that is travelling along the ground surface encounters a change in slope, the characteristics of the shock wave will change. If the terrain is characterized by large changes of slope, the changes in the blast wave can be significant. They can result in an overpressure increase by more than a factor of two or a decrease by more than a factor of three.

Interactions with real topography can be exceedingly complex. Therefore both experimental and theoretical studies have, for the most part, dealt with idealized, simplified terrain features. Techniques have been devised for predicting the characteristics of the shock waves that encounter changes in terrain, and methods for applying these techniques to real terrain have been devised.

If the level terrain in front of a slope is in the region of Mach reflection, the blast-wave incident on the slope will have a nearly vertical shock front, the Mach stem. (The nearly hemispherical shock front produced by a contact surface burst is considered a special case of an incident Mach stem.) If the level terrain in front of the slope is in the region of regular reflection, the first shock front striking the slope is the free air blast wave from the nuclear source. This

shock front is not vertical, but forms an angle of less than 90° with the level ground in front of the slope.

When the nearly vertical Mach stem strikes a rising slope, the incident wave undergoes either regular (two-shock) or Mach (three-shock) reflection, depending on the angle that the slope makes with the surface over which the shock wave has been moving and on the strength of the incident shock. For a falling slope, diffraction always occurs; the shock wave curves to orient itself normal to the slope. Differences between regular and Mach reflection on a rising slope are illustrated in Figure 2-47. Diffraction on a falling slope is illustrated in Figure 2-48 (in these figures, the shock wave direction of propagation is assumed to be normal to the slope contours).

Similar interactions occur when the direction of shock wave motion makes an angle  $\Phi$  with the line of steepest ascent or descent. The geometry of such an interaction is shown in Figures 2-49 and 2-50. In these figures, the angle that is important is  $\theta$ , the effective slope angle. Its relationship to  $\theta$ , the slope angle is

$$\sin \theta = \sin \theta_s \cos \Phi$$

This relationship is plotted in Figure 2-51. The relationship holds for both rising and falling slopes.

When a Mach stem encounters a rising slope, the incident overpressure and the effective slope angle determine whether regular or Mach reflection will occur. The conditions under which regular or Mach reflection occurs are shown in Figure 2-52.

Figure 2-53 shows how effective slope angle affects the peak overpressure produced by a 10-psi incident Mach stem. Similar data may be obtained from Figure 2-46 for other overpressures by noting that the angle of incidence to use with Figure 2-46 is equal to 90° minus the effective slope angle. The left-hand side of Fig-

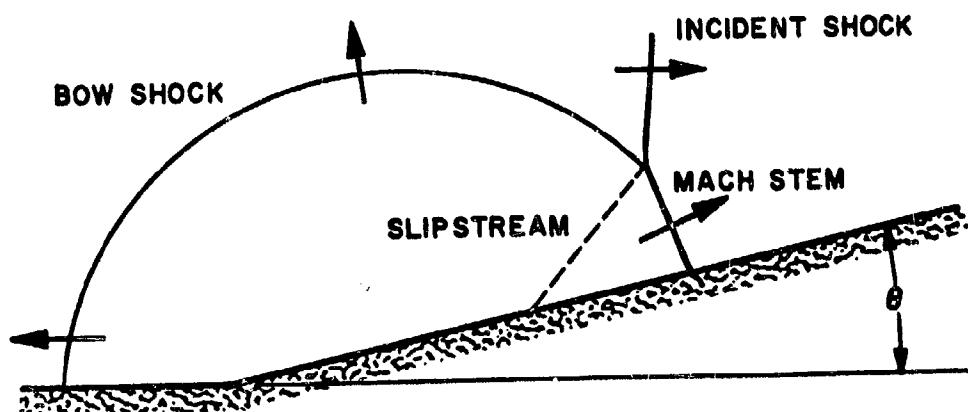
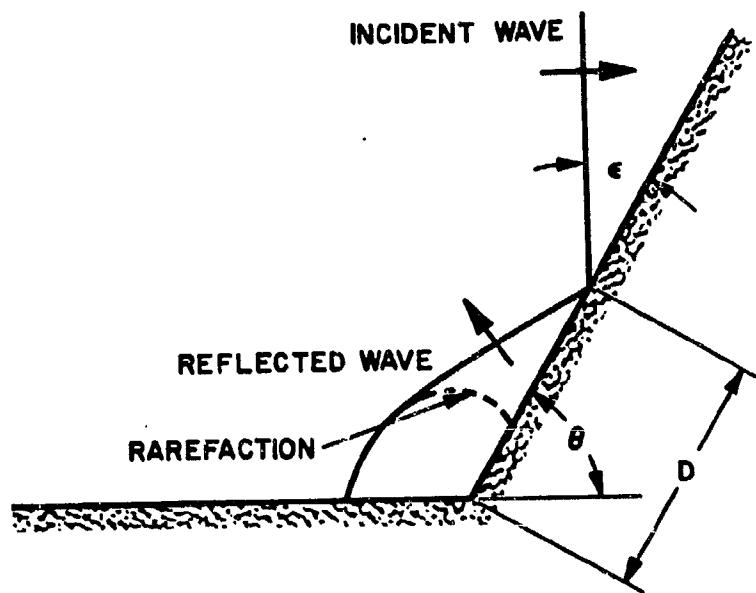


Figure 2-47. Regular and Mach Reflection Patterns Formed by a Mach Stem Striking a Rising Slope

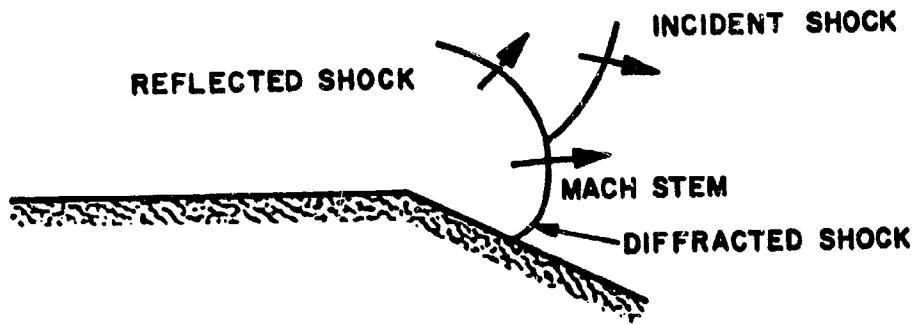


Figure 2-48. Diffraction Shock Front Pattern Formed  
by a Mach Stem at a Falling Slope

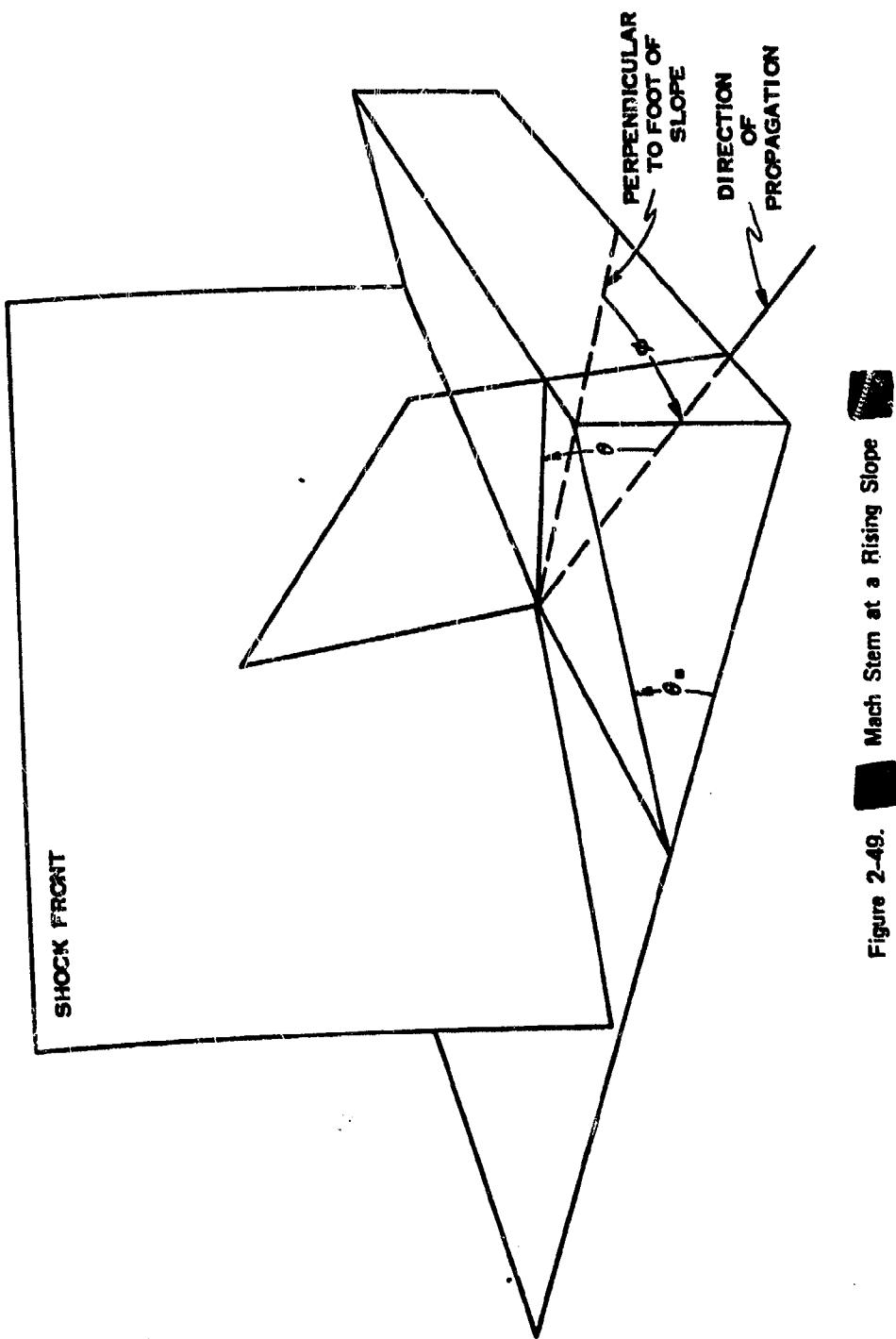


Figure 2-49. Mach Stem at a Rising Slope

### SECTIONAL VIEWS

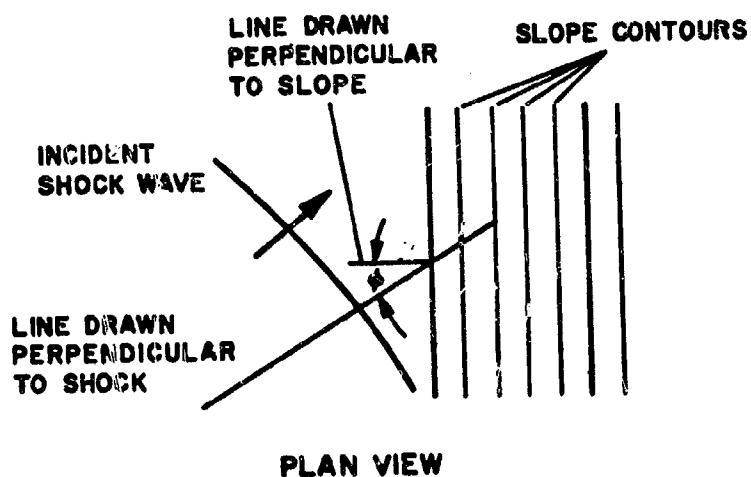
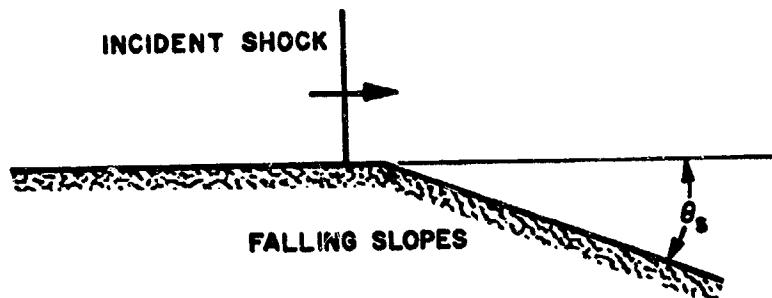
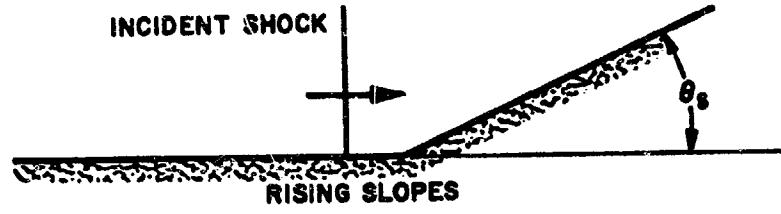


Figure 2-50. [REDACTED] Sectional and Plan Views of a Shock Front Approaching a Slope [REDACTED]

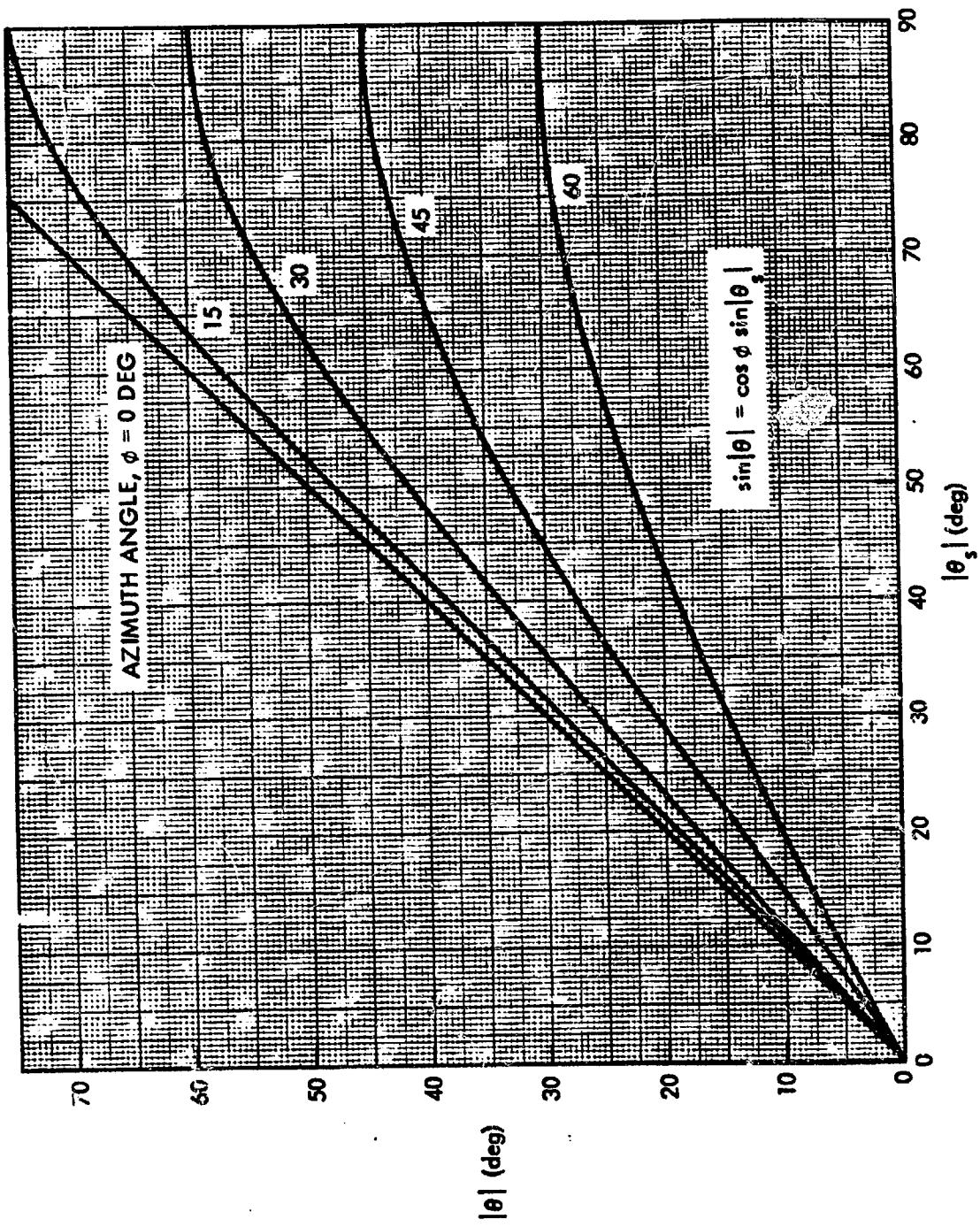


Figure 2-51. Effective Slope Angle  $\theta$  as a Function of Slope Angle  $\theta_s$  for Various Angles of Azimuth

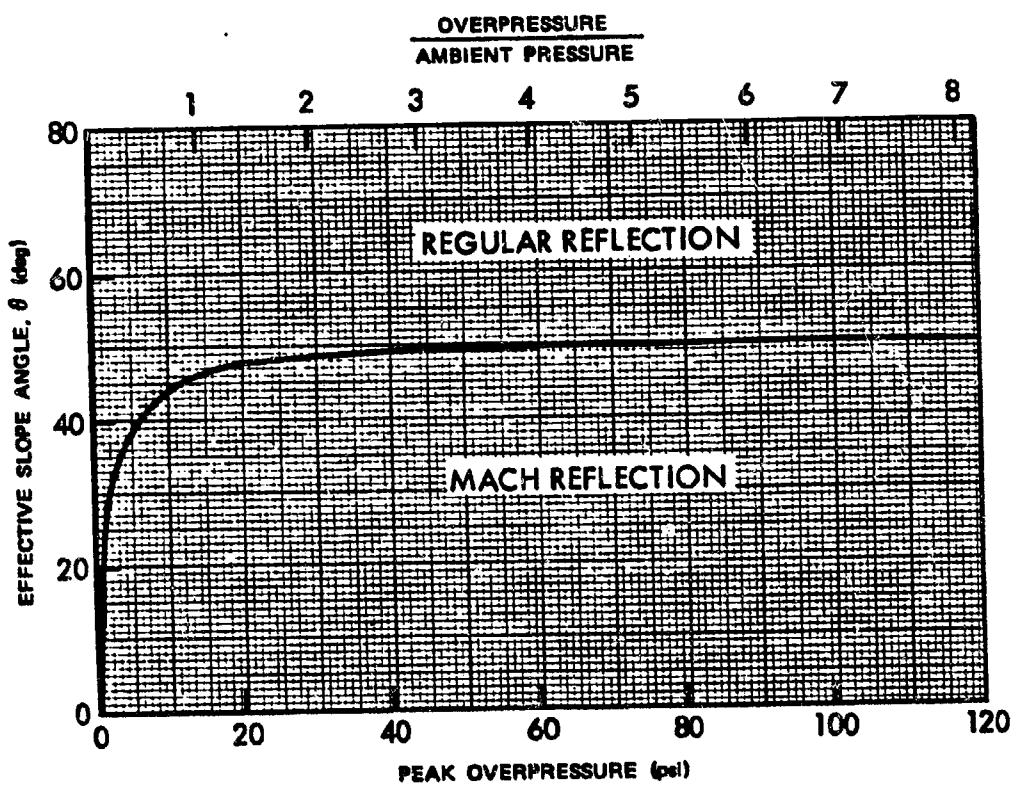


Figure 2-52. Conditions for Regular or Mach Reflection  
of Incident Mach Stem

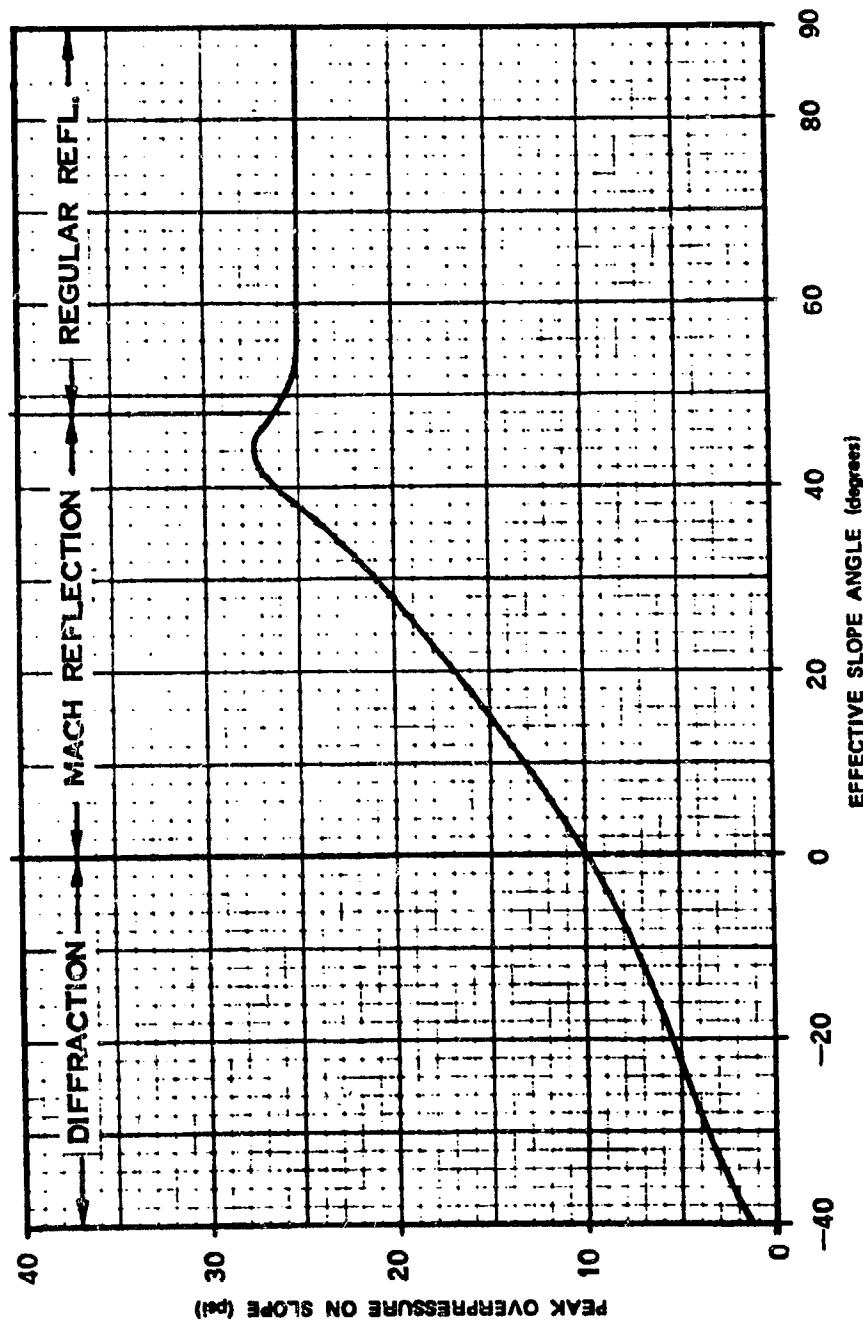


Figure 2-53. Peak Overpressure Produced on a Slope by a 10-psi Incident Mach Stem as a Function of a Slope Angle

ure 2-53 shows the effect of diffraction at a falling slope.

Figures 2-54, 2-55, and 2-56 show similar data in a more convenient form. The overpressure scales only apply to reflection of shock waves in a sea level atmosphere. At other ambient pressures, the scales marked "overpressure/ambient pressure" should be used. Note that Figure 2-54 is plotted for various values of the angle of incidence while Figures 2-55 and 2-56 are plotted for various values of the effective slope angle.

If the incident blast wave has been undergoing regular reflection before it encounters the rising or falling slope, approximate blast wave characteristics at the target can be determined by (1) constructing a sectional plot showing both the target area and the burst point, (2) drawing a "reference-plane line" through the target area showing the general plane in the vicinity of the target, and (3) drawing a line from the burst point perpendicular to the reference-plane line.

As Figure 2-57 shows, the length of the perpendicular is the effective height of burst; the length along the reference plane line between this perpendicular and the target area is the effective ground range or distance from ground zero, and shock-wave characteristics may be determined from height of burst charts. Although this technique does not take into account the effect of azimuth angle  $\Phi$  (where the shock wave moves at an angle to the line of steepest ascent or descent), further refinement is rarely justified.

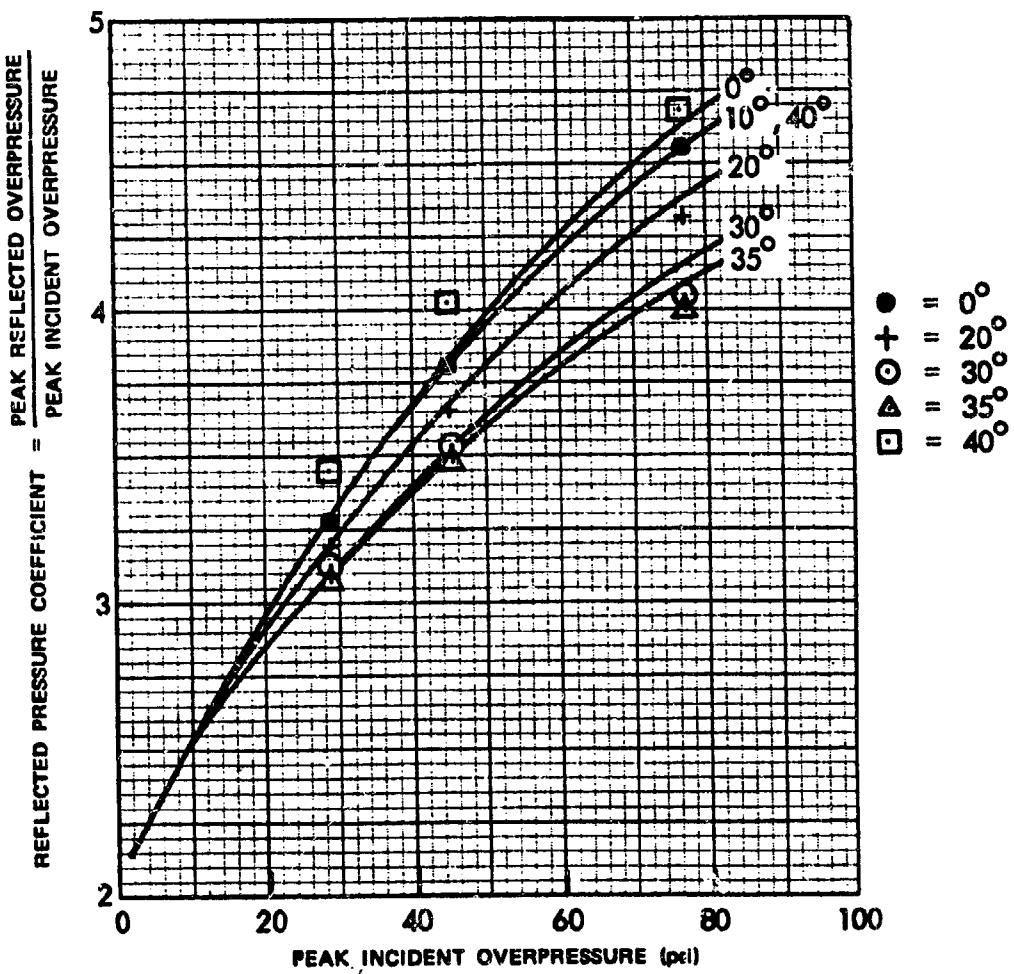


Figure 2-54. Reflected Overpressure Coefficients for Regular Reflection as a Function Incident Overpressure for Various Angles of Incidence

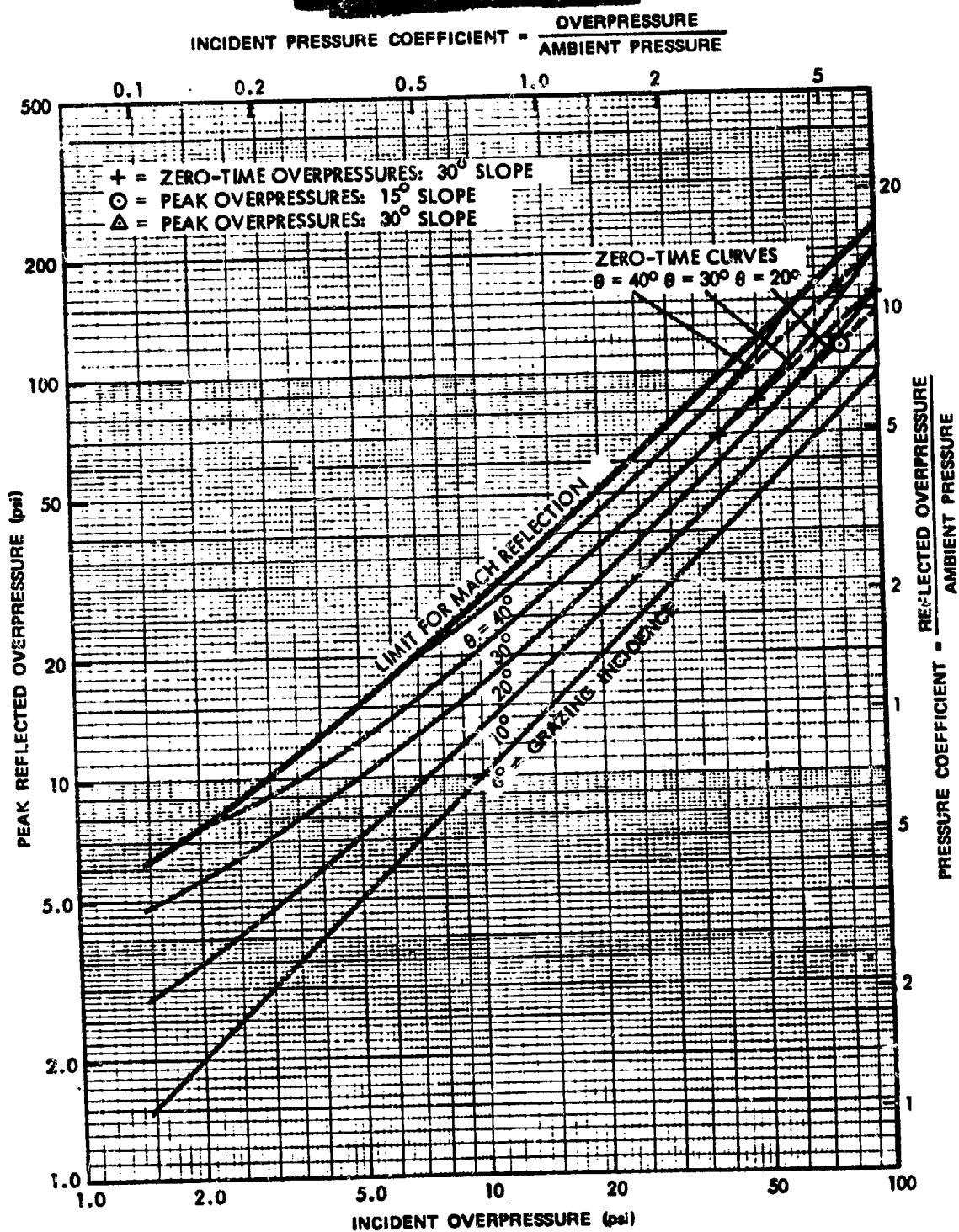


Figure 2-56. Reflected Overpressure as a Function of Incident Mach-Stern Overpressure for Mach Reflection for Various Slope Angles

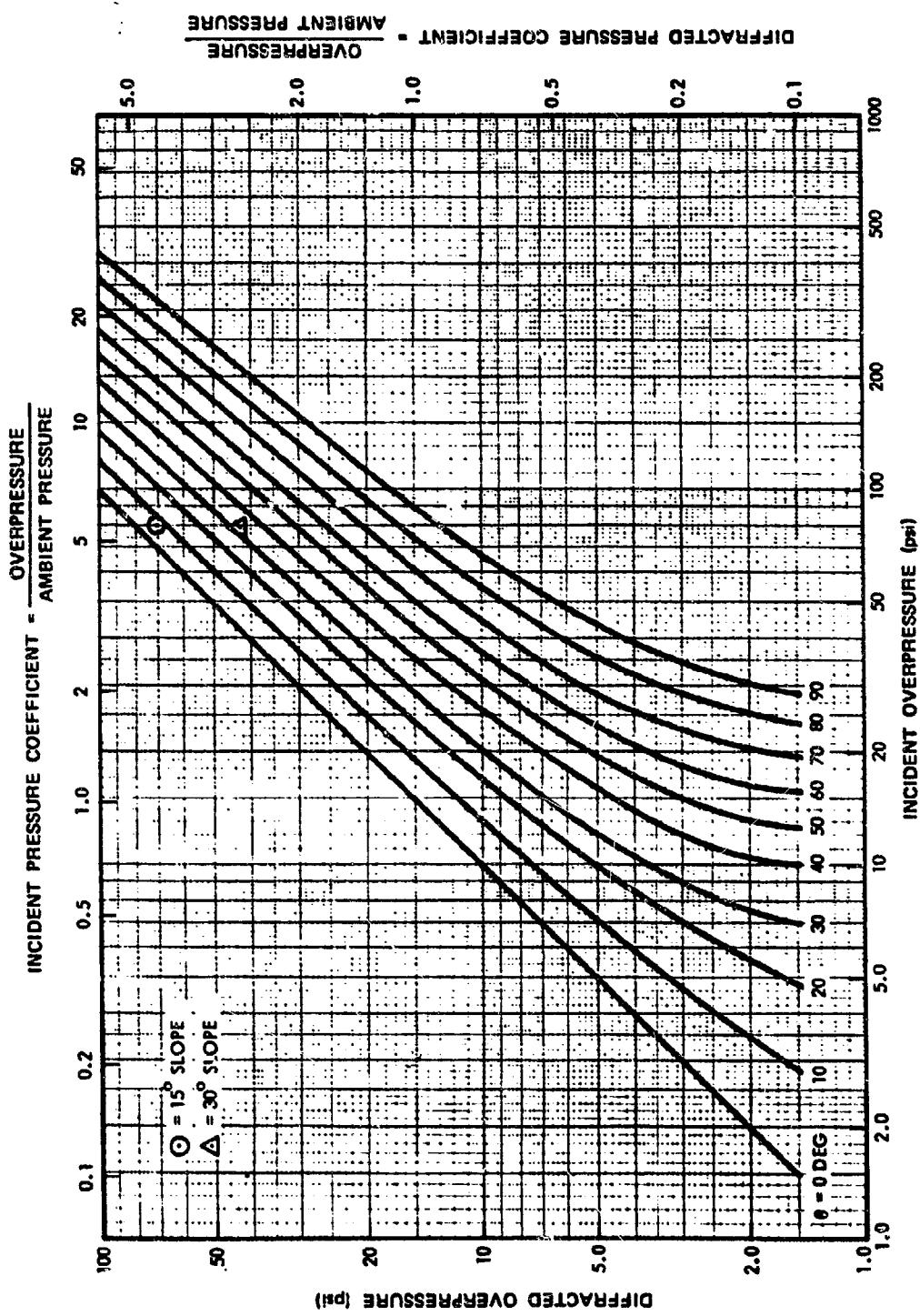


Figure 2-56. Diffracted Overpressure as a Function of Incident Mach-Stem Overpressure for Various Slope Angles

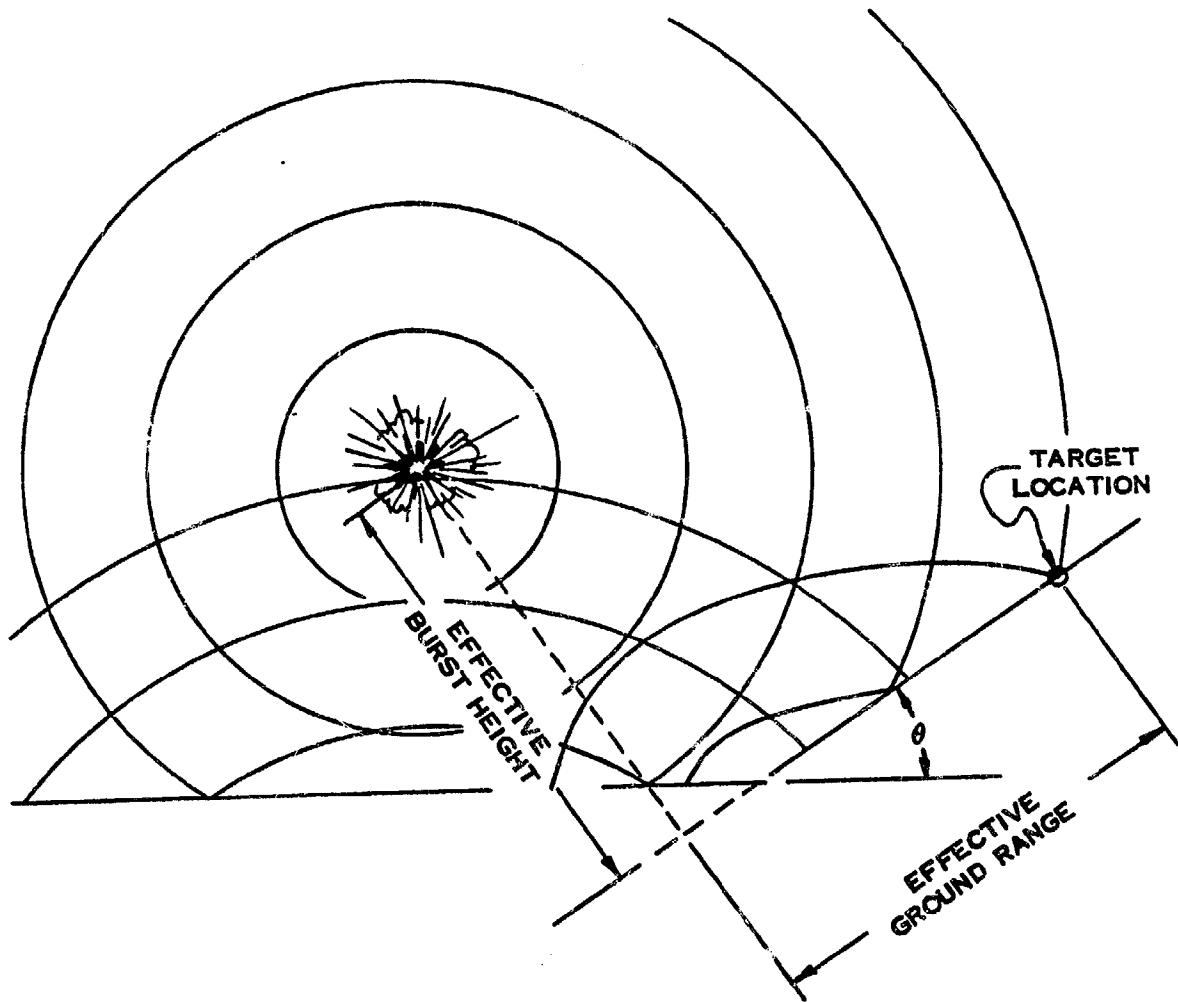


Figure 2-57. Construction Procedure Recommended When the Blast Wave Incident on a Slope Has Been Undergoing Regular Reflection on Level Ground

### Problem 2-17. Calculation of Overpressure on a Slope

The information provided in paragraph 2-37 and in Figures 2-47 through 2-57 provides the data to calculate peak reflected overpressures when a blast wave encounters a rising or falling slope. The data are given relative to the incident overpressures that would be expected over flat terrain in a standard sea level atmosphere. These latter values may be obtained from Figures 2-17 through 2-22.

**Scaling.** For target altitudes above 5,000 feet, both the incident and the reflected overpressures scale according to the altitude scaling procedures described in paragraph 2-14, i.e.,

$$\frac{\Delta p_t}{\Delta p_{ro}} = \frac{\Delta p}{\Delta p_o} = S_p,$$

where  $\Delta p_{ro}$  and  $\Delta p_o$  are the reflected and incident peak overpressures, respectively, in a standard sea level atmosphere,  $\Delta p_t$  and  $\Delta p$  are the corresponding pressures at the desired altitude, and  $S_p$  is the pressure scaling factor described in paragraph 2-14 and tabulated in Tables 2-1 and 2-2.

#### Example

**Given:** A ridge with a slope angle of  $27^\circ$  on otherwise flat terrain at an altitude of 7,500 feet. For a particular set of burst conditions, the predicted blast wave in the absence of the ridge (but including altitude corrections) is a Mach stem with a peak overpressure between 10 and 15 psi. The direction of propagation of the blast wave makes an angle of  $20^\circ$  with the line of steepest ascent.

**Find:** The range of peak overpressures that may be expected on the side of the ridge facing the explosion.

**Solution:** From the equation given in paragraph 2-37 (or by interpolation in Figure 2-51),

the effective slope angle is found as follows:

$$\begin{aligned}\sin \theta &= \sin \theta_s \cos \Phi \\ &= (\sin 27^\circ) (\cos 20^\circ) \\ &= 0.427, \\ \theta &= 25^\circ.\end{aligned}$$

From Table 2-1, the altitude scaling factor for pressure at 7,500 feet is

$$S_p = 0.76.$$

Under sea level conditions, the predicted value of the incident Mach stem overpressure would lie between

$$\Delta p_o = \frac{\Delta p}{S_p} = \frac{10}{0.76} = 13.2 \text{ psi, and}$$

$$\Delta p_o = \frac{15}{0.76} = 19.7 \text{ psi.}$$

Figure 2-55 shows that a rising slope will increase these sea level values to

$$\Delta p_{ro} = 19 \text{ psi, and}$$

$$\Delta p_{ro} = 28 \text{ psi, respectively.}$$

An uncertainty of about 20 percent exists in these values (see "Reliability" below). In order to bracket the range of expected values, the lower will be decreased by 20 percent, and the upper will be increased by 20 percent. The resulting sea level reflected overpressures are

$\Delta p_{r_0} = 15.2$  psi, and

$\Delta p_{t_0} = 33.6$  psi, respectively.

*Answer:* The corresponding values of reflected overpressure at an altitude of 7,500 feet are

$$\Delta p_r = \Delta p_{r_0} S_p = (15.2)(0.76) = 11.5 \text{ psi, and}$$

$$\Delta p_t = (33.6)(0.76) = 25.5 \text{ psi, respectively.}$$

**Reliability:** Full scale nuclear tests indicate that the increase or decrease in peak overpressure at a rising or falling slope is generally within 10 or 20 percent of the predicted value. In the presence of a precursor, less accuracy may be expected. Accuracy also decreases if the slope angle is close to the critical angle that separates the regions of regular and Mach reflection.

**Related Material:** See paragraphs 2-14, 2-17 through 2-20, 2-22 through 2-24, and 2-37. See also Tables 2-1 and 2-2.

### **2-38 Effects of Slopes on Other Blast Wave Parameters**

Methods for determining peak overpressures at rising and falling slopes are described in paragraph 2-37. This paragraph relates the peak dynamic pressure and the duration of the positive phases of the overpressure and the dynamic pressure to the expected overpressures that are determined by the methods described in paragraph 2-37. The relations of the dynamic pressure and positive phase durations to the overpressure will be discussed for three types of interactions of the blast wave with slopes: regular reflection of an incident Mach stem; Mach reflection of an incident Mach stem; and diffraction of an incident Mach stem.

Figure 2-58 shows the reflected dynamic pressure as a function of incident Mach stem overpressure in the regular reflection region for various effective slope angles. The duration of the positive phase overpressure after regular reflection can be considered to be the same as that of the incident pulse. The dynamic pressure pulse, on the other hand, changes as the shock wave proceeds up the slope as a result of the presence and growth of a rarefaction wave from the slope corner (see Figure 2-47). The dynamic pressure pulse effectively terminates where the rarefaction wave intersects the reflected wave. The effect depends on the distance up the slope that the shock wave has moved, the slope angle, and the overpressure coefficient in the manner shown in Figure 2-59. In this figure, the number 1116 is the velocity of sound (in feet/sec) for standard sea level conditions ( $15^{\circ}\text{C}$  or  $59^{\circ}\text{F}$ ). For different ambient temperatures, the appropriate sound speed should be used (see Tables 2-1 and 2-2).

In the case of Mach reflection of the incident Mach stem, the peak dynamic pressure at the shock front may be determined from Figure 2-13 once the reflected overpressure is determined as described in paragraph 2-37. Figure

2-13 is only valid when a single shock front is involved. If the rising slope is sufficiently steep to cause regular reflection (Figure 2-52), the peak dynamic pressure should be determined from Figure 2-58. The duration of the positive phase overpressure pulse in the Mach stem after Mach reflection can be assumed to be the same as that of the incident wave, while the positive phase dynamic pressure pulse is shorter than that of the incident wave. Over a range of overpressure coefficients from 2 to 11, and slope angles from 11.8 to 38 degrees, the reflected pulse after Mach reflection may be assumed to be 0.55 times as long as that of the incident blast wave.

Figure 2-13 also may be used to determine the peak dynamic pressure from the peak overpressure in a diffracted wave. Although the positive phase duration of both the overpressure and dynamic pressure pulses are known to decrease as a result of the formation of low pressure vortices at the slope change point, neither experiment nor theory is sufficiently extensive to provide a satisfactory prediction technique. As an approximation, the positive phase duration of the diffracted overpressure pulse may be taken to be the same as that of the incident pulse, and the duration of the diffracted dynamic pressure pulse may be shortened by the ratio of diffracted peak dynamic pressure to incident peak dynamic pressure.

### **2-39 Channelling of an Incident Mach Stem Along the Axis of a Valley**

Figure 2-60 illustrates a third type of idealized topographic feature: an elongated valley. Shock waves reflecting from the walls of such a valley tend to enhance each other in the vicinity of the axis of the valley. The simple relations shown in Figure 2-61 have been shown to hold for a wide range of valley forms and for incident overpressures below about 60 psi. The relation for "flat-bottomed valleys" holds for

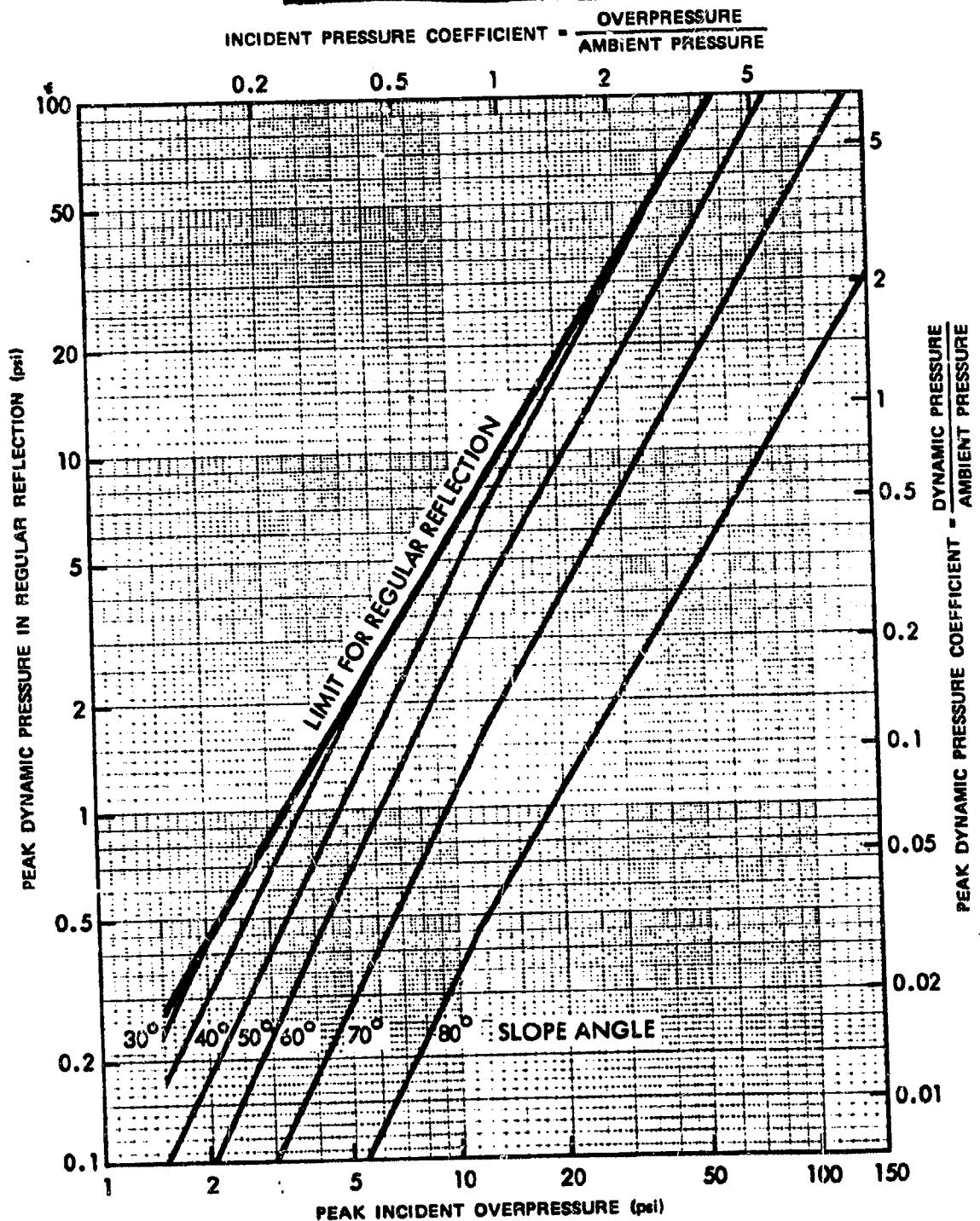


Figure 2-58. Reflected Dynamic Pressure as a Function of Incident Mach Stem Overpressure for Regular Reflections for Various Effective Slope Angles

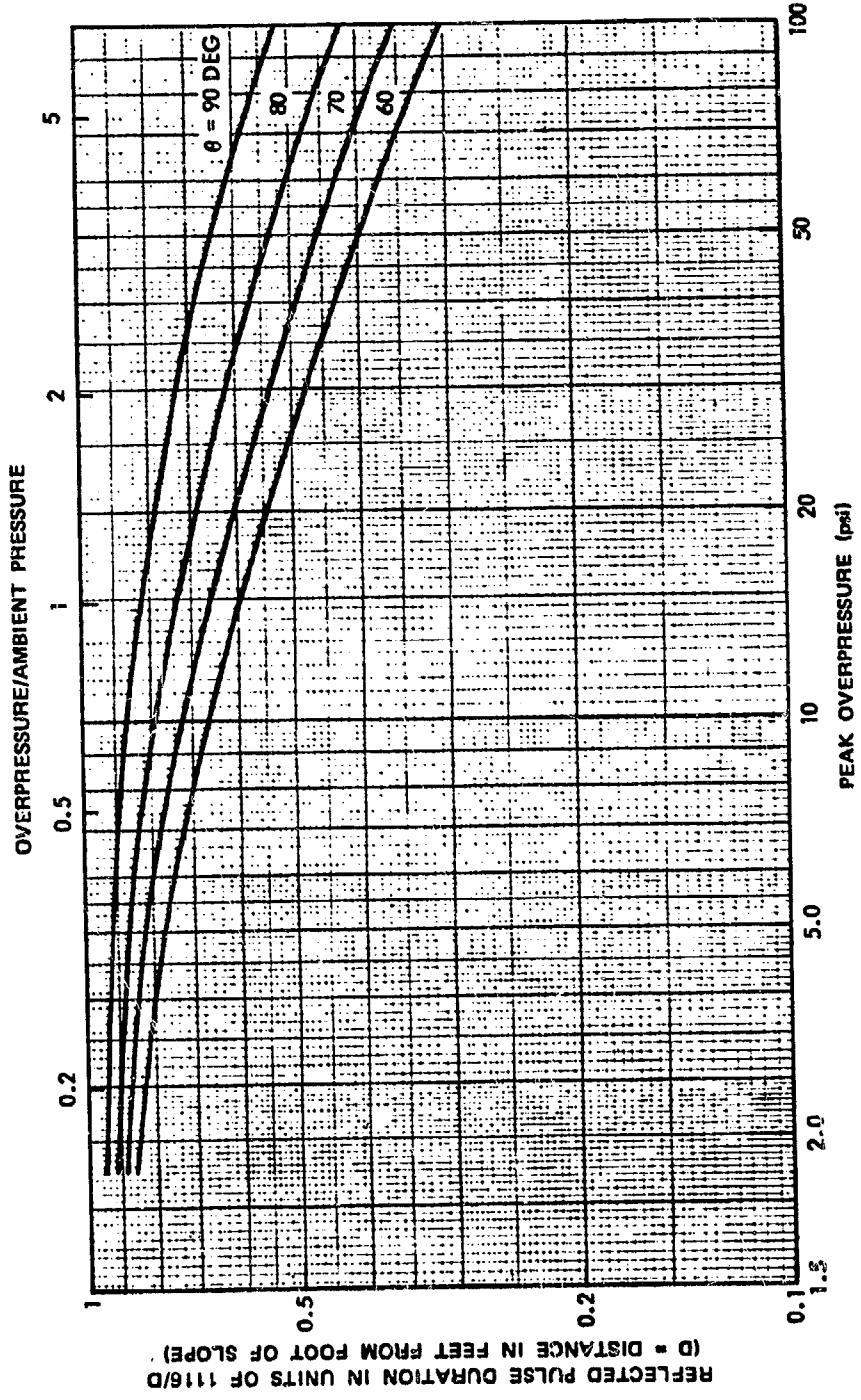


Figure 2-59. [REDACTED] Duration of the Reflected Dynamic Pressure Pulse for Regular Reflection

1

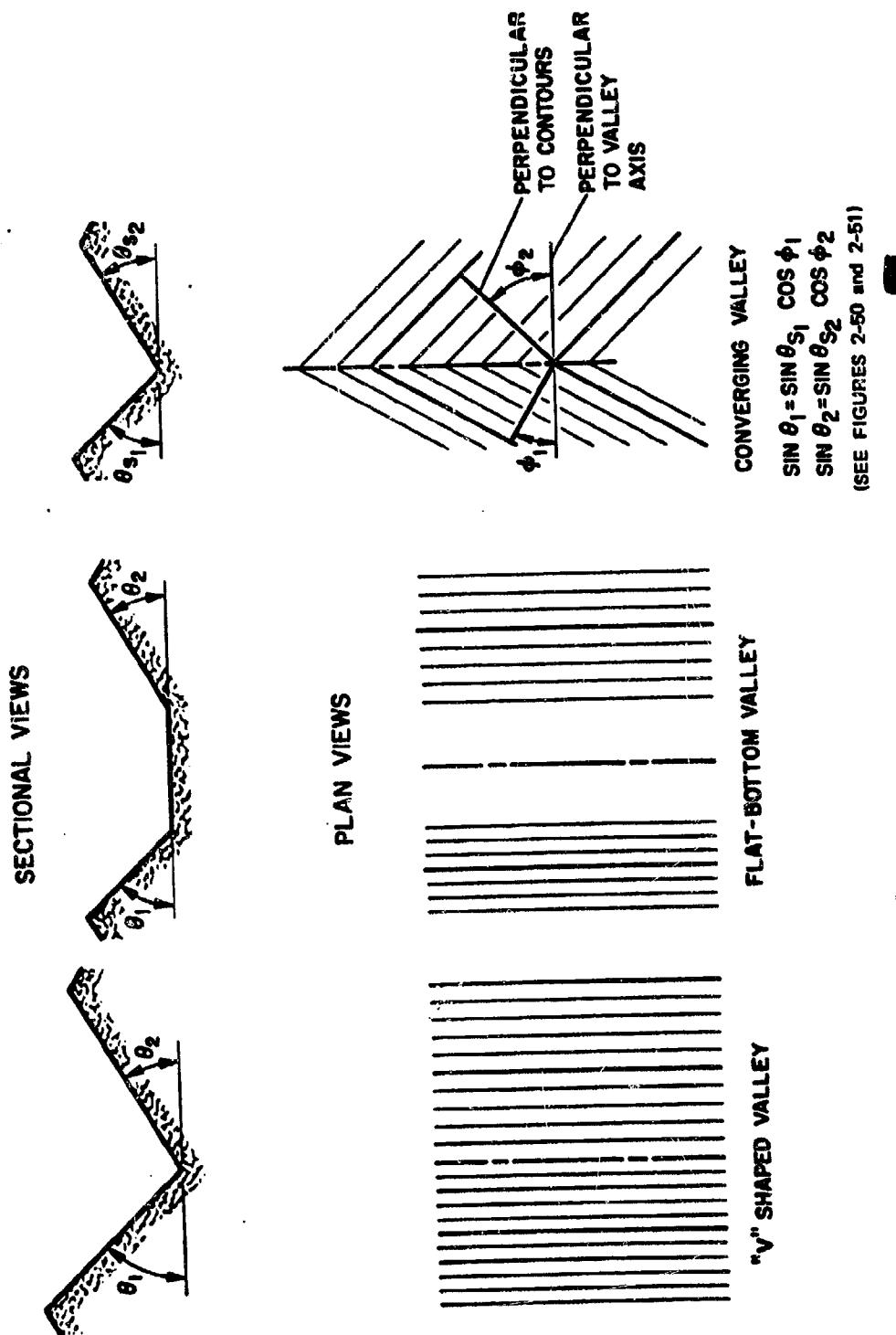
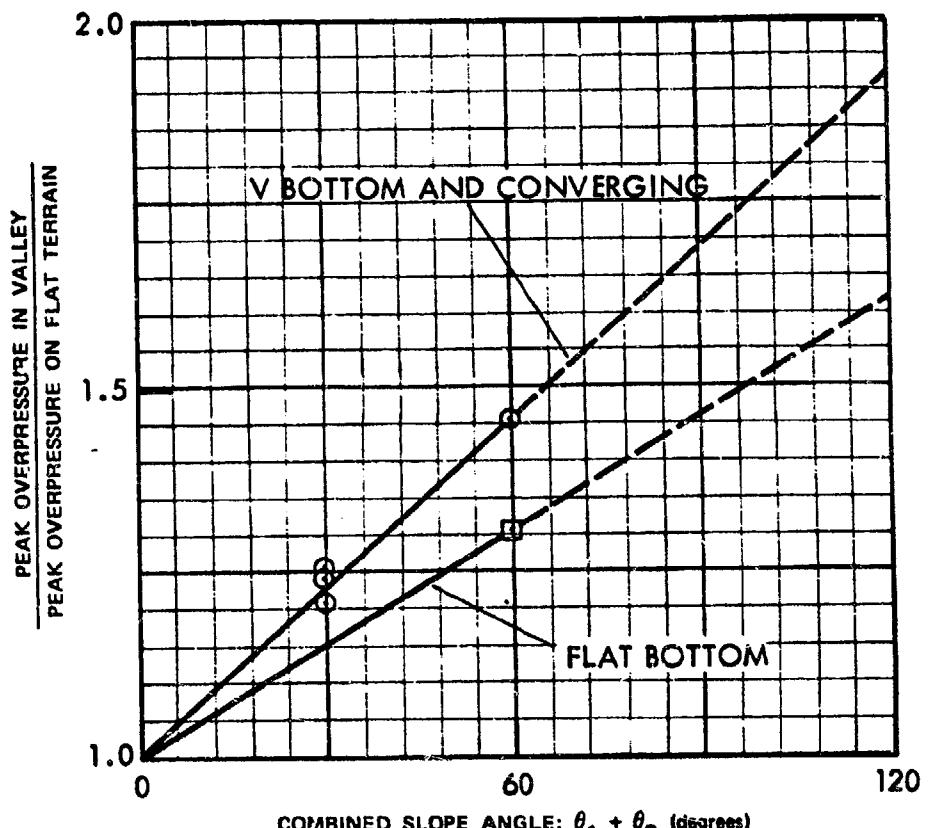


Figure 2-60. ■ Sectional and Plan Views of Idealized Valley Shapes ■



(SEE FIGURE 2-60)

Figure 2-61. █ Average Peak Overpressure Amplification Factors at the Bottom of Valleys as a Function of Combined Slope Angle █

valleys whose floor widths (measured perpendicular to the valley axis) are of the same order as, or shorter than, the slope heights of the valley walls (also measured perpendicular to the valley axis). For wider flat-bottomed valleys, each side of the valley and a portion of the adjacent valley floor may be considered independently as a V-shaped valley.

#### 2-40 General Application of Prediction Techniques to Actual Topographical Features

Paragraphs 2-37 and 2-38 provide data for only the most significant shock wave characteristics — peak pressures and positive phase durations. More detailed information, e.g., data on pressure waveforms, may be obtained from DASA 1200, "Nuclear Weapons Blast Phenomena" (see bibliography).

Applicability of the curves that have been presented depends largely on the size of a terrain feature relative to the size of the incident shock wave. If the incident shock is very much longer than a terrain feature of interest, the predicted changes in peak values of overpressure and dynamic pressure will occur on the slope; but the duration will not be affected greatly. The incident pulse length in feet is slightly more than  $11\frac{1}{16}$  times the incident pulse duration in seconds, and if this pulse length is more than about three times as long as the slope being considered, no changes in pulse duration can be expected.

Much of the complexity of actual terrain may be eliminated from blast wave calculations by application of the *local-slope* concept. This concept is based on the observation that, in many situations, a shock wave that has passed over a succession of terrain features (hills, valleys, etc.) before encountering a feature of interest interacts with that feature as if the shock wave had previously passed over flat terrain.

This trend was noted during testing programs and has been supported by theoretical inference. The Ranier nuclear test over fairly complex terrain, provided additional checks. Although much of the area around this explosion was subject to precursor type waves, sharp fronted waves traversed many regions that were protected from direct thermal radiation. Predictions of peak overpressures generally were within 10 to 20 percent of observed values.

Determining whether the local slope approximation will give reasonably accurate results requires application of judgment in an examination of the region between the target area and the presumed burst point to determine whether there are significant terrain features between the two, especially in the vicinity of the target. This examination is often based on a sectional plot of the terrain, made along a line between ground zero and the target. Although it is sometimes difficult to draw conclusions from this examination, the following criteria are helpful:

- Features that show slope angles of less than 10 degrees on a sectional plot of the terrain, i.e., about a 20 percent grade, will not create significant effects.
- Symmetrical features at an appreciable distance from the target generally can be ignored. Effects that occur on the front slope of such features compensate for effects that occur on the back slope.
- Terrain features near ground zero have a small effect on the blast wave at large ground distances.
- If the average slope of the terrain tends to follow a straight line, particularly if the deviations from this straight line are small or random, the local slope approximation is justified. However, if the average slope of the sectional plot clearly follows two straight lines, and the angle between these

lines exceeds 10 degrees, and if the break occurs in the region of Mach reflection, the blast wave calculations may have to treat the effects of two slopes in sequence.

Unless the average slope between ground zero and the target is essentially horizontal, use of the local slope concept requires establishment of the primary reference plane (PRP). Over complex terrain, the PRP often follows the average slope of the terrain between ground zero and the foot of the feature upon which the target lies. If the PRP does not seem clearly defined by this criterion, it is better to allow the terrain within the region of Mach reflection suggest the slope of the PRP. If the target is in the region of regular reflection, the average slope of the terrain near the target should be given more weight than the average slope of terrain closer to ground zero.

After the PRP has been established, effective burst height and ground distance *with respect to this plane* may be determined by means of a geometrical construction similar to that suggested by Figure 2-57. Properties of the blast wave incident on the terrain feature of interest may be read directly from height of burst curves in terms of these effective values of distance and height.

Although there are many cases in which the local slope concept will fail in detail if applied to features that are regular and uniform, ordinary terrain is so complex that the uncertainties engendered by terrain irregularities generally will exceed errors resulting from application of the local slope concept. Furthermore, the process of determining *approximate* terrain effects with the local slope concept is generally far simpler than that of obtaining more refined, *but still approximate*, effects with more rigorous techniques.

Once the blast wave properties are determined from height of burst curves, appropriate sectional plots should be made of the target area

slope. Azimuth angle and valley slopes must be determined where appropriate.

#### 2-41 Application of Prediction Techniques to Specific Topography

Figure 2-62 is a topographical map with a target area (designated by T) to be investigated. It is desired to determine the locus of ground zeros that would subject the target to an overpressure of 10 psi from a 1 Mt weapon burst at a height of 5,000 feet above the terrain.

Examination of Figure 2-62 shows that the highest point on the terrain around the target area is just over 4,000 feet (note that the grid lines and elevations are given in meters in Figure 2-62, and the highest point in the vicinity of the target is at an elevation of 1,243 meters), so altitude corrections are not required.

In accordance with the instructions in paragraph 2-20, the blast-wave parameters for explosions over mechanically nonideal surfaces are performed by first finding the desired blast parameters over a near-ideal surface. The results then are corrected for the change in the blast wave properties introduced by the mechanically nonideal features. The corresponding height of burst for a 1 kt explosion is

$$h_1 = \frac{h}{W^{1/3}} = \frac{5,000}{(1,000)^{1/3}} = 500 \text{ feet.}$$

From Figure 2-18, a 1 kt explosion at a height of burst of 500 feet will produce an overpressure of 10 psi at a ground distance of 1,315 feet (about 400 meters). The corresponding ground distance for a 1 Mt explosion is

$$d = d_1 W^{1/3} = (1,315)(1,000)^{1/3}$$

$$\approx 13,150 \text{ feet (or about 4,000 m).}$$

A circle, centered on the target, with this radius is shown in Figure 2-62. A 1 Mt explosion at a

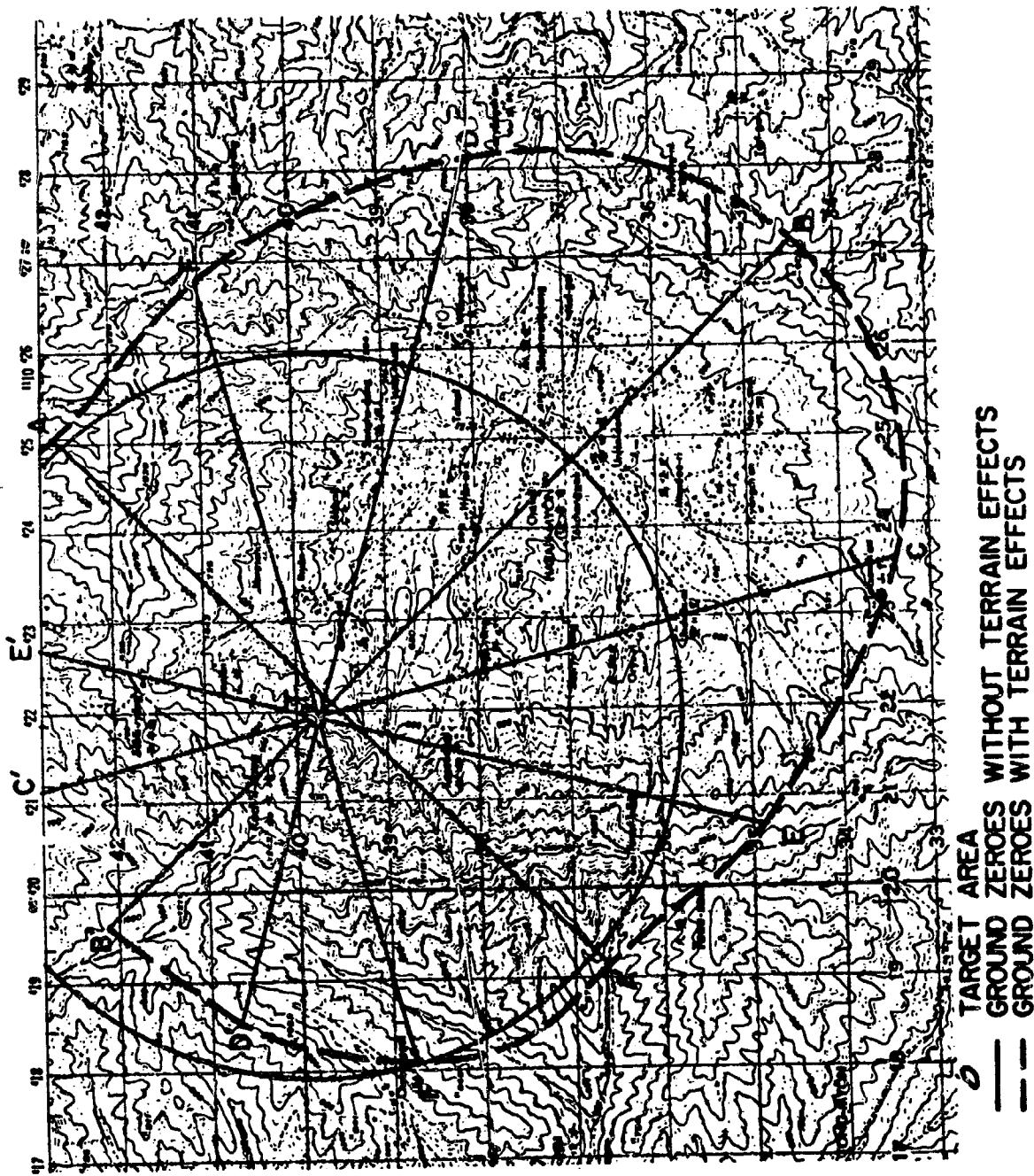


Figure 2-62. Terrain Map Used in Example

height of burst of 5,000 feet over any point on the circle would produce an overpressure of 10 psi at the target area (burst over points within the circle would produce overpressures in excess of 10 psi at the target).

The target area includes two small converging valleys that are relatively shallow and have relatively flat slopes normal to their axes. Figure 2-61 shows that relatively steep slopes are required to produce large effects in converging valleys, so these minor terrain irregularities may be ignored.

The general direction of the contours in the target area is established as being parallel to line AA'; and a sectional plot along line BB', perpendicular to AA' and through the target area, is constructed (this sectional plot is shown in Figure 2-63 with the distance scales in meters for ease in comparison with the map). The plot in Figure 2-63 is not extended to the ground-zero circle (though it could easily be), since inspection of the area between the target and this circle, and reference to Figure 2-15 shows that Mach reflection would take place long before the shock would arrive at the target area. Furthermore, inspection of the area within the ground zero line indicates that an assumption of a horizontal datum for the slope of the primary reference plane is fairly good.

From Figure 2-63, it can be determined that the tangent of the slope angle (vertical rise/horizontal distances) is 0.57. Thus, the slope angle is

$$\theta_s = 30^\circ.$$

It is therefore necessary to determine the incident overpressure that will produce an overpressure of 10 psi when the shock wave encounters a 30 degree rising slope (along the line BT) or a 30 degree falling slope (along the line B'T'). Figure 2-55 (Mach Reflection) gives an incident overpressure of 3.5 psi for the rising-slope condition,

and Figure 2-56 (diffraction) shows an incident overpressure of 20 psi for the falling-slope condition. Figure 2-19 shows that 3.5 psi would occur at a ground distance of about 2,450 feet from a 1 kt burst or 24,500 feet (about 7,500 m) from a 1 Mt burst at heights of burst of 500 feet and 5,000 feet, respectively. Figure 2-18 shows that, for the same heights of burst, 20 psi occurs at a ground distance of 870 feet from a 1 kt burst or 8,700 feet (about 2,650 meters) from a 1 Mt burst.

Lines CC' and DD' are drawn at  $30^\circ$  to line BB'. For these lines, the angle between the direction of shock wave propagation and the angle of steepest ascent or descent is

$$\Phi = 30^\circ,$$

and the effective slope angle is determined by

$$\sin \theta = \sin \Phi_s \cos \Phi$$

$$= \sin 30^\circ \cos 30^\circ = 0.43$$

which yields

$$\theta = 26^\circ.$$

The angle  $\Phi$  for lines EE' and FF' is  $60^\circ$ , from which  $\theta = 14.5^\circ$ . Using these two values of  $\theta$  with Figures 2-55, 2-56, 2-18, and 2-19 provides the results shown in Table 2-5.

Along line AA' the hill on which the target lies is, for all intents, a V-shaped valley with combined slope angle (see Figure 2-62) of  $30^\circ$ . Figure 2-60 indicates that an amplification factor of about 1.25 holds for such a valley, so an 8 psi incident overpressure ( $10/1.25$ ) will yield 10 psi at the target area. Figure 2-19 shows that 8 psi would occur at a distance of approximately 1,375 feet for 1 kt or 13,750 feet for 1 Mt (about 4,200 meters for 1 Mt).

When the various distances given above

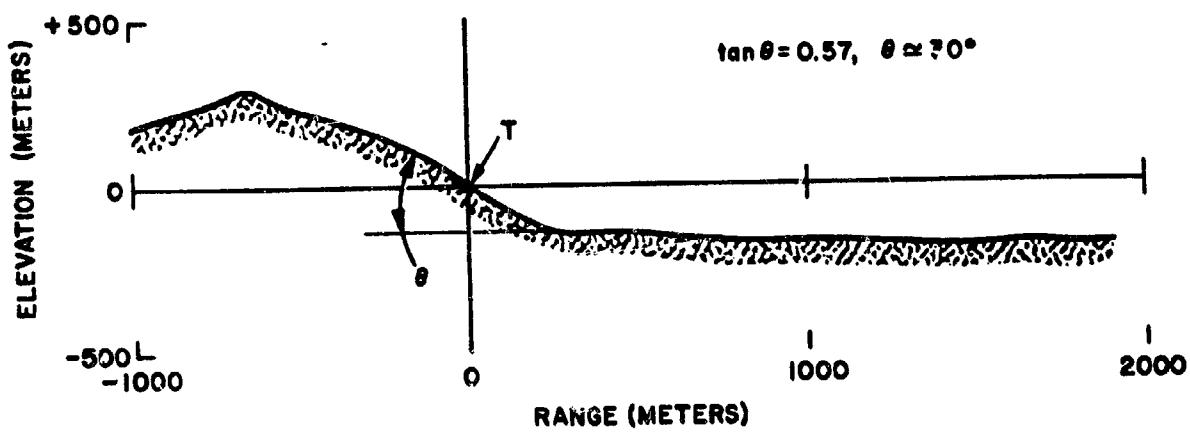


Figure 2-63. [redacted] Sectional Plot of the Terrain Along  
BB' in Figure 2-62 [redacted]

Table 2-5. Incident Overpressure and Ranges

Line	$\Phi$	$\theta$	Rising Slope Incident Overpressure (psi)	Approximate Distance	
				Feet	Meters
BT	0°	30°	3.5	24,500	7,500
CT, DT	30°	26°	4.1	21,500	6,600
ET, FT	60°	15°	6.0	17,000	5,000
<u>Falling Slope</u>					
B'T	0°	30°	20.0	8,700	2,650
C'T, D'T	30°	26°	18.5	9,500	2,900
E'T, F'T	60°	15°	15.0	10,900	3,300

are measured from the target area T along the appropriate lines, the points are connected, the dashed line shown in Figure 2-62 is the result. This line is the approximate locus of ground zeroes that will subject the target area to a peak overpressure of 10 psi.

### THE BLAST WAVE AT HIGH ALTITUDES

Nearly all of the energy from a nuclear burst detonated within the atmosphere is absorbed by air molecules. Within a few seconds, most of this energy evolves to three forms: blast energy, radiated thermal energy, and thermal energy retained in a large volume of air. The first two components of energy are useful nuclear effects; the third is harmlessly dissipated over a relatively long period of time. Deviations from Sachs' scaling laws (paragraphs 2-13 and 2-14) above 40,000 feet are caused principally by differences in the partitioning of these three energy components. Between sea level and 130,000 feet, blast energy decreases and radiated thermal energy increases with yield.

These changes are, to a large degree, caused by changes in characteristic times. The blast wave develops more slowly at higher altitudes, and the thermal pulse radiates more rapidly. Thus, energy is radiated at high altitudes that would, at lower altitudes, have contributed to the blast wave. At altitudes higher than 130,000 feet, both blast and thermal\* efficiencies drop.

#### 2-42 Effective Blast Yield at High Altitudes

To account for the smaller fraction of the yield that appears as blast energy at higher altitudes, the actual yield is multiplied by the blast efficiency factor shown in Figure 2-64 to obtain the effective blast yield. Effective blast yield is that value of yield which, when used in Sachs' scaling laws, predicts the correct value of peak overpressure.

Figure 2-64 shows approximate upper and lower limits rather than a single value for

\*Thermal radiation as used here includes ultraviolet through infrared, but excludes higher frequency radiations, e.g., X-rays. See Chapters 3 and 4.

the blast efficiency factor. At high altitudes, overpressure varies with distance in such a way that effective blast yield is different at different distances. For example, a 100 kt burst at 100,000 feet has an effective blast yield that varies from about 50 kt to 85 kt. It appears impossible to formulate simple rules that state where these numbers apply. It is preferable to consider the upper and lower effective blast yields as defining a range of uncertainty. Methods for making more detailed and complex calculations are suggested in DASA-1200 "Nuclear Weapons Blast Phenomena" (see bibliography).

Although blast efficiency is a correction factor established to determine peak overpressure, it also may be used to calculate other blast-wave parameters. However, because of the non-linear properties of air, blast waves with high shock strengths cannot be scaled exactly, and shock-front parameters other than peak overpressure are defined less accurately by effective blast yield. The waveform behind the shock front is subject to additional variations, and the blast efficiency is least dependable when applied to parameters such as impulse and positive phase duration.

### Problem 2-18. \*Calculation of Peak Overpressure at High Altitudes

Figure 2-64 shows the blast efficiency factor as a function of height of burst. This efficiency factor when multiplied by the weapon yield provides the effective blast yield. The effective blast yield may then be used to obtain peak overpressure as a function of distance by the methods described in paragraph 2-7 and Problem 2-1 as modified by the altitude correction procedures described in paragraph 2-14. Other blast parameters may be obtained by using the effective blast yield in the manner described for total yield in paragraphs 2-8 through 2-11, as modified by the altitude scaling described in paragraph 2-14.

**Scaling.** After obtaining the effective blast yield, the various blast parameters are scaled according to the procedures described in Problems 2-1 through 2-5, as modified by the altitude scaling described in paragraph 2-14 and Problem 2-6.

#### Example

**Given:** A 200 kt explosion at an altitude of 100,000 feet.

**Find:** The highest value of peak overpressure that might be expected 5,000 feet below the explosion.

**Solution:** Since Figure 2-64 shows that the highest value of blast efficiency factor for a burst at 100,000 feet is 85 percent, the calculation is based on an effective yield,  $W_{\text{eff}}$ , of

$$W_{\text{eff}} = (0.85)(200) = 170 \text{ kt.}$$

While the blast efficiency factor is based on burst altitude, the altitude scaling factors are based on target altitude (paragraph 2-14). From Table 2-1, the distance and pressure scaling factors at 95,000 feet are

$$S_d \approx 4.2$$

$$S_p \approx 0.014.$$

The distance from a 1 kt explosion that corresponds to a distance of 5,000 feet from a 170 kt explosion is

$$d_1 = \frac{d}{S_d W^{1/3}} = \frac{5,000}{(4.2)(170)^{1/3}} = 215 \text{ feet.}$$

From Figure 2-2, the peak overpressure at this distance at sea level is 210 psi.

**Answer:** The corresponding peak overpressure at 95,000 feet is

$$\Delta p = \Delta p_0 S_p = (210)(0.014) = 2.9 \text{ psi.}$$

The reliability statement of Problem 2-1 indicates that for scaled distances (distances from a 1 kt explosion) less than 1,000 feet the values of peak overpressure obtained from Figure 2-2 are accurate to within  $\pm 15$  percent. The probable upper limit of the required overpressure is

$$\Delta p = 2.9 + (0.15)(2.9) = 3.3 \text{ psi.}$$

**Reliability:** The data curves in Figure 2-64 are based on computer calculations supported by limited data from full-scale nuclear tests. As a result of the experimental checks, the computed data are believed to be accurate at high overpressures; however, this accuracy is not considered confirmed. At low overpressures (scaled radii under 300 feet, shock strengths less than 7), some of the numerical methods used by the computer introduce errors, and reliable esti-

mates of effective blast yield are not available; however, even at low shock strengths, the blast efficiency factor is believed to be approximately within the limits shown in Figure 2-64. Yield scaling appears to be relatively accurate, introducing errors of only a few percent. Uncertain-

ties in the overpressure values obtained from Figure 2-2 are described in Problem 2-1.

**Related Material:** See paragraph 2-41. See also paragraphs 2-7 through 2-11 and 2-14. See also Problems 2-1 through 2-6.

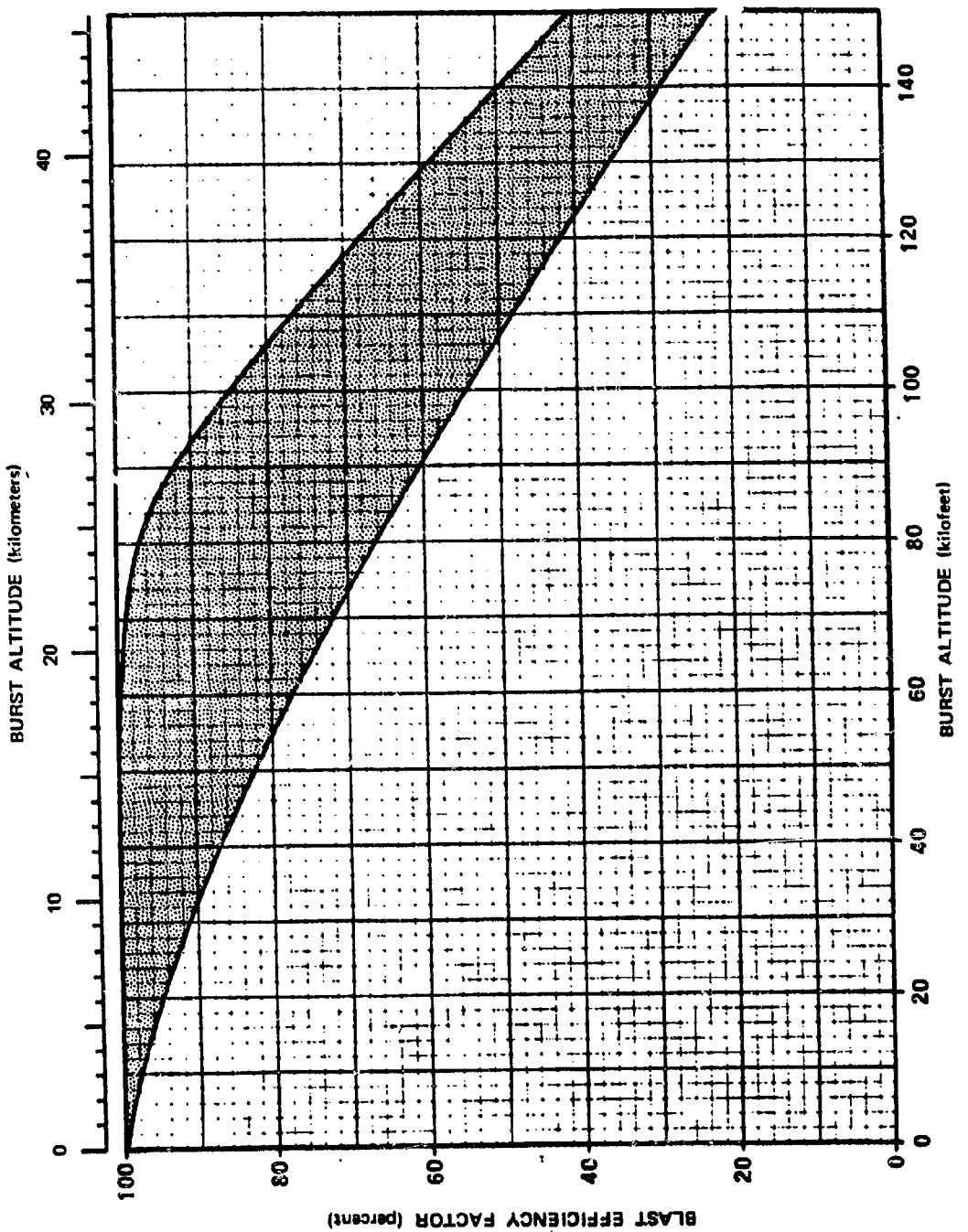


Figure 2-64. Blast Efficiency Factor for High-Altitude Bursts

#### **2-43 Peak Overpressure on the Ground from High-Altitude Bursts**

The conventional procedure for finding blast-wave parameters at one altitude produced by a burst at another altitude is modified Sachs' scaling (paragraph 2-14). Figure 2-65 uses this principle for the prediction of peak reflected overpressure at ground zero as a function of yield and burst altitude. The curves are based on computer calculations and are compatible with the curves in Figure 2-3, which show peak overpressure in free air.

The curves are drawn as though effective blast yield (paragraph 2-41) were always equal to actual weapon yield. If the burst is above 40,000 feet, a correction for effective blast yield is appropriate, and this reduced yield (rather than actual weapon yield) should be used to enter Figure 2-65.

Since the abscissa is slant range, Figure 2-65 may be used to predict peak reflected overpressure at locations other than at ground zero, provided the locations are within the region of regular reflection and are not too close to the range at which Mach reflection begins. Figure 2-46 may be used to determine the range over which the reflection coefficient has essentially the same value that it has at ground zero.

Since modified Sachs' scaling is an empirical method, there may be doubt as to its application over a wide altitude range. However, comparisons of reflected overpressures at ground

zero from Figure 2-65 with calculations performed in a way that is independent of the technique of modified Sachs' scaling show substantial agreement up to burst altitudes of about 150,000 feet, the limit of the latter calculations.

#### **2-44 Effects of Early Blast Phenomena**

At the overpressures that are ordinarily of interest in blast calculations, the blast wave from a sea level burst has propagated well away from the region in which it originated. At high altitudes, however, the blast wave forms at relatively low overpressures and at long ranges. In making a blast calculation at these altitudes, a possibility exists that the range of interest is closer than that at which a scalable shock front forms.

The first stage of blast-wave formation occurs when the air around the burst, under high pressure because of its suddenly increased temperature, starts to move. In the analysis of computer runs, a convenient criterion for shock front formation is that the ratio of air density behind the shock to ambient air density ( $\rho_s/\rho$ ) rises at some point to a value exceeding 1.5. This criterion indicates that the pressure waves originating in the air near the burst are starting to merge to form a shock front. Formation of the hydrodynamic shock front then proceeds rapidly, and the actual time and radius of shock formation are close to the values based on the  $\rho_s/\rho = 1.5$  criterion.

**Problem 2-19. Calculation of Peak Reflected Overpressure  
at Ground Zero from a High Altitude Explosion**

Figure 2-65 shows the peak reflected overpressure at the ground as a function of slant range for a selected family of weapon yields. The curves in Figure 2-65 are applicable at ground zero and at locations away from ground zero that are in the regular reflection region.

**Scaling.** No scaling is required with Figure 2-65; however, for explosions above 40,000 feet, the effective yield obtained by use of Figure 2-64 should be used to enter Figure 2-65.

**Example**

**Given:** A 100 Mt explosion at an altitude of 120,000 feet.

**Find:** The maximum peak reflected overpressure expected at ground zero.

**Solution:** From Figure 2-64, the maximum blast efficiency factor for bursts at 120,000 feet is 68 percent. The effective yield is

$$W_{\text{eff}} = (0.68)(100) = 68 \text{ Mt.}$$

**Answer:** Interpolation in Figure 2-65 indi-

cates that peak reflected overpressure at ground zero is about 2.5 psi.

**Reliability**

The few available experimental data points tend to substantiate the curves in Figure 2-65. A certain amount of uncertainty occurs at low overpressures because the overpressure distance curves in Figure 2-65 are not identical to the results of the calculations independent of Sachs' scaling that were mentioned in paragraph 2-42.

No reliability estimate has been made for these curves; however, it should be observed that, for the extreme range of atmospheric conditions found along the path of the blast wave, overpressure values that are within a factor of 2 often represent satisfactory agreement.

**Related Material:** See paragraphs 2-7, 2-13, 2-14, and 2-42. See also Tables 2-1 and 2-2.

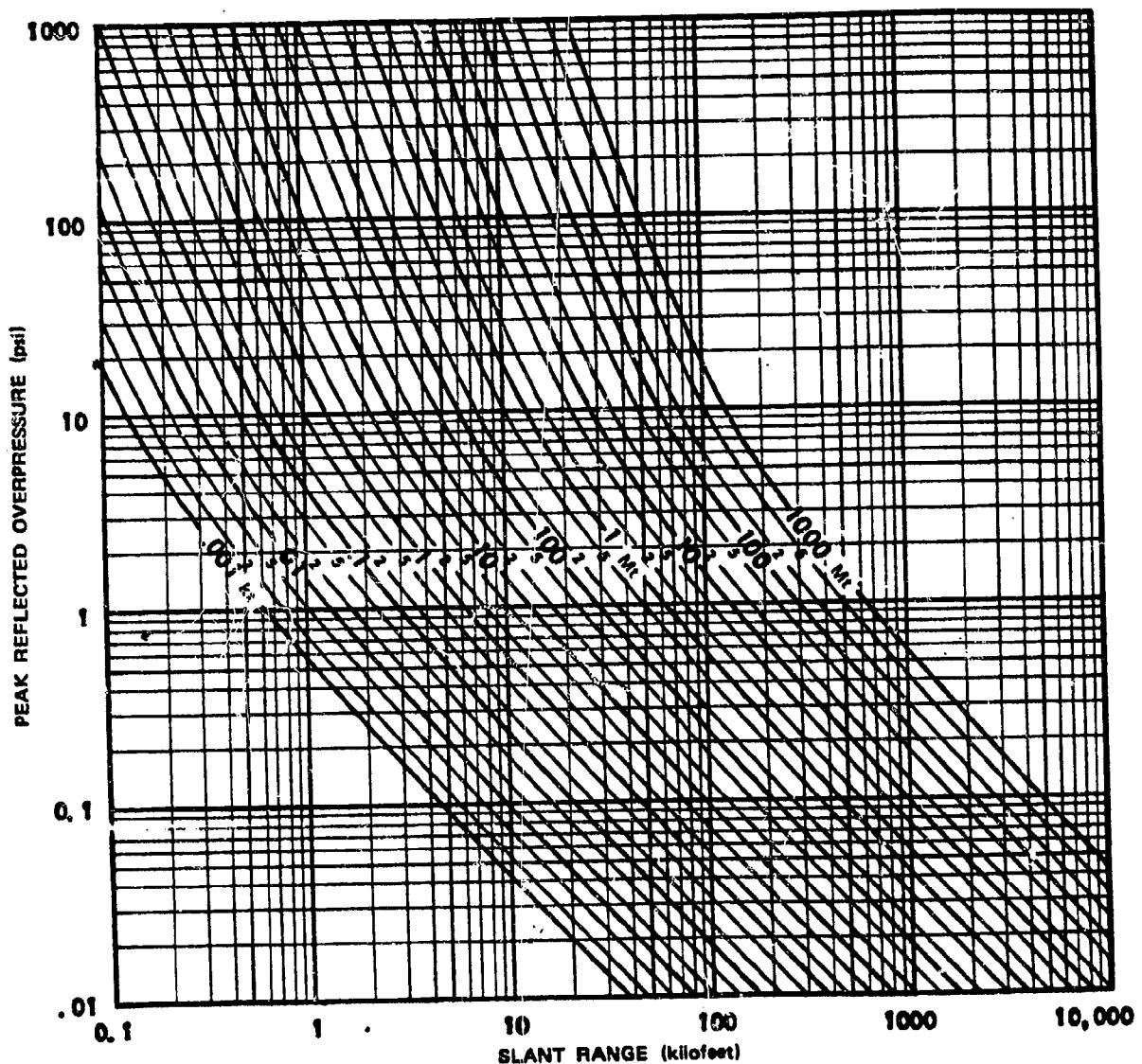


Figure 2-65. Peak Reflected Overpressure at Ground Zero  
as a Function of Yield and Slant Range

The kinetic energy of the bomb debris, which is typically about 25 percent of the total yield, makes an important contribution to the strength of the blast wave. These high velocity debris atoms, pushing away the air surrounding the burst point, create a shock wave that is known as the nuclear shock or case shock. Until this shock front overtakes and merges with the hydrodynamic shock front, the blast wave will not have acquired its full energy. The fraction of the total energy carried by the debris is a function of weapon design. Therefore the arrival of the case shock at the hydrodynamic shock front, which marks the beginning of a scalable shock wave, also is a function of weapon design.

Figure 2-66 shows the approximate ranges of shock-front formation and case-shock arrival as a function of burst altitude for a 1 kt explosion. These ranges were calculated for conventional nuclear devices. Different curves would be required to show these ranges accurately for weapons with enhanced radiation outputs (paragraph 2-45).

Figure 2-66 also shows curves of blast-wave overpressure levels as a function of range and altitude. Since peak overpressure cannot be scaled accurately until the case-shock front joins the hydrodynamic shock front, the overpressure curves terminate on the curve for case-shock arrival. To emphasize the increasing uncertainty of peak overpressure data with increasing altitude, the overpressure contour lines are dashed above 100 kft.\*

These overpressure curves were obtained directly from Figure 2-2 and Sachs' scaling laws, including altitude corrections described in paragraph 2-14. However, correction for effective

blast yield at high altitudes must be made, as illustrated in Problem 2-20.

This procedure will give a reasonably accurate answer only if the range that is used exceeds the range for case-shock arrival. The latter range is obtained by multiplying range obtained from Figure 2-66 for case-shock arrival by  $W^{1/3}$  (note that actual yield  $W$ , not effective yield  $W_{\text{eff}}$ , is required in this calculation). Similarly, the approximate range for shock front formation is obtained by multiplying the scaled range by  $W^{1/3}$ .

If a blast-wave calculation closer to the burst than the range of case-shock arrival is required, data from Figure 2-2 may be scaled to obtain a rough estimate of peak overpressure. If the calculation is for a range closer than the range for  $\rho_s/\rho = 1.5$ , the discrepancy between the actual overpressure and the calculated overpressure will probably be excessive. Requirement for a calculation of this type generally is a sign that other nuclear effects should be considered. Blast damage at ranges closer than shock-front formation usually is less serious than damage caused by neutrons, X-rays, gamma rays, and thermal energy.

The stages of development of a nuclear blast wave are most accurately known in terms of time, because accurate comparisons can be made between experimental data and points in computer calculations. Approximate equations for determining three times of interest are given below.

See NOTE in Reliability paragraph of Problem 2-20.

### Problem 2-20. Calculation of Case-Shock Arrival and Peak Overpressure at High Altitudes

Figure 2-66 shows the approximate ranges of shock-front formation and case-shock arrival as a function of burst altitude and distance from a 1 kt explosion.

**Scaling.** For yields other than 1 kt, the range for case-shock arrival scales as follows:

$$\frac{d}{d_1} = W^{1/3},$$

where  $d_1$  is the range for case-shock arrival for 1 kt (obtained from Figure 2-66), and  $d$  is the corresponding range for a yield of  $W$  kt. For heights of burst above 40,000 feet the range for a given overpressure scales as follows:

$$\frac{d}{d_1} = (W_{\text{eff}})^{1/3},$$

where  $d_1$  is the range for the desired overpressure for a 1 kt explosion and  $d$  is the corresponding range for a yield of  $W_{\text{eff}}$  kt ( $W_{\text{eff}}$  is the effective yield for a high altitude burst obtained from Figure 2-64 as illustrated in Problem 2-18).

#### Example

**Given:** A 100 kt explosion at an altitude of 110 kilofeet above sea level.

**Find:** The peak overpressure at a range of 1,000 feet.

**Solution:** From Figure 2-66, the range for case shock arrival from a 1 kt burst at 110 kft is about 180 feet. The corresponding range for 100 kt is

$$d = d_1 W^{1/3} = (180)(100)^{1/3} = 935 \text{ feet.}$$

Since this is less than 1,000 feet, peak overpres-

sure is scalable at the range of interest. From Figure 2-64, the blast efficiency for a burst at 110 kft is expected to be between 48 percent and 77 percent. The effective blast yield is therefore between 48 and 77 kt. The corresponding distances for a 1 kt explosion are

$$d_1 = \frac{d}{(W_{\text{eff}})^{1/3}} = \frac{1,000}{(48)^{1/3}} = 275 \text{ feet,}$$

and

$$d_1 = \frac{d}{(W_{\text{eff}})^{1/3}} = \frac{1,000}{(77)^{1/3}} = 235 \text{ feet.}$$

**Answer:** From Figure 2-66, the overpressures are 90 and 150 psi at these ranges from a 1 kt explosion at 110 kft. The 15 percent uncertainty in overpressure data (see "Reliability") extends the range of 1 kt overpressure values to between 75 and 170 psi.

#### Reliability

Ranges for shock formation and case-shock arrival were obtained from computer calculations. Case-shock arrival has been observed in nuclear tests, and the experimentally determined ranges substantiate the computer data. For conventional weapons (unconventional weapons are discussed in the following subsection), the range for case-shock arrival is believed correct within a few percent. Yield scaling appears to be fairly accurate for these phenomena.

Below 40,000 feet peak overpressure data are considered reliable within 15 percent for shock strengths greater than 1.5 (7 psi at sea level), within 20 percent for shock strengths between 1.5 and 1.03, and within 30 percent for shock strengths below 1.03 (~1/2 psi at sea

level). Above 40,000 feet, the additional uncertainty implied by Figure 2-64 should be considered.

Note: Although Figure 2-66 was used in this example to calculate peak overpressure, it is not the preferred source of overpressure data. More accurate values may be obtained by scaling data from Figure 2-2 and, at high altitudes, following the method of Problem 2-18. Figure 2-66

is convenient for rough calculations, because it eliminates the requirement for altitude scaling. However, the important information in this figure is given by the curves that show the approximate ranges of shock-front formation ( $\rho_s/\rho = 1.5$ ) and the beginning of a scalable shock wave (case-shock arrival).

*Related Material:* See paragraphs 2-7, 2-41, and 2-43. See also Problem 2-18.

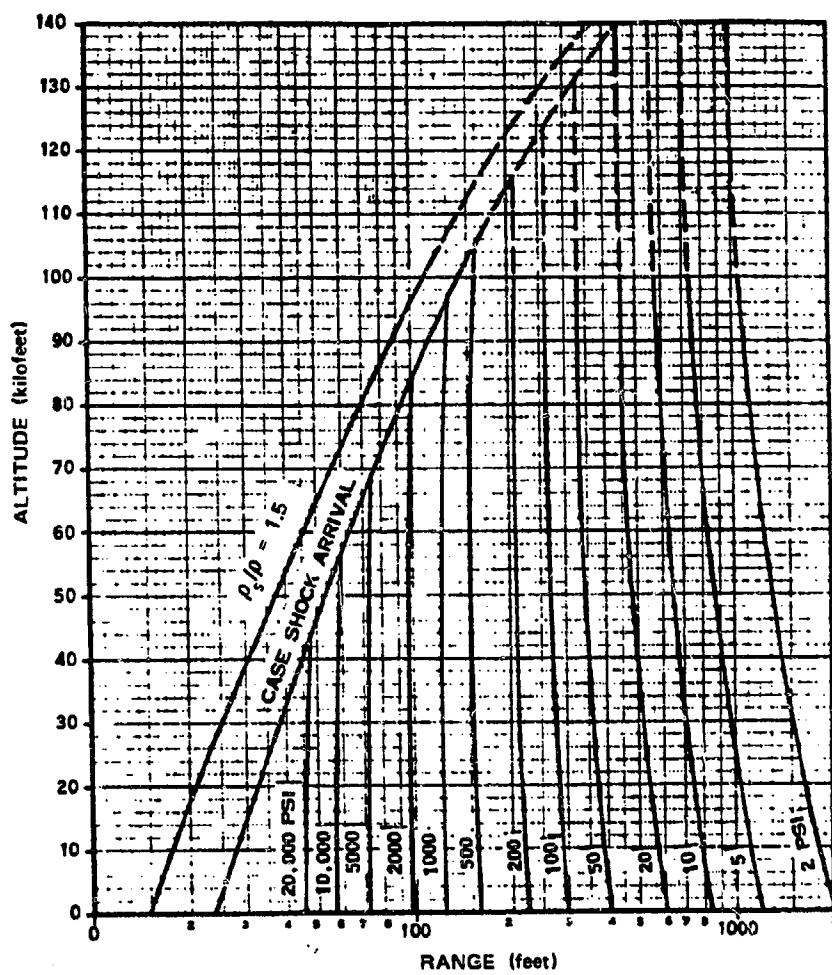


Figure 2-66. Limits of Scalable Shock Wave and Calculated Peak Overpressure as a Function of Altitude as a Function of Distance from a 1 kt Explosion

## WEAPONS WITH ENHANCED OUTPUTS

The initial output energy of a conventional nuclear weapon consists mainly of black body radiation.

and kinetic energy of bomb debris as shown in Table 2-6. Table 2-7 shows the mean free path of various forms of energy that can be generated by a nuclear device. Most of the output of a conventional nuclear weapon interacts with air atoms near the burst.

### 2-45 Air Blast from Weapons with Enhanced Radiation Outputs

The strength of the blast wave from enhanced radiation weapons is a complex function of the radiant energy distribution. Accurate blast wave calculations require detailed energy transport calculations, followed by hydrodynamic calculations to account for the motion of the heated air and the bomb debris. Frequently, the variation of ambient air density with altitude is sufficiently important to be included in the calculations. A large digital computer is required to account for all of these factors.

The unit keV is commonly used in two senses. Strictly speaking, it is a unit of energy ( $1 \text{ keV} = 1,000 \text{ electron volts} = 1.602 \times 10^{-9} \text{ erg}$ ) which has a magnitude that is convenient for specifying the energies of X-ray photons. However, by extension of its original meaning, the unit is used to define temperature ( $1 \text{ keV} \approx 11,600,000^\circ\text{K}$ ).

The term  $1 \text{ keV}$  spectrum means the spectrum of thermal radiation from a black body, i.e., a perfect radiator of thermal energy, that has a temperature of  $1 \text{ keV}$ . Note, however, that an energy of  $1 \text{ keV}$  is not representative of the energy of the photons constituting such a spectrum: about 15 percent of the photons have energies of  $1 \text{ keV}$  or less, and these photons represent less than 3.5 percent of the total spectral energy. Half of the energy is carried by photons with energies greater than  $3.5 \text{ keV}$ . The spectrum extends roughly to  $10 \text{ keV}$ ; photons with energies higher than this constitute only 1 percent of the spectral energy. See Chapter 4 for further discussion of black body radiators.

Table 2-7

Representative Mean Free Paths of Nuclear Weapon Radiation

Source	Energy	Mean Free Path	
		Sea Level	80,000 ft
[REDACTED]	[REDACTED]	[REDACTED]	[REDACTED]

\* The mean free paths shown in this table are for individual particles in ambient air. Collectively, the particles may travel farther. Debris atoms, for example, assist one another in pushing the air atoms away from the burst point. X-ray photons completely ionize a small region of air near the burst, thus creating a nearly transparent region through which other X-ray photons can travel freely.

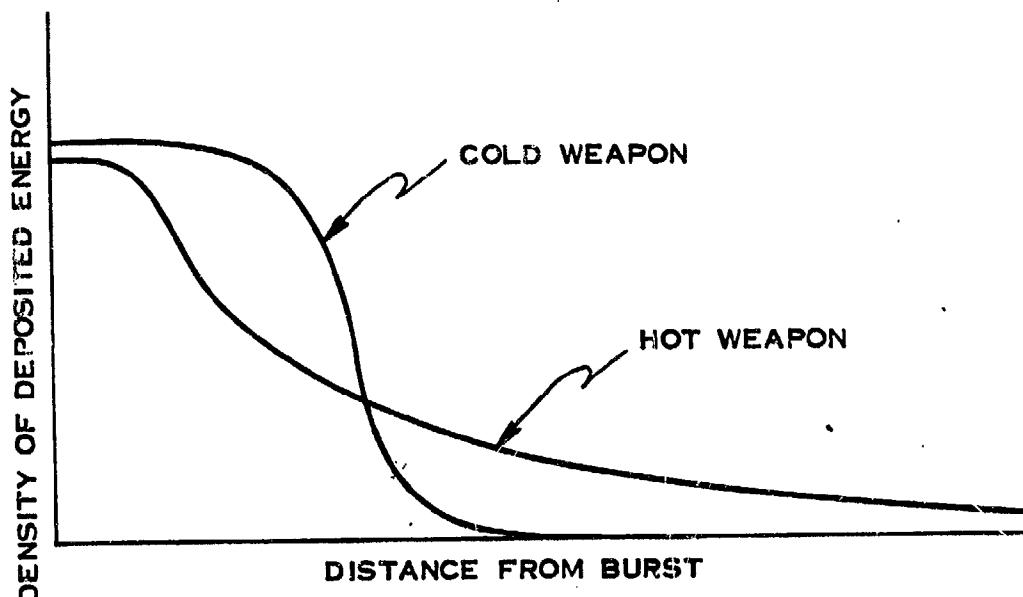


Figure 2-6  
Energy Deposition in Air as a Function of Nuclear Source Characteristics (Not to Scale)

Rough calculation may be made, however, by applying the following rule of thumb to weapons with enhanced outputs: blast calculations for a given radius may be based on a weapon yield that is equal to the amount of energy contained in the sphere defined by that radius. As this rule implies, the blast wave, as it propagates outward, picks up hydrodynamic energy from the heated air through which it passes.

DNA  
(6)(3)

DNA  
(6)(3)

[REDACTED] Many problems that require blast yield correction because of output spectrum will also require a blast yield correction because of altitude (paragraph 2-41). One correction factor does not replace the other, as illustrated in Problem 2-21.

[REDACTED] Effective blast yield, in percent, tends to increase with (1) increased range, (2) decreased radiating temperature, (3) increased yield, and (4) decreased altitude.

DNA  
(k)(3)

[REDACTED] As yield increases, the range for a given overpressure increases, but the distance that a given form of prompt energy can travel

[REDACTED] remains essentially the same; therefore, at a given overpressure level the blast wave from a higher yield encloses a greater fraction of the weapon output.

DNI  
(k)(3)

[REDACTED] As altitude decreases, the denser air confines the radiated energy to a smaller volume. Since the range for a given peak overpressure is relatively insensitive to altitude (Figure 2-66), the sphere defined by this range encloses an increasing fraction of the source energy as altitude decreases.

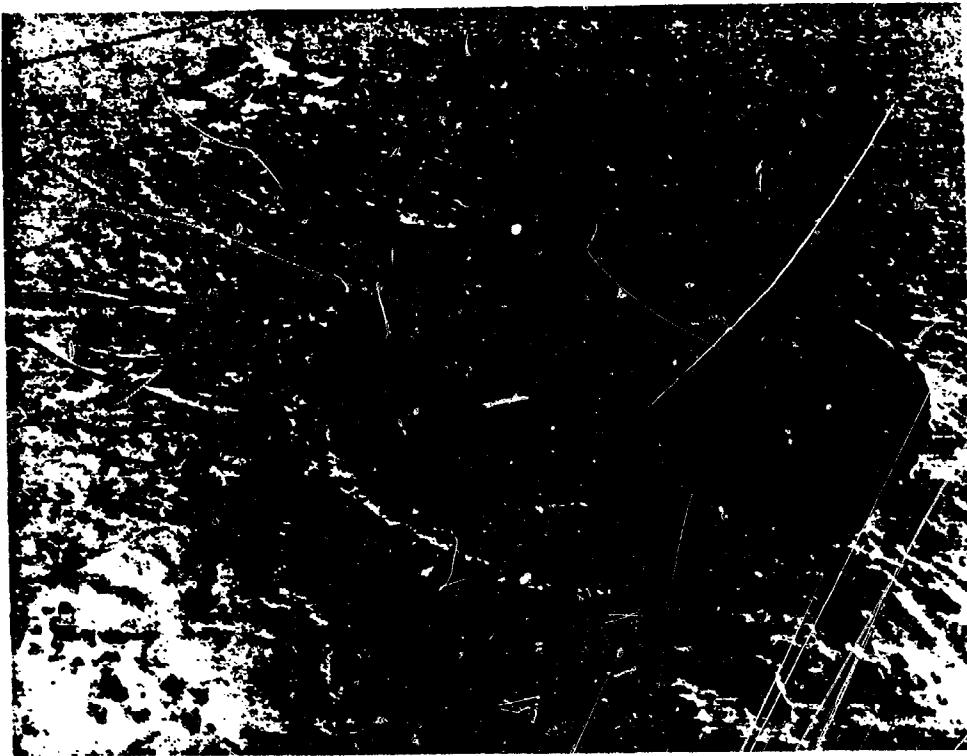


Figure 2-71a. SEDAN Event; Typical Crater Formed by a 100 kt Detonation in a Soil Medium at Optimum DOB:  $R_g = 186$  m (611 ft.);  $D_g = 98.5$  m (323 ft.); DOB = 194 m (635 ft.)

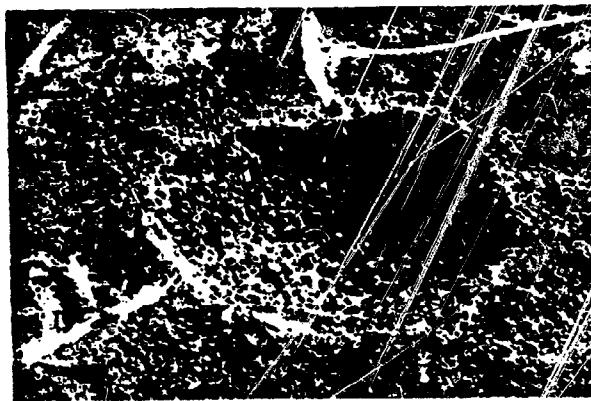


Figure 2-71b. DANNY BOY Event; Typical Crater Formed by a 0.43 kt Detonation in a Hard Rock Medium (Basalt) at Optimum DOB:  $R_g = 33.5$  m (110 ft.);  $D_g = 18.9$  m (62 ft.); DOB = 33.5 m (110 ft.)



Figure 2-72a. SULKY Event; Mound Created by the Bulking of Rock Material in a Deeply Buried  
0.087 kt Nuclear Detonation:  
Mound Diameter = 48.8 m (160 ft.); Mound Height = 7.6 m (25 ft.); DOB = 27 m (90 ft.).

2-153

Reproduced from  
best available copy.

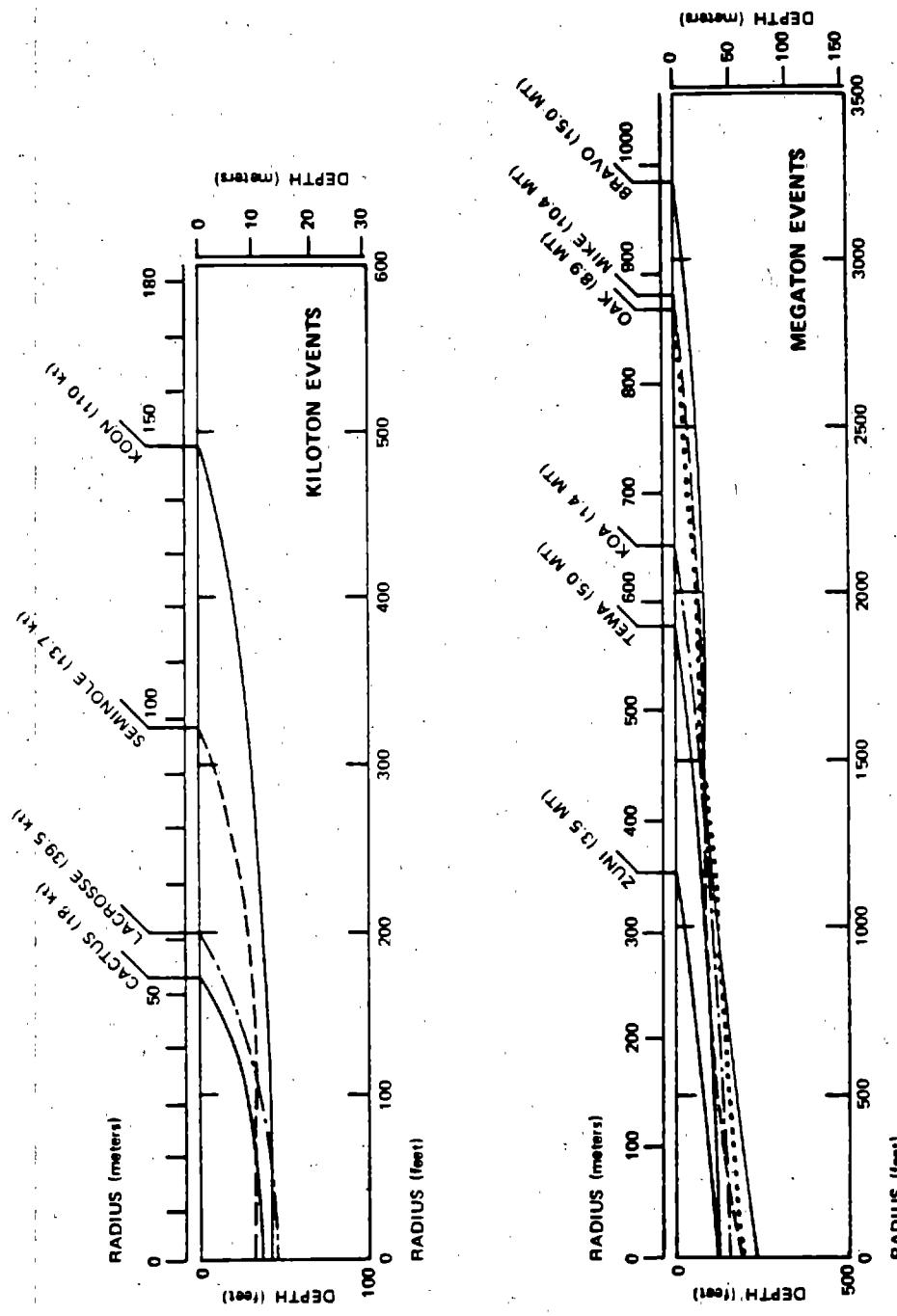


Figure 2-73. Typical Pacific Proving Ground Crater Profiles

In the shallow-buried region where the  $DOB/W^{1/3}$  is less than  $5 \text{ m}/\text{kt}^{1/3}$ , the yield scaling exponent,  $a$ , is a function of depth of burial.\* It is in this region that an interpolation procedure is required to determine  $a$ , as will be discussed in paragraph 2-49.

The near-surface region ( $HOB/W^{1/3} \leq 3 \text{ m}/\text{kt}^{1/3}$  to  $DOB/W^{1/3} \leq 5 \text{ m}/\text{kt}^{1/3}$ ) and the buried burst ( $DOB/W^{1/3} > 5 \text{ m}/\text{kt}^{1/3}$ ) region will be examined separately in the succeeding paragraphs. Five generic geologies have been chosen to describe the effect of various homogeneous media on cratering efficiency.

#### 2-49 Volume of Craters from Surface and Near-Surface Bursts ( $HOB/W^{1/3} \leq 3 \text{ m}/\text{kt}^{1/3}$ to $DOB/W^{1/3} \leq 5 \text{ m}/\text{kt}^{1/3}$ )

Figures 2-74a through 2-75e show the apparent crater volume, as a function of height of burst,<sup>†</sup> for a near-surface 1 kt explosion in various homogeneous generic geologies. Figures 2-74a through 2-74e are valid for yields less than or equal to 1 kt and Figures 2-75a through 2-75e are valid for yields greater than 10 kt.

For yields between 1 and 10 kt, the crater volume may be estimated by using the best estimate curve of the appropriate geology for either 1 kt or 10 kt or a weighted average, depending upon the output characteristics of the warhead. The higher the radiative fraction, the

\*Craters from detonations on the islands of the Pacific Proving Ground (Eniwetok and Bikini atolls) indicate that, for a saturated coral medium, the scaling exponent for the apparent crater radius may be greater than  $1/3$  and for the crater depth, smaller than  $1/3$ . Until the reason that it is necessary to depart from cube-root scaling in saturated coral is understood, it will not be possible to determine similar departures in other media.

<sup>†</sup>In this group of figures, HOB is used to indicate both HOB and DOB, i.e., buried bursts are shown with a negative HOB.

closer the crater volume will be to the  $W > 10 \text{ kt}$  curve. If, for example, it is known that a 3 kt weapon of interest has a high radiative output, the  $W > 10 \text{ kt}$  curve should be used to determine the apparent crater volume. If, however, no information is available concerning the radiative output, the crater volume should be determined by interpolation, assigning a 60 percent weight to the  $W < 1 \text{ kt}$  curve and 40 percent weight to the  $W > 10 \text{ kt}$  curve, i.e., for a 3 kt weapon with no further information

$$V_a(3) = 0.6 V_a(W < 1) + 0.4 V_a(W > 10).$$

The yield scaling parameter,  $a$ , for near-surface bursts is determined as follows:

$$\frac{HOB}{W^{1/3}} > 0; a = 0.333$$

$$-5 \leq \frac{HOB}{W^{1/3}} < 0 \text{ (m}/\text{kt}^{1/3}\text{)}; a = (\text{see Figure 2-76a}).$$

Once the value of  $a$  is known, the apparent scaled crater volume can be obtained from Figures 2-74a through 2-75e for a specified yield ( $W$ ) and  $HOB/W^a$  in the appropriate geology. The value obtained by this procedure is the "best estimate" of the apparent crater volume for a 1 kt explosion ( $V_{a1}$ ).

The crater volume for yields other than 1 kt may be obtained by the following scaling relation:

$$\frac{V_a}{V_{a1}} = W^3 a,$$

where  $V_{a1}$  is the apparent crater volume for a 1 kt explosion, and  $V_a$  is the corresponding volume for a yield of  $W$  kt. The height of burst scaling relation is

$$\frac{HOB}{HOB_1} = W^a,$$

where  $HOB_1$  is the height of burst for a 1 kt explosion, and  $HOB$  is the corresponding height of burst for a yield of  $W$  kt.

The uncertainty in the crater volume for  $W \leq 1$  kt is based on HE cratering results. It is assumed that the uncertainty is independent of geology and yield. The bounds shown in Figures 2-74a through 2-74e are not the results of a detailed statistical analysis. These bounds contain 95 percent of the experimental data, but statistical implications should not be drawn from this fact.

The best estimate for the  $W > 10$  kt curve was determined by nuclear data from the Pacific Proving Ground. The lower bound was suggested by calculations, and was influenced by the fact that all the nuclear data were obtained from devices that were very dissimilar to modern weapons.

## 2-50 Crater Shapes and Dimensions for Surface and near-Surface Bursts

The shape of the crater from a near-surface burst must be known to determine the radius and depth from the crater volume and the explosive yield. The shape depends mainly on the yield, the scaled height of burst, and the geology. Table 2-8 shows the shape to be expected as a function of these three variables. The succeeding discussion provides the necessary scaling relationships to determine the dimensions for the various shapes. Separate procedures are provided for each of the yield/HOB combinations shown in Table 2-8.

Table 2-8. Classification of Crater Shapes from Near Surface Bursts as a Function of Yield, Height of Burst, and Geology

Yield	Scaled HOB (m/kt <sup>1/3</sup> )	Geology	Crater Shape
$W \leq 1$ kt	All	All	Bowl
$W > 1$ kt	$HOB/W^{1/3} > 0$	All	Dish
$W > 1$ kt	$-5 \leq HOB/W^{1/3} < 0$	Unsaturated Saturated	Dish/Bowl Dish

### a. $W \leq 1$ kt

The crater shape for near-surface bursts ( $-5 \text{ m}/\text{kt}^{1/3} \leq \text{HOB}/W^{1/3} \leq 3 \text{ m}/\text{kt}^{1/3}$ ) in all geologies for  $W \leq 1$  kt is best described as bowl-shaped. The dimensions of the apparent crater radius,  $R_a$ , and apparent crater depth ( $D_a$ ) for these bursts are given by the following expressions:

$$1.1 V_a^{1/3} \leq R_a \leq 1.4 V_a^{1/3},$$

$$0.35 V_a^{1/3} \leq D_a \leq 0.7 V_a^{1/3}.$$

The best estimates for  $R_a$  and  $D_a$  are

$$R_a = 1.2 V_a^{1/3},$$

$$D_a = 0.5 V_a^{1/3},$$

where  $V_a$  = the best estimate apparent volume.

### b. $W > 1$ kt

The crater shape for near-surface bursts in which  $W > 1$  kt depends on the yield and HOB.

#### (1) $HOB/W^{1/3} \geq 0$ .

For above-surface bursts ( $HOB/W^{1/3} \geq 0$ ), in which  $W > 1$  kt, the crater shape is best described as dish-shaped and the crater dimensions are determined by the expressions

$$1.1 W^{0.08} \leq \frac{R_a}{V_a^{1/3}} \leq 1.4 W^{0.08},$$

$$0.35 W^{-0.12} \leq \frac{D_a}{V_a^{1/3}} \leq 0.7 W^{-0.12}.$$

The best estimates for  $R_a$  and  $D_a$  are

$$\frac{R_a}{V_a^{1/3}} = 1.2 W^{0.08},$$

$$\frac{D_a}{V_a^{1/3}} = 0.5 W^{-0.12}.$$

where  $V_a$  = the best estimate apparent volume.

$$(2) HOB/W^{1/3} < 0$$

For near-surface buried events

$$\left( 0 < \frac{DOB}{Wa} \leq 5 \text{ m/kt}^a \right),$$

in which  $W' > kt$ , the shape of the crater may be either "bowl" or "dish" in nature or some combination of the two extremes. Mechanisms such as compaction, rebound, bulking, slumping and layering effects play a significant role in the final crater shape. Cratering experience to date is not sufficient to make quantitative judgments regarding the impact of each mechanism.

The apparent crater dimensions for near-surface buried events are determined by the expressions

$$\frac{R_a}{V_a^{1/3}} = 1.2 W^b \text{ meters},$$

$$\frac{D_a}{V_a^{1/3}} = 0.5 W^{-c} \text{ meters}.$$

The values of the exponents (b, c), as a function of DOB, are found in Figures 2-76b and 2-76c. These exponents are necessary to ensure a smooth continuous curve for the radii of large yield (1 Mt) bursts as the depth of burial increases. Existing data indicate that above-surface bursts of high yield nuclear explosions produce dish-shaped craters and buried nuclear explosions produce bowl-shaped craters. However, since no data exist in the region

$$0 < \frac{DOB}{Wa} \leq 5 \text{ (m/kt}^a\text{)},$$

it is necessary to provide a transition region in which the crater produced is neither dish-shaped nor bowl-shaped, but some intermediate of the two extremes. The above equations produce this smooth transition region for the crater dimensions.

It has been noted, however, that in highly saturated media slope failure and/or liquefaction can produce a shallow crater for buried events. High explosive tests conducted at Fort

Polk, Louisiana are good examples of these phenomena.

Other pertinent crater dimensions may be related to the above dimensions as follows:

- The radius to the crater lip crest is

$$R_{al} = 1.25 R_a.$$

- The height of the apparent lip is

$$.25 D_a \leq H_{al} \leq .33 D_a$$

(near-surface bursts).

A summary of the procedures for calculating craters from near-surface bursts is given on page 2-161, immediately preceding the applicable figures.

## 2-51 Dimensions of Craters from Deep-Buried Explosions

Cratering experiments with chemical explosives (HE) and nuclear explosions (NE) suggest that linear dimensions of craters from buried explosions scale according to a modified overburden rule. This scaling rule is somewhat cumbersome to use for the computation of crater dimensions, and the available data do not conclusively prove the validity of any single scaling rule. Therefore, a simplified yield scaling exponent, yield (kt) to the 1/3.4 power, has been chosen for scaling apparent crater dimensions for scaled DOBs greater than 5 m/kt<sup>1/3</sup>. Figures 2-77 through 2-81 may be used to obtain apparent crater volumes for buried bursts in each of the soil types indicated. The curves in these figures are valid for all yields. The uncertainty in crater volume is independent of geology and yield, and is based on HE cratering results.

Crater radius and depth are given by the following expressions

$$1.1 V_a^{1/3} \leq R_a \leq 1.4 V_a^{1/3},$$

$$0.35 V_a^{1/3} \leq D_a \leq 0.7 V_a^{1/3}.$$

These expressions are valid for deep-buried bursts in *all* geologies for *all* yields. The best estimates for the crater dimensions are

$$R_a = 1.2 V_a^{1/3},$$

$$D_a = 0.5 V_a^{1/3},$$

where  $V_a$  is the best estimate of the apparent volume.

It is possible that slumping of the walls will produce a wide, shallow crater for some yield-DOB combinations in a saturated geology. The resulting crater shape is neither "bowl" nor "dish" in nature; it is some combination of the two. The only explosions to date that resulted in such occurrences in the craters have been in a very wet clay soil with the explosive charge at or near the optimum depth of burial.

The uncertainty in crater dimensions obtained from the expressions given above is, however, approximately correct for any specified crater volume. If the crater volume is chosen as the lower or upper uncertainty band from Figures 2-77 through 2-81, then the expressions for the radius and depth are still valid. A new range of crater dimensions is determined by using the equations and the chosen volume.

Figure 2-82 contains the best estimate prediction for high-explosive detonations in the five generic homogeneous geologies. These curves show the relative crater volumes for the geologies. The curves can be used as a guide as to the proper nuclear curve to use for a new or unknown geology. If some HE cratering data are available, the curves of Figure 2-82 can be used to determine which homogeneous geology is best for the problem. This figure should not be used to calculate crater volume for nuclear explosions.

Other pertinent crater dimensions may be related to the above dimensions as follows:

- The radius to the crater lip crest is

$$R_{al} = 1.25 R_a.$$

- The height of the apparent lip is

$$.20 D_a \leq H_{al} \leq .25 D_a$$

(deep-buried bursts).

A summary of the procedures for calculating craters from deep-buried bursts is given on page 2-179, immediately preceding the applicable figures.

## SUMMARY OF PROCEDURES FOR CALCULATING CRATERS FROM NEAR-SURFACE BURSTS ( $-5 \text{ m}/\text{kt}^{1/3} \leq \text{HOB}/W^{1/3} \leq 3 \text{ m}/\text{kt}^{1/3}$ )

Figures 2-74a through 2-75e and 2-76a, b and c, together with appropriate scaling laws, may be used to obtain crater volumes and dimensions from near-surface bursts in a variety of situations. The following summary provides a step-by-step procedure for obtaining such information. Example problems are provided on the pages immediately following the figures.

### *Required (either given or estimated)*

Yield ( $W$ ) in kt

Actual HOB or DOB (may be zero if required)

Soil type (one of the five generic types or a combination; see Figure 2-86b).

1. Determine yield scaling parameter,  $a$ , for burst position:
  - a.  $\text{HOB}/W^{1/3} \geq 0 \rightarrow a = 1/3 \equiv 0.333$ ,
  - b.  $0 < \text{DOB}/W^{1/3} \leq 5 \text{ m}/\text{kt}^{1/3} \rightarrow a$  from Figure 2-76a.
2. Compute  $\text{HOB}_1$  (HOB for 1 kt) = 
$$\frac{\text{Actual HOB}}{W^a}$$
 or  $\text{DOB}_1$  (DOB for 1 kt) = 
$$\frac{\text{Actual DOB}}{W^a}$$
3. Determine  $V_{al}$  (apparent-crater volume for 1 kt):
  - a. If  $W \leq 1 \text{ kt}$ , use curve for given soil type from Figures 2-74a through 2-74e.
  - b. If  $W > 10 \text{ kt}$ , use curve for given soil type from Figures 2-75a through 2-75e.
  - c. If  $1 \text{ kt} < W \leq 10 \text{ kt}$ , with *low or unknown* radiative output, interpolate using  $V_{al} = 0.6 V_{al}$  (from  $W \leq 1 \text{ kt}$  curve) + 0.4  $V_{al}$  (from  $W > 10 \text{ kt}$  curve).
  - d. If  $1 \text{ kt} < W \leq 10 \text{ kt}$  with *known high* radiative output, use curve for given soil type from Figures 2-75a to 2-75e.

4. Compute  $V_a$  (actual crater volume for yield other than 1 kt):

$$V_a (\text{actual volume}) = V_{al} (W^{3a}).$$

These curves are provided for each soil type: best estimate, upper bound, and lower bound. Using the following guidelines, select the curve most appropriate to the problem.

- a. Use *best estimate*  $V_{al}$  if no specific geologic data are given. If actual HE tests are available for a specific site, compare them with the HE curves in Figure 2-82, and move toward the upper or lower bound NE curve to adjust for these data, depending on where the data are grouped.
- b. Use *lower bound*  $V_{al}$  (if desirable) for target-oriented calculations (offensive-conservative) to calculate  $R_a$  or  $D_a$ . Consider lower-bound  $V_{al}$  for targeting when calculating crater volume-related phenomena, such as ejecta, transient velocity or displacement.\*
- c. Use *upper-bound*  $V_{al}$  (if desirable) for design-oriented calculations (defense-conservative) to calculate  $R_a$  or  $D_a$ . Consider upper bound  $V_{al}$  for design when calculating crater-related phenomena affected by volume.
- d. For  $W > 10 \text{ kt}$ , the discrepancy between the theoretical calculations and the empirical data in our understanding of the energy coupling produced by modern weapons detonated at low HOBs or in contact with the earth (HOB = 0.5 m)

---

\*In all instances it is recommended that upper and lower bound values be calculated in order to gain an appreciation of the effects of uncertainties on the particular problem under consideration.

must be considered. (See paragraph 2-49.) Since this discrepancy only occurs in the lower-bound  $V_a$  values, it principally influences targeting, or offensive-conservative, problems.

It is recommended that the lower-bound  $V_a$  values be considered in calculating kill probabilities ( $P_k$ ) due to the crater, but that high credence in cratering  $P_k$  not be used in assessing overall system  $P_k$ .

*Note:* This cratering discrepancy is a systematic uncertainty and should not be treated as a random uncertainty.

5. Calculate  $R_a$  and  $D_a$  using the expression from the following table that fits the yield and HOB and inserting the appropriate  $V_a$ :

Yield	Near-Surface Bursts	
	Above Surface HOB $(\frac{W^{1/3}}{W^{1/3}} \geq 0)$	Below Surface DOB $(\frac{W^{1/3}}{W^{1/3}} \leq 5 \text{ m}/\text{kt}^{1/3})$
$W \leq k_t$	$R_a = 1.2 V_a^{1/3}$ $D_a = 0.5 V_a^{1/3}$	same same
$W > 1 \text{ kt}^*$	$R_a = 1.2 W^{0.08} V_a^{1/3}$ $D_a = 0.5 W^{-0.12} V_a^{1/3}$	$R_a = 1.2 W^b V_a^{1/3}$ $D_a = 0.5 W^{-c} V_a^{1/3}$

\*See Figures 2-76b and 2-76c for determining b and c.

The dimensions  $R_a$ ,  $D_a$ , and  $V_a$  can be related to other pertinent crater dimensions as follows:

- The radius to the crest of the apparent crater lip is

$$R_{al} = 1.25 R_a$$

- The height of the apparent lip is

$$0.25 D_a \leq H_{al} \leq 0.33 D_a$$

for near-surface bursts.<sup>†</sup>

Variations in the thickness of the ejecta as a function of range from the surface ground zero (SGZ) are discussed in paragraphs 2-52 and 2-53.

<sup>†</sup>An exception to this is a similar crater formed by an explosion at the Pacific Proving Ground. The crater had no lip and greatly reduced ejecta. It is thought that such a crater shape may have been the result of a late-time reconsolidation/liquefaction process, which caused the crater lip to be below the water surface.

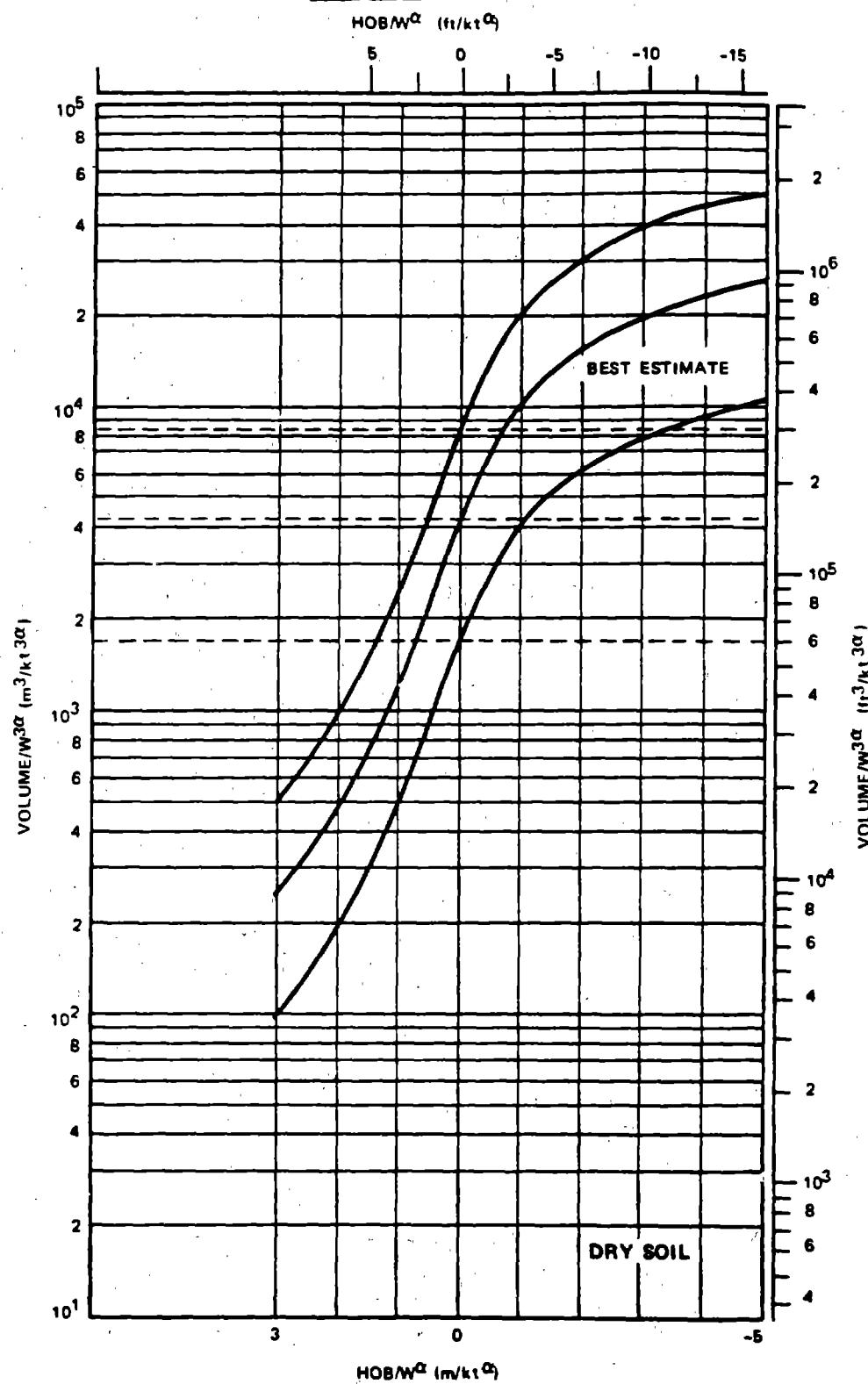
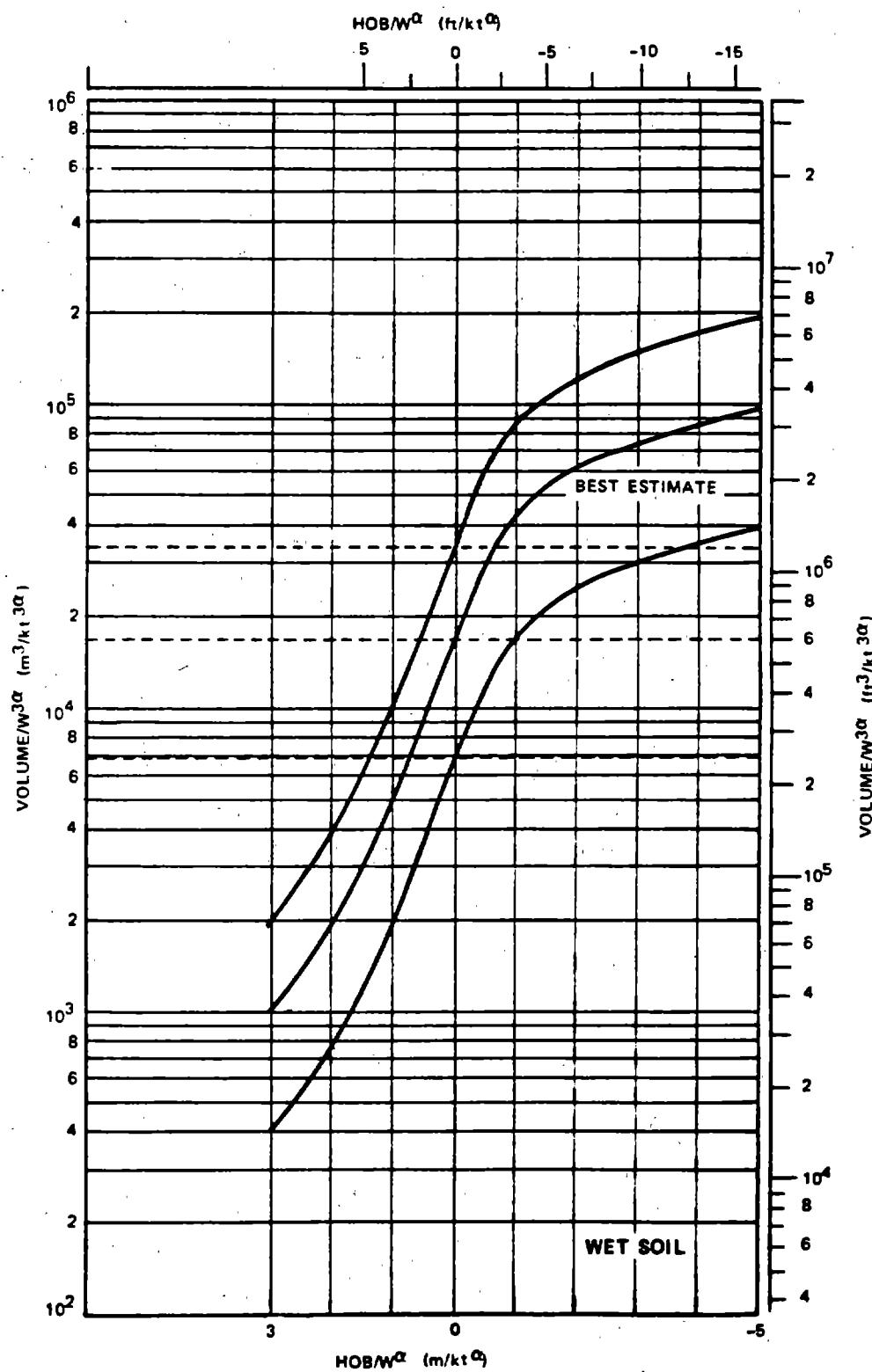


Figure 2-74a. Apparent Crater Volume for a 1-Kiloton Near-Surface Explosion in Dry Soil;  
Applicable for  $W \leq 1$  kt



2-164

Figure 2-74b. Apparent Crater Volume for a 1-Kiloton Near-Surface Explosion in Wet Soil; Applicable for  $W \leq 1 \text{ kt}$

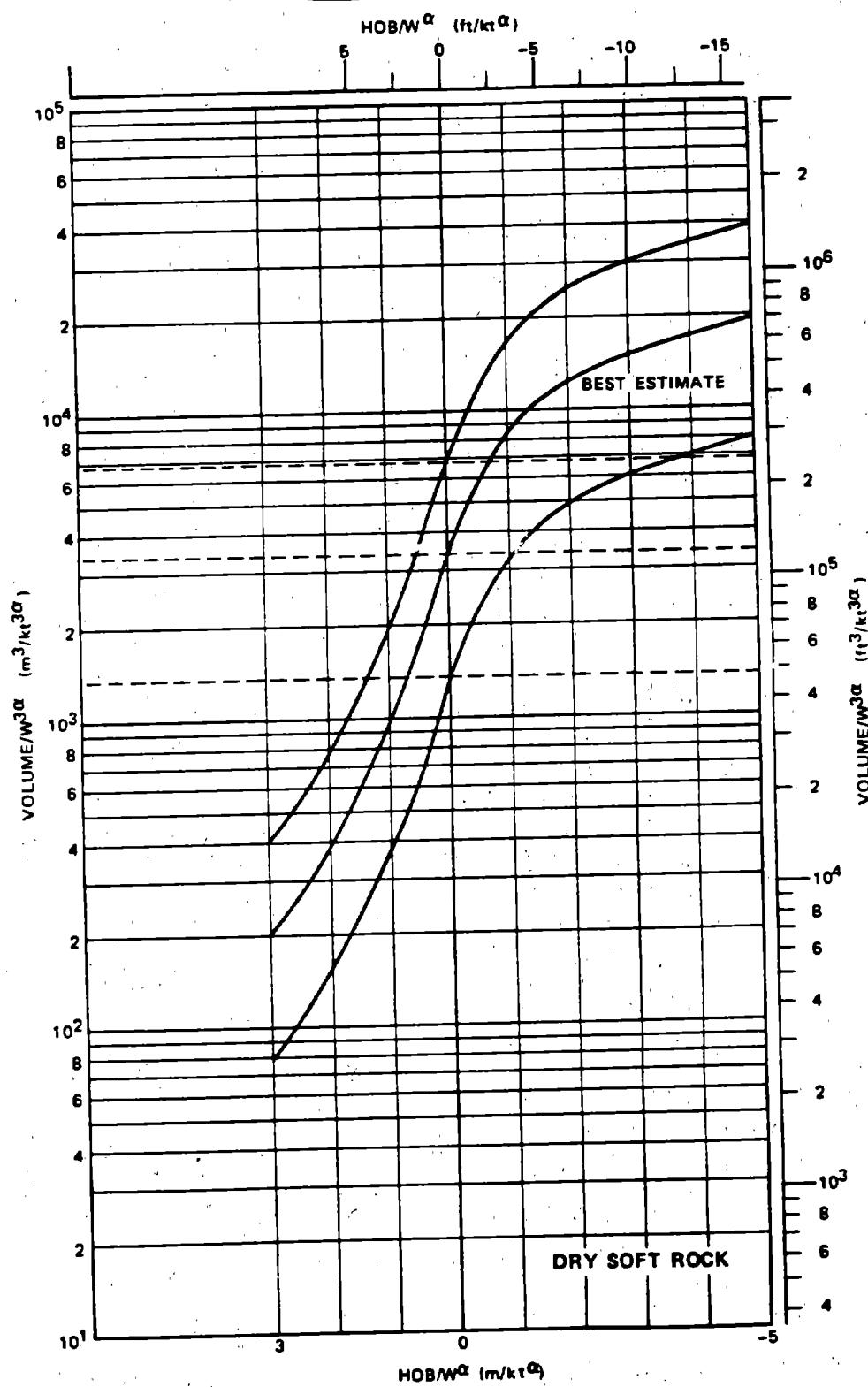
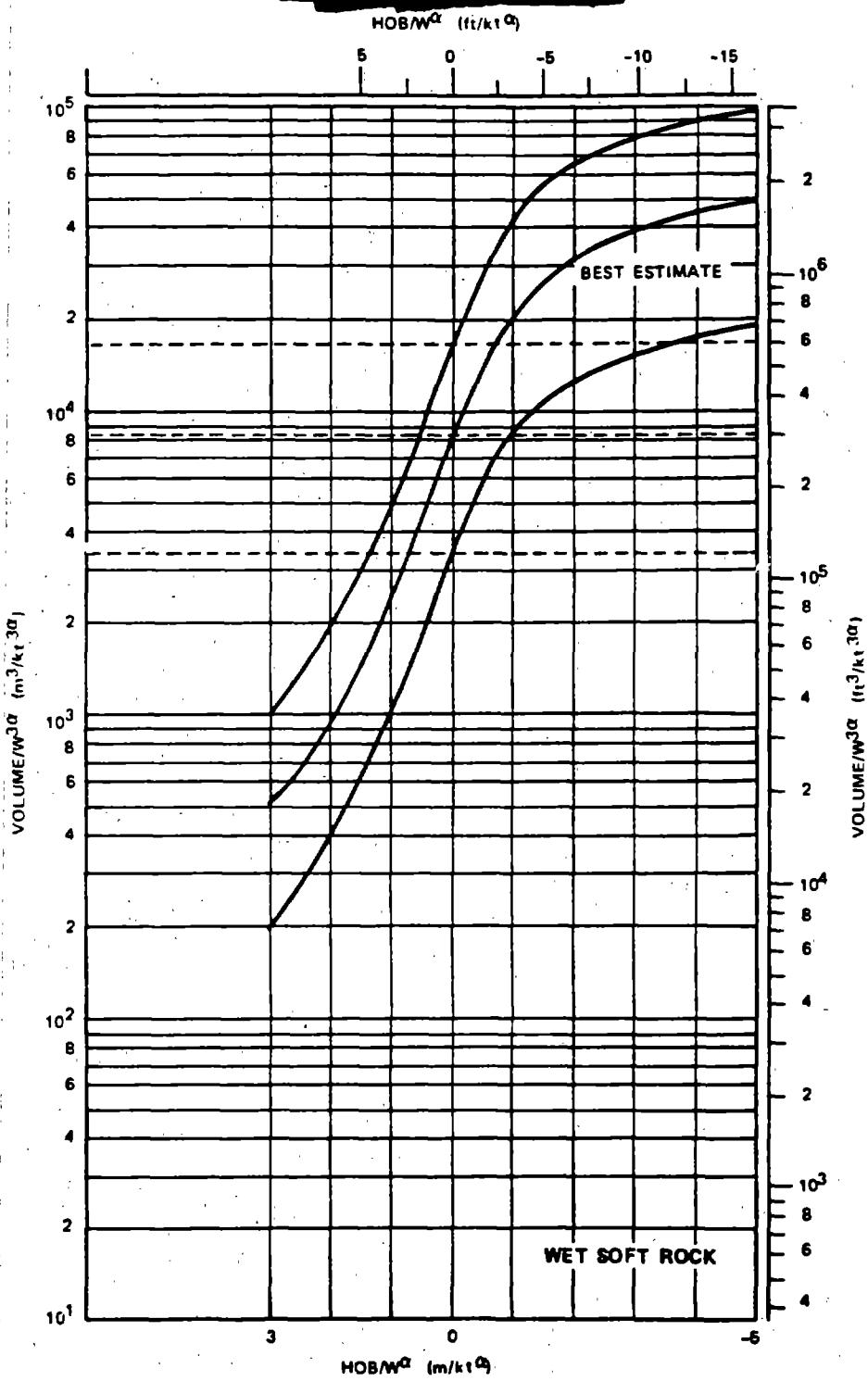


Figure 2-74c. Apparent Crater Volume for a 1 Kiloton Near-Surface Explosion in Dry Soft Rock; Applicable for  $W \leq 1 kt$



2-166

Figure 2-74d. Apparent Crater Volume for a 1-Kiloton Near-Surface Explosion in Wet Soft Rock; Applicable for  $W \leq 1 \text{ kt}$

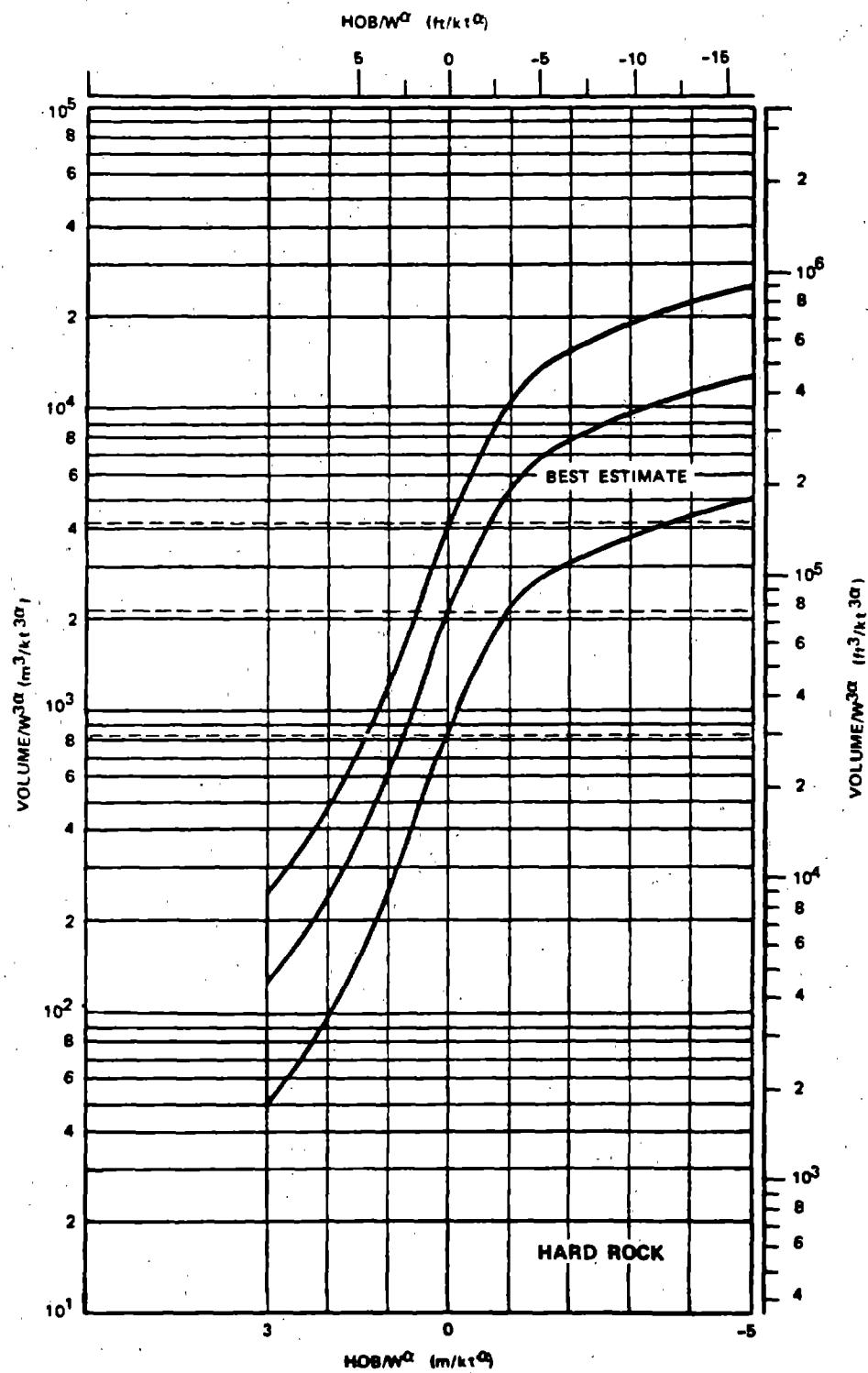
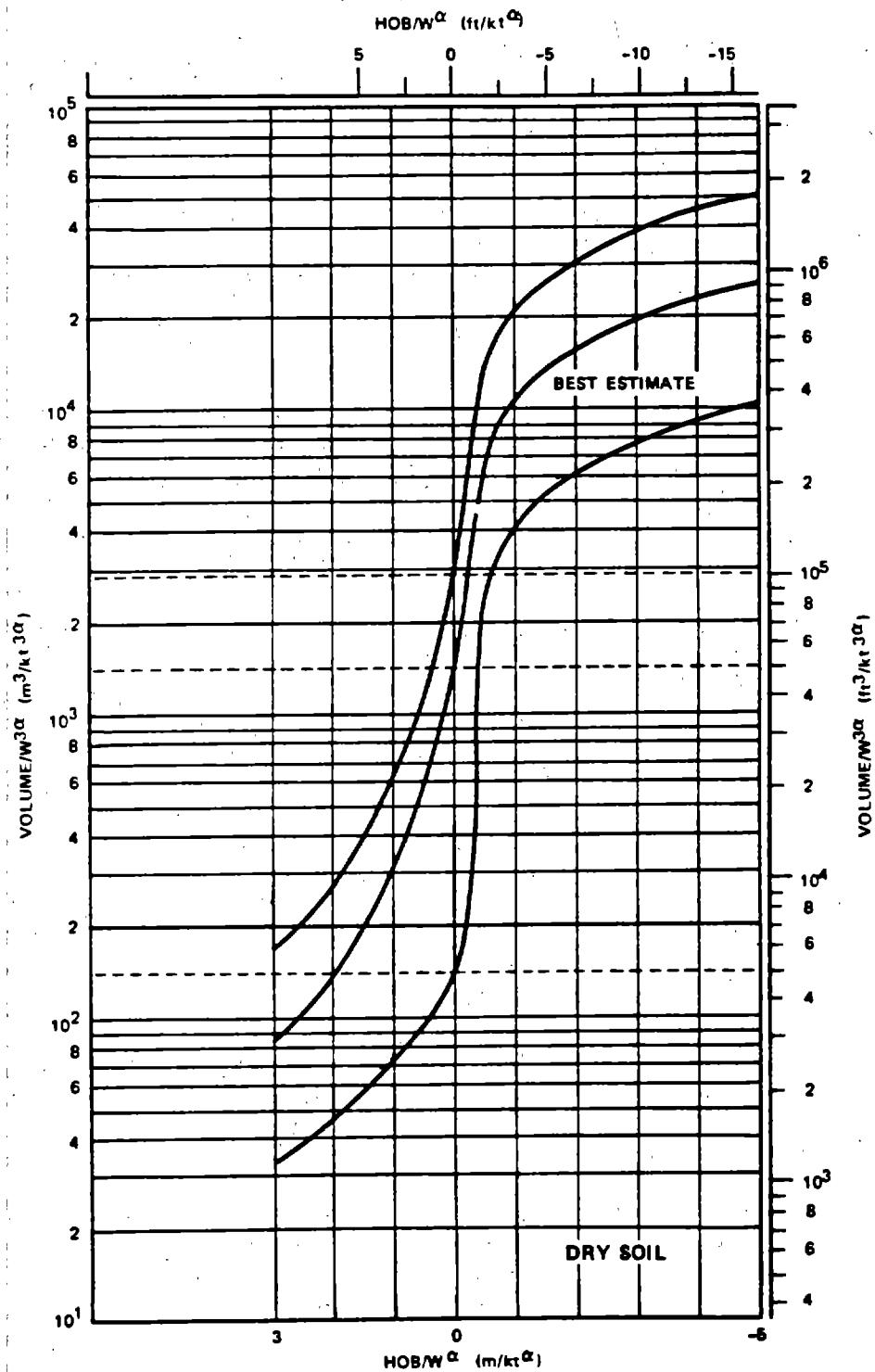


Figure 2-74e. Apparent Crater Volume for a 1 Kiloton Near-Surface Explosion in Hard Rock; Applicable for  $W \leq 1$  kt



2-168

Figure 2-75a. Apparent Crater Volume for a 1 Kiloton-Near-Surface Explosion in Dry Soil; Applicable for W > 10 kt

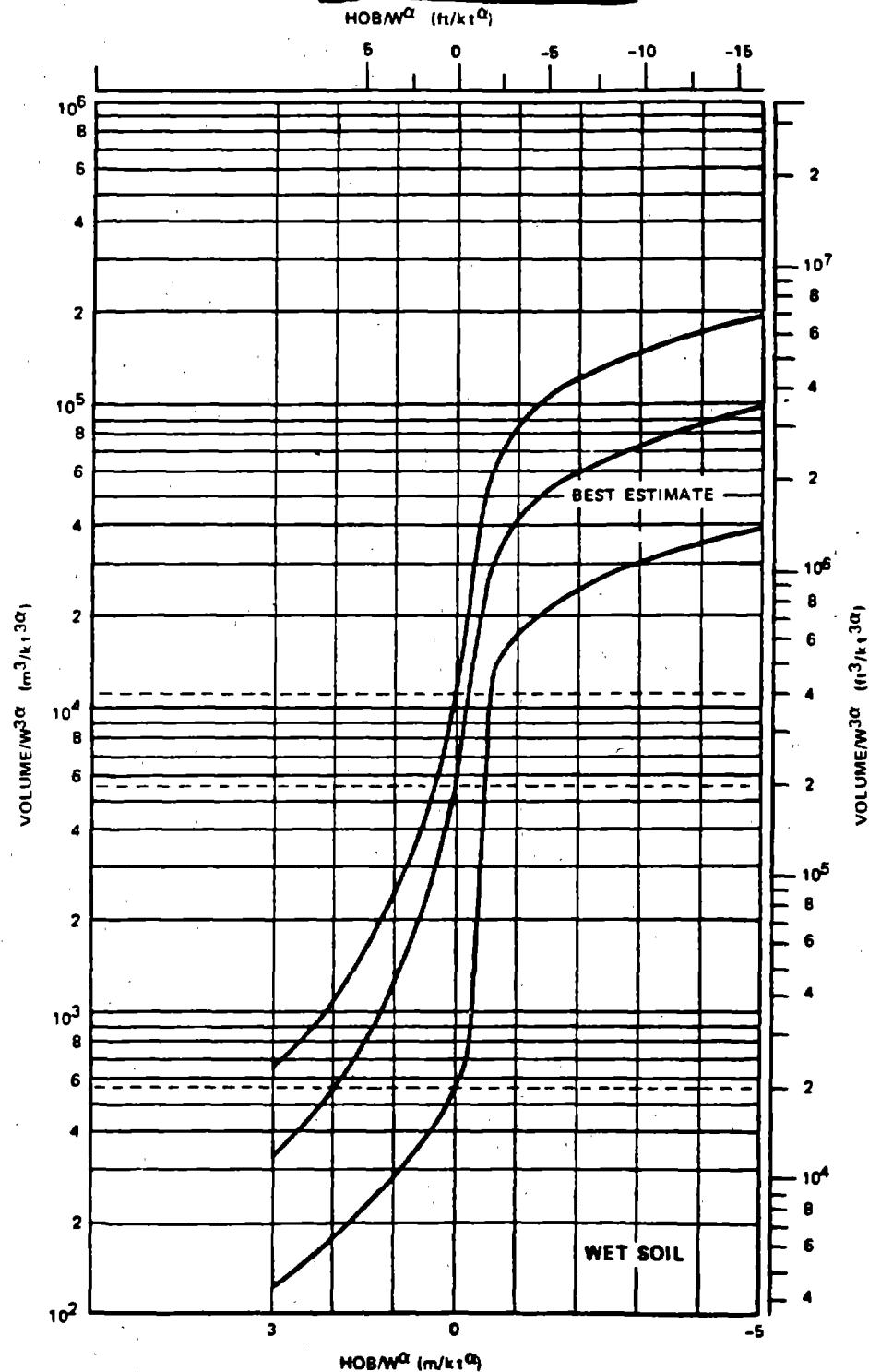
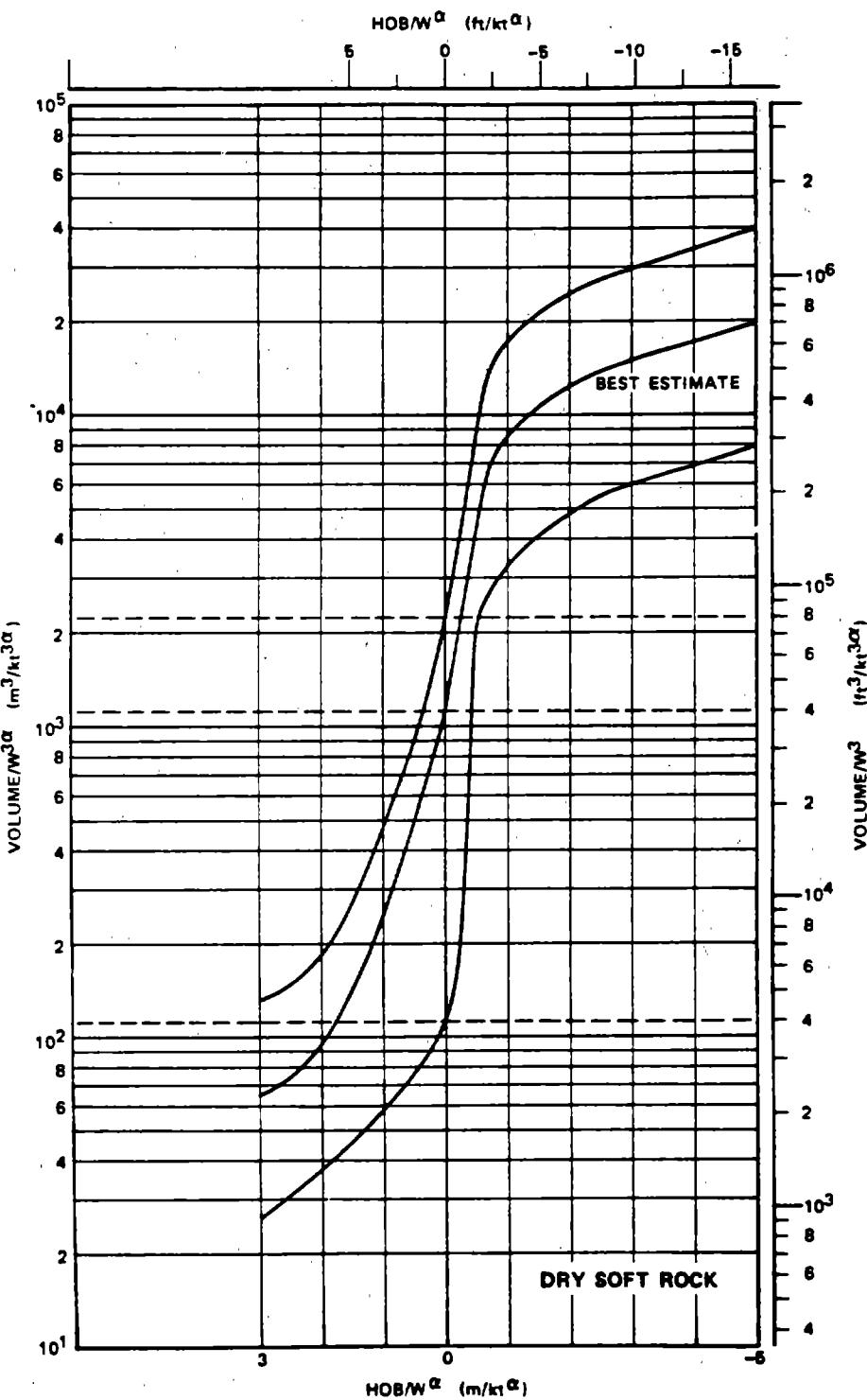
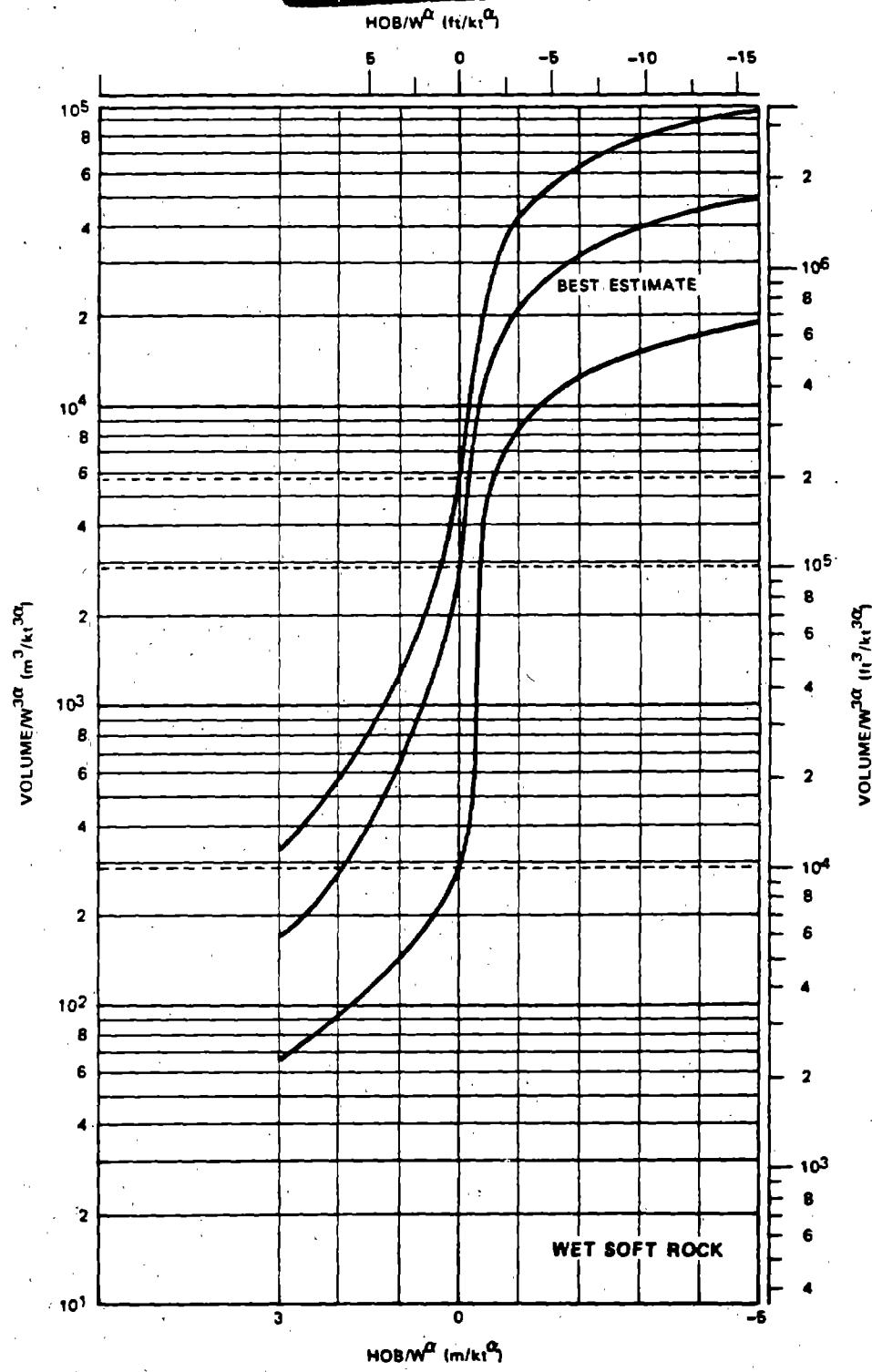


Figure 2-75b. Apparent Crater Volume for a 1 Kiloton Near-Surface Explosion in Wet Soil; Applicable for W > 10 kt



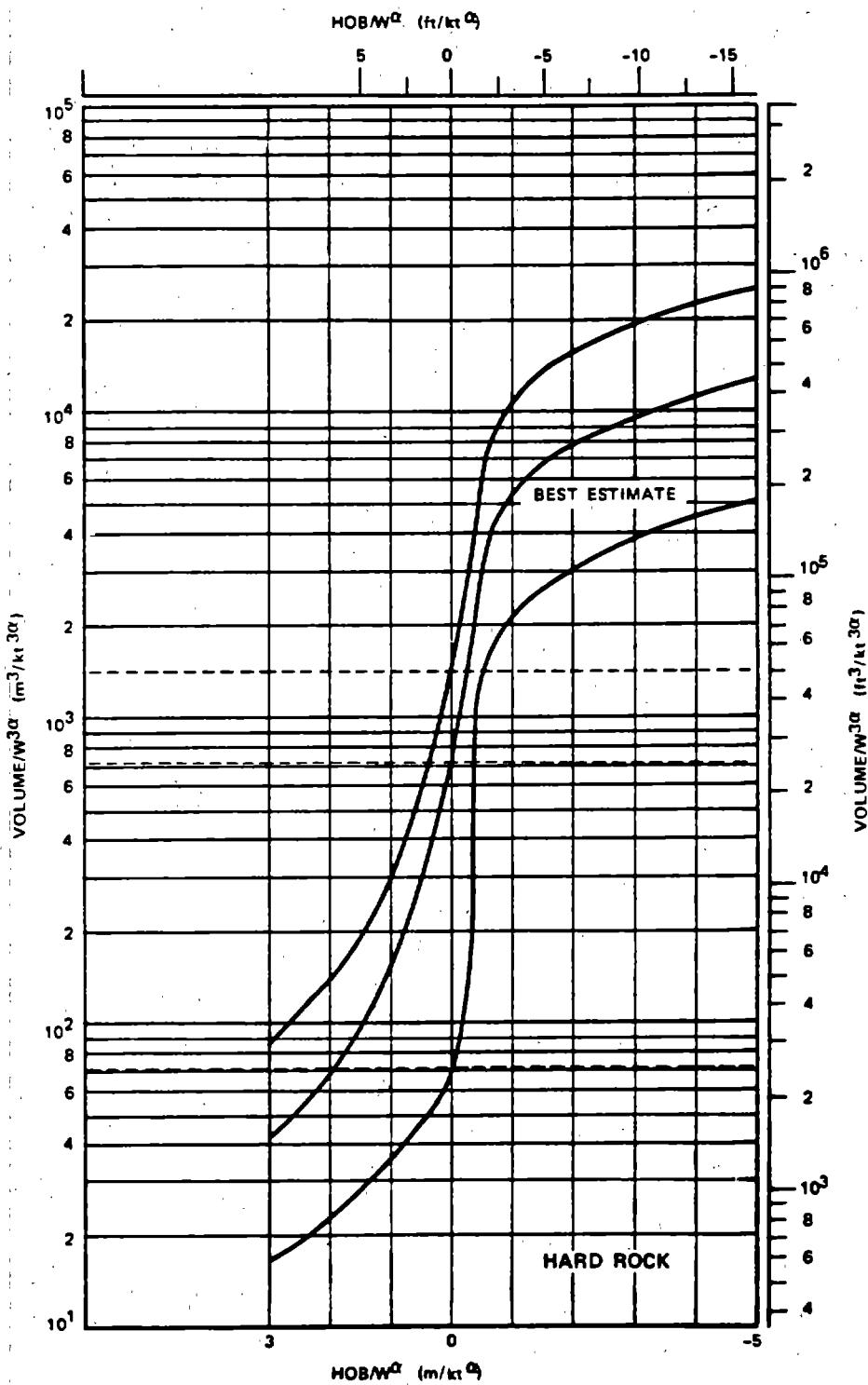
2-170

Figure 2-75c. Apparent Crater Volume for a 1 Kiloton Near-Surface Explosion in Dry Soft Rock; Applicable for W > 10 kt



2-171

Figure 2-75d. Apparent Crater Volume for a 1-Kiloton Near-Surface Explosion in Wet Soft Rock; Applicable for W > 10 kt



2-172

Figure 2-75e. Apparent Crater Volume for a 1 Kiloton Near-Surface Explosion in Hard Rock; Applicable for W > 10 kt

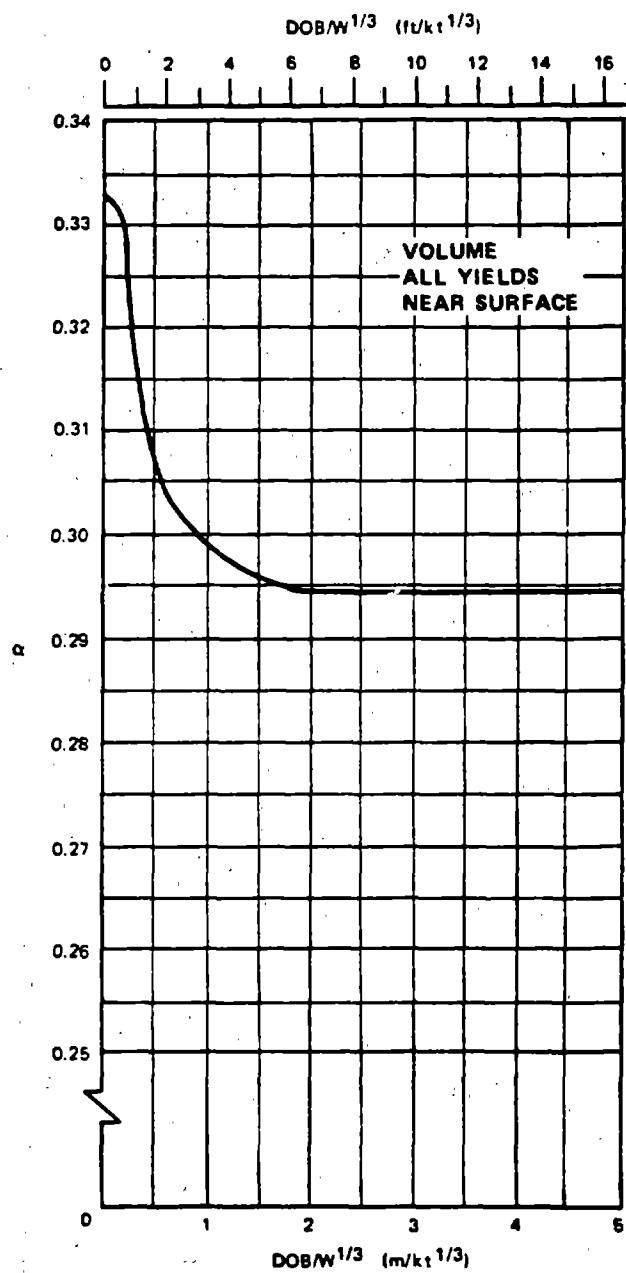
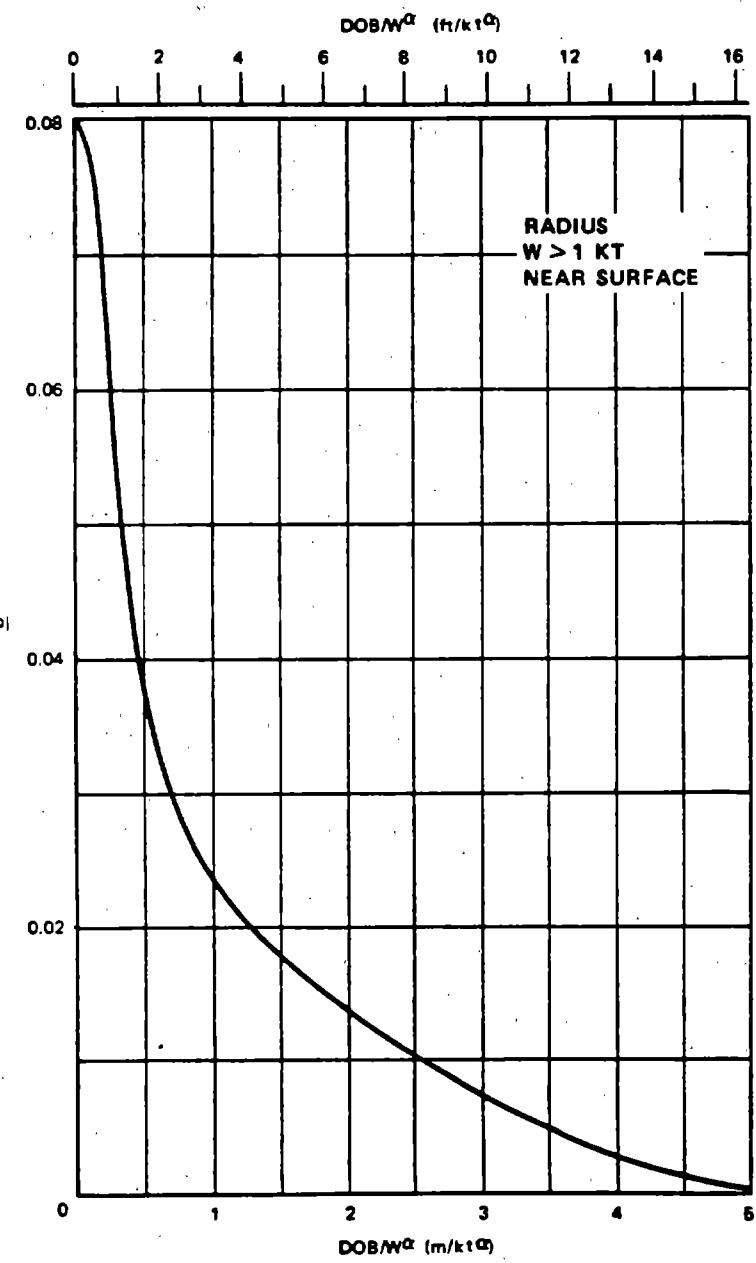


Figure 2-76a. Volume Scaling Exponent,  $\alpha$ , as a Function of Scaled DOB for Near-Surface Explosions, All Yields



2-174

Figure 2-76b. Yield Transition Exponent,  $b$ , for Calculation of the Radius of Near-Surface, Buried Explosions  $W > 1 \text{ kt}$

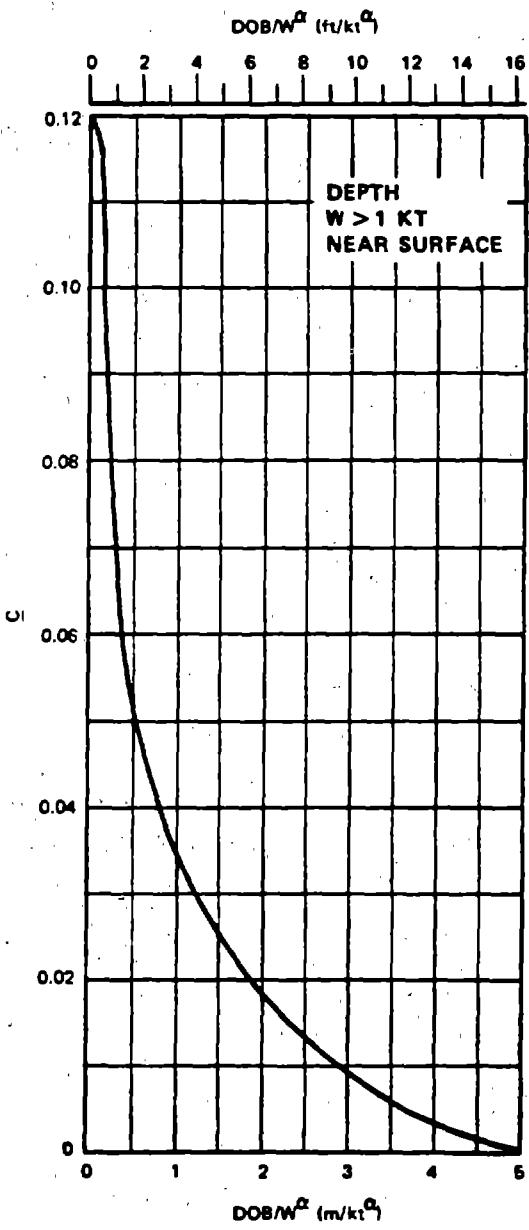


Figure 2-76c. Yield Transition Exponent,  $c$ , for Calculation of the Depth of Near-Surface, Buried Explosions,  $W > 1$  kt

**Problem 2-22. Crater Dimensions for Above-Surface Bursts  
(HOB > 0)**

Figures 2-74a through 2-75e include curves that indicate the apparent crater volume as a function of HOB for a 1 kt explosion in various homogeneous media.

*Scaling:* For yields other than 1 kt, the crater volume scales as follows:

$$V_{al} = W^{3a},$$

where  $V_{al}$  is the apparent crater volume for a 1 kt explosion, and  $V_a$  is the corresponding volume for a yield of  $W$  kt. The height of burst scales as

$$\frac{HOB}{HOB_1} = W^a$$

*Example:*

*Given:* A hypothetical 300 kt contact burst on dry soil.

*Find:* The apparent crater radius and depth.

*Solution:* The HOB for a contact nuclear explosion is 0.5 meters. From paragraph 2-49,

$$a = 0.333$$

for  $HOB \geq 0$ . Therefore,

$$HOB_1 = \frac{HOB}{W^a} = \frac{0.5}{(300)^{1/3}} = 0.075 \text{ m/kt}^{1/3}.$$

From Figure 2-75a, the apparent crater volume for a 1 kt explosion at a scaled HOB of 0.075 m/kt<sup>1/3</sup> in dry soil is

$$V_{al} = 1.25 \times 10^3 \text{ m}^3/\text{kt}^{3a}$$

$$V_a = V_{al} (W)^{3a} = 1.25 \times 10^3 (300)^{1.0} \\ = 3.75 \times 10^5 \text{ m}^3.$$

*Answer:* The dimensions of the crater for a 300 kt contact burst are

$$\frac{R_a}{V_a^{1/3}} = 1.2 W^{0.08} = 1.2 (300)^{0.08} = 1.89,$$

$$R_a = 1.89 (V_a)^{1/3} = 1.89 (3.75 \times 10^5)^{1/3} \\ = 137 \text{ meters},$$

and

$$\frac{D_a}{V_a^{1/3}} = 0.5 W^{-0.12} = 0.5 (300)^{-0.12} = 0.252,$$

$$D_a = 0.252 (V_a)^{1/3} = 0.252 (3.75 \times 10^5)^{1/3} \\ = 18.2 \text{ meters.}$$

*Uncertainty.* The dimensions of the apparent crater obtained for the above problem have a range of uncertainties that are defined by the following:

$$1.1 W^{0.08} \leq \frac{R_a}{V_a^{1/3}} \leq 1.4 W^{0.08}$$

$$125 \leq R_a \leq 159 \text{ meters,}$$

and

$$0.35 W^{-0.12} \leq \frac{D_a}{V_a^{1/3}} \leq 0.7 W^{-0.12}$$

$$13 \leq D_a \leq 25 \text{ meters.}$$

The characteristics of the medium represent a major uncertainty in the crater data presented in Figure 2-74a through 2-75e. Details concerning material properties and geologic structure are not usually known about any particular site, but, in many cases small changes in these media characteristics can cause large changes in crater dimensions. The largest changes usually occur in the presence of an intersecting water table or a layered medium. Therefore, the range of uncertainty for a generic geology such as "wet soil" can be quite large, especially in the prediction of the apparent crater depth.

*Related Material:* See paragraphs 2-46 through 2-50; see also paragraphs 1-14 and 1-33.

### Problem 2-23. Crater Dimensions for a Shallow Buried Burst

Figures 2-74a through 2-75e include curves that indicate the apparent crater volume as a function of HOB for 1 kt explosion in various homogeneous media.

*Scaling:* For yields other than 1 kt, the crater volume scales as follows:

$$\frac{V_a}{V_{a1}} = W^{3a}$$

where  $V_{a1}$  is the apparent crater volume for a 1 kt explosion, and  $V_a$  is the corresponding volume for a yield of  $W$  kt. The height of burst scales as

$$\frac{\text{HOB}}{\text{HOB}_1} = W^a$$

*Example:*

*Given:* A hypothetical 30 kt burst in wet soft rock at a depth of burial of 3 meters.

*Find:* The apparent crater radius and depth.

*Solution:* The value of  $a$  is obtained from Figure 2-76a, which must be entered with the scaled DOB.

The scaled DOB is

$$\frac{\text{DOB}}{W^{1/3}} = \frac{3}{(30)^{1/3}} = 0.965 \text{ m/kt}^{1/3}$$

From Figure 2-76a,

$$a = 0.299$$

The scaled HOB is

$$\text{HOB}_1 = \frac{\text{HOB}}{W^a} = \frac{-3}{(30)^{0.299}} = -1.09 \text{ m/kt}^a$$

From Figure 2-75d., the apparent crater volume for a 1 kt explosion, at  $\text{HOB} = -1.09 \text{ m/kt}^a$  in wet soft rock, is,

$$V_{a1} = 2.20 \times 10^4 \text{ m}^3/\text{kt}^{3a}$$

and

$$\begin{aligned} V_a &= V_{a1} (W)^{3a} = 2.20 \times 10^4 (30)^{0.897} \\ &= 4.65 \times 10^5 \text{ m}^3 \end{aligned}$$

The dimensions for the 30 kt explosion are determined from the following expressions:

$$\frac{R_a}{V_{a1}^{1/3}} = 1.2 W^b$$

$$\frac{D_a}{V_{a1}^{1/3}} = 0.5 W^c$$

From Figures 2-76b and 2-76c the values of the yield transition exponents,  $b$  and  $c$ , at a scaled DOB of 1.09 m/kt<sup>a</sup> ( $\text{HOB} = -1.09 \text{ m/kt}^a$ ) are:

$$b = 0.023$$

$$c = 0.033$$

*Answer:* The dimensions of the crater for a 30 kt explosion at a DOB of 3 meters are:

$$\frac{R_a}{V_{a1}^{1/3}} = 1.2 W^{0.023} = 1.2 (30)^{0.023} = 1.30$$

$$R_a = 1.30 (4.65 \times 10^5)^{1/3} = 101 \text{ meters}$$

and

$$\frac{D_a}{V_{a1}^{1/3}} = 0.5 W^{-0.033} = 0.5 (30)^{-0.033} = 0.447$$

$$D_a = 0.447 (4.65 \times 10^5)^{1/3} = 34.6 \text{ meters}$$

*Uncertainty.* The ranges of uncertainty for the radius and the depth are

$$1.1 W^{0.023} \leq \frac{R_a}{V_{a1}^{1/3}} \leq 1.4 W^{0.023}$$

$$92 \leq R_a \leq 117 \text{ meters}$$

and

$$0.35 W^{-0.033} \leq \frac{D_a}{V_{a1}^{1/3}} \leq 0.7 W^{-0.033}$$

$$24 \leq D_a \leq 49 \text{ meters}$$

*Related Material:* See paragraphs 2-46 through 2-50; see also paragraphs 1-14 and 1-33.

\*This could be written  $\text{DOB}_1 = \frac{\text{DOB}}{W^a} = \frac{3}{(30)^{0.299}} = 1.09 \text{ m/kt}^a$ , i.e.,  $\text{HOB} = -1.09$  is equivalent to  $\text{DOB} = 1.09$ .

### Problem 2-24. Crater Dimensions for a Low Yield Near-Surface Explosion

Figures 2-74a through 2-75e include curves that indicate the apparent crater volume as a function of HOB for 1 kt explosion in various homogeneous media.

*Scaling.* For yields other than 1 kt, the crater volume scales as follows

$$\frac{V_a}{V_{a1}} = W^{3\alpha},$$

where  $V_{a1}$  is the apparent crater volume for a 1 kt explosion, and  $V_a$  is the corresponding volume for a yield of  $W$  kt. The height of burst scales as

$$\frac{\text{HOB}}{\text{HOB}_1} = W^{\alpha}.$$

*Example:*

*Given:* A hypothetical 3 kt burst over wet soil at a height of burst of 1 meter.

*Find:* The apparent crater radius and depth.

*Solution:* From paragraph 2-49,

$$\text{HOB}_1 = \frac{\text{HOB}}{W^{\alpha}} = \frac{1.0}{(3)^{1/3}} = 0.693 \text{ m/kt}^{1/3}.$$

The apparent crater volume for a 3 kt burst will be determined by interpolating between the best estimate values from Figures 2-74b and 2-75b.

$$V_a(3) = 0.6 V_{a1}(W \leq 1) + 0.4 V_{a1}(W > 10).$$

From Figure 2-74b, the apparent crater volume for a 1-kt explosion (for  $W \leq 1$ ), at a scaled HOB = 0.693 m/kt<sup>1/3</sup>, in wet soil is

$$V_{a1} = 7.00 \times 10^3 \text{ m}^3/\text{kt}^{3\alpha},$$

and

$$V_a(W \leq 1) = V_{a1}(W)^{3\alpha} = 7.00 \times 10^3 (3)^{1.0} = 2.10 \times 10^4 \text{ m}^3.$$

From Figure 2-75b, the apparent crater volume for a 1 kt explosion ( $W > 10$ ), at a scaled HOB = 0.693 m/kt<sup>1/3</sup>, in wet soil is

$$V_{a1} = 1.80 \times 10^3 \text{ m}^3/\text{kt}^{3\alpha},$$

and

$$V_a(W > 10) = V_{a1}(W)^{3\alpha} = 1.80 \times 10^3 (3)^{1.0} = 5.40 \times 10^3 \text{ m}^3.$$

Therefore, for a 3 kt burst

$$V_a = 0.6 (2.10 \times 10^4) + 0.4 (5.40 \times 10^3) = 1.48 \times 10^4 \text{ m}^3.$$

*Answer:* The apparent crater dimensions for a 3 kt explosion with HOB of 1 meter are:

$$\frac{R_a}{V_a^{1/3}} = 1.2 W^{0.08} = 1.2 (3)^{0.08} = 1.31,$$

$$R_a = 1.31 (V_a)^{1/3} = 32.2 \text{ meters},$$

and

$$\frac{D_a}{V_a^{1/3}} = 0.5 W^{-0.12} = 0.5 (3)^{-0.12} = 0.438,$$

$$D_a = 0.438 (V_a)^{1/3} = 10.8 \text{ meters.}$$

*Uncertainty.* The dimensions of the apparent crater obtained for the above problem have a range of uncertainty that is defined by the following:

$$1.1 W^{0.08} \leq \frac{R_a}{V_a^{1/3}} \leq 1.4 W^{0.08}$$

$$29 \leq R_a \leq 38 \text{ meters}$$

and

$$0.35 W^{-0.12} \leq \frac{D_a}{V_a^{1/3}} \leq 0.7 W^{-0.12}$$

$$8 \leq D_a \leq 15 \text{ meters.}$$

If the 3 kt weapon in the preceding example were known to have a high radiative output, similar to weapons of larger yield (10 kt), then the best estimate for the apparent crater volume would be found using only Figure 2-75b. Therefore,  $V_a$  would be given by

$$V_a = 5.40 \times 10^3 \text{ m}^3,$$

and

$$R_a = 1.31 (V_a)^{1/3} = 23.0 \text{ meters},$$

$$D_a = 0.438 (V_a)^{1/3} = 7.7 \text{ meters}$$

*Related Material:* See paragraphs 2-46 through 2-50; see also paragraphs 1-14 and 1-33.

## SUMMARY OF PROCEDURES FOR CALCULATING CRATERS FROM DEEP-BURIED BURSTS ( $DOB/W^{1/3} > 5 \text{ m}/\text{kt}^{1/3}$ )

Figures 2-77 through 2-81, together with appropriate scaling laws may be used to obtain crater volumes from deep-buried bursts in a variety of situations. The following summary provides a step-by-step procedure for obtaining such information. An example problem is provided immediately following the figures.

Required (either given or estimated):

Yield ( $W$ ) in kt

Actual DOB

Soil Type (one of the five generic types or a combination; see Figures 2-82 and 2-86b).

Yield-scaling parameters,  $a$ , for burst position:

$$DOB/W^{1/3} > 5 \text{ m}/\text{kt}^{1/3} \rightarrow a = 1/3.4$$

1. Compute DOB<sub>1</sub>

$$(DOB \text{ for } 1 \text{ kt}) = \frac{\text{Actual DOB}}{W^a}$$

2. Determine  $V_{al}$  (apparent-crater volume for 1 kt), using curve for given soil type from Figures 2-77 to 2-81.

3. Compute  $V_a$  (actual crater volume for yield other than 1 kt):

$$V_a (\text{actual volume}) = V_{al} (W^{3a}).$$

Three curves are provided for each soil type: best estimate, upper bound, and lower bound. Using the following guidelines, select the curve most appropriate to the problem.

a. Use *best estimate*  $V_{al}$  if no specific geologic data are given. If actual HE test are available for specific site, compare them with the HE curves in Figure 2-82, and move toward the upper or lower bound HE curve to adjust for these data, depending on where the data are grouped.

b. Use *lower-bound*  $V_{al}$  (if desirable) for target-oriented calculations (offensive-conservative) and to calculate  $R_a$  or  $D_a$ . Consider *lower-bound*  $V_{al}$  for targeting when calculating crater-volume-related phenomena such as ejecta, transient velocity, or displacement.\*

c. Use *upper-bound*  $V_{al}$  (if desirable) for design-oriented calculations (defense-conservative) and to calculate  $R_a$  or  $D_a$ . Consider *upper-bound*  $V_{al}$  for design when calculating crater-related phenomena affected by volume.

4. Calculate  $R_a$  and  $D_a$  using the following expressions:

$$R_a = 1.2 V_a^{1/3}$$

$$D_a = 0.5 V_a^{1/3}$$

The dimensions  $R_a$ ,  $D_a$ , and  $V_a$  can be related to other pertinent crater dimensions as follows:

- The radius to the crest of the apparent-crater lip is

$$R_{al} = 1.25 R_a.$$

- The height of the apparent lip is

$$0.20 D_a \leq H_{al} \leq 0.25 D_a$$

for deep-buried bursts.

Variations in the thickness of the ejecta as a function of range from the surface ground zero (SGZ) are discussed in paragraphs 2-52 and 2-53.

---

\*In all instances it is recommended that upper and lower bound values be calculated in order to gain an appreciation of the effects of uncertainties on the particular problem under consideration.

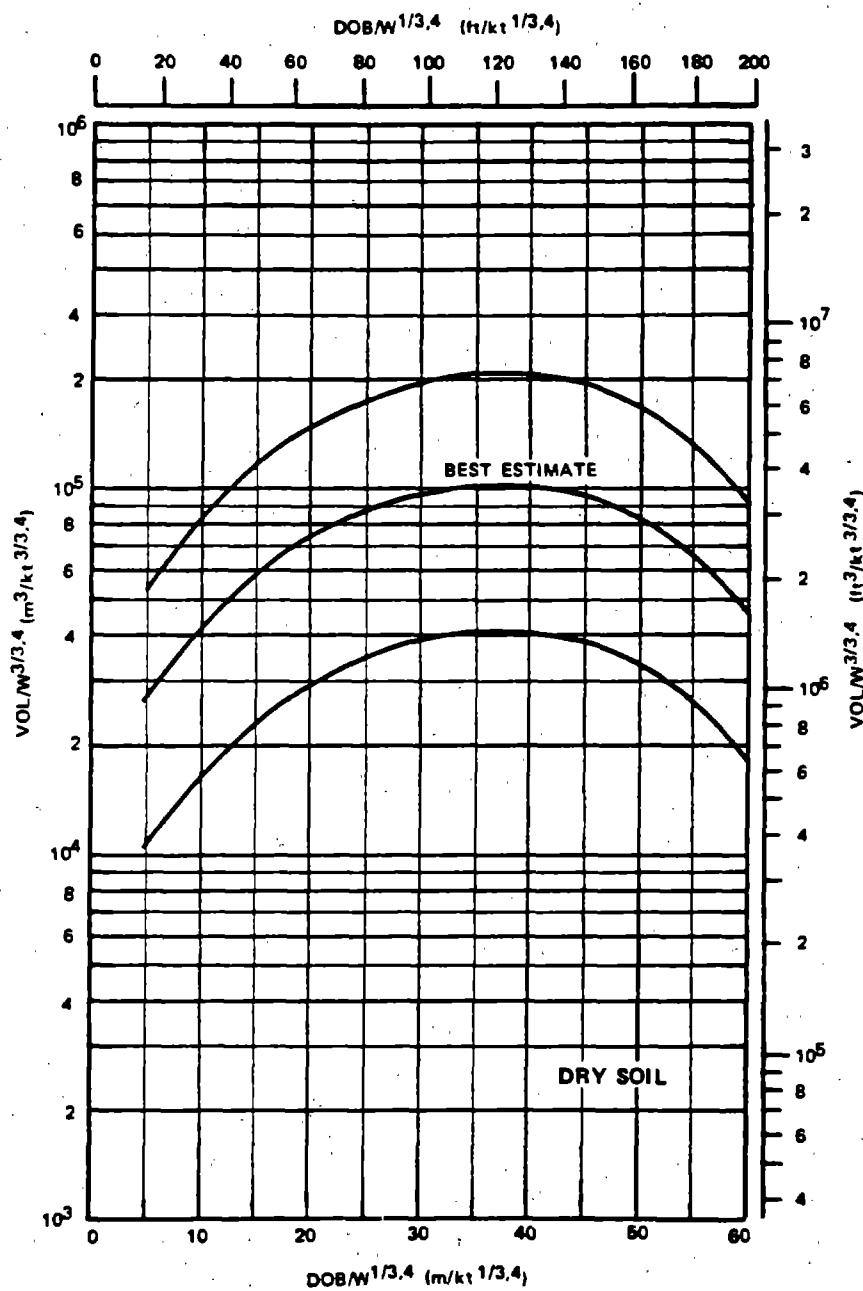


Figure 2-77. Crater Volume as a Function of Depth of Burial for a 1 Kiloton Explosion Buried in Dry Soil

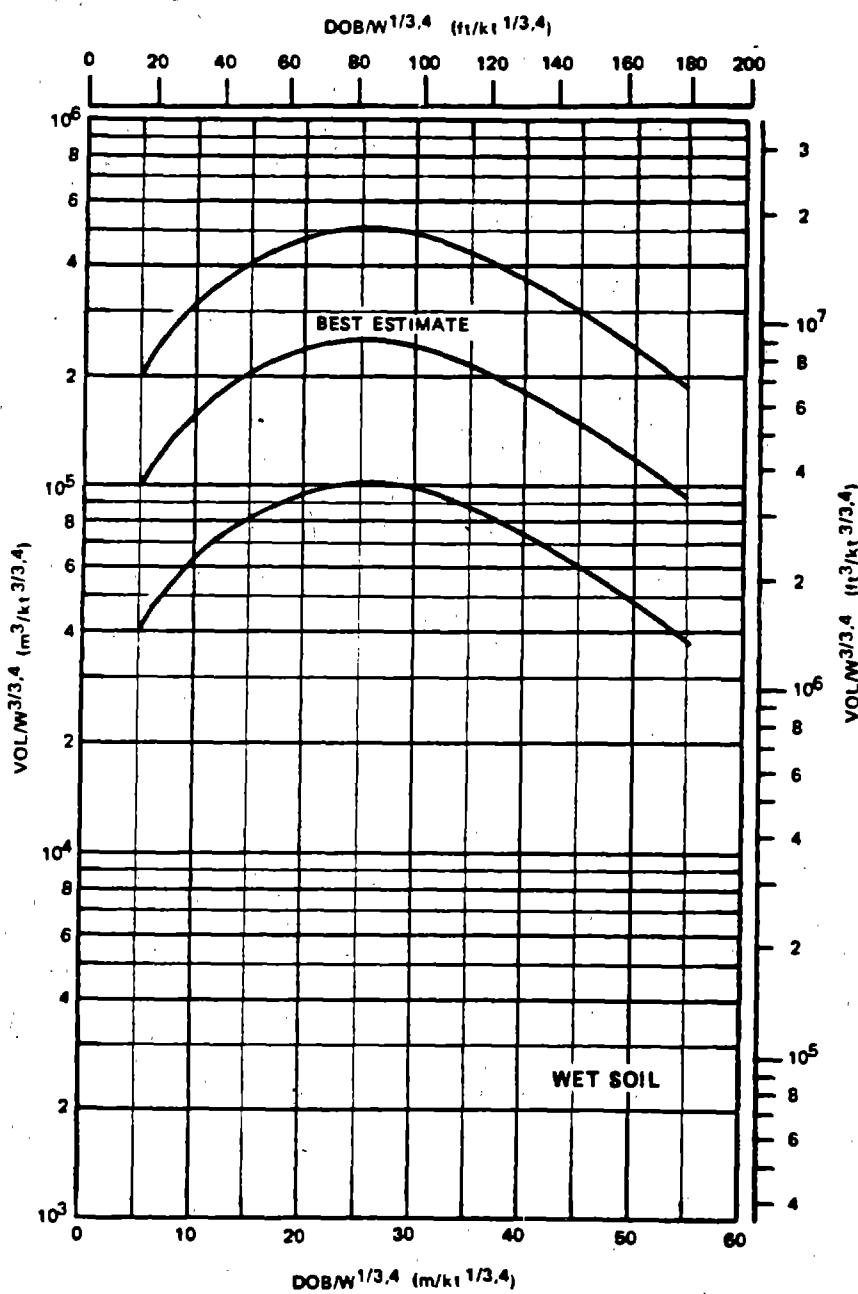


Figure 2-78. Crater Volume as a Function of Depth of Burial for a 1 Kiloton Explosion Buried in Wet Soil

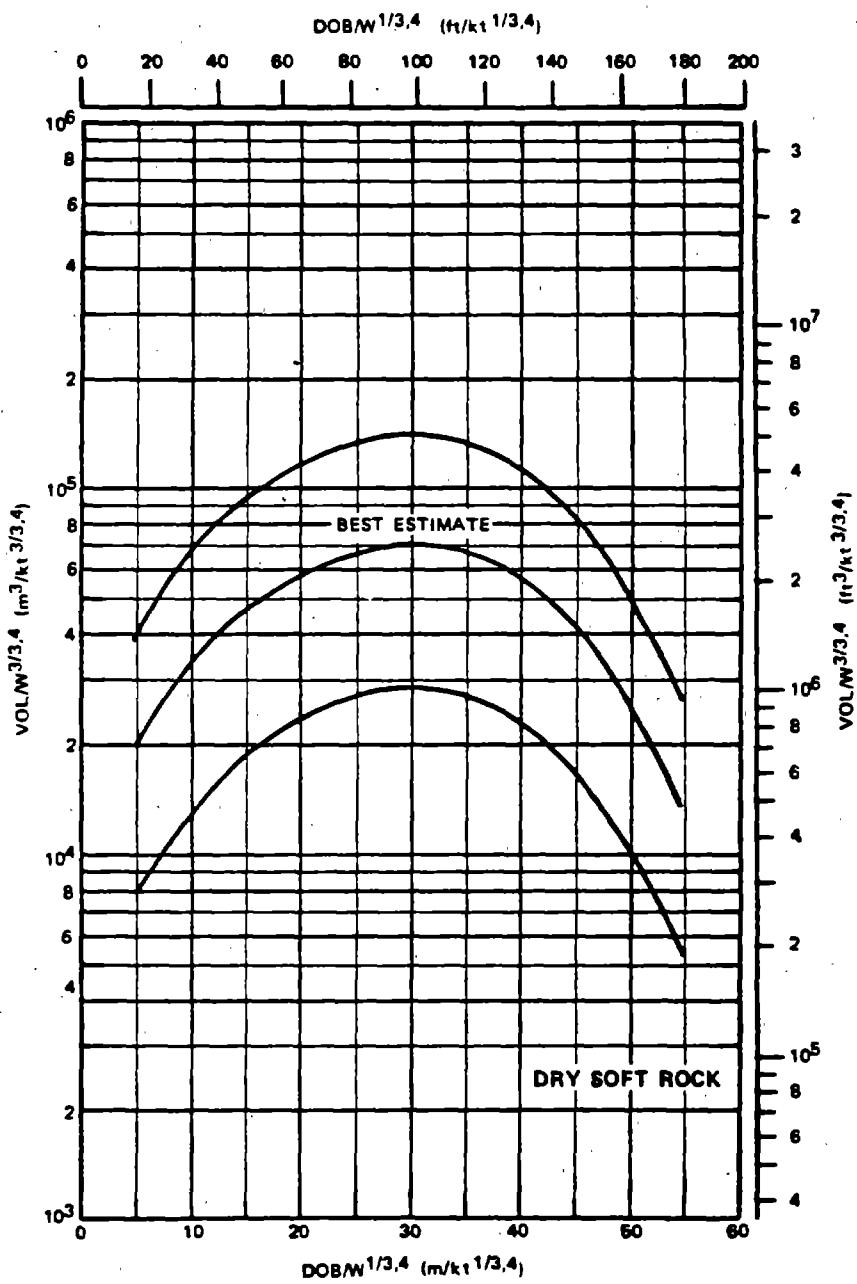


Figure 2-79. Crater Volume as a Function of Depth of Burial for a 1 Kiloton Explosion Buried in Dry Soft Rock

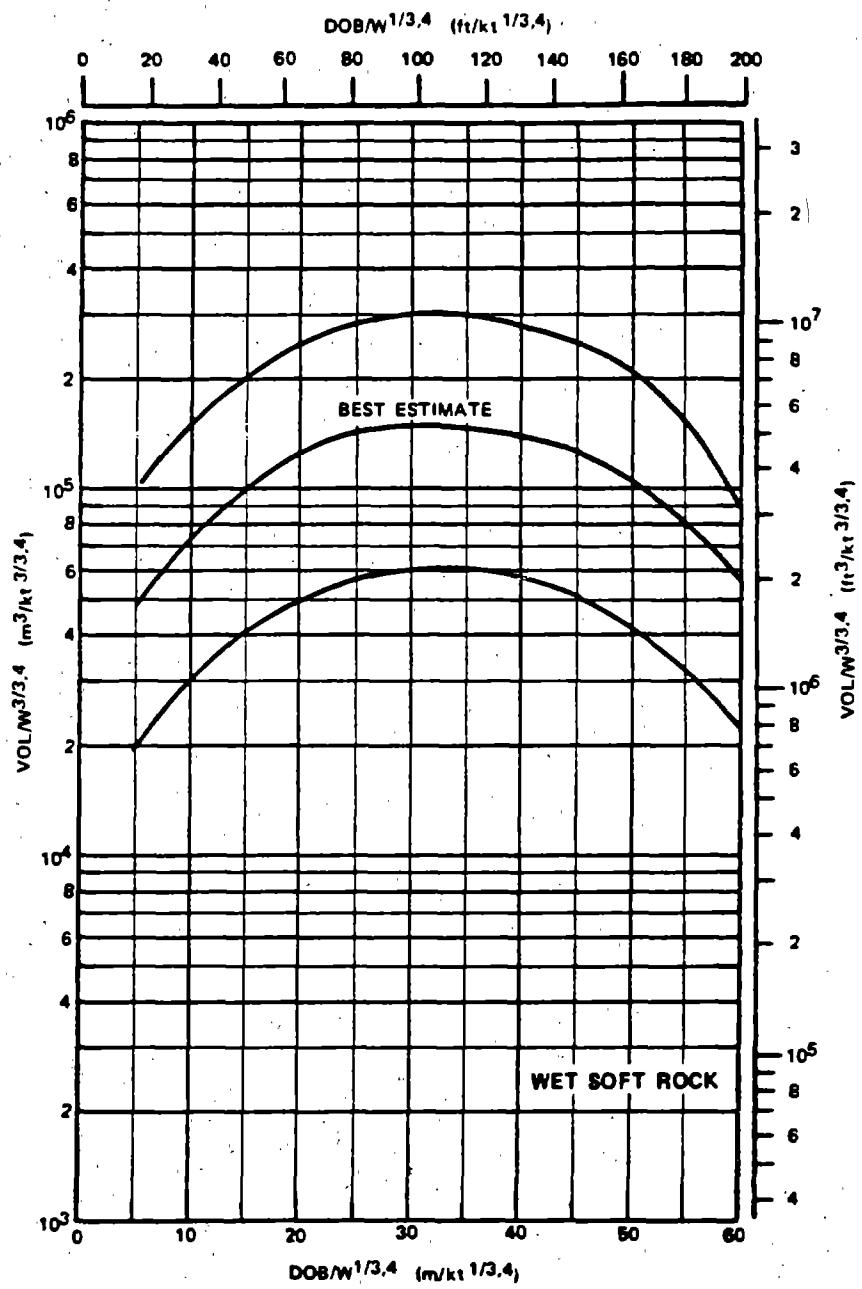


Figure 2-80. Crater Volume as a Function of Depth of Burial for a 1 Kiloton Explosion Buried in Wet Soft Rock

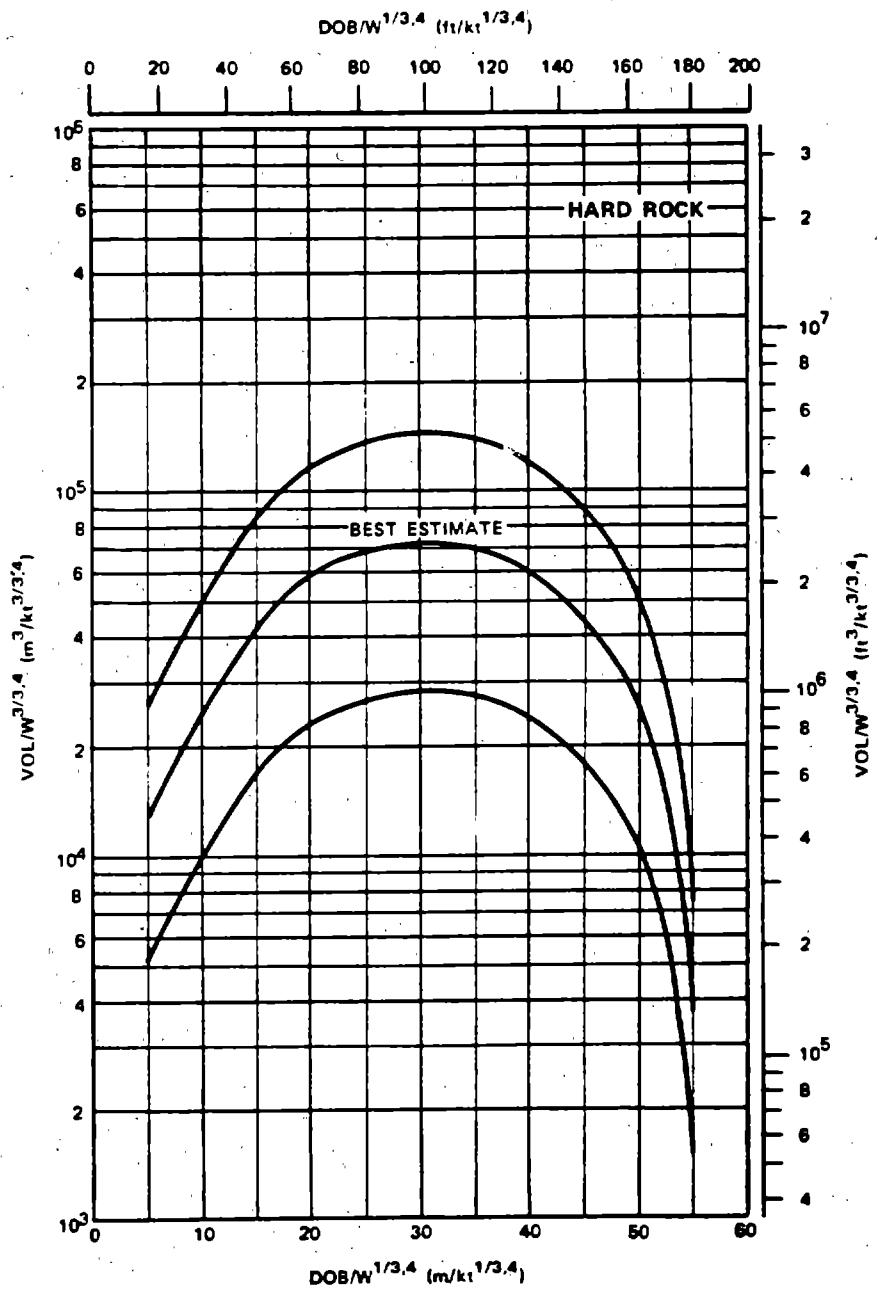


Figure 2-81. Crater Volume as a Function of Depth of Burial for a 1 Kiloton Explosion Buried in Hard Rock

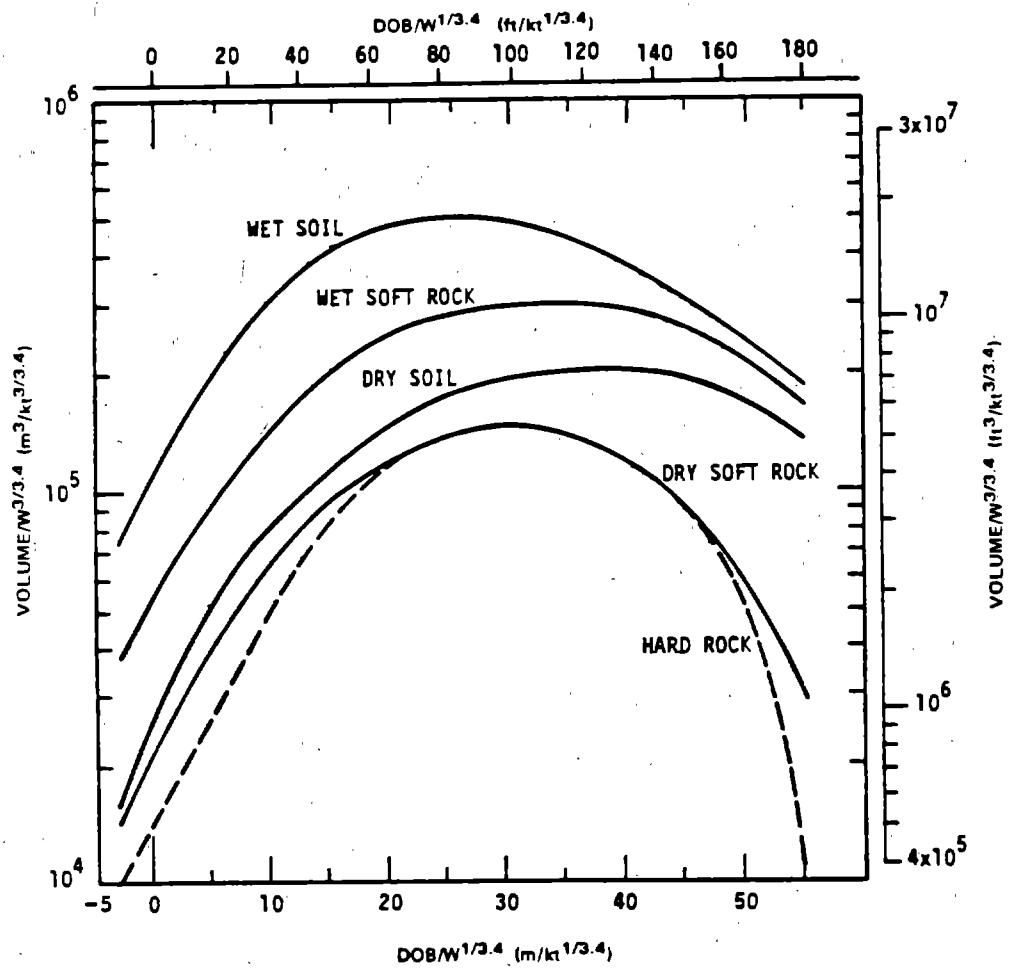


Figure 2-82. Crater Volume as a Function of Depth of Burst for HE Explosions in Five Homogenous Geologies

(This page is intentionally blank)

### Problem 2-25. Calculation of Depth of Burial for Optimum Crater

Figures 2-77 through 2-81 show curves that indicate the apparent crater volume as a function of DOB for a 1 kt explosion in various media which are indicated in each figure.

*Scaling.* For yields other than 1 kt the crater volume and depth of burial scale as

$$\frac{DOB}{DOB_1} = W^{1/3.4},$$

$$\frac{V_a}{V_{a1}} = W^{3/3.4},$$

where  $DOB_1$  and  $V_{a1}$  are the depth of burst and apparent crater volume for a 1 kt explosion, and  $DOB$  and  $V_a$  are the corresponding quantities for a yield of  $W$  kt.

*Example:*

*Given:* A hypothetical 3 kt explosion in hard rock.

*Find:* The depth of burst at which the maximum apparent crater will occur, and the dimensions of the apparent crater at this depth of burst.

*Solution:* From Figure 2-81, the maximum crater volume from a 1 kt explosion in hard rock occurs at a  $DOB_1$  of 30.5 meters (note that the curve is flat in this region, and a variation of a few meters in DOB will have a small effect on  $V$ ). The apparent volume of the crater from such a burst is

$$V_1 = 7.20 \times 10^4 \text{ m}^3.$$

*Answer:* The corresponding depth of burst and crater volume for a 3 kt explosion are

$$DOB = (DOB_1)(W)^{1/3.4} = 30.5 (3)^{1/3.4}$$

$$= 42.1 \text{ meters,}$$

$$V_a = (V_{a1})(W)^{3/3.4} = 7.20 \times 10^4 (3)^{3/3.4}$$

$$= 1.90 \times 10^5 \text{ m}^3.$$

The apparent crater dimensions are defined by the expressions

$$R_a = 1.2 V_a^{1/3} = 1.2 (1.90 \times 10^5)^{1/3}$$

$$= 69.0 \text{ meters,}$$

$$D_a = 0.5 V_a^{1/3} = 0.5 (1.90 \times 10^5)^{1/3}$$

$$= 28.7 \text{ meters.}$$

*Uncertainty:* The dimensions of the apparent crater have a range of uncertainty that is defined by the expressions

$$1.1 V_a^{1/3} \leq R_a \leq 1.4 V_a^{1/3},$$

$$63 \leq R_a \leq 80 \text{ meters,}$$

$$0.35 V_a^{1/3} \leq D_a \leq 0.70 V_a^{1/3},$$

$$20 \leq D_a \leq 40 \text{ meters.}$$

In addition, the uncertainty in crater volume is given by

$$V_a (\min) = V_{a1} (\min) W^{3/3.4},$$

$$V_a (\min) = 2.80 \times 10^4 (3)^{3/3.4},$$

$$= 7.38 \times 10^4 \text{ m}^3,$$

$$V_a (\max) = V_{a1} (\max) W^{3/3.4},$$

$$V_a (\max) = 1.45 \times 10^5 (3)^{3/3.4},$$

$$= 3.82 \times 10^5 \text{ m}^3.$$

*Related Material:* See paragraph 2-51; see also paragraph 1-14 and 1-33.

## EJECTA

Crater ejecta consists of soil or rock debris that is thrown beyond the boundaries of the apparent crater by an explosion. Together with the fallback, which lies between the true and apparent crater boundaries, ejecta comprises all material that is completely dissociated from the parent medium by the explosion. The ejecta field is divided into two zones:

- The crater lip, including the continuous ejecta surrounding the apparent crater.
- The discontinuous ejecta, comprised of the discrete natural missiles that fall beyond the limit of continuous ejecta.

The principal parameters used to describe the ejecta are:

- The average lip crest height.
- The radius to the crest of the crater lip from surface ground zero (SGZ).
- The depth of deposition.
- The ejecta mass density.
- The missile size distribution, which is a function of the azimuthal and radial distance from SGZ, the radius to the outer boundary of continuous ejecta, and the maximum missile range.

The principal variables that control the ejecta parameters are the yield and geometry, and the physical characteristics of the earth medium. Figure 2-83a shows the throwout of ejecta from the SEDAN Event, a 100 kt explosion at a depth of 635 feet.

### 2-52 Ejecta Thickness

The amount and linear extent of the continuously deposited ejecta in the crater lip are determined primarily by the yield. The radial limit of continuous ejecta, which is the outer edge of the lip, will usually vary between 2 and 3 times the apparent crater radius. The lip crest height above the original surface is estimated to be one-fourth

of the apparent crater depth ( $H_{\text{ap}} = 0.25 D_a$ , paragraphs 2-50 and 2-51). The depth of ejecta decreases rapidly in an exponential fashion as the distance from SGZ increases. About 80 to 90 percent of the entire ejecta volume generally is deposited within the area of continuous ejecta. Analysis of data for craters formed by near-surface bursts over soil indicates that ejecta mass represents approximately 55 percent of the apparent crater mass (the remainder being found in fallback, compaction, and the dust cloud, which is blown away). When the same yields explode at successively greater depths, ejecta mass increases significantly until the optimum DOB is reached. Ejecta thickness can be estimated for soil as follows (all dimensions are in feet):

$$t_e = 0.9 V_a^{1.6} R^{-3.86}, \text{ for } R > 2.2 V_a^{1/3}$$

where  $t_e$  is the ejecta thickness,  $V_a$  is the apparent crater volume, and  $R$  is the distance from SGZ to the point of interest. This formula for ejecta thickness assumes that the ejecta mass density will be approximately equal to the original in-situ density of the medium. The equation may be considered valid for a soil medium; however, the bulking, which is inherent in a disturbed rock medium would result in greater ejecta thicknesses than predicted by the formula. Therefore, in a rock medium, the ejecta thickness should be increased by 30 percent to account for the bulking, i.e., the formula for a rock medium is

$$t_e = 1.17 V_a^{1.6} R^{-3.86}, \text{ for } R > 2.2 V_a^{1/3}$$

### 2-53 Maximum Missile Range

Figure 2-83b shows the maximum missile range as a function of depth of burst for a 1 kt explosion in two soil types. These data are based on empirical results from several nuclear explosions.



Figure 2-83a. Throwout of Ejecta from the 100-kt SEDAN Event

2-189

Reproduced from  
best available copy.

### Problem 2-26a. Calculation of Ejecta Thickness

Paragraph 2-52 provides formulas for the prediction of ejecta thickness as a function of distance from surface ground zero and the apparent crater volume ( $V_a$ ).  $V_a$  may be obtained from Figures 2-74a through 2-76c for near surface bursts and 2-77 through 2-81 for deep-buried bursts by the methods described in paragraphs 2-49 through 2-51.

*Example:*

*Given:* A hypothetical 300 kt contact surface burst (center of gravity of the weapon 0.5 meters above the surface) will produce a crater predicted to have an apparent radius of 137 meters, an apparent depth of 18.2 meters and an apparent volume of  $3.75 \times 10^5$  cubic meters in dry soil. (See problem 2-22).

*Find:* The thickness of the ejecta at a distance of 300 meters from SGZ.

*Solution:*

$$R = 300 \text{ meters,}$$

$$2.2V_a^{1/3} = 2.2(3.75 \times 10^5)^{1/3} = 159 \text{ meters}$$

$$R > 2.2V_a^{1/3}$$

Therefore the equation for soil given in paragraph 2-52 applies.

*Answer:* The ejecta thickness is

$$t_e = 0.9V_a^{1.6} R^{-3.86}$$

$$t_e = 0.9 (3.75 \times 10^5)^{1.6} (300)^{-3.86} = \\ 0.20 \text{ meters}$$

*Reliability:* Based on empirical formulas derived from high explosive and nuclear burst. Specific reliability has not been estimated.

*Related Material:* See paragraph 2-49 through 2-52. See also Problem 2-22.

### Problem 2-26b. Calculation of Maximum Missile Range

Figure 2-83b shows the maximum range to which missiles might be expected from a 1 kt explosion as a function of depth of burial in two soil types.

*Scaling.* For yields other than 1 kt, the maximum missile range and depth of burst scale as follows:

$$\frac{R_m}{R_{m1}} = \frac{\text{DOB}}{\text{DOB}_1} = W^{0.3}$$

where  $R_{m1}$  is the maximum missile range for 1 kt,  $\text{DOB}_1$  is the depth of burst for 1 kt, and  $R_m$  and  $\text{DOB}$  are the corresponding range and burial depth for  $W$  kt.

*Example:*

*Given:* A hypothetical 3 kt explosion at a depth of 85 meters in hard rock.

*Find:* The maximum missile range for the explosion.

*Solution:* The corresponding depth of burst for a 1 kt explosion is

$$\text{DOB}_1 = \frac{\text{DOB}}{W^{0.3}} = \frac{85}{(3)^{0.3}} = 61 \text{ meters.}$$

From Figure 2-83b, the maximum missile range for a 1 kt explosion at a depth of 61 meters in hard rock is 440 meters.

*Answer:* The corresponding maximum missile range for a 3 kt explosion at a depth of 85 meters in hard rock is

$$R_m = R_{m1} W^{0.3} = (440) (3)^{0.3} = 612 \text{ meters.}$$

*Reliability:* Based on empirical results from several nuclear explosions, but no specific reliability has been estimated.

*Related Material:* See paragraphs 2-46 through 2-52.

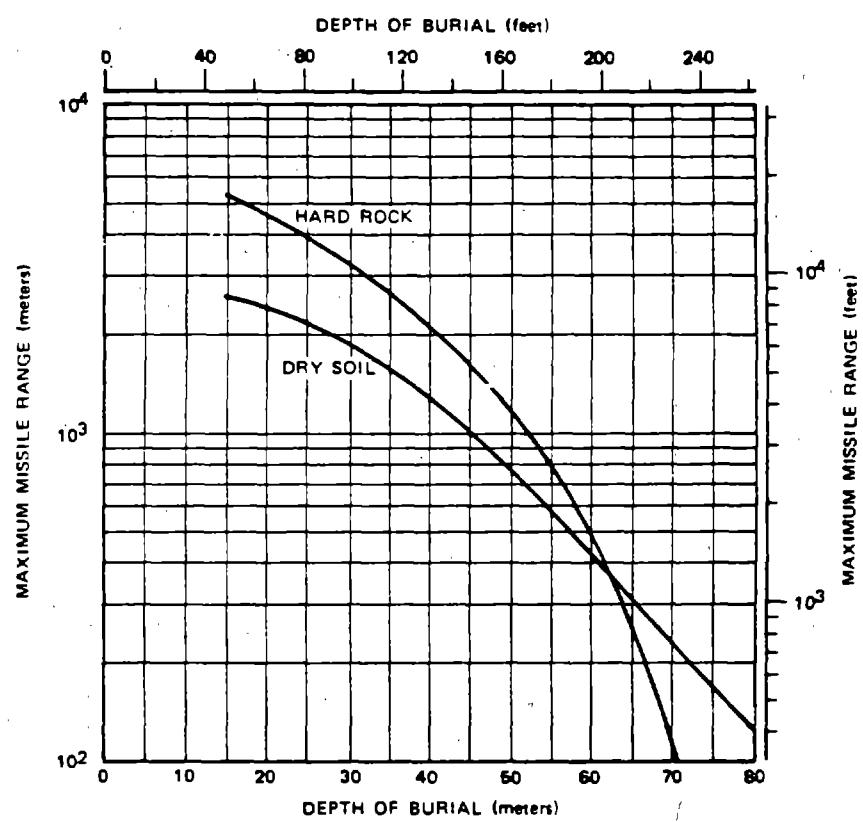


Figure 2-83b. Maximum Missile Range as a Function of Depth of Burial for a 1 kt Explosion

## CHARGE STEMMING

The term charge stemming refers to the backfilling of material in the charge-emplacement hole. Ideally, charges should be completely stemmed and tamped to contain the explosive energy temporarily, which increases its coupling with the medium. Typical stemming materials are concrete, gravel, sand and water. The cratering curves shown in preceding paragraphs provide predictions for fully stemmed charges. There are, however, operational considerations that may require reduced stemming or the capability to emplace or remove the stemming material in a short period of time. Therefore, modified stemming geometries, including various degrees of stemming or no stemming at all, are important considerations in the evaluation of nuclear cratering phenomena.

The following changes in cratering phenomena generally may be expected when less than full stemming is used:

- Air blast and the fraction of radioactive materials that vents will be increased.
- Energy loss out of the emplacement hole will reduce the coupling effectiveness of the explosion. This will result in crater dimensions that are smaller than those from fully stemmed explosions.
- Energy deposited in the emplacement hole will cause a modification to the energy deposition pattern in the medium. The source will appear to be a distorted cylindrical source rather than a concentrated spherical source. Lip height, ejecta distribution, and maximum missile range will vary from those of a fully stemmed explosion.

### 2-54 Guidelines for Assessing the Effect of Stemming

The crater dimensions from a partially stemmed or an unstemmed emplacement hole

will be affected primarily by the amount of stemming, the diameter of the emplacement hole, and the depth of burial. The following are some general conclusions concerning stemming that are based largely on HE experiments.

- The crater radius, which is the dimension of greatest military importance, does not increase significantly with increased stemming.
- Stemming about one-half of the emplacement hole (50% stemming) provides most of the crater depth that would be expected from a fully stemmed charge.
- Water appears to be a very efficient stemming material.

Figures 2-84a, b, and c illustrate the HE experimental results concerning the effect of stemming on crater volume, diameter, and depth, respectively.

## EFFECTS OF GEOLOGICAL FACTORS

In most situations a weapon will *not* be burst in a homogeneous medium such as dry soil or wet soft rock. Instead, typical geologies may contain a water table at a shallow depth, a layering of one type of media over another (e.g., soil over rock), parallel planes of distant jointing in rock, or a steeply sloping ground surface. All of these factors can influence the formation of a crater and, in some cases, can change the size or characteristics of the crater significantly. The following paragraphs describe the general effects of geologic variations on cratering phenomena.

### 2-55 Sloping Topography

Terrain slopes of about five degrees or more will affect the geometry of a crater formed by either a surface or buried explosion. The ejecta distribution will also be affected. If the slope is gentle, the crater volume will be comparable

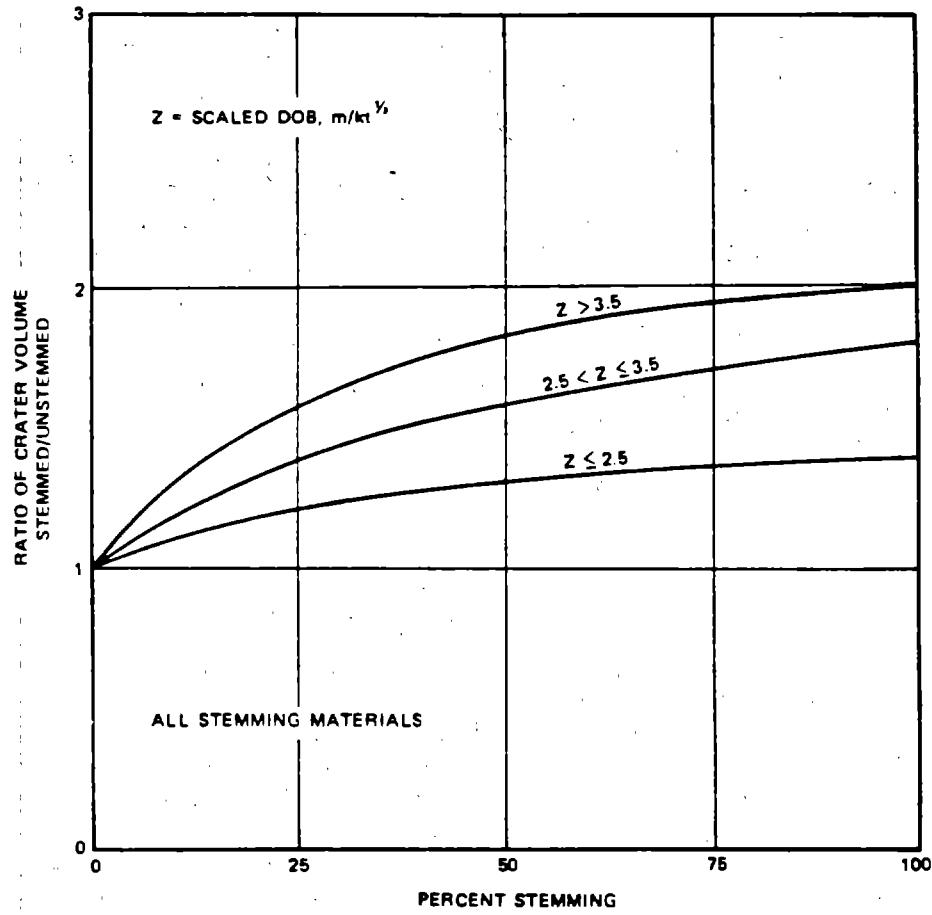


Figure 2-84a. Increase in HE Crater Volume as a Function of Stemming for Various DOBs

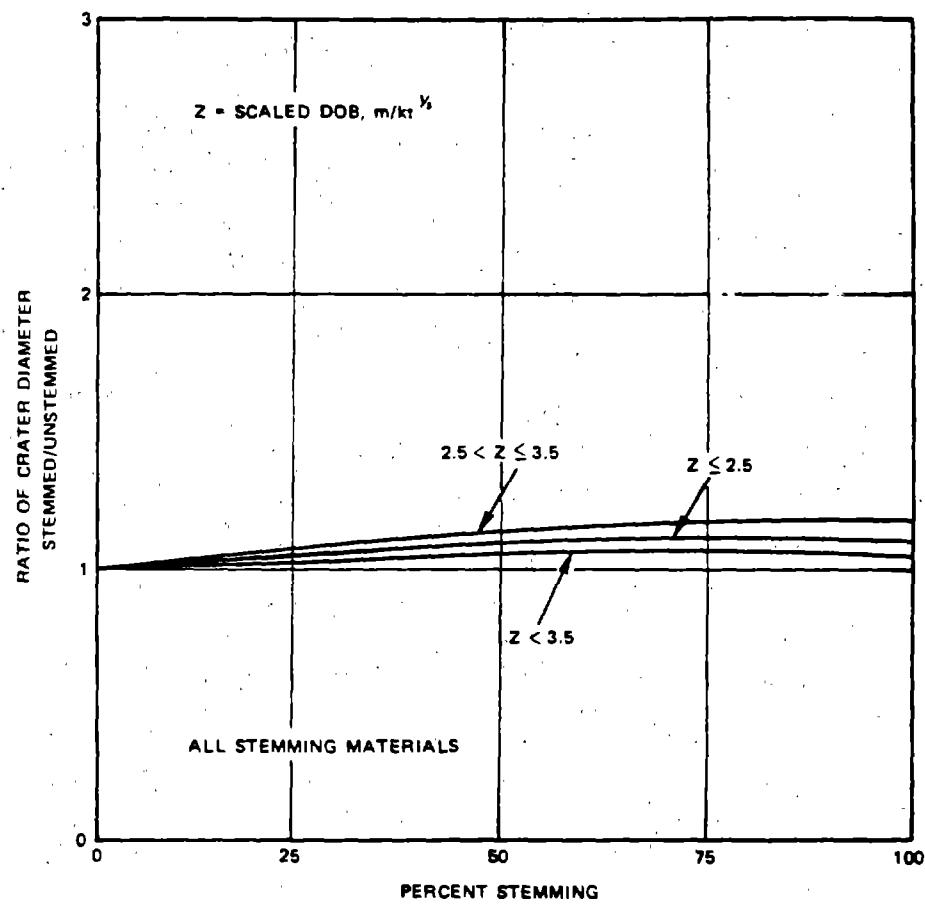


Figure 2-84b. Increase in HE Crater Diameter as a function of Stemming for Various DOBs

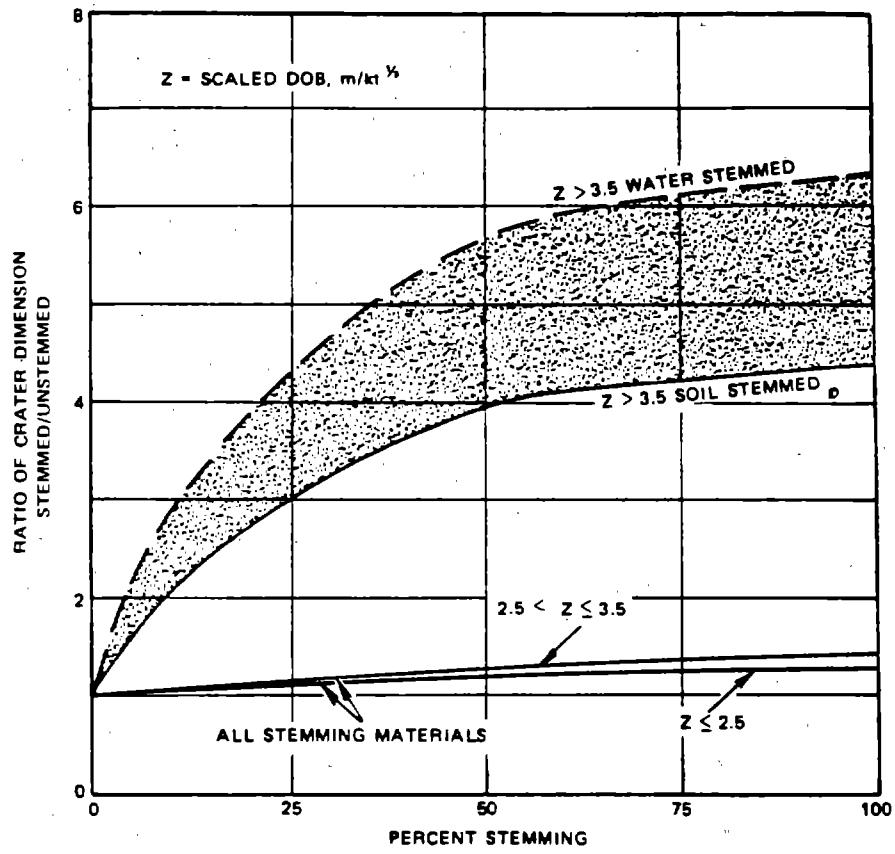


Figure 2-84c. Increase in HE Crater Depth as a Function of Stemming for Various DOBs

with that of craters on level ground, but the resulting crater will be asymmetrical; it will be wider up-slope and will have a larger lip down-slope. Figures 2-85a and b show a photograph and a schematic drawing, respectively, of the crater from a nuclear event buried 30 meters below a 30 degree slope in tuff. The shape of the crater formed by this explosion was influenced by the slope of the surface because almost all the debris formed a rock slide originating at the lower edge of the crater and terminating about 240 meters down the slope.

Limited small-scale cratering experiments have been conducted in moist, sandy soil and in desert alluvium on slopes ranging from 40 degrees to vertical wedges. For charges buried on severe but nonvertical slopes, with DOB measured normal to the sloping surface and with the vertical depth of overburden being greater than containment depth, crater dimensions decrease with increasing slope. Optimum vertical DOB appears larger by about one-third than optimum DOB on level terrain.

## 2-56 Water Tables

A subsurface ground water table in a soil medium will begin to influence the size and shape of the crater when its depth below the surface is equal to or less than three-fourths the predicted apparent crater depth. Its effect is to flatten and widen the crater. Figure 2-86a illustrates the effect of a shallow water table on the shape of the crater. As the water table depth decreases, its effect becomes more evident. Based upon HE experiments, it can be concluded that for a surface detonation, the influence of the water table is not significant for scaled water table depths greater than about  $3.5 \text{ m}/\text{kt}^{1/3}$ , and the apparent radius, volume and lip height increase exponentially as the water table approaches the ground surface. For shallow buried bursts ( $\text{DOB}/W^{1/3} < 3 \text{ m}/\text{kt}^{1/3}$ )

the final crater radius may be as much as 50 percent greater than the predicted value and the depth as little as one-third that of the predicted value.

Figure 2-86b shows a normalization technique that has been developed for plotting crater volume for surface and shallow buried explosions in a layered geology. A shallow water table effectively causes a homogeneous medium to act as a two layered medium

$d$  = depth to water table (thickness of upper layer)

$V_a$  = apparent crater volume

$V_u$  = apparent crater volume predicted in the upper layer alone (usually dry soil)

$V_L$  = apparent crater volume predicted in the lower layer alone (usually wet soil).

The curve fitted to the water table crater volume data in Figure 2-86b is given by the expression

$$\frac{V_a - V_L}{V_u - V_L} = 1 - \exp(-5.4 d/V_a^{1/3}).$$

Iteration is required to solve this expression for  $V_a$ ; however, the technique converges very rapidly. It is recommended that the curve in Figure 2-86b be used to predict crater volume for sites having a shallow water table.

## 2-57 Bedrock

The influence of a bedrock layer below a soil medium is similar to that of a water table, though somewhat less pronounced. For surface explosions it appears that a hard layer may limit the crater depth while causing the crater shape to be more nearly trapezoidal than parabolic or conical (see Figure 2-86c). The bedrock layer may increase the crater radius slightly (5 to 10



Figure 2-85a. NEPTUNE Crater and its Position on Slope of Mesa

2-198

Reproduced from  
best available copy.

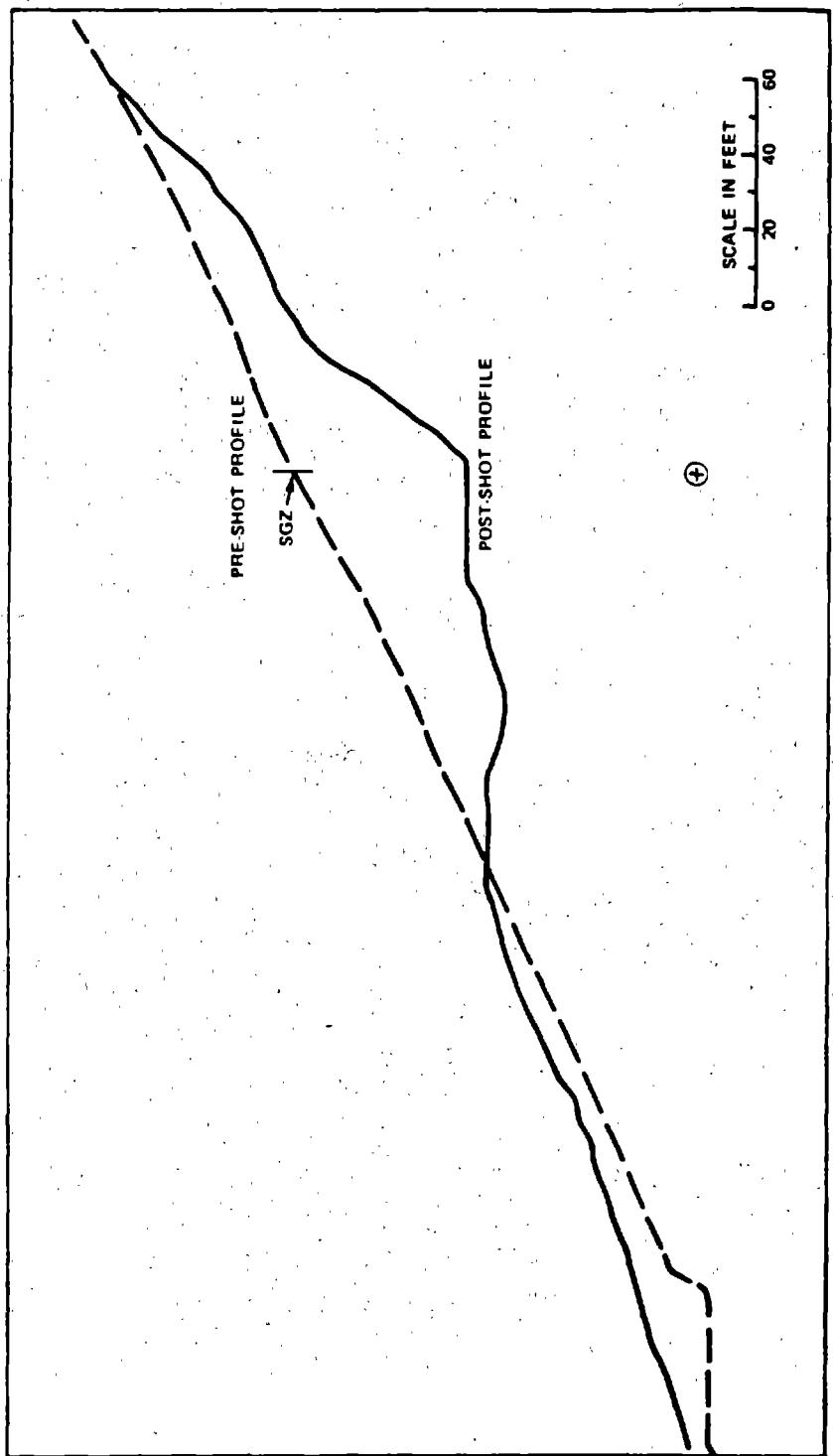


Figure 2-85b. Section of NEPTUNE Crater Normal to Slope Contours



Figure 2-86a. Crater Formed by a Surface Detonation of a 0.5 kt High Explosive Charge In a Wet Soil Medium with a Shallow Water Table (DIAL PACK Event); a 8.2 m (27 ft.) Diameter Sphere with the Bottom Tangent to the Ground:  
 $R_g = 30.48$  m (100 ft.);  $D_g = 4.6$  m (15 ft.)

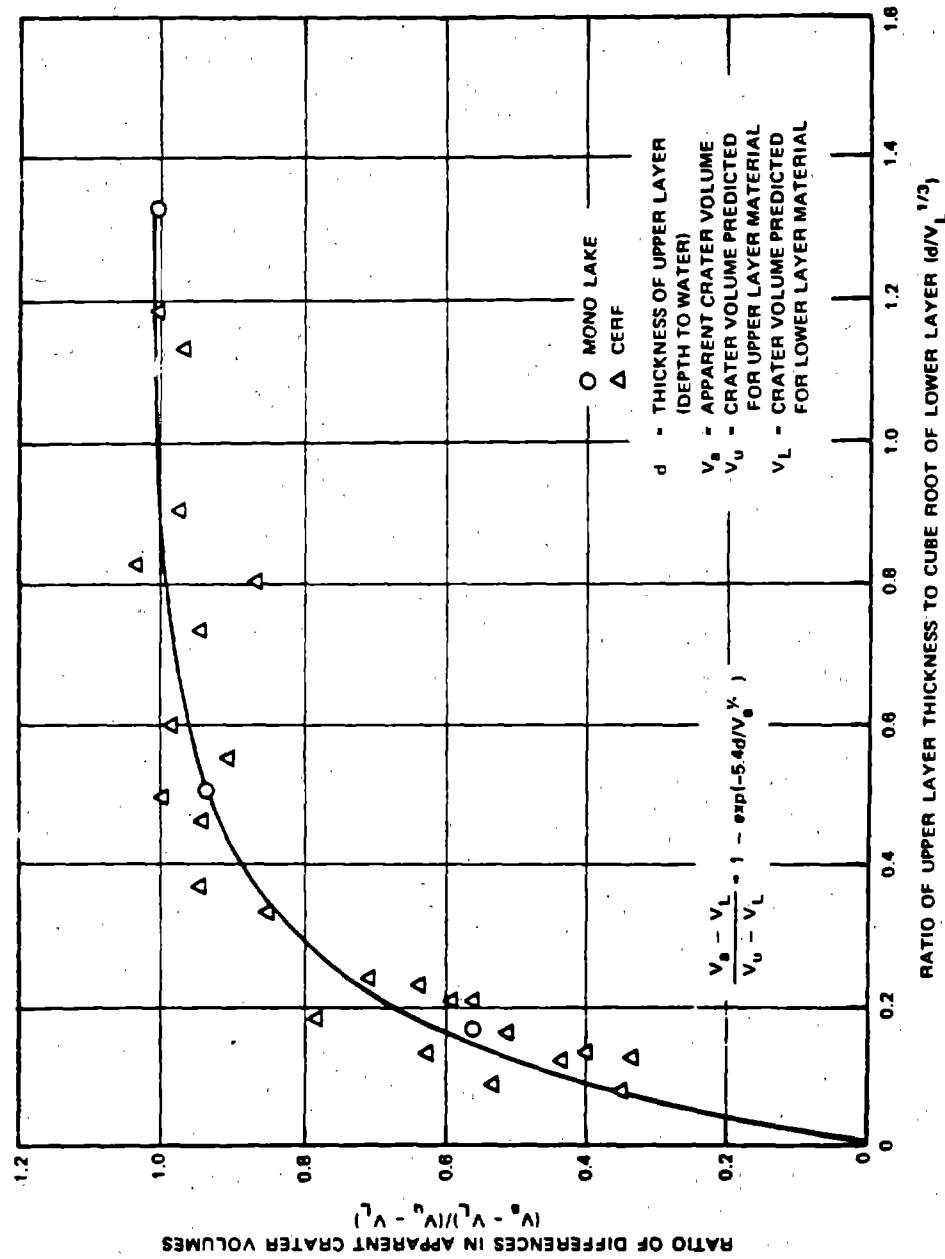


Figure 2-86b. Cratering Data for Dry Soil over Wet Soil

percent). The layer may decrease the final crater depth by as much as one-third when the overburden layer is as shallow as one-fourth the predicted apparent crater depth.

Although the effect of a water table and the effect of a hard layer are different, the water table curve is a good approximation for predicting the crater volume in a layered geology involving a gradual transition to rock. The water table curve should *not* be used for geologies involving a sharp transition to rock.

The two-layer problem can be generalized to three layers. Let  $V_1$ ,  $V_2$ , and  $V_3$  be the crater volume associated with the top, middle, and bottom materials considered separately. Then,  $V_{23}$  is the crater volume associated with the middle layer and bottom layer, and  $V$  is the crater volume in the total layered medium.

$V_{23}$  is calculated by neglecting the top layer and then solving a two-layer problem with  $V_2$  as the upper layer and  $V_3$  as the lower layer. The thickness of the middle layer  $d_2$  is used as the depth to the lower layer. This gives

$$\frac{V_{23} - V_3}{V_2 - V_3} = 1 - \exp(-5.4 d_2 / V_{23}^{1/3})$$

$V$  is then calculated by solving another two-layer problem with  $V_1$  as the upper layer and  $V_{23}$  as the lower layer. The thickness of the upper layer  $d_1$  is used as the depth of the lower layer. This gives

$$\frac{V - V_{23}}{V_1 - V_{23}} = 1 - \exp(-5.4 d_1 / V^{1/3}).$$

## 2-58 Rock Bedding/Jointing

If a low-yield explosion occurs at or very near the surface, the bedding or jointing planes in rock can influence the shape of the crater produced. The direction of the ejection process

will also be affected. The formation of the crater will tend to follow the direction of the predominant joints, and the crater radius will be increased by as much as one-third in the direction parallel to the joints and decreased by as much as one-third in the direction normal to the joints. The magnitude of the crater depth is usually not affected significantly, but the deepest point may be shifted to one side of the crater. As the yield or the DOB is increased, the influence of rock jointing is reduced.

The dip of bedding planes will influence energy propagation, and this will cause the maximum crater depth to be offset in the down-dip direction. Little overall effect is noted on the size of the crater radius, but differences in ejection angles cause the maximum lip height and ejecta radius to occur down-dip.

## 2-59 Snow and Ice

Measured craters in snow or ice are a rarity; however, data for a few craters have been recorded for surface HE explosions. In general, these craters are larger than would be predicted in soil and they are characteristically wide and flat. The trends in crater size and shape for a surface explosion in a snow/ice medium are given by the expressions

$$R_a = 38.8 W^{0.26} \text{ meters}$$

$$D_a = 5.75 W^{0.15} \text{ meters}$$

where  $W$  is the yield in kilotons.

## MULTIPLE BURST GEOMETRIES

Nuclear weapons may be detonated in close proximity to each other to create a linear crater or a series of interconnected craters. When simultaneous explosions are sufficiently close to cause interactions, the shot geometry is termed "multiple burst." A linear array of this nature is referred to as a row crater, as illustrated in Figure 2-87.

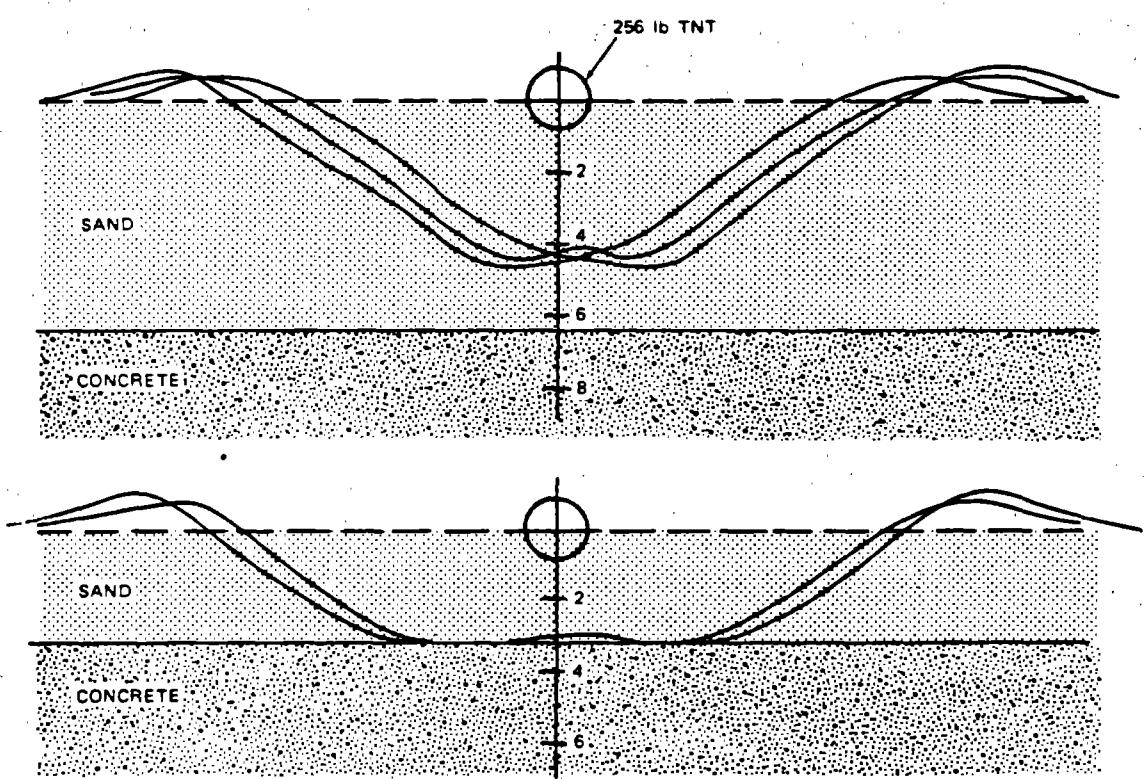


Figure 2-86c. Effects of a Hard Near-Surface Layer on Cratering



Figure 2-87. A Row Crater Produced by Simultaneous Explosions of Five 1.1 kt Nuclear Devices at Optimum DOB (BUGGY Event) in Basalt: DOB = 41 m (135 ft.); Spacing = 45.7 m (150 ft.); Width = 76.2 m (250 ft.); Depth = 19.8 m (65 ft.); Length = 262 m (860 ft.)

In addition to the parameters normally associated with an underground explosion, the results of a row charge also depend upon the spacing between charges ( $s$ ) and the degree of simultaneity of the explosions. Differences of only a few milliseconds in the times of explosion of adjacent charges can result in significantly degraded row charge crater dimensions. Close spacing of weapons (less than 1.4 times a single weapon crater radius) increases both the crater radius and depth compared to single weapon craters at the same scaled DOB. Experience has shown that a spacing of  $1.0 R_a$  (for explosions at optimum DOB) results in a smooth channel with crater depth and radius approximately 20 percent greater than those of single explosions. A spacing of  $1.25 R_a$  will still form a smooth channel, but with less enhancement of crater dimensions, while spacing of  $1.5 R_a$  will provide an adequate linear obstacle. The length of a row

crater  $L$  can be found in the equation:

$$L = s(n - 1) + 2 R_a,$$

where  $n$  is the number of charges in the row, and  $s$  is the spacing between charges.

### SECTION III

#### GROUND SHOCK PHENOMENA

##### 2-60 General Nature of Free-Field Effects

The position of the weapon at the time of detonation has a marked influence on the amount and nature of the energy transfer into the ground. The effects at depths below the surface from a high air burst will be primarily of the air-induced type. For surface or near surface bursts, both air-induced and direct-transmitted ground shock effects are produced, and both may be of importance. Deep underground bursts cause direct-transmitted effects almost exclusively.

The nuclear field tests of the past several decades involving air, surface, and fully contained bursts have provided the data that permit development of the expressions for predicting the peak values of air-induced and direct-transmitted acceleration, velocity, and displacement. Field observations for regions where the air blast overpressures are less than 1,000 psi generally indicate that, within about 50 to 100 feet of the surface, ground motions are predominantly air-induced. The relatively few measurements of acceleration and displacement that have been made at significant distances below the ground surface show the effects of attenuation and dispersion as the air-induced pulse travels through the ground.

A typical acceleration-time record from a gage mounted near the surface of the ground

exhibits a systematic pulse shape corresponding to the passage of the shock wave, with a random type disturbance often superimposed on this systematic pulse. In the superseismic case, when the air blast propagation velocity is greater than the ground seismic velocity, the downward acceleration is large compared with the following upward acceleration. The velocity-time record is similar in shape to the overpressure-time pulse, at least in the early stages. In cases in which the ground motion outruns the air blast, there is a slower rise in the acceleration; it may even be reversed in direction initially, i.e., upward rather than downward. In such cases, the signals may last for a longer time than the positive phase overpressure duration. The associated velocity wave form usually exhibits a velocity jump as the air-shock wave passes over the position, but the overall record is characterized by a considerable degree of oscillation. When precursors are present, the acceleration and velocity records may exhibit higher frequency components and more random type of oscillation. Wave front dia-

grams for the superseismic and outrunning cases are shown in Figure 2-88.

Most values of velocity have been obtained by integrating acceleration records. In general, velocities appear to be more predictable quantities than accelerations or displacements. Displacement data are even scarcer than velocity data, and only a few direct measurements have been made. For the most part, displacement data consist of integrated acceleration records or extrapolation of displacement spectra to zero frequency.

Knowledge of direct-transmitted ground shock effects is limited. Those data that exist were obtained from buried high explosive shots, from several surface and near surface nuclear detonations, and from a number of fully contained bursts. For a completely buried shot, measurements indicate that at any particular range  $R$ , the strain or velocity pulse rises in a parabolic manner to a peak value in a time roughly corresponding to  $T_r = R/6c_p$  to  $R/12c_p$ , where  $R$  is the range from the explosion, and  $c_p$

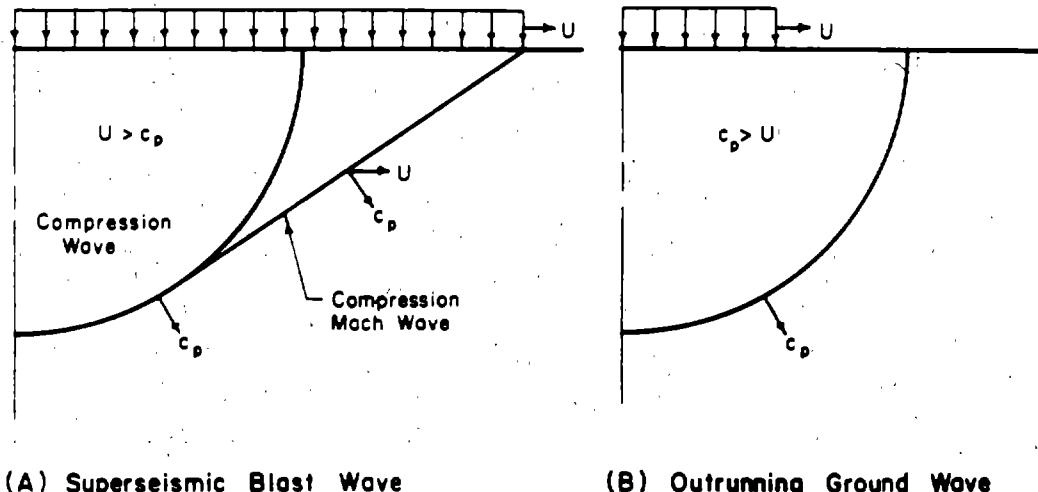


Figure 2-88. [REDACTED] Wave Front Diagram for Superseismic Air Blast and Outrunning Ground Wave [REDACTED]

[REDACTED]

is the effective seismic velocity of the medium. The signal then drops slowly with a total positive phase duration corresponding approximately to  $T_o = R/2c_p$  to  $R/c_p$ . The effects of layering, reflection, and refraction, tend to introduce high frequency and random components of motion.

### 2-61 Types of Effects

[REDACTED] It is convenient to consider the earth shock resulting from a nuclear explosion as producing both systematic and random effects. Systematic effects can be divided further into two major types:

- Air-induced shock associated with the passage of an air shock wave over the surface of the ground, and the overpressure at the surface above the structure transmitted downward with such attenuation and dispersion as may be consistent with the physical conditions at the site.
- Direct-transmitted ground shock that arises from direct energy transfer from surface, near surface, or underground bursts.

[REDACTED] Random effects include high frequency ground-transmitted shock, surface-wave effects, reflections, refractions, etc. The dominant effect depends on such factors as weapon yield, point of detonation with respect to the ground surface, range from ground zero, depth of the measurement, and, in particular, the geologic conditions.

[REDACTED] Reasonable estimates can be made of the maximum values of displacement, velocity, and acceleration associated with the air-induced shock and in more restricted cases for the direct-transmitted ground shock under more or less uniform geologic conditions.

### 2-62 Air-Induced Effects

[REDACTED] At the surface in a homogeneous medium the maximum transient elastic vertical displacement may be expressed as

2-178 ZOL

$$d_{\infty} = \frac{H p_{\infty}}{2 \bar{E}},$$

where  $H$  is the depth to which the air-induced shock wave extends during the effective duration of the shock,  $t_i$ ,  $p_{\infty}$  is the side-on overpressure at the surface, and  $\bar{E}$  is the restrained modulus. The duration of the shock may be approximated by

$$t_i \approx 0.37 \left( \frac{100}{p_{\infty}} \right)^{1/2} (W(Mt))^{1/3}$$

for

$$2 \leq p_{\infty} \leq 10,000 \text{ psi.}$$

Thus

$$H = c_p t_i = 0.37 \left( \frac{100}{p_{\infty}} \right)^{1/2} (W(Mt))^{1/3} c_p.$$

The restrained modulus is related to the effective seismic velocity, the mass density, and Young's modulus of elasticity of the medium as follows:

$$\frac{\bar{E}}{\rho} = c_p^2 = \left( \frac{E}{\rho} \right) \left( \frac{1 - \nu}{(1 + \nu)(1 - 2\nu)} \right),$$

where  $E$  is the Young's modulus of elasticity (psi),  $\rho$  is the mass density of the medium ( $\rho = \gamma/g$  lb sec<sup>2</sup>/ft<sup>4</sup>, where  $\gamma$  is the unit weight of the medium in pounds per cubic foot and  $g$  is the gravitational acceleration constant), and  $\nu$  is Poisson's ratio. For values of  $\nu$  of 0.25 or less, the relation may be approximated by:

$$\bar{E} = \rho c_p^2 \approx E.$$

If the unit weight of the soil is about 115 lb/ft<sup>3</sup>,

[REDACTED]  
[REDACTED]  
an approximate value of  $\bar{E}$  is

$$\bar{E} = 25,000 \left( \frac{c_p}{1,000} \right)^2, \text{ psi.}^*$$

Substituting the values for  $H$  and  $\bar{E}$  gives

$$d_{se} = 9 \left( \frac{p_{so}}{100} \right)^{0.5} \left( \frac{1,000}{c_p} \right) (W(Mt))^{1/3} \text{ inches.}$$

[REDACTED] The permanent vertical displacement is not so easily estimated; at present the best estimates can be made by considering the static stress-strain properties of the soil. In the absence of better information, it is suggested that the permanent displacement at the surface be taken to be the following for overpressures greater than 40 psi:

$$d_{sp} = \frac{p_{so} - 40}{30} \left( \frac{1,000}{c_p} \right)^2 \text{ inches,}$$

where  $c_p$  is the seismic velocity of the material near the surface.

[REDACTED] From wave propagation theory it may be demonstrated that the following relationship exists for particle velocities in terms of the dimensional units defined above.

$$v = c_p \frac{p_{so}}{\bar{E}} = c_p \epsilon,$$

where  $\epsilon$  is the strain. Upon substitution this gives the maximum velocity

$$v_s = 50 \left( \frac{p_{so}}{100} \right) \left( \frac{1,000}{c_p} \right) \text{ in./sec.}$$

[REDACTED] For a rise time of velocity of about 0.002 seconds, and considering a parabolic rise

with a 20 percent increase for nonlinearity, the maximum acceleration at the surface, computed as a rate of change of velocity, may be expressed by

$$a_s \approx 150 \left( \frac{p_{so}}{100} \right) \left( \frac{1,000}{c_p} \right), g.$$

[REDACTED] Since the surface acceleration is not related solely to the maximum velocity, but is partially dependent on the weapon yield and other factors, it is recommended that a value of  $c_p$ , no greater than 2,000 fps be used in this expression, regardless of the actual surface seismic velocity.

[REDACTED] Horizontal effects data are lacking for the surface. At present, it is recommended that the maximum horizontal deflection be taken as one-third the vertical, the maximum horizontal velocity as two-thirds the vertical, and the maximum horizontal acceleration as equal to the vertical.

[REDACTED] The same type of reasoning can be followed in arriving at maximum values of acceleration, velocity, and displacement at depths below the surface. The difference in deflection between the surface and some point at a depth  $y$  beneath the surface cannot exceed the surface stress divided by the lower restrained modulus of deformation,  $\bar{E}$ , in the interval  $y$ , and multiplied by the depth  $y$ . Thus between the surface and a depth  $y$ , not greater than 100 ft, assuming no attenuation of pressure with depth, an upper limit of the elastic component of differential displacement is given by

$$d_s - d_y \approx \frac{p_{so}}{\bar{E}} y.$$

[REDACTED] The actual difference in deflection is more likely to be one-half this value, and may be

[REDACTED] If the unit weight of the medium differs significantly from 1.5 lb/ft<sup>3</sup>, a representative value of  $\bar{E}$  should be used rather than the approximation given here.

considered to vary linearly to a depth of 100 ft, which results in the following expression

$$d_{se} - d_{ye} = 2.4 \left( \frac{p_{so}}{100} \right) \left( \frac{1,000}{c_p} \right)^2 \left( \frac{y^*}{100 \text{ ft}} \right) \text{ inches}$$

where  $y^* = y$  for depths of 0 to 100 ft, and  $y^* = 100$  ft for depths greater than 100 ft.

It is not generally considered desirable to assume any attenuation of displacement, except for very soft soils. Since total impulse must be preserved, the wavelength of the strain pulse probably increases with depth, and, therefore, it does not seem reasonable that there should be a reduction in elastic component of displacement consistent with the reduction in peak stress, as given by the attenuation relationships for stress or velocity with depth.

It is recommended that the permanent displacement of soils at depths below the surface be determined by multiplying the permanent displacement at the surface by  $(100 - y^*)/100$ , i.e.,

$$d_{yp} = d_{sp} \left( \frac{100 - y^*}{100} \right)$$

$$= \frac{p_{so}}{30} \left( \frac{1,000}{c_p} \right)^2 \left( \frac{100 - y^*}{100} \right) \text{ inches.}$$

Thus, permanent displacements below 100 feet would be taken to be zero. At depths less than 100 feet, the total displacement should be taken as the sum of the elastic displacement at the surface,  $d_{se}$ , shown previously, and the permanent displacement,  $d_{yp}$ , given above.

The value of maximum stress below the surface is given approximately, for any yield or overpressure, by the following expression

$$p_y = \alpha p_{so}$$

where

$$\alpha = \frac{1}{1 + \frac{y}{H}}$$

and for depths that are not near the surface

$$H = 230 \left( \frac{100}{p_{so}} \right)^{0.5} (W(Mt))^{1/3}.$$

Note: The attenuation factor,  $\alpha$ , that is used in this section is different than the corresponding attenuation factor  $1/\beta$  that is used in Section II, "Damage to Belowground Structures," of Chapter 11, "Damage to Structures." The attenuation factor given in Figure 11-29, Section II of Chapter 11 is the result of more recent studies. It reflects the influence of soil type (as represented by its seismic velocity) on peak pressure or soil particle velocity attenuation. The disparity between the two factors increases as the peak overpressure and/or the soil seismic velocity increase, but the disparity is relatively insensitive to variations in weapon yield. As a result of the influence of seismic velocity, the difference between the two factors also increases as the depth below ground surface increases. The factor given in Figure 11-29 gives substantially smaller attenuation rates under high overpressures and high seismic velocities than does the factor used in this section. Consequently, from the "vulnerability analysis" point of view, the factor of Figure 11-29 is more conservative, and its use in shock analysis studies is generally recommended. The attenuation factor obtained from Figure 11-29 may be introduced into the equations of this section by simply replacing " $\alpha$ " of this section with " $1/\beta$ ," where " $\beta$ " is obtained from Figure 11-29. As mentioned previously, it is recommended that this replacement be made, in general; however, there is

one important exception. The factor  $1/\beta$  is not compatible with the shortcut vulnerability curves shown in Figures 11-48 through 11-50, and calculations of similar curves that are compatible with the  $1/\beta$  attenuation factor have not been performed at this time. It is for this reason that the  $\alpha$  attenuation factor is introduced here, and its use will be illustrated in Problem 2-27. The use of the  $1/\beta$  attenuation factor is illustrated in Problems 11-3 and 11-4.

At depths below the surface, it is recommended that velocities be attenuated in about the same manner as the maximum stress. Thus, the vertical velocity at any depth  $y$  is given by

$$v_y = \alpha v_s$$

The peak downward acceleration attenuates sharply with depth, especially near the surface. The sharp attenuation is caused primarily by the increase of rise time in the stress or velocity with depth.

The time of rise of the maximum velocity from an initial zero value can be taken as one-half the transit time of the shock wave from the surface to depth considered. For a parabolic rise in velocity the acceleration can be considered to be twice the value for a linear rise, which leads to the expression

$$a_y = 2 \frac{v_y}{t_r} = 5 \left( \frac{P_{so}}{100} \right) \frac{100}{y} \alpha, g,$$

where  $t_r$  is the effective velocity pulse rise time. This expression gives values which appear to agree well with test data for depths greater than 10 ft.

In the absence of better information at depths below the surface, it is recommended that the ratios of horizontal to vertical effects be taken equal to those previously specified for the surface, i.e., horizontal deflection is one-third

the vertical, the maximum horizontal velocity is two-thirds the vertical, and the maximum horizontal acceleration is equal to the vertical.

Layered media pose a complicated situation, but with care and judgment, reasonable estimates of acceleration, velocity, and displacement can be made. A convenient method is to use the stepwise passage of a stress wave downward through the medium. In general, the basic concepts governing the computation of displacement, velocity, and acceleration are the same as those described for a uniform medium. The displacements at any particular time may be computed by dividing the average pressure in an interval by the modulus of elasticity to obtain the strain and then multiplying by the length of the interval to obtain the displacement; the total displacement occurring over the length of the pulse is the sum of the incremental displacements.

Complications arise at the interface of two media because of stress transmission and reflection. For soil and rock, the interface may not be sharply defined and the reflected and transmitted stresses probably do not follow the laws governing purely elastic media. If it is known that the interface is fairly sharp, an estimate of the reflected and transmitted stresses can be made from the following relationships:

$$p_t = \frac{1 - \psi}{1 + \psi} p_i$$

$$p_t = \frac{2}{1 + \psi} p_i$$

where  $\psi$  is the ratio of the impedances of the two media. The stresses at the interface must be taken as equal, and, from considerations of continuity, the displacements also are equal.

## 2-63 Outrunning Ground Motion

Outrunning ground motion occurs when the air-shock velocity  $U$  decays below the seis-

mic wave velocity  $c$  of the medium. In the most general sense, outrunning ground motions and direct-transmitted ground shock are different phenomena. Direct-transmitted ground shock is ground motion propagated through the ground media from the region of the crater (this is often denoted outrunning when it clearly arrives, as reflected or refracted waves from deep-seated layers, ahead of the blast front). Outrunning ground motion occurs when the air-induced ground motion begins to propagate more rapidly than the air blast shock front, as illustrated in Figure 2-88. In actual fact, the motion-time history at a point in the medium can be quite complicated, even random in nature, when air-induced, outrunning, and direct-transmitted effects all arrive at about the same time.

Some information on outrunning motions observed in field tests can be found in "Nuclear Geophysics" (see bibliography). Computer codes that are presently being developed should provide guides to even better estimates of outrunning motions.

#### 2-64 Direct-Transmitted Ground Shock

The energy transmitted directly to the earth from a surface or near-surface burst can be propagated effectively through competent material for long distances. Experimental data that demonstrate this are available from buried high explosive shots and from surface and contained nuclear weapon tests.

For a completely buried shot, the first portion of the strain or velocity record at a distance  $R$  from the point of burst has the form described in paragraph 2-60, i.e.,

$$T_R = \frac{R}{6c_p} \text{ to } \frac{R}{12c_p} \quad \text{and} \quad T_o = \frac{R}{2c_p} \text{ to } \frac{R}{c_p}$$

Without serious error, the relation between peak strain  $\epsilon$  and peak particle velocity  $v$  is given by the equation previously shown in

paragraph 2-62, i.e.,

$$v = c_p \frac{P_{so}}{E} = c_p \epsilon$$

Assuming that the steepest part of the velocity-time curve has a slope that is twice the average slope during the rise phase leads to the following relationship between the range of peak acceleration, peak velocity, and strain, all in the radial direction.

$$a_r = \frac{2v_r}{T_r} \approx \frac{12c_p^2}{R} \epsilon \text{ to } \frac{24c_p^2}{R} \epsilon$$

An estimate of the maximum displacement  $d$  in the radial direction may be obtained by integrating the area under the positive phase of the velocity curve. If the velocity waveform is parabolic, then

$$d_r = \frac{2}{3} v_r T_o \approx \frac{1}{3} R \epsilon \text{ to } \frac{2}{3} R \epsilon$$

If data for strain, acceleration, or displacement are available, approximate relations for the other quantities may be obtained. In general, the seismic velocity enters into the relationships as indicated in equations shown above.

Most of the available test data from which direct-transmitted shock effects may be estimated were obtained from buried nuclear and high explosive detonations. To extrapolate from the test data to estimate shock effects produced by surface nuclear detonations requires establishment of the equivalence factor relating buried HE to buried nuclear yield, and also establishment of the equivalence of fully buried detonations to surface detonations of the same type of explosive.

A yield effectiveness factor of 0.2 to 0.5 has been used to relate fully contained nuclear

explosions to fully contained HE explosions. To relate a surface nuclear burst to a fully contained nuclear burst, factors of 0.02 for a burst slightly above the surface to 0.05 for a burst slightly below the surface are recommended. Significant uncertainties exist regarding these equivalence factors.

Expressions for acceleration, velocity, and displacement have been derived on the basis of test data available for accelerations from shot RAINIER in Operation HARDTACK in volcanic tuff with a seismic velocity of 6,000 fps. For scaled ranges of 2,500 ft/Mt<sup>1/3</sup> and closer, and an equivalence factor of 0.05 as just discussed, the acceleration may be expressed as follows:

$$a_r = 0.4 \left( W(\text{Mt}) \right)^{5/6} \left( \frac{1,000}{R} \right)^{3.5} \left( \frac{c_p}{1,000} \right)^2, g.$$

Using the relations between acceleration, velocity, and displacement, and choosing the equations with coefficients of 12 and 1/3, respectively, this equation for acceleration may be used to arrive at the following equations for radial velocity and displacement for materials with seismic velocities less than 10,000 feet per second:

$$v_r = 12 \left( W(\text{Mt}) \right)^{5/6} \left( \frac{1,000}{R} \right)^{2.5} \left( \frac{c_p}{1,000} \right) \text{ in./sec}$$

$$d_r = 4 \left( W(\text{Mt}) \right)^{5/6} \left( \frac{1,000}{R} \right)^{1.5} \text{ inches.}$$

There is little or no information on tangential motions, and until additional information becomes available, it is recommended that maximum values of tangential acceleration, velocity, and displacement be taken as 1, 2/3, and 1/3 times the corresponding radial values.

It is desirable to consider the direct-transmitted effects as being applicable only at some distance below ground surface, except possibly at close in ranges. At scaled distances greater than 2,500 ft/Mt<sup>1/3</sup>, the limited available data suggest a decrease in the rate of decay of motion with distance. Approximate expressions for radial acceleration, velocity, and displacement for materials with an average seismic velocity less than 10,000 fps are as follows:

$$a_r = 0.081 \left( W(\text{Mt}) \right)^{0.25} \left( \frac{1,000}{R} \right)^{1.75} \left( \frac{c_p}{1,000} \right)^2, g.$$

$$v_r = 4.8 \left( W(\text{Mt}) \right)^{0.5} \left( \frac{1,000}{R} \right)^{1.5} \left( \frac{c_p}{1,000} \right) \text{ in./sec}$$

$$d_r = 3.19 \left( W(\text{Mt}) \right)^{0.75} \left( \frac{1,000}{R} \right)^{1.25} \text{ inches.}$$

These expressions give only very approximate values. Geologic conditions can produce large and random variations in the motions at large distances. For materials with seismic velocities greater than 10,000 fps, e.g., granite rock materials, the field test data suggest the following relationships as being applicable at scaled ranges of about 2,700 ft/Mt<sup>1/3</sup> and closer.

$$a_r = 180 \left( W(\text{Mt}) \right)^{5/6} \left( \frac{1,000}{R} \right)^{7/2} \left( \frac{165}{\gamma} \right)^{5/6} \left( \frac{c_p}{18,000} \right)^{1/3}, g,$$

$$v_r = 30 \left( W(\text{Mt}) \right)^{5/6} \left( \frac{1,000}{R} \right)^{5/2} \left( \frac{165}{\gamma} \right)^{5/6} \left( \frac{18,000}{c_p} \right)^{2/3}, \text{ ft/sec.}$$

(U)

$$d_r = 12 \left( W(Mt) \right)^{5/6} \left( \frac{1,000}{R} \right)^{3/2} \\ \left( \frac{165}{\gamma} \right)^{5/6} \left( \frac{18,000}{c_p} \right)^{5/3}, \text{ inches.}$$

As would be expected from the different scaling relationships, the expression for materials with seismic velocities less than 10,000 feet per second and those for materials with seismic velocities greater than 10,000 feet per second show lack of agreement at a seismic velocity of 10,000 feet per second, which divides the areas of applicability. This matter is currently receiving further attention, but in the interim it is believed that the expressions provide the best estimates of such motions.

No expressions exist for motions at large distances in hard materials that are comparable to the expressions presented above for soft materials. It was necessary to make approximate estimates to develop the relationships presented in Section III, Chapter 11.

## 2-65 Spectrum Concepts — Simple Systems

When structural systems or equipment are subject to a base disturbance, such as that arising from the ground motion associated with a nuclear explosion, the response of the system is governed by the distribution and magnitudes of the masses and resistance elements. A knowledge of the response of systems subjected to such loadings is extremely important from the standpoint of design in order to proportion the structure so that it will not undergo complete collapse, and to protect the structure, equipment, and personnel from shock damage. One of the simplest interpretations of ground motion data involves the concept of the response spectrum, which is a plot of the maximum response of a simple linear oscillator subjected to a given input motion as a function of frequency.

The time history of the actual motions of the earth caused by the passage of a shock wave over the surface is complex and is subject to considerable uncertainty. However, the principal effects on equipment and structural components can be described by use of the concept of the shock-response spectrum.

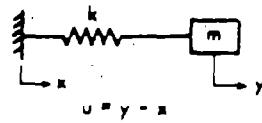
Consider a piece of equipment or an internal element of a structure supported at a point on an underground structure that is subjected to motion from blast. The equipment or element can be represented as a simple oscillator, consisting of a mass  $m$  attached by a linear spring of spring constant  $k$  to the base as shown in Figure 2-89(a). The natural frequency  $f$  of the oscillator is

$$f = \omega/2\pi = \frac{1}{2\pi} \sqrt{\frac{k}{m}}.$$

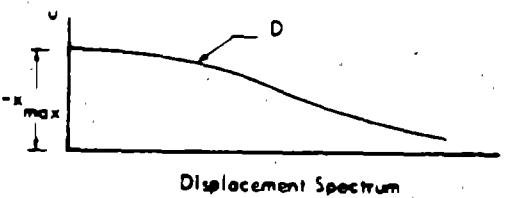
For a given transient ground motion  $x$ , the mass  $m$  will be set into motion. If the motion of the mass  $m$  is designated by the coordinate  $y$  and the motion of the base by the coordinate  $x$ , the deformation in the spring  $u$  is  $(y-x)$  and is positive when  $y$  exceeds  $x$ . For such a system the most useful spectra are found to be the following: the maximum relative displacement  $u$  of the system; the maximum relative velocity  $\dot{u}$ ; the maximum pseudo relative velocity or the quantity  $\omega u$ , the circular frequency  $\omega$  times the displacement  $u$ , which is not quite the same as  $\dot{u}$  and differs considerably from  $\dot{u}$  at low frequencies; and the absolute acceleration of the mass,  $\omega^2 u$ , which is nearly the same as  $\ddot{y}$ . A plot of the maximum values (denoted  $D$ ,  $\bar{V}$ ,  $V$ , and  $A_g$ , respectively) as a function of the frequency of the system for a given type of input constitutes a response spectrum for the particular function. These quantities are defined as follows:

$$A_g = |\omega^2 D| = (2\pi f)^2 D$$

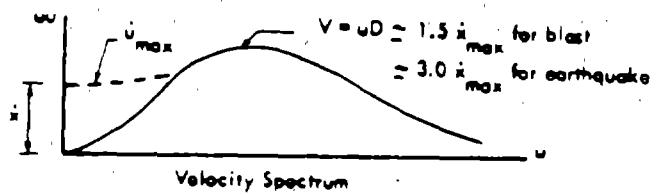
$$V = |\omega D| = 2\pi f D$$



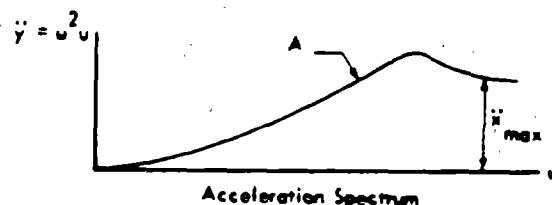
(a) SINGLE-DEGREE-OF-FREEDOM SYSTEM



Displacement Spectrum



Velocity Spectrum



Acceleration Spectrum

(b) TYPICAL SPECTRA

Figure 2-89. Single-Degree-of-Freedom System  
and Typical Response Spectra

The maximum energy absorbed in the spring is associated with  $V$ . The quantity  $\bar{V}$  is not particularly useful.

For inputs of the type associated with air-induced or direct-transmitted ground shock, the spectra for a simple system will have the characteristic appearances shown in Figure 2-89(b). The limiting conditions that apply to the spectra illustrated in Figure 2-89(b) are of particular interest. For example, as the frequency of the system approaches zero, the mass  $m$  does not move when the base of the system has a given motion applied. Then the relative displacement  $u$  is equal to the negative value of  $x$ , and the relative velocity  $\dot{u}$  is equal to minus the maximum base velocity  $\dot{x}$ . The dotted line in Figure 2-89(b) indicates the difference between  $\dot{u}_{\max}$  and  $V$  that may be observed in the region of low frequencies; likewise, there is some difference between  $\dot{u}_{\max}$  and  $V$  at the high frequency end, but these differences are of a smaller order of magnitude. Typical values of  $V$  that might be expected for blast conditions are shown in Figure 2-89(b). An additional control is that as the frequency of the system becomes large, the displacement  $y$  approaches the displacement  $x$ , i.e.,  $u$  approaches zero, and the acceleration  $\ddot{y}_{\max}$  approaches  $\ddot{x}_{\max}$ . These controls are of special importance in arriving at design shock spectra.

Ordinarily, the input for ground motion consists of two parts, a systematic portion on which is superimposed a series of random oscillations. The magnitude of the peaks of the random components may be either small or large compared to the systematic portion. The random part may exist over the entire range of the systematic portion, over only part of the range, or even may be prior to the systematic portion.

For a random series of pulses, the relative velocity peak of the spectrum compared with the maximum input velocity can be high, but it is not likely to be much higher than about 3, unless an almost resonant condition is obtain-

ed with several pulses of alternate positive and negative signs of exactly the same shape and duration. Such a resonant condition for velocity is extremely unlikely from blast loading, although it has been observed in long duration earthquake phenomena. Even if, for some reason, partial resonance is achieved, the dampening in the system being excited will reduce the peaks considerably.

In general, the combined effect of the two input motions, systematic and random, depends on their individual effects. It can be shown that the combined spectrum will be either equal to or less than the sum of the absolute values of the spectra corresponding to the individual inputs. It also appears reasonable that the combined spectrum can be expected to be approximately equal to the square root of the sum of the squares of the individual spectra, point by point. In most practical cases of the type under consideration, the frequencies for which the spectrum values are important differ by a considerable amount, and the sums of the spectra or the square root of the sums of the squares are nearly the same as the maximum individual modal value.

## 2-66 Shock Spectra for Free Field Ground Motion

Using the concepts discussed above, it is possible to derive shock spectra that can be used in design to assess the relative effects in a structure (above or below ground) or the effects on equipment within a structure. Such spectra can be described best by the use of a logarithmic plot that permits values of displacement, pseudo-velocity, and acceleration to be read versus frequency in accordance with the relations given by the equations in paragraph 2-65.

In accordance with the limiting conditions discussed for Figure 2-89, the response spectrum can be represented by three regions, each region defined by a straight line constituting an envelope to the actual spectrum. An

example of such a spectrum for air-induced shock for conditions of 100 psi surface pressure, 5 Mt yield, and an acoustic velocity of 2,500 ft/sec is shown in Figure 2-90 for situations at the surface and at a depth of 100 ft. The left hand region, at the low frequency side, is influenced primarily by the maximum elastic transient displacement. The intermediate part of the spectrum (horizontal line) is a function of the maximum velocity reached in the free field. The right hand side depends on the maximum acceleration. In brief, the approximate response spectrum "envelope" is described by three straight lines (actually there are discrepancies that may be as high as a factor of 2 in some areas, but the actual ground motions are now known even this accurately, and the simplification of the spectrum in this way is permissible).

- A line  $D = \text{constant}$ , parallel to the displacement scales, drawn with a magnitude equal to the maximum ground displacement.
- A line  $V = \text{constant}$ , drawn with a magnitude of 1.5 times the maximum ground velocity.
- A line  $A = \text{constant}$ , parallel to the acceleration scales, drawn with a magnitude equal to twice the maximum ground acceleration.

Spectra may be sketched for horizontal and vertical motions at various depths and employed as appropriate. Detailed procedures for constructing more accurate spectra may be found in "Effect of Inelastic Behavior on the Response of Simple Systems to Earthquake Motions," A. S. Veletsos and N. M. Newmark, and "Response Spectra Approach to Behavior of

Shock Isolation Systems," A. S. Veletsos and N. M. Newmark (see bibliography). In general, the air-induced and direct-transmitted ground motions, as well as the out-running ground motions, if applicable, are computed. The spectra of each are plotted, and the design is made according to the envelop of the spectra. If it is known that the motions will arrive at significantly different times, the design or analysis is only made for the worst case.

The response spectrum, such as that shown in Figure 2-90, may be used directly for elastic systems. If the frequency of equipment within a structure and its type and mode of support are known, it is possible to ascertain certain results in terms of the response of the system. For example, for a single-degree-of-freedom system, the number of gravities of acceleration corresponding to the natural frequencies may be considered as applied to the body to ascertain the dynamic stresses. For more complex systems, the analysis is more difficult, although consideration of the most significant mode will lead to useful estimates of dynamic loadings in many cases.

For purposes of comparison and interest, three shock spectra determined from reed gages or ground motion records in atomic field tests are shown in Figure 2-91. The Operation HARDTACK spectra exhibit high accelerations; this is likely to be the result of the high water table that tends to emphasize the high frequency end of the spectrum. The maximum velocity is much higher than would be expected in a typical soil site. The Operation PLUMBOB data approximate the type of response that would be expected for more normal soil conditions.

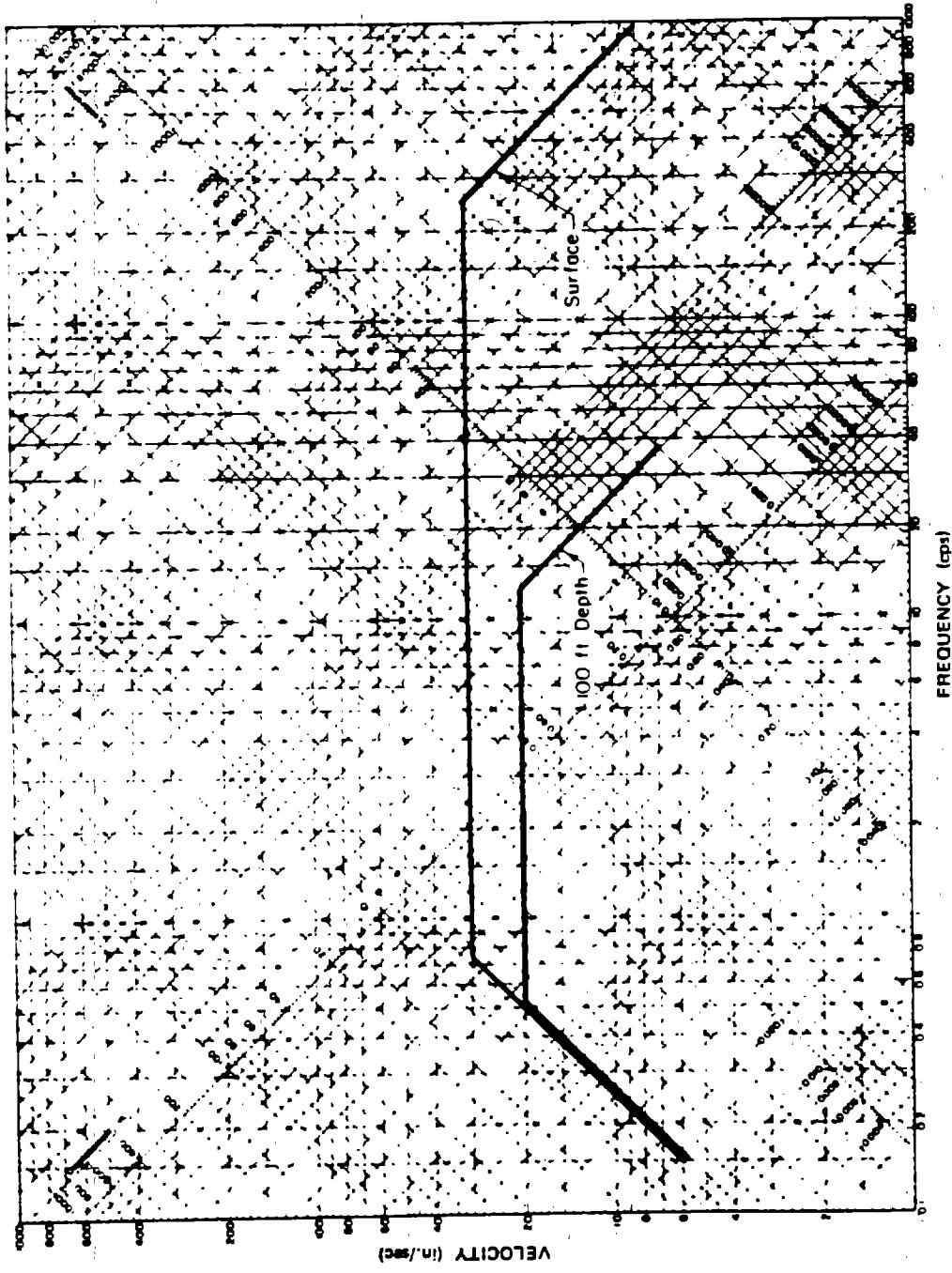


Figure 2-90. [REDACTED] Response Shock Spectra, 100 psi Overpressure, 5 Mt Yield.  
c = 2,500 fps (Vertical Motion - Air-Induced Effects) [REDACTED]

2-T88  
2/6

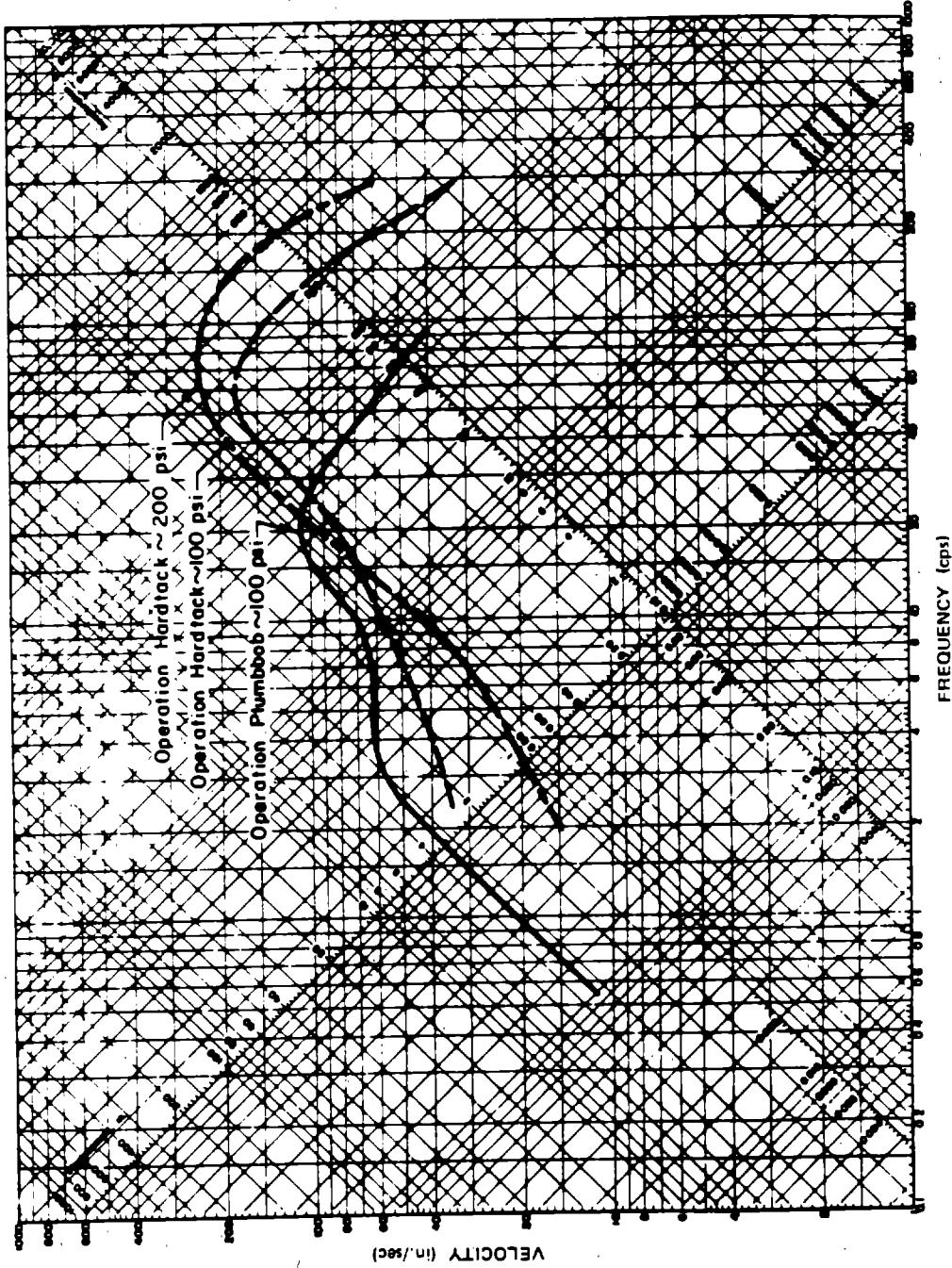


Figure 2-91. [ ] Typical Shock Spectra from Field Tests - Surface Data [ ]

2-700  
Z/7

**Problem 2-27. Calculation of the Ground Motions from  
a Nuclear Explosion at the Surface**

The nature of the free field effects of ground motion are described in paragraphs 2-60 through 2-66. The attenuation factor  $\alpha$  that is defined in paragraph 2-62 is used in the example presented below. As noted in paragraph 2-62, it generally is preferable to use the factor  $1/\beta$  for attenuation, where  $\beta$  is described in Section II of Chapter 11, and more specifically in Figure 11-29. However,  $1/\beta$  attenuation is not compatible with the equipment vulnerability curves in Figures 11-48 through 11-50. Therefore, the following example illustrates the use of the attenuation factor described in paragraph 2-62; use of the  $1/\beta$  attenuation is illustrated in Problems 11-3 and 11-4.

**Example**

**Given:** A 1 Mt weapon burst on the surface of a medium that has a seismic velocity of 5,000 ft/sec.

**Find:** The vertical and horizontal displacement, velocity, and acceleration at a point 50 feet below the surface and at a ground distance of 1,500 feet from the explosion.

**Solution:** The equivalent distance for 1 kt

$$d_1 = \frac{d}{(W(\text{kt}))^{1/3}} = \frac{1,500}{(1,000)^{1/3}} = 150 \text{ feet.}$$

From Figure 2-17, the overpressure at the surface is about 1,000 psi.

a. **Air Induced Motions:** The maximum elastic vertical displacement at the ground surface is given by the equation shown in paragraph 2-62:

$$d_{se} = 9 \left( \frac{P_{\infty}}{100} \right)^{0.5} \left( \frac{1,000}{c_p} \right) (W(\text{Mt}))^{1/3}$$

$$= 9 \left( \frac{1,000}{100} \right)^{0.5} \left( \frac{1,000}{5,000} \right) (1)^{1/3} = 5.7 \text{ inches.}$$

It is reasonable to assume that impulse is preserved in the stiff medium described in this case. Therefore, the vertical elastic displacement at a depth of 50 feet will be the same as that at the surface, i.e., 5.7 inches. As described in paragraph 2-62, the permanent displacement at a depth of 50 feet is

$$\begin{aligned} d_{yp} &= \frac{P_{\infty} - 40}{30} \left( \frac{1,000}{c_p} \right)^2 \left( \frac{100 - y}{100} \right) \\ &= \left( \frac{1,000 - 40}{30} \right) \left( \frac{1,000}{5,000} \right)^2 \left( \frac{100 - 50}{100} \right) \\ &= 0.6 \text{ inches.} \end{aligned}$$

Thus, from paragraph 2-62 the total vertical displacement is

$$d_y = d_{se} + d_{yp} = 5.7 + 0.6 = 6.3 \text{ inches.}$$

The peak vertical velocity given in paragraph 2-62 is:

$$v_y = \alpha v_s,$$

where

$$v_s = 50 \left( \frac{P_{\infty}}{100} \right) \left( \frac{1,000}{c_p} \right),$$

$$\alpha = \frac{1}{1 + \frac{y}{H}},$$

and

$$H = 230 \left( \frac{100}{P_{so}} \right)^{0.5} (W(Mt))^{1/3}$$

This gives

$$H = (230) \left( \frac{100}{1,000} \right)^{0.5} (1)^{1/3} = 73$$

$$\alpha = \frac{1}{1 + \frac{50}{73}} = 0.59$$

$$v_s = 50 \left( \frac{1,000}{100} \right) \left( \frac{1,000}{5,000} \right) = 100 \text{ in./sec.}$$

$$v_y = (0.59)(100) = 59 \text{ in./sec.}$$

The vertical acceleration is given by the equation in paragraph 2-62 as:

$$\begin{aligned} a_y &= 5 \left( \frac{P_{so}}{100} \right) \left( \frac{100}{y} \right) \alpha \\ &= (5) \left( \frac{1,000}{100} \right) \left( \frac{100}{50} \right) (0.59) = 59 \text{ g.} \end{aligned}$$

As described in paragraph 2-62, the horizontal values of the motions are taken to be  $1/3$ ,  $2/3$ , and 1 times the vertical displacement, velocity and acceleration, respectively, i.e.,

$$d_x = 1/3 d_y = \left( \frac{1}{3} \right) (6.3) = 2.1 \text{ inches,}$$

$$v_x = \frac{2}{3} v_y = \left( \frac{2}{3} \right) (59) = 39 \text{ in./sec,}$$

$$a_x = a_y = 59 \text{ g.}$$

b. *Direct Transmitted Motions:* The expressions given in paragraph 2-64 are applicable for direct transmitted motions. The radial motions are essentially horizontal for the distance and depth of this example. These are (note the distance is less than  $2,500 \text{ ft/Mt}^{1/3}$ ):

$$\begin{aligned} d_r &= 4 (W(Mt))^{5/6} \left( \frac{1,000}{R} \right)^{1.5} \\ &= (4) (1)^{5/6} \left( \frac{1,000}{1,500} \right)^{1.5} = 2.2 \text{ inches.} \end{aligned}$$

$$\begin{aligned} v_r &= 12 (W(Mt))^{5/6} \left( \frac{1,000}{R} \right)^{2.5} \left( \frac{c_p}{1,000} \right) \\ &= 12 (1)^{5/6} \left( \frac{1,000}{1,500} \right)^{2.5} \left( \frac{5,000}{1,000} \right) \\ &= 22 \text{ in./sec,} \end{aligned}$$

$$\begin{aligned} a_r &= 0.4 (W(Mt))^{5/6} \left( \frac{1,000}{R} \right)^{3.5} \left( \frac{c_p}{1,000} \right)^2 \\ &= (0.4) (1)^{5/6} \left( \frac{1,000}{1,500} \right)^{3.5} \left( \frac{5,000}{1,000} \right)^2 \\ &= 2.4 \text{ g.} \end{aligned}$$

In this case, the motions normal to the radial motions may be taken to be vertical. These are  $1/3$ ,  $2/3$ , and 1 times the corresponding radial values of displacement, velocity and acceleration, i.e.,

$$d_y = \frac{1}{3} d_r = \left( \frac{1}{3} \right) (2.2) = 0.7 \text{ inches,}$$

$$v_y = \frac{2}{3} v_r = \left( \frac{2}{3} \right) (22) = 15 \text{ in./sec,}$$

$$a_y = a_r = 2.4 \text{ g.}$$

**Answer:** The peak values of both horizontal and vertical motions, for air-induced and direct-transmitted shocks are:

	<u>d(in.)</u>	<u>v(in./sec)</u>	<u>a(g)</u>
<b>Vertical</b>			
Air-induced	6.3	59	59
Direct-transmitted	0.7	15	2.4
<b>Horizontal</b>			
Air-induced	2.1	39	59
Direct-transmitted	2.2	22	2.4

In this particular example the air-induced motions, with the exception of the horizontal displacement, are the largest values for both the vertical and horizontal directions. In the horizontal direction, the direct-transmitted value of displacement is nearly equal to that of the air-induced value. In many cases, especially at short range and for stiff media, it will be found that the direct-transmitted motions will be the largest, and will control the analysis. From paragraph 2-66, the bounds for the shock response

spectra are obtained by multiplying the controlling displacement, velocity, and acceleration values by 1, 1.5, and 2.0, respectively.

**Vertical Response Spectrum Bounds:**

$$D = 1.0d = 6.3 \text{ in.}$$

$$V = 1.5v = 89 \text{ in./sec}$$

$$A = 2.0a = 118g$$

**Horizontal Response Spectrum Bounds:**

$$D = 1.0d = 2.2 \text{ in.}$$

$$V = 1.5v = 59 \text{ in./sec}$$

$$A = 2.0a = 118g$$

These spectra bounds are shown in Figure 11-51. They show the response spectra for a single-degree-of-freedom system. These bounds are used in the analysis of the vulnerability of equipment mounted in an underground structure in Problem 11-8.

**Related Material:** See paragraphs 2-24, 2-60 through 2-66, and Sections II and III of Chapter 11.

## SECTION IV

### UNDERWATER EXPLOSION PHENOMENA

An underwater nuclear explosion is characterized initially by the formation and propagation of an underwater shock wave. The dissipation of heat at the shock front causes the water to vaporize in the vicinity of the explosion and results in the formation of a large bubble of steam. The interaction of the bubble and the shock wave with the air-water interface produces various surface phenomena, including spray domes, columns, plumes, base surges, radioactive pools and surface waves. If the explosion is on or near the bottom, a crater is formed.

An underwater nuclear explosion also can result in thermal, nuclear, and electromagnetic radiation above the surface, but these phenomena are insignificant, except in the case of a shallow burst. These phenomena, when caused by a shallow burst, should approximate those from a shallow underground explosion.

#### 2-67 Underwater Bubble

An underwater nuclear explosion releases large amounts of thermal and nuclear radiation, essentially all of which is absorbed by the surrounding water within several feet of the explosion (some radiation in the visible spectrum can be radiated to greater distances, depending on the transparency of the water).

During the early stages of the explosion, the warhead materials attain a very high temperature (tens of millions of degrees) and a very high pressure (on the order of millions of atmospheres). Energy acquired by these materials is transferred to the layer of water nearest the bomb, which is heated and compressed and which, then, heats and compresses the next outward layer. A compression wave (or hydrodynamic shock front) is formed by this mechanism, and this wave moves outward from the

explosion at a speed greater than that of sound. This shock front expands faster than the material that it engulfs, which also moves outward, but at a slower rate.

As the shock front moves away from the point of explosion, energy is dissipated as heat, which raises the temperature of the water engulfed by the shock front. The largest temperature increase occurs near the center of the explosion, where the water is not only vaporized but dissociated as well. At greater distances, the water is vaporized and turned to steam at the shock front. At still greater distances, the water is not heated by the shock front sufficiently to boil. The bubble that is formed does not have a clearly defined "surface." Figure 2-92 shows this progression in a highly stylized form.

Thus, shortly after an underwater burst an expanding bubble is formed, which is composed largely of vaporized water with radioactive bomb debris at its center, surrounded by heated water. Large quantities of neutron-activated elements in the sea water are also present in the steam and layer of surrounding water; however, the total induced radioactivity is relatively small compared to the fission product radioactivity. Continued expansion of this bubble reduces the pressure within it. As the bubble pressure falls below the vapor pressure of the heated water, additional water flashes to steam at the interface of the bubble and the water.

If the explosion is deep underwater, the bubble continues to expand at a decreasing rate until a maximum size is reached. If it is not too near the surface or the bottom, the bubble remains nearly spherical to this point. As a result of the inertia of the water surrounding the expanding bubble, the bubble actually overexpands; i.e., when it attains its maximum size, its pressure is below the ambient water pressure. The high pressure around the bubble then causes it to contract with an increase in its pressure and

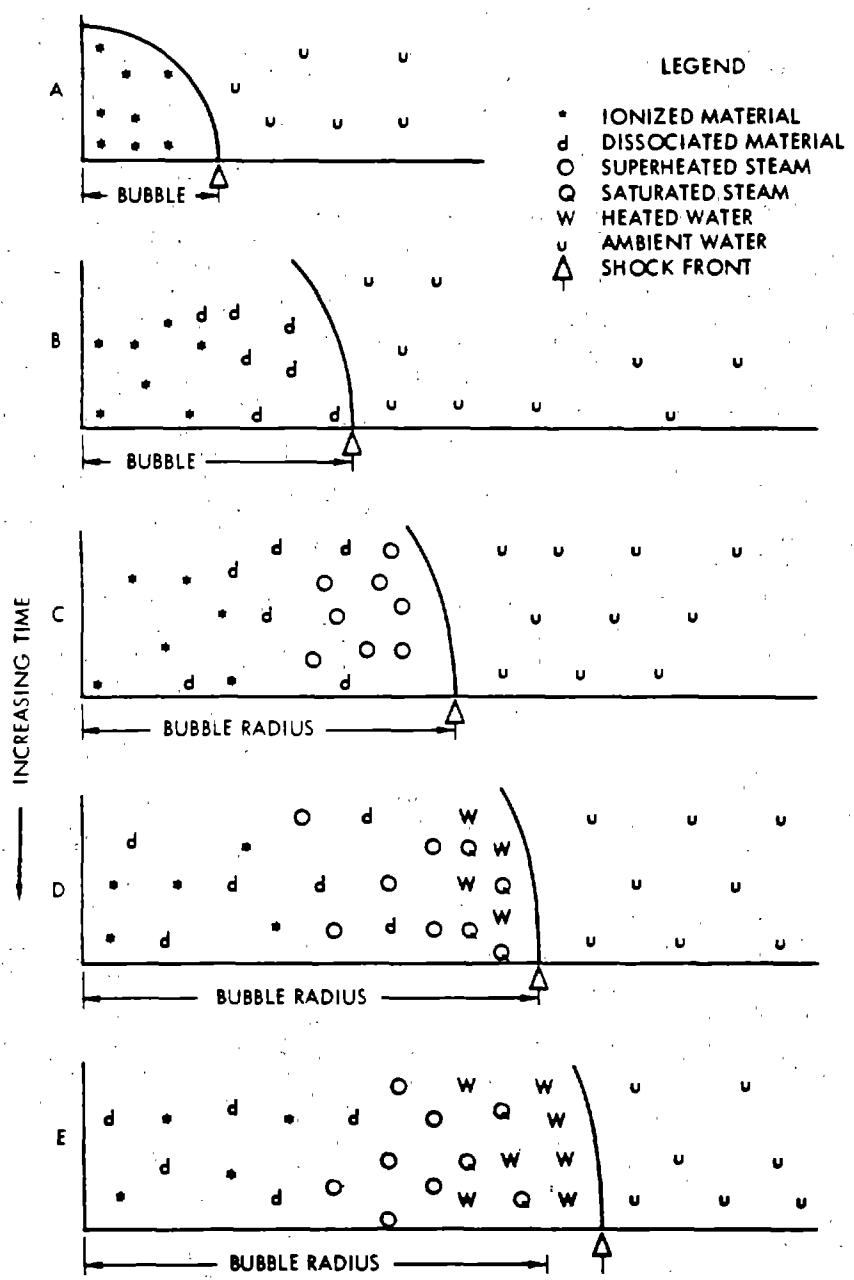


Figure 2-92. [REDACTED] Representation of Bubble Development [REDACTED]

2-194  
222

condensation of some of its steam. Since the hydrostatic pressure is larger at the bottom of the bubble than at the top, the bubble does not remain spherical during the contracting phase. The bottom moves upward faster than the top (which may even remain stationary) and contacts the top to form a toroidal, or doughnut-shaped, bubble as viewed from above. This causes turbulence and mixing of the bubble contents with the surrounding water.

The inertia of the water set in motion by the bubble contraction causes it to overcontract, and its internal pressure becomes very much higher than the ambient water pressure. A second compression wave (the first bubble pulse) commences when the bubble reaches its minimum volume. This wave has a lower peak pressure, but a longer duration, than the initial shock. A second cycle of bubble expansion and contraction begins.

When the bubble pulse is emitted, the bubble surface becomes exceedingly unstable; a multitude of water spray jets shoot inward, thereby condensing much of the steam and degrading the bubble energy. Figure 2-93 shows the relative partitioning of the energy of the explosion with time qualitatively.

The bubble is relatively stationary during the initial expansion cycle, but upon contracting, it begins to migrate upward under the action of buoyant forces. The rate of upward migration is greatest when it is contracted and nearly zero when it is expanded.

If the bubble is far enough below the surface, it continues to pulsate and rise, though after three complete cycles enough steam will have condensed to make additional pulsations unlikely. During the pulsation and upward motion of the bubble, the water surrounding the bubble acquires considerable upward momentum and eventually breaks through the surface with a high velocity (about 200 mph for Wigwam, a deep underwater shot) thereby creat-

ing a large plume.

If the explosion is at a shallow depth, the bubble may break through the surface during one of the early pulsations, or even during the first pulsation cycle. If such a breakthrough occurs when the bubble pressure is higher than ambient (as with a very shallow explosion), a phenomenon known as a "blowout" occurs. If a breakthrough occurs when bubble pressure is below ambient, "blowin'" occurs. The surface effects differ markedly for the two phenomena (see Figures 2-100 and 2-101 and accompanying text). A migrating bubble will not produce a bubble pulse if the bubble minimum occurs at or above the original water surface.

A strongly migrating bubble might continue to expand and not pass through a maximum size, somewhat like a balloon rising through the atmosphere. This is the balloon effect. A bubble migrating in this manner will not emit any bubble pulses. The conditions that cause a nuclear bubble to balloon rather than to pulsate are still subject to speculation; however, the absence of an expected bubble pulse might be explained by the balloon effect.

The maximum bubble radius and the first bubble period (time between burst and first minimum) are related to yield and depth of burst, as illustrated by the following two equations, which pertain to submerged bursts, i.e., the depth of burst,  $d_b$ , is greater than  $A_{\max}$ :

$$A_{\max} = J' \frac{W^{1/3}}{Z^{1/3}},$$

$$T_1 = K' \frac{W^{1/3}}{Z^{5/6}},$$

where

$A_{\max}$  = Maximum bubble radius (ft),

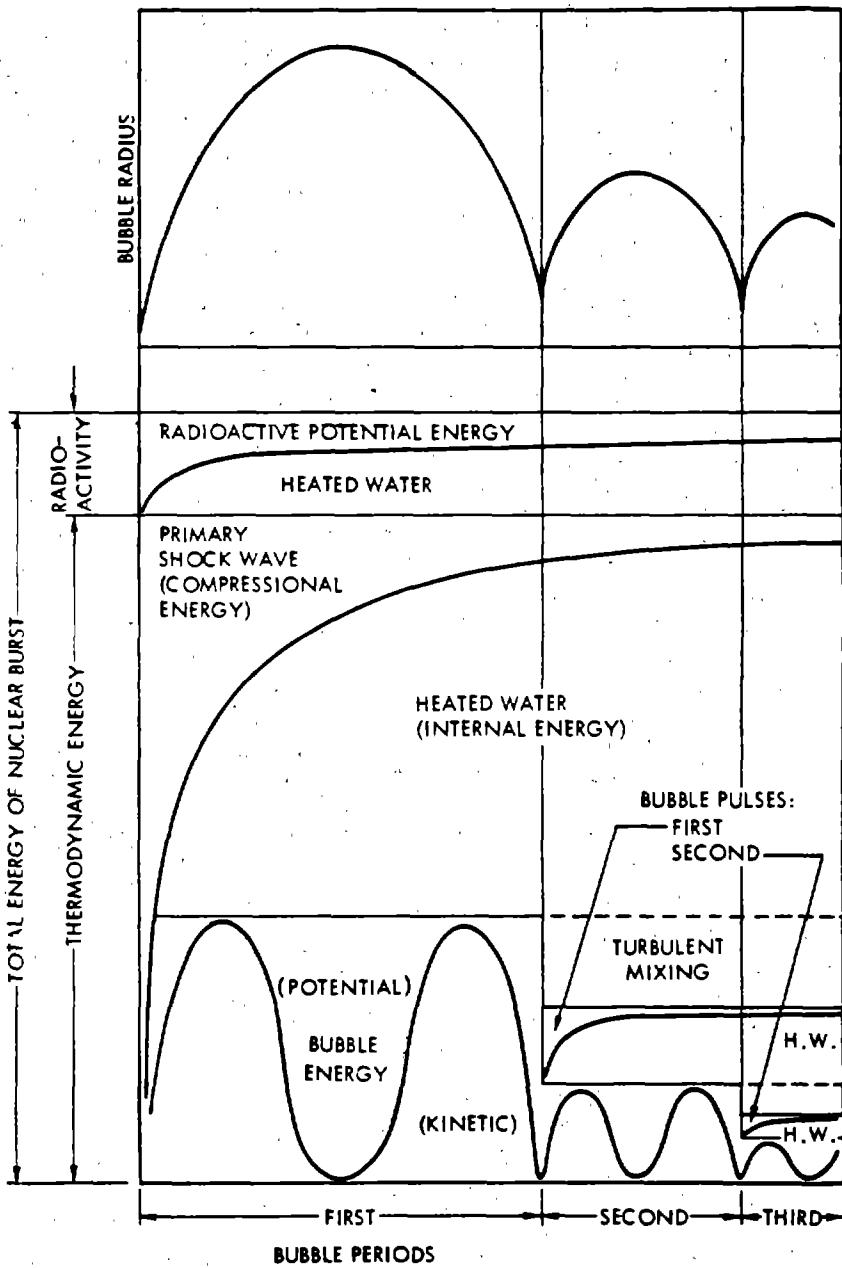


Figure 2-93. Energy Distribution Following an Underwater Nuclear Burst

$J'$  = Empirical constant, 1500,

$K'$  = Empirical constant, 515,

$T_1$  = First bubble period (sec),

$W$  = Yield (kt),

$Z$  = Hydrostatic head ( $d_b + 33$ ) (ft).

The form of the equations is the same as those given by Cole for high explosives. The constants,  $J'$  and  $K'$ , are slightly different because an underwater nuclear burst forms a steam bubble rather than gas bubble (as do high explosives) and because of other differences, mainly the distribution of total energy between bubble energy, shock wave energy, and residual radioactive energy.

It is likely that the constants  $J'$  and  $K'$  are actually somewhat dependent on depth. This can be understood qualitatively as follows:  $J'$  and  $K'$  implicitly include the fraction of explosion energy included in the bubble. As the depth of burst is increased, a smaller fraction of explosion energy is converted to steam by the expanding shock wave (and more energy goes into heating water) because of the greater hydrostatic pressure that must be overcome to boil water.

The second and third bubble maximum radii, the periods between minima, and the migration between periods, depend on the fraction of bubble energy that remains following succeeding bubble minima. The energy loss that occurs is due primarily to steam condensation at bubble minima as previously described, but the amount of energy loss is influenced by the depth at which the minimum occurs. An analytical representation of the energy as a function of bubble migration, which is best solved by use of a high-speed computer, has been developed,\* however, satisfactory solutions to bubble problems can be obtained by use of curves derived from the rep-

resentation, as illustrated in Problem 2-28.

### **WATER SHOCK WAVE AND OTHER PRESSURE PULSES**

The initial shock wave from an underwater explosion propagates radially from the source. This shock wave is characterized by an abrupt, virtually instantaneous, increase in pressure followed by a decrease that is approximately exponential. Near the explosion, the peak shock wave pressure is extremely high, but energy losses to the water cause the pressure to decrease somewhat faster than inversely with radius. Similarly, early shock wave propagation velocities are high, but by the time the peak pressure falls to about 3,000 psi, the propagation velocity becomes nearly equal to the acoustic speed in water (about 5,000 ft/sec), and the energy losses become small.

If an explosion takes place far from either the surface or the bottom, the shock wave remains spherical as long as it propagates into water having constant acoustic velocity. This velocity depends on temperature, hydrostatic pressure, and salinity, however, and in regions of the ocean in which significant sound velocity gradients exist, the shock wave can be bent or refracted. Refraction can either increase or decrease the shock wave pressures locally, depending on ambient water conditions. No general prediction techniques can be given, but the subject is discussed further in paragraph 2-71.

When a shock wave moving in water encounters another medium, it may be reflected as a tensile or rarefaction wave, as in the case of a water-air boundary; a compression or shock wave, as in the case of a water-bottom interface if the angle of incidence is not too far from the normal; or a distorted pulse having in general

\* This expression is described in "The Parameters of Underwater Nuclear Explosion Bubbles" (see bibliography).

both a positive and a negative phase, as in the case of more glancing incidence at the bottom. These are discussed separately in the following paragraphs.

### 2-68 Surface Reflection

The rarefaction wave, generated by the reflection of the primary shock wave from the surface, propagates downward and relieves the pressure behind the primary shock wave. If the shock wave is treated as a weak (acoustic) wave, this interaction instantaneously decreases the pressure in the primary shock wave to a value that might be well below the vapor pressure of the water, as shown by the broken line in Figure 2-94, Point A. Cavitation occurs in seawater when its pressure decreases to a value somewhat below its vapor pressure. The pressure of the primary shock wave is, therefore, reduced to a value which, when compared with the peak pressure, is usually so close to ambient water pressure that the shock wave pulse appears to have been truncated, i.e., reduced to ambient pressure.

For a strong primary shock wave, the reflected rarefaction wave propagates into water that has already been set in motion by the shock wave. Therefore, the rarefaction wave arrives earlier than predicted from the acoustic approximation, and the pressure cutoff is not instantaneous. This effect typically gives a pulse shape shown by the solid line for Point A of Figure 2-94. The shallower the point at which pressure measurements are made, the sooner the primary shock pulse is "cut off" and, hence, the shorter its duration (see Figure 2-94, Point B). At sufficiently shallow locations, the rarefaction wave interacts with the shock front and reduces the peak pressure (see Figure 2-94, Points C and D). The region in which peak pressure is reduced is known as the "anomalous region."

The effects of surface reflection decrease rapidly with increased depth of either the explo-

sion or the point of measurement. Conversely, as the depth of burst is decreased (or the yield increased for a given depth of burst), the effects increase. The size of the anomalous region increases with decreased depth of burst until, for a surface burst, the anomalous region <sup>includes</sup> all points beneath the water surface except those close to the explosion and directly under it.

A limited amount of data are available concerning the reflection of shock waves from an ice layer. To date all tests have been with relatively small explosive charges (a majority of the test shots have been in the 1- to 40-lb range, with one shot of 630 lb). The situation is complicated by reflection and refractions at both the water-ice boundary and the ice-air boundary.

### 2-69 Bottom Reflection

Under certain circumstances, the shock wave from the bottom can be more damaging to surface ships and shallow submarines than the primary shock. Although the peak pressure of the reflected wave is usually smaller, the wave arrives at a steeper angle, and therefore may induce more damaging shock motion to a target at or near the surface.

### 2-70 Secondary Shocks and Pressure Waves

An underwater burst can cause compression waves in addition to those described above, but these effects are usually negligible. These waves include retransmitted pulses, cavitation pulses, bubble pulses, and others that are described briefly below.

- **Retransmitted Pulses.** Upon reflecting from the surface and bottom, some primary shock energy is transmitted into the air or bottom material, and some of this energy can be retransmitted back into the water.
- **Cavitation Effects.** As noted earlier, the reflection of the shock wave from the sur-

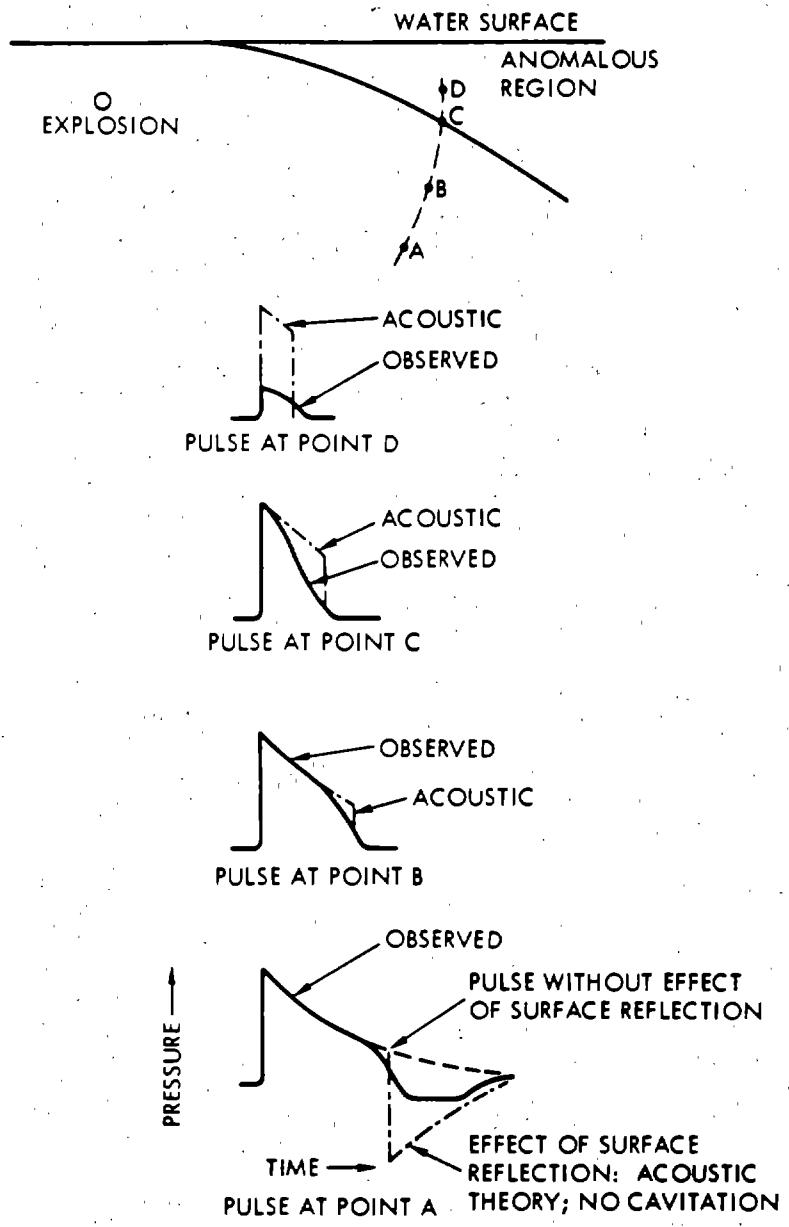


Figure 2-94. [REDACTED] Typical Pressure Pulses Affected by Surface Reflection [REDACTED]

face can lead to bulk cavitation below the surface. During the period of cavitation, the cavitated region can absorb further shock waves impinging on it. In the formation of the cavitation region, the rupture of the water by the shock wave causes a liquid surface layer (sometimes called "spall") to project upward in almost a ballistic trajectory. The impact of this spall when it returns to the surface can lead to further secondary shock waves. These shock waves account for the occasional larger damage to ships at intermediate ranges compared with the damage at shorter or longer ranges.

- *Bubble Pulses.* If an explosion is deep enough for one or more bubble pulsations to occur, compression waves are generated at the time of each bubble minimum.
- *Other Pulses.* All pressure waves are subject to multiple reflection from the surface and bottom. Also, in areas of irregular bottom topography, more than one reflected pulse can be generated.

Figure 2-95 shows typical shock wave and pressure pulse patterns for various burst and measurement conditions.

## 2-71 Refraction of Shock Waves

The shock front from an explosion far from a boundary (surface, bottom, etc.) remains spherical provided that it expands into water having constant acoustic velocity (isovelocity). However, the acoustic velocity in water depends on the temperature, salinity, and hydrostatic pressure, and these properties are not necessarily constant throughout a large body of water. As a result of variations in these properties, generally in horizontal layers, a region of water can have a characteristic acoustic velocity profile (sound velocity vs depth). Under such conditions, the shock wave is bent (refracted) because one part of the wave moves faster than another.

Refraction of the shock wave can result in convergence and reinforcement of the shock wave. This reinforcement commonly occurs along a surface called a "caustic." This effect may be illustrated by the use of a ray diagram\* (Figure 2-96). The acoustic velocity profile that corresponds to the ray diagram is also shown in the figure. The formation of several caustics for one burst is observed frequently. Regions of relatively low pressure also occur, such as the "shadow zone" above the caustic in the figure.

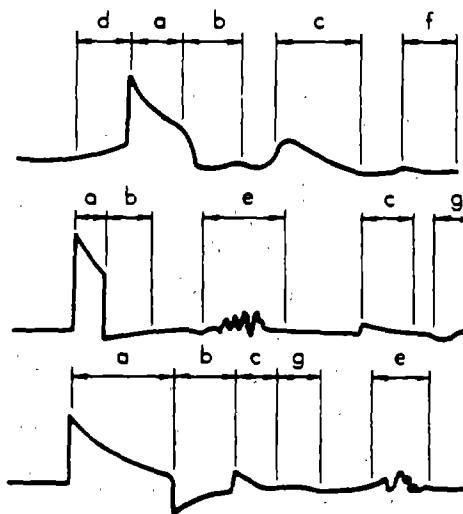
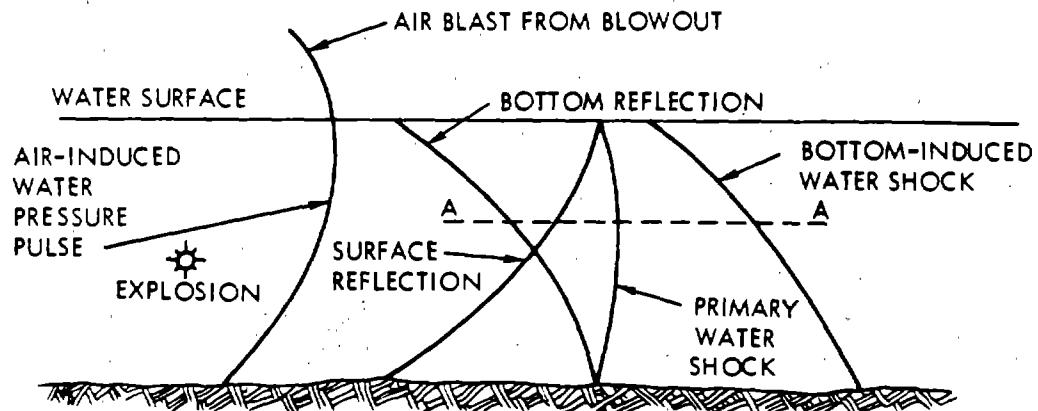
The caustic can reinforce the peak pressure by a factor of five or more over the isovelocity value, while the pressure observed deep in the shadow zone can be essentially negligible. Shock wave impulse amplification factors do not go through a maximum at the caustic position. They remain much closer to unity than do peak pressure and energy factors.

As a result of ocean currents and underwater swells, the acoustic velocity profile in the ocean is rarely stable. Thus, the location of the caustics can shift rather quickly and unpredictably (similar to optic mirages).

Common types of sound velocity profiles can give rise to caustics at various distances greater than about one mile. In particular, in about half of the areas of the oceans, a caustic occurs at what is known as the convergence zone, typically 30 (10 to 40) miles from an underwater burst. Therefore, it is conceivable that a submarine might suffer damage from its own multi-kiloton weapon detonated at a distance of about 30 miles if it happened to lie on the caustic of its shot.

In Figure 2-96, sound speed is considered to vary with depth only. Actually this would rarely happen. The velocity can vary considerably across the ocean within the range of interest. Generally, the region of focusing is sharper

\* A ray is generated by a curve that is always perpendicular to the expanding shock front.



1. SHALLOW EXPLOSION IN SHALLOW WATER  
MEASUREMENT IN SHALLOW WATER
2. DEEP EXPLOSION IN MUCH DEEPER WATER  
MEASUREMENT AT SHALLOW DEPTH
3. DEEP EXPLOSION IN MUCH DEEPER WATER  
MEASUREMENT AT DEEP DEPTH

a. PRIMARY SHOCK WAVE	d. BOTTOM-INDUCED PRESSURE PULSE
b. SURFACE REFLECTION	e. SHOCK FROM CAVITATION COLLAPSE
c. BOTTOM REFLECTION	f. AIR-INDUCED WATER SHOCK
	g. OTHER

Figure 2-95. [REDACTED] Typical Shock Wave Patterns Along Line A-A [REDACTED]

2-281  
229

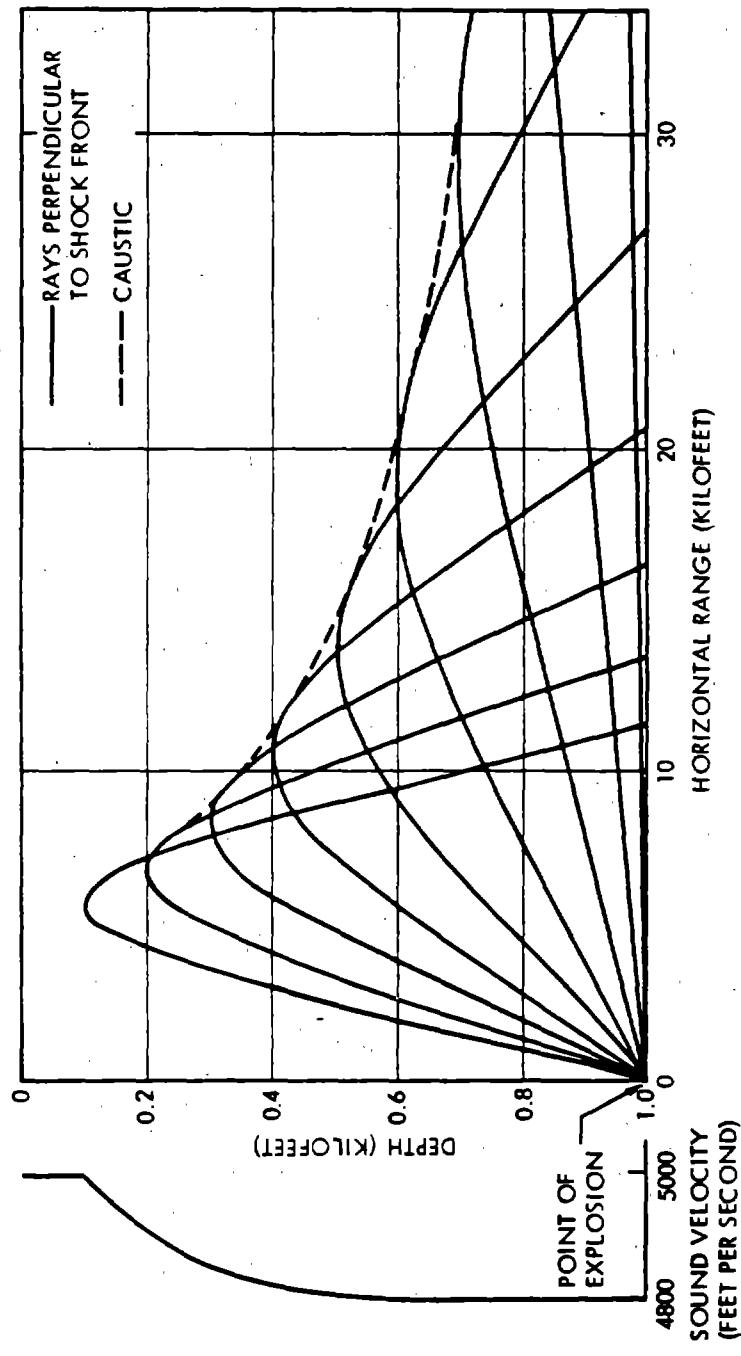


Figure 2-96. Ray Diagram for an Idealized Velocity Profile

and the maximum value of the amplification is greater for smaller yields.

## 2-72 Air Blast

The air blast wave has one to three pulses of various amplitudes, depending on the burst depth and the location of the observation point with reference to surface zero. These pulses are generated by two underwater explosion mechanisms: One is the underwater shock wave that transmits a portion of its energy across the water-air interface. The other is the underwater explosion bubble, which manifests itself in two ways: for burst depths shallower than about  $35W^{1/3}$  feet, the bubble vents, causing an air pressure pulse; for burst depths deeper than  $35W^{1/3}$  feet, a spray dome is pushed up by the expanding bubble, causing a bow wave.

For burst depths shallower than about  $50W^{1/3}$  feet the transmitted pulse and the bubble generated pulse are formed almost simultaneously, resulting in a single intense pressure pulse over surface zero. For burst depths between  $50W^{1/3}$  feet and about  $150W^{1/3}$  feet, up to three pulses can be seen. The transmitted shock in air bifurcates near surface zero to form two air pulses, and the bow shock causes the third air pulse. For burst depths deeper than about  $150W^{1/3}$  feet, the spray dome rises so slowly that no bow shock is formed and only the air pulse from the transmitted shock is important.

This discussion of the generation of air blast from underwater bursts is a simplified discussion of a complex subject. Much analytical, theoretical, and experimental work has been done to understand the physics of air blast generation. More complete discussions of the subject are given in Malme, Carbonell and Dyer (1966); Peckham and Pittman (1968); Pittman (1968); and Rudlin and Silva (1960) (see bibliography). Only a limited number of air blast measurements are available from nuclear weapon tests. The data are not sufficient to form a basis

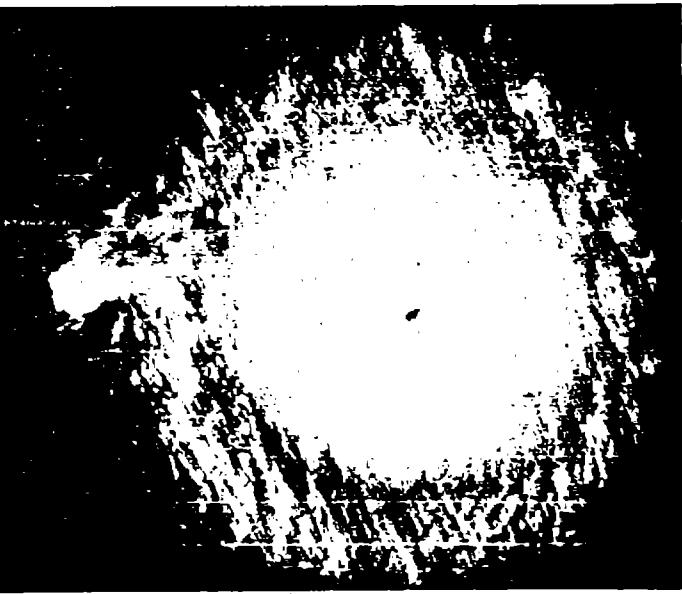
for predicting air blast for a spectrum of burst depths and pressure levels. The available predictive measures are based mainly on high explosive tests as described in Problem 2-31.

## SURFACE EFFECTS OTHER THAN WAVES

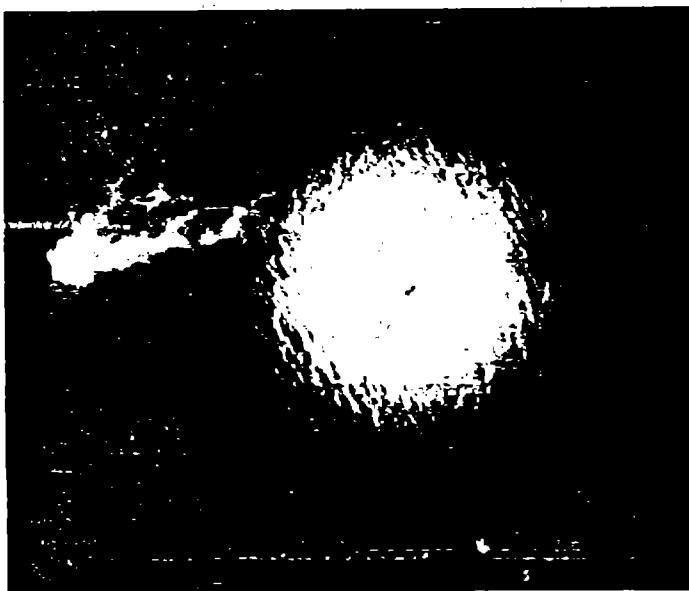
The first surface effect of an underwater burst is caused by the intersection of the primary shock wave and the surface. Viewed from above, the effect frequently appears to be a rapidly expanding ring of darkened water, often called the "slick" (Figure 2-97). A white circular patch (the "crack") follows closely behind the darkened region. The crack probably is caused by underwater cavitation produced by the reflected rarefaction wave. Shortly after appearance of the crack, the water above the explosion rises vertically and forms a white mound of spray, called the "spray dome" (Figure 2-98). This dome is caused by the velocity imparted to the water near the surface by the reflection of the shock wave and the subsequent breakup of the surface layer into drops of spray. Additional slick, crack, and spray dome phenomena may result if the bottom-reflected shock waves and bubble-pulse compression waves reach the surface with sufficient intensity (Figure 2-99).

The spray dome from a shallow burst changes rapidly to a shallow column formed by the upward and outward motion of the water surrounding the explosion bubble. If blowout occurs, the upper part of the column is likely to resemble a crown, which contains explosion products blown out of the column (Figure 2-100). If blowin occurs, the crown is likely to be absent (Figure 2-101a). In its later stages, the column may break up into column jets (relatively broad spouts of water that disintegrate into spray as they travel through the air) (Figure 2-101b).

If the burst is sufficiently deep to prevent blowout, but shallow enough for the bubble to continue to oscillate as it approaches the



(b) CAVITATION PULSE  
Slick and Spray Ring  
(0.73 sec after burn)



(a) PRIMARY SHOCK WAVE  
Slick and Spray Dome  
(0.20 sec after burn)

Figure 2-97. Slick Spray Dome and Cavitation Pulse Spray Ring (aerial view)

2-204  
232

Reproduced from  
best available copy.



Figure 2-98. Spray Dome (3.3 sec after burst)

2-206  
233

Reproduced from  
best available copy.

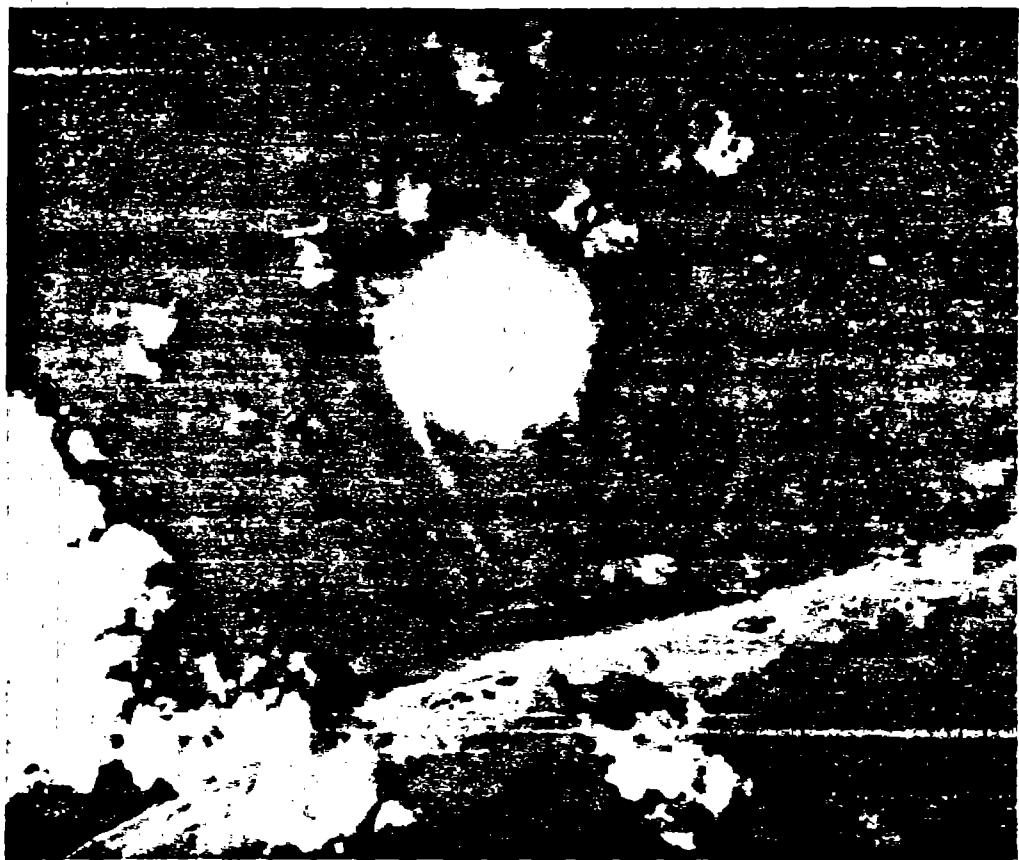


Figure 2-99. [REDACTED] Bottom-Reflected Shock Wave Slick  
(aerial view 1.38 sec after burst) [REDACTED]

2-266  
Z34

Reproduced from  
best available copy.

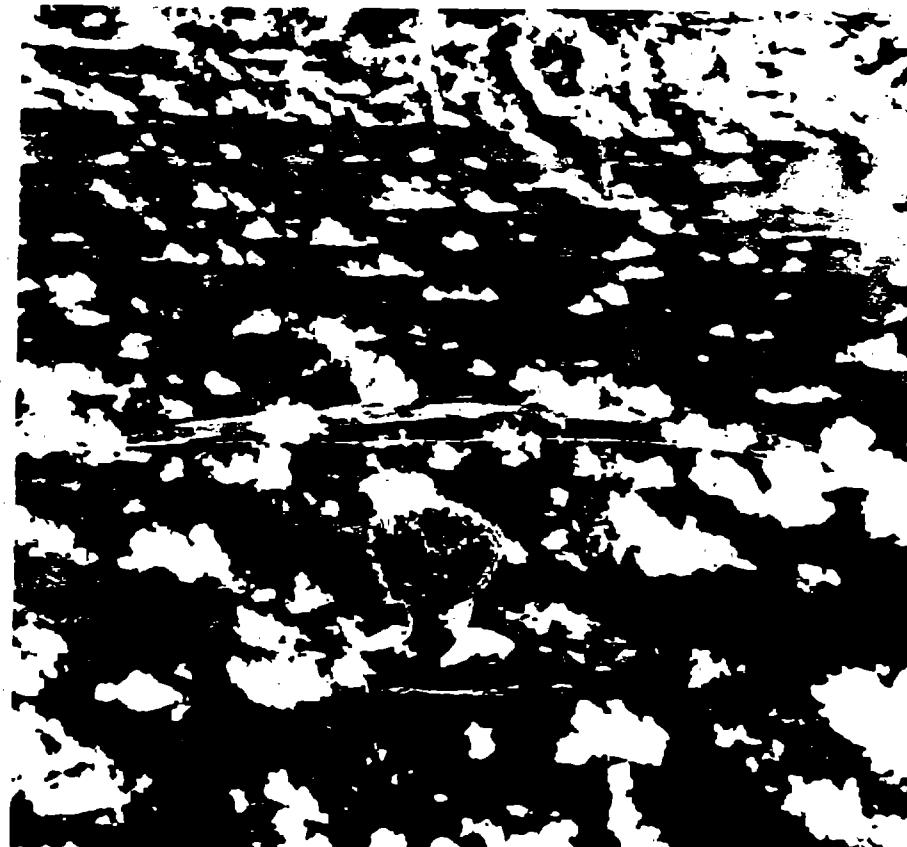


Figure 2-100. [REDACTED] Very Shallow Burst Showing Crown of Explosion Products on Column (oblique aerial view 0.7 sec after burst) [REDACTED]

2-202  
235

Reproduced from  
best available copy.



(a) EARLY STAGE  
(2.5 sec after burst)

(b) LATER STAGE SHOWING COLUMN JETS  
(8.2 sec after burst)

Figure 2-101. Column from Shallow Underwater Burst (no blowout)

2-268  
236

Reproduced from  
best available copy.

Table 2-8. Classification of Burst Depth Categories

Classification	Definition
Near surface	$0 < d_b < 21W^{1/3}$
Very shallow	$21W^{1/3} < d_b < 75W^{1/3}$
Shallow	$75W^{1/3} < d_b < 240W^{1/4}$
Deep	$240W^{1/4} < d_b < 700W^{1/4}$
Very deep	$700W^{1/4} < d_b$
Contained*	$1550W^{1/4} < d_b$
No spray dome*	$2500W^{1/3} < d_b$

\* These values are derived from H.E. tests. They have not been confirmed by nuclear tests; therefore, they are to be interpreted as "containment possible" and "possible limiting depth for spray dome formation."

surface, plumes of upwelled water and steam can occur (Figure 2-102).

Upon subsidence of the column and plumes from an underwater explosion, a "doughnut-shaped ring" of mist is formed, which is called the base surge and which is highly radioactive (Figure 2-103). This ring, or series of rings, expands radially in the absence of wind, but in the presence of wind, it elongates and drifts with the wind until it dissipates. A train of surface waves also expands radially from the explosion.

After dissipation of the base surge, the water surface around the explosion appears white (Figure 2-104). This "foam-patch" results from the upward motion of water and gaseous explosion products in the vicinity of the bubble, their spreading over the surface of the patch, and their downward motion at the edge of the patch. During its later stages, the foam-patch appears as a ring of foam and debris that is left floating where the water circulates downward.

As previously noted, the surface phenomena described above vary with the weapon yield and the depth of burst. Although clear-cut distinctions cannot be made in all cases, six explosion categories have been established to aid in establishing safe weapon delivery criteria. These categories are defined in Table 2-8. The classifications have been tested at yields as large as 30 kt, but they probably are valid for yields up to about 100 kt.

The limits of the relations given in Table 2-8 are plotted in Figure 2-105, and the phenomena that establish the categories are described below.

- **Near-surface bursts.** The layer of water above the burst is vaporized by the explosion. The surface phenomena for this type of burst and the associated hazards are unknown. The radiological hazard of the base surge is considered to be unimportant compared with air blast and fallout

hazards.

- **Very shallow bursts.** The bubble vents early during the first expansion cycle, i.e., when the bubble pressure is greater than ambient, and fission products are blown out at that time.
- **Shallow bursts.** The bubble vents late during the first cycle, after the bubble pressure has dropped below ambient, and fission products are blown in.
- **Deep bursts.** The depth of burst is equal to or greater than the radius of the fully expanded bubble, but not as deep as the very deep burst described below.
- **Very deep burst.** The explosion is at sufficient depth that the bubble breaks up, becomes a vortex ring, or loses its identity before reaching the surface.

The surface radioactivity from a very deep burst is operationally insignificant within about an hour and may be faint enough to escape detection.

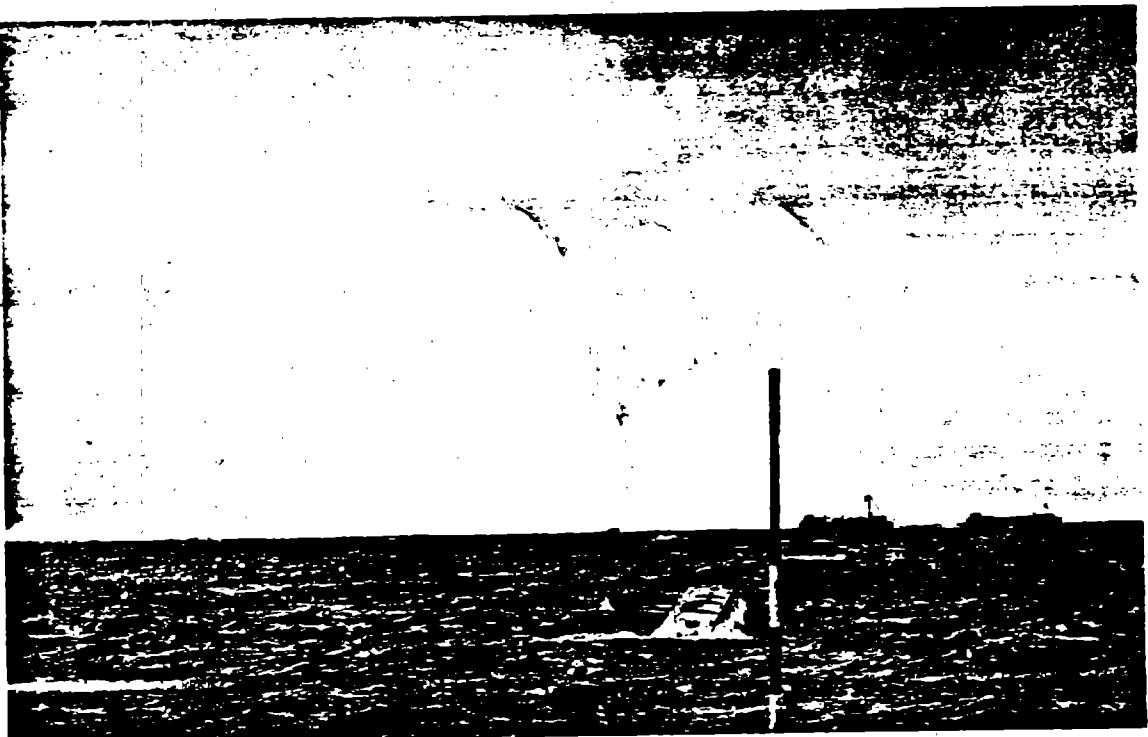


Figure 2-102. [REDACTED] Plume from Upwelling of Water from Very Deep Burst (24 sec after burst) [REDACTED]

2-246  
238

Reproduced from  
best available copy.



Figure 2-103. Base Surge "Doughnut-Shaped" Ring (oblique aerial view 100 sec after burst)

2-244  
239

Reproduced from  
best available copy.



Figure 2-104. [REDACTED] Foam Patch (oblique aerial view 8.3 min after burst) [REDACTED]

2-242  
240

Reproduced from  
best available copy.



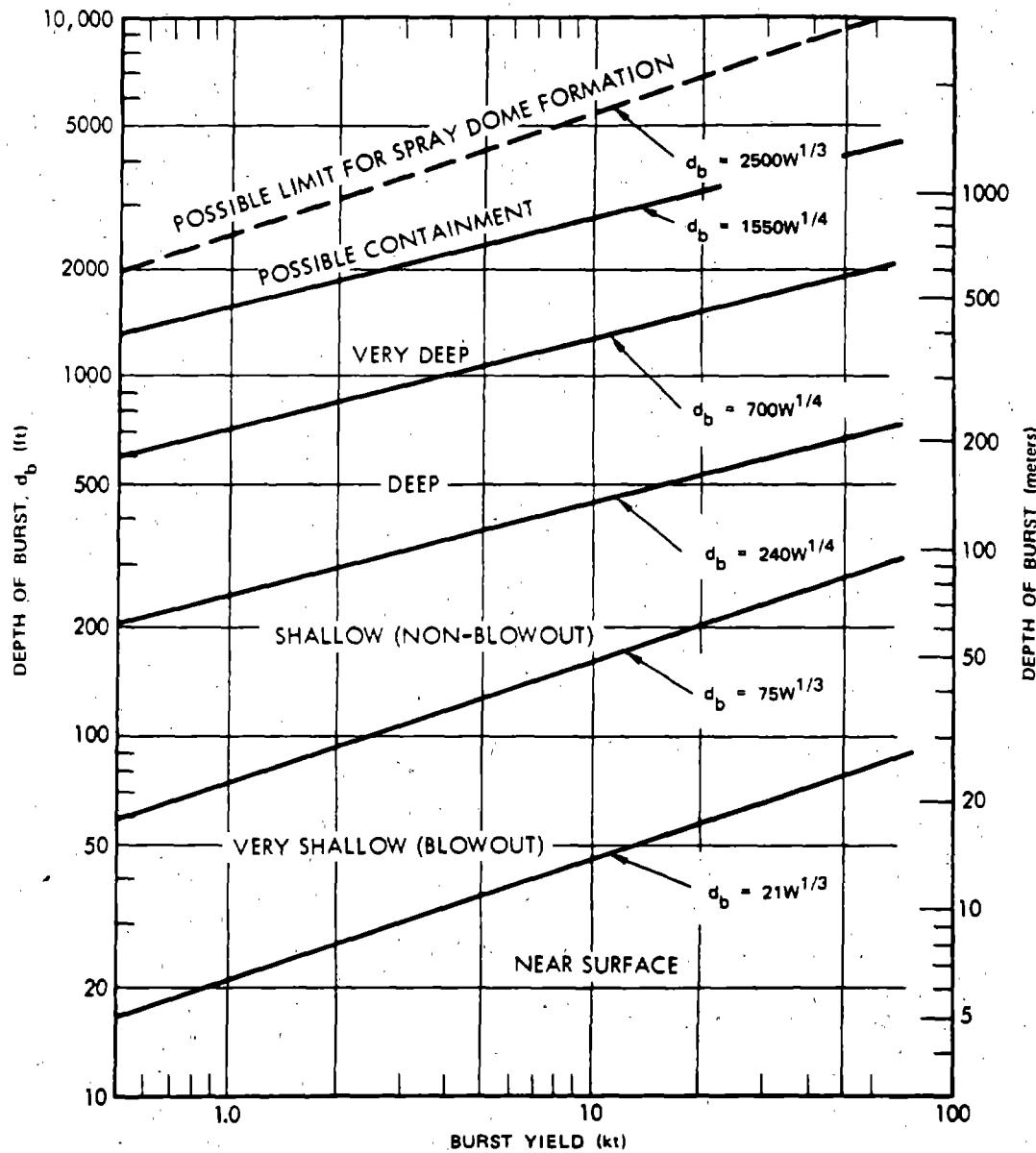


Figure 2-105. Classification of Underwater Nuclear Bursts

2-242  
241

## WATER SURFACE WAVES

### 2-77 Generation and Propagation of Water Surface Waves

A submerged nuclear explosion, like any other physical event that produces a localized disturbance on the water surface, generates a group of surface waves that expand radially. The characteristics of explosively generated waves depend upon the yield, the depth of burst, and the range to the point of observation. If the water is sufficiently shallow, the bottom contour also can affect the generation and propagation of the waves.

The following physical description of the wave generation process and the succeeding prediction technique are based on:

- Laboratory experiments with small H.E. charges
- Wave data for the nine nuclear shots that have been fired on or in the lagoons at Eniwetok and Bikini, as listed in Table 2-9.
- Wave data for all the known tests in water with H.E. charges larger than 10 lb, as listed and referenced in Table 2-10.

Surface waves produced by an underwater explosion are generated by pulsations of the cavity formed at the surface when the oscillating bubble breaks through the surface (vents).

At a short range, within a few cavity radii, the first wave crest is so high and steep that it is unstable, and it spills forward turbulently and dissipates much of its energy. However, as the wave train expands and attenuates, the waves become shallow and smooth, their number increases, their energy remains nearly constant, and the highest wave appears successively later in the train. A wave gage record for such an expanded wave train is shown in Figure 2-106. The height  $H$  of the highest wave (trough-to-crest) decreases nearly inversely with range  $R$ ; but the length, speed, and period all remain

nearly constant for this peak wave, which is the one temporarily located at the first anti-node of the wave envelope as the waves move back in the envelope.

An approximate mathematical theory has been developed for shallow waves propagating from a shallow disturbance on the surface of water with constant depth. The results of this theory compare well with measured wave trains when a motionless "pseudo-cavity" is selected to approximate the wave generator or initial conditions. The "pseudo-cavity" is a shallow motionless depression of the water surface near the explosion. Its shape is derived empirically to correspond with the waves measured far from an explosion, but it does not necessarily correspond accurately with the actual shape of the water surface at any time.

All of the known measurements of peak wave height over deep water for charges greater than 10 lb are plotted in Figure 2-107. The vertical bars indicate the variation of HR for repeated shots and/or various gage ranges  $R$ . There is little discernible effect of depth of burst except near the "upper critical depth," where the H.E. charges were only partially submerged and where the peak wave height nearly doubled. Although current studies indicate that the upper critical depth effect may exist for nuclear as well as for H.E. charges, there is no firm evidence to support the inference as yet.

A plot comparable with Figure 2-107 of the data for H.E. charges smaller than 10 lb exhibits a pronounced upward hump in wave height versus depth of burst at  $d_b \approx 3W_{HE}^{0.3}$  (and possibly also at  $d_b \approx 8W_{HE}^{0.3}$ ). This increase in wave generation efficiency at the "lower critical depth" occurs when the expanding underwater cavity ruptures the layer of water above it (or vents) just before it becomes fully expanded. For large submerged explosions, the expanded bubble becomes tangent to the surface when the

Table 2-9. Measured Wave Data from Nuclear Tests

NUMBER SERIES SHOT	YIELD $W \text{ (kt)}$ $100(W)^{1/4}$	WATER DEPTH AT CHARGE $d_w \text{ (ft)}$	DEPTH OF BURST $d_b \text{ (ft)}$	PEAK WAVE* HEIGHT $\times$ RANGE		CAVITY RADIUS $R_c \text{ (ft)}$	$d_w/100(W)^{1/4}$	$HR/2 \times 10^4 \sqrt{W}$
				HR/2,000 (ft) <sup>†</sup> min - max	HR/2,000 (ft) <sup>†</sup> min - max			
1 HARDTACK UMBRELLA			140	140				
2 HARDTACK WAHOO		3,000	500					
3 CROSSROADS BAKER	23.5 220	180	90	36 - 60		1,000 <sup>‡</sup>	0.82 Shallow	0.74 - 1.24
4 WIGWAM	32 238	15,000	2,000	118		490 <sup>†</sup>	63 Very Deep	2.08
5 REDWING FLATHEAD		120	0					
6 REDWING DAKOTA		140	0					
7 REDWING NAVAHO		230	0					
8 CASTLE UNION	7,000 916	145	7	232 - 312		1,000 <sup>†</sup>	0.16 Shallow	0.16 - 0.28
9 CASTLE YANKEE	13,500 1,080	220	7	426 - 438		1,000 <sup>†</sup>	0.20 Shallow	0.37 - 0.38

\*H is twice the measured height of the peak crest except for shots 8 and 9 where H is the measured height of the first crest from the following trough. H is corrected for uniform water depth =  $d_b$  by Green's law.

<sup>†</sup>Value deduced from measured surface wave train (Kaplan and Wallace, see bibliography) is a lower limit considerably smaller than actual values, which are unknown.

<sup>‡</sup>Measured values of the column radius (Young, DASA 1240-1(9)), see bibliography.

2-214  
245

Table 2-10. Measured Wave Data from Large H.E. Tests

SHOT	YIELD	WATER DEPTH	DEPTH OF BURST	PEAK WAVE HEIGHT	CAVITY RADIUS	$d_w/100(W)^{1/4}$	$HR/2 \times 10^4 \sqrt{W}$
	W (kt)	$d_w$ (ft)	$d_b$ (ft)	$HR/2$ (ft) <sup>2</sup>	R <sub>C</sub> (ft)		min - max
WES Test Series at Lake Ouachita (from Pinkston and from Whalin)							
125 lb	$0.625 \times 10^{-4}$	100	0 - 25	80 - 110		22.5	.90 - 1.24
385 lb	$1.97 \times 10^{-4}$	100	0 - 36	147 - 225		17.0	1.25 - 1.91
WES Test Series at Mono Lake (1965 - 1966)							
(Preliminary data by private communication with R. Whalin and M. Pinkston and from Walter)							
1965 - 6	$0.46 \times 10^{-2}$ (9,200 lb)	130	0	1650 - 1900	68	5.2	2.4 - 2.8
- 2			.67	2100 - 3900	69		3.1 - 5.7
- 4			1.04	2100 - 2850	71		3.1 - 4.2
- 3			1.40	1750 - 3000	74		2.6 - 4.4
-5, 7, 8, 9			9 - 51		61 - 80		
1966 - 3		$\approx 130$	5.2	1150 - 1250			1.7 - 1.8
- 2			23	850 - 1200			1.2 - 1.8
- 1			60	1300 - 1400			1.9 - 2.1
HYDRA 11a (Van Dorn) $W = 10^4$ lb HBX							
- 7	$0.723 \times 10^{-2}$ (14,450 lb)	300	140	1650 - 1970		10.3	1.94 - 2.31
- 8			80	975 - 1340			1.15 - 1.55
- 9			35.5	1260 - 1590			1.48 - 1.87
- 10			7.1	1610			1.88
- 11			15.9	1510 - 1840			1.77 - 2.16
- 12			15.9	1490			1.75
- 13			17.7	1450			1.71

2-248  
272

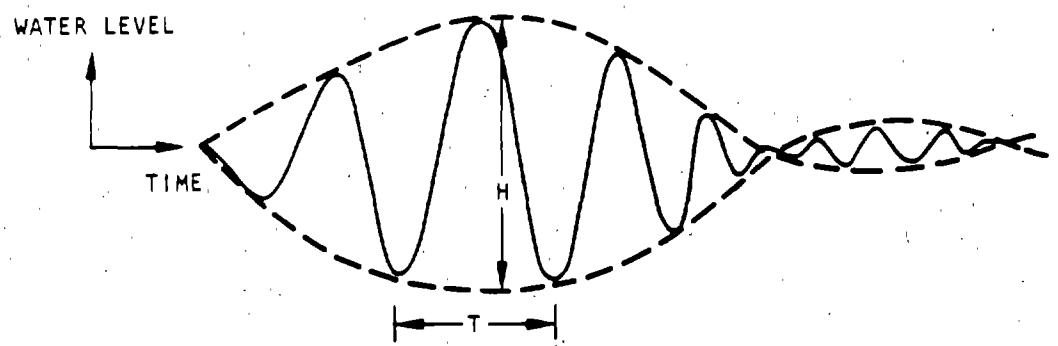


Figure 2-106. [REDACTED] Wave Gage Record for an Explosion-Generated Wave Train [REDACTED]

247  
2-218

burst depth  $d_b$  equals  $240W^{1/4}$ . The lower critical depth is somewhat smaller at about  $d_b = 170W^{1/4}$ . However, the effect on wave generation is much smaller for the larger charges in Figure 2-107, and the height of the peak wave generated by large explosions in "deep" water can be approximated simply by

$$HR/W_{HE}^{0.54} = 16 \pm 4,$$

where  $H$  is the amplitude of the maximum of the first envelope trough-to-crest in feet,  $R$  is the radial distance from the explosion in feet, and  $W_{HE}$  is the charge weight in equivalent pounds of TNT. An equivalent approximation is

$$HR = 40,500 (W)^{0.54} \pm 25 \text{ percent},$$

where  $W$  is the yield in kilotons and the other symbols are as defined above. Similarly, the length and period of the peak wave can be approximated by

$$L = 15.5 (W_{HE})^{0.288} \text{ ft.}$$

$$T = 1.74 (W_{HE})^{0.144} \text{ sec.}$$

These three relationships were derived empirically from test data for 125- and 385-lb H.E. charges and the two nuclear explosions shown in Figure 2-107. For a pseudo-cavity of a given shape, which has a potential (gravitational) energy comprising a fixed fraction of the explosive yield, all the dimensions of the cavity and the wave train are proportional to  $W_{HE}^{1/4}$  or  $W^{1/4}$  (Froude scaling), and the exponents in the three equations given above are 1/2, 1/4, and 1/8, respectively. Since the empirical exponent in the first equation was found to be 0.62 for small H.E. charges, it seems reasonable to suppose that the "theoretical" value of 1/2 may be the best

value to use for extrapolation to large yields (the high kiloton and megaton range). With this exponent, the data in Figure 2-107 have been replotted as a function of reduced water depth (rather than charge depth) for use in Problem 2-35 (Figure 2-128).

The horizontal line in Figure 2-128 can be used to predict the peak wave height in deep water. However, it can be derived by the following simple procedure to illustrate qualitatively the physical process of wave generation in "deep" water to define "deep." The approximation is made that an explosion in deep water at any depth of burst above the lower critical depth generates a parabolic (nearly hemispherical) cavity upon venting, and that the potential energy of this cavity  $E_c$  is equal to 5 percent of the explosive yield  $E_0$ . That is:

$$E_c = \frac{\pi}{6} \rho_w g R_c^4 = 0.05 E_0$$

$$= 0.05 \times 2.86 \times 10^{12} W \text{ ft-lb.}$$

This gives the following cavity radius, which is taken equal to the cavity depth and the radius of the plume (or column) of water projected upward:

$$R_c = 256 (W)^{1/4} \text{ ft.}$$

$$\text{if } d_w > R_c,$$

and if the density of seawater and the hydrodynamic yield of the explosion are taken as

$$\rho_w g = 65 \frac{\text{lb}}{\text{ft}^3}, \text{ and } e_0 = 1,025 \frac{\text{cal}}{\text{gm}}$$

This cavity radius is not much larger than the bubble radius and depth of burst corresponding to the lower critical depth. The restriction on

water depth  $d_w$  in the equation for  $R_c$  is taken as the minimum water depth that can be considered "deep" i.e., the depth for which the assumed cavity shape touches bottom as it vents.

The dissipative effects close to the cavity are approximated by the assumption that the leading peak wave crest spills forward and breaks turbulently at  $R = 2R_c$  to the limiting height of a wave that can propagate in a stable manner over deep water (the Michell limit, or  $H_{\max} = 0.14L$ ). Finally it is assumed that the amplitude of the wave envelope  $H$  is attenuated inversely with range  $R$  as it continues to expand without dissipation. This gives the "predicted" peak wave height when the water depth at the charge location is "deep" ( $d_w \geq 256W^{1/4}$ ) as

$$HR = 49,000 \sqrt{W},$$

which corresponds to the horizontal line in Figure 2-128. This "predicted" value can be used for depths of burst ranging from zero to at least five times the lower critical depth (at  $d = 170W^{1/4}$ ) judging by the comparison with WIG-WAM data, even though the cavity radius becomes too large for depths of burst much below the lower critical depth.

The line in Figure 2-128 can be extended into "shallow" water by a comparable simple procedure. In shallow water the cavity both touches bottom and vents to the atmosphere early during its expansion. Hence, much less work is done on the water by the expanding gaseous bubble, and much less energy is propagated as water surface waves over shallow water. Experimental data indicate that explosions in shallow water generate a dry cavity surrounded by a nearly vertical wall of water which extends upward as a thin lip to form the "column." A lower limit for the maximum radius of this cavity (or column) is given by the following relationship, which was derived from the energy calculated from measured wave trains

250  
2-223

over shallow water (Table 2-9) and which will be discussed in succeeding paragraphs.

$$R_c = 100 (W)^{1/4} \text{ if } d_w < R_c$$

Once again, the dissipative effects close to the cavity are approximated by the assumption that the leading peak wave breaks down to the limiting height of a stable progressive wave, but, for shallow water, the approximation is that  $H_{\max} = (3/4) d_w$  = Miche limit at  $R = 2R_c$ . If this peak wave height is then attenuated inversely with range  $R$ , the "predicted" peak wave height when the water depth at the charge location is "shallow," ( $d_w \leq 100W^{1/4}$ ), becomes

$$HR = 150 d_w W^{1/4},$$

which gives the line with the 45 degree slope in Figure 2-128. This "prediction" can be used for any depth of burst ( $0 < d_b < d_w$ ) as shown by measured data for H.E. charges in shallow water. As shown in Figure 2-128, there is much scatter in the nuclear wave data in shallow water and some of the measured peak wave heights are more than twice as large as "predicted" by the foregoing equation, which should be regarded only as a rough rule-of-thumb for correlating the measured data in Figure 2-128.

The only actual measured data for the radii of the water columns (or cavities) for nuclear bursts near the surface of water are for shots BAKER and UMBRELLA (Table 2-9). These values of  $R_c$  and those measured for submerged H.E. explosives are roughly equal to the value given by the equation for maximum bubble radius in paragraph 2-67, which gives a burst estimate for  $R_c$ .

DNA  
(4)(3)

TNA  
(X)(3)

In soil, TNT charges detonated at the surface generate crater radii approximately twice as large as nuclear explosions of the same yield, so the nuclear-TNT equivalence is only about 10 percent. The column radii observed for TNT detonations near the surface of the water are roughly equal to  $470W^{1/3}$ , which is the bubble radius given by the equation in paragraph 2-67 for a surface burst. This occurs even when the bubble radii exceed the water depth by a factor of 5. Therefore, it might be expected that a nuclear burst at the surface of water would produce a column radius about half as large as the H.E. value, or  $240W^{1/3}$ . This latter value is much larger than the lower limit estimated above ( $R_c = 100W^{1/4}$ ). This lower limit is also exceeded by the crater radii measured in the bottom after explosions in shallow water, and the water column radii probably exceed the crater radii. Although there are no substantiating data, nuclear explosions at the surface of water of any depth probably generate water columns with radii between  $100W^{1/4}$  and  $240W^{1/3}$  feet.

## 2-78 Refraction and Shoaling

Explosion-generated waves, in common with wind waves and tsunami (earthquake-generated) waves, are affected by changes in the depth over which they propagate. As the waves move into water shallower than about one-third their length (or shoal), their period remains fixed, but both their speed and their length decrease (between successive crests) and their height first decreases about 10 percent and then begins to increase. Because of the change in speed, a wave bends or refracts if it moves into shallow water at an angle to the bottom contours. Refraction can increase or decrease the localized wave height, depending on the hydrography over which the wave moves. No general

methods for determining refraction effects are given here; however, such techniques for calculating these effects are available ("Oceanographical Engineering," R. L. Wiegel, see bibliography).

The increase in height of a wave relative to its length (steepening) continues until the wave becomes unstable and breaks, unless the bottom slope is so shallow that bottom friction dissipates the wave before it breaks. In shallow water without dissipation, steepening increases the wave height as the inverse fourth root of the water depth. Many types of waves become unstable and break (or spill) when their height exceeds either 75 percent of the water depth (the Miche limit) or 14 percent of the wave length over deep water (the Michell limit) as described by Weigel (see bibliography).

## UNDERWATER CRATERING

If an explosion occurs in or even close to a layer of water overlaying bottom material, a significant crater forms in the bottom material whenever the gaseous bubble or water cavity formed by the explosion contacts the bottom. An underwater crater is similar to an onshore crater formed by an explosion near the ground since both are characterized by a dish-shaped depression, wider than it is deep, and surrounded by a lip raised above the undisturbed surface. In the case of most underwater craters, however, the observed ratio of crater radius to depth is larger and the lip height is smaller than for craters from comparable bursts in similar bottom materials onshore. These differences are caused by water displaced by the explosion washing back over the crater. This flow increases the crater radius by as much as 10 percent and decreases the crater depth by as much as 30 percent. An exception to this general rule occurs when the water layer is so shallow that the lip formed by the initial cratering extends above the surface of the water. Such craters (termed "un-

251  
2-282

washed craters") approach onshore craters in appearance, with higher lips and larger depth-to-radius ratios than washed craters. This section describes only the crater characteristics directly related to the explosion. The effects of tidal currents and the collapse of unwashed crater lips by hydrostatic forces are not considered.

The characteristics of underwater craters can be predicted at least qualitatively from the depth of burst, water depth, bottom composition, and weapon yield. The use of empirical curves relating the depth and radius of the crater for surface and bottom bursts over a clayey-sand bottom is described in Problem 2-36. Predictions for other bottom materials can be made by ap-

plying tabulated factors to the values predicted for clayey sand, as described in Problem 2-36. It is evident that larger craters are produced by moving the charge toward the bottom; increasing the water depth above a bottom burst (up to a point); or decreasing the water depth beneath a surface burst.

A very large yield is required to form an unwashed crater in water having a depth that is common to most harbors. For example, with 30 ft of water over clayey-sand, 4 Mt would be required on the bottom to produce a dry crater lip. It is quite unlikely that materials that tend to flow, such as oceanic ooze or fine-grained silt, could support the hydrostatic pressure exerted on a dry crater lip.

252  
2-234

**Problem 2-28. Calculations of Underwater  
Explosion Phenomena**

**■** Calculations can be performed to determine bubble characteristics described in paragraph 2-67. The characteristics include the maximum radii, bubble periods, and migration between maxima for events to the end of the second bubble period. The calculation methods do not apply to cases where the bubble touches the bottom; and the methods contain uncertainties not yet fully resolved when the bubble center is very close to or above the surface. Furthermore, predictions that are made for events increasingly removed in time from the first maximum have increasing uncertainty. Two methods for calculating these bubble characteristics are demonstrated in the example. The first method uses the equations given in paragraph 2-67 and Figures 2-108 through 2-110. The second method uses equations introduced in the example and Figure 2-111. The first method is graphical and is less accurate than the second, but it provides a quick estimate.

**■ Example ■**

Given: 32 kt fired at a depth of 2,000 ft in very deep water.

*Find:*

- a. The initial bubble period and radius,
- b. The depth of the second maximum radius,
- c. The second bubble period,
- d. The radius at second maximum,
- e. The depth of third maximum-radius,
- f. The third bubble period and radius at third maximum.

*Solution (Method 1):*

- a. Calculate the initial radius  $A_1$ , and the period  $T_1$ , by using equations given in paragraph 2-67:

$$A_1 = J' \frac{W^{1/3}}{Z^{1/3}},$$

$$A_1 = (1,500) \left( \frac{(32)^{1/3}}{(2,000 + 33)^{1/3}} \right) = 376 \text{ ft.}$$

$$T_1 = K' \frac{W^{1/3}}{Z^{5/6}},$$

$$T_1 = (515) \left( \frac{(32)^{1/3}}{(2,033)^{5/6}} \right) = 2.86 \text{ sec.}$$

b. Find the reduced hydrostatic head:

$$\frac{Z_1}{A_1} = \frac{2,033}{376} = 5.41.$$

From Figure 2-108, for  $n = 1$ ,

$$\frac{\Delta Z_1}{Z_1} = 0.28,$$

$$\Delta Z_1 = (0.28)(2,033) = 569 \text{ ft} \quad (\text{migration during first period}),$$

$$d_2 = d_b - \Delta Z_1,$$

$$d_2 = 2,000 - 569 = 1,431 \text{ ft.}^*$$

\* Note that results are sensitive to graph readings.

c. From Figure 2-109, for  $n = 2$ ,

$$T_2 = 0.90 T_1.$$

$$T_2 = (0.90)(2.86) = 2.57 \text{ sec.}$$

d. From Figure 2-110, for  $n = 2$ ,

$$A_2 = 0.77 A_1 = (0.77)(376) = 290 \text{ ft.}$$

e. From Figure 2-108, using  $Z_1/A_1 = 5.41$  and  $n = 2$ ,

$$\frac{\Delta Z_2}{Z_1} = 0.23,$$

$$\Delta Z_2 = 0.23 Z_1 = (0.23)(2,033) = 468 \text{ ft.}$$

$$d_3 = d_2 - \Delta Z_2,$$

$$d_3 = 1,431 - 468 = 963 \text{ ft.}$$

f. From Figure 2-109, for  $n = 3$ ,

$$T_3 = 0.66 T_1.$$

$$T_3 = (0.66)(2.86) = 1.89 \text{ sec.}$$

From Figure 2-110, for  $n = 3$ ,

$$\frac{A_3}{A_1} = 0.47,$$

$$A_3 = 0.47 A_1 = (0.47)(376) = 177 \text{ ft.}$$

**Solution (Method 2):** This method uses Figure 2-111 to obtain values for bubble energy ratio,  $r_n/r_{n-1}$ , and the following reduced equations:

$$\left( \frac{\Delta Z_n}{Z_n} \right) = 3.5 \left( \frac{A_1}{Z_1} \right)^{3/2} \left( \frac{r_n}{r_1} \right)^{1/2} \left( \frac{Z_1}{Z_n} \right)^2.$$

$$\left( \frac{A_n}{A_1} \right) = \left( \frac{Z_1}{Z_n} \right)^{1/3} \left( \frac{r_n}{r_1} \right)^{1/3}.$$

$$\left( \frac{T_n}{T_1} \right) = \left( \frac{Z_1}{Z_n} \right)^{5/6} \left( \frac{r_n}{r_1} \right)^{1/3}.$$

a. By the same procedures used in Method

1,

$$A_1 = 376 \text{ ft},$$

$$T_1 = 2.86 \text{ sec.}$$

b. Using the first reduced equation given above,

$$\left( \frac{\Delta Z_1}{Z_1} \right) = 3.5 \left( \frac{A_1}{Z_1} \right)^{3/2} \left( \frac{r_1}{r_1} \right)^{1/2} \left( \frac{Z_1}{Z_1} \right)^2.$$

$$\left( \frac{\Delta Z_1}{Z_1} \right) = 3.5 \left( \frac{375}{2,033} \right)^{3/2} (1)^{1/2} (1)^2 = 0.277,$$

$$\Delta Z_1 = 0.277 Z_1.$$

$$\Delta Z_1 = (0.277)(2,033) = 564,$$

$$d_2 = d_b - \Delta Z_1,$$

$$d_2 = 2,000 - 564 = 1,436 \text{ ft.}$$

c. The second bubble period  $T_2$  can be obtained from the third reduced equation given above, and  $T_1$  from (a) after finding the energy

[REDACTED]

ratio between the first and second bubbles. Using the reduced migration  $\Delta Z_1/Z_1 = 0.277$  to enter Figure 2-111, the energy ratio is  $r_2/r_1 = 0.324$ . Thus,

$$\left(\frac{T_2}{T_1}\right) = \left(\frac{Z_1}{Z_2}\right)^{5/6} \left(\frac{r_2}{r_1}\right)^{1/3},$$

$$\left(\frac{T_2}{T_1}\right) = \left(\frac{2,033}{1,469}\right)^{5/6} (0.324)^{1/3},$$

$$\frac{T_2}{T_1} = 0.90,$$

$$T_2 = (0.90)(2.86) = 2.57 \text{ sec.}$$

d. The radius of the second maximum is obtained from the second reduced equation given above.

$$\left(\frac{A_2}{A_1}\right) = \left(\frac{Z_1}{Z_2}\right)^{1/3} \left(\frac{r_2}{r_1}\right)^{1/3},$$

$$\left(\frac{A_2}{A_1}\right) = \left(\frac{2,033}{1,469}\right)^{1/3} (0.324)^{1/3},$$

$$\left(\frac{A_2}{A_1}\right) = 0.765,$$

$$A_2 = 0.765 A_1 = (0.765)(376) = 288 \text{ ft.}$$

e. To calculate the depth of the third maximum, it is first necessary to find the reduced migration  $\Delta Z_2/Z_2$ . From the first reduced equation,

$$\left(\frac{\Delta Z_2}{Z_2}\right) = 3.5 \left(\frac{A_1}{Z_1}\right)^{3/2} \left(\frac{r_2}{r_1}\right)^{1/2} \left(\frac{Z_1}{Z_2}\right)^2,$$

$$\left(\frac{\Delta Z_2}{Z_2}\right) = 3.5 \left(\frac{376}{2,033}\right)^{3/2} (0.324)^{1/2} \left(\frac{2,033}{1,469}\right)^2,$$

$$\left(\frac{\Delta Z_2}{Z_2}\right) = 0.303,$$

$$\Delta Z_2 = 0.303 Z_2 = (0.303)(1,469) = 445 \text{ ft.}$$

$$d_3 = d_2 - \Delta Z_2,$$

$$d_3 = 1,436 - 445 = 991 \text{ ft.}$$

f. From c.,  $r_2/r_1 = 0.324$ . Using the reduced migration  $\Delta Z_2/Z_2 = 0.303$  to enter Figure 2-111, the energy ratio  $r_3/r_2 = 0.158$ .

$$\left(\frac{r_3}{r_1}\right) = \left(\frac{r_2}{r_1}\right) \left(\frac{r_3}{r_2}\right)$$

$$\left(\frac{r_3}{r_1}\right) = (0.324)(0.158) = 0.0512.$$

From the third reduced equation

$$\left(\frac{T_3}{T_1}\right) = \left(\frac{Z_1}{Z_3}\right)^{5/6} \left(\frac{r_3}{r_1}\right)^{1/3},$$

$$\left(\frac{T_3}{T_1}\right) = \left(\frac{2,033}{1,024}\right)^{5/6} (0.0512)^{1/3} = 0.658,$$

$$T_3 = 0.658 T_1$$

$$T_3 = (0.658)(2.86) = 1.88 \text{ sec.}$$

From the second reduced equation,

$$\left(\frac{A_3}{A_1}\right) = \left(\frac{Z_1}{Z_3}\right)^{1/3} \left(\frac{r_3}{r_1}\right)^{1/3}$$

$$\left(\frac{A_3}{A_1}\right) = \left(\frac{2,033}{1,024}\right)^{1/3} (0.0512)^{1/3} = 0.467$$

$$A_3 = 0.467 A_1$$

$$A_3 = (0.467)(376) = 176 \text{ ft.}$$

*Answer:*      *Method 1*      *Method 2*

a. The initial       $A_1 = 376 \text{ ft}$       376 ft  
bubble period       $T_1 = 2.86 \text{ sec}$       2.86 sec  
and radius

b. The depth of       $d_2 = 1,431 \text{ ft}$       1,436 ft  
the second  
maximum radius

c. The second       $T_2 = 2.57 \text{ sec}$       2.57 sec  
bubble period

d. The radius at       $A_2 = 290 \text{ ft}$       288 ft  
second maximum

e. The depth of       $d_3 = 963 \text{ ft}$       991 ft  
third maximum  
radius

f. The third       $T_3 = 1.89 \text{ sec}$       1.88 sec  
bubble period       $A_3 = 177 \text{ ft}$       176 ft  
and radius at  
third maximum

**Reliability:** The uncertainty in the values for maximum radii calculated by the methods described above are about +20 percent and -35 percent, based on very limited information.

**Related Material:** See paragraph 2-67.

**Problem 2-29. Calculation of Shock Wave Parameters  
for Free Water (Deep Bursts)**

Figures 2-112 through 2-116 show the parameters for the primary shock wave from an underwater explosion in free, isovelocity water (no reflections, no refractions). Figure 2-112 shows the peak pressure as a function of slant range for various yields, where the peak pressure is lower than 3,000 psi, and as a function of reduced slant range ( $R/W^{1/3}$ ) for peak pressures above 3,000 psi. Figure 2-113 shows the shock wave impulse as a function of slant range for various yields, while Figure 2-114 shows the shock wave energy flux as a function of slant range for the same yields. These latter two families of curves show values of impulse and energy flux integrated to a time of  $6.7\theta$ , where  $\theta$  is the time constant for the shock wave, which is defined as the time for the shock wave pressure to fall to approximately 37 percent of its peak value.

The time constant  $\theta$  is shown in Figure 2-115 as a function of slant range for the same family of yields shown in Figures 2-113 and 2-114. Figure 2-116 shows a dimensionless pressure-time curve. Using values of  $\theta$  from Figure 2-115 and values of  $p_m$  from Figure 2-112, Figure 2-116 may be used to construct the pressure-time shape of the shock wave in free water at various ranges from underwater explosions of various yields.

**Scaling.** For yields other than those shown in Figure 2-112 through 2-115, use linear interpolation between appropriate curves.

**Example**

**Given:** A 50 kt burst at a depth of 1,000 ft in deep water.

**Find:** The peak shock pressure  $p_m$ , the shock wave impulse  $I$ , energy flux  $E$ , and time constant  $\theta$  at a 1,000 ft depth, 4,000 yd from

the burst.

**Solution:** The desired shock wave parameters can be read directly from Figures 2-112 through 2-115.

**Answer:**

$$p_m \approx 470 \text{ psi.}$$

$$I \approx 28 \text{ psi-sec.}$$

$$E \approx 10^3 \text{ in.-lb/in.}^2,$$

$$\theta \approx 50 \text{ msec.}$$

**Reliability:** Values shown in Figures 2-112 through 2-115 are estimated to be accurate within  $\pm 10$  percent for shock pressure, and  $\pm 20$  percent for the other parameters for yields between 1 kt and 1 Mt. For yields below 1 kt or above 1 Mt, the values are more uncertain. The assumption of isovelocity water becomes increasingly uncertain for ranges beyond a few kiloyards in the ocean.

**Related Material:**

See paragraphs 2-68 through 2-72.

Figures 2-112 through 2-115 are based on the following equations:

$$p_m = 4.38 \times 10^6 \left( \frac{W^{1/3}}{R} \right)^{1.13} \text{ psi}$$

$$I \text{ (to } 6.7\theta) = 1.176 \times 10^4 W^{1/3} \left( \frac{W^{1/3}}{R} \right)^{0.91} \text{ psi-sec}$$

$$E \text{ (to } 6.7\theta) = 3.976 \times 10^9 W^{1/3} \left( \frac{W^{1/3}}{R} \right)^{2.04} \frac{\text{in.-lb}}{\text{in.}^2}$$

$$\theta = 2.274 W^{1/3} \left( \frac{W^{1/3}}{R} \right)^{-0.22} \text{ msec.}$$

The values of these parameters are related to those for TNT (Cole, 1948) by an ap-

proximate equivalence factor. Snay and Butler (1957) (see bibliography) report that an underwater nuclear burst with a radiochemical yield of 1 kt gives approximately the same shock wave parameters at the same distance as a TNT charge weighing 0.67 kiloton (where 1 ton = 2,000 lbs).

2-234  
262

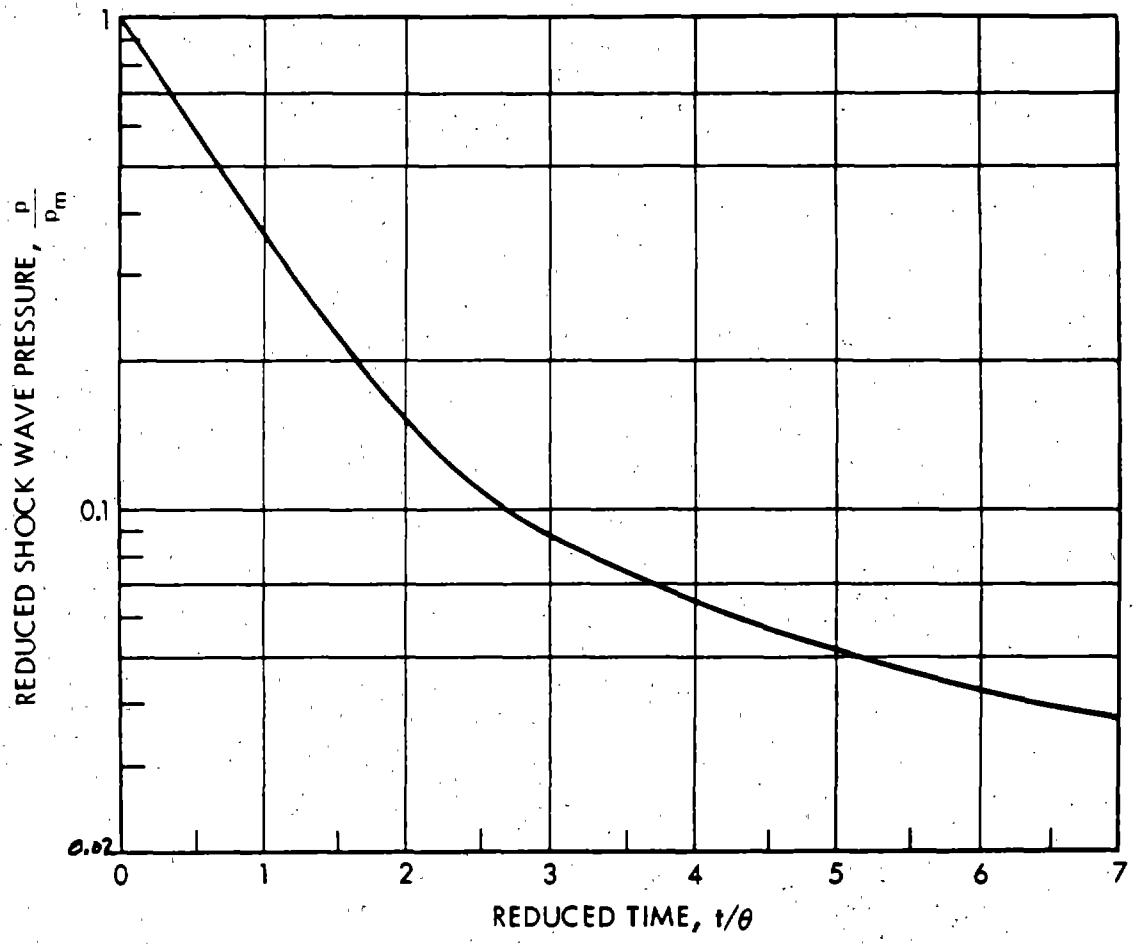
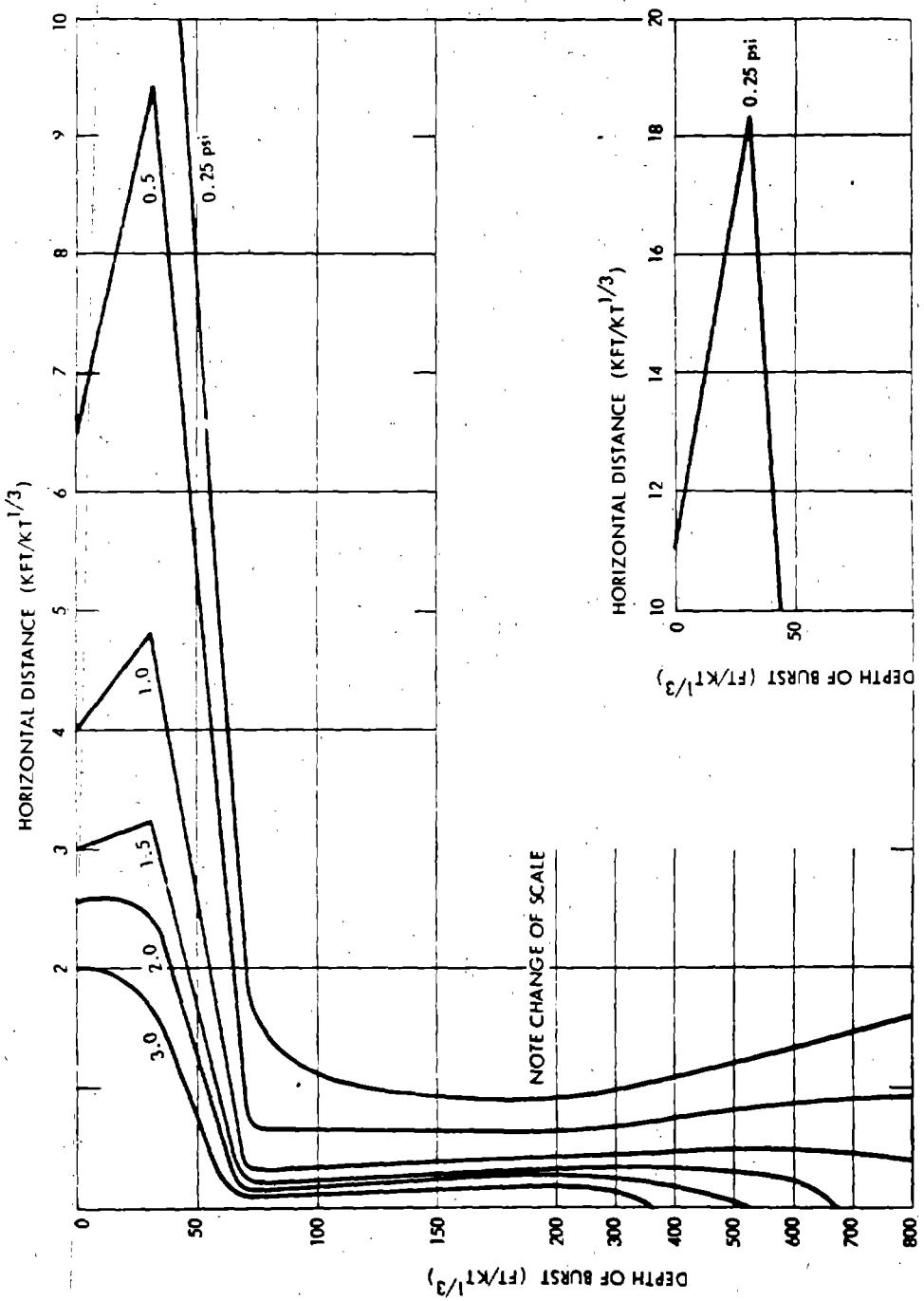


Figure 2-116. [REDACTED] Pressure-Time for Free Isovelocity Water  
Shock Waves from Nuclear Explosion [REDACTED]

267  
2-288



276  
2-248

Figure 2-121. [REDACTED] Peak Air Blast Overpressure Along the Water Surface [REDACTED] from Underwater Nuclear Explosions

**Problem 2-32. Calculation of the Extent, Initial Vertical Velocity, and Approximate Height of the Spray Dome**

The maximum extent of the spray dome can be estimated with the following relations, which are valid for reduced depths of burst as large as:

$$d_b/W^{1/3} \leq 1,260 \text{ ft/(kt)}^{1/3}$$

$$r_{sd} = d_b \tan \delta_{max}$$

$$\delta_{max} = 85.3 - 0.021 (d_b/W^{1/3})$$

where (as shown in the following sketch).

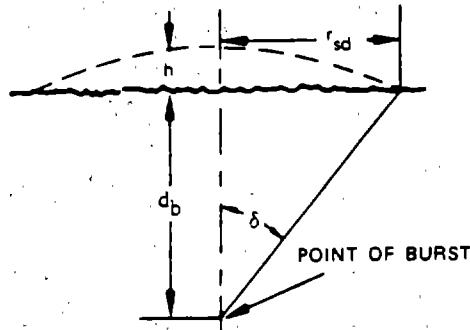
$r_{sd}$  = the horizontal extent of the spray dome (ft).

$\delta$  = the spray dome angle, the angle between a vertical line passing through the center of the burst and a line passing through the point of interest on the surface and the center of the burst (degrees).

$d_b$  = the burst depth (ft).

$W$  = the weapon yield (kt).

$h$  = maximum spray dome height (ft).



Initial spray velocities can be calculated from:

$$V_o = (144 \cos \delta) \frac{p_m}{U}$$

where at a point on the surface.

$p_m$  = peak shock pressure (psi).

$U$  = shock front propagation velocity (ft/sec).

$V_o$  = initial spray velocity (ft/sec.)

Values of  $p_m$  are given in Figure 2-112. Values of  $U$  are given in Figure 2-122 as a function of  $p_m$ . In practice, the presence of the bottom does not appear to have an influence upon the value for the spray velocity. However, for bursts on the bottom, the yield should be doubled (as an upper limit estimate) when calculating spray velocities.

Higher velocities than given by the above equation have been observed for deep bursts,\* therefore a 50 percent safety factor should be added to calculate values of initial dome velocity.

An upper limit of dome height  $h$  can be derived from:

$$h = V_o t - (f)t^2$$

where

$t$  = time (sec),

$f$  = retardation factor ( $\text{ft/sec}^2$ ),

Choppy sea, together with "Taylor instability" appear to account qualitatively for this observation.

by assuming that gravity is the only retarding force and, therefore, that  $f = 16 \text{ ft/sec}^2$ . The time that the upper limit height is reached can be determined that the first derivative of  $h$  with respect to time (that is, dome velocity) = zero at that time. Therefore,

$$\frac{dh}{dt} = 0 = V_0 - 2(f)t$$

Example

Given:

DNA  
(b)(3)

DNA  
(b)(3)

**Reliability:** Spray dome angles are estimated to be reliable to within  $\pm 10$  percent for  $d_b/W^{1/3} < 1,260 \text{ ft/(kt)}^{1/3}$ . Initial vertical velocities that are calculated by the equations given above might be low by as much as 50 percent, therefore, a safety factor is included in the method. The retardation factor  $f$  is taken to be  $16 \text{ ft/sec}^2$  to obtain an upper limit for dome height. Actual retardation factors as large as  $30 \text{ ft/sec}^2$  have been observed during nuclear tests.

**Related Material:** See paragraph 2-73.

278  
2-250

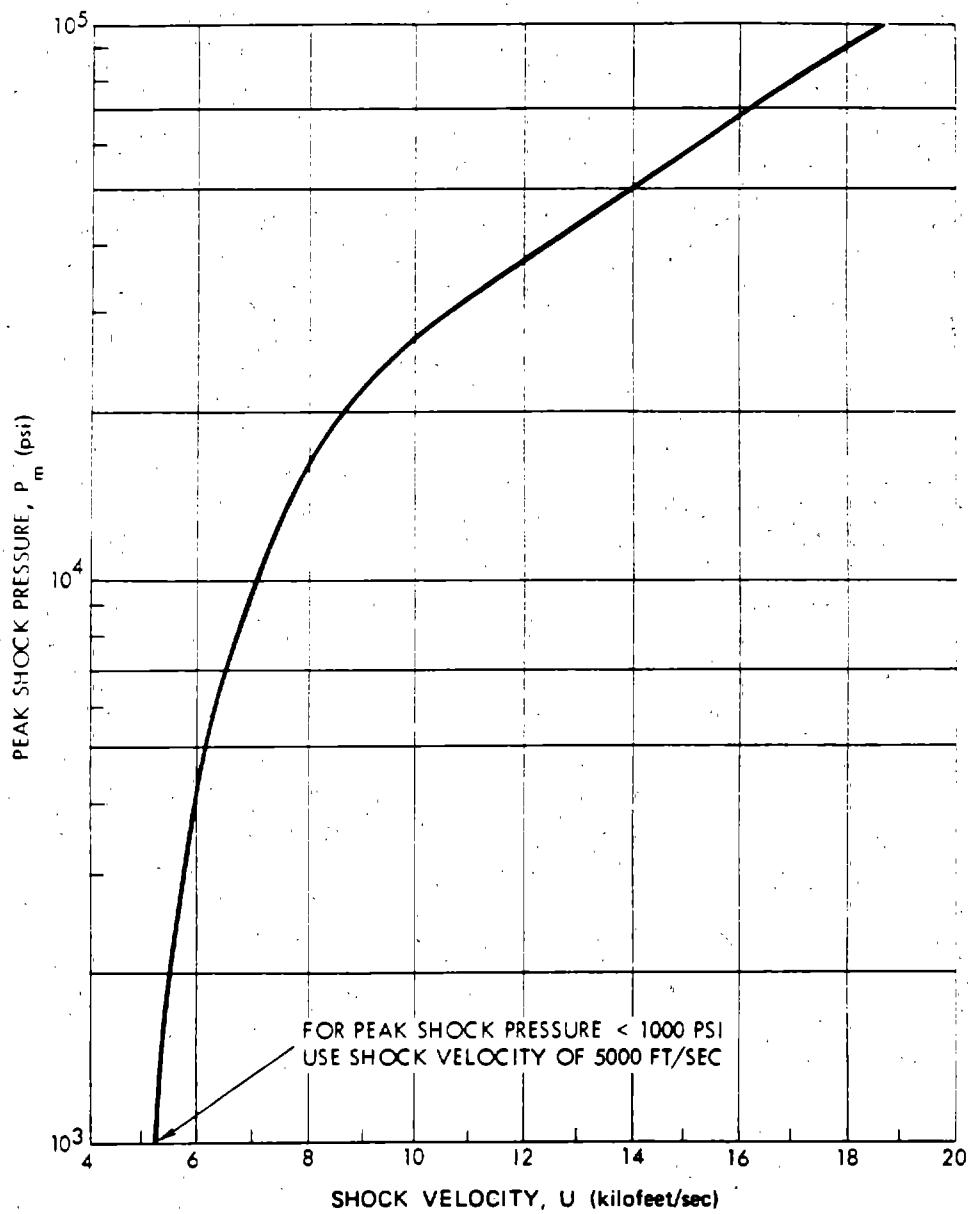


Figure 2-122: [REDACTED] Velocity of Shock Wave in Free Water  
vs Peak Shock Pressure [REDACTED]

2-251

DTIC FILE COPY

DTIC  
ELECTED

2 MAR 1989

②

S D

## Chapter 3

## THERMAL RADIATION PHENOMENA

Within a few seconds after the explosion a typical low altitude nuclear fireball emits about a third of the weapon yield as infrared, visible, and ultraviolet radiation (see Figure 4-1). This sudden pulse of thermal energy may damage any target that is susceptible to high temperatures. The damage may take many forms, but the effects that are most frequently of concern are fires that start as the result of ignition of thin combustible materials (e.g., paper or dried leaves) and injuries to personnel, in the form of burns.

The thermal pulse decays as the fireball fades, but there is no specific time that marks the end of the thermal radiation from the fireball. At late times, as the radioactive cloud rises, the heated air in the nuclear cloud still radiates some thermal energy; however, this radiant energy is released so slowly that it has little military importance. Therefore, in this chapter, the terms "thermal radiation phenomena," "thermal effects," and "thermal pulse" only pertain to the portion of the radiated energy that could be termed the "prompt thermal pulse."

This restriction in the meanings of terms such as "thermal effects" excludes a number of nuclear burst phenomena that are thermal in the broader sense. For example, fireball rise is a thermal effect; the fireball is buoyant for the same reason that a hot-air balloon is buoyant. Another effect that properly could be termed thermal is the radiation of X-ray energy by the nuclear source. The X-ray energy is the thermal radiation that is characteristic of an extremely high temperature source (see Chapter 4). In many situations, e.g., low altitude bursts, this

radiation has no direct effect on targets, because it is absorbed by air close to the source. In other situations, notably aerospace vehicles exposed to high altitude detonations, this X-ray energy becomes one of the most important direct damage mechanisms. This damage mechanism is discussed in Section V, Chapter 9.

## RADIANT EXPOSURE

Four variables determine the effects of the thermal pulse on a target:

- The amount of energy that is incident on the target.
- The time history of the thermal pulse.
- The spectral distribution of the radiant energy.
- The directional characteristics of the incident radiation, e.g., does it come directly from the source, or is it scattered and therefore arrives from many directions.

In most cases of military interest the first of the variables is dominant. A careful analysis cannot ignore the other three, but a *preliminary* evaluation of a thermal environment, for example, a calculation to determine whether a thermal problem exists, often can be based on the total energy received.

The energy delivered by the thermal pulse usually is specified in terms of *radiant exposure*, the energy per unit area incident on the target surface. It is denoted by the symbol  $Q$  and is conventionally measured in units of calories per square centimeter ( $\text{cal}/\text{cm}^2$ ). The factors that affect the radiant exposure are discussed separately in the following paragraphs.

This document has been approved  
for public release and makes its  
distribution unlimited.

3-1

89 3 02 046

### 3-1 Thermal Partition

The ratio of the thermal energy radiated by the fireball of a nuclear explosion to the total yield is *thermal partition* (sometimes called *thermal efficiency*), denoted by the symbol  $f$ . For burst altitudes below 100,000 feet and yields between 1 kt and 10 Mt, values of thermal partition may be determined from Figure 3-1. For higher burst altitudes, thermal partition must be determined by the method described in paragraph 3-19. If the burst is below  $180W^{0.4}$  feet (where  $W$  is the yield in kilotons), it is classed as a surface burst and the thermal partition should be determined by the method described in paragraph 3-9.

DNA  
U(3)

Accession For	
NTIS GRA&I	<input checked="" type="checkbox"/>
DTIC TAB	<input type="checkbox"/>
Unannounced	<input type="checkbox"/>
Justification <i>Code Doc</i>	
By _____	
Distribution/	
Availability Codes	
Dist	Avail and/or Special
A-1	



UNANNOUNCED

### 3-2 Range Effects

As the thermal energy propagates away from the fireball, the divergence that results from the increasing area through which it passes causes the radiant exposure to decrease as the inverse square of the slant range. At a slant range  $R$  centimeters from the source, the thermal energy is distributed over a spherical area of  $4\pi R^2$ . Since the thermal yield in calories is  $10^{12} Wf^*$ , where  $W$  is the yield in kilotons, the radiant exposure at a distance  $R$  cm in a clear atmosphere is

$$Q = \frac{10^{12} Wf}{4\pi R^2} \text{ cal/cm}^2.$$

Kilofeet and kilometers are more convenient units than centimeters for measuring the range from a nuclear burst. Appropriate conversion factors change the form of the equation to

$$Q = \frac{100 Wf}{4\pi R_{\text{km}}^2} = 7.96 \frac{Wf}{R_{\text{km}}^2} \text{ cal/cm}^2,$$

and

$$Q = 85.7 \frac{Wf}{R_{\text{kft}}^2} \text{ cal/cm}^2,$$

where  $R_{\text{km}}$  and  $R_{\text{kft}}$  are slant ranges in kilometers and kilofeet, respectively.

### TRANSMITTANCE

The equations presented above ignored the attenuation by the atmosphere that would affect the thermal energy received by a target. In many cases, particularly when the air is clear and the range is short, atmospheric attenuation is not important. In other situations, scattering and absorption of thermal energy by the atmosphere can reduce the amount of thermal energy reaching the target significantly.

In addition to atmospheric attenuation, other effects also must be considered. A cloud layer above a fireball can scatter radiation downward and can increase the thermal energy that reaches the ground. If the ground also is highly reflecting, e.g., if the ground is covered by a layer of snow, further enhancement of the thermal radiation may result.

All of these effects are approximated by one factor, the transmittance  $T$ . Transmittance is the ratio of the radiant exposure at a target facing the fireball to the radiant exposure that the target would receive if the intervening atmosphere were perfectly transparent.

Adding the transmittance factor to the equations given in paragraph 3-2 gives

$$Q = \frac{7.96 WfT}{R_{\text{km}}^2} \text{ cal/cm}^2,$$

and

$$Q = \frac{85.7 WfT}{R_{\text{kft}}^2} \text{ cal/cm}^2.$$

The corresponding expressions for slant range in terms of yield and transmittance are<sup>†</sup>

$$R_{\text{km}} = 2.82 \sqrt{WfT/Q}$$

$$R_{\text{kft}} = 9.26 \sqrt{WfT/Q}$$

### 3-3 Specification of Transmittance

A difficult task in applying transmittance data to a thermal problem is deciding which model atmosphere to use. Various model

<sup>\*</sup>One kiloton equals  $10^{12}$  calories (see Table 1-2).

<sup>†</sup>A relationship that is easy to remember and that is reasonably correct if it is assumed that the thermal partition,  $f = 1/3$ , and the transmittance,  $T = 1.0$ , is that the median exposure at one statute mile is about  $Q = 1 \text{ cal/cm}^2 \text{ per kt}$ .

sphere described in this chapter as having a visual range of 16 miles would be assigned a visibility of 12 miles by at least one author and a visibility of 24 miles by some others.

The extent to which the atmosphere impedes the flow of thermal energy and limits visibility depends largely on the amount of scattering of radiant energy by atmospheric particles. Absorption of energy also affects radiative transport, but absorption usually is less important than scattering. A description of these phenomena is the first step in explaining visual range and transmittance.

The thermal radiation of concern in this chapter consists of electromagnetic radiations from the ultraviolet to the infrared. The photons that make up electromagnetic radiations can react with matter in many complex ways, but the photons that constitute the thermal radiation spectrum of a nuclear fireball interact almost exclusively by being absorbed or elastically scattered. If the photon is absorbed, it gives up its energy to the absorbing particle, and this energy ultimately appears as heat. Scattering may be thought of as reflection from a small particle. Its effect is to change the direction in which the photon is traveling. The term "elastic" means that the photon does not lose energy during the scattering process. Other interactions of electromagnetic radiations with matter that are more probable for higher frequency (shorter wavelength) radiations than those of the thermal radiation are described in paragraph 4-3, Chapter 4.

The scattering and absorption properties of the atmosphere depend partly on the wavelength of the radiant energy. Wavelength is often measured in microns ( $1 \text{ micron} = 10^{-6} \text{ meter}$ ), for which the symbol is  $\mu$ . Wavelengths in the visible spectrum may be identified by the relation between wavelength and color: light with a wavelength of  $0.7 \mu$  is red;  $0.58 \mu$  light is yellow; and  $0.48 \mu$  light is blue. White light is a mixture

containing all wavelengths in the visible spectrum, which extends from  $0.38$  to  $0.78 \mu$ . The infrared spectrum consists of radiant energy at wavelengths longer than  $0.78 \mu$ , and the ultraviolet spectrum consists of radiant energy at wavelengths shorter than  $0.38 \mu$ .

The energy transport properties of atmospheric particles may be expressed in terms of scattering and absorption cross sections, which are fictitious areas that are a measure of the probability that scattering or absorption will occur. Particles that are small compared to the wavelength of light have scattering cross sections that are inversely proportional to the fourth power of the wavelength. Therefore, air molecules scatter light from the extreme blue end of the visible spectrum (wavelength =  $0.38 \mu$ ) about 16 times as effectively as they scatter light from the red end of the spectrum (wavelength =  $0.78 \mu$ ). Blue smoke, which consists of very small particles, has similar scattering properties. Particles that are large compared to the wavelength of light (e.g., haze or fog particles) have scattering cross sections that are much less dependent on wavelength. Individual particles have a scattering cross section that varies somewhat with wavelength, but the mixture of particle sizes found in a haze or fog usually results in an average cross section that is nearly independent of wavelength.

The sky is blue because most of the scattering at high altitudes is by air molecules, which scatter blue light more efficiently than they scatter other colors of the visible spectrum. A distant mountain appears blue on a clear day for the same reason.

The scattering properties of larger airborne particles may be observed on days when a very light haze reduces visibility to about 10 miles or less. Near the surface, scattering by haze particles contributes more to the light in the air than does scattering by air molecules. The sky still appears blue, but the color is not as deep as

[REDACTED]

it would be on a clearer day. Distant hills and the sky near the horizon appear to be more gray than blue, which indicates that the lower atmosphere is scattering all wavelengths of light about equally.

[REDACTED] Water droplets cause nearly all of the scattering that occurs in a fog or a thick cloud. Consequently, clouds are white and fogs tend to wash out all impressions of color.

[REDACTED] Absorption usually has little effect on visible light, but it can affect the infrared and ultraviolet portions of the spectrum significantly. The principal absorber of thermal energy usually is water vapor, which has strong absorption bands in the infrared spectrum. Dry air transmits infrared energy more efficiently than humid air. Carbon dioxide and other gases present in the atmosphere in small amounts also absorb infrared energy.

[REDACTED] Ultraviolet energy is absorbed most strongly at the shorter wavelengths: the limiting wavelength that air in the lower atmosphere will transmit is about 0.2 micron. Ozone, appreciable quantities of which are found between roughly 60,000 and 80,000 feet, absorbs ultraviolet radiation with wavelengths shorter than 0.29 micron. As a result of these absorption bands ultraviolet energy that reaches the earth from the sun is almost entirely limited to the spectral band between 0.38 micron (the violet edge of the visible spectrum) and 0.29 micron.

[REDACTED] Dark colored particles absorb appreciable energy in all regions of the thermal spectrum. Dust, smoke, and the smoky haze from large cities fall into this category.

[REDACTED] Detailed calculations of the complex scattering and absorption processes that can occur between a nuclear explosion and a target require computer codes that are capable of considering detailed changes in the atmosphere and the effect that these changes can have on the entire spectrum of frequencies emitted by the fireball. Monte Carlo calculations have been per-

formed for several model atmospheres and for several discrete wavelengths; however, as of this time, these calculations have not been generalized into a form that is suitable for inclusion in this manual. Therefore, the formulas and curves for atmospheric transmittance that are given below are based on a simplified model based on the concept of effective optical height for single wavelengths.

[REDACTED] One way to specify the attenuating properties of the atmosphere as a function of altitude is to assume that the transmittance between the point of burst and ground zero follows an equation of the form

$$T = e^{-\tau(h)},$$

where  $T$  is transmittance and  $\tau(h)$  is the *effective optical height* of the burst height  $h$ . This concept was applied in 1966 to specify one particular model atmosphere for which the visual range is 16 miles.\* The attenuation for light of 0.65 micron wavelength was used to specify  $\tau(h)$ . This choice was a purely empirical one, used because it brought the calculated values of transmittance into general agreement with experimentally determined values. The wavelength that was selected is attenuated less than is the thermal radiation spectrum as a whole;

\* [REDACTED] "Transmissivity of the Atmosphere for Thermal Radiation from Nuclear Weapons" (see bibliography). A 12 mile visual range was assigned to this model atmosphere. This choice was based on a comparison between a large number of visual range estimates at an airport weather station and simultaneous measurements with instruments designed to measure meteorological range. The 16 mile figure is used here because it is consistent with the definition of visual range given in this chapter. Qualitatively, this range is defined as the distance at which a dark object silhouetted against the sky is visible and recognizable. This range is more specifically defined in paragraph 3-7.

[REDACTED] Although the specification for this model atmosphere has been changed, the reason for having assigned the 12 mile figure carries a useful warning. There is no assurance that even trained meteorologists will make estimates that are consistent with a precise mathematical definition of visual range.

therefore, this choice makes allowance for additional energy that reaches the target by scattering. For bursts below one-quarter mile and surface targets, a wavelength of 0.55 microns was used together with a buildup factor, as described below.

Figure 3-2 shows  $\tau(h)$  as a function of altitude for this particular model atmosphere. This model shows no attempt to represent an abrupt increase in transparency at the top of the haze layer; optical height is a smoothly varying function of altitude. This approximation to the actual atmosphere does not appear to introduce serious error into the calculations, and it is more convenient than a model atmosphere that requires an estimate of the height of the haze layer as well as an estimate of visual range.

When visual range is different from 16 miles, the model atmosphere is specified by multiplying the values of effective optical height in Figure 3-2 by  $16/V$ , where  $V$  is visual range in miles. For example, if the visibility is 8 miles, all values of optical height are doubled, indicating that transparency at all altitudes is reduced by a factor of 2. This transformation may be stated mathematically as

$$\tau(h)_V = \tau(h)_{16} \frac{16}{V}$$

where  $\tau(h)_V$  is the effective optical height at a given altitude for the model atmosphere for which visual range is  $V$  and  $\tau(h)_{16}$  is the effective optical height of the 16 mile model atmosphere at the same altitude.

Visual range, a surface measurement, is a poor criterion for predicting the clarity of the air a few miles up. Although there is some correlation between these two quantities, the main justification for this somewhat arbitrary procedure is that the optical thickness assigned to the upper atmosphere, since it is a small fraction of the total optical thickness, has little influence

on the calculated transmittance to targets on the ground.

If the burst height is less than about one-quarter mile, the line-of-sight path from the burst to the target passes through air which, in most cases, has optical properties that are fairly uniform. In a uniform atmosphere, the attenuation of a direct beam of thermal energy may be related to the visibility of distant objects by the equation:

$$T_d = e^{-2.9 R/V},$$

where  $T_d$  is the transmission coefficient for direct flux over a path of slant range  $R$ , and  $V$  is visual range. As mentioned above, scattered as well as direct flux must be considered. Consequently, transmittance is larger than the transmission coefficient for direct flux and is given approximately by the following empirical equation:

$$T = e^{-2.9 R/V} (1 + 1.9 R/V).$$

The exponential factor in this equation accounts for energy loss from the direct beam by scattering. The expression in brackets is a buildup factor that accounts for energy scattered toward the target. This equation does not specifically involve any property of the model atmosphere other than visual range; however, the properties of the model atmosphere are involved implicitly, because the rate at which transparency changes with altitude helps determine the magnitude of the coefficient 1.9 in the buildup factor. Figure 3-3 shows this relation in graphical form.

When the burst height  $h$  is greater than about one-quarter mile, transmittance may be calculated from

$$T = e^{-\tau(h)} \frac{16}{V} \frac{R}{h}$$

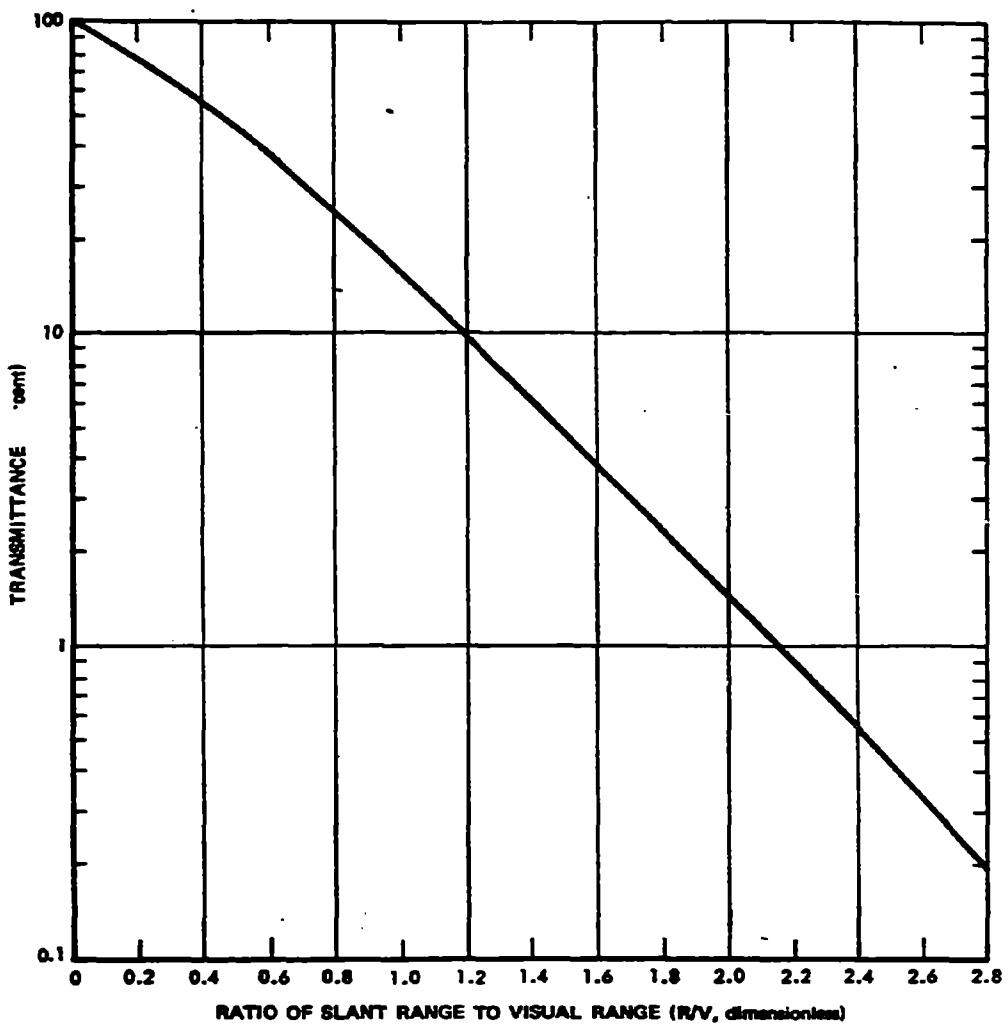


Figure 3-3. [REDACTED] Transmittance Between a Burst  
Within 1/4 Mile of the Surface  
and a Target on the Ground [REDACTED]

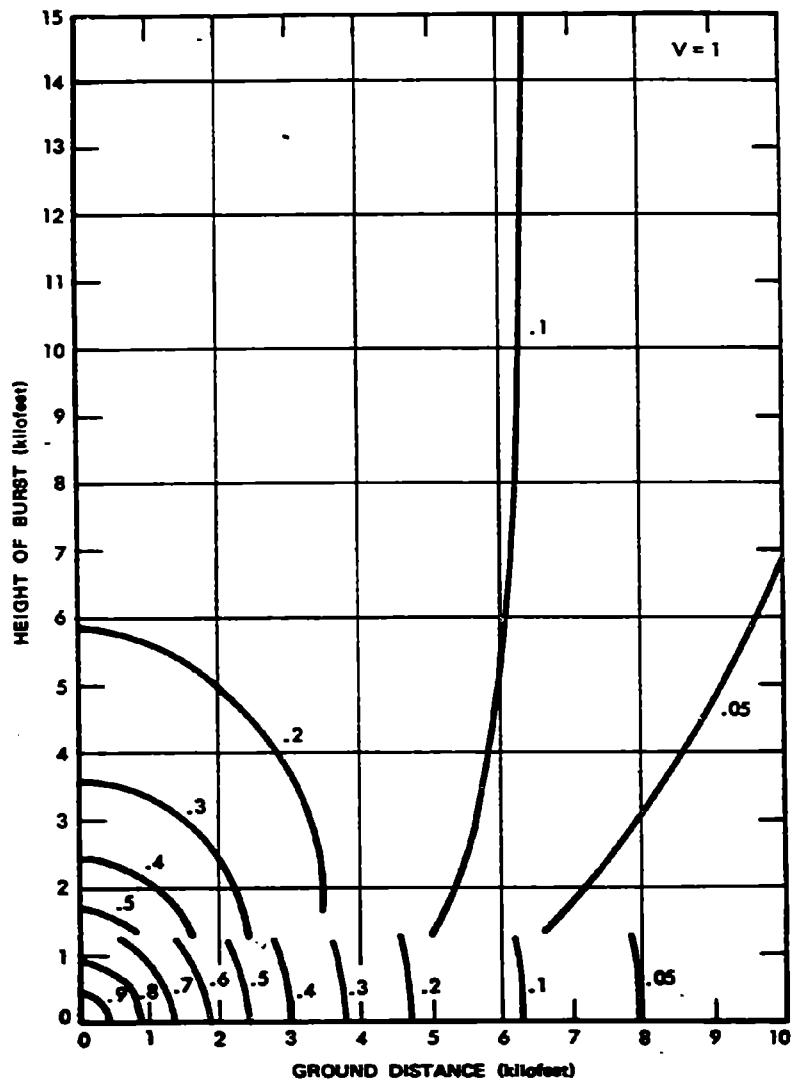


Figure 3-4. Transmittance to a Target on the Ground  
on a Clear Day (Visual Range = 1 Mile)

## SURFACE AND SUBSURFACE BURSTS

Clouds of dust (or spray) partly obscure the fireball of surface bursts and reduce the thermal radiation received by targets on the ground. Even less thermal radiation escapes from underground and underwater bursts. If the burst is deep enough, the earth or water absorbs almost all of the thermal energy; the amount of radiated thermal energy is insignificant.

### 3-9 Surface Bursts

The terms contact surface burst, surface burst, and air burst, when used in connection with thermal effects, have meanings similar to those assigned to the same terms in Chapter 2 (see paragraph 2-19). A contact surface burst is one that is no more than  $5 W^{0.3}$  feet above or below the surface. The region between  $5 W^{0.3}$  and  $180 W^{0.4}$  feet ( $\pm 20$  percent for yields between 10 and 100 kt, and  $\pm 30$  percent for other yields) is called the transition zone, and a burst within this region is a surface burst for purposes of thermal radiation phenomena. Since the fireball is approximately  $180 W^{0.4}$  feet in radius for explosions in the lower atmosphere, a surface burst is any burst above  $5 W^{0.3}$  feet but low enough that the fireball will interact strongly with the surface of the earth. As mentioned in paragraph 3-1, an air burst occurs above  $180 W^{0.4}$  feet.

Experimental data indicate that the thermal partition of contact surface bursts is about 0.21. Figure 3-18 assumes a thermal partition of 0.21 for a contact surface burst, assigns the air burst partition (Figure 3-1) to a burst at  $180 W^{0.4}$  feet, and provides intermediate values by linear interpolation. This procedure is arbitrary and is only supported in a general way by experimental data. Points above the dashed line in Figure 3-18 represent air bursts; points below the dashed line are surface bursts. The radiant

exposure from surface bursts may be calculated by the formulas given in paragraph 3-2 with the values of thermal partition,  $f$ , taken from Figure 3-18.

Figure 3-18 describes the fireball as it would be seen by targets on the surface. Clouds of dust would not obscure the fireball from above; consequently, radiant exposure of airborne targets should be calculated on the basis of the thermal partition of free air bursts given in Figure 3-1.

Since confinement of the fireball by the surface is roughly equivalent to reflection, the fireball radius for a contact surface burst is larger than that for the same burst in free air. Blast wave theory suggests that the fireball of a contact surface burst as viewed from above might resemble that of a free air burst with a yield of 2.0 W. In fact, determination of fireball yield by hydrodynamic scaling uses the 2.0 W assumption.

### 3-10 Subsurface Bursts

Two effects reduce the amount of thermal energy radiated by the nuclear explosions below the surface of the earth: a large amount of thermal energy is absorbed in fusing and vaporizing the earth; and the fireball that does develop above the surface is obscured to a great extent by earth that is thrown from the crater. Even relatively shallow underground bursts throw dirt up as a cone shaped cloud that screens surface targets from thermal radiation effectively.

Since surface reactions are complex and different types of surfaces react in different ways, the effects of underground bursts are extremely variable. As a result of these complexities as well as the fact that thermal effects from underground bursts usually are unimportant compared to other effects, methods for predicting thermal partition have not been developed for underground bursts.

**[REDACTED]** Underwater bursts are similar to underground bursts in that thermal radiation is greatly reduced by the heat absorbed by the water and by the screening effect of water thrown from

the crater. Thermal effects usually are insignificant. For example, a 20 kt burst in 90 feet of water produced negligible thermal radiation.

### Problem 3-5. Calculation of Thermal Partition for a Surface Burst

Figure 3-18 contains a family of curves that provide an effective thermal partition for surface targets from nuclear explosions that occur at heights of burst greater than  $5 W^{0.3}$  feet and less than  $180 W^{0.4}$  feet. A thermal partition of 0.21 should be used for surface targets for bursts  $5 W^{0.3}$  feet above or below the surface. Thermal partition for targets directly above the burst should be obtained from Figure 3-1 or from the upper portion (above the dashed line) of Figure 3-18.

#### Example

**Given:** A 500 kt explosion at a height of burst of 300 feet.

**Find:** The effective thermal partition.

**Solution:** From Figure 3-18, the effective thermal partition is 0.24.

**Answer:** The effective thermal partition for a surface target is 0.24. The effective thermal partition for a target directly above the burst is 0.45 (from Figure 3-1, or from the intersection of the dashed line in Figure 3-18 with a yield of

500 kt). The thermal partition for targets at intermediate altitudes would fall between these values. As a result of the uncertainties (see Reliability), the thermal partition for surface targets could fall between 0.44 and 0.1, and the thermal partition for targets directly over the burst could fall between 0.65 and 0.25.

**Reliability:** Interaction of the fireball with the surface produces complex effects, and thermal radiation from surface bursts cannot be predicted as reliably as thermal radiation from air bursts. Values of effective thermal partition obtained from Figure 3-18 are estimated to be reliable within  $\pm 0.20$  if the value is greater than 0.33. If the value that is read is less than 0.33, the lower limit of the expected range of values is 40 percent of the value that is read. The same tolerance is estimated for the effective thermal partition of the fireball as seen from above.

**Related Material:** See paragraphs 3-1 through 3-3. See also Figure 3-1.

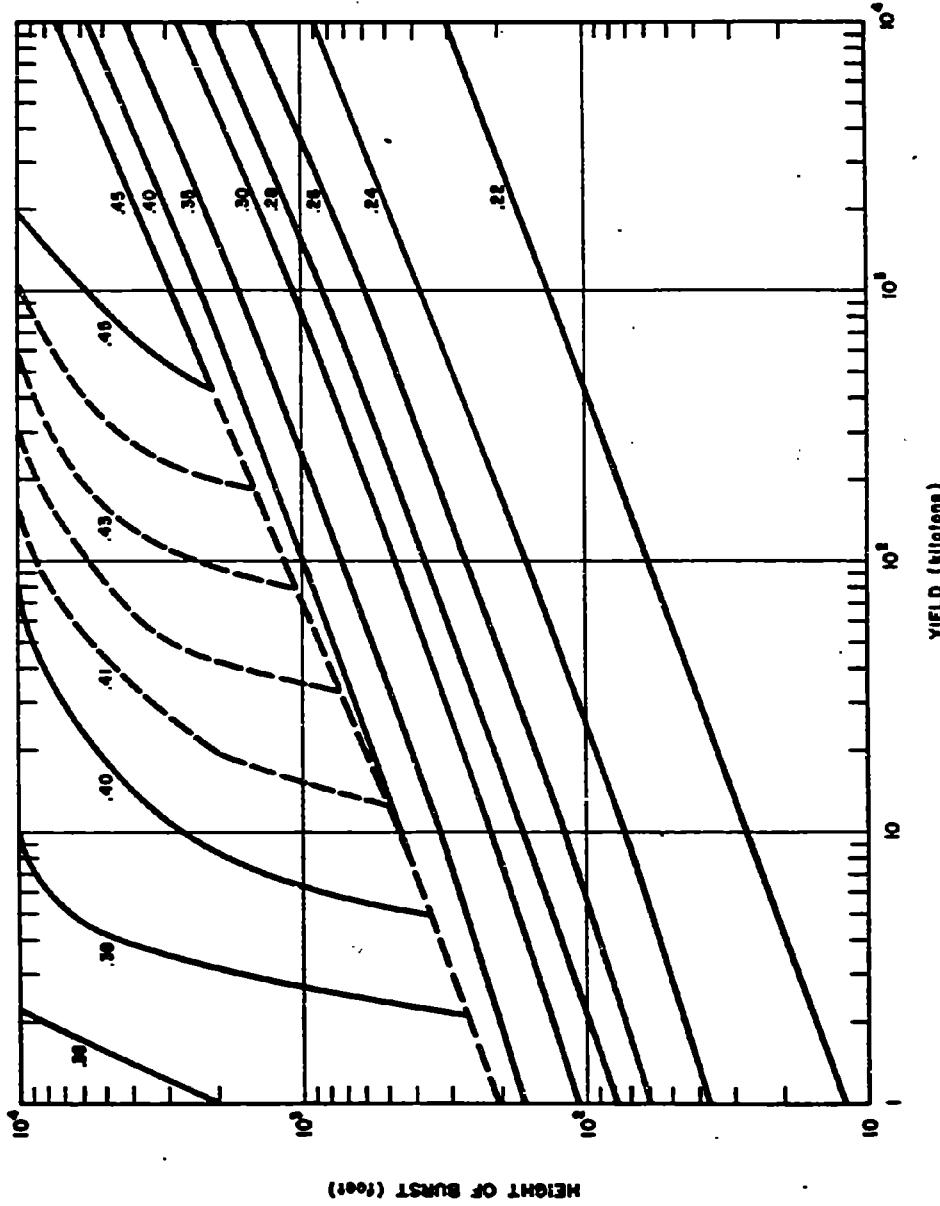


Figure 3-10. Thermal Partition for Surface Bursts

- Since the energy radiated after about  $10 t_{\max}$  produces little damage,  $10 t_{\max}$  is a logical cutoff time. This choice would have the effect of increasing the height of the energy curve so that it reaches 100 percent at  $10 t_{\max}$  in Figure 3-20.
- At times on the order of 20 or  $30 t_{\max}$ , fireball radiation becomes difficult to measure; therefore, the experimentally measured thermal pulse typically ends in this time range.

Precedent may be found for either alternative. The definition selected in this chapter is approximately equivalent to the second choice listed above: the portion of the pulse after  $10 t_{\max}$  is assigned a value of 15 percent of the total pulse energy. This definition of the prompt thermal pulse agrees within a few percent with the thermal pulse as described in most reports on thermal pulse measurements and on thermal damage effects.

Reports of theoretical calculations of the thermal pulse usually define the pulse energy in a way that corresponds roughly to the first alternative. The reason is a purely practical one: since calculation of the pulse beyond  $10 t_{\max}$  is neither accurate nor economical, the calculations usually are terminated at about  $10 t_{\max}$ . The reported energy content of the pulse is the energy contained in that portion of the pulse covered by the calculation. In reports describing these calculated results, a radiant exposure of  $8.5 \text{ cal/cm}^2$  may imply the identical thermal pulse that is implied in this chapter by a radiant exposure of  $10 \text{ cal/cm}^2$ . Similarly, a thermal partition of 0.34 as reported, for example, in DASA 1589 (see bibliography) is reported in this chapter as approximately 0.40.

The use of a standard thermal pulse introduces another problem. Since different thermal pulses have different shapes, the convenience of a standard pulse requires some sacrifice in accuracy. To minimize the effects of this

loss in accuracy, the most damaging portion of the pulse is matched carefully but substantial errors are tolerated where power levels are low. Comparison of the pulse for 200 kt at 100,000 feet (Figure 3-22) with the standard pulse (Figure 3-20) shows that the two pulses are nearly equivalent near the time of final maximum but quite different at late times.

To achieve this match, all parameters, including thermal partition, are chosen to give the correct power level and time scale at the time of final maximum. For the burst at 100,000 feet, the value of thermal partition so chosen is a few percent higher than a value based solely on total thermal energy. The standard pulse shape implies a level of late time radiation that the calculated thermal pulse for 100,000 feet fails to maintain. To match the high power portions of the calculated pulse to the standard pulse shape, thermal partition must be made artificially high.

These matters of definition present no particular problem within this manual. Thermal pulses below 100,000 feet are specified so that the standard pulse shape, the assigned value of thermal energy, and the time of final maximum imply a pulse that provides a close match to the actual pulse in its ability to produce thermal damage. On the other hand, the user must keep these details in mind if he wishes to compare thermal data as given in this chapter with similar data from other sources.

#### FIREBALL BRIGHTNESS

The surface of a nuclear fireball is many times brighter than the surface of the sun. The image of the fireball, brought to a focus on the retina of the eye, can produce burns and permanently damage the area covered by that image (see paragraph 10-20, Chapter 10). Fireball brightness is therefore one of the important parameters of the thermal source.

A detailed study of eye damage also re-

quires knowledge of the spectral distribution of thermal radiation and the transport properties of the air as a function of wavelength; however, the present discussion is limited to the most important and most easily used parameter, surface brightness. This quantity may be measured in terms of the total power per unit area radiated by the fireball. Convenient units are watts/cm<sup>2</sup>. Brightness of the sun provides a useful standard for comparison. As viewed from outside of the atmosphere, the surface brightness of the sun is 6,350 watts/cm<sup>2</sup>.

For bursts below 100,000 feet, the approximate brightness of the fireball at final maximum is

$$B = \frac{2.7 \times 10^4}{W^{0.14} (\rho/\rho_0)^{0.42}} \text{ watts/cm}^2,$$

where  $W$  is yield in kilotons and  $\rho/\rho_0$  is the ratio of ambient air density at burst altitude to ambient air density at sea level. This equation gives a rough approximation of fireball brightness; more complete and accurate data for a particular yield and altitude may be found from the equation.

$$B = \frac{P}{4 \times 10^4 \pi R_f^2}$$

where  $P$  is power in watts radiated by the fireball and  $R_f$  is fireball radius in meters. Values of  $P$  and  $R_f$  as functions of time may be found for a wide range of yields and altitudes in "Theoretical Models for Nuclear Fireballs," DASA 1589 (see bibliography).

Scattered light from a nuclear fireball can contribute to temporary flashblindness, but it is too diffuse to produce retinal burns. Consequently, the direct flux from the nuclear fireball is the only parameter of interest in the study of eye damage. Transmittance calculations are not appropriate, because they include scattered as well as direct flux.

The direct flux received from a low altitude burst (burst height about 1/4 mile or less) is attenuated by the factor

$$T_d = e^{-2R/V}$$

where  $T_d$  is the transmission coefficient of the atmosphere for direct flux,  $R$  is the slant range, and  $V$  is visual range. For higher altitude bursts, the transmission coefficient is

$$T_d = e^{-\tau(h)} \frac{R}{h} \frac{16}{V}$$

where  $\tau(h)$  is optical thickness of the model atmosphere with 16-mile visual range (Figure 3-2), and  $h$  is the height of burst.

These equations give average attenuation for the entire fireball spectrum and underestimate the amount of infrared energy that the atmosphere can transmit. Since infrared contributes substantially to eye damage, exposure to fireball radiation may be somewhat more serious than the equations given above would indicate. Figures 10-6 through 10-10 provide estimates of safe separation distances for eye damage for various observer and burst altitudes.

Cloud layers attenuate direct flux more than they attenuate radiant exposure. A cloud layer between the burst and the ground will produce the approximate attenuations shown in Table 3-3. The transmission coefficients shown in Table 3-3 are based on visible light, but they are expected to apply to the entire fireball spectrum within the limits to which a transmission coefficient can be matched to a particular sky condition.

#### THE THERMAL PULSE FROM SPECIAL WEAPONS

As stated in paragraph 2-45, Chapter 2, weapons that have enhanced radiation out-

Table 3-3. Attenuation of Direct Thermal Radiation by a Cloud or Haze Layer

Type of Atmosphere	Description of Sky	Transmission Coefficient for Direct Flux
Very clear	Visual range is 25 miles or more. This condition is rare except at high altitude locations.	90.0%
Clear	Sky deep blue. Shadows are distinct and dark.	80.0%
Light haze	Sky white; dazzling near the sun. Shadows visible, gray.	3.0%
Medium haze	Sky bright grayish white. Can view sun without discomfort. Shadows are visible but faint.	0.1%
Heavy haze	Sky dull gray-white. The sun's disk is just visible. Shadows are barely discernible.	0.003%

DNA  
KX3)

puts, i.e., weapons that produce a large fraction of their output in the form of neutrons, gamma rays, or X-rays. [redacted] will, in most cases, generate a weaker blast wave than a nominal weapon of the same yield. Similarly, the thermal pulse from such special weapons may be weaker than that from a nominal weapon. The explanation for the reduced thermal output is the same as the explanation for a weaker blast wave: neutrons, gamma rays, and [redacted] energy X-rays travel much farther through the atmosphere than the energy from a conventional weapon; therefore, a large portion of the weapon energy may be absorbed by air far from the burst. This air will not become sufficiently hot to contribute effectively to either the blast wave or to the thermal pulse.

[redacted] The terms "nominal weapon" and "conventional weapon" used in the preceding paragraph refer to a nuclear weapon that radi-

ates 70 to 80 percent of its energy as X-rays [redacted] and retains nearly all of the remaining energy as thermal and kinetic energy of the weapon debris (see paragraph 4-4, Chapter 4). Such a source serves as a convenient starting point for calculations involving weapons with other characteristics. The procedures described in this subsection apply to burst altitudes of 100,000 feet and lower.

### 3-17 Effective Thermal Yield of Special Weapons

[redacted] The modified thermal effects produced by weapons with enhanced outputs may be calculated in terms of an effective thermal yield. This is defined as the yield that a nominal warhead would have in order to radiate the same thermal energy as the special weapon. Effective thermal yield should not be interpreted to mean

thermal energy radiated (a quantity sometimes assigned to the term "thermal yield"). Effective thermal yield means the effective value of total yield to be used in thermal calculations.

The concept of effective thermal yield is an oversimplification, and it cannot describe the performance of special weapons precisely. For example, the effective thermal yield calculated on the basis of time of final maximum will, in general, be slightly different from the effective thermal yield that gives the correct value of total thermal energy radiated. A still different effective thermal yield would predict the correct power at final maximum.

In this subsection, effective thermal yield is the value that gives the correct value for thermal energy radiated, because, in most applications, this is the most important of the thermal parameters. Other parameters may be calculated by using this same value of effective thermal yield, but the calculation will be somewhat less accurate than if the procedure had been designed to calculate those parameters.

Effective thermal yield is roughly the amount of energy that the nuclear source deposits within a sphere the size of the fireball at the time of the principal minimum. This radius is

$$R_{min} = \frac{95 W^{0.36}}{(\rho/\rho_0)^{0.22}} \text{ feet}$$

$$= \frac{29 W^{0.36}}{(\rho/\rho_0)^{0.22}} \text{ meters,}$$

where  $W$  is the weapon yield in kilotons,  $\rho$  is the ambient air density at the burst altitude, and  $\rho_0$  is the ambient density at sea level. Table 3-4 shows the ratio  $\rho/\rho_0$  as a function of altitude. Energy that is deposited beyond the radius  $R_{min}$  is assumed to make a negligible contribution to the energy radiated by the fireball.

Table 3-4. Relative Air Density as a Function of Altitude

Altitude (feet)	Relative Density,* $\rho/\rho_0$	Altitude (feet)	Relative Density,* $\rho/\rho_0$
0	1.000	80,000	0.0361
1,000	0.971	85,000	0.0284
2,000	0.943	90,000	0.0224
3,000	0.915	95,000	0.0176
4,000	0.888	100,000	0.0140
5,000	0.862	110,000	8.69-3†
10,000	0.739	120,000	5.43
15,000	0.629	130,000	3.45
20,000	0.533	140,000	2.22
25,000	0.449	150,000	1.45
30,000	0.375	160,000	9.77-4
35,000	0.311	170,000	6.69
40,000	0.247	180,000	4.65
45,000	0.194	190,000	3.22
50,000	0.153	200,000	2.22
55,000	0.121	210,000	1.54
60,000	0.0949	220,000	1.05
65,000	0.0747	230,000	7.05-5
70,000	0.0586	240,000	4.62
75,000	0.0459	250,000	2.60

\*  $\rho_0 = 2.38 \times 10^{-3} \text{ slugs/ft}^3 = 1.225 \text{ gm/cm}^3$ .

† 8.69-3 means  $8.69 \times 10^{-3}$ .

Since the size of the fireball is determined by the thermal energy it contains, it would be logical to let  $W$  represent effective thermal yield rather than total weapon yield. To do this requires a trial-and-error approach. Effective yield is unknown until the equation given above has been solved and the energy deposited within  $R_{min}$  has been determined. In practice, the accuracy of this method for calculating effective thermal yield is sufficiently uncertain that this refinement is seldom justified. Unless

DNA

(f)(3)

the effective thermal yield is less than half of the total yield, it is recommended that  $W$  be equated to total yield in the equation.

To determine the amount of energy deposited within a radius  $R_{min}$  of the burst, the form of the energy emitted by the weapon must be determined.

The steps in calculating the energy contained within  $R_{min}$  are:

1. Find the scaled radius

$$(\rho/\rho_0) R_{min} = 95 W^{0.36} (\rho/\rho_0)^{0.78} \text{ feet}$$
$$= 29 W^{0.36} (\rho/\rho_0)^{0.78} \text{ meters.}$$

This is the path length at sea level that passes through the same amount of air that a path of length  $R_{min}$  passes through at the burst altitude. Use of this scaled radius makes further scaling unnecessary.

2. Assume that 100 percent of the debris is contained within the radius.

3.

4. In a similar manner, find the amount of gamma ray energy that is deposited within  $R_{min}$  of the burst. The 1 MeV gamma photon curve in Figure 3-24 is approximately representative of the energy deposition properties of the gamma spectrum of a nuclear weapon.

5.

6. The components of energy deposited within  $R_{min}$  of the burst are added together to obtain the effective thermal yield.

The calculation is then repeated on the basis of this new value of scaled radius.

The effective thermal yield calculated by the procedures described above may be used to calculate other thermal parameters by the methods described in preceding paragraphs. For example, the effective thermal yield may be used as the weapon yield to calculate thermal partition as described in paragraph 3-1.

### 3-18 Thermal Pulse Shape from Special Weapons

The two properties that characterize special weapons (in the sense that the term is used in this chapter) are that the initial deposition of energy fills a large volume and that the density of the deposited energy drops gradually with distance from the point of burst when compared to nominal weapons. The early fireball of a conventional weapon rapidly develops a sharply defined edge, formed by the shock front. The sharply defined edge results in a very bright fireball; the diffuse fireball from an enhanced weapon is relatively dim, becoming bright only when the shock wave propagates through the incandescent region of the initial fireball and reaches cooler air.

DNA  
(b)(3)

The thermal pulse assumes its conventional appearance at a time that depends on yield, altitude, and output properties of the nuclear device.

DNA  
(b)(3)

DNA  
(b)(3)

HIGH ALTITUDE THERMAL  
PHENOMENA

DNA  
(EX3)

DNA  
(EX3)

Both experimental and theoretical data are very limited, so the methods described are based on information that is sketchy at best. An additional problem affects theoretical data: the approximations necessary to limit computer programs to a usable size become poorer at higher altitudes. Although many points of agreement exist between experimental data and the corresponding computer calculations, the confidence that can be placed on theoretical results is less at high altitudes than at low altitudes.

3-19 Thermal Partition

Two factors affect thermal partition at high altitudes. First, shock waves form much less readily in the thinner air; consequently the fireball is able to radiate thermal energy that would have been transformed to hydrodynamic energy of the blast wave at lower altitudes. Second, the thinner air allows energy from the nuclear source to travel much farther than is possible at sea level. Some of this energy travels so far from the source that it makes no contribution to the energy contained in the fireball.

In general, the first of these factors becomes effective between about 100,000 and 140,000 feet, and, as a result, thermal efficiency rises. Above 140,000 feet, the second factor becomes the more important and efficiency drops.

As in the previous subsection on special weapons, this method requires that the X-ray output of the weapon be represented by the sum of several black body spectra. The energy density deposited at a given range may then be obtained from Figure 3-25a or 3-25b. Briefly, the scaling procedure is the following: the energy  $\Delta E_2 = 2,500 \text{ cal/gm}$  is scaled by the equation

$$\frac{\Delta E_2}{\Delta E_1} = \left( \frac{\rho}{\rho_0} \right)^2 \frac{W_2}{W_1}$$

This equation is solved for  $\Delta E_1$ , the value of energy to be read directly from Figure 3-25a or 3-25b. In this equation,  $\rho/\rho_0$  is the ratio of ambient air density at burst altitude to ambient

density at sea level (Table 3-4),  $W_1$  is a reference yield of 1 kt and  $W_2$  is the energy, in kilotons, contained in a particular black body temperature component of the nuclear source.

The scaled radius  $R_1$  is read directly from the horizontal axis of Figure 3-25a or 3-25b. This radius is related to the actual radius  $R_2$  by the scaling equation

$$\frac{R_1}{R_2} = \frac{\rho}{\rho_0}$$

However, the rest of the problem does not require that  $R_2$  be known; the calculation is based only on the scaled radius  $R_1$ . In general,  $R_1$  is determined by more than a single spectral component; the way in which this calculation is performed is made clear in Problem 3-7.

The method of treating debris, gamma, and neutron energy is identical to that described in paragraph 3-17.

time (see Figure 3-23), pulse duration no longer can be specified in terms of the time to final maximum. A number that is useful in many applications is  $t_{70}$ , the time required for a pulse to deliver 70 percent of the total energy. At low altitudes,

$$t_{70} \approx 2.9 t_{\max}$$

and it follows that at high altitudes it might be possible to assign an effective time of final maximum such that

$$t_{\max} \text{ (effective)} = t_{70}/2.9.$$

Analyses of a limited number of computer calculations of high altitude burst phenomena show the following trends: below 80,000 feet, the equation holds within the scatter of the data; above 80,000 feet, the thermal pulse is delivered more rapidly than this equation predicts, until at 160,000 feet the pulse is only about a third as long as predicted by the equation, above 200,000 feet, the pulse approaches and, in one case, exceeds the predicted value. This behavior is shown in Figure 3-26.

Since the thermal pulse

Since the thermal pulse from a high altitude explosion rises to its maximum in an extremely short time and declines from that

3-21 Bursts Above 250 Kilofeet

The calculations indicate that at heights of burst at or above about 290,000 feet the incandescent air heated by absorption of X-rays from the explosion is approximately at the same altitude, regardless of the actual height of burst. The heated region then reradiates at the longer wavelengths which could reach the ground. The reradiating region is in the form of a frustum of a cone, pointing upward, with a vertical thickness of approximately 45,000 feet and a mean altitude of 270,000. At this altitude, the radius of the frustum is roughly equal to the difference between the height of burst  $h$  and 270,000 feet, i.e.,  $h - 270,000$  feet. Consequently, as the burst altitude increases, the radius of the radiating region becomes greater but its thickness and altitude remain roughly constant. The shape of the region thus approaches a thick disk centered at about 270,000 feet altitude. The debris energy still is contained fairly locally until the height of burst reaches the debris stopping altitude of about 380,000 feet (see Table 8-1, Chapter 8), but the main effects of thermal energy delivered as a result of debris deposition at these altitudes are flashblindness or retinal burns (see Section

II, Chapter 10). The total thermal energy emitted as a result of the debris deposition is masked by that energy emitted at lower altitudes as a result of X-ray deposition insofar as total energy that reaches the earth is concerned.

About one-fourth of the X-ray energy from the explosion is absorbed in the low density air of the reradiating region, and only a small fraction, which decreases with the height of burst, is reradiated as secondary radiation. Consequently, only a few percent of the weapon energy is emitted as radiation capable of causing damage at the earth's surface. In fact, for bursts at altitudes exceeding about 330,000 feet the thermal radiation from a nuclear explosion even in the megaton range is essentially ineffective on the ground.

If the horizontal distance  $d$  from ground zero, i.e., from the point on the ground immediately below the center of the disk-like region, to the position where the incident thermal energy is to be calculated is less than the height of burst,  $h$ , the source may be regarded as being located at the median radius of the disk in an altitude of 270,000 feet; this is indicated by the point  $S$  in Figure 3-27. Hence, for the target point  $X$ , the appropriate slant range is given by

$$R \text{ (kilofeet)} = \left\{ (270)^2 + [1/2(h - 270) - d]^2 \right\}^{1/2},$$

with  $d$  and  $h$  in kilofeet. This expression holds even when  $d$  is greater than  $1/2(h - 270)$ ; although the quantity in the square brackets is then negative, the square is positive. The slant range,  $R_0$ , for ground zero is obtained by setting  $d$  equal to zero; thus,

$$R_0 \text{ (kilofeet)} = [(270)^2 + 1/2(h - 270)^2]^{1/2}.$$

If the distance  $d$  is greater than the height of burst, and equivalent point source is located at

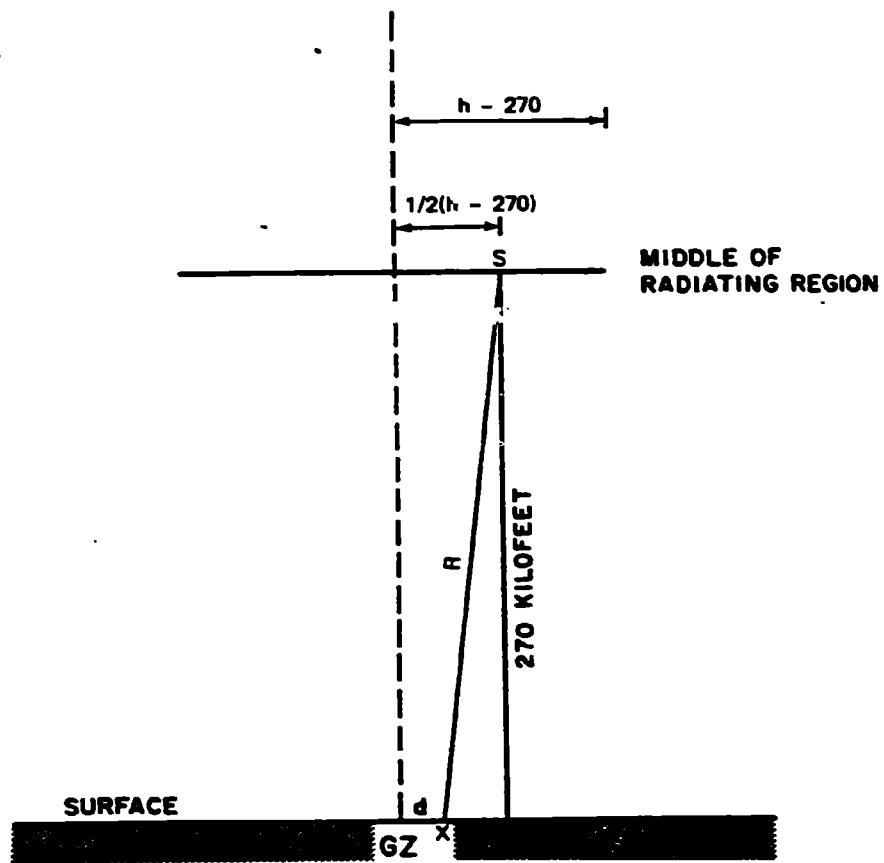


Figure 3-27. [REDACTED] Equivalent Point Source at Median Radius  
When Height of Burst Exceeds Distance of  
Target, X, from Ground Zero [REDACTED]

the center of the radiating disk at 270,000 feet altitude; then

$$R \text{ (kilofeet)} = [(270)^2 + d^2]^{1/2}$$

The calculations assumed that 80 percent of the total yield is emitted as X-ray energy and that 25 percent of this energy is absorbed in the radiating disk region. Hence,  $0.8 \times 0.25 = 0.2$  of the total yield is absorbed. For calculating the radiant exposure, the total yield  $W$  in the equations in paragraph 3-2 is consequently replaced by  $0.2 W$ . Furthermore, the equivalent of the thermal partition is called the "thermal efficiency,"  $\epsilon$ , defined as the effective fraction of the absorbed energy that is reradiated. Hence, if  $R$  is in kilofeet, the equation for radiant exposure given in paragraph 3-2 becomes

$$Q = \frac{17.1\epsilon WT}{R^2} \text{ cal/cm}^2$$

The values of  $\epsilon$  given in Figure 3-28 as a function of height of burst and yield were obtained by the theoretical calculations mentioned previously. The transmittance may be estimated from Figure 3-15, but no serious error would be involved by setting it equal to unity for the large burst heights involved. No attempt should be made to interpolate between values of radiant exposure obtained for a burst height of 250,000 feet by the method described in paragraph 3-19 and the values obtained for 290,000 feet by the method described in this paragraph. If values of radiant exposure from bursts between these altitudes are desired, it is recommended that the radiant exposure be calculated for each altitude (250,000 feet and 290,000 feet) and that the higher or lower value be taken as an estimate, depending on the direction of conservatism that is desired.

## RELIABILITY OF THERMAL SOURCE DATA

Most of the thermal radiation source data presented in this chapter were obtained from the series of computer runs reported in DASA 1589, "Theoretical Models for Nuclear Fireballs" (see bibliography). These data are not purely theoretical: development of the computer code included comparisons of calculated results with experimental data, and adjustments in the assumed weapon characteristics were made as a result of these comparisons.

The advantages of computer data (provided that this choice can be justified) are:

(1) This method eliminates many random errors that are inherent in experimental data. These random errors include uncertainty in the exact value of nuclear yield, instrument errors, uncertainty in atmospheric transmittances, blurring of some results as a result of finite time resolution of certain instruments, and uncertainty in the methods for transforming measured data to the parameters required for thermal calculations.

(2) Computer calculations can generate a large amount of data for a wide range of yields and altitudes that are not available from experiments.

(3) Errors that appear in the code results are likely to be consistent; therefore, the code probably predicts the trends produced by changes in yield or altitude more accurately than it predicts the results of any individual burst.

The disadvantage of using the code is that at best it gives only an approximation of the many processes that determine, directly or indirectly, the amount of thermal energy radiated. The method of accounting for spectral absorption lines is an example of the approximations that are required. A subroutine stores data for 151,528 different spectral lines, yet this is a small fraction of the number of lines that affect

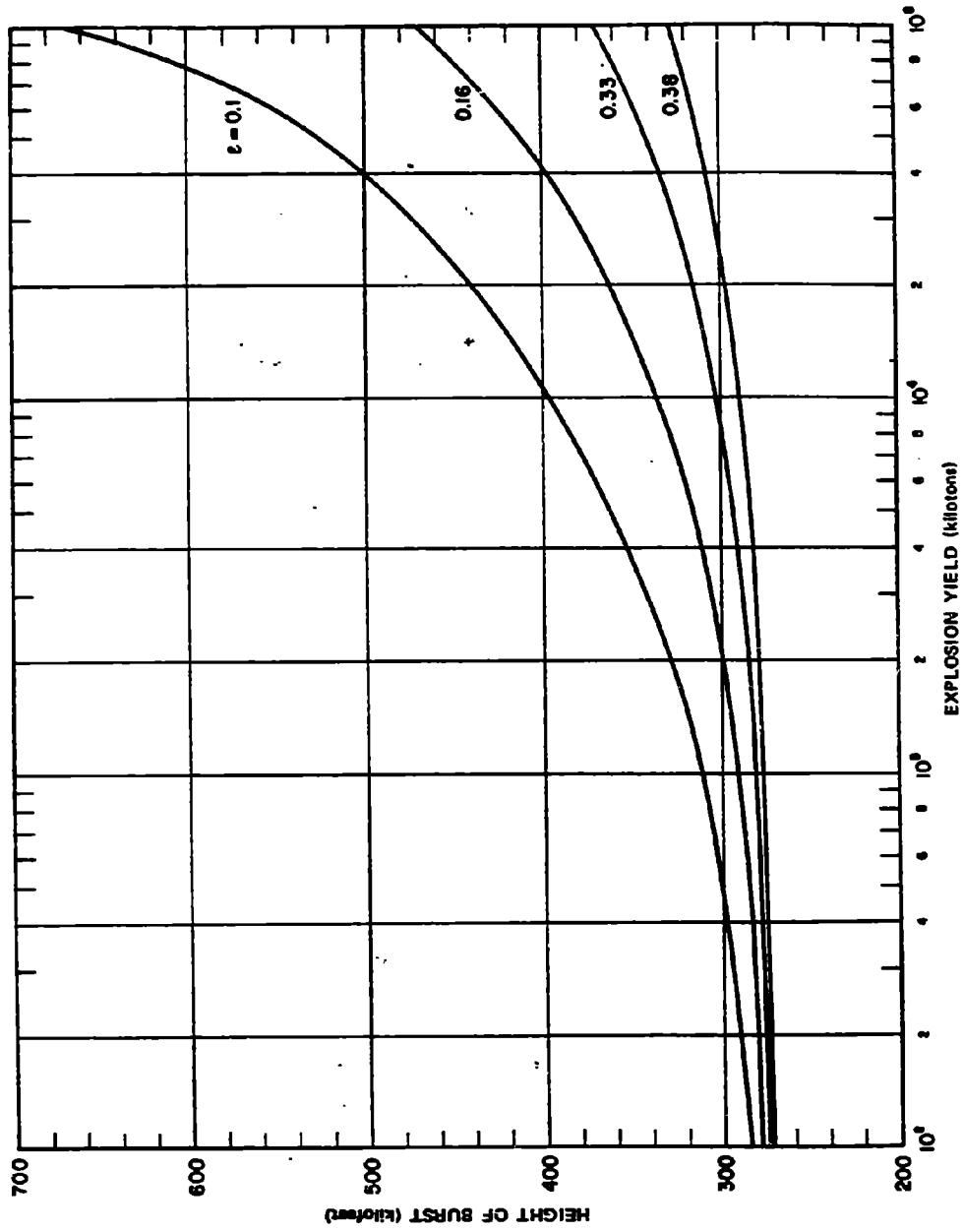


Figure 3-28. Fraction of Absorbed X-ray Energy Reradiated

[REDACTED] radiative transport within the fireball.

[REDACTED] Justification for using the code is the agreement between code results and measured data. The most striking areas of agreement are: (1) radius-time data, which are the most accurate experimental data, and (2) the ability of the code to reproduce intricate details of fireball evolution such as the fluctuations of the power-time curve (Figure 3-19) and the complex structure observed in high altitude fireballs.

[REDACTED] Unfortunately, the code-calculated parameters that are of more direct interest in this chapter (e.g., thermal partition) cannot be confirmed as accurately by experimental data. Since uncertainty in the experimental data generally is as great as the discrepancy between theory and experiment, the experimental data provide no clear indication of the reliability of the code results, e.g., the code reproduces observed fireball phenomena within the accuracy of most test measurements.

[REDACTED] This agreement has been obtained by comparisons of early code results with experimental data; however, changes in the code have never taken the form of arbitrary correction factors. Two examples illustrate the procedure used to correct the code.

[REDACTED] The code, as originally written, did not predict the correct level of radiation during the first maximum. Analysis of the radiative properties of the shock front revealed that a shock precursor (discussed in paragraph 3-25), a very thin layer of heated air ahead of the shock front, determines the radiative properties of the fireball during this interval. The fine structure of this precursor was lost by the approximate methods that were required to represent the shock front on the computer. A possible solution, much finer zoning in the region of the shock front, was rejected as uneconomical; however, a separate program to calculate shock-wave properties gave results that agree with the observed first maximum. This separate program

[REDACTED] was used to correct the radiation level that was calculated by the main computer program.

DNA  
(6X3)



[REDACTED] These illustrations show that the computed results are based on physical data. In a sense, experimental data are represented indirectly because they indicated the parts of the computer program that should be examined more closely. Nevertheless, agreement between code results and observations indicate that the physics of radiative transport and hydrodynamic motion is understood well enough that the computer program is an adequate representation of the fireball itself. Therefore, in this chapter these code results are tentatively accepted as the preferred source of data concerning the source of thermal radiation from nuclear fireballs.

#### RELATION OF RADIANT EXPOSURE TO PEAK OVERPRESSURE

[REDACTED] In many weapons effects problems, the first step is to determine which nuclear effect establishes the damage radius for a given burst. The series of figures in this subsection (Figure 3-29 through 3-56) show radiant exposure and peak overpressure as a function of height of burst and ground distance for 7 yields. The curves in these figures provide an aid in the determination of whether blast or thermal effects will be more important for specific situations. Four families of curves are presented for each yield. In each case the first two families of

curves are for no atmospheric attenuation of the thermal radiation, i.e., the worst case thermal exposure, and the second two families of curves are for a visual range of 16 miles (a clear day). Table 3-5 shows a summary of the data presented in the figures.

These curves reflect the data presented in preceding paragraphs of this chapter and the free field air blast data from Chapter 2 accurately for the yields and conditions shown on each figure; however, they do not provide the answers to all potential problems, e.g., only 7 yields are included, and no data are presented for visual

ranges less than 16 miles. The curves are intended to be used as an aid in determining the relative importance of blast and thermal radiation. Their use can be extended beyond the particular values that are plotted. For instance, the value of radiant exposure obtained from the curves for no atmospheric attenuation may be converted to the value for any visual range by multiplying by the transmittance appropriate to the given conditions. Interpolation between yields will provide a first order, and frequently sufficient, estimate of the more important effect.

Table 3-5. Summary of Blast-Thermal Curves

Figure Number	Yield (kt)	Atmospheric Attenuation	Blast Values (psi)
3-29	0.01	None	10-50
3-30	0.01	None	1- 4
3-31	0.01	16 Mile Visual Range	10-50
3-32	0.01	16 Mile Visual Range	1- 4
3-33	0.1	None	10-50
3-34	0.1	None	1- 4
3-35	0.1	16 Mile Visual Range	10-50
3-36	0.1	16 Mile Visual Range	1- 4
3-37	1.0	None	10-50
3-38	1.0	None	1- 4
3-39	1.0	16 Mile Visual Range	10-50
3-40	1.0	16 Mile Visual Range	1- 4
3-41	10	None	10-50
3-42	10	None	1- 4
3-43	10	16 Mile Visual Range	10-50
3-44	10	16 Mile Visual Range	1- 4
3-45	100	None	10-50
3-46	100	None	1- 4
3-47	100	16 Mile Visual Range	10-50
3-48	100	16 Mile Visual Range	1- 4
3-49	1,000	None	10-50
3-50	1,000	None	1- 4
3-51	1,000	16 Mile Visual Range	10-50
3-52	1,000	16 Mile Visual Range	1- 4
3-53	10,000	None	10-50
3-54	10,000	None	1- 4
3-55	10,000	16 Mile Visual Range	10-50
3-56	10,000	16 Mile Visual Range	1- 4

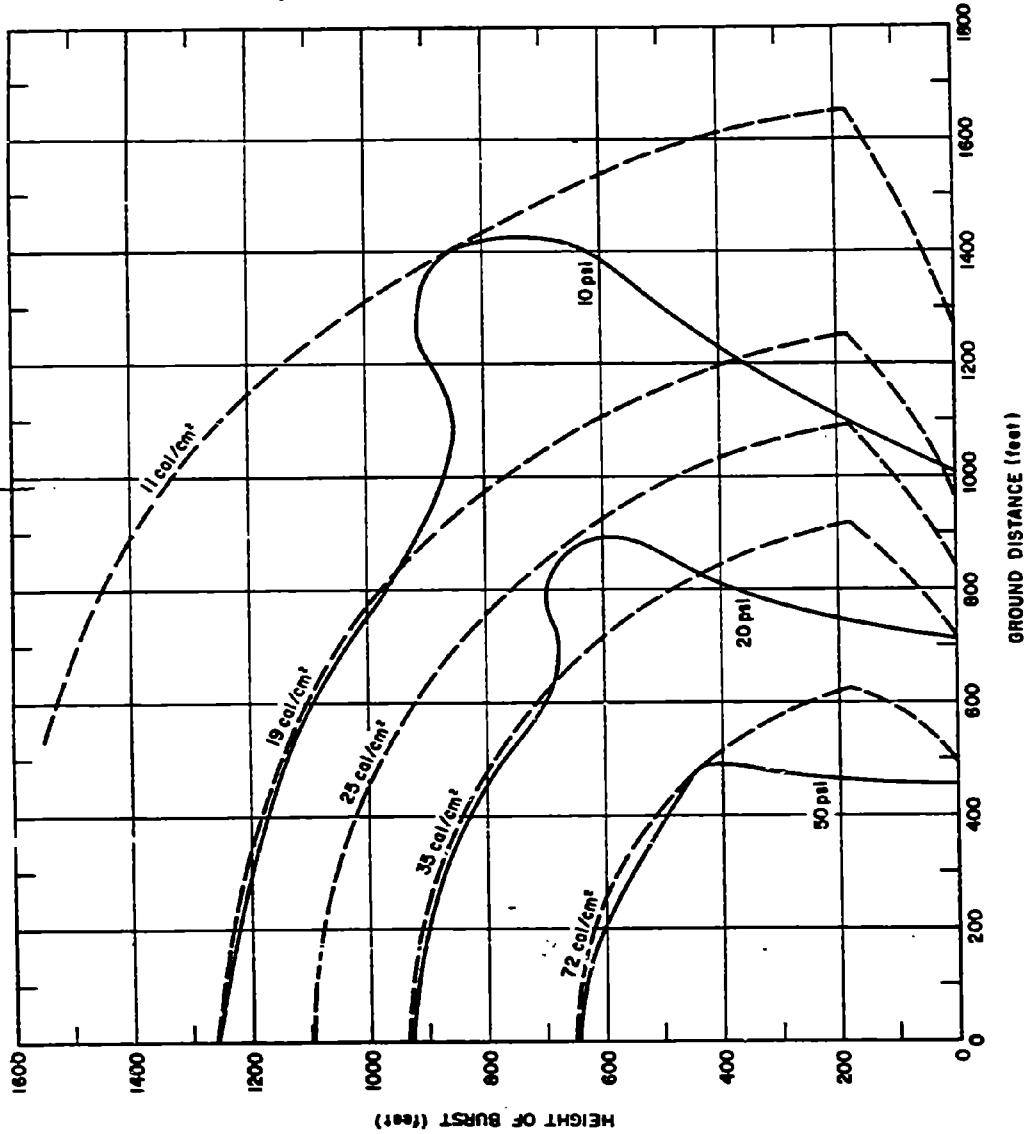


Figure 3-39. Free Field Radiant Exposure and Air Blast Overpressure at the Surface, as a Function of Height of Burst and Ground Distance, for 1 kiloton, 18 Mile Visual Range, High Overpressure Region

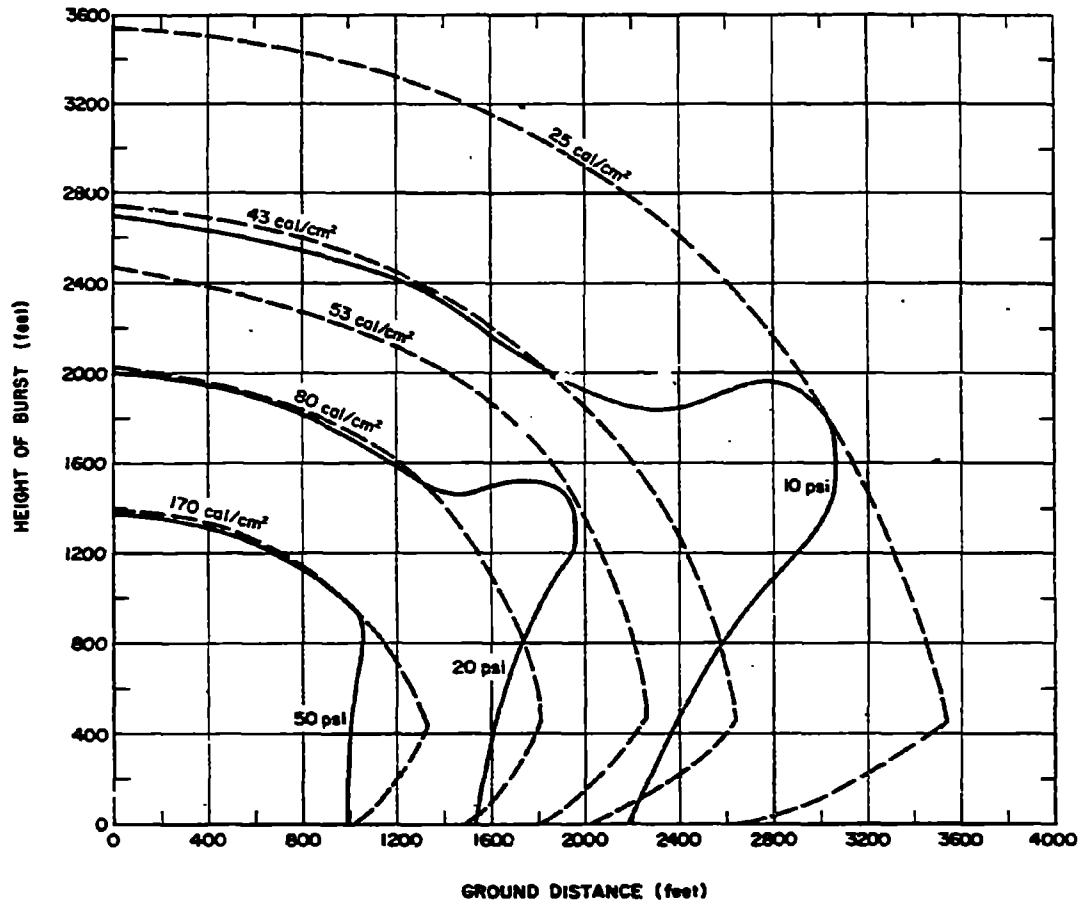


Figure 3-43. Free Field Radiant Exposure and Air Blast Overpressure at the Surface, as a Function of Height of Burst and Ground Distance, for 10 kilotons, 16 Mile Visual Range, High Overpressure Region

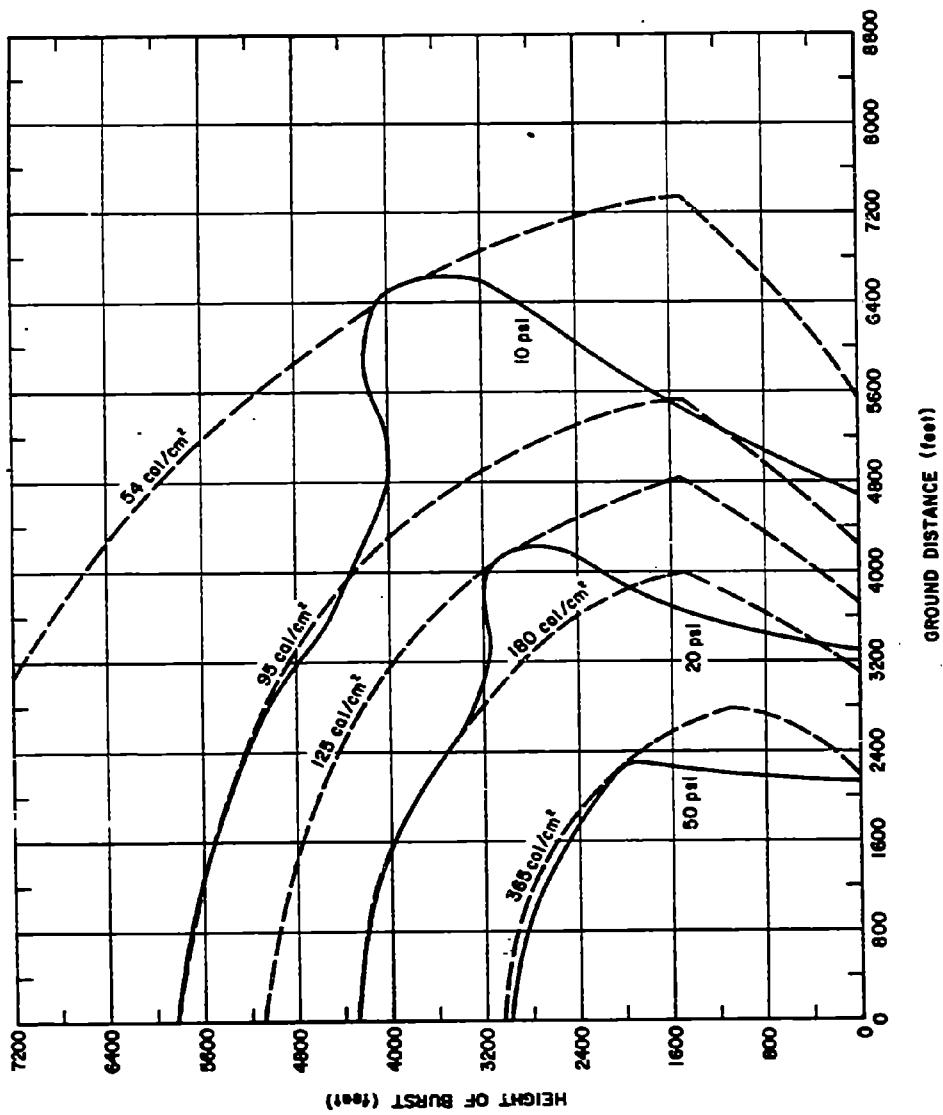


Figure 3-47. Free Field Radiant Exposure and Air Blast Overpressure at the Surface, as a Function of Height of Burst and Ground Distance, for 100 kilotons, 16 Mile Visual Range, High Overpressure Region

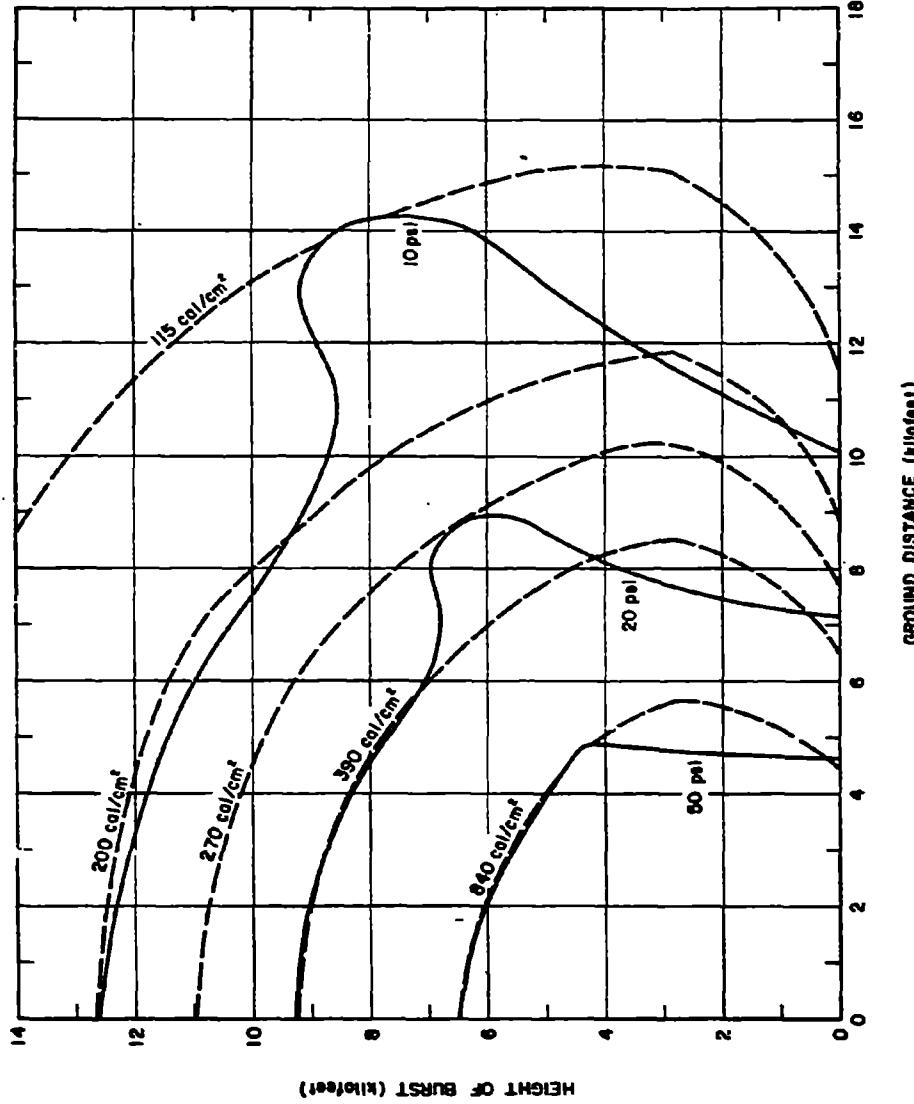


Figure 3-51. Free Field Radiant Exposure and Air Blast Overpressure at the Surface, a Function of Height of Burst and Ground Distance, for 1 megaton, 16 Mile Visual Range, High Overpressure Region

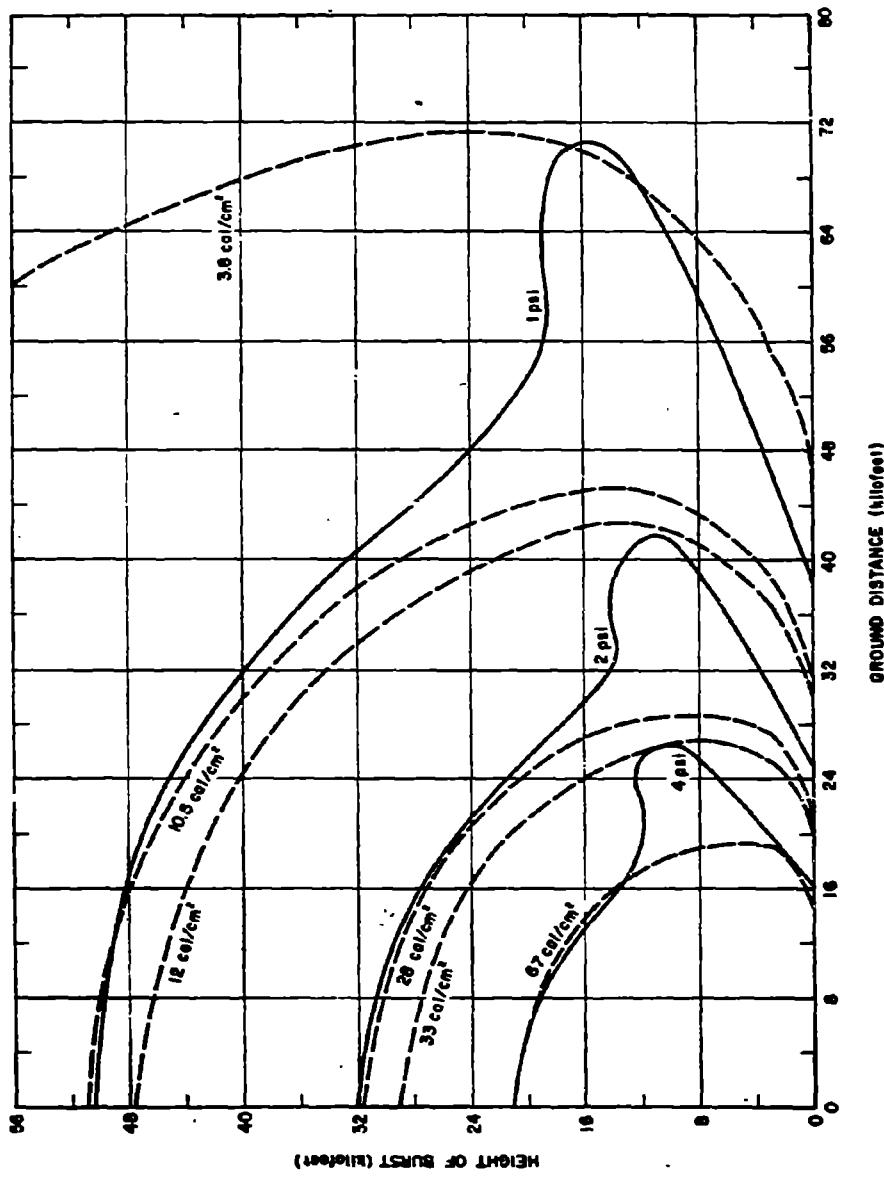


Figure 3-32. Free Field Radiant Exposure and Air Blast Overpressure at the Surface, as a Function of Height of Burst and Ground Distance, for 1 megaton, 16 Mile Visual Range, Low Overpressure Region

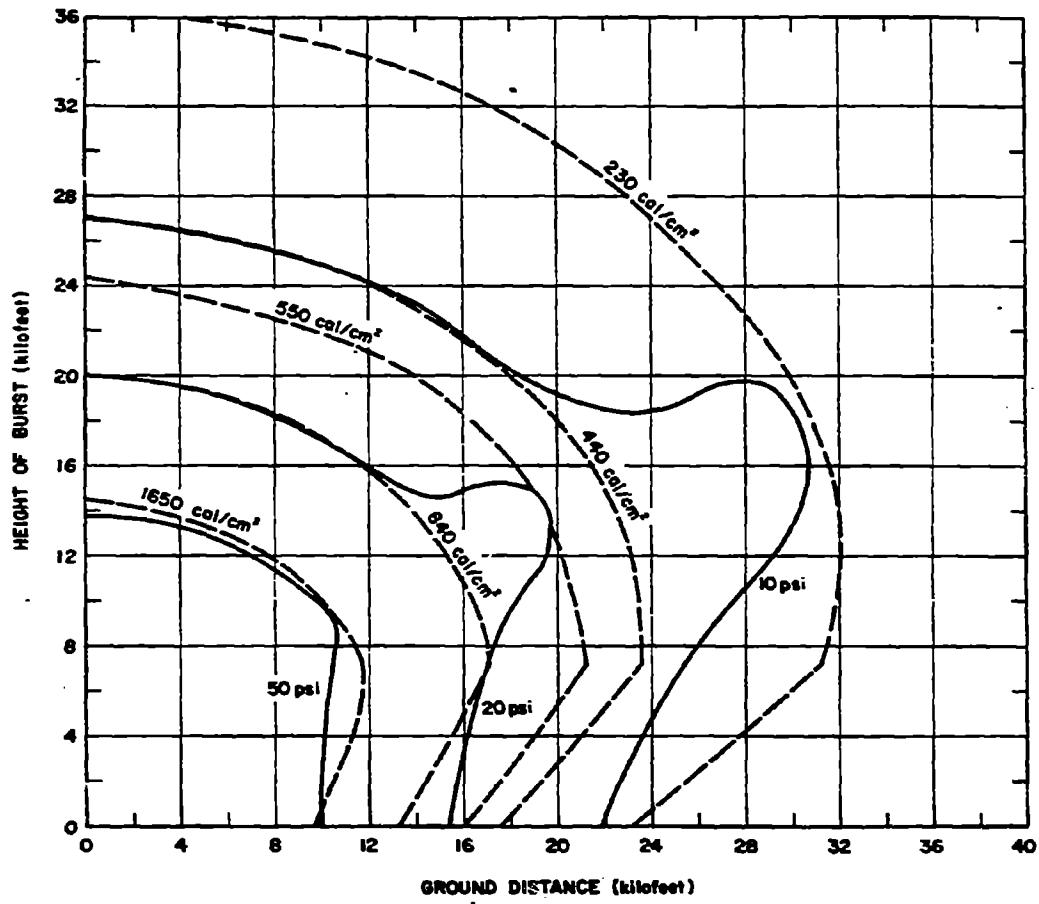


Figure 3-55. Free Field Radiant Exposure and Air Blast Overpressure at the Surface, as a Function of Height of Burst and Ground Distance, for 10 megatons, 16 Mile Visual Range, High Overpressure Region

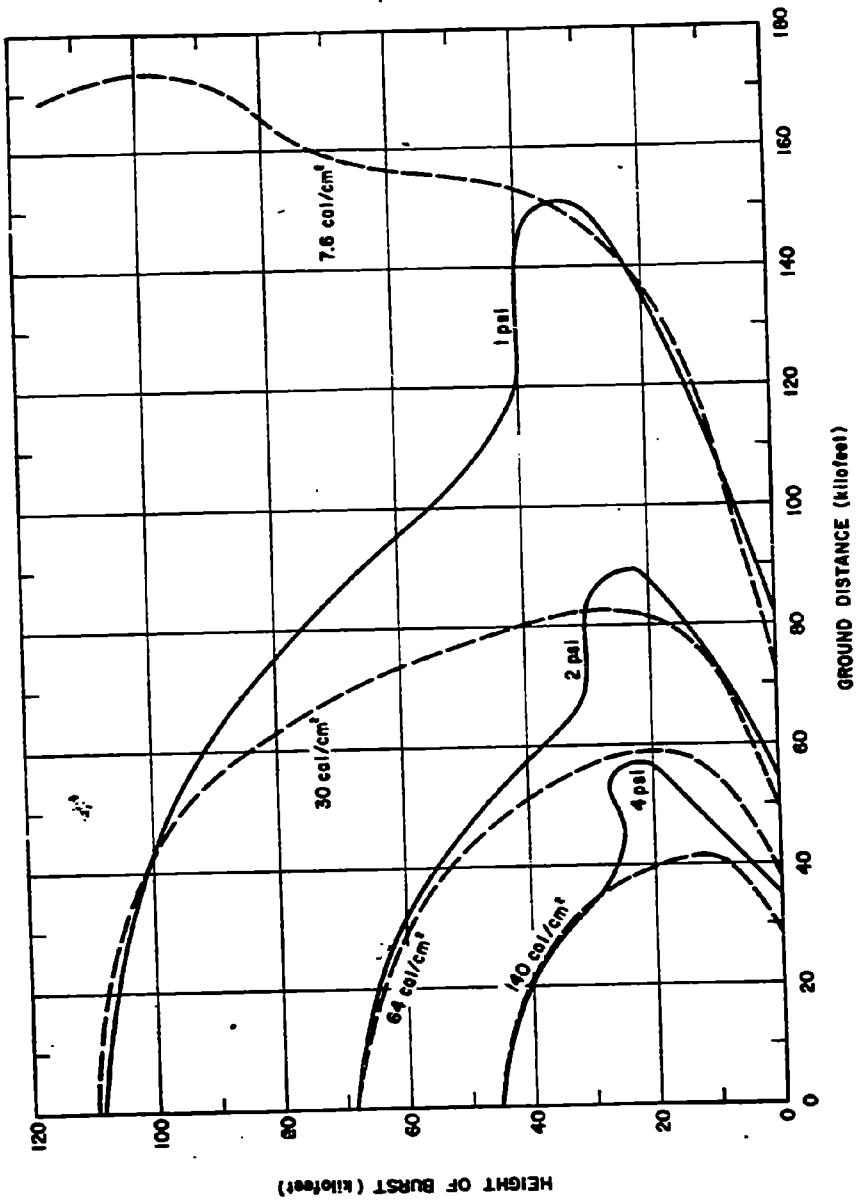


Figure 3-58. Free Field Radiant Exposure and Air Blast Overpressure at the Surface, as a Function of Height of Burst and Ground Distance, for 10 megatons, 16 Mile Visual Range, Low Overpressure Region

[REDACTED]  
[REDACTED] BIBLIOGRAPHY [REDACTED]

Duntley, S. O., *The Visibility of Distant Objects*, Journal of the Optical Society of America, 38, 237-249, 1948 [REDACTED]

Ellis, P. A., *A Note on the Prediction of Thermal Pulse from Special Nuclear Weapons* [REDACTED]  
DASA 2097, KN-717-68-3, Kaman Nuclear, Colorado Springs, Colorado, 20 March 1968  
[REDACTED]

Gibbons, M. G., *Transmissivity of the Atmosphere for Thermal Radiation from Nuclear Weapons*, USNRDL-TR-1060, U.S. Naval Radiological Defense Laboratory, San Francisco, California, 12 August 1966 [REDACTED]

Hillendahl, R. W., *Theoretical Models for Nuclear Fireballs* [REDACTED] (41 Volumes) DASA 1589,  
Lockheed Missiles and Space Company, Sunnyvale, California, 1965-1968 (Part A,  
[REDACTED] Part B, [REDACTED] Volumes 1-39, [REDACTED])  
[REDACTED]

Landshoff, R. M., *Thermal Radiation Phenomena* [REDACTED] (6 Volumes), DASA 1917, Lockheed  
Missiles and Space Company, Palo Alto, California, 1967 (Volumes 1-5, [REDACTED]  
Volume 6, [REDACTED])

*Manual of Surface Observations (WBAN)*, 7th Edition, Circular N., U.S. Government Print-  
ing Office, Washington, D.C., 1966 [REDACTED]

Middleton, W. E. Knowles, *Vision Through the Atmosphere*, University of Toronto Press,  
1958 [REDACTED]

Passell, T. O., and R. I. Miller, *Radiative Transfer from Nuclear Detonations Above 50-km  
Altitude*, Fire Research Abstracts and Reviews, Vol. 6, No. 2, 1964 [REDACTED]

Shnider, R. W., *A Compilation and Semi-Empirical Analysis of Thermal Pulse Times* [REDACTED]  
URS 7007, DASA 2677, URS Research Company, San Mateo, California, September  
1970 [REDACTED]

Wells, P. B., J. R. Keith, R. E. Welick, and D. C. Sachs, *Air Blast from Special Weapons* [REDACTED]  
(3 Volumes) KN-68-168(R), Kaman Nuclear, Colorado Springs, Colorado, October 1968  
(Volume 1, [REDACTED] Volume 2, [REDACTED] Volume 3, [REDACTED])



## Chapter 4

### X-RAY RADIATION PHENOMENA

#### INTRODUCTION

##### 4-1 Production of X-Rays

X-rays are electromagnetic radiations of frequencies from about  $10^{16}$  Hz\* to about  $10^{20}$  Hz, overlapping ultraviolet radiation at the low frequency end of the spectrum and gamma rays at the high end (see Figure 4-1). The wavelengths of the radiations are given by

$$\lambda = c/\nu \text{ cm.}$$

where  $\nu$  is the frequency in Hz, and  $c$  is the velocity of light ( $3 \times 10^{10}$  cm per sec). X-rays exhibit particle-like properties as well as wave-like properties, and are absorbed or emitted in quanta, or photons, of energy

$$E = h\nu \text{ ergs.}$$

where  $h$  is Planck's constant ( $6.625 \times 10^{-27}$  erg-sec). This energy is ordinarily expressed in kiloelectron-volts (keV).† Figure 4-2 shows X-ray wavelength and frequency as a function of photon energy. The more energetic X-rays of higher frequency are commonly known as "hard" X-rays, and the less energetic ones are correspondingly "soft."

The distinction between X-rays and other electromagnetic radiations is not made in terms of their respective frequencies but in terms of their method of production. Gamma rays, for instance, are those photons produced as a result of nuclear forces, whereas production of X-rays is associated with electromagnetic forces acting on electrons. Two basic physical mech-

anisms are principally responsible for X-ray production; the corresponding emissions are bremsstrahlung (braking radiation) and the characteristic radiation.

Bremsstrahlung is a result principally of inelastic (or radiative) scattering of fast electrons by atoms. If a beam of monoenergetic electrons impinges on a thick target, a spectrum of X-rays is produced with maximum energy equal to that of the electrons and a spectral distribution that depends on the atomic number,  $Z$ , of the target.

The spectrum of X-rays from such an experiment will contain (in addition to the bremsstrahlung spectrum) a number of intense, fairly sharp spectral lines. These lines are characteristic of the material being bombarded and result from X-rays that are emitted when the atomic electrons rearrange themselves into states of lower energy after one or more electrons have been knocked out of the atom by the bombarding electrons. Since the atomic electrons must be in one of a number of discrete energy stages, transitions between the states are accomplished by emissions of photons of discrete energies. If the initial beam has sufficient energy to remove the most tightly bound (K-shell) electrons from the atom, all possible transitions between states will result in X-rays and all of the characteristic spectral lines will be seen. At slightly lower incident beam energies, the K X-ray lines will disappear but the other lines will still be observed, and so on. The frequencies of the characteristic radiation depend on the atomic numbers of the

\*1 Hz (Hertz) = 1 cycle per second.

†1 keV =  $10^3$  ev; 1 ev =  $1.6 \times 10^{-12}$  erg

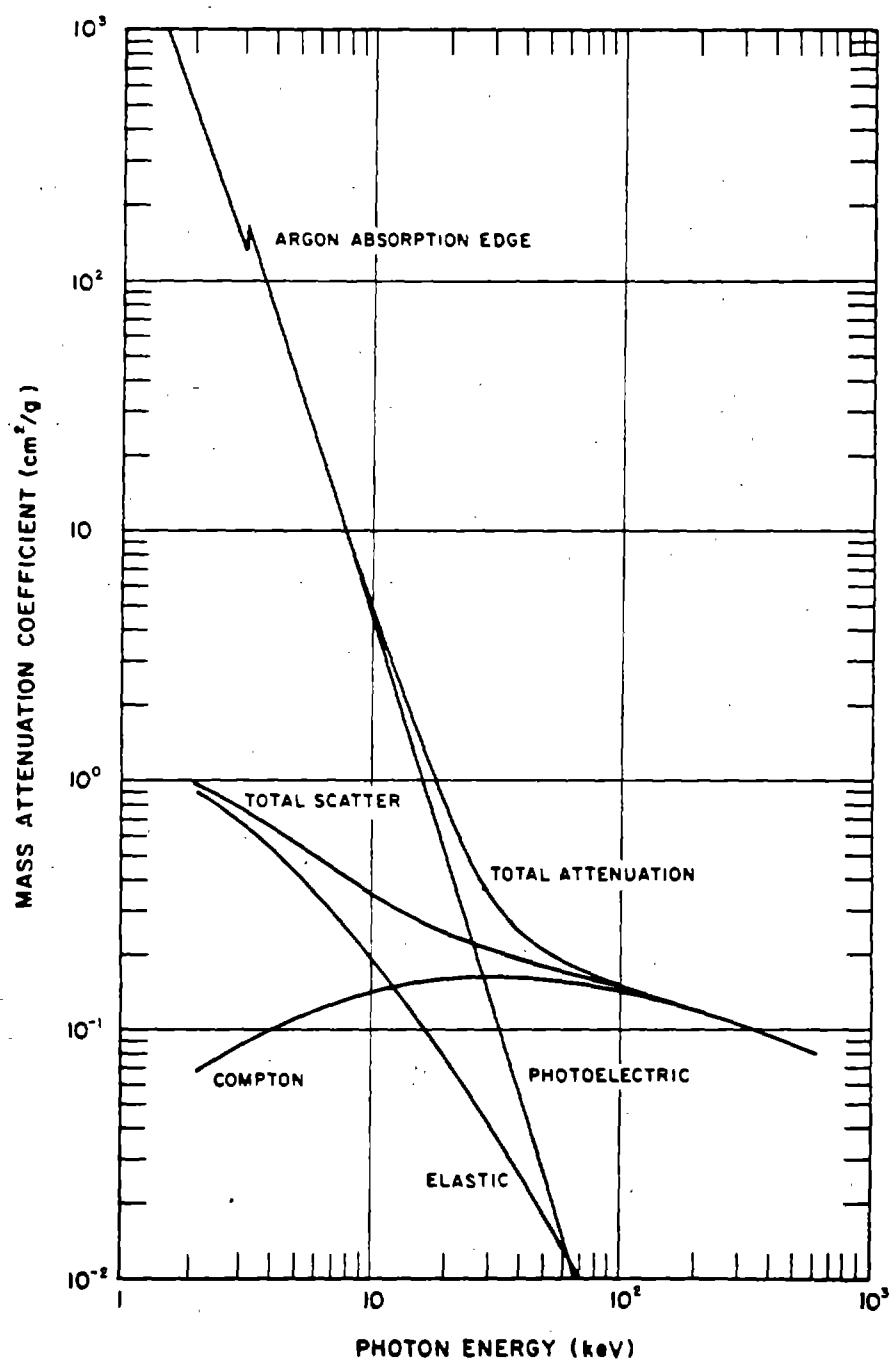


Figure 4-4. Mass Attenuation Coefficients for Air

as far as X-ray production is concerned, is that a very hot (tens of millions of degrees Kelvin) plasma is formed, consisting of electrons and the stripped nuclei of the fission and fusion products, of the elements in the casing materials, and of any other elements in the immediate vicinity of the detonation, such as nitrogen and oxygen in the air. Although the spectrum of emissions from this plasma is not that of a black body, particularly because the temperature is by no means uniform, it often approximates a black body spectrum, or a combination of two or more such spectra. The disposition of X-rays is further complicated by interactions with the atmosphere.

Approximately 70 to 80 percent of the total prompt yield of many nuclear weapons is radiated in the form of X-rays.

In recent years, considerable attention has been devoted to designing "hot" nuclear weapons with effective radiation temperatures greater than

#### 4-5 X-Ray Energy Emitted

A temperature gradient, decreasing outward, exists between the enormously hot interior nuclear materials and the somewhat cooler exterior bomb casing materials of the nuclear weapon. The X-rays, of course, are continuously being absorbed and reradiated, but with a temperature gradient, the conditions for an ideal black body with isotropic radiation at every point do not exist, and there is a net flow of energy outward from the point of detonation. The outward flux at the surface is, in fact, about twice what would be implied by black body radiation at the temperature of the surface because of X-rays from the interior escaping without interaction at the surface. If the actual surface temperature is  $T_s$ , then the surface energy flux is given by

$$\Phi_s = \sigma T_e^4$$

where

$$T_e = 2^{1/4} T_s = 1.19 T_s$$

The effective temperature,  $T_e$ , will be used in the succeeding discussions.

#### 4-6 Rate of X-Ray Emission

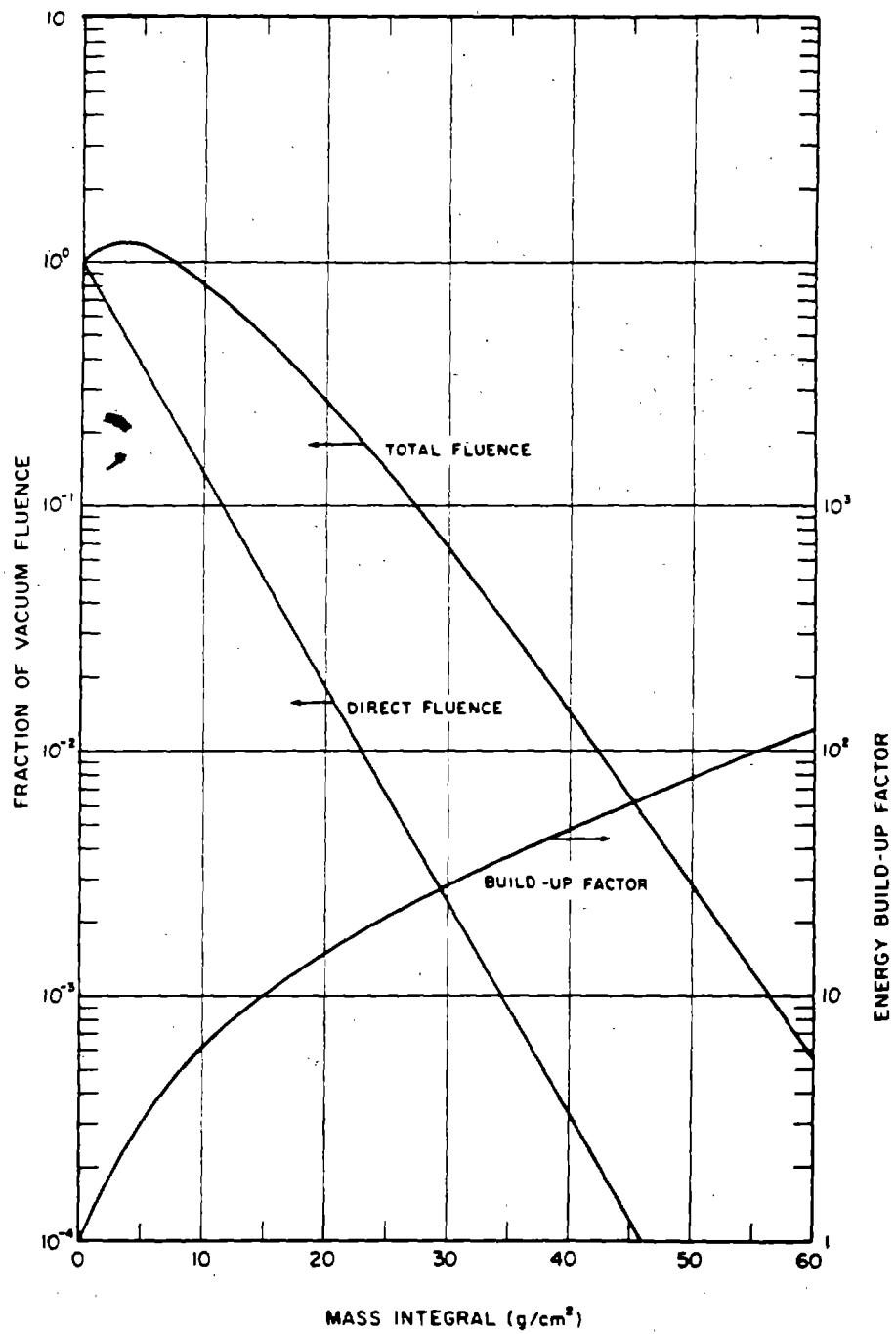


Figure 4-14. Energy Fluence and Build-up Factor for a 50 keV Monoenergetic Source in Homogeneous Air

Pages 4-32 + 4-33 are deleted. <sup>4-31</sup>

[REDACTED] BIBLIOGRAPHY [REDACTED]

Christian, R. H., and P. G. Fischer, *Phenomenology Estimates and a Proposed Experimental Program for Sentinel Environment Tests* [REDACTED] DASA 2116, 68TMP-30. General Electric Company. TEMPO, Santa Barbara, California, 29 February 1968 [REDACTED]

Evans, B. S. and F. H. Shelton, *A Table of the Planck Radiation Function and Its Integral*. KN-770-70-36. Kaman Nuclear, Colorado Springs, Colorado, 2 February 1970 [REDACTED]

Gilmore, F. R., *A Table of the Planck Radiation Function and Its Integral*. RM-1743, RAND Corporation, Santa Monica, California, 2 July 1956 [REDACTED]

Latter, A. L., *Another Vulnerability* [REDACTED] RM-3981-PR, RAND Corporation, January 1964 [REDACTED]

- Latter, A. L., *A High Temperature Nuclear Weapon* [REDACTED] RM-3978-AEC. RAND Corporation, Santa Monica, California, 23 December 1963 [REDACTED]

*LRL Warheads for Advanced Spartan* [REDACTED] LRL-CMA 68-154. Lawrence Radiation Laboratory, Livermore, California, 31 October 1968 [REDACTED]

Shelton, F. H., *Some Notes on the Spectral Distribution of Blackbody Sources* [REDACTED] KN-655-65-12. Kaman Nuclear, Colorado Springs, Colorado, 31 March 1965 [REDACTED]

Shelton, F. H., and J. R. Keith, *X-Ray Air Transport* [REDACTED] DASA 1981. KN-717-67-1, Kaman Nuclear, Colorado Springs, Colorado, 1 July 1967 [REDACTED]

Shelton, F. H., and J. R. Keith, *Time Dependent X-Ray Air Transport* [REDACTED] DASA 2138, KN-717-68-4. Kaman Nuclear, Colorado Springs, Colorado, 31 May 1968 [REDACTED]

Shelton, F. H., and J. R. Keith, *Initial Radiation Environments Produced by SPARTAN Events and Some of Their Aerospace Systems Effects* [REDACTED] DASA 2371, KN-774-69-4. Kaman Nuclear, Colorado Springs, Colorado, 24 July 1969 [REDACTED]

Shelton, F. H., *Nuclear Weapons as X-Ray Sources, the Environments They Produce, and Some Effects on Aerospace Systems* [REDACTED] Volume I – *X-Ray Sources and the Environments They Produce* [REDACTED] DASA 2397-1, KN-770-69-30, Kaman Nuclear, Colorado Springs, Colorado, September 1969 [REDACTED]

[REDACTED]

*U.S. Standard Atmosphere, 1962*, U.S. Committee on Extension to the Standard Atmosphere, available through the U.S. Government Printing Office, December 1962 [REDACTED]

[REDACTED]

*U.S. Standard Atmosphere Supplements, 1966*, U.S. Committee on Extension to the Standard Atmosphere, available through the U.S. Government Printing Office, 1966 [REDACTED]

## Chapter 5

## NUCLEAR RADIATION PHENOMENA

S &amp; E D

## INTRODUCTION

As described in Chapter 1, one of the special features of a nuclear explosion is the fact that it is accompanied by the emission of nuclear radiations. These radiations consist of gamma rays, neutrons, beta particles, and a small proportion of alpha particles. Most of the neutrons and part of the gamma rays are emitted during the actual fission or fusion processes (see paragraphs 1-1 and 1-2, Chapter 1). The remainder of the gamma rays are produced in various secondary nuclear processes, including decay of the fission products. The beta particles are also emitted as the fission products decay. Some of the alpha particles result from the normal radioactive decay of the uranium or plutonium that does not fission in the weapon, and others are formed during the fusion reactions (paragraph 1-2).

As a result of the nature of the phenomena associated with a nuclear explosion, it is convenient to consider the nuclear radiations as being divided into two categories; initial and residual. The line of demarcation is somewhat arbitrary, but it is generally accepted to be about 1 minute after the explosion. The initial nuclear radiations consequently refer to the radiations emitted within 1 minute of the explosion. These radiations are discussed in Section I of this chapter. The residual radiations are further subdivided into neutron induced activity, which results from neutron activation of the earth below an air burst, and fallout, which is the deposition of radioactive residues following a surface or near-surface burst. These latter two forms of nuclear radiation are discussed in Sections II and III of this chapter, respectively.

The ranges of alpha and beta particles are short, and they can be neglected in the consideration of initial radiation. The beta particles, however, may be a hazard to personnel if fallout particles are in contact with the skin for protracted periods of time. The beta particles emitted by radioactive debris from high altitude explosions also may cause intense patches of ionization in the atmosphere that can interfere with, or disrupt, radio or radar communications as described in Chapter 8.

SECTION I  
INITIAL NUCLEAR  
RADIATION

From the standpoint of total energy delivered, the principal sources of initial nuclear radiation (that delivered within 1 minute) are prompt neutrons (those emitted simultaneously with the fission or fusion events), gamma rays from the decay of fission products, and (in the case of an atmospheric burst) secondary gamma rays from neutron interactions with nuclei of the air and ground. Sources of lesser importance from the standpoint of energy delivered are delayed neutrons emitted by some fission products, secondary gamma rays from neutron interactions with the materials of the device, and gamma rays that are emitted simultaneously with fission. These latter components normally may be neglected in predicting total doses or exposures; however, the gamma components may be important for electronic components whose vulnerability is determined by dose rate rather than total dose.

## NEUTRONS

### 5.1 Neutron Source

As mentioned previously, the neutrons of interest originate during the fission and fusion processes. The neutron source of interest is that which exists at the weapon case, i.e., the source of interest consists of those neutrons that escape from the exploding weapon. Both the number of neutrons and their spectrum are altered during transit through the weapon materials. Thus, the source of interest may be quite different from the source of origin (fission or fusion). The neutron source can be defined properly only by considering the actual design of a specific weapon. No average source can be defined that will represent most weapons with any degree of accuracy. It is beyond the scope of this manual to describe the output of a sufficient number of weapon types to present the user with adequate information concerning the neutron output for any possible specific situation. The examples that are presented in succeeding paragraphs are truly examples and should not be taken to be representative for pur-

poses of generalization. Further information concerning nuclear weapons as neutron sources may be obtained from "Status of Neutron and Gamma Output from Nuclear Weapons," DASA 2567 (see bibliography). On the other hand, the curves shown in Figures 5-9 through 5-13 that provide the total dose to personnel on or near the surface of the earth were calculated for eight specific sources. It is believed that, with the descriptions of the eight sources provided in Table 5-3, one of the eight sources may be selected that will represent a reasonable estimate of the total dose to personnel on or near the surface of the earth for most situations.

Table 5-1 shows the spectra for two weapons, one pure fission and one thermonuclear, for which calculations are available.\* These spectra are also shown in Figure 5-1 and 5-2.

As mentioned before, the spectra shown in Table 5-1 should not be construed as

\*These spectra are those that were used in the calculation of dose to personnel from weapon types II and VIII, respectively, as shown in Figures 5-9 through 5-13.

Table 5-1. Weapon Neutron Output Spectra

Neutron Energy (MeV)	Fission Weapon (neutrons/kt)	Thermonuclear Weapon (neutrons/kt)
12.2 -15.0		$1.62 \times 10^{22}$
10.0 -12.2		$8.53 \times 10^{21}$
8.18 -10.0	$7.32 \times 10^{20}$	$6.08 \times 10^{21}$
6.36 - 8.18	$1.27 \times 10^{21}$	$5.46 \times 10^{21}$
4.06 - 6.36	$3.00 \times 10^{21}$	$6.41 \times 10^{21}$
2.35 - 4.06	$8.90 \times 10^{21}$	$1.22 \times 10^{22}$
1.11 - 2.35	$2.52 \times 10^{22}$	$2.84 \times 10^{22}$
0.111 - 1.11	$3.84 \times 10^{22}$	$6.18 \times 10^{22}$
0.0033- 0.111	$2.22 \times 10^{22}$	$1.71 \times 10^{23}$
Total	$9.97 \times 10^{22}$	$3.16 \times 10^{23}$

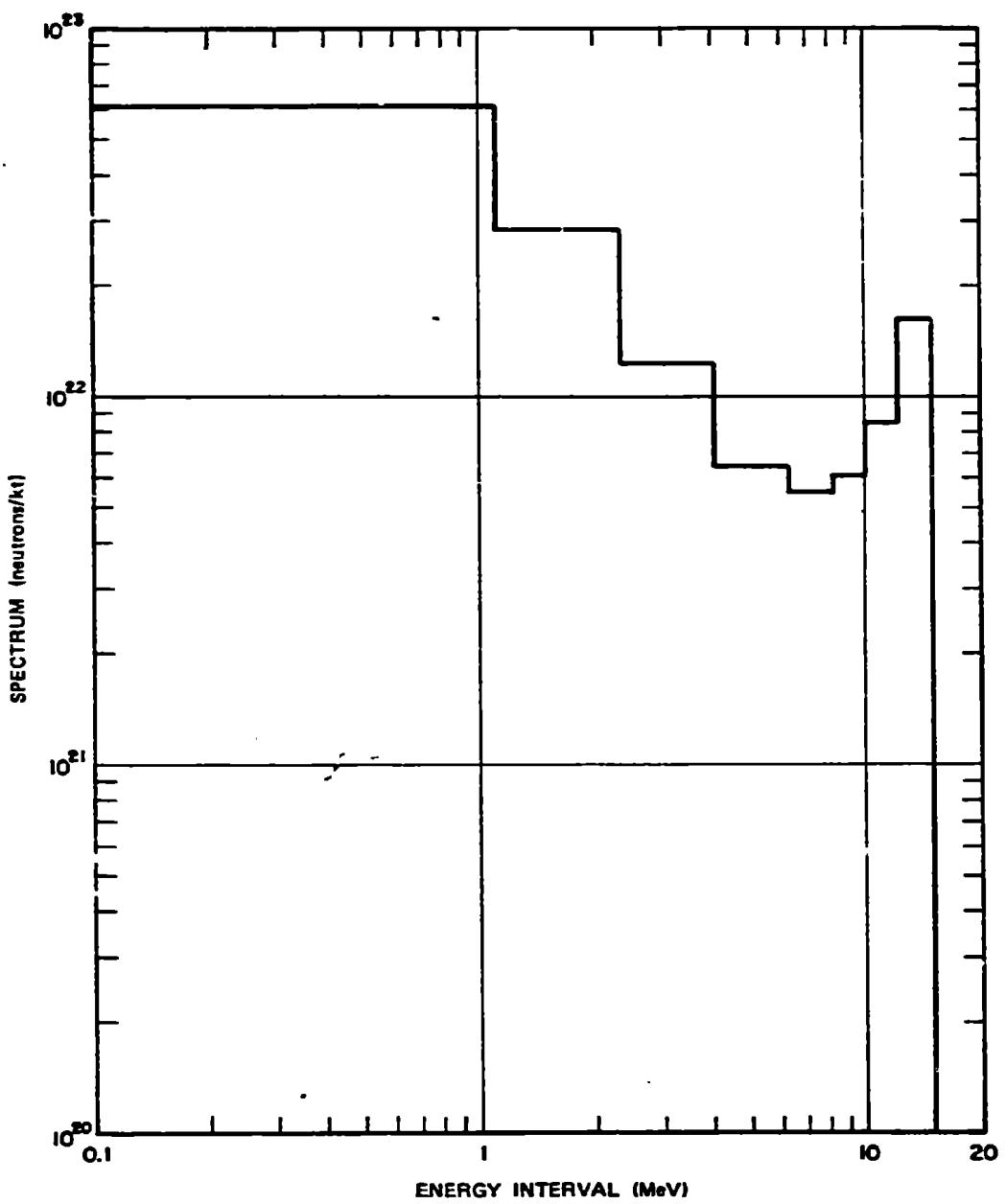


Figure 5-2. Spectrum for a Thermonuclear Weapon  
(Normalized to 1 kt)

DNA  
(b)(1)

being representative. They are merely examples.

The spectral characteristics, however, will vary with weapon design even for weapons with the same total neutron output per kiloton.

### 5-2 Exoatmospheric (Vacuum) Transport

Neutron environments are completely specified by the description of the source and the distance from the source to the point of interest if the explosion occurs in a vacuum. If an explosion occurs sufficiently high that essentially vacuum conditions prevail, it is designated an exoatmospheric explosion. Since in any case, the vacuum will be less than perfect, the distinction between exoatmospheric and endoatmospheric explosions will depend on the degree to which effects vary from those predicted for a vacuum.

For perfect vacuum conditions, the neutron fluence is given by

$$\varphi = \frac{N_0}{4\pi R^2} \text{ n/cm}^2$$

where  $N_0$  is the total number of neutrons emitted by the weapon and  $R$  is the distance in centimeters. Under these conditions the spectrum will remain constant, since no interactions can take place in a vacuum. However, as a result of the energy differences the flux (neutrons  $\text{cm}^{-2}$   $\text{sec}^{-1}$ ) will be a function of the distance from the source, i.e., the more energetic neutrons will arrive ahead of the less energetic ones. The energies associated with neutrons produced by nuclear explosions are sufficiently low compared

to their rest mass energy that their velocities may be determined from their kinetic energy by non-relativistic mechanics, i.e.,

$$\frac{1}{2} Mv^2 = \text{K.E.},$$

where  $M$  is the neutron mass,  $1.67 \times 10^{-24}$  gm,  $v$  is the velocity, cm/sec, and K.E. is the kinetic energy in ergs. Using the relationship

$$1 \text{ MeV} = 1.6 \times 10^6 \text{ ergs},$$

the velocity is related to the kinetic energy in MeV as follows

$$v = 1.38 \times 10^9 \sqrt{\text{K.E. (MeV)}} \text{ cm/sec.}$$

or

$$v = 1.38 \times 10^4 \sqrt{\text{K.E. (MeV)}} \text{ km/sec.}$$

Thus the velocities of 14 MeV, 4 MeV, and 1 MeV neutrons are

$$v_{14} = 1.38 \times 10^4 \sqrt{14} = 5.16 \times 10^4 \text{ km/sec.}$$

$$v_4 = 1.38 \times 10^4 \sqrt{4} = 2.76 \times 10^4 \text{ km/sec.}$$

$$v_1 = 1.38 \times 10^4 \sqrt{1} = 1.38 \times 10^4 \text{ km/sec.}$$

Expressed in a different manner, the times of flight will be 19.3, 36.2, and  $72.4 \mu \text{ sec}/\text{km}$  for the 14 MeV, 4 MeV, and 1 MeV neutrons, respectively. Thus, although the spectrum will remain unchanged, the neutrons will arrive at points several kilometers from the explosion over periods of tens of microseconds.

### 5-3 Neutron Transport Through Materials

Neutrons undergo three main types of reactions when traversing matter: elastic scatter-

ing; inelastic scattering; and capture. In the elastic scattering process, the neutron interacts with the nucleus of an atom and is scattered away from its original line of flight. If the nucleus is light (e.g., the proton that constitutes a hydrogen nucleus), the neutron may transmit a significant amount of its energy to the nucleus, and the scattered neutron will be less energetic than the incident neutron. If the nucleus is heavy, however, the energy transmitted to the nucleus will be insignificant, and the neutron will continue in a new direction with essentially the same energy as before the collision. In the inelastic scattering process, the neutron interacts with the nucleus with the subsequent emission of a gamma ray and a neutron with degraded energy. There are a variety of capture reactions, most of which result in the subsequent emission of a charged particle (generally a proton or alpha particle) and/or a gamma ray. When the reaction results solely in the emission of a gamma ray, it is generally referred to as a radiative capture reaction. As a rule, the probability for capture reactions is small compared to elastic and inelastic scattering when the neutron energy exceeds a few keV. The nuclei remaining after neutron capture are frequently radioactive. The fission process described in paragraph 1-1 is a special case of neutron-induced reactions. Neutrons that do not undergo any of the reactions described above will decay into a proton and an electron with a half life of about 12.8 minutes. The same is true of neutrons that undergo scattering, if they do not undergo some other reaction prior to decaying. The probabilities of the various reactions are such that the decay process is most important for neutrons traveling upwards from a relatively high altitude burst.

The primary reactions that occur during neutron transport through air are elastic scattering, inelastic scattering, and capture by nitrogen nuclei. These latter two reactions provide a source of secondary gamma rays that can be

important in some cases, as will be discussed in subsequent paragraphs.

The neutron environment produced by nuclear explosions within the atmosphere are much more complicated than those described in paragraph 5-2 for exoatmospheric cases because of the interactions that take place with the atmospheric constituents. Even for a monoenergetic source the interactions described above alter the total neutron fluence that reaches a given range, result in a spectral distribution at that point, and change the time rate and direction of arrival at the point. As a result of scattering, the neutrons may arrive at a given point from any direction. If the source consists of a spectrum such as those shown in Figures 5-1 and 5-2, the situation is even more complex. In practice, the calculation of neutron fluences, fluxes, and spectra at some point distant from an endoatmospheric nuclear explosion, or for the interior of a system that is operating exoatmospherically, is performed by complex computer codes. It is beyond the scope of this manual to provide the means for calculating all of these quantities or even to provide a description of the methodology. The latter is contained in Volume III of the "Weapons Radiation Shielding Handbook," DASA 1892-3 (see bibliography). Selected examples of the change in fluence and spectrum will be provided in succeeding paragraphs and figures.

An extensive set of tabulated results of computer calculations of neutron fluxes and doses is contained in "Time-Dependent Neutron and Secondary Gamma-Ray Transport in an Air-Over-Ground Geometry," ORNL-4289, Vol. II, (see bibliography). These data were used to obtain the spectra that would result from the source spectra shown in Figures 5-1 and 5-2 at slant ranges of 390, 1,050, and 1,500 meters. The resulting spectra are shown in Figures 5-3 and 5-4, respectively. Note that the spectra in Figures 5-3 and 5-4 show  $4\pi$  (slant range)<sup>2</sup> x

fluence. This does not mean that the spectra will be the same in all directions. The spectra shown in Figures 5-3 and 5-4 only apply to low air bursts and to targets located on or near the surface of the earth. The units for the ordinates in Figures 5-3 and 5-4 were chosen to allow a convenient visual comparison with Figures 5-1 and 5-2, respectively. Inspection of Figures 5-1 through 5-4 indicates that the shape of the fission source spectrum is not changed appreciably during transit through 1,500 meters of air (the relative abundance of extremely low energy neutrons, much lower energies than shown in Figures 5-1 through 5-4, will increase, however). The shape of the thermonuclear spectrum, on the other hand, does change as the neutrons penetrate air. The peak that exists at 14 MeV at the source becomes lower relative to the total, and the valley between about 8 and 12 MeV at the source becomes filled in as the higher energy neutrons are degraded to the 8 to 12 MeV range.

Figures 5-5 and 5-6 show the neutron fluence for a receiver located on or near the surface of the earth as a function of slant range for the source spectra shown in Table 5-1. The fluence is shown for each of the energy intervals in Table 5-1. The total number fluence for neutron energies above 3.3 keV is also shown for each source. Once again the user is cautioned that these fluences should not be considered representative. They are presented as illustrative examples. Changes in weapon design will change the source spectrum, and this will modify the spectrum as well as the total number fluence at some distance from the explosion. Figures 5-5 and 5-6 also illustrate the large change in the spectral characteristics of the thermonuclear spectrum when compared to the variations in the fission spectrum with slant range.

The preceding paragraphs have provided estimates of neutron fluences and spectra from low air bursts for detectors on or near the surface of the ground. The presence of an air-

ground interface can increase or decrease the neutron intensities by as much as an order of magnitude compared to intensities at corresponding distances in an infinite air medium as a result of reflections and absorption by the ground. For source-detector separation distances less than a mean-free path,\* localized reflection from the ground generally tends to increase the intensity of high energy neutrons; however, initial nuclear radiation is only of interest at very low yields at such short distances since other weapon effects normally will be dominant. At longer distances, the high energy neutron intensity may be reduced by a factor of five or more compared to infinite air when both the source and the detector are at the ground surface. These effects have been included in the calculations from which the preceding figures were derived.

The estimation of neutron environments around an endoatmospheric nuclear explosion for receivers away from the surface of the earth requires a knowledge of the atmospheric properties along any path that a neutron might traverse from the weapon to the point of interest. Although atmospheric properties can change from day to day and from place to place, most calculations are based on a standard atmosphere such as the one described by the National Bureau of Standards in 1962. The important atmospheric constituents that affect neutron transport are

Fraction by Weight	
Nitrogen	0.7553,
Oxygen	0.2318.

\* A mean-free path is the distance in which the radiation intensity is decreased by a factor of  $e$ , where  $e$  is the base of the natural logarithms (about 2.718). The length of a mean-free path depends on the neutron energy and on whether only the direct fluence or the total (direct plus scattered) fluence is being considered.

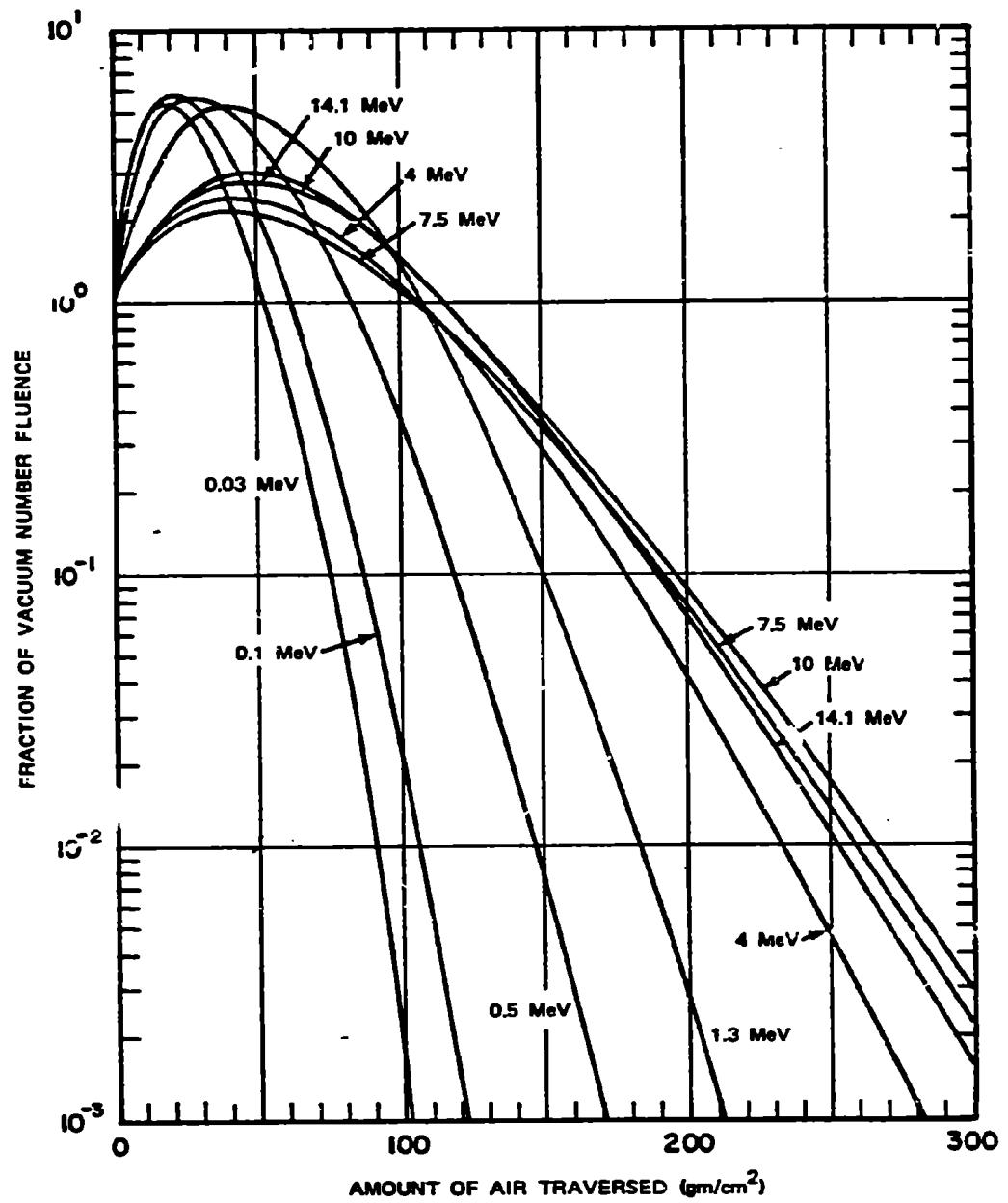


Figure 5-7. [REDACTED] Neutron Energy Build-Up Factors  
for Various Monoenergetic Sources  
in Homogeneous Air [REDACTED]

per kt from a large yield weapon. The dotted curves in Figure 5-8 show the source as it would exist in a vacuum, i.e., the gammas resulting from inelastic scattering and neutron capture in the air would not be present under vacuum conditions. Not shown in Figure 5-8, but of potential importance for receivers near the surface of the earth in the vicinity of a low air burst are gammas that result from neutron interactions with the ground. It is convenient to divide the initial gamma radiation into two components: prompt gamma rays that result from the fission process and some neutron interactions with weapon materials, and are generally emitted within 1 to 2 shakes,\* and delayed gamma radiation which originates from the sources described above subsequent to the prompt gamma ray emission and up to 1 minute after burst.

### 5-5 Prompt Gamma Rays

Prompt fission gamma rays are released essentially simultaneously with the fission process and thus their source rate behavior is determined by the rate profile of fission events in the weapon. These gamma rays escape before the detonation has appreciably deformed the weapon case or perturbed the atmosphere. The energy distribution of the fission gamma rays has been investigated using small samples of fissionable material; however, extrapolation of the small sample information to a weapon source involves considerable uncertainty because of the requirements to define the fission rate profile and to evaluate the attenuation provided by weapon materials as a function of time.

Another source of very early gamma rays that contributes to the prompt pulse results from the non-fission interaction of neutrons with weapon materials.<sup>†</sup> These two sources combine to form a pulse of extremely short duration. Although the total amount of radiation given off during this period is small relative to the total, the peak rate of the pulse is extremely

high. In some cases, such as for high altitude systems, the high ionization rate produced by this pulse may be the damage mechanism extending to the greatest range from the explosion. At low altitudes, the peak rate is attenuated rapidly, as a result of gamma ray absorption and scattering out of the time region of the peak rate.

The prompt gamma environment is very sensitive to weapon design and to weapon yield. Moreover, comparison of theory and experiment for specific weapons is poor. Most calculations and experiments agree that the prompt gamma yield ranges between 0.1 and 0.3 percent of the total yield. The prompt gamma energy output rate may be expressed as

$$\Phi_{\gamma p} = \frac{2.6 \times 10^{25} fW}{\tau} \text{ MeV/sec},$$

where  $f$  is the fraction of the weapon energy emitted as prompt gamma,  $W$  is the weapon yield in kt, and  $\tau$  is the emission time ( $2.6 \times 10^{25}$  is the energy equivalent of 1 kt in MeV; see paragraph 1-1). Using the limits quoted above for  $f$  and  $\tau$  would lead to

$$\frac{(2.6 \times 10^{25})(10^{-3})}{2 \times 10^{-8}} < \Phi_{\gamma p} (\text{MeV/sec/kt}) < \frac{(2.6 \times 10^{25})(3 \times 10^{-3})}{10^{-8}}$$

$$1.3 \times 10^{30} < \Phi_{\gamma p} (\text{MeV/sec/kt}) < 7.8 \times 10^{30}.$$

A shake is  $10^{-8}$  seconds.

Gamma rays from these interactions may continue to times on the order of 10 microseconds, but their contribution is generally small compared to other sources after one or two shakes beyond the time of peak gamma emission.

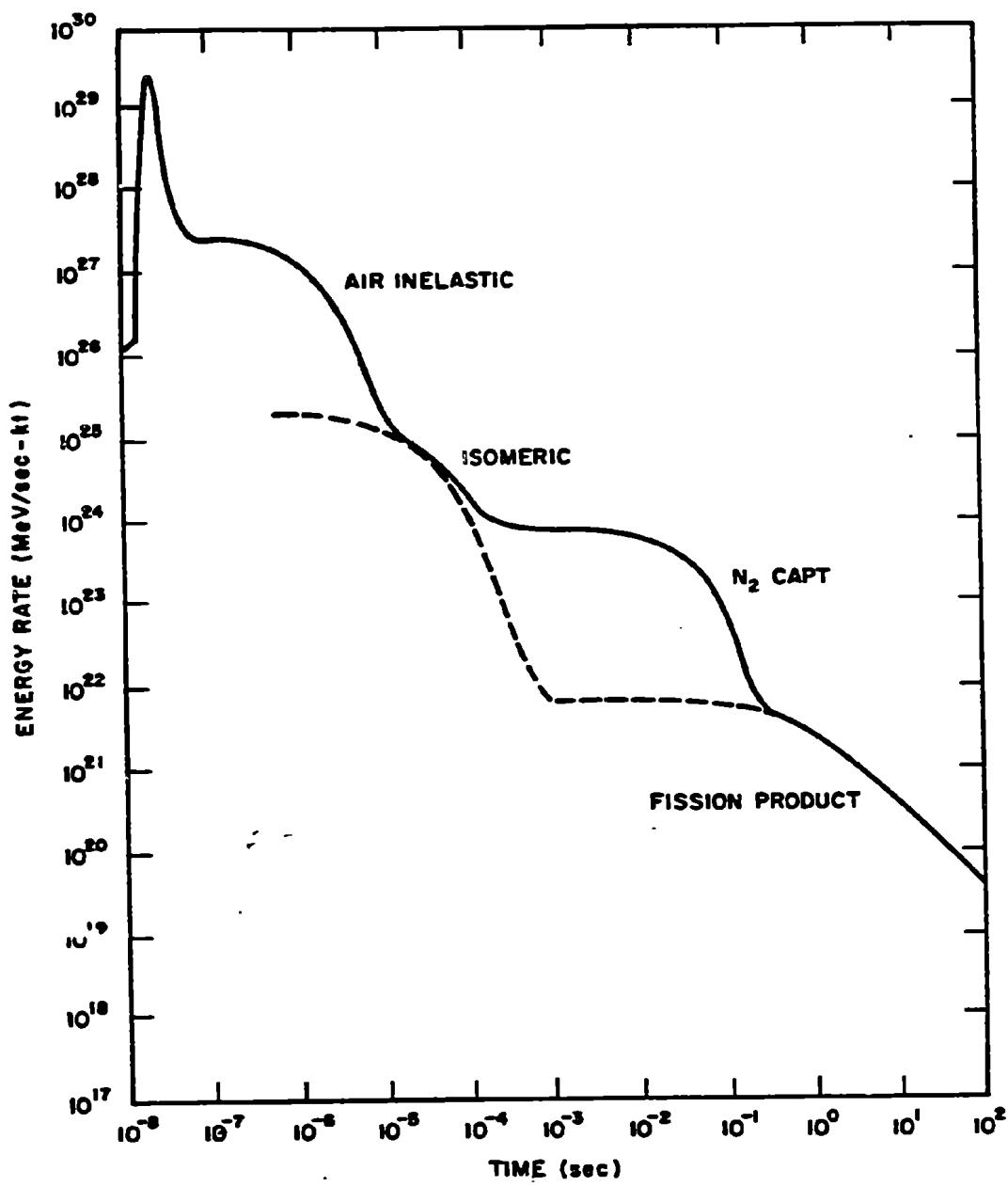


Figure 5-8. Calculated Time Dependence of the Gamma Ray Output from a Large Yield Explosion, Normalized to 1 kt

However, results of calculations and experiments indicate that the peak gamma energy output rate is more likely to lie between  $5 \times 10^{29}$  MeV/sec/kt and  $1 \times 10^{31}$  MeV/sec/kt. As mentioned previously, the peak gamma energy output rate depends on yield and on weapon design. The yield dependence shows a rough correlation as follows

$$\Phi_{\gamma p} = (W)^{-0.29} \times 10^{31} \text{ MeV/sec/kt},$$

at least between about 2 kt and 10 Mt. However, this does not account for the variation with weapon design, which might introduce differences on the order of plus or minus a factor of 3. Therefore, rather than use the yield dependent expression given above, it is recommended that the upper and lower limits given above be used for defensive and offensive estimates of the peak gamma energy output rate, respectively. Since no interactions take place in a vacuum, the peak prompt gamma exposure for exoatmospheric conditions should lie between

$$\Phi_{\gamma p} = \frac{10^{31} W}{4\pi R^2} \text{ MeV/cm}^2/\text{sec}, \text{ and}$$

$$\Phi_{\gamma p} = \frac{5 \times 10^{20} W}{4\pi R^2} \text{ MeV/cm}^2/\text{sec},$$

where  $W$  is the yield in kilotons, and  $R$  is the slant range in centimeters. These expressions are equivalent to

$$\Phi_{\gamma p} = \frac{8.57 \times 10^{20} W}{R_f^2} \text{ MeV/cm}^2/\text{sec}, \text{ and}$$

$$\Phi_{\gamma p} = \frac{4.28 \times 10^{19} W}{R_f^2} \text{ MeV/cm}^2/\text{sec},$$

where  $R_f$  is the slant range in kilofeet.

Gamma rays interact with matter in three ways. The first is called the Compton effect. In this type of interaction, a gamma ray (primary photon) collides with an electron, and its energy is transferred to the electron. A secondary photon, with less energy, is created and departs in a direction at an angle to the direction of motion of the primary photon. The second type of interaction of gamma rays with matter is the photoelectric effect. A gamma ray with energy somewhat greater than the binding energy of an electron in an atom, transfers all its energy to the electron, which is consequently ejected from the atom. Since the photon involved in the photoelectric effect transfers all of its energy, it ceases to exist and is said to be absorbed. The third type of interaction is pair production. When a gamma ray photon with energy in excess of 1.02 MeV passes near the nucleus of an atom, the photon may be converted into matter with the formation of a pair of electrons, equally but oppositely charged. The positive electron soon annihilates with a negative electron to form two photons, each having an energy of at least 0.51 MeV. In some cases, if the interaction takes place near the nucleus of a heavy atom, only one photon of about 1.02 MeV energy may be created. Figure 6-1, Chapter 6, illustrates the three processes qualitatively.

Any photon (e.g., an X-ray or a gamma ray) can produce ionization in a material by these processes of creating secondary electrons that deposit their kinetic energy by ionizing the medium in which they are created. The relative importance or frequency with which each process occurs depends upon the photon energy and the characteristics of the material. The Compton process is the dominant ionization mechanism for most gamma rays of interest, particularly in electronic materials such as silicon, of which many solid-state devices are fabricated.

The spectra of the prompt gamma rays are sensitive to weapon design and yield, just as

the gamma energy output rate is. It is beyond the scope of this manual to provide spectral information concerning sufficient samples of weapons spectra to be of general use (some such samples are provided in "Status of Neutron and Gamma Output from Nuclear Weapons (U)," DASA 2567 (see bibliography)). Moreover, with the wide range of prompt gamma output energy rates provided above, precise spectral data would be of little use. However, most of the prompt gamma rays lie in the energy range between 0.2 and 2 MeV, and in this energy range the Compton fractional energy loss is relatively constant. As mentioned above, the Compton process is the dominant energy transfer process for most electronic materials of interest (atomic number less than 20). These facts lead to a simplification in the relations between the incident prompt gamma energy fluence or energy flux and the energy absorbed by the material.

The unit of the absorbed energy, or dose, is the rad. One rad is the absorption of 100 ergs per gram of material being irradiated. Thus, the rad is independent of the type of radiation (e.g., gamma rays, neutrons, X-rays), but the material absorbing the radiation must be specified (e.g., rad (Si), rad (Ge), rad (tissue)). However, in view of the simplification mentioned above, in the case of *prompt gamma rays* and *materials with atomic numbers less than 20*, a simple conversion is possible, i.e.,

$$1 \text{ rad} = 2 \times 10^9 \text{ MeV/cm}^2, \text{ or}$$

$$1 \text{ rad/sec} = 2 \times 10^9 \text{ MeV/cm}^2/\text{sec.}$$

These are, of course, approximations. However, in view of the approximate nature of the prompt gamma energy flux that has been provided, and in view of the fact that effects of the prompt gamma dose rates on electronics given in Section VII of Chapter 9 and Section 4 of Chapter 14 are not provided for system design or for specific system vulnerability analyses but only as a

general guide to vulnerability, the approximation is considered to be adequate.

As an example of the use of the dose conversion, consider a system with essentially no shielding for gamma rays that is operating exo-atmospherically and that is 2,000 feet from a 100 kt explosion. It is desired to determine the peak gamma dose rate to a silicon transistor within the system. From the equations given previously, the maximum peak gamma energy flux incident on the system is expected to be

$$\Phi_{\gamma p} = \frac{8.57 \times 10^{20} W}{R_f^2},$$

$$\Phi_{\gamma p} = \frac{(8.57 \times 10^{20})(100)}{(2)^2}$$

$$\approx 2 \times 10^{22} \text{ MeV/cm}^2/\text{sec.}$$

and the minimum energy flux is expected to be

$$\Phi_{\gamma p} = \frac{4.28 \times 10^{19} W}{R_f^2},$$

$$\Phi_{\gamma p} = \frac{(4.28 \times 10^{19})(100)}{(2)^2}$$

$$\approx 1 \times 10^{21} \text{ MeV/cm}^2/\text{sec.}$$

Thus the peak dose rate is expected to lie between

$$\dot{D}_{\gamma p} = \frac{2 \times 10^{22}}{2 \times 10^9} = 10^{13} \text{ rads (Si)}/\text{sec. and}$$

$$\dot{D}_{\gamma p} = \frac{10^{21}}{2 \times 10^9} = 5 \times 10^{11} \text{ rads (Si)}/\text{sec.}$$

In view of the lack of spectral data that has been provided, the prompt gamma ener-

gy flux for endoatmospheric can only be determined by use of an effective mass attenuation coefficient (see the discussion of neutron transport in paragraph 5-3). A reasonable effective mass attenuation coefficient for prompt gammas is about  $2.8 \times 10^2 \text{ cm}^2/\text{gm}$ . Combining this with the exoatmospheric equations given previously, the direct peak prompt gamma ray energy may be estimated to lie between

$$\Phi_{\gamma p} = \frac{10^{31} W}{4\pi R^2} e^{-(2.8 \times 10^{-2})\rho R} \text{ MeV/cm}^2/\text{sec}, \text{ and}$$

$$\Phi_{\gamma p} = \frac{5 \times 10^{29} W}{4\pi R^2} e^{-(2.8 \times 10^{-2})\rho R} \text{ MeV/cm}^2/\text{sec},$$

where  $W$  is the yield in kt,  $\rho$  is the density in  $\text{gm/cm}^3$ , and  $R$  is the range in centimeters. As in the case for neutrons, the quantity  $\rho R$  may be replaced by the mass integral  $q(R)$ . The mass integral may be determined from the equations given in paragraph 5-3 and the data tabulated in Table 5-2.

The prompt gamma dose may be bounded by multiplying the minimum and maximum dose rates by 1 and 2 shakes, respectively.

## 5-6 Air-Ground Secondary Gamma Rays

Potentially important sources of secondary gamma rays result from the inelastic scattering of high-energy neutrons by the nuclei of the air and ground, and the capture of thermal neutrons by the nitrogen-14 in the air and by various elements in the ground. The relative importance of the inelastic and capture gamma rays depends strongly upon the neutron spectrum of the source.

Most of these gamma rays are produced near the neutron source where the neutron fluence is highest. The short neutron flight time to the regions of most intense interaction, and the practically instantaneous character of the nu-

clear interaction accounts for the early ( $10^7 < t < 10^5 \text{ sec}$ ) appearance of the secondary gamma components. The number of inelastic-scattering gamma rays relative to the total depends directly on the relative abundance of high-energy neutrons. The fraction of the total may be negligible in fission warheads or in large thermonuclear warheads. As the fusion yield fraction is increased the importance of the inelastic component will increase.

Any determination of the intensity of inelastic-scattering gamma rays must rely primarily upon analysis because of the difficulty in distinguishing the source of the different gamma rays measured in field tests. The first step in the analysis is that of neutron transport calculations. The local source strength of inelastic gamma rays is an energy dependent response to the local fluence of neutrons. Once the source intensity resulting from neutron interactions in air and ground is known, a gamma ray transport calculation must be performed to obtain the intensity at points of interest.

The energy spectrum of the gamma rays evolved in elastic scattering depends on the energy of the neutrons and the energy level structure of the nuclei with which the neutrons interact. However, the inelastic gamma rays are generally high in energy and, consequently, take on added significance when the target is behind a shield such as in a hardened military installation. Even though only a few percent of the gamma radiation incident on the shield results from inelastic scattering, it may be the source that is responsible for the maximum rate experienced by equipment inside the shielded installation since prompt gamma rays are attenuated more rapidly by shielding materials than the inelastic scattered gamma rays. Thus, where hardened installations are concerned, the inelastic gamma rays should be evaluated even in cases where they do not constitute a large fraction of the total free-field exposure. Methods for calculating the

tissue dose from secondary gamma rays are provided in the following subsection.

### 5-7 Fission Product Gamma Rays

Gamma rays produced by the decay of fission products following a fission detonation are an important source of radiation during the initial radiation time regime (the first minute following the explosion). The intensity of fission product gamma rays reaching a location of interest is affected by the complex source and media dynamics consisting of the formation and evolution of the fireball, the cloud expansion and rise, and the decay of the fission products with time. The fission products disperse throughout the cloud with the passage of time and the shape of the cloud may vary from spherical to toroidal as the materials forming the cloud rise through the atmosphere.

The formation of the fireball and the expansion and rise of the cloud depends upon weapon yield, weapon design, atmospheric conditions, and other parameters. The distribution of fission products in the cloud as a function of time is not well known, and, consequently, the attenuation of fission-product gamma rays within the cloud can only be approximated.

Atmospheric perturbation caused by the passage of the shock front also has a pronounced effect on the transport of fission-product gamma rays. The distribution of energy from a low altitude conventional fission weapon is such that roughly 50 percent of the energy is released in the form of blast and shock. The actual percentage depends on the weapon design and yield and on the nature of the surrounding environment (see Section I, Chapter 2). The percentage decreases for neutron enhanced weapons.

The sudden release of energy in the form of blast and shock produces an immediate increase in temperature and pressure thus produc-

ing hot, compressed gases from the weapon material. A pressure wave is initiated in the surrounding medium (paragraphs 1-4 through 1-6, 1-8, and Section I, Chapter 2). The characteristics of a shock wave is that there is a sudden increase of pressure at the front with a gradual decrease behind it. A severe change in the density of the heated air behind the shock front is associated with the pressure change. The large reduction in the air density, or optical depth, between the rising source and the receiver produces an enhancement of gamma ray intensities from hydrodynamic effects that is known as "hydrodynamic enhancement." These effects may last for several minutes and may extend to large distances from the explosion. The intensity and duration of hydrodynamic effects are yield dependent.

At early times when the shock front is located between the cloud and the receiver, the gamma ray intensity may increase because of the geometric displacement of the air. After the blast wave has passed the receiver, the gamma ray intensity is enhanced as a result of the reduced air density. This hydrodynamic enhancement becomes increasingly more important with higher weapon yields. For high yield weapons (in the megaton range), hydrodynamic enhancement can increase the fission-product gamma ray intensity by several orders of magnitude, with the result that fission product gamma rays can become the most important of all initial radiation sources.

With minimal hydrodynamic enhancement, as in the case of very low-yield weapons, the intensity of fission product gamma rays reaching a given point may be of approximately the same magnitude as that resulting from the secondary gamma ray sources. However, the average energy of the fission product gamma rays is considerably less than that of the secondary gamma rays, and the angle distribution of the fission product gamma rays is diffused by

the rise of the cloud. Each of these factors tends to reduce the penetrating power of fission product gamma rays relative to secondary gamma rays.

A reasonably accurate calculation of the transport of fission product gamma rays must consider such time-dependent parameters as cloud rise, source decay, and hydrodynamic enhancement. The curves presented in the following subsection that show tissue dose from fission product gamma rays were constructed by the use of such a model.\*

#### INITIAL RADIATION DOSE TO PERSONNEL

The preceding paragraphs have described the complexity of the calculations of the source and environments produced by the initial nuclear radiations. Simplified, but reasonably accurate, methods have been developed to predict the dose to personnel located on or near the surface of the earth. These methods are described in the succeeding paragraphs and figures, and illustrations of their use are provided in four problems.†

Various units have been used to describe the radiation dose to personnel. One of the earliest, originally used to describe X-ray environments, is the roentgen, which is defined in terms of ionization produced in air. In view of the long history of the roentgen, various attempts have been made to develop units that described the response of living creatures or physical objects in terms of "roentgen equivalent" units. None of these was completely satisfactory since they depended strongly on the type and energy of the radiation, and their relationship to an exposure measured in roentgens was not always descriptive of the response of the target. Since the response of a target to radiation generally can be related to the energy absorbed, the rad has come into general use for the description of dose to any target. As previously defined in paragraph

5-5, one rad is the absorption of 100 ergs per gram of material being irradiated. Thus, the rad is independent of the type of radiation, but the material absorbing the radiation must be specified. The curves provided in this subsection provide a methodology for determining the dose in rads (tissue) for the various components of the initial nuclear radiation. The response of personnel, as a function of absorbed dose, is given in Section III of Chapter 10.

In view of the strong dependence of the neutron and secondary gamma ray environments on weapon design, no one representative weapon could be chosen to provide a basis for calculating dose to humans. The fission product dose is relatively independent of design specifics, but it is strongly dependent on total yield and the ratio of fission yield to total yield. Consequently, eight different weapons, for which case output data were available, were selected to perform the basic calculations from which the curves presented below were developed. It is believed that these eight weapons provide a sufficiently wide spectrum of designs that one of the eight will represent a given weapon of interest in a reasonable manner. The eight weapons are described in Table 5-3.

#### 5-8 Initial Neutron Dose

Figures 5-9 through 5-11 provide all of the information necessary to calculate the contribution of neutrons to the initial nuclear radiation dose from each of the weapon types listed

\* The development of this model is explained in "Improved Models for Predicting Nuclear Weapon Initial Radiation Environments (U)," DASA 2615 (see bibliography).

† ATR, which stands for Atmospheric Radiation Transport library, may be used to obtain exact answers to problems involving radiation transport in the atmosphere without the necessity of making specific transport calculations. ATR is documented in DNA 28031, "Models of Radiation Transport in Air - the ATR Code" (see bibliography). The Code itself may be obtained from the Radiation Shielding Information Center (RSIC), Oak Ridge, Tennessee.

Table 5-3. Representative Types of Nuclear Weapons

Type	Description	Representative Yield Range
I	Subkiloton Fission	DNA (4)(3)
II	Pure Fission Implosion	
III	Large (physically) Boosted Fission	
IV	Small (physically) Boosted Fission	
V	Enhanced Neutron Weapon	
VI	Gun-Assembly Fission Weapon	
VII	Thermonuclear Weapon	
VIII	Thermonuclear Weapon	

in Table 5-3. Problem 5-1 describes the use of these figures to obtain the neutron dose.

#### 5-9 Air-Ground Secondary Gamma Ray Dose

Figures 5-11 through 5-13 provide all of the information necessary to calculate the contribution of air-ground secondary gamma rays to the initial nuclear radiation dose from each of the weapon types listed in Table 5-3. Problem 5-2 describes the use of these figures to obtain the air-ground secondary gamma ray dose.

#### 5-10 Fission Product Gamma Ray Dose

Figures 5-14 through 5-17 provide all of

the information necessary to calculate the contribution of fission product gamma rays to the initial nuclear radiation dose. Problem 5-3 describes the procedures for obtaining the fission product dose from these figures. Note the caution given in Problem 5-3 concerning interpolation between the hydrodynamic enhancement curves.

#### 5-11 Total Dose

The total initial radiation dose is simply the sum of the contributions of the neutrons, the secondary gamma rays, and the fission product gamma rays. Problem 5-4 illustrates the calculation of total initial radiation dose.

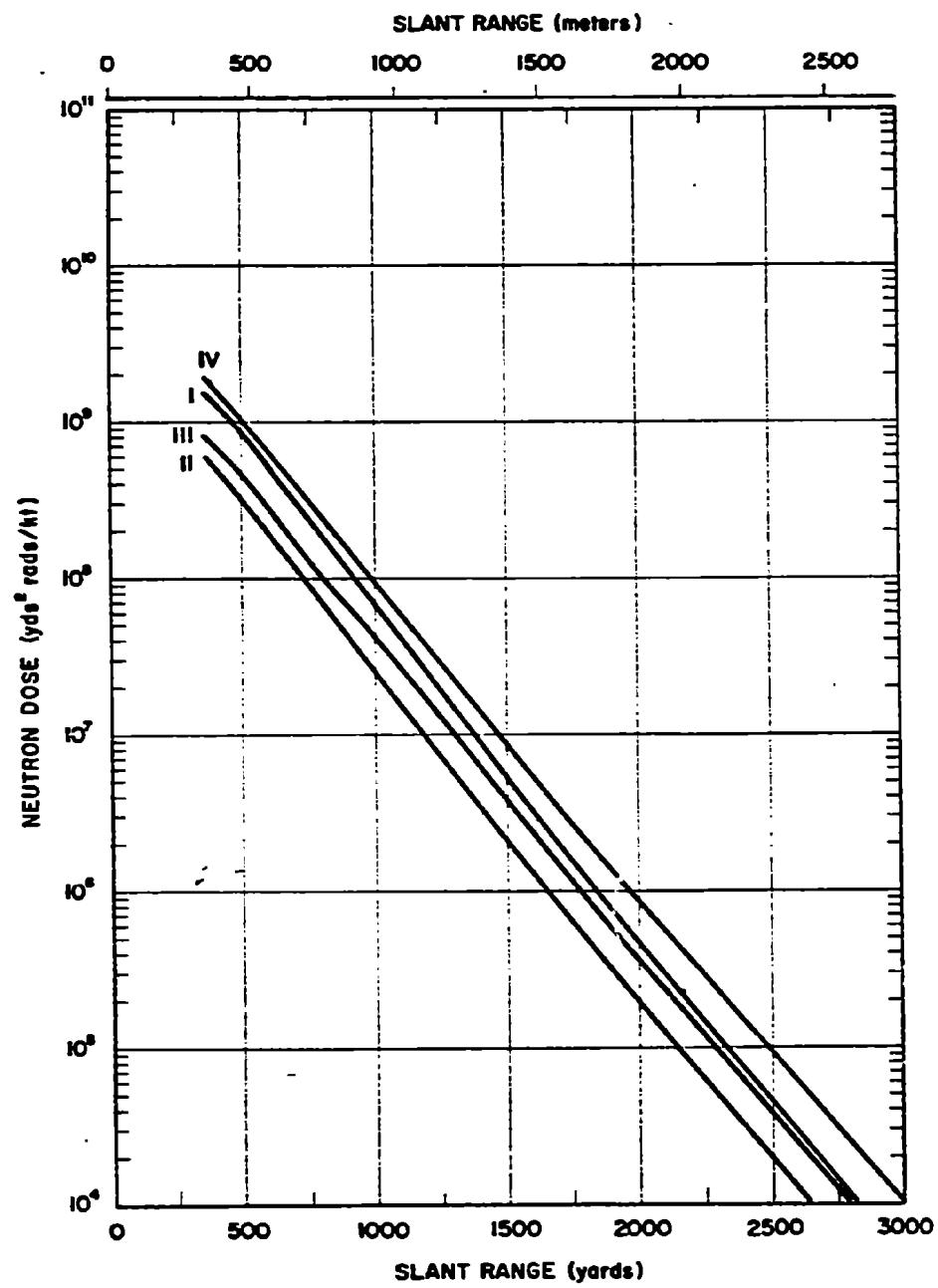


Figure 5-8a. [REDACTED] Neutron Dose as a Function of Slant Range from a 1 kt Surface Burst, Weapon Types I through IV, Short Ranges [REDACTED]

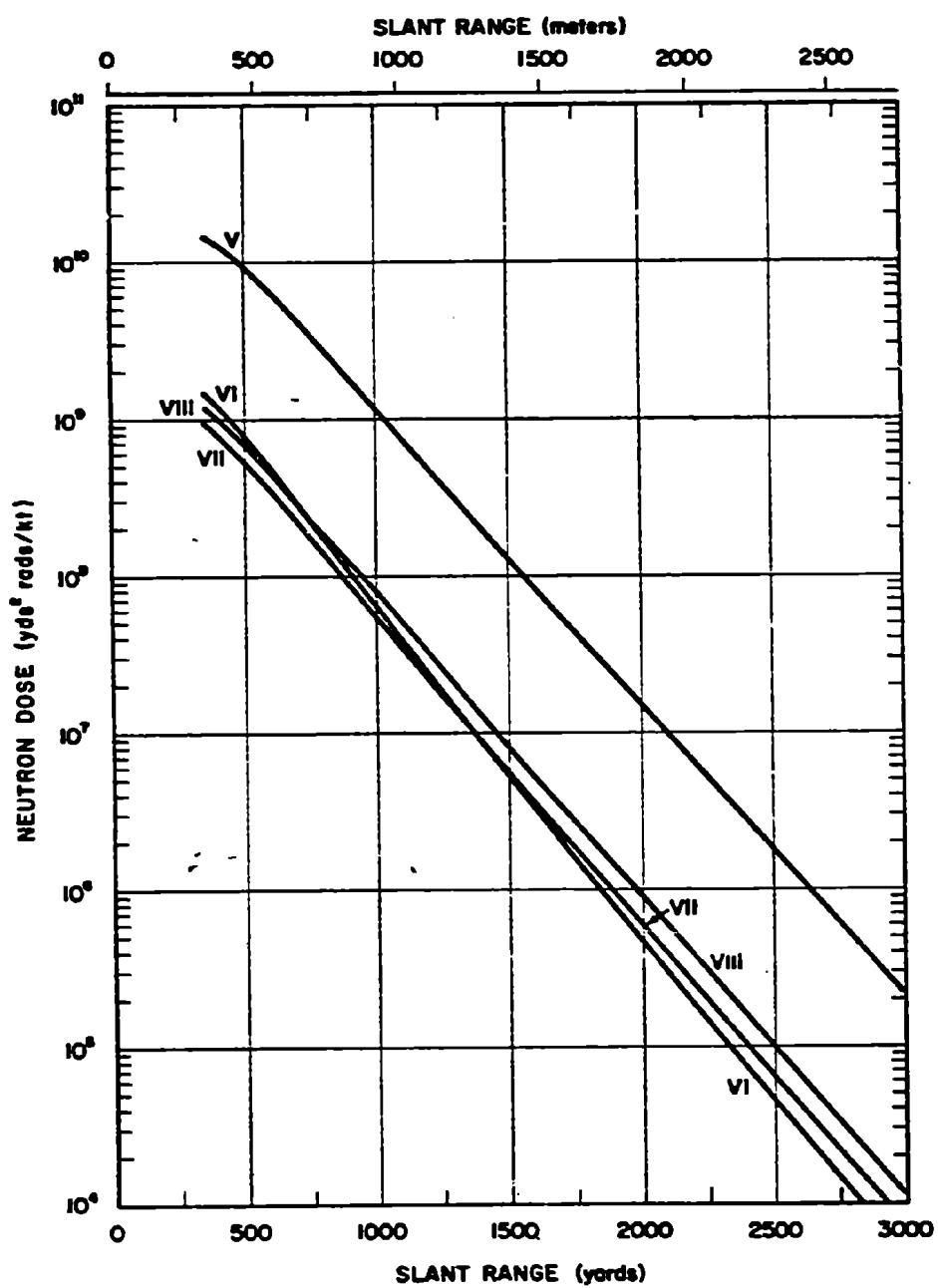


Figure 5-10a. [REDACTED] Neutron Dose as a Function of Slant Range from a 1 kt Surface Burst, Weapon Types V through VIII, Short Ranges [REDACTED]

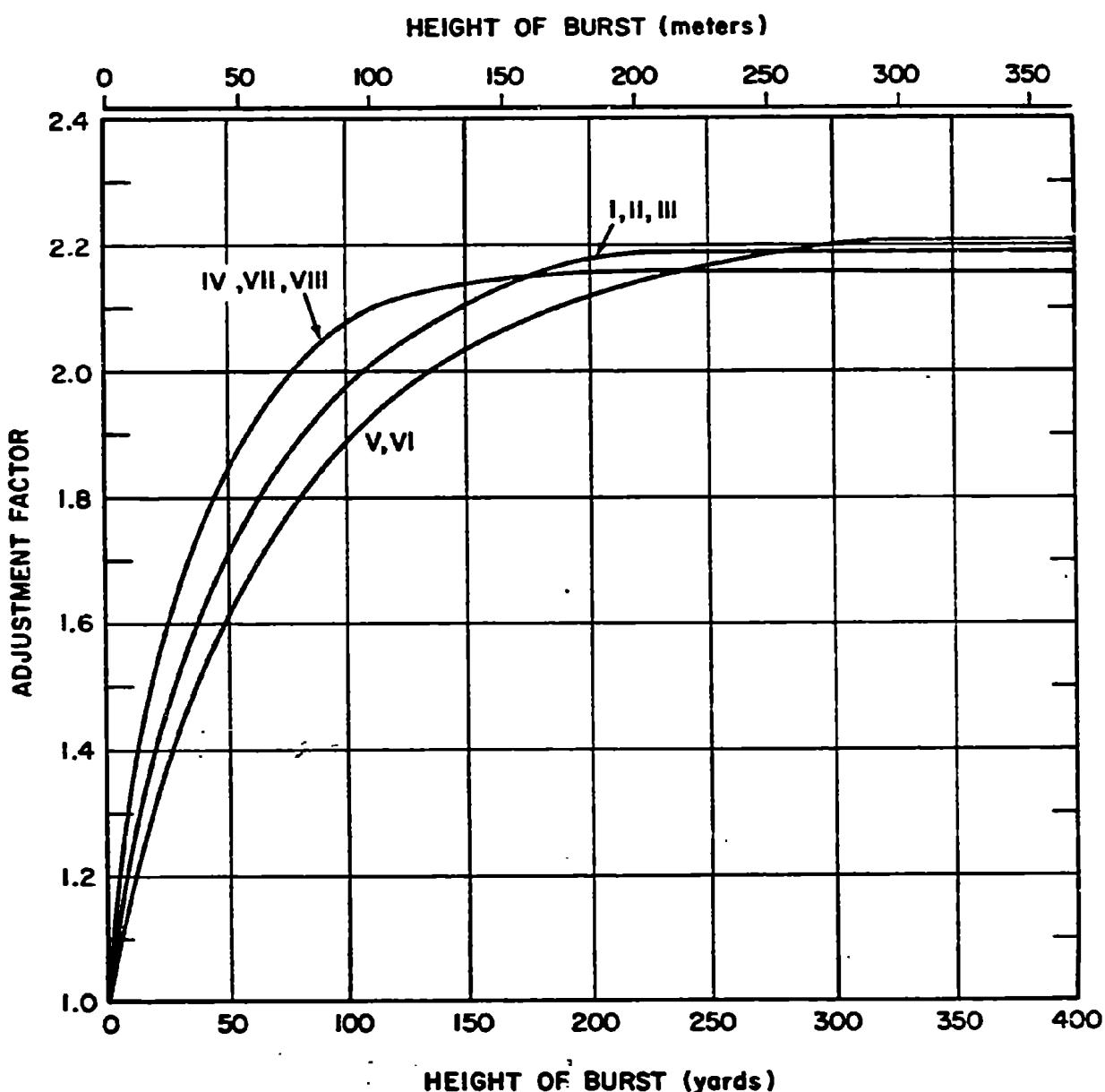


Figure 5-11. [REDACTED] Burst Height Adjustment Factors for Neutrons and Secondary Gamma Rays [REDACTED]

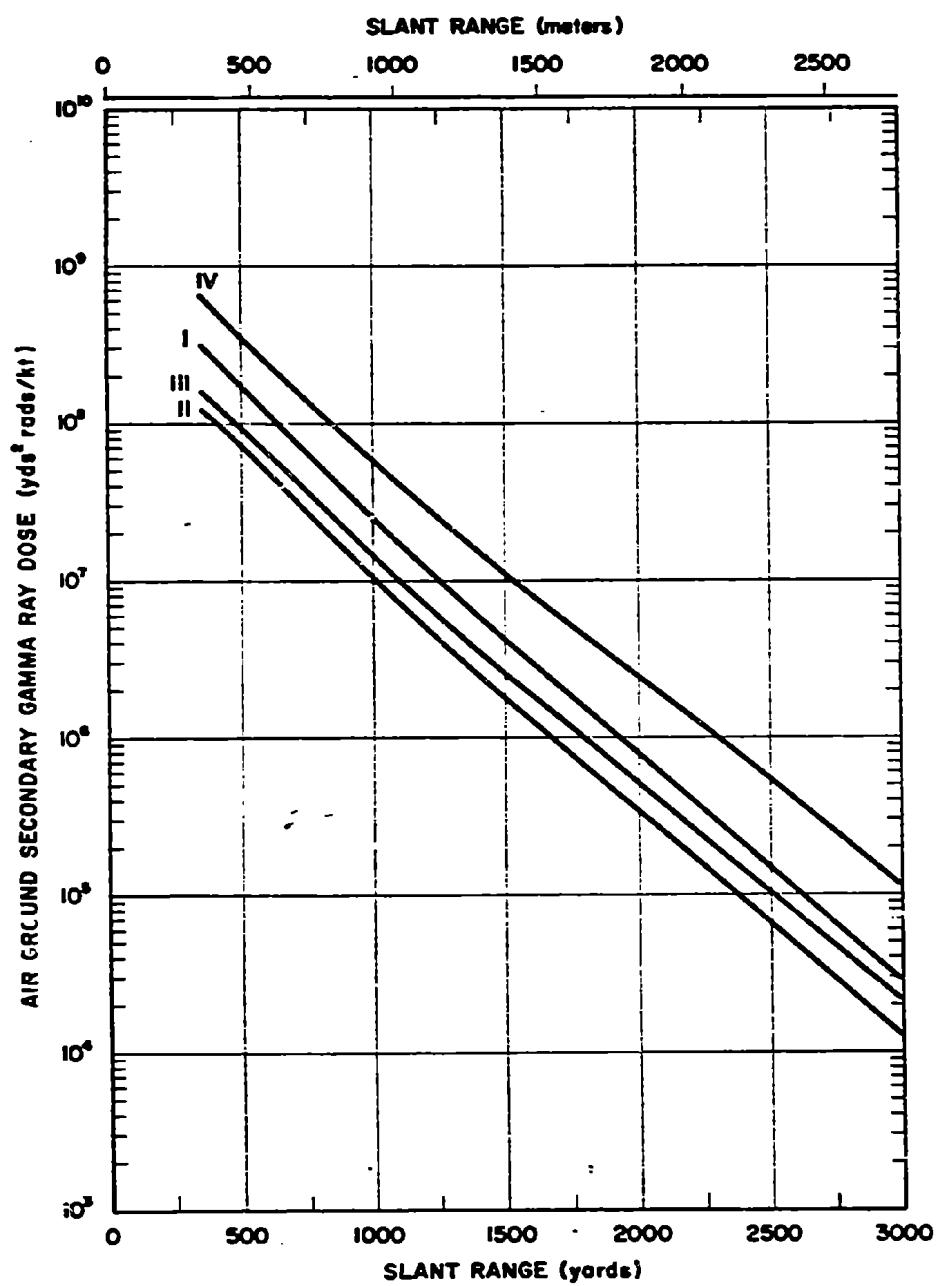


Figure 5-12a. Secondary Gamma Ray Dose as a Function of Slant Range from a 1 kt Surface Burst, Weapon Types I through IV, Short Ranges

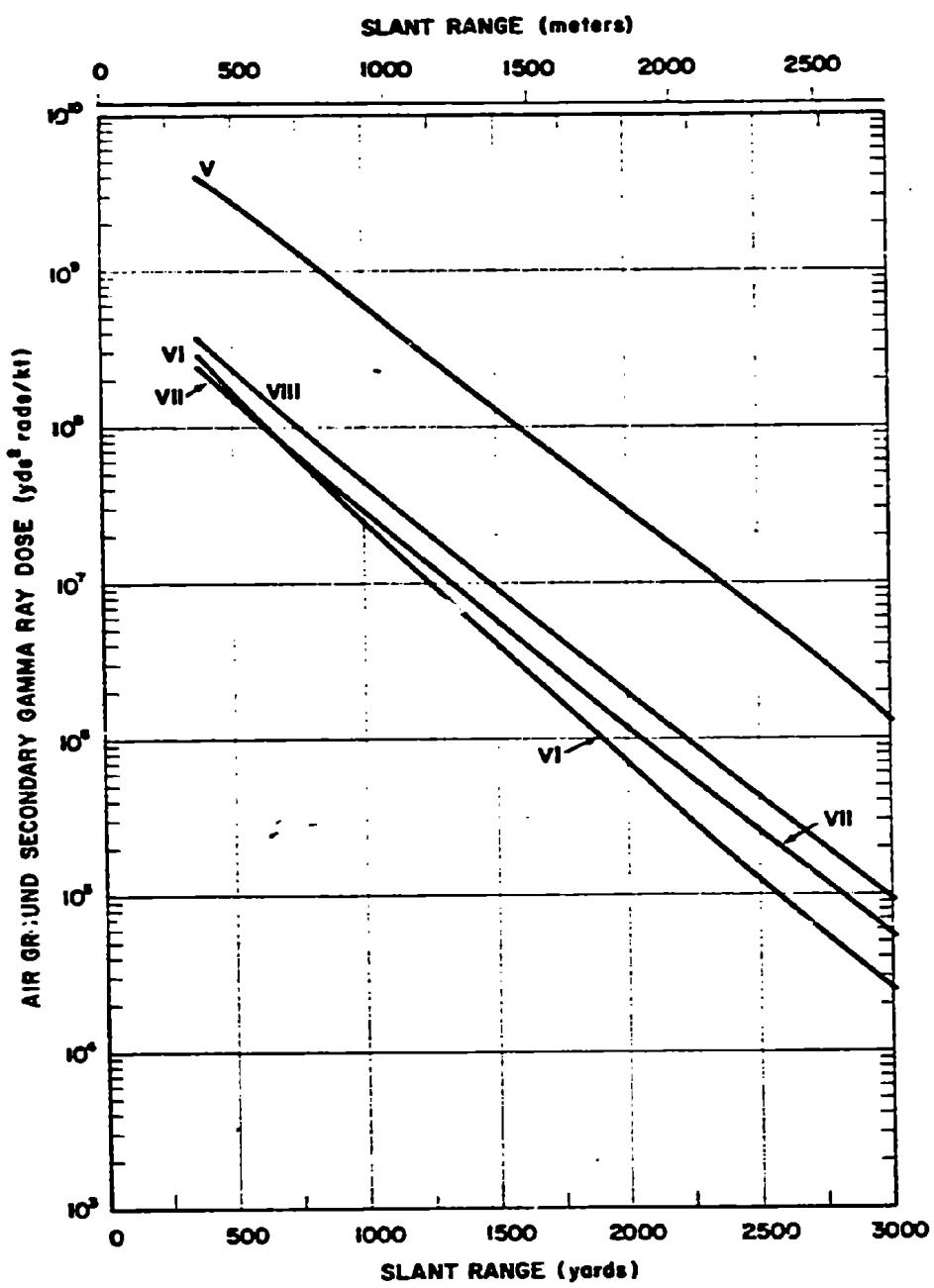


Figure 5-13a. [REDACTED] Secondary Gamma Ray Dose as a Function of Slant Range from a 1 kt Surface Burst, Weapon Types V through VIII, Short Ranges [REDACTED]

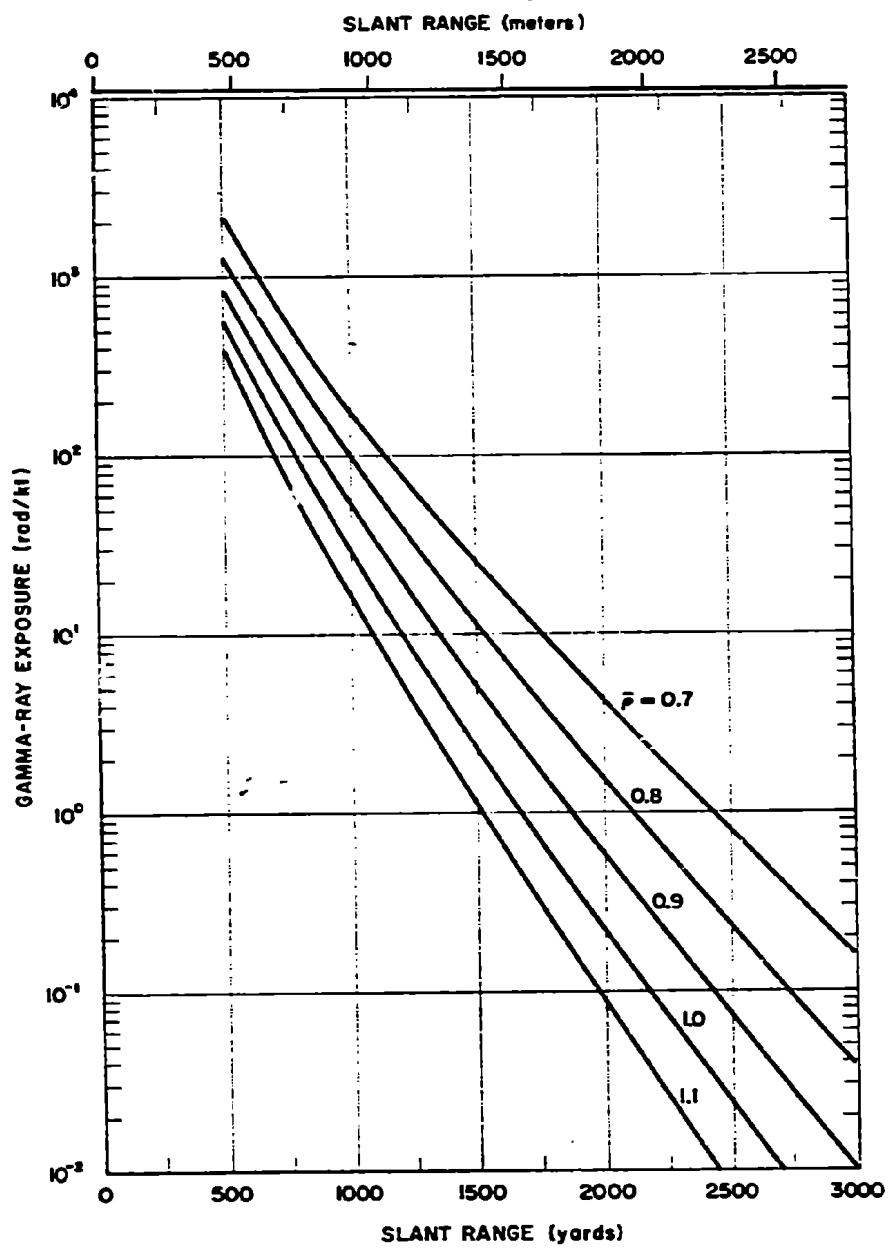


Figure 5-14a. [REDACTED] Fission Product Gamma Ray Dose as a Function of Slant Range from a 1 kt (Fission Yield) Surface Burst, Short Ranges [REDACTED]

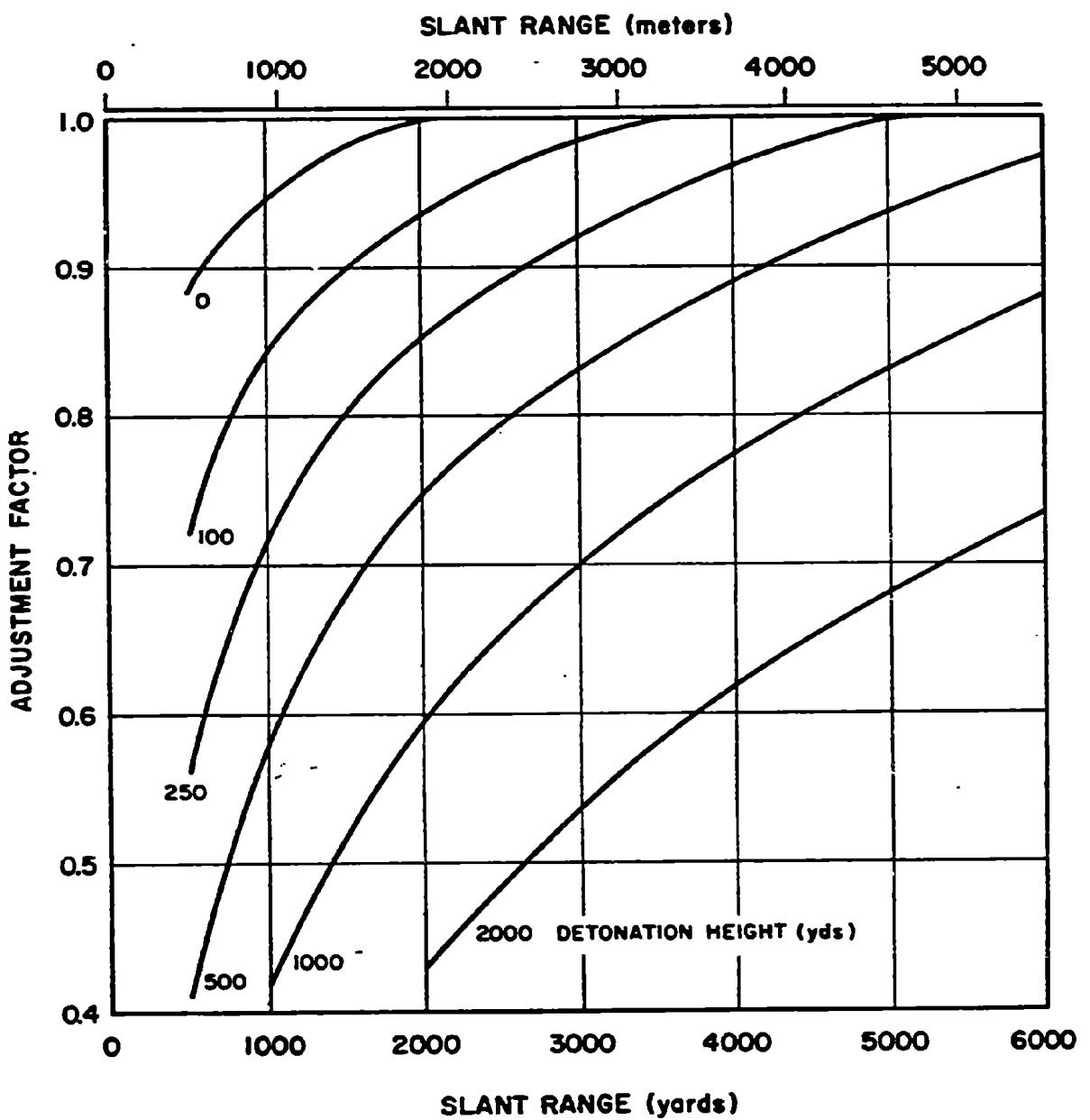


Figure 5-15. Range Dependent Burst Height Adjustment Factors for Fission Product Gamma Rays

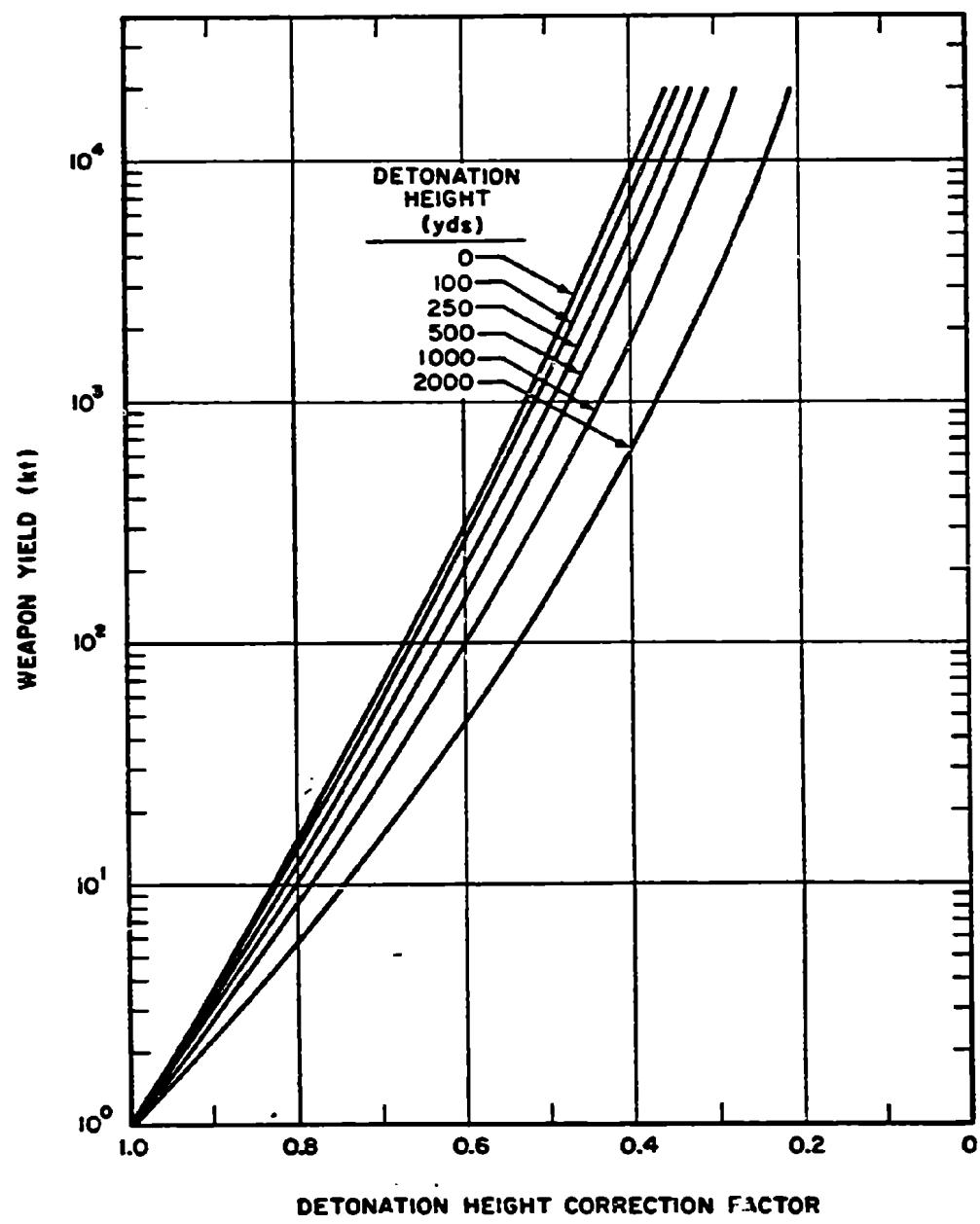


Figure 5-16. [REDACTED] Yield Dependent Burst Height Adjustment Factors for Fission Product Gamma Rays [REDACTED]

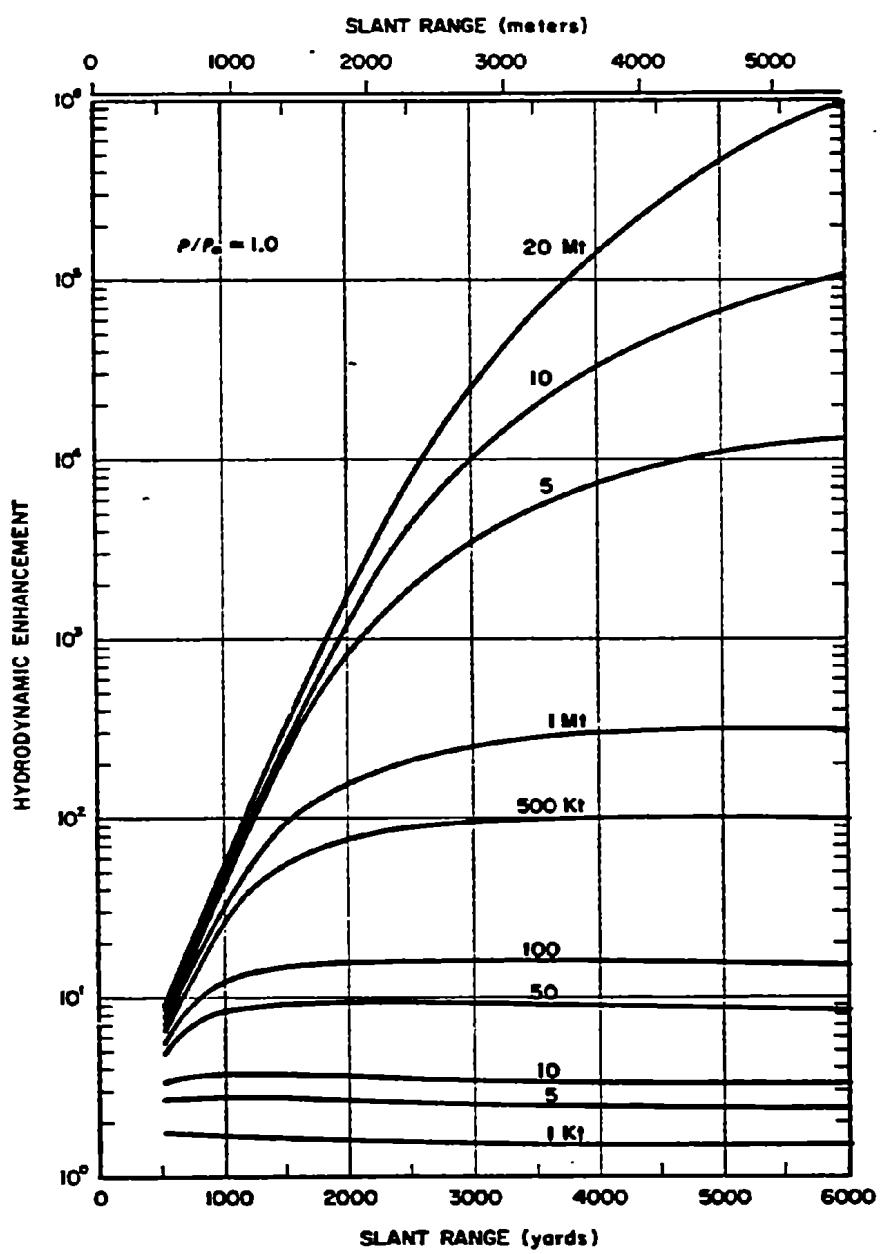


Figure 5-17b. [REDACTED] Fission Product Gamma Ray Hydrodynamic Enhancement Factors as a Function of Slant Range for Relative Air Density of 1.0 [REDACTED]

## **SECTION II**

### **NEUTRON-INDUCED ACTIVITY IN SOILS**

As mentioned in paragraph 5-3, the neutrons emitted during a nuclear explosion undergo three main types of reactions when traversing matter: elastic scattering; inelastic scattering; and neutron capture. There are a variety of capture reactions, most of which result in the subsequent emission of a charged particle (generally a proton or alpha particle) and/or a gamma ray. When the reaction results solely in the emission of a gamma ray, it is generally referred to as radiative capture. As a rule, the probability for capture reactions is small compared to elastic and inelastic scattering when the neutron energy exceeds a few keV. The nuclei remaining after neutron capture are frequently radioactive, generally emitting a beta particle, a gamma ray(s), or both. The extent of the hazard to personnel that results from radioactivity induced in the soil by neutrons from a nuclear explosion is described in this section.

#### **5-12 Height of Burst**

The residual radioactive contamination (fallout) that results from fission products that are distributed subsequent to a contact surface or subsurface burst (Section III of this chapter) is much greater than the radioactive contamination that results from the neutron activity discussed in this section. Thus, the neutron-induced activity may be neglected for contact surface and subsurface bursts.\* If a weapon is burst at such a height as to be in the transition zone as far as fallout is concerned, the neutron-induced activity generally can be neglected if the burst height is in the lower three-quarters of the fallout transition zone, i.e., if the burst is below about  $75W^{0.35}$  feet (see Section III). If the height of burst is in the upper quarter of the transition zone (between about  $75W^{0.35}$  feet

and  $100W^{0.35}$  feet), the neutron-induced activity may not be negligible compared to fallout. When fallout dose rate contours determined by the methods described in Section III are much smaller than those for a surface burst, the neutron-induced activity should be obtained by the methods described below. The overall contour values may be obtained by summing the dose rate values for induced activity and fallout at a particular time; however, as will be shown in succeeding paragraphs of this chapter, the radioactivity from fallout and that from neutron-induced activity decay at different rates. Therefore, the dose rate from each source must be determined separately for each time of interest, or the total doses over some period of time must be determined separately, and then the appropriate summing may be performed.

For burst heights that are sufficiently high, the various forms of attenuation described in paragraph 5-3 will result in a neutron fluence at the surface of the earth that is too small to produce significant induced activity. Since the neutron-induced gamma radiation depends on soil type as well as weapon type and yield, a height of burst above which neutron-induced activity will cease to be important cannot be defined. In general, however, this effect will only be important for low air bursts (just above the height of burst at which fallout ceases to be important).

#### **5-13 Soil Types**

The type, intensity, and energy distribution of the induced activity produced by the neutrons will depend on which isotopes are produced and in what quantity. These factors depend on the number and energy distribution of the incident neutrons and the chemical composi-

\* The induced activity contribution may, however, assume more importance if Plowshare type nuclear devices are adapted for military use.

tion of the soil. Induced contamination contours are independent of wind, except for some wind redistribution of the surface contaminant. The contours can be expected to be roughly circular.

■ Examination of several thousand analyses of the chemical composition of soils and the relative probabilities of neutron capture by the various elements present in the various samples has indicated that sodium, manganese, and aluminum generally will contribute most of the induced radioactivity. Small changes in the quantities of these materials can change the activity significantly. Other elements can also influence the radioactivity. Some elements have a relatively high probability for capturing neutrons (cross section), but the isotope that is formed after the capture either is not radioactive, does not emit gamma rays, or has such a long half life that the low activity does not produce a hazardous dose rate. The presence of such elements in the soil will tend to lower the hazard from neutron-induced activity.

■ As described in paragraph 5-3, scattering of neutrons from light elements may cause the neutron to transmit a significant amount of its energy to the nucleus, and the scattered neutron will be less energetic than the incident neutron. Since the probability of neutron capture generally increases as the neutron energy decreases (in particular, this is true for sodium, manganese, and aluminum), the presence of light elements in the soil will tend to cause a larger number of neutrons to be captured near the surface rather than at some depth (the peak intensity from neutron activated radionuclides generally is two to three inches below the surface). Thus, it might be expected that the presence of light elements might increase the hazard from neutron-induced activity by raising the primary gamma ray source to a level nearer the surface, where attenuation of the earth above the source would be less. A study of many soil samples indicates that the light element that is most likely to

cause such an effect is hydrogen that might be present in moisture (water) in the soil.\* Thus, it might be expected that soil saturated with water might be more hazardous from neutron-induced activity than the same soil when dry. However, competing effects occur because the hydrogen absorbs neutrons to form nonradioactive deuterium. These neutrons otherwise could produce gamma ray emitters. Experiments have confirmed that moisture content does increase the hazard from neutron-induced activity; however, this effect does not appear to be of major importance in view of the uncertainties in soil composition and variations in possible weapon neutron outputs.

■ Four soils have been chosen to illustrate the extent of the hazard that may be expected from induced activity. These soils were selected to show wide variations in predicted dose rates; the activity from most other soils should fall within the range of activities presented for these soils. Table 5-4 shows the chemical composition of the selected soils. The elements listed in Table 5-4 are in the order of probable importance so far as induced activity is concerned.

■ When applying the data presented in this section to soils other than the four types shown, the activity should be estimated by using the data for the type that most closely resembles the soil in question in chemical composition. If none of the four types resembles the soil in question very closely, the following points should be kept in mind. For times less than  $H + 1/2$  hour, aluminum is the most important contributor. Between  $H + 1/2$  hour and  $H + 5$  hours, manganese is generally the most important element. In the

■ Hydrogen, being the lightest element, will have many more atoms per unit volume for the same percentage concentration by weight. It is also the most effective element in reducing the energy of the neutron, since its nucleus (a proton) has essentially the same mass as a neutron and energy transfer by elastic collision is very effective.

Table 5-4. Chemical Composition of Illustrative Soils

Element	Percentage of Soil Type (by weight)			
	Type I (Liberia, Africa)	Type II (Nevada desert)	Type III (lava, clay, Hawaii)	Type IV (beach, sand, Pensacola, Florida)
Sodium	—	1.30	0.16	0.001
Manganese	0.008	0.04	2.94	—
Aluminum	7.89	6.90	18.79	0.006
Iron	3.75	2.20	10.64	0.005
Silicon	33.10	32.00	10.23	46.65
Titanium	0.39	0.27	1.26	0.004
Calcium	0.08	2.40	0.45	—
Potassium	—	2.70	0.88	—
Hydrogen	0.39	0.70	0.94	0.001
Boron	—	—	—	0.001
Nitrogen	0.065	—	0.26	—
Sulfur	0.07	0.03	0.26	—
Magnesium	0.05	0.60	0.34	—
Chromium	—	—	0.04	—
Phosphorous	0.008	0.04	0.13	—
Carbon	3.87	—	9.36	—
Oxygen	50.33	50.82	43.32	53.332

absence of manganese, the sodium content will probably govern the activity for this period. Between  $H + 5$  hours and  $H + 10$  hours, sodium and manganese content are both important. After  $H + 10$  hours, sodium will generally be the only large contributor. If the sodium, manganese, and aluminum contents are low, the neutron-induced activity generally will be low. Soil type IV is an example of such a soil. Using these guidelines, it may be possible to obtain better data for a given soil by using data for a different illustrative soil

at each of several times of interest. A word of caution is in order, however. While the content of sodium and aluminum will generally be relatively constant over fairly large areas, manganese generally is a trace element and the content may vary by an order of magnitude over a few hundred yards. Between  $H + 1/2$  hour and  $H + 5$  hours, the dose rate will vary almost directly in proportion to the magnitude of the variation in manganese content. In view of the uncertainty in the soil composition at any location under

operational conditions, and the possibility of variations in composition over short distances, the data presented herein should only be used for rough estimates and should not be used as the basis for operational planning.

#### 5-14 Dose Rate and Dose Predictions

As described in paragraph 5-1, both the spectrum and the total number of neutrons emitted during a nuclear explosion are sensitive functions of weapon design. Thus, no "representative" weapon was used for the prediction of neutron-induced activity, and, in view of the other uncertainties discussed above, presentation of prediction techniques for several weapon designs is not warranted. Figure 5-18 shows a broad band that indicates the variation of neutron-induced gamma activity as a function of slant range from the explosion. It is believed that the activity produced by most weapons will

fall within the band.\* Dose rates at  $H + 1$  hour after burst may be obtained by multiplying the dose rates from Figure 5-18 by the multiplying factors given in Problem 5-5.

Figure 5-19 represents the radioactive decay characteristics of the four soil types shown in Table 5-4. The decay factors taken from Figure 5-19 are multiplied by the  $H + 1$  hour dose rate for a particular soil to give the dose rate for that soil at any other time.

Figures 5-20 through 5-23 are presented to facilitate the computation of total dose. Multiplying factors may be obtained from these figures, which, when applied to the  $H + 1$  hour dose rate for the particular soil, will give the dose accumulated over any of several periods of time for various times of entry into the contaminated area.

\* This band considers the representative types of nuclear weapons shown in Table 5-3 with the exception of Type V.

**Problem 5-5. Calculation of Neutron-Induced Activity  
at 1 Hour After Explosion**

Figure 5-18 shows a range of normalized neutron-induced dose rates as a function of slant range from a 1 kt explosion. To estimate the  $H + 1$  hour dose rate, enter the slant range axis with the slant range in yards and read the range of normalized dose rates. Multiply these dose rates by the appropriate factor for the soil type of interest from the following list.

<u>Soil Type</u>	<u>Multiplying Factor</u>
I	1.0
II	9.1
III	109.0
IV	0.024

**Scaling.** For yields other than 1 kt, multiply the dose rates obtained from Figure 5-19 by the weapon yield in kt.

**Example**

**Given:** A 50 kt explosion at a height of burst of 900 feet above soil type III.

**Find:** The range of  $H + 1$  hour dose rates that might be expected: at ground zero and at a ground distance of 950 yards from ground zero.

**Solution:** The corresponding slant ranges are 300 yards to ground zero and 996 yards to a point at a ground distance of 950 yards from ground zero. From Figure 5-18, the normalized  $H + 1$  hour dose rate at a slant range of 300 yards from ground zero are expected to be be-

tween 0.8 rad/hr/kt and 1.8 rads/hr/kt. The corresponding dose rates at a slant range of 996 yards are  $1.6 \times 10^{-2}$  rad/hr/kt and  $5 \times 10^{-2}$  rad/hr/kt. The multiplying factor for soil type III is 109.

**Answer:** The  $H + 1$  hour dose rates at ground zero should be between

$$50 \times 109 \times 0.8 = 4,360 \text{ rads/hr.}$$

and

$$50 \times 109 \times 1.8 = 9,800 \text{ rads/hr.}$$

The  $H + 1$  hour dose rates at a ground distance of 950 yards from ground zero should be between

$$50 \times 109 \times 1.6 \times 10^{-2} = 87 \text{ rads/hr.}$$

and

$$50 \times 109 \times 5 \times 10^{-2} = 272 \text{ rads/hr.}$$

**Reliability.**  $H + 1$  hour dose rates are expected to fall within the limits of the band shown in Figure 5-19 for the specific soils shown. For other soils, even with small variations in the content of sodium and manganese, the data merely will furnish an estimate of the magnitude of the hazard.

**Related Material.** See paragraphs 5-1 through 5-3, and paragraphs 5-12 through 5-14.

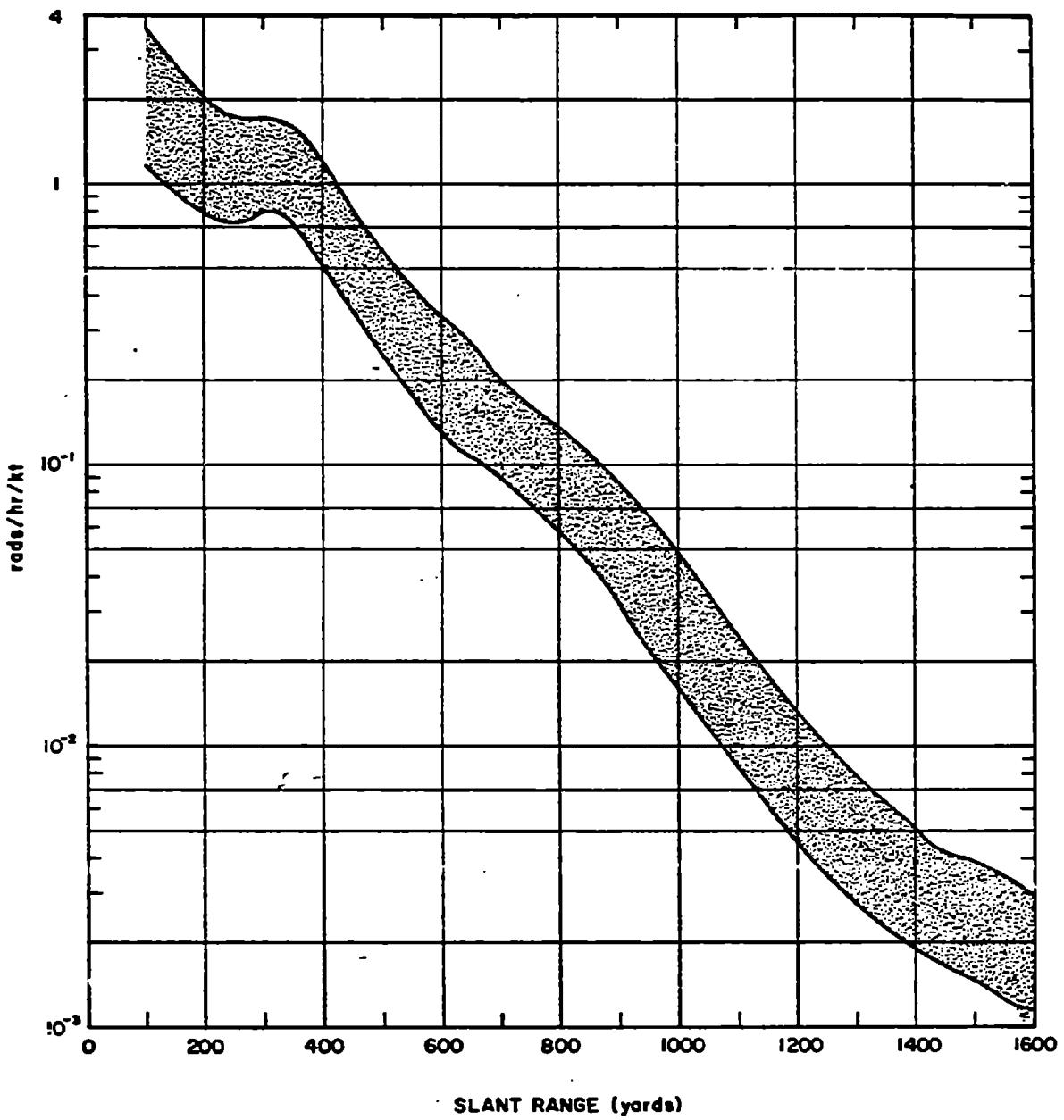


Figure 5-18. [REDACTED] Neutron-Induced Gamma Dose Rate as a Function of Slant Range at a Reference Time of 1 Hour After Burst [REDACTED]

### Problem 5-6. Calculation of Neutron-Induced Gamma Activity at Times Other than $H + 1$ Hour

The dose rate at any time after burst may be determined by multiplying the  $H + 1$  hour dose rate by the decay factor appropriate to the soil of interest from Figure 5-19. The decay curves may also be used to determine the value of the dose rate at  $H + 1$  hour from the dose rate at a later time. In this case, the measured dose rate is divided by the appropriate decay factor. The dose rate at any other time then may be determined from the  $H + 1$  hour dose rate.

#### Example 1

*Given:* The dose rate at a given point on soil type I is 30 rads/hr at  $H + 1$  hour.

*Find:* The dose rate at that point at  $H + 1/2$  hour and at  $H + 10$  hour.

*Solution:* From Figure 5-19, the decay factors for soil type I for  $1/2$  hour and 10 hours are 3 and 0.083, respectively.

*Answer:* The dose rate at  $1/2$  hour is:

$$30 \times 3 = 90 \text{ rads/hr}$$

and the dose rate at 10 hours is

$$30 \times 0.083 = 2.5 \text{ rads/hr.}$$

#### Example 2

*Given:* The measured dose rate at a point

over type II soil is 375 rads/hr 3 hours after the explosion.

*Find:* The dose rate at the same point 50 hours after the explosion.

*Solution:* From Figure 5-19, the decay factors for soil type II are 0.75 and 0.06 for times of  $H + 3$  and  $H + 50$  hours, respectively. The  $H + 1$  hour dose rate at the point is

$$\frac{375}{0.75} = 500 \text{ rads/hr.}$$

*Answer:* The  $H + 50$  hours dose rate at the point is

$$(500)(0.06) = 30 \text{ rads/hr.}$$

**Reliability.** The curves of Figure 5-19 are estimated to represent the decay of the soil compositions shown in Table 5-4 to within  $\pm 10$  percent; however, small changes in the chemical composition of the soil, particularly in the content of sodium, manganese, and aluminum, may change the decay characteristics drastically. Uncertainties associated with the prediction of  $H + 1$  hour dose rates will affect the prediction of dose rates at any other time.

**Related Material.** See paragraphs 5-13 and 5-14. See also Problem 5-5.

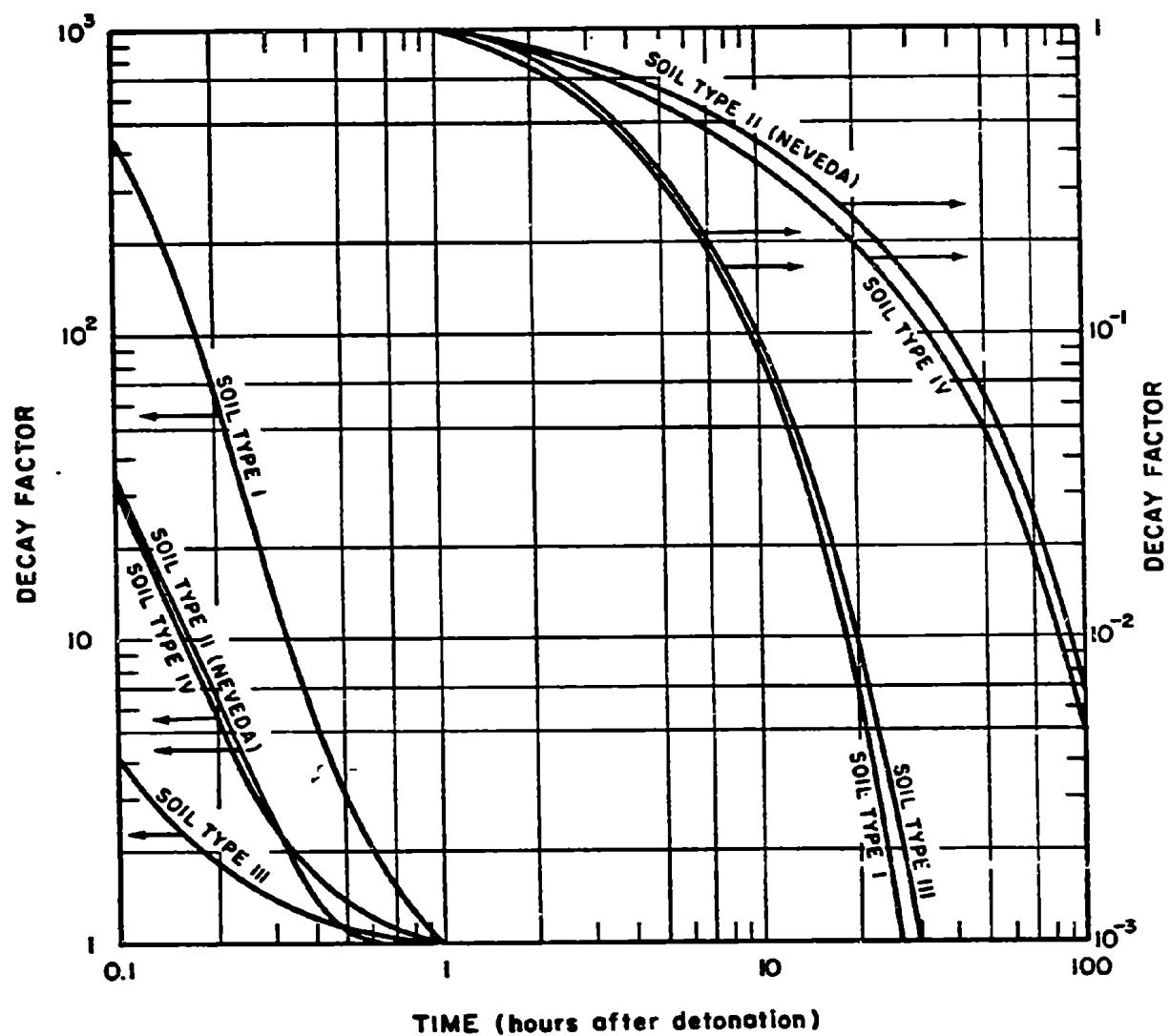


Figure 5-19. Decay Factors for Neutron-Induced Gamma Activity

**Problem 5-7. Calculation of Total Dose from Neutron-Induced Activity**

Figures 5-20 through 5-23 provide the means to obtain the total dose received when entering an area contaminated with neutron-induced activity and remaining for a specified interval of time. The various curves represent times that an individual remains in the contaminated area. To determine the dose, obtain the multiplying factor from the vertical axis that corresponds to the time of entry on the horizontal axis and the stay time from the appropriate curve (or by interpolation between curves).

**Example**

**Given:** A dose rate of 105 rads/hr was measured on entering a contaminated area of soil type III 5 hours after an air burst nuclear explosion.

**Find:** The total dose that would be received by an individual who remained in that area for 1 hour.

**Solution:** From Figure 5-19, the decay factor for soil type III at  $H + 5$  hours is 0.35. The 1

hour dose rate is therefore

$$\frac{105}{0.35} = 300 \text{ rads/hr.}$$

Figure 5-22 is the appropriate figure from which the dose multiplying factor should be obtained for soil type III. From this figure, the intersection of the line for a time of entry of 5 hours after burst with the 1 hour stay time curve gives a factor of 0.32.

**Answer:** If the individual remains in the area for 1 hour, the accumulated dose will be

$$(0.32)(300) = 96 \text{ rads.}$$

**Reliability.** Figures 5-20 through 5-23 are integrals of the curves in Figure 5-19. The same reliability statement given in Problem 5-6 applies.

**Related Material.** See paragraphs 5-13 and 5-14. See also Problems 5-5 and 5-6.

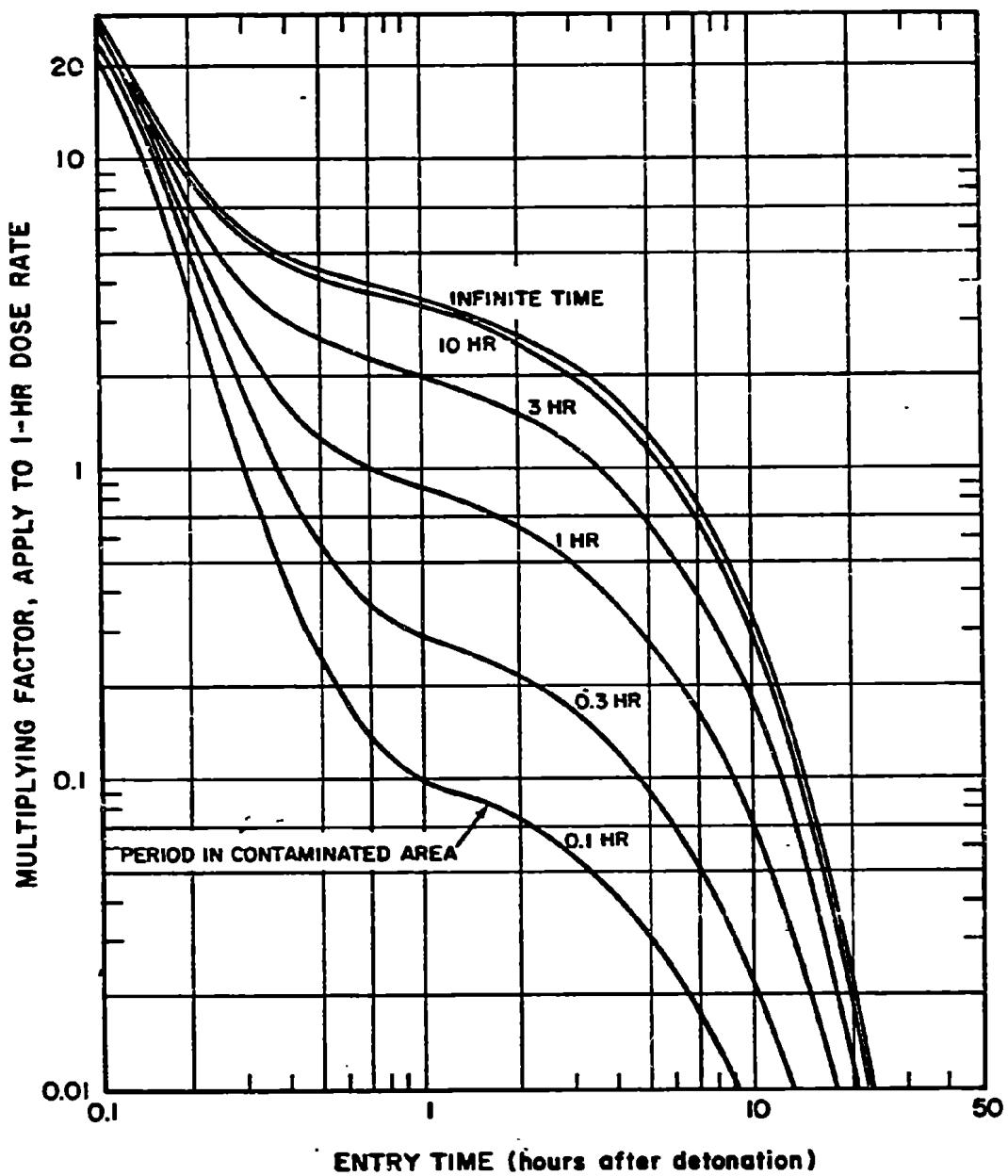


Figure 5-20. Total Radiation Dose Received in an Area Contaminated by Neutron-Induced Gamma Activity, Soil Type I

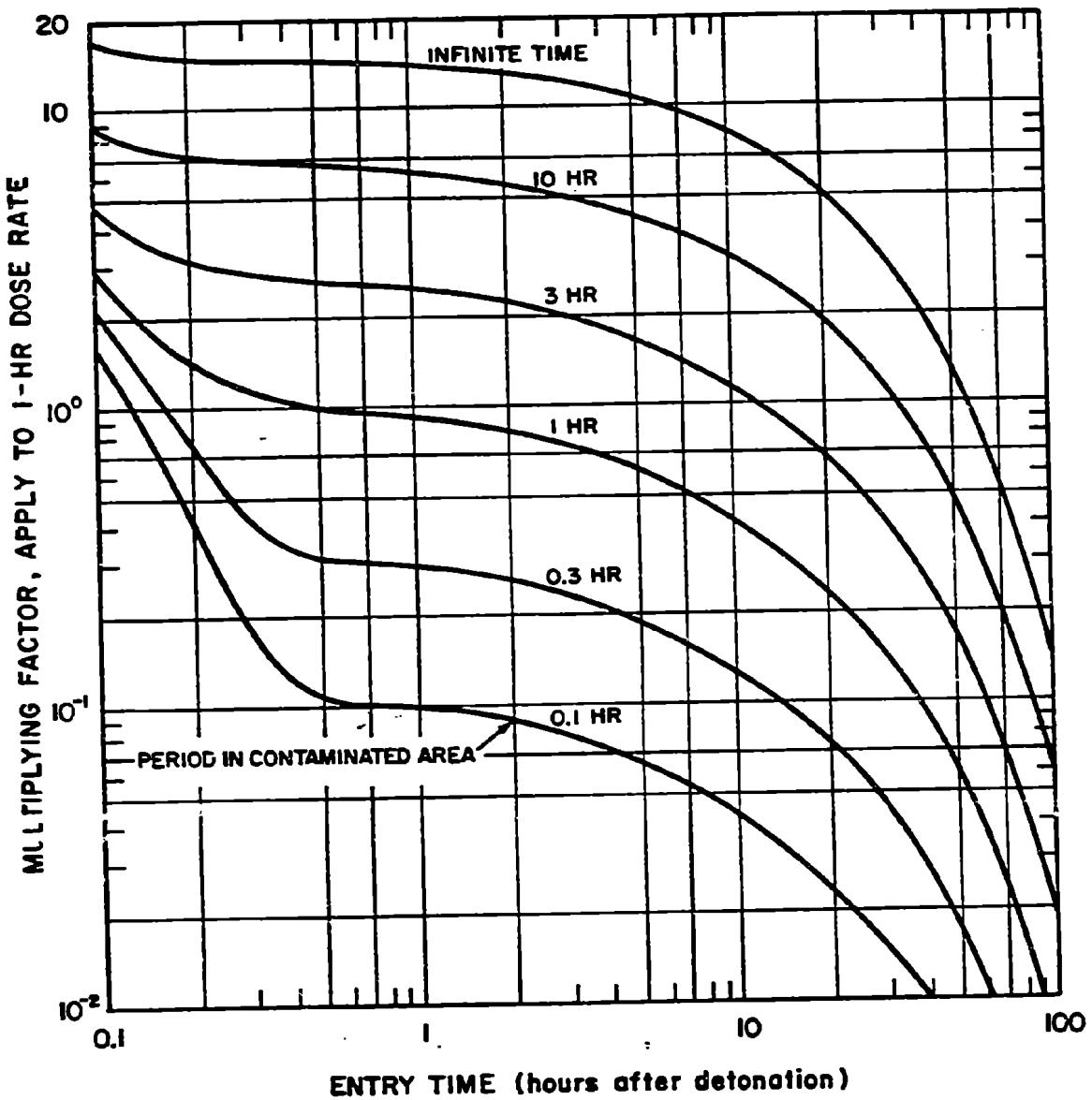


Figure 5-21. Total Radiation Dose Received in an Area Contaminated by Neutron-Induced Gamma Activity, Soil Type II

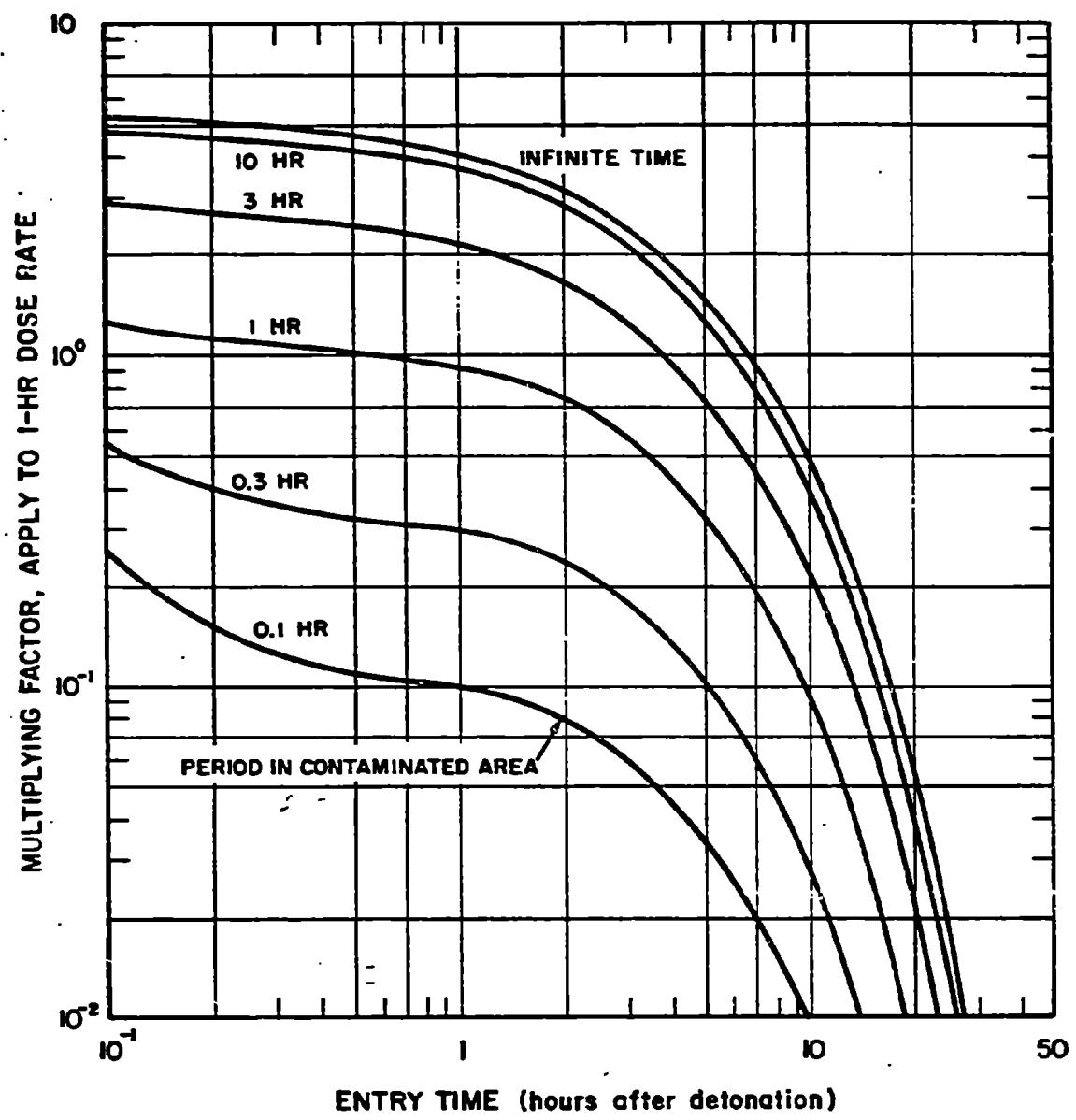


Figure 5-22. Total Radiation Dose Received in an Area Contaminated by Neutron-Induced Gamma Activity, Soil Type III

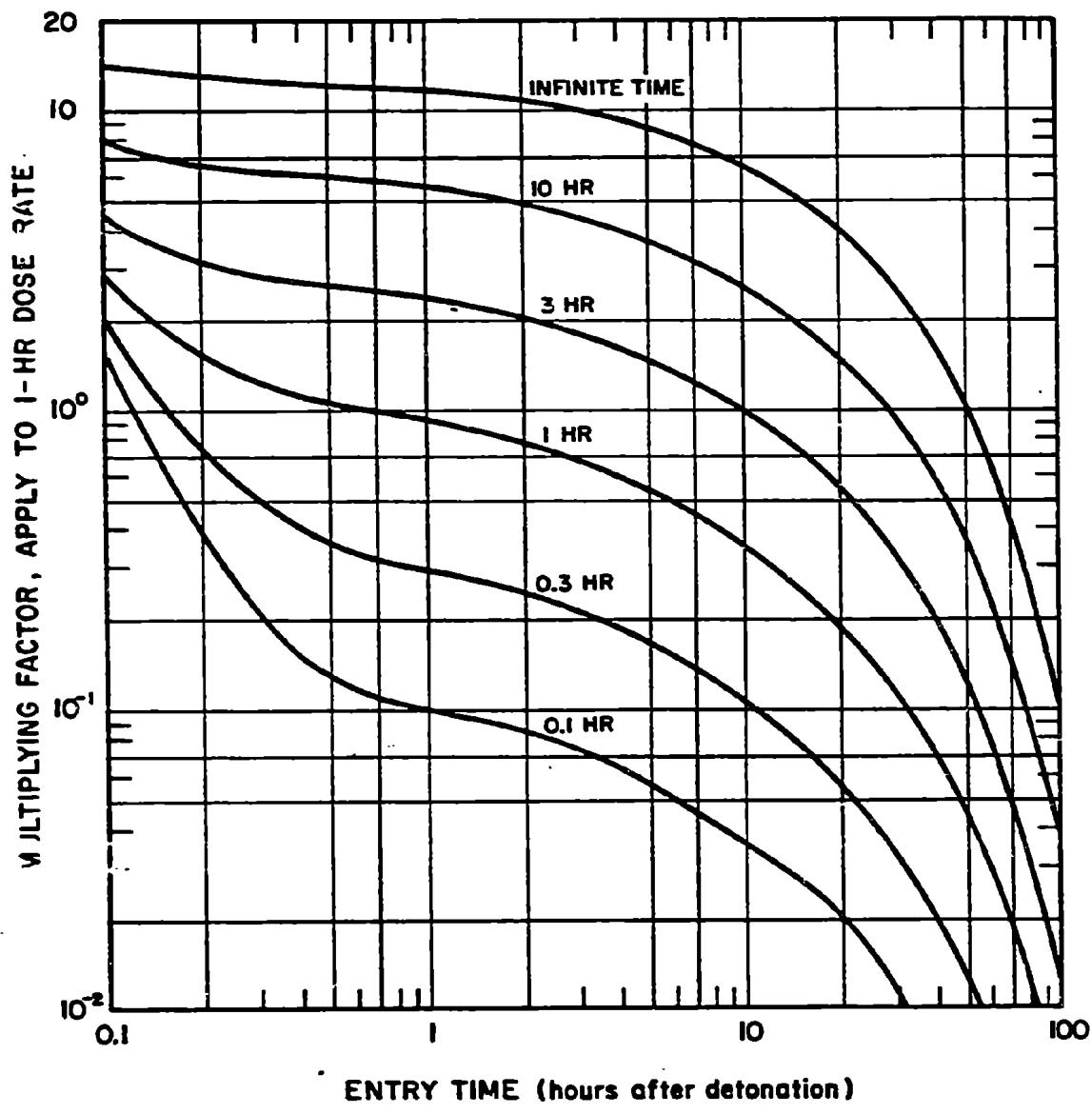


Figure 5-23. Total Radiation Dose Received in an Area Contaminated by Neutron-Induced Gamma Activity, Soil Type IV

### SECTION III

#### RESIDUAL RADIATION

Residual radiation is that radiation that is emitted later than one minute after the explosion. The sources and characteristics of this radiation vary depending on the extent to which fission and fusion reactions contribute to the energy of the weapon. Residual radiation from a fission weapon arises mainly from fission products and, to a lesser extent, from radioactive isotopes formed by neutron reactions in weapon materials and from uranium and/or plutonium that have escaped fission. Other sources of residual radiation hazard are the activity induced by neutrons that interact with various elements present in the earth, sea, air, or other substances in the explosion environment. The most important of these sources is the neutron-induced activity in soils that is discussed in Section II of this chapter. The radioactivity from a thermonuclear weapon will not contain the same quantity of fission products that are associated with a pure fission weapon of the same yield; however the large number of high energy neutrons will produce larger quantities of neutron-induced activity in weapon components and the surroundings. The total radioactivity from such a weapon will, however, generally be less than from a pure fission weapon of the same yield.

#### FALLOUT

The main hazard of residual radiation results from the creation of fallout particles that incorporate the radioactive weapon residues and the induced activity in the soil, water, and other materials in the vicinity of the explosion that are sucked up from the earth's surface into the rising fireball. The wind disperses these particles over large areas. Another hazard may arise from neutron-induced activity on the earth's surface in the immediate neighborhood of the burst

point. Both the absolute and relative contributions of the fission product and induced radioactivity will depend on the total yield and fission yield of weapon, the height of burst, the nature of the surface at the burst point, and the time after the explosion.

Two phases of fallout may be considered: early (local) and delayed (worldwide). Early fallout reaches the ground during the first 24 hours following a nuclear explosion. It is the early fallout from surface, subsurface, or low altitude bursts that produces radioactive contamination over large areas, with an intensity great enough to represent an immediate biological hazard. Delayed fallout, which arrives after the first day, consists of very fine, invisible particles that settle in low concentrations over a considerable part of the earth's surface. Radioactive decay during the relatively long time the delayed fallout remains suspended in the atmosphere reduces the radiation intensity from the fission products and other substances significantly. Because of these characteristics, the radiations from the delayed fallout pose no significant military effect and are not considered here.

#### 5-15 Early Fallout

The early fallout from a nuclear weapon consists of fission products and neutron activation products in quantities that are related to the fission and total yields of the weapon, respectively. In the case of a weapon in which large quantity of the energy is derived from fusion reactions, and especially for bursts high in the transition zone between surface (fallout producing) bursts and air bursts where little soil mixes with bomb debris to form fallout, the induced activity can be more important than that from fission products (see Section II). The relative importance of these two sources of residual radiation depends upon the fission-fusion ratio, type and composition of the surface material under the detonation and the height of burst.

For detonations over land, where the particles consist mainly of soil minerals, the fission-product vapors condense onto solid and diffuse into molten soil particles and other particles that may be present. The vapors of the fission products also may condense with vapors of other substances to form mixed solid particles of small size.

The fact that different materials condense at different temperatures, and at different times after detonation, changes the composition of fallout particles, giving rise to the phenomenon known as "fractionation." The occurrence of fractionation is shown, for example, by the fact that in a land surface burst the larger particles, which fall out of the fireball early and are found near ground zero, have radioactive compositions different from the smaller particles that leave the cloud later and reach the ground some distance downwind. The phenomena that account for fractionation are not all completely understood, but models have been developed to explain the phenomena reasonably satisfactorily. An example of fractionation is the change in physical state of fission products, such as krypton and xenon, as they decay. These two example products are gaseous in their normal state and do not combine with other elements to form compounds. During their radioactive decay, however, they form rubidium and cesium, respectively. These decay products can condense onto solid particles. In early fallout, the solid particles will be depleted not only in krypton and xenon, but also in their various decay (or daughter) products. In delayed fallout, small particles that have remained in the cloud for some time will have rubidium and cesium, and their daughters, strontium and barium, condensed upon them. Hence, the delayed fallout will be relatively richer in these elements.

#### 5-16 Air Bursts

The surface contamination effects of fallout from an air-burst weapon are militarily

insignificant in most cases, because the cloud carries most of the radioactive weapon debris to high altitudes. In general, by the time this material can fall back to earth, dilution and radioactive decay decreases the activity to levels that are no longer militarily important. An exception may occur in the case of a nuclear weapon cloud that is intercepted by a rainstorm from above. This special case of fallout, called "rainout" is discussed in a subsequent subsection.

#### 5-17 Land Surface Bursts

The activity available from a nuclear explosion at a reference time of 1 hour after burst corresponds roughly to 450 megacuries per kiloton of fission yield.\*

Roughly half of the available activity is deposited as early fallout during the first 24 hours following a surface burst. This deposited radioactivity can extend several hundred miles from the burst point, depending on the yield and the prevailing winds. The winds of the upper atmosphere (the stratosphere) slowly deposit the remainder of the activity, or the delayed fallout, over the earth's surface, mainly in the hemisphere of detonation. The land surface burst is used as the standard for the development of deposition patterns and idealized contours that are discussed below. Adjustments to correct these idealized contours for bursts in the transition zone (heights of burst between an air burst and a surface burst) and for underground bursts are described in paragraphs 5-22 and 5-23.

\* This value approximates the activity per kiloton in disintegrations per second at one hour. Actual values may range from about 430 to about 460 megacuries, depending on the fissile material and the neutron spectrum that causes the fission. The user may encounter other values in various sources, e.g., 550 gamma-megacuries per kiloton at 1 hour after explosion. This latter is a fictitious, but useful, relationship that relates the fission product gamma source to an equivalent monoenergetic source with an energy equal to the average photon energy of the fission products at 1 hour after the explosion.

### 5-18 Deposition Patterns

In a complete calm, the fallout contamination would form a roughly circular pattern around the point of detonation. Wind leads to an elongated area, the exact nature of which depends upon the speed and direction of the wind from the surface up to the altitude of the top of the stabilized cloud. If the direction of the wind does not vary excessively from the surface up to the top of the cloud, the ground fallout contours may be characterized by a semi-circular pattern upwind from ground zero and an elliptical pattern downwind. The upwind pattern is formed by the rapid settling of the heavier particulate matter in the stem and ejecta from the crater, whereas the downwind elliptical pattern is formed by fallout of smaller and lighter particles from the cloud.

Complicated wind patterns (wind shear) as well as variations of the wind pattern in time and space may cause extreme departures from a simple elliptical pattern. Also, the measured dose-rate contours have frequently been observed to occur in patterns that are best described as a series of islands of relatively high activity surrounded by areas of lower activity. The most common pattern of this type has been one in which the higher dose rate contours appear around two major areas and one or more smaller areas. One of the larger areas is in the immediate vicinity of ground zero; the other is in the general downwind direction from ground zero. The locations of the smaller areas of high activity have not demonstrated patterns that can be described simply in terms of the wind structure. The dose rates observed within these high activity areas have been of comparable magnitude when extrapolated back to some early time after detonation, such as  $H + 1$  hour. Because of the earlier arrival of the contaminant, however, the activities actually observed near ground zero have been higher than in the areas away from ground zero. A quantitative treatment of such

complicated deposition patterns is possible only through use of a complex computational model. The simplified method for obtaining deposition patterns presented below will not predict these islands of relatively high activity.

The area covered and the degree of localization of the contamination also depend to some extent on the character of the soil at the burst point. For example, a surface detonation over dry soil with small particle sizes probably would result in a larger area enclosed by low dose rate contours and a smaller area enclosed by high dose rate contours than for the average case. A similar detonation over water covered, finely divided soil such as clay probably would result in relatively high dose rate contours over larger areas close to the detonation, with a corresponding reduction in the areas of the lower dose rate contours farther out.

### 5-19 Idealized Contours

In any simplified discussion of the areas affected by residual contamination from fallout, it is convenient to set up a system of contamination dose rate contours which, although simplified and idealized, fit actual contours measured in the field as closely as possible. Figure 5-24 illustrates such a contour system. The idealized contour shown consists of a nearly semicircular upwind portion and a roughly elliptical continuation of the contour in the downwind direction. The radioactivity in the vicinity of ground zero is deposited soon after the detonation, largely from heavy particulate matter, ejecta from the crater, and soil made radioactive by neutron-capture reactions. The parameters that define the contour extent in this region are the upwind distance and ground zero width. The parameters that determine the shape of the downwind contours are the downwind distance, maximum width, and distance to the maximum width. To define the downward axis, it is assumed that the downwind direction and extent are determined by a single wind of constant velocity, the so-

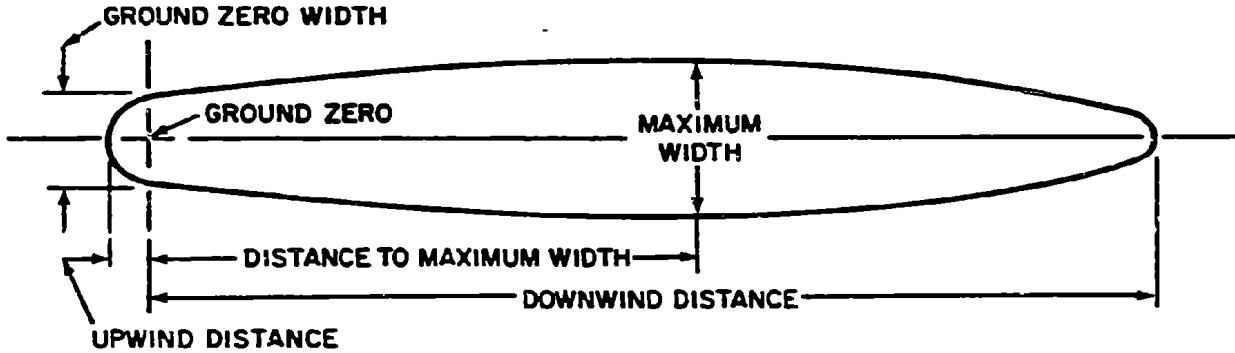


Figure 5-24. (U) Idealized Early Fallout Dose Rate Contour (U)

called effective wind, as described in paragraph 5-20. Usually wide discrepancy from the idealized pattern will result if there are large directional shears in the winds from the surface up to the altitudes of the stabilized cloud. Such shears can distort the idealized pattern seriously, so that, in practice, radical departures from the idealized patterns can be expected. Figure 5-25 compares the idealized dose rate contour pattern to the observed pattern normalized to 1 hour after shot SMALL BOY, a low yield shot in Nevada during which the wind shear was not excessive. The actual winds had an effective velocity of about 8 knots and an effective shear of about 30 degrees (effective velocity and effective shear are defined in paragraph 5-20). The idealized pattern is shown for an effective velocity of 10 knots and an effective shear of 15 degrees, for the reasons explained in paragraph 5-20. The downwind distance is expected to increase and the crosswind distance to decrease both with an increase in velocity and with a decrease in shear. These tendencies are noticeable in Figure 5-25; however, for this case of low yield and minimal shear, the idealized contours represent a reasonable approximation of the observed contours.

Figure 5-26 shows a hodograph of a typical summer wind structure over Fort Worth, Texas. This is an example of a severely sheared wind structure. The average wind speed to altitudes of the stabilized cloud from a 2 Mt burst is about 10 knots, but, as a result of directional changes, the effective velocity is only 2.5 knots. The direction of this effective wind is 43.5 degrees east of north.

Figure 5-27 shows a comparison of the idealized dose rate contours for a 2 Mt explosion on the surface and the contours computed by the "Defense Land Fallout Interpretive Code (DELFIC)" (see bibliography) for the wind hodograph shown in Figure 5-26 assuming that the winds stayed constant in time and distance. While this comparison is not a comparison with actual data, it is a comparison with the results of a complex computer code that was developed independent of empirical data and which has demonstrated a very good agreement with available data. The general direction as well as the areas of the two patterns are quite divergent. This comparison is intended to illustrate the lack of confidence that can be placed in the idealized contours for prediction of a fallout pattern for a particular explosion, even if meteorological data

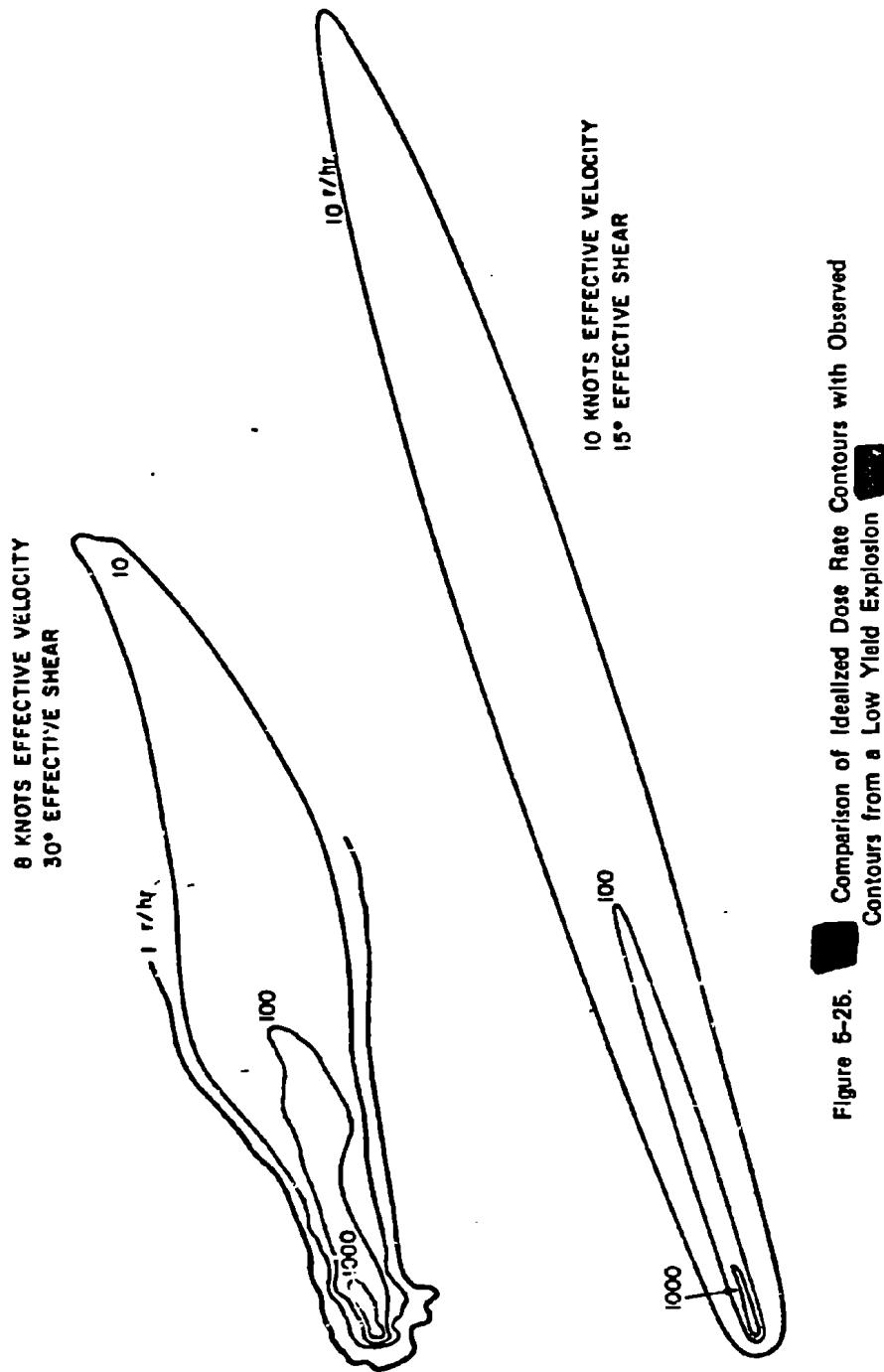
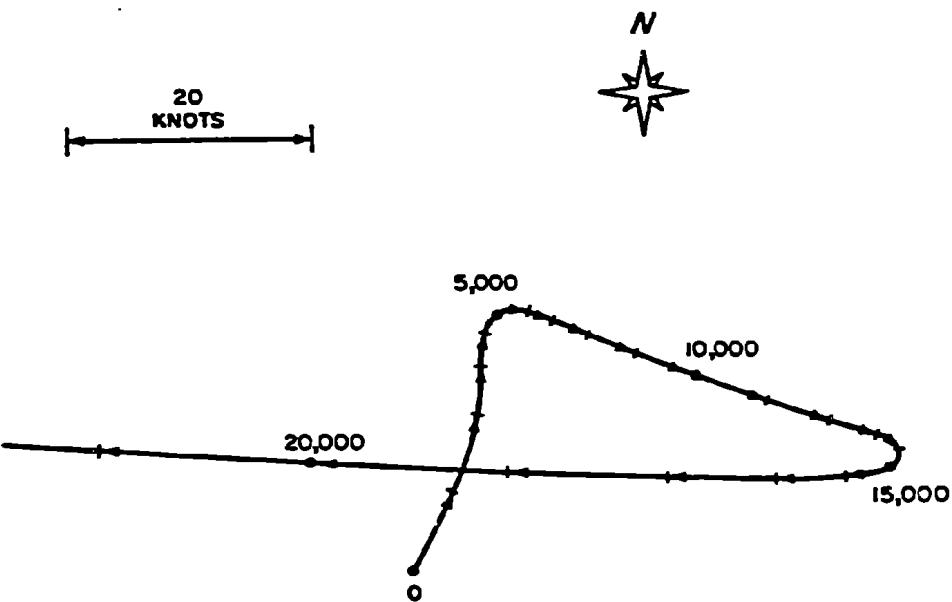


Figure 6-25. Comparison of Idealized Dose Rate Contours with Observed Contours from a Low Yield Explosion



NOTE: NUMBERS ARE METERS OF ALTITUDE.

Figure 5-26. Hodograph of a Typical Summer Wind Structure  
Over Fort Worth, Texas

at the burst point are known. The contours for the idealized curves were extrapolated to a speed of 25 knots even though extrapolation below 10 knots is not recommended. On the other hand, for small yields, or for the case of many weapons, the total dose predicted by the idealized contours over large areas probably would provide a reasonable basis upon which to base casualty predictions.

#### 5-20 Dose Rate Contour Dimensions

Figures 5-28 through 5-37 may be used to draw idealized dose rate contours for land surface explosions with yields between 0.01 kt and 30 Mt. Separate sets of curves are provided for downwind distance, maximum width, and

downwind distance to maximum width for effective wind speeds of 10, 20, and 40 knots. Since actual winds are seldom unidirectional and since the radioactive particles that cover the area around zero include many that were not carried to high altitudes, the ground zero width is presented independent of wind velocity in Figure 5-37. The upwind distance is estimated to be one-half the ground zero contour widths, i.e., they may be represented by a semi-circle, centered at ground zero, with a radius equal to one-half the ground zero width. The dose rate values obtained from the curves correspond to the values existing at a reference time of 1 hour after burst, 3 feet above a hypothetical smooth, infinite plane; therefore, they must be reduced to account for ground roughness. A reduction

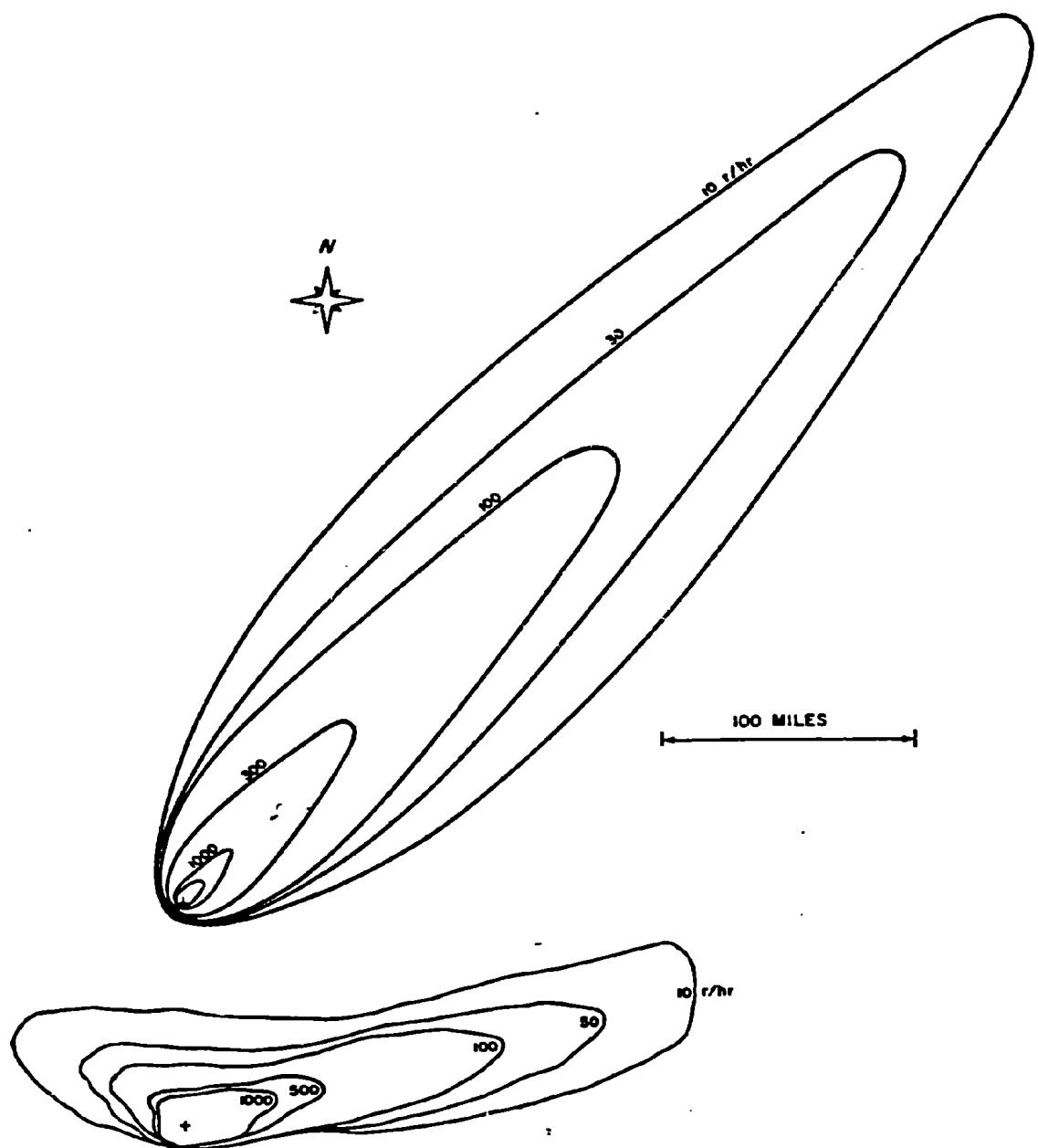


Figure 5-27. Comparison of Idealized Dose Rate Contours with Those Calculated by a Complex Computer Code for a 2 Mt Explosion and the Winds of Figure 5-25

factor of 0.7 is appropriate for reasonably level terrain. A factor of 0.5 to 0.6 would be more appropriate for rough and hilly terrain. If additional shielding exists (e.g., foxholes, buildings, tanks), additional shielding factors should be obtained from Section VI, Chapter 9.

To obtain the effective wind for use with Figures 5-28 through 5-36, a wind hodograph similar to that shown in Figure 5-26 should be prepared. The vector averages of the winds from ground zero to the base of the stabilized cloud and to the top of the stabilized cloud should then be obtained. The average of these two average vectors is the effective wind for use with Figures 5-28 through 5-36. The heights of the bottom and top of the stabilized cloud are shown as a function of yield in Figures 5-38 and 5-39, respectively. For wind speeds between the values of 10, 20, and 40 knots that are shown in Figures 5-28 through 5-36, contour values may be obtained by linear interpolation. Extrapolation to values below 10 knots or above 40 knots is not recommended.

As used herein the term "effective shear" refers to the angle between the average vectors to the bottom and top of the stabilized cloud. In the absence of a sufficient quantity of test data with which empirical curves for determining the idealized contours could be constructed, were generated by use of the Defense Land Fallout Interpretive Code (DELFIC) (see bibliography). An effective shear of 15 degrees was used in the computer calculations from which the curves of Figures 5-28 through 5-36 were derived. In general, increased wind velocity tends to lengthen and narrow the pattern, while increased directional shear tends to shorten and widen the pattern. An effective velocity and an effective directional shear do not define a unique wind structure, i.e., different wind structures could have the same effective velocity and directional shear. It is not recommended that any attempt be made to change the

contour values for effective directional shears different from 15 degrees; however, the user should be aware that differences from this value are more likely to result in idealized contours that are farther from reality than if the shear is nearly equal to 15 degrees.

### 5-21 Decay of Early Fallout

Fission products are composed of a complex mixture of over 200 different forms (isotopes) of 36 elements. Most of these isotopes are radioactive, decaying by the emission of beta particles, frequently accompanied by gamma radiation. About 2 ounces of fission products are formed for each kiloton (or 125 lb/Mt) of fission energy yield. The total radioactivity of the fission products initially is extremely large but it falls off rapidly as the result of radioactive decay.

At 1 minute after a nuclear explosion, when the residual nuclear radiation is postulated to begin, the gamma ray activity of the 2 ounces of fission products from a 1 kt fission yield explosion is comparable with that of about 30,000 tons of radium. For explosions in the megaton-energy range the amount of radioactivity produced is enormous. Although there is a decrease from the 1 minute value by a factor of over 6,000 by the end of a day, the radiation intensity still will be large.

Early fallout consists mainly, but not entirely, of fission products. The following rule indicates how the dose rate of the actual mixture decreases with time: for every seven-fold increase in time after the explosion, the dose rate decreases by a factor of 10. For example, if the radiation dose rate at 1 hour after the explosion is taken as a reference point, then at 7 hours after the explosion the dose rate will have decreased to 1/10; at  $7 \times 7 = 49$  hours (or roughly 2 days) it will be 1/100; and at  $7 \times 49 = 343$  hr (or roughly 2 weeks) the dose rate will be 1/1,000 of that at 1 hour after the burst.

Another aspect of the rule is that at the end of 1 week (7 days), the radiation dose rate will be 1/10 of the value after 1 day. This rule is accurate to within about 25 percent up to 2 weeks or so, and is applicable to within a factor of 2 up to roughly 6 months after the nuclear detonation. After 6 months, the dose rate decreases at a much more rapid rate than predicted by this rule.

Information concerning the decrease of dose rate in the early fallout can be obtained from the continuous curve in Figure 5-40, in which the ratio of the approximate exposure dose rate at any time after the explosion to a convenient reference value, called the 1 hour reference dose rate, is plotted as a function of time in hours.

Table 5-5 gives the results of Figure 5-40 in more convenient, although somewhat less complete, form. The dose rate, in any suitable units, is taken as 1,000 at 1 hour after a nuclear explosion; the expected dose rate in the same units at a number of subsequent times, for the same quantity of early fallout, is then as shown in the table. If the actual dose rate at 1 hour (or any other time) after the explosion is known, the value at any specified time, up to 1,000 hours, can be obtained by simple proportion.

It should be noted that Figure 5-40 and Table 5-5 are used for calculations of dose rates. To determine the total radiation dose received it is necessary to multiply the average dose rate by the exposure time. Since the dose rate is decreasing steadily during the exposure, however, appropriate allowance for this must be made. The results of the calculations based on Figure 5-40 are expressed by the curve in Figure 5-41, which gives the total dose received from early fallout, between 1 hour and any other specified time after the explosion, in terms of the 1 hour reference dose rate.

The continuous curve in Figure 5-40, which represents the decrease in dose rate due to

Table 5-5. [REDACTED] Relative Theoretical Dose Rates from Early Fallout at Various Times After a Nuclear Explosion [REDACTED]

Time (hr)	Relative Dose Rate	Time (hr)	Relative Dose Rate
1	1,000	36	14.0
1-1/2	615	48	9.6
2	435	72	5.9
3	268	100	4.0
5	145	200	1.7
6	116	400	0.75
10	63	600	0.46
15	40	800	0.33
24	22	1,000	0.25

gamma radiation from radioactive fallout, sums up the contributions of the more than 200 isotopes in the fission products and in the activity induced by neutrons in the weapons materials for various times after fission. The effects of fractionation, resulting from the partial loss of gaseous krypton and xenon (and their daughter elements), and from other circumstances, have also been taken into account (see paragraph 5-15). The dose rates calculated in this manner vary with the nature of the weapon, but the values plotted in Figure 5-40 are reasonable averages when the fallout activity arises mainly from fission products. The decrease in the dose rate with time cannot be represented by a simple equation that is valid at all times, but it can be approximated to within 25 percent by the straight dashed lines labeled  $t^{-1.2}$  for times between 30 minutes to about 5000 hours (about 200 days) after the explosion. After 200 days, the fallout decays more rapidly than indicated by the  $t^{-1.2}$  (broken) line, so the continuous

curve should be used to estimate dose rates from fallout at these times.

(U) While the approximation is applicable, the decay of fallout activity at a given location may be represented by the simple expression

$$\dot{D}_t = \dot{D}_1 t^{-1.2},$$

where  $\dot{D}_t$  is the gamma radiation dose rate at time  $t$  after the explosion, and  $\dot{D}_1$  is the 1 hour dose rate, which is also the reference dose rate that is used in Figures 5-28 through 5-37. The actual value of  $\dot{D}_1$  will depend on the time units, that is, minutes, hours, days, and so on. In this chapter, time is generally expressed in hours, so that the unit time for the reference dose rate  $\dot{D}_1$  is 1 hour.

The curves in Figure 5-40 and the equation given above apply so long as there is no change in the quantity of fallout during the time interval under consideration. Therefore, it cannot be used while the fallout is still descending, but only after it is essentially complete, at the particular location. If during the time  $t$ , any fallout material is removed, for example, by weathering or by washing away, or if any additional material is brought to the given point by wind or by another nuclear explosion, neither the curves nor the equation will predict the decay of the fallout activity correctly.

Measurements made on actual fallout from weapons tests indicate that, although the  $t^{-1.2}$  decay represents a reasonable average, exponents in the range of -0.2 to -2, rather than -1.2, are sometimes needed to represent the rate of decay. In fact, different exponents are sometimes needed for different times after the explosion. These anomalies, which apparently arise from the particular circumstances of the explosion, are very difficult to predict, except in cases where a large quantity of neutron-induced activity is known to have been produced, either in the ground or in weapon components or both.

Furthermore, fallout from two or more explosions occurring at different times will change the observed decay rate completely. For measurements made over a long period of time after the burst, weathering will tend to alter the dose rates unpredictably. In an actual situation following a nuclear detonation, estimates based on either the  $t^{-1.2}$  decay rule or even on the continuous curves in Figures 5-40 and 5-41 must be used with caution and should be verified by actual measurements as frequently as possible.

In principal, either Figures 5-40 and 5-41, or the  $t^{-1.2}$  decay equation could be used to estimate the total dose received from fallout in a contaminated area, provided that all of the fallout arrives in a short time. Actually, the contaminated particles may descend for several hours, and without knowing the rate at which the fission products reach the ground, useful calculations cannot be made. However, after the fallout has ceased to arrive, either the figures or the equation will provide rough estimates of radiation doses up to about 200 days after the explosion, provided one measurement of the dose rate is available. After 200 days, the solid curve of Figure 5-40 together with Figure 5-41 should be used. However, at such long times after the explosion, it is not likely that the standard decay pattern will persist. It is advisable to make frequent measurements and to derive an appropriate decay scheme.

Table 5-6 shows the percentage of the infinity (residual radiation) dose that would be received from a given quantity of early-fallout, computed from 1 hour to various times after a nuclear explosion. The infinity dose is that which would be received as a result of continued exposure to a certain quantity of early fallout for many years. These data can be used to determine the proportion of the infinity dose received during any specified period following the complete deposition of the early fallout from a nuclear explosion. If the decay followed the

Table 5-6. Percentage of the Infinite Residence Dose Received from 1 Hour to Various Times After Explosion

Time (hr)	Percent of Infinite Dose	Time (hr)	Percent of Infinite Dose
2	15	72	68
4	28	200	78
6	33	500	85
12	44	1,000	89
24	53	2,000	93
48	63	5,000	98

$r^{1/2}$  decay law given above beyond 200 days, the infinite residence dose, starting at 1 hour, would be equal to 5 times the  $H + 1$  hour dose rate, and this convenient rule of thumb has been used frequently. However, in view of the more rapid decay of the actual fission product mix after about 5,000 hours (see Figure 5-40), a better rule of thumb is that the infinite residence dose is equal to 4 times the  $H + 1$  hour dose rate.

Figure 5-42 provides a convenient means for determining the total dose received during various times of occupancy of a contaminated area as a function of time of entry. For purposes of prediction, the time of entry may be taken to be the time of arrival of the fallout. Within the accuracy of Figures 5-28 through 5-37, this time may be taken to be equal to the distance from ground zero divided by the effective wind speed, i.e., the buildup of activity during the finite arrival time is neglected.

### 5-22 Bursts in the Transition Zone

The deposition patterns and decay rate of the contamination from weapons that are

burst very close to the surface will be similar to those for a weapon of the same yield burst on the surface. However, as the height of burst increases, the activity deposited locally as fallout decreases, and the residual contamination resulting from the neutron-induced activity becomes more important. The exact scaling of the fallout dose rate contour values with height of burst is uncertain. Residual contamination from tests at heights of burst immediately above or below  $100W^{0.35}$  feet has been small enough to permit approach to ground zero within the first 24 to 48 hours after detonation without exceeding reasonable peacetime dosages. In these tests the mass of the tower, special shielding, and other test equipment contributed to considerable part of the fallout actually experienced, and neutron-induced activity in the soil added further to the total contamination. Thus, for heights of burst of  $100W^{0.35}$  feet or greater, contamination from fallout will probably not be sufficiently extensive to affect military operations materially. Figure 5-43 shows this relation plotted as minimum height of burst versus weapon yield. It must not be assumed that even low to intermediate yields will never present a residual radiation problem when burst above  $100W^{0.35}$  feet. The neutron-induced gamma activity can be intense in a relatively small area around ground zero. A better idea of the contamination pattern, dose rate contour values, and decay rate of the residual radiation from the above types of explosions generally will be obtained by basing the predictions on the induced activity as described in Section II of this chapter. In view of the uncertainty involved and the lack of experimental data for high yields burst over land at heights of burst near  $100W^{0.35}$  feet, a more conservative estimate of  $180W^{0.4}$  feet may be desirable for use under some circumstances as the height at which fallout becomes negligible.

A rough estimate of the dose rate contour values for bursts in the transition zone may

be obtained by applying an adjustment factor from Figure 5-44 to the dose rate contour values obtained from Figures 5-28 through 5-37. For bursts in the upper quarter of the fallout transition zone, neutron-induced activity must also be considered. For bursts in the lower three-quarters of the transition zone the neutron-induced gamma activity generally can be neglected compared to the fallout activity.

### 5-23 Underground Bursts

A large amount of residual contamination is deposited in the immediate vicinity of the burst point after an underground detonation, because most of the radioactive material falls from the column and cloud to the surface rapidly. A very shallow underground burst conforms closely to the contamination mechanisms and patterns described in paragraphs 5-19 and 5-20 for land surface bursts. As depth of burst increases, a greater percentage of the total available contaminant is deposited as local fallout, until for the case of no surface venting, all of the contamination is contained in the volume of ruptured earth surrounding the point of detonation.

Figure 5-45 shows a depth multiplication factor as a function of scaled depth of burst for yields between 1 kt and 1 Mt. These factors

are applied to the linear dimensions of the dose rate contours for a land surface burst of the same yield, which must be obtained from Figures 5-28 through 5-37. This treatment yields dose rate contours for underground bursts that have shapes similar to the comparable surface burst dose rate contours. Although there is some reason to believe that this is not a valid representation, this treatment does yield a fair representation of the total activity deposited in early fallout patterns. Variations in soil type and other factors introduce additional uncertainties, which are reflected by the broad band in Figure 5-45.

### 5-24 Beta Radiation

The hazard from the gamma rays of the residual radiation generally will exceed that from beta particles, except in those cases where intimate contact with beta emitting particles occurs. Such contact may result when an individual lies prone in a contaminated area, or when particles fall directly on the scalp. Burns that range from being superficial to severe may result from such exposures (see paragraph 10-27, Chapter 10). The severity of the burn will depend both on the intensity of the radiation source in contact with the body and on the promptness with which the particles are washed from the skin, i.e., the length of exposure.

**Problem 5-8. Calculation of Fallout Gamma Radiation  
Dose Rate Contours for Surface Bursts**

[REDACTED] Figures 5-28 through 5-37 show idealized dose rate contour parameters for residual fallout radiation from surface bursts of weapons with yields between 0.01 kt and 30 Mt. The dose rates are given in terms of exposure rate in roentgens per hour as calculated by the DELFIC computer code for a receiver 3 feet above an infinite plane surface. Within the accuracy of the data, 1 roentgen may be taken to be equal to 1 rad. The actual exposure will be about 0.7 times that shown for the plane surface if the terrain is smooth, and 0.5 to 0.6 times the values for the plane surface if the terrain is rough or hilly. The basic data are presented for weapons from which all the yield results from fission; but, as described below, the data can also be used to obtain fallout contours for weapons for which the fission yield is only a fraction of the total yield, and for which essentially all of the contamination produced (90 percent or more) results from fission products. The dose rate values are given for a reference time of  $H + 1$  hour. The more distant parts of the larger contours do not exist at  $H + 1$  hour, because the fallout that eventually reaches some of these more distant areas is still airborne at that time. The dose rate contours do exist at later times when fallout is complete, but with dose rate contour values reduced according to the appropriate decay factor from Figure 5-40. Visual interpolation may be used for dose rate contour values between those for which curves are given. Extrapolation to dose rate contour values higher or lower than those shown in the families of curves cannot be done accurately and should not be attempted.

[REDACTED] An approximate estimate of the area within particular dose rate contour may be calculated by assuming that the roughly elliptical contour obtained by plotting the parameters

[REDACTED] given in Figures 5-28 through 5-37 is an ellipse. The formula for this area is: Area =  $\pi ab/4$  where  $a$  is downwind distance plus upwind distance, and  $b$  is maximum crosswind distance. It must be realized that the dose rate contours are not true ellipses, and that this formula is only an approximation.

[REDACTED] The decay factors from Figure 5-4 should be used to obtain dose rate values for times other than  $H + 1$  hour. To obtain contour values for effective winds other than those given in the curves, that is, 10, 20, and 40 knots, linear interpolation may be used. Thus, the downward distance for a 30 knot effective wind speed would be midway between the 20 knot and 40 knot downwind distances.

[REDACTED] Contour shapes and sizes are a function of the total yield of the weapon, whereas the dose rate contour values are determined by the fission yield. Thus, if only a fraction of the total yield of the weapon results from fission, and this fraction is known, Figures 5-28 through 5-37 may be used to estimate fallout contours resulting from the detonation of such a weapon. The dose rate for the dimension of interest as read from the figures opposite the total yield must be multiplied by the ratio of fission yield to total yield to obtain the true dose rate value for that dimension. Similarly, to obtain contour dimensions for a particular dose rate, the value of the desired dose rate must be divided by the ratio of fission to total yield, and the dimension of the resultant dose rate read from the figure opposite the total yield.

[REDACTED] *Example* [REDACTED]

*Given:* A hypothetical weapon with a total yield of 600 kt, of which 200 kt results from fission, is detonated on a land surface with 10 knot effective wind conditions.

**Find:** The contour parameters for a dose rate of 50 rads/hr at  $H + 1$  hour reference time over rough, hilly terrain.

**Solution:** The 50 rads/hr contour for a fission yield to total yield ratio of  $200/600 = 1/3$  corresponds to the contour of  $50 \div 1/3 = 150$  rads/hr for a weapon for 600 kt fission yield. The dose rate above contaminated rough and hilly terrain is about one-half that above an ideal smooth plane. Thus the desired contour parameters can be obtained by entering Figures 5-28, 5-31, 5-34, and 5-37 with a yield of 600 kt and reading the parameter values corresponding to an  $H + 1$  hour dose rate of  $2 \times 150 = 300$  rads/hr (the factor 2 corrects for the rough, hilly

terrain).

**Answer:** The  $H + 1$  hour dose rate parameter values are shown below.

**Reliability.** The degree to which wind and other meteorological conditions affect these contour parameters cannot be overemphasized. The contours presented in these curves have been idealized in order to make it possible to present average, representative values for planning purposes. Due to these limitations, a meaningful percentage reliability figure cannot be assigned to the idealized fallout pattern.

**Related Material.** See paragraphs 5-17 through 5-20.

Parameter	Source Figure	Parameter Value for a 10 Knot Effective Wind (miles)
Downwind Distance	5-28	80.0
Maximum Width	5-31	9.0
Distance to Maximum Width	5-34	25.0
Ground Zero Width	5-37	4.4
Upwind Distance	5-37*	2.2

Upwind distance equals one-half the ground zero width.

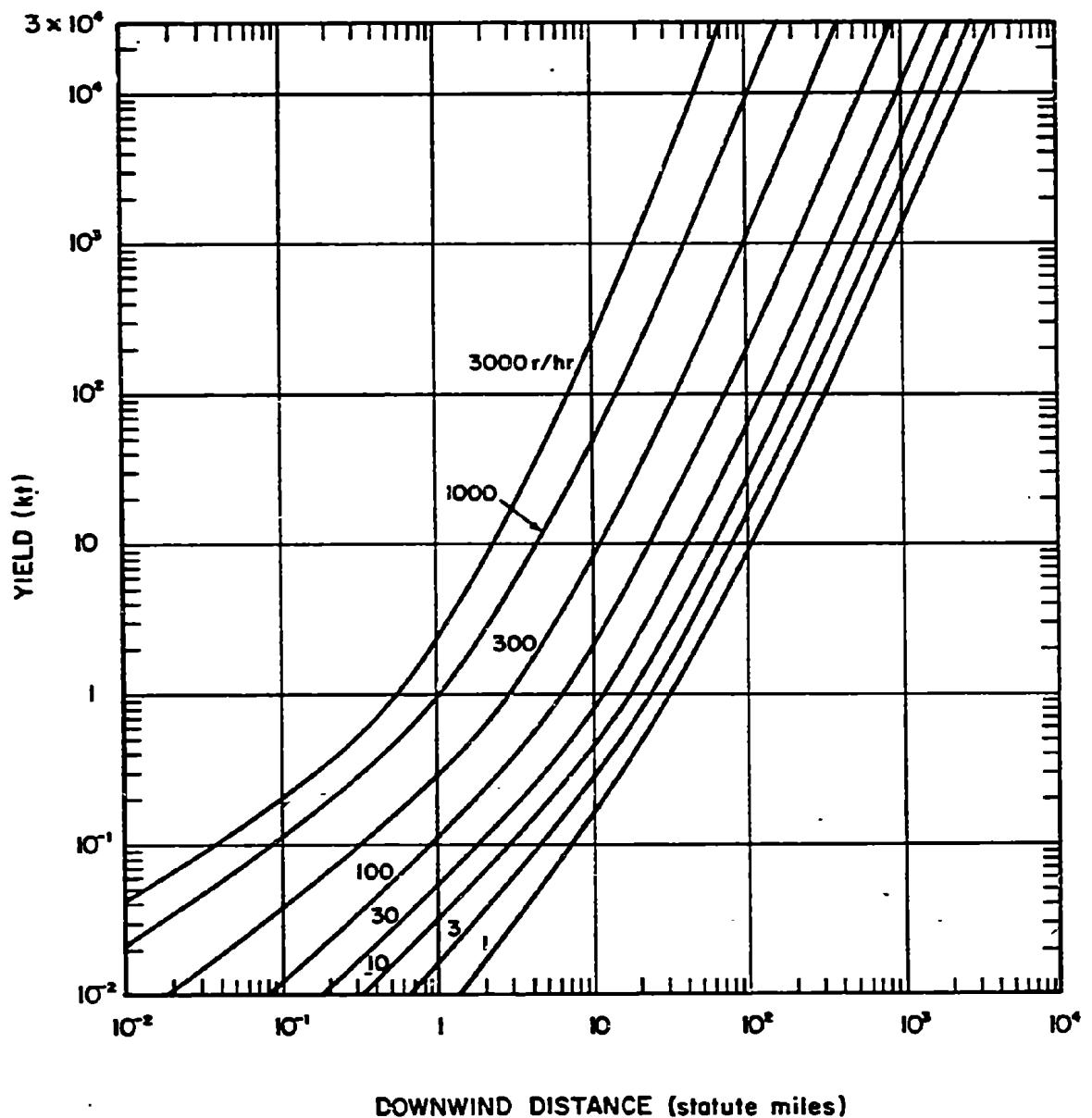


Figure 5-28. [REDACTED] Downwind Distance as a Function of Yield,  
10 Knot Effective Wind [REDACTED]

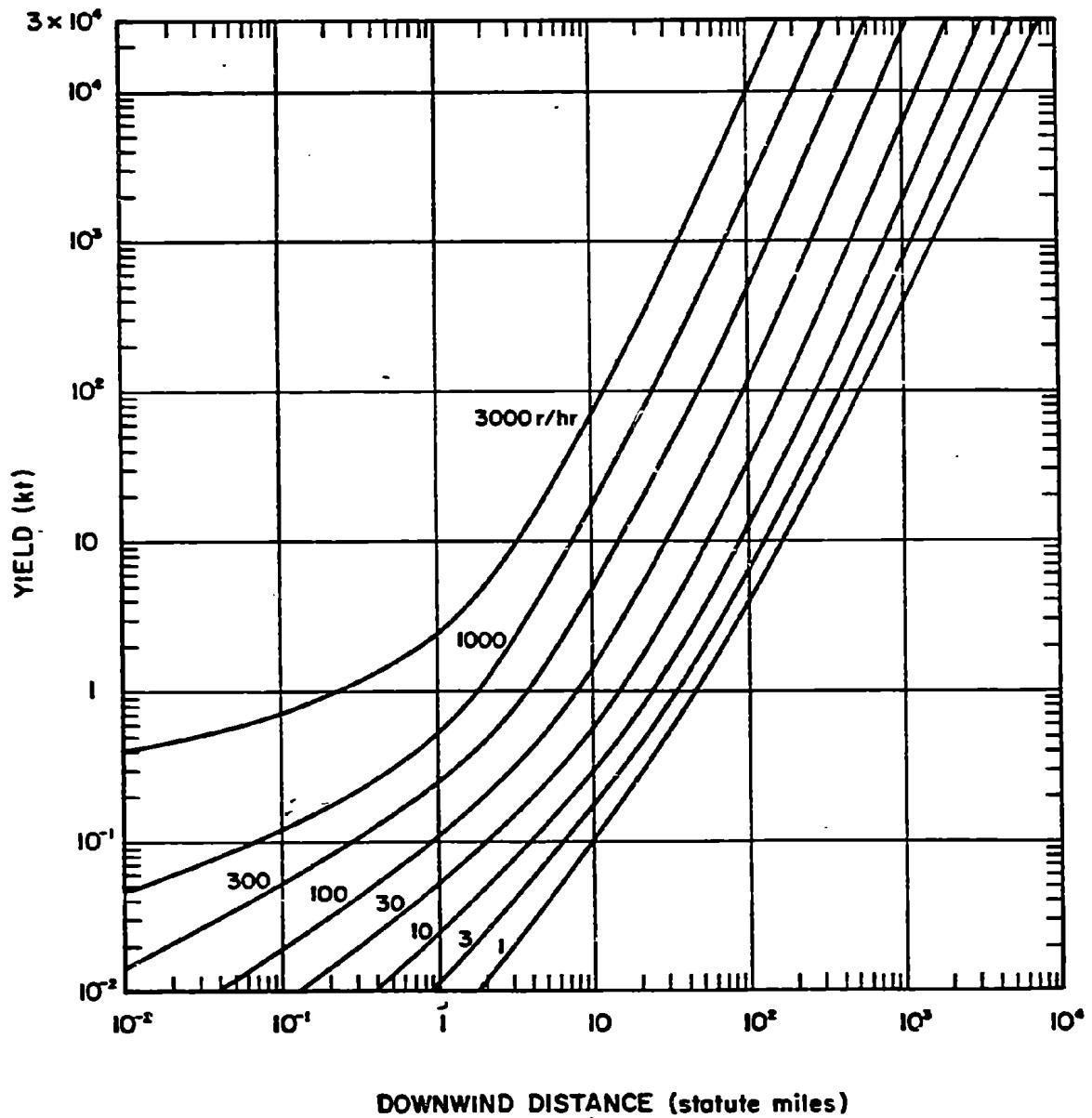


Figure 5-30. [REDACTED] Downwind Distance as a Function of Yield,  
40 Knot Effective Wind [REDACTED]

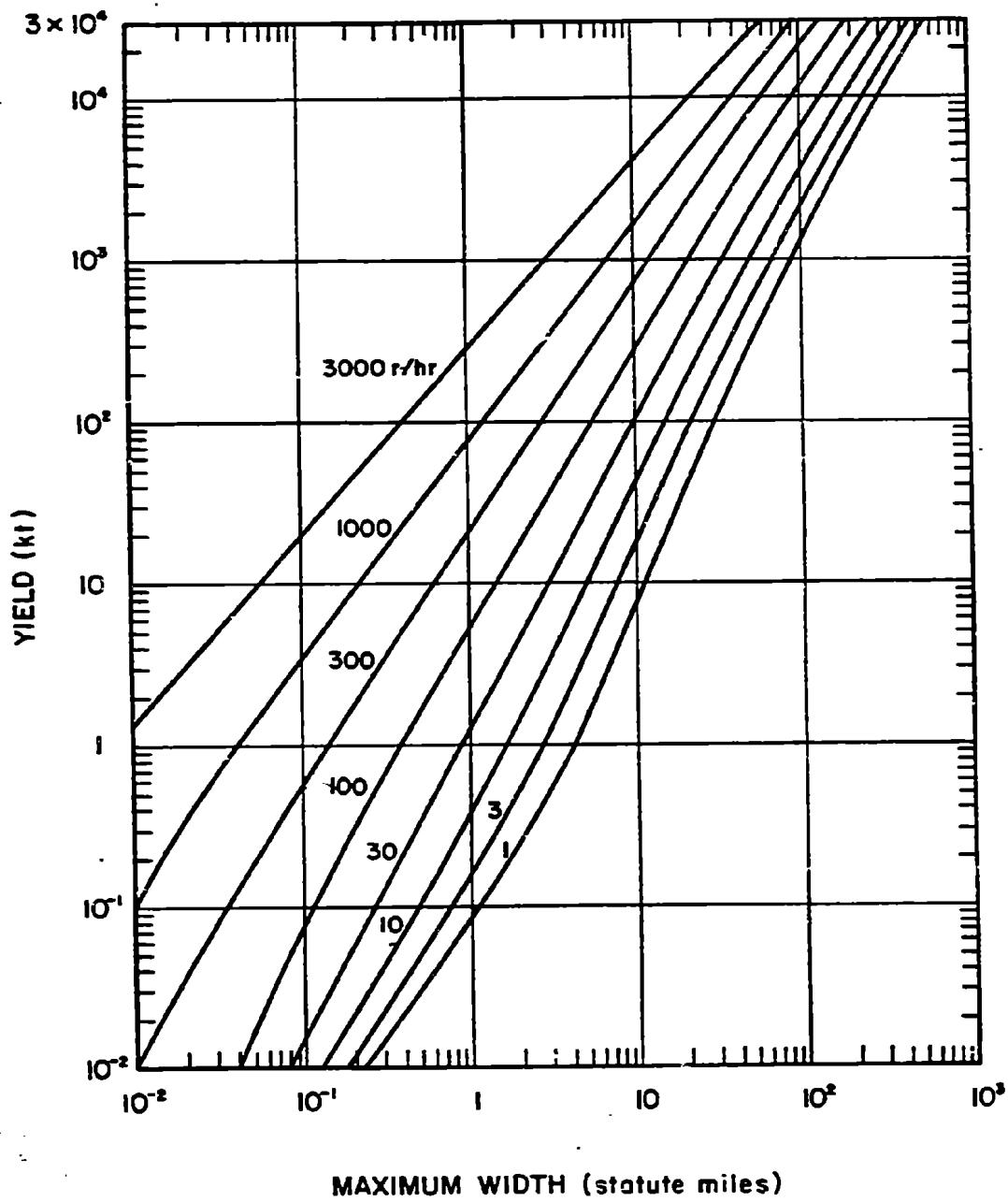


Figure 5-31. Maximum Width as a Function of Yield,  
10 Knot Effective Wind

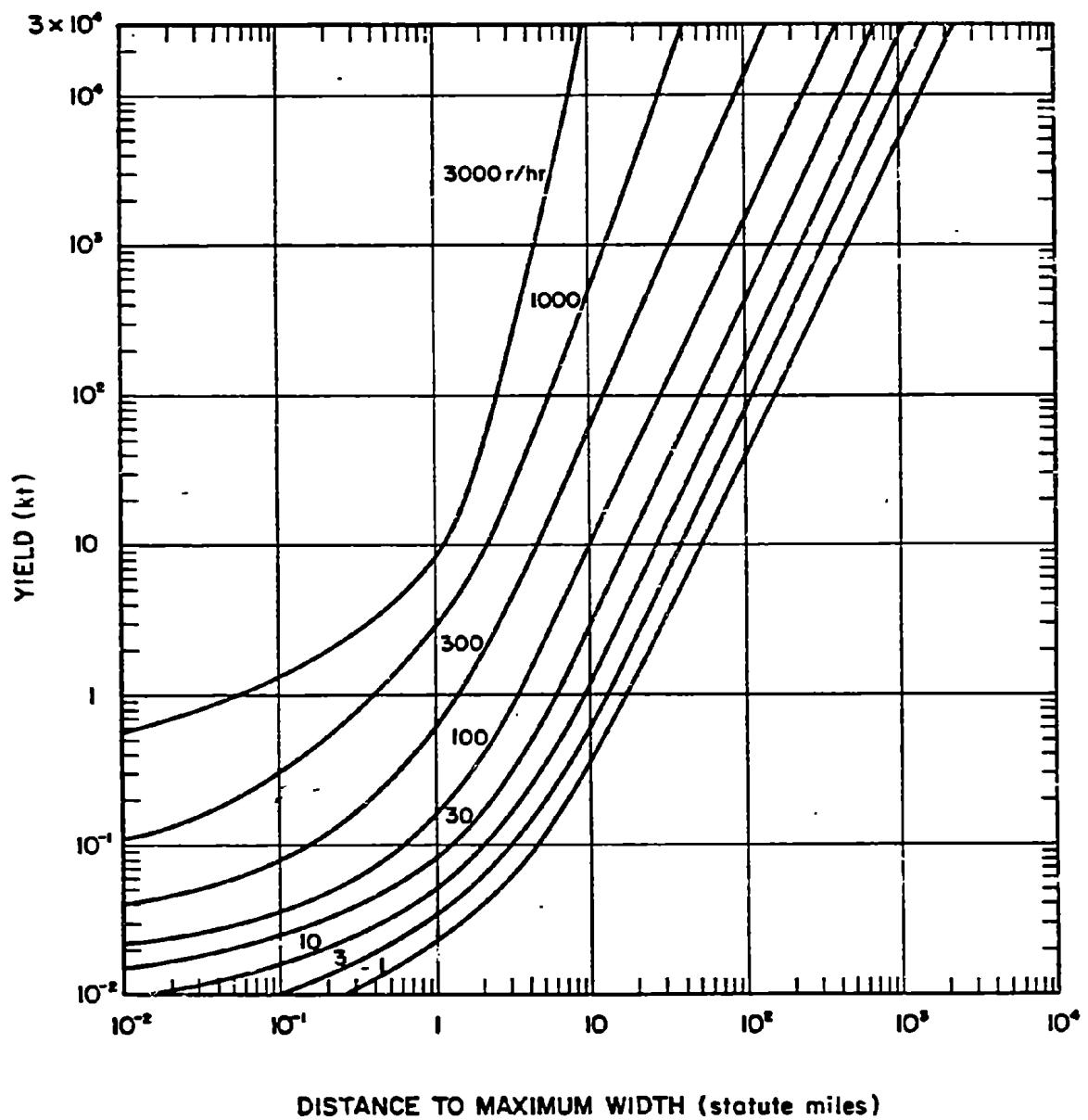


Figure 5-34. [REDACTED] Distance to Maximum Width as a Function of Yield,  
10 Knot Effective Wind [REDACTED]

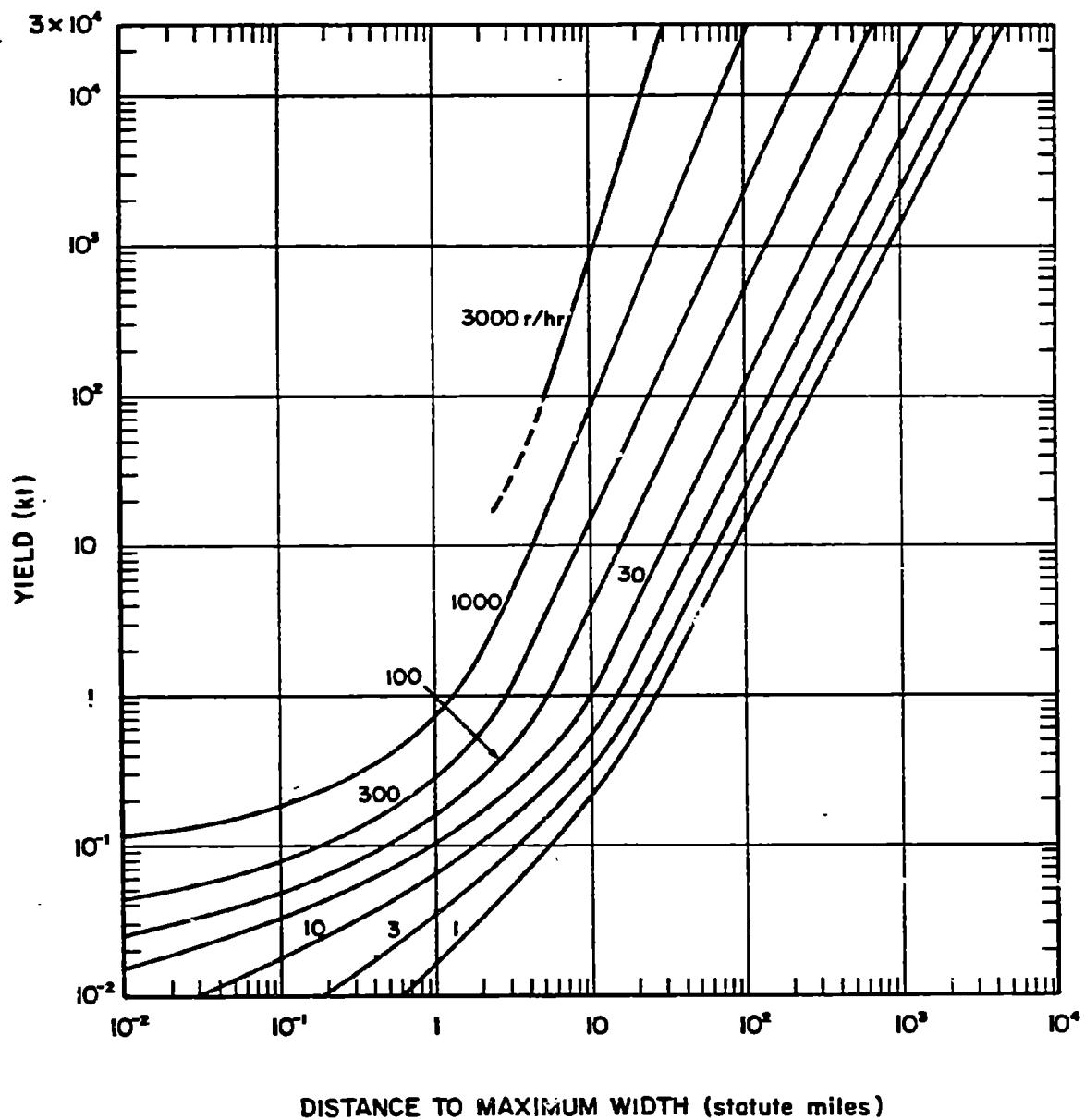
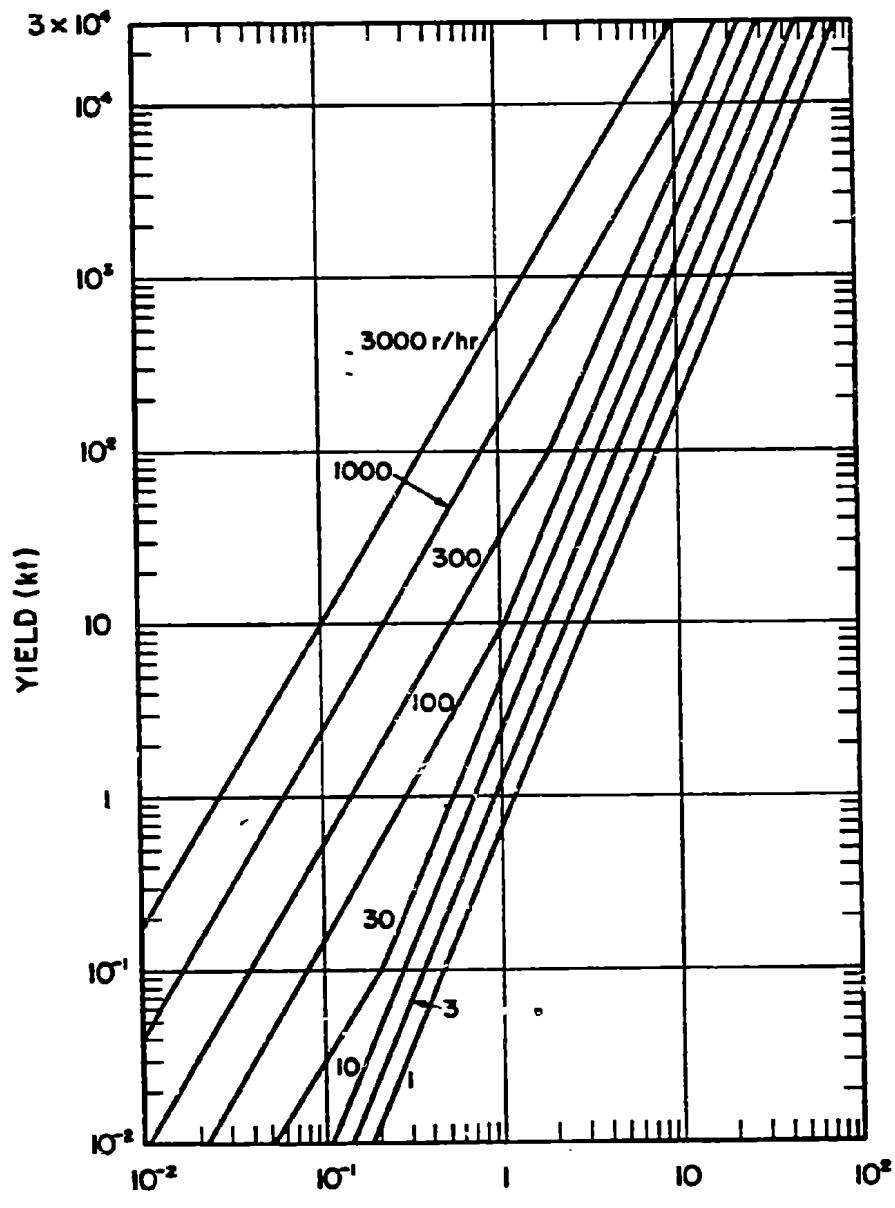


Figure 5-36. Distance to Maximum Width as a Function of Yield,  
40 Knot Effective Wind



GROUND ZERO WIDTH (statute miles)

Figure 5-37. Ground Zero Width as a Function of Yield

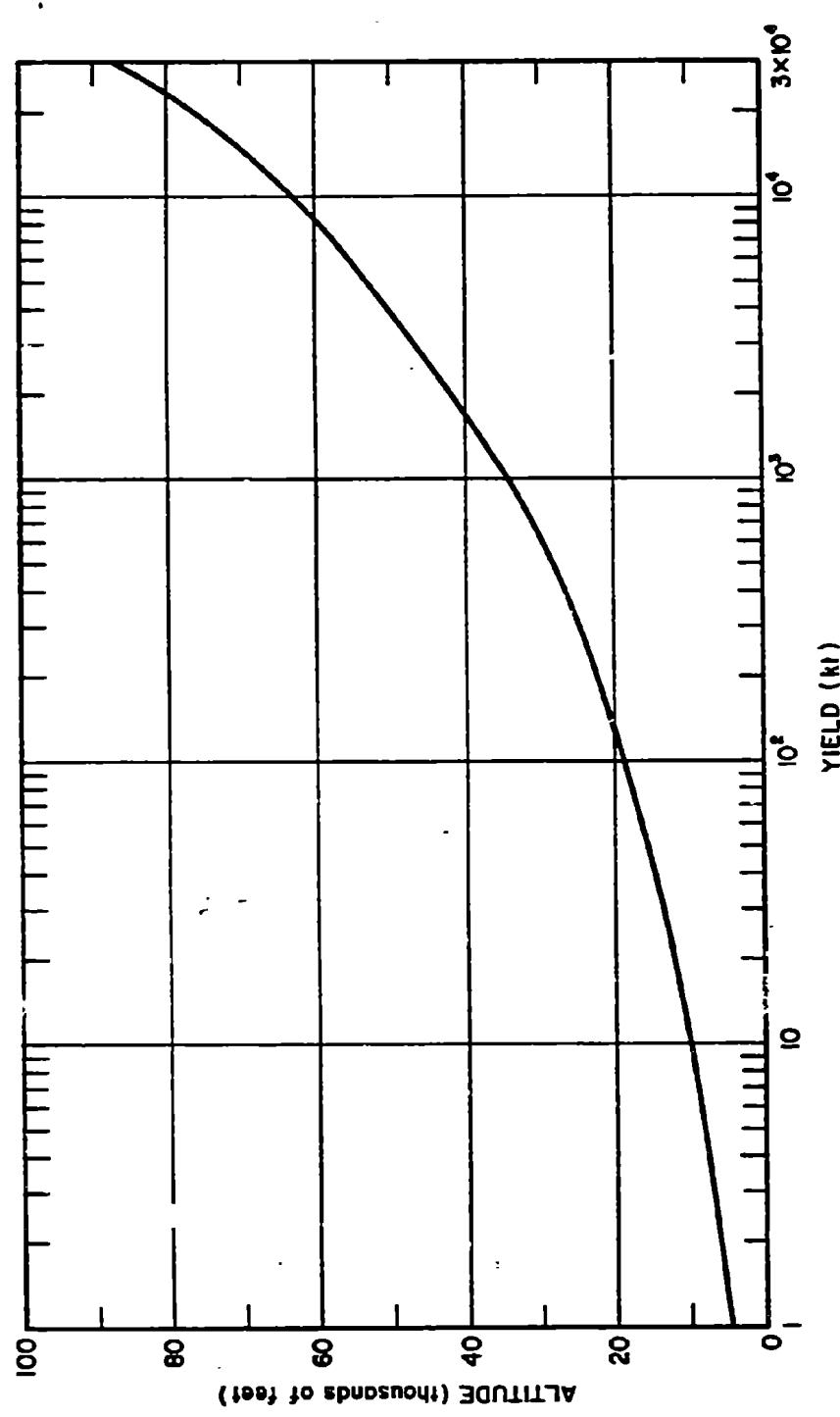


Figure 6-38. Height of the Stabilized Cloud Bottom  
as a Function of Yield

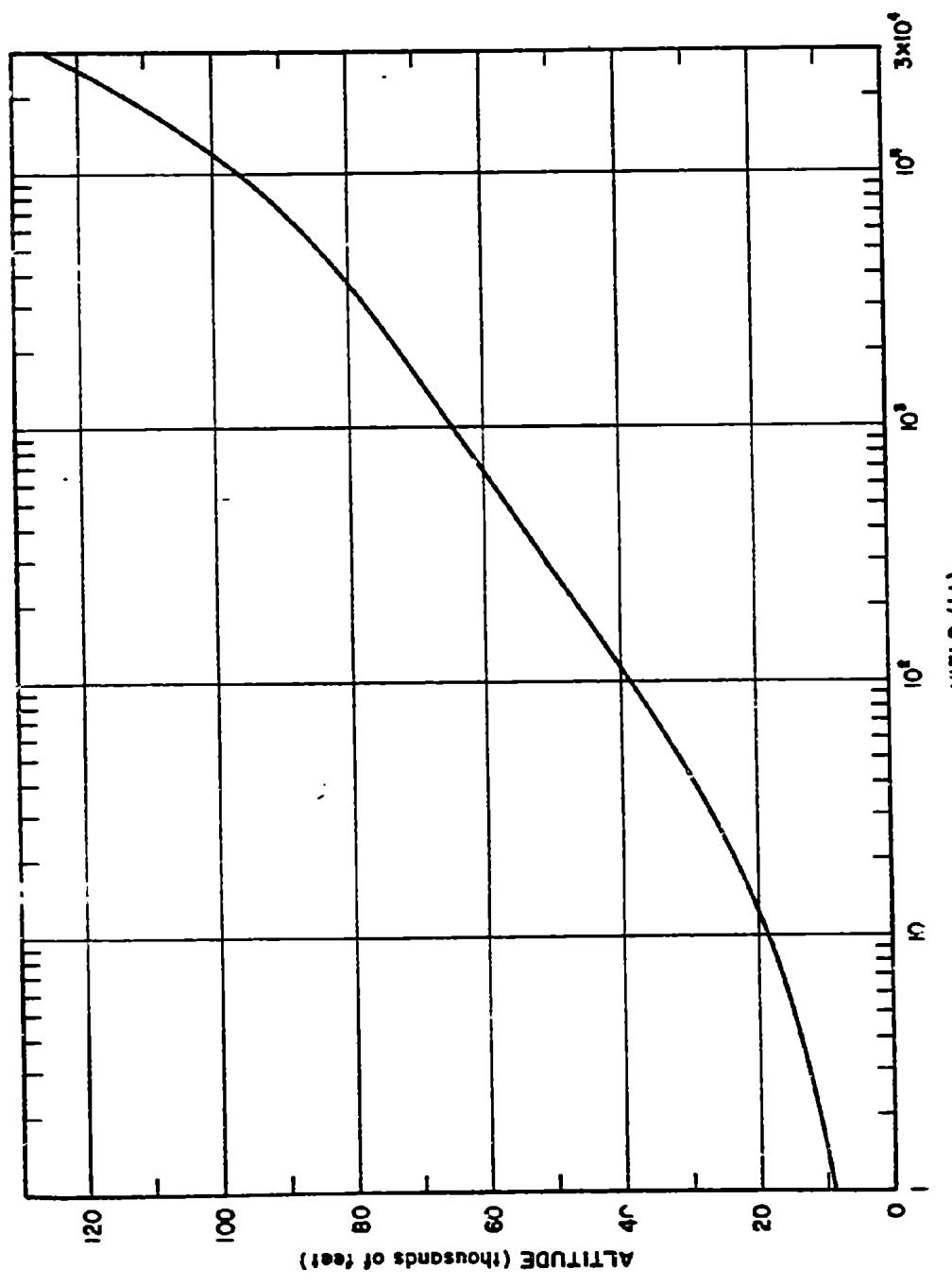


Figure 6-39. Height of the Stabilized Cloud Top  
as a Function of Yield

### Problem 5-9. Calculation of Fission Product Decay

Figure 5-40 provides fission product decay factors as a function of time after burst. The dose rate at any time can be obtained by multiplying the  $H + 1$  hour dose rate by the appropriate decay factor from Figure 5-40. The decay curve also may be used to determine the value of the  $H + 1$  hour dose rate from the dose rate measured at a later time. In this case the measured dose rate is divided by the appropriate decay factor.

#### Example 1

**Given:** The dose rate at a given point at 1 hour after a nuclear explosion is 500 rads/hr.

**Find:** The dose rate at that point 12 hours after the explosion.

**Solution:** From Figure 5-40, the decay factor at 12 hours is 0.05.

**Answer:** The dose rate at 12 hours is

$$500 \times 0.05 = 25 \text{ rads/hr.}$$

#### Example 2

**Given:** The dose rate at a given point 10 hours after detonation is 72 rads/hr.

**Find:** The dose rate at the same point 1 hour after the detonation.

**Solution:** From Figure 5-40, the decay factor at 10 hours is 0.06.

**Answer:** The dose rate at 1 hour is

$$\frac{72}{0.06} = 1,200 \text{ rads/hr.}$$

**Related Material.** See paragraph 5-21.

See also Figure 5-42.

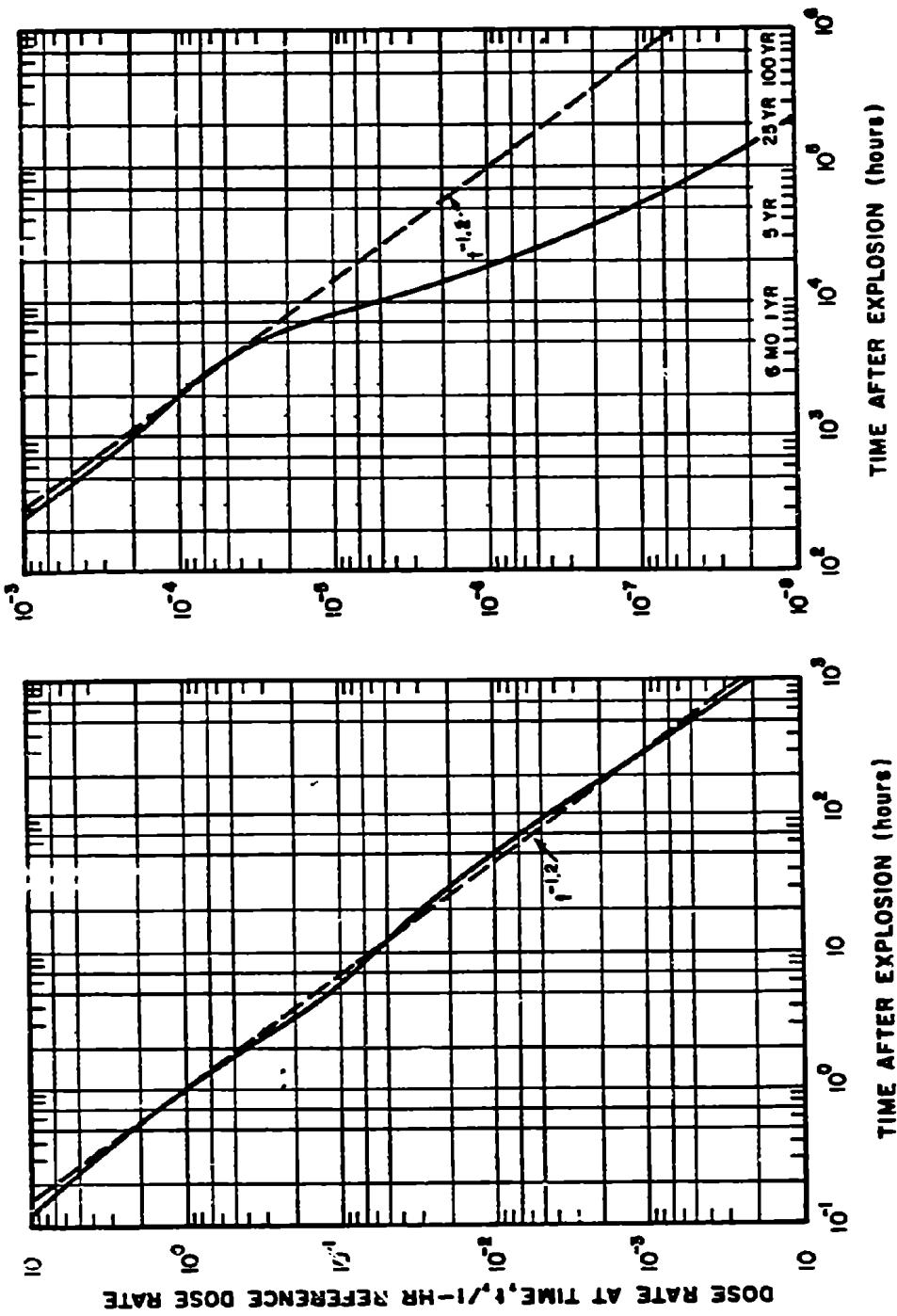


Figure 5-40. ■ Fission Product Decay Factors Normalized  
to Unity at 1 Hour After Detonation

### Problem 5-10. Calculation of Gamma Radiation Dose as a Function of Time

Figure 5-41 shows the integrated gamma dose received in a fallout-contaminated area as a function of time after  $H + 1$  hour ( $\sim 0.042$  day). This curve was generated by integrating the solid curve of Figure 5-40. If the true dose rate at some time between  $H + 1$  hour and  $H + 1,000$  days is known, Figure 5-41 can be used to estimate the dose accumulated during any time interval in this time range, provided the fallout decays as shown in Figure 5-40.

#### Example

**Given:** A dose rate of 20 rads/hr is measured in a fallout contaminated area 4 hours after the explosion (fallout had ceased to arrive at this time).

**Find:** The dose received by personnel who enter the area at  $H + 4.8$  hours and remain for 2.5 hours before leaving the area.

**Solution:**

$$H + 4.8 \text{ hr} = H + 0.2 \text{ day}$$

$$(H + 4.8 + 2.5) \text{ hr} = H + 7.3 \text{ hr}$$
$$= H + 0.304 \text{ day}$$

From Figure 5-41, the normalized dose that would be received between  $H + 1$  hour and  $H + 0.304$  day is 1.55. Similarly, the normalized dose received between  $H + 1$  hour and  $H + 0.2$

day is 1.3. Therefore, the normalized dose received by these personnel between  $H + 0.2$  and  $H + 0.304$  day would be:

$$1.55 - 1.3 = 0.25$$

To convert this to actual dose received, use is made of the  $H + 4$  hour dose rate (20 rads/hr). From Figure 5-40, the normalized dose rate at  $H + 4$  hour is found to be 0.18. The  $H + 1$  hour dose rate is

$$\frac{20}{0.18} = 111 \text{ rads/hr.}$$

**Answer:** The dose that the personnel can expect to receive is found by multiplying the  $H + 1$  hour dose rate by the normalized dose obtained from Figure 5-41:

$$111 \times 0.25 \approx 28 \text{ rads.}$$

**NOTE:** The dose calculated above is only the dose received during the stay at the particular spot in question. Additional dose would be accumulated during entry and exit. The amount of the additional dose would depend on the means of transportation and the size of the contaminated area.

**Related Material.** See paragraph 5-21. See also Figure 5-42.

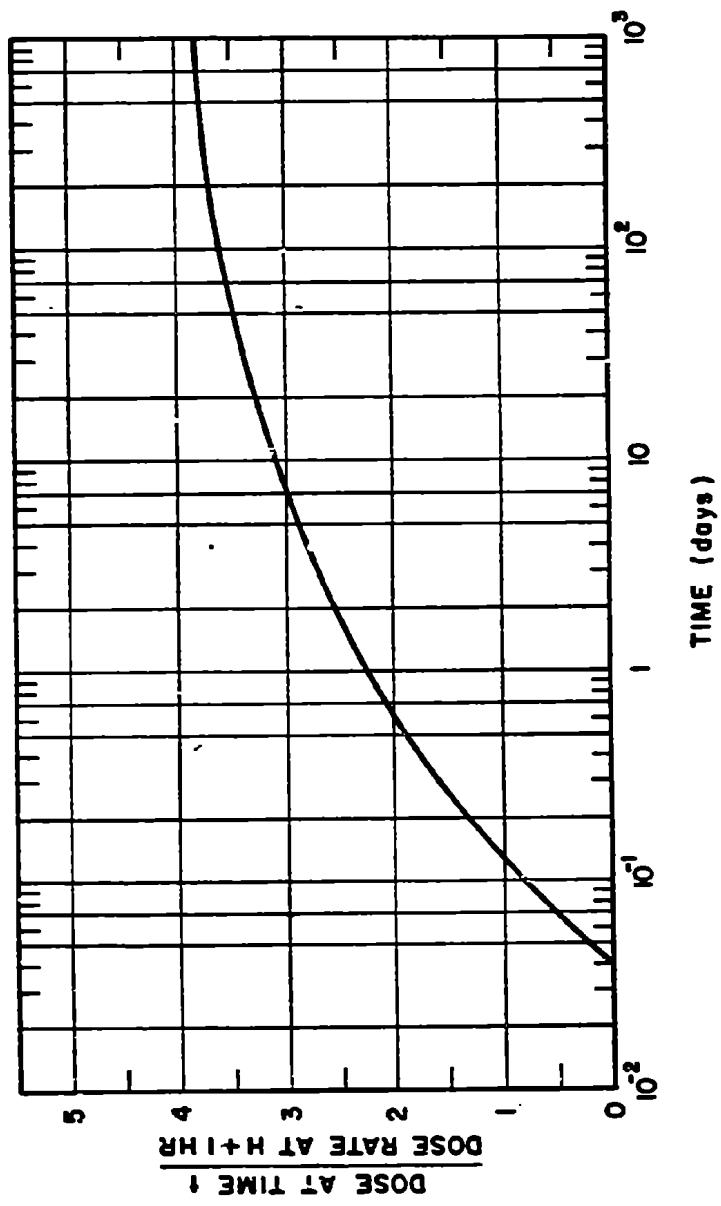


Figure 6-41. [REDACTED] Normalized Dose Accumulated in a Fallout Contaminated Area  
from  $H + 1$  Hour to  $H + 1,000$  Days [REDACTED]

**Problem 5-11. Calculation of Total Gamma Radiation Dose Received in a Contaminated Area**

Figure 5-42 gives the total dose received if a contaminated area is entered at a specified time and occupied for a specified interval of time. The vertical axis gives the accumulated dose for each unit (rads/hr) of dose rate at one hour after the detonation. The various curves represent time of stay in the contaminated area. To determine the accumulated dose, a factor is taken from the vertical axis corresponding to the time of entry and the time of stay. The product of this factor and the dose rate at one hour is the accumulated dose.

**Example**

Given: The dose rate in a given area at 1

hour after a nuclear explosion is 500 rads/hr.

*Find:* The total dose received by a man who enters the area 2 hours after the explosion and remains 4 hours.

*Solution:* From Figure 5-42, the intersection of the line for a time of entry of 2 hours after burst with the 4 hour curve gives a factor of 0.8.

*Answer:* The accumulated dose is:

$$500 \times 0.8 = 400 \text{ rads.}$$

**Related Material.** See paragraphs 5-21. See also Figures 5-40 and 5-41.

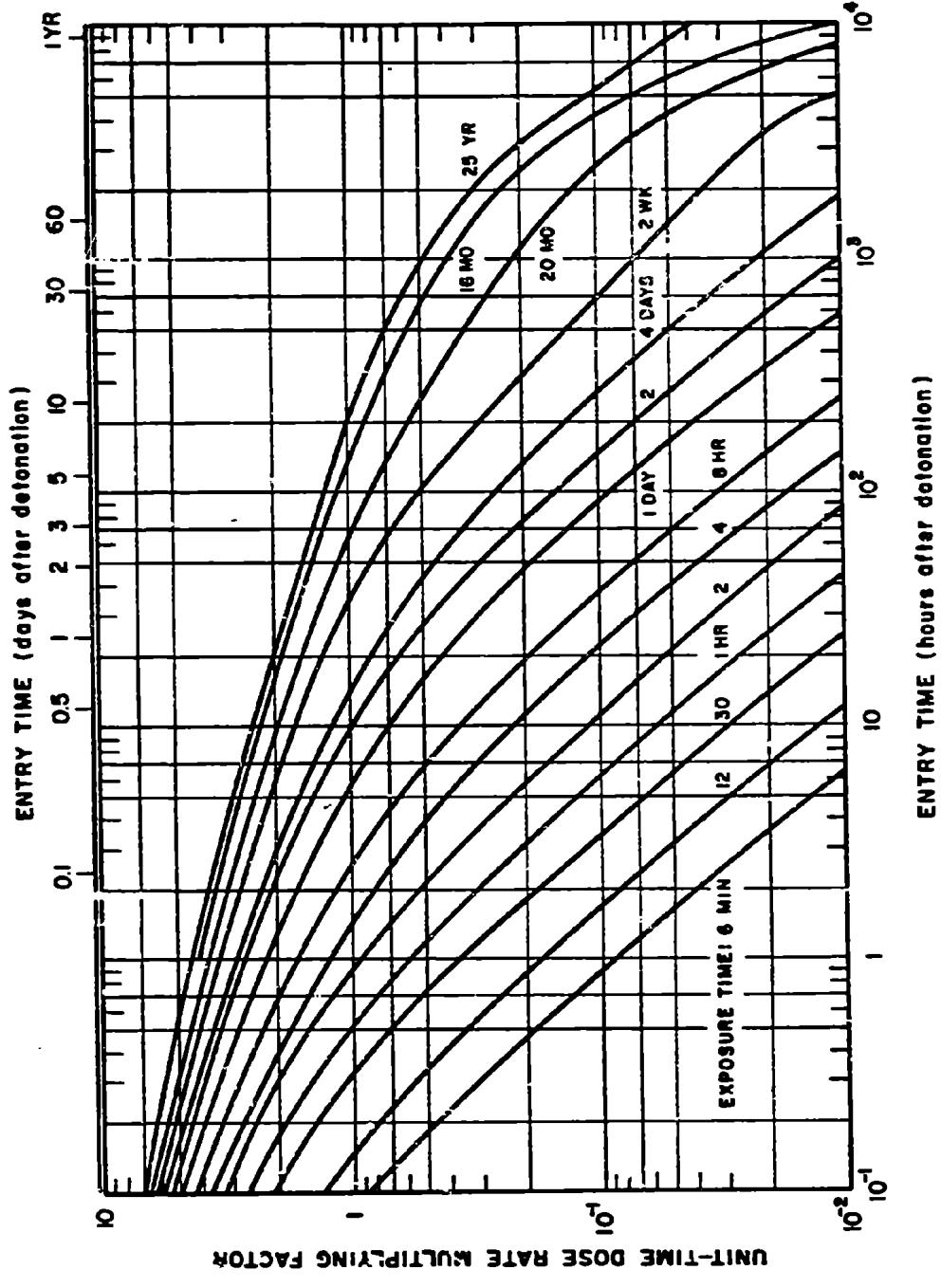


Figure 5-42. Total Radiation Dose from Early Fallout as a Function of Entry Time and Stay Time, Normalized to Unit Time Reference Dose Rate

**Problem 5-12. Calculation of Fallout Gamma Radiation Dose Rate  
Contours for Bursts in the Transition Zone**

Figure 5-43 may be used to determine whether or not a burst is in the transition zone, i.e., below a height of burst of  $100W^{0.35}$  feet. Burst heights below the curve in Figure 5-43 are in the transition zone. Burst heights above the curve are air bursts. In some situations, it may be desirable to consider bursts below  $180W^{0.4}$  feet to be in the transition zone for conservative estimates. The means for doing this are discussed below. When a burst occurs in the transition zone, an approximation of the resulting fallout contamination patterns may be obtained by multiplying the dose rate contour values for a contact surface burst weapon of the same yield by an adjustment factor from Figure 5-44. The curves of Figure 5-44 were constructed under the assumption that the ratio of the dose rate values from a burst in the transition zone to the dose rate values for the same contour from a surface burst are proportional to the ratio of the volume of a segment of a sphere intercepted by the ground surface to the volume of the hemisphere, where the radius of the sphere is  $100W^{0.35}$  feet, i.e.,

$$\text{Adjustment Factor} = \frac{\left(100 - \frac{h}{W^{0.35}}\right)^2 \left(200 + \frac{h}{W^{0.35}}\right)}{2 \times 10^6},$$

where  $h$  is the actual height of burst in feet, and  $W$  is the total weapon yield in kilotons.

In view of the lack of data from bursts in the transition zone over a land surface, a more conservative estimate may be desired. In this case, the height of burst for the upper limit of the transition zone is taken to be  $180W^{0.4}$  feet. The adjustment factor to be applied to dose rate values for the same contours from a surface burst of the same yield can be calculated from:

$$\text{Adjustment Factor} = \frac{\left(180 - \frac{h}{W^{0.4}}\right)^2 \left(360 + \frac{h}{W^{0.4}}\right)}{1.17 \times 10^7}$$

**Example**

*Given:* A hypothetical weapon with a total yield of 600 kt, of which 200 kt results from fission, is burst 560 feet over a land surface with 10 knot effective wind conditions.

*Find:* The contour parameters for a dose rate of 15 rads/hr at  $H + 1$  hour reference time over smooth terrain.

*Solution:* From Figure 5-43, a 600 kt weapon burst below about 940 feet would be in the transition zone. A height of burst of 560 feet is less than three quarters of the limiting altitude of the transition, so fallout is the only residual radiation to be considered. The 15 rads/hr contour for a fission yield to total yield ratio of  $200/600 = 1/3$  corresponds to the contour for  $15 \div 1/3 = 45$  rads/hr for a weapon of 600 kt fission yield. The dose rate over reasonably level terrain is about 70 percent of that over an ideal smooth plane. Thus, the ideal smooth plane contour parameters for this weapon burst on the surface would correspond to

$$\frac{45}{0.7} = 64 \text{ rads/hr.}$$

From Figure 5-44 (or from the normal adjustment factor equation given above) the height of burst adjustment factor for a 600 kt weapon burst at 560 feet is 0.21. Therefore, the desired contour parameters can be obtained by entering Figures 5-28, 5-31, 5-34, and 5-37 with a yield of 600 kt and reading the parameter values corresponding to an  $H + 1$  hour dose rate of

$$\frac{64}{0.21} = 300 \text{ rads/hr.}$$

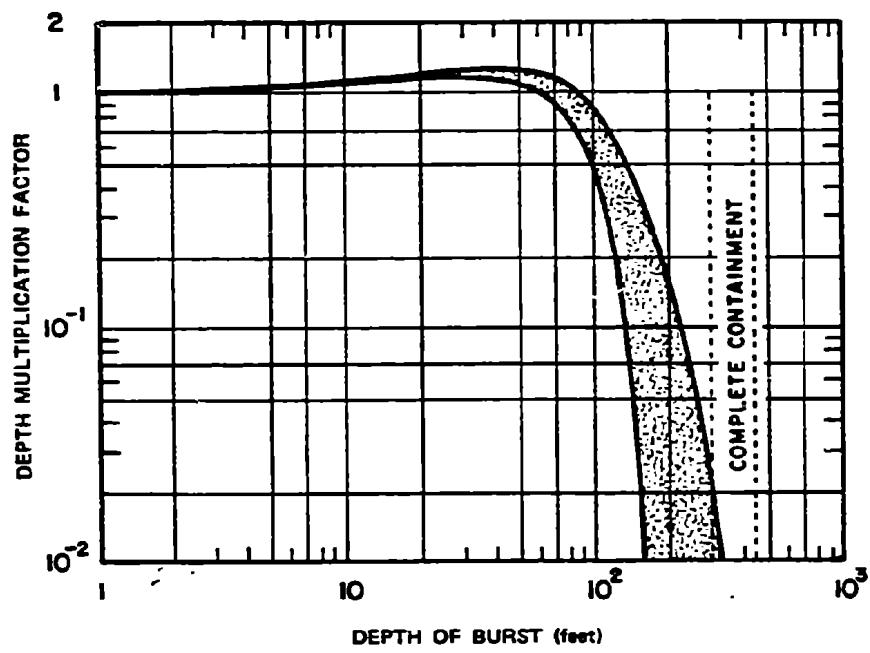


Figure 5-45. [REDACTED] Depth Multiplication Factor for Linear Dimensions of the Fallout Pattern from a 1 kt Explosion as a Function of Depth of Burst [REDACTED]

## RESIDUAL RADIATION FROM WATER SURFACE AND UNDERWATER BURSTS

The distinction between initial and residual radiation from underwater bursts is much less distinct than it is for air bursts or land surface or subsurface bursts. The radiation accompanying the base surge expands sufficiently rapidly as to become merged with what is normally considered initial radiation. In the case of water surface bursts, the distinction between initial and residual radiation is somewhat more clear cut, but in most cases the residual radiation will not be of great significance.

### 5-25 Water Surface Bursts

A base surge (paragraph 2-75, Chapter 2) is not expected to form as a result of a water surface burst, consequently a separation between initial and residual nuclear radiation can be made as in the case of a land surface explosion. An approximation of the initial nuclear radiation dose may be obtained from Figures 5-9 through 5-17 in Section I of this chapter. It must be emphasized, however, that the dose so obtained will be an approximation. The curves of Figures 5-9 through 5-17 are based on extensive computer calculations for a receiver on or near a *land* surface. These calculations included the effect of the ground-air interface, and a number of comparisons with measured data have substantiated the validity of the calculations. A limited number of comparisons of the same computer calculations have also indicated good agreement with initial gamma ray dose measurements made near a water surface after high yield explosions; however, these were not true water surface explosions, and no comparisons with neutron dose are available. Thus, in the absence of data and in the absence of comprehensive computer calculations, the curves of Figures 5-9 through 5-17 provide the best available data for

simplified calculations of initial nuclear radiation dose from water surface bursts.

For yields of more than a few kilotons, the cloud from a sea water surface burst is similar to that from a land surface or low air burst of the same yield. The cloud height and horizontal extent are determined primarily by the yield and by atmospheric conditions. For megaton yields, the maximum cloud height may be somewhat greater than that for a land surface burst, as a result of the release of latent heat from condensation of vaporized sea water. For very low yields, it is possible that the maximum cloud height may be less than for a land or low air burst, as a result of interference from the disturbed water. It is also possible, under certain atmospheric conditions, that the sea salt raised and dispersed in the atmosphere by low yield explosions may have a cloud-seeding effect. In this event, the water burst could produce a larger, higher cloud than a land burst, and the dispersion of salt would trigger a rainout of radioactivity.

The possible cloud seeding described above is only one example of the extreme sensitivity of fallout from water surface bursts to atmospheric conditions, especially relative humidity. This sensitivity results from the hygroscopic (water-absorbing) nature of the fallout particles. These particles consist mainly of sea salt and water. When dry, they are generally much smaller and lighter than fallout particles from land surface bursts. Because water burst particles are smaller than those from land bursts, water bursts produce less close-in fallout than land bursts. In particular, water bursts, unlike land bursts, generally will not produce a region of intense fallout (several thousand r/hr) near surface zero. The one possible exception is a water burst in an extremely humid atmosphere. Water surface bursts are even less likely to produce regular cigar-shaped fallout patterns than land surface bursts. The effect of atmo-

spheric humidity introduces further irregularities in fallout patterns. Also, because water surface burst particles take longer to fall than particles from land surface bursts, wind and weather conditions are more likely to change during the time of fallout transport and deposition. It is often difficult to define a downwind direction in the fallout pattern. The apparent downwind direction may vary with yield and with time after burst at which the pattern is observed or calculated.

In almost all cases, the region of maximum deposit intensity is not around surface zero but considerably downwind. Thus, for a 10 Mt burst, the calculated region of a normalized dose rate of at least 300 r/hr at 1 hour extends from about 125 to 300 miles from surface zero. The dose rate would, of course, be much lower at the time of arrival and would vary throughout the area as a result of varying arrival times.

As material in the cloud rises, it cools by entraining ambient air, and by expanding with increasing altitude. Fallout particles form by condensation of vapor and grow by coagulation; that is, by collision and adhesion of smaller particles to form larger particles. The vapor condensation may be considered a 3-stage process.

In the first stage, calcium and magnesium from the sea water and iron, and other metals from the weapon condense as oxides. In the second stage sodium chloride, which is about 90 percent of dried sea salt, condenses on the nuclei provided by the stage 1 particles. In the third stage, water vapor condenses to liquid water or to ice, on the stage 2 particles.

The median diameter of the stage 1 particles is about 1 micron contrasted to a few hundred microns for a land surface burst. The size is expected to increase slightly with yield, because the particles are formed by diffusion onto nuclei while the fireball is cooling by thermal radiation. The larger the fireball, the slower the cooling rate. The slower the cooling

rate, the more time is available for diffusive growth.

During and after the three condensation stages, coagulation causes particle growth. Particles of sub-micron size coagulate as a result of Brownian motion. Somewhat larger particles coagulate due to turbulent accelerations in the cloud. Turbulent coagulation only appears to be of importance in clouds from megaton bursts. Even larger particles grow by gravitational coagulation; that is, as they fall through the cloud they overtake and capture smaller particles. Gravitational coagulation is particularly important for low-yield bursts in humid atmospheres. The process is similar to one of the mechanisms for growth of ordinary raindrops. The largest particles formed, i.e., those from low yield bursts in a humid atmosphere, may have actual diameters of 2,000 microns. Particles of this size fall out of the cloud rapidly. Thus, there is a practical limit on the growth of particles in the cloud.

Moisture effects play a dominant part in water surface burst fallout. In general, the more humid the atmosphere, the more radioactivity is deposited as close-in fallout. Most of the moisture contained in the clouds of low yield bursts comes from entrained air. Consequently, the higher the humidity, the greater the cloud moisture content. In turn, the salt particles absorb more water, and, as they get larger, gravitational coagulation proceeds faster.

Moisture not only has a direct effect on particle formation, but also has an indirect effect on cloud height. The top of the cloud from a 20 kt water surface burst in a very humid tropical atmosphere may reach the tropopause at about 55,000 feet. In a less humid atmosphere, the cloud from a burst of the same yield may rise less than half as high (see Figure 5-39). Salt particles absorb moisture from humid air; the moisture evaporates when the particles are exposed to relatively dry air. Consequently the

[REDACTED]

size, falling rate, and time and place of deposit of water surface burst fallout particles vary with the atmospheric humidity the particles encounter during their trajectories. As the particles fall, they usually shrink by evaporation and may become completely dry, with a diameter of at most 100 to 200 microns. They then fall very slowly, and move large horizontal distances as a result of the forces exerted by the wind. Finally, the particles reach the more humid air near sea level, begin to grow by absorbing moisture, and fall faster. Thus, although particles from a megaton burst may leave the cloud with a water content almost entirely derived from sea water, this water may evaporate completely during fall, and the water content of the particles that reach the surface is entirely atmospheric moisture. An exception to this situation could occur for a burst in an arctic atmosphere. The cold air retards evaporation, even if humidity is low, and some of the original sea water could remain on the particles.

[REDACTED] Maximum fallout intensity, as well as the area covered by fallout from a water surface burst increases with weapon yield. For yields between 1 kt and 100 kt, the normalized  $H + 1$  hour exposure rates are expected to be negligible. The highest normalized intensities from a 100 kt explosion are expected to be more than 50 roentgens per hour (r/hr), but less than 100 r/hr. The highest intensities from a 1 Mt burst are expected to be over 100 r/hr but less than 300 r/hr. Finally, a 10 Mt burst is expected to produce intensities over 300 r/hr, but less than 1,000 r/hr. Since all of these exposure intensities are normalized to  $H + 1$  hour, and the fallout will arrive at significantly longer times after burst for the larger yields (depending upon the wind), the radioactivity will have decayed to much smaller levels prior to the time of arrival and fallout generally is not expected to be a governing effect from water surface bursts.

### 5-26 Underwater Bursts [REDACTED]

[REDACTED] An underwater burst creates a highly energetic bubble, whose history determines the major above-surface effects. For very shallow explosions, the bubble expands through the water surface with a high internal pressure, and develops a hollow column through which the bubble blows out into the atmosphere in the form of a cloud at the column top. For a somewhat greater depth, the bubble expands through the water surface at lower internal pressure and a column again forms, but no blowout occurs. Transition from columnar formations to plume-like eruptions, hemispherical in shape, takes place as the depth increases. The migration of the underwater bubble through the surface near its minimal phase at or shortly after its maximum-expansion phase creates the plumes. For deep explosions, the bubble may experience several oscillations as it migrates upwards. If the explosion is very deep, the bubble will degenerate and break up before reaching the surface. It is possible that an explosion may take place at such a great depth that little, if any, disturbance will be noted on the surface.

[REDACTED] The ejected water, whether a column or a plume, will fall back to the surface rapidly. This massive subsidence creates a radially expanding aerosol cloud, or base surge, at the water surface. The base surge expands as a ring or disk until it dissipates energy received from the subsidiary plumes or columns. After expanding, it drifts with the surface winds. Some evidence suggests the base surge has the same initial bulk density as that of the plumes or columns from which it is formed, being several times the density of air. As it travels downwind, it will react to the existing atmospheric conditions; e.g., evaporating or developing into low-cloud formations. These physical phenomena are described in more detail in Section IV, Chapter 2.

[REDACTED] Three sources of radioactivity are the

major contributors to the radiation above the surface subsequent to an underwater explosion: initial, above surface nuclear radiation; base surge; and residual radioactivity deposited in the mixed layer of the ocean. These sources are very time dependent, and they are affected by atmospheric and oceanic variables.

Even for a shallow underwater explosion the neutron and secondary gamma portions of the initial nuclear radiation are essentially negligible. The initial above-surface source includes the fission product activity contained in the visible column and crown, or plume. This source contains radioactivity ejected into the atmosphere as a result of underwater hydrodynamic phenomena. The scaled depth of burst is a major factor in determining the extent to which this initial radiation contributes to the total above surface exposure. The rapid development and spread of the base surge (paragraph 2-75, Chapter 2) causes the initial and residual radioactivity from an underwater burst to merge into one more or less continuous source.

The base surge develops as a result of both underwater flow phenomena and the collapse of the water masses associated with the initial source. This radially expanding surge grows to large dimensions as a dense, fog-like aerosol carrying with it a substantial fraction of suspended fission products. This source is either annular or disk-shaped in geometry and extends from the ocean surface to a height of several thousand feet. The base surge is influenced strongly by the wind, moving as an entity at the existing wind speed and direction. Initially it is highly radioactive; however, as it expands and dilutes, the concentration of the fission products decreases. This dispersion, coupled with rapid radioactivity decay, results in comparatively low exposure rates by the first half-hour after burst.

The residual radioactivity in the surface layer of the ocean is the third, and final, major source of radiation. This radioactive pool is

moved by the local currents, which depend on the existing oceanographic conditions. The pool is initially a disk which upon expansion approximates an annulus, although at times significantly later than a half-hour, it reverts to an irregular disk shape. Eventual mixing down to the top of the thermocline and the action of horizontal turbulent diffusion result in rapid dilution of the pool, reducing its hazard as time progresses.

The gamma radiation hazard created by the initial source, base surge, and pool resulting from an underwater nuclear explosion varies significantly with weapon yield and burst depth, proximity of the ocean bottom to the point of detonation, wind velocity and current velocity. Consequently, a description of the radiation fields (exposure rate and total exposure) associated with an underwater burst is complex, and no simplified prediction system suitable for general application has been developed.

A prediction system, DAEDALUS, has been developed to compute the radiological effects of underwater nuclear bursts. In this system, all above-surface sources, as well as the radioactive pool, are approximated by cylinders homogeneously contaminated with mixed fission products. The dimensions, water concentrations, and fission product contents of these cylindrical sources are estimated from empirical and theoretical considerations. Having defined the radioactive sources, DAEDALUS calculates, for each time of interest, exposure rates from these sources at specified detector locations. At each location the exposure rates are summed over time and the total exposure is thus cumulated. In the absence of a simple prediction system suitable for inclusion in this manual, examples of the results of DAEDALUS calculations are presented to provide an appreciation of the potential magnitude of the problems associated with radioactivity from underwater nuclear bursts.

Table 5-7. Examples Selected for Base Surge and Pool Exposure Rates

Yield (kt)	Explosion Depth (ft)	Depth of Water (ft)	Base Surge Figure Number	Pool Figure Number
10	65	5,000	S-46	S-52
10	65	65	S-47	S-53
10	150	5,000	S-48	S-54
10	500	5,000	S-49	S-55
10	1,000	5,000	S-50	S-56
10	1,500	5,000	S-51	S-57

A yield of 10 kt was selected to illustrate the effects of depth of burst and water depth on the time dependence of the gamma ray exposure rates from the base surge and the pool. Table 5-7 shows combinations of depth of burst and water depth that were selected. Table 5-7 also indicates the corresponding figures that show exposure rates as a function of time and radial distance from the source for the base surge and the pool respectively. A no-wind environment was chosen for these examples, and, in the case of the pools, a no-current environment was assumed.

Figures 5-58 through 5-75 show the accumulated exposures for two scaled depths ( $d_b \approx 30W^{1/3}$  and  $d_b \approx 280W^{1/4}$ ), corresponding to very shallow and deep explosions, respectively (Figure 2-105, Chapter 2). The doses are shown for 1, 10, and 100 kt explosions at each scaled depth. Two minute, 10 minute, and 30 minute exposures are shown for each yield at each scaled depth. In all cases it was assumed that the depth of the water was 5,000 feet, the effective wind was 15 knots, and a no-current condition existed. Table 5-8 identifies the figure for each combination of yield, burst depth, and exposure time.

Table 5-8. Examples Selected for Total Exposure

Yield (kt)	Explosion Depth (ft)	Exposure Time		
		2 Minutes	10 Minutes	30 Minutes
1	30	Fig. 5-58	Fig. 5-59	Fig. 5-60
10	65	Fig. 5-61	Fig. 5-62	Fig. 5-63
100	140	Fig. 5-64	Fig. 5-65	Fig. 5-66
1	280	Fig. 5-67	Fig. 5-68	Fig. 5-69
10	500	Fig. 5-70	Fig. 5-71	Fig. 5-72
100	890	Fig. 5-73	Fig. 5-74	Fig. 5-75

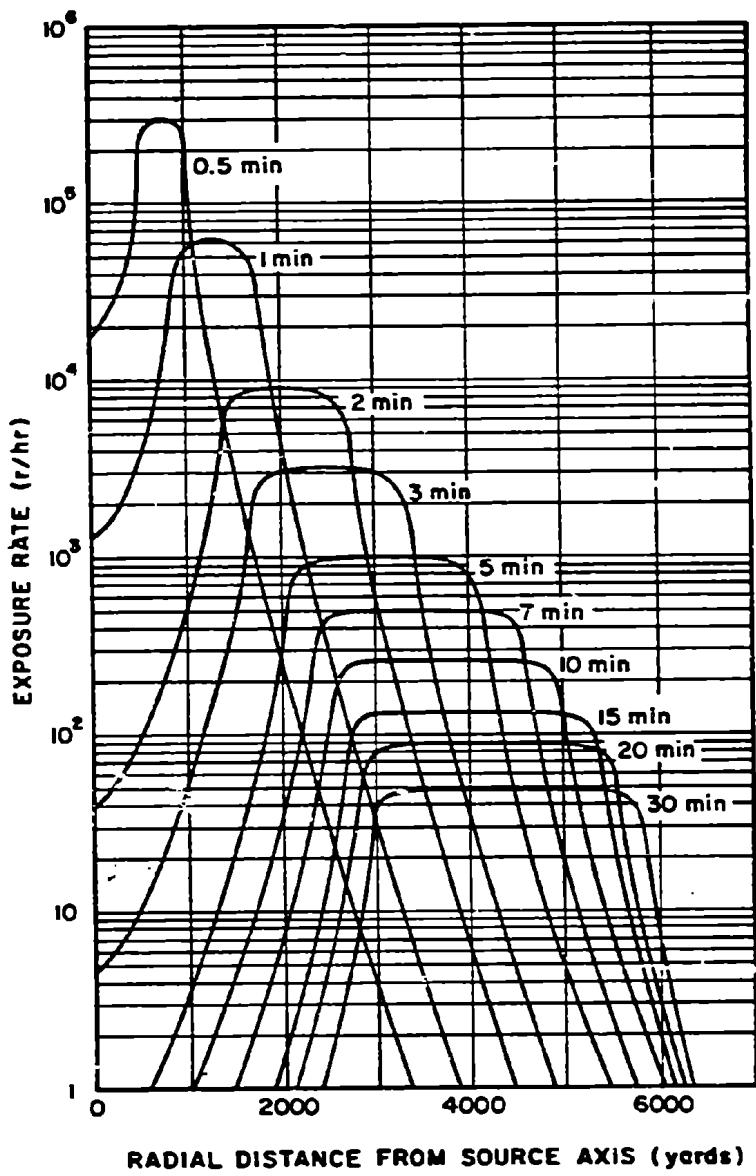


Figure 5-46. [REDACTED] Base Surge Radiation Exposure Rate 15 Feet Above the Water Surface from a 10 kt Explosion at a Depth of 65 Feet in 5,000 Feet of Water, No-Wind Environment [REDACTED]

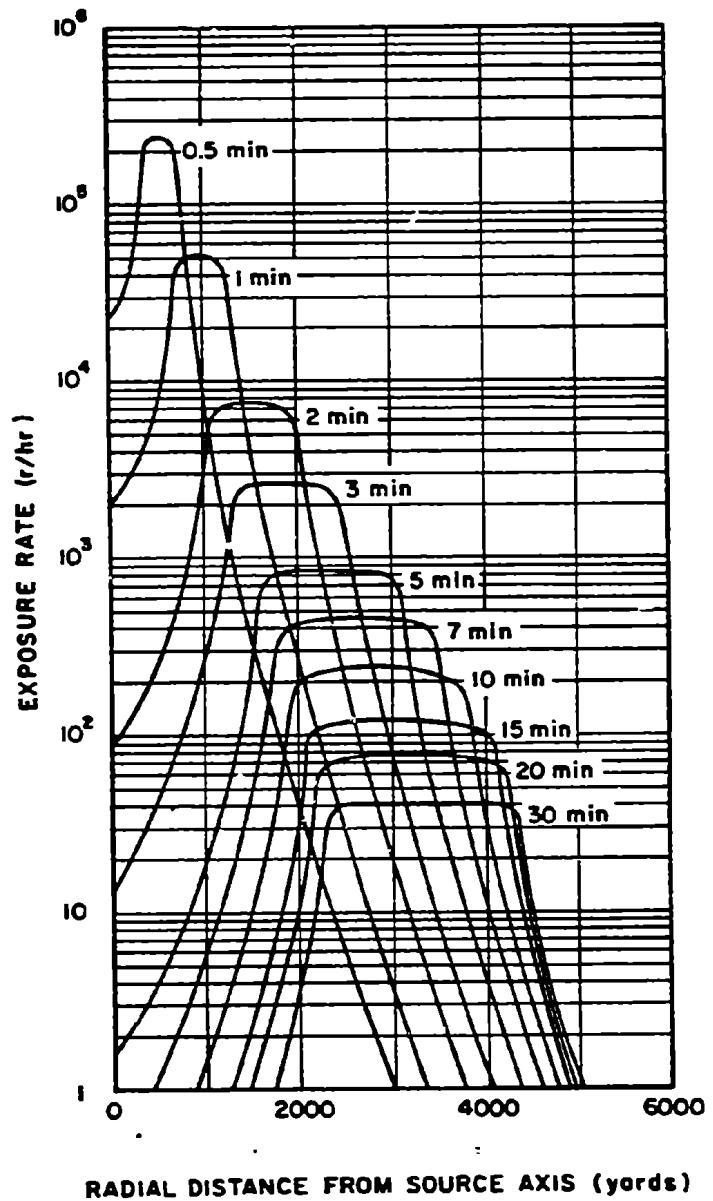


Figure 5-47. [REDACTED] Base Surge Radiation Exposure Rate 15 Feet Above the Water Surface from a 10 kt Explosion on the Bottom in 65 Feet of Water, No-Wind Environment [REDACTED]

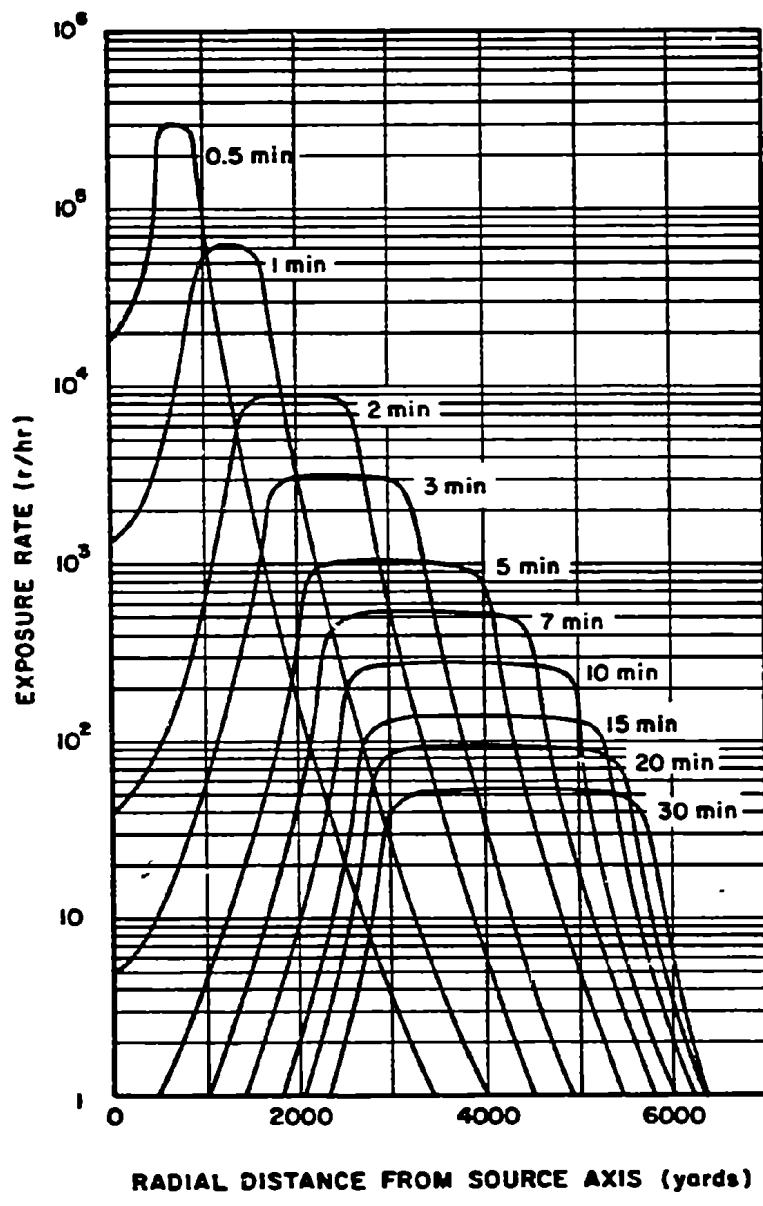


Figure 5-48. [REDACTED] Base Surge Radiation Exposure Rate 15 Feet Above the Water Surface from a 10 kt Explosion at a Depth of 150 Feet in 5,000 Feet of Water, No-Wind Environment [REDACTED]

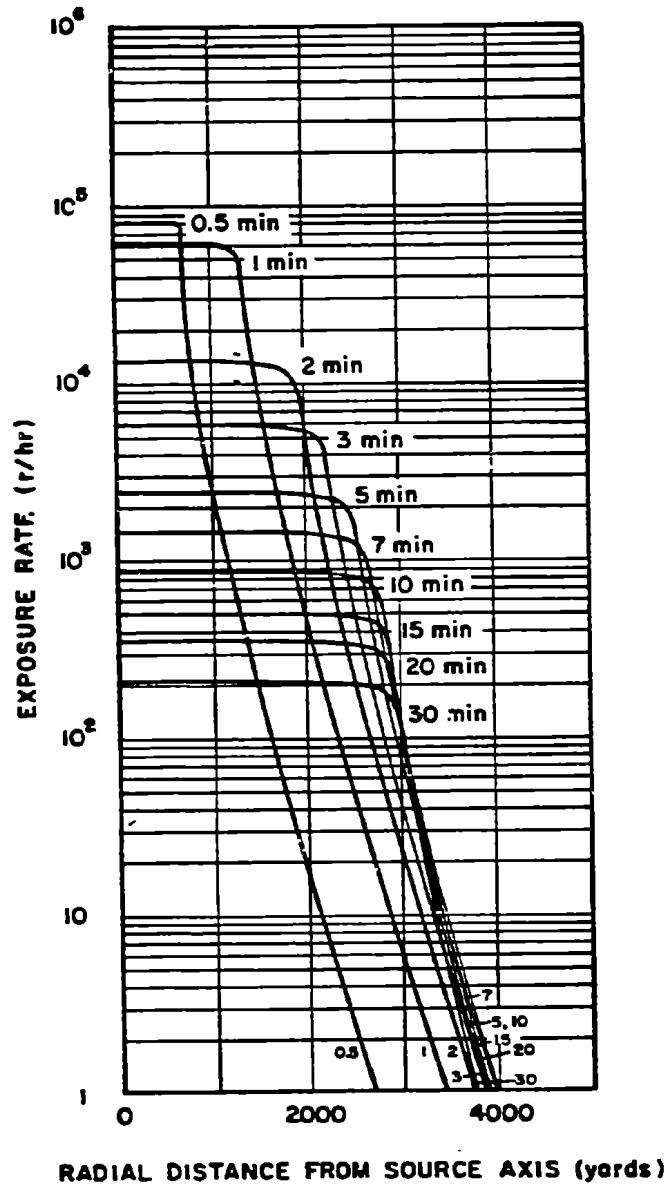


Figure 5-49. [REDACTED] Base Surge Radiation Exposure Rate 15 Feet Above the Water Surface from a 10 kt Explosion at a Depth of 500 Feet in 5,000 Feet of Water, No-Wind Environment [REDACTED]

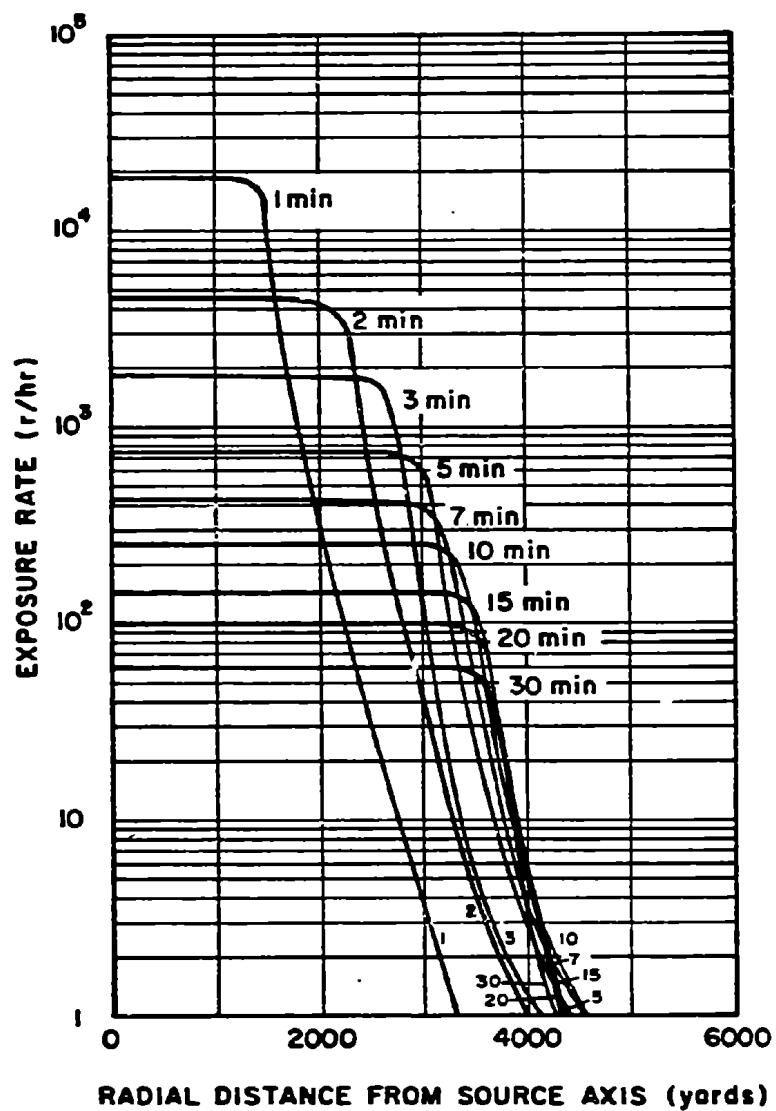


Figure 5-50. [REDACTED] Base Surge Radiation Exposure Rate 15 Feet Above the Water Surface from a 10 kt Explosion at a Depth of 1,000 Feet in 5,000 Feet of Water, No-Wind Environment [REDACTED]

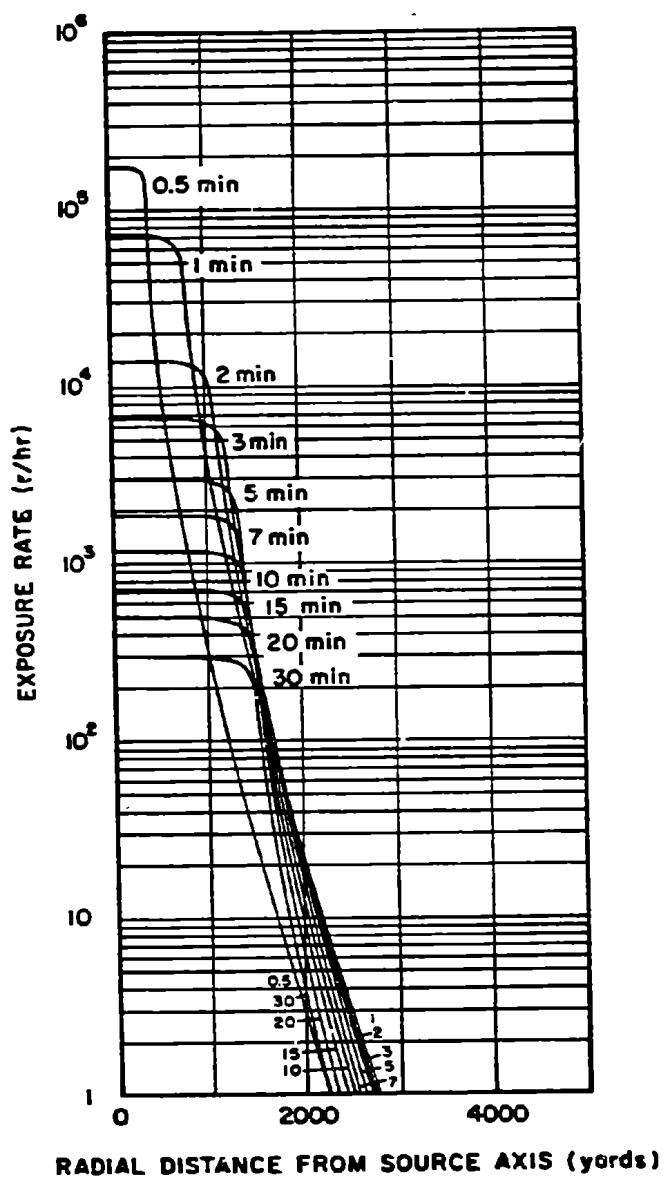


Figure 5-51. [REDACTED] Base Surge Radiation Exposure Rate 15 Feet Above the Water Surface from a 10 kt Explosion at a Depth of 1,500 Feet in 5,000 Feet of Water, No-Wind Environment [REDACTED]

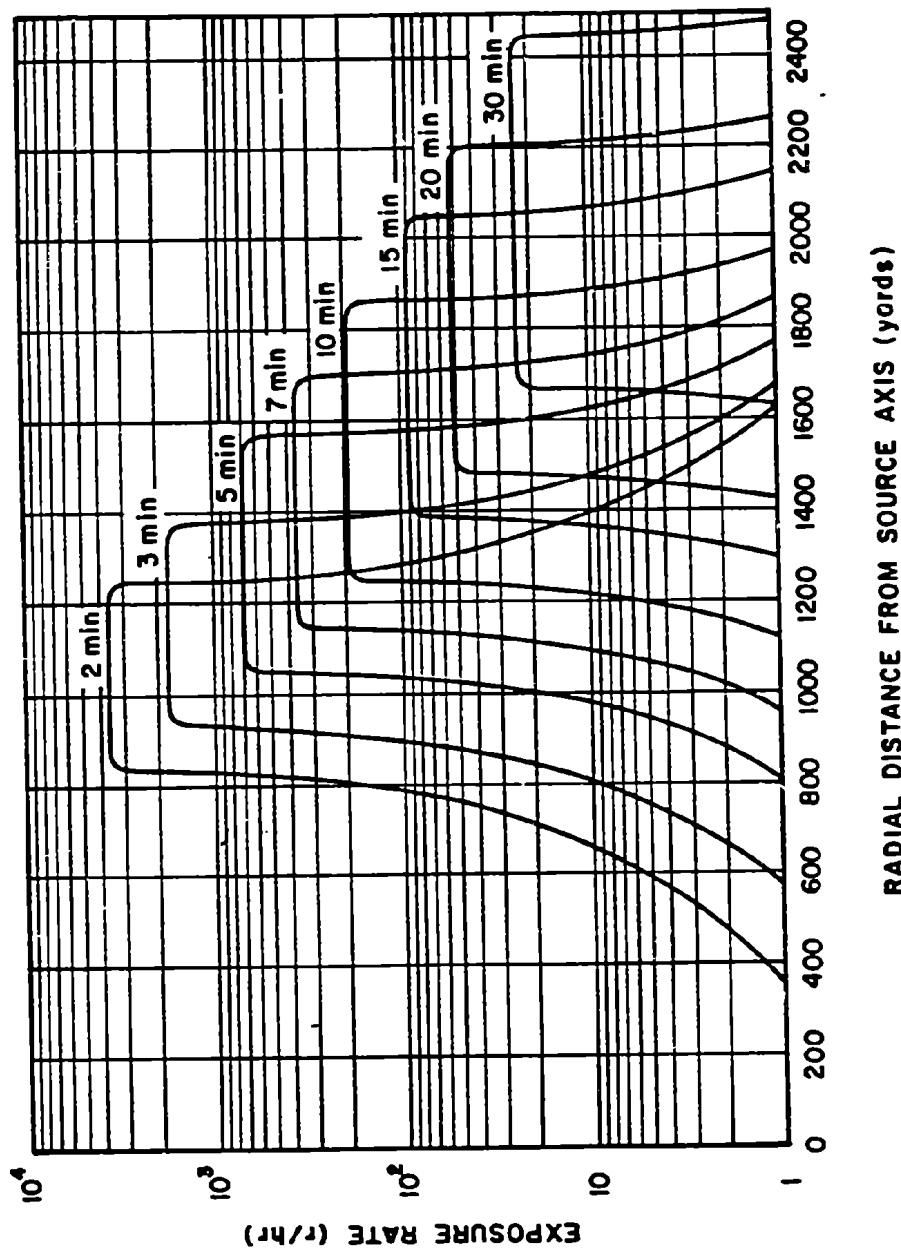


Figure 6-62. [REDACTED] Pool Radiation Exposure Rate 15 Feet Above the Water Surface from a 10 kt Explosion at a Depth of 65 Feet in 5,000 Feet of Water, No-Current Environment [REDACTED]

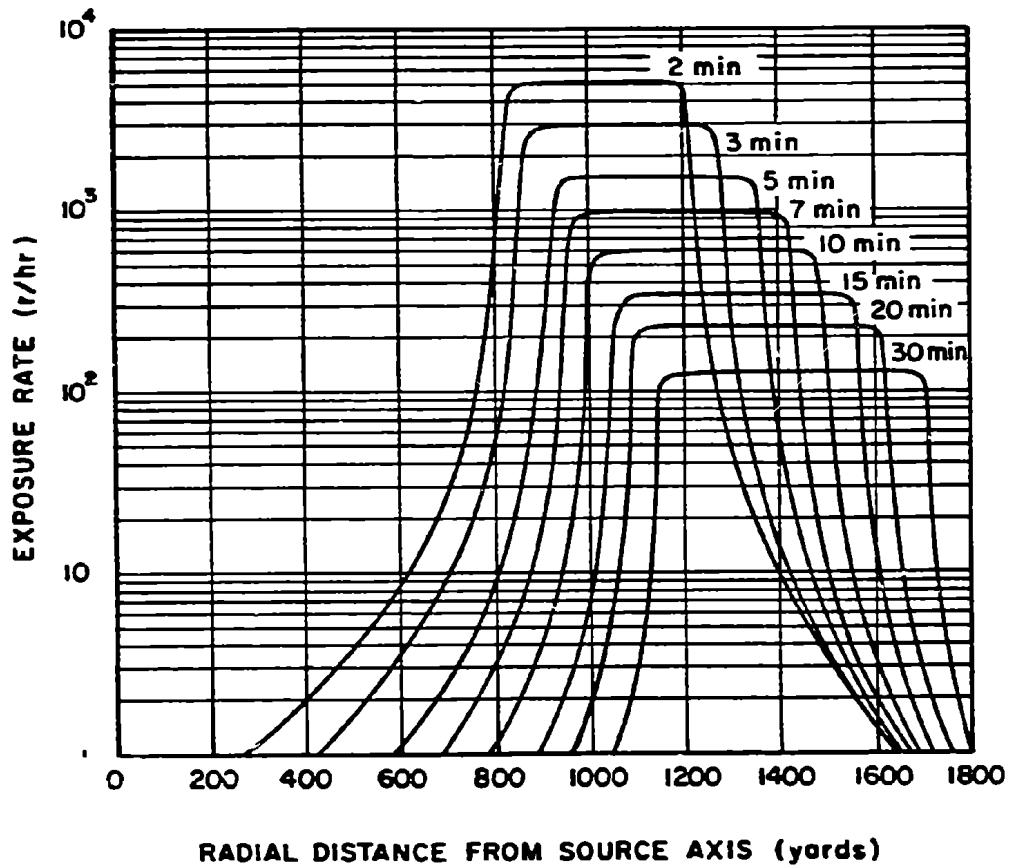


Figure 5-53. [REDACTED] Pool Radiation Exposure Rate: 15 Feet  
Above the Water Surface from a 10 kt Explosion  
on the Bottom in 65 Feet of Water,  
No-Current Environment [REDACTED]

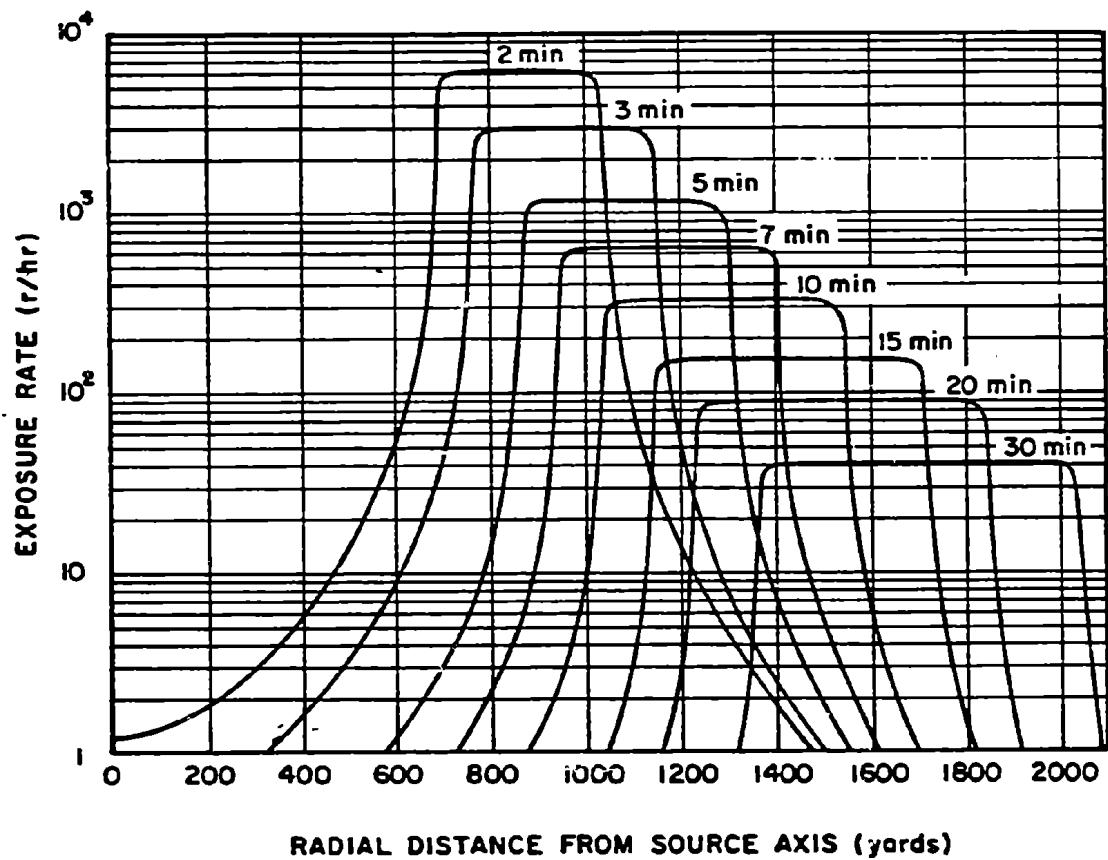


Figure 5-54. [REDACTED] Pool Radiation Exposure Rate 15 Feet Above the Water Surface from a 10 kt Explosion at a Depth of 150 Feet in 5,000 Feet of Water, No-Current Environment [REDACTED]

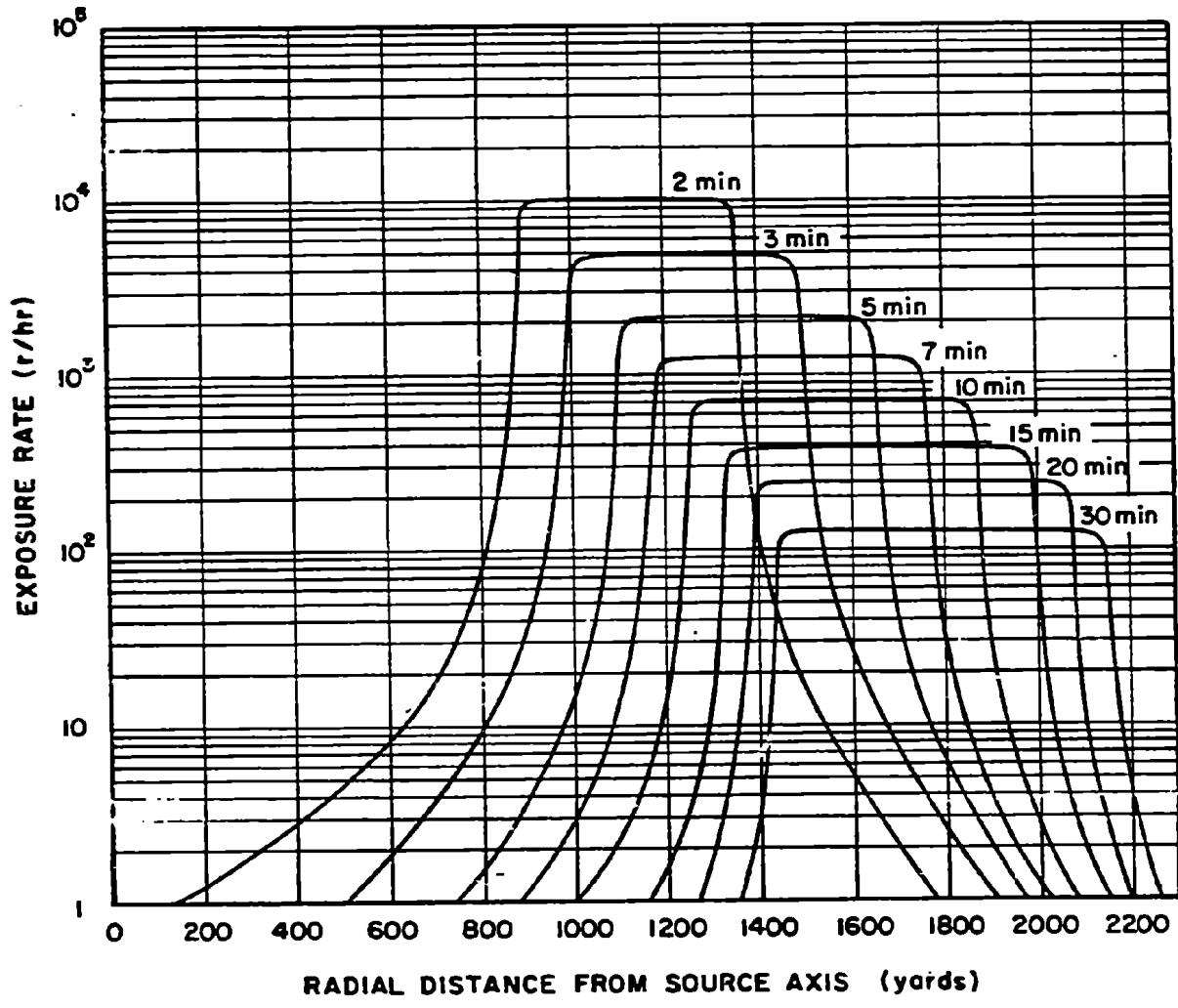


Figure 5-55. [REDACTED] Pool Radiation Exposure Rate 15 Feet Above the Water Surface from a 10 kt Explosion at a Depth of 500 Feet in 5,000 Feet of Water, No-Current Environment [REDACTED]

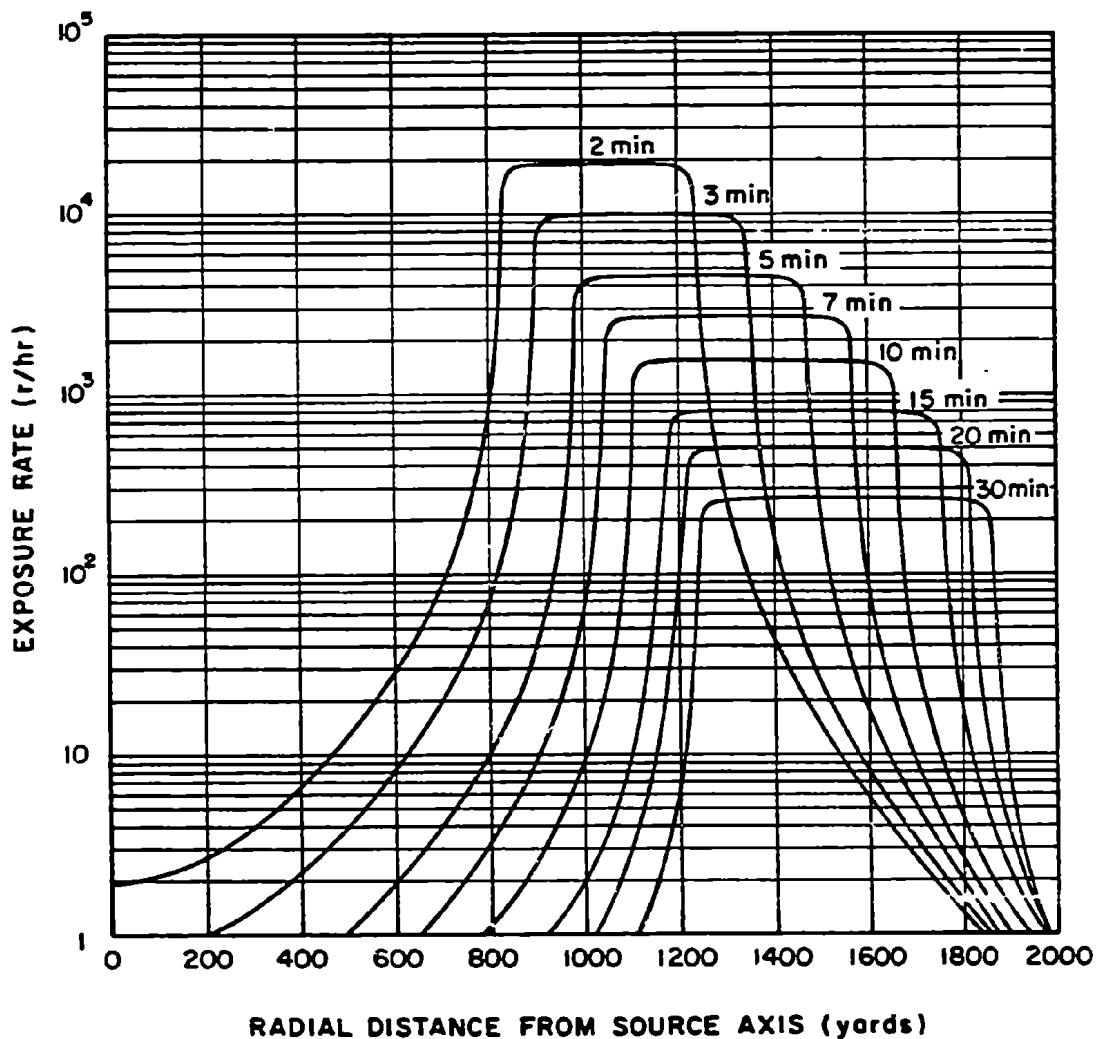


Figure 5-56. [REDACTED] Pool Radiation Exposure Rate 15 Feet Above the Water Surface from a 10 kt Explosion at a Depth of 1,000 Feet in 5,000 Feet of Water, No-Current Environment [REDACTED]

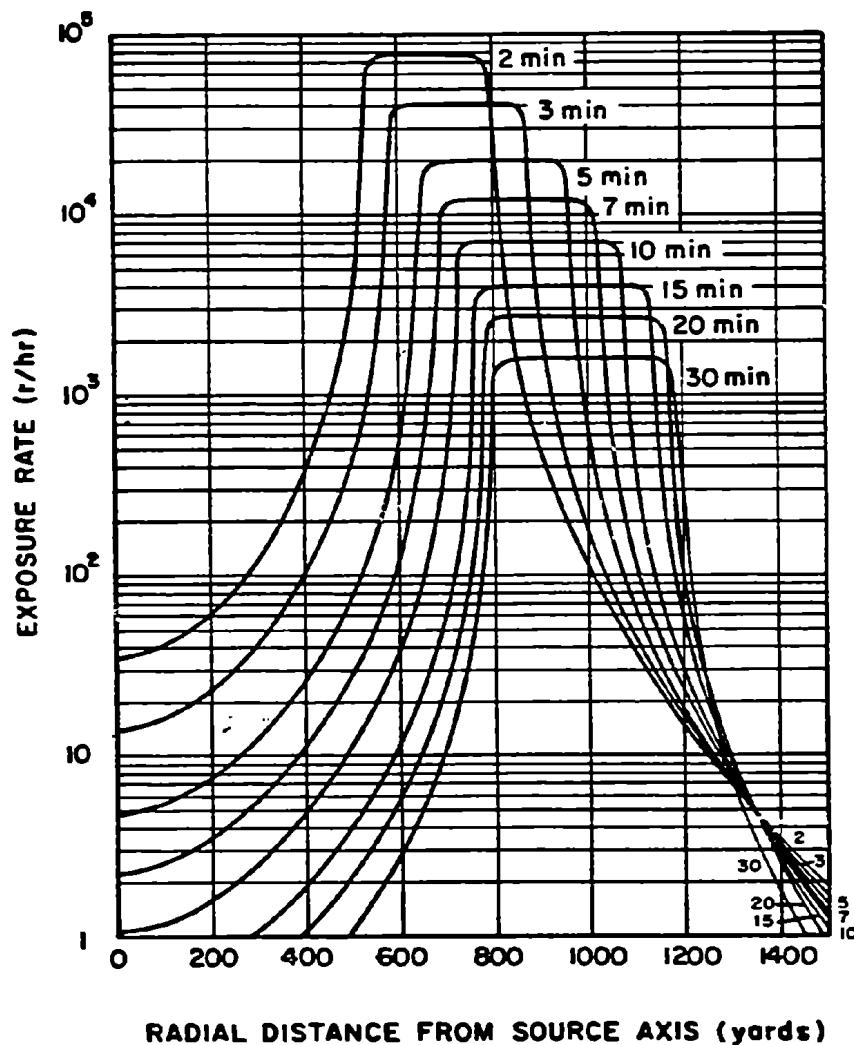
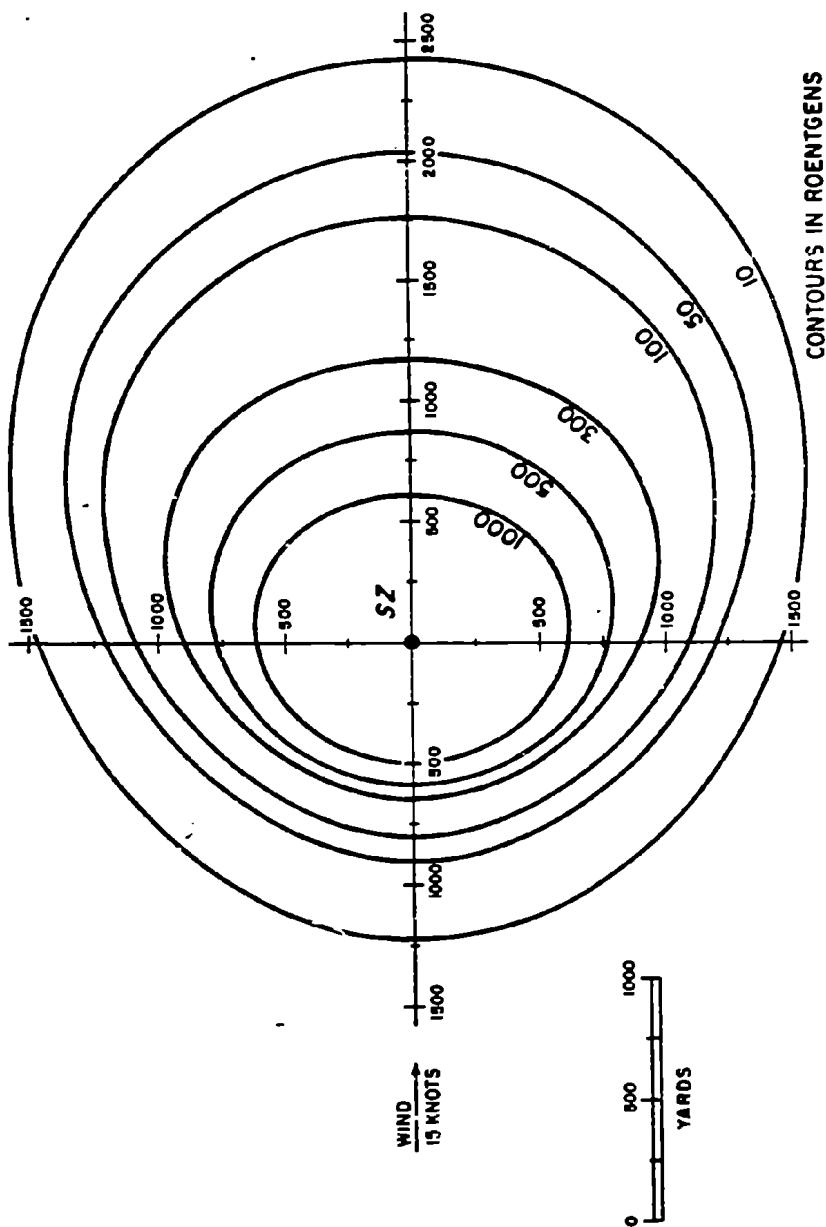


Figure 5-57. [REDACTED] Pool Radiation Exposure Rate 15 Feet  
Above the Water Surface from a 10 kt Explosion  
at a Depth of 1,500 Feet in 5,000 Feet  
of Water, No-Current Environment [REDACTED]



**Figure 6-58.** Two-Minute Total Exposure 15 Feet Above the Water Surface from a 1 kt Explosion at a Depth of 30 Feet In 5,000 Feet of Water, 15 Knot Wind, No-Current Environment

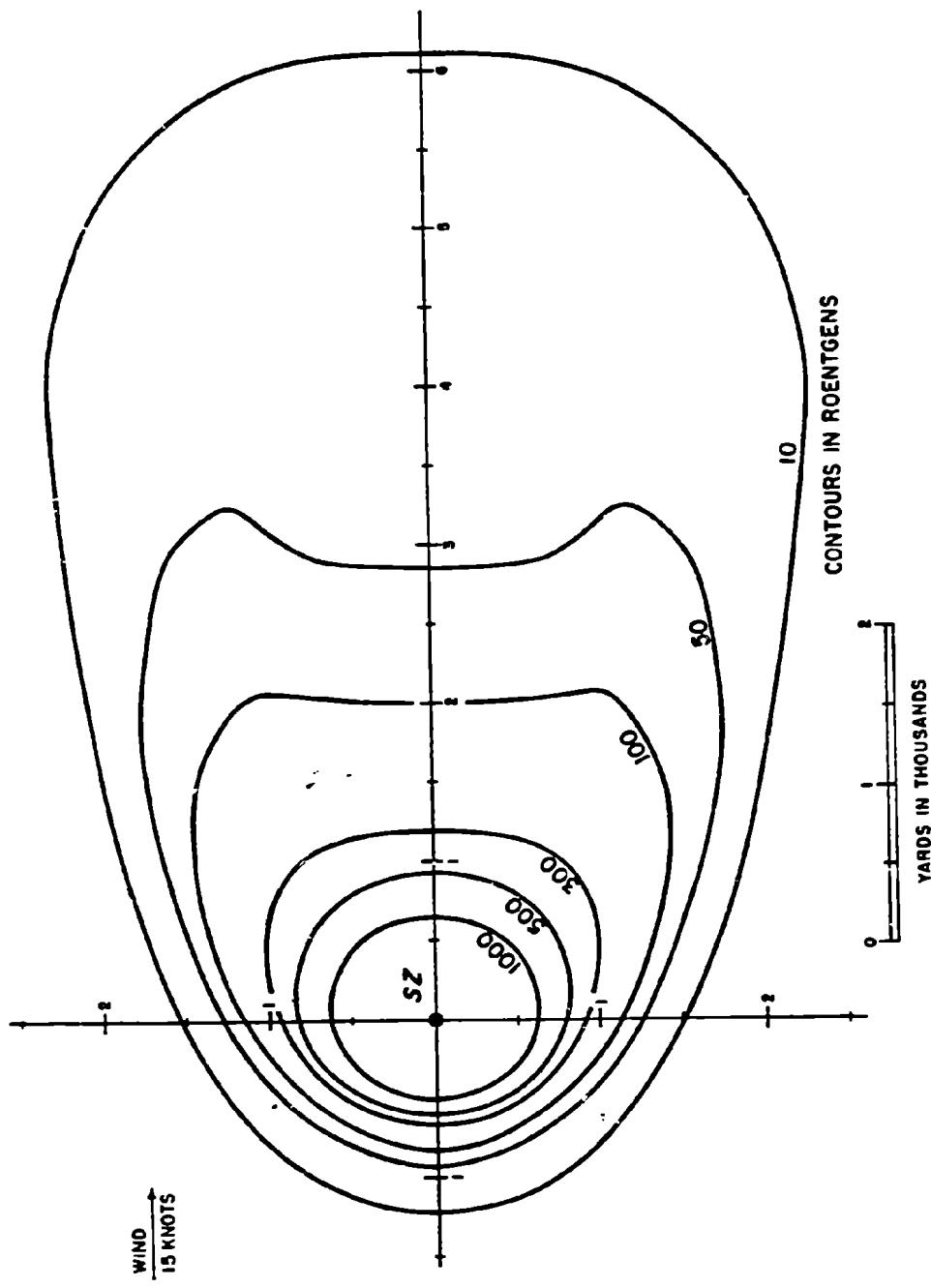
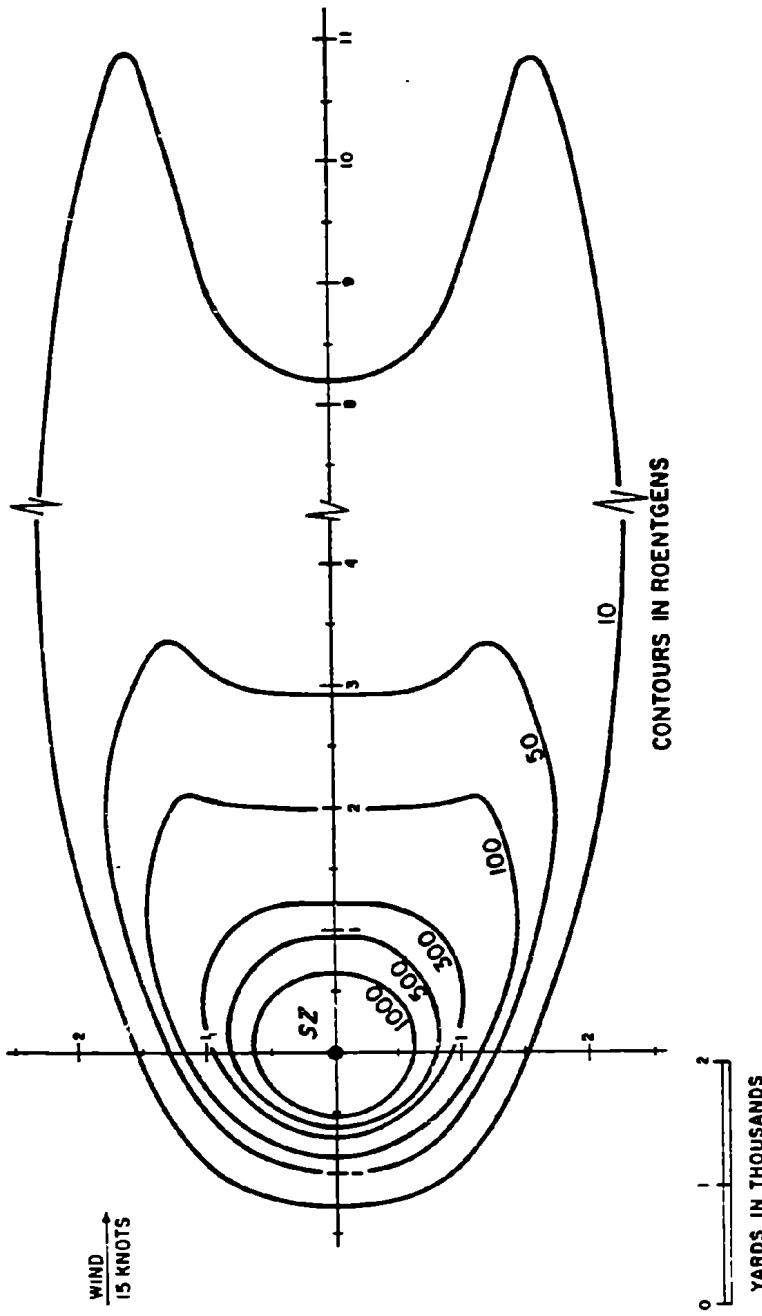


Figure 5-59. [REDACTED] Ten-Minute Total Exposure 15 Feet Above the Water Surface from a 1 kt Explosion at a Depth of 30 Feet in 5,000 Feet of Water, 16 Knot Wind, No-Current Environment



**Figure 5-60.** [REDACTED] Thirty-Minute Total Exposure 15 Feet Above the Water Surface from a 1 kt Explosion at a Depth of 30 Feet in 5,000 Feet of Water, 15 Knot Wind, No-Current Environment [REDACTED]

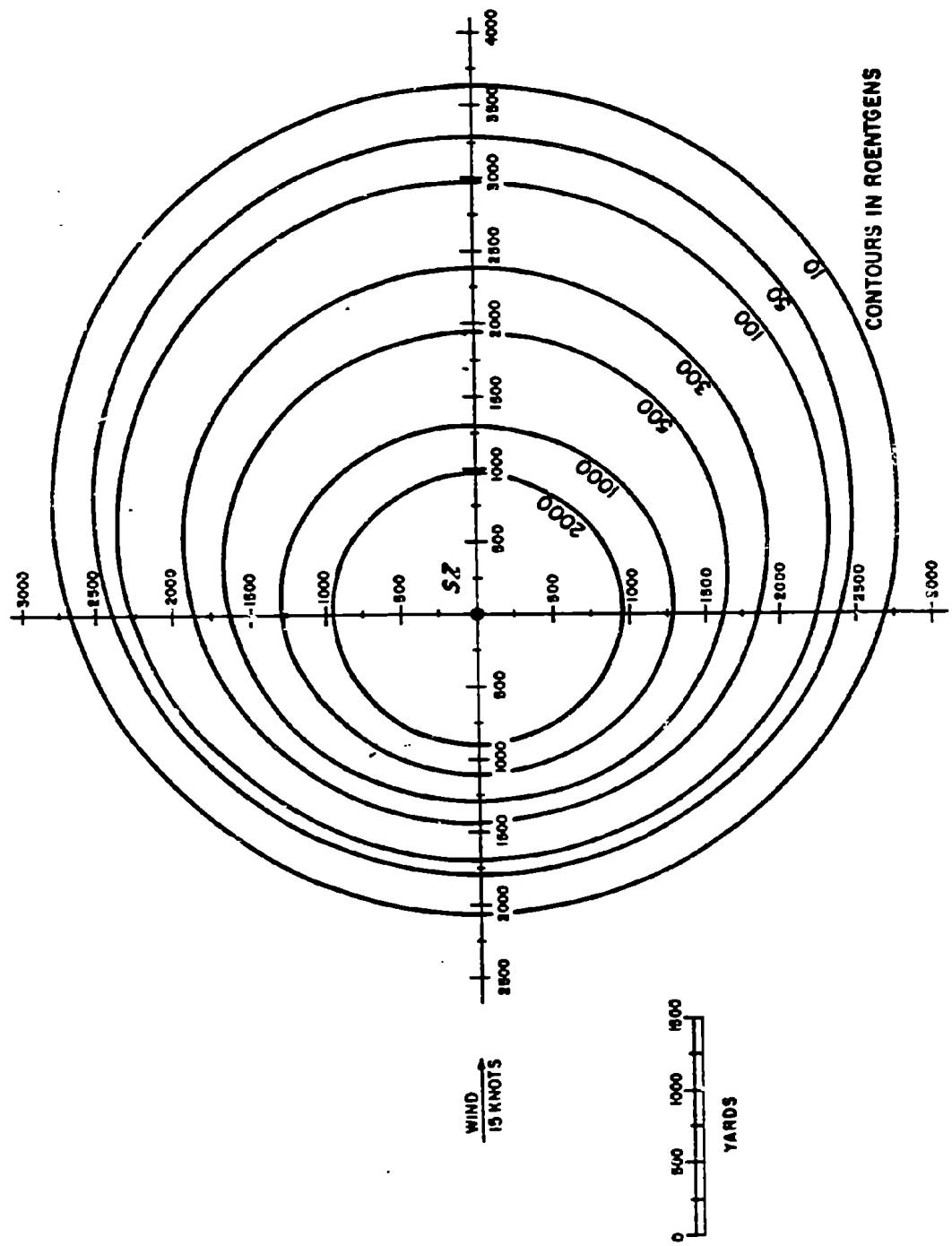


Figure 5-61. Two-Minute Total Exposure 16 Feet Above the Water Surface  
from a 10 kt Explosion at a Depth of 65 Feet in 5,000 Feet of Water,  
15 Knot Wind, No-Current Environment

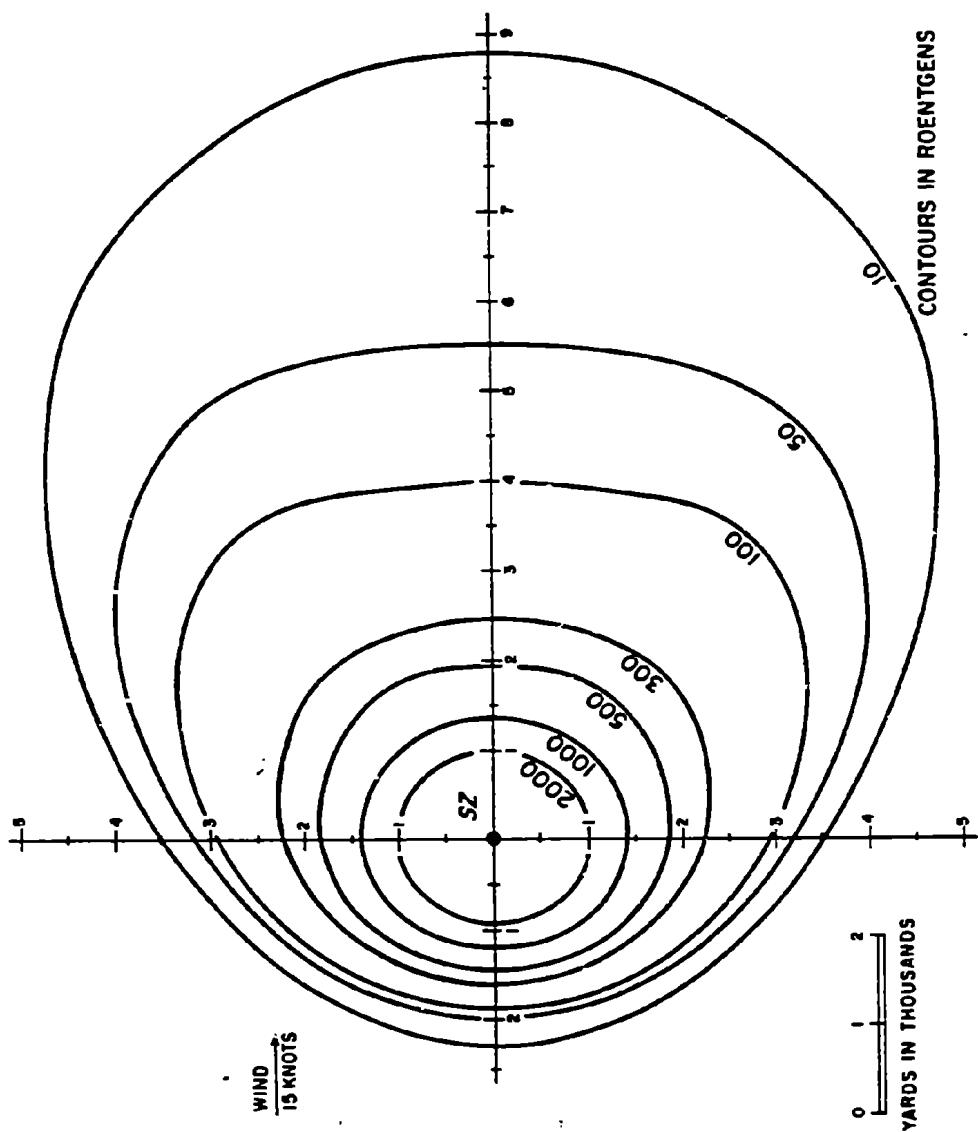


Figure 5-62. [REDACTED] Ten-Minute Total Exposure 15 Feet Above the Water Surface from a 10 kt Explosion at a Depth of 65 Feet in 5,000 Feet of Water, 15 Knot Wind, No-Current Environment [REDACTED]

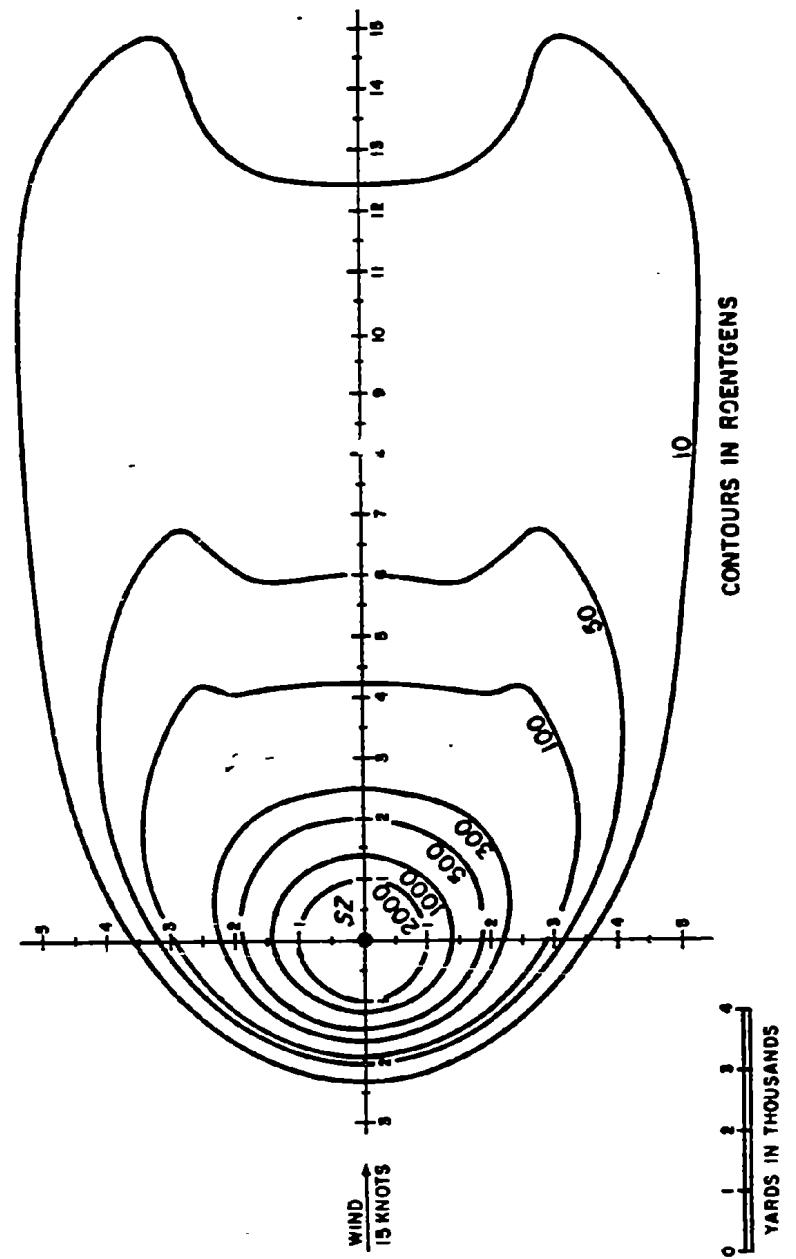


Figure 6-62. [REDACTED] Thirty-Minute Total Exposure 15 Feet Above the Water Surface from a 10 kt Explosion at a Depth of 65 Feet in 5,000 Feet of Water, 15 Knot Wind, No Current Environment [REDACTED]

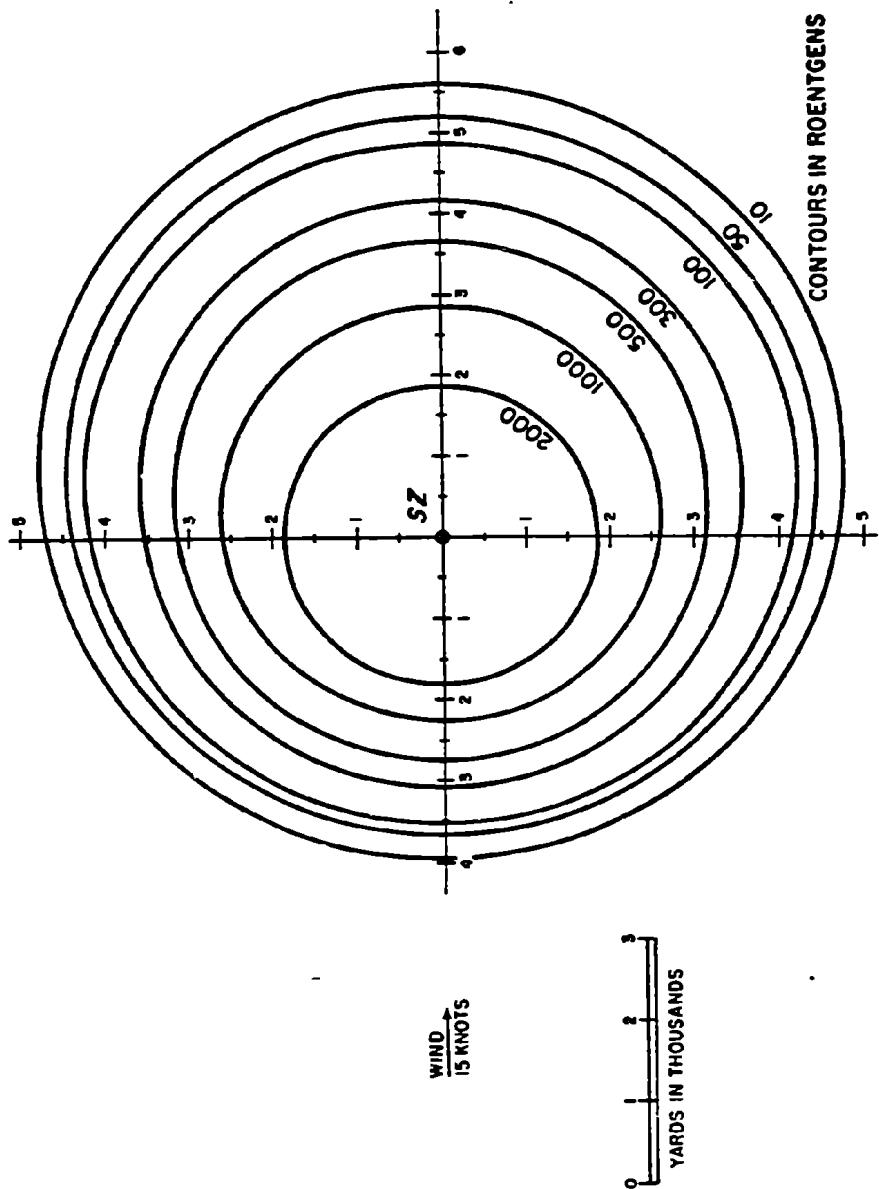


Figure 5-64. [REDACTED] Two-Minute Total Exposure 15 Feet Above the Water Surface from a 100 kt Explosion at a Depth of 140 Feet in 5,000 Feet of Water, 16 Knot Wind, No-Current Environment [REDACTED]

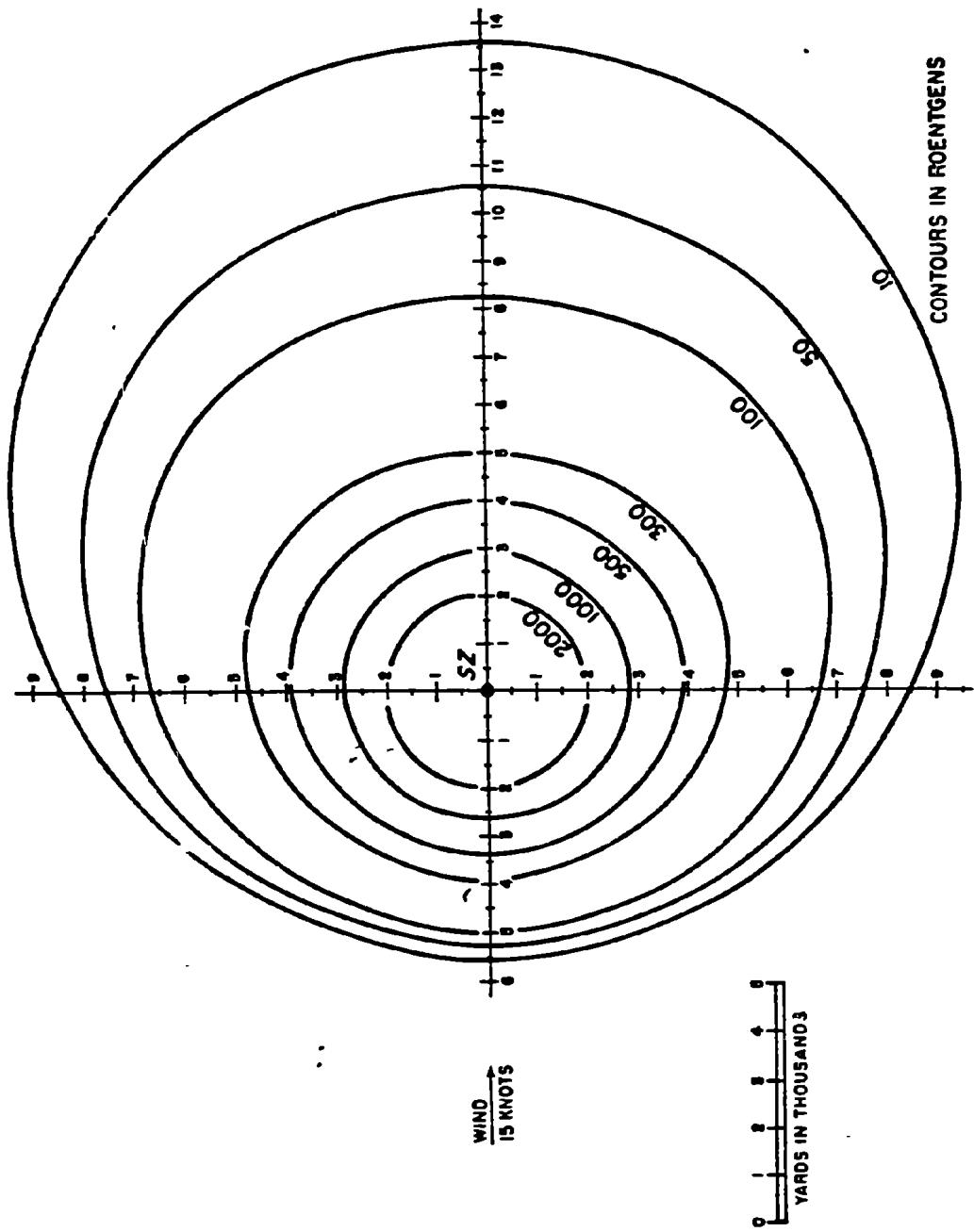
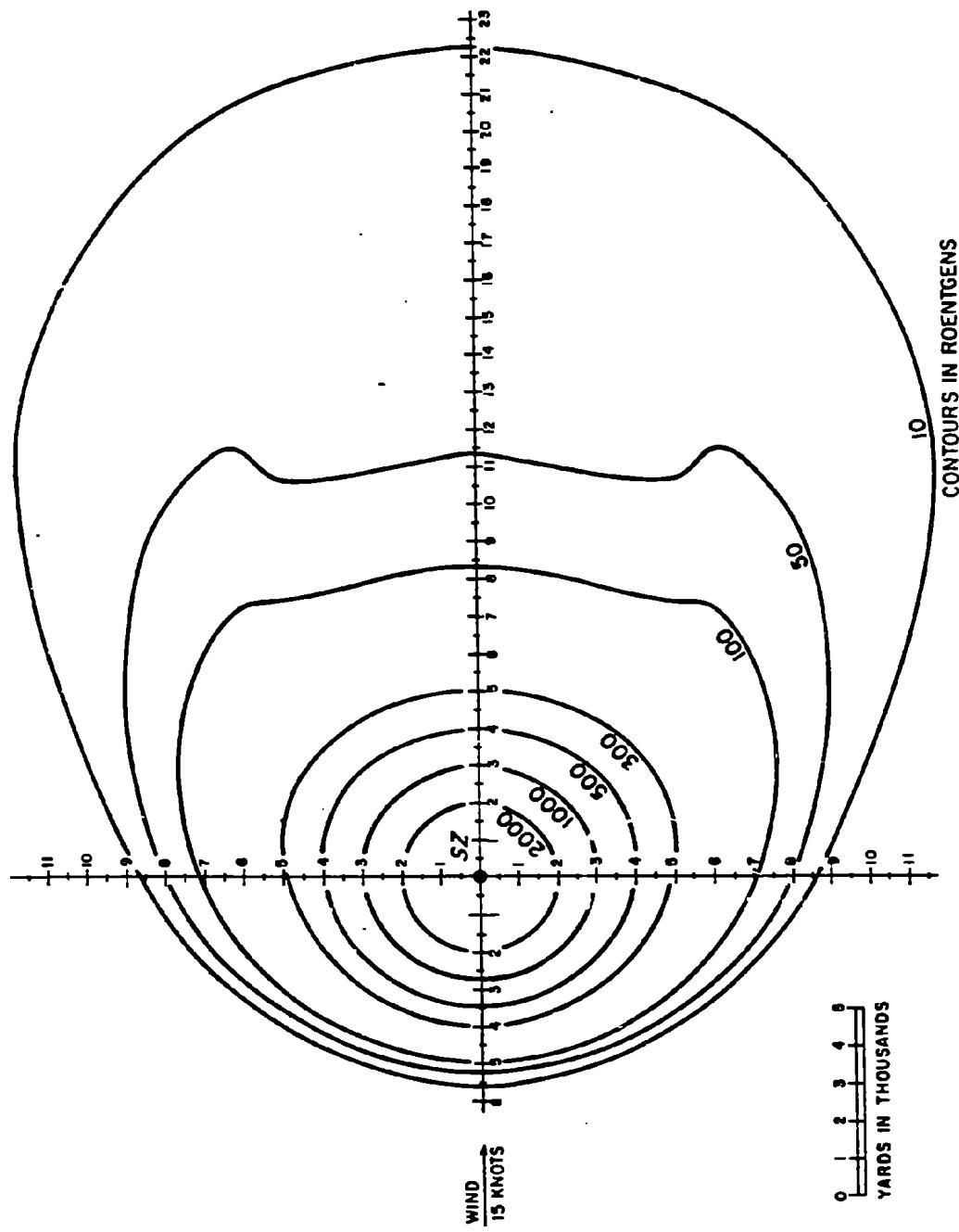


Figure 5-85. [REDACTED] Ten-Minute Total Exposure 15 Feet Above the Water Surface from a 100 kt Explosion at a Depth of 140 Feet in 5,000 Feet of Water, 16 Knot Wind, No-Current Environment [REDACTED]



**Figure 5-66.** [REDACTED] Thirty-Minute Total Exposure 15 Feet Above the Water Surface from a 100 kt Explosion at a Depth of 140 Feet in 6,000 Feet of Water, 15 Knot Wind, No-Current Environment [REDACTED]

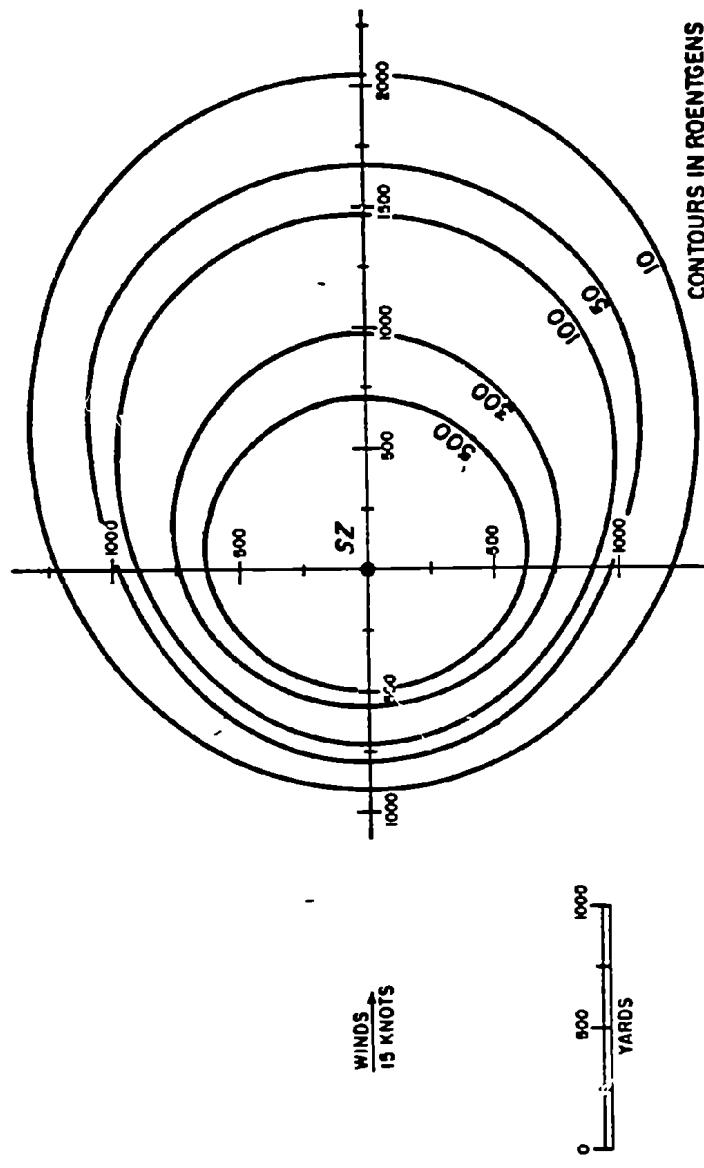


Figure 5-67. Two-Minute Total Exposure 16 Feet Above the Water Surface from a 1 kt Explosion at a Depth of 280 Feet In 5,000 Feet of Water, 15 Knot Wind, No-Current Environment

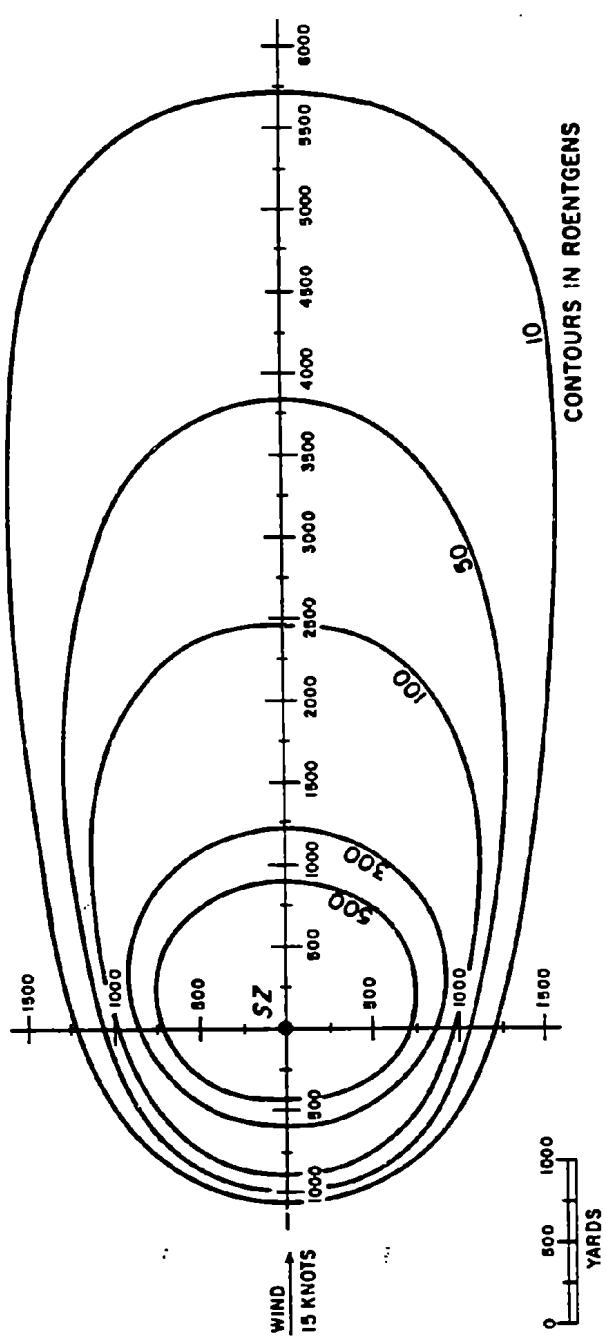


Figure 5-6P. [REDACTED] Ten-Minute Total Exposure 15 Feet Above the Water Surface from a 1 kt Explosion at a Depth of 280 Feet in 5,000 Feet of Water, 15 Knot Wind, No-Current Environment [REDACTED]

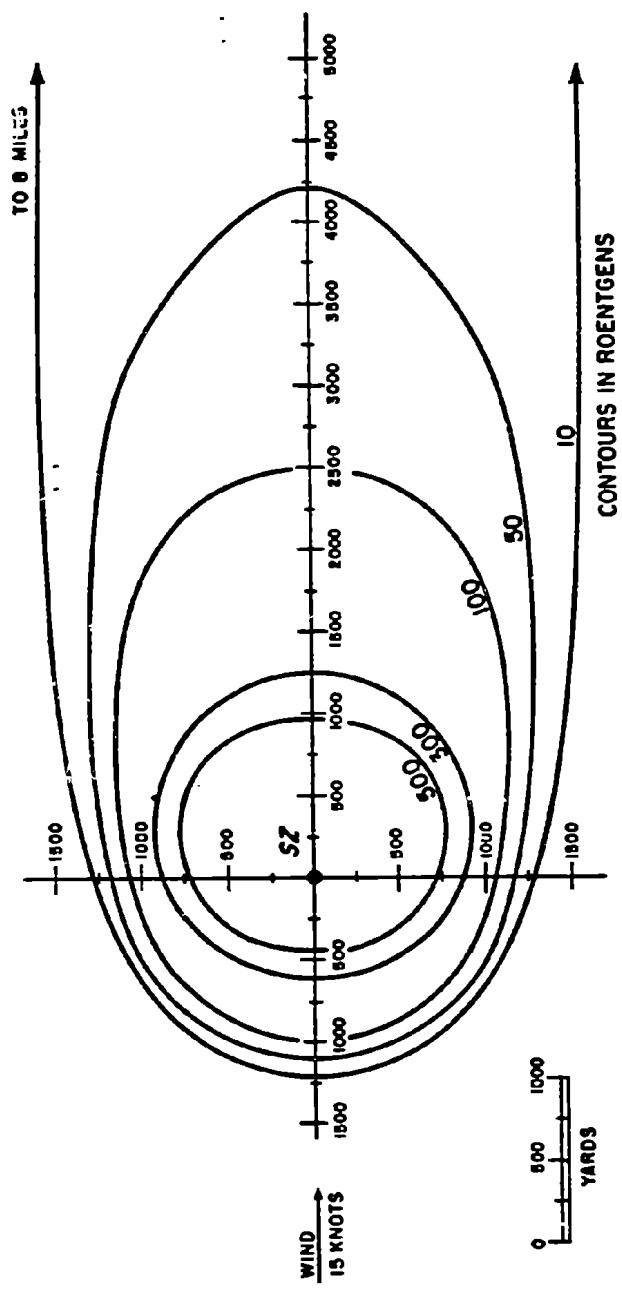


Figure 6-69. [REDACTED] Thirty-Minute Total Exposure 16 Feet Above the Water Surface  
from a 1 kI Explosion at a Depth of 280 Feet in 5,000 Feet of Water,  
15 Knot Wind, No-Current Environment [REDACTED]

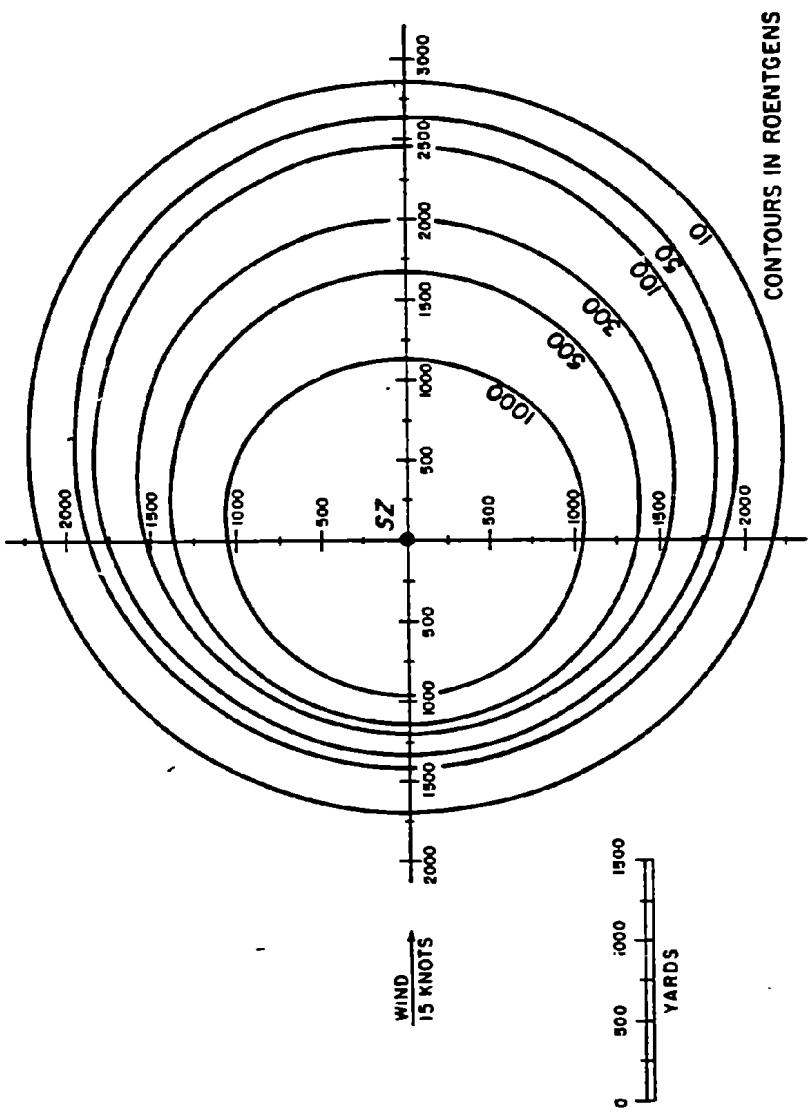


Figure 6-70. [REDACTED] Two-Minute Total Exposure 16 Feet Above the Water Surface from 10 kt Explosion at a Depth of 500 Feet in 6,000 Feet of Water,  
15 Knot Wind, No-Current Environment [REDACTED]

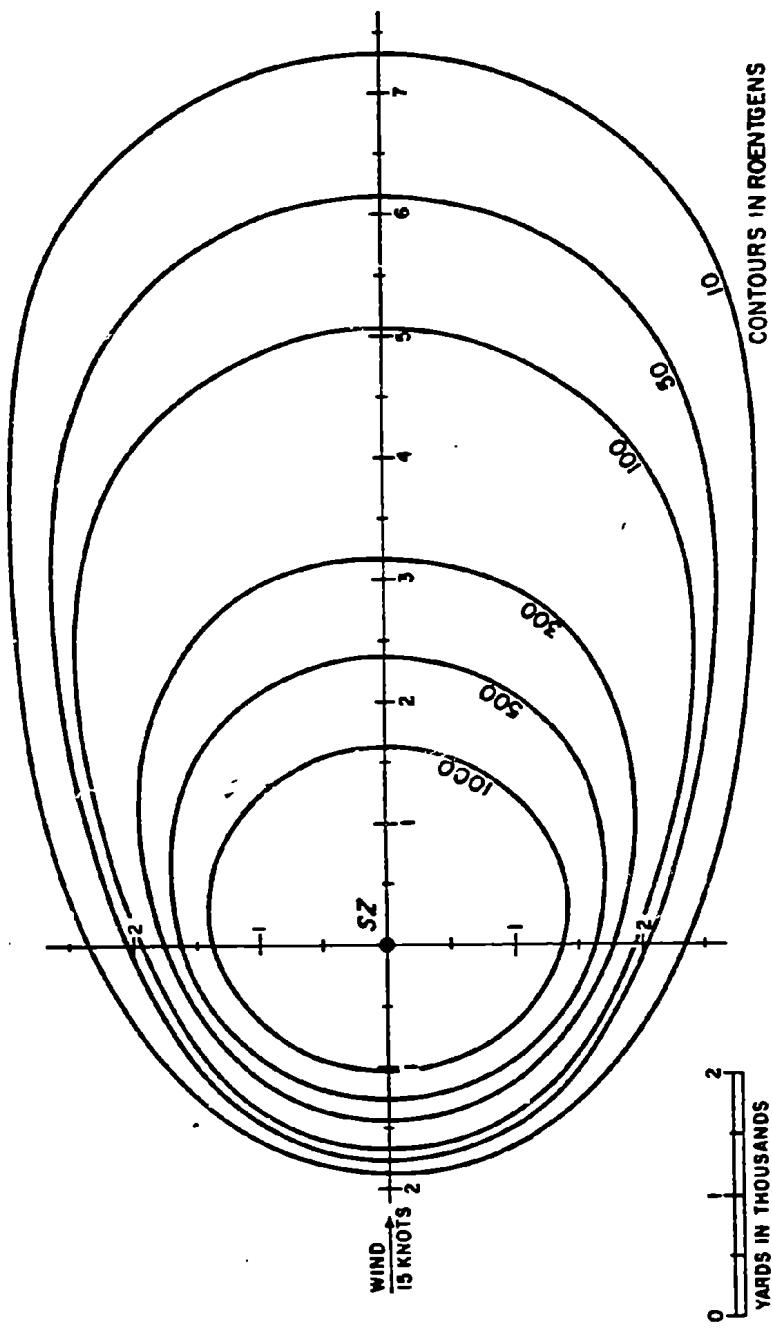


Figure 5-71. [REDACTED] Ten-Minute Total Exposure 16 Feet Above the Water Surface  
from a 10 kt Explosion at a Depth of 500 Feet in 5,000 Feet of Water,  
16 Knot Wind, No-Current Environment [REDACTED]

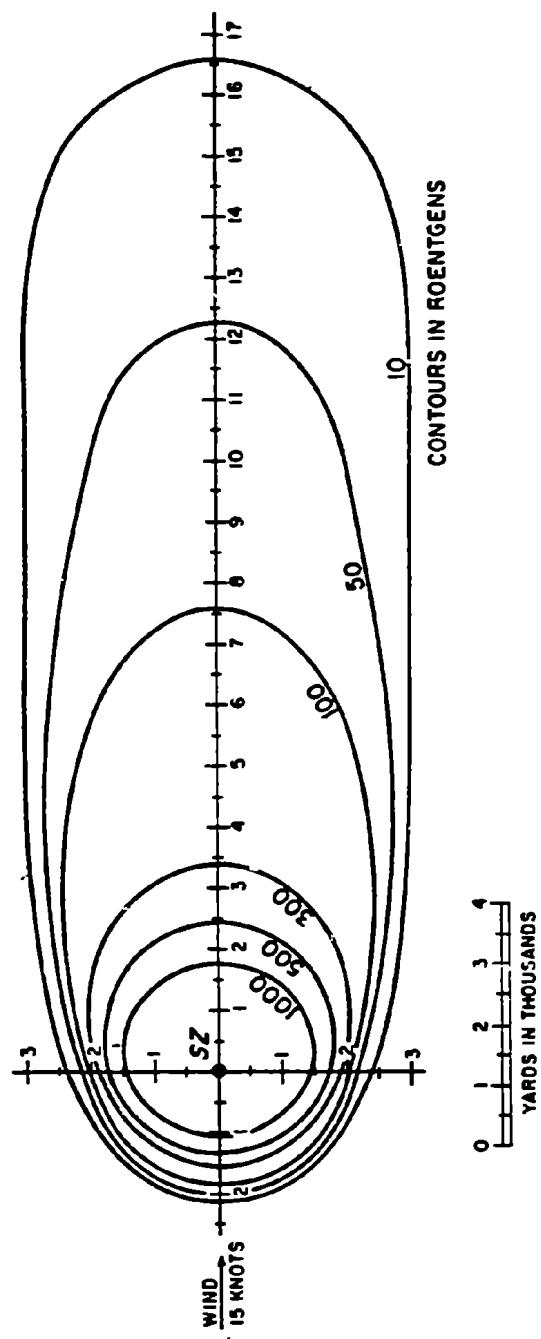
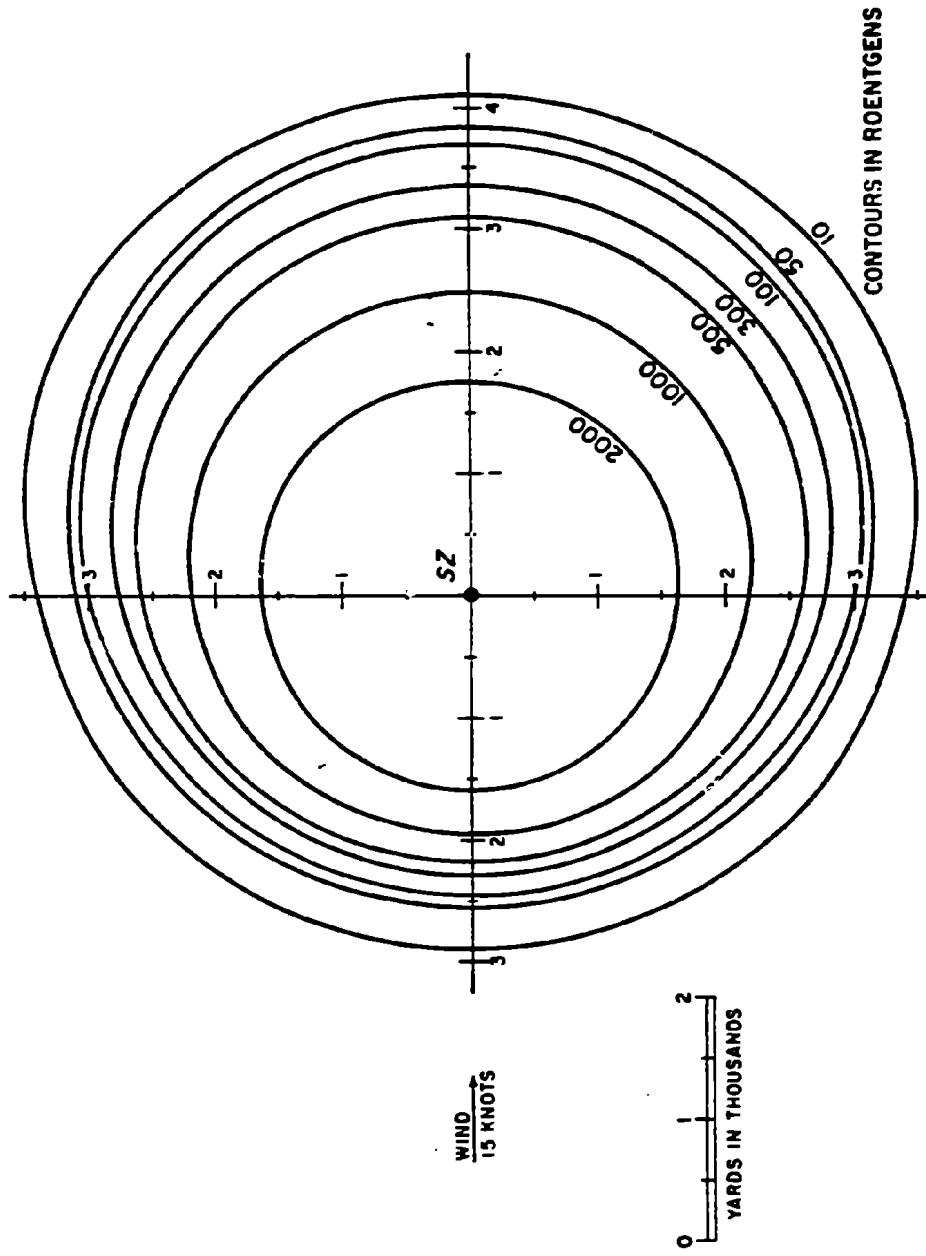


Figure 6-72. [REDACTED] Thirty-Minute Total Exposure 15 Feet Above the Water Surface  
from a 10 kt Explosion at a Depth of 500 Feet in 5,000 Feet of Water,  
15 Knot Wind, No-Current Environment



**Figure 5-73.** Two-Minute Total Exposure 15 Feet Above the Water Surface  
from a 100 kt Explosion at a Depth of 890 Feet in 5,000 Feet of Water,  
15 Knot Wind, No-Current Environment

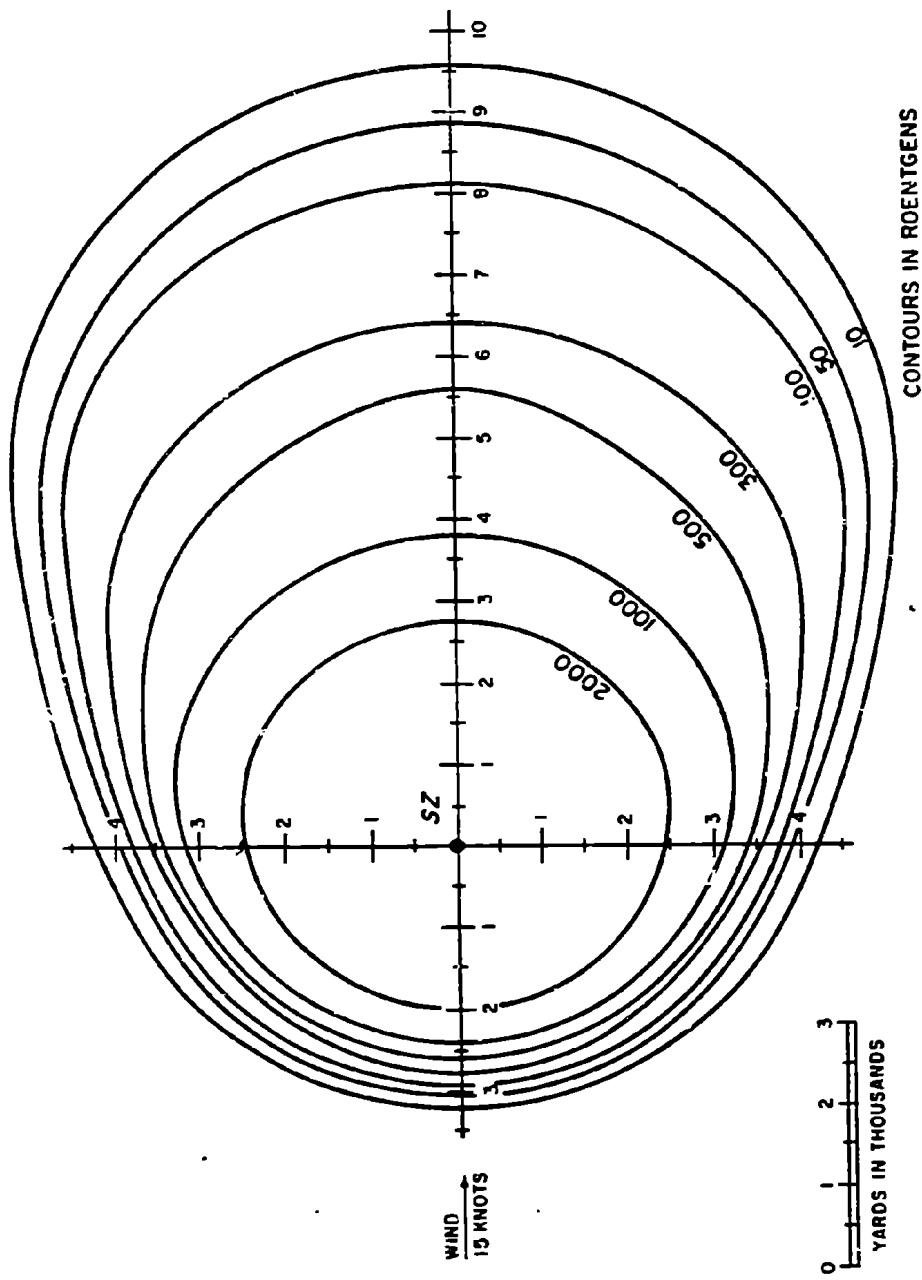
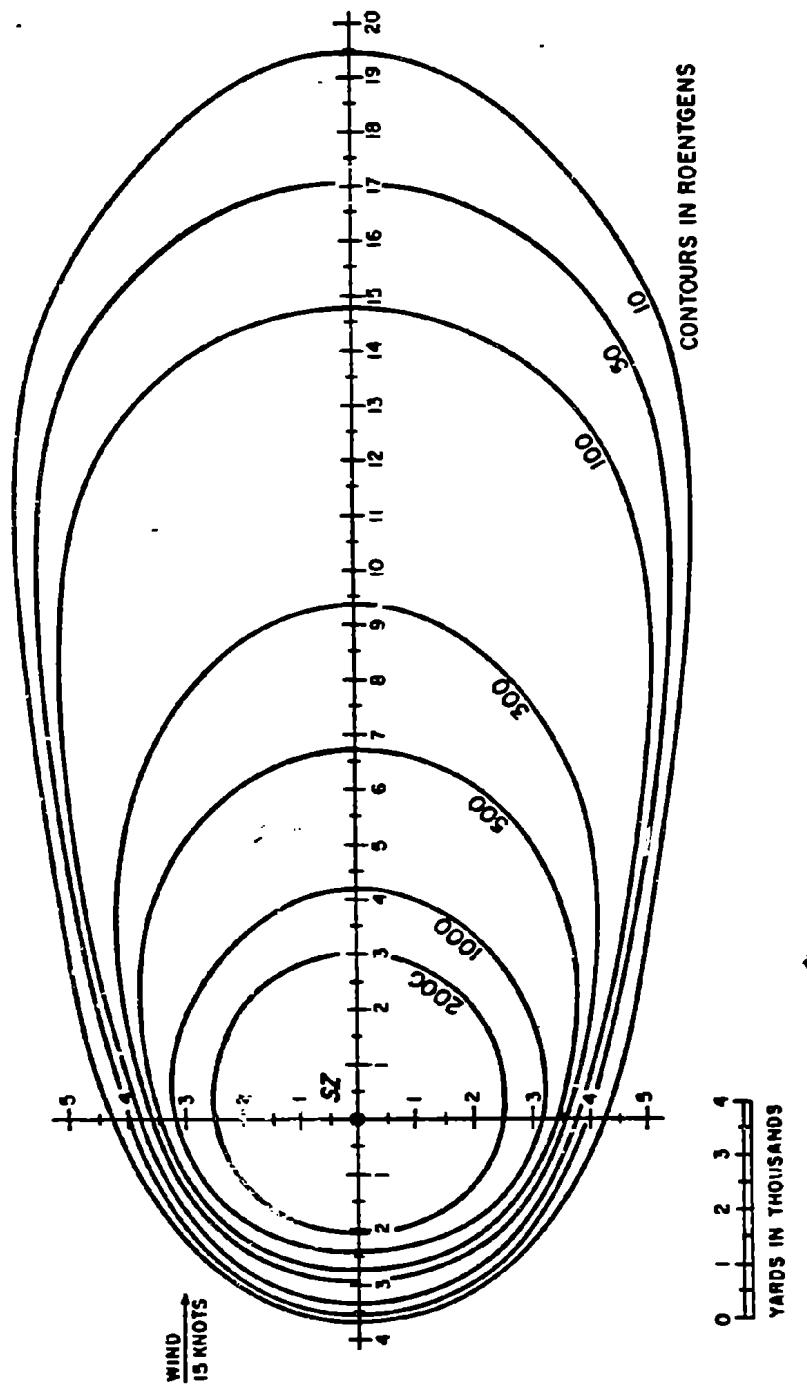


Figure 6-74. Ten-Minute Total Exposure 15 Feet Above the Water Surface from a 100 kt Explosion at a Depth of 890 Feet in 5,000 Feet of Water, 15 Knot Wind, No-Current Environment



**Figure 6-75.** [REDACTED] Thirty-Minute Total Exposure 15 Feet Above the Water Surface from a 100 kt Explosion at a Depth of 880 Feet in 5,000 Feet of Water, 15 Knot Wind, No-Current Environment [REDACTED]

[REDACTED] DOSE RECEIVED WHILE  
FLYING THROUGH A  
NUCLEAR CLOUD [REDACTED]

[REDACTED] The radioactive nuclear cloud represents a potential hazard to crews of aircraft that fly through the cloud. The dose that a crew might receive will depend upon many variables including the time after burst (which determines the intensity of the radiation as well as the size of the cloud), the portion of the cloud traversed, and the length of transit time through the cloud.

[REDACTED] After stabilization, the particles that make up the radioactive cloud will travel with the winds as they fall, and, since the wind speed and direction are both likely to vary with altitude and time, the size and shape of the cloud can only be described by complex computer codes that can accept temporal and spatial variations in weather data. No simple idealized shape can describe the cloud adequately. Even during the time of cloud rise, the winds will act on the

particles, and the cloud probably will not stabilize directly above ground zero; however, the shape can be approximated roughly by a right circular cylinder, with a stem of smaller diameter below it, at the time of stabilization. Figures 5-76 through 5-78 show the cloud diameter, the height of the cloud bottom, and the height of the cloud top, respectively, as functions of time after burst for various yields. These figures allow approximations of the cloud dimensions during the first few minutes after an explosion.

[REDACTED] Even if the cloud geometry were known, no satisfactory model exists from which simple scaling procedures could be developed to predict the dose received while flying through the cloud. Figure 5-79 shows estimates of the transit dose as a function of transit time for several entry times. These estimates were extrapolated from a limited amount of test data. The relative hazard for flight through the stem is even less certain, but it is believed to be less than that from flight through the center of the cloud.

[REDACTED]

**Problem 5-14. Calculation of Dose Received While Flying Through a Nuclear Cloud**

[REDACTED] The curves in Figure 5-79 show the total dose received while passing through nuclear clouds at various times after burst. Figures 5-76 through 5-78 provide the dimensions of the cloud as a function of time after burst.

[REDACTED] *Example* [REDACTED]

*Given:* An aircraft flying at 235 knots at an altitude of 23,000 feet passes through a nuclear cloud from a 50 kt weapon 5 minutes after the explosion.

*Find:* The probable maximum exposure of the crew, assuming that the shielding of the aircraft structure is negligible.

*Solution:* From Figure 5-77, the height of the cloud bottom will be about 16,000 feet 5 minutes after a 50 kt explosion, and from Figure 5-78, the corresponding height of the cloud top is 30,000 feet. Thus, the aircraft is flying at an altitude corresponding to the vertical center of the cloud. The maximum dose (corresponding to maximum transit time) will occur if the aircraft flies through the horizontal center of the cloud, i.e., if the aircraft traverses the entire diameter. From Figure 5-76, the diameter of a cloud from a 50 kt explosion will be 2.7 miles at 5 minutes after the burst. The aircraft speed is

$$235 \times 1.15 = 270 \text{ mph.}$$

The transit time is

$$\frac{2.7}{270} = 0.01 \text{ hr}$$
$$= 0.6 \text{ min.}$$

*Answer:* From Figure 5-79, with an entry time of 5 minutes and a transit time of 0.6 minutes, the expected dose is 37 rads. The maximum dose might be twice this value (see Reliability below), or

$$2 \times 37 = 74 \text{ rads.}$$

[REDACTED] *Reliability.* The doses obtained from Figure 5-79 are estimated to be accurate within a factor of 2 for flight paths that pass near the cloud center. If the path is near the cloud boundary, the predicted dose probably will be higher than the actual dose, although the magnitude of the error is unknown. Additional uncertainties of unknown magnitude are introduced by the prediction of the cloud size, but these uncertainties are not believed to be large for times of entry soon after burst and for short transit times.

[REDACTED] *Related Material:* See paragraphs 5-15 through 5-19.

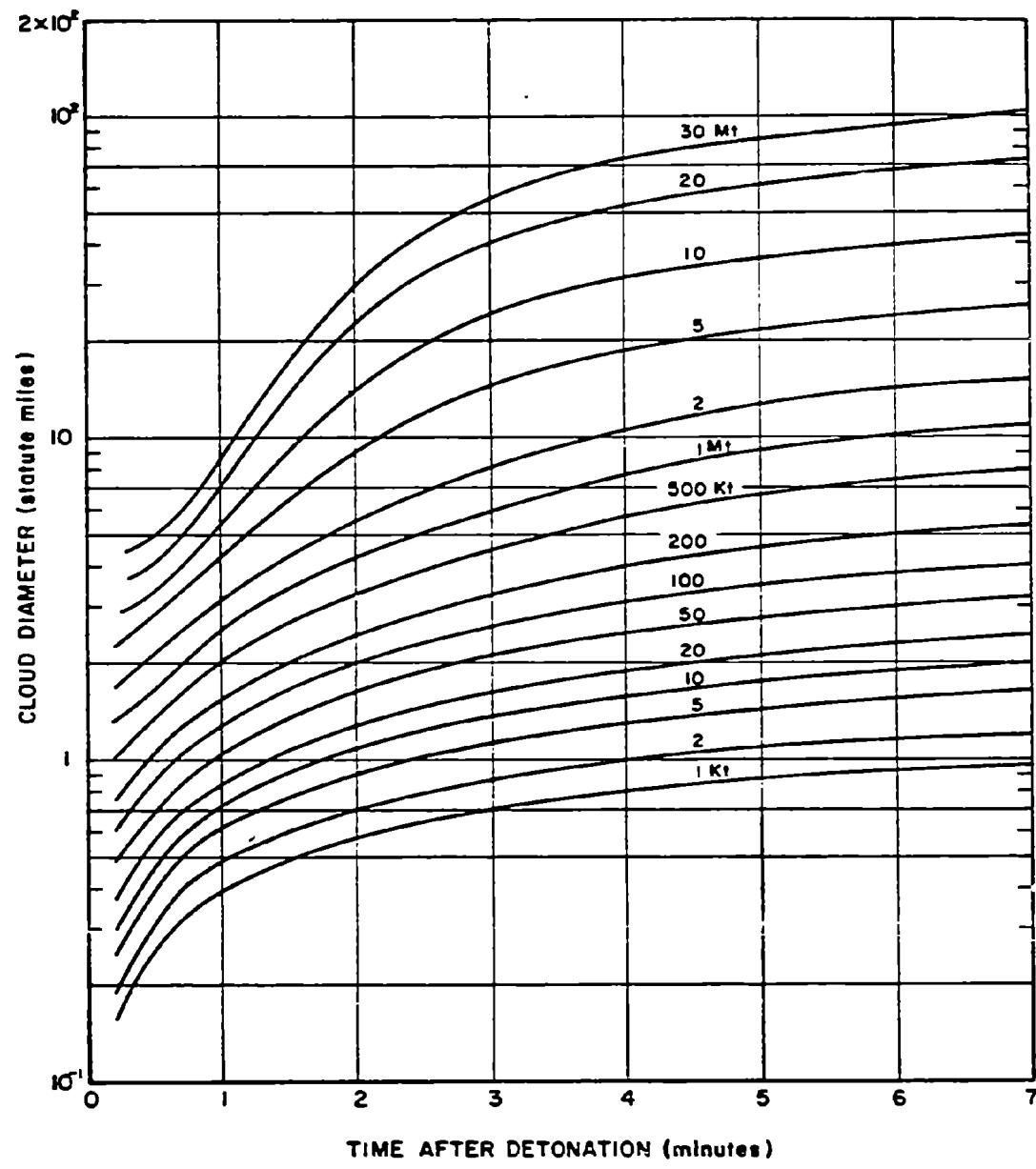
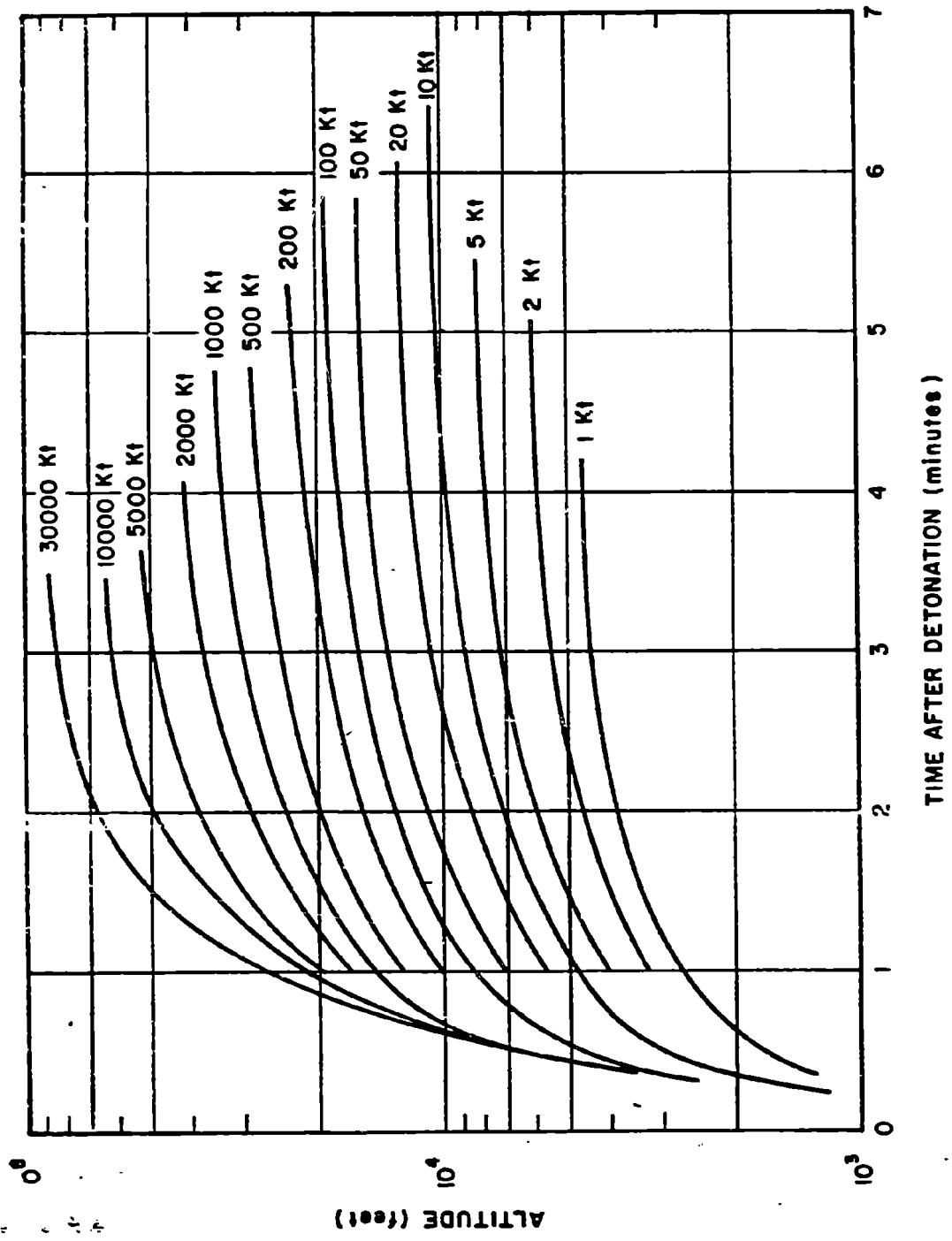


Figure 5-76. [REDACTED] Cloud Diameter as a Function of Time After Burst for Various Weapon Yields [REDACTED]



5-142

Figure 6-77. [REDACTED] Height of Cloud Bottom as a Function of Time for Various Weapon Yields [REDACTED]

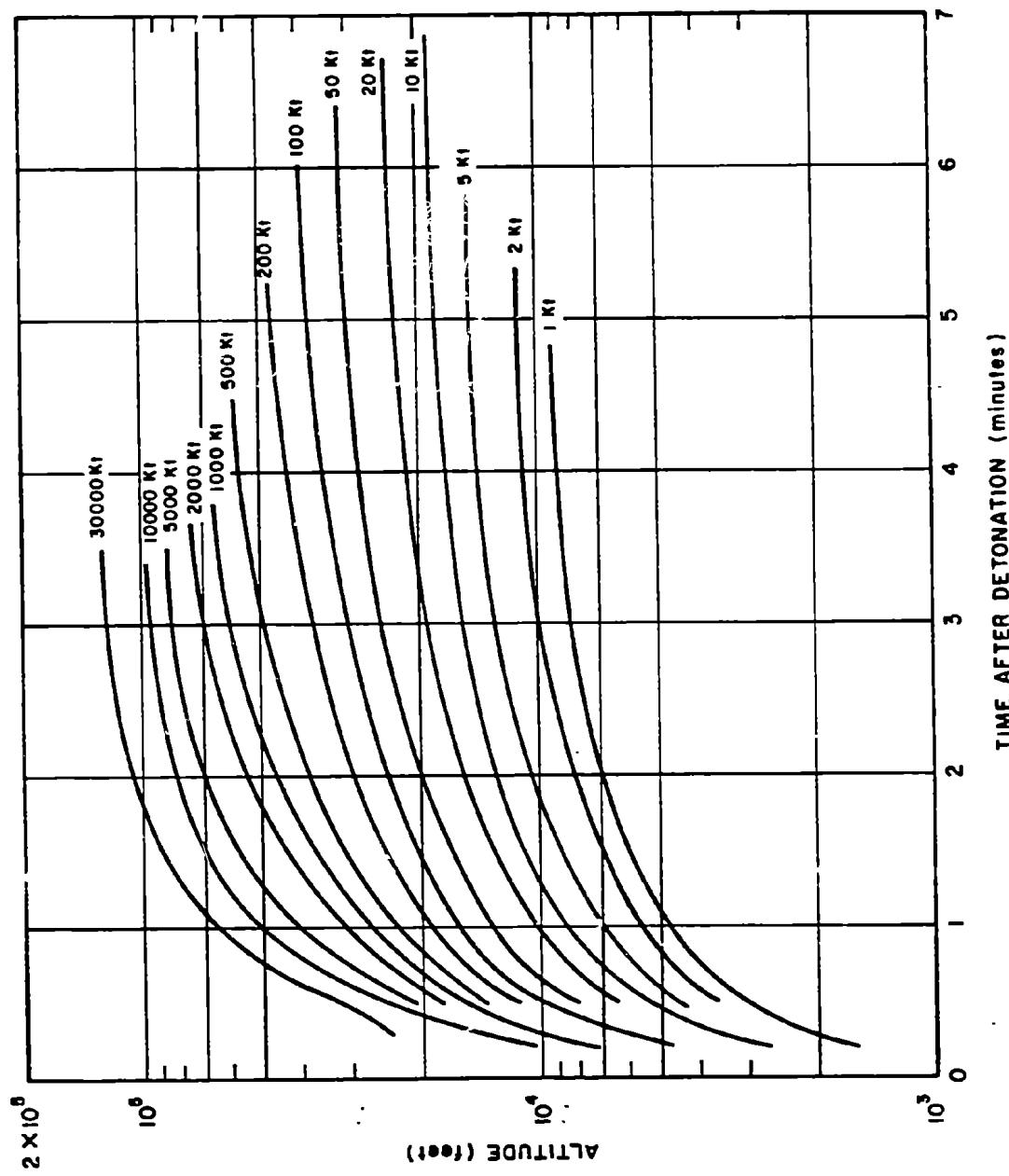


Figure 6-78. Height of Cloud Top as a Function of Time  
for Various Weapon Yields

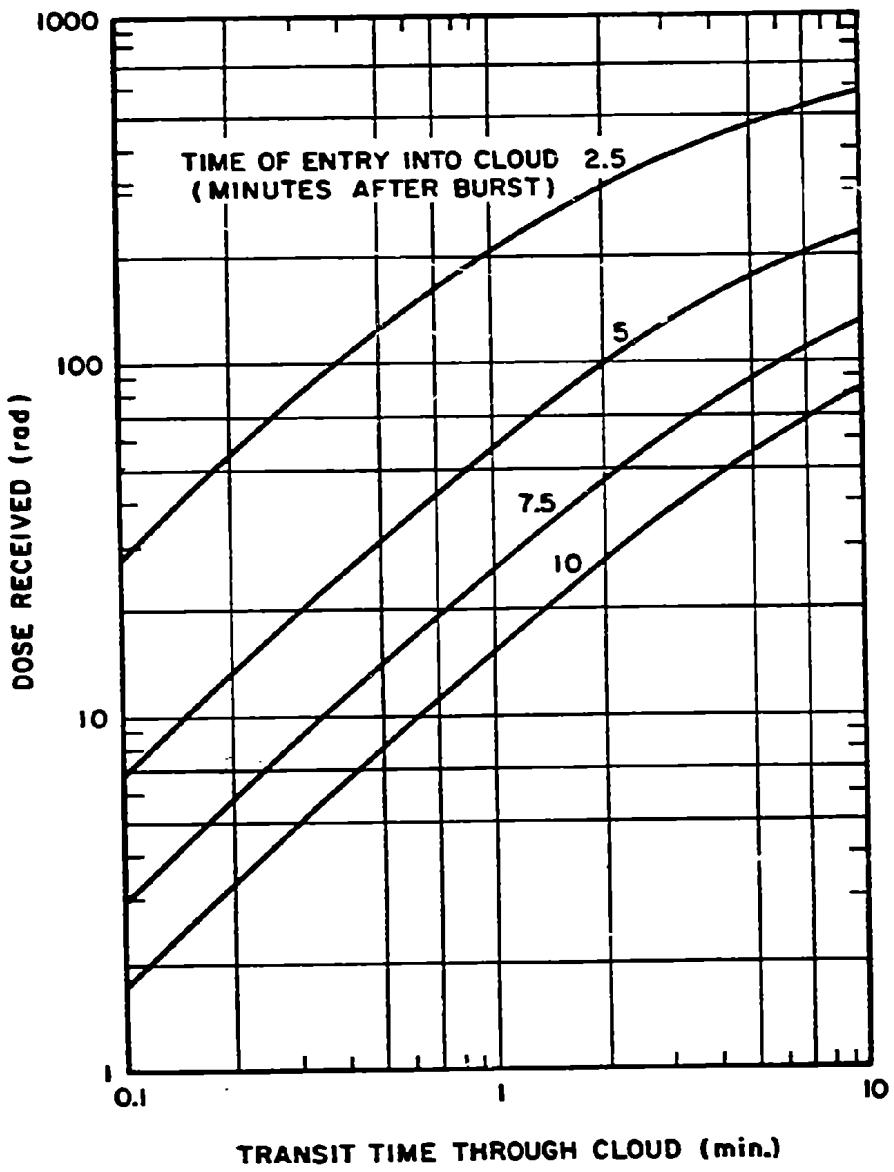


Figure 5-79. [REDACTED] Dose Received While Flying Through a Nuclear Cloud as a Function of Transit Time Through the Cloud [REDACTED]

## PRECIPITATION EFFECTS

As mentioned in paragraph 5-16, the surface contamination from an air burst weapon will be militarily insignificant in most cases. The radioactive particles remaining from the weapon debris are extremely small, having diameters that range roughly between 0.01 and 20 micrometers. The weapon cloud carries these particles to high altitudes, with the exact altitude being dependent on the weapon yield and atmospheric conditions. These particles are too small to fall, but they can diffuse downward and can be deposited by atmospheric turbulence processes. In the absence of precipitation, the deposition process takes place over sufficiently long periods of time that the cloud will have spread over a large volume as a result of diffusion and the action of winds at different levels, thereby reducing the particle concentration. Over this same period of time the radioactive decay decreases the activity levels. The net result is that dry deposition of particles from air burst weapons will not be militarily significant although there may be some long-term effects, e.g., thyroid exposures from radioactive iodine. If precipitation occurs in or above the nuclear cloud, however, there is a possibility that contamination that could be considered militarily significant may be deposited on the ground as a result of scavenging of the radioactive particles by the rain or snow. Precipitation also can affect the fallout from a surface or subsurface burst, but contamination is expected from these bursts with or without precipitation. The primary effect of precipitation on the contamination resulting from surface or subsurface bursts would be to change the location and shape of the militarily significant fallout contours. If precipitation scavenges and deposits that portion of the radioactive debris from surface or subsurface bursts that would have been delayed fallout rather than early fallout (see Section III,

"RESIDUAL RADIATION," "FALLOUT"), the resulting contamination on the ground is not expected to be militarily significant.

### 5-27 Precipitation Scavenging

Precipitation scavenging may be divided into two types: scavenging when the nuclear cloud is within the rain cloud, usually called rainout or snowout; and scavenging when the nuclear cloud is below the rain (snow) cloud, usually called washout. Rainout is generally considered to be a much more efficient form of scavenging than washout, but there are many factors that affect precipitation scavenging and the ground contamination resulting therefrom. These factors are discussed in the succeeding paragraph.

### 5-28 Factors Affecting the Prediction of Ground Contamination from Precipitation Effects

The prediction of the contamination patterns that may result from precipitation scavenging of air burst nuclear weapons is complicated by many factors. Some of the important factors are discussed below.

- *The burst occurs during precipitation.* If the burst occurs during heavy precipitation, or if heavy precipitation begins at the burst location during stabilization time, the pattern will be roughly circular around ground zero, and will be roughly the size of the nuclear cloud (if the rain cloud extends to distances beyond the nuclear cloud radius).
- *The weapon yield.* The cloud from low yield weapons will be completely contained beneath the rain layers; as the yield is increased, the percentage of the nuclear cloud beneath the rain layer decreases; at a sufficiently high

yield, the entire stabilized cloud will be above the rain layers. Specific yields will, of course, depend upon the height of the rain layer.

- *The size and shape of the nuclear cloud.* If no precipitation occurs during or very soon after burst, the nuclear cloud will reach its stabilized altitude. The size and shape of the radioactive cloud will depend upon the meteorological conditions after the stabilization time (the stabilization altitudes of both the top and bottom of the cloud will depend on the atmosphere within which the explosion occurs, and the position of the stabilized cloud will depend upon the winds that act on it during its rise, but these effects are generally small compared to the changes in cloud shape and size after stabilization). In the absence of precipitation or velocity shear in the wind, the dominant physical phenomena responsible for reducing the activity concentration in a nuclear cloud is diffusion produced by turbulent eddies in the atmosphere. Reasonable estimates of the diffusion in a horizontal plane exist. Less is known about vertical diffusion; however, unless the vertical diffusion causes the particles to enter a zone where the wind speed or direction changes, it will not affect the horizontal concentration. Changes in wind speed and direction can have a significant effect on the size and shape of the nuclear cloud. Since the particles from an air burst are so small that they will not actually "fall," they will be acted on by winds within a specific altitude layer. Frequently, several such layers will exist within the thickness of the cloud at stabilization, each having a different speed and/or direction. Changes in both speed and direction of the wind are likely to occur as a function of time and space. Since most of the particles within any one altitude layer will remain in that layer for long periods of time, differences in wind ve-

locity (speed and direction) between layers, as well as changes within a layer, generally will tend to decrease the horizontal concentration as viewed from above (exceptions may occur, of course, e.g., changes in direction may cause two layer that have separated to overlap after some time). The net result of all of the factors acting on the nuclear cloud from a low altitude air burst is that it generally will tend to increase in size horizontally without drastic changes in the vertical dimension for relatively long periods of time, unless precipitation scavenging occurs. This increase in horizontal dimensions will decrease the concentration of radioactive particles available for scavenging.

- *Radioactive decay.* While the nuclear cloud is drifting, the radioactive isotopes decay continuously. Thus, the longer the time between the explosion and the time that the nuclear cloud encounters precipitation, the smaller the total intensity of radiation that will be available (see Problem 5-9 and Figure 5-40). This, together with the general decrease in horizontal concentration described above, reduces the potential hazard with increasing time.
- *The rain cloud size, and the type and during of the precipitation.* If the rain cloud is smaller than the nuclear cloud, only that portion of the nuclear cloud that is in or below the rain cloud will be available for scavenging (any part of the nuclear cloud that is above the rain cloud is not available, as discussed under the effects of yield above). If the rain cloud is larger than the nuclear cloud in horizontal dimensions, any portion of the nuclear cloud that is in or below the rain cloud will be available for scavenging. The length of time during which the nuclear cloud is available for scavenging will depend on the relative directions and speed of travel of the nuclear and

rain clouds. The efficiency of the scavenging process will depend on the debris characteristics, scavenging mechanisms, and the type of rain. Heavy precipitation generally is considered to be more efficient in the scavenging process than light rainfall. Finally, strong updrafts and downdrafts of wind are frequently found around and within a rain cloud. These vertical air motions could prevent the intersection of the nuclear cloud and the rain cloud, but under some circumstances the air motions could enhance the mixing of the two clouds.

- *The effects of precipitation on the contamination once it reaches the ground.* After radioactive particles are brought to the ground by precipitation, they may or may not stay in place. There is a possibility that water run-off will create hot spots in some areas while decreasing the activity in other areas. Some of the radioactive particles may be leached into the ground and, as a result of the attenuation by the ground between the particle and the ground-air surface, the dose rate above the ground will be reduced.

[REDACTED] There are no data concerning precipitation effects where the resulting contamination was militarily significant. Also, no computer model has been developed that can include all of the factors described above either on a deterministic or a statistical basis. The results of theoretical studies, field simulations, and laboratory experiments have, however, provided some general conclusions concerning the importance of precipitation effects. First, contamination resulting from precipitation scavenging is *not* considered to be a major problem from the standpoint of effects on military operations. Second, weapons may be separated into three groups according to their relative importance with regard to precipitation effects: 1. weapons in the yield range from 1 to 10 kt are most likely to have an effect on military operations, if any such effect occurs; 2. weapons with yields greater than 10 kt and less than about 60 kt may have some effect on military operations, with the probability of such an effect decreasing with increasing yield; 3. weapons with yields greater than 60 kt or less than 1 kt are not expected to have any effect on military operations. The potential hazard may be reduced by making use of available shelter.

[REDACTED]  
[REDACTED] BIBLIOGRAPHY [REDACTED]

Baum, S., P. W. Wong, and P. J. Dolan, *NUCROM: A Model of Rainout from Nuclear Clouds*, DNA 3389F, Stanford Research Institute, Menlo Park, California, August 1974

Biggers, W. A., and K. C. Kohr, *Neutron Outputs from Selected LASL Nuclear Devices* LA 3688, Los Alamos Scientific Laboratory, Los Alamos, New Mexico, April 1967

Beyster, J. R., et al., *Status of Neutron and Gamma Output from Nuclear Weapons* SAI 70-205, DASA 2567, Science Applications Incorporated, La Jolla, California, May 1971

Bunney, L. R., and D. Sam, *Gamma-Ray Spectra of Fractionated Fission Products*, NOLTR 71-103, Naval Ordnance Laboratory, White Oak, Silver Spring, Maryland, 18 June 1971

Canu, J. F., and P. J. Dolan, *Prediction of Neutron Induced Activity in Soils* Technical Analysis Report AFSWP 518, Headquarters, Armed Forces Special Weapons Project, Washington, D.C., 4 June 1957

Crawford, T. V., and K. R. Peterson, *BANEERRY - Discussion of Diffusion Calculations Including Potential Exposure to Child's Thyroid from I-131 Via the Forage-Cow-Milk Pathway* COPK 71-20, Lawrence Radiation Laboratory, Livermore, California, 3 March 1971

Crawford, T. V., *Precipitation Scavenging and 2BUFFF*, UOPKA 71-14, Lawrence Livermore Laboratory, Livermore, California, 6 December 1971

Crocker, G. R., *Fission Product Decay Chains: Schematics with Branching Fractions, Half-Lives, and Literature References*, USNRDL-TR-67-111, U.S. Naval Radiological Defense Laboratory, San Francisco, California, 24 June 1967

Crocker, G. R., and T. Turner, *Calculated Activities, Exposure Rates, and Gamma Spectra for Unfractionated Fission Products*, USNRDL-TR-1009, U.S. Naval Radiological Defense Laboratory, San Francisco, California, 28 December 1965

Crocker, G. R., and M. A. Connors, *Gamma-Emission Data for the Calculation of Exposure Rates from Nuclear Debris, Volume I, Fission Products*, USNRDL-TR-876, U.S. Naval Radiological Defense Laboratory, San Francisco, California, 10 June 1965

Crocker, G. R., J. D. O'Connor, and E. C. Freiling, *Physical and Radiochemical Properties of Fallout Particles*, NRDL-TR-899, Naval Radiological Defense Laboratory, San Francisco, California, 15 June 1965

*Department of Defense Land Fallout Prediction System*, DASA 1800-I through 1800-VII, Defense Atomic Support Agency, Washington, D.C.; U.S. Army Nuclear Defense Laboratory, Edgewood Arsenal, Maryland; U.S. Naval Radiological Defense Laboratory, San Francisco, California; Technical Operations Research, Burlington, Massachusetts; 1966

Dolan, P. J., *Gamma Spectra of Uranium-235 Fission Products at Various Times After Fission*, AFSWP 524, Headquarters, Armed Forces Special Weapons Project, Washington, D.C., March 1959 [REDACTED]

Dolan, P. J., *Gamma Spectra of Uranium-238 Fission Products at Various Times After Fission*, DASA 526, Headquarters, Defense Atomic Support Agency, Washington, D.C., May 1959 [REDACTED]

Dolan, P. J., *Theoretical Dose Rate Decay Curves for Contamination Resulting from Land Surface Burst Nuclear Weapons*, DASA 528, Defense Atomic Support Agency, Washington, D.C., 6 August 1959 [REDACTED]

Englemann, R. J., and W. G. N. Slinn, *Precipitation Scavenging (1970)*, AEC Symposium Series, U.S. Atomic Energy Commission, Washington, D.C., 22 December 1970 [REDACTED]

Englemann, R. J., *Priorities in Scavenging Research*, AEC Symposium Series U.S. Atomic Energy Commission, Washington, D.C., 22 December 1970 [REDACTED]

French, R. L., *A First-Last Collision Model of the Air/Ground Interface Effects on Fast-Neutron Distributions*, Nucl. Sci. Engr., 19, 151-157, 1964 [REDACTED]

Freiling, E. C., and N. E. Ballou, *Nature of Nuclear Debris in Sea Water*, Nature 195, No. 4848, pp. 1283-1287, 29 September 1962 [REDACTED]

Fritzsche, A. E., N. E. Lorimier, and Z. G. Burson, *Measured Low-Altitude Neutron and Gamma Dose Distributions Due to a 14-MeV Neutron Source*, EGG 1183-1449, E. G. and G., Inc., 1969 [REDACTED]

Fritzsche, A. E., N. E. Lorimier, and Z. G. Burson, *Measured High-Altitude Neutron and Gamma Dose Distributions Due to a 14-MeV Neutron Source*, EGG 1183-1438, E. G. and G., Inc., 1969 [REDACTED]

Harris, R. J., Jr., et al., *Models of Radiation in Air - The ATR Code*, DNA 28031, SAI-71-557-LV, Science Applications Incorporated, La Jolla, California, May 1972 [REDACTED]

Huebsch, I. O., *Fallout Predictions for Water-Surface Nuclear Bursts*, USNRDL-TR-67-147, U.S. Naval Radiological Defense Laboratory, San Francisco, California, 28 November 1967 [REDACTED]

Heubsch, I. O., *Development of a Water-Surface-Burst Fallout Model: The Formation, Dispersion and Deposition of Fallout Particles*, USNRDL Technical Report, U.S. Naval Radiological Defense Laboratory, San Francisco, California [REDACTED]

Keith, J. R., and F. H. Shelton, *Neutron Transport in Non-Uniform Air by Monte Carlo Calculation, Volume 1*, DASA 2236-1 KN-774-69-1, Kaman Nuclear, Colorado Springs, Colorado, 15 January 1969 [REDACTED]

Keith, J. R., and F. H. Shelton, *Neutron Transport in Non-Uniform Air by Monte Carlo Calculation* [REDACTED] Volume II, KN-774-69-1, DASA 2236-II, Kaman Nuclear, Colorado Springs, Colorado, 15 January 1969 [REDACTED]

Knox, J. G., and A. L. Williams, *Rainout Studies at Lawrence Livermore Laboratory*, UCRL S1530, Lawrence Livermore Laboratory, University of California/Livermore, Livermore, California, 11 February 1974 [REDACTED]

Krey, P. W., et al., *Soil Activation by Neutrons* [REDACTED] Project 2.1, WT-1410, U.S. Army Chemical Warfare Laboratories, Army Chemical Center, Maryland, 16 May 1960 [REDACTED]

Lee, H., P. W. Wong, and S. L. Brown, *SEER II: A New Damage Assessment Fallout Model*, DNA 3008F, Stanford Research Institute, Menlo Park, California, May 1972 [REDACTED]

Marshall, J. D., and M. B. Wells, *The Effects of Cut-Off Energy on Monte Carlo Calculated Gamma-Ray Dose Rates in Air*, RRA-M67, Radiation Research Associates, Fort Worth, Texas, 1966 [REDACTED]

Mooney, L. G., and R. L. French, *Improved Models for Predicting Nuclear Weapon Initial Radiation Environments* [REDACTED] RRA-T93, DASA 2615, Radiation Research Associates, Fort Worth, Texas, 31 December 1969 [REDACTED]

Norment, H. G., and E. J. Tichovolsky, *A New Fallout Transport Code for the DELFIC System: The Diffusive Transport Module*, DASA 2669, Arcon Corporation, Wakefield, Massachusetts, 1 March 1971 [REDACTED]

Norment, H. G., *A Precipitation Scavenging Model for Studies of Tactical Nuclear Operations, Volume I - Theory and Preliminary Results, Volume II - The DELFIC-PSM Code*, DNA 3661F-1, -2, Mt. Auburn Research Associates, Inc., Newton, Massachusetts, 18 June 1975 [REDACTED]

Read, P. A., *Neutron Induced Activity on a Beach: A Method for Calculating the Dose Rate*, USNRDL-TR-67-133, U.S. Naval Radiological Defense Laboratory, San Francisco, California, 27 October 1967 [REDACTED]

Ritchie, R. H., and V. E. Anderson, *Some Monte Carlo Results on the Penetration of Neutrons from Weapons in an Air-Over-Ground Geometry* [REDACTED] ORNL-3116, Oak Ridge National Laboratory, Oak Ridge, Tennessee, 26 July 1962 [REDACTED]

Schuert, E. A., *Distribution of the Radioactive Debris and Associated Nuclear Radiation from Underwater Nuclear Explosions* [REDACTED] USNRDL-TR-67-28, DASA 1240, Part 1, Chapter 11, U.S. Naval Radiological Defense Laboratory, San Francisco, California, 15 December 1966 [REDACTED]

Selph, W. E., and M. B. Wells, *Weapons Radiation Shielding Handbook. Chapter 6, Methods for Predicting Radiation Fields Produced by Nuclear Weapons*, DASA-1892-4, Oak Ridge National Laboratory, Oak Ridge, Tennessee, December 1969

Shelton, F. H., *Nuclear Weapons as Neutron Sources, The Neutron Environments They Produce, and Some Neutron Effects on Aerospace Systems*, DASA-2383-1, Volume I, Neutron Sources, KN 774-69-6, Kaman Nuclear, Colorado Springs, Colorado, October 1969

Shelton, F. H., and J. R. Keith, *Nuclear Weapons as Neutron Sources, The Neutron Environments They Produce, and Some Neutron Effects on Aerospace Systems*, Volume II, *Neutron Environments and Some Effects*, DASA 2383-2, KN 774-69-6, October 1969

Slade, D. H. (Ed.), *Meteorology and Atomic Energy - 1968*, USAEC Report TID-24190, Environmental Science Services Administration, Washington, D.C., July 1968

Smith, R. J., R. F. Benck, and E. E. Lissak, *Initial Gamma Data from Nuclear Weapon Tests, 1948 Through 1962*, NDL-TR-53, U.S. Army Nuclear Defense Laboratory, Edgewood Arsenal, Maryland, July 1965

Snay, H. G., *The Hydrodynamic Background of the Radiological Effects of Underwater Nuclear Explosions*, Proceedings of the Tripartite Symposium on the Technical Status of Radiological Defense in the Fleets, U.S. Naval Radiological Defense Laboratory, San Francisco, California, 16-20 May 1960, Vol. II, USNRDL Reviews and Lectures, No. 103

Stensland, G. J., *Further Numerical Model Studies of the Washout of Hygroscopic Particles in the Atmosphere*, UCRL-51614, Lawrence Radiation Laboratory, University of California/Livermore, Livermore, California, 2 July 1974

Stevens, E. A., *Time-Dependent Neutron and Secondary Gamma-Ray Transport in an Air-Over-Ground Geometry, Volume II. Tabulated Data*, ORNL 4289, Vol. II, Oak Ridge National Laboratory, Oak Ridge, Tennessee, September 1968

Williams, A. L., *Rain Scavenging of Radioactive Particles*, UCRL-517765, Lawrence Radiation Laboratory, University of California/Livermore, Livermore, California, 28 February 1975

Wong, P. W., and H. Lee, *Utilization of the SEER Fallout Model in a Damage Assessment Computer Program (DACOMP)*, DNA 3608F, Stanford Research Institute, Menlo Park, California, 27 February 1975

Young, F. H., et al., *The Radiological Effects from Underwater Nuclear Explosions*, USNRDL-TR-68-1, U.S. Naval Radiological Defense Laboratory, San Francisco, California, 17 October 1967

## Chapter 6

### TRANSIENT-RADIATION EFFECTS ON ELECTRONICS (TREE) PHENOMENA

#### INTRODUCTION

This chapter introduces the subject of transient-radiation effects on electronics and provides a basic description of the interaction of nuclear radiation with matter as it applies to electronic components. The response of electronics to the radiation from a nuclear weapon burst depends not only on the radiation present at the electronics but also depends on the specific operating state of the electronics at the time of the radiation exposure and on the specific electronics in the system. A knowledge of the individual characteristics of the circuits contained in an electronics package, of the exact electronic components used in the circuits, and of the specific construction techniques and materials used in making the electronic components constitutes the necessary background for determining the radiation response of the electronic system. This chapter explains how the radiation interacts with different materials to produce a wide variety of effects. These material effects are used in the discussions of the component-part responses in Section VII of Chapter 9. Section IV of Chapter 14 contains a brief discussion of circuit and electronic-system response supplemented with discussions of general electrical responses of classes of systems (radios, radar, etc.).

The cumbersome name applied to the class of effects that are the subject of this chapter, transient-radiation effects on electronics, is generally abbreviated to the acronym TREE. In general, TREE means those effects occurring in

electronics as a result of the transient radiation from a nuclear weapon explosion or as a result of an environment designed to simulate that radiation. It should be understood that the transient-radiation from a nuclear explosion can be and is simulated by the use of controlled sources of steady-state and transient radiation since the environment produced can be correlated to the actual environment of interest, and thereby the effects on electronics can be studied.

Although the weapons radiation environment lasts for a very short time, its effect on electronics can be both short or long term. For emphasis, it must be stated that the word transient in TREE modifies the word radiation and does not modify the word effects: the effects may be transient, semipermanent, or permanent.

The term electronics means any one or all of the following: electronic component parts, electronic component parts assembled into a circuit, and circuits assembled into a system. TREE studies also may include the response of electro-mechanical components connected to the electronics, e.g., gyros, inertial instruments, etc. TREE does, however, specifically exclude other types of component parts or systems such as hydraulic cylinders and hydraulic systems, fuel lines and fuel systems, etc. This exclusion is made since electronics as a group or as part of a hybrid system are one of the most radiation-sensitive portions of a system.

There are several points to be emphasized about TREE. The TREE interest is in the environment at the electronics produced by the

initial nuclear radiation (i.e., that radiation emitted within 1 minute following the burst) which, in turn, consists of both prompt and delayed radiation. The weapon-burst radiations of interest are neutrons, gamma rays, X-rays, and to a much less extent, electrons. The effects of interest are both temporary and permanent even

though the radiation persists only for a short time.

[REDACTED] Examples of system responses to TREE and their consequences are given below. These examples represent only a small sample and are not necessarily representative of present day problems.

#### **Effect in System Due to Temporary Disturbances of the Electronics**

- Change in logic state in missile-borne guidance computer
- Spurious (ill-timed) fuzing signal
- Excess currents in transistors and capacitors in servo control loop
- Excess currents in memory write circuits
- Microcircuit latchup following ionization pulse

#### **Typical Consequence**

- Program jump or disturbance of key data causing mission failure
- Warhead dudding or premature detonation
- Excessive steering maneuvers causing structural instability
- Writing erroneous data in memory, usually causing mission failure
- Functional disabling of microcircuit until power is cycled off and on

#### **Effect in System Due to Permanent Degradation of the Electronics**

- Neutron-induced loss of gain in lower-frequency transistors
- Delamination of semiconductor wire bonds due to thermomechanical shock
- Neutron-induced loss of gain in higher-frequency transistor structures
- Metalization burnout due to excess ionization-induced currents

#### **Typical Consequence**

- Loss of power supply regulation; decreased servo-loop gain
- Functional failure of the affected device, usually leading to mission failure
- Decreased fan-out capability in computer logic
- Functional failure of affected device, usually causing mission failure

## ENVIRONMENT

In order to specify the hardness required of an electronic system, or to formulate an analysis or test program on which its hardness level will be established, it is necessary to describe the radiation environment to which the electronic systems may be exposed. Since the multitude of components of this environment leads to confusion in understanding the variety of mechanisms whereby a nuclear explosion can affect the operation of electronic systems, the primary outputs of a nuclear weapon and the mechanisms whereby secondary radiation are generated will be reviewed. In quantifying the environment to which the electronics are exposed, it is first necessary to treat the primary output of the nuclear explosion, then transport this radiation through the atmosphere and generate secondary radiations by interaction with the atmosphere. At this point, the radiation incident at the system of interest can be quantified. Since most of the electronics are enclosed by some structural material, there is the additional effect of transport through such shields, and it becomes necessary to describe the radiation field as it interacts with the affected part.

This step-wise description of the radiation explains the variety of methods and units by which the radiation field is described. The weapon designer usually describes the output from the nuclear explosion-total energy output, total number of neutrons emitted, total gamma-ray energy, and reaction pulse shape. The person who formulates specifications for system design usually describes the radiation field as it impinges on the system, e.g., energy per unit area, neutron fluence, gamma exposure, pulse shape as affected by radiation transport through intervening material. Finally, the designer of the individual electronic piece-part or circuit is concerned with describing the radiation in units that are convenient for quantifying the radiation ef-

fect that he has to take into account, e.g., energy deposition per unit mass or volume, 1-MeV equivalent neutron fluence, gamma dose, radiation pulse shape at the device.

### 6-1 Weapon Output

The weapon radiation output and its interaction with the atmosphere will be summarized in succeeding paragraphs, together with the units in which these radiations are usually described. Following this summary, the individual radiation effects of concern will be discussed, and the appropriate methods of describing the radiation at the affected parts or circuits will be described for each type of effect.

The majority of the energy released in a nuclear explosion heats the material of which the nuclear device was composed, to temperatures of tens and hundreds of millions of degrees. A smaller fraction (0.1 to 10%) escapes promptly in the form of fast neutrons and prompt gamma rays (see Chapters 4 and 5). The intense thermal source radiates most of its energy in the form of X-rays. If the explosion occurs in a vacuum, or, if the weapon is a "hot" X-ray device (see Section II, Chapter 4) that explodes in relatively thin atmosphere, these X-rays can produce important TREE effects. Depending upon the specific temperature of the source, the X-rays have energies varying from a few to a few hundred kilovolts. One method by which the energy spectrum from such a source is frequently described is by specifying the temperature of a black body which would emit a spectrum that approximates the observed X-ray spectrum (Chapter 4). It should be noted that even though the temperature is usually specified as a number in units of keV (kilo-electron-Volts), this unit describes a spectrum of photon energies extending significantly below and above the quoted number.

DNA  
(4)(3)

[REDACTED]

[REDACTED]

After the prompt radiations have been emitted from the nuclear explosion, a residue of hot and radioactive debris remains. Some of its energy continues to be irradiated as thermal energy in the ultra violet and visual regions of the spectrum. Subsequent radioactive decay of the debris produces lower intensity gamma rays as well as emitting high energy electrons. These electrons are particularly important for high altitude nuclear detonations, which may inject the electrons into orbits trapped by the earth's magnetic field. These electrons are of particular concern to space vehicles whose orbits intercept the earth's radiation belts, because continued exposure to the electrons can cause significant permanent degradation.

If the explosion occurs within or near the atmosphere, the prompt radiations interact with the constituents of the atmosphere, producing secondary effects. The X-rays are absorbed most strongly and, depending upon altitude, the air is heated by the interaction to produce an intense thermal source and a blast wave in the air (Chapters 1 through 4). The gamma rays interact to produce secondary electrons. In concert with the earth's magnetic field and/or inhomogeneities, such as the surface of the earth, these electrons create a radiating electromagnetic pulse (EMP) (Chapter 7). The neutrons interact with the atmosphere to produce secondary gamma rays (Chapter 5).

## 6-2 Time Considerations

[REDACTED]

The general time frame for the arrival of the various radiation components at the electronics package is sometimes important. In general, for the purposes of electronic vulnerability, the prompt gamma radiation can be considered as a single pulse. Since the flight time for X-rays and gamma rays of all energies equals the speed

of light, *unscattered* photons arrive at the equipment with the same time distribution they had at the source, with a time delay of  $3.33 \mu\text{sec}/\text{km}$  from the weapon burst. The arrival of the gamma pulse approximately coincides with the unscattered prompt X-rays.

[REDACTED] The neutrons arrive after the initiation of the gamma- and X-radiation. Their arrival time depends on the neutron energy and the range to the receiver. The first neutrons to arrive will be the unscattered 14-MeV neutrons. Their time of flight is  $19.3 \mu\text{sec}/\text{km}$ , therefore, they will arrive  $16 \mu\text{sec}/\text{km}$  after photon arrival. The photons resulting from neutron inelastic-scattering (Chapter 5) will also begin to arrive at about this time. Within  $32.8 \mu\text{sec}/\text{km}$  (the arrival time after photon arrival for 4-MeV neutrons), the photons resulting from neutron inelastic-scattering will be completed, since the inelastic-scatter contribution is negligible for lower energy neutrons. Within  $69.0 \mu\text{sec}/\text{km}$ , the bulk of the unscattered 1-MeV neutrons will have been deposited. The photons resulting from neutron capture (or thermalization) typically will peak shortly after the arrival of the 1-MeV neutrons depending on the system configuration being studied. Both the thermalization time and the capture time following thermalization depend strongly on the interacting materials and the system configuration. The radiation of interest to TREE is complete in less than 1 minute.

## 6-3 Description of Radiation Fields

[REDACTED] A complete description of the radiation field produced at the system should include the time dependence, angular distribution, and energy spectrum of each of the components. Of course, this should be done for a wide variety of conditions to cover all possible interaction scenarios. In practice, it is not necessary to be so thorough, and the following approximations are usually made:

- A worst case radiation environment is spe-

cified and the objective is to have the system tolerate all combinations of environments that are less stringent than the specification.

- The incident radiation is assumed to be unidirectional. This is usually the worst case angular distribution, and it represents a reasonable approximation to reality.
- Where possible, the individual radiation fields are specified in units that facilitate conversion to those units that are convenient for describing the effect.

For example, it is possible to specify the time dependent neutron energy spectrum incident on the system. Since the time dependence of arrival of unscattered neutrons is correlated with neutron energy, as discussed above, specifying the neutron energy spectrum, and the range of distances between nuclear explosion and the irradiated system, also is equivalent to specifying the time dependence. Finally, if the only effect of interest is permanent neutron-induced displacement effects, the spectrum can be replaced by a single quantity such as the 1-MeV damage equivalent neutron fluence. The meaning of these units and the method of calculating them will be discussed in following paragraphs. It must be emphasized, however, that such convenient units are intended for simplification only. They are useful only if the assumptions underlying their use are valid. In the foregoing example, specifying only the 1-MeV damage equivalent neutron fluence is useless for determining the magnitude of neutron-induced ionization effects quantitatively.

The degree to which such simplifications can be used depends in large measure upon the simplicity of the interaction of the incident radiation with the target materials. A particularly simple case is the description of the gamma-ray environment. High energy gamma rays suffer negligible attenuation in passing through significant quantities of material, and they interact with matter to produce approxi-

mately the same energy deposition, independent of atomic composition of the target. Therefore, it has been possible to describe the gamma ray environment fairly simply and this has frequently led to carelessness. A more complicated situation, in which carelessness cannot be tolerated, is represented by the X-ray interactions. X-rays of energies of tens to a few hundred kilovolts are attenuated significantly even by thin missile skins and electronic subsystem boxes, and the energy deposition produced by such X-rays is a strong function of the atomic number of the target material. For this reason, it is invariably necessary to specify not only the total X-ray energy fluence incident on the system (usually given in calories/cm<sup>2</sup>), its pulse width (usually given in nanoseconds), but also a range of possible energy spectra (sometimes given as explicit spectra, and at other times specified by a range of characteristic black body temperatures). The relating of such an exposure to the intensity of the radiation present at the affected area, such as the junction region of a transistor, requires detailed and specific calculations of the transport of the spectrum through the intervening material and the resultant energy deposition in the affected volume.

The transport of the various radiation components to the site of the equipment of interest is discussed in Chapters 4 and 5. It is of value, however, to note that typical electronic packaging materials will not produce significant attenuation of the neutron and gamma ray components of the environment. They do represent significant shields of X-rays, particularly if high-Z materials are used for electronic envelopes. Only the higher energy photons penetrate to the electronics of interest. Since the lower energy photons produce the highest energy deposition per unit volume when they interact, such shielding is especially useful because it removes preferentially that portion of the photon energy spectrum that would be most damaging if it were

allowed to penetrate to the sensitive devices. This fact reinforces the observation that it is necessary to specify both the X-ray energy fluence and its spectrum outside and inside the shield. Indicating only the energy-fluence attenuation factor of a shield would ignore the fact that remaining photons are less effective in producing damage.

## INTERACTIONS BASIC TO TREE

### 6-4 Ionization

[REDACTED] Ionization is that process by which electrons are freed from their parent atoms in a material. A free electron carries a negative charge. After losing an electron, the atom (then called an ion) carries a net positive charge. Thus, the process of ionization results in the formation of electron-ion pairs in a material. If none of the electrons or ions leave the material, the material remains electrically neutral, since the positive and negative charges balance one another. Nevertheless, characteristics of the material may be altered considerably by ionization. The number of electron-ion pairs formed and their subsequent behavior are of prime interest in determining the effects of ionization.

[REDACTED] Gamma rays interact with matter in three ways. The first is called the Compton effect. In this type of interaction, a gamma ray (primary photon) collides with an electron, and some of its energy is transferred to the electron (see Figure 6-1a). A secondary photon, with less energy, is created and departs in a direction at an angle to the direction of motion of the primary photon. The second type of interaction of gamma rays with matter is the photoelectric effect (see Figure 6-1b). A gamma ray, with energy somewhat greater than the binding energy of an electron in an atom, transfers all its energy to the electron, which is consequently ejected from the atom. Since the photon involved in the photoelectric effect transfers all of its energy, it ceases

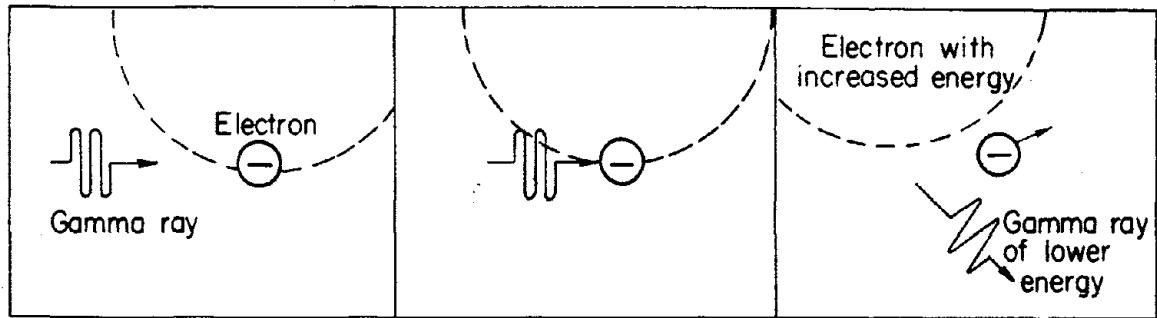
[REDACTED] to exist and is said to be absorbed. The third type of interaction is pair production (see Figure 6-1c). When a gamma ray photon with energy in excess of 1.02 MeV passes near the nucleus of an atom, the photon may be converted into matter with the formation of a pair of electrons, equally but oppositely charged. The positive electron soon annihilates with a negative electron to form two photons, each having an energy of at least 0.51 MeV. In some cases, if the interaction takes place near the nucleus of a heavy atom, only one photon of about 1.02 MeV energy may be created.

[REDACTED] Any photon (e.g., an X-ray or a gamma ray) can produce ionization in a material by these processes of creating secondary electrons that deposit their kinetic energy by ionizing the medium in which they are created. The relative importance or frequency with which each process occurs depends upon the photon energy and the characteristics of the material. The Compton process is the dominant ionization mechanism for most gamma rays of interest, particularly in electronic materials such as silicon, of which many solid-state devices are fabricated.

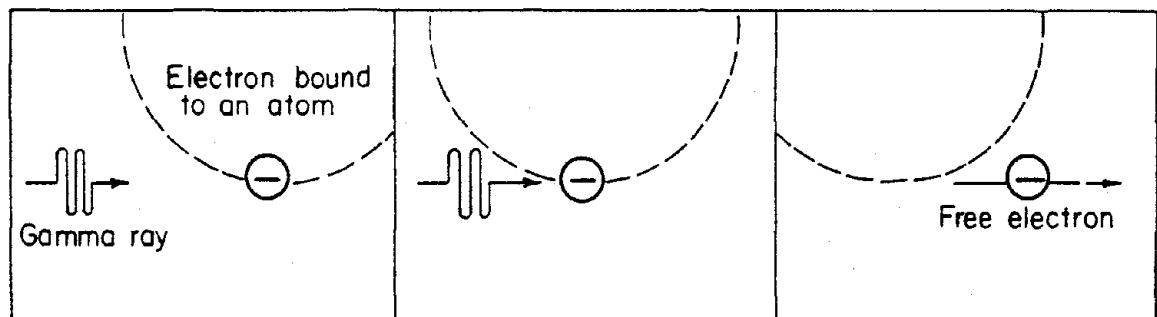
[REDACTED] Fast neutrons can produce ionization indirectly. As neutrons undergo inelastic scattering and capture in a material (see Section I, Chapter 5), gamma rays that are emitted can cause ionization. In addition, collision of a neutron with an atom may impart sufficient energy to the atom for it to cause ionization. Only high-energy neutrons ( $E > 1$  MeV) contribute significantly to ionization. The 14-MeV neutrons arising from fusion reactions in a weapon are particularly important.

[REDACTED] The types of radiation that cause ionization in materials — namely, gamma rays, electrons, X-rays, and, to a lesser extent, fast neutrons — are known collectively as ionizing radiation.

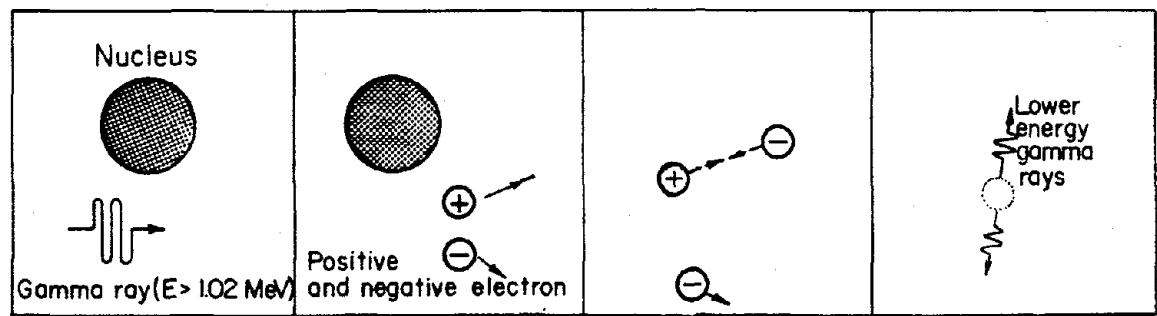
[REDACTED] Once created by the ionization processes (either primary or secondary), the charged par-



a. Compton Effect



b. Photoelectric Effect



c. Pair Production

Figure 6-1. Gamma Ray Interaction with Matter

ticles (electrons or ions) are free to move in a material, scattering frequently and following a random-walk pattern. If the concentration of electric charge carriers throughout the material is not uniform, and if no externally applied electric field is present, the carriers will move from regions of high concentration to regions of low concentration. This movement is known as diffusion and it would be superimposed on the normal random-movement. If an electric field is present (e.g., as a result of an intentionally applied voltage), the carriers drift in the electric field while they undergo a predominantly random scattering. If impurities are present in the material (as they always are in solid-state devices, such as transistors and diodes), carriers may be captured (trapped) and immobilized by impurity atoms (traps). Eventually, the trapped carriers will be annihilated by their mates (oppositely-charged carriers) in a process called recombination. The net result of these processes is that the carriers diffuse and/or drift until they are trapped and usually recombined.

## 6-5 Displacement

As described above, ionization involves the movement of electrically charged electrons and ions in a material. Displacement involves the movement of atoms (which are electrically neutral).

Any material may be described as being either crystalline or amorphous. The atoms of a crystalline material (a crystal) are arranged in a definite, repeated, three-dimensional pattern called a lattice; the atoms of an amorphous material have no definite arrangement. Displacement is an important phenomenon in crystalline materials, and it is a very important phenomenon in TREE because many electronic devices (e.g., transistors, diodes, integrated circuits) are constructed from crystalline semiconductors — primarily silicon and germanium. Lattice defects result from the displacement of atoms from their

usual sites in crystal lattices. The simplest lattice defects are extra atoms inserted between lattice positions (interstitials) and unoccupied lattice positions (vacancies). At least part of the resultant damage to the material is stable and accounts for permanent property changes of irradiated crystalline materials.

The production of displacement damage in a crystalline solid is a complex process. An abbreviated history of this process follows.

- (1) Radiation of an appropriate form enters the material, interacts with a lattice atom, and imparts to it a certain energy.
- (2) The target (recoil) atom leaves its lattice site, thus creating a vacancy, and collides with other lattice atoms (see Figure 6-2).
- (3) Other atoms are displaced from their sites, creating more vacancies.
- (4) Eventually, most recoil atoms come to rest in interstitial positions, while a few fall into vacancies. Some of the interstitials and vacancies may be isolated, but most of them will be associated with other defects in cluster formations.
- (5) The simple defects and defect clusters migrate through the crystal.
- (6) Eventually, the mobile defects are annihilated by recombination of vacancy-interstitial pairs, are immobilized by the formation of stable defect clusters with other impurities or lattice defects (either present in the original material or created by the irradiation), or escape to a free surface.
- (7) Meanwhile, the physical properties of the material are changed by the presence of the defects.

Fast neutrons are very effective in producing displacement damage. Energetic electrons can also produce displacement damage; however, their displacement effects are negligible compared to those of fast neutrons.

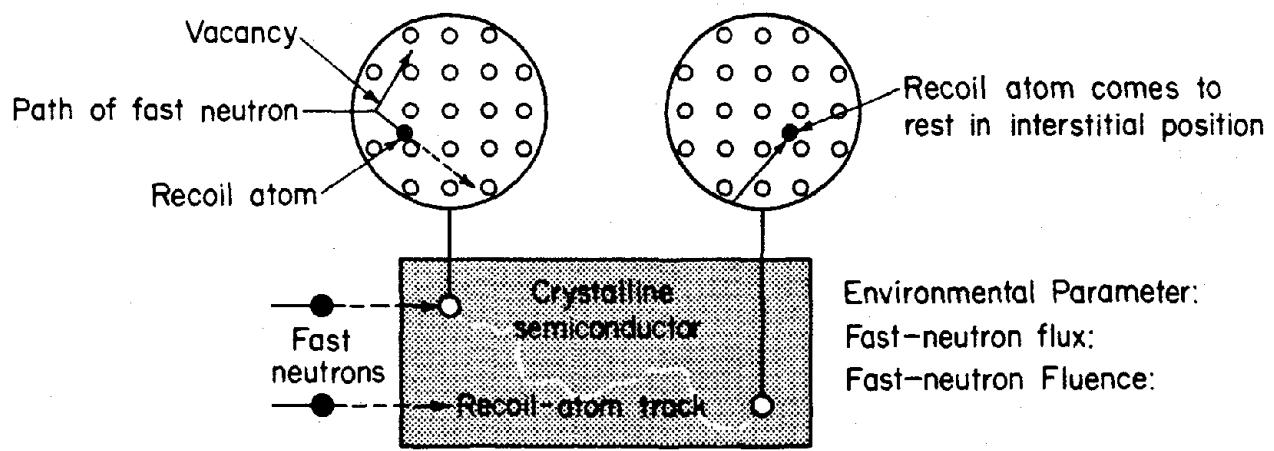


Figure 6-2. Displacement Damage in a Crystalline Solid

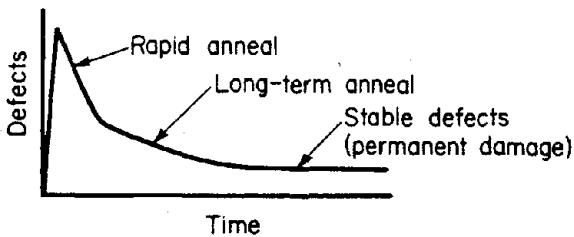
The absolute magnitude of damage in a material caused by neutrons is difficult to predict because some of the defects that are produced will effectively disappear at room temperature, that is, anneal. However, much useful information can be gained from the relative value of the concentration of defects produced before annealing. Assuming the same fraction anneals, the relative concentration of stable defects would be in the same ratio. It has been found that the number of unannealed defects that are generated depends on the energy of the impinging neutron. The number of unannealed defects generated by a 14-MeV neutron (one from a fusion weapon) is about 2.5 times the number of unannealed defects generated by a 1-MeV neutron (roughly the average energy for a neutron from a fission weapon). As will be discussed below, the number of defects generated in semiconductor materials is directly related to the change in semiconductor device parameters.

Not all of the defects produced in the displacement process are stable. Some defects are annihilated by recombination of vacancy-interstitial pairs, some combine with pre-existing lattice defects, and some eventually escape to a

free surface of the material. The stable defects contribute to the permanent damage of the material. The unstable defects are said to disappear, or anneal, with time. In practice, this means that the degree of displacement damage in a crystalline semiconductor varies with time, reaching a peak rapidly and then partially annealing with time. The temperature of the material exerts a considerable influence on the amount of annealing that takes place. More annealing is observed at elevated temperatures.

Annealing may be divided roughly into two time frames. Rapid, or short term, annealing occurs in times of the order of hundredths of a second. Long term annealing continues at a slower rate for times of the order of tens of seconds (see Figure 6-3). If the temperature remains constant, annealing will be essentially complete after one-half hour. The ratio of the damage observed at early times (number of defects present) to the damage after a very long time is called the annealing factor, which is a function of the time of measurement and other parameters. The maximum damage created at short times following the fast-neutron burst frequently is important to electron-system perfor-

mance. Therefore, the maximum annealing factor is an important quantity, because it indicates the peak damage that must be tolerated above the permanent damage in the steady state. Values of the annealing factor depend on the temperature and on the electrical condition of the material. An annealing factor of three is commonly used for room temperature at  $\sim 10$  msec. Larger factors have been observed at shorter times, or low injection conditions (e.g., cut-off transistors).



Environmental Parameters:

Fast-neutron flux:

Fast-neutron Fluence:

Figure 6-3. [REDACTED] Annealing Due to Vacancy-Interstitial Recombination and Escape of Defects from Semiconductor [REDACTED]

## 6-6 Heating

[REDACTED] Whenever a material absorbs energy from its surroundings and cannot instantaneously dissipate that energy, the temperature of the material will rise, i.e., the material will be heated. The temperature will return to ambient at a rate determined by the efficiency with which the material can dissipate heat to its surroundings. If the energy deposition is great, and the mechanisms for heat dissipation are inadequate, the temperature rise will be significant and will persist for a considerable time (see Figure 6-4).

[REDACTED] X-rays are the primary contributors to heating. Therefore, the relevant environmental parameters are the X-ray dose rate, and the

X-ray dose. Predictions of the X-ray environment from nuclear weapon bursts and the X-ray absorption mechanisms are discussed in Chapter 4. Responses of electronic components to heating are discussed in Section VII, Chapter 9.

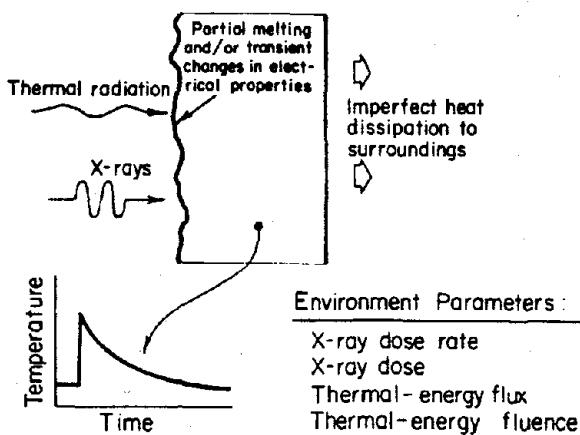


Figure 6-4. [REDACTED] Heating [REDACTED]

## MANIFESTATIONS OF TREE IN MATERIALS

### 6-7 Ionization Effects

[REDACTED] The important manifestations of ionization include (1) charge transfers, (2) bulk-conductivity increases, (3) excess minority-carrier generation, (4) charge trapping, and (5) chemical effects.

[REDACTED] Charge transfer results from the escape of some electrons produced during ionization from the surface of the material being ionized. If the net flow of electrons is out of the material, the material will be left with a net positive charge. If these electrons are stopped in an adjacent material, a transfer of charge will have occurred from one material to the other, and a difference of potential (or voltage) will exist between the two materials.

The transfer of charge from one material to another can have a number of effects. The most obvious one is that a current will flow through any electrical circuit connecting the two materials to restore charge neutrality. The charge will produce electric and magnetic fields during transit. If there is matter in the gap between the materials, the charge transfer also will produce ionization and conduction in response to local electrical fields. Finally, if the charge either originates or embeds itself in an insulator, a long-lived local space charge may result. Charge transfer, therefore, may result in either a temporary or a semipermanent effect.

The free carriers produced during ionization respond to an applied electric field by producing a net drift current. This is precisely the mechanism by which a material conducts electricity. Therefore, ionization induces a transient increase in conductivity. An example of a detrimental effect to the operation of electronic equipment resulting from an increase in bulk conductivity occurs in a capacitor exposed to a weapon burst environment. The ability of a capacitor to retain, or restore, electrical charge is dependent upon the low conductivity of the dielectric, or insulating material, that is contained within the capacitor. In an ionizing environment the increase in bulk conductivity results in a decrease of stored charge in the capacitor.

The ionization effect of excess minority carriers is a prime concern in many semiconductors and is usually the most important manifestation of TREE. Semiconductor devices, such as transistors and diodes, employ both positive and negative charge carriers, either of which may be in the minority with respect to concentration. The characteristics of many such devices depend strongly upon the instantaneous concentration of minority carriers in various regions of the device. Since ionizing radiation creates large (and equal) numbers of positive and negative charge carriers, the concentration of minority

carriers in the device is temporarily enhanced by a large percentage, and the electrical operation of the device may be affected adversely. The most familiar example of this effect is the current flow across a reverse-biased PN junction, such as those that are found in a diode or the base-collector junction of a transistor (see Section VII, Chapter 9).

When free carriers are created in insulating materials, and are trapped at impurity sites, many may not undergo recombination with their mates, which may be trapped elsewhere. In these cases, the material properties may be altered semipermanently, even though there is no net charge in the material. This ionization effect is known as charge trapping.

Trapped charge can change the optical properties of materials (e.g., F centers in alkali halides, coloration of glasses). The trapped carriers may be released thermally, either at the irradiation temperature or by elevating the temperature. In either case the resultant creation of some free carriers is manifested by an increase in conductivity and sometimes by the emission of light.

The chemical effects of ionization occur during the processes of trapping and recombination when sufficient energy is available to disrupt chemical bonds. At the completion of the ionization cycle (i.e., after recombination is complete), the material may return to electrical inactivity, but its chemical composition may be altered permanently. The resulting chemical changes may be manifested as permanent changes in physical and/or electrical properties of the material. The radiation dose required to cause such effects is larger than normally will be encountered; therefore, the effect will not be discussed further.

Since ionization effects do not occur and/or recover in the same time period, the time domain for their occurrence and recovery must be considered. There are three categories of time

dependence – prompt, delayed, and long term.

Prompt effects are those in which the width of the ionization pulse is longer than the times required for atoms or electrons within the material being exposed to make a specified amount of recovery. The magnitude of the effect is a function of the density of the positive and negative particles created during the ionization, which in turn is a function of the dose rate. Examples of prompt effects are charge transfer and prompt bulk-conductivity increases in insulating and semiconductor materials.

Delayed effects are those in which the width of the ionization pulse is shorter than the times required for atoms or electrons within the material being exposed to make a specified amount of recovery. The initial response of the material or device is a function of dose, and its persistence is determined by the length of the specified recovery time. An example of this effect is delayed bulk conductivity of insulator materials. In this particular example the recovery times for the prompt and delayed effects are based on different mechanisms of carrier generation (ionization induced or thermal trapping) and, hence, they have very different time periods.

Long-term effects are those which persist for periods longer than minutes. These effects can be, but are not necessarily, permanent. Recovery may be so slow that it takes days, months, or years for apparent complete recovery. Examples of long-term effects are some cases of trapped charge and chemical effects.

An important point, emphasized here, is that a general class of materials or devices (plastics, transistors, etc.) could be both dose and dose-rate sensitive with respect to the ionization effects observed.

It has been established that, with the exception of charge transfer, the magnitude of the ionization effects is primarily a function of the total concentration of thermalized charge car-

riers (electrons and holes). These carriers are generated at a rate proportional to the instantaneous ionization energy deposition and independent of the nature of the radiation producing that energy deposition. Therefore, it is appropriate to use units that quantify the energy deposition in the material of interest when describing the radiation field at the responding device. Such units include ergs/gram (material), rads (material), and calories/gram (material). Since these are descriptions of energy deposition in a given material, they are called units of dose. The time dependence of energy deposition can be specified by these same units per second, and are called dose rate.

Unfortunately, the magnitude of charge transfer depends not only on the energy deposition but the spectrum of the secondary electrons. Therefore, quantitative evaluations of systems in which charge transfer represents a significant vulnerability mode must use a more complex characterization of the spectrum of the incident photons, together with a calculation of the photon interactions, to produce the spectrum of secondary electrons.

In some materials, particularly insulators, the ionization effects are also a weak function of the microscopic concentration of the ionization around individual particle tracks. For example, neutron-induced ionization created by intensively ionizing recoil atom may be less effective in producing conductivity in an insulator than the same dose or dose rate imparted by lightly ionizing gamma rays. Units for describing this process include specific ionization (ratios of ionization to the minimum level of ionization at high velocities of a singly charged particle), and linear energy transfer (MeV/cm or MeV cm<sup>2</sup>/gram). Fortunately, these effects are of second order importance for most TREE applications. A specification of dose rate and dose is adequate in the majority of applications.

The gamma-ray field incident on a

system is frequently described by its exposure measure in roentgens. The roentgen is determined by specifying the energy deposition in a standard material (dry air under standard temperature and pressure conditions). For high energy gamma rays that interact primarily via the Compton process, exposure of almost any material to one roentgen of gamma rays produce (within 20%) approximately one rad of energy deposition in any material. This factor has enabled the users of these units to become somewhat careless, without serious consequence, so long as only high-energy photons are of interest. However, these relations do not carry over into photons of lower energies (200 kilovolts or less in medium atomic-number materials) and careful treatment of the units is required. One way of minimizing the chances of misinterpretation is to use units of calories/cm<sup>2</sup> with a defined spectrum for external exposure and units of cal/gram (material) for dose.

#### 6-8 Displacement Effects

The displacement effects of prime concern to TREE are those generated in semiconductor materials. The lattice damage resulting from displacement degrades the electrical characteristics of semiconductor devices by increasing the number of trapping, scattering, and recombination centers. The effect of displacement in semiconductors is, therefore, threefold: (1) the trapping centers remove charge carriers from the electrical conduction process (reduces electrical current flow), (2) the additional scattering centers reduce the capability of the charge carriers to move through the semiconductor material (reduces charge-carrier mobility), and (3) the recombination centers reduce the time that the minority charge carriers are available for electrical conduction (reduces the lifetime of the minority-charge carriers). This last effect is most important for prediction of semiconductor device performance in radiation environments that cause displacement. The decrease in minority-

carrier lifetime ( $\tau$ ) is predicted according to the relationship

$$\frac{1}{\tau_\varphi} = \frac{1}{\tau_0} + K\varphi,$$

where

$\tau_\varphi$  = minority-carrier lifetime at fluence  $\varphi$  in seconds,

$\tau_0$  = initial minority-carrier lifetime in seconds

$K$  = lifetime damage constant, cm<sup>2</sup>/(neutron · second)

$\varphi$  = total fast-neutron fluence, neutrons/cm<sup>2</sup>.

Typical values for  $\tau_0$  in device materials of interest are  $10^{-8}$  to  $10^{-4}$  seconds. The value of the lifetime damage constant,  $K$ , is dependent on the type of material, the type and amount of impurities in the material, the operating voltage applied to the material, the temperature, the energy spectrum of incident neutrons, and, because of defect annealing, the time after the nuclear radiation is incident on the material. A general value for silicon, the prime material used in transistors, diodes, and integrated circuits, is  $K \approx 1 \times 10^{-6}$  cm<sup>2</sup>/(n · sec).

To illustrate the magnitude of displacement effects that occur in semiconductors compared to those that occur in other materials, a comparison of neutron fluences that will cause significant effects is made in the following paragraph. Interest is focused only on those property changes that affect the normal use of the materials being compared.

Semiconductor lifetime can begin to show significant effects in devices at a fluence of  $10^{11}$  n/cm<sup>2</sup> (Pu, fission)\* and by  $10^{16}$  n/cm<sup>2</sup>

\*Accurate neutron dosimetry requires that the foil used for making the neutron measurement and the energy spectrum of the neutrons be specified with the value measured. Therefore, in the example presented here,  $10^{11}$  neutrons per square centimeter were detected with a plutonium foil and the energy spectrum of the neutrons was a nominal fission spectrum.

(Pu, fission) the lifetime in most semiconductor devices is so short that the device is no longer useful. Metals such as nickel and copper start to show effects in material strength at a fluence of  $10^{18}$  n/cm<sup>2</sup> (Pu, fission). As a general rule, the electrical properties will not start to change in structural materials until the material properties change. Glasses and ceramics are much less susceptible to neutron damage than semiconductors, but they are more susceptible than metals. The point that is emphasized is that semiconductors are among the devices that are most susceptible to displacement effects.

[REDACTED] It is frequently desirable to express neutron effects data observed by different experimenters using different neutron-energy spectra in terms of an equivalence fluence unit in addition to the measured flux and fluence units. This permits easy comparison of damage levels obtained from different neutron test facilities. Since silicon is the material of most interest to displacement effects, the equivalence is usually based upon damage in silicon. The energy spectrum typically used as a standard for comparison is a hypothetical 1-MeV monoenergetic neutron source. The damage caused by the neutrons (of some known spectrum) is compared to the damage done by the neutron spectrum which is used as a standard. The neutron fluence of the standard which would cause the same damage in the given material as observed for the known spectrum is then specified as the damage equivalent fluence for that material. An example of this equivalence unit for 1-MeV neutrons standard spectrum and silicon material is:  $10^{13}$  n/cm<sup>2</sup> (1-MeV damage equivalence in silicon). The procedures for obtaining a 1-MeV equivalent fluence for any known neutron spectrum are specified in the TREE Handbook (see bibliography).

### 6-9 Heating Effects [REDACTED]

[REDACTED] The radiation environment, especially the X-rays, produced by nuclear weapons

can deposit considerable energy in electronic materials. The energy deposited is sufficient to heat some materials to such an extent as to cause partial melting, and it is sufficient to change electrical properties in other materials. These temperature transients may last from fractions of a second to minutes. If the energy is deposited in the material in a very short time (deposition time is typically  $10^{-8}$  seconds for a nuclear weapon) an additional effect is observed; the material is heated very rapidly but does not have time to expand. The result is the instantaneous creation of a shock wave, or pressure pulse, which tends to compress the material. This compression wave starts at the point of energy absorption, typically close to the material's front surface upon which the incident energy impinges, and quickly propagates to the back surface. When it reaches the back surface, it is reflected, becomes a tension wave, and propagates toward the front surface. For energy deposition of sufficient magnitude delivered in a sufficiently short interval, the tension wave can be intense enough to exceed the strength of the material. Several consequences are possible.

- (1) Portions of the material may be removed from the back surface — spallation (see Figure 6-5).
- (2) Fragments of the material may separate from the front surface — blowoff.
- (3) The material may separate between front and back surfaces — delamination.
- (4) Agglomerates or layers of dissimilar materials bonded together will tend to separate at the interfaces — also called delamination.
- (5) In brittle crystalline materials (e.g., Si or Ge), crystal fracture can occur.

Generally, effects of this nature are referred to as thermomechanical shock effects. Obviously, the consequences of these effects can be catastrophic. An example important to transistors and inte-

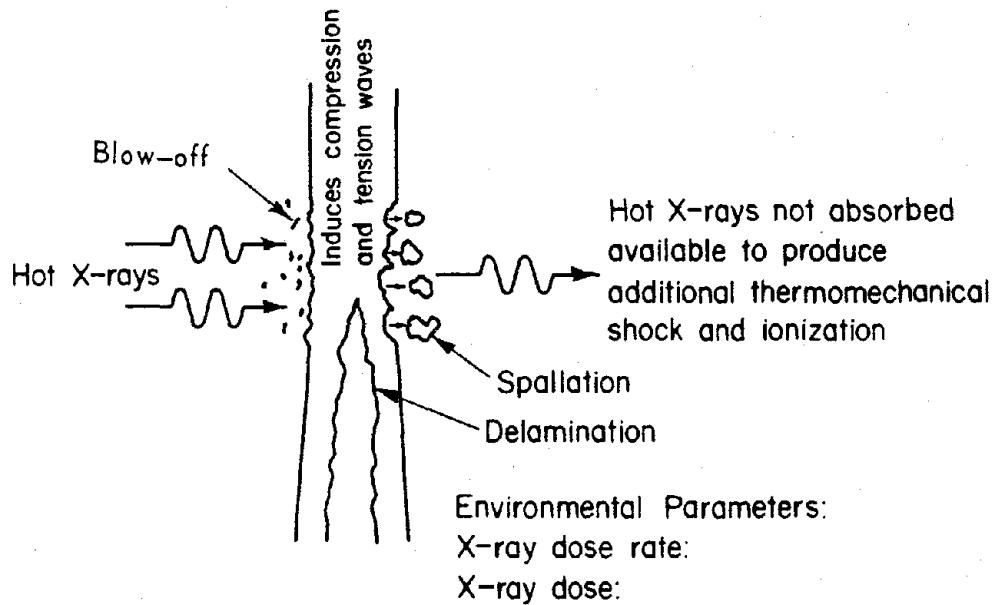


Figure 6-5.

#### Thermomechanical Shock Effects

grated circuits is the delamination of the electrical contacts to the semiconductor chip, resulting in complete loss of the device function. The thermomechanical-effect damage threshold is difficult to determine. It depends not only on the energy deposition and energy spectrum but

also on the thickness of the materials, the compressibility, the expansion coefficient, and the dynamic strength of the materials. Thermomechanical effects on materials are discussed in more detail in Section VII of Chapter 9.

## BIBLIOGRAPHY

DASA EMP (*Electromagnetic Pulse*) Handbook, DASA 2114-1, DASIAC, Santa Barbara, California, September 1968, [REDACTED] (to be replaced by DNA 2114H-1 during calendar year 1972).

DASA EMP (*Electromagnetic Pulse*) Handbook, *Classified Supplement* [REDACTED] DASA 2114-2, DASIAC, Santa Barbara, California, September 1968, [REDACTED] (to be replaced by DNA 2114H-2, 2114H-3, and DNA 2114H-4 during calendar year 1972).

Gwyn, C. W., D. L. Scharfetter, and J. L. Wirth, *The Analysis of Radiation Effects in Semiconductor Junction Devices*, SC-R-67-1158, Sandia Corporation, Albuquerque, New Mexico, July 1967 [REDACTED]

Kalinowski, J. J., *A Management Guide to Transient-Radiation Effects on Electronics (TREE)* [REDACTED] DNA 2051H, Battelle Memorial Institute, Columbus, Ohio, February 1972 [REDACTED]

Larin, F., *Radiation Effects in Semiconductor Devices*, John Wiley and Sons, Inc., New York, 1968 [REDACTED]

TREE (*Transient-Radiation Effects on Electronics*) Handbook [REDACTED] Vol. 1 Edition No. 3, DNA 1420H-1, Battelle Memorial Institute, Columbus, Ohio, December 1971 [REDACTED]

TREE (*Transient-Radiation Effects on Electronics*) Handbook [REDACTED] (*Classified Supplement*), Edition 2, Revision 2, DASA 1420-1, Battelle Memorial Institute, Columbus, Ohio, September 1970, [REDACTED] (to be replaced by DNA 1420H-2 during calendar year 1972).

TREE Preferred Procedures (*Selected Electronic Parts*), DASA 2028, Defense Atomic Support Agency, Washington, D.C., May 1968, [REDACTED] (to be replaced by DNA 2028H during calendar year 1972).

Vook, F. L., Editor, *Radiation Effects in Semiconductors*, Proceedings of the Santa Fe Conference on Radiation Effects in Semiconductors, Plenum Press, New York, 1968 [REDACTED]

## Chapter 7

### ELECTROMAGNETIC PULSE (EMP) PHENOMENA

The nuclear electromagnetic pulse (EMP) is the time-varying electromagnetic radiation resulting from a nuclear burst. It has a very broad frequency spectrum, ranging from near dc to several hundred MHz.

The generation of EMP from a nuclear detonation was predicted even before the initial test, but the extent and potentially serious degree of EMP effects were not realized for many years. Attention slowly began to focus on EMP as a probable cause of malfunction of electronic equipment during the early 1950s. Induced currents and voltages caused unexpected equipment failures during nuclear tests, and subsequent analysis disclosed the role of EMP in such failures. Finally in 1960 the possible vulnerability of hardened weapon systems to EMP was officially recognized. Increased knowledge of the electric and magnetic fields became desirable for both weapons diagnostics and long-range detection of nuclear detonations. For all these reasons a more thorough investigation of EMP was undertaken.

Theoretical and experimental efforts were expanded to study and observe EMP phenomenology and to develop appropriate descriptive models. A limited amount of data had been gathered on the phenomenon and its threat to military systems when all aboveground testing was halted in 1962. From this time reliance has been placed on underground testing, analysis of existing atmospheric test data, and nonnuclear simulation for experimental knowledge. Extended efforts have been made to improve theoretical models and to develop associated computer codes for predictive studies. At the same time, efforts to develop simulators capable of produc-

ing threat-level pulses for system coupling and response studies have been expanded.

This chapter describes the EMP generation mechanism and the resulting environment for various burst regimes. The description is largely qualitative, since the complexity of the calculations requires that heavy reliance be placed on computer code calculations for specific problems. Some results of computer code calculations are presented, but generalization of these results is beyond the scope of this chapter. More complete treatments of the EMP phenomena may be found in the "DNA EMP (Electromagnetic Pulse) Handbook (U)" (see bibliography).

#### ENVIRONMENT - GENERAL DESCRIPTION

##### 7-1 Weapon Gamma Radiation

The gamma radiation output from a nuclear burst initiates the processes that shape the development of an electromagnetic pulse. The gamma radiation components important in EMP generation are the prompt, air inelastic, and isomeric gammas (see Chapter 5). Briefly, the prompt gammas arise from the fission or fusion reactions taking place in the bomb and from the inelastic collisions of neutrons with the weapon materials. The fraction of the total weapon energy that may be contained in the prompt gammas will vary nominally from about 0.1% for high yield weapons to about 0.5% for low yield weapons, depending on weapon design and size. Special designs might increase the gamma fraction, whereas massive, inefficient designs would decrease it. This component is generated within

Change 1 7-1

less than a microsecond of detonation time. High energy neutrons, which result from the fusion process, emerge from the bomb debris with energies on the order of four to fourteen MeV. For a surface or air burst, these neutrons lose their energies primarily through a large number of inelastic collisions with the surrounding air molecules over a time period of many microseconds. This gives rise to a source of gammas over the same time span. Isomeric gammas are given off by nuclei of certain fission products in decaying from excited states to the ground state. They are important at times after the peaks in prompt and air inelastic contributions (see Section 1, Chapter 5).

## 7-2 Compton Current

When gamma radiation from any of the sources mentioned in the preceding paragraph impinges upon air molecules, high energy electrons are created by the Compton effect. In this effect, illustrated in Figure 7-1, the incident gamma ray interacts with an electron in the shell of an atom, imparting to it a large amount of energy. Both the electron and a less energetic

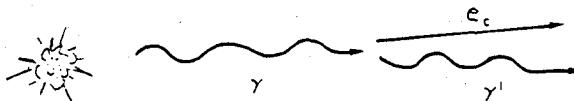


Figure 7-1. (U) The Compton Effect (U)

gamma ray scatter, primarily in the forward direction, and the scattered gamma rays frequently retain sufficient energy to repeat the process. In addition to the generation of Compton electrons, over ten percent of the gamma rays with energy above 5 MeV may generate electron-positron pairs (pair production). The

## 7-2 Change 1

positrons will cause ionization by inelastic collisions and eventually will be annihilated on collision with an electron, resulting in two 0.511 MeV gamma rays. The radial beams of scattered high energy electrons comprise a current termed the Compton current. If certain spatial and time conditions are met by a current, an electromagnetic field is generated. Since the prompt gamma ray pulse increases rapidly to a peak value and then decays (Section 1, Chapter 5), and since the Compton electrons lose energy as described in the following paragraph, the Compton current rises to a peak value rapidly and then decays as illustrated in Figure 7-2.

## 7-3 Air Conductivity

The high energy electrons in the Compton current lose some energy to the surrounding air molecules through inelastic collisions. The energy lost in these collisions goes into the freeing of additional electrons from the air molecules, i.e., further ionization. A drastic change in the conductivity of air takes place as it is ionized to become a plasma consisting of molecules, atoms, ions, electrons and accompanying electromagnetic radiation (see paragraph 4-2, Chapter 4). The conductivity will vary in space and time with the density and mobility of the ions and electrons, and the mobility depends on the electric field strength. Under certain conditions of air density and distance the x-rays from the bomb may contribute significantly to the air conductivity. Further complications are introduced by the recombination of ions and electrons. Initially the dominant process is the attachment of electrons to neutral oxygen molecules, reducing their mobility. Later the negative ions and electrons recombine with positive ions, reducing the charge density. Both processes, which are strongly dependent on air density, water content of the air, and the electric field, tend to reduce the conductivity of this partially ionized plasma. Figure 7-3 shows an example of air conductivity. The sudden rise at 8 microseconds



UNANNOUNCED

7-4 Change 1

Deleced

DNA  
4-X(1)

Figure 7-3 [redacted] Conductivity at 500 Meters from a 4200 TJ (1 Mt) Low-Altitude Burst [redacted]

is due to the local arrival of the neutron flux that produces ionization by nuclear reactions other than inelastic collision, namely  $(n,p)$  and  $(n,\gamma)$  reactions; however, earlier times are of greatest interest for the generation of EMP.

#### 7-4 Radical Electric Field

If a nuclear burst occurs in homogeneous (constant density) atmosphere, with no geomagnetic fields present, a charge-separation model may be used to describe the resulting electric fields. Positive and negative charges are separated as the Compton electrons sweep off in a radial direction from the explosion, while the heavier ions tend to remain behind. Thus, two shells of charge are created, an inner positive ion shell and an outer shell of electrons. This separation produces a large local electric field in the radial direction shown as  $E_r$  in Figure 7-4. The magnitude of the field is limited as the air conductivity rises to permit return currents. Conductivity is higher closer to the burst where the current are more dense, so this region is the first to saturate and to limit the radial field although the radial electric field is higher when saturation occurs. These effects are depicted schematically in Figure 7-5.

It is to be noted, however, that the total current distribution and the resulting radial electric field are perfectly spherically symmetric in this hypothetical illustration. It is a fundamental property of such a current distribution that no magnetic field is generated and no electromagnetic field is radiated away. The various asymmetries that occur in practice, and the resulting fields that are generated in the source region or radiated away are discussed in the following paragraphs.

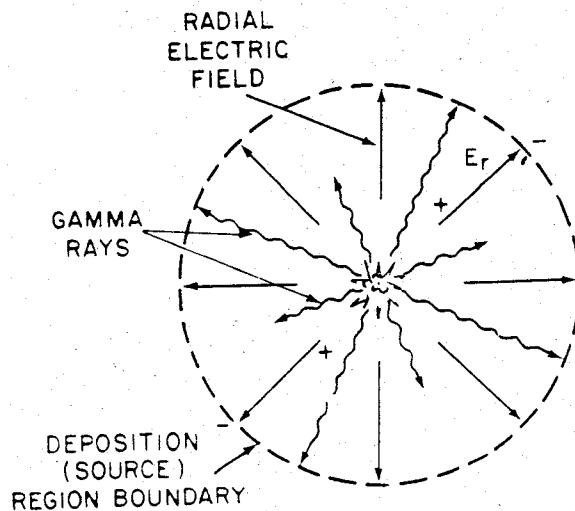


Figure 7-4. Charge Separation Model

#### ELECTROMAGNETIC FIELD GENERATION

##### 7-5 Medium Altitude Air Burst

This category of nuclear explosions is defined to include weapon bursts under about 30 kilometers (19 miles) altitude, but sufficiently high that the deposition region containing the source currents does not touch the earth. In this case there are three principal factors tending to destroy the spherical symmetry of the current distribution discussed in the preceding paragraph: the atmospheric density gradient, the earth's magnetic field, and the configuration of the weapon itself. Since the earth's magnetic field is a much more important influence in less dense atmosphere, it will be discussed in succeeding paragraphs in connection with high-altitude bursts.

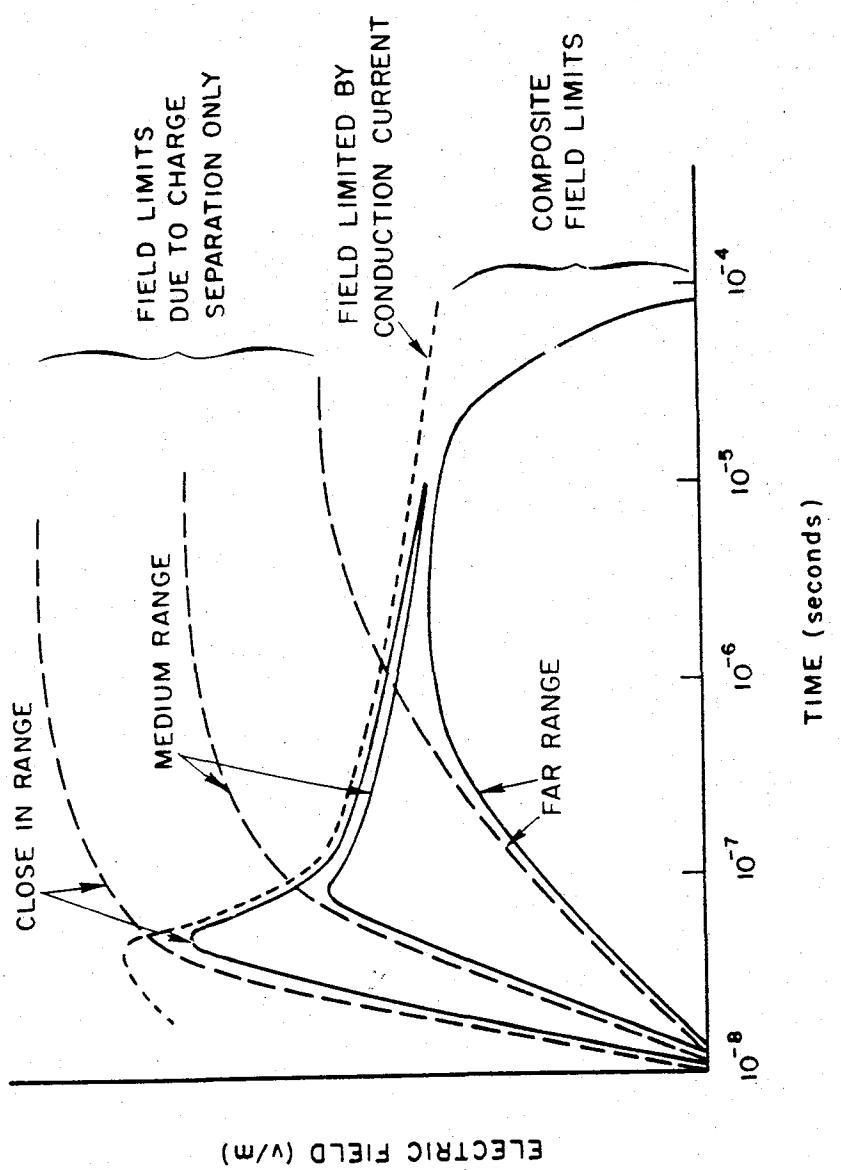


Figure 7-5. Limits on Electric Field Waveforms

The density gradient in the lower atmosphere leaves the current distribution in the deposition region symmetric in azimuth only, since the strength of all the deposition region interactions depends on the density of its constituents. Thus there is a net vertical current component, the strength of which is expressed in terms of a dipole moment. This quantity is responsible for the generation of a magnetic field in the deposition region and the radiation of an electromagnetic wave from this region. These effects are shown in Figure 7-6, assuming no weapon asymmetry. The radiation, which is in the form of a simple vertical electric dipole, is a high intensity brief pulse that includes a broad spectrum of frequencies up to many MHz. Figure 7-7 demonstrates the relationship of energy per unit frequency as a function of frequency. The electric field as a function of range,  $R$ , and azimuth,  $\theta$ , follows the form

$$E(t) = \frac{R}{R_0} E_0(t) \sin \theta$$

where  $R_0$  is the radius of the deposition region and  $E_0$  is the time dependent electric field at  $R_0$ . The angular dependence of radiated electromagnetic radiation is such that maximum intensity is radiated horizontally from the burst and is minimum directly above or below the burst. Simplified general waveforms of the quantities discussed here are presented in Figure 7-8.

### 7-6 Surface Burst

The presence of the ground introduces a strong asymmetry in addition to the ones described above. The ground is a very good absorber of neutrons and gamma rays and a good conductor of electricity compared with air. Therefore, the deposition region consists approximately of a hemisphere, resulting in a very large dipole moment and consequently large radiated fields. Further, the conducting ground allows an effective return path for the electron shell near the surface with the result that current loops are formed. That is, electrons travel outward from the burst in the air, then return through the higher conductivity ground toward the burst point. These current loops form a toroidal shaped solenoid resulting in very large azimuthal magnetic fields in the deposition region, especially close to the ground. These effects are shown in Figure 7-9. Figure 7-10 shows a typical toroidal magnetic field waveform in the deposition region near the surface.

There can be extremely large electric and magnetic fields as well as the presence of a highly conducting plasma within the deposition region. As a result of the number of variables that can affect the magnitude and shape of the fields, it is not possible to provide a simple description of the fields.

The peak radiated electric fields are ten to a hundred times stronger than for a similar air burst. The range,  $R_0$ , at which the radiation region begins is a function of weapon yield as shown in Table 7-1.

The magnitude of the peak value of the radiated electric waveform for a surface burst is a weak function of yield, varying from about 1,300 volts per meter at  $R_0$  for a 4.2 TJ (1KT)

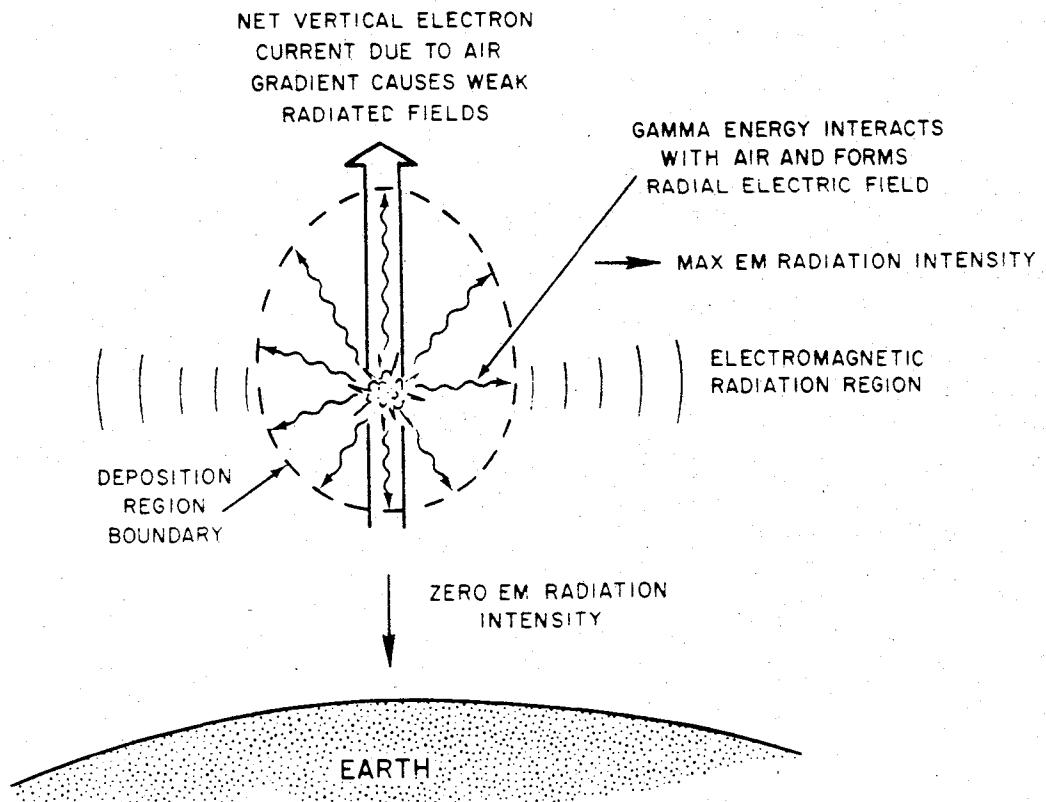


Figure 7-6. [REDACTED] Simple Illustration of Air-Burst EMP [REDACTED]

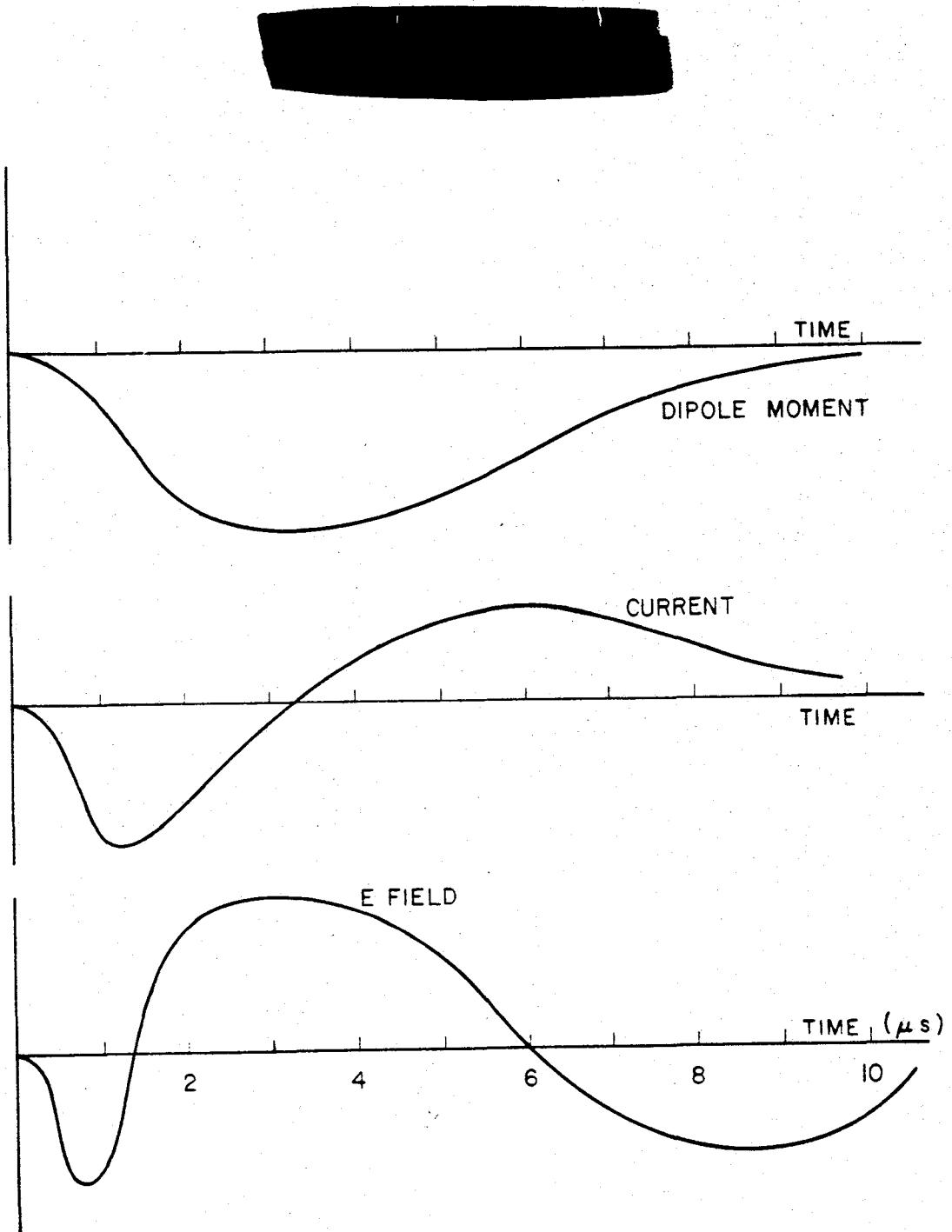


Figure 7-8 Comparison of General Waveforms for the Dipole Moment, the Current, and the E-Field for an Air Burst

7-10 Change 1

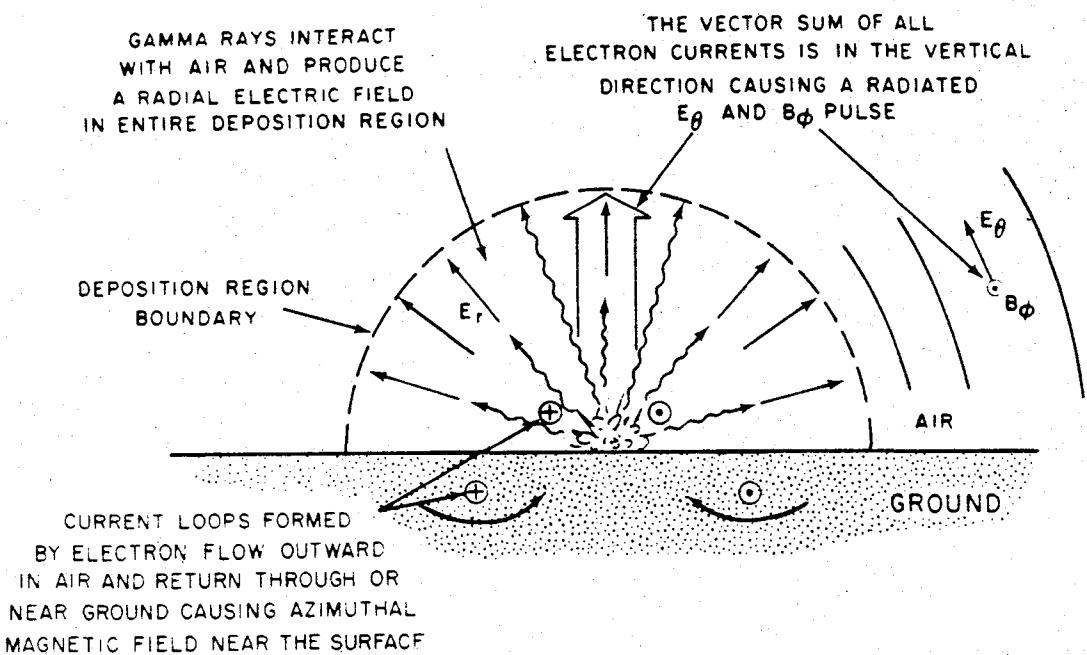


Figure 7-9 Simple Illustration of Surface Burst EMP

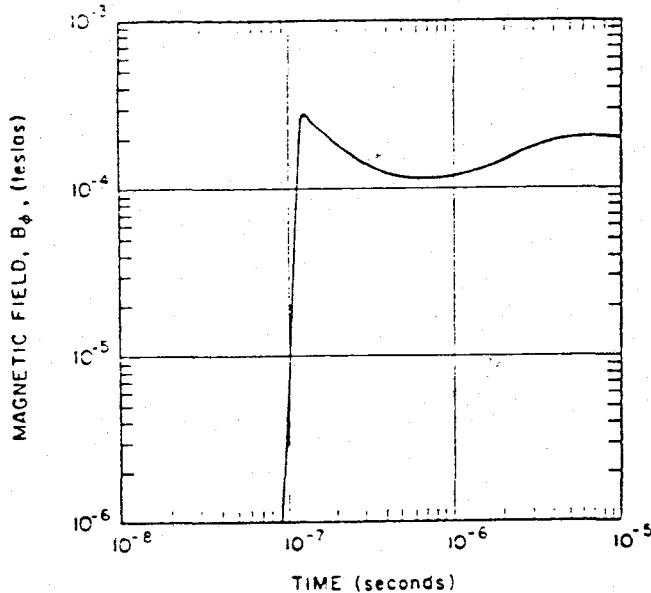


Figure 7-10 Shape of Magnetic Field for Toroid Model

explosion to about 1,670 volts per meter for a  $4.2 \times 10^4$  TJ (10 MT) explosion. For most cases, a value of 1,650 volts per meter may be assumed. At ranges along the surface beyond  $R_o$ , the peak radiated electric field varies inversely with the distance from the burst. Thus, the magnitude of the peak radiated electric field along the surface may be estimated from the equation

$$E = \frac{R_o}{R} E_o ,$$

where  $R_o$  is the range to the beginning of the radiation region,  $R$  is the distance along the surface to the point of interest,  $E_o$  is the peak value of the radiated field at  $R_o$  (assumed to be about

DIA  
K13

Table 7-1. Variation of Range,  
 $R_O'$  at which the Radiation Region  
Begins, with Yield

1.650 volts per meter), and E is peak value of the radiated field at R. For example, the peak electric field 10 kilometers from a 4200 TJ (1 MT) surface burst would be

$$E = \left(\frac{5.2}{10}\right) (1.650) \approx 1.200 \text{ v/m.}$$

The peak electric field at the same distance from a 420 TJ (100 KT) surface burst would be

$$E = \left(\frac{5.8}{10}\right) (1.650) \approx 950 \text{ v/m.}$$

The spatial distribution of the radiated signal involves not only the inverse range attenuation discussed above, but also the polar angle. The magnitude of the  $R \cdot E_\theta$  product follows a complicated function of the polar angle,  $\theta$ . Figure 7-11 shows the computed variation of the radiated EMP signals as a function of  $\theta$ . The variation in the waveform shape, as well as in the peak amplitude, as a function of angle should be noted. Because of the greater rise time of the

waveforms as the vertical is approached, it is apparent that the high frequency content of the signals decreases. The frequency spectrum is an important parameter for coupling analysis. Figure 7-12 shows the normalized frequency spectrum of the horizontally radiated EMP from a surface burst. Comparing this spectrum with that shown in Figure 7-7 shows significantly greater high frequency content for the surface burst.

The preceding discussion was intended to illustrate the general characteristics of the EMP fields generated by surface bursts and the variation of the peak radiated electric fields in space. In addition to the behavior of the electric and magnetic fields, the air conductivity is important for more accurate coupling analysis. A few selected examples of these quantities are presented in later sections of this chapter; however, it is beyond the scope of this manual to provide complete EMP environmental data upon which vulnerability analyses may be based.

### 7-7 High Altitude Burst

This burst regime is defined to include any nuclear burst at an altitude above about 30 kilometers (19 miles). In this regime the atmosphere is so sparse above the burst that relatively little Compton current is generated there. The deposition region, departing far from spherical symmetry, consists principally of a pancake shaped volume extending from about 20 to 50 kilometers (12 to 30 miles) in altitude and to the horizon as viewed from the burst. Thus, very high altitude bursts may cover vast geographical areas. A further asymmetry, the earth's magnetic field, is responsible for the form of the radiation. The Compton electrons, which result from collisions of the prompt gammas and x-rays with the air molecules in the deposition regions, are deflected by the earth's field to follow helical paths significantly long

during the time between collisions in the rare-field medium. The accelerated electrons produce the characteristic synchrotron radiation with a large high-frequency content. The peak amplitude of the electric field near the surface may be quite large, a few tens of thousands of volts/meter for high bursts. Figure 7-13 illustrates the basic geometry of this burst.

DNA  
(f)(1)

DNF  
(u)

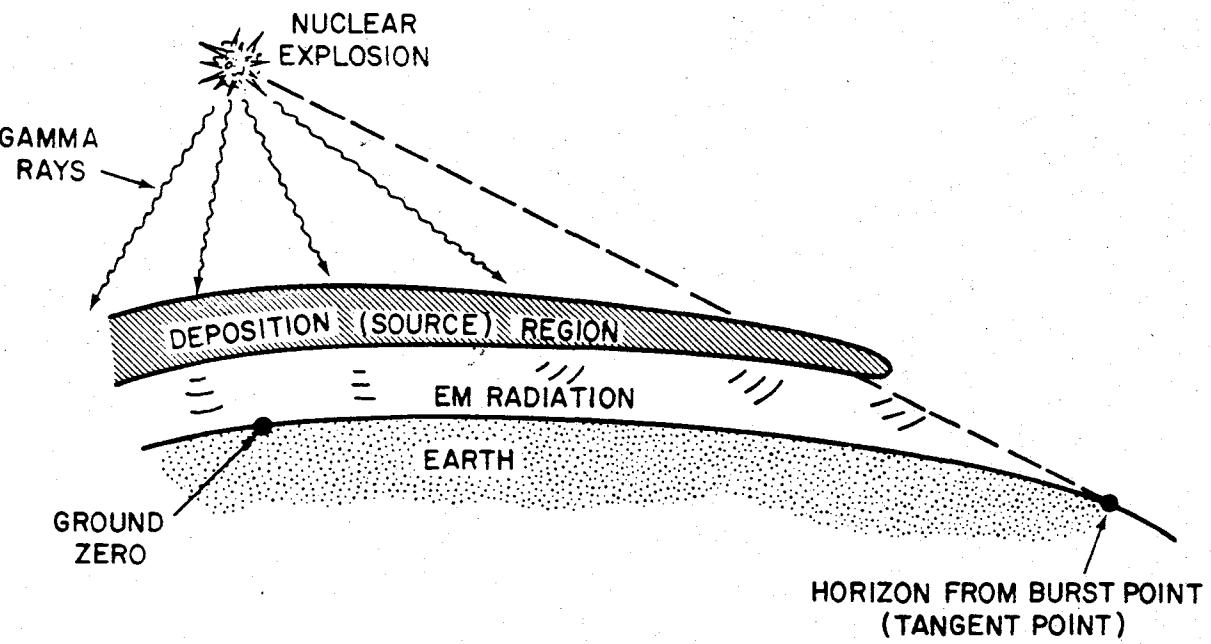


Figure 7-13 Illustration of the Basic Geometry of the High-Altitude Burst

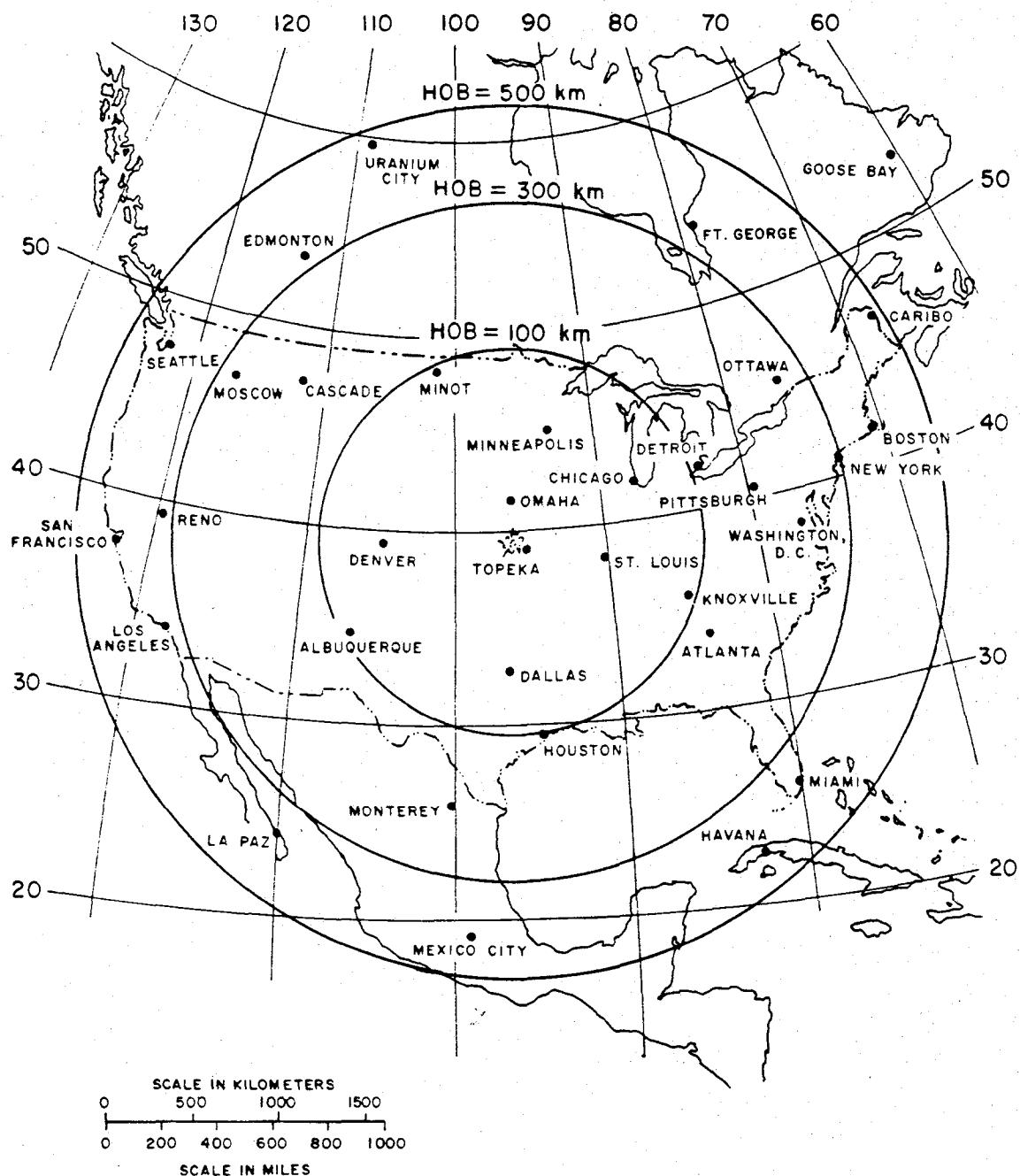


Figure 7-14 [REDACTED] Ground Coverage for Bursts of 100, 300, and 500 km (about 62, 186, and 310 miles) for a Large Yield Burst Above the Geographical Center of the (counterminous) United States [REDACTED]

7-16 Change 1

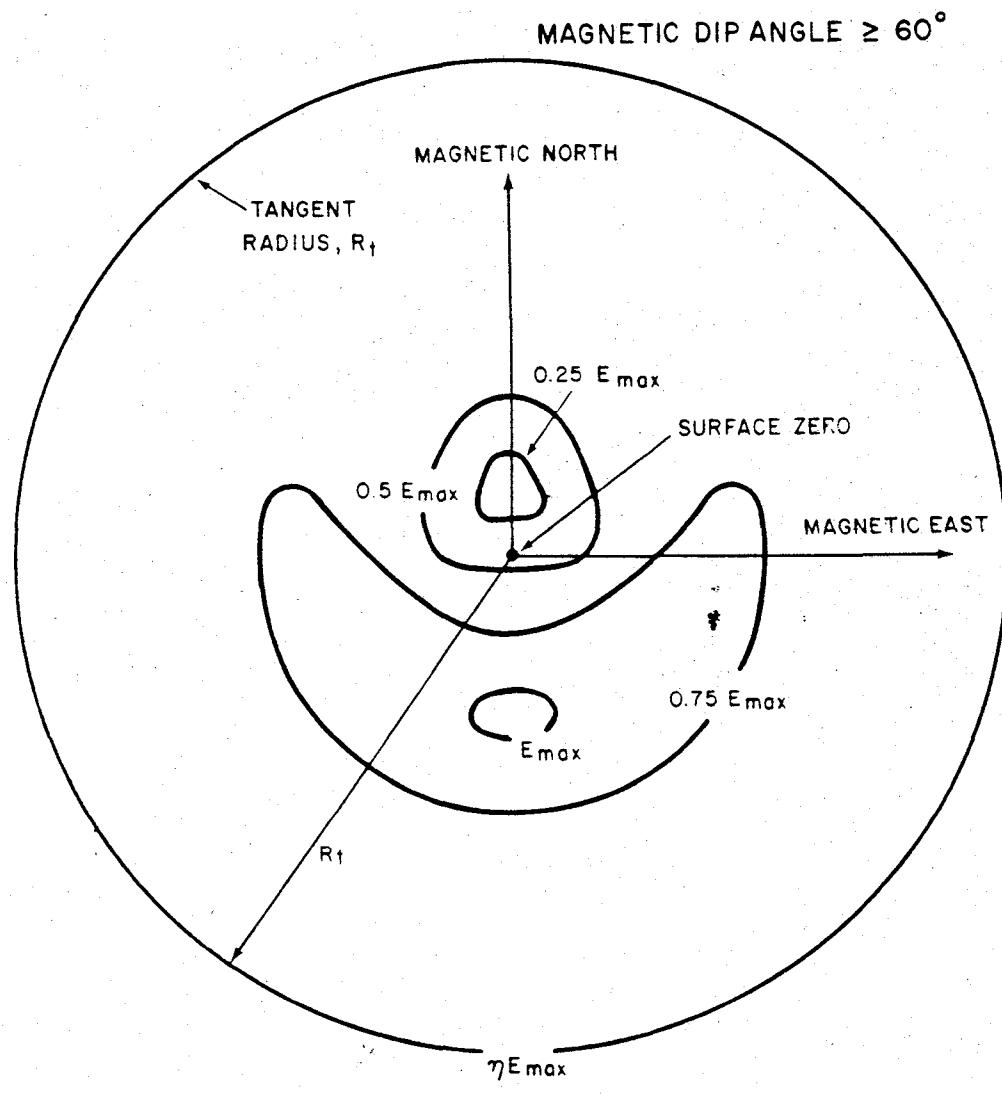


Figure 7-15 [REDACTED] Basic Variations in Incident Peak Electric Field for Locations on the Earth's Surface for HOB above 500 km [REDACTED]

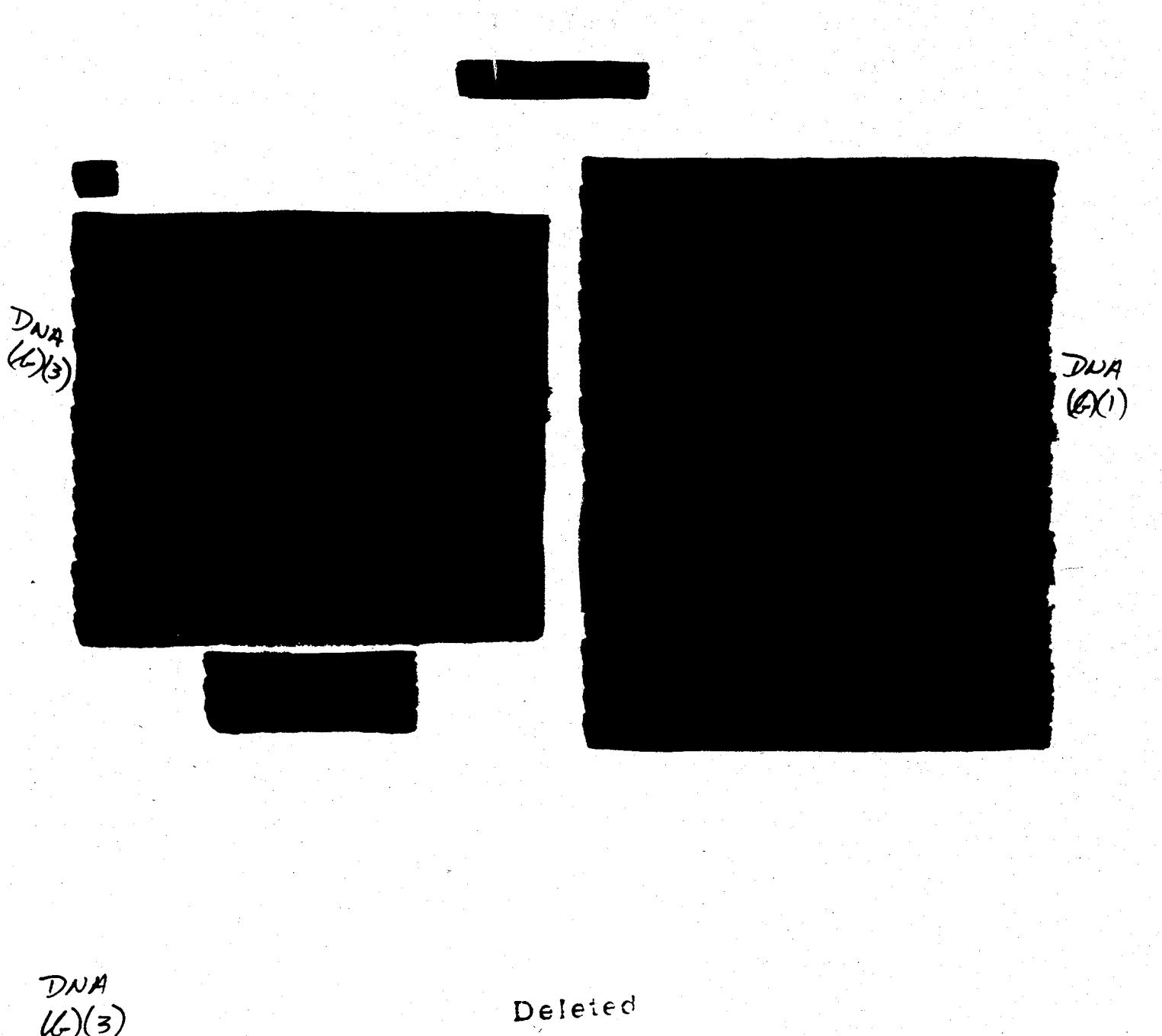


Figure 7-16 [REDACTED] Maximum Peak Electric Field as a Function of Gamma Ray Yield for Selected Burst Heights [REDACTED]

7-18 Change 1

DND  
(b)(1)

than that from a surface or low air burst. Figure 7-17 illustrates the time waveform of the radiated signal from a high altitude burst. The analytic expression

$$E(t) = 5.3 \times 10^4 (e^{-4t} - e^{-476t}) \text{ V/m},$$

where  $t$  is in microseconds, describes the waveform in Figure 7-17. The frequency spectrum of this pulse is illustrated in Figure 7-18. As the gamma yield of the weapon decreases, the pulse width tends to increase, decreasing the relative high frequency content of the signal. Similarly, increasing the angle between the line-of-sight and the vertical through the burst point increases the pulse width.

The high altitude burst is the dominant threat to exoatmospheric systems. The most severe EMP environment for such a system comes from a line-of-sight path that passes

The radiated EMP from a high altitude burst rises to a peak value much more rapidly

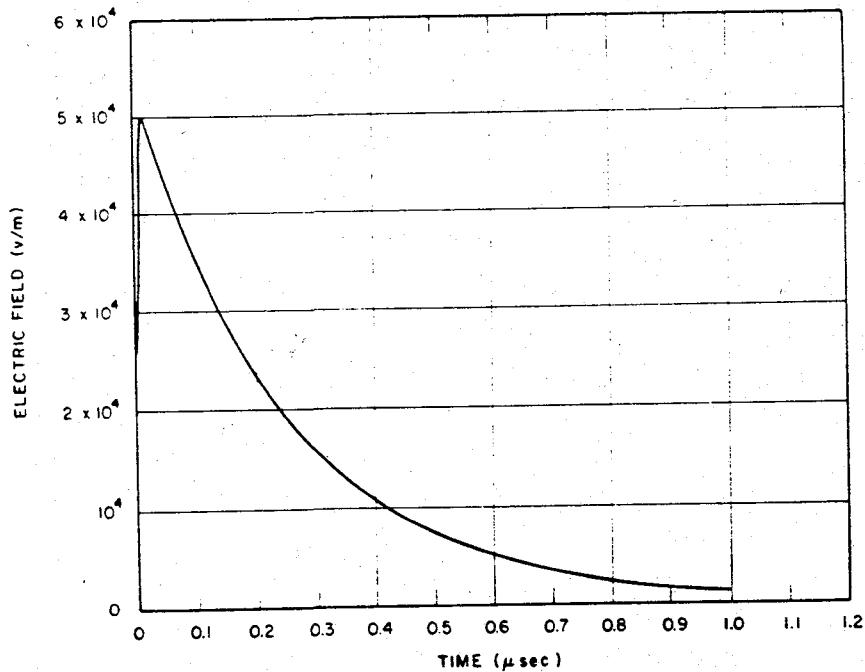


Figure 7-17 Time Waveform of High-Altitude Radiated

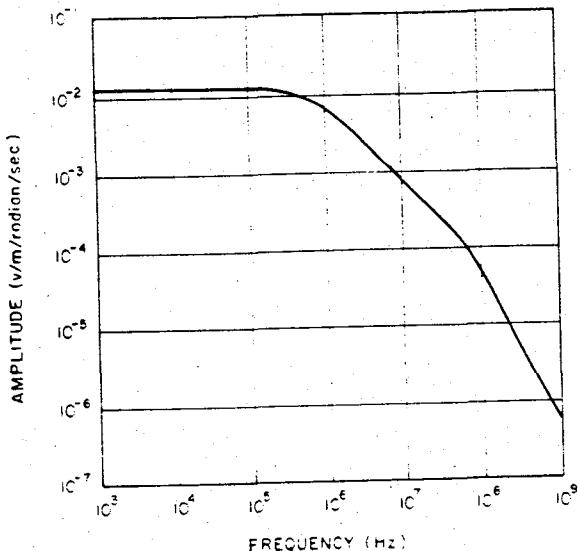


Figure 7-18 Amplitude of High-Altitude Radiated Signal

through the deposition region but misses the earth and is propagated through the ionosphere (see Figure 7-19). The ionosphere acts as a high pass filter, and only frequencies above a given cutoff are observed. The cutoff frequency depends on the altitude, time of day and sunspot activity, and, for example, varies between about 3 and 14 MHz at night, depending on the altitude of the observer. Daytime cutoff frequencies, of 30 MHz may be encountered for a 1000 km high observer. In addition, the effective index of refraction, and therefore the group velocity of the EMP signal also varies, with the higher frequencies traveling fastest. Also, the transmission for frequencies near the cutoff is very large, rising to near unity for higher frequencies. Although the amplitude of the dispersed pulse will be much smaller than that of the undispersed pulse, the signal will be stretched out greatly in

time. For frequencies above the cutoff there will be little energy loss. Figure 7-20 shows a predicted dispersed EMP (DEMP) signal from a high altitude burst as viewed by an observer at 100 km altitude. This is based on a nighttime ionosphere at sunspot minimum.

## SYSTEM GENERATED EMP

### 7-8 General Description

The term System Generated Electromagnetic Pulse (SGEMP) refers to the fields and currents generated by the interaction of weapons-produced radiation (principally X-rays and gamma rays) with a system or portion of a system. The system generated electromagnetic pulse is produced inside or in the vicinity of a system when an incident photon pulse interacts with the material of the system. Photoelectric and Compton electrons are created, and the resulting emission current produces electric and magnetic fields. Internal EMP, or IEMP, which refers to the electromagnetic fields interior to systems and containers, and which is generally generated by gamma rays, or high energy X-rays, is included in the general category of SGEMP. SGEMP specifically excludes the internal effects associated with transient radiation effects on electronics (TREE).

The system-generated EMP is most important for electronic components in satellites and ballistic systems above the deposition region that would be exposed directly to the nuclear radiations from a high-altitude burst. The system-generated EMP can also be significant for surface and moderate-altitude bursts if the system is within the deposition region but is not subject to damage by other weapons effects. This could possibly occur for surface systems exposed to a burst of relatively low yield or for airborne (aircraft) systems and burst of higher yield.

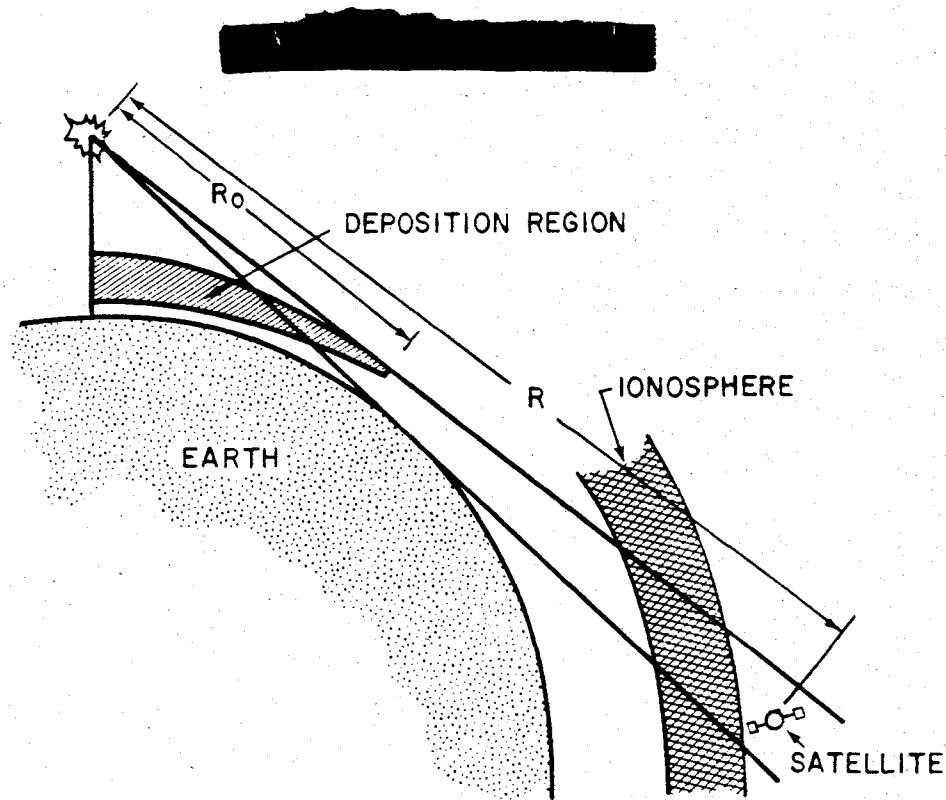


Figure 7-19 ■ The Geometry for Producing Dispersed EMP for Exoatmospheric Systems ■

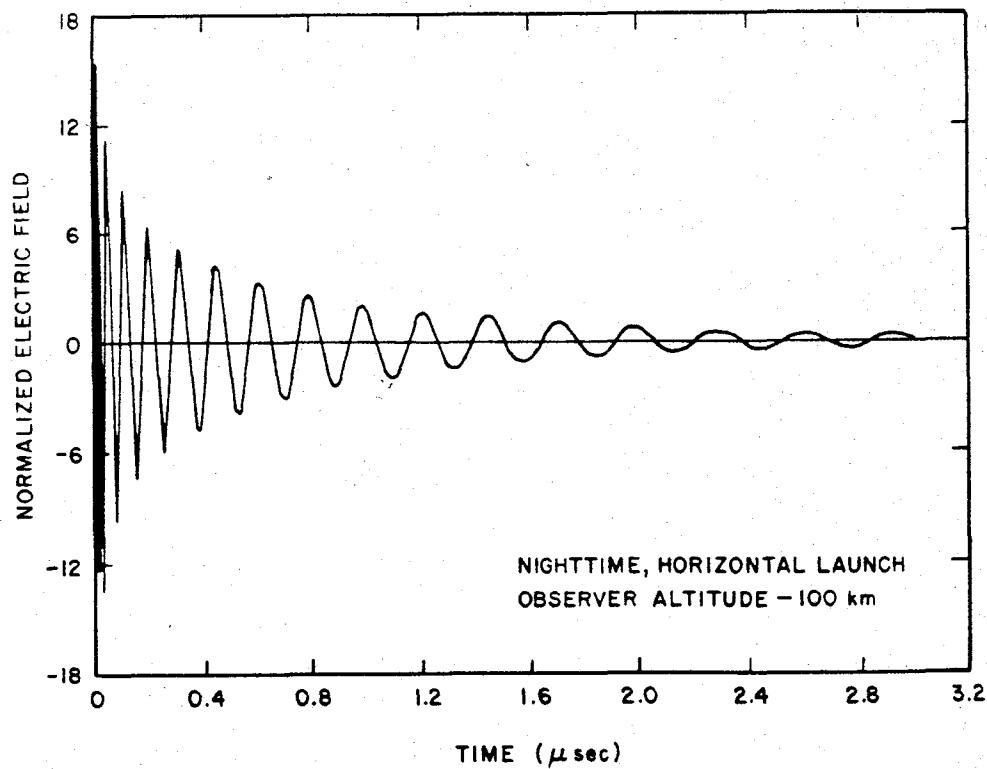


Figure 7-20 ■ Electric Field Time Waveform of High-Altitude EMP after Dispersion by Nighttime Ionosphere ■

Change 1  
7-21

## 7-9 SGEMP Generation

The generation of SGEMP is a complex function of many physical phenomena. The complexity of the problem precludes quantifying SGEMP generation for any broad class of systems. This section, therefore, will attempt to describe some of the generation phenomena for one simple problem. The "DNA EMP (Electromagnetic Pulse) Handbook," DNA 2114H-3, Volume 3, should be consulted for an in-depth treatment of the subject (see bibliography).

Figure 7-21 illustrates SGEMP generation in a cavity. The incident X-rays and gamma rays create photo- and Compton electrons, respectively, within the cavity walls. The generation is, of course, dependent on the energy flux of the incoming photons and the properties of the wall material. The photo- and Compton electrons subsequently interact with the atoms of the wall material to produce secondary electrons. Those electrons created near the surface (within an electron mean-free-path) with velocity vectors toward the surface generally will be emitted. The net electron currents, both within and without the cavity, gives rise to a magnetic field which will induce currents in circuit loops via magnetic coupling.

For this discussion, it is assumed that the electron emission and subsequent field generation are separable problems. Further, the electron emission from the external wall surfaces will be ignored. The problem under consideration is thus one in which electrons are emitted from two internal surfaces of the cavity in the forward and reverse directions, the emission being described as a time and energy dependent electron flux.

As the emitted electrons traverse the cavity, a net forward current will be observed within the cavity while a space charge is established concurrently. If the cavity is at vacuum or

near-vacuum conditions ( $0.13 \text{ pascal} - 10^{-3} \text{ Torr}$  or less) and of appropriate size, space charge limitation will occur. This will result in the creation of high electric fields ( $10^5 - 10^6 \text{ volts/meter}$ ) near the walls.

If the cavity pressure is above 0.13 pascal, another phenomenon will occur in sufficient intensity to alter the SGEMP. The emission electrons will interact with the gas molecules to produce additional secondary electrons (hereafter called gas electrons) and positive ions. The gas electrons will tend to "stream" to the cavity walls in comparison to the heavier and slower gas ions that are created concurrently. The gas ions will neutralize the space charge, thereby allowing more electrons to traverse the cavity. Thus the E-field intensity near the walls will decrease while the current in the cavity, and concurrently the magnetic field, will increase. It should be noted that quantitative analysis of the electron emission and subsequent SGEMP generation for even this simple problem requires the use of complex computer codes on large computers.

## 7-10 Problem Definition

It is emphasized that the above discussion dwells on only one small aspect of the SGEMP problem: the generation of an idealized SGEMP in a simplified geometry. A complete treatment of the SGEMP for a given system must start with the threat definition and the incoming photon flux. This must then be translated into electron emission from all surfaces, cables, components, etc., of the system. From the emission, fields and currents throughout and external to the system must be determined in a self-consistent manner. Next, coupling of the fields and currents to the system electronics must be established. Finally, the reaction of the electronics to the coupled energy must be determined and evaluated.

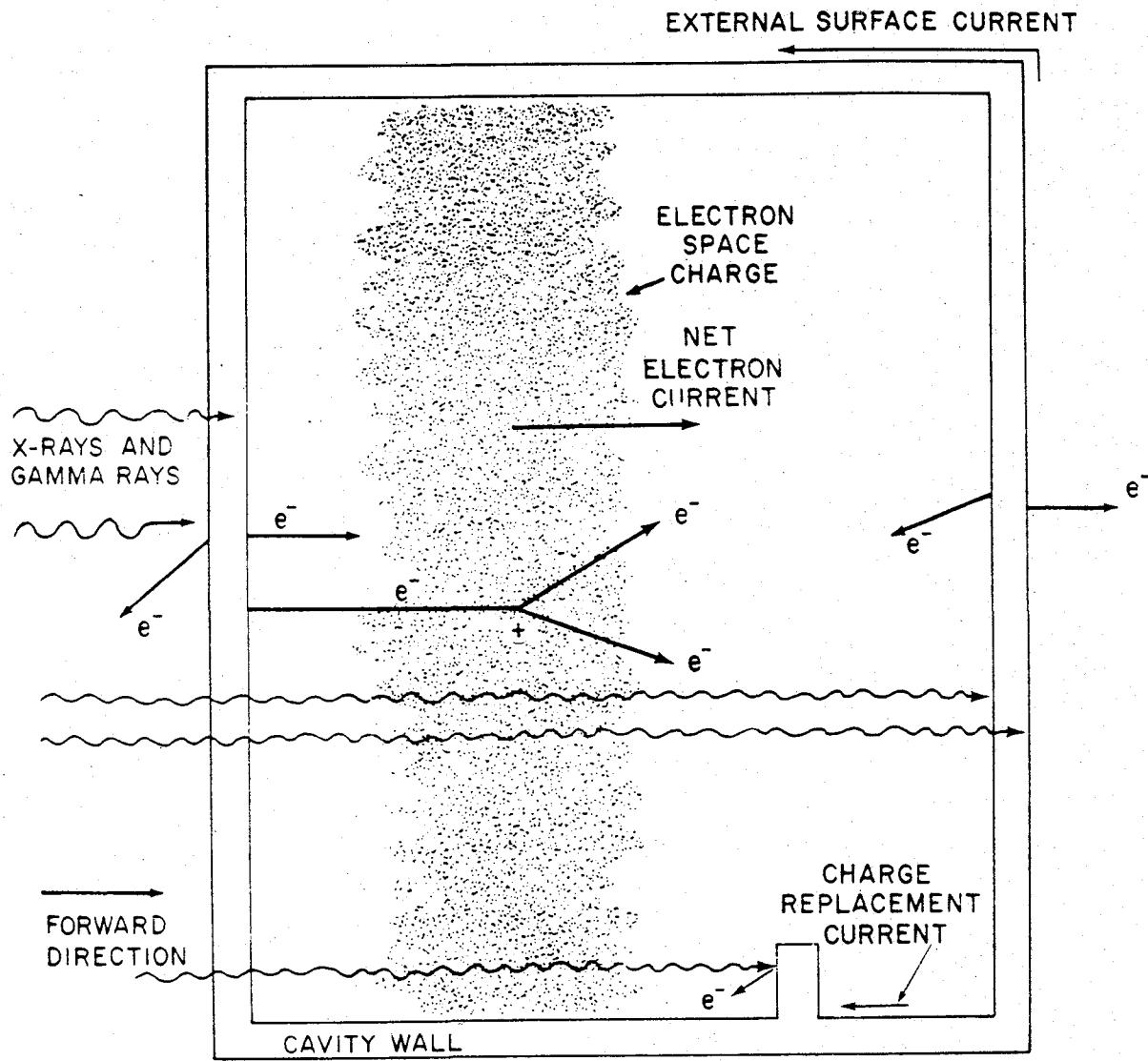


Figure 7-21 SGEMP Generation

Change 1 7-23

It is possible that this evaluation procedure may be terminated after any given step. For example, consider an electronically very "hard" system for which the "threat" is specified as  $4.2 \times 10^4$  joules/meter<sup>2</sup> (1 cal/cm<sup>2</sup>) received uniformly over a period of a year. By inspection, SGEMP is not a problem. At the other extreme, consider a system that is easily upset by small (milliamp), short duration (30 nsec) electrical pulses. If the threat for this system is  $4.2 \times 10^5$  joules/meter<sup>2</sup> (10 cal/cm<sup>2</sup>) in a period of 100 nanoseconds, SGEMP may be a significant problem. An in-depth analytical/experimental program must be undertaken to make an evaluation of SGEMP effects.

Clearly, the above examples are extremes. They only serve to illustrate that an all encompassing definition of SGEMP problems is impossible because of the highly complex, system-specific nature of this phenomenon. Likewise, it is not possible to formulate a specific solution to the SGEMP threat for general application. Thus, the susceptibility and vulnerability of each system to SGEMP effects must be considered separately.

## COMPUTER CODE DESCRIPTIONS

### 7-11 Code Utility

From the physical descriptions provided in the preceding paragraphs, it is apparent from the large number of variables involved that even approximate solutions to practical problems of interest demand a large investment in electronic computation. The complete problem of the coupling of the EMP from a specific detonation into the components of a specific system is an extremely complex problem. There are no computer codes which even remotely approach a treatment of the complex problem. As a consequence, various aspects of the EMP problem are

studied individually with the aid of existing codes, and good engineering judgment must be used to couple these various parts of the solution into a quantitative estimate of the effects of EMP upon a given system.

### 7-12 Code Classes

There are three general classes of computer codes in use: environment codes, system generated EMP codes, and circuit-analysis codes. The codes that are currently in use are described in the "DNA EMP (Electromagnetic Pulse) Handbook," Volume 4 (see bibliography).

## SYSTEMS EFFECTS

### 7-13 System Definitions

Many systems that are physically different can be grouped together in terms of the EMP environments they will encounter. For this purpose it is useful to consider classification of systems in terms of operating altitude and nuclear hardness.

From the previous description of the EMP environment, the altitude categories suggested in Figure 7-22 are evident. It should be noted that certain systems may operate successively in more than one category.

For the purposes of this manual it is adequate to consider system hardness in only two categories. A hard system is one that has been designed to operate in some nuclear environment. A soft system is not so designed, and its hardness is due solely to its inherent design. For a ground system, the blast usually is considered to be the indicator of the nuclear hardness of the system. The dominant effect will change from blast to nuclear radiation, defined here in terms of the total dose in rad (Si), as the system altitude increases. A system is considered to be

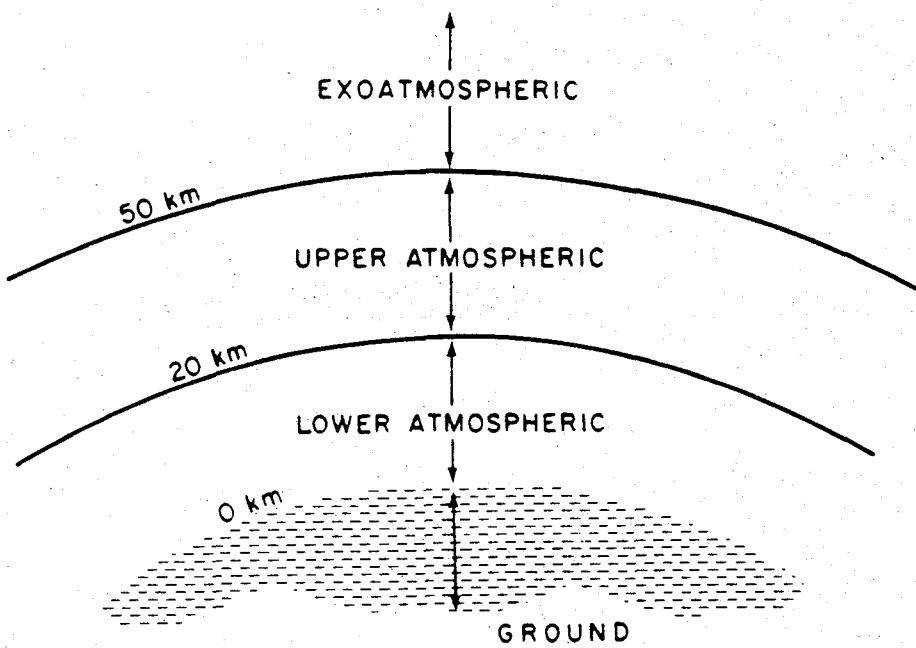


Figure 7-22 Categories of System Operation Regions

hard if it is built to withstand blast overpressures of about 70 kilopascals (10 psi) or more or a radiation dose of 1 rad (Si) or more. Corresponding figures for a soft system are 7 kilopascals (1 psi) or less and 0.1 rad (Si) or less. Systems marginal with respect to either criterion should be reviewed in both categories.

#### 7-14 Threat Definition

DNA  
(b)(1)

		EMP ENVIRONMENT								
		DEPOSITION			RADIATION			PROPAGATION		
		SURFACE	AIR	HIGH ALTITUDE	SURFACE	AIR	HIGH ALTITUDE	SURFACE	AIR	HIGH ALTITUDE
MISSION	HARD	GROUND	X					X		
		LOWER ATMOSPHERIC		X				X		
		UPPER ATMOSPHERIC			X			X		
		EXO ATMOSPHERIC								X
MISSION	SOFT	GROUND			X		X			
		LOWER ATMOSPHERIC			X	X	X			
		UPPER ATMOSPHERIC					X			
		EXO ATMOSPHERIC								X

Figure 7-23 Mission/Environment Matrix

DNA  
(b)(1)

Blocks are shaded in on the diagram on the basis of dominant environments for a given mission, not on the basis of whether EMP exists at all for that situation. Thus, based on the definitions given, Figure 7-23 may be used as a guide for which environments constitute a dominant threat for given situations of interest.

### 7-15 Effects Comparisons

It is well beyond the scope of this chapter to attempt meaningful effects comparisons for every system altitude, burst altitude, and environment combination for which EMP may be the dominant threat. However, it is instructive to consider one such combination in order to gain some impression of how the magnitude of the threat might be compared to other effects. Accordingly, the deposition region environment created by a surface burst will be examined with regard to the effects on hardened ground systems, a category in which the EMP threat may dominate according to Figure 7-23. As mentioned previously, the nuclear hardness of such a system is generally described in terms of its over-pressure level. Using this quantity as an indicator of hardness, the EMP field waveforms, peak values and frequency content for the principal field components  $B_\varphi$ ,  $E_r$ , and  $E_\theta$ , as defined in Figure 7-24 and the associated air conductivity waveforms and peak values will be examined.

The peak values as a function of overpressure are considered first. Figures 7-25, 7-26, and 7-27 show these values for the three field components for two yields and two values of ground conductivity ( $\sigma_g$ ). It should be kept in mind that a large shift in frequencies present can

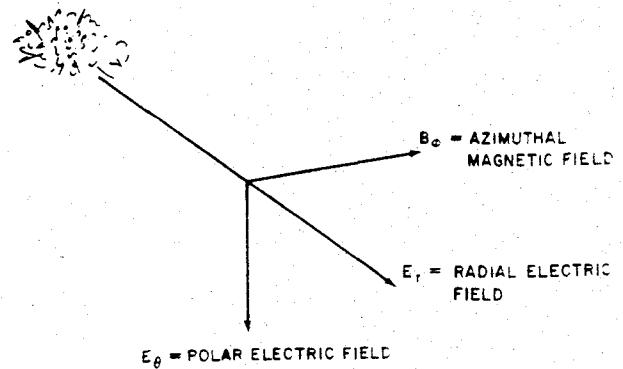


Figure 7-24 Field Directions of Ground-Burst EMP

occur between 70 and 7,000 kilopascals (10 and 100 psi). The coupling of systems to the fields in this intense region is complicated by the high air conductivity. Figure 7-28 shows how peak air conductivity varies with overpressure. It should be noted that the lower yield weapon produces higher conductivity for a given overpressure level.

The variation of these same quantities in time for the 4,200 terajoules (1 MT) yield and a ground conductivity of  $10^{-2}$  mho/m is illustrated next. The waveform for the  $B_\varphi$  component is shown for various overpressure levels in Figure 7-29, and the frequency spectrum is illustrated in Figure 7-30. Corresponding waveforms and spectra for  $E_r$  and  $E_\theta$  components are shown in Figures 7-31, 7-32, 7-33, and 7-34. Finally, the corresponding air conductivity waveforms are presented in Figure 7-35.

It is apparent from these figures that meaningful effects comparisons can be made and presented to the systems designer for a given set of physical conditions. However, it is also clear that the results vary drastically with changes in

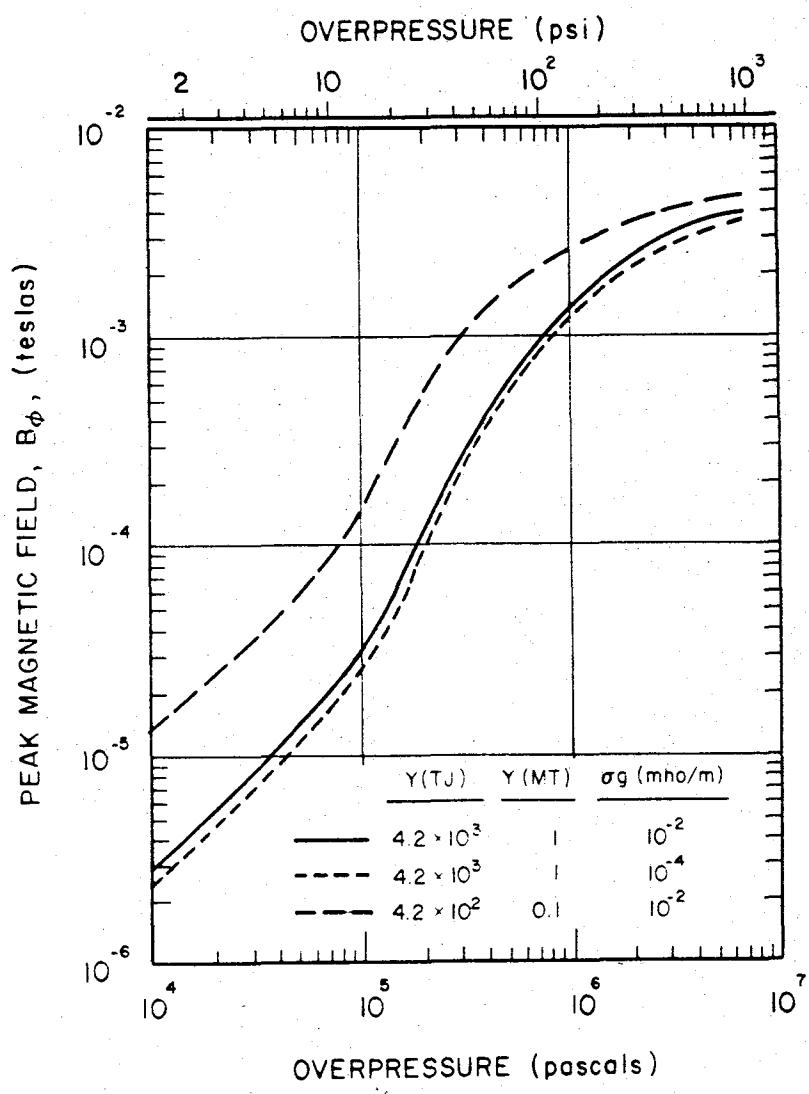


Figure 7-25 [REDACTED] Peak Magnetic Field  $B_\phi$  Versus Overpressure for Varying Ground Conductivities and Yields [REDACTED]

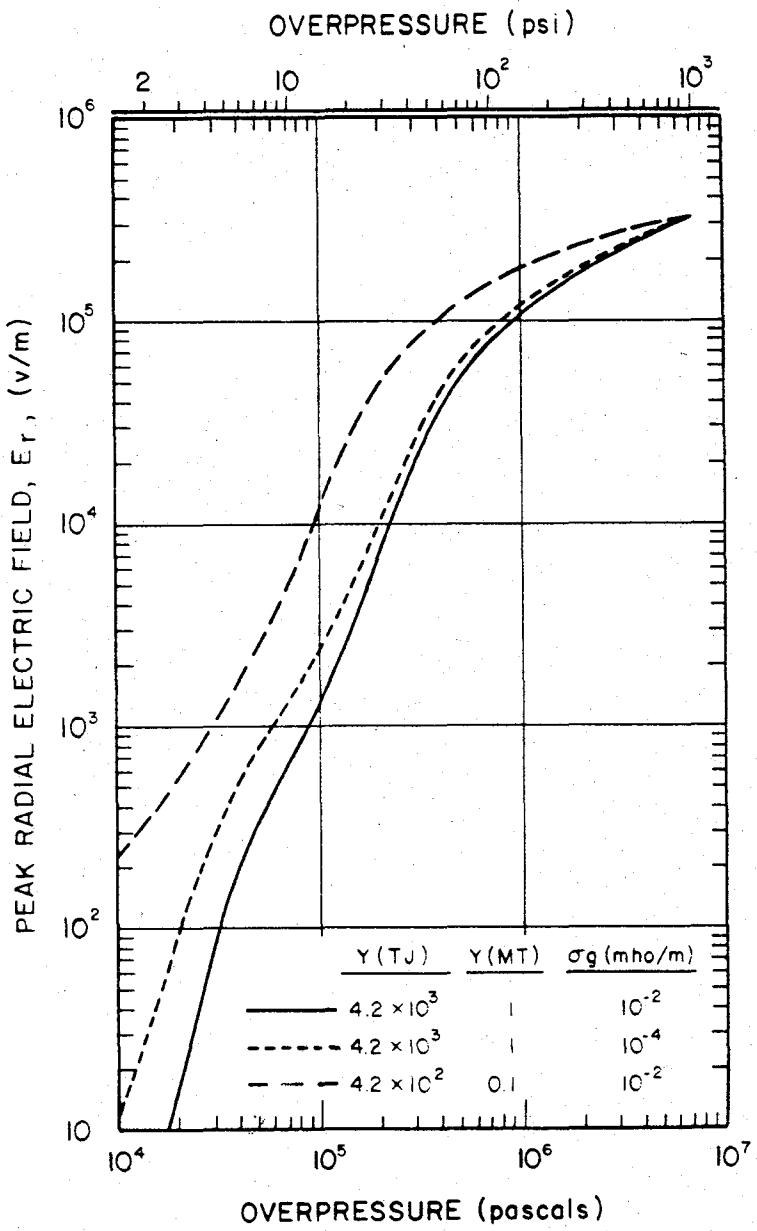


Figure 7-26 Peak Radial Electric Field  $E_r$  Versus Overpressure  
for Varying Ground Conductivities and Yields

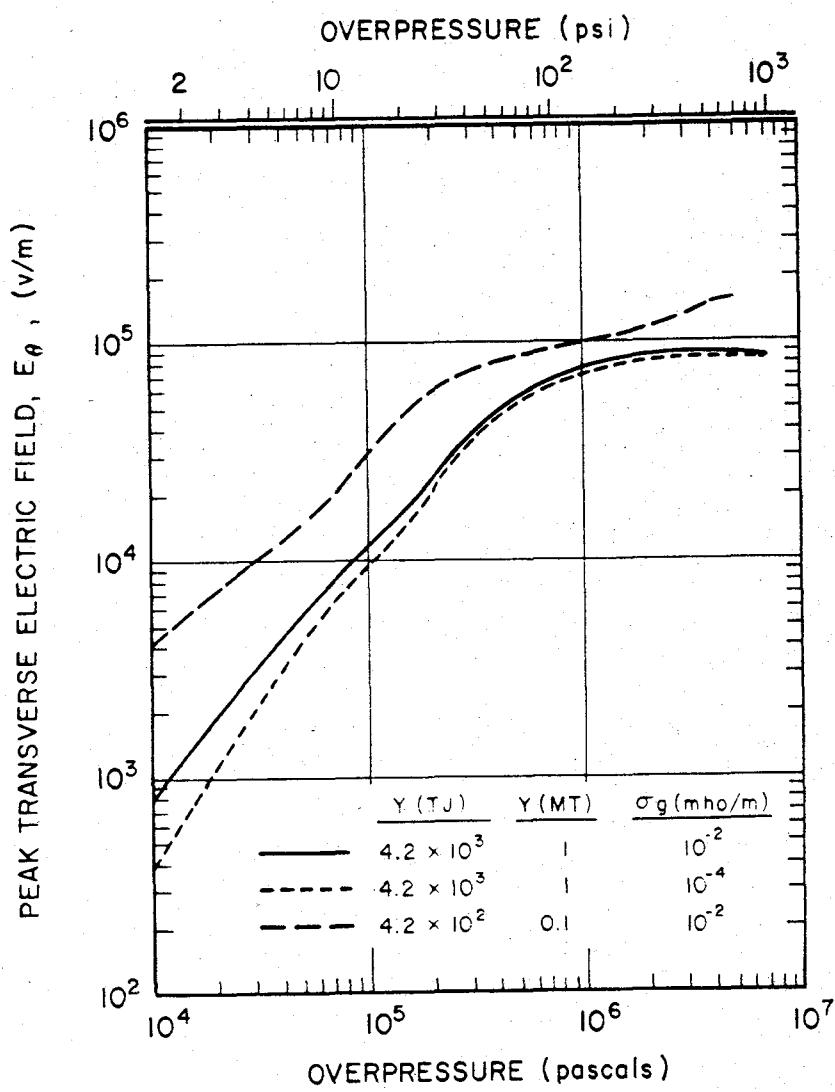


Figure 7-27 Peak Transverse Electric Field  $E_\theta$  Versus Overpressure  
for Varying Ground Conductivities and Yields

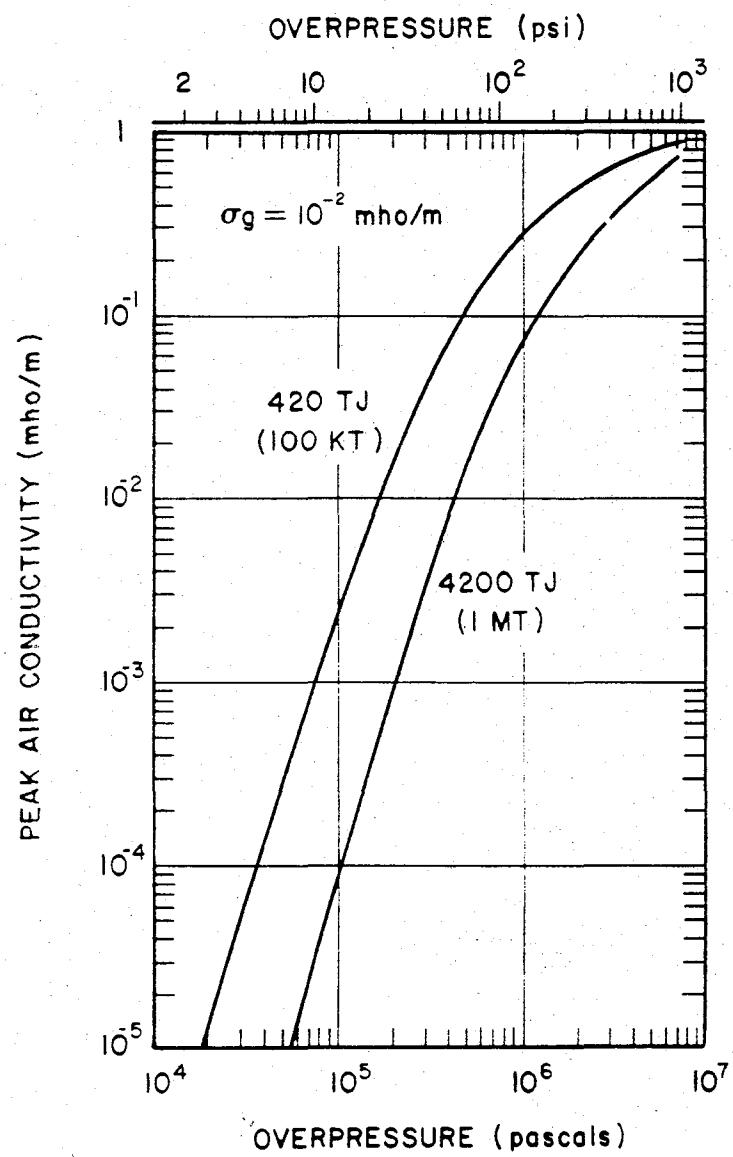


Figure 7-28 Peak Air Conductivity Versus Overpressure for Yields of 420 TJ (100 kt) and  $4.2 \times 10^3$  TJ (1 Mt)

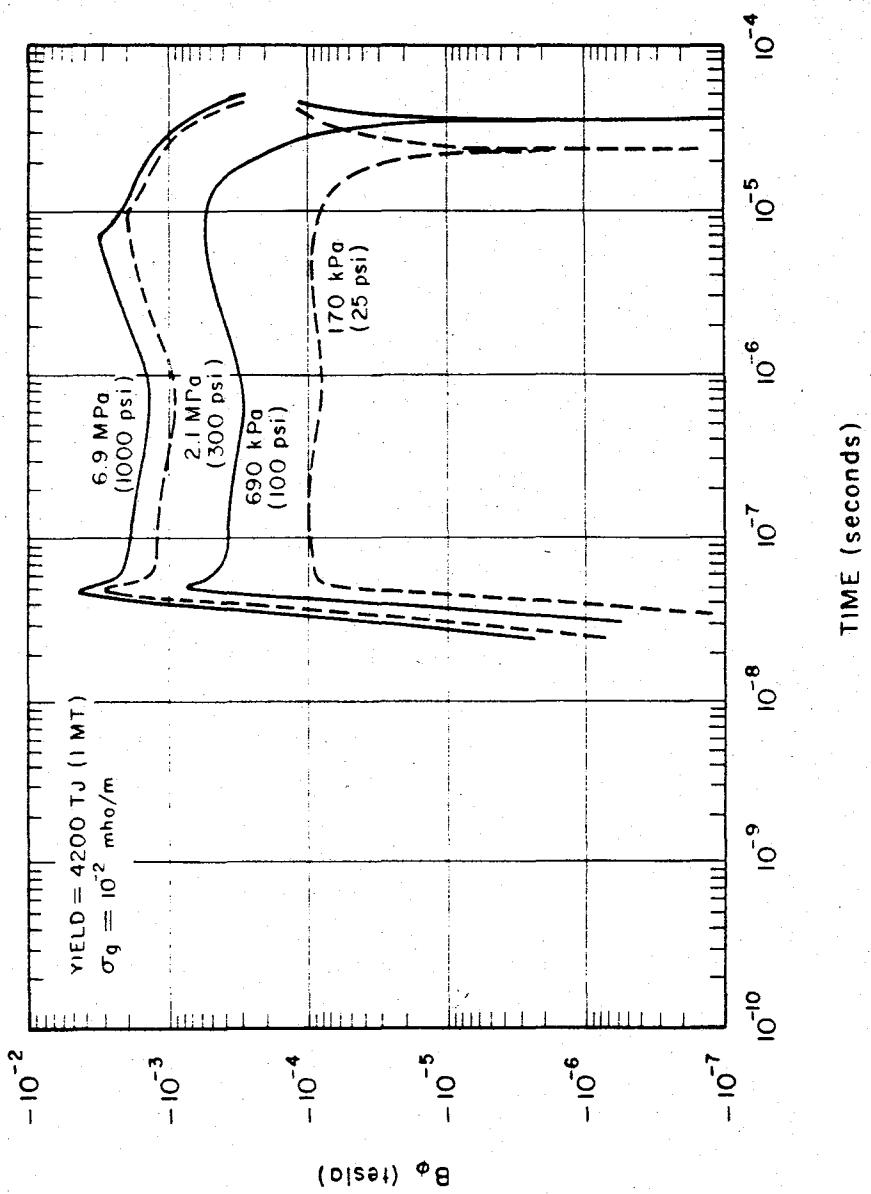


Figure 7-29 B<sub>φ</sub> Time Waveform at the Air-Ground Interface for Several Pressure Levels

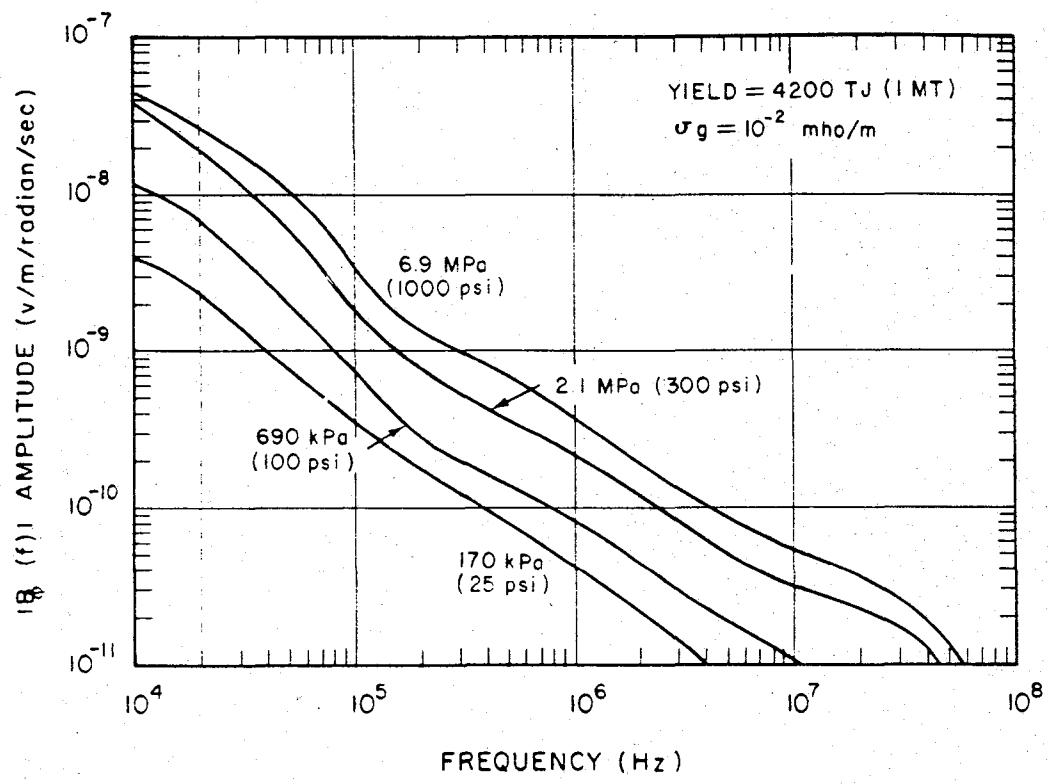


Figure 7-30 [REDACTED] Fourier Amplitude of  $B_\phi$  Waveform of Figure 7-29 [REDACTED]

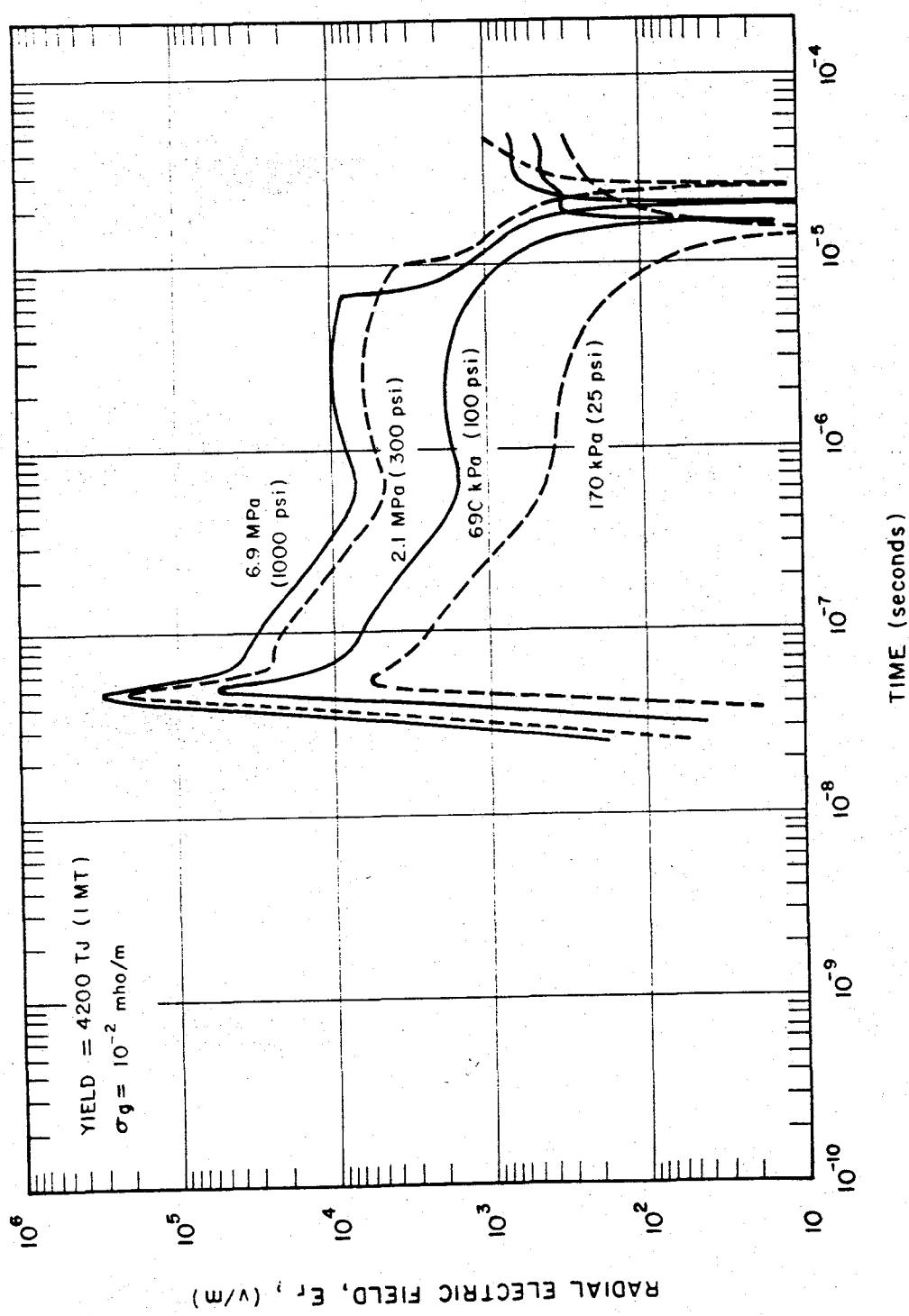


Figure 7-31  $E_r$  Time Waveform at the Air-Ground Interface for Several Pressure Levels,  
 $\sigma_g = 10^{-2}$  mho/m

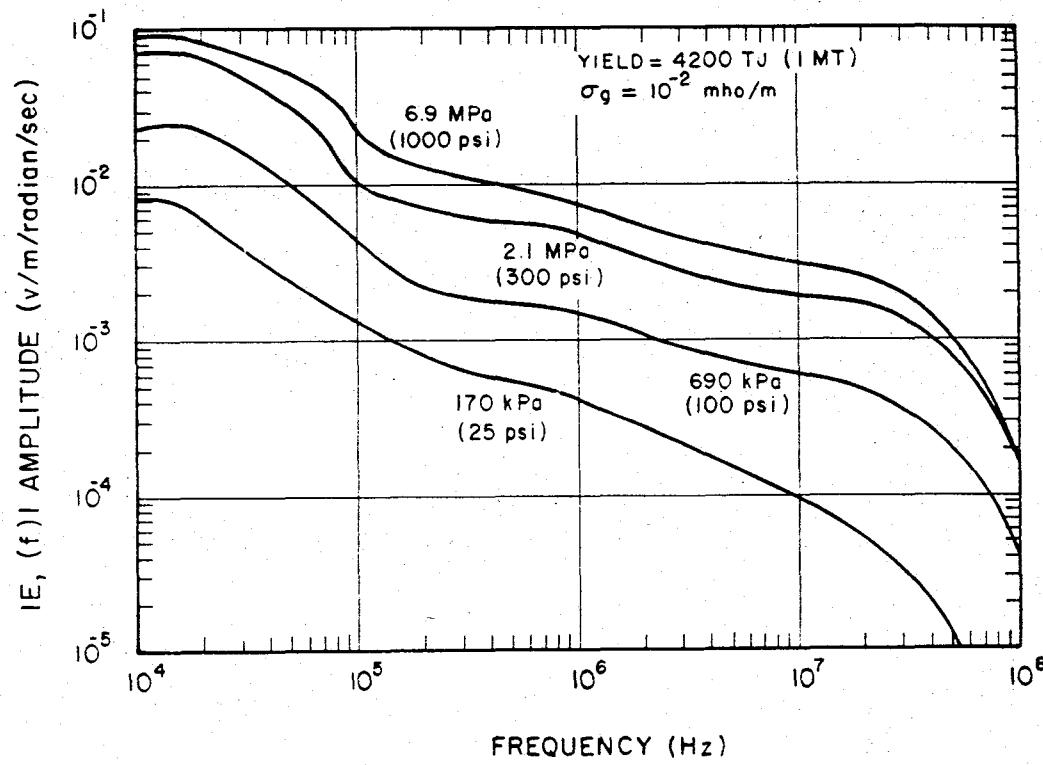
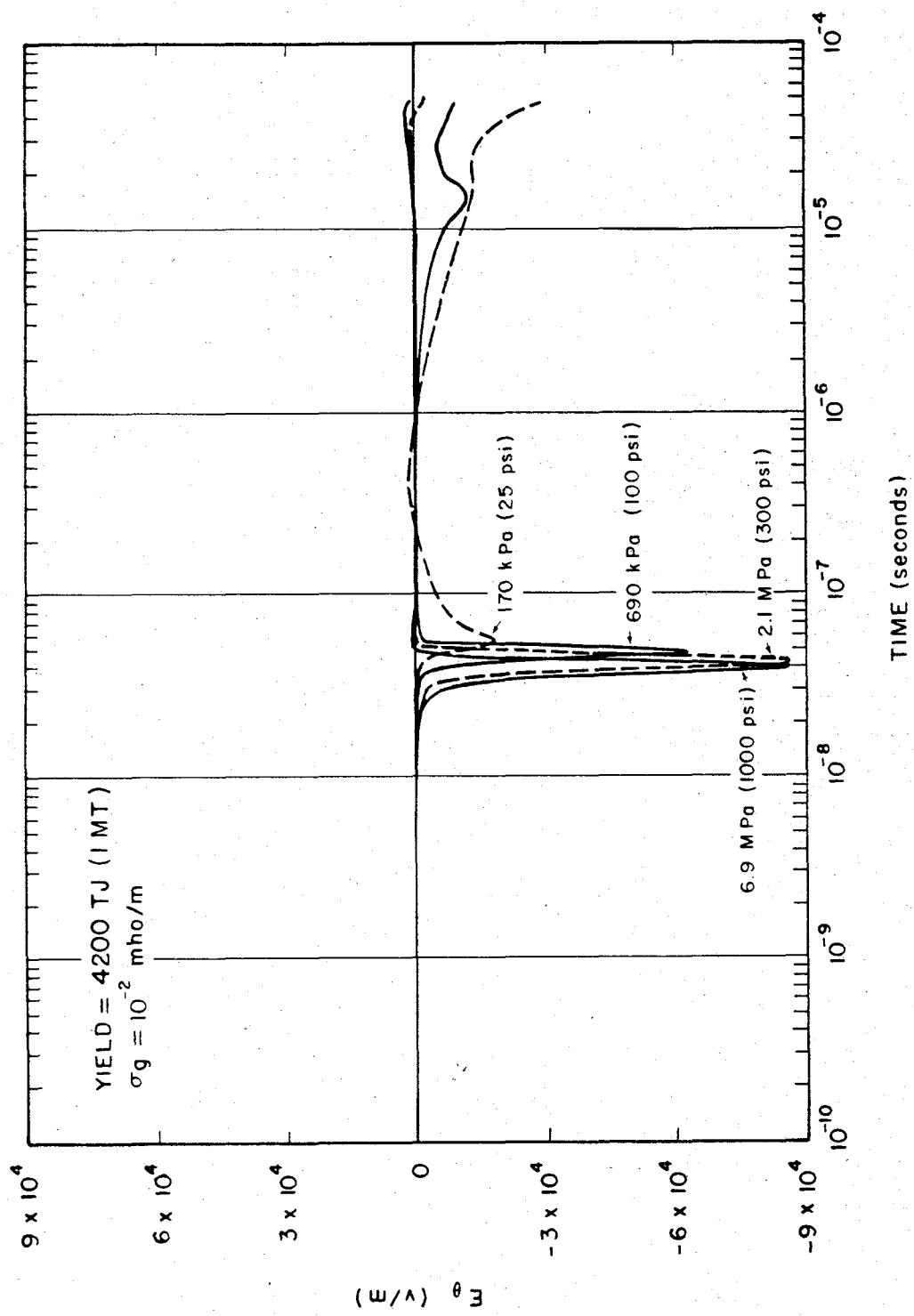


Figure 7-32 [REDACTED] Fourier Amplitude of  $E_r$  Waveform of Figure 7-31 [REDACTED]



7-36 Change 1

Figure 7-33 [REDACTED]  $E_\theta$  Time Waveform at the Air-Ground Interface for Several Pressure Levels,  
 $\sigma_g = 10^{-2}$  mho/m [REDACTED]

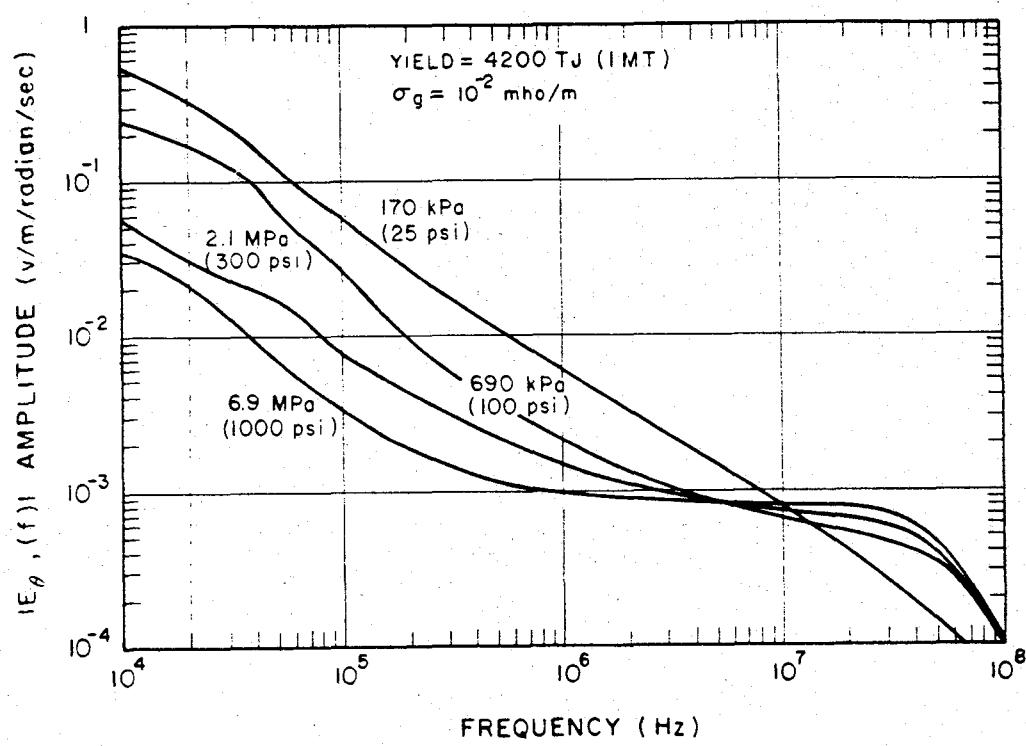


Figure 7-34 Fourier Amplitude of  $E_\theta$  Waveform of Figure 7-33

Change 1 7-37

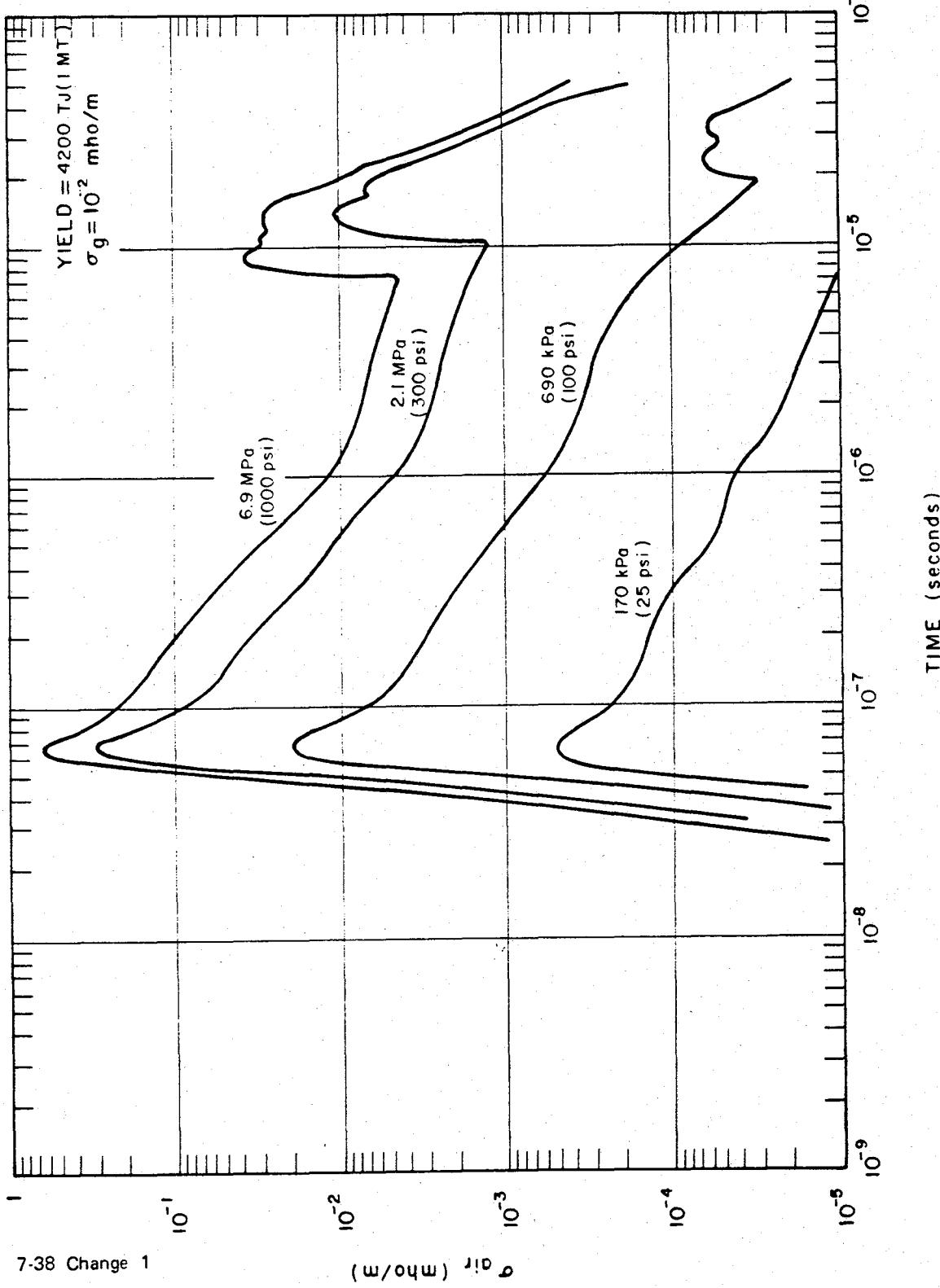


Figure 7-35 [REDACTED] Air Conductivity Time Waveforms at the Air-Ground Interface for Several Pressure Levels,  $\sigma_g = 10^{-2}$  mho/m [REDACTED]

[REDACTED]

[REDACTED]

the conditions, and that the very many combinations possible in the conditions preclude concise generalizations to cover every situation. Strictly speaking, a system imbedded in the deposition region must be included as part of the environment itself in formulating the problem. This limitation should be kept in mind while examining the figures described.

[REDACTED] BIBLIOGRAPHY [REDACTED]

DNA EMP (Electromagnetic Pulse) Handbook [REDACTED] DNA 2114H-1, DNA 2114H-2, DNA 2114H-3, DNA 2114H-4, Defense Nuclear Agency, Washington, D.C., August 1976. (I, II, IV - [REDACTED] III - [REDACTED])

EMP Simulator Study [REDACTED] DASA 2049, DASIAC SR-92, DASIAC, Santa Barbara, California, May 1968 [REDACTED]

Glasstone, S. and P. J. Dolan, eds., *The Effects of Nuclear Weapons*, Third Edition. U.S. Department of Defense and U.S. Department of Energy, December 1977 [REDACTED]

Jordan, T. M., et al., *Prediction of Internal Electromagnetic Pulse* [REDACTED] DNA 2966D. Defense Nuclear Agency, Washington, D.C., August 1972 [REDACTED]

Longmire, C. L., *Ground Fields and Cable Currents Produced by Electromagnetic Pulse from a Surface Nuclear Burst* [REDACTED] DASA 1913, DASIAC SR-54, DASIAC, Santa Barbara, California, March 1968 [REDACTED]

Proceedings: DASA EMP Technical Conference - 1969 [REDACTED] DASA 2280, DASIAC SR-91, DASIAC, Santa Barbara, California, March 1969 [REDACTED]

Schlegel, G. K., M. A. Messier and W. A. Radasky. (edited by W. C. Hart). *Electromagnetic Pulse Environment Handbook* [REDACTED] AFWL EMP PHENOMENOLOGY 1-1. Air Force Weapons Laboratory, Albuquerque, N.M., January 1972 [REDACTED]

Tompkins, J. E., and J. A. Rosado, *Internal Electromagnetic Pulse: Electric and Magnetic Fields in Complex Enclosures* [REDACTED] HDL-TR-1500. Harry Diamond Laboratories, Washington, D.C., June 1970 [REDACTED]

2 MAR 1989

## Chapter 8

PHENOMENA AFFECTING ELECTROMAGNETIC  
PROPAGATION<sup>1</sup>

## INTRODUCTION

The two principal phenomena caused by a nuclear detonation that affect electromagnetic propagation are electromagnetic emissions and ionization of the atmosphere. The short duration electromagnetic pulse described in Chapter 7 is in the first category. Also included in this first category are continuing thermal radiation and emissions from various chemical reactions within the atmosphere. These radiations and emissions produce noise throughout the radio and optical spectra. The second phenomenon, atmospheric ionization, involves alterations of the electrical properties of the atmosphere that can affect the propagation of electromagnetic waves. Both types of effects are caused by energy radiated from the nuclear explosion, from the subsequent fireball, and from the radioactive debris. The severity of the effects on the propagation of electromagnetic waves may vary from being completely negligible to intolerable degradation of system performance.

For the purpose of discussing the effects on propagation, the electromagnetic spectrum is divided into two frequency bands: the radio band, which includes radar applications, and the optical band, as shown in Figure 8-1. The most important effects in the radio band usually are those that affect the propagation of the desired electromagnetic signal (effects that change the amplitude, phase, direction, etc.). Electromagnetic radiations from the fireball and other regions can interfere with desired signals, and in some cases, interference from other sources (e.g., atmospheric noise) will be enhanced or diminished. The most important effect in the optical band is radiation from the fireball and other regions

that interferes with desired signals. The source of this radiation is described in Chapter 3.

The current state of knowledge concerning the effects of nuclear detonations on electromagnetic wave propagation stems from full scale tests, laboratory experiments, theoretical studies, and simulation with certain atmospheric phenomena. Meaningful testing of high-altitude nuclear weapon effects requires a sophisticated space capability (e.g., instrumented rocket probes), and only a relatively few high-altitudes tests were performed prior to the test moratorium in 1962.

While those tests provided information to develop models to calculate the various phenomena, considerable uncertainty exists in scaling to burst or atmospheric conditions that are much different from those of the tests. All of the high-altitude tests have been single bursts. Significant differences are expected when two or more nuclear detonations occur near one another in time and space.

Detailed theoretical descriptions for most burst phenomena are highly complex and require specification of poorly known parameters for quantitative results. Laboratory measurements have been used to obtain estimates of some parameters, but usually the results have to be scaled to conditions much different than those

Although the English system of units for measuring distance is given priority throughout most chapters of this manual, wavelengths and other dimensions dealing with electromagnetic wave propagation usually are given in the metric system. Therefore, in this chapter and in Chapter 17, the metric system is used for distance dimensions. Conversion factors from the metric system to the English system are provided in Appendix B.

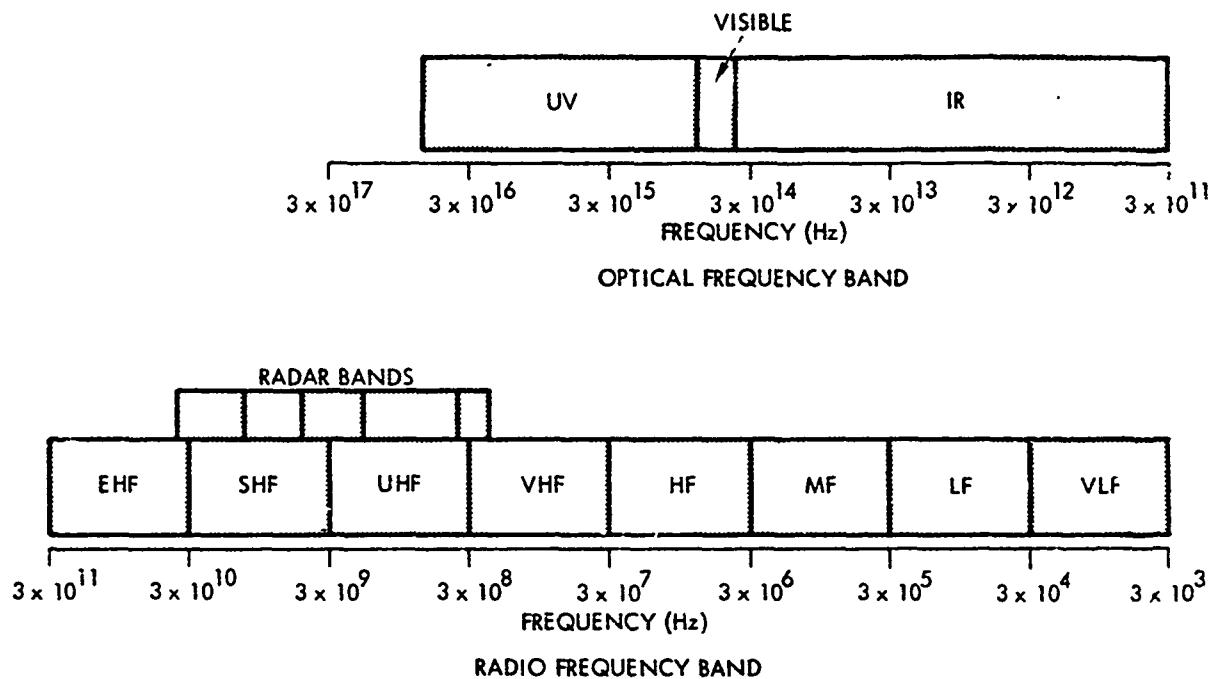


Figure 8-1. [REDACTED] Optical and Radio Frequency Bands [REDACTED]

used in the measurements. Some understanding of electromagnetic propagation in disturbed environments has been obtained from propagation measurements during eclipses, solar flares, and auroral disturbances. However, natural phenomena often involve the superposition of different phenomena than those brought about by nuclear bursts, and extrapolation to burst conditions can be misleading.

## SECTION I PHENOMENA AFFECTING RADIO FREQUENCIES

The number of free electrons in the atmosphere is increased greatly by weapon radiations from high altitude bursts. These free electrons can absorb energy from electromagnetic waves and can change the phase velocity of the waves (changing the direction of propagation

and signal characteristics). Electromagnetic radiations from heated regions and from trapped electrons are a source of noise.

### IONIZATION AND DEIONIZATION

Most of the energy of a nuclear detonation is emitted in forms that can produce ionization.<sup>2</sup> Some of this energy is in particulate matter (neutrons, beta particles, and high-speed debris that originally constituted the warhead and adjacent structure), and some is in photons (thermal radiation from the weapon case and gamma rays). Between 90 and 95 percent of the energy is emitted promptly (within a microsecond); about 5 to 10 percent is delayed radiation from the radioactive decay of fission debris.

<sup>2</sup>The ionization process is described in paragraph 6-4, Chapter 6.



Distribution/	
Availability Codes	
Dist	Avail and/or Special

UNANNOUNCED

If a nuclear explosion occurred in a vacuum with no magnetic field, the flux of radiated energy would decrease as the square of the distance traveled. In the atmosphere, collisions and scattering processes absorb energy and produce ionization and excitation. (See Chapters 3, 4, and 5 for discussion of atmospheric absorption of photons, neutrons, and beta particles.)

Radiation entering the atmosphere from above is absorbed rapidly when it reaches the altitude, termed the stopping altitude, where the mean-free path equals one scale height (an altitude region over which the atmospheric density changes by a factor of e (approximately 2.7). Stopping altitudes for the principal radiations from a nuclear weapon are shown in Table 8-1.

Table 8-1 [REDACTED] Approximate Stopping Altitudes for Principal Weapon Outputs Causing Ionization [REDACTED]

Weapon Output	Stopping Altitude (km)
Prompt Radiation	
x-rays (1 kev radiator)	80
Neutrons	25
Gamma rays	25
Debris (kinetic energy)	115
Delayed Radiation	
Gamma rays	25
Beta particles (1 Mev)	60

[REDACTED] For detonations below the stopping altitude of a particular radiation, most of that radiation will be contained locally. When detonations occur above the stopping altitude of a particular radiation, that radiation can spread large distances before being deposited and causing ionization. About  $3 \times 10^4$  ion pairs are produced for each 1 Mev of energy deposited in the atmosphere.

Since about  $3 \times 10^{28}$  Mev are released per megaton of weapon yield, even a small fraction of the weapon output can cause large electron densities. The lifetime for many of the electrons produced is short, however, and it depends critically on the altitude at which they are produced.

[REDACTED] Electrons and ions produced by the ionization sources undergo various atmospheric reactions that change their number density. Four principal reactions must be considered:

1. Attachment. Electrons can attach to neutral air particles (primarily to oxygen molecules and/or atoms) to form negative ions.
2. Detachment. Once attached, electrons can be detached from negative ions by collisions, solar radiation, or radiation from the fireball.
3. Recombination. Electrons and positive ions can recombine to form neutral particles.
4. Mutual Neutralization. Positive ions can combine with negative ions formed by attachment, to produce neutral particles.

[REDACTED] The rate at which these reactions proceed is a strong function of altitude. Thus, the altitude distribution of electron density after a period of time generally will not coincide with the altitude distribution immediately after the deposition of weapon energy. Detailed solutions of the time history of electron density require consideration of a large number of atmospheric species. Many reaction-rate coefficients are not well known, even for the natural atmosphere. The uncertainties in these coefficients provide a significant source of uncertainty in the prediction of electron density time history. In the natural atmosphere above about 70 km, where neutral particle density is low, recombination accounts for the major electron loss. At lower altitudes, attachment becomes increasingly important in the removal of free electrons, particularly at night.

[REDACTED]  
when there is no photodetachment of electrons from negative ions by sunlight.

[REDACTED] In heated or highly ionized regions, the air chemistry (interaction between species) is modified, and electron loss processes are changed. The expansion of heated regions also reduces the electron density.

[REDACTED] In discussing electron density caused by nuclear weapons, it is convenient and useful to consider the electron density resulting from prompt radiation and delayed radiation separately. Also, since ionization and deionization processes are significantly different inside and outside the fireball, these regions will be discussed separately. Although electrons are the principal cause of effects on electromagnetic propagation, ions can affect propagation in the VLF and LF bands (frequencies below a few hundred kilohertz).

### 8-1 Electron Density Within the Fireball

[REDACTED] Initially the incandescent region termed the fireball is highly ionized. For detonations below about 60 km, thermal ionization of air and debris from the weapon and carrier maintains high electron densities until the fireball cools below about 2500°K. For cooler fireballs, beta particles deposited within the fireball may be a significant ionization source. Predictions of electron density within the fireball require knowledge of the distribution of temperature and debris within the fireball, the shape of the fireball as a function of time, and the detailed chemistry of heated regions.

[REDACTED] Detailed calculations, which have been performed for a few burst conditions, are imprecise, particularly with regard to inhomogeneities and gradients in fireball properties. However, for many cases, relatively simple fireball models in which the mass density and temperature are assumed uniform within the fireball can be used. Figures 8-2 and 8-3 show calculated values of average fireball electron density and temperature

following 1-Mt detonations at altitudes of 25 and 50 km, respectively. The calculations contained the assumption that the fireball gas was in thermal equilibrium, as well as being homogeneous.

[REDACTED] When detonations occur above about 60 km, losses of free electrons within the fireball are slower and the electron density does not decay rapidly enough to remain in equilibrium with the cooling fireball. Volume expansion controls the decline of electron density during the first few tens of seconds following detonation. Later, recombination of electrons with positive atomic ions predominates.

[REDACTED] For detonations at altitudes above about 80 km, the geomagnetic field influences the fireball expansion and location. After a few tens of seconds, magnetic forces cause the expansion across the magnetic field to become slower, while expansion along the magnetic field continues. Thus, the fireball becomes elongated along the magnetic field in a roughly cylindrical or tube shape. Figures 8-4 and 8-5 show calculations of average fireball electron density and temperature following 1-Mt detonations at altitudes of 75 and 150 km, respectively.

[REDACTED] Photographs of fireballs affected by the magnetic field show many field-aligned striations within the fireball (see Figure 1-4C). The optical striations also indicate large variations of electron density within the fireball. The size of the striations and the variation of electron density from the average value cannot be scaled accurately with burst parameters at present.

[REDACTED] For detonations at altitudes above about 300 km, the mean-free path of both X-rays and debris particles is large, and localized fireball may not form around the detonation point. However, debris particles initially directed downward may heat and ionize a region below the detonation point. This region, if sufficiently disturbed, is termed a fireball region. The formation of a fireball region depends on the detonation altitude, the weapon yield, and the atmospheric density

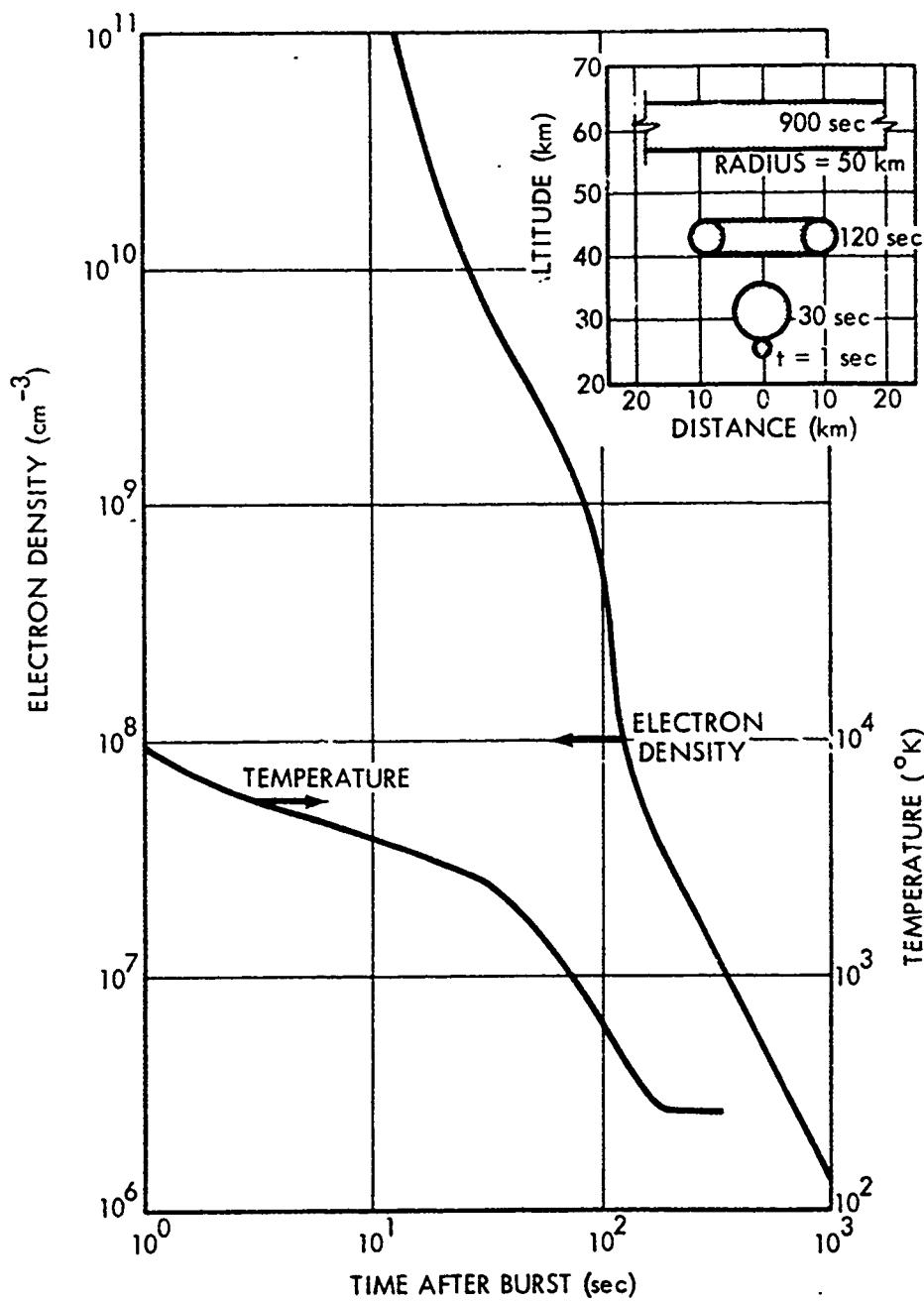


Figure 8-2. Fireball Electron Density and Temperature, 1-Mit at 25 km

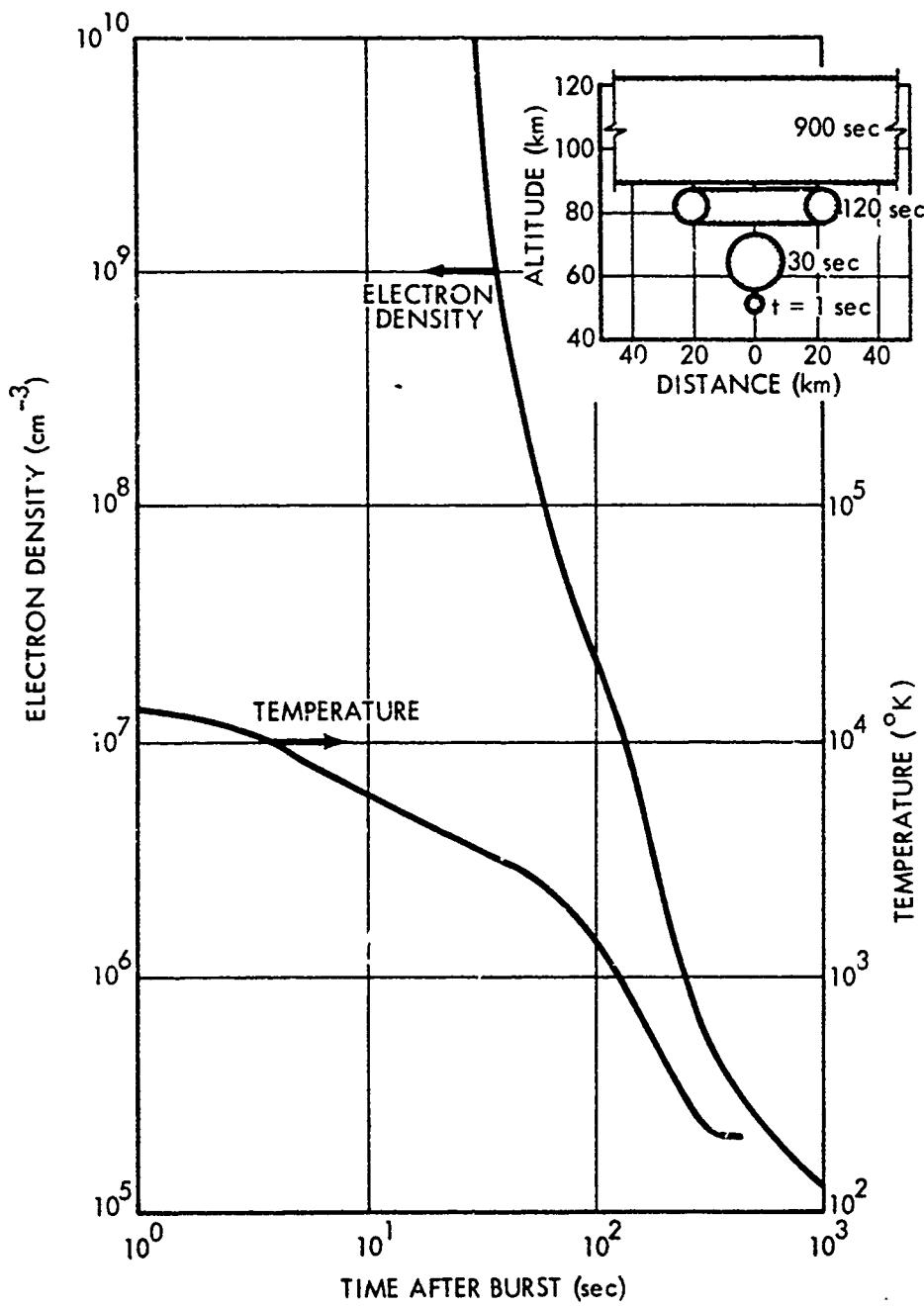


Figure 8-3. Fireball Electron Density and Temperature, 1-Mt at 50 km

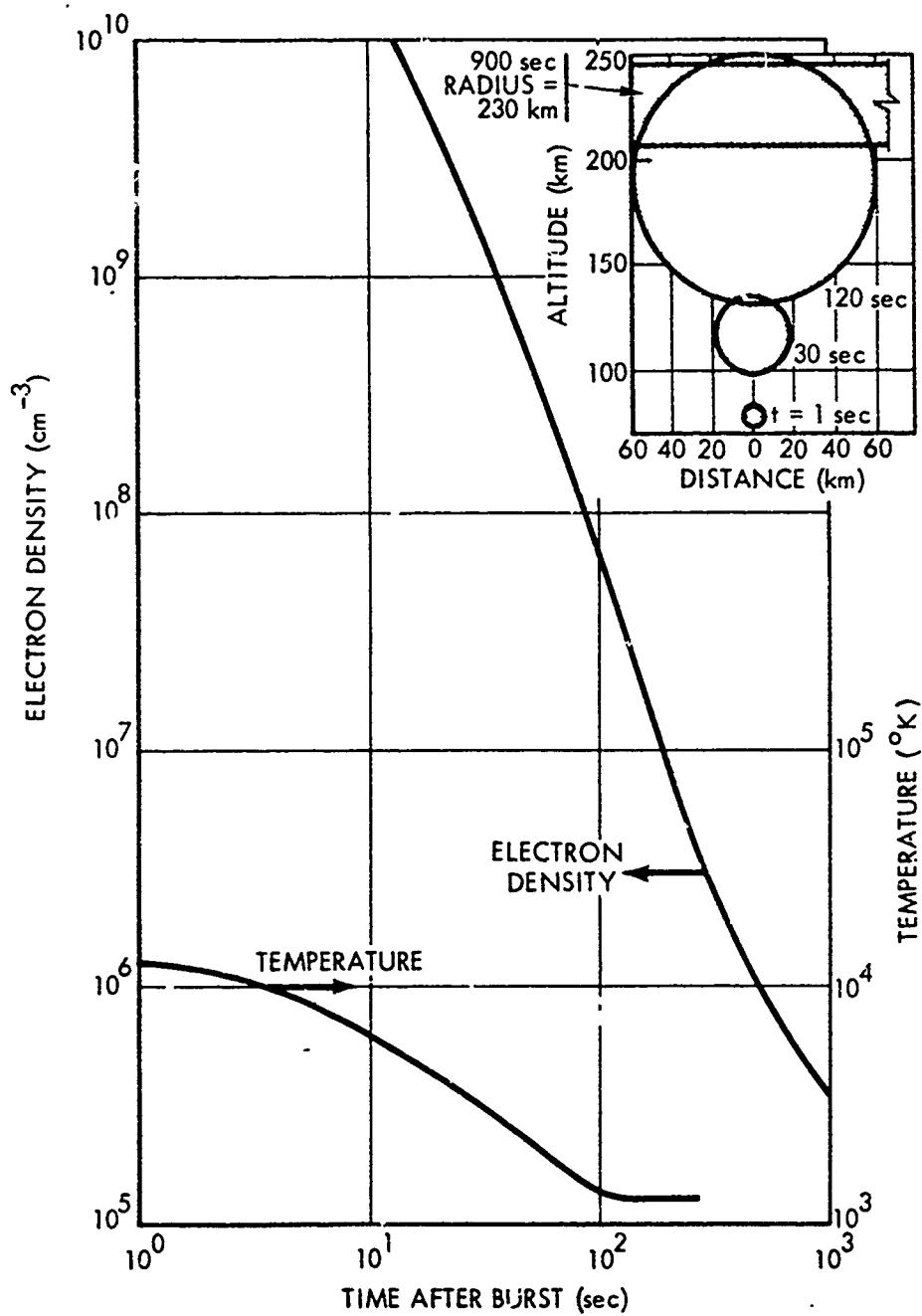


Figure 8-4. Fireball Electron Density and Temperature, 1-Mt at 75 km

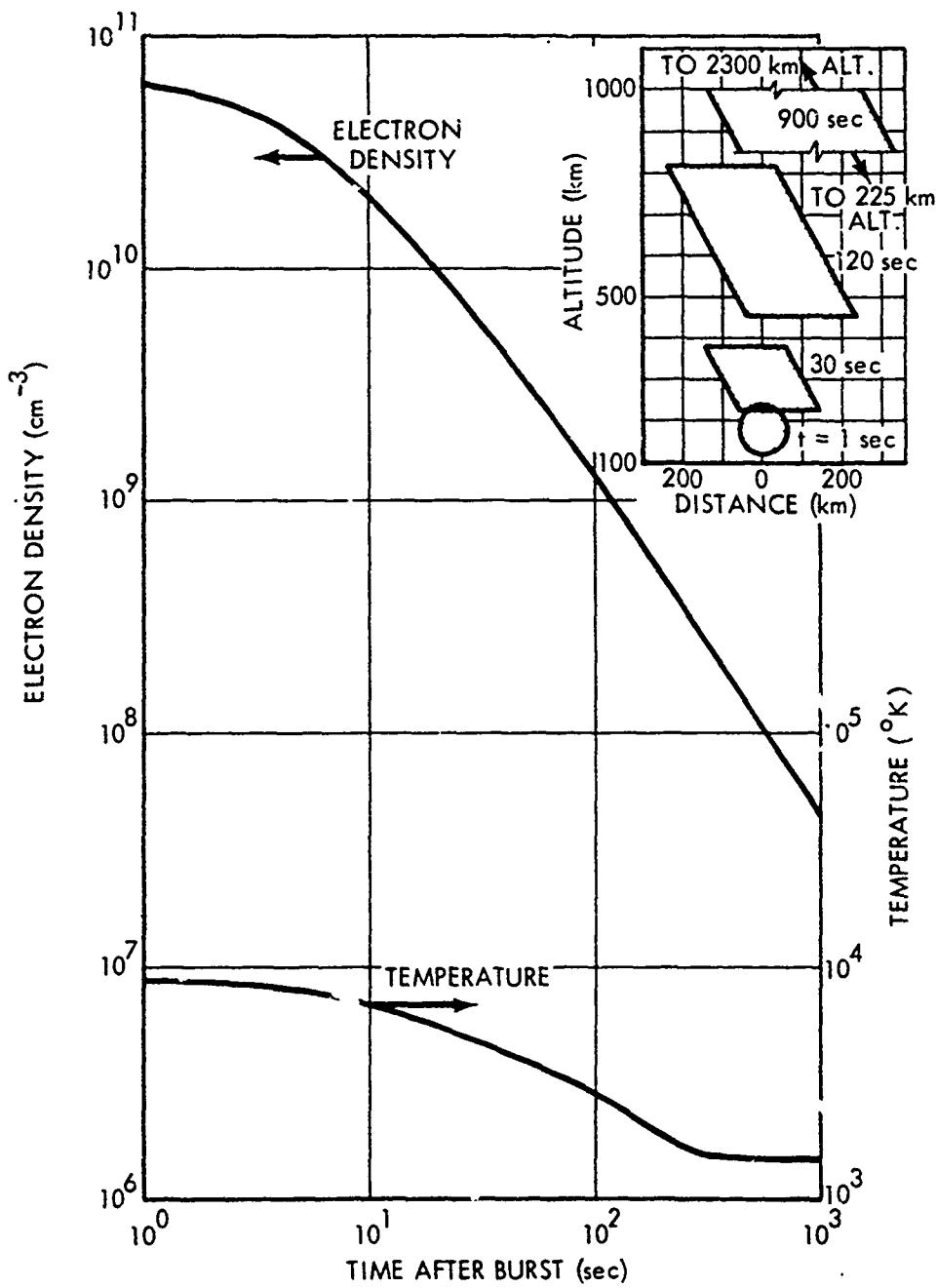


Figure 8-5. Fireball Electron Density and Temperature, 1-MeV at 150 km

at burst time. Figure 8-6 shows calculated values of electron density and temperature within the fireball following a 1-Mt detonation at an altitude of 400 km.

Only a few nuclear tests have been carried out by the U.S. at detonation altitudes above 80 km; therefore, theoretical calculations of fireball formation, size, location, and properties are dependent on parameters that are poorly known. Calculations of fireball properties for detonations at altitudes above 80 km should be considered illustrative of the general order of magnitude rather than as detailed quantitative results.

## 8-2 Electron Density Caused by Prompt Radiation Outside the Fireball

Ionization produced outside the fireball by prompt gamma rays can be neglected insofar as effects on radio propagation are concerned. For detonations at altitudes below about 25 km, both neutrons and X-rays are deposited within or close to the fireball, and the effects of prompt radiation outside the fireball are minimal. For detonation altitudes between 25 and about 80 km, X-rays are largely confined, but neutrons produce ionization over distances of several hundred kilometers. For higher altitude detonations, both X-rays and neutrons cause widespread ionization. Figure 8-7 shows the initial ionization caused by prompt radiation from a nominal megaton weapon detonated at 120 km. Because of earth's curvature, radiation reaching a given altitude at large horizontal distances from the source must pass through lower altitudes where it is strongly attenuated by the denser air.

The decay of electron and ion densities following the ionization impulse depends on electron and ion loss rates, which are functions of altitude and time of day. Below about 100 km, the electron and ion density after 1 second will be essentially independent of the initial ionization if the initial ion pair density is greater than  $10^7$  ion pairs  $\text{cm}^{-3}$ . This condition is termed

saturation; larger initial ionization will not increase the electron or ion density remaining after 1 second. Figure 8-7 shows that the initial ion pair density below 100 km exceeds  $10^7$  ion pairs  $\text{cm}^{-3}$  out to about 500 km from the burst.

Figure 8-8 shows the altitude dependence of the electron density for several times after a saturation impulse. At night the electron concentration decays rapidly, particularly at low altitudes where attachment of electrons to neutral particles is the predominant reaction. During the day, electron densities greater than normal can persist for tens of minutes. The insert in Figure 8-8 illustrates the horizontal extent of the region that can be saturated by prompt radiation as a function of detonation altitude. The decay of electron and ion densities above 100 km depends on processes that may be affected by atmospheric chemistry changes caused by the deposition of prompt radiation. Because of the additional complications introduced at those altitudes, a simple representation of the decay is not possible.

Many of the neutrons produced by the explosion will travel upward and will escape the atmosphere. Since neutrons are not affected by the geomagnetic field, they will spread isotropically over a large area. Each neutron eventually disintegrates spontaneously into a proton, a neutrino, and a beta particle (half-life for disintegration is about 12 minutes). Since the beta particle (a high-energy electron) is charged, it can move only in the direction of the geomagnetic field (motion normal to the magnetic field direction causes the beta particle to spiral around the magnetic field lines). The beta particles are guided by the geomagnetic field until reaching altitudes near the beta-particle stopping altitude (see paragraph 8-4 and Figure 8-10), where they deposit their energy to produce ionization. The amount of ionization caused by neutron-decay beta particles is small, but it has been noted at distances of many thousands of kilometers from the burst point.

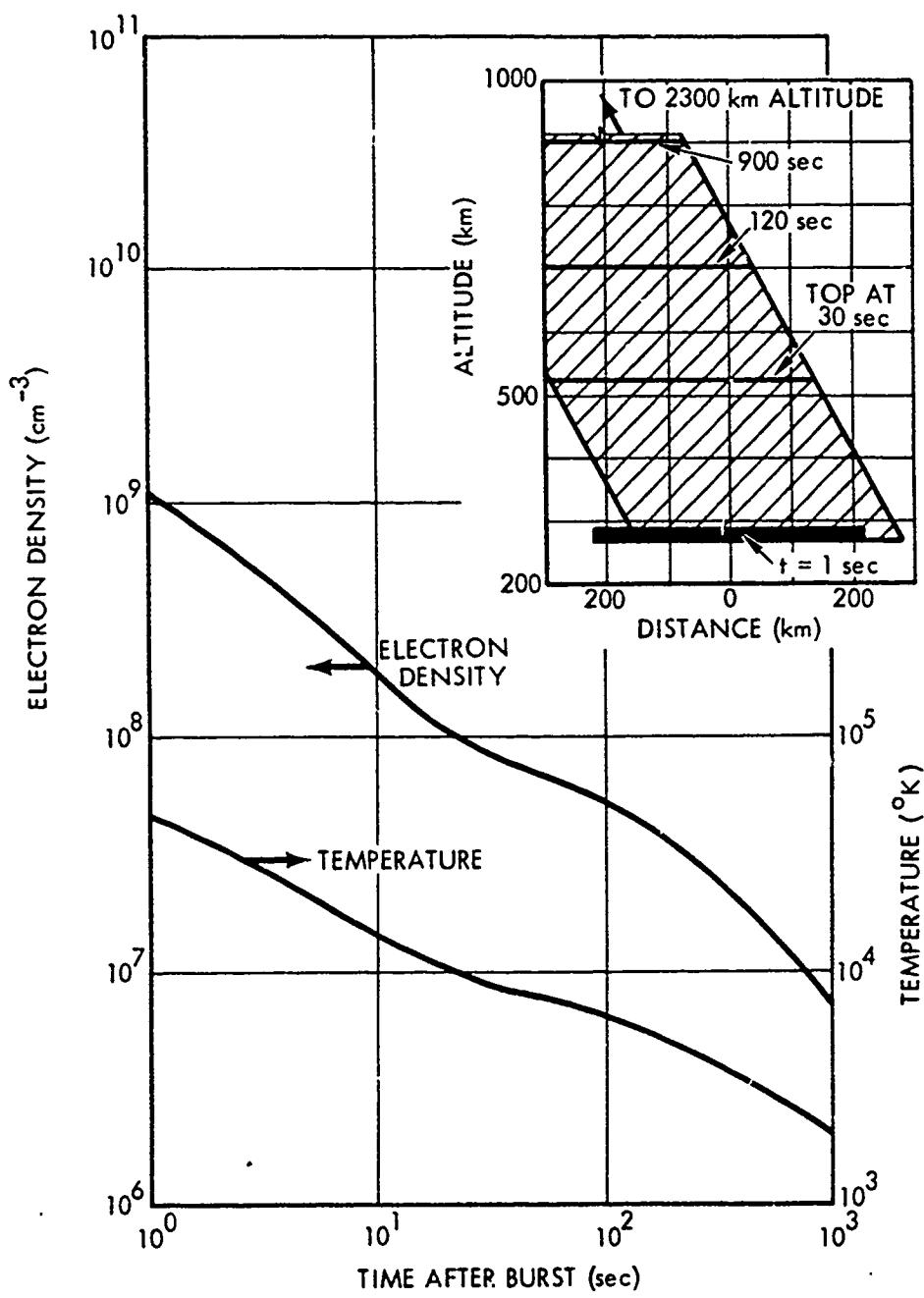


Figure 8-6. [REDACTED] Fireball Electron Density and Temperature, 1-Mt at 400 km [REDACTED]

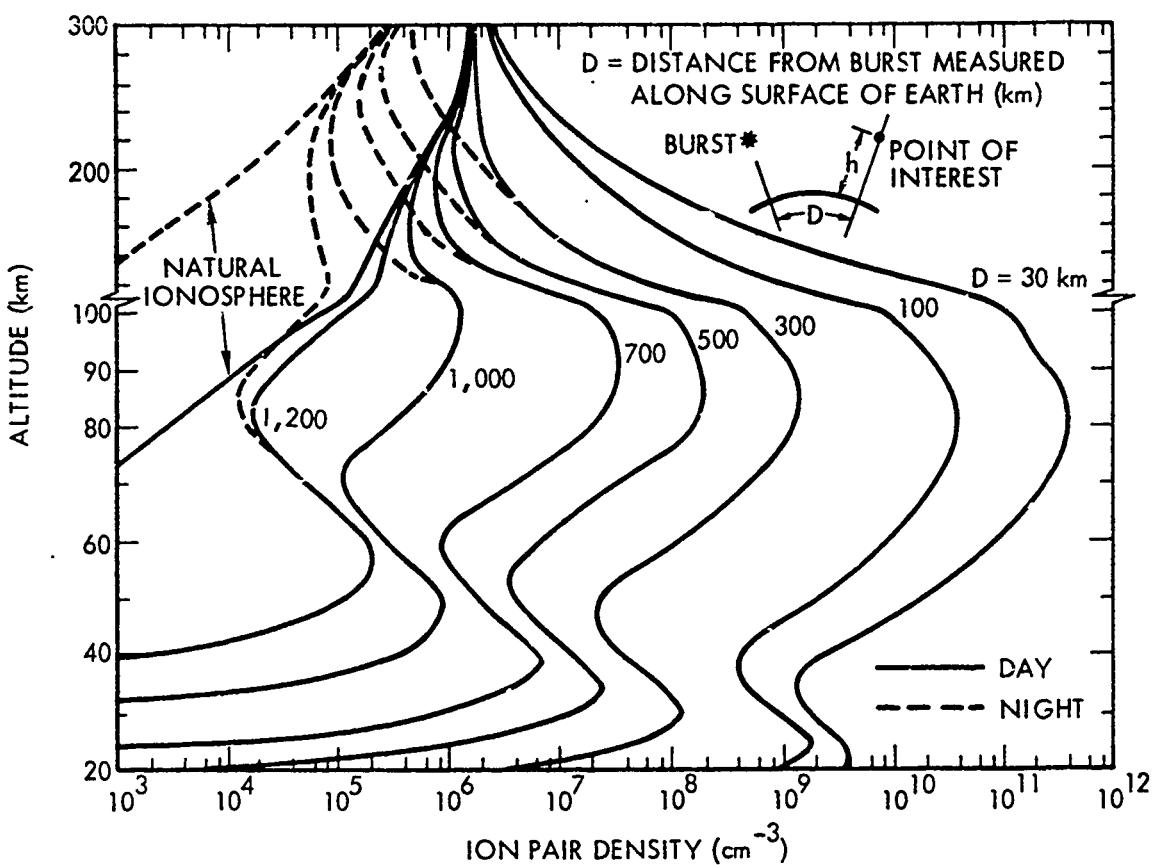


Figure 8-7. Ion-Pair Density Due to Prompt Radiation from a 1-Mt Burst Detonated at 120 km,  $t = 0$

### 8-3 Electron Density Caused by Delayed Gamma Radiation Outside the Fireball

In addition to prompt radiation, delayed gamma rays and beta particles (discussed in Section III, Chapter 5) are produced during the radioactive decay of the fission debris. This continuing radiation produces ionization characterized by a production rate of ion pairs per unit volume per unit time. For detonations below several hundred kilometers, the fission debris (assumed to be mixed with the total weapon debris) is initially within the fireball and is carried upward as the fireball rises and expands.

When the debris is below the gamma-ray stopping altitude, gamma rays can only penetrate a short distance, and the ionized region that they produce around the fireball is small. If the debris rises above the gamma-ray stopping altitude, gamma rays produce ionization over larger distances. The resulting electron and ion densities are a function of both the ion-pair production rate and the electron and ion loss processes. Most of the gamma-ray energy is deposited near the stopping altitude, but the electrons produced below about 40 km are lost quickly by attachment. Maximum electron density usually occurs at higher altitudes where the electron lifetimes

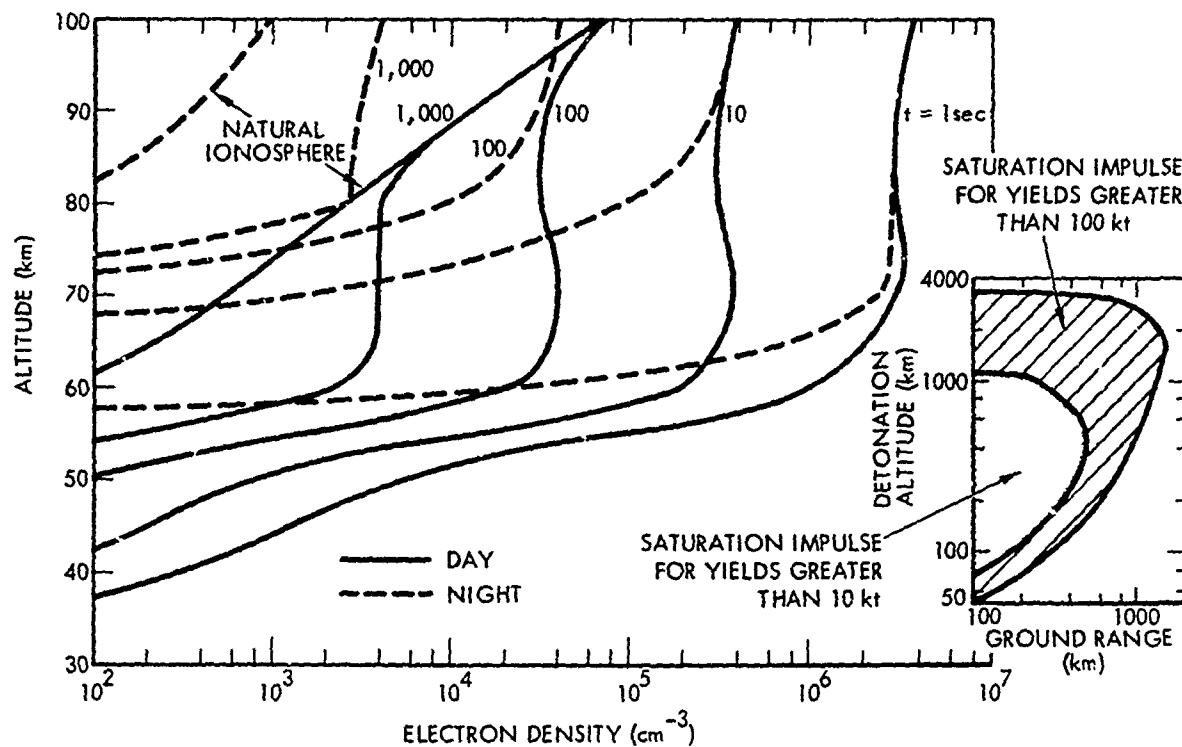


Figure 8-8. D-Region Electron Density Caused by Prompt Radiation (Saturation)

are longer. Near the debris region, where the gamma ray flux is large, substantial electron densities can be maintained even though the debris is at an altitude where free electrons are lost by attachment rapidly.

When the fission debris and the point of interest are both well above the gamma-ray stopping altitude, the ion-pair production rate and electron and ion densities caused by gamma rays can be expressed conveniently in terms of a radiation intensity parameter,  $I_\gamma$ , defined by

$$I_\gamma = \frac{4 \times 10^{-7} W_F}{4\pi R^2 (I+t)^{1.2}} \text{ watts m}^{-2},$$

where

$W_F$  = fission yield in megatons,

$R$  = radial distance from debris center to point of interest in km,

$t$  = time after detonation in seconds.

Figure 8-9 shows quasi-equilibrium electron densities for particular values of  $I_\gamma$ . The values are called quasi-equilibrium because they are the values that would be reached if the production rate remained constant and if sufficient time were allowed for equilibrium conditions to be reached. In an actual situation, the production rate changes with time because of the radioactive decay of the fission debris and the changing geometry as the debris moves. However, for most cases, the time to reach equilibrium is short, and the quasi-equilibrium values are close approximations to the electron densities. The insert in Figure 8-9 illustrates the horizontal extent as a function of

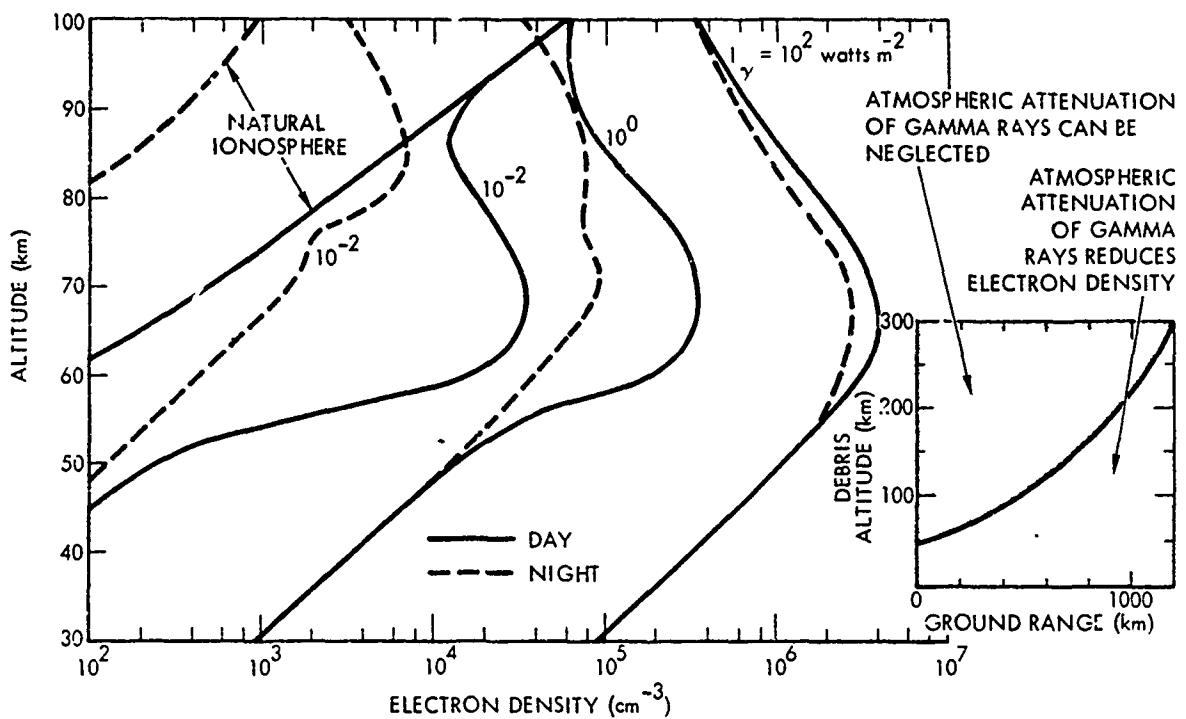


Figure 8-9. Quasi-Equilibrium Electron Density Due to Gamma Rays

debris altitude for which the electron densities are applicable.

Most delayed gamma rays deposit their energy in the atmosphere by first producing high-energy electrons (Compton electrons). Compton electrons travel very short distances in the lower atmosphere; however, some Compton electrons produced above about 60 km can escape to the conjugate region, as described for beta particles in paragraph 8-4. Ionization in the conjugate region caused by Compton electrons is of interest primarily for studies of propagation in and below the HF band (frequencies below 30 megahertz).

#### 8-4 Electron Density Caused by Beta Particles Outside the Fireball

Since beta particles are electrically charged, their motion in the atmosphere is affected by the geomagnetic field. When the fission

debris is above the beta-particle stopping altitude, about half of the betas will travel down the geomagnetic field lines, producing ionization (similar to auroral ionization at high latitudes) until they are deposited near the stopping altitude. The other half of the betas (those emitted upward) will follow the geomagnetic field lines across the geomagnetic equator and will produce ionization at the geomagnetic conjugate.<sup>3</sup>

Figure 8-10 illustrates the location of the beta-particle ionization regions. Because of the slope (dip angle) of the magnetic field lines, the beta-particle ionization region is offset from the debris. When the geomagnetic field is undisturbed by the detonation, the location of the

<sup>3</sup> As used herein, geomagnetic conjugate points are points at the north and south ends of a geomagnetic field line that are at corresponding altitudes.

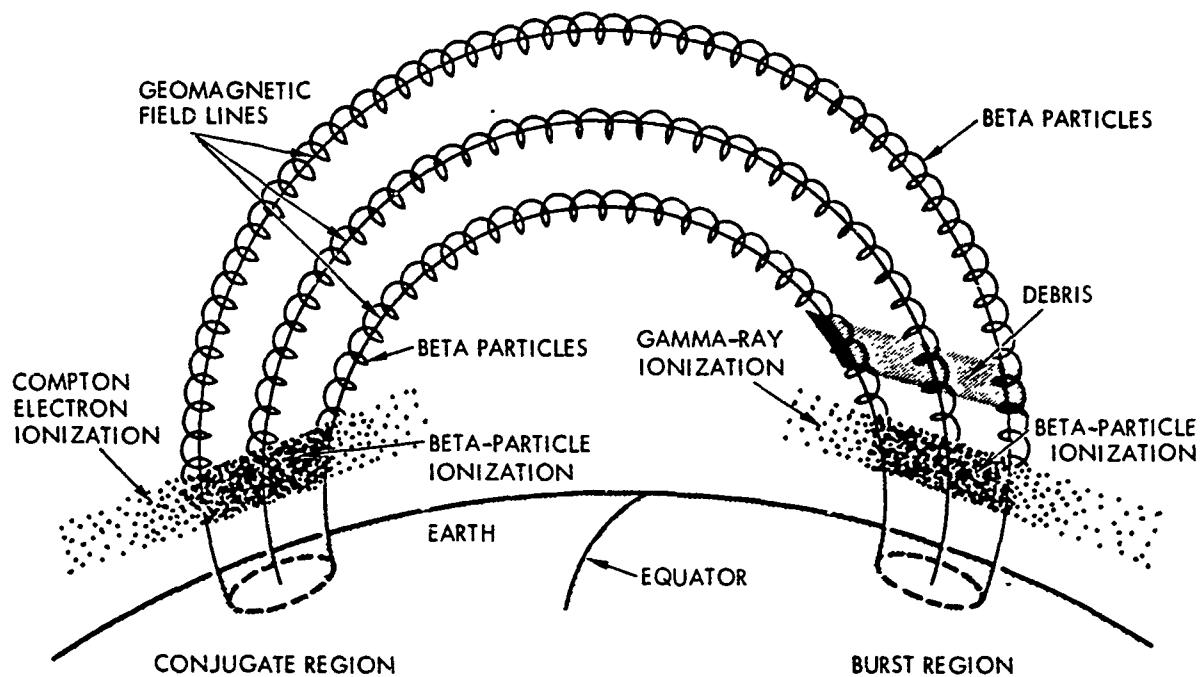


Figure 8-10. Location of Delayed Ionization Regions

beta-particle ionization region can be determined from a knowledge of the size and location of the debris region and the geomagnetic field lines. However, the geomagnetic field can be severely distorted for tens of seconds after a nuclear detonation. Determination of the magnetic dip angle and location of the conjugate point for undisturbed magnetic-field conditions are discussed in Problems 8-8 and 8-9.

The location of the gamma-ray ionization region and the region ionized by Compton electrons escaping to the conjugate region are also illustrated in Figure 8-10.

The ion-pair production rate and electron density caused by beta particles can be expressed conveniently in terms of a radiation intensity parameter,  $N_\beta$ , defined by:

$$N_\beta = \frac{8.8 \times 10^{15} W_F}{A(1+t)^{1.2}} \text{ betas } cm^{-2} sec^{-1}, \quad (8.1)$$

where

$A$  = area covered by fission debris in square kilometers.

Figure 8-11 shows the quasi-equilibrium electron density caused by beta particles for particular values of  $N_\beta$ . These curves apply if the fission debris is well above the beta stopping altitude and if the debris is uniformly distributed over the area  $A$ .

### 8-5 Electromagnetic Propagation in Ionized Regions

An electromagnetic wave propagating through an ionized region does work on charged particles in the region and transfers a portion of the wave energy to charged-particle kinetic energy. The electric field exerts a force on all charged particles; however ions, because of their larger mass, absorb less energy than electrons and can usually be neglected (an exception is wave

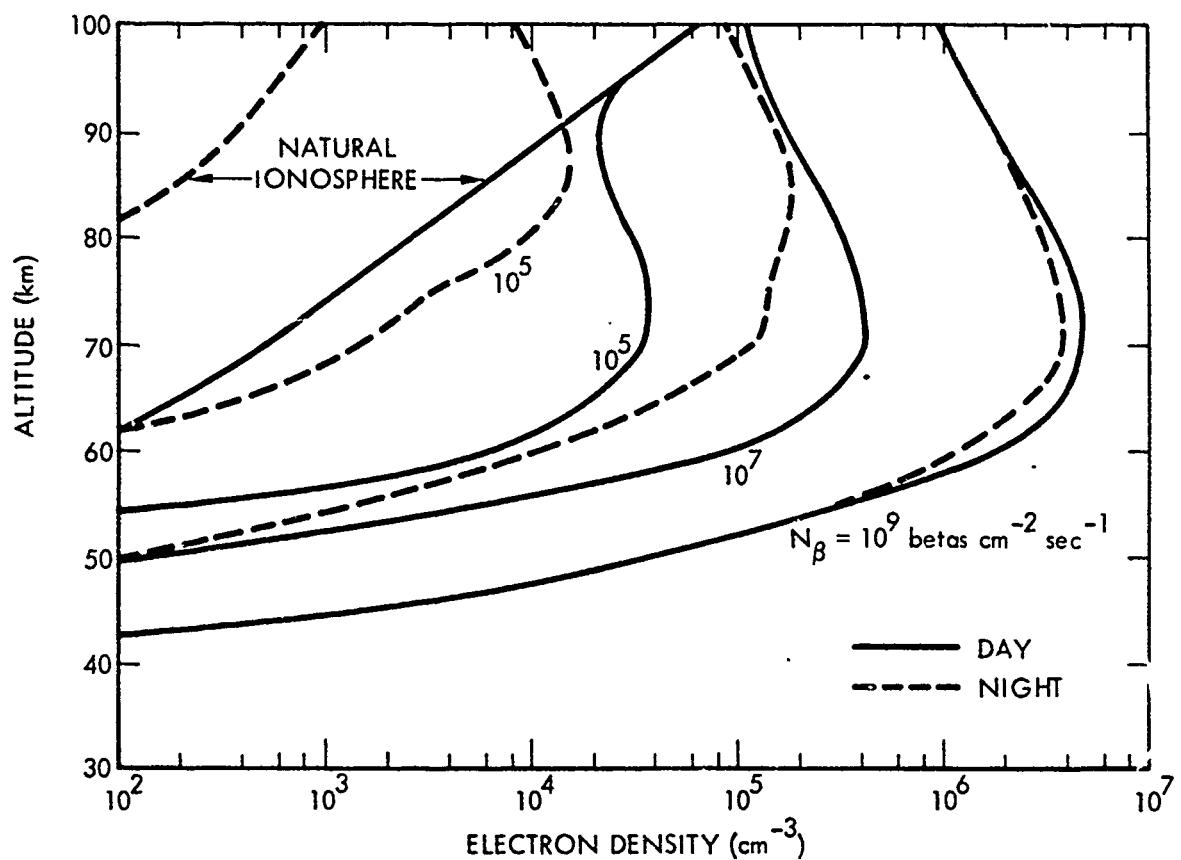


Figure 8-11. Quasi-Equilibrium Electron Density Due to Beta Particles,  
Debris Altitude Greater than 60 km

propagation at frequencies below a few hundred kilohertz). If the electrons do not collide with other particles, the energy is returned to the propagating wave without loss, but the phase of the wave is modified. Unless the geomagnetic field is parallel to the electric field of the propagating wave, some of the energy returned to the wave will have an electric field that is perpendicular to the incident electric field. The propagation wave then can be described as the sum of two plane waves termed the ordinary and the extraordinary waves—which have different phase velocities. One effect is to change the polarization of the propagation wave as it travels through the

ionized medium. Electron collisions with other particles change the ordered motion of electrons into random motion (heat), and energy is absorbed from the wave. For many cases of interest, detonation-produced absorption is the overriding effect on electromagnetic propagation and it is the effect that is understood best.

#### TRAVELING DISTURBANCES IN E AND F REGIONS OF IONOSPHERE

The preceding paragraphs discuss ionization sources from a nuclear explosion that add to the free electron content of the atmosphere. Following Teak and Orange (megaton

DRA  
(b) (3)

[REDACTED]

detonations at altitudes of 76 and 43 kilometers, respectively: 1958 test series) and again during Operation Fish Bowl (1962 test series), the normal E-region and F-region electron content appeared to be disturbed by hydrodynamic or hydromagnetic waves created by the detonation (the E-region includes the volume from 90 to 160 kilometers altitude, and the F-region begins at about 160 kilometers).

DRA  
(b) (5)

## ELECTROMAGNETIC RADIATIONS

[REDACTED]

A heated region emits thermal radiation according to its temperature and emissivity. The emissivity at a given frequency approaches unity as the absorption becomes large (10 decibels or more). The fireball may remain hotter than several thousand degrees Kelvin for about a hundred seconds. It may be sufficiently emissive for fre-

quencies less than a few gigahertz that systems with antennas pointing at the fireball would register antenna temperatures equal to the fireball temperature if there were no intervening absorption outside the fireball. Generally, absorption caused by prompt and delayed radiation outside the fireball will reduce the escaping thermal radiation. The effective antenna noise temperature will depend on the size of the fireball relative to the antenna beam width, the location of the fireball relative to the antenna beam, and the absorption outside the fireball, as well as the temperature and emissivity of the fireball.

[REDACTED] A second source of electromagnetic radiation in the radio band is synchrotron radiation, which is caused by beta particles spiraling along geomagnetic field lines. A spiraling beta particle continually accelerates, and, therefore, it radiates electromagnetic energy. The radiation is maximum in the HF band, and it is approximately inversely proportional to frequency cubed for higher frequencies. The radiation is concentrated in the direction of the vector of electron motion. Because of its directivity, low intensity, and frequency dependence, synchrotron radiation does not appear to degrade present military systems seriously.

## ABSORPTION

[REDACTED] Exact expressions for the absorption or energy loss involve components of the earth's magnetic field as well as electron density, collision frequency (number of collisions an electron makes per second), and wave frequency. For frequencies above about 10 megahertz and when bending of the wave is negligible, the incremental path absorption can be found from the following equation.

$$a = 4.6 \times 10^4 \frac{N_e v}{\omega^2 + v^2} dB/km, \quad (8.2)$$

where

$N_e$  = electron density (electrons/cm<sup>3</sup>)

$v$  = collision frequency (collisions/sec)

$\omega$  = wave frequency (radians/sec).

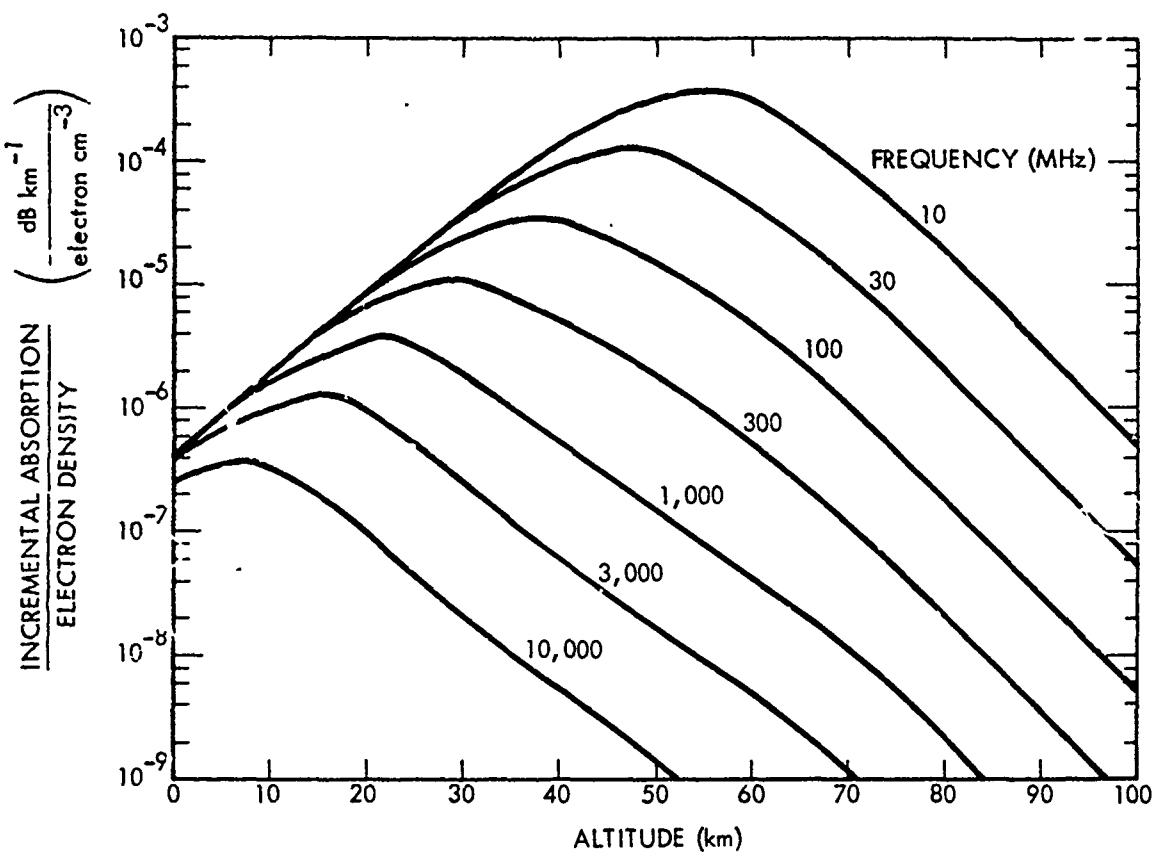


Figure 8-12. Incremental Absorption Due to Electron-Neutral Collisions

Figure 8-12 shows incremental path absorption per electron per cubic centimeter as a function of altitude due to electron-neutral collisions. Above about 100 km, where the neutral particle density is low, absorption due to electron-neutral collisions is small; however, absorption due to electron-ion collisions may be important. Figure 8-13 shows incremental absorption due to electron-ion collisions for a temperature of 1000°K (approximate value of the atmospheric temperature above 200 km). The incremental absorption is proportional to  $(1000/T)^{3/2}$  for other temperatures. The dotted portion of the curves indicates the volume where the electron density causes considerable bending

of the wave, and a more detailed solution is required to obtain better values for the absorption. Figures 8-12 and 8-13 can be used with estimates of electron density (obtained from Figures 8-2 through 8-9 and 8-11) to determine incremental path absorption. The integral of the incremental path absorption along the propagation path gives the total path loss. Equation 8.1 and Figures 8-12 and 8-13 neglect ion-neutral collisions, which are important at low frequencies (VLF and LF bands). Problems 8-4 through 8-7 provide methods for estimating total one-way path absorption for various propagation paths.

As was the case for electron density, it is convenient and useful to present absorption in-

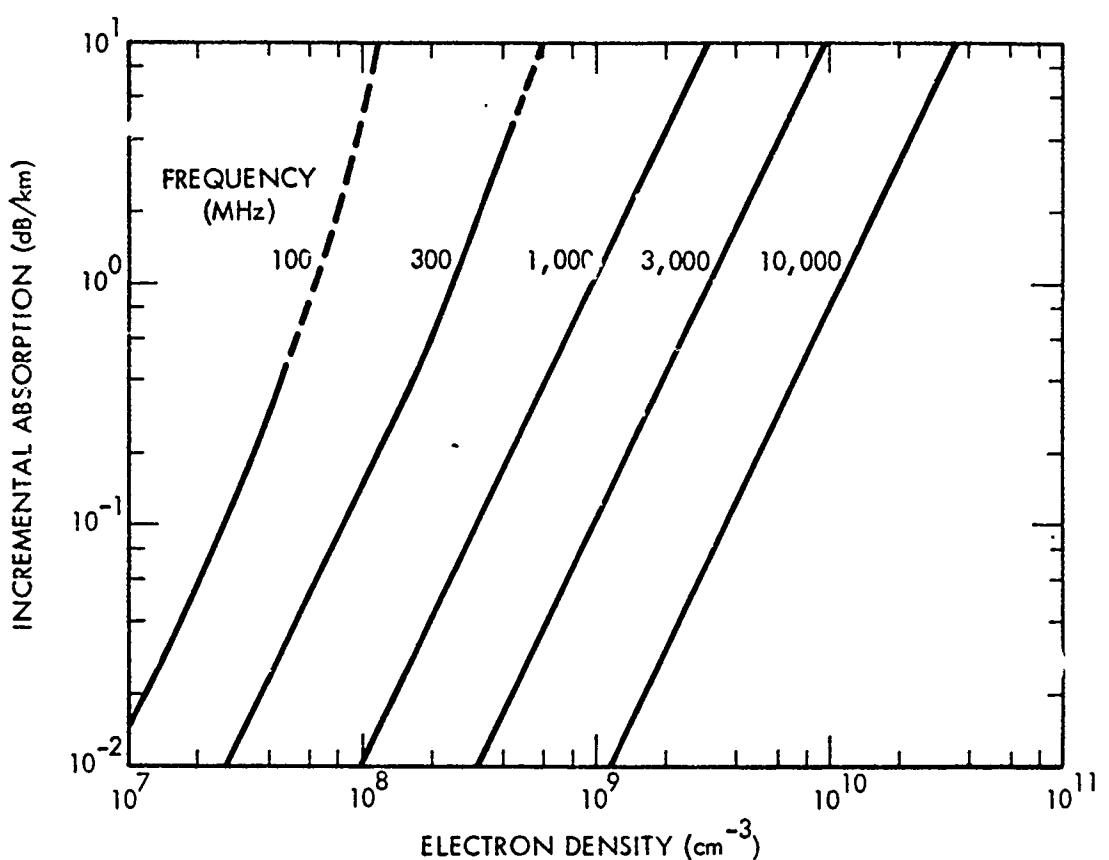


Figure 8-13. Incremental Absorption Due to Electron-Ion Collisions,  
Electron Temperature = 1,000°K

side the fireball) and absorption caused by prompt and delayed radiation outside the fireball separately. With the exception of propagation paths that pass close to the fireball, absorption outside the fireball is maximum in the D-region (40 to 90 km). Generally it is sufficiently accurate to consider the largest of the separate absorptions as the total absorption along a particular propagation path.

Scaling relations for the attenuation of low frequencies (VLF and LF bands) are difficult to present, because the amount of absorption for a particular propagation path depends in detail on the penetration of the wave into the atmosphere.

A description of low-frequency propagation in nuclear environments is given in Chapter 17. Scaling relations for absorption of propagation at frequencies greater than a few megahertz are given in succeeding paragraphs; however detailed solutions of absorption for propagation paths associated with communication and radar systems usually require numerous calculations that cannot be obtained readily from simple hand-computation procedures. Figure 8-14 shows the burst conditions (detonation altitudes and yield) for which prompt and delayed radiation can cause absorption outside the fireball. The figure can be used in conjunction with the discussion in para-

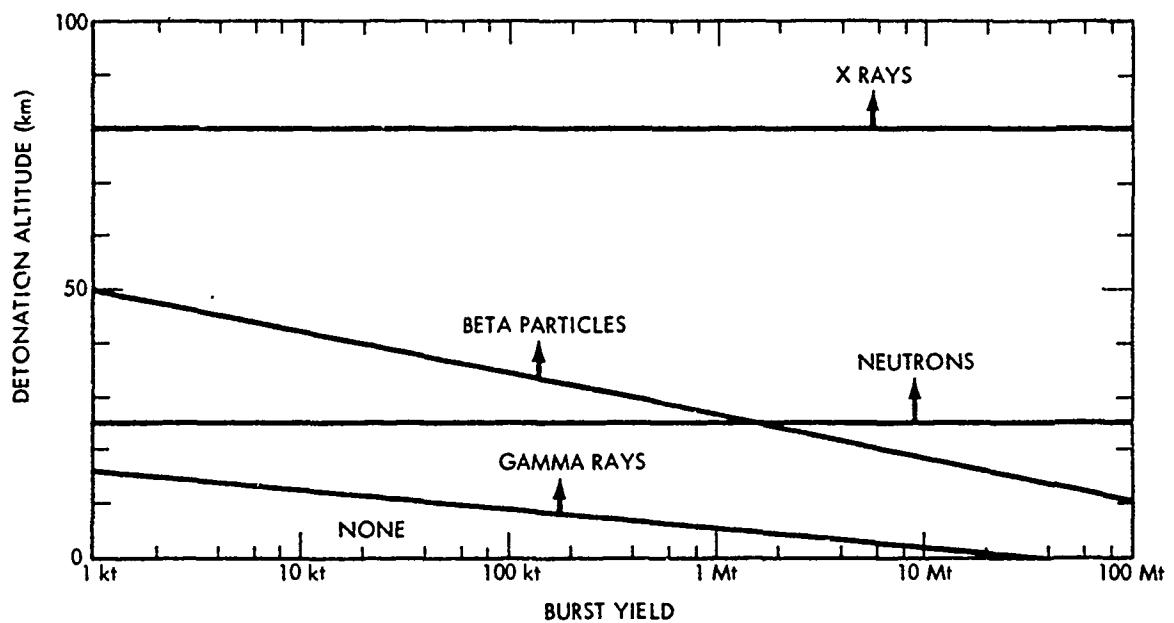


Figure 8-14. Radiation Sources Causing Absorption Outside the Fireball

graphs 8-7 and 8-8 to determine whether absorption outside the fireball need be considered and which radiation sources are important.

#### 8-6 Absorption Within the Fireball

Fireball ionization is localized and very intense: for most purposes, the fireball may be considered opaque at all radio frequencies for at least a few seconds. Calculations of the magnitude of absorption at a given time, or the duration of a given magnitude of absorption, are subject to considerable error because of uncertainties in predictions of the electron density within the fireball (see paragraph 8-1) and the fireball geometry. Methods for estimating fireball size and absorption through the fireball are given in Problems 8-1 through 8-4.

For detonations below about 80 km and weapon yields greater than 100 kt, absorption through the fireball is expected to exceed 25 decibels for about 50 seconds at 10 gigahertz and for longer than 100 seconds at 1 gigahertz.

Because the fireball rises a significant distance during these time periods, the duration of degradation due to absorption will generally be determined by the relative motion of fireball and propagation path.

(1)(3)

(b)(3) A

### 8-7 Absorption Caused by Prompt Radiation Outside the Fireball

Absorption outside the fireball caused by prompt radiation may last from tens of seconds in the VHF band to tens of minutes in the HF band for daytime conditions. At night the absorption decreases more rapidly. For bursts below about 100 kilometers, the horizontal radius of the prompt absorption region only extends a few hundred kilometers from the burst point; for higher detonations the extent can be much longer.

### 8-8 Absorption Caused by Delayed Radiation Outside the Fireball

Absorption caused by delayed radiation (gamma rays and beta particles) is a function of the location and distribution of the fission debris. Estimates of debris rise and expansion for use in computing delayed-radiation effects are given in Problems 8-1 through 8-3.

Delayed gamma rays can produce significant absorption when the debris is at altitudes above about 25 kilometers. Problem 8-6 describes methods that can be used to estimate one-way path absorption. The horizontal extent of the absorption region caused by gamma rays depends on weapon fission yield, debris altitude, time after burst, and wave frequency. The insert in Figure 8-9 shows the maximum possible extent of ionization and, thus the maximum extent of absorption; for most cases the region of significant absorption will be smaller.

When the debris is above about 60 kilometers, beta particles produce D-region absorption at the burst locale and on the opposite side of the magnetic equator. Figures 8-49 through 8-51 can be used to obtain estimates of absorption caused by beta particles in terms of the beta-radiation intensity parameter that was defined in

paragraph 8-4 for debris above the beta-particle stopping altitude (60 km). The location of the absorption region is offset from the debris region because of the effect of the geomagnetic field on the motion of beta particles, as illustrated in Figure 8-10. The horizontal radius of the absorption region is approximately equal to the debris radius. This radius can vary from a few kilometers to a few thousand kilometers depending on weapon yield, detonation altitude, and time after burst.

### PHASE CHANGES

Phase changes resulting from propagation through a region of uniform electron density affect propagation velocity and signal characteristics. Relative phase changes due to gradients in electron density change the direction of propagation and scatter energy from the propagating wave. Some phase effects become important only for electron densities that cause significant absorption. Evaluation of direction changes and scattering requires detailed information concerning the spatial distribution of electron density, which is difficult to predict theoretically and for which there is only limited experimental data.

### 8-9 Velocity of Propagation

Within an ionized region the phase velocity is increased over that in vacuum, but the group velocity, associated with the transmission of energy, is reduced. The increased time required to propagate energy through the region is proportional to the integral of electron density along the propagation path. Typical values of time delays associated with ionization caused by nuclear bursts range from a few nanoseconds to a few tens of microseconds. The larger time delays usually are accompanied by significant absorption when the ionized region occurs below 100 km.

The phase velocity in an ionized region depends on the frequency. Therefore, the region

[REDACTED]  
[REDACTED]  
separates waves of different frequencies, i.e., the region is dispersive. The significance of dispersion depends critically on the type of signal being propagated and the type of signal processing being employed. For frequency-modulated signals, dispersion causes intermodulation and harmonic distortion. For digital systems, dispersion causes pulse-envelope distortion. Dispersion effects caused by electrons below 100 kilometers appear to be negligible when compared to absorption. At higher altitudes, electrons can only cause important dispersion effects for wide-band signals (bandwidths of the order of 1 percent or more of the carrier frequency), and these effects will probably only occur for propagation paths through fireball regions after the electron density has decreased sufficiently that absorption is not overriding.

#### 8-10 Frequency of Propagation [REDACTED]

[REDACTED] A time-dependent phase change is equivalent to a frequency shift. The frequency shift is proportional to the time rate of change of the electron density integral along the propagation path. Frequency changes may be caused by changes in electron density with time along a fixed propagation path or by motion of the propagation path in a region of inhomogeneous electron density. For a fixed propagation path, frequency changes caused by nuclear-weapon-produced ionization are small (a few hertz for a 10 megahertz signal) by a few seconds after burst. Larger frequency changes may occur when the propagation path moves through regions of high electron density, such as the fireball; however, in those cases absorption generally will be overriding.

#### 8-11 Direction of Propagation [REDACTED]

[REDACTED] Spatial gradients in electron-density can change the direction of propagation. When the electron density gradient is steep, part of the energy can be reflected. Reflection is important in the propagation of low frequencies (tens of

kilohertz) over paths that are remote from the fireball. It also may be important in the propagation of much higher frequencies for paths that pass near the fireball, where high electron density gradients can exist.

[REDACTED] Smaller electron-density gradients cause ray bending (refraction). Refraction in the ambient ionosphere (E- and F-region) is important for beyond-the-horizon propagation in the HF band. For radar systems, refraction in the D-region caused by nuclear-burst-produced ionization normally is accompanied by significant absorption. Possible exceptions may occur if the propagation path passes close to the fireball or close to regions ionized by beta particles (particularly when the propagation path is nearly parallel to the geomagnetic field lines). Changes in the E- and F-region electron density caused by the fireball or by traveling disturbances may modify HF and VHF propagation significantly. E- and F-region electron densities sufficient to change the direction of propagation at higher frequencies by a few degrees can occur without causing significant absorption.

#### 8-12 Scatter and Scintillation [REDACTED]

[REDACTED] Inhomogeneities in the propagation medium (variations in the dielectric constant of the medium) cause a small amount of incident energy to be scattered away from the original propagation direction. The direction of scatter depends on the shape of the inhomogeneities and their orientation relative to that of the incident beam. Energy that is forward scattered as the wave traverses inhomogeneous regions can cause fluctuations in the amplitude and the phase of the wave, called scintillation. The phase fluctuations are equivalent to fluctuations in the direction of propagation that result in random variations in the angle of arrival of received signals. Small amounts of backscattered energy can produce interference to radar systems called clutter.

[REDACTED] The analysis and quantitative description

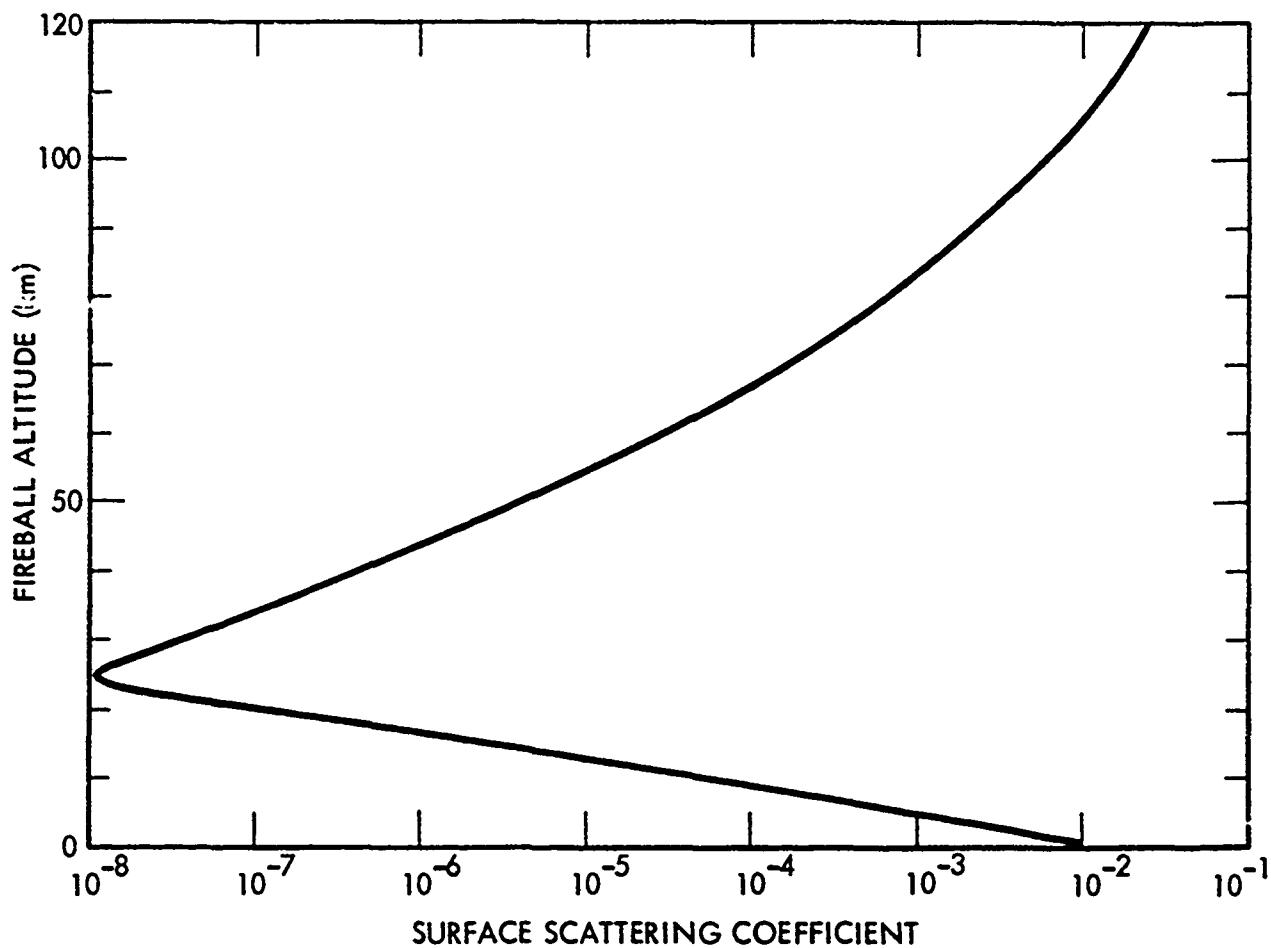


Figure 8-15. [REDACTED] Apparent Fireball Surface Scattering Coefficient at 400 MHz [REDACTED]

of scatter requires a statistical model of the spatial distribution of inhomogeneities in the propagating medium. Sufficient information from which such models could be constructed for nuclear-weapon-produced ionization is not available. There are limited experimental data from nuclear weapon tests concerning backscatter; however, interpretation of these data is difficult, and sufficient information for the construction of a complete empirical model is not available.

Significant backscatter has been observed from fireball regions from a few tens of seconds to a few minutes after burst. Figure 8-15 shows the general order of magnitude of the surface scattering coefficient (multiply by the area of the scattering surface to obtain radar cross section) derived from experimental data. Below about 20 km, scattering is apparently due to variations in air density across fireball boundaries and across shock waves. For surface bursts, dust, dirt, and water vapor appear to cause backscatter

from the stem of the rising cloud. Backscatter from fireballs above 20 km can be explained in terms of partial reflection, or scatter from inhomogeneities in electron density in the fireball or in the shock fronts. The cross section appears to decrease with increasing frequency. The minimum in the apparent cross section near 20 km is due to several mechanisms, the prime of which is the absorption sheath caused by beta particles escaping from the fireball. The scattering coefficients shown in Figure 8-15 are only illustrative; observed values vary over an order of magnitude, depending on the relative geometry of propagation path and fireball, the characteristics of radars used in obtaining the data, and the time after burst.

Backscatter is also observed from regions of field-aligned ionization (ionized regions that are elongated along the geomagnetic field, often referred to as auroral ionization) which can be produced above about 80 km by beta particles. Field-aligned ionization can also occur within the fireball after a few tens of seconds for detonations above about 80 kilometers. The magnitude of backscatter is aspect sensitive; maximum backscatter occurs when the propagation path is normal to geomagnetic field lines. Backscatter from field-aligned ionization is thought to be a volume effect; volume scattering coefficients of about  $10^{-13} \text{ m}^2/\text{m}^3$  at 400 MHz have been observed from beta-particle ionization regions. Significantly larger coefficients may occur from field-aligned ionization caused by the fireball. The cross section scales inversely as about the 4.5 power of frequency. Returns have been recorded for several hours after burst.

## SECTION II METHODS FOR CALCULATING ABSORPTION OF RADIO FREQUENCIES

As discussed previously, absorption fre-

quently is the most important phenomena affecting propagation of radio frequencies; however, detailed solutions of absorption for propagation paths associated with communication and radar systems usually require numerous computations that cannot be obtained readily by hand calculations. The procedure for calculating absorption that are described below offer a means for obtaining reasonable estimates of radio frequency absorption for many situations of interest, however, the user should maintain awareness of the limitations defined for each of the calculations.

The calculation of the absorption of radio frequencies will be described separately for three conditions: absorption of propagation paths going through the fireball, absorption caused by prompt radiation outside of the fireball, and absorption caused by delayed radiation outside of the fireball (this last condition is divided further into absorption caused by delayed gamma rays and absorption caused by delayed beta particles).

Prior to the determination of the absorption along any of the paths discussed above, the size and location of the fireball region and/or the debris region must be determined. The spatial and temporal characteristics of the fireball and the debris regions created by nuclear bursts are complex. Idealized geometric models have been adopted for the purpose of analysis. The dimensions of three scaling models, based largely on interpolations of data from high-altitude nuclear tests, are used to represent detonations in three burst altitude regimes; below 80 kilometers, between 85 and 120 kilometers, and above 120 kilometers. The characteristics of the fireball and the debris are discussed separately for these three burst altitude regimes in succeeding paragraphs. Figure 8-16 illustrates the idealized geometric models referred to in the discussions. Dimensions shown in Figure 8-16 are defined in the discussions or in the illustrative problems that follow.

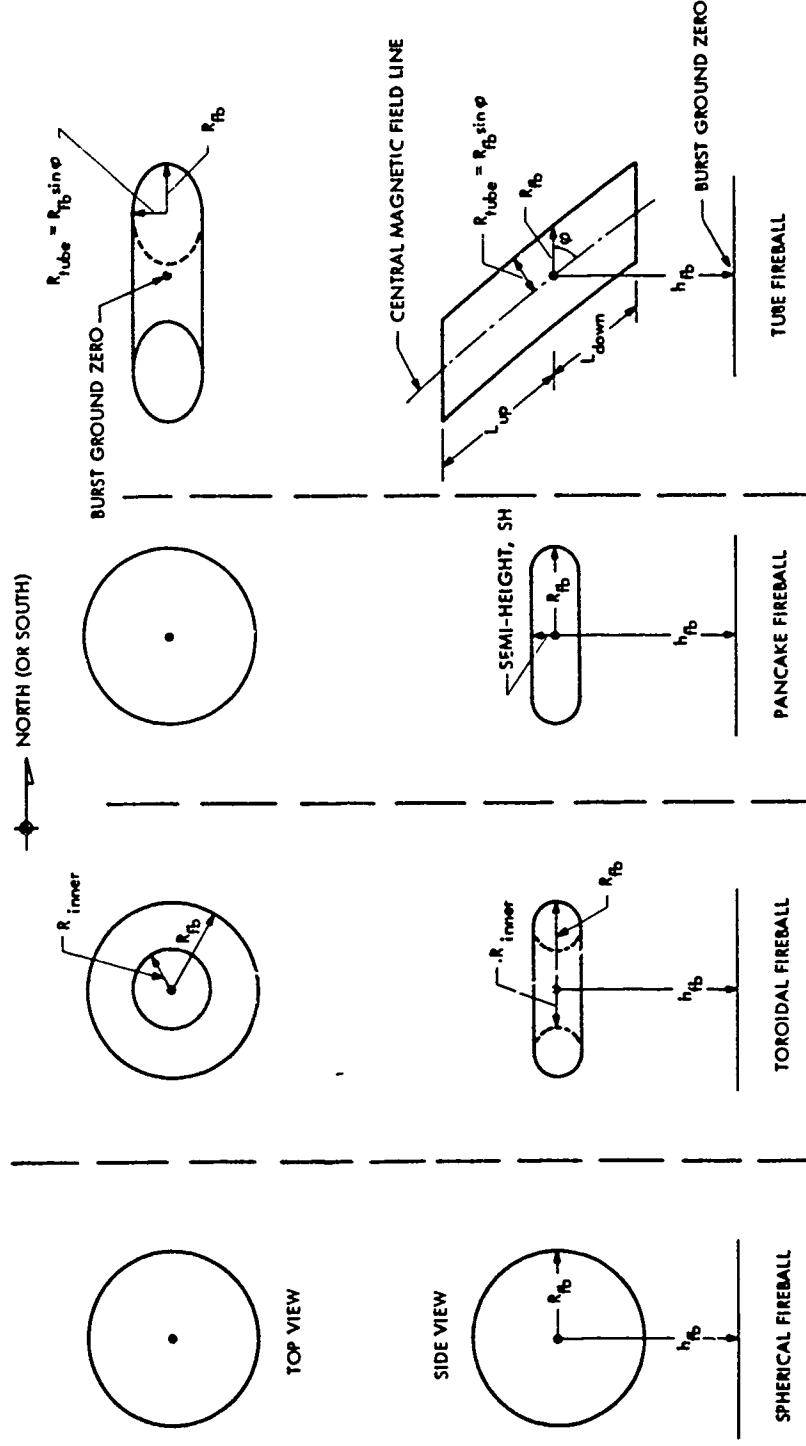


Fig. 2-16. Examples of Fireball Geometry

**8-13 Size and Location of Fireball and Debris Regions for Detonations Below 85 Kilometers**

When a nuclear weapon is detonated at an altitude below about 85 kilometers, the fireball initially is a reasonably well defined and relatively small spherical region (see Chapter 1). After the fireball is formed, it expands and rises above the detonation point, carrying the fission debris with it. Depending on the weapon yield and the detonation altitude, the fireball may become toroidal in shape as it rises. After rising, the fireball will become stabilized in altitude and will diffuse into a pancake shape.

If the fireball rises above 200 kilometers, it is assumed to fall back to 200 kilometers. If the peak altitude of the fireball is less than 200 kilometers, it is assumed to stabilize at its peak altitude.

The initial fireball radius is the parameter used to determine whether the fireball will form a toroid. The toroid is assumed to transform into a pancake at 7 minutes after burst, with a vertical thickness equal to the vertical dimension of the toroid at 7 minutes. If the fireball does not form a toroid, the fireball is assumed to transform from a sphere to a pancake when the radius becomes 100 kilometers. The vertical thickness of the pancake is assumed to be 100 kilometers.

The model provided for determining the location of the debris is intended for calculation of delayed-radiation (gamma rays and beta particles) effects. For times later than a few tens of minutes after burst, the size and location of the debris region will depend on atmospheric winds and diffusion, and the model may be considerably in error.

Figures 8-19 through 8-25 are used to determine the spatial and temporal history of the fireball (and the debris), for bursts that occur below 85 kilometers.

**8-14 Size and Location of Fireball and Debris Regions for Detonations Between 85 and 120 Kilometers**

When a nuclear detonation occurs between 85 and 120 kilometers, the fireball transforms from a sphere to a cylinder or tube aligned along the geomagnetic field. The model used for the calculations described herein assumes that the fireball stabilizes at its maximum altitude above ground zero. The fireball radial dimension also is assumed to remain constant after 7 minutes. A fireball region is not defined for times longer than 2 hours after burst.

Delayed radiation (gamma rays and beta particles) is assumed to be emitted from a single debris pancake, which is assumed to rise with the fireball and then to settle slowly along the geomagnetic field until it reaches 200 kilometers altitude at approximately 2 hours after burst. As the debris settles, the center is offset from ground zero toward the nearest magnetic pole, as illustrated in Figure 8-17. Figures 8-19 through 8-29 are used to determine the spatial and temporal history of the fireball (and the debris) for bursts that occur at altitudes between 85 and 120 kilometers.

**8-15 Size and Location of Fireball and Debris Regions for Detonations Above 120 Kilometers**

Theoretical and experimental data are incomplete for this altitude region; therefore, scaling relations are given only for a few parametric yields and detonation altitudes. Three shapes are used to model the fireball region: a sphere, a pancake, and a cylinder or tube aligned along the geomagnetic field. Figure 8-16 illustrates the fireball geometry.

As the detonation altitude is increased above 120 kilometers, the debris is distributed over a larger region. Some debris can be transported across the magnetic equator. The single-pancake debris region used at lower altitudes to

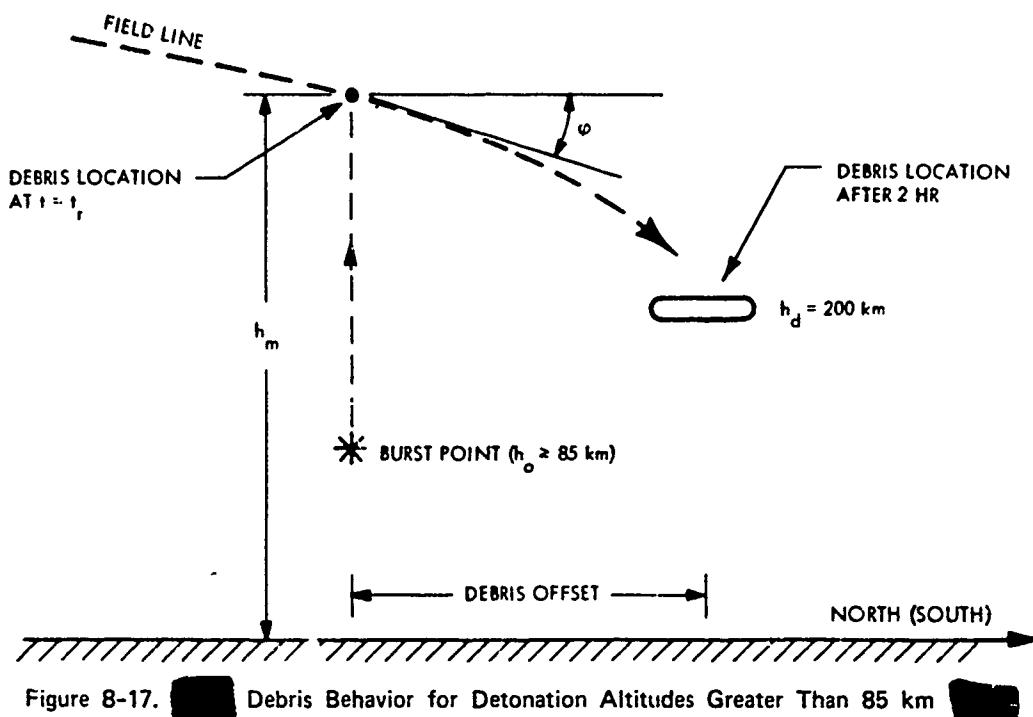


Figure 8-17. Debris Behavior for Detonation Altitudes Greater Than 85 km

model delayed radiation effects is not adequate, so multiple regions are used.

Up to three debris regions are used to determine the delayed radiation resulting from detonations above 120 kilometers. Figure 8-18 illustrates the geometry. Two of these regions (Regions 1 and 2) model debris in the burst region, and the third (Region 3) models debris transported across the magnetic equator to the conjugate region. For convenience and because little is known about the debris location in the conjugate region, the beta-particle ionization in the burst and conjugate regions associated with Debris Region 3 is assumed to coincide with that associated with Debris Region 1. Debris Region 3 is used to compute gamma-ray ionization in the conjugate region. For weapons detonated above 250 kilometers, Region 2 is used to determine both gamma-ray and beta-particle ionization.

In the model used herein, the fraction of

debris transported across the magnetic equator is assumed to be independent of geomagnetic dip angle for detonations above 250 kilometers. A small amount of debris can reach the conjugate region for detonations below 250 kilometers and low dip angles. The time required for the debris to reach the conjugate region depends on detonation altitude and geomagnetic dip angle; however, for purposes of calculating delayed gamma radiation, the debris can be assumed to reach the conjugate region immediately after burst.

About 20 percent of the debris for detonations above 120 kilometers is not accounted for in the model. This debris is assumed to escape to large distances; some may be carried into space and some may be spread world-wide. At least part of this debris will be trapped on the magnetic field lines above the burst. While this debris probably is not important for single bursts, it could cause significant delayed radiation after

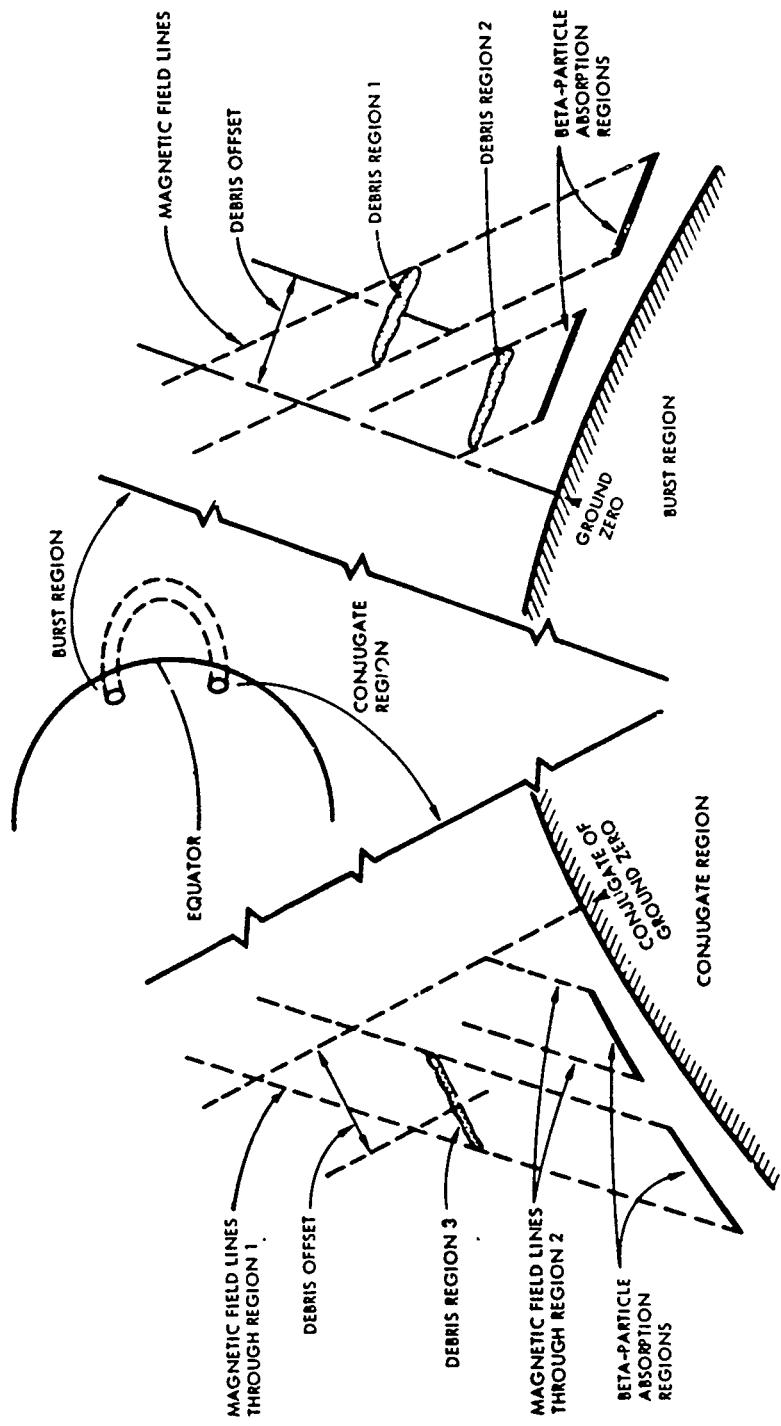


Figure 8-18. Illustration of Debris and Beta-Particle Absorption Regions for Times Later Than 10 Minutes After Burst,  $H_0$  Above 120 km

[REDACTED]  
[REDACTED]  
multiple weapon detonations.

[REDACTED] After rising to peak altitude, the three debris regions are assumed to settle along the geomagnetic field lines until they reach 200

kilometers altitude at about 2 hours after burst. The debris regions are offset from ground zero or the conjugate of ground zero toward the magnetic pole.

### Problem 8-1 Calculation of Fireball Size, Shape, and Location for a Burst Below 85 Kilometers

Figures 8-19 through 8-25 contain families of curves with which the size, shape, and location of the fireball resulting from a nuclear detonation below 85 kilometers may be estimated. For bursts in this altitude regime, the debris altitude  $h_d$  is assumed to be the same as the fireball altitude  $h_{fb}$ . The debris is distributed non-uniformly within the fireball region. However, for simplified calculations of delayed radiation effects, the debris region can be assumed to be a thin pancake region with radius  $R_d$  equal to the fireball radius  $R_{fb}$ .

The altitude of the fireball at a time  $t$  after burst is obtained from Figures 8-19 through 8-22 by a series of steps, as follows:

1. Enter Figure 8-19 with the weapon yield and detonation altitude  $h_o$  to obtain  $h_r$ , the distance the fireball will rise above the detonation point. The maximum fireball altitude,  $h_m$ , is

$$h_m = h_o + h_r \text{ km.}$$

Enter Figure 8-20 with  $h_r$  to obtain the time required to reach maximum altitude  $t_r$ . If  $t \geq t_r$  and  $h_m \leq 200$  km, go to 3; otherwise go to 2.

2. If  $t < t_r$ , enter Figure 8-21 with time after burst and  $h_r$  to obtain  $h_N$ , an altitude normalizing factor. If  $h_m > 200$  km, enter Figure 8-22 with  $\tau = t/t_r$  to obtain  $f_h$ , the fireball height factor.

3. Compute  $h_{fb}$ , the fireball altitude at time  $t$ :

$$h_{fb} = \begin{cases} (h_o + h_N h_r) \text{ km} & \text{when } t < t_r \\ h_m \text{ km} & \text{when } t \geq t_r, h_m < 200 \\ [200 + f_h (h_m - 200)] \text{ km} & \text{when } t > t_r, h_m > 200 \end{cases}$$

The radius and shape of the fireball at a time  $t$  after burst are obtained from Figures 8-23 through 8-25, as follows:

1. Enter Figure 8-23 with weapon yield and detonation altitude  $h_o$  to obtain the initial fireball radius  $R_o$ . If  $R_o < 4$  km, go to 2; otherwise go to 3 when  $t < 7$  minutes or go to 4 when  $\geq 7$  minutes.

2. Determine  $t_{toroid}$ , the time of toroid formation, from Figure 8-24 by selecting the fireball radius curve for the value of  $R_o$  determined above, by locating the intercept of this curve with the toroid formation time curve, and by reading  $t_{toroid}$  on the abscissa.

3. Enter Figure 8-24 with the time of interest  $t$  and the initial fireball radius  $R_o$ . Determine  $R_{fb}$ , the fireball radius at time  $t$ , then go to 5.

4. Enter Figure 8-24 with  $t = 7$  minutes and the initial fireball radius  $R_o$ ; obtain the fireball radius at 7 minutes after burst,  $R_{fb}(7)$ . Enter Figure 8-25 with  $t$  and  $h_m$  to obtain  $\Delta R$ . Compute  $R_{fb}$ , as follows:

$$R_{fb} = R_{fb}(7) + \Delta R.$$

5. The fireball will be a

sphere if  $R_o \leq 4$  km and  $t < t_{toroid}$ , or if

$R_o > 4$  km and  $R_{fb} < 100$  km;

toroid if  $R_o < 4$  km and  $t_{toroid} \leq t < 7$  minutes;

pancake if  $R_o \leq 4$  km and  $t \geq 7$  minutes, or if

$R_o > 4$  km and  $R_{fb} \leq 100$  km.

If the fireball shape is a toroid, compute the inner toroid radius:

$$R_{inner} = \frac{R_{fb}}{2}$$

If the fireball shape is a pancake, compute the pancake semithickness:

$$SH = \begin{cases} \frac{1}{4} R_{fb}(7) & R_o \leq 4 \text{ km} \\ 50 & R_o > 4 \text{ km.} \end{cases}$$

**Example**

**Given:** A 1 Mt weapon burst at an altitude of 50 km.

**Find:** The size, shape, and location of the fireball and debris region 2 minutes after the burst.

**Solution:**

a. From Figure 8-19  $h_r \approx 50$  km for a 1 Mt weapon burst at 50 km.

b.  $h_m = h_o + h_r = 50 + 50 = 100$  km.

c. From Figure 8-20,  $t_r = 10$  min for  $h_r = 50$  km.

d. From Figure 8-21,  $h_N = 0.6$  for  $t = 2$  min and  $h_r = 50$  km.

e. Since  $t < t_r$ .

$$h_{fb} = h_o + h_N h_r = 50 + (0.6)(50) = 80 \text{ km}$$

f. From Figure 8-23,  $R_o = 2$  km for a 1 Mt weapon detonation at 50 km.

g. From Figure 8-24,  $t_{toroid} = 1.7$  min for  $R_o = 2$  km.

h. From Figure 8-24,  $R_{fb} = 30$  km 2 min after a burst with  $R_o = 2$  km.

i. Since  $t_{toroid} < t < 7$  minutes, the fireball shape is a toroid, and

$$R_{inner} = \frac{R_{fb}}{2} = \frac{30}{2} = 15 \text{ km.}$$

**Answer:** The fireball is a toroid centered at 80 kilometers altitude. The outer radius is 30 kilometers and the inner radius is 15 kilometers (see Figure 8-16). The altitude and radius of the debris pancake are 80 kilometers and 30 kilometers, respectively.

**Reliability** The size and location of the debris region depend on atmospheric winds and diffusion. Since these effects are neglected in the model described herein, the results predicted by the model may be considerably in error.

**Related Material** See paragraph 8-13.

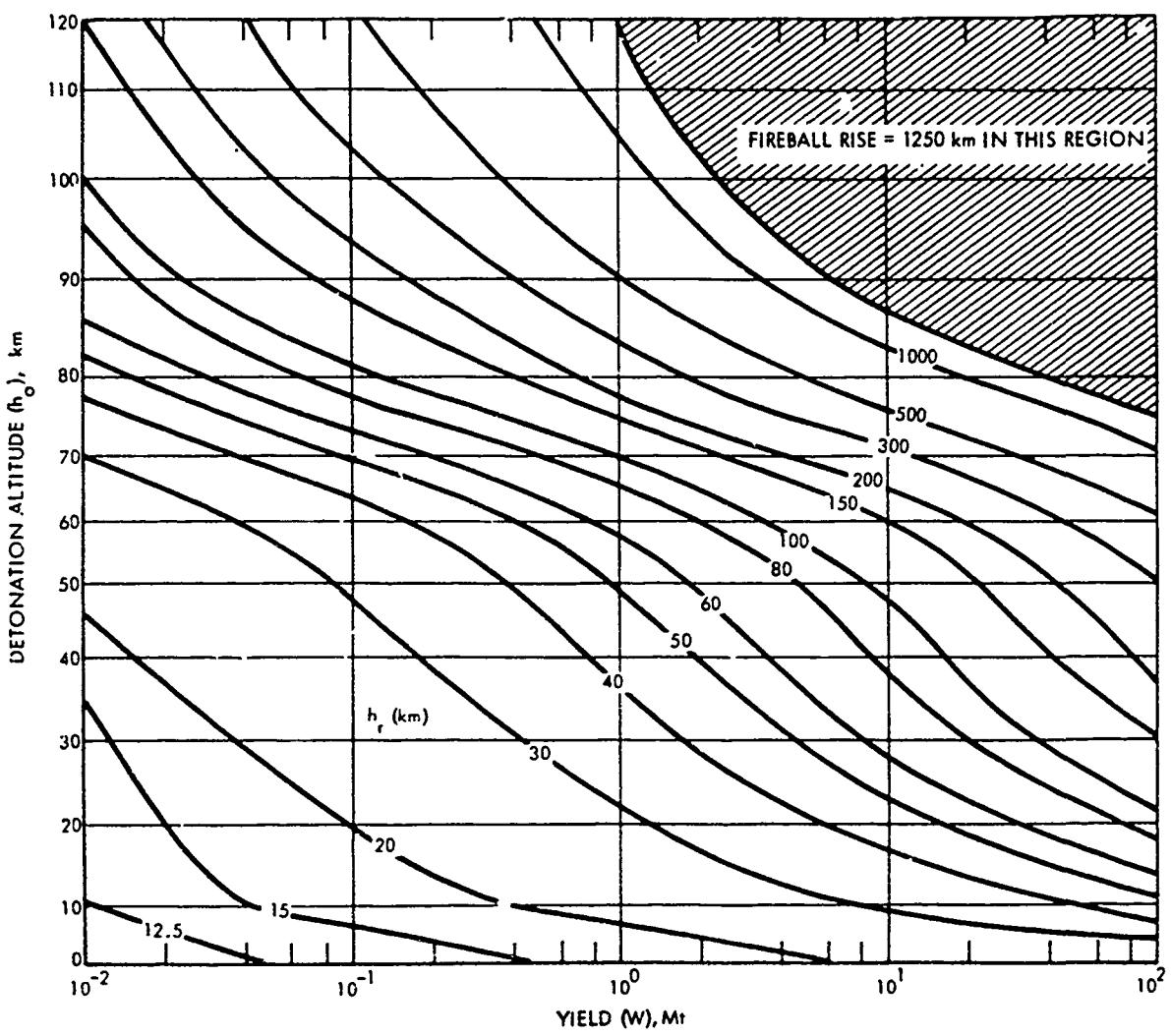


Figure 8-19. Maximum Fireball Rise

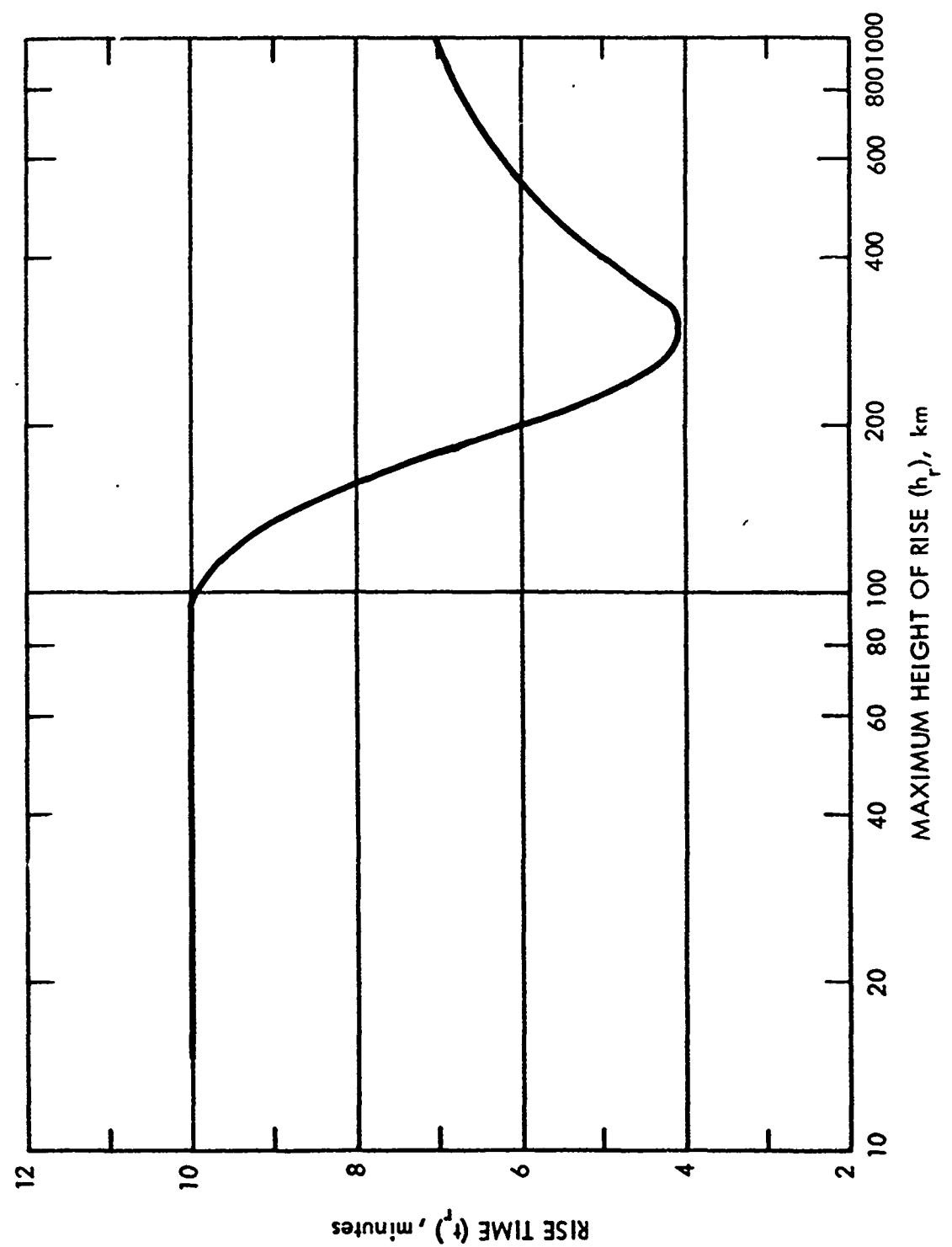


Figure 8-20. Time for Fireball to Reach Its Maximum Altitude

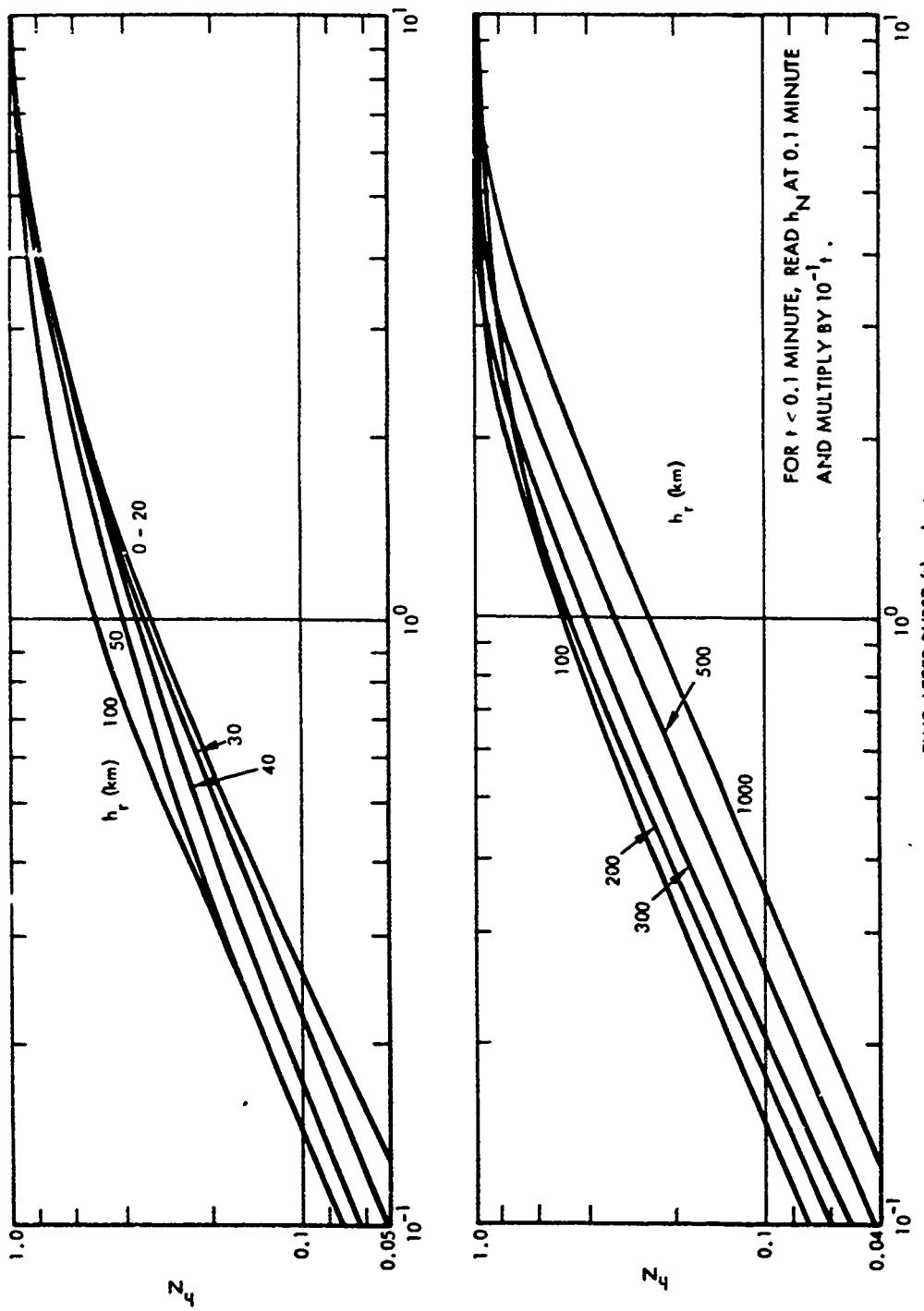


Figure 8-21. [REDACTED] Altitude Normalizing Factor  $h_N$  [REDACTED]

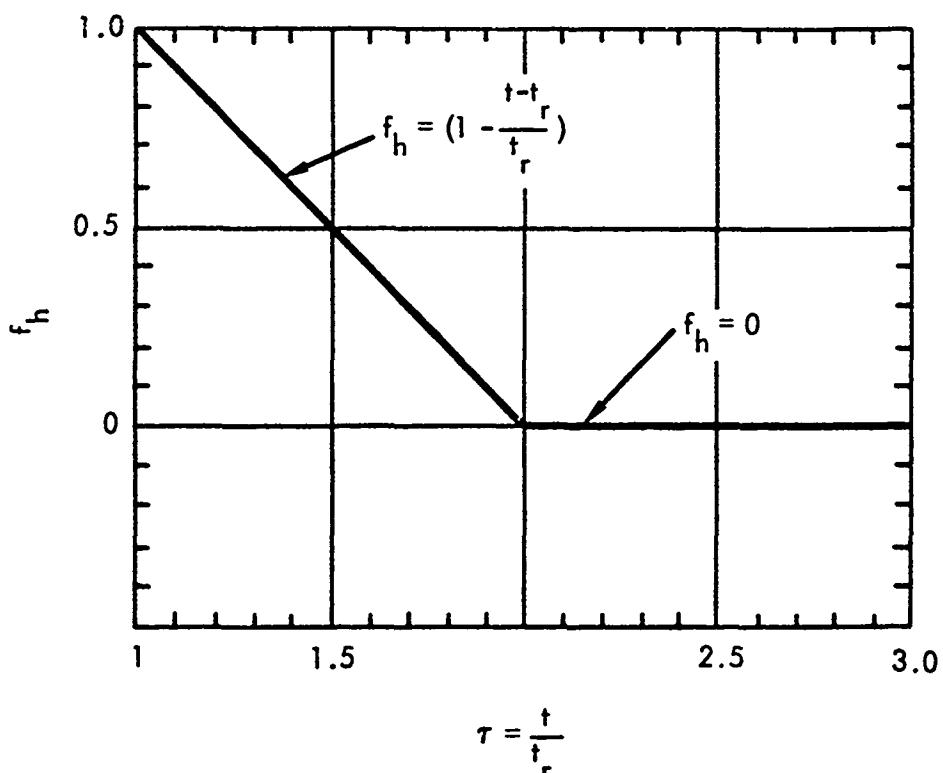


Figure 8-22. Fireball Height Factor

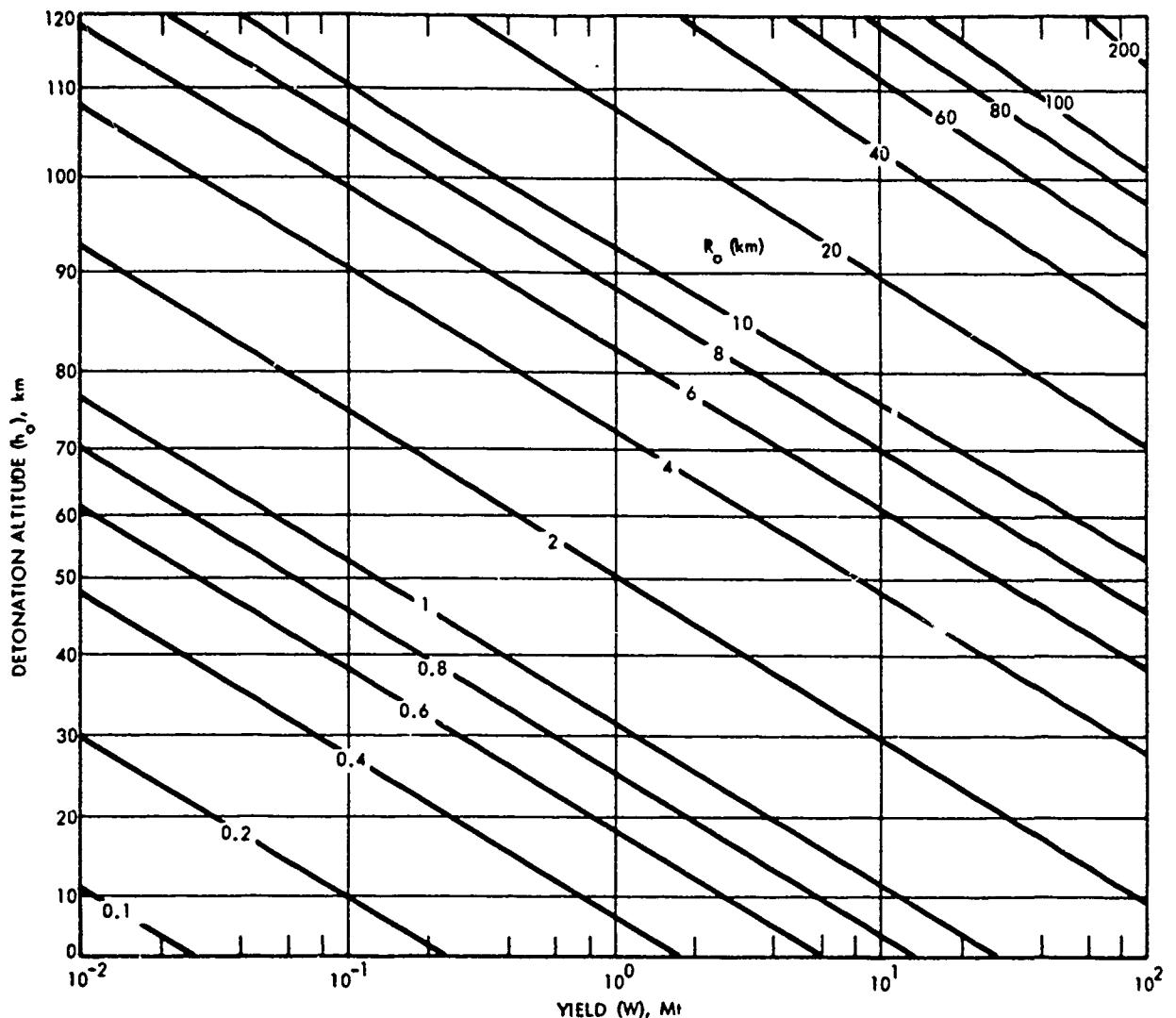


Figure 8-23. Initial Fireball Radius

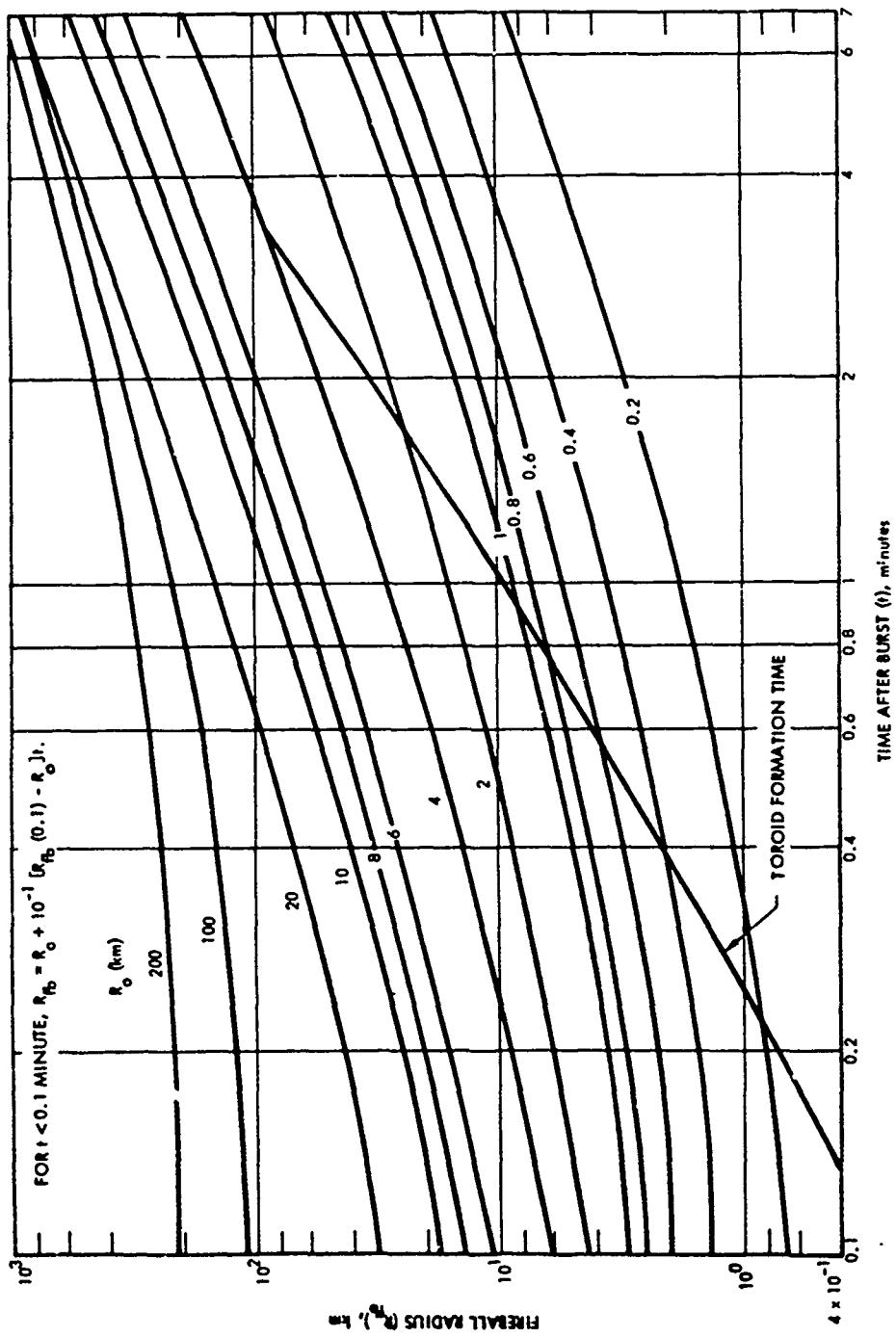


Figure 8-24. [REDACTED] Fireball Radius [REDACTED]

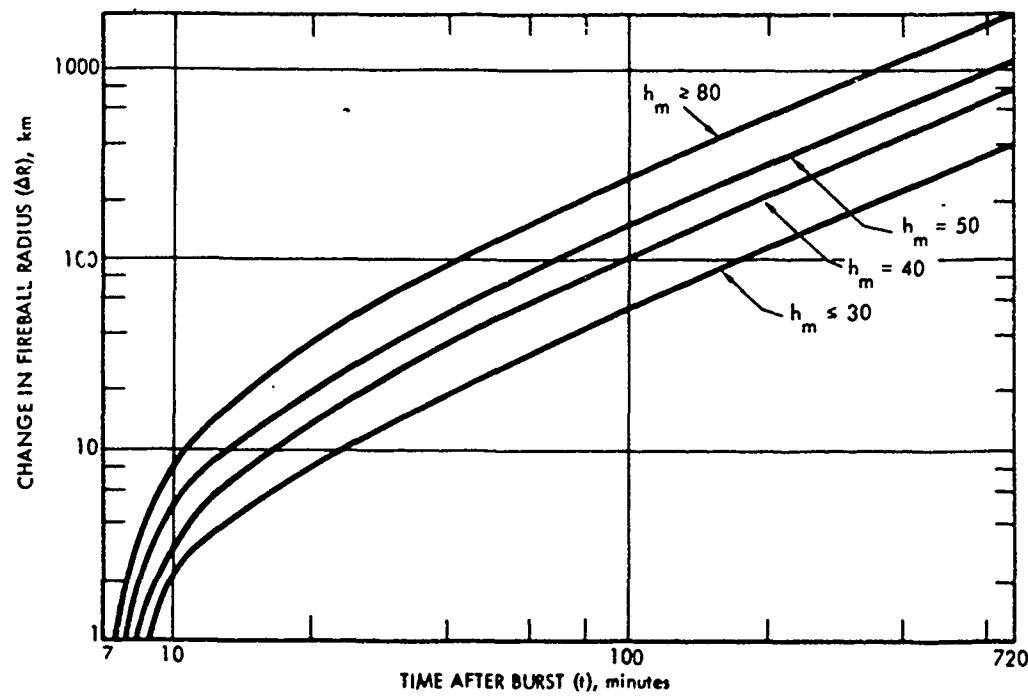


Figure 8-25. [REDACTED] Change in Fireball/Debris-Region Radius After Several Minutes [REDACTED]

### Problem 8-2 Calculation of Fireball Size, Shape, and Location for a Burst Between 85 and 120 kilometers

Figures 8-19 through 8-29 contain families of curves with which the size, shape, and location of the fireball resulting from a nuclear detonation between 85 and 120 kilometers may be estimated. For bursts in this altitude regime, the fireball transforms from a sphere to a cylinder or tube aligned along the geomagnetic field line. A fireball region is not defined for times after burst greater than 2 hours.

The altitude of the fireball at a time  $t$  after burst is obtained from Figures 8-19 through 8-21 by a series of steps, as follows:

1. Enter Figure 8-19 with weapon yield  $W$  and detonation altitude  $h_o$  to obtain  $h_r$ , the distance the fireball will rise above the detonation point. The maximum fireball altitude,  $h_m$ , is

$$h_m = h_r + h_o \text{ km.}$$

Enter Figure 8-20 with  $h_r$  to obtain the time to reach maximum altitude  $t_r$ . If  $t \geq t_r$ , go to 3; otherwise go to 2.

2. If  $t < t_r$ , enter Figure 8-21 with time after burst and  $h_r$  to obtain  $h_N$ , and altitude normalizing factor.

3. Compute  $h_{fb}$ , the fireball altitude at time  $t$ :

$$h_{fb} = \begin{cases} (h_o + h_N h_r) \text{ km} & t < t_r \text{ minutes} \\ h_m \text{ km} & t_r < t < 120 \text{ minutes} \end{cases}$$

The radius and shape of the fireball at a time  $t$  after burst are obtained from Figures 8-23, 8-24, and 8-26, as follows:

1. Enter Figure 8-23 with weapon yield and detonation altitude  $h_o$  to obtain fireball radius

$R_o$ . Enter Figure 8-26 with weapon yield to obtain the magnetic equilibrium radius  $R_{eq}$ . Determine the time to reach  $R_{eq}$ ,  $t'$ , from Figure 8-24 by selecting the fireball radius curve for the value of  $R_o$  obtained from Figure 8-23 and by determining the time when the fireball radius ( $R_{fb}$ ) is equal to  $R_{eq}$ . If  $t > t'$ , go to 3; otherwise go to 2.

2. Enter Figure 8-24 with  $t$  and  $R_o$  to obtain  $R_{fb}$ , the fireball radius at time  $t$ . Go to Step 4.

3. Compute  $R_{fb}$ :

$$R_{fb} = \begin{cases} (R_{eq} + (t - t') R_o) \text{ km} & t < 7 \text{ minutes,} \\ (R_{eq} + (7 - t') R_o) \text{ km} & t \geq 7 \text{ minutes.} \end{cases}$$

4. The fireball shape will be a

sphere if  $t < t'$   
tube if  $t \geq t'$ .

If the time of interest  $t$  is greater than  $t'$ , the time to reach the magnetic equilibrium radius, the tube fireball dimensions are obtained as follows:

1. If  $t' > t_r$  (obtained from Figure 8-20 above), go to 2; otherwise enter Figure 8-21 with  $t = t'$  and  $h_r$  (from Figure 8-19) and obtain  $h_N(t')$ .

2. Compute  $h_{fb}(t')$ :

$$h_{fb}(t') = \begin{cases} (h_o + h_N(t') h_r) \text{ km} & t' \leq t_r \text{ minutes,} \\ h_m \text{ km} & t' > t_r \text{ minutes.} \end{cases}$$

Compute the altitude of the base of the

tube  $h_b$  ( $h_b$  is taken as the altitude of the base if  $h_b > 200$  km):

$$h_b = h_{fb}(t') - R_{eq} \text{ km.}$$

Compute the length of the fireball up the tube in the direction of the magnetic field line,  $L_{up}$ :

$$L_{up} = 6(t - t')R_o + R_{fb} \text{ km.}$$

Compute the quantity  $L'$ :

$$L' = \begin{cases} \frac{h_{fb} - h_b}{\sin \varphi} \text{ km} & h_b \leq 200 \text{ km} \\ \frac{h_{fb} - 200}{\sin \varphi} \text{ km} & h_b > 200 \text{ km,} \end{cases}$$

where  $\varphi$  is the magnetic dip angle at the burst location. If the magnetic dip angle is not known for the burst location, it can be determined from Figure 8-54. The length of the fireball down the tube will be the smaller of  $L_{up}$  and  $L'$ .

If the time of interest  $t$  is equal to or less than  $t_r$ , the time to reach maximum altitude, or if the maximum fireball altitude,  $h_m$ , is less than 200 kilometers, the debris altitude,  $h_d$ , is determined from the fireball altitude as described below. If the time of interest is equal to or greater than the time to reach maximum altitude ( $t \geq t_r$ ), and the maximum fireball altitude is greater than 200 kilometers ( $h_m > 200$ ), Figure 8-27 is entered with the quantity  $(t - t_r)$  to obtain the debris height factor  $f_h$ . The debris altitude is then determined as follows:

$$h_d = \begin{cases} h_{fb} \text{ km} & t \leq t_r \text{ min} \\ h_m \text{ km} & t \geq t_r \text{ min, } h_m \leq 200 \text{ km} \\ [200 + f_h(h_m - 200)] \text{ km} & t \geq t_r \text{ min, } h_m > 200 \text{ km} \end{cases}$$

If the maximum fireball altitude,  $h_m$ , is equal to or less than 200 kilometers, the debris offset is zero (see Figure 8-17). If  $h_m$  is greater than 200 kilometers, enter Figure 8-28 with  $h_m$  and the magnetic dip angle,  $\varphi$ , to obtain the maximum debris offset  $D_d$ . Then enter Figure 8-29 with the quantity  $(t - t_r)$  to obtain a value of the debris offset correction factor  $f_o$ . The debris offset,  $\Delta d$ , is:

$$\Delta d = f_o D_d \quad (h_m > 200 \text{ km}).$$

The radius of the debris is obtained from previously determined dimensions, as follows:

$$R_d = \begin{cases} R_{fb} \text{ km} & t \leq 120 \text{ minutes} \\ [R_{eq} + (7 - t')R_o + 3(t - 120)] \text{ km} & t > 120 \text{ minutes} \end{cases}$$

#### Example

*Given:* A 1 Mt weapon burst at an altitude of 100 km, at a location where the magnetic dip angle,  $\varphi$ , is  $60^\circ$ .

*Find:* The shape, size, and location of the fireball, and the altitude, radius, and offset of the debris region 20 minutes after the burst.

*Solution:*

a. From Figure 8-19,  $h_r = 800$  km for a 1 Mt weapon burst at 100 km.

$$b. h_m = h_r + h_o = 800 + 100 = 900 \text{ km.}$$

c. From Figure 8-20,  $t_r = 7$  minutes for  $h_r = 800$  km.

d. Since  $t_r < t$ ,

$$h_{fb} = h_m = 900 \text{ km}$$

e. From Figure 8-23,  $R_o = 15$  km for a 1 Mt burst at 100 km altitude.

f. From Figure 8-26,  $R_{eq} = 100$  km for a 1 Mt weapon.

g. From Figure 8-24,  $t' = 0.9$  min for  $R_o = 15$  km and  $R_{fb} = R_{eq} = 100$  km.

h. Since  $t > 7$  min, the fireball shape is a tube, and

$$R_{fb} = R_{eq} + (t - t') R_o \\ = 100 + (6.1)(15) = 192 \text{ km}$$

i. From Figure 8-21,  $h_N(t) = 0.25$  for  $t = t' = 0.9$  min and  $h_r = 800$  km.

j. Since  $t' < t_r$ ,

$$h_{fb}(t') = h_o + h_N(t') h_r \\ = 100 + (0.25)(800) = 300 \text{ km.}$$

k. The height of the fireball base is

$$h_b = h_{fb}(t') - R_{eq} = 300 - 100 = 200 \text{ km}$$

l. The length up the fireball tube is

$$L_{up} = 6(t - t') R_o + R_{fb} \\ = (6)(19.1)(15) + 192 = 1911 \text{ km}$$

m. Since  $h_b = 200$  km, the quantity  $L'$  is

$$L' = \frac{h_{fb} - h_b}{\sin \varphi} = \frac{900 - 200}{0.87} = 810 \text{ km}$$

n. Since  $L' < L_{up}$

$$L_{down} = L' = 810 \text{ km.}$$

o. Since  $t > t_r$  and  $h_m > 200$  km, the quantity  $f_h$  must be determined from Figure 8-27. Entering Figure 8-27 with  $t - t_r = 13$ , the quantity is determined to be

$$f_h = 0.9.$$

The altitude of the debris is, therefore,

$$h_d = 200 + f_h(h_m - 200) \\ = 200 + (0.9)(900 - 200) = 830 \text{ km.}$$

p. From Figure 8-28, the maximum debris offset  $D_d = 350$  km for  $\varphi = 60^\circ$  and  $h_m = 900$  km. From Figure 8-29, the debris offset correction factor is  $f_o = 0.1$  for  $(t - t_r) = 13$  min. Therefore, the debris offset is

$$\Delta d = f_o D_d = (0.1)(350) = 35 \text{ km.}$$

q. Since  $t < 120$  minutes,

$$R_d = R_{fb} = 192 \text{ km.}$$

Answer:

a. The fireball is a tube with dimensions as follows (refer to Figure 8-16):

$$h_{fb} = 900 \text{ km,} \\ R_{fb} = 192 \text{ km,} \\ L_{up} = 1911 \text{ km,} \\ L_{down} = 810 \text{ km.}$$

b. The debris region is a pancake with a radius of 192 km centered at an altitude of 830 km. It is offset 35 km towards the north pole from the burst point (refer to Figure 8-17).

**Reliability** The size and location of the fireball and debris, particularly late time debris expansion, are affected by atmospheric winds and diffusion. Since these effects are neglected in the model described herein, the results predicted by the model may be considerably in error.

**Related Material** See paragraph 8-14.

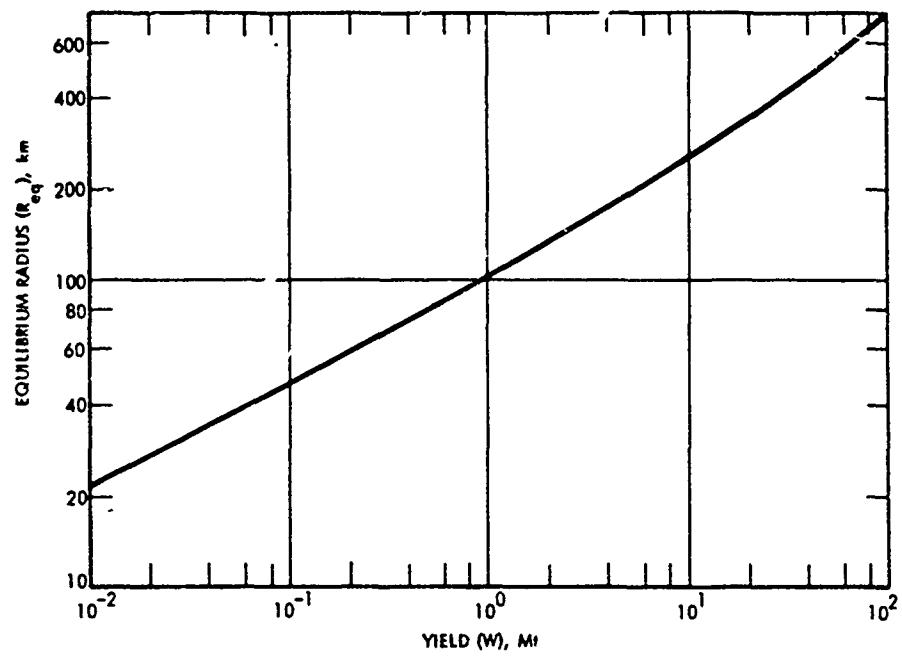


Figure 8-26. Magnetic Equilibrium Radius

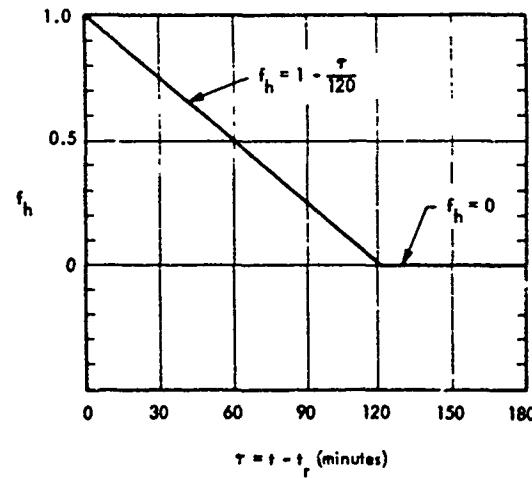


Figure 8-27. Debris Height Factor

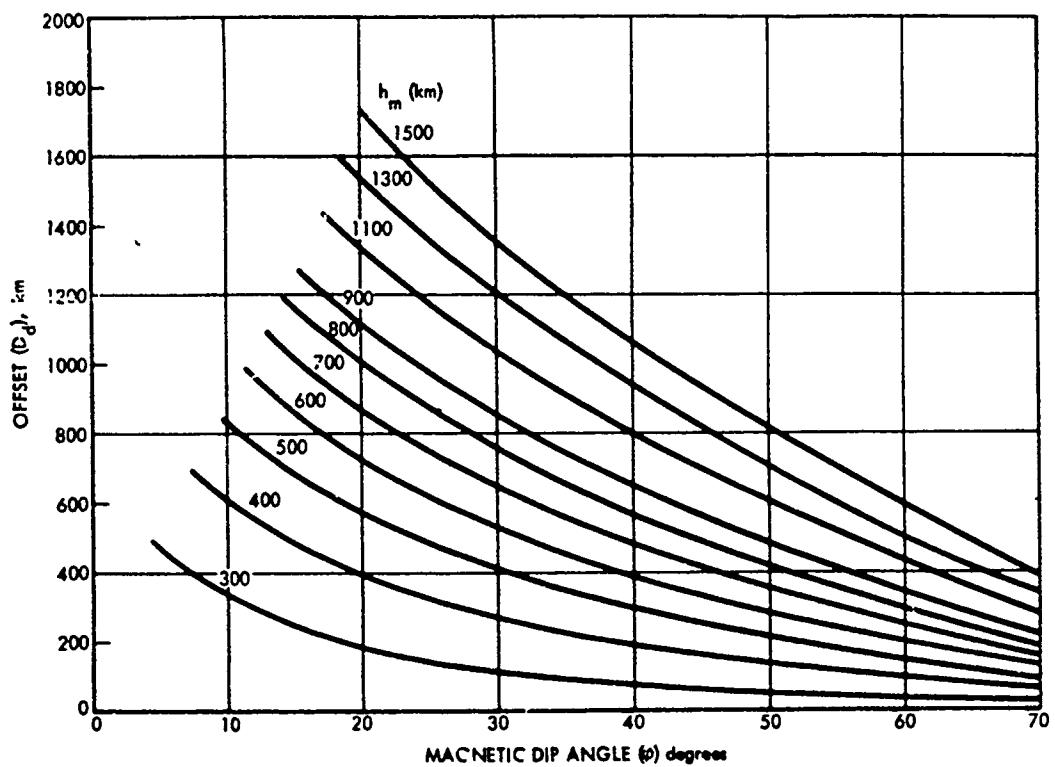


Figure 8-28. Maximum Debris Offset

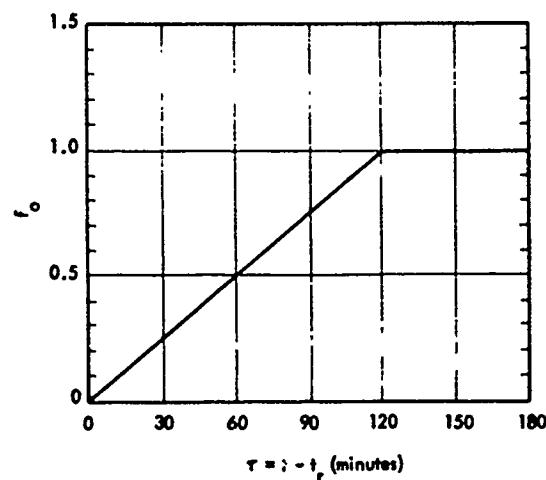


Figure 8-29. Debris Offset Correction Factor

### Problem 8-3 Calculation of Size, Shape, and Location of Fireball and Debris Regions for a Burst Above 120 kilometers

Table 8-2 and Figures 8-27 through 8-38 contain data with which estimates may be made of the size, shape, and location of the fireball and the debris regions for nuclear detonations above 120 kilometers. As discussed in paragraph 8-15 and shown in Figure 8-18, three separate debris regions are considered. Three shapes are used to model the fireball region: a sphere, a pancake, and a tube (cylinder) along the geomagnetic field. The shapes are illustrated in Figure 8-16.

Table 8-2 is used to determine the fireball size, shape, and location (note that time after burst is given in seconds in Table 8-2). The table provides relations for a few parametric yields and detonation altitudes. In view of the uncertainties in both theoretical and experimental data in this burst altitude regime, interpolation between sections of Table 8-2 is not warranted. Data provided in the table for the yield and altitude combination nearest to those desired should be used. If either the desired yield or the desired detonation altitude is midway between values given in the table, values for the next higher yield and/or detonation altitude should be used. The phenomenology is very uncertain for yields greater than 10 Mt. If estimates are required for yields greater than 10 Mt, the dimensions and location given for a 10 Mt burst should be used. Table 8-2 indicates the shape of the fireball for the various yields and burst altitudes as a function of time (in seconds) after burst. The size and location of the fireball are determined as described below.

1. If the fireball is a sphere, the fireball altitude,  $h_{fb}$ , and fireball radius,  $R_{fb}$ , are read directly from Table 8-2 for the time of interest.
2. If the fireball is a pancake, the fireball altitude,  $h_{fb}$ , and the fireball radius,  $R_{fb}$ , are read directly from Table 8-2 for the time of interest. The semithickness of the pancake in kilo-

meters (see Figure 8-16) is equal to the value shown in the column headed "x" in Table 8-2. Together, these values provide the size and location of the fireball at the desired time.

3. If the fireball is a tube, the fireball altitude,  $h_{fb}$ , and fireball radius,  $R_{fb}$ , are once again read directly from Table 8-2. The fireball lengths up and down the tube (see Figure 8-16) are determined from the values in the columns headed "x" and "y" in Table 8-2, as follows:

$$L_{down} = \frac{h_{fb} - 200}{|\sin \varphi|} \text{ km, or}$$

$$L_{down} = \frac{x}{2|\sin \varphi|} \text{ whichever is smaller,}$$

$$L_{up} = \frac{y}{2|\sin \varphi|} \text{ km,}$$

where  $\varphi$  is the magnetic dip angle at the burst point. If the magnetic dip angle is not known, it can be obtained from Figure 8-54. A negative value for y in Table 8-2 means that both x and y are dimensions down the geomagnetic field and the fireball is below  $h_{fb}$ .

Figures 8-30 through 8-38 contain families of curves with which the size and location of the three debris regions may be estimated. Once again, the uncertainties in the data are such that interpolation between figures is not warranted. Data on the figure for the yield nearest to that desired should be used. If the desired yield is midway between values provided, data for the next higher value should be used.

The fraction of the total weapon debris in each of the debris regions is obtained by use of Figure 8-30 and the calculations described below. Enter Figure 8-30 with the magnetic dip angle  $\varphi$  and the altitude of detonation  $h_o$  to obtain the fraction of debris going to debris region

3, X (see Figure 8-18). Compute the fraction of the debris in each of the three regions as follows:

$$FF1 = \begin{cases} 0.8 - X & h_o \leq 250 \text{ km}, \\ 0.6 - X & h_o > 250 \text{ km}, \end{cases}$$

$$FF2 = \begin{cases} 0 & h_o \leq 250 \text{ km}, \\ 0.2 & h_o > 250 \text{ km}, \end{cases}$$

$$FF3 = X,$$

where FF1, FF2, and FF3 are the fractions of total weapon debris in regions 1, 2, and 3, respectively. The sum of the three fractions is always less than 1.0, since some debris is assumed to escape to long distances (see paragraph 8-15).

The altitude,  $h_d$ , for debris region 1 is obtained from Figures 8-31 through 8-34 by selecting the figure with the yield closest to that desired, and by determining  $h_{d1}$  for the time and burst altitude of interest. The maximum altitude to which the debris rises in region 1,  $h_{m1}$  should also be obtained for use in determining the debris offset as described later.

The debris radius,  $R_{d1}$ , for debris region 1 is obtained from Figures 8-35 through 8-38 by selecting the figure with the yield closest to that desired, and by determining  $R_{d1}$  for the time and burst altitude of interest.

If  $t \leq 10$  minutes, the offset for debris region 1,  $\Delta d$ , is zero. If  $t > 10$  minutes, the offset of debris region 1 is determined as follows.

1. Obtain the maximum debris offset  $D_d$  from Figure 8-28 for  $h_m = h_{m1}$ , as determined above, and the magnetic dip angle,  $\varphi$ , of interest.

2. Calculate  $\tau$ :

$$\tau = t - 10 \text{ min.}$$

Enter Figure 8-29 with  $\tau$  to obtain the debris offset correction factor  $f_o$ .

3. The offset of debris region 1 is

$$\Delta d_1 = f_o D_d \text{ km.}$$

Debris region 2 is only defined for bursts above 250 km. The size and location are determined by a series of steps, as follows. If  $t \leq 10$  minutes, go to 2; otherwise go to 1.

1. Enter Figure 8-27 with  $\tau = t - 10$  min to obtain the debris height correction factor  $f_h$ .

2. Compute the maximum altitude,  $h_{m2}$ , for debris region 2:

$$h_{m2} = h_o + 500 W^{1/3} \text{ km}$$

Compute the altitude for debris region 2 at time  $t$ :

$$h_{d2} = \begin{cases} h_{m2} \text{ km} & t \leq 10 \text{ min}, \\ 200 + f_h(h_o + 500 W^{1/3} - 200) \text{ km} & t > 10 \text{ min}, \end{cases}$$

where  $W$  is the weapon yield in megatons.

3. Compute the radius for debris region 2,  $R_{d2}$ :

$$R_{d2} = \begin{cases} 500 W^{1/3} \text{ km} & t \leq 120 \text{ min}, \\ 500 W^{1/3} + 3(t - 120) \text{ km} & t > 120 \text{ min}, \end{cases}$$

4. If  $t \leq 10$  minutes, the debris offset,  $\Delta d_2$ , equals zero. If  $t > 10$  minutes,  $\Delta d_2$  is determined from Figures 8-28 and 8-29. Enter Figure 8-28 with magnetic dip angle,  $\varphi$ , and  $h_m = h_{m2}$  to obtain  $D_d$ . Calculate  $\tau$ :

$$\tau = t - 10 \text{ min.}$$

Enter Figure 8-29 to obtain the debris offset

correction factor,  $f_o$ . Calculate  $\Delta d_2$ , the debris offset for region 2:

$$\Delta d_2 = D_d f_o.$$

The debris altitude, radius, and offset for debris region 3 are assumed to be the same as those determined for debris region 1, but they are located in the magnetic conjugate area (see Figure 8-18).

*Example*

*Given:* A 1 Mt weapon detonated at 250 km altitude at a location where the magnetic dip angle is  $60^\circ$ .

*Find:* The shape, size, and location of the fireball, and the altitude, radius, and offset of the debris regions 2 minutes after the burst.

*Solution:*

a. Since the altitude of interest is midway between the altitudes provided in Table 8-2, the larger (300 km) is used. From the data provided in Table 8-2 for 1 Mt at a burst altitude of 300 km, the following values are obtained for  $t = 120$  sec:

Fireball shape is a tube.

$$h_{fb} = 290 \text{ km}$$

$$R_{fb} = 150 \text{ km}$$

$$x = 160$$

$$y = 300$$

b.

$$(1) \frac{h_{fb} - 200}{|sin \varphi|} = \frac{290 - 200}{0.87} = 103 \text{ km.}$$

$$(2) \frac{x}{2|sin \varphi|} = \frac{160}{(2)(0.87)} = 92 \text{ km.}$$

Since the result obtained in (2) is less than that obtained in (1),

$$L_{down} = 92 \text{ km.}$$

$$L_{up} = \frac{y}{2|sin \varphi|} = \frac{300}{(2)(0.87)} = 172 \text{ km.}$$

c. From Figure 8-30, the fraction of debris transported to debris region 3, X, is 0.2 for a burst altitude of 250 km. Therefore,

$$FF1 = 0.6$$

$$FF2 = 0$$

$$FF3 = 0.2$$

d. From Figure 8-33,

$$h_{dl} = 625 \text{ km, and}$$

$$h_{ml} = 800 \text{ km.}$$

e. From Figure 8-37,

$$R_{dl} = 150 \text{ km.}$$

f. Since  $t < 10$  min,  $\Delta d_1 = 0$ .

g. Since the burst altitude is not greater than 250 km, no debris region 2 is defined.

h. The size and altitude of debris region 3 are the same as those of debris region 1, but debris region 3 is centered over the magnetic conjugate of the burst point.

*Answer:*

a. The fireball is a tube with the following dimensions (see Figure 8-16 for illustration of the meaning of the dimensions):

$$h_{fb} = 290 \text{ km}$$

$$R_{fb} = 150 \text{ km}$$

$$L_{down} = 92 \text{ km}$$

$$L_{up} = 172 \text{ km}$$

b. There are two debris pancake regions for use in determining delayed radiation effects. Debris region 1 is a pancake centered over the burst point with an altitude and radius of 625 km and 150 km, respectively. Debris region 3 is a pancake directly over the conjugate of the burst

[REDACTED]  
point, and it has the same altitude and radius as debris region 1. Sixty percent of the fission debris is in debris region 1, and twenty percent is in debris region 3. (Twenty percent is assumed to escape to large distances.)

[REDACTED] Reliability [REDACTED] Because of the theoretical

[REDACTED]  
and experimental uncertainties concerning bursts above 120 km, together with the uncertainties introduced by using fixed parametric yield/detonation altitude combinations, results predicted by the model described above may be considerably in error.

[REDACTED] Related Material [REDACTED] See paragraph 8-15.

Table 8-2 Fireball Location and Dimensions for Detonations Above 80 km  
 Time is in seconds, distances are in kilometers. E refers to the power of 10, e.g.,  $1.5E4 = 1.5 \times 10^4$ .

10 kt, 150 km							10 kt, 200 km						
t	Shape	$h_{fb}$	$R_{fb}$	x	y		t	Shape	$h_{fb}$	$R_{fb}$	x	y	
1	Sphere	1.5E2	1.2E1				1	Sphere	2.0E2	1.8E1			
3	"	1.6E2	1.3E1				3	"	2.1E2	1.9E1			
10	"	1.6E2	1.7E1				10	Tube	"	2.2E1	4.0E1	4.0E1	
30	Tube	1.9E2	2.2E1	3.0E1	3.0E1		30	"	2.3E2	2.3E2	5.0E1	5.0E1	
60	"	2.1E2	2.6E1	6.0E1	6.0E1		60	"	2.6E1	6.0E1	6.0E1		
120	"	2.4E2	3.2E1	1.0E2	1.0E2		120	"	2.8E2	3.2E1	1.0E2	1.0E2	
300	"	2.6E2	5.1E1	1.4E2	2.2E2		300	"	3.0E2	4.9E1	1.4E2	2.0E2	
600	"	2.7E2	6.3E1	1.6E2	4.4E2		600	"	"	6.1E1	"	4.2E2	
900	"	"	"	6.4E2	900	"	"	"	"	6.0E2	"		
1800	"	"	"	1.4E3	1800	"	"	"	"	"	1.3E3		

10 kt, 300 km							10 kt, 400 km						
t	Shape	$h_{fb}$	$R_{fb}$	x	y		t	Shape	$h_{fb}$	$R_{fb}$	x	y	
1	Tube	3.1E2	3.2E1	4.0E1	4.0E1		1	Tube	4.1E2	4.7E1	6.0E1	6.0E1	
3	"	"	"	"	"		3	"	"	4.8E1	"	"	
10	"	3.2E2	3.3E1	5.0E1	5.0E1		10	"	4.2E2	4.9E1	8.0E1	8.0E1	
30	"	3.4E2	3.5E1	6.0E1	6.0E1		30	"	4.3E2	5.1E1	1.0E2	1.0E2	
60	"	3.7E2	3.8E1	8.0E1	8.0E1		60	"	"	5.5E1	1.2E2	1.2E2	
120	"	4.0E2	4.5E1	1.4E2	1.4E2		120	"	5.2E2	6.3E1	1.6E2	1.6E2	
300	"	4.2E2	6.5E1	2.6E2	2.6E2		300	"	5.4E2	8.4E1	3.0E2	3.0E2	
600	"	4.3E2	7.8E1	4.0E2	4.8E2		600	"	5.5E2	1.0E2	5.6E2	5.6E2	
900	"	"	"	"	7.0E2		900	"	"	"	"	8.0E2	
1800	"	"	"	"	1.5E3		1800	"	"	"	"	1.9E3	

Table 8-2 Fireball Location and Dimensions for Detonations Above 80 km (Continued)

Time is in seconds, distances are in kilometers. E refers to the power of 10, e.g.,  $1.5E4 = 1.5 \times 10^4$ .

10 kt, 500 km							100 kt, 150 km						
t	Shape	$h_{fb}$	$R_{fb}$	x	y	t	Shape	$h_{fb}$	$R_{fb}$	x	y		
1	Tube	5.1E2	6.5E1	8.0E1	8.0E1	1	Sphere	1.6E2	2.7E1				
3	"	5.2E2	6.5E1	"	"	3	"	"	2.9E1				
10	"	"	6.6E1	1.0E2	1.0E2	10	"	1.8E2	3.6E1				
30	"	5.6E2	6.9E1	1.2E2	1.2E2	30	Tube	2.3E2	4.8E1	8.0E1	8.0E1		
60	"	5.9E2	7.3E1	1.4E2	1.4E2	60	"	2.9E2	5.5E1	1.2E2	1.2E2		
120	"	6.4E2	8.2E1	2.0E2	2.0E2	120	"	3.9E2	6.8E1	2.0E2	2.0E2		
300	"	6.6E2	1.0E2	3.4E2	3.4E2	300	"	4.8E2	1.0E2	4.4E2	4.4E2		
600	"	6.7E2	1.2E2	6.2E2	6.2E2	600	"	"	1.3E2	5.2E2	8.4E2		
900	"	"	"	8.8E2	8.6E2	900	"	"	"	"	1.2E3		
1800	"	"	"	"	1.9E3	1800	"	"	"	"	2.6E3		

100 kt, 200 km							100 kt, 300 km						
t	Shape	$h_{fb}$	$R_{fb}$	x	y	t	Shape	$h_{fb}$	$R_{fb}$	x	y		
1	Sphere	2.1E2	4.0E1			1	Tube	3.2E2	7.0E1	1.0E2	1.0E2		
3	"	2.2E2	4.2E1			3	"	3.3E2	7.1E1	8.0E1	8.0E1		
10	Tube	2.3E2	4.7E1	6.0E1	6.0E1	10	"	"	3.4E2	7.2E1	1.2E2	1.2E2	
30	"	2.7E2	5.1E1	8.0E1	8.0E1	30	"	"	3.9E2	7.6E1	1.4E2	1.4E2	
60	"	3.3E2	5.6E1	1.2E2	1.2E2	60	"	"	4.6E2	8.3E1	1.8E2	1.8E2	
120	"	4.2E2	6.8E1	2.0E2	2.0E2	120	"	"	5.7E2	9.6E1	2.6E2	2.6E2	
300	"	4.8E2	1.0E2	4.2E2	4.2E2	300	"	"	6.7E2	1.3E2	5.2E2	5.2E2	
600	"	"	"	5.2E2	7.8E2	600	"	"	"	1.6E2	9.0E2	8.6E2	
900	"	"	"	"	1.2E3	900	"	"	"	"	1.3E3	1.3E3	
1800	"	"	"	"	2.4E3	1800	"	"	"	"	2.9E3	2.9E3	

Table 8-2 Fireball Location and Dimensions for Detonations Above 80 km (Continued)

Time is in seconds, distances are in kilometers. E refers to the power of 10, e.g.,  $1.5E4 = 1.5 \times 10^4$ .

100 kt, 400 km							100 kt, 500 km						
t	Shape	$h_{fb}$	$R_{fb}$	x	y		t	Shape	$h_{fb}$	$R_{fb}$	x	y	
1	Tube	4.3E2	1.1E2	1.4E2	1.4E2		1	Tube	5.5E2	1.4E2	2.0E2	2.0E2	
3	"	4.4E2	"	"	"		3	"	"	1.5E2	"	"	
10	"	4.6E2	"	1.6E2	1.6E2		10	"	5.7E2	"	"	2.2E2	
30	"	5.1E2	"	1.8E2	1.8E2		30	"	6.3E2	"	2.4E2	2.4E2	
60	"	5.8E2	1.2E2	2.2E2	2.2E2		60	"	7.1E2	1.6E2	3.0E2	3.0E2	
120	"	7.1E2	1.3E2	3.4E2	3.4E2		120	"	8.5E2	1.8E2	5.0E2	5.0E2	
300	"	8.5E2	1.7E2	7.0E2	7.0E2		300	"	1.0E3	2.2E2	6.4E2	8.0E2	
600	"	"	2.0E2	1.1E3	1.1E3		600	"	"	2.5E2	1.1E2	1.2E3	
900	"	"	"	1.3E3	1.5E3		900	"	"	"	1.6E2	1.8E3	
1800	"	"	"	"	"		1800	"	"	"	"	3.6E3	

1 Mt, 150 km							1 Mt, 200 km						
t	Shape	$h_{fb}$	$R_{fb}$	x	y		t	Shape	$h_{fb}$	$R_{fb}$	x	y	
1	Sphere	1.8E2	6.1E1				1	Sphere	2.4E2	9.1E1			
3	"	1.9E2	6.4E1				3	"	2.5E2	9.5E1			
10	"	2.2E2	7.7E1				10	Tube	2.8E2	1.1E2	1.4E2	1.4E2	
0	Tube	3.0E2	1.1E2	1.4E2	1.4E2		30	"	3.5E2	1.1E2	2.0E2	2.0E2	
60	"	4.2E2	1.2E2	2.2E2	2.2E2		60	"	4.6E2	1.2E2	2.4E2	2.4E2	
120	"	6.5E2	1.4E2	3.6E2	3.6E2		120	"	6.7E2	1.4E2	4.0E2	4.0E2	
300	"	1.1E3	2.0E2	8.0E2	8.0E2		300	"	1.0E3	2.0E2	8.0E2	8.0E2	
600	"	1.2E3	2.5E2	1.4E3	1.4E3		600	"	1.1E3	2.4E2	1.4E3	1.4E3	
900	"	"	"	2.0E3	2.0E3		900	"	"	"	1.8E3	2.0E3	
1800	"	"	"	"	"		1800	"	"	"	"	4.6E3	

Table 8-2 Fireball Location and Dimensions for Detonations Above 80 km (Continued)

Time is in seconds, distance; are in kilometers. E refers to the power of 10, e.g.,  $1.5E4 = 1.5 \times 10^4$ .

## 1 Mt, 300 km

t	Shape	$h_{fb}$	$R_{fb}$	x	y
1	Pancake	2.2E2	1.5E2	9.1E0	
3	"	"	"	1.7E1	
10	"	2.5E2	"	4.6E1	
30	Tube	2.9E2	"	1.1E2	
60	"	"	"	1.6E2	
120	"	"	"	"	
300	"	"	"	3.0E2	
600	"	"	"	6.5E2	
900	"	"	"	2.4E3	
1800	"	"	"	3.6E3	
				8.0E3	

## Mt, 400 km

t	Shape	$h_{fb}$	$R_{fb}$	x	y
1	Pancake		2.8E2	2.2E2	1.1E1
3	"	"	2.9E2	"	2.2E2
10	"	"	3.3E2	"	6.2E2
30	Tube		3.9E2	"	2. E2
60	"	"	"	"	2.8E2
120	"	"	"	"	"
300	"	"	"	"	"
600	"	"	"	"	"
900	"	"	"	"	"
1800	"	"	"	"	"

## 1 Mt, 500 km

t	Shape	$h_{fb}$	$R_{fb}$	x	y
1	Pancake	3.4E2	3.0E2	1.2E1	
3	"	3.5E2	"	2.7E1	
10	"	4.0E2	"	8.0E1	
30	Tube	4.8E2	"	3.2E2	
60	"	"	"	3.4E2	
120	"	"	"	4.6E2	
300	"	"	"	7.2E2	
600	"	"	"	1.4E3	
900	"	"	"	2.6E3	
1800	"	"	"	3.8E2	
				8.2E3	

## 10 Mt, 400 km

t	Shape	$h_{fb}$	$R_{fb}$	x	y
1	Sphere		2.5E2	1.5E2	
3	"	"	2.6E2	1.5E2	
10	"	"	2.9E2	1.7E2	
30	Tube		3.9E2	2.1E2	
60	"	"	5.2E2	2.7E2	
120	"	"	7.9E2	3.0E2	
300	"	"	1.3E3	3.7E2	
600	"	"	1.5E3	4.1E2	
900	"	"	"	"	
1800	"	"	"	"	

## 10 Mt, 150 km

t	Shape	$h_{fb}$	$R_{fb}$	x	y
1	Sphere		2.5E2	1.5E2	
3	"	"	2.6E2	1.5E2	
10	"	"	2.9E2	1.7E2	
30	Tube		3.9E2	2.1E2	
60	"	"	5.2E2	2.7E2	
120	"	"	7.9E2	3.0E2	
300	"	"	1.3E3	3.7E2	
600	"	"	1.5E3	4.1E2	
900	"	"	"	"	
1800	"	"	"	"	

Table 8-2 Fireball Location and Dimensions for Detonations Above 80 km (Concluded)

Time is in seconds, distances are in kilometers. E refers to the power of 10, e.g.,  $1.5E4 = 1.5 \times 10^4$ .

10 Mt, 200 km

t	Shape	$h_{fb}$	$R_{fb}$	x	y
1	Sphere	3.4E2	2.2E2		
3	"	3.5E2	2.3E2		
10	"	3.8E2	2.4E2		
30	Tube	4.8E2	2.7E2	3.8E2	3.8E2
60	"	6.1E2	2.8E2	4.4E2	4.4E2
120	"	8.8E2	3.0E2	5.2E2	6.2E2
300	"	1.4E3	3.7E2	1.0E3	1.0E3
600	"	1.6E3	4.2E2	2.0E3	2.0E3
900	"	"	"	2.8E3	2.8E3
1800	"	"	"	"	5.6E3

10 Mt, 300 km

t	Shape	$h_{fb}$	$R_{fb}$	x	y
1	Pancake	1.6E2	3.1E2	7.6E0	
3	"	1.7E2	"	1.3E1	
10	"	1.8E2	"	3.1E1	
30	Tube	2.1E2	"	1.2E2	1.6E2
60	"	"	"	"	2.8E2
120	"	"	"	"	5.4E2
300	"	"	"	"	1.2E3
600	"	"	"	"	2.4E3
900	"	"	"	"	3.6E3
1800	"	"	"	"	8.0E3

10 Mt, 500 km

t	Shape	$h_{fb}$	$R_{fb}$	x	y
1	Pancake	2.4E2	6.4E2	9.6E0	
3	"	2.5E2	"	1.9E1	
10	"	2.8E2	"	5.1E1	
30	Tube	3.2E2	"	1.3E2	2.4E2
60	"	"	"	"	3.6E2
120	"	"	"	"	6.2E2
300	"	"	"	"	1.3E3
600	"	"	"	"	2.6E3
900	"	"	"	"	3.8E3
1800	"	"	"	"	8.2E3

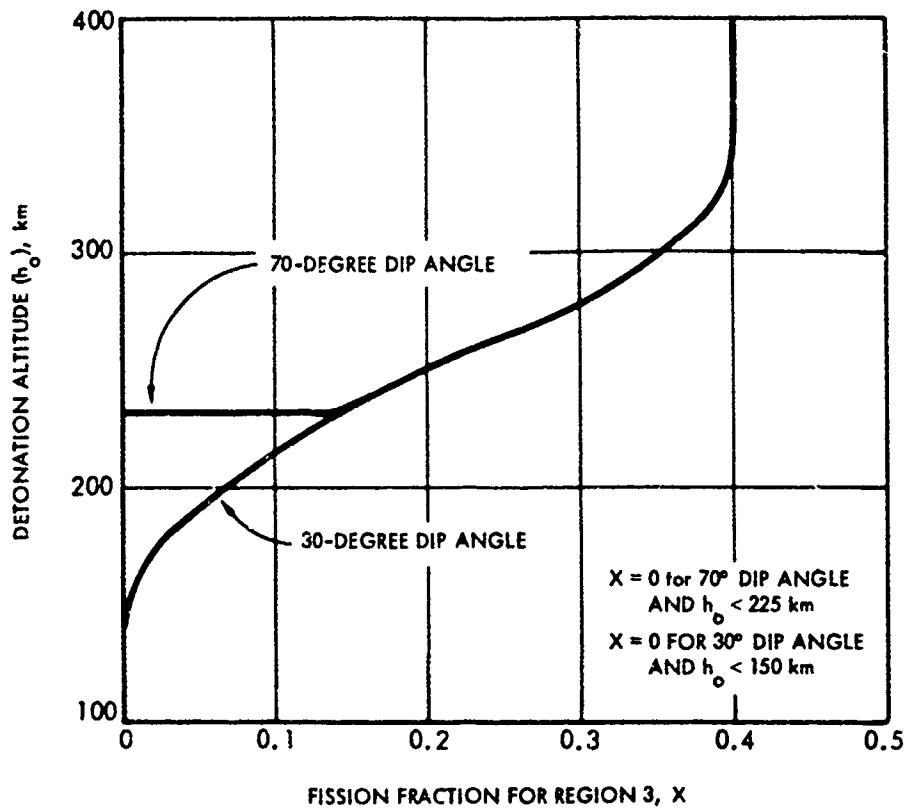


Figure 8-30. Fraction of Total Debris Transported to Conjugate Region (Region 3)

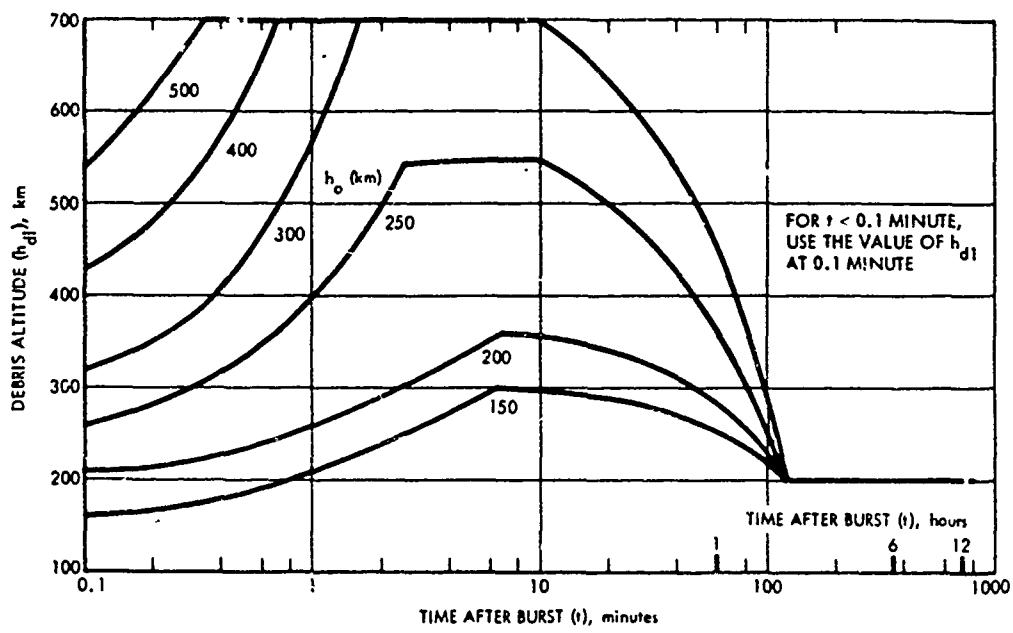


Figure 8-31. Altitude of Debris Region 1, 10-kt Burst

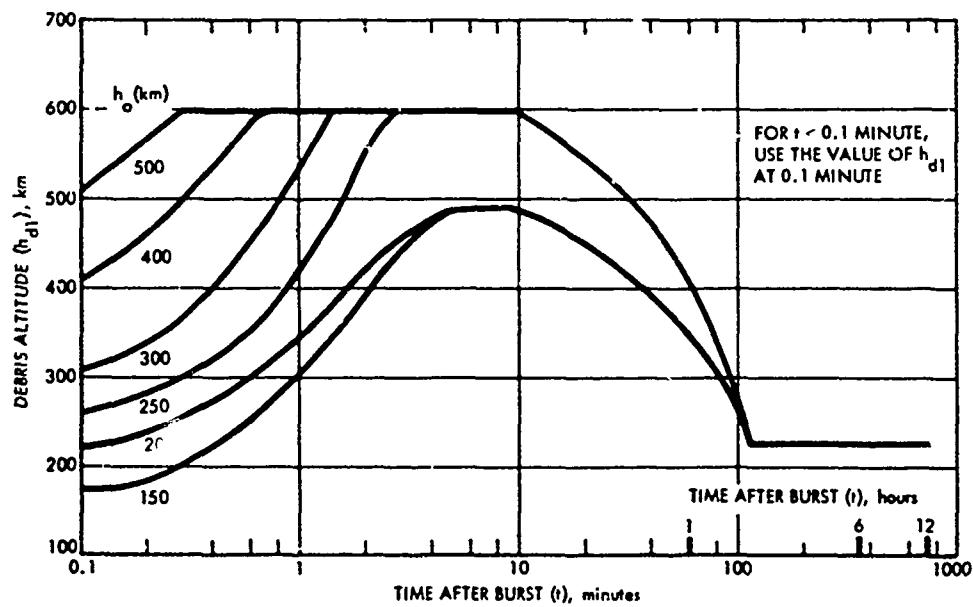


Figure 8-32. Altitude of Debris Region 1, 100-kt Burst

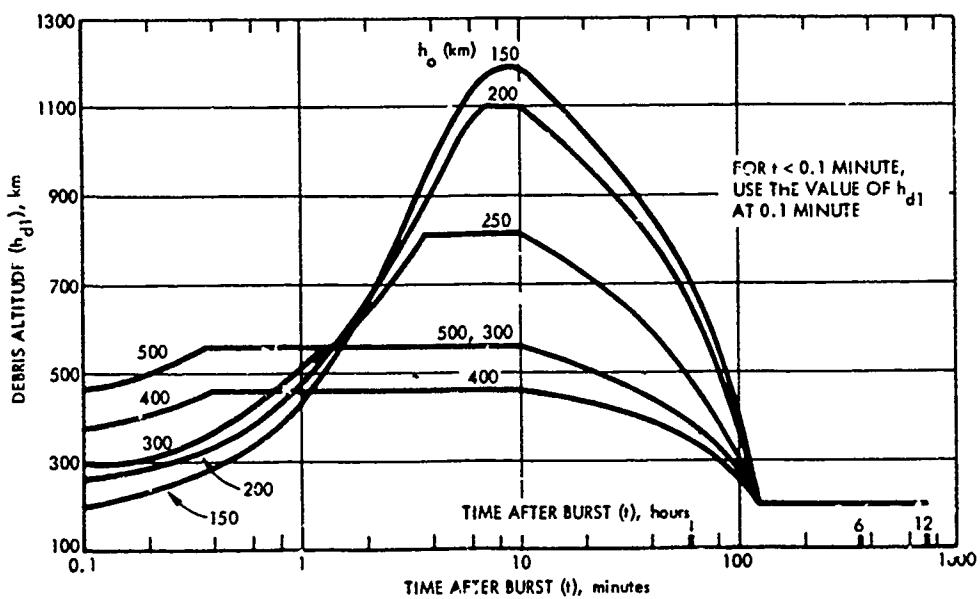


Figure 8-33. Altitude of Debris Region 1, 1-Mt Burst

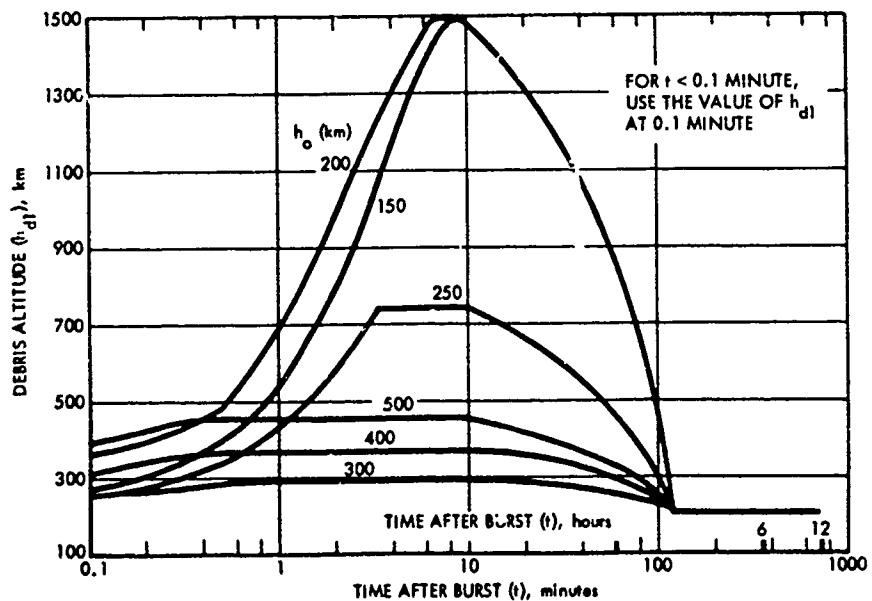


Figure 8-34. Altitude of Debris Region 1, 10-Mt Burst

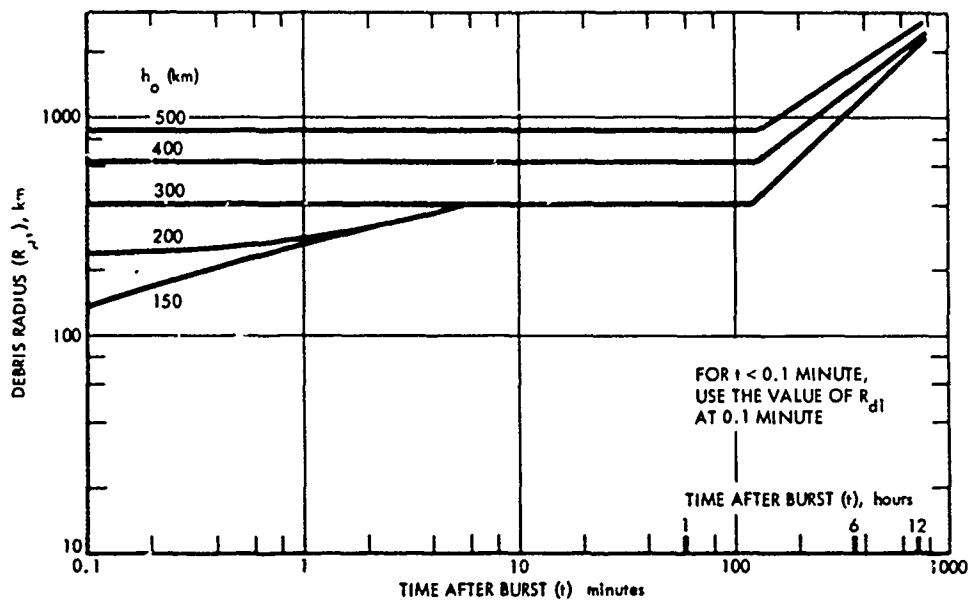


Figure 8-35. [REDACTED] Radius of Debris Region 1, 10-kt Burst [REDACTED]

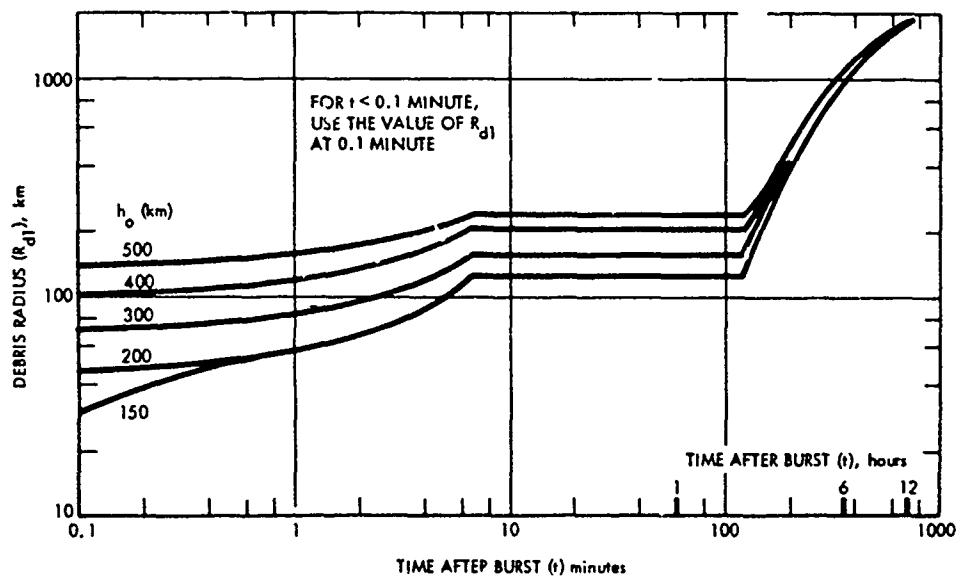


Figure 8-36. [REDACTED] Radius of Debris Region 1, 100-kt Burst [REDACTED]

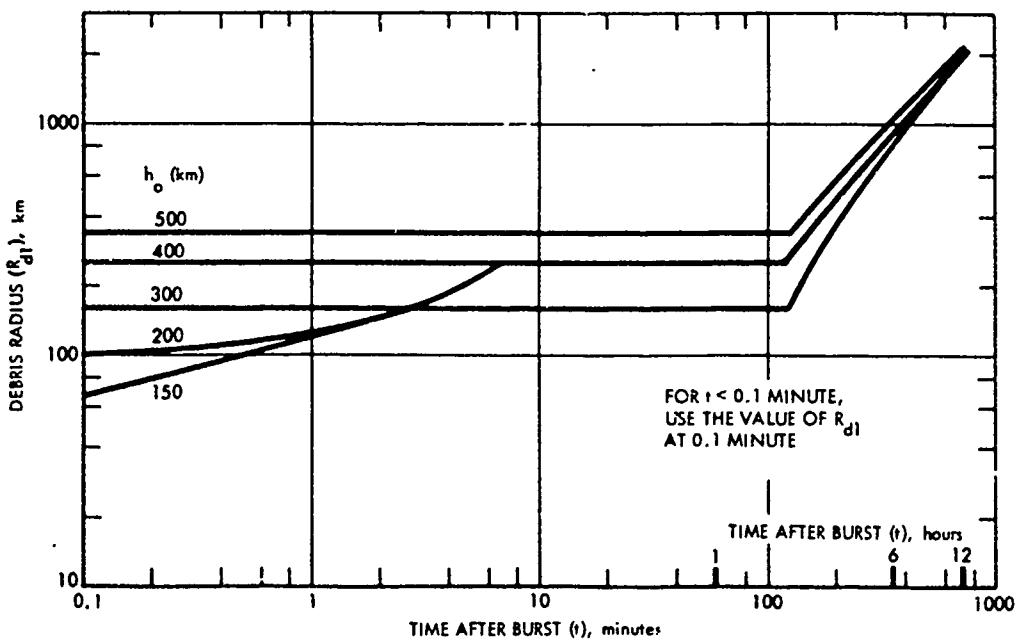


Figure 8-37. Radius of Debris Region 1, 1-Mt Burst

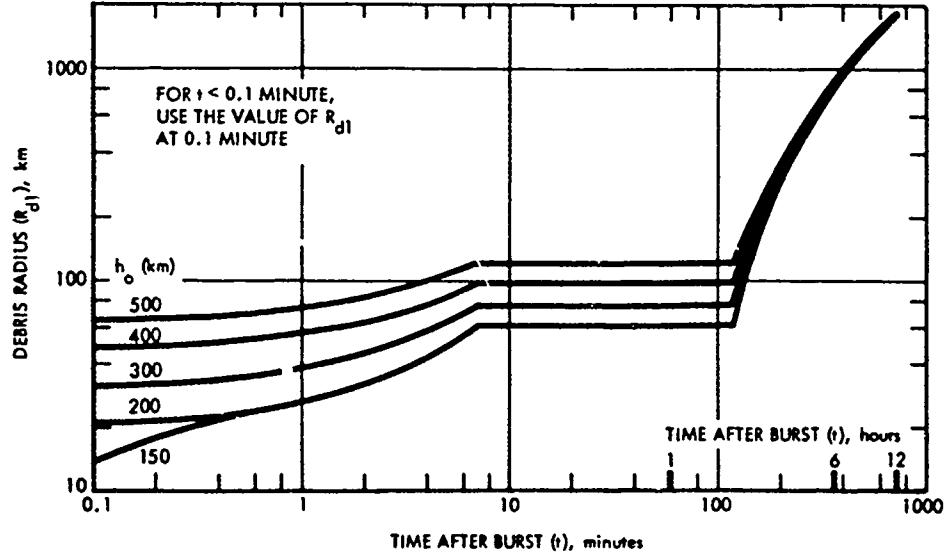


Figure 8-38. Radius of Debris Region 1, 10-Mt Burst

#### Problem 8-4 Absorption through the Fireball

Tables 8-3 through 8-7 and Figure 8-39 are used to obtain estimates of the absorption of signals propagating through the fireball for parametric burst yields and detonation altitudes. The temperature and electron density within the fireball are assumed to be uniformly distributed; thus, the absorption through the fireball is linearly dependent upon the distance the propagation path travels through the fireball. The fireball location and size can be determined from Table 8-2 and Figures 8-16 through 8-38, as described in Problems 8-1 through 8-3.

The absorption data are given for a path length through the fireball equal to the fireball diameter if the fireball is a sphere, equal to the diameter of the toroid arm if the fireball is a toroid, equal to the vertical thickness of a pancake if the fireball is a pancake, or equal to the diameter of the tube if the fireball is a tube. For detonations that occur above about 50 km, the fireball absorption scales inversely with the square of the frequency.

When the fireball is below an altitude of about 60 km, beta particles deposit their energy within the fireball, and they are the major source of ionization and absorption after the fireball has cooled to the atmospheric temperature. When the altitude of the fireball is greater than 60 km, absorption caused by beta-particle ionization should be determined by the methods described in Problem 8-7.

Tables 8-3 through 8-6 provide data to determine absorption of signals propagating through the fireball of bursts that occur below 80 km at times after burst less than 300 seconds and fireball altitudes greater than 60 km (the fireball altitude at the time of interest may be obtained by the methods described in Problem 8-1). If the detonation altitude is below 50 km, the absorption  $A_{fb}$  is read directly from the table

with the weapon yield closest to the desired yield at the closest detonation altitude, time after burst, and frequency given in the table. If the detonation altitude is 50 km or greater (but not greater than 80 km), the absorption for 1000 MHz,  $A'_{fb}$ , is read from the appropriate table at the closest detonation altitude and time after burst. The absorption is then calculated as follows:

$$A_{fb} = A'_{fb} \frac{10^6}{f^2},$$

where  $f$  is the desired frequency in MHz.

If the time after burst is greater than 300 seconds and the fireball altitude is less than 60 kilometers, the absorption of signals propagating through the fireball may be estimated from Figure 8-39. The quantity  $L'_a$  is obtained from Figure 8-39 for the appropriate fireball altitude and frequency. The absorption is then calculated as follows:

$$A_{fb} = L'_a \frac{N_\beta}{10^9},$$

where  $N_\beta$  is the beta particle radiation intensity parameter defined by equation 8.1 in paragraph 8-4.

Table 8-7 provides data to determine absorption of signals propagating through the fireball of bursts that occur at altitudes above 80 km. The absorption of a 1000 MHz signal ( $A'_{fb}$ ) is read from Table 8-7 for the weapon yield and altitude closest to those desired. The absorption at the desired frequency ( $A_{fb}$ ) is then calculated as follows:

$$A_{fb} = A'_{fb} \frac{10^6}{f^2},$$

where  $f$  is the frequency in MHz.

**Example 1**

*Given:* A 1 Mt weapon burst at an altitude 50 km.

*Find:* The absorption of a 400 MHz signal propagating through the fireball 2 min after burst.

*Solution:* From Table 8-5, the absorption of a 1000 MHz signal 10 min after a 1 Mt burst at 150 km is

$$A'_{fb} = 0.2 \text{ dB};$$

therefore,

$$A'_{fb} = (0.2) \frac{10^6}{(400)^2} = 1.25 \text{ dB.}$$

*Answer:* The absorption of a 400 MHz signal propagating through the fireball of a 1 Mt weapon 2 min after the weapon was detonated at an altitude of 50 km is 1.25 dB.

**Example 2**

*Given:* A 4 Mt weapon burst at an altitude of 150 km.

*Find:* The absorption of a 400 MHz signal propagating through the fireball 15 min after burst.

*Solution:* The yield and time nearest to

those desired that are tabulated in Table 8-7 are 1 Mt and 10 min (600 sec). The absorption for a 1000 MHz signal 10 min after a 1 Mt burst at 150 km is

$$A'_{fb} = 3.2 \text{ dB};$$

therefore,

$$A'_{fb} = (3.2) \frac{10^6}{(400)^2} = 20 \text{ dB.}$$

*Answer:* The absorption of a 400 MHz signal propagating through the fireball of a 4 Mt weapon 15 min after the weapon was detonated at an altitude of 150 km is approximately 20 dB.

**Reliability** The uncertainties in predicting fireball dimensions and electron density are such that estimates of the duration of a given level of absorption are uncertain by at least a factor of two. In general, the duration of absorption caused by the rising fireball will be determined by how long the fireball interdicts the propagation path, rather than the time period that the fireball remains absorbing at a given frequency.

**Related Material** See paragraph 8-6 and Problems 8-1 through 8-3.

Table 8-3 Absorption (dB) Through Fireball for Detonations Below 80 km, W = 10 kt

Time (sec)	Freq. (MHz)	Detonation Altitude (km)								
		0	10	20	30	40	50	60	70	80
10	100	8.5E3	2.0E4	2.7E5	9.1E6	1.7E7				
	400	8.5E3	1.9E4	2.4E5	2.5E6	1.4E6				
	1,000	8.5E3	1.9E4	1.4E5	5.0E5	2.2E5	1.4E5	1.1E3	3.8E2	1.7E2
	4,000	8.2E3	1.2E4	1.7E4	3.3E4	1.4E4	2.2E3			
	10,000	6.7E3	3.7E3	2.8E3	5.3E3					
20	100	3.1E3	1.2E4	2.9E4	5.2E4	3.0E5				
	400	3.2E3	1.2E4	2.4E4	1.2E4	2.2E4				
	1,000	3.1E3	1.2E4	1.3E4	2.3E3	3.6E3	1.3E4	3.7E2	1.0E2	2.7E1
	4,000	3.0E3	6.7E3	1.4E3	1.5E2	2.3E2				
	10,000	2.4E3	2.0E3	2.3E2	2.3E1	3.6E1				
30	100	7.4E2	8.5E3	2.2E4	3.8E4	1.5E4				
	400	7.4E2	8.4E3	1.8E4	7.5E3	1.1E3				
	1,000	7.3E2	8.0E3	8.7E3	1.4E3	1.7E2	7.5E1	1.7E1	4.2E2	8.8E0
	4,000	7.0E2	4.1E3	8.5E2	8.7E1	1.1E1				
	10,000	5.4E2	1.1E3	1.4E2	1.4E1	1.7E0				
40	100	7.3E1	3.2E3	1.7E4	2.9E4	9.9E3				
	400	7.3E1	3.1E3	1.4E4	5.0E3	6.9E2				
	1,000	7.3E1	3.0E3	6.0E3	8.9E2	1.0E2	1.7E1	1.8E1	2.0E1	3.8E0
	4,000	6.9E1	1.4E3	5.5E2	5.7E1	7.0E0				
	10,000	5.2E1	3.5E2	9.0E1	9.1E0	1.1E0				
50	100	4.6E0	4.7E2	1.2E4	2.3E4	7.0E3				
	400	4.6E0	4.7E2	8.6E3	3.5E3	4.8E2				
	1,000	4.6E0	4.3E2	3.5E3	6.1E2	7.6E1	1.1E1	1.1E1	2.2E0	1.9E0
	4,000	4.3E0	1.8E2	3.0E2	3.9E1	4.9E0				
	10,000	3.2E0	4.4E1	4.9E1	6.2E0	7.7E-1				
60	100	2.6E-1	3.9E1	3.8E3	1.8E4	5.1E3				
	400	2.6E-1	3.9E1	2.7E3	2.4E3	3.4E2				
	1,000	2.6E-1	3.5E1	1.0E3	4.1E2	5.5E1	8.0E0	6.6E0	1.3E0	1.1E0
	4,000	2.3E-1	1.4E1	8.3E1	2.6E1	3.4E0				
	10,000	1.7E-1	3.1E0	1.4E1	4.2E0	5.5E-1				
90	100	5.6E-3	4.8E-1	3.3E1	6.5E2	1.5E3				
	400	5.6E-3	4.6E-1	2.0E1	6.9E1	9.0E1				
	1,000	5.6E-3	4.0E-1	6.1E0	1.2E1	1.6E1	3.3E0	2.1E0	3.4E-1	7.7E-2
	4,000	5.0E-3	1.2E-1	4.5E-1	7.2E-1	9.9E-1				
	10,000	3.2E-3	2.4E-2	7.3E-2	1.2E-1	1.6E-1				
120	100		3.1E-1	1.7E1	2.2E-2					
	400		2.9E-1	8.4E0	1.9E-1					
	1,000		2.3E-1	2.2E0	3.2E0	1.7E0	9.0E-1	7.8E-1	1.1E-1	3.5E-2
	4,000		5.8E-2	1.7E-1	2.1E-1					
	10,000		1.0E-2	2.4E-2	3.2E-2					
150	100		2.7E-1	1.5E1	1.7E2					
	400		2.6E-1	6.4E0	1.4E1					
	1,000		2.0E-1	1.5E0	2.3E0	1.2E0	5.5E-1	4.3E-1	6.0E-2	2.3E-2
	4,000		3.8E-2	1.0E-1	1.4E-1					
	10,000		6.9E-3	1.7E-2	2.3E-2					
180	100		2.4E-1	1.3E1	1.3E2					
	400		2.2E-1	4.9E0	1.0E1	1.7E0	8.8E-1	4.0E-1	2.6E-1	3.6E-2
	1,000		1.6E-1	1.1E0	1.7E0					
	4,000		2.6E-2	6.9E-2	1.0E-1					
	10,000		4.9E-3	1.2E-2	1.7E-2					
300	100		1.3E-1	5.7E0	5.0E1					
	400		1.2E-1	1.7E0	3.5E0					
	1,000		6.9E-2	3.2E-1	5.6E-1	3.4E-1	1.7E-1	4.4E-2	4.9E-3	1.2E-3
	4,000		8.2E-3	2.1E-2	3.5E-2					
	10,000		1.4E-3	3.3E-3	5.6E-3					

Notes: E refers to the power of 10, e.g.,  $1.5E4 = 1.5 \times 10^4$ . If  $f^{-2}$  scaling applies, only 1,000 MHz values are given.

Table 8-4 Absorption (dB) Through Fireball for Detonations Below 80 km, W = 100 kt

Time (sec)	Freq. (MHz)	Detonation Altitude (km)								
		0	10	20	30	40	50	60	70	80
10	100	1.3E5	6.5E5	4.3E6	2.5E7	4.8E7				
	400	1.3E5	6.4E5	3.7E6	6.5E6	3.8E6				
	1,000	1.3E5	6.2E5	2.1E6	1.3E6	6.1E5	4.8E5	2.1E3	9.5E2	9.2E2
	4,000	1.2E5	3.7E5	2.3E5	8.2E4	3.8E4				
	10,000	1.0E5	1.1E5	3.9E4	1.3E4	6.1E3				
20	100	9.0E3	4.3E4	1.0E5	3.5E6	4.7E6				
	400	9.0E3	4.3E4	8.3E4	6.9E5	3.3E5				
	1,000	3.3E3	2.4E4	2.5E4	3.4E3	3.7E3	4.0E3	2.3E2	3.1E1	2.5E1
	4,000	8.6E3	2.2E4	3.9E3	8.0E3	3.4E3				
	10,000	6.8E3	6.0E3	6.5E2	1.2E3	5.4E2				
30	100	3.3E3	2.6E4	8.1E4	1.3E5	3.3E5				
	400	3.3E3	2.6E4	6.1E4	2.0E4	2.3E4				
	1,000	5.8E2	1.4E4	1.7E4	2.1E3	2.5E2	1.1E2	1.1E2	1.2E1	1.1E0
	4,000	3.1E3	1.1E4	2.2E3	2.2E2	2.3E2				
	10,000	2.3E3	2.8E3	3.7E2	3.5E1	3.7E1				
40	100	5.8E2	1.5E4	6.7E4	9.4E4	2.3E4				
	400	5.8E2	1.5E4	4.7E4	1.2E4	1.6E3				
	1,000	5.8E2	1.4E4	1.7E4	2.1E3	2.5E2	1.7E2	1.1E2	1.2E1	9.1E0
	4,000	5.4E2	5.5E3	1.4E3	1.3E2	1.6E1				
	10,000	4.0E2	1.3E3	2.3E2	2.1E1	2.5E0				
50	100	5.5E1	5.5E3	5.7E4	7.1E4					
	400	5.5E1	5.4E3	3.6E4	8.0E3					
	1,000	5.5E1	4.8E3	1.2E4	1.3E3	1.6E2	9.2E1	6.0E1	5.7E0	4.2E0
	4,000	5.0E1	1.7E3	8.8E2	8.5E1					
	10,000	3.5E1	3.6E2	1.4E2	1.4E1					
60	100	4.0E0	8.9E2	4.2E4	5.5E4					
	400	4.0E0	8.7E2	2.4E4	5.5E3					
	1,000	4.0E0	7.5E2	6.9E3	9.1E2	1.1E2	1.4E1	3.3E1	3.0E0	2.2E0
	4,000	3.6E0	2.2E2	5.0E2	5.7E1					
	10,000	2.4E0	4.5E1	8.1E1	9.1E0					
90	100	2.3E-2	3.6E0	7.0E2	1.5E4					
	400	2.3E-2	3.5E0	2.8E2	1.2E3					
	1,000	2.2E-2	2.7E0	6.3E1	2.0E2	3.9E1	4.5E0	1.7E0	1.3E-1	5.4E-1
	4,000	2.0E-2	5.4E-1	4.3E0	1.2E1					
	10,000	1.1E-2	1.0E-1	6.9E-1	2.0E0					
120	100	1.4E-2	2.2E0	1.7E2	1.1E3					
	400	1.4E-2	2.0E0	4.7E1	8.0E1					
	1,000	1.4E-2	1.3E0	9.2E0	1.3E1	7.7E0	1.6E0	4.6E-1	4.8E-2	3.5E-2
	4,000	1.2E-2	2.1E-1	6.7E-1	9.1E-1					
	10,000	5.4E-3	3.3E-2	9.6E-2	1.3E-1					
150	100	1.2E-2	2.2E0	1.6E2	8.2E2					
	400	1.2E-2	2.0E0	3.4E1	5.6E1					
	1,000	1.2E-2	1.1E0	6.2E0	9.1E0	3.6E0	7.8E-1	2.2E-1	4.9E-2	1.7E-2
	4,000	9.0E-3	1.4E-1	4.0E-1	5.7E-1					
	10,000	4.0E-3	2.4E-2	6.4E-2	9.1E-2					
180	100	1.0E-2	2.2E0	1.5E2	6.1E2					
	400	1.0E-2	1.8E0	2.6E1	4.1E1					
	1,000	1.0E-2	9.8E-1	4.7E0	6.6E0	2.5E0	4.5E-1	1.2E-1	1.9E-2	7.9E-3
	4,000	7.2E-3	1.0E-1	2.9E-1	3.9E-1					
	10,000	3.0E-2	1.7E-2	4.8E-2	6.6E-2					
300	100	6.1E-3	1.7E0	8.5E1						
	400	6.1E-3	1.2E0	9.3E0						
	1,000	5.8E-3	4.2E-1	1.6E0	2.2E0	9.3E-1	8.6E-2	1.5E-2	2.6E-3	5.7E-4
	4,000	3.4E-3	3.4E-2	9.8E-2						
	10,000	1.0E-3	5.5E-3	1.6E-2						

Notes: E refers to the power of 10, e.g.,  $1.5E4 = 10^4$ . If  $f^{-2}$  scaling applies, only 1,000 MHz values are given.

Table 8-5 Absorption (dB) Through Fireball for Detonations Below 80 km, W = 1 Mt

Time (sec)	Freq. (MHz)	Detonation Altitude (km)								
		0	10	20	30	40	50	60	70	80
10	100	3.4E5	1.8E6	1.4E7	9.7E7	1.8E8				
	400	3.4E5	1.8E6	1.2E7	1.9E7	1.3E7				
	1,000	3.4E5	1.8E6	3.4E7	2.2E6	7.5E6	7.5E6	1.6E4	1.4E4	3.2E3
	4,000	3.3E5	1.0E6	6.2E5	2.2E5	1.4E5				
	10,000	2.7E5	3.0E5	1.0E5	3.5E4	2.2E4				
20	100	5.2E4	2.4E5	1.5E6	1.1E7	9.2E6				
	400	5.2E4	2.3E5	1.1E6	1.4E6	6.0E5				
	1,000	5.2E4	2.2E5	4.5E5	2.4E5	9.7E3	6.8E4	1.2E3	9.2E2	2.3E2
	4,000	5.0E4	1.0E5	3.8E4	1.5E4	6.0E3				
	10,000	3.8E4	2.6E4	6.3E3	2.4E3	1.0E3				
30	100	1.4E4	8.8E4	9.0E5	1.4E6	9.5E5				
	400	1.4E4	8.6E4	5.7E5	1.5E5	6.1E4				
	1,000	1.4E4	7.8E4	1.9E5	2.4E4	9.7E3	4.2E3	2.4E2	1.7E2	4.7E1
	4,000	1.3E4	3.0E4	1.4E4	1.5E3	6.0E2				
	10,000	1.0E4	6.8E3	2.3E3	2.5E2	9.7E1				
40	100	5.8E3	6.3E4	2.7E5	1.0E6	1.1E5				
	400	5.8E3	6.1E4	1.4E5	8.4E4	6.7E3				
	1,000	5.7E3	5.4E4	4.0E4	1.4E4	1.1E3	4.0E2	7.0E1	4.6E1	1.6E1
	4,000	5.3E3	1.7E4	2.9E3	8.6E2	1.7E1				
	10,000	3.7E3	3.4E3	4.6E2	1.4E2	1.1E1				
50	100	1.3E3	4.5E4	2.4E5	6.5E5	6.2E4				
	400	1.3E3	4.3E4	1.0E5	5.1E4	3.9E3				
	1,000	1.3E3	3.6E3	2.5E4	8.3E3	6.2E2	4.0E1	2.6E1	1.7E1	6.8E0
	4,000	1.1E3	8.9E3	1.7E3	5.2E2	8.3E1				
	10,000	7.4E2	1.7E3	2.7E2						
60	100	1.6E2	2.5E4	2.2E5	1.0E5					
	400	1.6E2	2.4E4	7.4E4	7.4E3					
	1,000	1.6E3	1.9E4	1.6E4	1.2E3	3.8E2	2.2E1	1.1E1	7.4E0	3.5E0
	4,000	1.4E2	3.8E3	1.1E3	7.5E1					
	10,000	8.7E1	6.9E2	1.7E2	1.2E1					
90	100	2.4E-1	2.2E2	7.8E4	3.4E4					
	400	2.4E-1	1.9E2	1.5E4	2.3E3					
	1,000	2.4E-1	1.2E2	2.6E3	3.6E2	2.4E1	4.5E0	1.6E0	1.3E0	6.4E-1
	4,000	1.9E-1	1.5E1	1.7E2	2.3E1					
	10,000	9.4E-2	2.6E0	2.7E1	3.6E0					
120	100	7.0E-2	2.7E1	3.1E3	7.6E3					
	400	7.0E-2	2.1E1	3.6E2	4.8E2					
	1,000	6.9E-2	9.3E0	6.1E1	7.8E1	6.8E0	2.0E-1	3.5E-1	3.2E-1	1.3E-1
	4,000	5.2E-2	9.6E-1	4.9E0	6.6E0					
	10,000	1.9E-2	1.4E-1	6.2E-1	7.8E-1					
150	100	6.9E-2	2.8E1	2.1E3						
	400	6.8E-2	1.9E1	2.0E2						
	1,000	6.6E-2	7.1E0	3.3E1						
	4,000	4.3E-2	5.8E-1	2.1E0						
	10,000	1.4E-2	9.4E-2	3.4E-1						
180	100	6.8E-2	3.2E1	1.8E3						
	400	6.7E-2	1.9E1	1.5E2						
	1,000	6.5E-2	6.0E0	2.5E1	1.6E1	1.5E0	3.2E-2	1.8E-2	7.4E-2	3.9E-3
	4,000	3.6E-2	4.3E-1	1.7E-1						
	10,000	1.1E-2	7.3E-2	2.5E-1						
300	100	5.2E-2	3.6E1	8.5E2						
	400	5.1E-2	1.2E1	5.8E1						
	1,000	4.6E-2	2.5E0	9.3E0	4.7E0	4.7E0	2.4E-3	3.3E-3	1.0E-3	1.8E-4
	4,000	1.7E-2	1.7E-1	5.8E-1						
	10,000	3.8E-3	2.7E-2	9.3E-2						

Notes: E refers to the power of 10, e.g., 1.5E4 =  $1.5 \times 10^4$ . If  $t^{-2}$  scaling applies, only 1,000 MHz values are given.

Table 8-6 Absorption (dB) Through Fireball for Detonations Below 80 km, W = 10 Mt

Time (sec)	Freq. (MHz)	Detonation Altitude (km)								
		0	10	20	30	40	50	60	70	80
10	100	1.2E6	7.4E6	8.4E7	8.8E8	1.0E10				
	400	1.1E6	7.4E6	6.2E7	2.9E8	5.2E9				
	1,000	1.1E6	7.0E6	2.5E7	6.0E7	1.4E9	1.2E10	7.8E4	2.5E4	8.2E3
	4,000	1.1E6	3.7E6	2.1E6	4.0E6	1.0E8				
	10,000	8.8E5	1.0E6	3.4E5	6.4E5	1.6E7				
20	100	1.3E5	6.6E5	1.2E7	5.0E7	1.8E8				
	400	1.3E5	6.4E5	4.9E6	4.5E6	1.2E7				
	1,000	1.3E5	5.9E5	1.1E6	7.3E5	2.0E6	8.8E6	4.8E3	1.6E3	5.9E2
	4,000	1.2E5	2.3E5	7.8E4	4.6E4	1.2E5				
	10,000	9.1E4	5.3E4	1.0E4	7.4E3	2.0E4				
30	100	9.0E4	5.3E5	4.3E6	2.4E6					
	400	8.9E4	5.1E5	1.1E6	1.6E5					
	1,000	8.9E4	4.4E5	2.2E5	2.6E4	4.5E4	7.1E4	7.4E2	2.5E2	1.2E2
	4,000	8.2E4	1.3E5	1.4E4	1.6E3					
	10,000	5.7E4	2.5E4	2.3E3	2.6E2					
40	100	6.8E4	4.7E5	3.4E6						
	400	6.8E4	4.4E5	6.1E5	4.0E3	1.8E3	2.3E3	1.8E2	6.7E1	3.9E1
	1,000	6.7E4	3.5E5	1.1E5						
	4,000	6.1E4	7.4E4	6.9E3						
	10,000	3.9E4	1.4E4	1.1E3						
50	100	2.1E4	4.3E5	2.7E6						
	400	2.1E4	4.0E5	3.4E5	1.4E3	2.5E2	5.9E1	6.0E1	2.4E1	1.7E1
	1,000	2.1E4	2.8E5	5.9E4						
	4,000	1.8E4	4.5E4	3.7E3						
	10,000	1.1E4	7.9E3	5.9E2						
60	100	9.2E3	2.0E5	2.0E6						
	400	9.2E3	1.7E5	2.1E5	6.9E2	9.2E1	1.6E1	2.4E1	1.1E1	1.7E0
	1,000	9.1E3	1.1E5	3.4E4						
	4,000	7.6E3	1.3E4	2.2E3						
	10,000	4.0E3	2.3E3	3.4E2						
90	100	7.4E1	7.7E4	2.3E5						
	400	7.3E1	5.4E4	1.7E4	1.4E2	8.9E2	1.3E0	3.1E0	1.8E0	2.0E-1
	1,000	7.2E1	2.1E4	2.7E3						
	4,000	5.1E1	1.7E3	1.7E2						
	10,000	2.0E1	2.8E2	2.7E1						
120	100	6.6E-1	1.3E3	6.2E4						
	400	6.5E-1	6.3E2	4.1E3	6.8E0	1.2E0	1.7E-1	6.4E-1	6.1E-2	3.1E-2
	1,000	6.2E-1	1.6E2	6.5E2						
	4,000	4.3E-1	2.0E1	5.2E1						
	10,000	1.0E-1	1.8E0	6.5E0						
150	100	5.5E-1	7.6E2							
	400	5.4E-1	2.5E2	1.8E2						
	1,000	5.1E-1	5.3E1	5.3E0						
	4,000	2.3E-1	3.5E0							
	10,000	5.6E-2	5.6E-1							
180	100	5.9E-1	8.2E2							
	400	5.7E-1	2.0E2	9.6E1	1.0E0	2.7E-2	2.0E-2	2.2E-2	8.9E-3	4.5E-3
	1,000	5.2E-1	3.8E1							
	4,000	1.9E-1	2.3E0							
	10,000	4.3E-2	3.9E-1							
300	100	6.5E-1	9.3E2							
	400	6.1E-1	9.8E1							
	1,000	4.6E-1	1.6E1	2.1E1	5.3E-2	5.8E-4	9.8E-4	4.0E-4	2.0E-4	2.7E-4
	4,000	8.7E-2	1.0E0							
	10,000	1.6E-2	1.6E-1							

Notes: E refers to the power of 10, e.g., 1.5E4 =  $1.5 \times 10^4$ . If f<sup>-2</sup> scaling applies, only 1,000 MHz values are given.

Table 8-7 Absorption (dB) Through Fireball at 1000 MHz for Detonations Above 80 km

Time (sec)	Yield (Mt)	Detonation Altitude (km)								
		100	150	200	250	300	350	400	450	500
10	0.01	5.2E2	7.9E2	1.7E2	1.4E1	6.1E0	2.1E0	6.1E-1	2.0E-1	7.3E-2
	0.1	1.1E3	2.0E3	3.8E2	3.1E1	1.4E1	4.8E0	1.4E0	4.5E-1	1.6E-1
	1	3.2E3	5.4E3	9.0E2	5.0E1	5.5E0	7.9E-1	1.5E-1	3.3E-2	8.7E-3
	10	1.4E4	2.0E4	3.3E3	2.6E3	3.5E2	6.9E1	1.7E1	4.9E0	1.6E0
20	0.01	7.2E1	2.1E2	1.2E2	1.2E1	5.4E0	1.9E0	5.5E-1	1.8E-1	6.8E-2
	0.1	1.4E2	5.8E2	2.8E2	2.6E1	1.2E1	4.3E0	1.3E0	4.2E-1	1.5E-1
	1	4.1E2	1.8E3	6.7E2	4.3E1	5.1E0	7.6E-1	1.4E-1	3.2E-2	8.4E-3
	10	2.2E3	8.0E3	1.9E3	1.4E3	2.7E2	5.9E1	1.5E1	4.5E0	1.5E0
30	0.01	2.2E1	1.3E2	9.6E1	1.0E1	4.8E0	1.7E1	5.1E-1	1.7E-1	6.4E-2
	0.1	3.8E1	3.0E2	2.2E1	2.3E1	1.1E1	4.0E0	1.2E0	3.9E-1	1.5E-1
	1	1.2E2	7.2E2	5.3E2	4.6E1	6.2E0	1.0E0	2.0E-1	4.8E-2	1.30E-2
	10	6.6E2	4.0E3	1.5E3	3.2E3	8.4E2	2.2E2	6.5E1	2.1E1	7.4E0
40	0.01	9.2E0	8.8E1	7.7E0	9.1E0	4.4E0	1.6E0	4.7E-1	1.6E-1	6.0E-2
	0.1	1.5E1	2.0E2	1.8E2	2.1E1	1.0E1	3.7E0	1.1E0	3.7E-1	1.4E-1
	1	4.6E1	4.9E2	4.3E2	3.6E1	5.3E0	9.1E-1	1.8E-1	4.4E-2	1.2E-2
	10	2.7E2	2.3E3	1.2E3	1.0E3	5.9E2	1.7E2	5.4E1	1.8E1	6.5E0
50	0.01	4.6E0	6.4E1	6.4E1	8.2E0	4.0E0	1.5E0	4.4E-0	1.5E-1	5.7E-0
	0.1	7.1E0	1.5E2	1.5E2	1.9E1	9.2E0	3.4E0	1.0E0	3.5E-1	1.3E-1
	1	2.2E1	3.6E2	3.5E2	3.0E1	4.6E0	8.2E-1	1.7E-1	4.1E-2	1.1E-2
	10	1.4E2	1.4E3	1.0E3	1.3E3	4.4E2	1.4E2	4.5E1	1.6E1	5.8E0
60	0.01	2.3E0	4.9E1	5.4E1	7.5E0	3.7E0	1.4E0	4.2E-1	1.4E-1	5.4E-2
	0.1	4.8E0	1.1E2	1.2E2	1.7E1	8.6E0	3.2E0	9.7E-1	3.3E-1	1.3E-1
	1	1.1E1	2.7E2	3.0E2	2.4E1	4.1E0	7.4E-1	1.6E-1	3.9E-2	1.1E-2
	10	7.3E1	9.3E2	8.7E2	9.3E2	3.4E2	1.1E2	3.9E1	1.4E1	5.2E0
90	0.01	9.9E-1	2.7E1	3.6E1	6.0E0	3.1E0	1.8E0	3.6E-1	1.2E-1	4.7E-2
	0.1	1.5E0	6.0E1	8.2E1	1.4E1	7.1E0	2.7E0	8.4E-1	2.9E-1	1.1E-1
	1	3.7E0	1.4E2	2.0E2	1.5E1	2.9E0	5.7E-1	1.3E-1	3.2E-2	9.2E-3
	10	2.0E1	4.1E2	5.8E2	4.2E2	1.8E2	6.8E1	2.0E1	9.9E0	3.9E0
125	0.01	4.7E-1	1.6E-1	2.5E1	5.0E1	2.6E0	1.0E0	3.1E-1	1.1E-1	4.2E-2
	0.1	5.5E-1	3.5E1	5.7E1	1.1E1	6.0E0	2.4E0	7.4E-1	2.6E-1	9.9E-2
	1	1.5E0	8.3E1	1.4E2	9.7E0	2.1E0	4.4E-1	1.0E-1	2.7E-2	7.8E-3
	10	6.8E0	2.3E2	3.9E2	1.8E2	1.0E2	4.2E1	1.8E1	7.1E0	3.0E0
180	0.01	2.8E1	9.9E0	1.8E1	4.0E0	2.1E0	8.6E-1	2.7E-1	9.4E-2	3.7E-2
	0.1	2.1E-1	2.1E1	3.8E1	9.2E0	5.0E0	2.0E0	6.4E1	2.2E1	8.7E0
	1	5.6E-1	4.8E1	9.0E1	5.9E0	1.4E0	3.3E-1	8.0E-2	2.1E-2	6.4E-3
	10	2.6E1	1.3E2	2.5E2	6.8E1	5.0E1	2.5E1	1.1E1	4.9E0	2.1E0
300	0.01	4.5E-2	4.6E0	1.0E1	2.8E0	1.6E0	6.5E-1	2.1E-1	7.5E-2	2.9E-2
	0.1	5.9E-2	7.7E0	2.0E1	6.4E0	3.6E0	1.5E0	4.9E-1	1.8E-1	6.9E-2
	1	1.3E-1	2.0E1	4.5E1	2.4E0	7.0E-1	1.8E-1	4.9E-2	1.4E-2	4.4E-3
	10	5.6E-1	4.9E1	1.2E2	1.4E1	1.2E1	9.1E0	5.0E0	2.4E0	1.2E0
600	0.01	7.3E-3	9.3E-1	3.3E0	1.3E0	7.1E-1	3.1E-1	1.2E-1	4.6E-2	1.8E-2
	0.1	1.1E-2	1.6E0	5.8E0	2.6E0	1.6E0	8.1E-1	3.0E-1	1.1E-1	4.4E-2
	1	1.7E-2	3.2E0	1.2E1	4.1E-1	2.4E-1	7.6E-2	2.3E-2	7.2E-3	2.4E-3
	10	7.0E-2	1.2E1	3.6E1	1.6E0	1.5E0	1.4E0	1.1E0	8.5E-1	4.5E-1
2000	0.01	2.2E-4	2.7E-2	1.2E-1	1.1E-1	8.5E-2	5.1E-2	2.2E-2	9.1E-3	4.0E-3
	0.1	2.8E-4	5.3E-2	2.5E-1	2.4E-1	2.1E-1	1.3E-1	5.9E-2	2.6E-2	1.2E-2
	1	5.7E-4	1.2E-1	5.7E-1	1.2E-2	10.0E-3	7.0E-3	4.1E-3	1.7E-3	6.4E-4
	10	2.2E-3	5.2E-1	2.3E0	3.5E-2	3.7E-2	3.9E-2	3.8E-2	3.5E-2	3.0E-2

Note: E refers to the power of 10, e.g., 1.5E4 =  $1.5 \times 10^4$ .

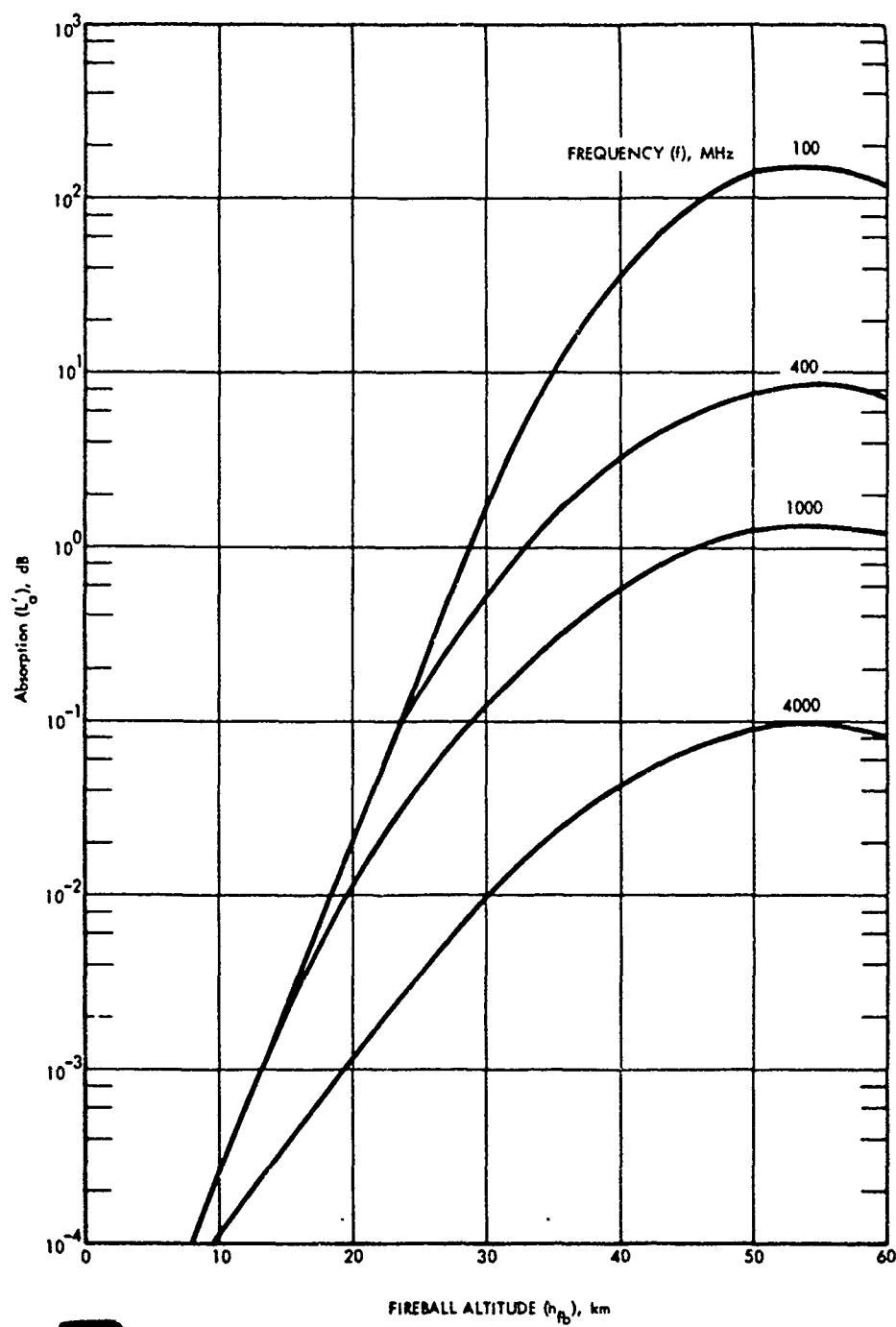


Figure 8-39. One-Way Absorption Through Debris Region Due to Beta-Particle Ionization

### Problem 8-5 Absorption Due to Prompt Radiation Outside the Fireball

Figures 8-40 and 8-41 are used to obtain the one-way absorption along a propagation path caused by prompt radiation in terms of the one-way vertical absorption (the absorption for a single vertical traversal of the atmosphere) at a time  $t$  after burst. The absorption for the vertical path may be converted to that for an oblique path by using the secant of the angle of incidence at the altitude of peak absorption (approximately 65 km, see Problem 8-10).

Using the detonation altitude and the ground range between the burst and the point where the propagation path intersects 65 km altitude, a reference yield  $W_r$  is obtained from Figure 8-40 (note that  $W_r$  differs for night and day). The location of the 65-km intersect point with respect to the propagation-path ground location can be determined from Figure 8-55 as described in Problem 8-10. If the actual weapon yield,  $W$ , is less than  $W_r$ , go to 2; otherwise go to 1.

1. Enter Figure 8-41 with time after burst in seconds and the radio frequency to obtain  $A_p'$ , the one-way vertical absorption (note that the absorption differs for night and day). Go to 2.

2. Compute  $t_r$ :

$$t_r = \frac{W_r}{W} \text{ sec},$$

where  $W_r$  and  $W$  are both in Mt or kt. If  $t > t_r$ , go to 4; otherwise go to 3.

3. Enter Figure 8-41 with time after burst equal to  $t_r$  and the frequency to obtain  $A_p'(t_r)$ . Compute  $A_p'$ :

$$A_p' = \frac{t_r A_p'(t_r)}{0.5t_r + 1.5t}.$$

Go to 5.

4. Enter Figure 8-41 with time after burst,  $t$ , and the frequency to obtain  $A_p'(t)$ . Compute  $A_p'$ :

$$A_p' = \frac{t A_p'(t)}{t + t_r}.$$

5. Compute  $A_p$ , the one-way path absorption along the oblique path:

$$A_p = A_p' \sec \theta,$$

where  $\sec \theta$  is the secant of the angle of incidence at 65 km determined from Figure 8-55.

#### Example 1

*Given:* A 1 Mt weapon detonated at an altitude of 300 km. The ground range between the burst and the propagation path is 800 km; the secant of the angle of incidence ( $\sec \theta$ ) at 65 km is 3 for the propagation path.

*Find:* The one-way path absorption due to prompt radiation for a 100 MHz signal 10 seconds after the burst during the daytime.

*Solution:*

a. From Figure 8-40,  $W_r = 100$  kt for a detonation altitude of 300 km and a ground range of 800 km.

b. Since  $W_r < W$ ,  $A_p'$  is determined to be 12 dB from Figure 8-41.

$$c. A_p = A_p' \sec \theta = (12)(3) = 36 \text{ dB}.$$

*Answer:* The one-way path absorption for a 100 MHz signal having a propagation path with an angle of incidence at 65 km whose secant is 3, resulting from prompt radiation from a 1 Mt weapon detonated at an altitude of 300 km, is 36 dB 10 seconds after burst at a ground range of 800 km from the burst point.

#### Example 2

*Given:* A 1 Mt weapon detonated at an

altitude of 200 km. The ground range between the burst and the propagation path is 1000 km; the secant of the angle of incidence ( $\sec \theta$ ) at 65 km is 3 for the propagation path.

*Find:* The one-way path absorption due to prompt radiation for a 100 MHz signal 10 seconds after the burst during the daytime.

*Solution:*

a. From Figure 8-40,  $W_r = 5$  Mt for a detonation altitude of 200 km and a ground range of 1000 km.

$$b. t_r = \frac{W_r}{W} = 5.$$

c.  $t > t_r$ ; therefore, from Figure 8-41  $A_p'(t) = 12$  dB, and

$$A_p' = \frac{t A_p'(t)}{t + t_r} = \frac{(10)(12)}{10 + 5} = 8 \text{ dB.}$$

d.  $A_p = A_p' \sec \theta = (8)(3) = 24 \text{ dB.}$

*Answer:* The one-way path absorption for a 100 MHz signal having a propagation path with an angle of incidence at 65 km whose secant is 3, resulting from prompt radiation from a 1 Mt weapon detonated at an altitude of 200 km, is 24 dB 10 seconds after burst at a ground range of 1000 km from the burst point.

*Reliability* [REDACTED] The procedures given for computing absorption due to prompt radiation outside the fireball are based on simplified weapon design, atmospheric chemistry, and geometry models. More detailed models are required for specific communications and radar system problems.

[REDACTED] *Related Material* [REDACTED] See paragraph 8-2 and Problem 8-10.

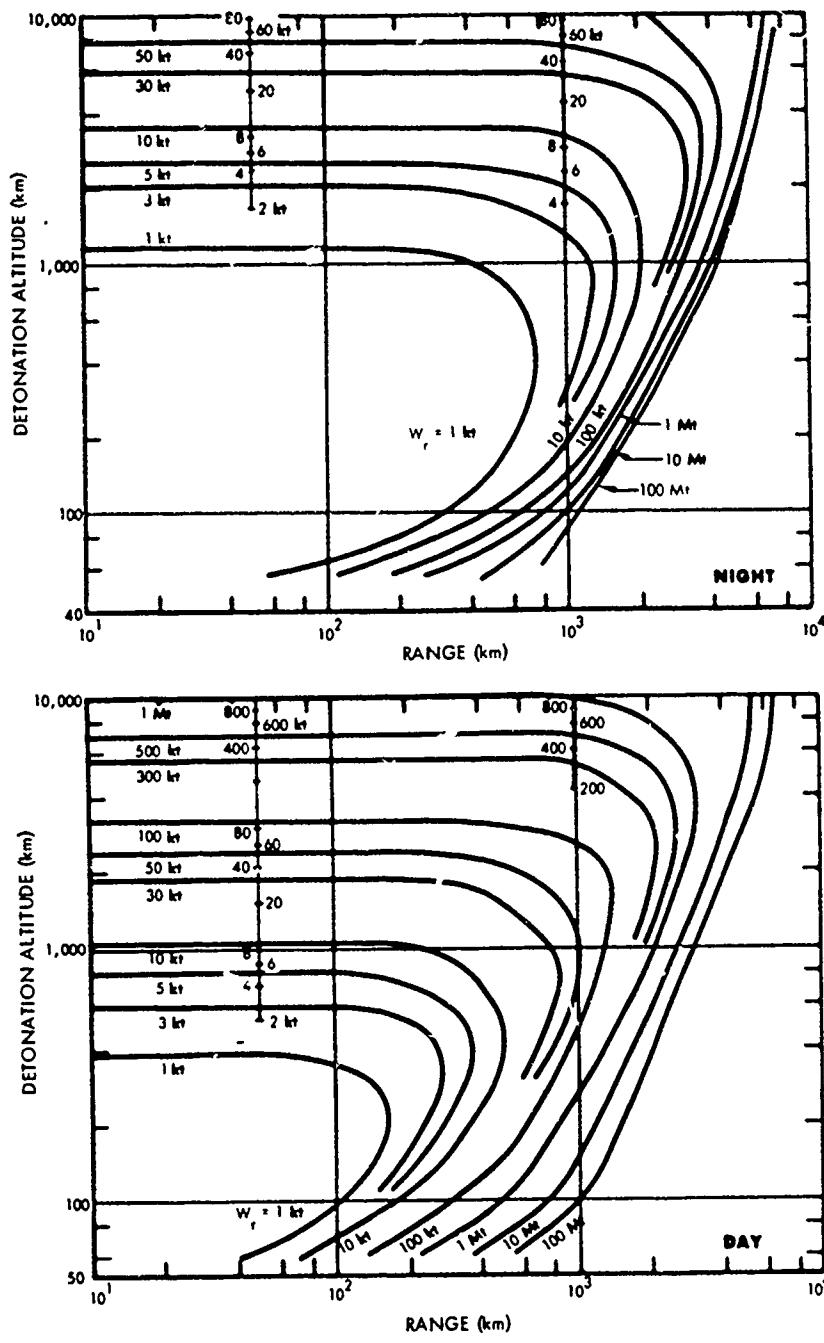


Figure 8-40. Reference Weapon Yield  $W_r$

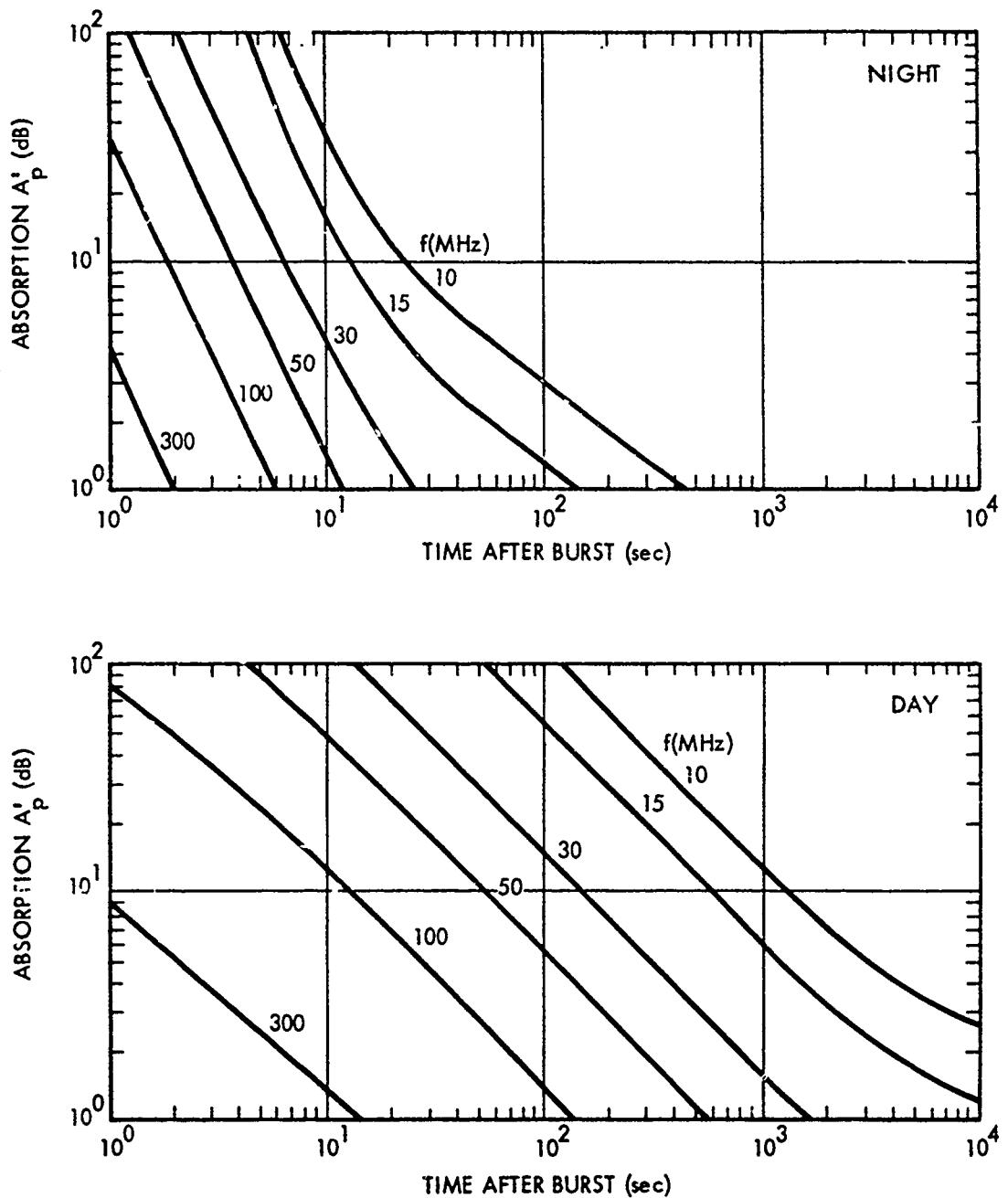


Figure 8-41. One-Way Vertical Absorption Due to Prompt Radiation

### Problem 8-6 Absorption Outside the Fireball Due to Delayed Gamma Rays

Figures 8-42 through 8-48 are used to estimate the absorption caused by gamma rays emitted by the radioactive decay of fission debris. When the propagation path is within 100 km of the debris region and the debris region is below 120 km, the absorption depends on the orientation of the propagation path with respect to the debris region. Data are provided for three cases: a vertical path, a path passing above the debris region, and a path passing below the debris region. The geometry is illustrated in Figure 8-42.

If the debris is at an altitude greater than 120 km or if the propagation path passes farther than 100 km from the debris region, absorption caused by gamma rays is given in terms of the gamma ray intensity parameter,  $I_\gamma$ . In determining  $I_\gamma$ , the debris region is modeled as a thin pancake region. Methods to determine the altitude and radius of the pancake debris region as a function of the burst parameters are described in Problems 8-1 through 8-3. If the altitude of detonation is below 85 km, the debris region is centered over the burst point (see Problem 8-1). For higher detonation altitudes, the center of the debris region is offset horizontally from the burst point toward the nearest magnetic pole after reaching maximum altitude (see Problem 8-2 and Figure 8-17). If the detonation altitude is greater than 120 km, up to three debris regions are defined (see Problem 8-3 and Figure 8-18).

Figures 8-42 through 8-45 are used to obtain the one-way path absorption for bursts below 120 km and ground ranges from the debris less than 100 km. Choose the figure with the angle  $\theta_d$  (see Figure 8-42) closest to the case of interest. Enter the figure with debris altitude,  $h_d$ , closest point of approach,  $X_d$  (see Figure 8-42), and time of day (day or night); obtain  $A'_\gamma$ , the one-way path absorption for a 1000

MHz signal 10 seconds after a 1 Mt fission yield detonation. Compute  $A_\gamma$ , the one-way path absorption:

$$A_\gamma = A'_\gamma W_F \frac{18}{(1+t)^{1.2}} \frac{10^6}{f^2}$$

where  $W_F$  is the fission yield in Mt,  $t$  is the time in sec, and  $f$  is the propagation frequency in MHz.

Figures 8-46 through 8-48 are used to obtain the one-way path absorption for bursts above 120 km or for cases where the ground range from the debris to the point where the propagation path intersects the altitude of 65 km is greater than 100 km. The following series of steps describe the procedure for obtaining the absorption.

1. Compute the quantity  $R'$ , as follows:

$$R' = \begin{cases} [D^2 + (h_d - 60)^2]^{1/2} & D > R_d/2 \\ \left[ \left(\frac{R_d}{2}\right)^2 + (h_d - 60)^2 \right]^{1/2} & D \leq R_d/2 \end{cases}$$

where  $D$  is the ground range between the debris center and the point where the propagation path intersects 65 km altitude (see Figures 8-42 and 8-55 and Problem 8-10), and  $h_d$  and  $R_d$  are the debris altitude and radius, respectively (see Problems 8-1, 8-2, and 8-3).

2. Determine the debris-region fission yield  $W'_F$ :

$$W'_F = W_F \quad h_o \leq 120 \text{ km}$$

$$W'_F = FF W_F \quad h_o > 120 \text{ km}$$

where  $FF$  is the fraction of the total weapon fission yield in the debris region (see Problem 8-3).

3. Enter Figure 8-46 with debris-region fission yield ( $W'_F$ ), time after burst  $t$ , and  $R'$  to obtain  $I'_\gamma$ .

4. Enter Figure 8-47 with debris altitude  $h_d$ , debris radius  $R_d$ , i.e. the ground range where the propagation path intersects 65 km altitude  $D$ , to obtain  $C_\gamma$ . Compute  $I_\gamma$ :

$$I_\gamma = C_\gamma I'_\gamma.$$

If there is more than one debris region (if the detonation is above 120 km or if there are multiple bursts), the radiation intensity parametric  $I_\gamma$  should be found for each debris region and the sum of the radiation intensity parameters used to obtain the absorption.

5. Enter Figure 8-48 with  $I_\gamma$ , time of day (day or night), and frequency to obtain  $A'_\gamma$ , the one-way vertical absorption. Compute  $A_\gamma$ , the one-way path absorption:

$$A_\gamma = A'_\gamma \sec \theta$$

where  $\sec \theta$  is the secant of the angle of incidence at 65 km (see Problem 8-10).

#### *Example 1*

*Given:* A 1 Mt weapon, 50% fission ( $W_F = 0.5$  Mt), detonated at an altitude of 30 km during the daytime.

*Find:* The one-way absorption resulting from gamma ray ionization for a 1000 MHz signal 2 min after burst if the ground range between debris center and the propagation path is less than 100 km, the closest point of approach of the propagation path to the debris center,  $X_d$ , is 20 km, and  $\theta_d$  is  $60^\circ$  (see Figure 8-42).

*Solution:* By the methods described in Problem 8-1, the debris altitude is determined to be:

$$h_d = 49 \text{ km.}$$

From Figure 8-43,  $A'_\gamma = 14$  dB for  $h_d = 49$  km and  $X_d = 20$  km. Therefore,

$$A_\gamma = A'_\gamma W_F \frac{18}{(1+t)^{1.2}} \frac{10^6}{f^2},$$

$$A_\gamma = (14)(0.5) \frac{18}{(121)^{1.2}} \frac{10^6}{10^6} = 0.4 \text{ dB}$$

*Answer:* The one-way path absorption for a 1000 MHz signal propagating on a path as described above 2 min after a daytime 1 Mt burst ( $W_F = 0.5$  Mt) is 0.4 dB.

#### *Example 2*

*Given:* A 1 Mt weapon, 50% fission, detonated at an altitude of 30 km during the nighttime.

*Find:* The one-way path absorption resulting from gamma ray ionization for a 100 MHz signal 2 min after burst if the ground range between the debris center and the point where the propagation path intersects 65 km is 200 km and  $\sec \theta = 3$ .

#### *Solution:*

a. By the methods described in Problem 8-1, the debris height,  $h_d$ , and radius,  $R_d$ , are determined to be:

$$h_d = 49 \text{ km,}$$

$$R_d = 15 \text{ km.}$$

b. Since  $D > R_d/2$ ,

$$R' = [D^2 + (h_d - 60)^2]^{1/2}$$

$$R' = [(200)^2 + (49 - 60)^2]^{1/2} \approx 200 \text{ km}$$

c. From Figure 8-46,  $I'_\gamma = 0.15 \text{ watts m}^{-2}$ , for  $W_F = 0.5$  Mt,  $(1+t) = 121$  sec, and  $R' = 200$  km.

d. From Figure 8-47,  $C_\gamma = 0.8$  for  $(D - R_d) = 185$  km and  $h_d = 49$  km. Therefore,

$$I_\gamma = C'_\gamma I'_\gamma = (0.8)(0.15) = 0.12 \text{ watts m}^{-2}$$

e. From Figure 8-48,  $A'_\gamma = 1.0$  dB for  $I_\gamma = 0.12$  watts  $\text{m}^{-2}$  and  $f = 100$  MHz during the night. Therefore,

$$A_\gamma = A'_\gamma \sec \theta = 3.0 \text{ dB.}$$

**Answer:** The one-way path absorption for a 100 MHz signal propagating on a path as described above 2 min after a nighttime 1 Mt burst ( $W_F = 0.5$  Mt) is 3.0 dB.

### Example 3

**Given:** A 1 Mt weapon, 50% fission, detonated at an altitude of 300 km during the day at a location where the magnetic dip angle  $\theta$  is  $60^\circ$ :

**Find:** The one-way path absorption resulting from gamma ray ionization for a 30 MHz signal 60 min after burst if the ground range between the point where the propagation path intersects 65 km is 1000 km due magnetic north of the burst point and  $\sec \theta = 3$ .

**Solution:**

a. By the methods described in Problem 8-3, the height,  $h_d$ , radius,  $R_d$ , offset,  $\Delta_d$ , and fraction of the debris,  $FF$  for the three debris regions (see Figure 8-18), are found to be:

Debris Region	$h_d$ (km)	$R_d$ (km)	$\Delta_d$ (km)	FF
1	390	170	75	0.25
2	550	500	125	0.2
3	390	170	75	0.35

Debris region 1 is centered 75 km magnetic north of the burst point. The ground range,  $D$ , between the debris center and the point where the propagation path intersects 65 km is  $1000 - 75 = 925$  km. The ground range between the center of debris region 2 and the propagation path is 375 km. Debris region 3 is offset 75 km south of the conjugate of the burst point and is too far from the propagation path to produce gamma ray ionization.

b. The quantity  $R'$  for debris region 1 is:

$$R'_1 = [D^2 + (h_d - 60)^2]^{1/2} = [(925)^2 + (330)^2]^{1/2} = 980 \text{ km.}$$

c. The debris region 1 fission yield is:

$$W'_{F1} = FF_1 W_F = 0.125 \text{ Mt.}$$

d. From Figure 8-46,  $I'_{\gamma 1}$  is  $2 \times 10^{-5}$  watts  $\text{m}^{-2}$  for  $W'_{F1} = 0.125$  Mt,  $t = 3600$  sec, and  $R'_1 = 980$  km.

e. From Figure 8-47,  $C_{\gamma 1}$  is 1 for  $(D - R_d) = 775$  km and  $h_d = 390$  km.

$$f. I_{\gamma 1} = C_{\gamma 1} I'_{\gamma 1} = 2 \times 10^{-5} \text{ watts m}^{-2}.$$

g. The quantity  $R'$  for debris region 2 is:

$$R'_2 = [(875)^2 + (490)^2]^{1/2} = 1000 \text{ km}$$

h. The debris region 2 fission yield is:

$$W'_{F2} = FF_2 W_F = 0.1 \text{ Mt}$$

i. From Figure 8-46,  $I'_{\gamma 2}$  is  $1.5 \times 10^{-5}$  watts  $\text{m}^{-2}$  for  $W'_{F2} = 0.1$  Mt,  $t = 3600$  sec, and  $R'_2 = 1000$  km.

j. From Figure 8-47,  $C_{\gamma 2}$  is 1 for  $(D - R_d) = 375$  km and  $h_d = 550$  km.

$$k. I_{\gamma 2} = C_{\gamma 2} I'_{\gamma 2} = 1.5 \times 10^{-5} \text{ watts m}^{-2}.$$

$$l. I_\gamma = I_{\gamma 1} + I_{\gamma 2} = 3.5 \times 10^{-5} \text{ watts m}^{-2}.$$

m. From Figure 8-48,  $A'_\gamma = 1$  dB for  $I_\gamma = 3.5 \times 10^{-5}$  watts  $\text{m}^{-2}$  and  $f = 30$  MHz.

$$n. A_\gamma = A'_\gamma \sec \theta = 3 \text{ dB.}$$

**Answer:** The one-way path absorption for a 30 MHz signal propagating on a path as described above 60 min after a daytime burst ( $W_F = 0.5$  Mt) is 3 dB. If the propagation path had been located near the conjugate of the burst point, gamma rays from debris regions 1 and 2 would not reach the path, and only debris region 3 would have been considered.

[REDACTED] Reliability [REDACTED]. The procedures given for computing absorption due to gamma ray ionization are based on simplified-debris, atmospheric-chemistry, and geometry models. More detailed models are required for most radar and commun-

cation system problems.

[REDACTED] Related Material [REDACTED]. See paragraphs 8-3, 8-8, 8-13, 8-14, and 8-15, and Problems 8-1, 8-2, and 8-3.

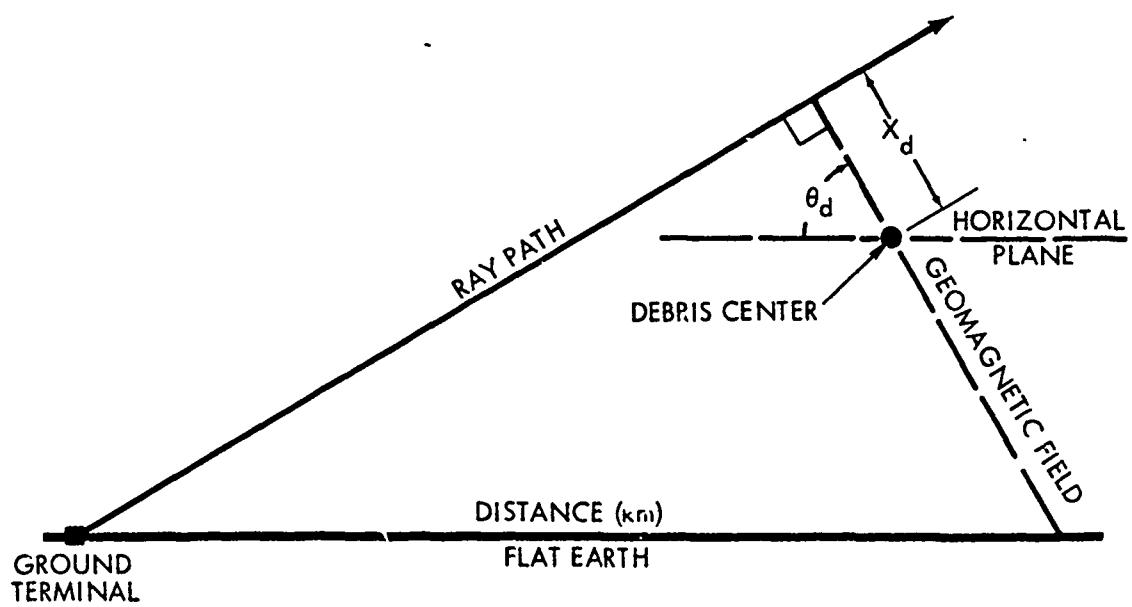


Figure 8-42. Geometry for Gamma Ray Absorption

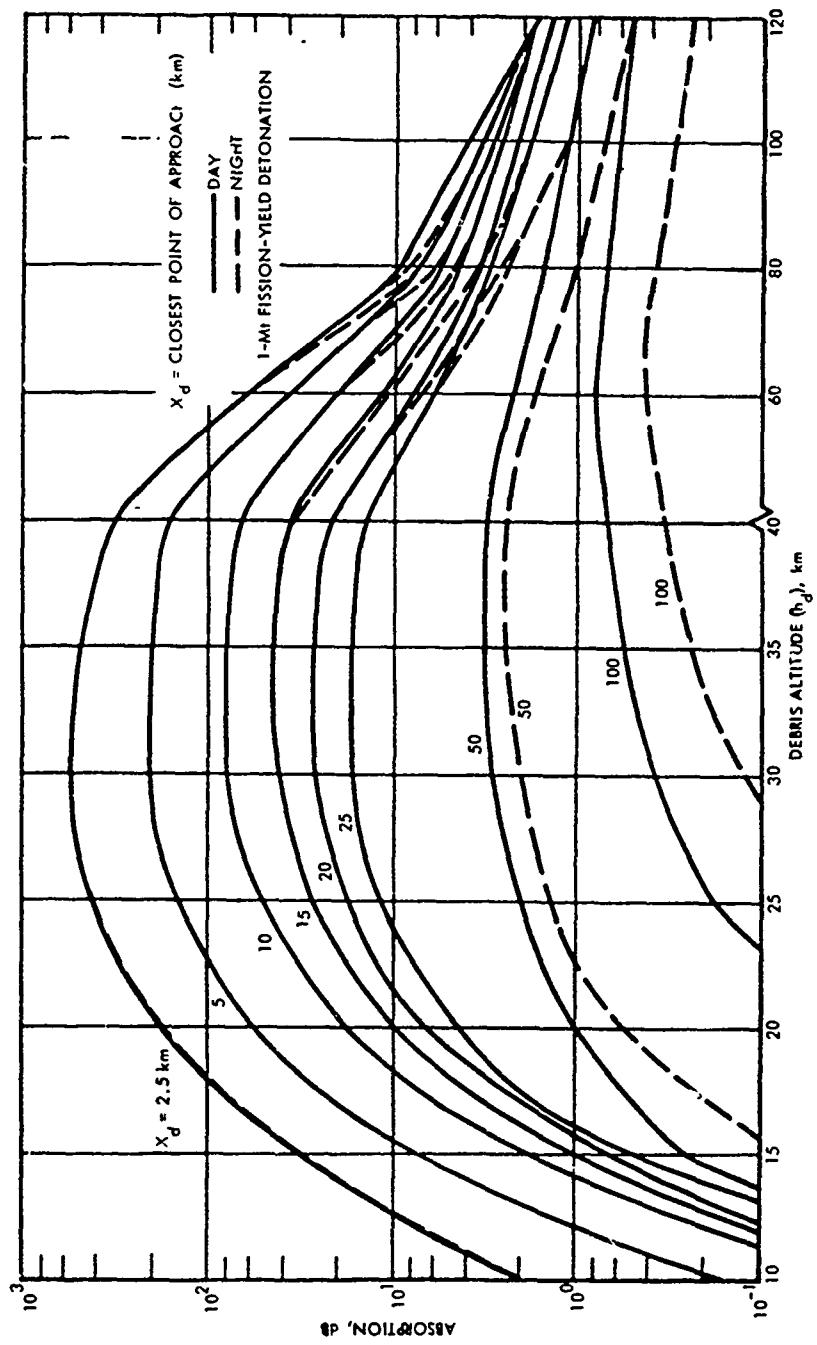


Figure 8-43. One-Way Absorption Due to Gamma Rays,  $f = 1000 \text{ MHz}$ ,  $\theta_d = +60^\circ$

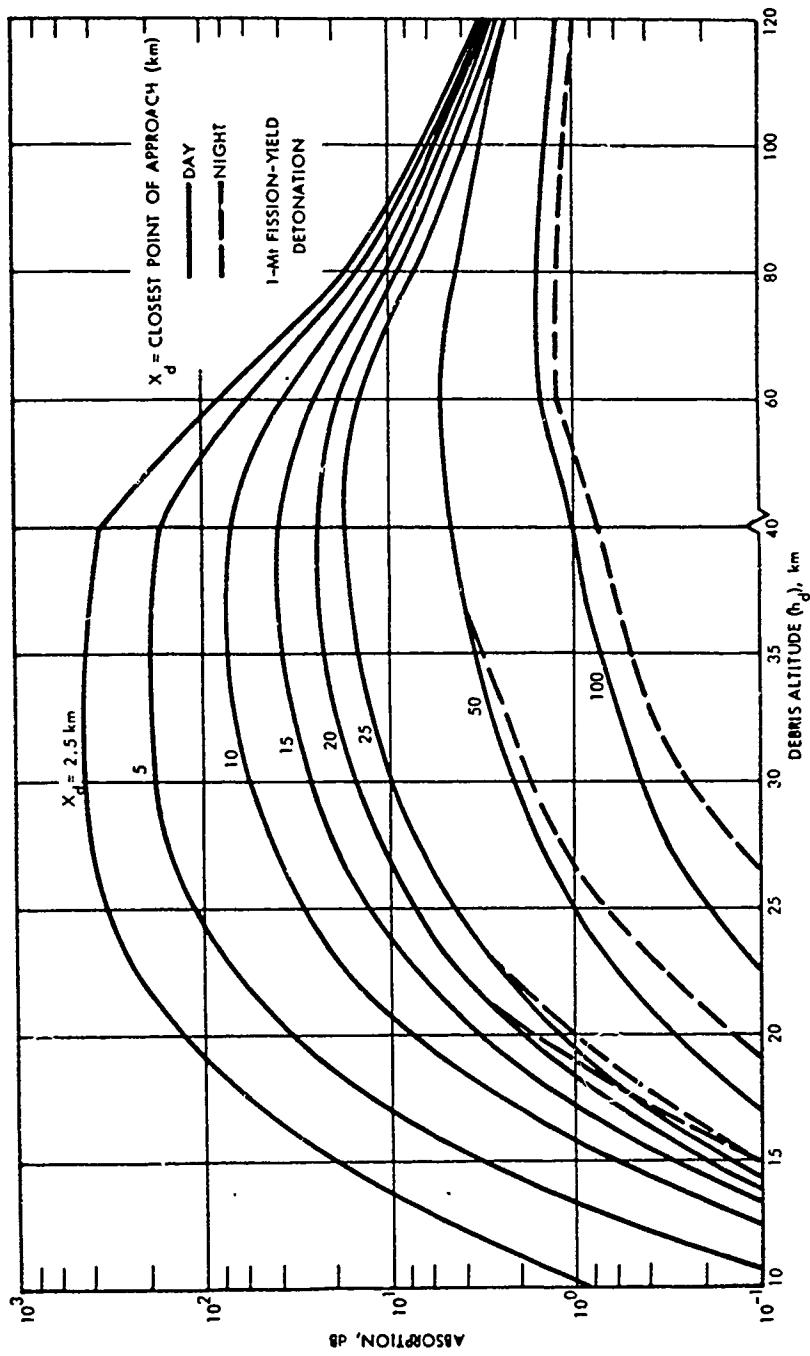


Figure 8-44. [REDACTED] One-Way Absorption Due to Gamma Rays,  $f = 1000$  MHz,  $\theta_d = 0$  Degrees [REDACTED]

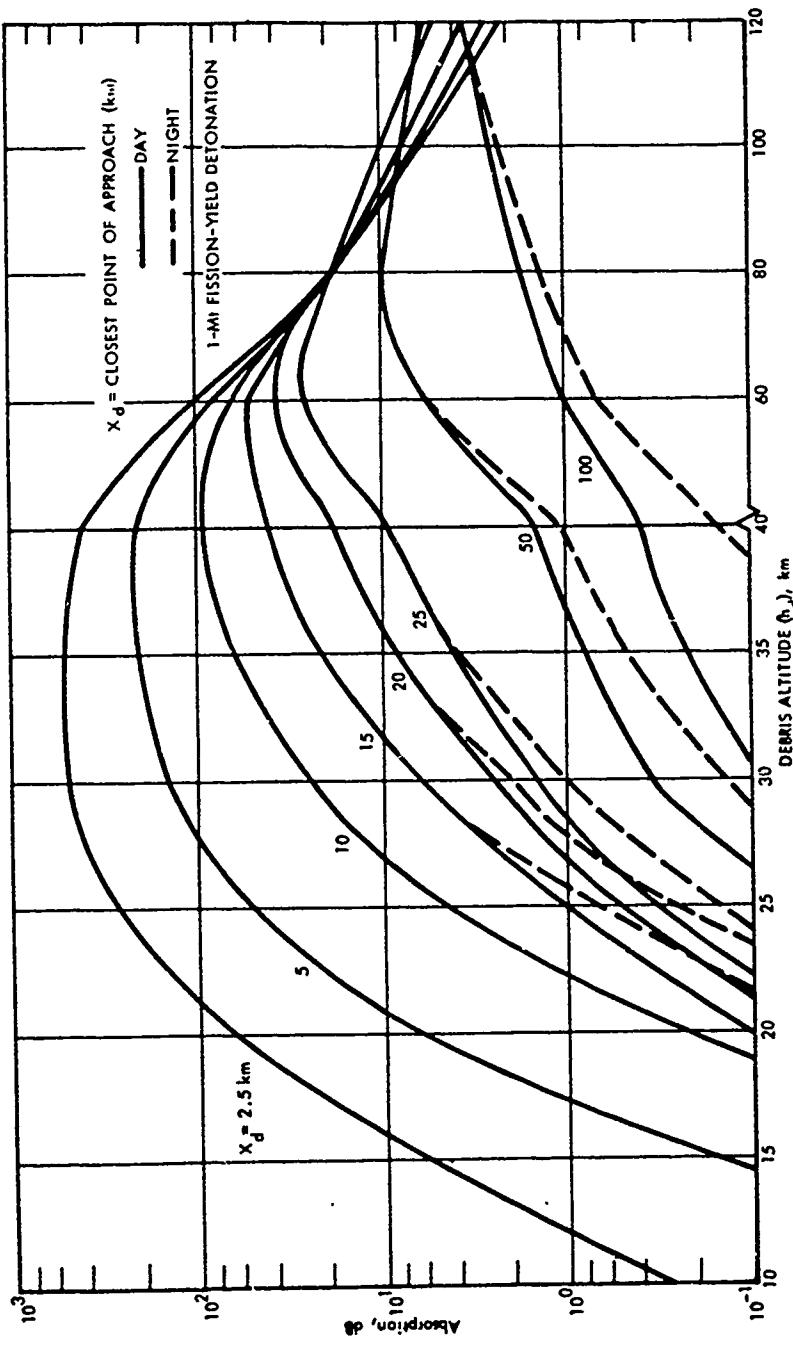
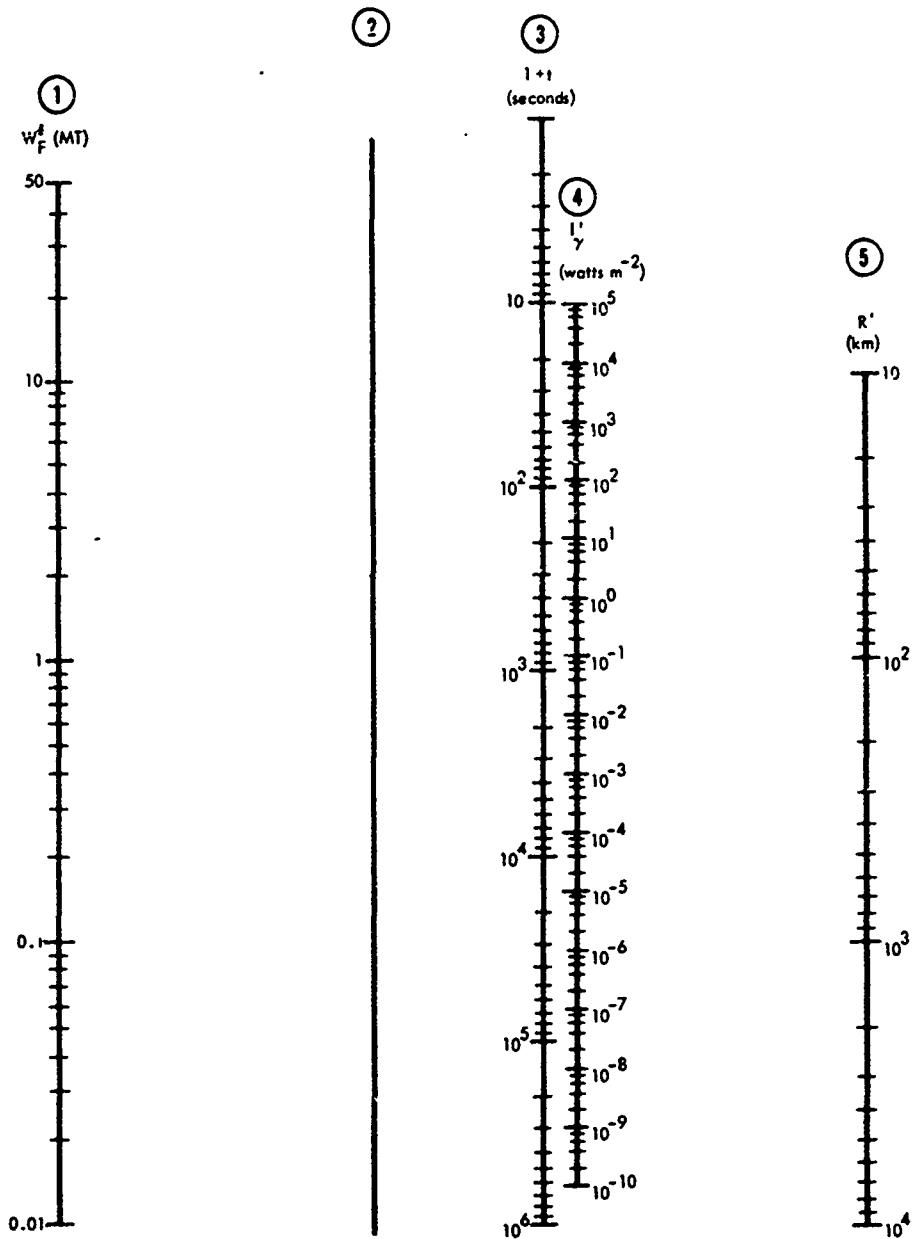


Figure 8-45. One-Way Absorption Due to Gamma Rays,  $f = 1000$  MHz,  $\theta_d = -60$  Degrees



INSTRUCTIONS: To find  $I_\gamma'$ , connect a straight line from fission yield (Scale 1) to time after detonation on Scale 3 (note this is a  $1+t$  scale). Mark the intersection on Scale 2. Connect a straight line from the point determined on Scale 2 to the appropriate distance,  $R'$ , on Scale 5. The intersection with Scale 4 is  $I_\gamma'$ .

Figure 8-46. Gamma Radiation Intensity Nomogram

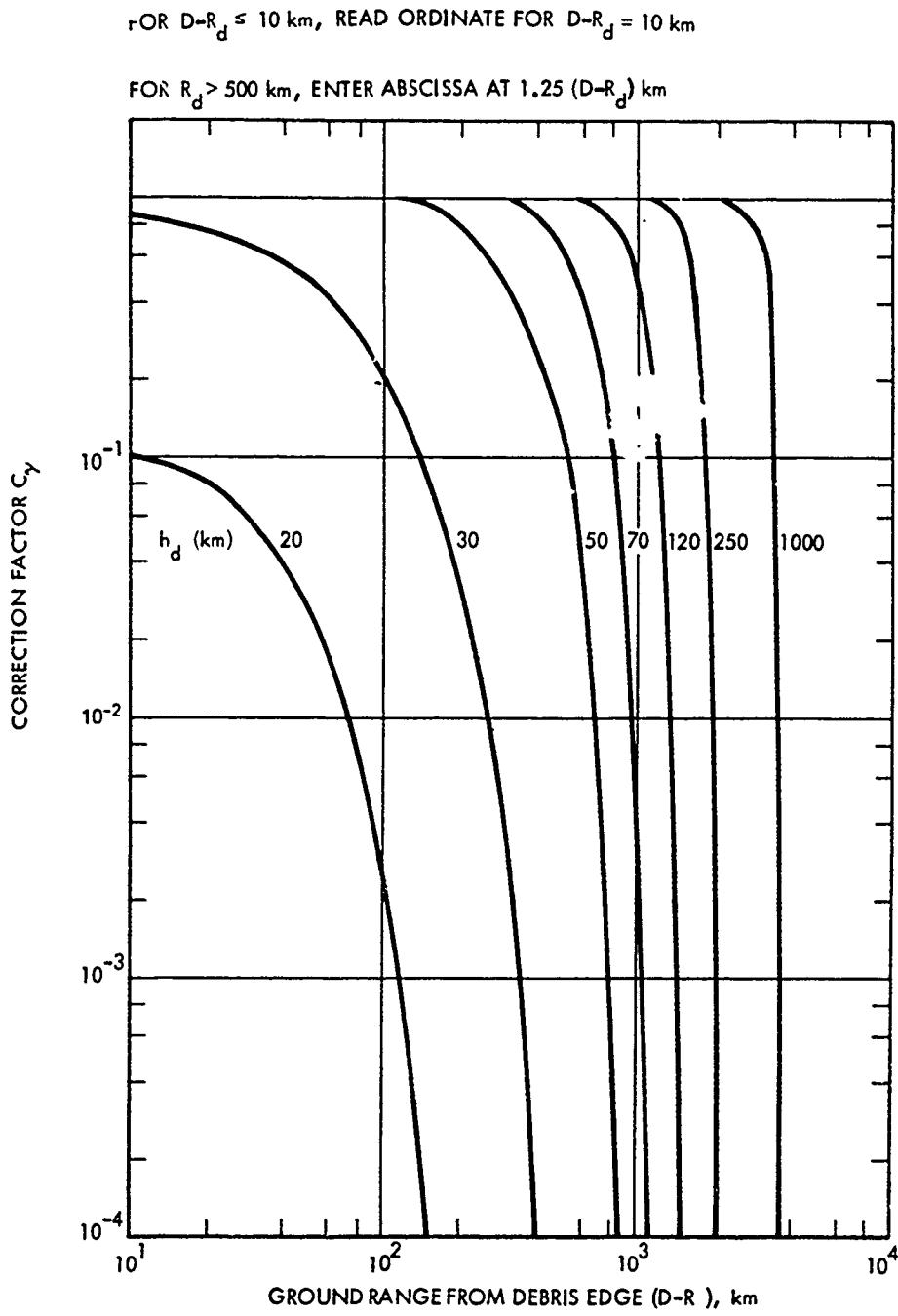


Figure 8-47. [REDACTED] Correction Factor for Gamma Ray Flux [REDACTED]

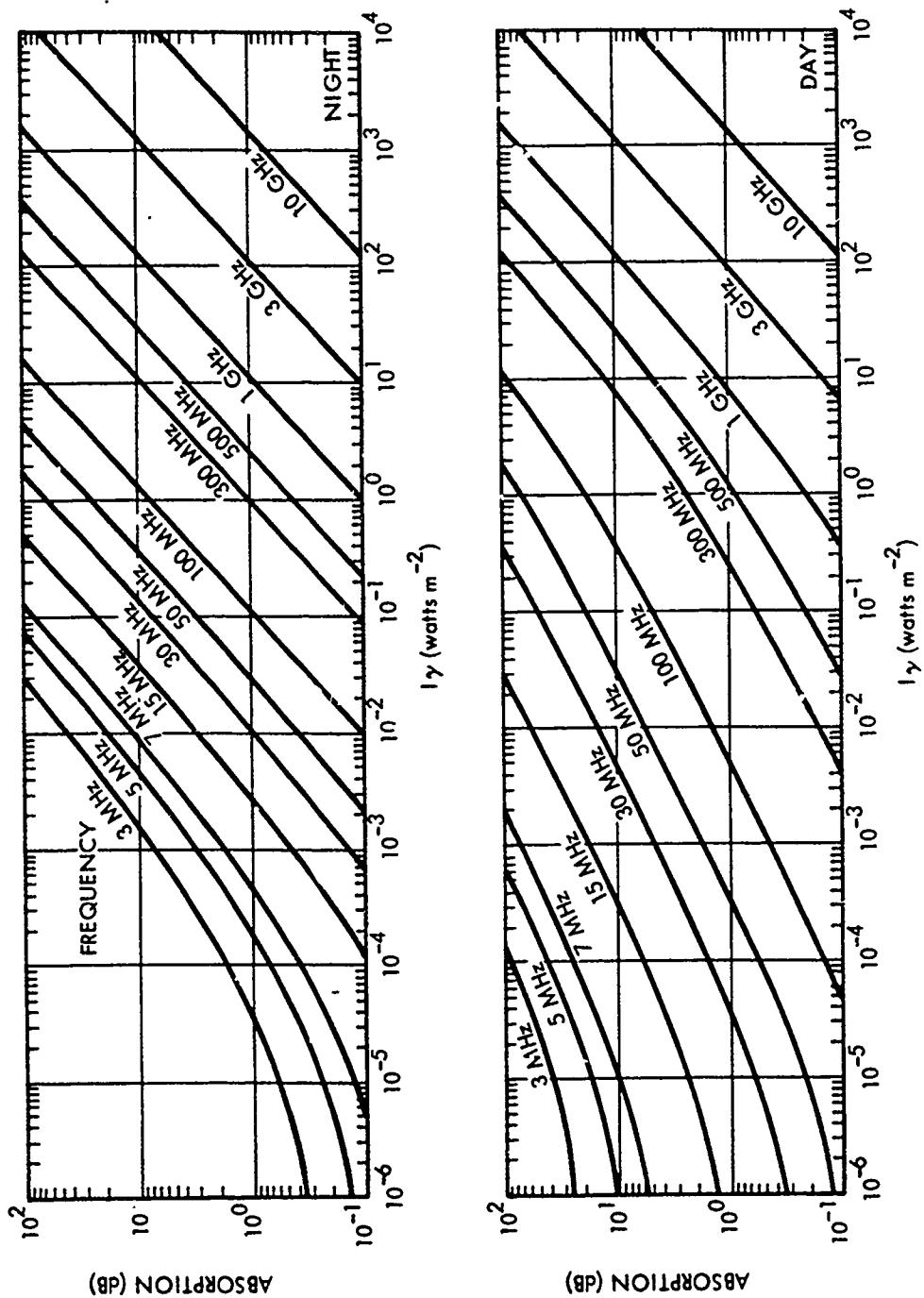


Figure 8-48. One-Way Vertical Absorption Due to Gamma Rays

### Problem 8-7 Calculation of Absorption Outside the Fireball Due to Beta Particles

Figures 8-49 through 8-51 are used to estimate the absorption outside the fireball region caused by beta particle ionization when the fission debris is above 60 km. If the debris is below 60 km, the absorption caused by beta particle ionization can be computed by the methods described in Problem 8-4.

When the fission debris is above 60 km, the location of the beta particle absorption region with respect to the debris region is determined by the geomagnetic field (see paragraph 8-4). Most of the absorption occurs between the altitudes of 60 and 80 km. The predictions of absorption apply to beta particle radiation from fission debris that is uniformly distributed in a thin pancake-shaped region.

Obtain the debris altitude,  $h_d$ , and debris radius,  $R_d$ , by the methods described in Problems 8-1, 8-2, or 8-3. If the detonation altitude,  $h_o$ , is greater than 85 km and the time after burst is greater than 10 minutes, determine the maximum debris altitude,  $h_m$  (km). Compute  $h$ :

$$h = h_d \quad \begin{cases} h_o < 85 \text{ or if} \\ h_o \geq 85 \text{ and } t < 10 \text{ minutes.} \end{cases}$$

$$h = h_m \quad h_o \geq 85 \text{ and } t > 10 \text{ minutes.}$$

Enter Figure 8-49 with  $h$  and  $\varphi$ , the magnetic dip angle at the burst point to obtain  $\Delta_\beta$ , the offset of the beta particle absorption region. If the magnetic dip angle at the burst point is not known, it can be obtained from Figure 8-54 as described in Problem 8-9.

There are two beta particle absorption regions for each debris region; one is in the burst region and is offset a distance  $\Delta_\beta$  from ground zero toward the nearest magnetic pole (see Figure 8-49), and the other is in the conjugate

region and is offset from the conjugate of ground zero toward the nearest magnetic pole. Location of the conjugate of ground zero can be estimated from Figure 8-53 as described in Problem 8-8. The horizontal extent of the beta particle absorption region is approximately the same as that of the debris region (this neglects convergence of the magnetic field).

If the propagation path passes through a beta particle absorption region, the one-way absorption can be found by the following procedure:

1. Determine the debris region fission yield,  $W'_F$ :

$$W'_F = W_F \quad h_o \leq 120 \text{ km}$$

$$W'_F = FF \cdot W_F \quad h_o > 120 \text{ km}$$

where  $FF$  is the fraction of the total weapon fission yield in the debris region (see Problem 8-3).

2. Enter Figure 8-50 with debris region fission yield,  $W'_F$ , time after burst,  $t$ , and debris radius,  $R_d$ , to obtain  $N_\beta$ . If the propagation path passes through more than one beta particle absorption region, compute the value of  $N_\beta$  for each region and use the sum to compute the one-way vertical absorption.

3. Enter Figure 8-51 with  $N_\beta$ , the frequency,  $f$ , and the time of day (day or night) to obtain  $A'_\beta$ , the one-way vertical absorption. Compute  $A_\beta$ , the one-way absorption:

$$A_\beta = A'_\beta \sec \theta,$$

where  $\sec \theta$  is the secant of the angle of incidence of the propagation path at 65 km which may be determined by the methods described in Problem 8-10.

**Example 1**

*Given:* A 1 Mt weapon, 50% fission, detonated at an altitude of 80 km at a location where the magnetic dip angle is 60° during daytime.

*Find:* The one-way absorption resulting from beta particle ionization for a 400 MHz signal 5 min after burst if  $\sec \theta = 3$ .

*Solution:*

a. By the methods described in Problem 8-1, the debris height and radius are determined to be:

$$h_d = 305 \text{ km},$$

$$R_d = 200 \text{ km}.$$

b. Since  $h_o < 85 \text{ km}$ ,

$$h = h_d = 305 \text{ km}.$$

c. From Figure 8-49,  $\Delta_\beta = 150 \text{ km}$  for  $h = 305 \text{ km}$ , and  $\theta = 60^\circ$ .

d. Since  $h_o < 120 \text{ km}$ ,

$$W'_F = W_F = 0.5 \text{ Mt}.$$

e. From Figure 8-50,  $N_\beta = 4 \times 10^7 \text{ betas cm}^{-2} \text{ sec}^{-1}$  for  $W'_F = 0.5 \text{ Mt}$ ,  $t = 300 \text{ sec}$ , and  $R_d = 200 \text{ km}$ .

f. From Figure 8-51,  $A_\beta = 2 \text{ dB}$ ; therefore,

$$A_\beta = A_\beta \sec \theta = 6 \text{ dB}.$$

*Answer:* There are two absorption regions caused by beta particle ionization. One is in the burst locale and is centered 150 km towards the nearest magnetic pole. The other is on the opposite side of the magnetic equator and is centered 150 km towards the nearest magnetic pole from the conjugate of the burst point. The horizontal radius of each absorption region is 200 km. The one-way path absorption for a 400 MHz signal passing through either absorption region is 6 dB.

**Example 2**

*Given:* A 1 Mt weapon, 50% fission, detonated at an altitude of 300 km at a location

where the magnetic dip angle is 60° during daytime.

*Find:* The one-way absorption resulting from beta particle ionization for a 400 MHz signal 60 min after burst if the ground terminal is at burst ground zero, the propagation path is at an elevation of 15° along a zero degree magnetic azimuth, and  $\sec \theta = 3.4$ .

*Solution:*

a. By the methods described in Problem 8-3, the height,  $h_d$ , radius,  $R_d$ , maximum altitude of rise, and fraction of the debris,  $FF$ , for the three debris regions (see Figure 8-18) are found to be:

Debris Region	$h_d$ (km)	$R_d$ (km)	$h_m$ (km)	$FF$
1	390	170	550	0.25
2	550	500	800	0.2
3	390	170	550	0.35

b. Since  $h_o > 85 \text{ km}$  and  $t > 10 \text{ min}$ :

$$h_1 = h_{m1} = 550 \text{ km},$$

$$h_2 = h_{m2} = 800 \text{ km},$$

$$h_3 = h_{m3} = 550 \text{ km}.$$

c. From Figure 8-49, the beta particle absorption region offsets are:

$$\Delta_{\beta 1} = 300 \text{ km},$$

$$\Delta_{\beta 2} = 450 \text{ km},$$

$$\Delta_{\beta 3} = 300 \text{ km}.$$

d. Since  $W_F = 0.5 \text{ Mt}$ , the fission yields contained in the debris regions are:

$$W'_{F1} = 0.125 \text{ Mt},$$

$$W'_{F2} = 0.1 \text{ Mt},$$

$$W'_{F3} = 0.175 \text{ Mt}.$$

e. Entering Figure 8-50 with the debris radii from "a," the fission yields from "d," and a time  $t = 3600$  sec, the following values of  $N_\beta$  are obtained:

$$N_{\beta 1} = 10^6 \text{ betas cm}^{-2} \text{ sec}^{-1},$$

$$N_{\beta 2} = 8 \times 10^4 \text{ betas cm}^{-2} \text{ sec}^{-1},$$

$$N_{\beta 3} = 1.75 \times 10^6 \text{ betas cm}^{-2} \text{ sec}^{-1},$$

f. A sketch of the location of the absorption regions in the burst locale caused by beta particle ionization is shown in Figure 8-52. The propagation path chosen for this example traverses the absorption regions caused by all three debris regions. Thus, the values of  $N_\beta$  for each debris region are added together before finding the absorption.

$$\begin{aligned} N_\beta &= N_{\beta 1} + N_{\beta 2} + N_{\beta 3} \\ &= 2.8 \times 10^6 \text{ betas cm}^{-2} \text{ sec}^{-1} \end{aligned}$$

g. From Figure 8-51, the one-way vertical absorption for a 40 MHz signal is

$$A'_\beta = 40 \text{ dB}$$

and

$$A_\beta = A'_\beta \sec \theta = 136 \text{ dB.}$$

*Answer:* The one-way path absorption for a 40 MHz signal propagating on the path as described above 60 min after a 1 Mt ( $W_F = 0.5$  Mt) daytime burst at 300 km is the sum of the absorptions caused by all three debris regions and is 136 dB.

*Reliability:* The procedures given for computing absorption due to beta particle ionization are based on simplified debris, atmospheric chemistry, and geometry models. More detailed models are required for most radar and communication system problems.

*Related Material:* See paragraphs 8-4, 8-5, 8-8, 8-13, 8-14, and 8-15, and Problems 8-1, 8-2, and 8-3.

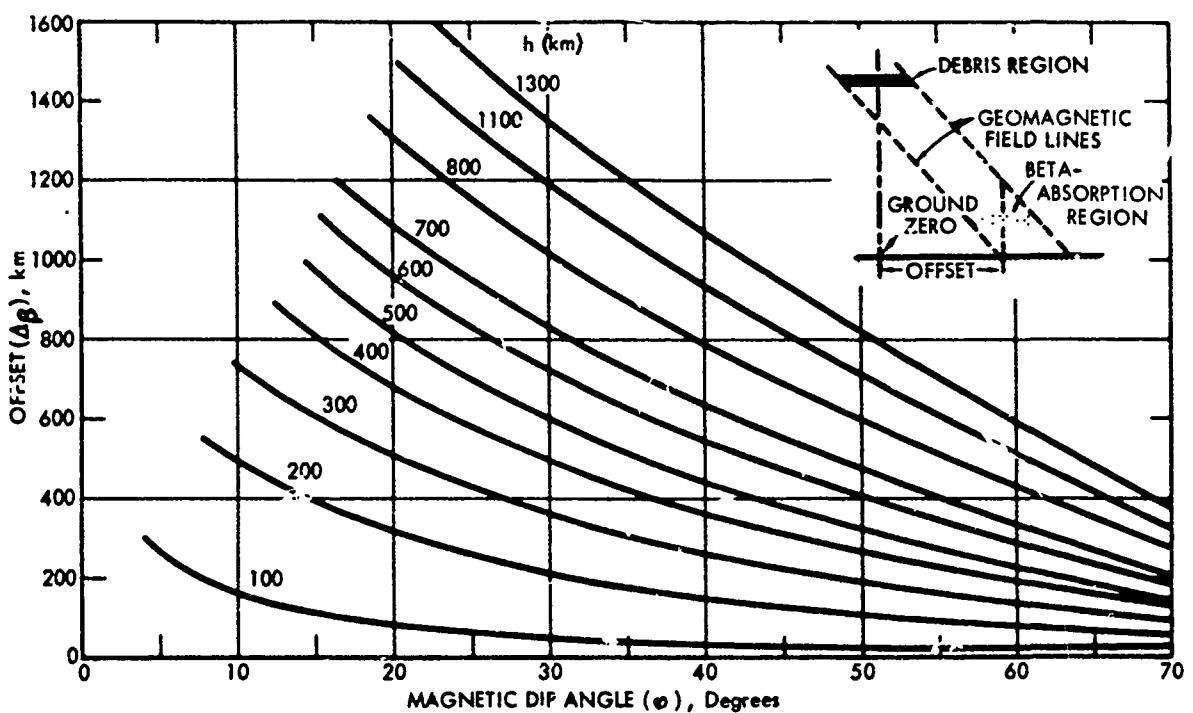
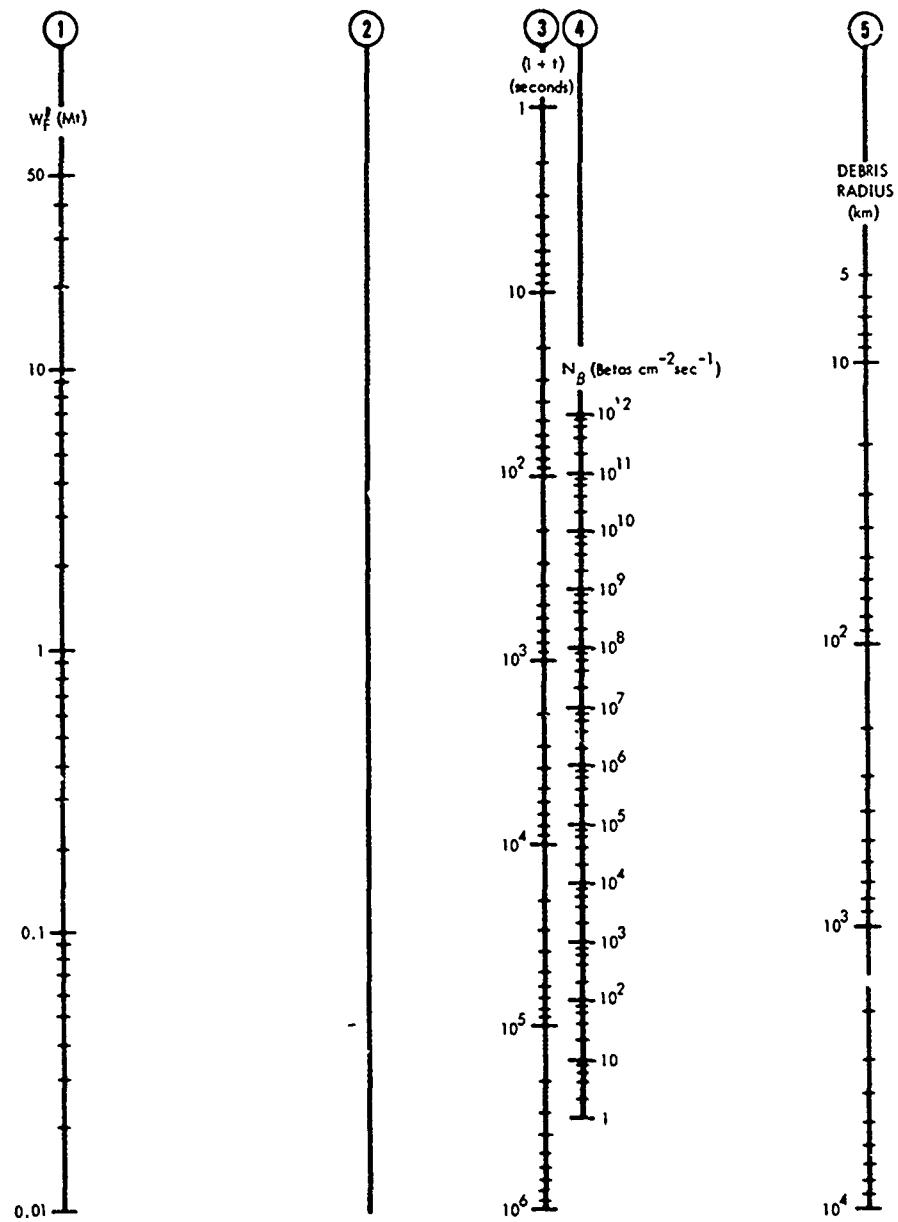


Figure 8-49. Offset of Beta-Absorption Region



INSTRUCTIONS: To find  $N_B$  connect a straight line from fission yield (Scale 1) to time after detonation (Scale 3 - this is a  $t + t$  scale). Mark the point of intersection of this line with Scale 2. Then draw a straight line from this point to the appropriate debris radius on Scale 5. The intersection of the latter line with Scale 4 is  $N_B$ .

Figure 8-50. Beta Radiation Intensity Nomogram

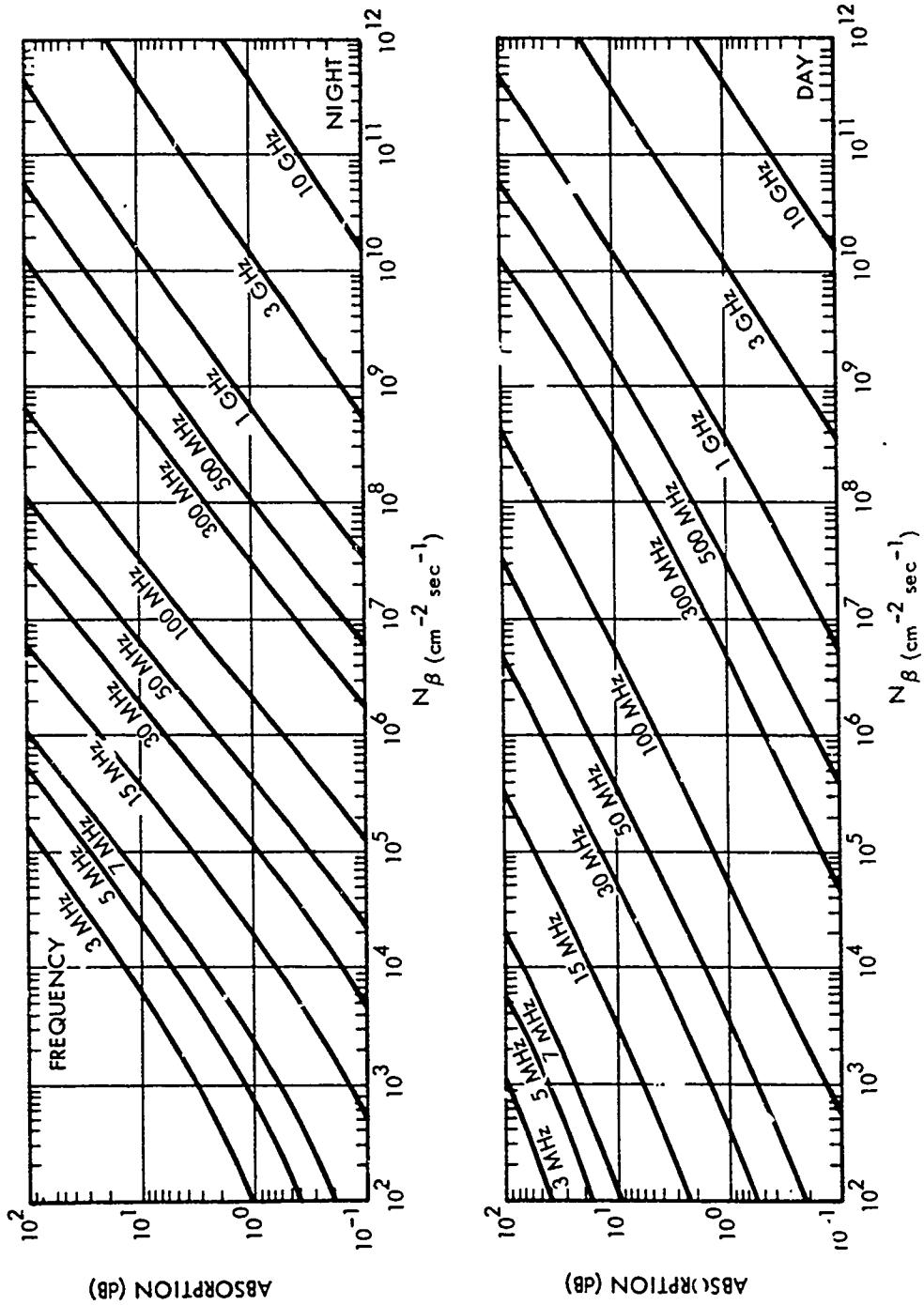


Figure 8-51. One-Way Vertical Absorption Due to Beta Particles, Debris Altitude Above 60 km

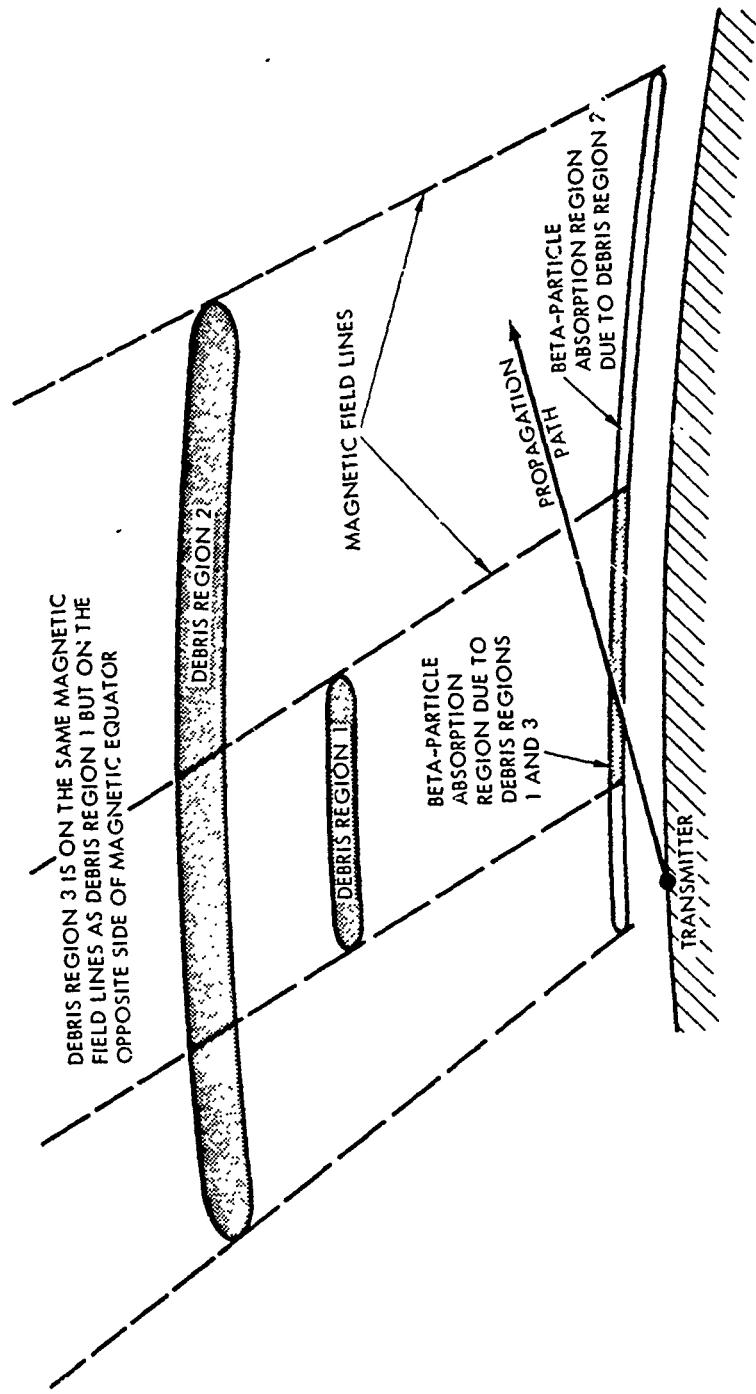


Figure 8-52. Sketch of Absorption-Region Geometry for Example 2

### Problem 8-8 Magnetic Conjugate Map

Figure 8-53 presents the location of geomagnetic conjugate points on the earth's surface. Using the geographic coordinates of a given point, enter Figure 8-53 on the straight-line rectangular grid, and read the geographic coordinates of the magnetic conjugate point on the heavy curved grid.

In reading Figure 8-53, note that the east-west curved dashed lines indicate conjugate latitude, plus for degrees north latitude and minus for degrees south latitude. Similarly, the north-south curved solid lines indicate conjugate longitude, plus for degrees east longitude and minus for degrees west longitude:

*Example*

Given: Geographic coordinates  $45^{\circ}\text{N}$ ,  $77^{\circ}\text{W}$

(point near Ottawa, Canada).

*Find:* The coordinate of the conjugate point.

*Solution:* The given coordinates occur at the intersection of the  $-71^{\circ}$  and  $-93^{\circ}$  heavy grid lines.

*Answer:* The approximate geographic coordinates of the conjugate point are  $71^{\circ}\text{S}$  and  $93^{\circ}\text{W}$ .

*Reliability* In addition to uncertainties in the geomagnetic field, distortions of the geomagnetic field caused by the burst may persist for tens of seconds. Thus, the locations of conjugate debris and beta particle ionization regions may be significantly different than predicted by Figure 8-53.

*Related Material* See paragraph 8-4.

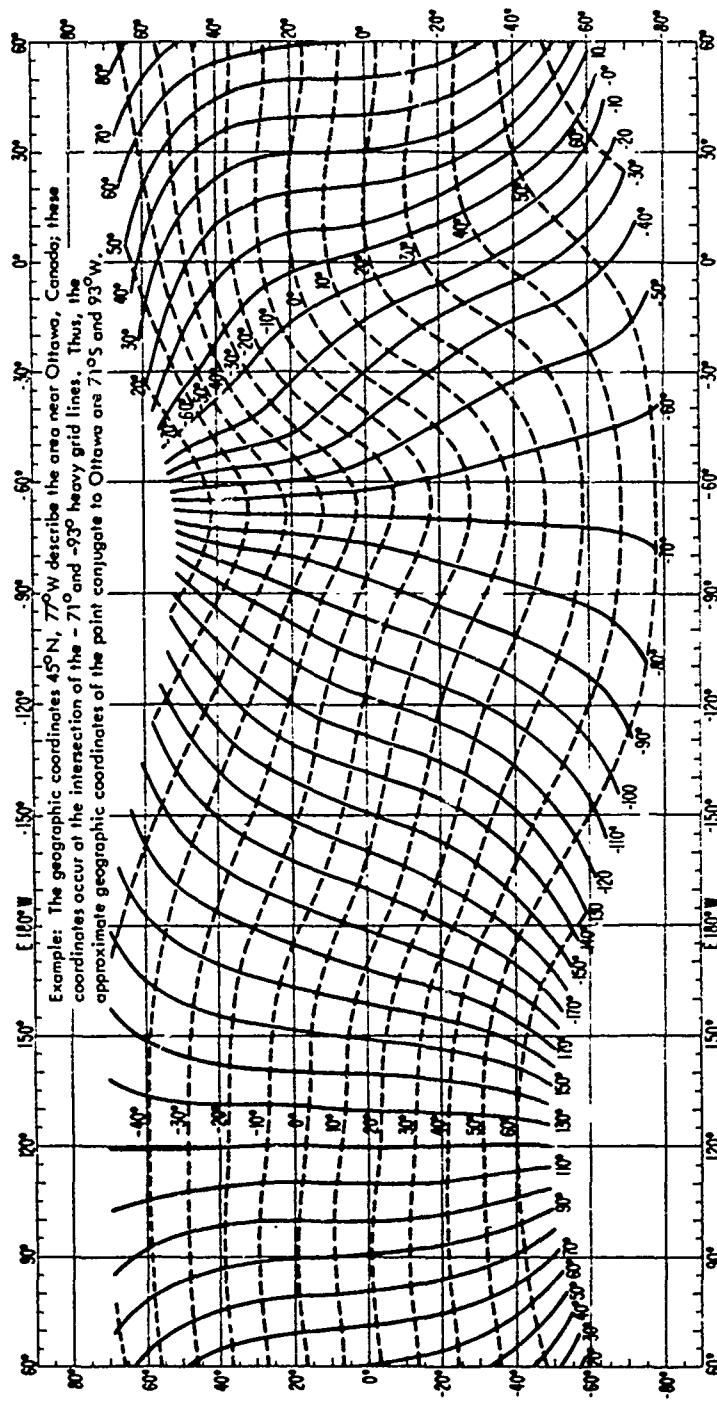


Figure 8-53. Magnetic Conjugate Map

### Problem 8-9 Geomagnetic Dip Angle Map

Figure 8-54 presents the geomagnetic dip angle (declination) as a function of the geographic coordinates of a position on the earth's surface.

#### Example

Given: A point with geographic coordinates 40°N latitude, 100°W longitude.

Find: The geomagnetic dip angle.

Answer: From Figure 8-54 the magnetic

dip angle is 70°.

#### Reliability

Figure 8-54 shows the geomagnetic dip angle for undisturbed magnetic field conditions. The geomagnetic field may be distorted for tens of seconds after a nuclear detonation. Therefore, the locations of the debris and beta particle ionization regions may differ significantly from those predicted by Figure 8-54.

#### Related Material

See paragraph 8-4.

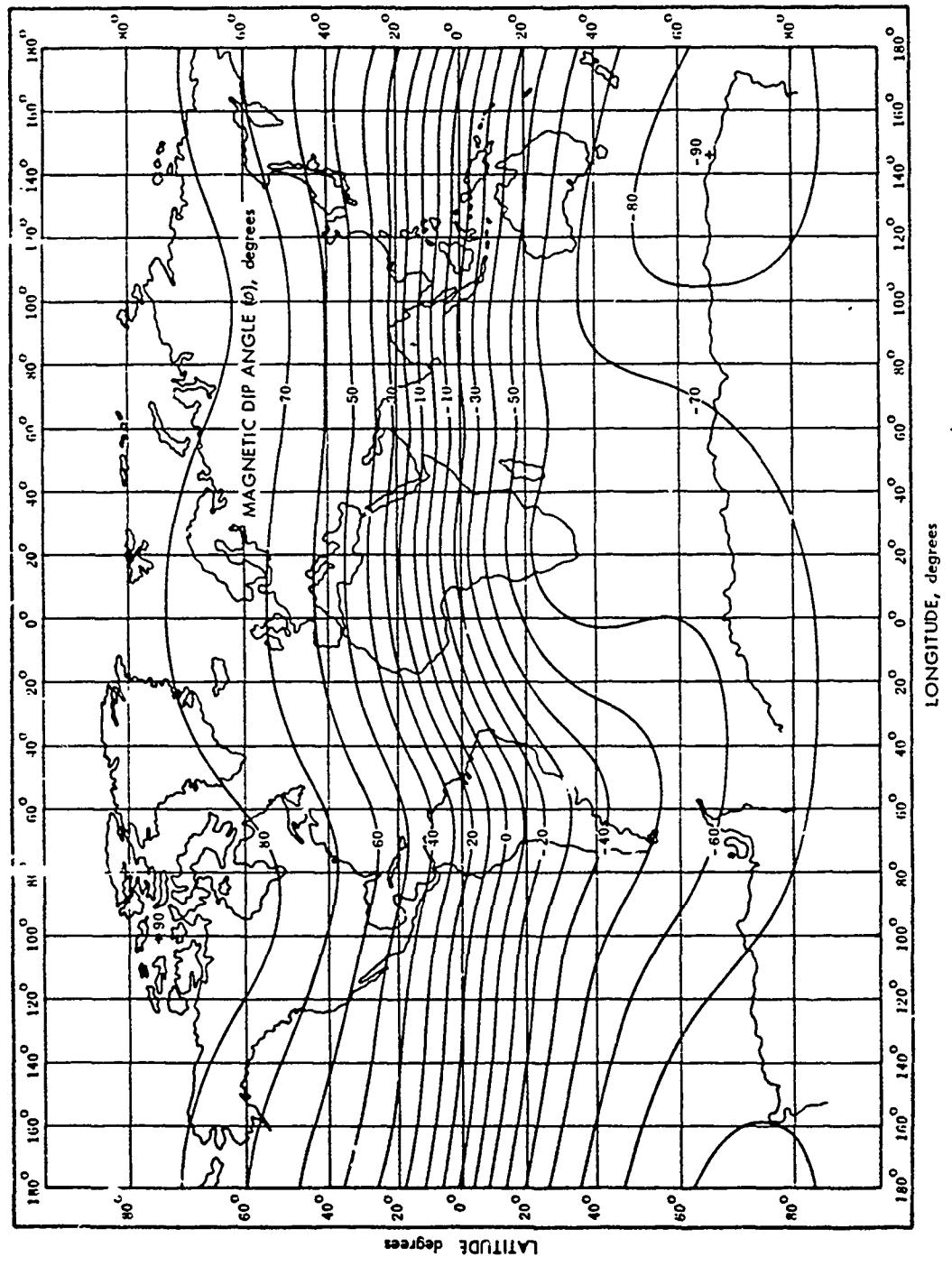


Figure 8-54. [REDACTED] World Map of Magnetic Dip [REDACTED]

### Problem 8-10 Secant $\theta$ Chart

Figure 8-55 presents the secant of the angle of incidence of a ray path at 65 km altitude as a function of elevation angle or distance from the ground terminal to E- and F-region reflection points. The angle of incidence,  $\theta$ , is illustrated in the sketch in Figure 8-55.

#### Example 1

*Given:* A propagation path with a 10-degree elevation angle ( $\beta$ ).

*Find:* The horizontal distance from the ground terminal to the point where the propagation path intersects 65 km altitude, and the secant of the angle of incidence  $\theta$  at the intersection.

*Solution:* Enter Figure 8-55 on the line sloping downward to the right labeled 10 degrees. Locate the intersection of this line with the line sloping upward to the right labeled  $h = 65$  km. The abscissa of this intersection is the horizontal distance, and the ordinate is secant  $\theta$ .

*Answer:* The horizontal distance from the ground terminal to the point where the propagation path intersects 65 km altitude is 320 km. The secant of the angle of incidence at the intersection is 4.6.

#### Example 2

*Given:* A HF propagation path that reflects from the F-region (300 km), 1500 km from the ground terminal.

*Find:* The horizontal distance from the

ground terminal to the point where the propagation path intersects 65 km altitude, and secant  $\theta$  at the intersection.

*Solution:* Enter the abscissa of Figure 8-55 at 1500 km. Proceed upward to the line labeled F-region Reflection Altitude (300 km). Note the elevation angle ( $\beta$ ) corresponding to this point. Find the intersection of the elevation angle line with the line labeled D-region Absorption Altitude (65 km). The abscissa of this intersection is the desired horizontal distance, and the ordinate is secant  $\theta$ .

*Answer:* The horizontal distance from the ground terminal to the point where the propagation path intersects 65 km altitude is 500 km. The secant of the angle of incidence at the intersection is 6.

*Reliability:* The curves of Figure 8-55 are accurate for the simplified geometry assumed; however, the D, E, and F absorption and reflection altitudes are not single lines but occupy a volume of space which changes in altitude with time of day and which may be affected by solar activity. Therefore, more detailed models are generally required for radar and communication system problems.

*Related Material:* See paragraphs 8-1, 8-3, 8-4, 8-6, 8-7, 8-8, and Problems 8-1 through 8-6.

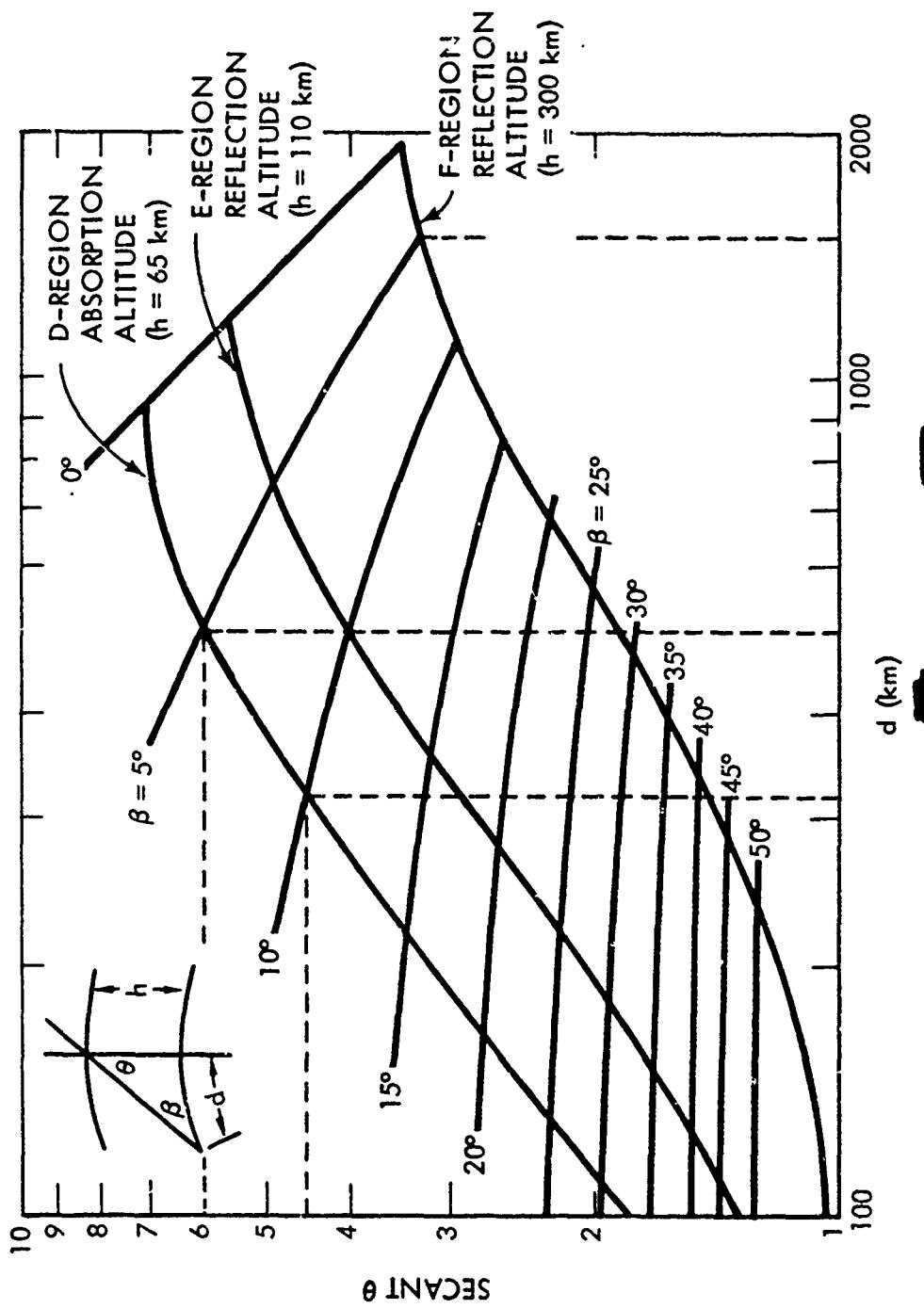


Figure 8-55. Secant  $\theta$  Chart

## BIBLIOGRAPHY

*Atmospheric Ionization and Effects on Radar and Communications, A Bibliography*,  
DASA 2069, Defense Atomic Support Agency, Washington, D.C., January 1968

*Bibliography of Open and Unclassified Literature Pertaining to the Effects of High Altitude Nuclear Explosions, Parts I and II*, Final Report, DASA 1795, Defense Atomic Support Agency, Washington, D.C., May 1966

*DASA Reaction Rate Handbook*, DASA 1948, Defense Atomic Support Agency, Washington, D.C., October 1967 [REDACTED] (will be revised as DNA 1948H during calendar year 1972).

*Electromagnetic Blackout Handbook* [REDACTED] Second Edition, Volume I: *Guide to Systems Effects* [REDACTED] DASA 1580, Defense Atomic Support Agency, Washington, D.C., December 1964 [REDACTED]

*Electromagnetic Blackout Handbook* [REDACTED] Second Edition, Volume II: *Nuclear Weapons Effects* [REDACTED] DASA 1580-1, Defense Atomic Support Agency, Washington, D.C., February 1965 [REDACTED]

*High Altitude Tests Measurement Summary* [REDACTED] DASA 1970, Defense Atomic Support Agency, Washington, D.C., September 1967 [REDACTED]

Knapp, W. S., and P. G. Fischer, *Aids for the Study of Electromagnetic Blackout*, DASA 2499, General Electric, TEMPO, Santa Barbara, Calif., July 1970 [REDACTED]

*RANC IV, Computer Simulation of Radar Propagation in a Nuclear Environment, Volume I: Computational Models*, DASA 2497-1, Defense Atomic Support Agency, Washington, D.C., July 1970 [REDACTED]

*Weapon Effects Computer Code Directory*, DASA 1727, Special Report 43, Defense Atomic Support Agency, Washington, D.C., April 1969 [REDACTED]

## PART II

# DAMAGE CRITERIA

### Chapter 9

#### INTRODUCTION TO DAMAGE CRITERIA

Part I of this manual describes the basic phenomena associated with a nuclear explosion for various burst conditions. These phenomena include: blast and shock, thermal radiation, X-ray radiation, nuclear radiation, transient radiation effects on electronics (TREE), electromagnetic pulse (EMP) phenomena, and phenomena affecting electromagnetic wave propagation. Part II treats the mechanisms of casualty production and damage to military targets, and describes the response of these targets by correlating the basic physical phenomena with various defined degrees of damage.

#### SECTION I CONTENT AND LIMITATIONS OF PART II

##### 9-1 Introduction to Chapter 9

The information in Part I is divided according to the phenomenology, with one chapter being devoted to each of the seven phenomena listed above. This chapter provides a general discussion of the physical damage mechanisms associated with each of the first six phenomena listed above (the last phenomenon does not produce physical damage; the degradation of signals from radio and radar systems is discussed in Chapter 17). Separate sections describe the damage mechanisms associated with each of the six phenomena. In addition, Section IV of this chapter discusses the degradation of equipment

by thermal radiation that might affect its response to the blast wave.

##### 9-2 Organization of Part II

Part II of this manual is divided into chapters according to types of targets that exhibit similar response characteristics. Further subdivisions within the chapters separate the types of targets into subtypes, and for each subtype there are frequently further subdivisions according to the phenomena that cause the damage.

The data presented here are interpretations of complex results of the nuclear weapons effects research and test programs of the Department of Defense. A constant effort is made to deduce theoretical models and scaling laws for the various weapons effects that permit a quantitative prediction of the extent of a given effect from a weapon of one yield related to weapons of other yields. Since the initiation of the limited nuclear test ban treaty, a large amount of effort has been devoted to the development of complex computer codes to predict the environments created by the various phenomena resulting from nuclear explosions and the interactions of these environments with personnel and military systems. A large number of scaling laws presented in Part I that are useful in predicting the environment from a given explosion were derived from the calculations performed with these codes. Many additional scaling laws,

derived from field and laboratory experiments, and theoretical studies, as well as the codes, are presented in the chapters of Part II to aid in the predictions of the response of personnel and systems to the environment. Graphical presentation is used in preference to tabular or purely computational presentations wherever possible. The damage curves are drawn for a probability of 50 percent of producing the indicated damage. Curves of 90 and 10 percent probability are included when the quantity and quality of the data permit. In addition, Appendix C provides the methodology for estimating any probability of damage, provided that the median values of the response of a given system are known. Estimates of such median values for the equipment discussed in Sections I through III of Chapter 11 are provided in Appendix C. Effort has been made to provide a comprehensive set of data in a readily usable form; however, certain categories of damage are not amenable to generalization. Some limitations in the content of Part II are discussed in paragraph 9-3.

An estimate of the degree of reliability accompanies most of the data presented herein. Statements of the reliability of damage data only pertain to the basic response data, which, for the target analyst represent the "radius of effect." They should not be confused with the terms variability and probability of damage, which pertain to target response; nor do these estimates include operational considerations such as linear, circular, or spherical aiming and fuzing errors, yield variations, and target intelligence.

### 9-3 Limitations in Part II

As mentioned in paragraph 9-2, the remaining chapters of Part II each contain descriptions of damage to a category of targets that exhibit similar response characteristics. Unfortunately, the response to certain of the phenomena depends so strongly on a specific system design that it is impossible to present response

data for a "category" of targets (e.g., communications equipment, aircraft, missiles). These phenomena include X-ray radiation and EMP. Therefore, general discussions of the types of systems that are likely to be affected by these phenomena and the general nature of the responses are given in Sections V and VIII of this chapter. No response criteria are provided in subsequent chapters; however, the potential importance of these phenomena are mentioned where appropriate. TREE response is also very dependent on specific system design. The response of electronic components and circuits is described in Section VII of this chapter. Section IV of Chapter 14 contains a brief review of component and circuit response supplemented with discussions of general electrical responses of classes of systems. This latter discussion is intended to include a cross section of systems that should provide some basis for estimating the radiation damage threshold of other similar equipment.

## SECTION II BLAST AND SHOCK DAMAGE

When a blast or shock wave strikes a target, the target may be damaged (distorted sufficiently to impair usefulness) by the blast or shock wave itself, by being translated by the blast wave and striking another object or the ground, or by being struck by another object translated by the blast wave. For example, the air blast wave can shatter windows, dish in walls, collapse roofs, deflect structural frames of buildings, and bend or rupture aircraft panels and frames. Vehicles, tanks, artillery pieces, and personnel can strike other objects on the ground while being hurled through the air or tumbled along the ground by the blast wave. Ship hulls may be split or crushed by the water shock wave. Buried structures or structural founda-



UNANNOUNCED

Distribution/	
Availability	
Dist	Avail and/ Special
A-1	23

ssion For

GRA&I

TAB

ounced

Location

tions can be displaced, collapsed, or ruptured by the ground shock wave. Usually, the degree of damage sustained by a particular target cannot be correlated specifically to a single blast or shock parameter. The total damage received by the target may depend on a combination of air blast and ground or water shock parameters. The orientation of the target with respect to the blast wave, and the type of surface (the topography or the type of soil) associated with the target also determine damage.

## LOADING

The blast loading on an object is a function not only of the blast characteristics of the incident wave (rise time, peak overpressure, peak dynamic pressure, decay, and duration), but also of the size, shape, orientation, and response of the object. The influence of the target characteristics on the loading is discussed below, with emphasis on air blast loading.

### 9-4 Air Blast Loading in the Mach Reflection Region

The loading on an object exposed to air blast is a combination of the forces exerted by the overpressure and the dynamic pressure of the incident blast wave. The loading at any point on a surface of an object can be described as the sum of the dynamic pressure, multiplied by a local drag coefficient, and the overpressure after any initial reflections have cleared the structure. Since the loading changes rapidly while the blast wave is reflecting from the front surfaces and diffracting around the object, loading generally comprises two distinct phases: the initial diffraction phase; and the phase following diffraction when the object is completely engulfed by the blast wave. This latter phase approaches a steady state and usually is referred to as the drag phase, because during this phase the drag forces (i.e., the forces resulting from the dynamic pressures) are the predominant factors in the production of

a net translational force on the object. The following discussion of the loading process is based on an ideal blast wave as described in Section I (Figure 2-1), Chapter 2. Where nonideal blast waves, with slow rise time, irregular shapes, and high dynamic pressures (paragraphs 2-21 through 2-31, Chapter 2) introduce complications into the loading process, further explanation is provided. The loading on an object can be described conveniently in three parts: diffraction loading, drag loading, and net loading. These are discussed separately below.

*Diffraction Loading.* The side of an object facing the shock front of an air blast wave bears overpressures several times that of the incident overpressure because it both receives and reflects the shock. In the Mach reflection region the overpressure incident on the object is actually that of the original free air blast wave which has been reflected from the ground surface to a higher value. The reflection off the object therefore constitutes a second reflection process. In the regular reflection region, the incident overpressure is that of the free air blast wave (see paragraph 9-6). The magnitude of the reflected overpressure depends on the angle between the shock front and the face of the object, the rise time of the incident blast wave, and the initial incident shock strength. The greatest reflected overpressures occur when the direction of propagation of the shock front is normal to the face of the object, when the rise to the peak overpressure is essentially instantaneous, and when the incident shock strength is high. As the blast wave progresses it bends or diffracts around the object, eventually exerting overpressures on all sides. Before the object is entirely engulfed in the pressure region, however, overpressure is exerted on the front side of the object, whereas only ambient air pressure exists on the back side. During the diffraction phase this pressure differential produces a translational force on the object in the direction of blast wave propagation.

tion. When the blast wave has completely surrounded a small object, the translational force that results from diffraction loading is reduced essentially to zero, because the pressures on the front and on the back are almost equal. In the cases of long objects or short duration blast waves, the net force may actually reverse, because the overpressure on the front face may decay to a value lower than that on the rear face. The importance of this translational loading in the production of damage to the target depends on the duration of the loading or on the time required for the shock front to traverse the target and, therefore, on the size of the target. The effects of the translational load decrease as the duration of the load is decreased until, in some instances, translational load effects can be ignored. The overpressures continue on all sides of the object until the positive phase of the blast wave has passed. These pressures may be sufficient to crush an object (a 55-gallon drum may be damaged in this manner in addition to damage that might be incurred by translation). Thus, the diffraction phase translational loading depends primarily on the object size, pressure pulse duration, and on increases in differential overpressures resulting from reflection on the front face.

*Drag Loading.* During the time of diffraction and until the blast wave has passed, the wind behind the shock front causes dynamic pressures to be exerted on the object as drag loading. Except in the case where shock strengths are high, these pressures are much lower than the reflected overpressures; however, they produce a translational force that the target component receives for the entire positive phase duration of the blast wave. For a given blast wave, the loading that results from dynamic pressure depends principally on the shape and orientation of the object, ranging from less than four-tenths of the dynamic pressures in the case of a cylinder (when normal to the cylindrical

axis), to over twice the dynamic pressures for an irregular, sharp-edged object.

*Net Loading.* Net loading is the combined load on the element that tends to translate it in the direction of propagation of the blast wave. Thus, it is the difference between the load on the front face and the load on the back face; the loads on the sides are of no effect in producing translation.

### 9-5 Qualitative Examples of Net Loading

The net load on a target can be developed most simply by considering the idealized case shown in Figure 9-1, in which a classical, sharp fronted blast wave moving along the surface of the ground encounters a simple, rigid, fixed cube. When the blast wave arrives at the front face of the target, this face experiences a sudden rise in overpressure to a value  $p_r$  that is greater than the peak overpressure  $\Delta p$  of the incident blast wave (also frequently called "side on" overpressure). As the shock wave moves over the cube, subjecting its top and side faces to side on overpressure, the pressure on the front face of the cube begins to drop as the result of rarefaction waves that are generated at the edges of the front face, and which move across that face. When the wave encounters the back face of the cube, that face experiences a gradual pressure increase. The air behind the front of the incident shock wave is in motion, and as the wave envelopes the cube this air motion also affects the pressures experienced by the various faces of the cube.

After a time that is related to the cube dimensions and to the velocity of the incident shock wave, the pressure on the front face becomes

$$p_f = \Delta p(t) + C_{df}q(t)$$

where

$\Delta p(t)$  = the overpressure in the incident shock wave as a function of time,  $t$ ,

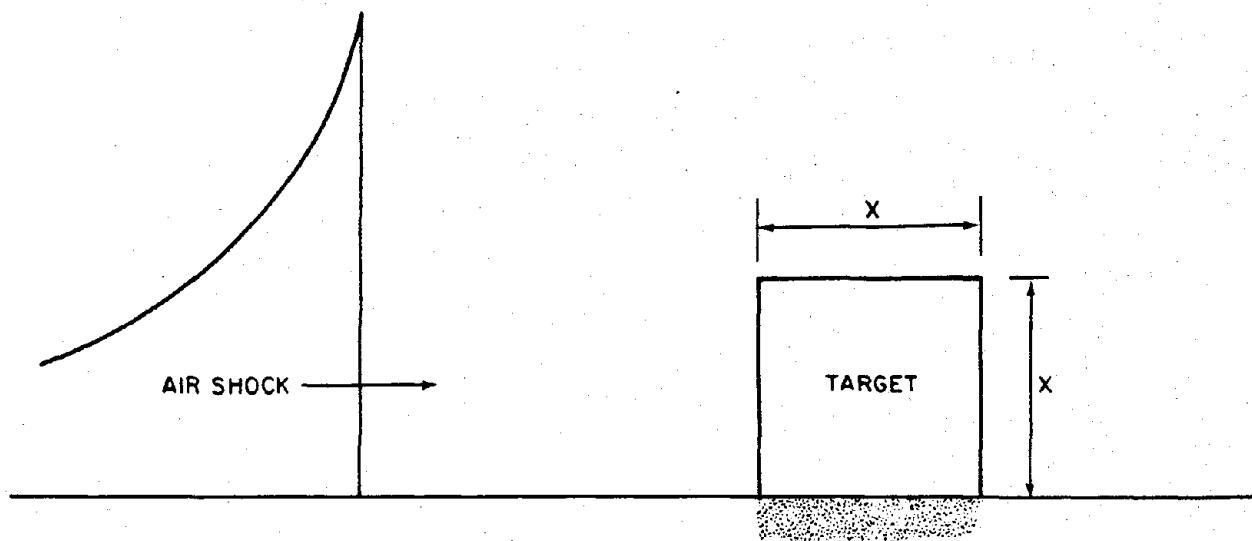


Figure 9-1. [REDACTED] Initial Conditions for Loading of a Rigid, Fixed Cube [REDACTED]

$C_{df}$  = the drag coefficient of the front face of the cube,

$q(t)$  = the dynamic pressure in the incident shock wave as a function of time,  $t$ .

After the shock wave has passed over the cube and has reached the back face, the pressure on that face begins to rise and, at a later time also related to the cube dimensions and the velocity of the incident shock wave, the pressure becomes

$$p_b = \Delta p(t) - C_{db} q(t)$$

where

$C_{db}$  = the drag coefficient of the back face of the cube.

Note that both expressions contain overpressure and dynamic pressure components. As far as the net horizontal (translational) loading on the

cube is concerned (i.e., the pressures tending to move the cube to the right in Figure 9-1), the overpressure contributions must be subtracted from one another (pressure on the back face tends to move the cube to the left) while the dynamic pressure contributions must be added to each other.

[REDACTED] It is convenient to consider the two contributions separately. Figure 9-2 illustrates the overpressure loadings only (dynamic pressure contributions are not included) experienced by the front and back faces of the cube both during the early (diffraction) phases — up to time  $t_1$  on the front face and time  $t_3$  on the back face of the cube — and after the times that the equations given above apply.

[REDACTED] The incident shock wave is of the classical (peaked) form with peak overpressure and overpressure duration of  $\Delta p$  and  $t_p^+$  respectively;  $t_1$  is the time after which the total front face loading is represented by the equation for  $p_f$

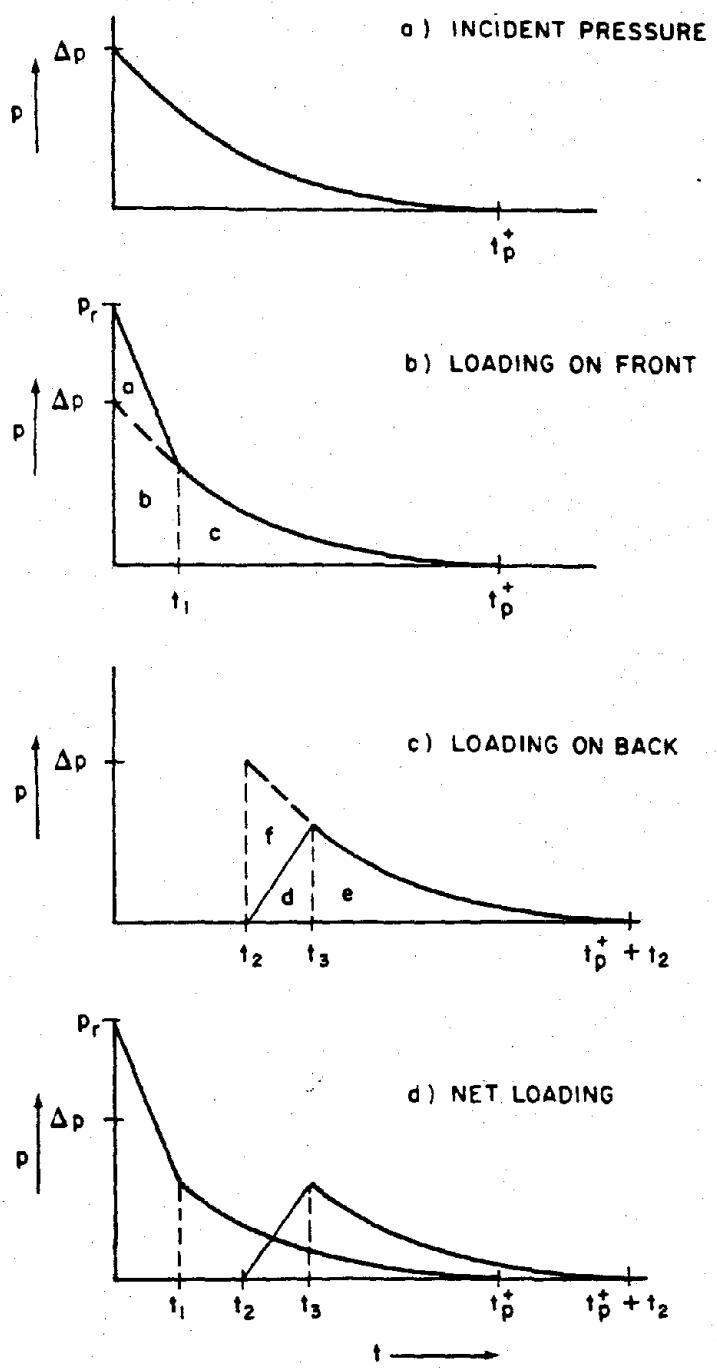


Figure 9-2. [REDACTED] Target Loading by Overpressure [REDACTED]

above;  $t_1$  is the time for the shock wave to reach the back face, and  $t_3$  is the time after which the total back face loading is represented by the equation for  $p_b$  above.

From Figure 9-2b, the total impulse on the front face,  $I_F$  (i.e., the area under the curve multiplied by the area of the cube face,  $A$ ) is equal to the sum of the areas  $a$ ,  $b$ , and  $c$ .

$$I_F = (a + b + c)A$$

The total impulse on the back face,  $I_B$ , is (Figure 9-2c)

$$I_B = (d + e)A$$

The net overpressure impulse is  $I_F - I_B$ . If the cube is not too large compared to the duration of the blast wave, the following approximations hold among the areas:

$$b = d + f,$$

$$c = e.$$

Thus, the net overpressure impulse is

$$I_N = (a + f)A.$$

If the initial drop of pressure on the front face and the build up of pressure on the rear face are assumed to be linear, the net impulse is

$$I_N = A \left[ \frac{1}{2} (p_r - \Delta p) t_1 + \frac{1}{2} \Delta p (t_3 - t_2) \right]$$

in which the term containing  $t_1$  is area "a," and the term containing  $t_2$  and  $t_3$  is area "f" of Figure 9-2. Note in particular that the only times are  $t_1$ ,  $t_2$ , and  $t_3$ , i.e., those times related to the initial envelopment of the cube by the blast wave.  $I_N$  does not, in this simple analysis, depend on overpressure duration  $t_p^+$ .

Substitution of commonly accepted values of  $t_1$ ,  $t_2$ , and  $t_3$  for a curve leads to the following expression for the net impulse from overpressure diffraction around the target:

$$I_N = A \left[ \frac{X}{2U} (3p_r + \Delta p) \right]$$

where

$X$  = one-half the width or the height, whichever is smaller,

$U$  = velocity of the shock wave.

These values of  $t_1$ ,  $t_2$  and  $t_3$  originally were derived from early shock tube experiments and full scale nuclear tests on structures at low pressure levels. Consequently, they are used for illustrative purposes only in this simple analysis. More recent work with two and three dimensional models in the shock tube has shown that the exact values for these times depend strongly on model shape and pressure level as well as sound velocity in the reflected pressure region on the face of the model rather than shock front velocity.

The impulse on the cube due to dynamic pressure  $I_q$  is

$$I_q = A \int_0^{t_p^+} q(t) C_d dt$$

where

$I_q$  = drag impulse,

$q$  = dynamic pressure,

$C_d$  = drag coefficient of the entire object, a combination of  $C_{df}$  and  $C_{db}$ .

By expressing  $p_r$  in terms of  $\Delta p$  and shock strength  $\xi$ , and  $U$  in terms of the sound velocity,  $c$  and the shock strength  $\xi$ , the drag impulse equation may be solved in terms of  $\Delta p$ ,

$\xi$ ,  $C_d$ , and shock wave duration\*  $t^+$ . The combined impulse is

$$I_T = \left\{ \left[ \frac{X\Delta p}{2c} \left( \frac{42 + 24\xi}{\xi + 7} + 1 \right) \left( 1 + \frac{6\xi}{7} \right)^{-1/2} \right] + \left[ \frac{0.54\Delta p C_d t^+ \xi}{\xi + 7} \right] \right\}.$$

The first expression in brackets, which is independent of duration, is the overpressure contribution. The second expression is the contribution of dynamic pressure.

If height of burst and ground distance are scaled as the cube root of the yield  $W$  for weapons of different yields,  $\Delta p$  remains constant, but the shock wave duration  $t^+$  varies as the cube root of the yield. Thus, the yield dependence is

$$I_T = A [B + C(W^{1/3})]$$

where  $B$ , the overpressure contribution ( $I_N$  for a 1 kt yield), and  $C$ , the dynamic pressure contribution ( $I_q$  for a 1 kt yield), are both constants. Thus, the contribution to total impulse from overpressure remains constant, while that from dynamic pressure increases as the cube root of the yield. For very low fractional kiloton yields, the loading is highly impulsive with most of the load coming from the overpressure contribution. As the yield increases, at a constant scaled height of burst and ground distance, the total impulse also increases, with an increasing fraction resulting from dynamic pressure.

Figures 9-3a and b show representative net loadings for two classes of weapon yield and two classes of structures, one small and one large. A small element would be about the size of a telephone pole or a jeep; a large element would be the size of a house or larger. Since the

reflected overpressure is more than twice the incident pressure on the front face of the element, the loading displays an initial peak value. The reflected pressure decays or clears the front face at a time that depends on the size of the element. The rapid decay for the small element may make the reflected pressure spike of no significance, whereas the slow decay for the large element creates a load that may govern the response of the target entirely. For the representative cases shown, the diffraction phase terminates at time  $t_{\text{diff}}$ , the time at which the reflected pressure has decayed to the incident pressure. At this time the drag phase begins. It continues until the end of the positive phase of the incident blast wave. The load during the drag phase is shown to be equal to the dynamic pressure, i.e., the drag coefficients of the elements are equal to 1.0. The characteristics of the target element determine whether the response of the element is governed primarily by the diffraction phase or the drag phase. Figures 9-3a and b show that for medium and high yield weapons and small elements, a much greater impulse (the area under the loading curve) occurs during the drag phase than during the diffraction phase. As the yield increases the drag phase impulse increases in importance. For large elements and large yield weapons, the diffraction phase and drag phase impulses are about equal. In this latter case the drag phase impulse may still be of no importance, because the significant target response may occur during the diffraction phase. The diffraction phase impulses are not changed by the yield of the weapon (this is true for all but very large structures exposed to low yield weapons), whereas the drag phase impulses are directly related to the weapon yield (for the same peak dynamic pressures).

\* In this solution it is assumed that the difference between  $t_p^+$  and  $t_q^+$  may be neglected, and  $t_p^+ = t_q^+ = t^+$ .

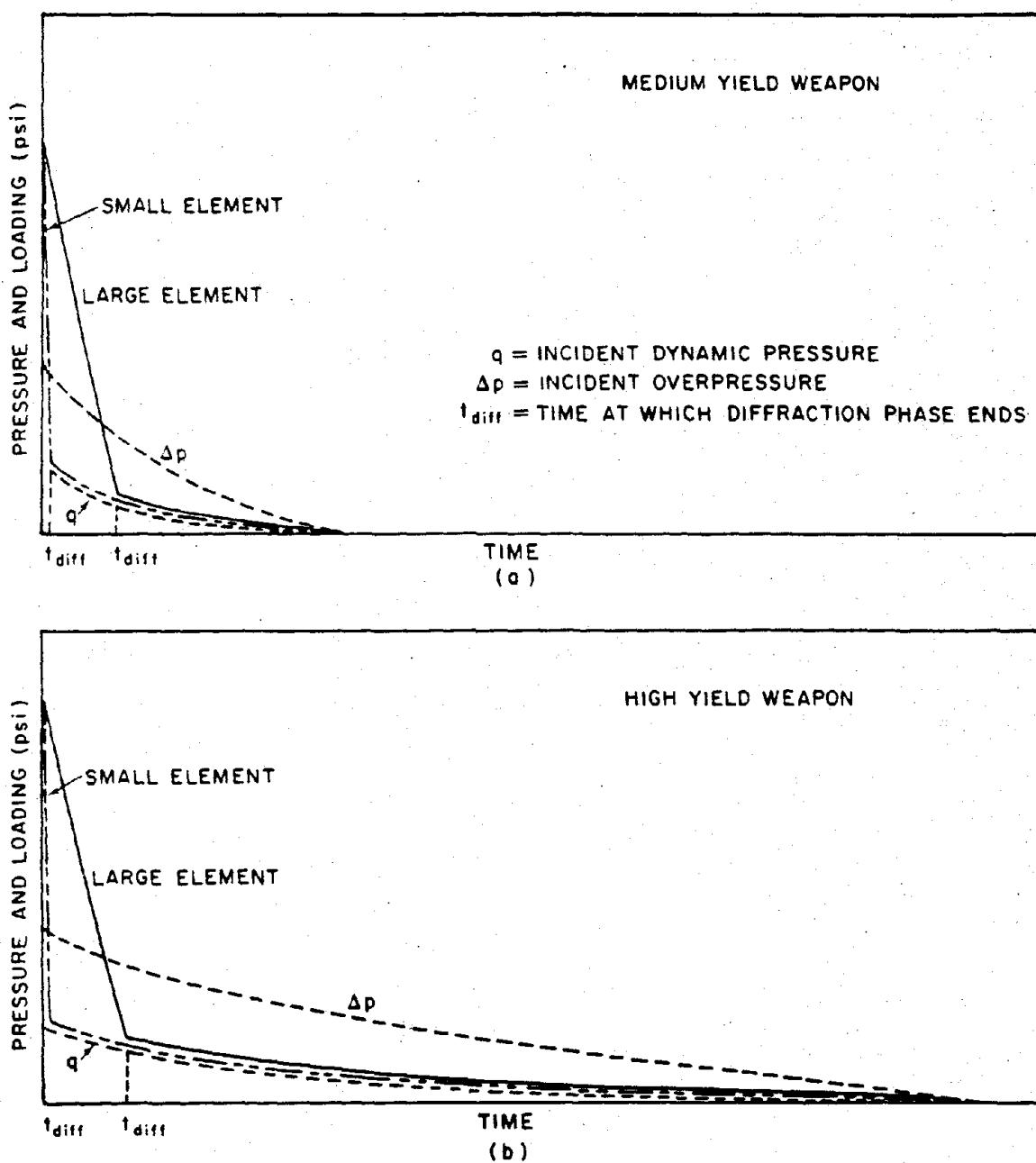


Figure 9-3. Net Blast Loading on Representative Structures

## **9-6 Regular and Mach Reflection**

Specific aspects of the blast wave propagation must be considered when computing the load on a target. The loading of a surface target in the regular reflection region (paragraph 2-18, Chapter 2) is complicated by the vertical component of the incident blast wave, which causes multiple reflections between the ground and the target and additional reflected pressures on horizontal surfaces. In the Mach reflection region (paragraph 2-18), the loading is simplified because the blast wave propagation is horizontal. Near the surface of the ground, the vertical component of the drag forces in the regular reflection region is cancelled by the reflected wave rapidly; therefore, the brief vertical drag loading is ignored, except when the target is near the ground zero of an air burst. For aircraft in flight, the loading may be a single horizontal shock from a Mach stem or two separate shocks; the first from the free air wave and the second from the ground reflected wave. In establishing the damage curves for surface targets, the loadings on targets in the regular reflection region during the diffraction phase are considered separately from the loadings on similar targets in the Mach reflection region. The surface conditions are assumed to be average unless otherwise indicated in the figures that provide the damage curves. Objects that are primarily susceptible to horizontal drag loading in the Mach reflection region may become primarily susceptible to crushing action if they are in the early regular reflection region.

## **9-7 Target Motion**

When air blast loading is considered, the movement of the target component during loading is assumed to have negligible effect on the loading itself. Aircraft and missiles in flight are exceptions. Their speed, orientation, and movement during loading assume increased importance (see Chapters 13 and 16).

**9-10**

## **9-8 Nonideal Waveforms**

As discussed in paragraphs 2-31 and 2-32, ideal waveforms are seldom found along the surface for overpressure levels above 6 psi. The description of the diffraction and drag phases given in preceding paragraphs is not true in regions of nonideal waveforms. If the overpressure wave has a long rise time (30 to 40 msec) to a peak value, full reflection of the wave from the surface of a structure will not occur. At the same time, the relationship between dynamic pressure and overpressure is different from that described for the ideal blast wave. During the diffraction phase, the drag forces caused by high dynamic pressures may be the predominant damage-producing criteria. Since many conventional surface structures sustain severe damage at low peak overpressure levels, and nonideal waveforms occur only in the higher overpressure regions, such waveforms were not considered in determining damage criteria for such structures. Careful consideration must be given to nonideal waveforms when assessing the vulnerability of protective structures that were designed to withstand high overpressures. The dynamic pressures for such waveforms generally will be higher than would be expected if the blast wave were ideal. There are few data on blast loading in the high pressure regions.

## **9-9 Underwater Shock Wave Loading**

The air blast wave operates in a compressible fluid, while the water shock wave operates in a noncompressible fluid. This difference in medium accounts for the differences in detail between air blast and water shock loading. The peak values in water are higher than they would be at the same distance from an explosion of the same yield in air. However, the duration of the shock wave in water is shorter than in air. When the shock wave strikes a rigid, submerged surface, such as the sea bottom, it is reflected.

When the shock wave reaches the air-water surface (a less rigid medium), however, a refraction (or negative pressure) wave occurs. The combination of the surface reflected shock wave and the direct shock wave produces a sharp decrease or "cutoff" in the water shock overpressure, as shown in Figure 9-4. Incidence of a shock wave on a ship or structure produces damage through the direct mechanism of overpressure (or excess impulse) and by imparting a transitional velocity to the target structure.

#### 9-10 Ground Shock Loading

The loading of buried structures by ground shock is connected intimately to the response of the structures. For certain underground structures, serious damage will only occur if the ground shock is so intense that the damage area for those structures is confined closely to the crater area of a surface or underground explosion. For structures near the surface, air blast induced ground shock may cause significant damage. The damage to these structures is more closely related to air blast pressures than it is to crater dimensions. Loading pressures are numerically equal to the ground stress normal to the structure. Such pressures do not produce detectable reflected pressures. Internal equipment of a structure may be subjected to ground shock accelerations that will severely damage the equipment without damaging the structure. For a discussion of accelerations resulting from ground shock see Section III, Chapter 2, and Sections II and III, Chapter 11.

#### RESPONSE AND DAMAGE

Damage to a target is closely related to, and is a direct derivative of, its response. For targets anchored to the ground, damage is usually the result of displacement of one part of the target with respect to another part, resulting in permanent distortion, collapse, or toppling. For movable targets, however, the target may be

moved by the loading with or without a resulting damage. In the latter case, the damage to the target is governed primarily by the manner in which the moving target comes to rest. Whether drag phase loading or diffraction phase loading causes the greater damage will depend upon the weapon yield, target characteristics, and the damage level considered.

#### 9-11 Surface Structures

The predominant cause of failure to large targets, such as buildings that have small window areas compared to wall areas that either support the structure or are as strong as the structural frames, is the pressure differential between the front and rear faces that exists for a relatively long period of time. If the window area is large, the pressure on each wall is equalized quickly by the entry of the blast wave through the windows. The pressures exerted on the inside of the wall reduce the translational force on the wall. This translational force also is reduced because of a smaller wall area on which the pressures can act; however, the force exerted on interior partitions and rear walls tends to offset the reduction in front face loading in the production of total damage. When the overpressures causing translational force on the structural component are equalized quickly as a result of the geometry or construction of the building, the primary damaging forces are those that are significant in damaging structural components that have fairly small cross sections, such as columns and beams. Structures that are normally damaged by drag forces include smoke stacks, telephone poles, truss bridges, and steel or reinforced concrete frame buildings with light walls. These buildings are drag sensitive, because the light walls of corrugated steel, asbestos, or cinder block fail at low reflected pressures, and they do not transmit a significant load to the structure frame. Only the frame is exposed to the blast, and, being composed of small cross

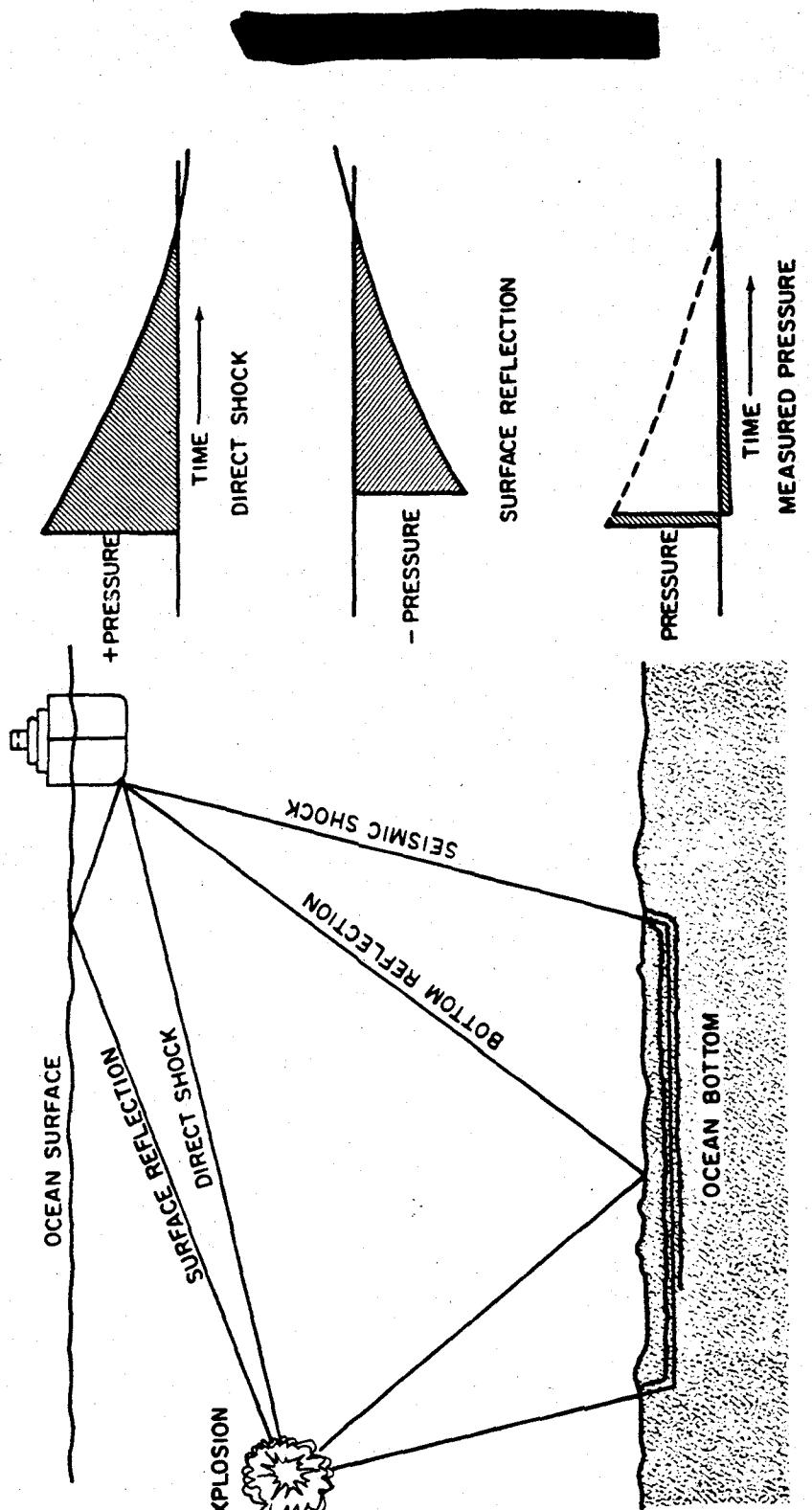


Figure 9-4. Direct and Reflected Shock Waves from an Underwater Burst

section structural elements, it is distorted primarily by drag forces. These buildings are not considered severely damaged unless the structural frame has collapsed or is near the point of collapse. A tree is a good example of a drag sensitive target, because the duration of the diffraction phase is extremely short and there is considerable force applied by the high wind velocity drag loading. Most military field equipment is drag sensitive, because damage generally results from the tumbling or overturning caused by the drag forces.

#### 9-12 Shielded Structures

If the target is shielded from the drag forces, or if it lies within the early regular reflection region, high overpressures may become the damage producing criteria. For blast resistant aboveground structures designed to resist more than 5 to 10 psi overpressure, the distinction between diffraction and drag sensitivity cannot be defined well, because full reflection from the surface of the structure does not occur, and dynamic pressures exceed those expected in the case of the incident waveform. As a result, drag forces may be predominant in producing damage, even during the diffraction phase.

#### 9-13 Aircraft

Aircraft may be damaged by the forces developed in the diffraction phase, in the drag loading phase, or in both. Parked aircraft can receive light, crushing forces corresponding to low overpressures. For example, light skins and frames are easily dished and buckled at relatively low overpressures. At higher overpressure levels, drag loading (referred to as "gust loading" with respect to aircraft) adds to the damage. At these levels, much of the damage may result from translation and overturning of the aircraft. For aircraft in flight, the diffraction and drag forces combine with the existing aerodynamic forces to develop destructive loads on airfoils at low over-

pressure levels. The diffraction or crushing overpressure effects on the fuselage and other thin skinned components, however, are usually of secondary importance for most in-flight aircraft. Responses of aircraft are discussed in more detail in Chapter 13.

### SECTION III THERMAL RADIATION DAMAGE

#### INTRODUCTION

Two important effects of thermal radiation are injuries to personnel (burns) and fires that might be ignited in the target area. Burns to personnel are treated in Section II of Chapter 10. Section VII of Chapter 11 discusses fires in urban areas. Section III of Chapter 15 discusses fires in forest stands. The effects of thermal radiation on various classes of equipment are described in other chapters of Part II. This section contains a description of the properties of materials that might result in ignition or degradation of their physical properties. A brief discussion of survival in fire areas is also provided. Section IV describes the degradation of structural resistance to air blast of materials, primarily metals, as a result of thermal radiation.

Chapter 3 provides the data necessary to estimate the thermal environment. In general, thermal damage is likely to be more important than blast damage for surface targets for high yield weapons that are air bursts rather than surface bursts. As discussed in Chapter 3, the influence of weather makes thermal effects much less predictable than blast effects. Clouds or haze can provide a protective screen, and moisture from an earlier rain can reduce the number of fires in outdoor targets. In some cases, cloud cover can enhance thermal effects on the ground. The criteria for thermal damage given in succeeding paragraphs are representative values

for dry materials directly exposed to the thermal source. These values should be applied with the understanding that they can be modified by a variety of factors discussed briefly in the following paragraphs.

#### 9-14 Radiant Exposure

The thermal damage inflicted on a target depends upon the incident energy per unit area. This quantity is called radiant exposure and, as described in Chapter 3, it usually is expressed in calories per square centimeter ( $\text{cal}/\text{cm}^2$ ). Radiant exposures below  $2 \text{ cal}/\text{cm}^2$  will produce little damage other than possible eye injury (Section II, Chapter 10). Radiant exposures above  $10 \text{ cal}/\text{cm}^2$  usually produce significant damage in unprotected target areas.

#### 9-15 Thermal Pulse Duration

The radiant exposure required to damage a particular target varies with the duration of the thermal pulse. The reason is readily seen from the following example: about 3 to 5  $\text{cal}/\text{cm}^2$  from a short thermal pulse, e.g., from a 1 kt detonation, will produce a second degree burn on bare skin, but direct sunlight delivers the same radiant exposure in a little over 2 minutes with no serious effects.

The time scale of the thermal pulse from low altitude nuclear weapon bursts may be characterized by the parameter  $t_{\max}$ , the time during the final pulse at which the fireball is radiating maximum power. This time increases with increasing yield and decreases with increasing altitude. The relation of  $t_{\max}$  to pulse duration and the method for calculating  $t_{\max}$  are given in Chapter 3. As described in Chapter 3, the time scale of the thermal pulse may be specified indirectly in terms of yield for low altitude bursts. The thermal pulse for high altitude bursts (up to about 100,000 feet) may be described in terms of an equivalent sea level burst. Specifying the thermal pulse duration in terms of yield is convenient since it eliminates the necessity to calcu-

late  $t_{\max}$ ; therefore, many damage criteria are given in terms of radiant exposure and yield rather than radiant exposure and time to final maximum.

#### 9-16 Target Response

For most materials, the heat absorbed from the thermal pulse initially is confined to a thin surface layer. Damage usually results from high surface temperatures. The nature and the degree of the damage depend not only on the intensity and duration of the thermal pulse, but also on several properties of the material that are described below.

**Thickness.** Thick organic materials such as wood, plastics, and heavy fabrics char and may burst into flame while exposed to the thermal pulse; however, this flaming is only a transient effect. As the radiant pulse decays, the absorbed thermal energy continues to penetrate the material. This flow of heat allows the surface to cool to a temperature too low to support combustion.

**Thin materials,** such as light fabrics, newspaper, dry leaves, and dry grass tend to become hotter than the surfaces of thicker materials since the absorbed thermal energy is confined to a relatively small volume of material. Also, since these materials are heated throughout, they usually continue to burn once they are ignited. Moreover, subsequent arrival of the blast wave frequently will fail to extinguish the fire.

**Thermal Conductivity.** Most metals allow rapid penetration of thermal energy to depths below the surface as a result of their high values of thermal conductivity. Consequently, the peak surface temperatures induced in thick pieces of metal are considerably less than the peak surface temperatures induced in most nonmetallic materials. Thin pieces of metal may fail as a result of the combined effects of the thermal pulse, which reduces the strength of the metal by heating it, and the blast wave, which causes it to bend or collapse. This effect is dis-

cussed in more detail in Section IV. Dry rotted wood (or punk) has a lower thermal conductivity than sound wood as a result of its porous structure. When the surface of punk is ignited by a thermal pulse, conduction of heat to the interior is too slow to allow significant cooling of the surface, and burning continues.

**Color.** Light colored objects of a given thickness are more resistant to thermal radiation than dark colored objects, because they reflect more of the incident energy. Color has little effect on the response of materials that blacken (char) early in the thermal pulse, because the energy delivered during the remainder of the pulse is absorbed efficiently by the charred surface.

**Transparency.** Transparent materials are relatively resistant to thermal damage (even though transparency in the visible region does not assure that the material is transparent to infrared) because the radiant energy that passes through them usually does not contribute to heating. Partially transparent materials are thermally resistant because the incident thermal energy is deposited over a range of depths rather than being confined to a thin surface layer. Peak temperatures induced in partially transparent materials therefore are likely to be lower than the peak temperatures produced at the surfaces of opaque materials.

**Moisture Content.** Thermal damage to materials that absorb moisture depends on the percentage of water in such materials. Usually, the moisture content varies with the prevailing relative humidity. Exposure to recent rain, however, may alter the moisture content significantly. Scorching or charring of an organic surface by radiant energy is preceded by vaporization of the water. Consequently, more energy is required to produce a given damage effect on wet surfaces or on targets in highly humid atmospheres. Materials located indoors and exposed to thermal radiation through windows are damaged more readily during the latter part of the heating

season (late winter and early spring), largely because of decreased interior humidities.

### 9-17 Target Orientation

In clear atmospheres and in the absence of reflecting surfaces, the amount of energy incident on a unit area of a target surface is greatest when the surface is directly facing the burst. If the target surface is not facing the burst, the energy per unit area depends on the angle between the perpendicular to the surface and the direction of the incoming radiation.

When the atmosphere is hazy, much of the energy received at the target is scattered by atmospheric particles, arrives from all directions, and reaches portions of the target that are not exposed to direct radiation. Scattered energy is likely to be a large fraction of the total energy received when the slant range from the burst to the target exceeds about half the visual range. Reflection from clouds and from the ground can produce similar effects.

### 9-18 Shielding

Any object that casts a shadow is capable of shielding objects behind it from the direct component of thermal radiation. Trees, buildings, foxholes, hills, etc. offer effective protection except when the scattered component of thermal radiation is large. After leaves have been stripped by the dynamic pressure (wind) of a nuclear burst, the trees offer little shielding from the thermal radiation produced by a second burst. Reflection of thermal radiation from exposed walls of foxholes is about 5 percent.

## THERMAL RESPONSE OF MATERIALS

The amount of thermal radiation that a material will absorb depends on the properties of the material discussed in paragraph 9-16. The amount of energy absorbed usually is determined by multiplying the incident energy by an

absorption coefficient. The absorption coefficient cannot be measured directly, but a good estimate can be made by performing spectral measurements of reflectance (the fraction of incident energy reflected from the surface) over the range of wave lengths of the nuclear spectral distribution and by finding an average value of reflectance. The coefficient of absorptance is equal to one minus the average value of the reflectance. The absorptance determined in this manner is valid only as long as the surface does not change as a result of the absorbed thermal energy. Another approach is to divide the quantity of energy absorbed by the incident energy. The absorbed energy is determined from experimentally determined temperature vs time relationships and appropriate theoretical energy balance relationships. Absorptance is a function of time and temperature although an average value is usually employed. This function when known may be found as an input specification for certain computer programs. In the absence of more definitive data for a specific system, an absorption coefficient of 0.5 is a reasonable value to assume for many materials, particularly metals. For a conservative defensive assumption, the absorption coefficient may be taken to be 1.0 (i.e., total absorption), particularly for dark porous materials.

In many cases, it is appropriate to consider only one or two fuel types, assuming that these fuels are the critical items that will determine whether fires are started in a particular area. In other cases, more detail is required. For example, an estimate of the thermal energy that will ignite a particular type of material used in military uniforms may be desired. The data contained in the succeeding paragraphs is intended as a guide in the solution of more specific problems.

### 9-19 Thickness Effects

The time required for thermal energy to penetrate very thin materials is short compared

to the duration of the thermal pulse. At the end of the pulse, the absorbed thermal energy is distributed more or less uniformly throughout the material. In very thick materials, the end of the pulse finds most of the absorbed thermal energy in a surface layer, with the bulk of the material almost unaffected.

If the terms thermally "thin" and thermally "thick" are used to distinguish between materials that are heated throughout from those that are initially heated only at the surface, it is apparent that physical thickness is not the only parameter involved. For example, as a result of the rapid penetration of heat into metals, a sheet of metal is more likely to be thermally thin than is a sheet of insulating material of the same physical thickness.

The ability of a short pulse of energy to penetrate a target material is most readily measured in the laboratory and most readily treated analytically if the thermal pulse is given a rectangular waveform rather than the more complex waveform produced by a nuclear weapon. A parameter that is useful for calculating thermal response of materials is the characteristic thermal response time  $\tau_o$ , given by the equation

$$\tau_o = \rho C_p L^2 / k \text{ sec},$$

where  $k$  is thermal conductivity ( $\text{cal}\cdot\text{sec}^{-1}\text{cm}^{-1}\text{C}^{-1}$ ),  $\rho C_p$  is heat capacity per unit volume ( $\rho$  = density in  $\text{g}\cdot\text{cm}^{-3}$  and  $C_p$  = specific heat at constant pressure in  $\text{cal}\cdot\text{g}^{-1}\text{C}^{-1}$ ), and  $L$  is the thickness, in centimeters, of the layer of material.

The quantity

$$\alpha = \frac{k}{\rho C_p}$$

is called thermal diffusivity ( $\text{cm}^2/\text{sec}$ ). Use of this quantity simplifies the previous equation to

$$\tau_o = \frac{L^2}{\alpha} \text{ sec.}^*$$

Thermal diffusivity and other properties of a number of materials are shown in Table 9-1.

Characteristic time may be related in several ways to the thermal response of a target. Most important is that the ignition of thin fuels by a rectangular thermal pulse requires the least radiant exposure when pulse duration is about equal to  $\tau_o$ .

Two other relations apply to a thick slab of material. For any particular material exposed to a rectangular pulse of length  $\tau$ , the previous equation can be transformed to give a characteristic thickness

$$\delta = \sqrt{\alpha\tau} \text{ cm.}$$

for which the characteristic time is equal to the pulse duration. If a thick slab of this material is exposed to a pulse of length  $\tau$ , the temperature rise at the surface is the same as would be produced by uniformly distributing the absorbed thermal energy in a slab of thickness  $\delta$ , and the peak temperature rise at depth  $\delta$  in the thick slab is about half as great as the peak temperature rise at the surface.

For example, consider a block of red pine that is exposed to  $15 \text{ cal/cm}^2$  from a rectangular pulse of 3 seconds duration. From Table 9-1, the properties of red pine are

$$\rho = 0.51 \text{ g/cm}^3,$$

$$C_p = 0.4 \text{ cal/g} \cdot {}^\circ\text{C},$$

$$\alpha = 24 \times 10^{-4} \text{ cm}^2/\text{sec.}$$

The characteristic depth is

$$\delta = \sqrt{\alpha\tau} = \sqrt{(24 \times 10^{-4})(3)} = 0.085 \text{ cm.}$$

The mass of wood per unit area in a slab of this thickness is

$$\rho\delta = (0.51)(0.085) = 0.043 \text{ g/cm}^2.$$

The heat absorbed by the wood before it begins to scorch is equal to the product of the incident radiant energy,  $Q$ , and the absorption coefficient,  $A$ . If the absorption coefficient is assumed to be 0.5.

$$QA = (15)(0.5) = 7.5 \text{ cal/cm}^2.$$

Absorption of this amount of energy in a layer of thickness  $\delta$  would result in an energy density of

$$\frac{QA}{\rho\delta} = \frac{7.5}{0.043} = 174 \text{ cal/g.}$$

If the energy were evenly distributed through this layer, the resulting temperature rise would be

$$\frac{QA}{\rho\delta C_p} = \frac{174}{0.4} = 435^\circ\text{C.}$$

and the peak temperature rise at the surface of the wood would be about the same.

The result obtained above may be generalized as follows:

$$\Delta T_s = \frac{QA}{\rho\delta C_p} = \frac{QA}{\rho C_p \sqrt{\alpha\tau}} = \frac{QA}{\rho C_p \sqrt{\tau k/C_p}}$$

\* This equation is useful, but it is by no means exact. The simplified heat-flow analysis from which this equation is derived neglects the effects of radiation and convection heat losses from the surfaces of the exposed sample. It also assumes an isotropic medium, i.e., a medium whose structure and properties in the neighborhood of any point are the same relative to all directions through the point. It also neglects the changes in thermal properties that occur as the exposed material heats, volatilizes, chars, and bursts into flame.

Table 9-1. Thermal Properties of Materials

Materials	Density, $\rho$ (gm/cm <sup>3</sup> )	Specific Heat, $C_p$ (cal/gm $\cdot$ °C)	Conductivity, $k$ (cal/sec $\cdot$ cm $\cdot$ °C)	Diffusivity, $\alpha$ (cm <sup>2</sup> /sec)
<u>Insulating Materials</u>				
Air	9.46 $\times 10^{-4}$	0.24	0.55 $\times 10^{-4}$	0.22
Asbestos	0.58	0.20	4.6 $\times 10^{-4}$	40. $\times 10^{-4}$
Balsa	0.12	0.4	1.2 $\times 10^{-4}$	25. $\times 10^{-4}$
Brick (common red)	1.8	0.2	16. $\times 10^{-4}$	18. $\times 10^{-4}$
Celluloid	1.4	0.35	5.0 $\times 10^{-4}$	10. $\times 10^{-4}$
Cotton, sateen, green	0.70	0.35	1.5 $\times 10^{-4}$	2.5 $\times 10^{-4}$
Fir, Douglas-				
spring growth	0.29	0.4	2. $\times 10^{-4}$	17. $\times 10^{-4}$
summer growth	1.00	0.4	5. $\times 10^{-4}$	12. $\times 10^{-4}$
Fir, white	0.45	0.4	2.6 $\times 10^{-4}$	14. $\times 10^{-4}$
Glass, window	2.2	0.2	19. $\times 10^{-4}$	43. $\times 10^{-4}$
Granite	2.5	0.19	66. $\times 10^{-4}$	140. $\times 10^{-4}$
Leather sole	1.0	0.36	3.8 $\times 10^{-4}$	11. $\times 10^{-4}$
Mahogany	0.53	0.36	3.1 $\times 10^{-4}$	16. $\times 10^{-4}$
Maple	0.72	0.4	4.5 $\times 10^{-4}$	16. $\times 10^{-4}$
Oak	0.82	0.4	5.0 $\times 10^{-4}$	15. $\times 10^{-4}$
Pine, white	0.54	0.33	3.6 $\times 10^{-4}$	18. $\times 10^{-4}$
Pine, red	0.51	0.4	5. $\times 10^{-4}$	24. $\times 10^{-4}$
Rubber, hard	1.2	0.5	3.6 $\times 10^{-4}$	60. $\times 10^{-4}$
Teak	0.64	0.4	4.1 $\times 10^{-4}$	16. $\times 10^{-4}$
<u>Metals (100°C)</u>				
Aluminum	2.7	0.22	0.49	1.0
Cadmium	8.65	0.057	0.20	0.45
Copper	8.92	0.094	0.92	1.1
Gold	19.3	0.031	0.75	1.2
Lead	11.34	0.031	0.081	0.23
Magnesium	1.74	0.25	0.38	0.87
Platinum	21.45	0.027	0.17	0.29
Silver	10.5	0.056	0.96	1.6
Steel, mild	7.8	0.11	0.107	1.2
Tin	6.55	0.056	0.14	0.38
<u>Miscellaneous Materials</u>				
Ice (0°C)	0.92	0.492	54. $\times 10^{-4}$	120. $\times 10^{-4}$
Water	1.00	1.00	14. $\times 10^{-4}$	14. $\times 10^{-4}$
Skin (porcine, dermis, dead)	1.06	0.77	9. $\times 10^{-4}$	11. $\times 10^{-4}$
Skin (human, living, averaged for upper 0.1 cm)	1.06	0.75	8. $\times 10^{-4}$	30. $\times 10^{-4}$
Polyethylene (black)	0.92	0.55	8. $\times 10^{-4}$	17. $\times 10^{-4}$

where  $\Delta T_s$  is the peak temperature rise at the surface. The parameters that define the thermal pulse may be separated from those that define the material properties, and

$$\Delta T_s = \left( \frac{Q}{\sqrt{\tau}} \right) \left( \frac{A}{\sqrt{k\rho C_p}} \right).$$

For a fixed rectangular pulse,  $Q/\sqrt{\tau}$  is a constant, and the equation may be written

$$\Delta T_s = (K) \left( \frac{A}{\sqrt{k\rho C_p}} \right).$$

In practice, the surface temperature rise produced in a thick material is approximately proportional to  $A/\sqrt{k\rho C_p}$  over a wide range of pulse shapes and pulse times. Thus, this parameter may be used as a measure of the relative susceptibility of various materials to surface heating.

Direct measurements of the ignition properties of a representative cellulosic fuel have been reported. The material is  $\alpha$ -cellulose, blackened by the addition of carbon, and made into sheets of various thicknesses. This material has the uniformity required to obtain repeatable test results, and its thermal properties are similar to those of common cellulosic fuels, such as paper and dry leaves.

Figure 9-5 shows the results of exposing this material to the idealized rectangular thermal pulse. Figure 9-6 shows the results obtained in the more practical case of a simulated weapon pulse. These curves show data for black  $\alpha$ -cellulose sheets of a variety of thicknesses by using normalized coordinates. The ordinate is normalized radiant exposure. One unit on this scale corresponds to the energy per unit area that will raise the temperature of the entire sheet  $1^\circ\text{C}$ . Thus, a given value of the ordinate represents a higher radiant exposure for a thicker sheet of cellulose. The abscissa of Figure 9-5

is normalized pulse duration, the duration of the rectangular pulse divided by  $\tau_o$ , the characteristic thermal response time of the sheet of material. The abscissa of Figure 9-6 is a similar normalized time,  $t_{\max}/\tau_o$ . Normalization fails in the case of long pulses, and the curves break into families of curves for different thicknesses of material.

If the pulse has such a short duration that the exposed surface reaches the ignition temperature while the back surface remains cool, two distinct ignition thresholds appear. Low values of radiant exposure produce high surface temperatures and flames, but the flames do not persist after the end of the thermal pulse. This region is labeled transient ignition in Figures 9-5 and 9-6. Sustained ignition only occurs when higher radiant exposures raise the temperature throughout the thickness of the cellulose to a level that is sufficiently high to sustain the flow of combustible gases from breakdown of the fuel. It is difficult to supply sufficient energy with short pulses, since a large amount of the energy that is deposited is carried away by the rapid ablation of the thin surface layer. This transient flaming phenomenon is typical of the response of sound wooden boards to a thermal pulse.

If the pulse is of long duration, the ignition threshold rises because the exposed material can dissipate an appreciable fraction of the energy while it is being received. For very long rectangular pulses an irradiance of about  $0.5 \text{ cal} \cdot \text{cm}^{-2} \text{ sec}^{-1}$  is required to ignite the cellulose. Heat supplied to the material at a slow rate is just sufficient to offset radiative and convective heat losses, while maintaining the cellulose at the ignition temperature of about  $300^\circ\text{C}$ .

Materials respond to the thermal pulse from a nuclear weapon in much the same way that they respond to a rectangular thermal pulse; however, a number of practical effects make a thorough analysis of ordinary fuels ignited by

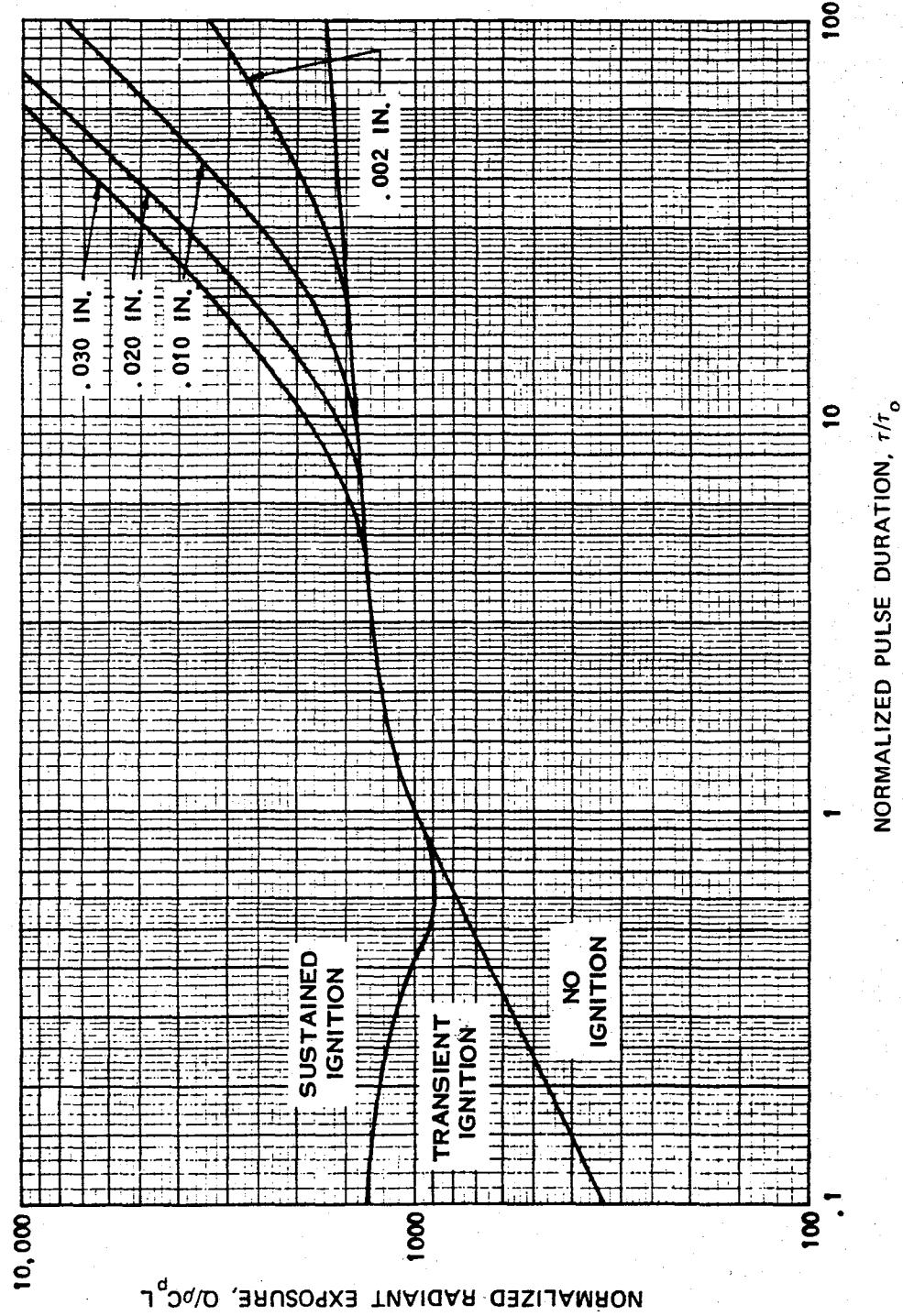


Figure 9-5. Ignition Thresholds for Black  $\alpha$ -Cellulose Exposed to a Rectangular Thermal Pulse

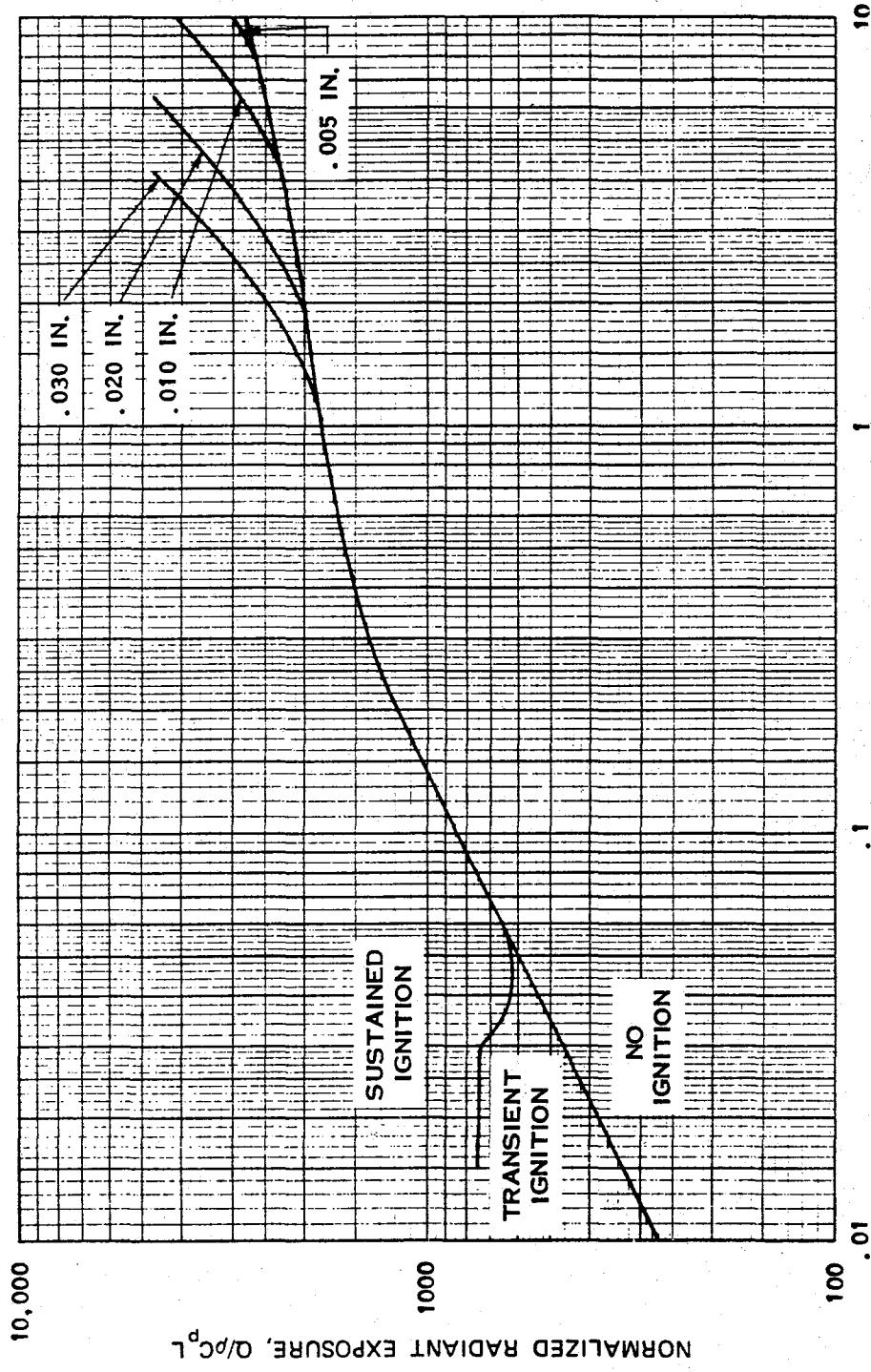


Figure 9-6. Ignition Thresholds for Black [redacted] Cellulose  
 Exposed to a Simulated Weapon Pulse

weapon pulses difficult. While the fuel absorbs heat and its surface chars, its absorption coefficient changes. As a result, the shape of the energy pulse actually absorbed by the material differs from that of the incident energy pulse (this effect is avoided in the  $\alpha$ -cellulose by making the material black initially). A weapon pulse has no single rectangular wave equivalent, since the nature of material response to a thermal pulse varies with pulse shape as well as pulse length. However, for many calculations a rough equivalence may be obtained by assigning between 2.5 and 3 times the irradiance of the rectangular pulse to the weapon pulse.

Both rectangular and weapon pulse data show an optimum pulse length for igniting materials. For the rectangular pulse, this optimum occurs with a pulse length slightly shorter than the characteristic thermal response time of the material. A pulse of this optimum duration lasts long enough to allow an appreciable amount of heat to penetrate to the back face, but it is short enough that only a small heat loss occurs during the pulse.

For example, consider newsprint that is 0.008 cm thick, which has a thermal diffusivity,  $\alpha$ , of  $10^{-3}$  cm<sup>2</sup>/sec. From the equation given previously

$$\tau_o = \frac{L^2}{\alpha}.$$

From Figure 9-6, the threshold for sustained ignition of black  $\alpha$ -cellulose is a minimum when

$$\frac{\tau_{\max}}{\tau_o} = \frac{\tau_{\max} \alpha}{L^2} = 0.045.$$

The properties of newspaper are similar to those of  $\alpha$ -cellulose, so the same relation may be assumed to hold for the newsprint. Thus,

$$t_{\max} = 0.045 \frac{L^2}{\alpha} = \frac{(0.045)(0.008)^2}{0.001}$$

$$t_{\max} = 2.9 \times 10^{-3} \text{ sec.}$$

From the equation given in Chapter 3

$$t_{\max} = 0.043 W^{0.43} (\rho/\rho_o)^{0.42} \text{ sec.}$$

At sea level  $\rho = \rho_o$ , and

$$W = (t_{\max}/0.043)^{2.3}$$

$$W = \left( \frac{2.9 \times 10^{-3}}{4.3 \times 10^{-2}} \right)^{2.3} = 0.002 \text{ kt.}$$

This yield is so small that little confidence may be placed in the result; however, this example demonstrates the general rule that short thermal pulses are more likely to ignite newsprint than long pulses over the range of yields that probably will be of practical importance.

#### 9-20 Color

Although thermal damage depends on the radiant exposure to which a target is subjected, it depends in a much more direct manner on the amount of thermal energy absorbed. Thus color, which indicates the amount and spectral distribution of the visible energy reflected, is one indication of the resistance of a material to thermal damage.

White materials reflect most of the energy in the visible portion of the spectrum that is incident on them, but all cellulosic fuels (which constitute the commonest potential ignition sites) absorb energy in the near infrared region. Cellulosic materials also char in response to high radiant exposures, and once the surface begins to blacken they absorb strongly. The total amount of energy absorbed depends on the absorption coefficient averaged not only over the spectrum of energies contained in the thermal pulse, but also over the interval of time during which the pulse is received. For a thin cellulosic material exposed to a moderately high level of radiant energy (just enough to ignite the ma-

material) blackening will not occur immediately, and the following rules give an effective average for the absorption coefficient that is roughly correct.

- If the material is white or nearly white, the effective absorption coefficient for the thermal pulse is about the square root of the absorption coefficient for visible light. *Example:* If the visible absorption coefficient is 0.1, the effective absorption coefficient for the thermal pulse is about 0.3.
- If the material has a color that is as dark as or darker than dove gray (a fairly light shade of gray), the effective absorption coefficient for thermal radiation is about equal to the visible absorption coefficient.
- The response of most of the nonwhite materials that provide potential ignition sites may be approximated by assigning an effective absorption coefficient of 0.5.

### 9-21 Transparency

The energy that passes through a partially transparent material cannot heat it. Thus, the energy deposited in the material is the incident energy minus the reflected energy minus the transmitted energy.

The depth of penetration of thermal energy into a partially transparent material is determined by two mechanisms: heat absorbed at or near the surface penetrates by diffusion; and heat penetrates as radiant energy before it is absorbed. As shown in paragraph 9-19, the diffusion of heat may be associated with a transient thickness  $\delta$ . Similarly, the penetration of thermal energy due to diathermancy (partial transparency) may be associated with a characteristic depth of  $1/\beta$ , where  $\beta$  is the extinction coefficient. In a practical situation, both of these mechanisms work simultaneously, and the heat penetrates deeper than it would if only one mechanism were effective.

Usually, one or the other of the two mechanisms is dominant. If the product  $\beta\delta$  exceeds 3 or 4, penetration will occur principally by diffusion. If the product is less than about 1/4, penetration will be principally by transmission of radiant energy. Temperature profiles in a semi-infinite solid are shown in Figure 9-7 in terms of dimensionless parameters, where  $\Delta T$  is temperature rise,  $k$  is thermal conductivity,  $\rho$  is density,  $C_p$  is specific heat,  $H$  is energy absorbed (not the incident energy) per unit area,  $\tau$  is rectangular pulse duration, and  $\delta$  is characteristic depth defined in paragraph 9-19.

### 9-22 Effect of Humidity

The water content of thin fuels responds rapidly to changes in humidity. The radiant exposure that is required to ignite a thin cellulosic fuel is approximately

$$Q = Q_0 (1 + h/2),$$

where  $h$  is relative humidity and  $Q_0$  is the radiant exposure that will ignite the fuel when it is completely dry.

In general, ignition data give radiant exposure thresholds for average rather than extremely dry conditions. If the tabulated value of radiant exposure  $Q_1$  applies to a relative humidity of  $h_1$ , the equation given above becomes

$$Q = Q_1 \frac{1 + h/2}{1 + h_1/2}.$$

For example, if the radiant exposure from a 1 Mt explosion that is required to ignite new white bond paper is 30 cal/cm<sup>2</sup> when the relative humidity is 65 percent, the ignition threshold for the same explosion when the relative humidity is 15 percent is

$$Q = (30) \left( \frac{1 + 0.15/2}{1 + 0.65/2} \right) = 24 \text{ cal/cm}^2.$$

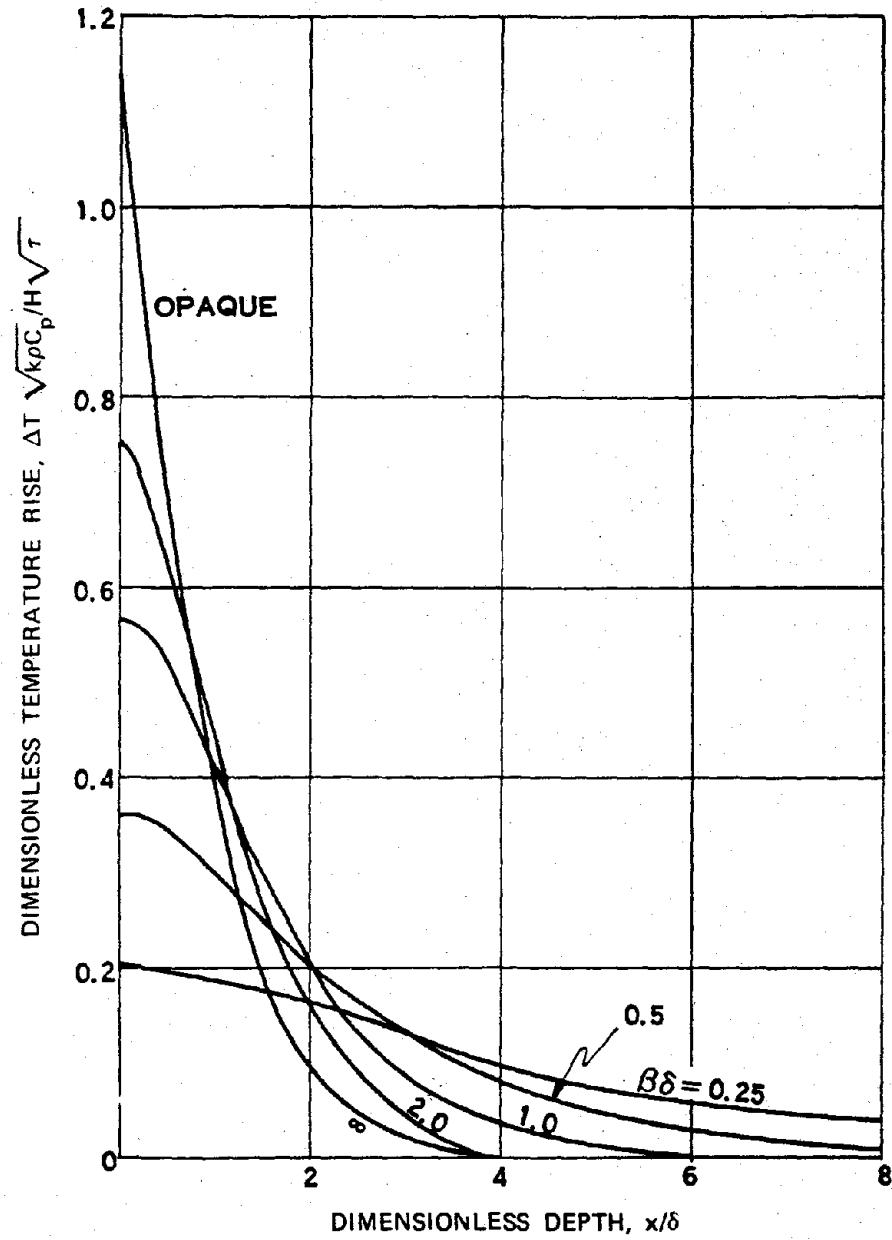


Figure 9-7. [REDACTED] Dimensionless Temperature Profiles in Opaque and Diathermanous Semi-Infinite Solids Exposed to a Rectangular Thermal Pulse [REDACTED]

### 9-23 Response of Metal Sheets

Both the tensile strength and the elastic modulus of metals tend to decrease with increasing temperature. Thus, thermal energy has the potential to weaken metallic structural members. If exposed metal parts are essential to the strength of a structure or a piece of equipment, weakening the metal by heating it may make the unit more susceptible to damage by the blast wave.

Most structural metal is relatively immune to this form of damage in the loading levels of interest. If a heavy part such as a steel I-beam is subjected to a thermal pulse that is sufficiently intense to weaken it appreciably, it is probably so close to the burst that the blast wave could demolish the structure without assistance from the thermal pulse. Walls or roofs usually shield heavy structural members from the thermal pulse.

Light weight units are more likely to be vulnerable to this synergistic damage. The outer covering and the materials that give these units mechanical strength are frequently one and the same. The material is likely to be an aluminum alloy, which loses strength at a much lower temperature than steel.

(U) The degradation of the response of metals to the blast wave as a result of thermal exposure is discussed in more detail in Section IV of this chapter.

### 9-24 Thermal Damage to Various Materials

The general trends discussed in the preceding paragraphs are illustrated by a number of specific examples in Tables 9-2 and 9-3. These tables show the critical radiant exposures for specified damage to fabrics and to various other materials, respectively. The radiant exposures are shown for three weapon pulse durations. The corresponding yields are shown in the footnote for low air bursts (note that altitude scaling is

required for a 24 Mt burst to be considered an air burst (see Chapter 3)). Various yield/altitude combinations that will give the same values of  $t_{max}$  may be obtained by the methods described in Chapter 3.

The values presented in Table 9-2 for fabrics apply for an ambient relative humidity of 65 percent and an ambient temperature of 20°C. For extremely dry conditions, the values shown for fabrics should be reduced by 25 percent. For extremely high relative humidities, near 100 percent (at 20°C), the values for fabrics should be increased by 25 percent. If the fabrics are water-soaked, the critical radiant exposures should be increased by 300 percent. The values for uniforms in Table 9-2 refer to damage to the material itself. They are not applicable for predicting skin burns under uniforms. However, when the outer garment ignites, the probability of skin burns should be considered.

The effect, "tears on flexing," indicates the radiant exposure level at which the outer garment ceases to serve as a reliable barrier to the environment. Under certain environmental conditions the garment would require immediate replacement.

Cotton or rayon fabrics generally can be ignited by exposure to thermal radiation. Nylons, dacrons, and similar synthetics generally are not ignited but melt at relatively low radiant exposures. Woolens do not ignite, but the fibers scorch and coalesce. When a sufficient thickness of the woolen fabric is scorched it becomes brittle and can be torn or crumbled readily.

Most thick, dense materials that ordinarily are considered inflammable do not ignite to persistent flaming ignition when exposed to transient thermal radiation pulses. Wood, in the form of siding or beams, may flame during the exposure but the flame is extinguished when the exposure ceases.

Table 9-2. Approximate Radiant Exposures for Ignition of Fabrics

Material	Weight (oz/yd <sup>2</sup> )	Color	Effect on Material	Radiant Exposure* (cal/cm <sup>2</sup> )		
				t <sub>max</sub> 0.2 sec	t <sub>max</sub> 1.0 sec	t <sub>max</sub> 3.2 sec
<u>Clothing Fabrics</u>						
Cotton	8	White	Ignites	32	48	85
		Khaki	Tears on flexing	17	27	34
		Khaki	Ignites	20	30	39
		Olive	Tears on flexing	9	14	21
		Olive	Ignites	14	19	21
		Dark blue	Tears on flexing	11	14	17
		Dark blue	Ignites	14	19	21
Cotton corduroy	8	Brown	Ignites	11	16	22
Cotton denim, new	10	Blue	Ignites	12	27	44
Cotton shirting	3	Khaki	Ignites	14	21	28
Cotton-nylon mixture	5	Olive	Tears on flexing	8	15	17
	5	Olive	Ignites	12	28	53
Wool	8	White	Tears on flexing	14	25	38
		Khaki	Tears on flexing	14	24	34
		Olive	Tears on flexing	9	13	19
		Dark blue	Tears on flexing	8	12	18
	20	Dark blue	Tears on flexing	14	20	26
Rainwear (double-neoprene-coated nylon twill)	9	Olive	Begins to melt	5	9	13
	9	Olive	Tears on flexing	8	14	22
<u>Drapery Fabrics</u>						
Rayon gabardine	6	Black	Ignites	9	20	26
Rayon-acetate drapery	5	Wine	Ignites	9	22	28
Rayon gabardine	7	Gold	Ignites	**	24†	28‡
Rayon twill lining	3	Black	Ignites	7	17	25
Rayon twill lining	3	Biege	Ignites	13	20	28
Acetate-shantung	3	Black	Ignites	10†	22†	35‡
Cotton heavy draperies	13	Dark colors	Ignites	15	18	34
<u>Tent Fabrics</u>						
Canvas (cotton)	12	White	Ignites	13	28	51
Canvas	12	Olive drab	Ignites	12	18	28
<u>Other Fabrics</u>						
Cotton chenille bedspread		Light blue	Ignites	**	11†	15†
Cotton venetian blind tape, dirty		White	Ignites	10	18	22
Cotton venetian blind tape		White	Ignites	13†	27†	31†
Cotton muslin window shade	8	Green	Ignites	7	13	19

\* Radiant exposures for the indicated responses (except where marked †) are estimated to be valid to  $\pm 25\%$  under standard laboratory conditions. Under typical field conditions the values are estimated to be valid within  $\pm 50\%$  with a greater likelihood of higher rather than lower values. For materials marked †, ignition levels are estimated to be valid within  $\pm 50\%$  under laboratory conditions and within  $\pm 100\%$  under field conditions. For low air bursts, values of t<sub>max</sub> of 0.2, 1.0, and 3.2 sec correspond roughly to yields of 40 kt, 2 Mt, and 24 Mt, respectively.

\*\* Data are not available or appropriate scaling not known.

Table 9-3. Approximate Radiant Exposures for Ignition of Various Materials

Material	Weight (oz/yd <sup>2</sup> )	Color	Effect of Material	Radiant Exposure*		
				t <sub>max</sub> 0.2 sec	t <sub>max</sub> 1.0 sec	t <sub>max</sub> 3.2 sec
<u>Household Tinder Materials</u>						
Newspaper, shredded	2		Ignites	4	6	11
Newspaper, dark picture area	2		Ignites	5	7	12
Newspaper, printed text area	2		Ignites	6	8	15
Crepé paper	1	Green	Ignites	6	9	16
Kraft paper	3	Tan	Ignites	10	13	20
Bristol board, 3 ply	10	Dark	Ignites	16	20	40
Kraft paper, carbon, used (flat side)	16	Brown	Ignites	16	20	40
New bond typing paper	2	White	Ignites	24 <sup>†</sup>	30 <sup>‡</sup>	50 <sup>‡</sup>
Cotton tags		Black	Ignites	10	15	20
Rag tags		Black	Ignites	9	14	21
Cotton string scrubbing mop (used)		Gray	Ignites	10 <sup>‡</sup>	15 <sup>‡</sup>	21 <sup>‡</sup>
Cotton string scrubbing mop (weathered)		Cream	Ignites	10 <sup>‡</sup>	19 <sup>‡</sup>	26 <sup>‡</sup>
Paper book matches, blue head exposed			Ignites	11 <sup>‡</sup>	14 <sup>‡</sup>	20 <sup>‡</sup>
Exhaust ponderosa pine	2 lb/ft <sup>3</sup>	Light yellow	Ignites		23 <sup>‡</sup>	23 <sup>‡</sup>
<u>Outdoor Tinder Materials**</u>						
Dry rotted wood puni (fir)			Ignites	4 <sup>‡</sup>	6 <sup>‡</sup>	8 <sup>‡</sup>
Deciduous leaves (beech)			Ignites	4	6	8
Fine grass (cheat)			Ignites	5	8	10
Coarse grass (sedge)			Ignites	6	9	11
Pine needles, brown (ponderosa)			Ignites	10	16	21
<u>Construction Materials</u>						
Roll roofing, mineral surface			Ignites	**	>34	>116
Roll roofing, smooth surface			Ignites	**	30	72
Plywood, douglas fir			Flaming during exposure	9	16	20
Rubber, pale latex			Ignites	50	80	110
Rubber, black			Ignites	10	20	25
<u>Other Materials</u>						
Aluminum aircraft skin (0.020 in. thick) coated with 0.002 in. of standard white aircraft paint			Blisters	15	30	40
Cotton canvas sandbags, dry filled			Failure	10	18	32
Coral sand			Explodes (popcorning)	15 <sup>‡</sup>	27 <sup>‡</sup>	47 <sup>‡</sup>
Siliceous sand			Explodes (popcorning)	11	19	35

\* Radiant exposures for the indicated responses (except where marked ‡) are estimated to be valid to  $\pm 25\%$  under standard laboratory conditions. Under typical field conditions the values are estimated to be valid within  $\pm 50\%$  with a greater likelihood of higher rather than lower values. For materials marked ‡, ignition levels are estimated to be valid within  $\pm 50\%$  under laboratory conditions and within  $\pm 100\%$  under field conditions. For low air burst, values of t<sub>max</sub> of 0.2, 1.0, and 3.2 sec correspond roughly to yields of 40 kt, 2 Mt, and 24 Mt, respectively.

\*\* Data are not available or appropriate scaling not known.

† Radiant exposures for ignition of these substances are highly dependent on the moisture content.

## SURVIVAL IN FIRE AREAS

The best documented fire storm in history (but not the one causing the greatest loss of life) occurred in Hamburg, Germany during the night of July 27-28, 1943, as a result of an incendiary raid by Allied forces. Factors that contributed to the fire included the high fuel loading of the area and the large number of buildings ignited within a short period of time.

The main raid lasted about 30 minutes. Since the air raid warning and the first high explosive bombs caused most people to seek shelter, few fires were extinguished during the attack. By the time the raid ended, roughly half the buildings in the 5 square-mile fire storm area were burning, many of them intensely. The fire storm developed rapidly and reached its peak in two or three hours.

Many people were driven from their shelters and then found that nearly everything was burning. Some people escaped through the streets; others died in the attempt; others returned to their shelters and succumbed to carbon monoxide poisoning.

Estimates of the number that were killed range from about 40,000 to 55,000. Most of the deaths resulted from the fire storm. Two equally heavy raids on the same city (one occurred two nights earlier; the other, one night later) did not produce fire storms, and they resulted in death rates that have been estimated to be nearly an order of magnitude lower.

More surprising than the number killed is the number of survivors. The population of the fire storm area was roughly 280,000. Estimates have been made that about 45,000 were rescued, 53,000 survived in non-basement shelters, and 140,000 either survived in basement shelters or escaped by their own initiative.

### 9-25 Causes of Death

The evidence that can be reconstructed from such catastrophes as the Hamburg fire

storm indicates that carbon monoxide and excessive heat are the most frequent causes of death in mass fires. Since the conditions that offer protection from these two hazards generally provide protection from other hazards as well, the following discussion is limited to these two causes of death.

*Carbon Monoxide.* Burning consists of a series of physical and chemical reactions. For most common fuels, one of the last of the reactions is the burning of carbon monoxide to form carbon dioxide near the tips of the flames. If the supply of air is limited, as it is likely to be if the fire is in a closed room or at the bottom of a pile of debris from a collapsed building, the carbon monoxide will not burn completely. Fumes from the fire will contain a large amount of this tasteless, odorless, toxic gas.

During the Hamburg fire, many basement shelters were exposed to fumes. Imperfectly fitting doors and cracks produced by exploding bombs allowed carbon monoxide to penetrate these shelters. The natural positions of many of the bodies recovered after the raid indicated that death had often come without warning, as is frequently the case for carbon monoxide poisoning.

Carbon monoxide kills by forming a more stable compound with hemoglobin than either oxygen or carbon dioxide will form. These latter are the two substances that hemoglobin ordinarily carries through the blood stream. Carbon monoxide that is absorbed by the blood reduces the oxygen carrying capacity of the blood, and the victim dies from oxygen deficiency.

As a result of the manner that carbon monoxide acts, it can contribute to the death of a person who leaves a contaminated shelter to attempt escape through the streets of a burning city. A person recovering from a moderate case of carbon monoxide poisoning may feel well while he is resting, but his blood may be unable

[REDACTED]  
to supply the oxygen his body needs when he exerts himself. After the air raid at Hamburg, victims of carbon monoxide poisoning, apparently in good health, collapsed and died from the strain of walking away from a shelter. It is suspected that many of the people who died in the streets of Hamburg were suffering from incipient carbon monoxide poisoning.

[REDACTED] *Heat.* The body cools itself by perspiration. When the environment is so hot that this method fails, body temperature rises. Shortly thereafter, the rate of perspiration decreases rapidly, and, unless the victim finds immediate relief from the heat, he dies of heat exhaustion. Death from excessive heat may occur in an inadequately insulated shelter; it also may occur in the streets if a safe area cannot be located in a short time.

#### 9-26 Shelters [REDACTED]

[REDACTED] The results of the Hamburg fire storm illustrate the value of shelters during an intense mass fire. The public air raid shelters in Hamburg had very heavy walls to resist large bombs. Reinforced concrete three feet thick represented typical walls. Some of these shelters were fitted with gas proof doors to provide protection from poison gas. These two features offered good protection from the heat and toxic gases generated by the fire storm.

[REDACTED] The public shelters were of three types:  
• *Bunkers.* These were large buildings of several shapes and sizes, designed to withstand direct hits by large bombs. The fire storm area included 19 bunkers designed to hold a total of about 15,000 people. Probably twice this number occupied the bunkers during the fire storm, and all of these people survived.

• *Splinterproof Shelters.* These were long single story shelters standing free of other buildings and protected by walls of reinforced concrete at least 2-1/2 feet thick.

No deaths resulting from the fire storm were reported among occupants of these shelters. These structures were not gas-proof. Distance from burning structures and low height of the shelters probably provided protection from carbon monoxide.

• *Basement Shelters.* The public shelters that were constructed in large basements had ceilings of reinforced concrete 2 to 5 feet thick. Although reports indicate that some of the occupants of these shelters survived and some did not, statistics to indicate the chance of survival in such structures are not available.

• *Private Basement Shelters.* Private basements were constructed solidly, but most of them lacked the insulating value of very thick walls and the protection of gas-tight construction. Emergency exits (usually leading to another shelter in an adjacent building) could be broken if collapse of the building caused the normal exit to be blocked. As a result of the total destruction in the fire storm area, this precaution was of limited value. Many deaths occurred in these shelters as a result of carbon monoxide poisoning, and the condition of the bodies indicated that intolerable heat followed the carbon monoxide frequently. In some cases, the heat preceded the poisonous gas and was the cause of death. Generally, these shelters offered such a small amount of protection that the occupants were forced out within 10 to 30 minutes. Most of these people were able to move through the streets and escape. Others were forced out later when the fire storm was nearer its peak intensity, and few of these escaped. A few people survived in private basement shelters.

[REDACTED] Experience in Hamburg and other mass fire areas suggests the following requirements for

shelters for fire protection:

- **Location.** Shelters should be located as far away from combustible structures as possible. The bottom of a mass of burning debris is very hot and can remain so for days. An open area also may be exposed to considerable heat, but not so much as the basement of a burned-out building. Three feet of earth will provide sufficient insulation for a shelter if no heavy fuels are nearby. However, material scattered by the blast wave could fall on a shelter and render it less safe. The choice of a suitable location for a shelter is most difficult in heavily built-up areas, where mass fires are most likely to occur. Shelters in such areas would have to be designed to withstand the severe environment to which they would be subjected in case of a mass fire. When the shelters in Hamburg were built, the problems of mass fires were not anticipated.
- **Ventilation.** Any shelter that is large enough to house its occupants in reasonable comfort contains sufficient air to sustain life for the duration of a mass fire. The shelter should be constructed so that it can be sealed from the entry of gases from the outside during the period of active burning. After the fire subsides, air will be available inside the shelter if burning debris has not fallen on or near the air intake.
- **Provisions.** If escape from a shelter is necessary, wet coats or blankets would improve the chance of survival in the open. Since any shelter built for protection against a mass fire would logically serve also as a fallout shelter, such items as blankets and water normally would be available.

#### 9-27 Escape from the Fire Areas

A large number of people, chiefly the occupants of basement shelters, escaped from

the Hamburg fire simply by leaving while the streets were still passable. In areas where damage is sufficiently light that people can attempt escape, the rate at which the fire builds up is expected to be slow enough to allow 30 minutes or more before movement through the streets will become dangerous.

Escape from the Hamburg fire storm area was simplified by the limited size of the fire. In the event of a mass fire caused by a nuclear attack, the fire area probably will be much larger. Although escape to the edge of the fire may be impossible, parks, bodies of water, or even areas that are not heavily built up may offer relative safety from the fire.

As the fire grows in intensity, selection of a suitable escape route becomes important. Moving through a narrow street, with tall buildings burning intensely on both sides, will subject people to an excessive amount of heat.

Preplanned escape routes are desirable. The safest routes are those that minimize exposure to thermal radiation from burning structures. A safe street would be wide compared to the heights of the buildings facing it. Masonry buildings with few windows would be a lesser threat than buildings with many windows. The solid wall blocks radiant exposure from fires burning inside the building, and it also protects the contents of the building from direct ignition by the thermal pulse from the nuclear weapon.

Simple rules for distinguishing safe from unsafe streets are not available; however, calculations of the street width for which the thermal radiation would be intense enough to ignite clothing in a short time have been made, assuming that buildings on both sides of the street were burning. The results of these calculations are shown in Table 9-4.

Whether or not such streets are safe will depend on many factors, such as fire intensity, percentage of the building fronts occupied by windows, wind speed and direction, protective

clothing, and exposure time. In general, the streets of Hamburg were 45 to 60 feet wide, and the buildings were 3 to 5 stories high. Table 9-4 predicts that such streets would be dangerous, and experience shows that they were. However, even these streets provided escape for some.

Table 9-4. [REDACTED] Minimum Structure Separation for Escape Route [REDACTED]

Building Height (feet)	Distance Between Buildings (feet)
20	40
30	57
40	67
50	83
60	96

#### 9-28 Safe Areas Within the Fire [REDACTED]

[REDACTED] Experience indicates that large open areas within a fire storm area probably are safe. A park 1,000 feet in diameter provided adequate protection from the Hamburg fire storm; a similar area of 400 x 400 feet did not.

[REDACTED] In Tokyo, during the Kanto earthquake and fire of 1923, fire whirlwinds sweeping across some large open areas killed many who would otherwise have survived. Thus, safety in a particular location depends to some extent on unpredictable aspects of the fire.

### SECTION IV

#### THERMAL RADIATION DEGRADATION OF STRUCTURAL RESISTANCE TO AIR BLAST [REDACTED]

[REDACTED] Section III of this chapter contains a description of the properties of materials that might result in ignition or degradation of their physical properties. The emphasis of the discus-

sion in Section III concerns the ignition of combustible materials. This section provides a somewhat expanded treatment of the degradation of structural resistance to air blast that is brought about by exposure to thermal radiation.

[REDACTED] The problem of integrated thermal/blast effects can be divided into several elements. One element is the free field thermal and air blast environments to which a system element is exposed. Methods of predicting these environments are presented in Chapters 2 and 3. As pointed out in Chapter 3, prediction of the thermal environment is difficult because of the importance of climatic conditions. A statistical or probabilistic description of weather conditions frequently will have to be used to form some estimate of the validity of the results.

[REDACTED] The first element of the overall problem treated in this section is the coupling of thermal energy into the structure or system element of interest. The condition of the target surface, its orientation to the detonation, and coatings employed all can affect the amount of thermal energy that is absorbed by the target.

[REDACTED] The second element is the mechanisms for the loss of energy from the structure through convective heat losses or reradiation. The third element is the effect of absorbed energy on the state of the target material. The primary effect of this change of state is the fourth element, which is the change in material properties.

[REDACTED] The final and fifth element of the problem is the effect of changes in material properties on the structural resistance to air blast loading.

[REDACTED] Insufficient data are available concerning the thermophysical properties of nonmetallic materials to provide a realistic discussion of the combined blast/thermal effects on such materials. Any current prediction would be highly uncertain, both with regard to the occurrence of any specific physical phenomena and to the quantitative evaluation of the phenomena. Con-

sequently the discussion in this section will be limited to metallic materials.

## THERMAL ENERGY ABSORBED

### 9-29 Absorption

The amount of thermal radiation that a metallic element will absorb depends on the properties of the metal, color, surface condition, orientation to the burst, the absence or presence of some type of coating (either accidental such as dirt or grease or intentional such as a paint system).<sup>\*</sup> The amount of thermal energy absorbed by a target usually is determined by multiplying the incident energy by an absorption coefficient. The absorption coefficient cannot be directly measured; however, a good estimate can be made by performing spectral measurements of reflectance over the range of wavelengths representative of the nuclear radiation spectral distribution, and finding an average value of reflectance. The coefficient of absorptance then equals one minus this average value of reflectance. The absorptance determined in this manner is valid only as long as the surface does not change as a result of the absorbed thermal energy. Another approach is to divide the quantity of energy absorbed by the incident energy. The absorbed energy is determined from experimentally determined temperature vs time relationships and appropriate theoretical energy balance relationships.<sup>†</sup> Some typical values for absorption coefficients for bare metals are shown in Table 9-5. A value of 0.5 would be a good value to assume for the absorption coefficient in the absence of more definitive data for a specific system under investigation.

A coating or surface treatment on a metal substrate can alter the effective absorption coefficient significantly, and thereby can alter the amount of energy absorbed by the metal structure. The amount of energy absorbed depends on color, thickness, adhesiveness, and heat transfer characteristics of the coating. The

Table 9-5. Absorption Coefficients for Bare Metals

Material	Absorption Coefficient
Polished metals	0.25-0.5
Especially clean aluminum	0.2-0.4
Clean aluminum	0.5
Unpolished metals	0.45-0.55
Average over aircraft	0.5

most common type of coating is, of course, paint. The importance of paint in altering the amount of thermal radiation absorbed was noted in early investigations where it was found that the thin aircraft skin under painted insignia had melted, whereas the skin of adjacent areas was not affected. It should not be assumed, however, that paint or other coating is necessarily a detriment. In some instances the smoke that results from the breakdown of the paint can reduce the amount of energy absorbed and thereby reduce the maximum temperature reached by the substrate. Figure 9-8 illustrates this factor. The only true general statement that can be made about coatings is that they can alter the amount of thermal energy absorbed by the substrate. In fact some coatings, even paint systems, can be designed to reduce the amount of energy absorbed. As a general rule, however, most coating systems on present tactical military equipment

\* Implicit in this statement and throughout this discussion is the fact that energy coupling depends on the wavelength of the incident radiation.

† Absorptance is a function of time and temperature, although an average value usually is employed. This function when known may be found as an input specification for certain computer programs.

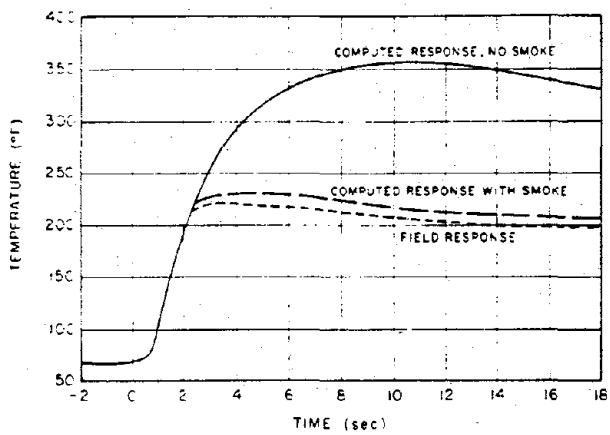


Figure 9-8. [REDACTED] Exposed Facing Temperature-Time Histories of Aluminum Honeycomb. Facing, 0.016-in. Gray Painted Skin; Core 1/8-in., Cell Size 1/2-in. Thick. 21.24.2 cal/cm<sup>2</sup>, 3.8 Mt [REDACTED]

will cause an increase in the amount of energy absorbed. The mechanisms of the response of coatings and the transfer of energy to the substrate are so complex that theoretical descriptions have not been successful. The response of coatings depends upon both the rate at which thermal radiation is received and the total incident energy. A given amount of radiation received at a slow rate may only cause discoloration or slight scorching, whereas if it were received at a very rapid rate it would cause charring or blistering. The latter response is more typical in a nuclear environment. The change in state of the coating reduces the amount of energy available to be transferred to the substrate, because these processes are irreversible. However, the change in state usually increases the absorption coefficient of the coating, and the net result usually is an increase on the amount of energy absorbed by the substrate. An exception occurs if the absorption coefficient was initially high, and energy was absorbed by the smoke layer generated by the decomposing paint. Coatings that respond by

physically separating from the surface, i.e., blister, potentially can reduce the amounts of energy transferred to the substrate. Since the response of the coating-substrate system to nuclear weapon thermal radiation is so complex, effective absorption coefficients usually are determined experimentally.

[REDACTED] The average value of the absorption coefficient,  $A$ , depends on the properties of the substrate as the flow of thermal energy from the coating influences the response of the coating. A series of experiments with laser heating provides data to illustrate this point. Various metallic samples were prepared with a Silicon-carbide-synar binder coating (spectrophotometric measurements gave an average absorption coefficient of 0.85 for the coated aluminum sample for equilibrium temperatures of 70 and 600°F for a 10.6 micron wavelength). The average values of the absorption coefficients for a range of irradiances based on temperature vs time data are shown in Table 9-6. The effect of substrate properties is significant.

[REDACTED] Values of absorption coefficients are shown in Table 9-7. Generally, values range from 0.3 to 0.6 for light or reflective paints, and from

Table 9-6. [REDACTED] Average Absorption Coefficients for Laser Heated Coated Substrates [REDACTED]

Substrate	Average Absorption Coefficient
2024-T81 clad aluminum alloy	0.7 ± 0.1
6AL-4V annealed titanium	0.35 ± 0.1*
301 full hard stainless steel	0.80 ± 0.05

[REDACTED] Evaluation of titanium specimens showed considerable scatter. Erratic behavior probably resulted from improper bonding of the coating and cracking or flaking of the coating during straining.

Table 9-7. Representative Values of Absorption Coefficients for Metals with Various Coatings or Surface Treatments

Substrate	Coating or Surface Treatment	Absorption Coefficient
Metallic skins	Aluminum paint	0.5
Painted metals (aircraft skins)	White paint	0.3 - 0.5
	White paint (clean)	0.25
	White paint w/oil film	0.30
	Yellow paint	0.4 - 0.55
	Olive paint	0.6 - 0.7
	Gray paint (clean)	0.6
	Black paint	0.65 - 0.95
	Insignia blue	0.9
5032-H32AL	Black paint	0.7 - 1.0
Aluminums	Reflecting white paint	0.32
	Camouflage paint	1.00
6061 Al-Mg alloy	Haze gray Navy paint	0.78 ± 0.04
	Volcanol	0.99 ± 0.05
2024-T3	Anodized black	0.67

0.6 to 1.0 for dark paints or treated surfaces.

It is apparent that the selection of an absorption coefficient based on the information in Table 9-7 for use in analyzing the response of a military system could be in error by as much as ±50 percent. Currently, the best solution is to perform upper and lower bound calculations. The upper and lower bound calculations should be based on the best estimate of the condition of the surface at the time of exposure, i.e., dirty, corroded, prior exposures, etc.

One additional factor affects the amount of energy absorbed. This factor is the orientation of the surface to the thermal pulse. Ideally, if incident parallel rays are assumed, with no scattering, reflection or refraction, the target

surface receives all of the radiation if it is oriented normal to the rays. If the surface is rotated about an axis normal to the rays, it cuts fewer of the rays, and the amount of thermal energy received is reduced. The energy received by a differential area on a curved surface also can be treated in this manner. With such assumptions, the absorbed energy function takes the following form:

$$Q_a = Q A_e \cos \theta$$

where

$Q$  = incident energy, usually expressed in cal/cm<sup>2</sup>

$Q_a$  = absorbed energy, usually expressed in cal/cm<sup>2</sup>

$A_e$  = effective absorption coefficient

$\theta$  = incident angle, angle between a line from the source to the surface and a line normal to the plane of the surface.

Under those ideal conditions, the amount of absorbed energy follows the cosine law; however, there will be conditions where scattering, reflection, and refraction, will invalidate the parallel ray assumption in addition to altering  $Q$ . This would principally occur at large angles of incidence such as shown schematically in Figure 9-9. A computer program called TRAP has recently been developed to handle these conditions.

Figure 9-9 also illustrates the amount of energy received by the surface of a cylinder with its axis oriented normal to the ray paths. The quantity  $\theta$  then becomes the distance, in ra-

dians, along the circumference, from the point nearest the source.

Both the absorption coefficient and orientation are important in determining the amount of energy absorbed into the target. Errors in orientation are of greater significance at large angles on incidence; however, orientation usually can be inferred, at least for worst cases, whereas the absorption coefficient usually is not well known unless it has been determined experimentally.

### 9-30 Energy Losses

The absorption of thermal radiation energy into a material has been discussed in the previous paragraph. Before discussing the effect of this absorbed energy on material properties or change in structural resistance, the form and significance of energy losses from the material

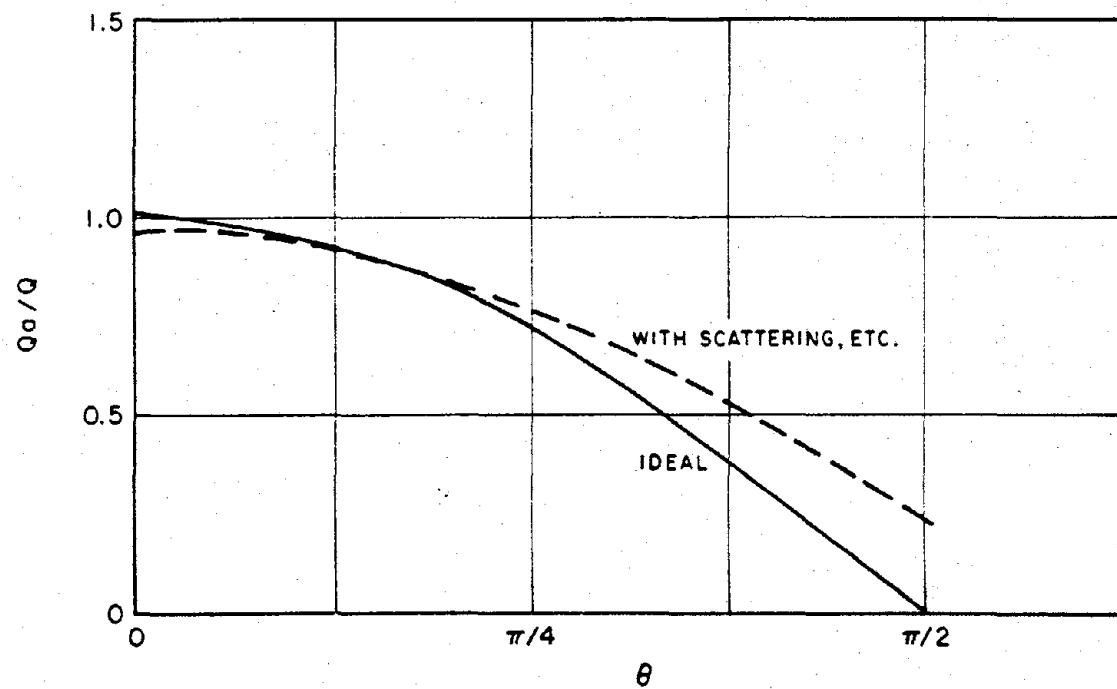


Figure 9-9. Schematic Comparison of Ideal Cosine Law with Function Including Scattering, Reflection, and Refraction

must be discussed. The three ways in which thermal energy can be dissipated are conduction, radiation, and convection. For purposes of this discussion, conductive dissipation is not really a loss, in that energy is redistributed throughout the material system rather than lost from the system. This form of heat dissipation is considered in more detail in the following subsection that discusses the change in material state, and the discussion of temperature profiles.

Radiation losses normally are considered negligible, because the temperature rises in a material are relatively small, even though the radiation heat loss is a function of the fourth power of absolute temperatures. The heat loss through radiation is expressed by:

$$Q_r = \sigma\epsilon(T^4 - T_0^4)$$

where

$Q_r$  = radiative heat loss, cal/cm<sup>2</sup>·sec,

$\sigma$  = Stephan Boltzmann Coefficient =  $1.36 \times 10^{-12}$  cal/cm<sup>2</sup> sec °K<sup>-4</sup>,

$\epsilon$  = emissivity, nondimensional,

$T$  = absolute temperature, °K, of radiator (may be time dependent),

$T_0$  = absolute temperature, °K, of surrounding air.

If a 200°C temperature difference is assumed, and an emissivity of 0.2 (for oxidized aluminum at temperatures of a few hundred °C), and the ambient air temperature is 300°K, the radiative heat loss becomes:

$$\begin{aligned} Q_r &= (1.36 \times 10^{-12})(0.2)(500^4 - 300^4) \\ &= 1.48 \times 10^{-2} \text{ cal/cm}^2 \cdot \text{sec} \end{aligned}$$

If the temperature rise is 400°C then  $Q_r$  becomes equal to  $6.3 \times 10^{-2}$  cal/cm<sup>2</sup> sec. Thus, it

can be seen that even at high elevated temperatures, the heat loss through radiative processes is small.

Convective heat losses occur when there is a flow of air over the heated surface. This type of heat loss is most important for aircraft in flight and is a weak function of position on the airfoil, and the speed and altitude of the aircraft. The rate of convective heat loss also depends on whether the boundary layer flow is laminar or turbulent. These processes are generally understood, and a number of formulas that are available are given below:

$$h_{cv} = 0.67(10)^{-4} T^{0.3} \frac{(V\rho)^{0.8}}{x^{0.2}}$$

where

$h_{cv}$  = convective heat loss coefficient for turbulent flow,

$T$  = air temperature, °R,

$V$  = flight speed, ft/sec,

$\rho$  = density of air, lb/ft<sup>3</sup>,

$x$  = distance from leading edge of airfoil, ft.

$$h_{cv} = 0.176 \rho V C_p (\log_{10} Re)^{-2.45},$$

$$h_{cv} = 0.01445 k/x (Re)^{0.8} (Pr)^{0.33},$$

$$h_{cv} = 0.0282 k/x (Re)^{0.8} (Pr)^{0.33},$$

$$h'_{cv} = 0.318 k/x (Pr)^{1/3} (Re)^{1/2},$$

$$h'_{cv} = 0.332 \rho V C_p (Pr)^{-2/3} (Re)^{-1/2},$$

where

$h_{cv}$  = convective heat loss coefficient for turbulent flow, cal/cm<sup>2</sup> sec °C

$h'_{cv}$  = convective heat loss coefficient for laminar flow,  $\text{cal}/\text{cm}^2 \cdot \text{sec} \cdot {}^\circ\text{C}$

$\rho$  = density of air,  $\text{gm}/\text{cm}^3$

$V$  = flight speed,  $\text{cm}/\text{sec}$

$C_p$  = specific heat of air,  $\text{cal}/\text{gm} \cdot {}^\circ\text{C}$

$Re$  = Reynolds number,  $\rho Vx/\mu$ , dimensionless

$k$  = thermal conductivity of air,  $\text{cal}/\text{cm} \cdot \text{sec} \cdot {}^\circ\text{C}$

$x$  = distance from leading edge of airfoil, cm

$Pr$  = Prandtl number,  $C_p\mu/k$ , dimensionless

$\mu$  = viscosity of air,  $\text{gm}/\text{sec} \cdot \text{cm}$

These formulas are based on the assumption that a reasonable approximation may be obtained by analysis of airflow over a heated flat plate. Experimental data indicate that the average error in using this approximation may be as much as 30 percent with a mean error of from 10 to 15 percent. The value for  $h_{cv}$  ranges from zero to 0.03  $\text{cal}/\text{cm}^2 \cdot \text{sec} \cdot {}^\circ\text{C}$  for a range of reasonable air properties and velocities. Generally, convective heat losses are marginally important for relatively low yield weapons; however, for long duration thermal pulses and under conditions when the temperature difference between the aircraft skin and the air boundary layer is large, the convective heat loss can be significant for high speed aircraft.

Values of  $h_{cv}$  have been calculated (see Table 9-8) for purposes of comparing the results of the equations given above, under the following assumed conditions.

Aircraft type = fixed wing

Aircraft speed = 100 mph ( $4.47 \times 10^3$   $\text{cm}/\text{sec}$ )

Aircraft altitude = 1,000 ft

Air temperature =  $70^\circ\text{F}$ ,  $20^\circ\text{C}$

$x = 4$  ft, 121.92 cm

$\rho = 7.5(10)^{-2}$   $\text{lb}/\text{ft}^3$

Table 9-8. Values of  $h_{cv}$  Obtained from Various Functions in the Order in Which the Equations are Given Above

Flow Condition	$h_{cv}$ ( $\frac{\text{cal}}{\text{cm}^2 \cdot \text{sec} \cdot {}^\circ\text{C}}$ )
Turbulent	$2.27(10)^{-3}$
	$2.27(10)^{-3}$
	$1.14(10)^{-3}$
	$2.23(10)^{-3}$
Laminar	$2.15(10)^{-4}$
	$2.82(10)^{-4}$

$$= 1.2(10)^{-3} \text{ gm}/\text{cm}^3$$

$$k = 6.0874(10)^{-5} \text{ cal}/\text{cm} \cdot \text{sec} \cdot {}^\circ\text{C}$$

$$C_p = 0.2404 \text{ cal}/\text{gm} \cdot {}^\circ\text{C}$$

$$\mu = 1.798(10)^{-4} \text{ gm}/\text{cm} \cdot \text{cm}$$

The use of the convective heat loss coefficient,  $h_{cv}$ , is shown below:

$$Q_{cv} = h_{cv} (T_s - T)$$

where

$Q_{cv}$  = convective heat loss,  $\text{cal}/\text{cm}^2 \cdot \text{sec}$

$T_s$  = surface temperature,  ${}^\circ\text{C}$  (may be time dependent)

$T$  = surrounding air temperature,  ${}^\circ\text{C}$

For high speed aircraft, it may not be appropriate to assume that the temperature of the surrounding air is the temperature of the air boundary layer next to the heated surface. This

is particularly true if aerodynamic heating occurs. For this situation, the recovery temperature  $T_r$  should replace  $T$  in the equation given above.

For tactical systems of interest to this section, radiative and convective heat losses generally can be neglected. However, these are and normally should be included in detailed analyses and computer calculations for completeness, particularly for high speed aircraft and large yield weapons.

## CHANGES IN MATERIAL STATE AND MATERIALS PROPERTIES

### 9-31 Changes in Material State

The change in material state of primary interest is the change in temperature caused by absorbed thermal radiation. The temperature changes are controlled by the energy absorbed in the material as a function of time and position and by the geometry of the member being analyzed. Geometry can have a significant impact on heat flow through the member as well as heat absorption and losses. There are a number of techniques available for determining temperature changes. These techniques vary from simple formulas to large computer programs depending on the simplifying assumptions that are made and the complexity of the system geometry. The greatest amount of effort has been devoted to the study of temperature changes in flat plates, primarily because of the interest in aircraft safety/survivability problems. Therefore, the following discussion is dominated by analysis of flat plates, although most of what can be learned about the processes affecting plate temperature applies to other geometries because the basic equations describing the processes are the same.

Plates can be divided into several types according to the temperature profile through the plate. A thermally "thin" plate usually is defined as a plate where the temperature gradient

between the front and back of the plate is small. Thermally thin plates simplify the analysis problem, because, if a significant thermal gradient exists, the thermal stresses become more complex. Plates usually are assumed to be one dimensional, with no heat flow to a supporting structure, so heat sink effects can be neglected, unless the plate is part of a fuel tank.

Whether a plate is thermally thin depends not only on the thermophysical properties of the material, but also on the thermal pulse characteristics and the time during the pulse that the criterion is applied. Some materials conduct heat more quickly than others, and the temperature on the back face of these materials will not lag behind the temperature on the front as much as for materials with lower conductivities. For example, the thermal conductivity of aluminum is about  $0.4 \text{ cal/sec} \cdot \text{cm} \cdot {}^\circ\text{C}$ , and that of titanium is about  $0.04 \text{ cal/sec} \cdot \text{cm} \cdot {}^\circ\text{C}$ . Therefore, aluminum conducts 10 times as much heat as titanium in a given amount of time. Other material factors that control the ratio of front to back temperature are specific heat, density, and thickness.

The temperature difference also depends on pulse characteristics. For a pulse that is delivered slowly, there may be sufficient time for energy to be conducted to the back face, so the thermal gradient at the time of interest is minimized. Conversely, a pulse that is delivered rapidly may cause a steep thermal gradient. For a given pulse, material, and thickness, the time at which the temperature response is of interest determines whether the thermal gradient is small.

A number of techniques have been developed to determine whether a plate can be considered to be thermally thin. One technique that gives a good approximation is illustrated in Figure 9-10. The values of  $\eta = t/t_{\max}$  and  $\alpha t_{\max}/b^2$  must be evaluated to use the curves in Figure 9-10. From Chapter 3

$$t_{\max} = 0.043 W^{0.43} (\rho/\rho_0)^{0.42} \text{ sec.}^*$$

where  $t_{\max}$  is the time to the principle thermal maximum,  $W$  is the weapon yield in kilotons, and  $\rho/\rho_0$  is the ratio of the air density at the burst altitude to the air density at sea level. The parameter  $\alpha$  is defined as

$$\alpha = k/\rho_m C_p \text{ cm}^2/\text{sec}$$

where

$k$  = thermal conductivity of air, cal/cm · sec · °C.

$\rho_m$  = material density, gm/cm<sup>3</sup>.

$C_p$  = specific heat of air, cal/gm · °C

and  $b$  is the thickness of the plate in centimeters. The point where the values of  $\eta$  and  $\alpha t_{\max}/b^2$  meet determines whether the plate is

thin, finite, or thick. A thin plate is one in which the difference between back and front temperatures is less than 10 percent. A thick plate is one in which there is no temperature rise on the back face. A finite plate falls between the other two criteria.

A technique for predicting the temperatures of thermally thin plates uses the relationships shown in Figure 9-11. This technique is believed to provide good results over a fairly wide range of problems of interest. The technique assumes that thermophysical properties and the rate of convective heat loss are constant, that radiation losses are negligible, and that there is no heat loss from the back of the plate.

The examples provided in this section will all be concerned with air bursts that are sufficiently low that the term  $(\rho/\rho_0)^{0.42}$  is near enough to 1.0 to be neglected (e.g., at 4,000 feet  $(\rho/\rho_0)^{0.42} \approx 0.99$ ). Therefore, the approximation  $t_{\max} \approx 0.043 W^{0.43}$  will be used throughout the remainder of this section.

### Problem 9-1. Calculation of Thermal Thickness of a Metal Plate

Figure 9-10 contains curves that define regions where metal plates may be considered thermally thin, finite, and thick, respectively. The curves are plotted as a function of the parameters  $\eta$  and  $\alpha t_{\max}/b^2$ , which are defined in paragraph 9-31. Their use is demonstrated in the following example.

*Example*

*Given:* A 5086 Aluminum alloy plate is an important part of a structure under analysis. The plate is 0.875 cm thick and the range of air blast exposures for the system of which it is a part are expected to be from 8 to 15 psi from a 100 kt explosion at a height of burst of 1,000 feet.

*Find:* Whether the plate can be considered thermally thin.

*Solution:* The corresponding height of burst for a 1 kt explosion is

$$h_1 = \frac{h}{(W^{1/3})} = \frac{1,000}{(100)^{1/3}} = 215 \text{ feet.}$$

From Figures 2-18 and 2-19, Chapter 2, the ground distances from a 1 kt explosion at a height of burst of 215 feet that correspond to 15 and 8 psi overpressure are 895 and 1,250 feet respectively. From Figure 2-28, Chapter 2, the times of arrival of the blast wave from a 1 kt explosion to these distances are 0.37 seconds and 0.61 seconds, respectively. The corresponding times for a 100 kt explosion are

$$t = t_1 W^{1/3}$$

$$t = (0.37)(100)^{1/3} = 1.72 \text{ sec for 15 psi,}$$

and

$$t = (0.61)(100)^{1/3} = 2.83 \text{ sec for 8 psi.}$$

The time to final maximum for a 100 kt low air burst is

$$t_{\max} \approx 0.043 W^{0.43}$$

$$= (0.043)(100)^{0.43} = 0.31 \text{ sec.}$$

Therefore,

$$\eta = t/t_{\max}$$

$$\eta = \frac{1.72}{0.31} = 5.5 \text{ for 15 psi,}$$

and

$$\eta = \frac{2.83}{0.31} = 9.1 \text{ for 8 psi.}$$

The properties of the alloy are

$$k = 0.28 \text{ cal/sec} \cdot {}^{\circ}\text{C},$$

$$C_p = 0.22 \text{ cal/gm} \cdot {}^{\circ}\text{C},$$

$$\rho = 2.66 \text{ gram/cm}^3.$$

Since

$$\alpha = \frac{k}{\rho C_p},$$

$$\begin{aligned} \frac{\alpha t_{\max}}{b^2} &= \frac{kt_{\max}}{\rho C_p b^2} \\ &= \frac{(0.28)(0.31)}{(2.66)(0.22)(0.875)^2} \\ &= 0.19. \end{aligned}$$

*Answer:* From Figure 9-10, at the 15 psi overpressure level where  $\eta = 5.5$ , the plate should be considered finite; at the 8 psi overpressure level, where  $\eta = 9.1$ , the plate can be considered thermally thin.

*Related Material:* See paragraph 9-31.

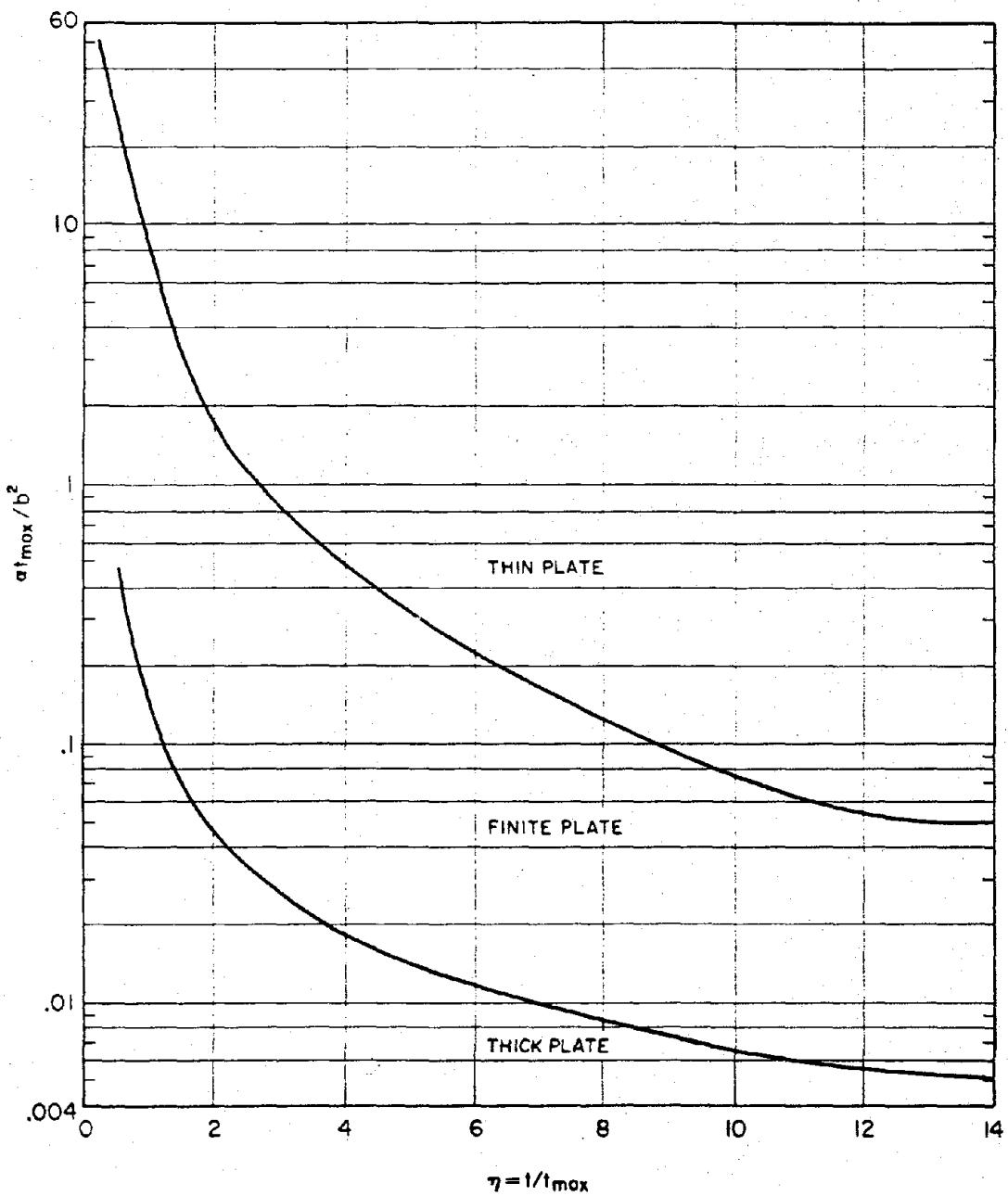


Figure 9-10. [REDACTED] Thin Plate, Thick Plate, and Finite Plate Regions for Exposure to Nuclear Weapons Thermal Radiation [REDACTED]

The variables used in this technique have units in the cgs system and have been defined previously; however, they are listed below for convenience.

$T_0$  = temperature of the plate prior to exposure,

$\Delta T$  = temperature rise,  $^{\circ}\text{C}$ ,

$A$  = absorption coefficient

$Q$  = thermal exposure,  $\text{cal}/\text{cm}^2$  (effective

thermal exposure may be used where  $Q = Q \cos \theta$ ),

$\rho_m$  = specific gravity of material,  $\text{gm}/\text{cm}^3$ ,

$C_p$  = specific heat,  $\text{cal}/\text{gm} \cdot ^{\circ}\text{C}$ ,

$b$  = plate thickness, cm,

$h_{cv}$  = convective heat loss,  $\text{cal}/\text{cm}^2 \cdot \text{sec} \cdot ^{\circ}\text{C}$ ,

$\eta = t/t_{max}$ .

Use of the technique is illustrated in Problem 9-2.

### Problem 9-2. Calculation of Temperature Rise in a Thermally Thin Plate

Figure 9-11 contains a family of curves that relate thermophysical properties of a thin metal plate to thermal pulse parameters in a manner that allows calculation of the temperature rise in the plate. The procedures for the calculation are made clear in the following examples. Symbols for the various parameters are listed in paragraph 9-31.

#### Example 1

*Given:* A 6061-16 Aluminum alloy plate is exposed to the thermal pulse from a 100 kt low air burst at a location where the incident radiant energy is 76 cal/cm<sup>2</sup> and arrives at an angle of incidence of 30°. Properties of the plate are

$$T_0 = 30^\circ\text{C},$$

$$A = 0.8,$$

$$\rho_m = 2.7 \text{ gm/cm}^3,$$

$$C_p = 0.216 \text{ cal/gm} \cdot ^\circ\text{C},$$

$$b = 0.15875 \text{ cm},$$

$$h_{cv} = 0.$$

*Find:* The temperature of the plate when  $\eta = 2, 4$ , and  $6$ .

*Solution:* The effective radiant exposure is

$$Q_e = Q \cos \theta = 76 \cos 30^\circ = 65.8 \text{ cal/cm}^2.$$

From Figure 9-11, with

$$\frac{h_{cv} t_{max}}{\rho C_p b} = 0,$$

when

$$\eta = 2, \frac{\Delta T}{AQ/\rho C_p b} = 0.47,$$

when

$$\eta = 4, \frac{\Delta T}{AQ/\rho C_p b} = 0.67,$$

and when

$$\eta = 6, \frac{\Delta T}{AQ/\rho C_p b} = 0.74.$$

The value of  $AQ/\rho C_p b$  is

$$\frac{AQ_e}{\rho C_p b} = \frac{(0.8)(65.8)}{(2.7)(0.216)(0.15875)} = 569^\circ\text{C}.$$

The temperature rises are

$$\Delta T = (0.47)(569) = 267^\circ\text{C} \text{ for } \eta = 2,$$

$$\Delta T = (0.67)(569) = 381^\circ\text{C} \text{ for } \eta = 4,$$

and

$$\Delta T = (0.74)(569) = 421^\circ\text{C} \text{ for } \eta = 6.$$

*Answer:* The plate temperatures are

$$T = T_0 + \Delta T.$$

Therefore,

$$T_{\eta=2} = 30 + 267 = 297^\circ\text{C}$$

$$T_{\eta=4} = 30 + 381 = 411^\circ\text{C}$$

$$T_{\eta=6} = 30 + 421 = 451^\circ\text{C}.$$

#### Example 2

*Given:* The same conditions as Example 1,

except that  $h_{cv} = 3.0 \times 10^{-2} \text{ cal/cm}^2 \cdot ^\circ\text{C}.$ \*

Find: The temperature of the plate when  $\eta = 2, 4, \text{ and } 6.$

Solution:

$$t_{\max} = 0.043 \text{ } W^{0.43} = (0.043)(100)^{0.43}$$
$$= 0.31 \text{ sec.}$$

$$\frac{h_{cv} t_{\max}}{\rho C_p b} = \frac{(3.0 \times 10^{-2})(0.31)}{(2.7)(0.216)(0.15875)} = 0.1.$$

From Figure 9-11, when

$$\eta = 2, \frac{\Delta T}{AQ/\rho C_p b} = 0.44,$$

when

$$\eta = 4, \frac{\Delta T}{AQ/\rho C_p b} = 0.53,$$

and when

$$\eta = 6, \frac{\Delta T}{AQ/\rho C_p b} = 0.51.$$

From Example 1,

$$\frac{AQ}{\rho C_p b} = 569^\circ\text{C}.$$

The temperature rises are

$$\Delta T = (0.44)(569) = 250^\circ\text{C} \text{ for } \eta = 2,$$

$$\Delta T = (0.53)(569) = 302^\circ\text{C} \text{ for } \eta = 4,$$

and

$$\Delta T = (0.51)(569) = 290^\circ\text{C} \text{ for } \eta = 6.$$

Answer: The plate temperatures are

$$T = T_o + \Delta T.$$

Therefore,

$$T_{\eta=2} = 30 + 250 = 280^\circ\text{C},$$

$$T_{\eta=4} = 30 + 302 = 332^\circ\text{C},$$

and

$$T_{\eta=6} = 30 + 290 = 320^\circ\text{C}.$$

Related Material: See paragraph 9-31.

\* This value corresponds roughly to an airplane speed of 200 mi/hr.

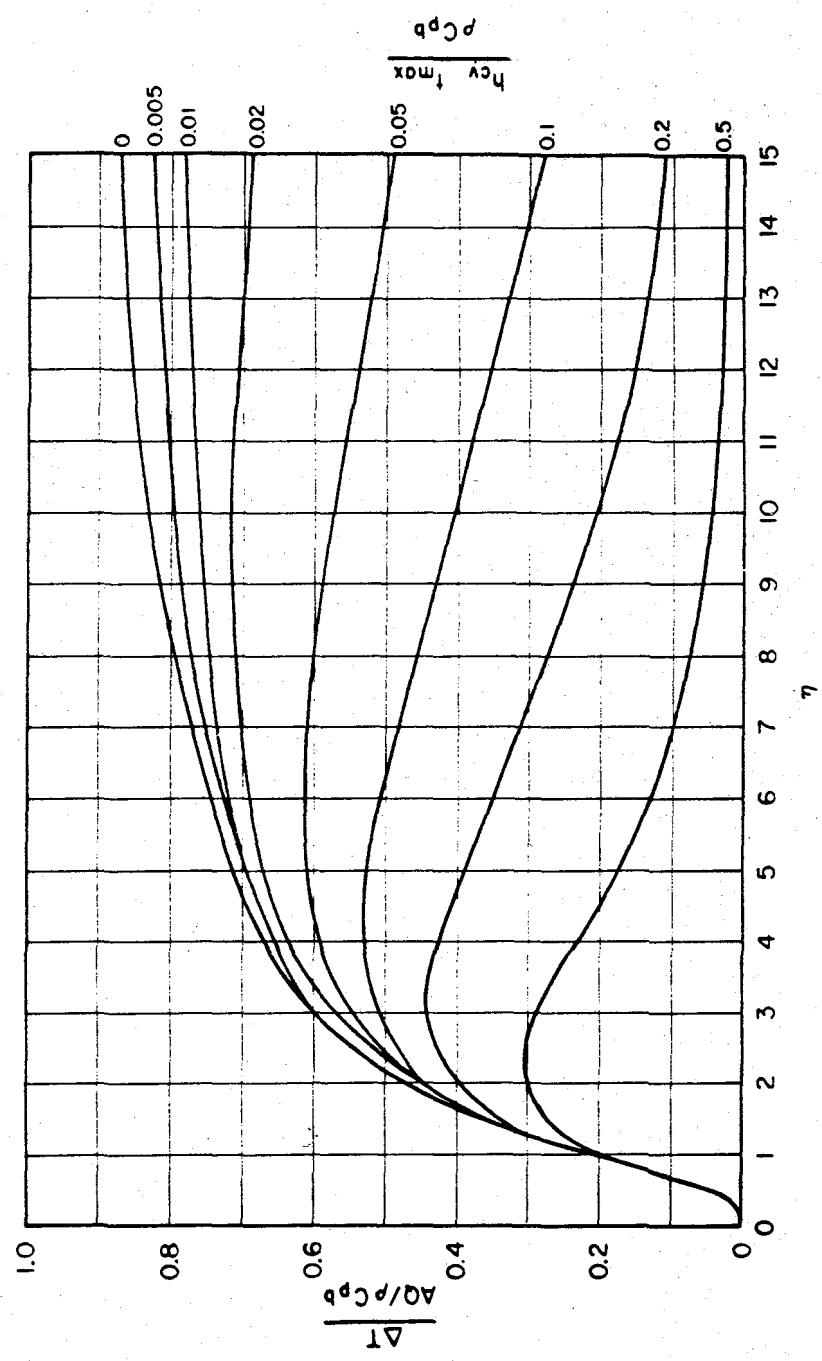


Figure 9-11. Thermal Response of a Thin Plate to Nuclear Weapons Thermal Radiation Pulse

Thermally thick plates are those that do not have a temperature rise on the back surface at the time of interest. Finite plates have a temperature gradient between the front and back surfaces and a temperature rise at both surfaces.

Computer codes generally are required to calculate the temperature history of thermally thick and thermally finite plates. Simple graphical techniques have been developed to determine the temperature rise on the front face of a thermally thick plate and on the front face, mid place, and back face of thermally finite plates. These are not included herein because the techniques depend upon thermal source characteristics that are very different from the source characteristics described in Chapter 3.\* If graphical techniques that are compatible with the thermal source data of Chapter 3 become available, they will be included in revisions to this manual. In the meantime, users who are interested in the techniques should consult "Thermal Degradation of Structural Resistance to Air Blast" (see bibliography).

Requirements to analyze geometries that are more complex than single layer plates (even if they are layered thin plates) or to examine plates with temperature dependent thermo-physical properties or heat losses require the use of a computer code. Codes for more complex geometries, such as cylinders and tee beams, have been developed specifically for the types of analysis of concern to this section. As noted previously, the TRAP computer program can calculate temperatures and stresses for two dimensional structures.

Honeycomb structures or sandwich construction must be considered as a multi-layered system. A five layer system was used to examine thin sandwich construction. The five layers consisted of the core, the two skins, and the two bonding layers between the skins and core. Most sandwich construction has been found to fail at the bonding layer. Consequently, the tempera-

ture of the bond and the thermal stresses in the face sheets (or skins) can be of equal importance. Studies and experiments show that a calculational procedure that includes five layers was required to duplicate experimental results accurately. A code developed for dual layer plates has been used to calculate thick single layer plates by considering both layers to be the same material.

### 9-32 Change in Materials Properties

The rise in temperature that occurs when thermal radiation is absorbed can be expected to cause changes in materials prop-

\* The important differences in source characteristics are the time to final maximum, where

$$t_{\max} = 0.032 W^{1/2} \text{ sec}$$

was used in developing the graphical techniques, while a more recent value

$$t_{\max} = 0.043 W^{0.43} (\rho/\rho_0)^{0.42} \text{ sec}$$

is given in Chapter 3, and the power at thermal maximum, where

$$P_{\max} = 4 W^{1/2} \text{ kt/sec}$$

was used in developing the graphical techniques while a more recent value of

$$P_{\max} = \frac{4.3 W^{0.6}}{(\rho/\rho_0)^{0.44}} \text{ kt/sec}$$

is given in Chapter 3. The latter determines the maximum irradiance (thermal energy per unit area per unit time) incident on the target. Actually, the procedures described in Problems 9-1 and 9-2 were developed for use with the older expression for  $t_{\max}$ ; however, since the two expressions agree within a few percent for low air bursts and for yields from a few kt to a few Mt, the use of the techniques with the value of  $t_{\max}$  from Chapter 3 was illustrated. The values of  $P_{\max}$ , on the other hand, differ widely at all yields. Since the temperature histories presented in the graphical techniques for finite and thick plates depend strongly on irradiance, it is not possible to use the thermal source data with the curves derived for use with the older expression for  $P_{\max}$ .

erties. Properties of mechanical strength are of greatest concern, since these properties influence structural resistance.

Thermal stresses may be present in either unrestrained or restrained structures or elements thereof if thermal gradients, which usually are caused by increased temperatures, are present. The magnitude of the stresses depends upon the amount of expansion the structure experiences, which depends on the value of the coefficient of thermal expansion,  $\alpha_e$ , for the material. The dimensions of this coefficient are length per length per temperature unit, often expressed as in./in. $^{\circ}$ F or cm/cm. $^{\circ}$ C. The value of  $\alpha_e$  depends on the temperature, as shown in Figures 9-12 through 9-15 for a number of materials. Use of an improper value of  $\alpha_e$  can cause serious errors in the estimation of the thermal stress level in some materials. For example, the use of the room temperature value of  $\alpha_e$  for AISI 301 stainless steel when the value of 1200 $^{\circ}$ F ( $\sim$ 650 $^{\circ}$ C) should have been used, would result in a value of thermal stress that is 20 percent too low. For 2024 Aluminum Alloy, the error would be about 18 percent, whereas for Ti-8Mn Titanium Alloy, the error would be 45 percent. Thus, for large temperature rises, the assumption of a constant value for the coefficient of thermal expansion could lead to significant errors. However, for small temperature rises, on the order of 200 $^{\circ}$ F (110 $^{\circ}$ C), the error would not be significant. For most metallic materials, the error in thermal stress is about 2 percent per 100 $^{\circ}$ F or 3 percent per 100 $^{\circ}$ C temperature rise above room temperature values of  $\alpha_e$ . Additional data may be obtained from "Metallic Materials and Elements for Aerospace Vehicle Structures" (see bibliography).

Changes in mechanical strength are the prime reason for concern about the effects of absorbed thermal radiation. Data from several sources are incorporated into Figures 9-16 through 9-18 to provide some indication of the

effects of elevated temperature on the tensile strength properties of 2014-T6 Aluminum Alloy, Titanium Alloy 6AL-4V, and 301 full, hard stainless steel. The various curves in these figures provide some indication of the effect of elevated temperature and also the effects of the speed at which the sample was heated and the time it remained at a given temperature.

The data that will be discussed comes from several sources. Since the techniques for testing that were used in these sources differ considerably, it will be of value to discuss the various techniques employed.

The four basic types of loading tests that have been used to determine mechanical properties at elevated temperatures are illustrated in Figure 9-19 and 9-20. Figures 9-19a and b illustrate an adaptation of the conventional tensile test for elevated temperature. The sample is heated rapidly to an equilibrium temperature. At some finite time after thermal equilibrium, called the soak time, a conventional tensile loading test is conducted with a constant strain rate loading mechanism. Two loading rates are shown in Figure 9-19a. Figure 9-19b illustrates the type of results that are obtained from the type of test illustrated in Figure 9-19a.

Figures 9-19c and d illustrate another type of tensile test where the sample is loaded with a constant load, then heated at some rate until rupture occurs. Figure 9-19d illustrates the type of results that are obtained from the type of test illustrated in Figure 9-19c. Figure 9-20 illustrates two types of short time creep tests and their results.

Results from these types of tests are shown for three aluminum alloys in Figures 9-21 through 9-23. Some data shown in Figure 9-21 were obtained by the type of the test illustrated in Figure 9-19a. The soak time of the sample was one-half hour before a standard constant strain rate of 0.00033 in./in./sec tensile test was performed. Other data in Figure 9-21 also were

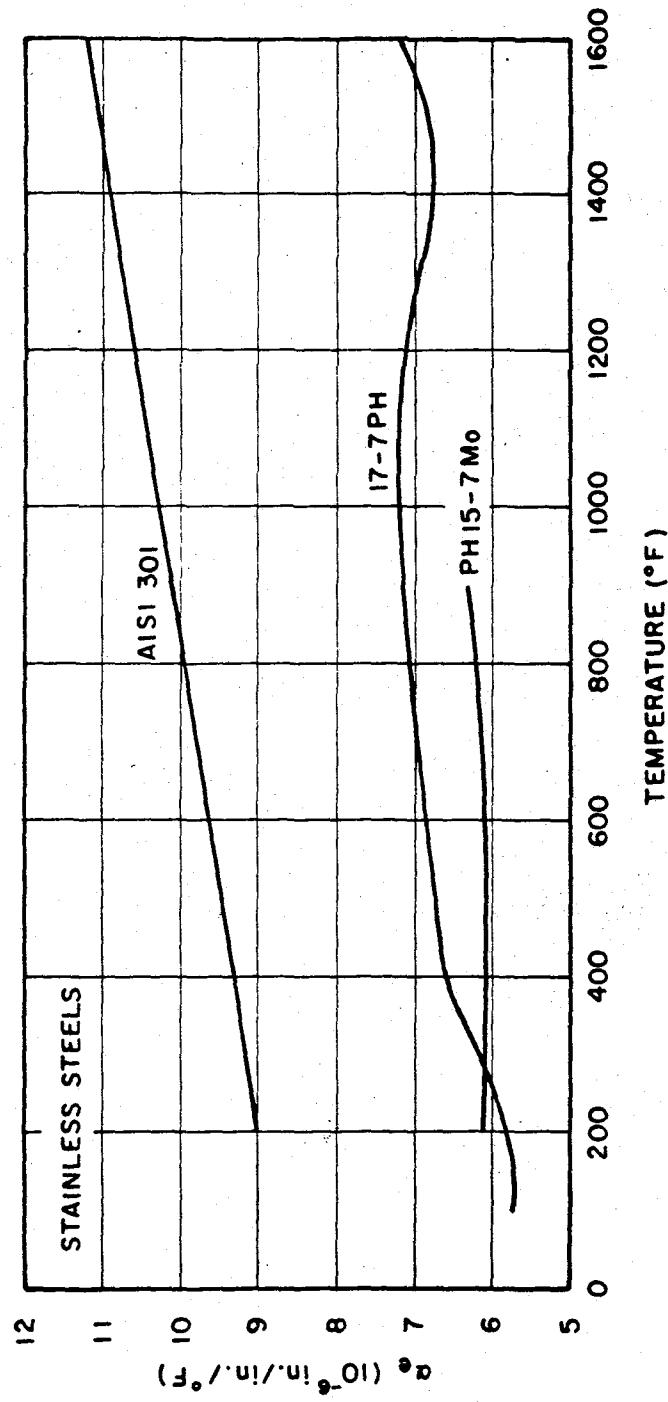


Figure 9-12. [REDACTED] Coefficient of Linear Expansion as a Function of Temperature for Stainless Steels [REDACTED]

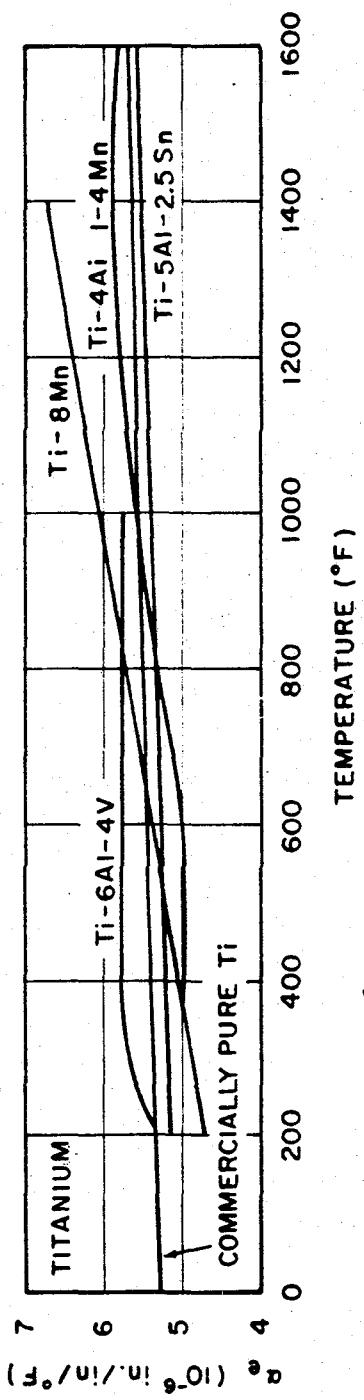


Figure 9-13. Coefficient of Linear Expansion as a Function of Temperature for Titanium Alloys

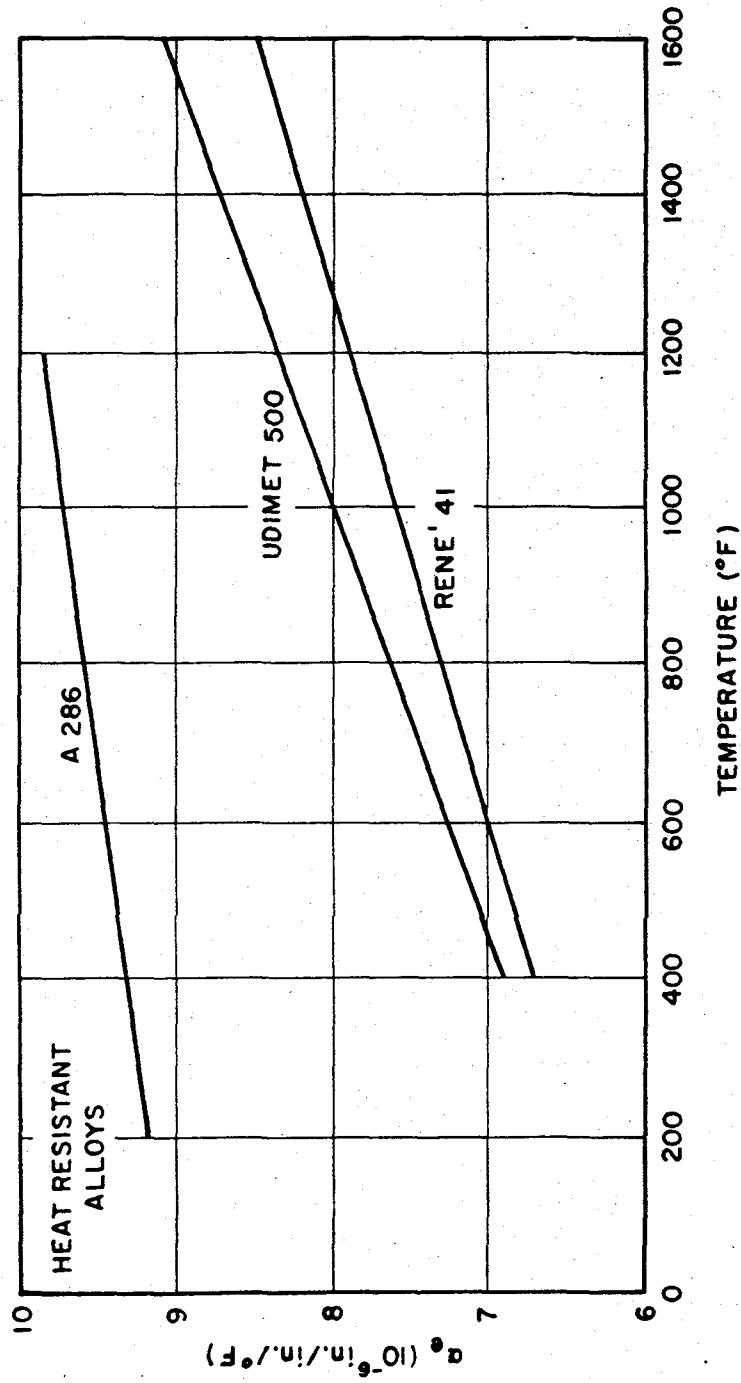


Figure 9-14. [REDACTED] Coefficient of Linear Expansion as a Function of Temperature for Heat Resistant Alloys [REDACTED]

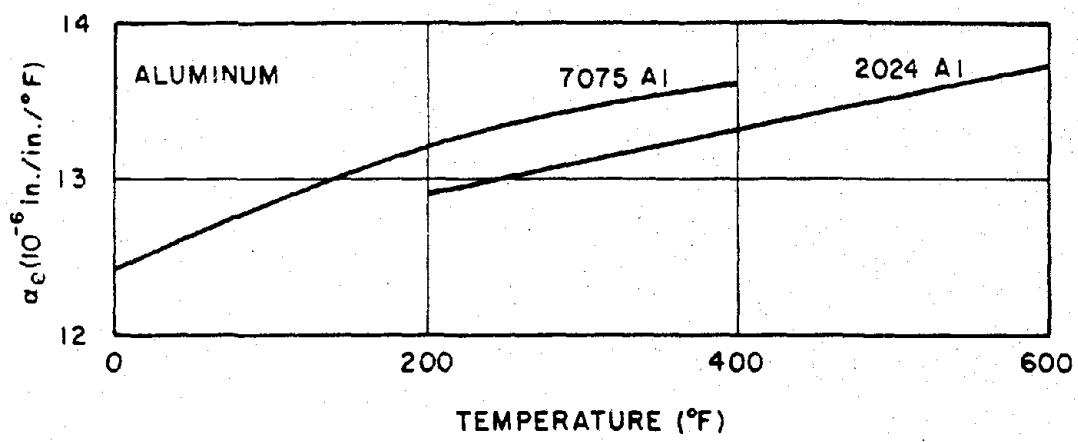


Figure 9-15. [REDACTED] Coefficient of Linear Expansion as a Function of Temperature for Aluminum Alloys [REDACTED]

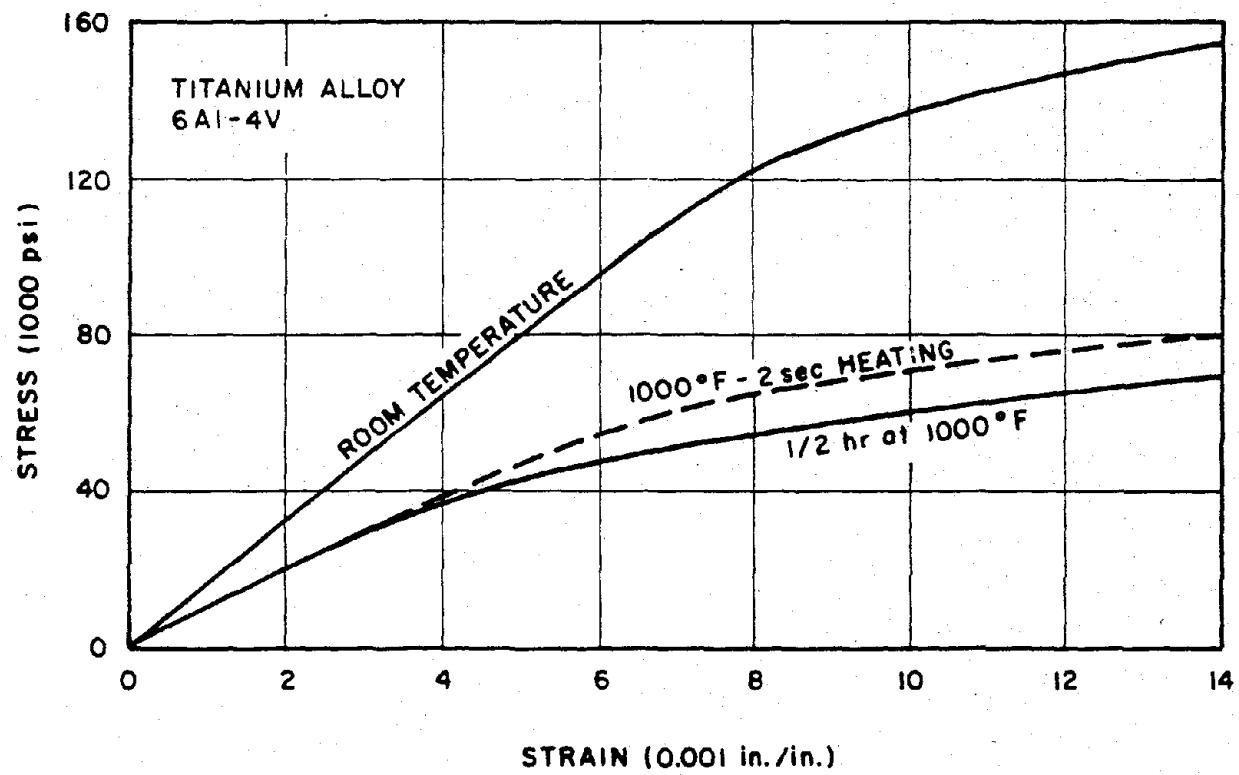


Figure 9-16. [REDACTED] Typical Stress-Strain Curves for Titanium 6Al-4V Alloy at Room and Elevated Temperatures [REDACTED]

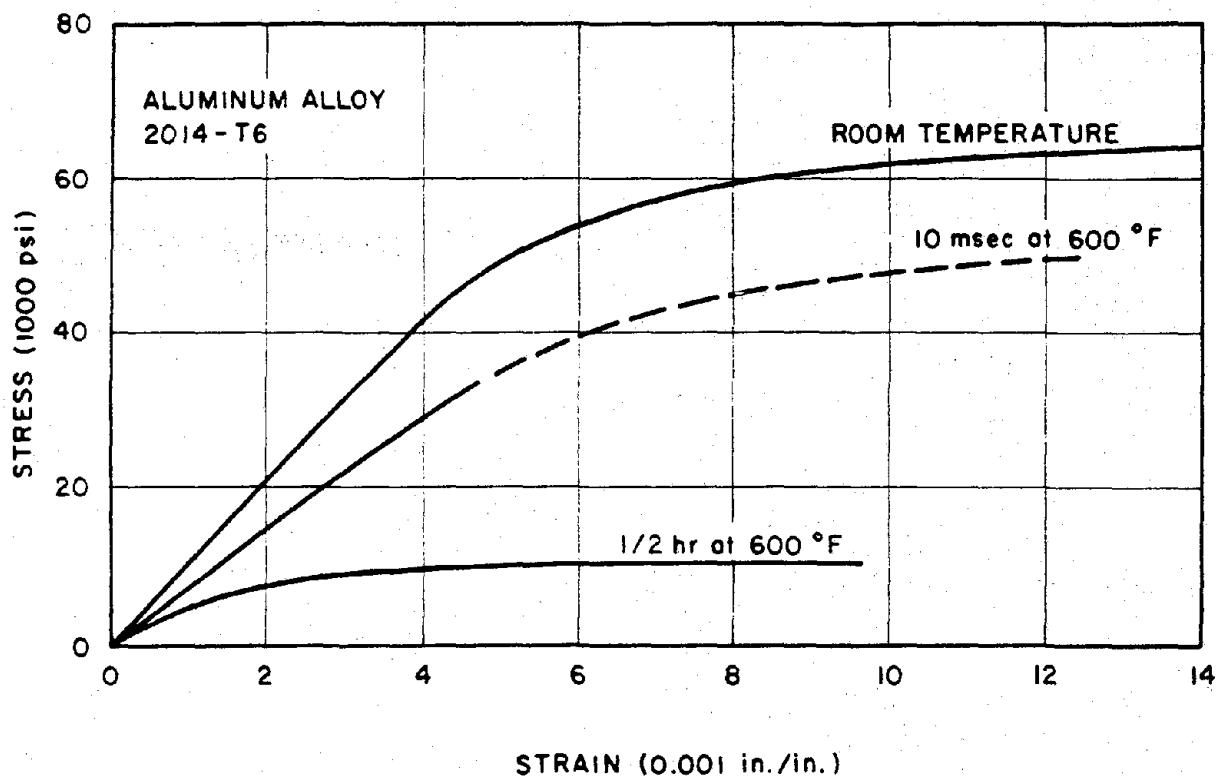


Figure 9-17. [REDACTED] Typical Stress-Strain Curves for 2014-T6 Aluminum Alloy at Room and Elevated Temperatures [REDACTED]

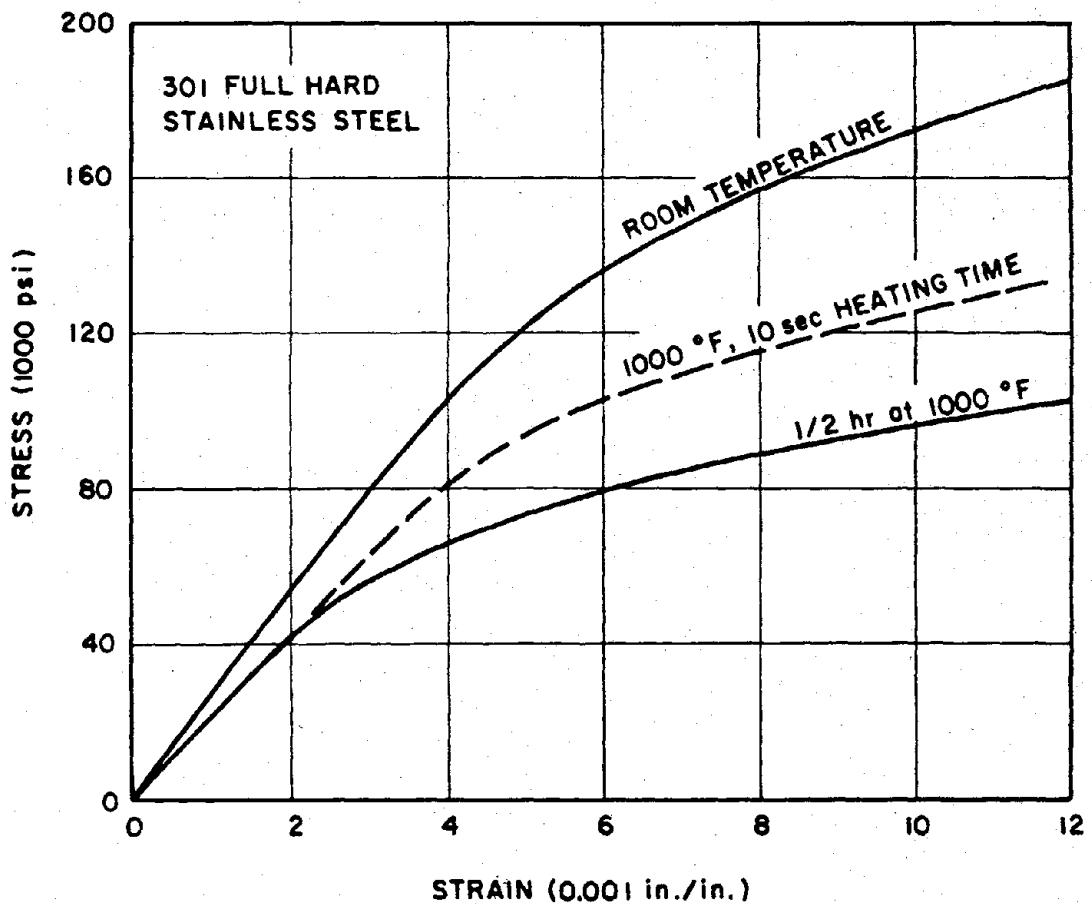
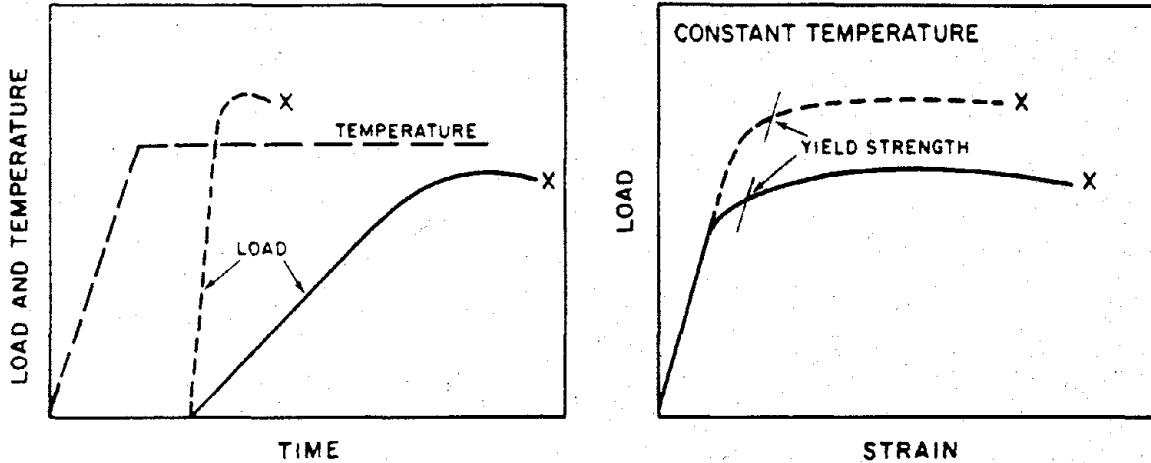
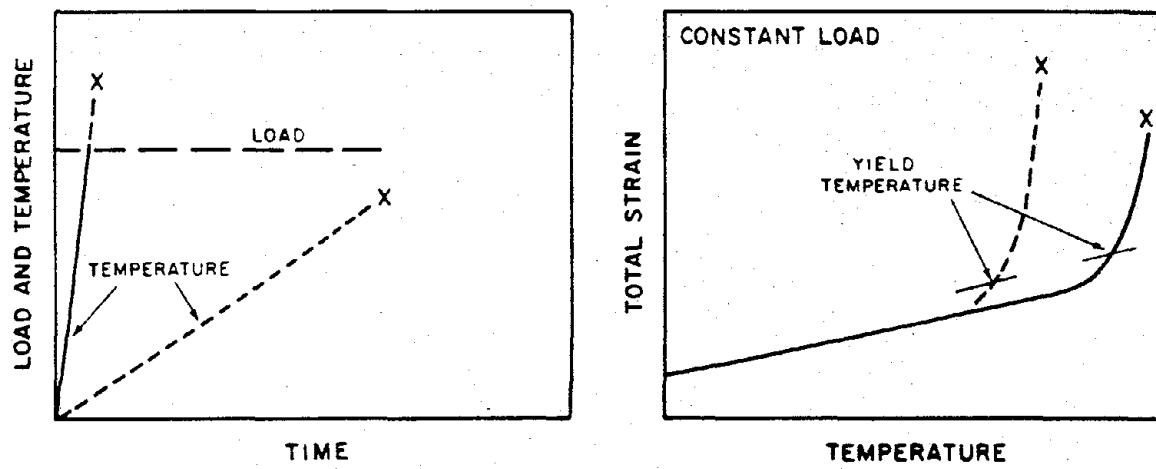


Figure 9-18. [REDACTED] Typical Stress-Strain Curves for 301 Stainless Steel at Room and Elevated Temperatures [REDACTED]



a. Tensile Tests After Rapid Heating

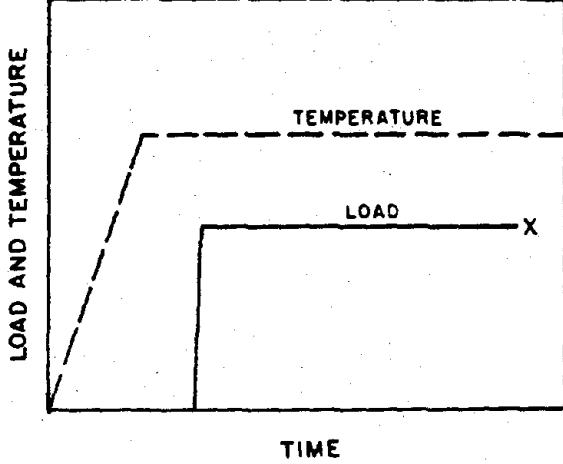
b. Load-Strain Curves from Tests  
Illustrated in Figure 9-19a.



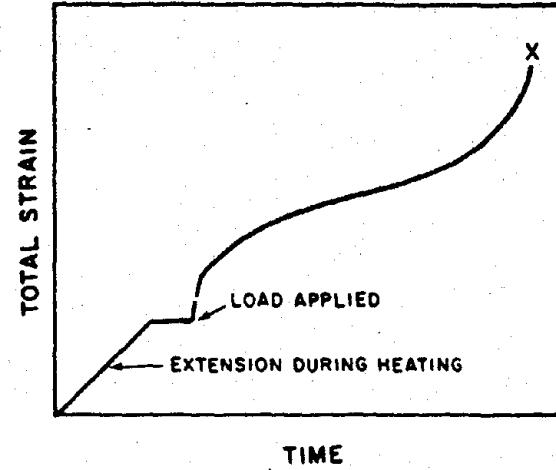
c. Rapid-Heating Constant-Load  
Tensile Tests

d. Strain-Temperature Curves from  
Tests Illustrated in Figure 9-19c.

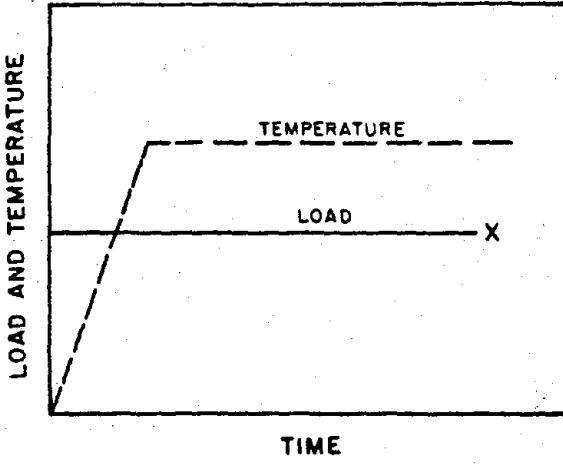
Figure 9-19. [redacted] Types of Rapid Heating Tensile Tests [redacted]



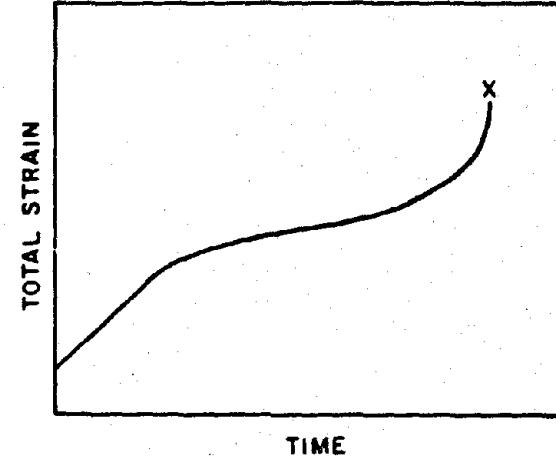
a. Very Short-Time Creep Tests  
After Rapid Heating



b. Time-Strain Curve



c. Very Short-Time Rapid-Heating  
Creep Tests



d. Time-Strain Curve

Figure 9-20. [REDACTED] Types of Short Time Creep Tests [REDACTED]

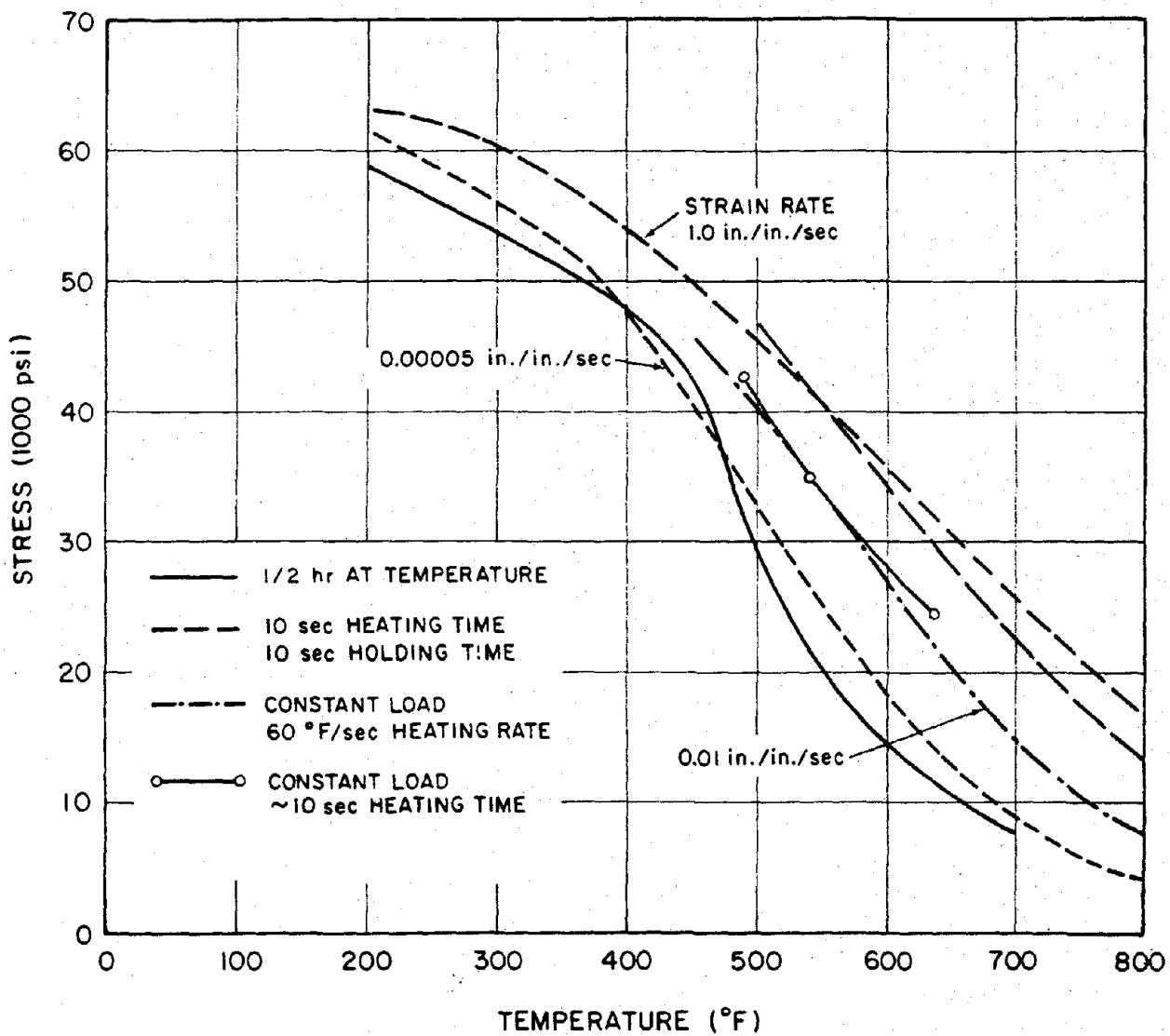


Figure 9-21. [REDACTED] 2024-T3 Aluminum Alloy Ultimate Strength at Elevated Temperature [REDACTED]

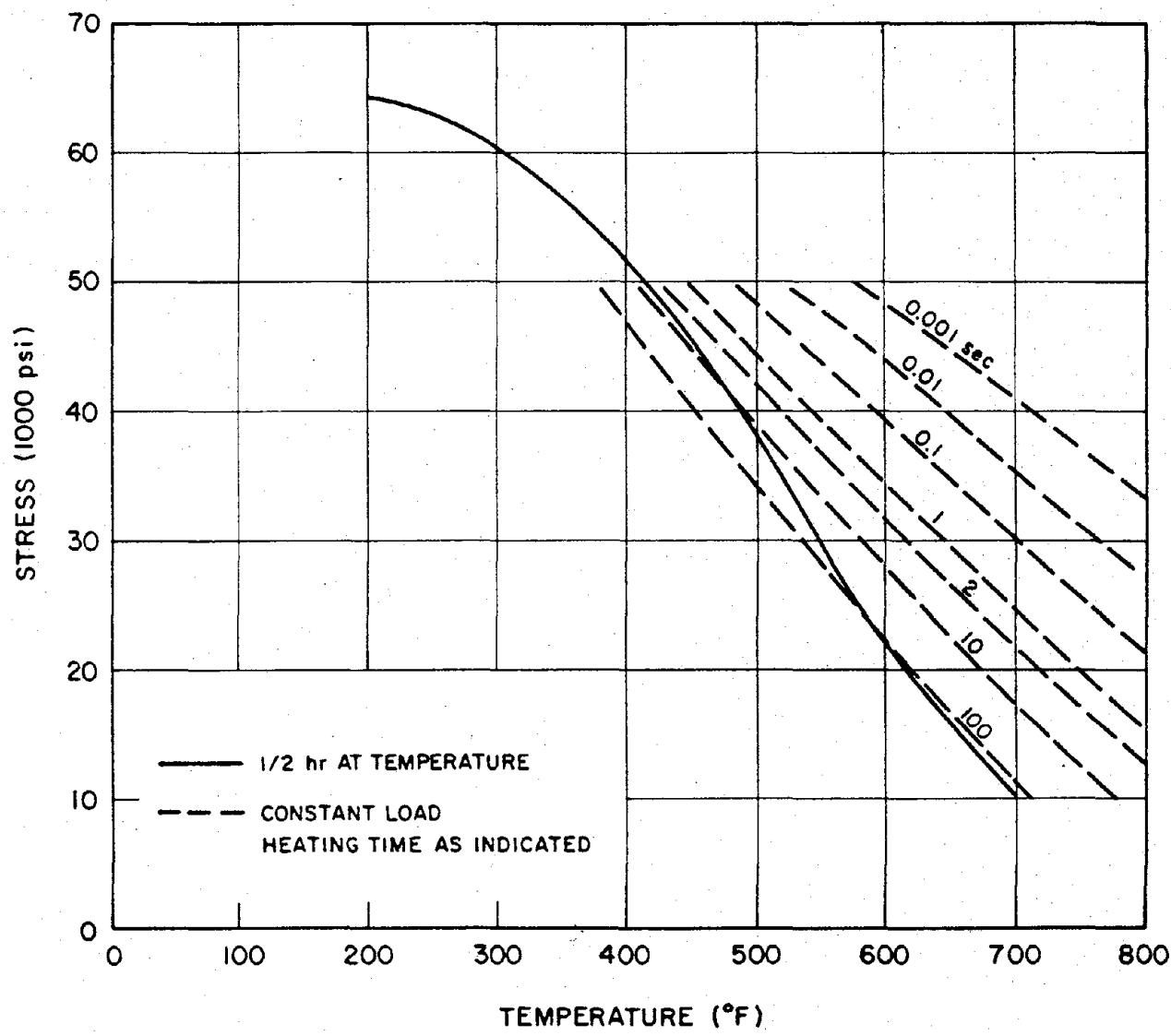


Figure 9-22. [REDACTED] 2024-T81 Aluminum Alloy Ultimate Strength  
at Elevated Temperature [REDACTED]

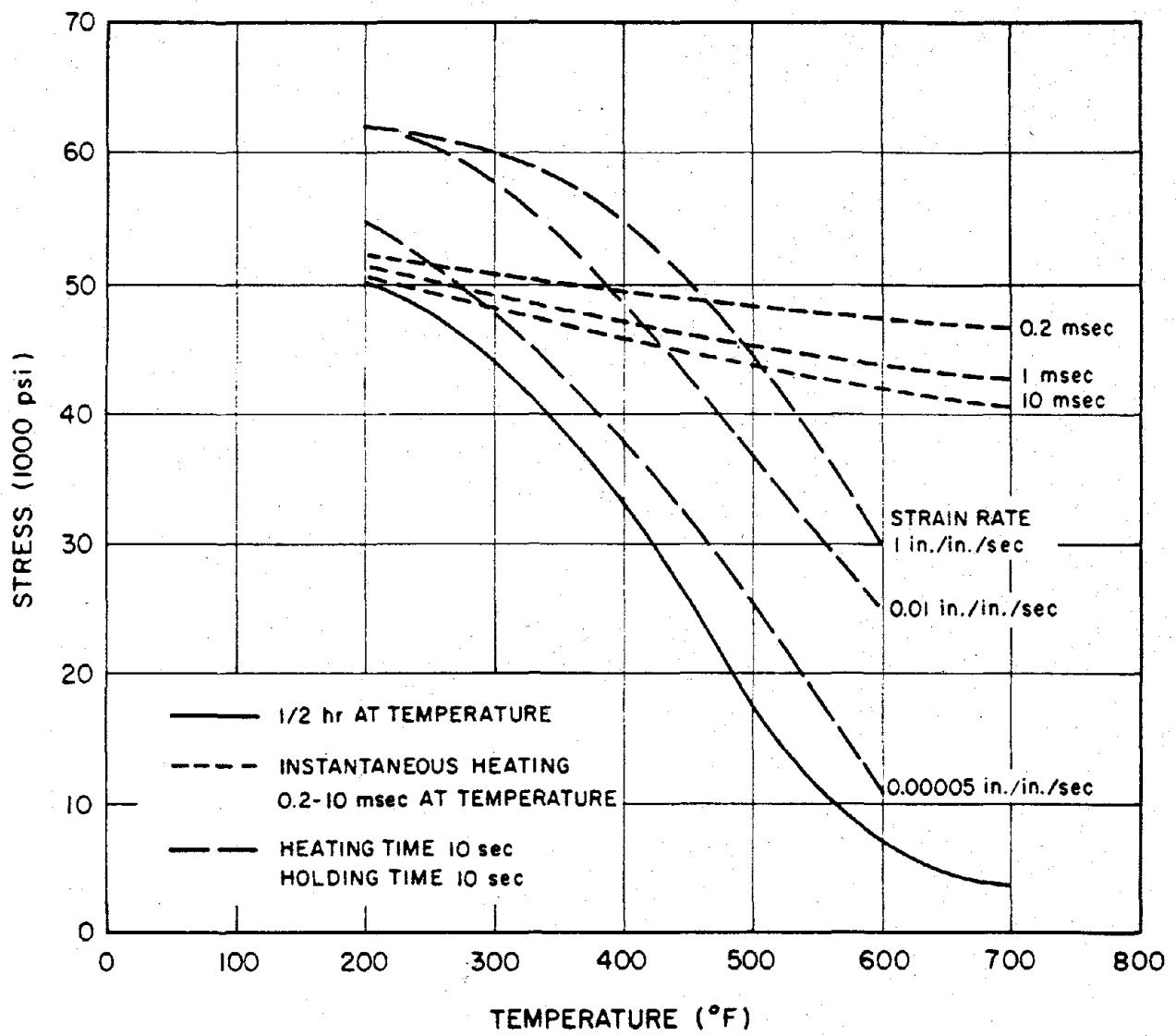


Figure 9-23. [REDACTED] 2014-T6 Aluminum Alloy Yield Strength  
at Elevated Temperature [REDACTED]

obtained in the manner illustrated in Figure 9-19a, but with the equilibrium temperature being reached in 10 sec and with a 10 sec soak time, and with three different strain rates used in the tensile tests. Other data were obtained in the manner illustrated in Figure 9-19c with a heating rate of 60°F/sec. The final data in Figure 9-21 also were obtained in a manner similar to that illustrated in Figure 9-19c with a heating time and time of rupture each approximately 10 sec.

The ultimate strength data in Figure 9-21 tend to show the importance of temperature and strain rate, but the data from the different sources are not consistent and are, therefore, difficult to evaluate. For example, the 0.00005 in./in./sec strain rate curve for 10 sec soak times from one source lies close to the 0.00033 in./in./sec strain rate curve for one-half hour soak times from a different source. Interpolation between the strain rate data for 10 sec soak times would indicate that a 0.00033 in./in./sec strain rate curve for a 10 sec soak time would lie slightly to the right of the 0.00005 in./in./sec curve and, therefore, slightly to the right of the one-half hour soak time curve. However, there are ample data, as shown in Figures 9-16 through 9-18, to justify the expectation that the 10 second curve should fall significantly to the right of the one-half hour curve; that is, for a given temperature and strain rate, the shorter the soak time, the smaller the decrease in tensile strength. It should also be noted that constant load curves should agree more closely.

The ultimate strength data in Figure 9-22 suggest a similar inconsistency although the data were taken from two different types of loading tests. The one-half hour data is from loading tests similar to that shown in Figure 9-19a, and "constant load, heating time as indicated" data is from loading tests similar to that shown in Figure 9-19c. The latter data clearly shows the influence of heating times or heating

rates on rapid heating, constant load tensile test results.

The yield strength data shown in Figure 9-23 for 2014-T6 Aluminum Alloy is somewhat more consistent. The instantaneous heating data were obtained in a manner similar to that illustrated in Figure 9-19a, although times are very short. Specimens were heated instantaneously by an electron beam, then a stress wave was sent up the specimen. An analysis of the stress wave characteristics on either side of the heated region provided yield and ultimate strength data as well as elastic modulus data. The times indicated for these data are the delay times between time of heating and the arrival of the stress wave. Thus, the data are for instantaneous heating, very short soak times, and extremely high strain rates ( $\sim 10^9 \text{ sec}^{-1}$ ). The comparable strain rate data for 1/2 hour and 10 sec soak times are in the relative positions that would be expected. The one factor that may explain why the comparable strain rate data of Figures 9-21 and 9-23 are relatively close together despite the different soak times is the heating rate.

Similar data from a single source are shown in Figures 9-24 and 9-25 for 6AL-4V Titanium Alloy and full, hard 301 stainless steel. The data in these figures also illustrates the inconsistencies in data discussed for Figures 9-21 through 9-23.

One other mechanical strength property of interest is the elastic or Young's modulus of the material. One source indicates that for soak times of from 1/2 to 10,000 hours, the elastic modulus depends only on temperature and not on soak time for a number of different materials. A separate source indicates that this is true for 6061-T6 and 2014-T6 Aluminum Alloys with soak times of 0.2, 1, and 10 msec. Although this conclusion has not been validated for other materials at small soak times, it appears reasonable to assume that the elastic

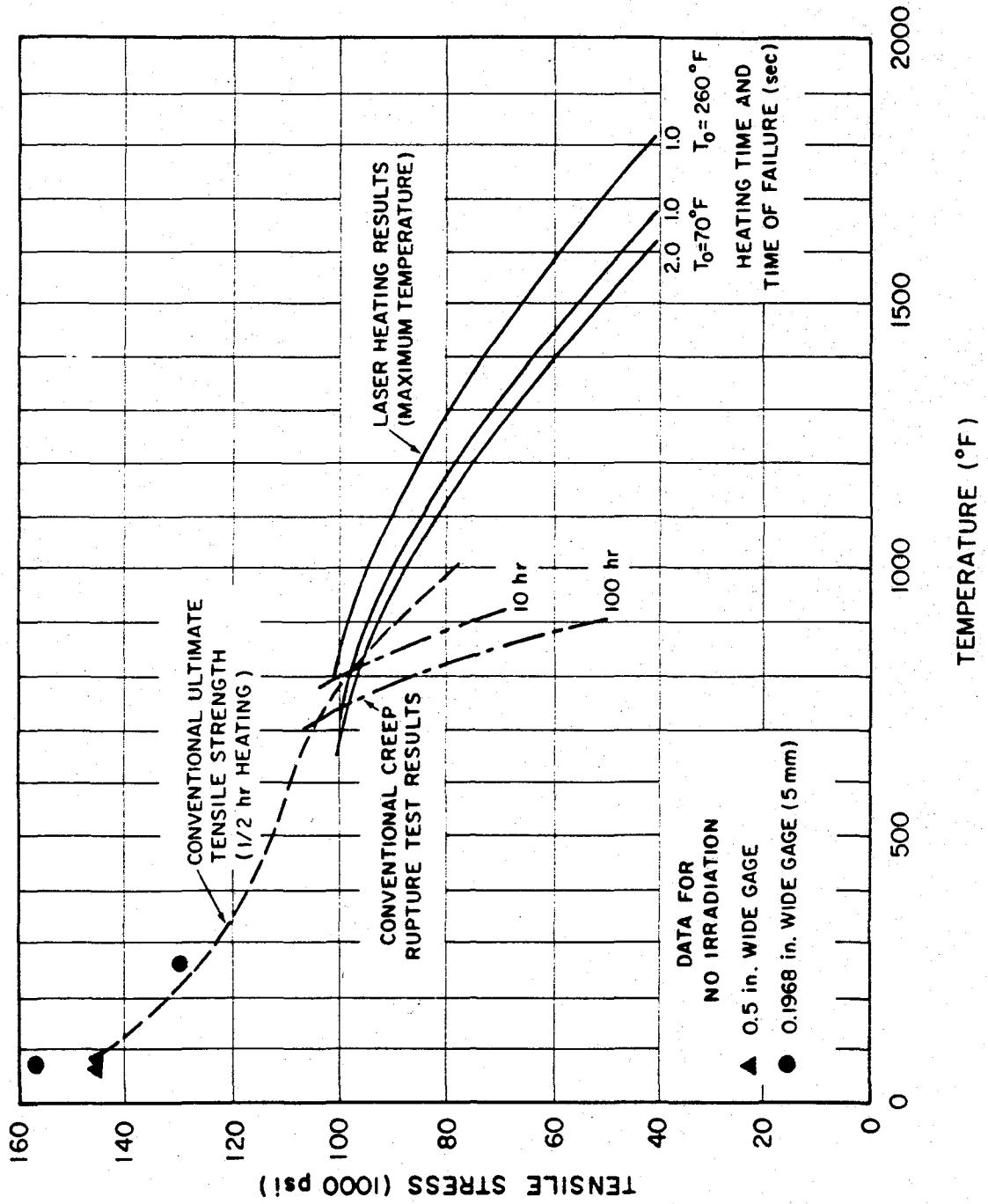


Figure 9-24. [REDACTED] Ultimate Strength Test Results for 6Al-4V Titanium Alloy at Elevated Temperatures [REDACTED]

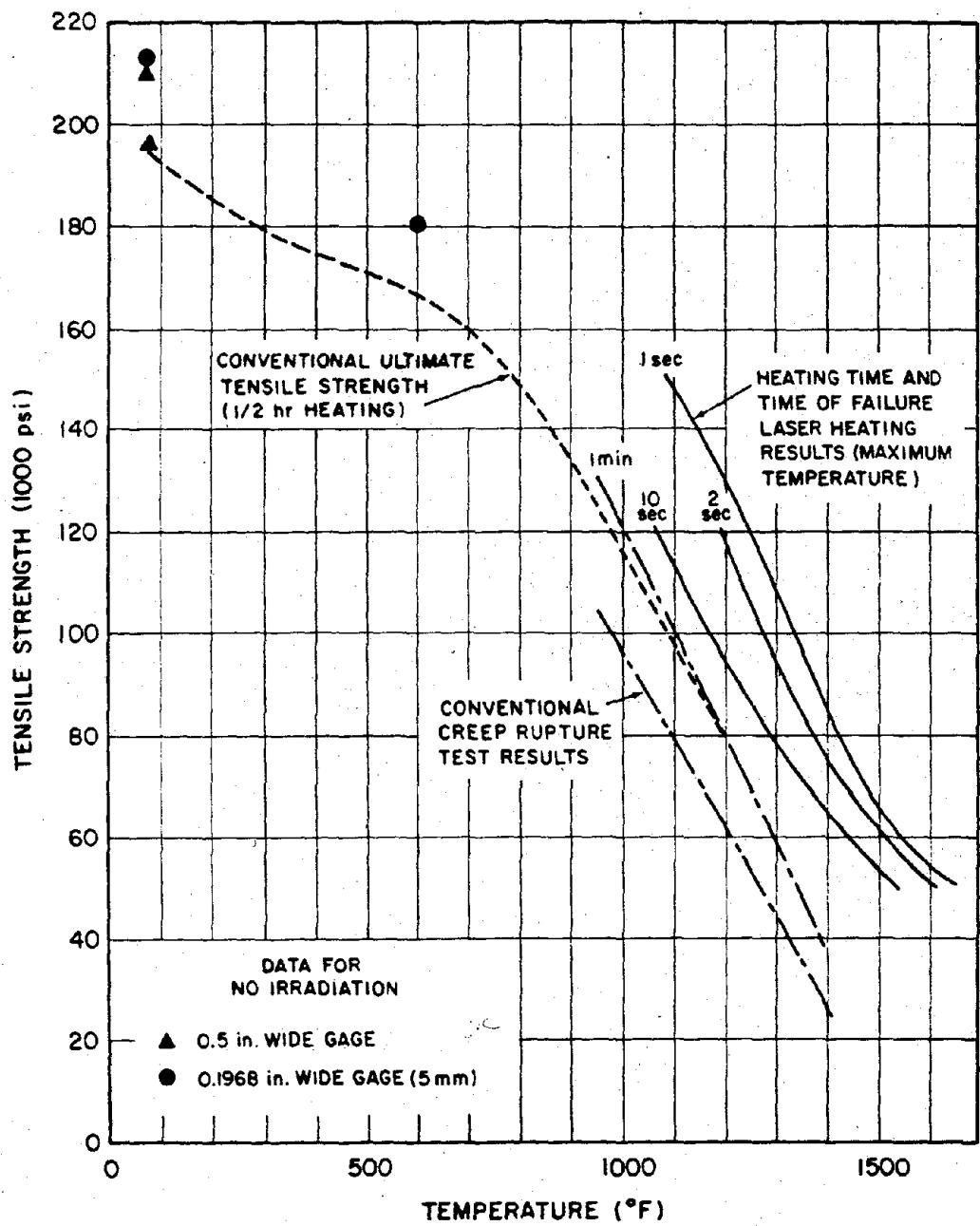


Figure 9-25. [REDACTED] Ultimate Strength Test Results for Full Hard Stainless Steel at Elevated Temperature [REDACTED]

[REDACTED] modulus only depends on temperature for metallic materials.

[REDACTED] In evaluating the information available on changes in mechanical strength properties of materials, it should be reemphasized that a variety of testing techniques have been used to obtain the data presented in this section. Constant strain rate and constant load techniques have both been used. A variety of heating techniques have been used, including ovens, resistance heating, inductive heating, hot-fluid bath heating, radiant heating, lasers, and electron beams. A considerable amount of data have been obtained on a number of different materials.

[REDACTED] The data indicate that there are five basic variables that influence the degradation of mechanical strength properties at elevated temperature for particular materials: initial temperature, heating rate, final temperature, soak time, and strain rate. Not much is known about the effect of initial temperature since most data report "room temperature" as the reference temperature. Increases in heating rate, final temperature, or soak times cause a decrease in ultimate and yield strengths. An increase in strain rate at a particular final temperature apparently increases the strength. Because of the different testing techniques employed, the relative importance of these variables in determining material strengths is difficult to determine; however, it appears that soak time and final temperature are most important, followed closely by strain rate, and finally heating rate as long as final temperature is reached in less than one minute.

[REDACTED] Although there are considerable data available on rapid heating effects, it is difficult to extrapolate to other than test conditions with any confidence. In any event, in estimating strength, data available on rapid heating and short times appear to be more appropriate than those for slow heating, long soak times for the general class of problems of interest in this manual.

## RESISTANCE TO LOAD

[REDACTED] The ultimate concern of combined thermal/blast effects is the change, if any, in the vulnerability/survivability of tactical systems compared to vulnerability/survivability to thermal or blast effects separately.

[REDACTED] Figure 9-26 illustrates typical experimental stress-strain curves for 2014-T6 Aluminum Alloy with two approximations to this curve: the more or less classical straight line; and the so-called Bell's stress-strain law for dynamic deformation:

$$\sigma = \beta \left(1 - \frac{T}{T_m}\right) \epsilon^{1/2}$$

where

$\sigma$  = stress, psi,

$\epsilon$  = strain, in./in.,

$T$  = temperature of interest, °K.

$T_m$  = melting temperature, °K,

$\beta$  = parabolic coefficient.

The area under each of these curves is equal to the strain energy absorbed by the material. For the straight line approximation the area under the room temperature curve equals about 433 in. · lb/in.<sup>3</sup> to a strain ( $\epsilon$ ) of 0.01 in./in. This compares well with the area of 432 in. · lb/in. under the typical curve to the same  $\epsilon$ . The Bell stress-strain law gives an area of 441 in. · lb/in.<sup>3</sup>.

[REDACTED] The change in allowable uniform equivalent static load that will give the same maximum deflection as a uniform dynamic load has been determined for degraded 2014-T6 Aluminum alloy properties using elastic theory for large deflections of simply supported square plates.\* The allowable load was defined as the maximum

[REDACTED] An air blast loading of long duration, or a flat top wave, was assumed.

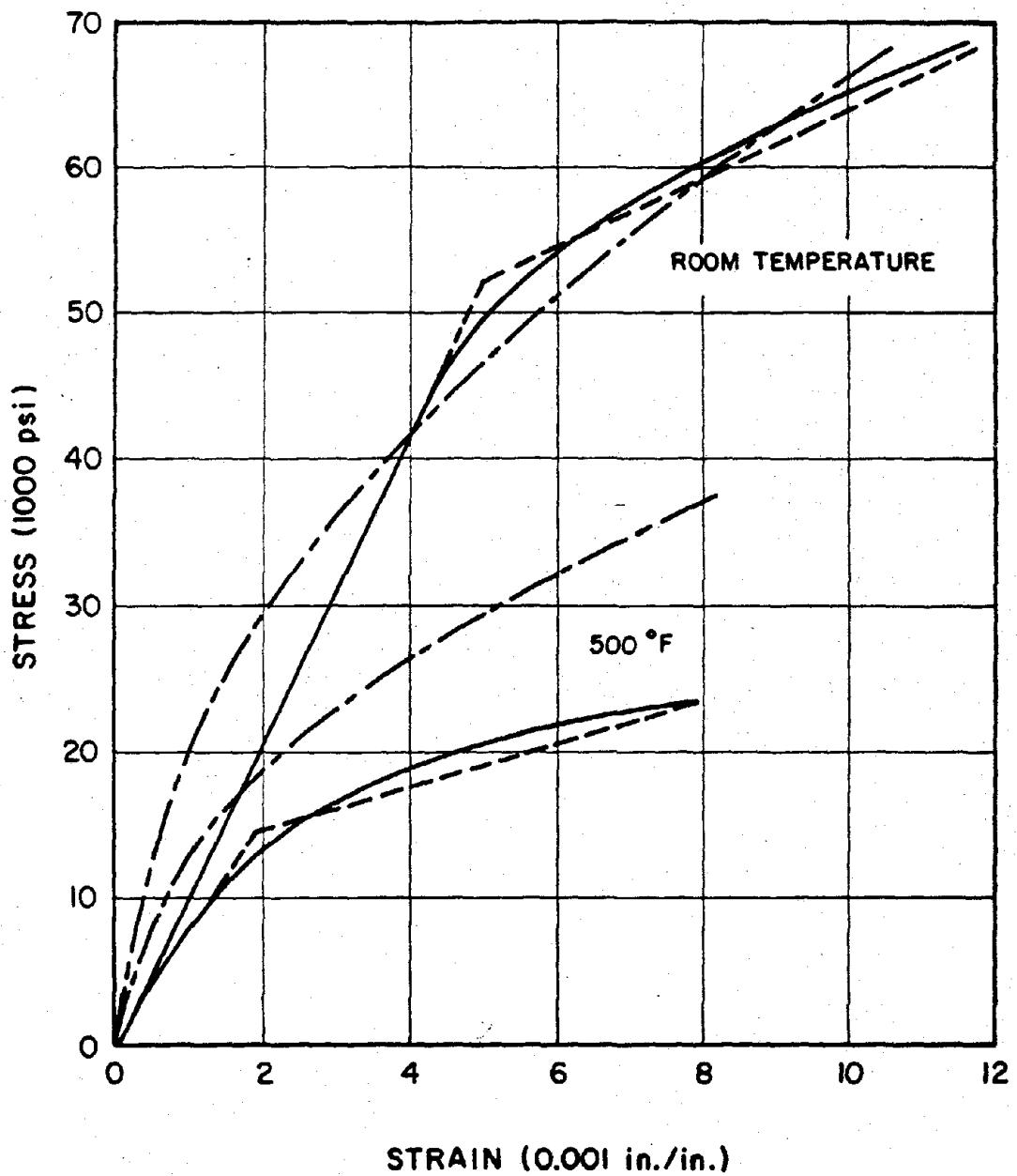


Figure 9-26. Stress-Strain Approximation for 2014-T6  
Aluminum Alloy

static load the plate could carry without exceeding the yield stress. One-half hour soak time data were used to determine the strength properties, and a 20-in. square plate, 1/4-in. thick was assumed. The results are shown in Table 9-9. As can be seen, the maximum allowable load is almost a linear function of allowable stress. The explanation of this can be seen in the following equation, which is the elastic stress equation for the plate under study.

$$\sigma = 7,356.8p + 4.632E^{1/3}p^{2/3}$$

The second term of the equation is for membrane stresses and is the only term that contains the temperature dependent Young's modulus. As the temperature increases, the value of  $E$  decreases, so the contribution from the second term is further decreased, and a fairly linear dependence on the pressure,  $p$ , remains.

The allowable stress in the above example was taken from 1/2 hour soak time data. This provides a lower bound for the allowable load. Examination of Figure 9-21 through 9-25 indicates that the rapid heating, short soak time data generally fall above the 1/2 hour soak time curves. More reliable estimation of allowable loads will depend on the availability and appropriateness of the material data that is required for the type of analysis and calculation

techniques being employed by an investigator.

The truly dynamic case may be analyzed similarly. In both cases, however, the basic factor that influences structural degradation is allowable stress as long as the elastic analysis approach is used.

Where deformation or plastic response is responsible for failure, allowable stress no longer can be used to determine allowable load; either total deformation or total energy absorbed must be used.

The energy approach consists of stating that the energy absorbed by a structure as it deforms is proportional to the product of the overpressure and the impulse values,  $\Delta pI$ , of the blast wave that causes the deformation. Thus, for a constant value of absorbed energy used as a measure of damage, any combination of overpressure and impulse that yields the same product will cause the same amount of "damage."

The effect of elevated temperature on the damage values has been investigated. One source indicates that for face-centered cubic materials, such as aluminum, the value of the parabolic coefficient of Bell's stress-strain law varies linearly with the temperature. For 2014-T6 Aluminum, the equation would be

$$\sigma = 9.65 \times 10^5 \epsilon^{1/2}$$

Table 9-9. Allowable Uniform Static Load for Aluminum Plate at Three Temperatures

Temperature (°F)	$\sigma_y$ ( $10^3$ psi)	Young's Modulus, E ( $10^6$ psi)	Deflection (in.)	Allowable Load (psi)
70	57	10.5	0.323	7.25
350	43	9.77	0.261	5.45
500	17	8.4	0.117	2.10

where the value of  $\beta$  was obtained by fitting the curve to pass through the room temperature yield stress for the material. The Bell's law equation indicates that the energy under the stress-strain curve is a linear function of temperature by varying values of  $\beta$  linearly. This infers that the damage value,  $\Delta pI$ , should depend on a linear function of temperature, i.e.,

$$(\Delta pI)_{T_2} = (\Delta pI)_{T_1} \left[ \frac{1 - \frac{T_2}{T_m}}{1 - \frac{T_1}{T_m}} \right]$$

where

$(\Delta pI)_{T_1}$  = damage value at temperature  $T_1$

and

$(\Delta pI)_{T_2}$  = damage value at temperature  $T_2$ .

If this relation were true, it would be a simple matter to evaluate the vulnerability of a structure. Once the value of  $\Delta pI$  had been determined for ambient temperatures, the  $\Delta pI$  value at elevated temperatures could be determined easily.

The Bell's law equation also indicates that yield strength, ultimate strength, and Young's modulus are linear functions of temperature for dynamic deformation. The data that were used to develop the equation were obtained from impact tests of oven heated samples. No information was provided as to what the heating rates or soak times were. The only other comparable data, at least in the dynamic sense, were shown in Figure 9-24, which indicate that data from dynamic tests do seem to approximate a straight line to some degree.

Thus, with further testing and research, it may be that a relatively simple approach to assessing structural vulnerability to combined thermal/blast effects will be possible for dynamic deformation damage criteria.

The previous discussion has been concerned primarily with unstressed, unrestrained structural elements. There are three main structural conditions that are encountered in the analysis of structural response to combined thermal/blast effects. These are: unstressed members with no edge or end restraints; unstressed members with restraints; and prestressed members with restraints. These conditions refer to the status of a structure before either thermal or blast loading. The first condition is the easiest to analyze since there are no restraints to dimensional changes during or after heating so the thermal degradation of mechanical strength properties is the main concern. The second condition is more complex since dimension changes are prevented in varying degrees and appreciable thermal stresses may exist at the time of blast loading. The inclusion of these thermal stresses is not uncommon in structural elastic analysis. Thermal stresses caused by thermal gradients in the structural member also are included under this condition. The inclusion of stresses induced by the thermal gradient in an elastic structural analysis generally will require the use of a finite element structural analysis computer code. Unfortunately, it cannot be assumed that either form of thermal stress will be inconsequential, and they should both be addressed specifically in the solution of a particular problem. The final condition is the most difficult to analyze because a member may be stressed prior to thermal or blast loading.

The final factor to consider in determining structural response is the possibility of changes in failure modes, particularly materials rupture. Visual examination of a 1/4-in. by 0.040-in. 2024-T3 Aluminum specimen that fail-

ed indicated little necking down at the failure point. This may be due to the small area (about 17 mm diameter) exposed to thermal radiation. Failure occurred on a 45° plane, with no cupping. Postshot photos of cylindrical/aluminum shells, exposed to HE air blast after rapid heating, indicated an almost brittle-like fracture mode of failure. Failure of similar shells at normal temperature under the same type of loading was of a ductile deformation type. The possibility of a change in failure mode under dynamic loading at elevated temperatures has not been investigated, but is of concern since residual load carrying capabilities of deformed structures are sometimes used in determining vulnerability.

In summary, if elastic criteria are used to determine survivability/vulnerability, and if the necessary materials strength properties are known, a fairly straight forward but not necessarily simple stress analysis may be performed. If dynamic or deformation criteria are necessary, the problem becomes very difficult, if not impossible, because of the lack of validated analysis techniques. A third criterion, material melting, may be used to bound the problem. A temperature criterion may be chosen that is or nearly equal to the melting point of the material with the inference that, at that temperature, the material has no strength, and therefore, no resistance to load. This latter criterion has been used, for example, to establish kill criteria for Army aircraft.

## SECTION V

### X-RAY DAMAGE EFFECTS

#### INTRODUCTION

Nuclear weapons as X-ray sources and the environments they produce are described in Chapter 4. This section discusses the interaction of the X-ray environment with aerospace systems and some typical damage mech-

anisms that result from the interaction. The damage mechanisms depend on the fluence and energy, or temperature, of the X-rays and on the protective and structural materials involved in the interaction. For purposes of discussion the damage mechanisms can be divided conveniently into the effects caused by hot X-rays and those caused by cold X-rays. Some familiarity with the material discussed in Chapter 4 is assumed in the following discussion.

Cold X-rays (typically 1 to 3 keV black body temperatures) are absorbed in a thin surface layer. At sufficiently high fluence, a short pulse of X-rays can heat the surface rapidly and may cause it to vaporize and blow off. This results in: (1) an impulse imparted to the total structure; and (2) generation of a strong shock wave that propagates into the structure, and which may cause spallation of material at free boundaries and internal fracture of materials and bonds. These latter effects are produced by shock wave propagation through the thickness of a surface structure such as the thermal protection shell of a reentry vehicle. The former effects may produce damage by whole vehicle modes of response to the net impulse.

The hot X-rays are more penetrating. They can cause: (1) thermally generated shock waves in the vehicle structural materials and internal components; (2) melting and vaporization of the substructure; (3) internal deposition of energy in electronic components producing transient or permanent damage (see Chapter 6 and Section 7 of this chapter); or (4) produce internal EMP signals (see Chapter 7).

While some nuclear weapons emit only cold X-rays, all hot X-ray weapons have a cold component. Hence, for exoatmospheric events the hot X-ray effects are accompanied by cold X-ray effects. On the other hand, for endoatmospheric explosions, the cold X-rays have short mean free paths, and the X-ray effects beyond distances of a few tens of meters are produced by hot X-rays alone.

[REDACTED] Damage to a particular system depends on the structural details of the system as well as the X-ray spectrum. Accurate damage prediction even for the simplest geometries, generally require elaborate computer programs to calculate the energy deposition and the response of the system. All vulnerability analyses follow similar computational steps:

1. The X-ray energy deposition is computed using known processes for the materials and structure. This energy is assumed most often to be deposited instantaneously.

2. From the calculated energy deposition and the equation of state for the materials in the structure (if known) for the liquid, solid, and vapor phases of the material, a stress wave, which propagates through the surface structure, is calculated.

3. Damage to the surface structure that results from the stress wave (spallation, internal fracturing, delamination and debonding), is determined. These calculations generally are based on experimentally derived damage response curves. A good deal of progress has been made in the last few years in understanding and predicting fractures in most homogeneous and some composite materials. Even a small amount of fracturing may cause a significant loss in strength of material. One of the most complicating factors involved in making reliable damage predictions is that of in-depth heating prior to stress wave propagation through the material.

4. The response of the whole structure that results from the impulse imparted to it is determined. This response also is generally based on experimentally determined damage or properties degradation measurements. In these computations, the effects of the loss of strength of the structural material as a result of fracturing caused by the immediately preceding stress wave or by in-depth heating must be included. The structure may be broken by the impulse loading, or it may be weakened (buckled) so that it will

fail under subsequent stresses, for example, re-entry into the atmosphere.

### X-RAY ENERGY DEPOSITION CALCULATIONS

[REDACTED] The starting point of all X-ray vulnerability analysis is a calculation of the X-ray energy deposition. The determination of the transmitted X-ray fluence, or shine through, into the interior of the aerospace system, is implicit in these calculations. Calculation of X-ray energy deposition involves the use of energy dependent photon absorption cross sections and energy and angle dependent scattering cross sections. Corrections for fluorescence, i.e., reradiation of X-rays, may be significant for high energy photons in certain materials. Sophisticated energy deposition and transport calculations, using detailed energy dependent cross sections and their angular dependence can be made by computers using Monte Carlo techniques. The results serve as an accuracy check and provide "effective" cross section data for simpler techniques. Approximation techniques greatly reduce the amount of effort and time involved in system analysis. Fairly accurate approximate values sometimes can be obtained even by hand calculations, as will be shown with examples.

#### 9-33 X-ray Cross Sections

[REDACTED] The probability of a photon of energy  $h\nu$  traversing a distance of absorbing material  $x$  is  $e^{-\mu x}$ , where  $\mu$  is the linear attenuation coefficient. This probability also can be written as  $e^{-(\mu/\rho)\rho x}$ , where  $\mu/\rho$  is the mass attenuation coefficient for the material (see paragraph 4-3). In this representation,  $\mu/\rho$  is in  $\text{cm}^2/\text{gm}$  and  $\rho x$  is the thickness in  $\text{gm}/\text{cm}^2$ , i.e., the mass of material in the column of 1 square centimeter cross section and  $x$  centimeters long.

[REDACTED] If the monoenergetic X-ray fluence incident normal (perpendicular) to the material sur-

face is  $\varphi_o$ , the direct fluence after traversing a thickness  $\rho x$  of absorbing material is

$$\varphi_{\text{dir}} = \varphi_o e^{-(\mu/\rho)\rho x} \text{ cal/cm}^2.$$

The total mass attenuation coefficient  $\mu/\rho$  is the sum of several components that represent the various mechanisms that can remove a primary photon from the direct flux, while it traverses a material. These mechanisms are described in paragraph 4-3, Chapter 4, and are: the photoelectric process, Compton inelastic scattering, Compton elastic scattering (incoherent elastic scattering) and Rayleigh elastic scattering (coherent elastic scattering). The first two processes result in photon energy being absorbed and the production of secondary electrons, the photoelectrons and Compton recoil electrons, respectively. The kinetic energy of these electrons is dissipated in the material and heats it. Energy deposition usually is calculated to have occurred at the depth at which the electrons are produced. However, in the case of very thin samples, the range of the freed electrons can exceed the material thickness, and energy deposition cannot be considered to be local. The energy removed from the primary photon beam in the Compton elastic process or the Rayleigh elastic process is not locally absorbed. A clear distinction must be made between attenuation of the primary flux and absorption of energy from the primary flux. For this reason the total linear attenuation coefficient usually is written as  $\mu = \mu_a + \mu_s$ . Here,  $\mu_a$  is an absorption coefficient. It represents the first two processes mentioned above, which result in energy absorption. The second term,  $\mu_s$ , is an elastic scattering coefficient, which contributes to the attenuation of the primary flux but not to local energy absorption. It is sometimes convenient to ignore the Rayleigh coherent scattering coefficient in the total attenuation coefficient. The coherent radiation has the same energy, and nearly the same

direction, as the primary photon and cannot be distinguished from it in the "bad" geometry situations that usually occur in nuclear effects applications.\*

Mass attenuation coefficients for the elements beryllium, aluminum, iron, copper, tungsten, and uranium are given in Tables 9-10 through 9-15, and Figures 9-27 through 9-32, respectively. These are representative of metallic materials used in aerospace systems. Mass attenuation coefficients for ablator materials, carbon phenolic and tape-wound silicon phenolic are shown in Figures 9-33 and 9-34, respectively. In these tables and figures,  $Z$  is the atomic number,  $\mu_{ce}/\rho$  is the coherent elastic scattering coefficient,  $\mu_{ie}/\rho$  is the incoherent Compton elastic coefficient,  $\mu_{is}/\rho$  is the inelastic Compton coefficient, and  $\mu_p/\rho$  is the photoelectric coefficient. As designated previously,  $\mu_a/\rho$  and  $\mu/\rho$  are the energy absorption coefficient and the total attenuation coefficient.<sup>†</sup>

### 9-34 X-ray Energy Deposition and Shine Through Fluences

X-ray energy deposition in a thickness  $\delta$  at a depth  $x$  due to direct fluence photons is given by

$$A'_{\text{dir}} = \varphi_o \left[ 1 - e^{-\left(\frac{\mu_a}{\rho}\right)\rho\delta} \right] e^{-\left(\frac{\mu}{\rho}\right)\rho x}.$$

If  $\mu_a \delta \ll 1$ , and if  $\varphi_o$  is in  $\text{cal/cm}^2$ , this expression can be written as

$$A'_{\text{dir}} = \varphi_o \left( \frac{\mu_a}{\rho} \right) \rho \delta e^{-\left(\frac{\mu}{\rho}\right)\rho x} \text{ cal/cm}^2.$$

\* A "good" geometry is one in which the distinction between primary and scattered photons can be made accurately.

<sup>†</sup> The symbols  $K$ ,  $L_1$ ,  $L_2$ , etc., in the tables and figures indicate the binding energies of the various electron shells (see paragraph 4-3, Chapter 4).

Frequently, the absorption is written in terms of cal/gm by dividing out the thickness  $\rho\delta$ ,

$$A_{\text{dir}} = \varphi_0 \left( \frac{\mu_a}{\rho} \right) e^{-\left(\frac{\mu}{\rho}\right) \rho x} \text{ cal/gm.}$$

This expression for the absorption is in terms of a dose; however, this assumes that very little of the flux is absorbed in the deposition region at depth  $x$ , i.e., the deposition region considered is very thin. Clearly, more energy than is in the incident flux cannot be absorbed.

The equation for direct fluence ( $\varphi_{\text{dir}}$ ) given in paragraph 9-32 can be used to represent a small energy band of photons in X-ray energy spectra such as those tabulated in Table 4-3, Chapter 4, for various black body spectra. The total energy in the direct X-ray fluence after

traversing thickness  $x$  is obtained by summing over the energy bands.

$$\varphi = \sum_i \varphi_{oi} e^{-\left(\frac{\mu}{\rho}\right)_i \rho x} \text{ cal/cm}^2.$$

In a like manner, the total direct fluence X-ray energy absorption at depth  $\rho x$  is obtained by summing for each energy band.

$$A = \sum_i \left( \frac{\mu_a}{\rho} \right)_i \varphi_{oi} e^{-\left(\frac{\mu}{\rho}\right)_i \rho x} \text{ cal/cm}^2.$$

Problems 9-3 and 9-4 illustrate how these equations can be used to calculate approximate values for energy deposition and shine through.

Problem 9-3. Calculation of X-ray Energy Deposition at the Surface

The information contained in Tables 9-10 through 9-15 and Figures 9-27 through 9-34 together with the equation for energy absorption given in paragraph 9-34 provide the means to obtain the approximate X-ray energy absorbed for various spectra and several materials. If the energy deposition at the surface on which the X-rays are incident is desired, the thickness,  $x$ , reduces to zero, and the energy deposition equation becomes.

$$A = \sum (\mu_a / \rho)_i \varphi_{oi} \text{ cal/gm.}$$

**Problem 9-4. Calculation of X-ray Energy Deposition at a Depth  
in a Material and the Shine Through Fluence**

The information contained in Tables 9-10 through 9-15 and Figures 9-27 through 9-34 together with the equation for energy absorption given in paragraph 9-34 provide the means to obtain the approximate X-ray energy absorbed for various spectra and several materials at a depth  $x$  in the materials, as well as the fluence at that depth or the fluence emerging from the back face of the material (shine through).

DNA  
(L)(3)

Problem 4-1, Chapter 4, describes the method to obtain energy distributions for various source temperatures from the normalized Planck distributions given in Table 4-1, Chapter 4.

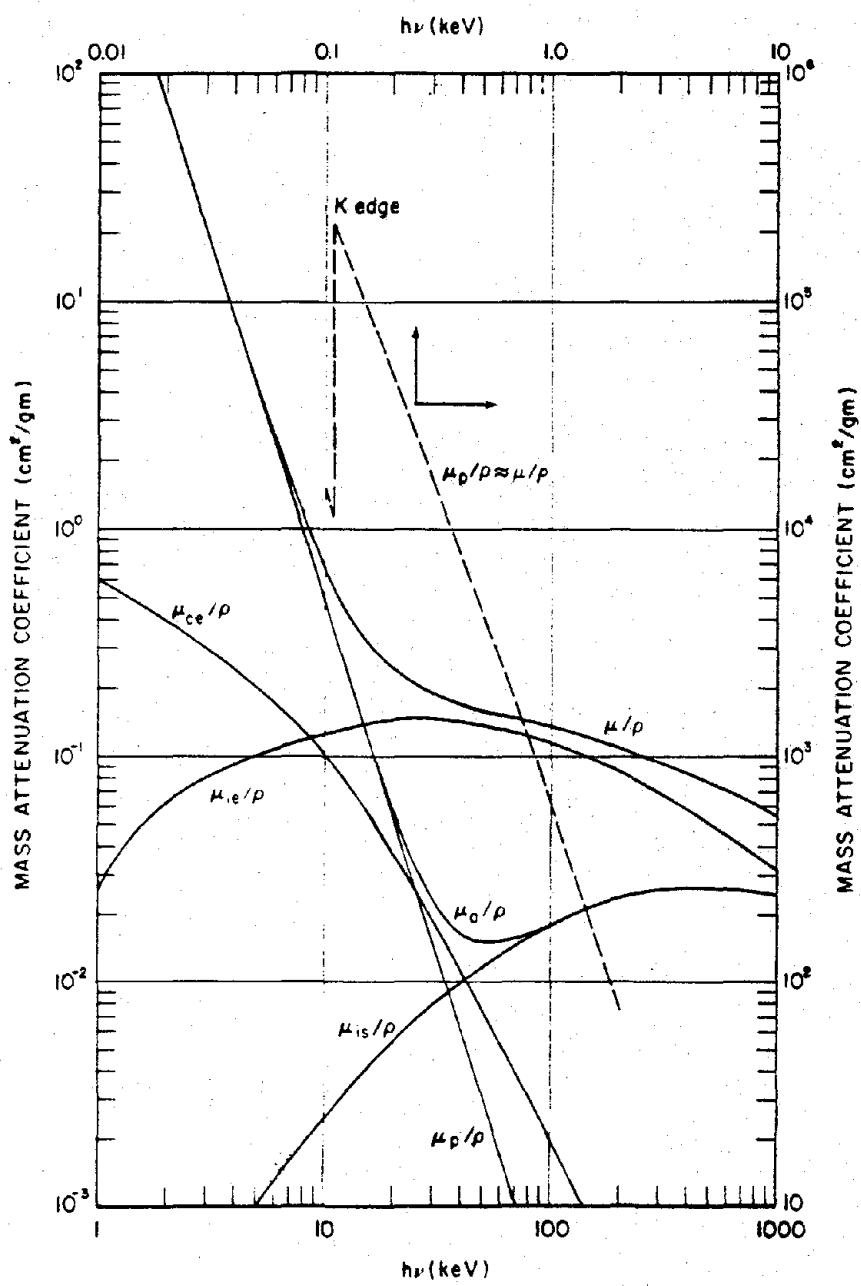


Figure 9-27. Photon Cross Sections in Beryllium

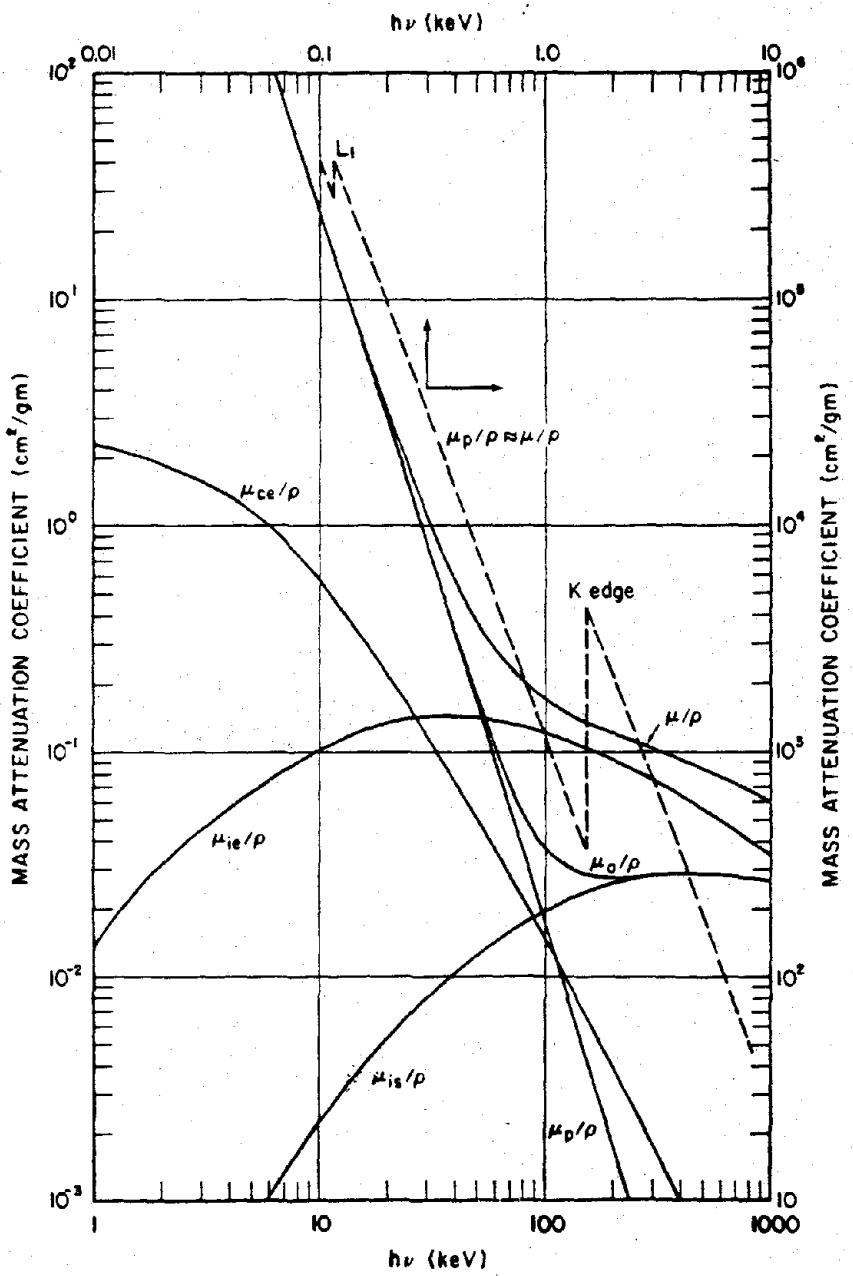


Figure 9-28. Photon Cross Sections in Aluminum

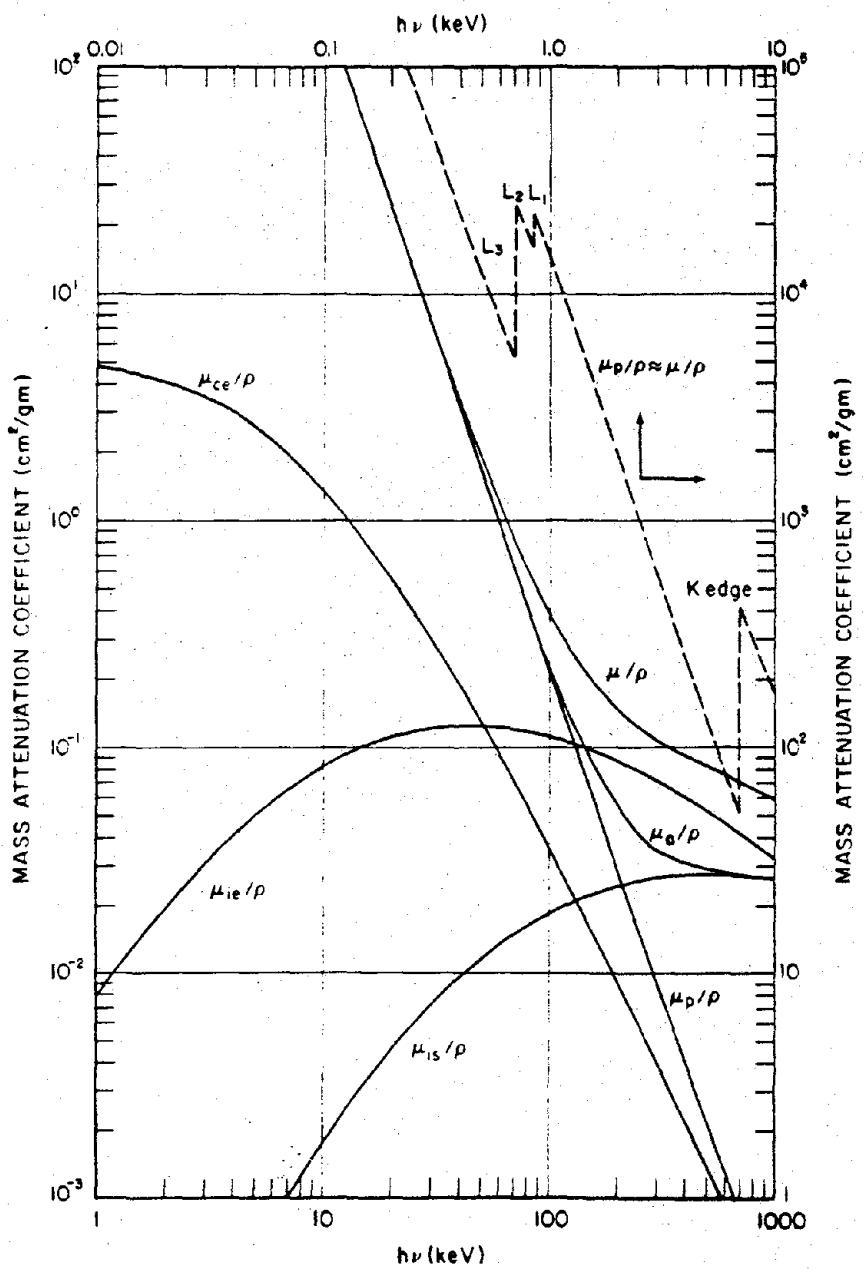


Figure 9-29. Photon Cross Sections in Iron

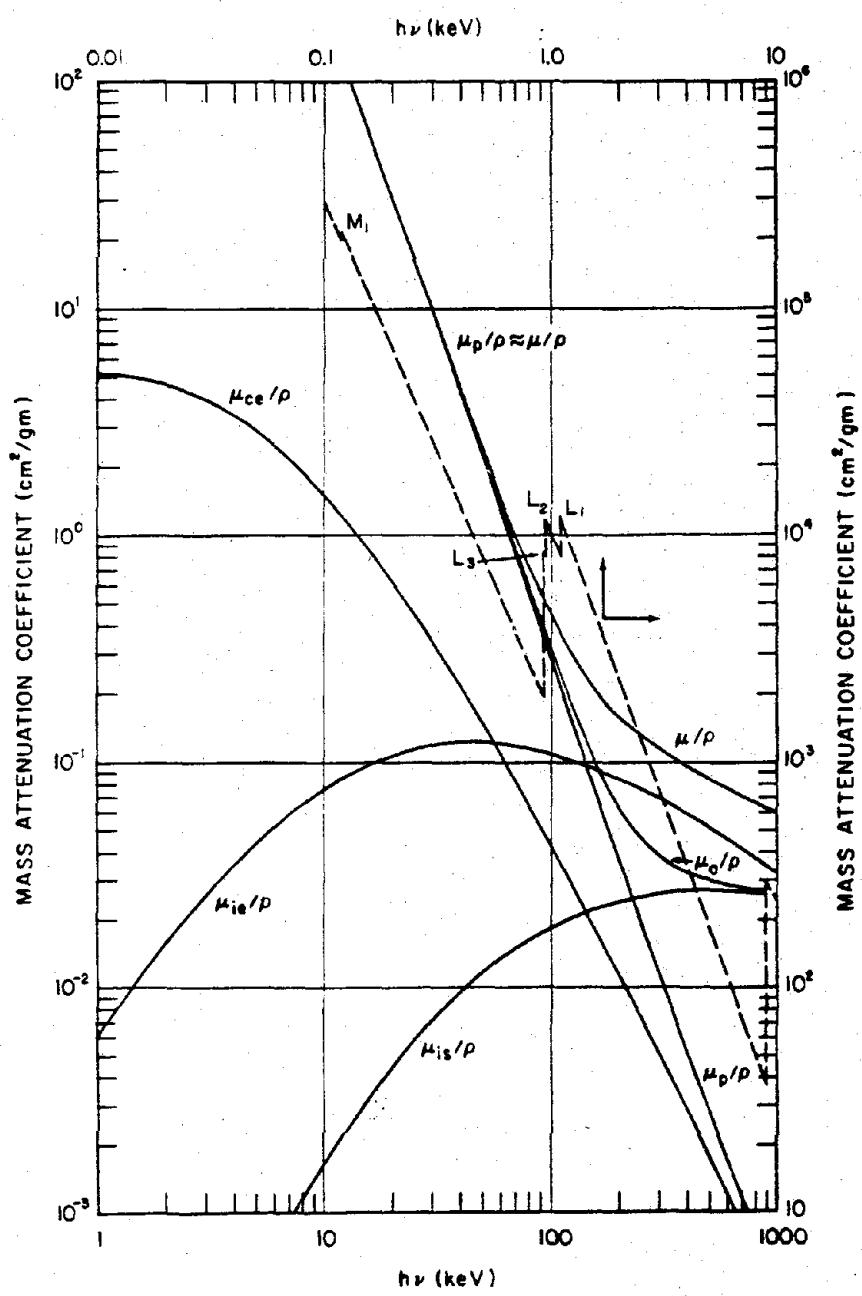


Figure 9-30. Photon Cross Sections in Copper

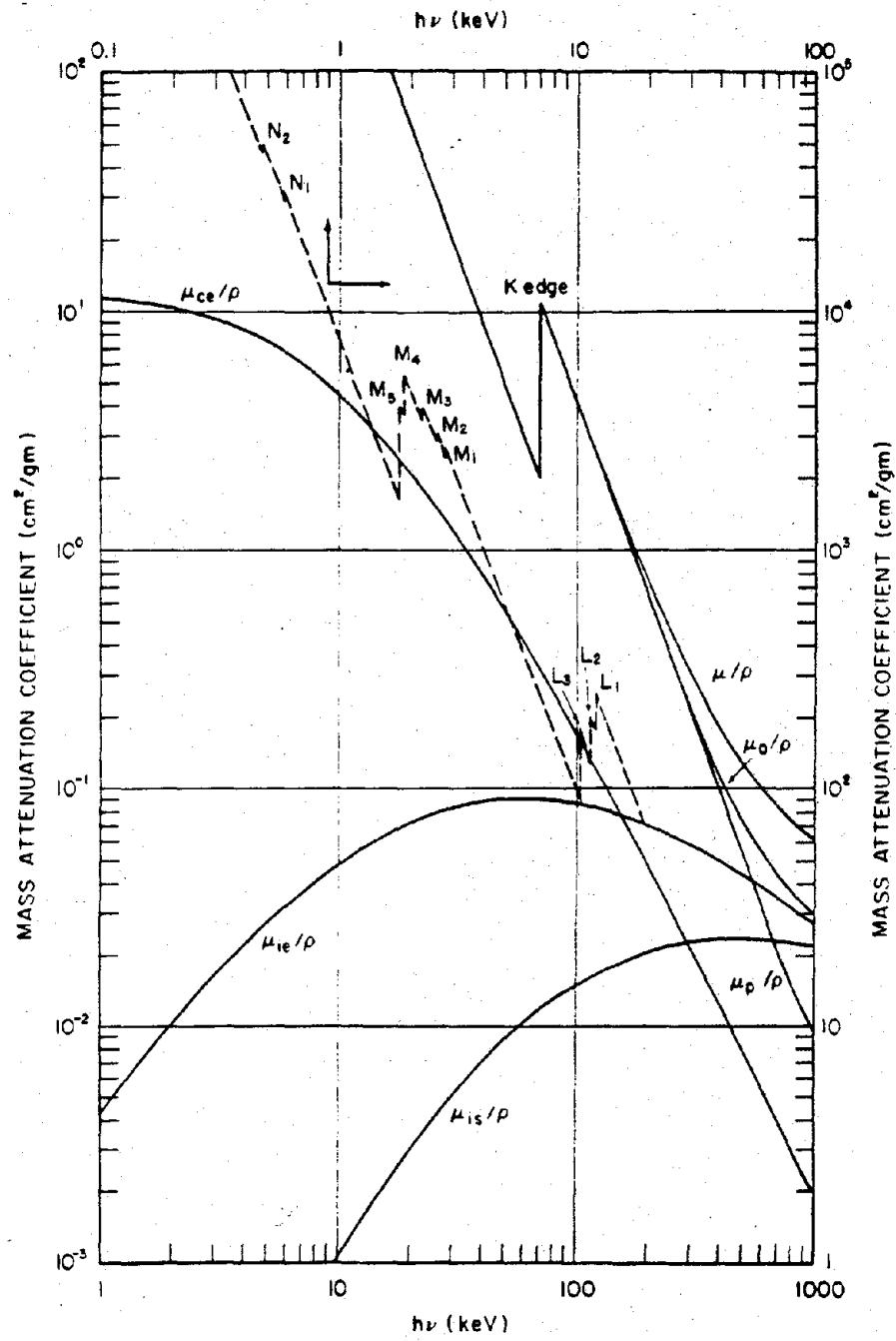


Figure 9-31. Photon Cross Sections in Tungsten

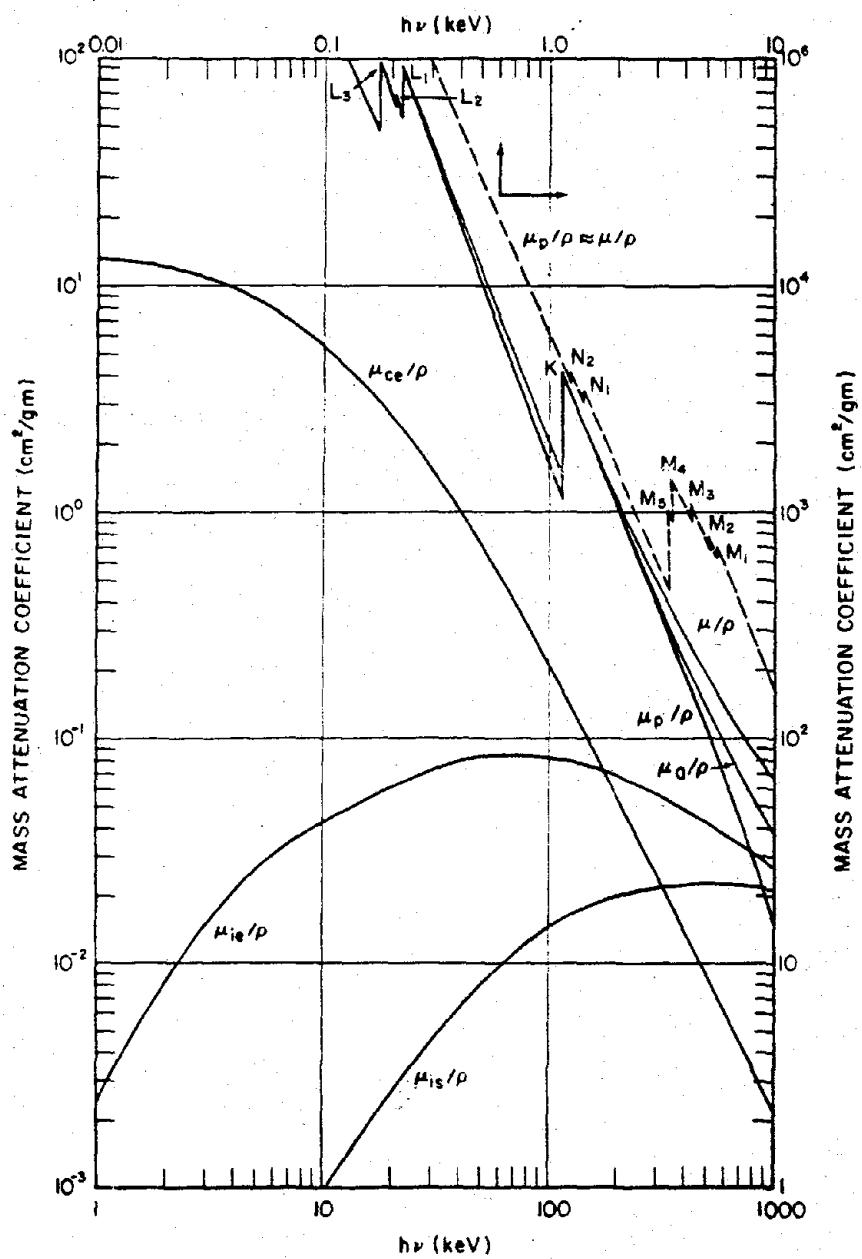


Figure 9-32. Photon Cross Sections in Uranium

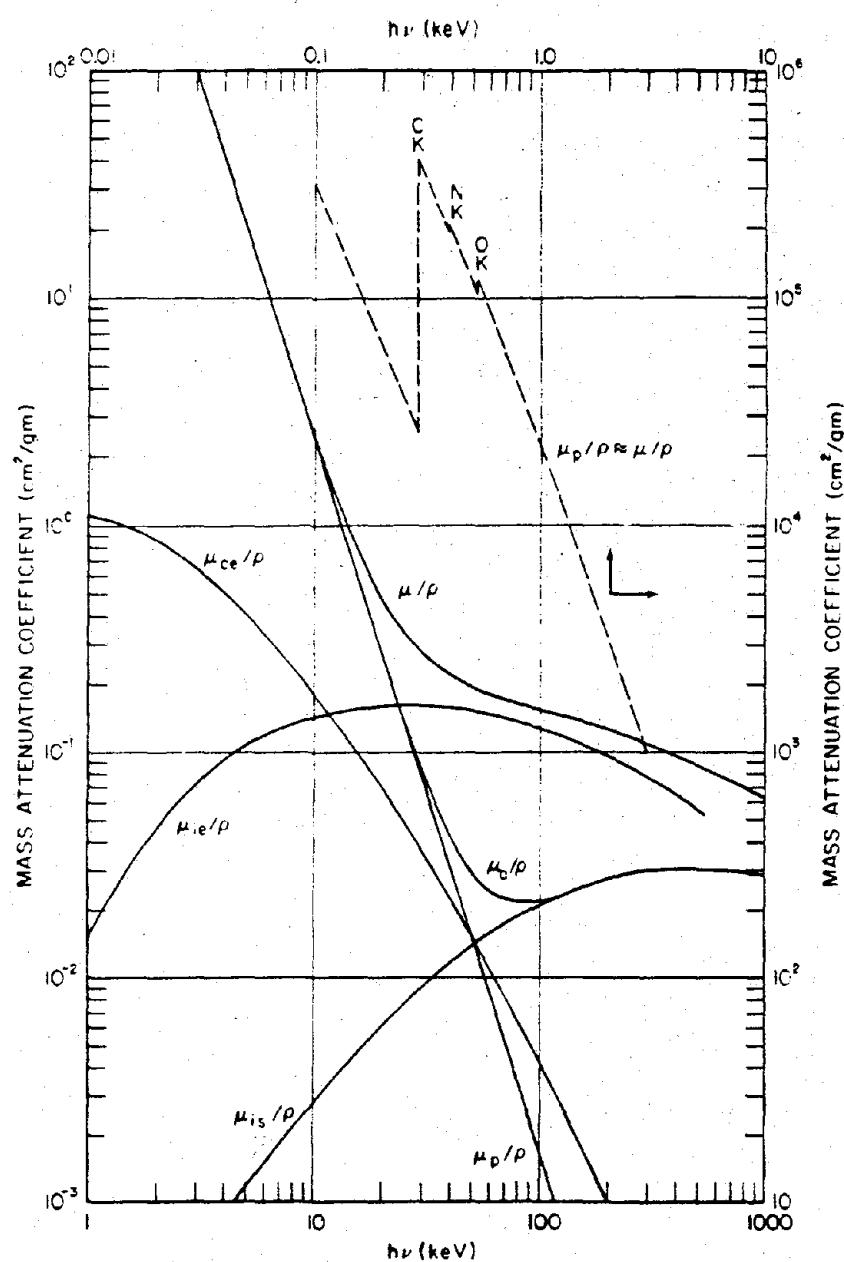


Figure 9-33. Photon Cross Sections in Carbon  
Phenolic (CP),  $\bar{Z} = 6.08$

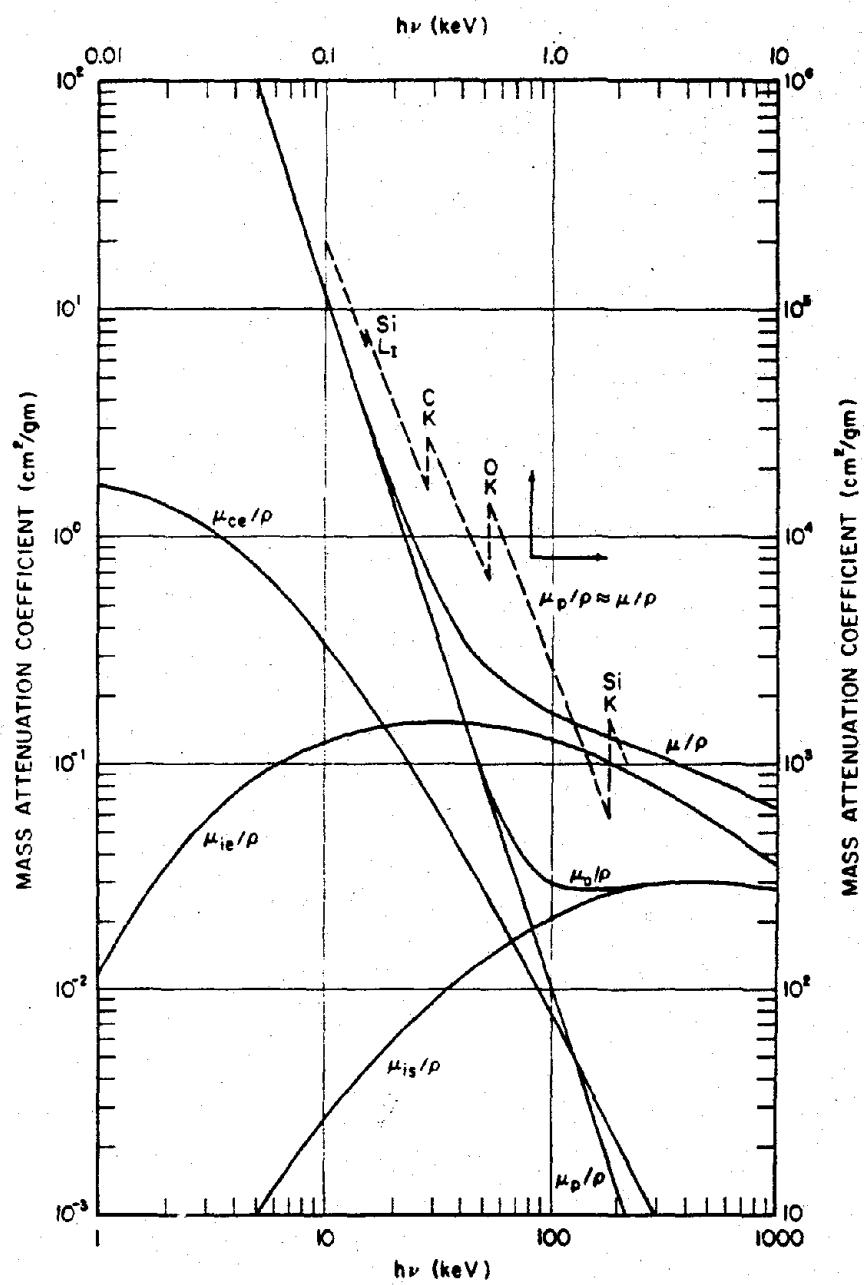


Figure 9-34. Photon Cross Sections in Tape Wound  
Silicon Phenolic (TWSP),  $\bar{Z} = 9.01$

### **9-35 X-ray Energy Deposition Summary**

The methods described in paragraphs 9-33 and 9-34 and illustrated in Problems 9-3 and 9-4 allow the calculation of curves that show approximations of energy deposition as a function of depth for black body spectra incident on any material, if the cross sections are known for the material.

### **INITIAL PRESSURIZATION OF MATERIALS DUE TO X-RAY DEPOSITION**

An immediate consequence of the deposition of X-ray energy is the rapid heating of the material. This heating causes an initial pressure distribution as a function of depth in the structure. The initial pressurization generates shock waves that propagate through the thickness of the shell of the structure. The heating can result in a solid material changing phase, that is, melting or vaporizing. The melting and vaporization cause blowoff, which imparts an impulse to the structure and excites whole structure modes of response.

### **9-36 Phase Changes Induced by X-ray Heating**

In most nuclear weapon X-ray environments, the X-ray energy is deposited in a very short time, a few nanoseconds to a few hundred nanoseconds. The material cannot expand appreciably during this time, so the energy deposition process can be considered to occur at a constant volume or at normal material density,  $\rho_0$ . Rapid melting and vaporization are accompanied by enormous pressure increases. Values

for enthalpy changes for melting and vaporization for the metals discussed in the previous subsection are given in Table 9-17. These values are for one atmosphere pressure. In most X-ray problems of interest the material is initially at very high pressure, so these values can be considered to be only approximate. This approach is not correct for ablators as a class although it might apply to carbon phenolic in a cold environment. Confining the discussion to metals will not restrict the transfer of principles.\*

The rising pressure that results from heating at constant density is illustrated in Figures 9-39 and 9-40 where isoenergy lines of aluminum are shown in pressure-density plots. If the internal energy is above the critical energy, 3,016 cal/gm for aluminum, the material can be considered as a vapor. Figure 9-40 shows the high pressure, high energy intercepts with the normal density abscissa ( $\rho_0 = 2.7 \text{ gm/cm}^3$ ). The release adiabats for expansion from density  $\rho_0$  to low density and pressure also are shown in this figure. Expansion along the adiabat results in decreasing internal or potential energy as the material develops kinetic energy during "blow-off." For example, a 6,000 cal/gm energy depo-

sition in aluminum at  $\rho_0 = 2.7 \text{ gm/cm}^3$  results in a pressure of about 1.5 megabars (Mb). The aluminum would expand from that state to low pressure and density, with final internal energy of about 3,000 cal/gm and about 3,000 cal/gm of kinetic energy. The 3,000 cal/gm of internal or potential energy is used to overcome the physical and chemical forces that bind the atoms together in the solid. This leads to the concept of heat of sublimation. The heat of sublimation at absolute zero,  $E_{so}$ , is the energy required to form the saturated vapor from the solid at a temperature of absolute zero. Thus,  $E_{so}$  does not include any energy of kinetic motion. The energy of sublimation generally is a function of temperature becoming larger for larger deposition energies (temperatures).

\* The problem of phase changes in a composite heat shield ablator is more complicated since different deposition profiles, material enthalpy, and thermal conductivities are involved in the calculations. While some materials, e.g., tape-wrapped carbon phenolic, may behave like metals in a cold environment, the techniques described here generally are not applicable to the description of the blowoff process in the broad category of composite materials that use three dimension (3-D) weaves for heat shields or for X-ray shields that use dispersed high Z materials for loading.

Table 9-17. Enthalpy Change for Selected Metals (cal/gm)

Metal- Atomic Weight	To Melt	Through Melt	To Vapor	Through Vapor	Sublimation Energy
Be 9.013	876.0	1,187.0	2,147.0	10,040.0	8,682.0
Al 26.98	160.4	255.3	771.1	3,347.0	2,891.0
Fe 55.85	250.8	315.8	573.0	2,071.0	1,782.0
Cu 63.54	110.0	160.0	336.0	1,481.0	1,275.0
W 183.85	153.9	200.0	304.0	1,353.0	1,110.0
U 238.00	49.0	64.5	171.9	596.1	492.1

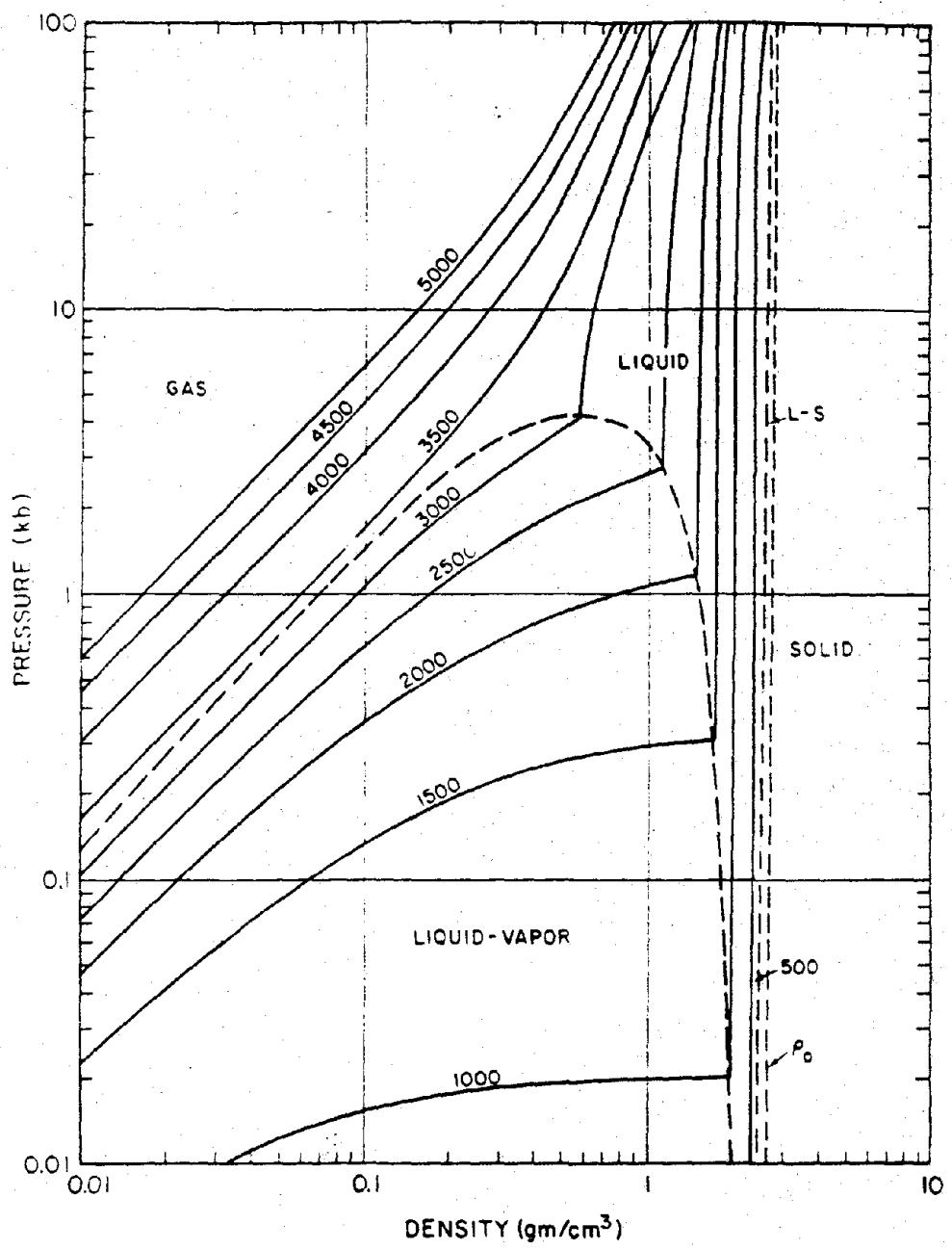


Figure 9-39. Aluminum Isoenergy Lines.  
Parameter is Energy in cal/gm

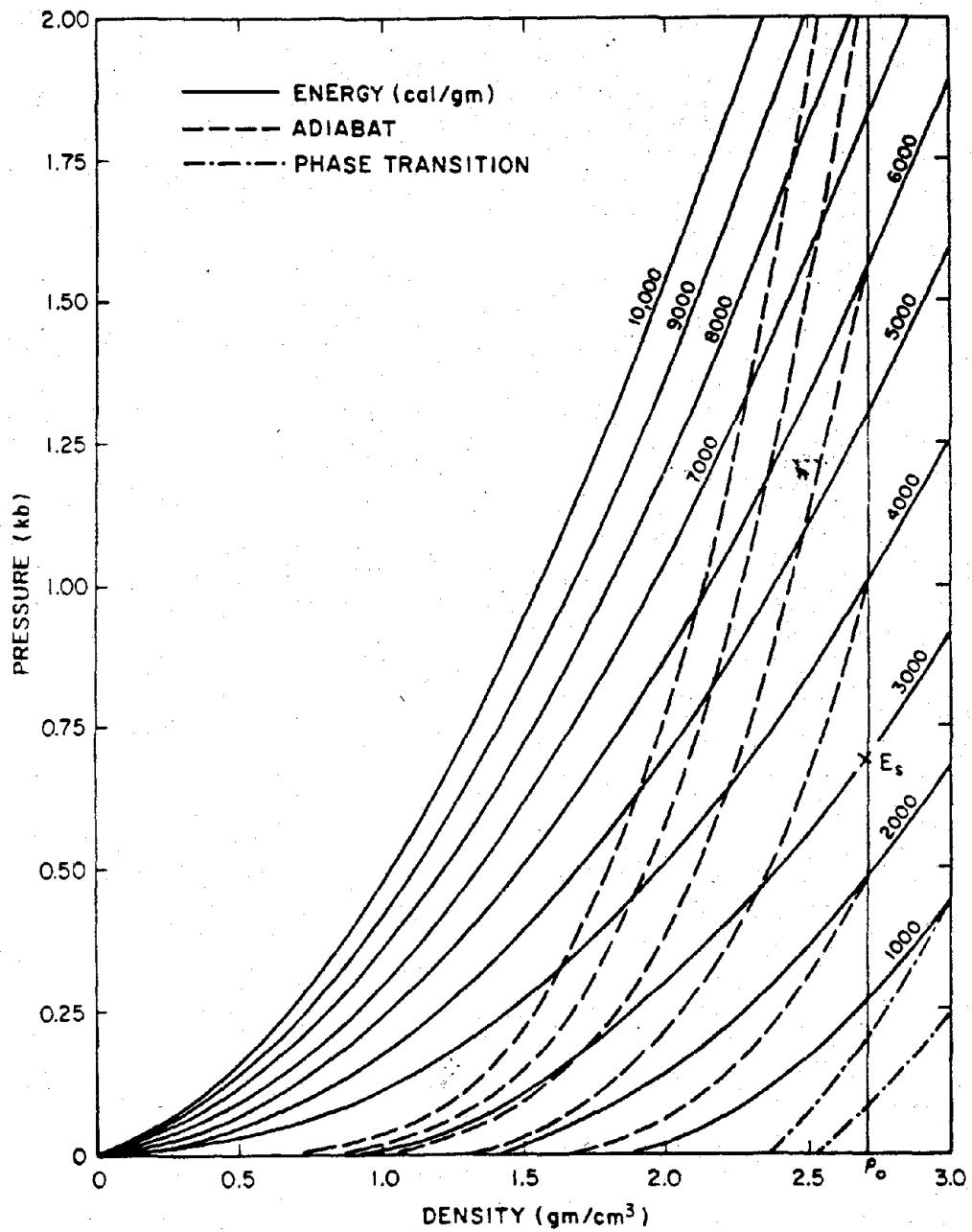


Figure 9-40. Aluminum Isoenergy Lines and Adiabats

9-37. The Grüneisen Parameter and  
the Equation of State

As a first approximation to the equation of state of material, it is assumed that the pressure in the material increases linearly with the deposited internal energy per unit volume,

$$P = G\eta\epsilon,$$

where  $G$  is the Grüneisen ratio for the material,  $\epsilon$  is the internal energy per unit volume, and  $\eta =$

$\rho/\rho_0$ , the ratio of the density to a normalized density of the material, usually the ambient density. In codes used to calculate shock wave propagation, for example the PUFF type codes, more elaborate equations of state are used to fit the experimentally determined behavior of the solid and vapor phases. The equations used in the PUFF codes reduce to the equation given above when  $\eta = 1$ , and generally only one value of  $G$  is used to specify a material.

Although there may be small errors in calculating the X-ray energy deposition as a function of depth, the significant sources of errors in pressure predictions are the accuracy and validity of the Grüneisen parameter for solid and vapor equations of state. Experimental values of  $G$  obtained by different methods result in factors of about two uncertainty even for some of the common materials such as aluminum, beryllium, and tungsten. Even though indications are that  $G$  is not well known as a function of deposited energy, some very good correlations have been obtained for computed and measured values of pressure waves in X-ray tests, when careful calculations are made employing elastic plastic properties of the materials.

Initial pressurization in distended materials such as porous metals and foams present a particularly difficult and uncertain condition for current analytical techniques.

The units for  $\epsilon$  in the equation given above are energy per unit volume, which have the same dimensions as pressure. Therefore, the energy required in cal/gm for a phase change can be expressed in units of pressure, if the density of the material is specified. If the internal energy,  $E$ , is given per unit mass, the relation to  $\epsilon$  is

$$\epsilon \text{ (cal/cm}^3\text{)} = E \text{ (cal/gm)} \rho_0 \text{ (gm/cm}^3\text{)}.$$

The value of  $\epsilon$  in megabars may then be obtained by the relation

$$\epsilon \text{ (Mb)} = \epsilon \text{ (cal/cm}^3\text{)} \times 4.18 \times 10^7 \left( \frac{\text{erg}}{\text{cal}} \right) \times 1 \left( \frac{\text{Mb}}{10^{12} \text{ dyne/cm}^2} \right)$$

$$\epsilon \text{ (Mb)} = 4.8 \times 10^{-5} \epsilon \left( \frac{\text{cal}}{\text{cm}^3} \right) \\ = 4.18 \times 10^{-5} \rho_0 E \left( \frac{\text{cal}}{\text{gm}} \right).$$

Thus, the previous equation for pressure may be written

$$P \text{ (Mb)} = G \frac{\rho}{\rho_0} \epsilon \text{ (Mb)},$$

or

$$P \text{ (Mb)} = 4.18 \times 10^{-5} G \rho E \text{ (cal/gm)}.$$

The enthalpy changes of the metals shown in Table 9-17 in cal/gm are given in Table 9-19.

Table 9-19. Enthalpy Changes  $\epsilon$  (Mb)

Metal	$\rho_0$ (gm/cm <sup>3</sup> )	To Melt	Through Melt	To Vapor	Through Vapor	Sublimation Energy, $E_s$
Be	1.85	0.068	0.0918	0.166	0.776	0.671
Al	2.70	0.0181	0.0288	0.087	0.378	0.326
Fe	7.86	0.0824	0.1036	0.188	0.680	0.585
Cu	8.92	0.0410	0.0596	0.125	0.552	0.475
W	19.3	0.124	0.161	0.245	1.092	0.895
U	18.7	0.0383	0.0504	0.134	0.466	0.385

Table 9-20. Pressure Change,  $P$  (Mb)  
 $(\rho = \rho_0, \eta = 1)$

Metal	G	To Melt	Through Melt	To Vapor	Through Vapor	Sublimation Energy, $E$
Be	1.45	0.009	0.133	0.241	0.12	0.973
Al	2.13	0.0366	0.0613	0.185	0.805	0.694
Fe	1.69	0.139	0.175	0.318	1.15	0.989
Cu	2.00	0.082	0.119	0.250	1.10	0.950
W	1.43	0.177	0.230	0.350	1.56	1.28
U	2.03	0.078	0.102	0.273	0.946	0.782

The pressures associated with these changes at ambient density, i.e., when  $\rho = \rho_0$ , and  $P$  (Mb) =  $Ge$  (Mb), are shown in Table 9-20.

From Table 9-20, aluminum has a sublimation pressure of about 0.7 Mb at ambient density, corresponding to sublimation energy of about 2,900 cal/gm (Table 9-17). This point is shown in Figure 9-40, labeled  $E$ , at about 3,000 cal/gm. Table 9-20 indicates that the pressures associated with vaporization of metals at ambient density are with some exceptions about 1 Mb. A survey of more than 30 common metal elements indicates that an average of 1 Mb for vaporization is a good approximation, especially if the Grüneisen value for the material is uncertain. Since a bar corresponds to 14.7 psi a Mb is the enormous pressure of about  $1.45 \times 10^7$  psi. Thus, tremendous forces are involved in the pressure gradients associated with metal vaporization at ambient density. Table 9-17 shows that vaporization usually involves several thousand calories per gram of energy. High explosive materials (TNT, etc.) release about 1,000 cal/gm. Therefore, on a mass basis there is more energy associated with metal vaporization than with high explosives. Generally, the thicknesses of material evaporated by X-ray absorption is

small, and, the total mass of material that is vaporized generally is small.

### SHOCK WAVE PROPAGATION AND DAMAGE PREDICTIONS

The sequence of events for the generation and propagation of a stress wave through the thickness of an aerospace shell and the damage produced is illustrated in Figure 9-41. Cold X-rays are deposited primarily in a relatively thin sheet of material at the front surface (Figure 9-41a). After the energy is deposited a compression wave propagates inward from the front surface, followed by a rarefaction that causes the vapor and liquid to blow off (Figure 9-41b). This rarefaction also may cause a spall of solid material from the front surface (Figure 9-41c). Later the compression wave reflects from the back surface and returns as a rarefaction wave. This rarefaction wave, or the coincidence of this wave with the rearward moving rarefaction may cause the rear surface to spall (Figure 9-41d), or may cause fracturing or debonding. This process occurs within the order of a microsecond and generally is complete before the overall structural motion occurs. The shock effects are

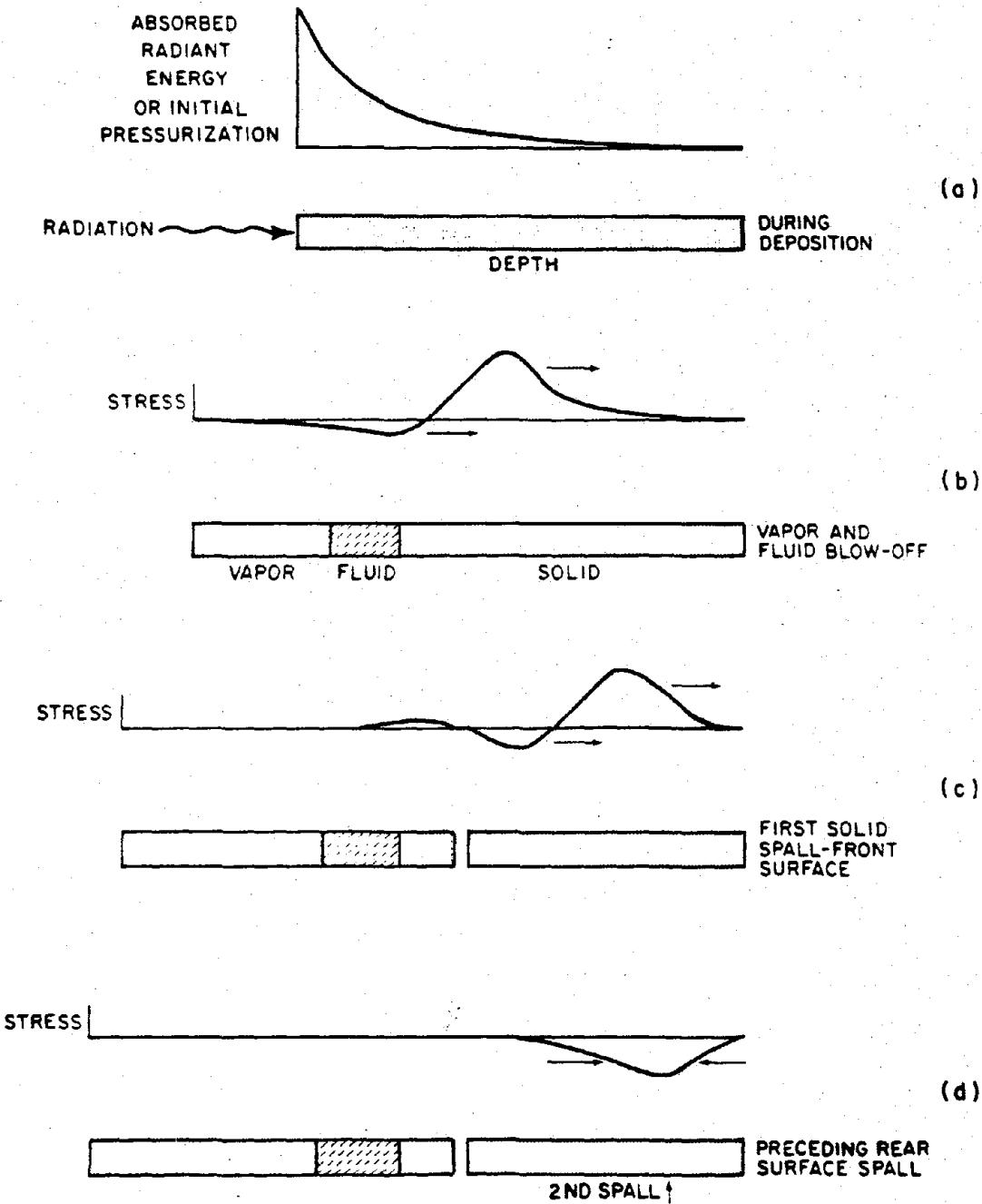


Figure 9-41. [REDACTED] Sequence of Spallation Following  
Radiation Deposition [REDACTED]

extremely local, depending on the sheet thickness and not on the overall geometry of the structure, so spall damage, including fracturing and debonding, usually cannot be scaled according to the laws that govern structural behavior. Since the spall damage occurs early, possibly weakening the structure, it can have a strong effect on the subsequent response to the structure to the impulse that has been imparted.

Propagation of stress waves and the damage predictions are not amenable to hand calculations. Most stress wave propagation calculations are performed on computers using one dimensional (1-D) models to represent a cross section of an aerospace vehicle shell. These stress wave propagation calculations are used routinely in design analysis and are the direct outputs of PUFF-like codes or their variations. The stress wave propagation predictions are used to:

1. Obtain a calculated pressure time history at the rear surface of a 1-D sample for direct comparison to experimental values that are obtained by laboratory simulation or by underground nuclear tests. The agreement or lack of correlation serve as an important criteria for judging the adequacy of analytical techniques. The conclusions are almost universal that the largest sources of error in stress wave propagation codes are associated with the mechanical aspects of the material behavior, such as failure criteria, and the elastic-plastic models, which should include strain rate and temperature dependence.

2. Obtain maximum tension as a function of depth in the materials to indicate regions of potential material failure, debonding, and spalling. Definitions that are required for the materials failure level under these dynamic tensile loads are obtained experimentally.

3. Obtain input data for structural response analysis.

There also are some 2-D shock propagation codes being used for specific calculations

involving cylinders, nose tips, etc. Peak pressure predictions using pure hydrodynamic representations of the material in code calculations are generally high by a factor of 2 to 4. If a dynamic elastic-plastic constitutive relationship is included, the predictions are improved significantly.

### 9-38 Through-the-Thickness Elastic-Plastic Shock Propagation

Considerable progress has been made in correlating measured and calculated through-the-thickness shock propagation in one dimension by using the elastic-plastic materials description in PUFF-type codes. The stress strain diagram shown in Figure 9-42 illustrates a two-wave nature of the elastic-plastic shock wave propagation. The total stress,  $\sigma$ , is the sum of the hydrostatic pressure,  $P$ , and an elastic stress offset of  $2/3 Y_0$ , where  $Y_0$  is the yield strength of the material (its compressive yield strength if that is different from its yield strength in simple tension). The effect of the yield stress path OAB is to propagate two stress waves having different velocities into the undisturbed material. The slope of the elastic portion, OA, is larger than the plastic portion, AB. The propagation speed is larger if the slope of the stress strain curve is larger. Hence, an elastic precursor shock traveling with the elastic velocity,  $c_E$ , runs in front of the slower total stress wave which propagates with a bulk sound speed,  $c_o$ .

$$c_E = \sqrt{\frac{K}{\rho_0} + \frac{4/3 S^*}{\rho_0}}$$

$$c_o = \sqrt{\frac{K}{\rho_0}}$$

where  $K$  is the bulk modulus and  $S^*$  is the shear modulus.

An elastic rarefaction stress ( $4/3 Y_0$  or twice the stress offset) propagates from the rear of the shock wave at velocity  $c_E$  and overtakes

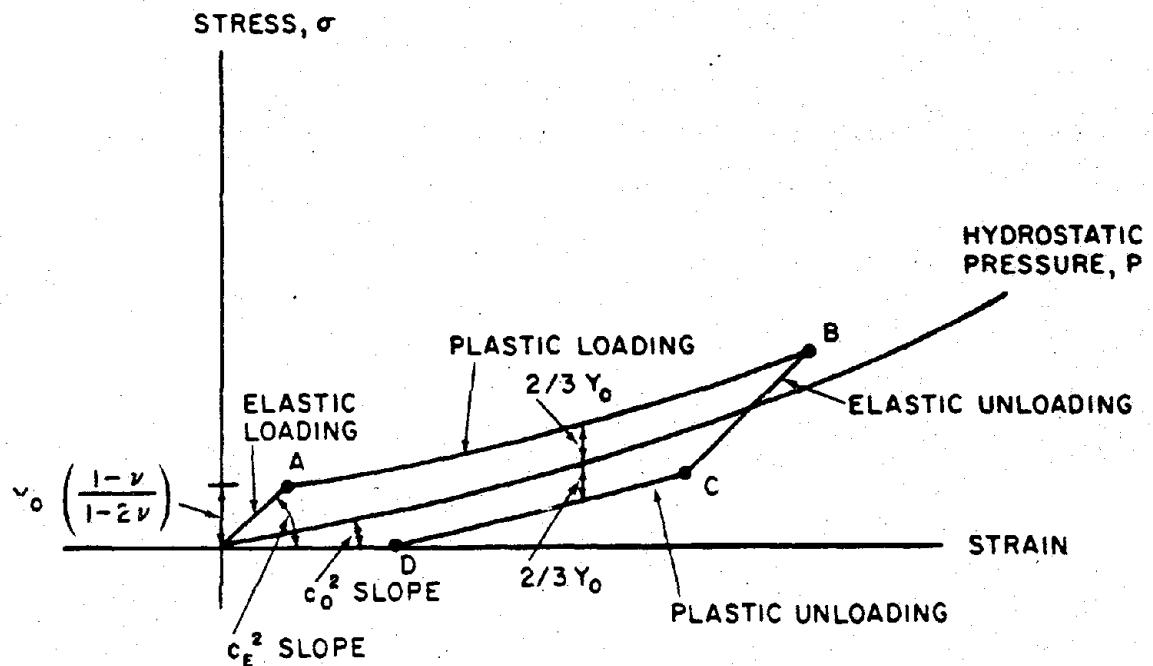


Figure 9-42. [REDACTED] Equation of State for Elastic-Plastic Material Description [REDACTED]

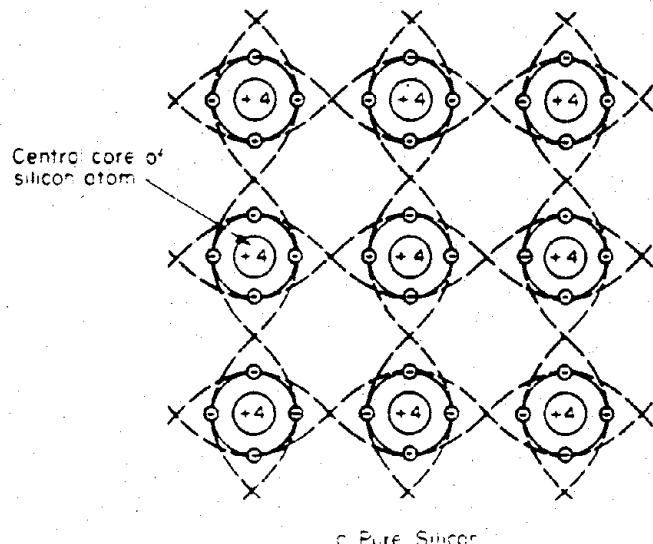
the slower plastic wave (path BC). This rarefaction wave causes a greater attenuation of the main stress pressure wave than is obtained in pure hydrodynamic calculations (up and down the Hugoniot). This greater attenuation of the elastic plastic wave propagation compared to purely hydrodynamic calculations results in better correlation with measured values of stress. The plastic unloading to a stress-free condition, path CD in Figure 9-42, also propagates with velocity  $c_0$  and completes the cycle.

Although the elastic-plastic code calculations improved the correlation of measured and computed through-the-thickness stresses for some materials, if a material has strong strain rate or temperature dependence these features also must be incorporated into the calculations. Stress wave propagation through materials such as foams require an entirely different constitu-

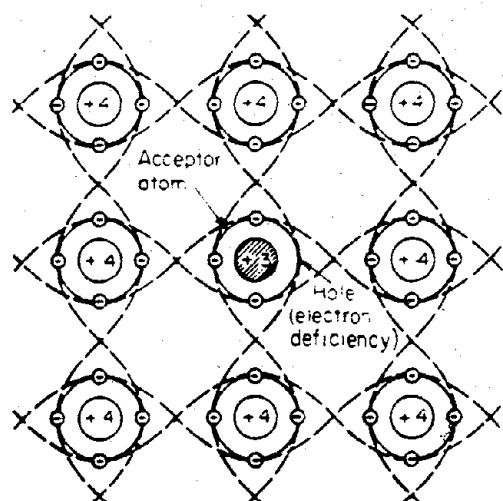
tive expression, and anisotropic materials such as three-dimensional quartz phenolic, can have quite different material properties in different directions. Similarly, propagation characteristics of inhomogeneous materials or materials that contain small radiation absorbers lead to complicated propagation analysis. Propagation in these materials has not been treated in an analytically satisfactory manner. Most of the current analytical techniques used in the solution of stress wave propagation in the materials are deficient in varying degrees in the following ways.

1. There is incomplete understanding of the material behavior under the types of conditions that result from X-ray energy deposition, so the material representations are inadequate in most cases.

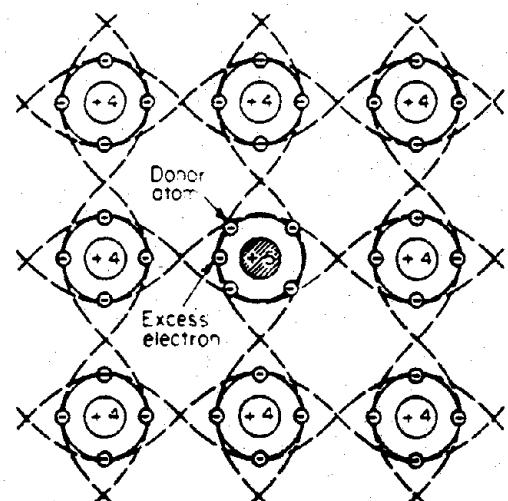
2. Experimental data for verification and modification of the equations of state and con-



c. Pure Silicon



b. Silicon with Acceptor Impurity Atom



c. Silicon with Donor Impurity Atom

Figure 9-45. Two-Dimensional Lattice Structure of Silicon

three orbiting electrons does not have sufficient electrons to share with its neighboring silicon atoms. This lack of an electron is called a hole. For conceptual purposes, the hole can be treated like an electron with a positive charge. Consequently, in semiconductor discussion the term charge carriers refers to the electrons and holes made available for the conduction process by the impurity doping.

Figure 9-46 illustrates a semiconductor junction (diode), with the two impurity regions shown separated by a solid line. This represents what conceptually would be the junction of the two materials. However, in reality the silicon is all one crystal, and there is really no physical junction. There are, as illustrated, regions at both ends of the crystal which are predominantly either P type (excess of free holes) or N type (excess of free electrons). A transition region, called the depletion region, exists in the center. Within this region, holes from the P region combine with equal numbers of electrons from the N region. As a result, only a few free charge carriers remain in the region when equilibrium has been reached. Depending on the number of charges removed from each region, a voltage (electric field) will be developed across the depletion region. The voltage across the depletion region under equilibrium is such that any

holes (positive charge carriers) introduced into the region would migrate by the drift process to the P region, and a negative charge carrier (electron) introduced into the depletion region would migrate by the drift process to the N region. Under normal conditions conventional current flow\* would allow current to flow for ideal diodes only from the P side to the N side. If, however, free carriers were generated in the depletion region, conventional current flow would dictate that a current, proportional to the number of free charge carriers generated, would flow from the N region to the P region. This is in the reverse direction from the normal conventional current flow through an ideal diode. This reverse current, if generated in the depletion region by ionizing radiation, is called the drift component of the photocurrent in a PN junction. The diffusion component of the photocurrent is the result of free carrier generation by the ionizing radiation in the P and N regions near the depletion region. Those hole-electron pairs generated far from the depletion region will be trapped and recombined before they can become effective. The effect of the radiation is to

\* In this chapter, normal current flow is considered to be conventional current flow. This is opposite to actual electron flow.

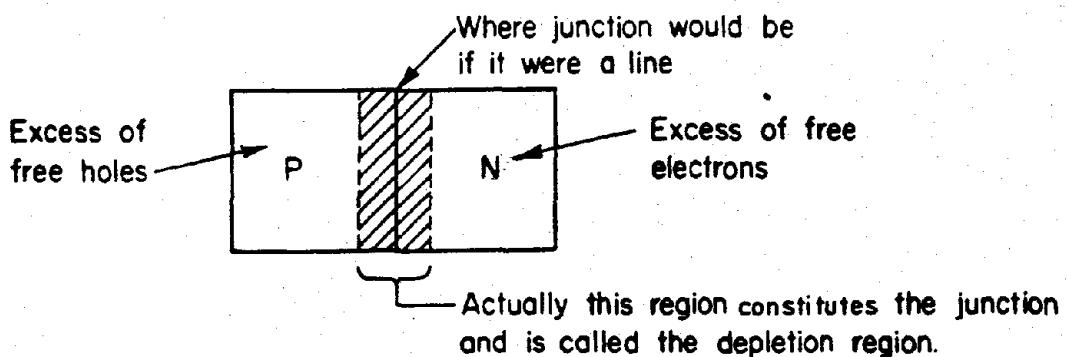


Figure 9-46. Illustration of a Semiconductor Junction

generate a current in the reverse direction through the diode junction, which tends to forward bias the diode. An expression that generally will predict the photocurrent for many cases of interest is:

$$I_{pp\ max} = qK_g \dot{D}A (w + L),$$

where

$I_{pp\ max}$  = the maximum\* primary photocurrent for a PN junction

$q$  = electronic charge  $1.60 \times 10^{-19}$  coulombs

$K_g$  = the energy-dependent free-charge-carrier-generation constant (electron-hole pairs/cm<sup>3</sup> · roentgen)

$K_g$  (for silicon) =  $4.2 \times 10^{13}$  electron-hole pairs/cm<sup>3</sup> · R

$K_g$  (for germanium) =  $1 \times 10^{14}$  electron-hole pairs/cm<sup>3</sup> · R

$\dot{D}$  = the gamma exposure rate, R/sec (The gamma ray photons have energies which would give best results with the  $K_g$  constants given above.)

$A$  = junction area in cm<sup>2</sup> ( $A$  can typically vary from  $0.3 \times 10^{-4}$  to  $0.2 \times 10^{-1}$  cm<sup>2</sup>)

$w$  = depletion layer width in cm ( $w$  varies with applied voltage and is best expressed as  $w = w_1 (V_o - V_j)^b$  where  $V_o$  is the built-in junc-

tion potential ( $\sim 0.35$  volts for germanium and  $\sim 0.72$  volts for silicon)  $w_1$  typically varies from  $0.5 \times 10^{-4}$  cm to  $1 \times 10^{-3}$  cm,  $V_j$  is the junction voltage, and  $b$  typically varies from 0.05 to 0.5.

$L$  = diffusion length for minority carriers on the side of the junction with the longer diffusion length in cm ( $L$  can vary typically from  $0.15 \times 10^{-1}$  cm to  $0.2 \times 10^{-4}$  cm).

The duration of the photocurrent depends on the time required for free holes and free electrons to be trapped and to recombine. Since these times are short, the photocurrent is a pulse of current of relatively short duration. Typical pulse shapes are shown in Figure 9-47.

Tunnel diodes are at least an order of magnitude more radiation resistant than diodes in general, since they are characterized by small geometry, heavily doped PN regions, and narrow junctions. The short-circuit photocurrent can be estimated from the equations applicable to general diodes. Since the lifetime of minority carriers in tunnel diodes is very short, the response of a tunnel diode to a pulse of radiation is expected to follow the radiation pulse. Normally, the width of the depletion region for tunnel diodes is so narrow that the photocurrent will consist primarily of the diffusion component. The maximum photocurrent under short

\* For those more theoretically inclined this equation applies in the case where  $\tau < t_p/4$  and  $t_p$  is the steady-state value. A more detailed equation and development is the *TREE Handbook*.

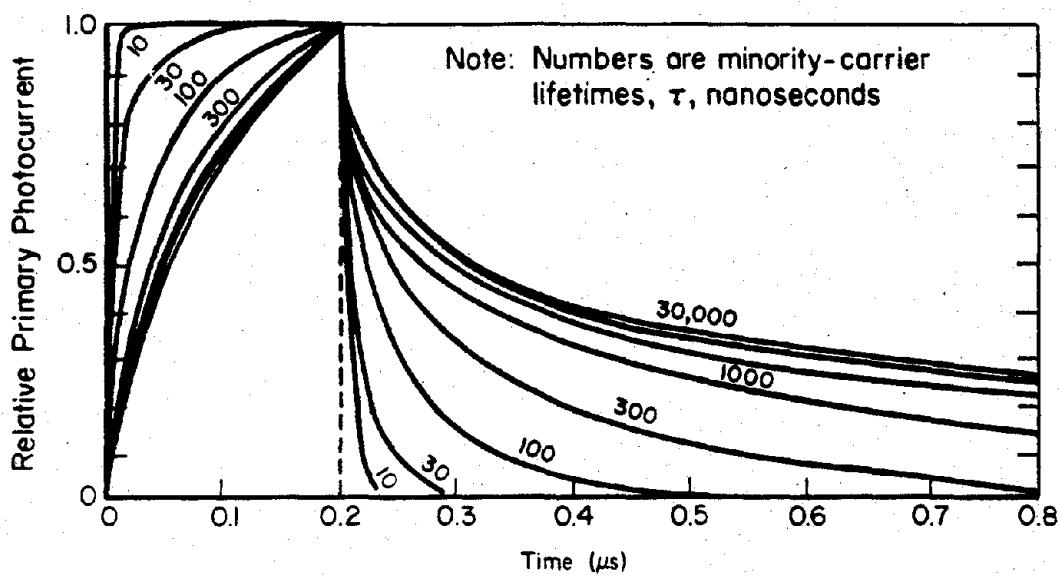


Figure 9-47. Relative Shapes of Diffusion Component of Primary Photocurrent

circuit conditions can thus be estimated as follows:

$$I_{pp \text{ max}} = qK_g \dot{D}A (L_n + L_p)$$

where

$q$ ,  $K_g$ ,  $\dot{D}$  and  $A$  are defined as in the diode expression, and  $L_n$  and  $L_p$  are the diffusion lengths in the N and P regions, respectively. Diffusion lengths are comparable on each side of the junction.

The radiation induced offset voltage in an open circuited tunnel diode is influenced by the tunneling current at low dose rates, but at higher dose rates a tunnel diode behaves like a conventional diode. This behavior occurs because very little induced voltage is required to set up a tunneling current equal to the diffusion current of excess carriers. When the tunneling current reaches a maximum, the induced voltage

rises sharply to the value for a conventional diode.

A transistor is a more complicated device than a diode, both structurally and functionally. The main functional advantage of the transistor is the fact the transistor has the ability to amplify its input signal. The transistor has three impurity regions that alternate, i.e., NPN or PNP. When an operating transistor\* is exposed to transient ionizing radiation, a current pulse is observed in the external circuit. This current pulse, which may be orders of magnitude larger than that of a diode with comparable dimensions, can reach a peak value at a time later than the radiation peak, and can, in some cases, continue for milliseconds.

The following paragraphs are concerned with bipolar transistors; not to MOS, junction field-effect transistors, or thin-film transistors.

This characteristic behavior of transistors is the result of the amplifying properties acting on the primary radiation induced photocurrents. The electrical action of the transistor creates a secondary photocurrent that is typically greater than the primary photocurrent by a factor equal to the gain (a measure of ability of the transistor to amplify) of the transistor. Analysis of the radiation response of a transistor involves the determination of the primary photocurrent, followed by a calculation of the magnitude and duration of secondary photocurrents under the given circuit conditions.

In transistors, the primary photocurrent is generated in five regions: in the collector- and emitter-junction depletion regions, in the base, and in the emitter and collector bodies lying

within a diffusion length of the junctions. In most cases, the generation of primary photocurrent in the emitter body and within the junctions can be neglected since the emitter body and the junction volumes are a relatively small part of the total generating volume (see Figure 9-48).

The secondary photocurrent is produced by the accumulation of excess majority carriers in the base region as a result of the flow of primary photocurrents across the PN junctions of the device. This excess charge, which is confined in the base by the built-in junction fields, is the correct polarity to forward bias the emitter-base junction and to cause normal current to flow. The collector current that is produced is called secondary photocurrent. This collector

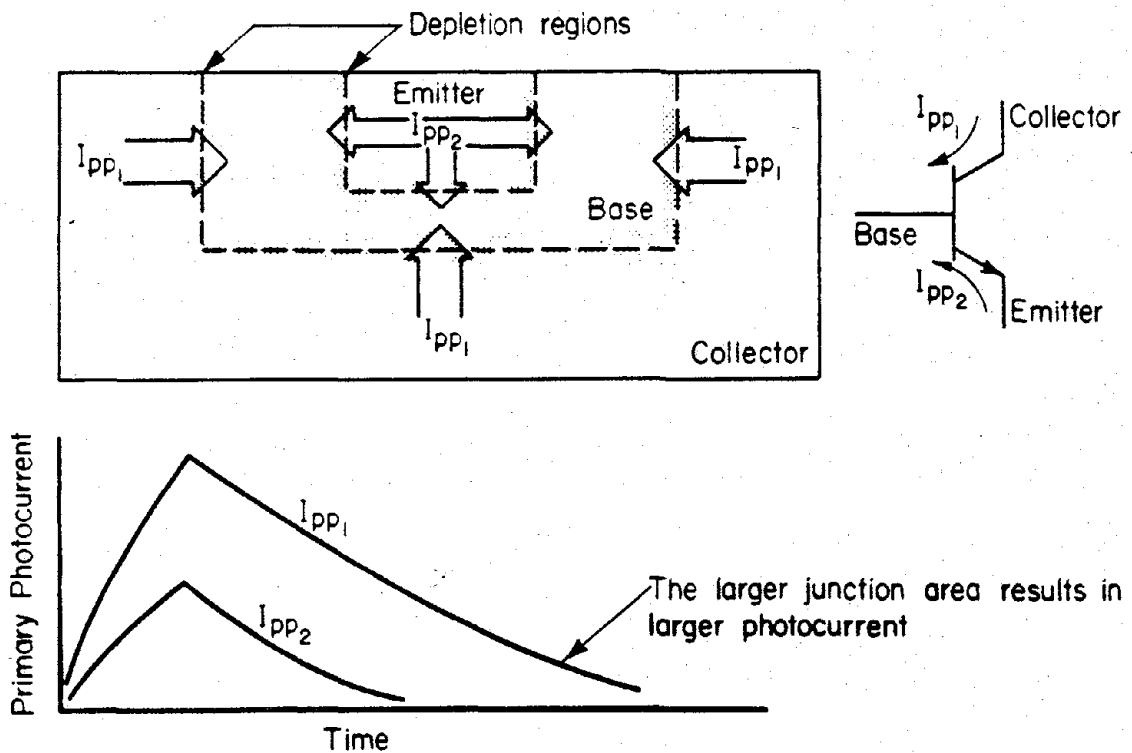


Figure 9-48. [REDACTED] NPN Transistor Illustrating the Primary Photocurrent [REDACTED]

current continues to flow until the excess charge stored in the base can either recombine with minority carriers or flow out through the external base lead.

The magnitude of the collector current pulse will depend on the dose rate if the radiation pulse is long compared to the lifetimes of the transistor base and collector, but it will depend on the total dose if the pulse is shorter than those lifetimes. This results from the charge transferred from the collector by the primary photocurrent being stored in the base region. Since many transistors have lifetimes that are as long as or longer than typical nuclear weapon radiation pulses, the prompt dose is quite often the most important factor.

A simplified linear approximation of the primary photocurrent in a transistor can be estimated with the following equation:

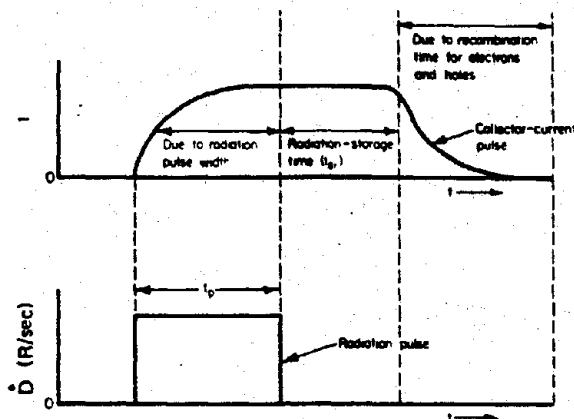
$$I_{pp} = \frac{D}{CONST.} [t_s + 0.03],$$

where

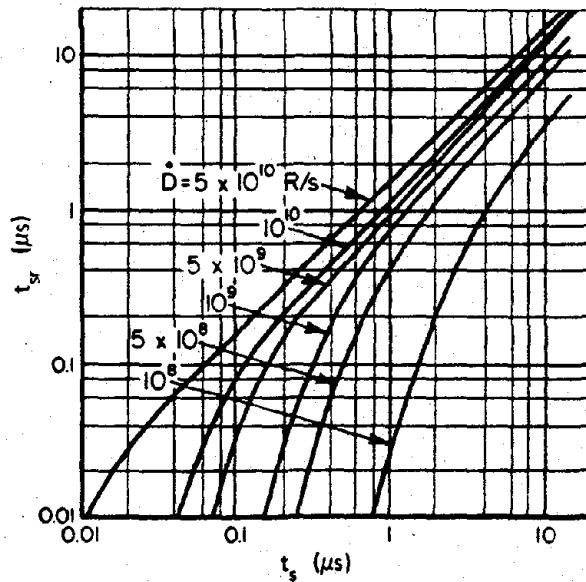
$D$  = the gamma ray exposure rate, R/s  
 $CONST.$  =  $0.83 \times 10^8$  for NPN devices and  
 $0.42 \times 10^8$  for PNP devices\*

$t_s$  = charge storage time (in  $\mu\text{s}$ ) for the device of interest ( $t_s$  typically can vary from a few nanoseconds to hundreds of microseconds).

The duration of the photocurrent response depends on the radiation pulse width, the radiation storage time (which is different than the charge storage time ( $t_s$ )), and the time for holes and electrons to recombine. The radiation pulse width is determined by the weapon. The time for holes and electrons to recombine is illustrated for a diode in Figure 9-47, which applies generally for transistors. The radiation storage time,  $t_{sr}$ , is defined by Figure 9-49a. The radiation storage times for several dose rates are shown in Figure 9-49b. These latter curves are



a. Definition of the Device Radiation-Response Times



b.  $t_{sr}$  vs  $t_s$  Curves

Figure 9-49. Radiation Storage Time

\*These equations only apply for the steady-state estimate of the primary photocurrent for silicon planar and mesa transistors with rated maximum continuous collector dissipation below 0.8 watt at 25°C. More detailed information about prediction is available in the TREE Handbook (see bibliography).

for a particular bias and radiation condition during storage. They are presented as being illustrative, and no attempt should be made to generalize from the curves. It is necessary to analyze a transistor or diode in the particular circuit configuration in which it is used to determine the threshold for circuit malfunction. As a result of the many different circuit configurations and bias conditions that can occur for transistors and diodes, failure thresholds that would be of value can not be specified generally for the TSEE environment.

A silicon controlled rectifier (SCR) is a solid state semiconductor device composed of four layers of alternate-impurity semiconductor material containing three PN junctions. The SCR is an active switching element that will remain in a nonconducting or "off" state until turned on or "fired" by a low-level control signal on the gate. It will then remain "on" without need for a sustaining control signal. The SCR is turned "off" by reducing its output (anode) current below the "dropout" level. Radiation induced currents, like those discussed for diodes and transistors, are a direct function of the junction areas, diffusion lengths, etc., and thus are difficult to predict since values for the parameters usually are not available. Since these currents, above a threshold, can induce changes in the state of an SCR, some method is required to predict the magnitude of the radiation induced currents, or, more specifically, the radiation threshold above which switching occurs.

It has been found that the transient radiation switching thresholds (critical radiation exposure rate) for SCR's are functions of the radiation pulse width. The exposure rate required to trigger an SCR becomes constant for pulse widths longer than a critical value. This critical value is a function of the device minority carrier lifetime and the device delay "turn on" time. For pulse widths less than the critical value, the exposure rate required to trigger an

SCR increases rapidly as the pulse width approaches zero. The dependence of the switching threshold of a 3A60A SCR on pulse widths and gamma ray exposure rate is shown in Figure 9-50. The critical pulse width for this device is approximately 2 microseconds.

Typically the SCR type of device would not be expected to fire below  $10^6$  rads (Si)/sec. For most cases, however, the pulse width is sufficiently short that the devices are dose dependent. Failures occur typically at prompt doses between 0.1 and 1 rad (Si).

Field-effect transistors (FET) are a family of unipolar devices that have pentode-like characteristics. The three major categories within this family are the junction FET, the metal-oxide insulated-gate FET (MOSFET), and the thin-film insulated-gate FET (TFT). The geometry and construction features of typical field-effect transistors are shown in Figure 9-51. The basic structure of the FET devices involves a source, a gate, and a drain in rough functional correspondence to the familiar cathode, grid, and plate of vacuum tube technology.

The mechanisms by which radiation generates photocurrents in an FET are not substantially different from those for bipolar transistors and diodes. The important radiation parameters in an FET are the transient gate and drain-to-source currents. Possible sources of transient currents in FET's can be grouped into the following categories:

- Leakage currents across PN junctions that behave like PN junction photocurrents discussed previously.
- Direct modulation of the channel conductivity and mobility (usually applicable at high ( $>10^8$  rads (Si)/s) dose rates).
- Leakage currents through the gate oxide layer (applicable to the metal oxide and thin-film FET's).
- Secondary emission (see Chapter 6) and atmosphere ionization currents.

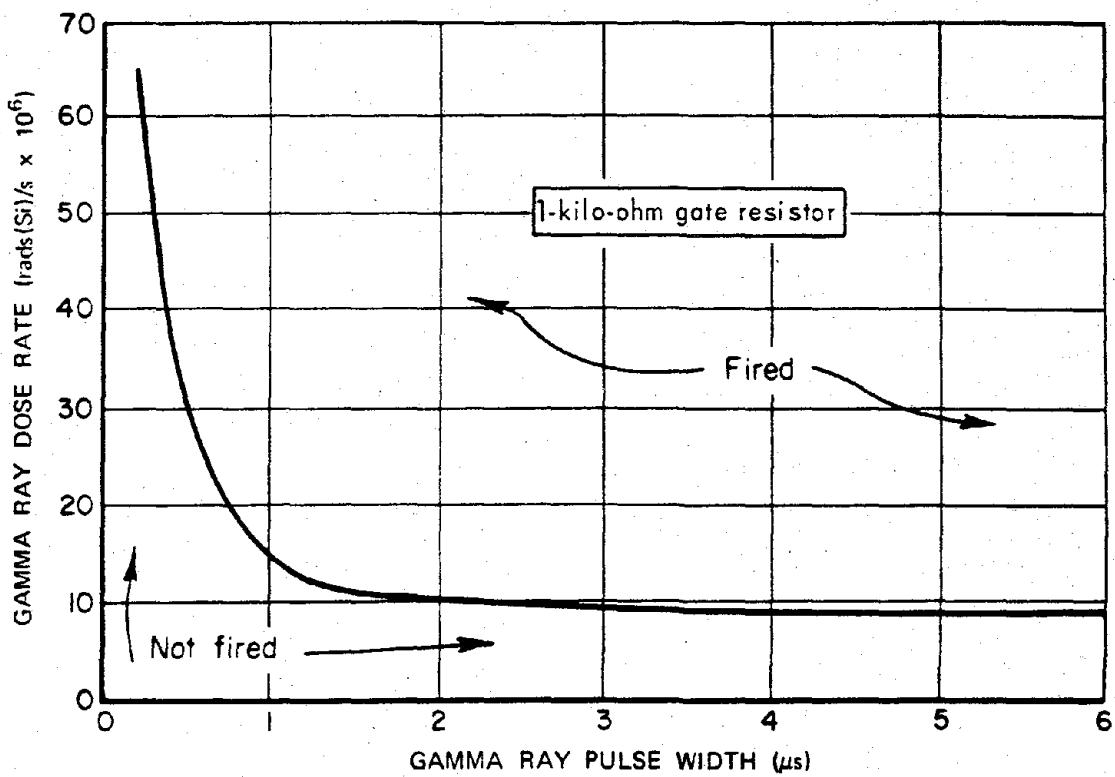
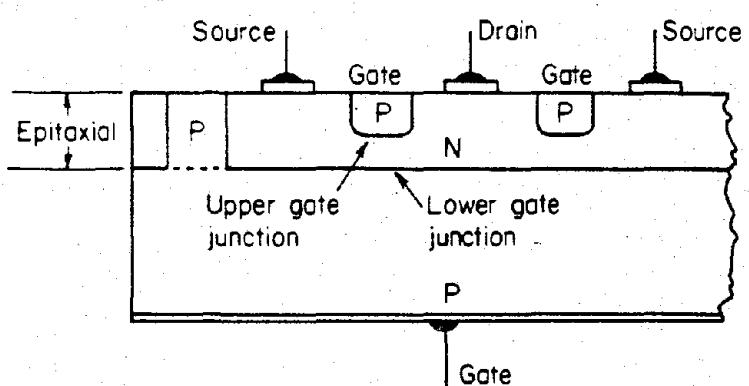
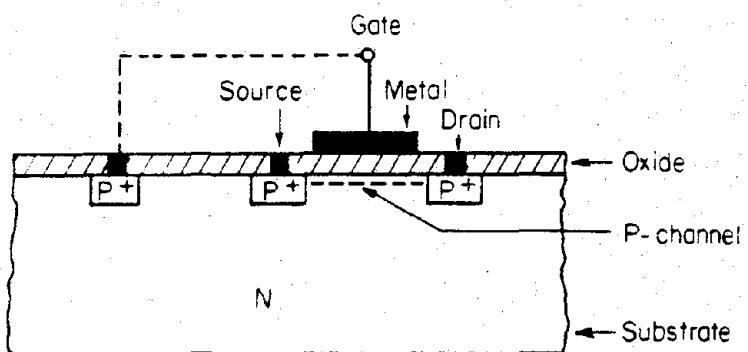


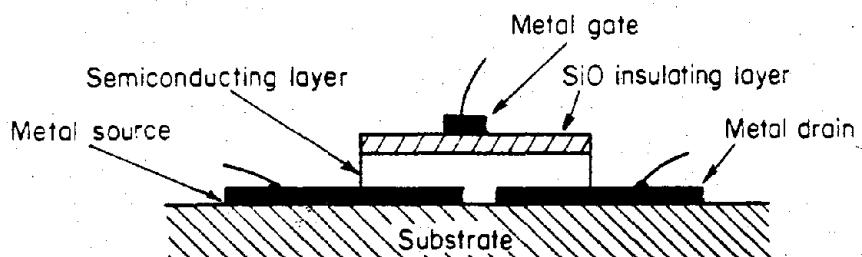
Figure 9-50. [REDACTED] Gamma Ray Exposure Rate as a Function of Pulse Width  
Switching Thresholds for a 3A60A SCR [REDACTED]



a. Junction Field-Effect Transistor



b. MOS Field-Effect Transistor



c. Thin-Film Field-Effect Transistor

Figure 9-51. Construction of Typical Junction, MOS, and Thin-Film Field-Effect Transistors

Significant problems generally are not caused in field-effect transistors at dose rates below  $10^6$  rads (Si)/sec.

#### 9-45 Permanent Effects

Permanent effects in semiconductor devices are those that can be attributed to physical property changes that result from the direct interaction of the radiation with the material of interest. These property changes typically last for periods that are long with respect to the recovery times of the components. These property changes occur in a very short time period and result in a rapid change in the operating characteristics of the device. A closely related effect is called rapid annealing, which is the process by which an initially large change in device parameters recovers very rapidly, approaching the smaller change observed several minutes after the radiation exposure.

Most permanent effects in semiconductor devices subjected to a nuclear radiation pulse result from damage to the semiconductor material by energetic neutrons ( $E > 10$  keV); however, the effects of gamma rays and secondary electrons must not be underestimated. In certain devices such as MOS field-effect transistors the effects of ionizing radiation can be the principal causes of permanent failure.

Permanent effects can be grouped into two categories – bulk, and surface effects. Bulk effects are changes in the device characteristics that can result from damage to the bulk material. Surface effects are changes that are generally caused by radiation induced ionization near the surface of the device. Bulk damage effects from neutron radiation usually can be predicted within a factor of 2, while surface effects are generally unpredictable.

Bulk effects result from electron, gamma ray, and neutron induced lattice displacements in the bulk of the material (see Chapter 6). Fast neutrons lose energy primarily by elastic colli-

sions with the semiconductor atoms and cause large disordered clusters to be formed within the material. Gamma radiation loses energy by creating Compton electrons (see Section I, Chapter 5), which may cause lattice displacements. Since electrons have such a small mass, they primarily cause vacancy-interstitial pairs rather than clusters of defects that are typical of neutron damage. Lattice damage that results from gamma radiation usually is of secondary importance, unless a large gamma dose ( $>10^5$  rads) is absorbed by the material.

Lattice damage degrades the electrical characteristics of semiconductor devices by increasing the number of trapping, scattering, and recombination centers.

- The trapping centers remove carriers from the conduction process.
- The additional scattering centers reduce the mean free path of the free carriers. Since the mobility is directly proportional to the mean free path, radiation exposure reduces the mobility of charge carriers.
- The recombination centers decrease the minority carrier lifetime according to the relationship (see Chapter 6).

$$\frac{1}{\tau_\varphi} = \frac{1}{\tau_0} + K\varphi,$$

where

$\tau_\varphi$  = minority-carrier lifetime at fluence  $\varphi$  in seconds,

$\tau_0$  = initial minority-carrier lifetime (bulk lifetime), in seconds,

$K$  = lifetime damage constant,  $\text{cm}^2/(\text{neutron-seconds})$ ,

$\varphi$  = fast neutron fluence,  $\text{neutrons}/\text{cm}^2$ .

Permanent effects also can be caused by radiation induced changes in the semiconductor surface. The changes in the surface conditions

attributed to radiation that can cause permanent effects are surface charging mechanisms and changes in the surface recombination velocity. The most likely charging mechanisms are the collection of ions from a gas in the atmosphere surrounding the semiconductor device and the ejection of electrons from dielectric materials which are either deposited on the semiconductor surface or in which the device is encapsulated. These ions migrate under the influence of electric fields. As a result of the collection of these charges, inversion layers can form near the surface, causing large increases in leakage currents. In silicon devices these leakage currents result from recombination-generation in the enlarged depletion region.

[REDACTED] Ionizing radiation can cause changes in recombination velocity, which has deleterious effects on the effective lifetime according to the relation

$$\frac{1}{\tau_{\text{eff}}} = \frac{1}{\tau_{\varphi}} + \frac{1}{\tau_{\text{surf}}},$$

where

$\tau_{\text{eff}}$  = effective lifetime,

$\tau_{\varphi}$  = bulk lifetime,

$\tau_{\text{surf}}$  = surface lifetime (an inverse function of recombination velocity).

Surface effects usually are negligible compared to bulk lifetime damage for most conventional devices in a transient radiation environment. Field-effect devices, where radiation induced surface changes are the primary damage mechanisms, represent an important exception. [REDACTED] The general effects of nuclear radiation on semiconductor diodes are summarized below and are illustrated in Figure 9-52 and 9-53.

- The forward voltage of the diode at constant current normally will increase as a

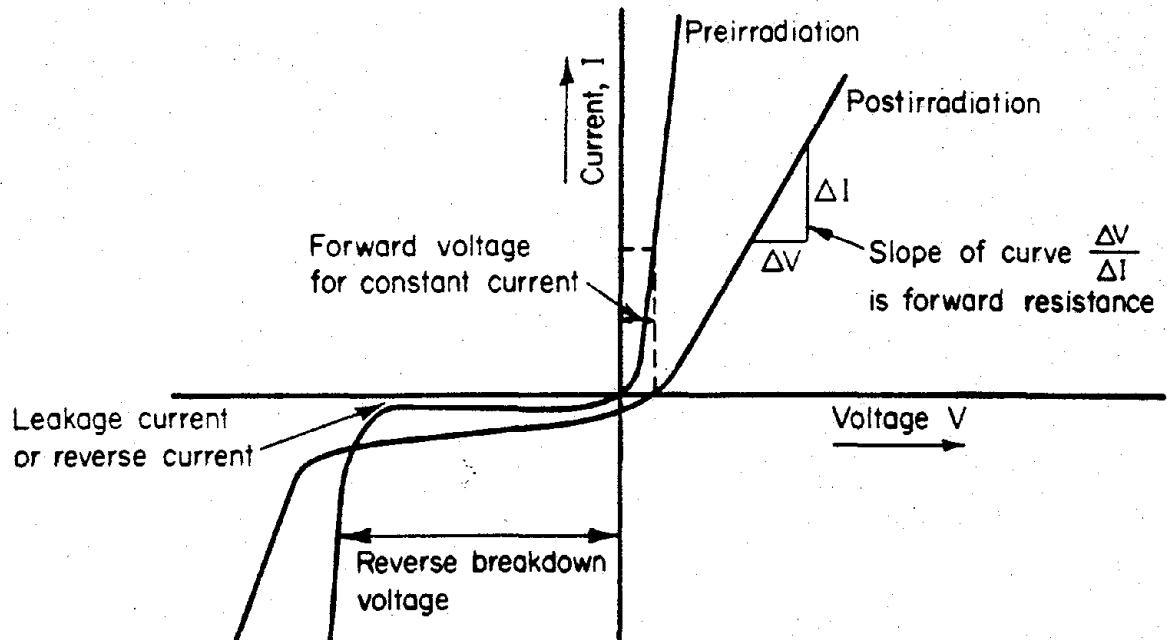


Figure 9-52. [REDACTED] An Illustrative Diode Characteristic for Pre- and Post-irradiation by Neutrons [REDACTED]

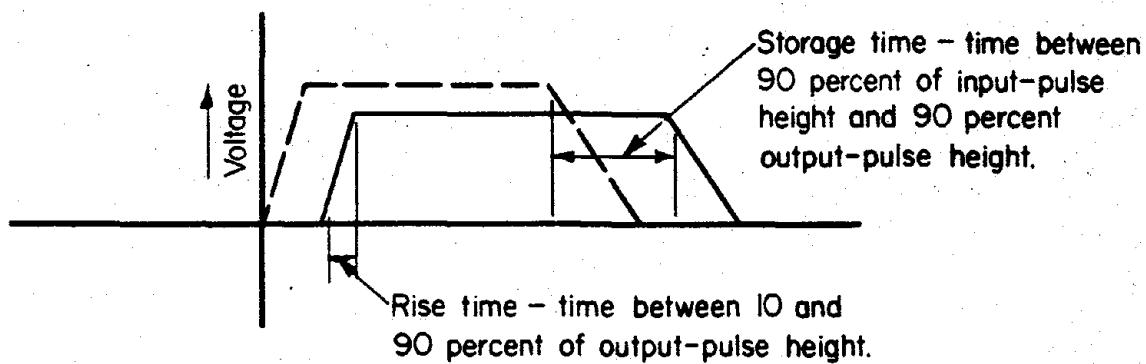


Figure 9-53. An Illustration of Rise Time and Storage Time

result of changes in resistivity and mobility in the bulk material.

- The dynamic forward resistance will increase as a result of changes in resistivity and conductivity modulation.
- The surface effects and increases in carrier generation in the space-charge region will cause the reverse current to increase.
- The reverse breakdown voltage normally will increase because of an increase in resistivity.
- The switching characteristic of the diode generally will be changed. The rise time will increase, and the storage time will decrease as a result of lifetime damage.

Diodes generally are an order of magnitude more resistant to radiation than transistors of similar type. For this reason, theoretical and experimental studies have concentrated on transistors rather than diodes. Prediction techniques for diodes are complicated by the fact that the various bulk and surface damage mechanisms interact in an intricate manner. The wide variety of diode types, i.e., material, doping level and profile, geometry, etc., all tend to make comprehensive prediction schemes difficult and inaccurate. However, some quantitative trends in the changes in diode parameters can be given. The

more important changes in diode characteristics, from a circuits point of view, are the increase in forward voltage at constant current and the increase of reverse leakage current. Changes in the dynamic forward resistance, breakdown voltage, and switching characteristics usually are of secondary importance.

The forward voltage at constant current generally starts to increase at a fluence of  $10^{13}$  to  $10^{14} \text{ n/cm}^2$  ( $E > 10 \text{ keV}$ , fission), though some diodes exhibit changes at fluences as low as  $10^{12} \text{ n/cm}^2$  ( $E > 10 \text{ keV}$ , fission) while others show no change up to fluences as large as  $10^{15} \text{ n/cm}^2$  ( $E > 10 \text{ keV}$ , fission). Usually, fluences of about an order of magnitude greater than the fluences required to cause the initial change will double the forward voltage.

The reverse leakage current usually increases with exposure, but decreases also have been observed. Nominally, changes begin at fluences from  $10^{13}$  to  $10^{14} \text{ n/cm}^2$  ( $E > 10 \text{ keV}$ , fission). Gamma ray doses as low as  $5 \times 10^4$  rads (Si) have caused significant leakage currents. Germanium devices generally have larger changes in leakage current than silicon devices.

The changes in breakdown voltage are typically the largest for diodes with high breakdown voltage. Reference voltage diodes (zener

diodes) are relatively resistant to radiation with reference voltage changes less than 5 percent at  $10^{15} \text{ n/cm}^2$  ( $E > 10 \text{ keV}$ , fission).

The storage time is directly proportional to lifetime. Hence, the fluence at which the storage time will be reduced to one-half the preirradiation value will be

$$\varphi = \frac{1}{\tau_0 K}$$

where

$\tau_0$  is the minority carrier lifetime,

$K$  is the damage constant (see Chapter 6).

Other diode types are specifically designed for rectifier application where high breakdown voltage and a low voltage drop are required even at high current. These diodes usually are designed with a PIN junction, which results in a device that is less sensitive to radiation than the standard type diodes.

Selenium rectifiers and hot carrier diodes (metal semiconductor junction) appear to be more radiation resistant than either germanium or silicon diodes because of their material and structural differences. Reactor tests conducted on the HPA-2300 series hot carrier diodes confirm the relative radiation hardness of these devices. Most units tested remained within manufacturer's specifications at fluences of  $3 \times 10^{15} \text{ n/cm}^2$  ( $E > 0.1 \text{ MeV}$ , fission) and  $9 \times 10^5 \text{ rads (Si)}$ .

Diodes classified as "tunnel diodes" are easily recognized by their forward current characteristic, which shows a region of negative resistance. The effect of radiation on tunnel diodes is observable on the current-voltage (I-V) characteristic at fluences between  $10^{15}$  and  $10^{16} \text{ n/cm}^2$  ( $E > 10 \text{ keV}$ , fission), and can be summarized as follows:

- The slope of the primary tunneling current is not changed; however, the peak current

is slightly reduced as a result of the redistribution of the electrons in the defect states.

- The valley current at a given voltage increases due to the additional tunneling via defect states.
- For voltages larger than valley voltage, there is an increased current for a given voltage due to the excess current, which predominates over the diminishing normal diode current.

Figures 9-54 and 9-55 show representative germanium and silicon tunnel diodes under neutron irradiation. The figures show that tunnel diodes are still operational at  $5 \times 10^{15} \text{ n/cm}^2$  ( $E > 10 \text{ keV}$ , fission), which indicates the relative radiation hardness of these devices.

The general effects of nuclear radiation on bipolar transistors can be summarized as follows:

- The current gain (amplification) of the transistor will be degraded as a result of lifetime damage to the bulk material. Degradation of gain will be greatest immed-

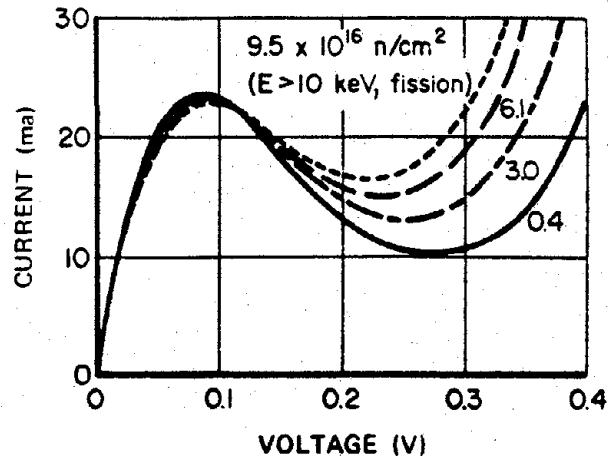


Figure 9-54. Fast Neutron Bombardment Effect on Voltage-Current Characteristic of a Germanium Tunnel Diode

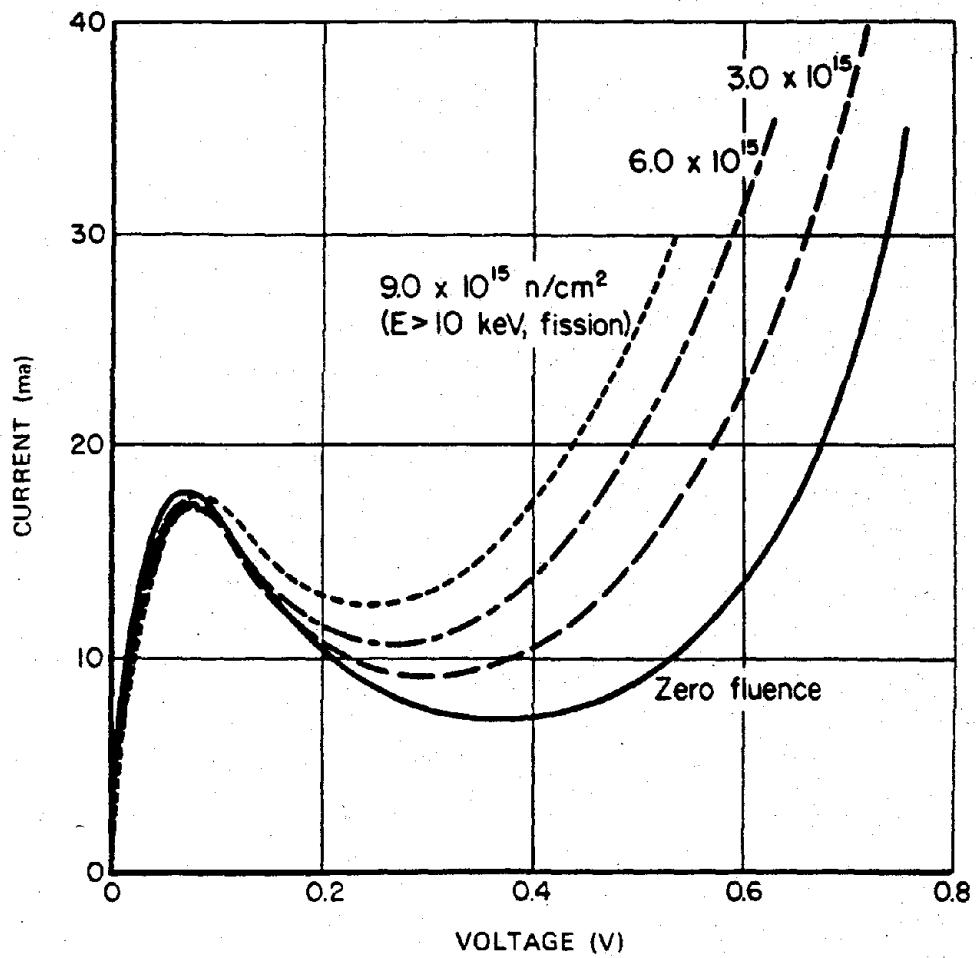


Figure 9-55. Fast Neutron Bombardment Effect on Voltage-Current Characteristic of a Silicon Tunnel Diode

iately following a burst of nuclear radiation, and the gain will recover rapidly to a quasi steady-state value. The annealing can go on for weeks, but usually the current gain recovery is small or negligible after the initial recovery.

- The reverse leakage current will increase as a result of surface effects and carrier generation in the space-charge region.
- Changes occur in the punch-through voltage, and the base-to-emitter and collector-to-base breakdown voltage as a result of changes in resistivity.
- Increases in base-spreading resistance, collector body resistance, and saturation voltage result from changes in resistivity and conductivity modulation.
- The switching characteristics also are changed slightly — exemplified by decreased storage time and increased turn-on time as a result of changes in lifetime and resistivity.

Since transistors usually are the most vulnerable devices used in conventional circuits, predictions of circuit response under radiation conditions will be limited by the accuracy with which transistor behavior can be predicted. The reduction of current gain generally will limit the usefulness of the component before the other factors listed above become a serious problem. Therefore, emphasis is placed on the prediction of current gain degradation. However, in some applications saturation voltages and/or leakage currents across reverse biased junctions may be the limiting factors.

The structure of a device is an important factor in determining its radiation resistance. A general rule is that the thinner base, higher frequency, and smaller junction area devices usually have better radiation resistance. For example, the diffused-junction devices usually offer a resistance to radiation about one order of

magnitude better than that offered by the alloy-junction devices.

Experimental data for conventional transistors in the form of generalized gain degradation curves are shown in Figure 9-56 for some common transistor types. The ratio  $\beta_\varphi/\beta_0$  represents the ratio of gain at some fast neutron fluence to the gain prior to irradiation. Figure 9-56 is representative of preliminary data from steady-state reactor experiments. The transistor types have been placed in their respective regions on the basis of where a majority of samples of a given type fell on the graph. Caution should be exercised in using and interpreting the information in the figure, since irradiation temperature, irradiation source, measurement conditions, etc. are not specified.

A further word of caution should be injected concerning the interpretation of gain degradation data. A sharp decrease in  $\beta$  occurs during exposure and then rapidly anneals to a final value that is commonly measured. The time dependence of gain degradation can best be interpreted with the use of the annealing factor,  $F$ , defined as follows:

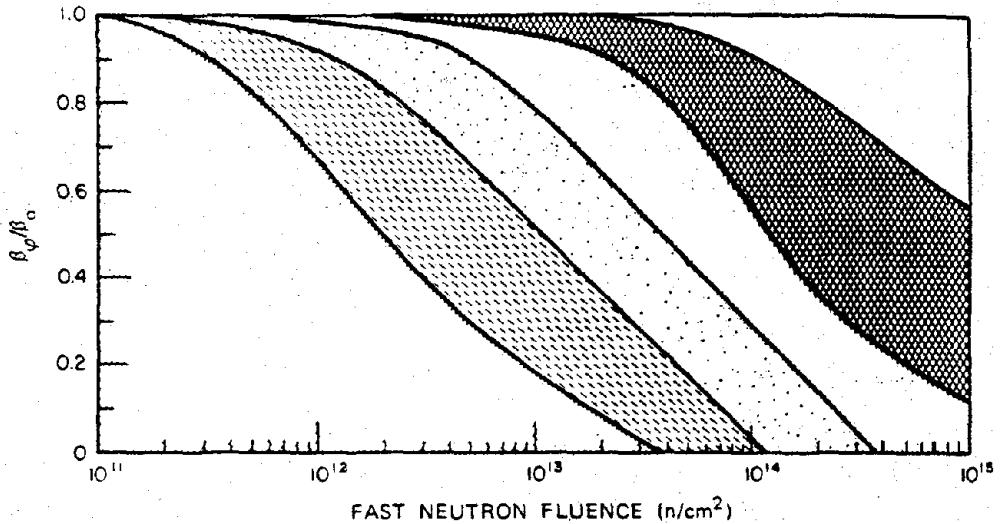
$$F(t) = \frac{\frac{1}{\beta_\varphi(t)} - \frac{1}{\beta_0}}{\frac{1}{\beta_\varphi(\infty)} - \frac{1}{\beta_0}} = \frac{K(t)}{K(\infty)},$$

where

$\beta_\varphi(t)$ ,  $K(t)$  are gain and damage constants as a function of time after a fast burst of nuclear radiation.

$\beta_\varphi(\infty)$ ,  $K(\infty)$  are the steady-state values of gain and damage constants.

The magnitude and form of  $F$  varies with temperature, injection level, doping level, and impurity content. Typical values for the annealing factor at 1 msec range from approximately two to three for NPN transistors and



I	II	III	IV	V
2N329A	2N336	2N697	2N3244	2N404
2N1016E	2N699	2N708	2N3251	2N2784
2N1486	2N861	2N718	2N3252	2N2808
2N1653	2N917	2N720A	2N3300	2N705
2N1722	2N1016	2N722	2N3444	2N706A
2N2187	2N1132	2N869	2N3486	2N708
2N2484	2N1184	2N910	2N3497	2N2894
	2N1613	2N1306	2N3499	2N743
	2N1711	2N1342	2N3509	2N744
	2N1900	2N1506	3TE240	2N834
	2N1936	2N1717	BR100A	2N835
	2N2187	2N1893	7900302	2N914
	2N2219	2N2192A	7900329	2N915
	2N2223	2N2193A		2N3227
	2N2243A	2N2217		2N3252
	2N2297	2N2222		2N3287
	2N2411	2N2223		2N3287
	2N2878	2N2368		2N3287
	2N3072	2N2481		2N3287
	2N3439	2N2699		2N3287
	2N3499	2N2801		2N3287
	2N3501	2N2887		2N3287
	2N3502	2N2907		2N3287
	2N3637			

Figure 9-56. [REDACTED] Current Gain Degradation Characteristics for Some Common Transistor Types [REDACTED]

slightly smaller for PNP transistors. The annealing factor can be as high as 7 for low injection situations and immediately after turning on a device that was off during the neutron pulse.

Other transistor parameters also can be degraded. Permanent increases occur in leakage currents across reverse-biased junctions. In general, the discussion of diode leakage is applicable to transistor leakage.

Changes in breakdown voltages, punch-through voltage, and collector and emitter body resistances are negligible at fluences where the gain is still usable. The effects of nuclear radiation on these parameters can be analyzed from comments made about diodes.

The changes in saturation voltage and in the switching time as a result of nuclear radiation are of interest for switching applications. In many cases the saturation voltage may appear to increase at relatively low levels of radiation, but actually the transistor is losing base drive and is coming out of saturation. The only significant increases in saturation voltage are seen at high collector currents. These increases, however, occur at high neutron fluences.

The switching time of a transistor is referred to as the turn-on time and the turn-off time, which consist of the delay time,  $t_d$ , the rise time,  $t_r$ , the storage time,  $t_s$ , and the fall time,  $t_f$ . First-order theory indicates that, with the exception of the rise time, these parameters either remain relatively constant or decrease with radiation. Normally, the decreases are larger than the increases in these parameters; thus a net reduction of transistor switching time occurs with radiation, which usually is desirable. The largest changes occur in the storage time, which is proportional to the lifetime. Thus,

$$\varphi = \frac{1}{K\tau_0}$$

is the fluence at which the storage time is reduced by one half.

The general effects of nuclear radiation on field-effect transistors can be summarized as follows:

- Changes occur in the threshold voltage,  $V_T$ . These changes in threshold voltage affect most of the field-effect transistor parameters.
- Increases in leakage current occur.
- Changes in channel resistivity and carrier mobility occur.

Damage in MOS field-effect transistors is due primarily to ionizing radiation. For this reason damage is reported in terms of dose (in rads) or exposure (in Roentgens) rather than fluence (in n/cm<sup>2</sup>). The most sensitive parameter to radiation in field-effect transistors is the threshold voltage,  $V_T$ . In general, degradation in  $V_T$  proceeds rapidly in the range of  $10^3$  and  $10^4$  rads (Si), but becomes more gradual above this dose. Complete failures, i.e., complete degradation in transconductance, have been observed at doses of  $10^6$  to  $10^7$  rads (Si).

Considerable interest has been shown in the use of junction field-effect transistors (JFETs) in a radiation environment, since these are unipolar devices and do not depend on minority-carrier lifetime for operation. The primary effect of radiation on JFET's is the removal of carriers in the channel region. Radiation induced carrier removal is a strong function of resistivity. Thus, increased radiation tolerances is expected from JFET's with a high initial carrier concentration. The planar process has allowed heavily doped JFET's to be manufactured with the necessary control to make them commercially available. These heavily doped JFET's have demonstrated a very significant improvement in radiation hardness, e.g., approximately 15 percent degradation in transconductance after a neutron fluence of  $7 \times 10^{14}$  n/cm<sup>2</sup> ( $E > 10$  keV, fission).

Thin-film field-effect transistor (TFT) devices have been found to be more radiation

resistant than conventional field-effect transistors. Tests indicate that both the cadmium selenide and the silicon on sapphire type TFT's are operational at  $10^6$  rads (Si) or  $10^{15}$  n/cm<sup>2</sup> ( $E > 10$  keV, fission).

The negative resistance characteristic of the unijunction transistor depends upon the conductivity modulation of a moderately high resistivity silicon bar by means of injected minority carriers from the rectifying emitter contact. This transistor is highly sensitive to radiation induced changes in minority-carrier lifetime and resistivity. Typical failure thresholds for unijunction transistors are of the order of  $5 \times 10^{11}$  to  $5 \times 10^{12}$  n/cm<sup>2</sup> ( $E > 10$  keV, fission). The degradation is manifested by an increase in valley voltage, a decrease in valley current, and increases in the interbase and emitter-base resistances.

The three basic types of silicon PNPN devices are: the silicon-controlled rectifier, SCR; the silicon-controlled switch, SCS, and the Shockley diode. All of these devices may be considered to consist of overlapping NPN and PNP transistors, the primary difference being the external accessibility of the various layers; that is, the Shockley diode provides external access to only the outer P- and N-layers, the SCR has leads to all but the central N-region, and the SCS has leads to all four regions. The "two transistors" of the PNPN structure operate in a positive-feedback configuration, and the current-transfer ratios of the two sections add together for the composite device.

As previously discussed for transistors, radiation induced defects reduce the current gain for both "transistors" so that the required gate current, holding current, and breakdown voltage should increase with radiation at fluences comparable to the bulk damage fluence levels in silicon transistors. Theoretical considerations of the mechanisms of PNPN device operation also indicate that excessive leakage currents will cause premature triggering of the devices.

Hence, increases in surface and bulk leakage currents induced by radiation may cause the device to conduct continuously. This effect will depend upon the bias level applied in the application.

Since PNPN devices are used in medium-to high-power applications, they cannot be compared to high-frequency transistors in radiation resistance. Typical failure thresholds for PNPN devices range between  $10^{12}$  and  $5 \times 10^{14}$  n/cm<sup>2</sup> ( $E > 10$  keV, fission). Some narrow base PNPN devices have performed well at  $10^{15}$  n/cm<sup>2</sup> ( $E > 10$  keV, fission).

#### 9-46 Heating and Thermomechanical Damage

Any electronic component parts in which sufficient energy has been deposited by the electronic system environment will experience a transient rise in its temperature. The performance characteristics of most component parts are sensitive to temperature. Therefore, a temporary perturbation in the response of electronic component parts can be expected. The severity of the perturbation is a function of the deposited energy and the manner in which components are interconnected and mounted. Semiconductor devices are particularly vulnerable to temperature transients.

Fortunately, most of the common circuit design techniques for compensation for temperature rises are directly applicable to the circumvention of heating effects caused by the TREX environment. Consequently, heating effects seldom are emphasized, and other effects predominate. However, in some particularly sensitive components such as inertial-guidance devices, heating effects remain a serious problem.

The thermomechanical-shock effects arise from the deposition of short pulses of high intensity X-ray energy. The component part response differs from the effects discussed so far in that the primary manifestation is the loss of

mechanical integrity. The processes of spallation, blowoff, and delamination combine to produce mechanical damage. In most cases, this mechanical damage results in a permanent, catastrophic electrical failure of the component parts.

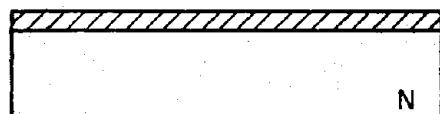
All electronic components are potentially vulnerable to thermomechanical shock, but semiconductor devices are among the most vulnerable components. The failure modes for transistors exposed to X-rays depend on the materials and geometries employed in their construction. It is, therefore, worthwhile to consider device fabrication in some detail.

Transistors are composed of a combination of materials, and the relationship of these materials to each is best illustrated in terms of the processes by which these devices are fabricated. Transistors are produced from single crystal semiconducting material, which is processed into regions of desired type and resistivity to form the junctions necessary for transistor action. The many techniques employed to achieve the required junction configurations include growing the desired material from suitably doped melts and alloying-in the dopant impurities from appropriately metallized surfaces. However, the most prevalent technology being used to fabricate silicon transistors is the so-called "planar" process in which the required dopants are allowed to diffuse through area-defining masks formed on the surface of the silicon. These masks are made of silicon dioxide, which (1) is thermally grown on the surface of the silicon, (2) may be etched to form windows for diffusion, and (3) is a natural barrier to the diffusion of phosphorous and boron (the most commonly employed dopants for producing N- and P-type silicon, respectively). The windows in the silicon dioxide are defined by photoetching techniques initially developed and employed in the fabrication of etched wiring boards and subsequently refined in resolution to permit application in the fabrication of semiconductor devices.

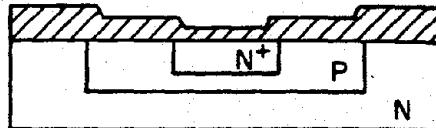
Figure 9-57 shows the steps employed in the fabrication of a typical transistor by the planar process. The oxide layer grown in Step (a) is removed in a selected area by photoetching (Step b), and a P-type dopant is allowed to diffuse into the starting N-type silicon to form what will be the base region of the transistor (Step c). A new oxide is grown next (Step d) and is photoetched to form a window over a smaller area, and an N-type dopant in high concentration is allowed to diffuse into this portion of the P-type region (Step e), converting it to  $(N^+)$ -type silicon. This forms the emitter region of the transistor. Depth of penetration of the dopant materials is controlled by the times and temperatures at which the diffusion operations are conducted. A final oxide growth (Step f) and selective photoetching (Step g) expose the emitter and base contact points. The whole surface is subsequently coated with aluminum (Step h) and selectively etched to produce the desired current paths and land areas (tabs) for connection (Step i).

Since transistors fabricated in the above manner usually are prepared in multiple arrays containing hundreds of identical devices, the next steps are the separation of the individual devices by some technique such as diamond scribing and the mounting of each of the resultant chips (or dice) into a separate package. Typical chips for high-frequency transistors are less than  $0.025 \times 0.025$  in. in area.

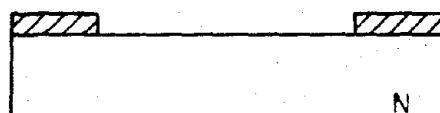
The transistor package can take many forms (see Figure 9-58a), but in each form there is usually a section of the package that contains the lead wires to which the emitter, base, and collector portions of the device must be connected. This section is called the header. In a typical package this is the bottom section of the can, which contains the three lead wires. A cap is attached to complete the package. The header usually is made of Kovar, a nickel-iron alloy frequently used for glass-to-metal seals because of their comparable thermal-expansion coefficients.



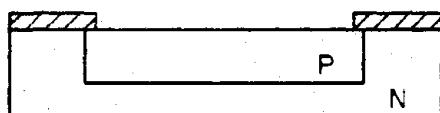
a. Growth of the  $\text{SiO}_2$  Layer



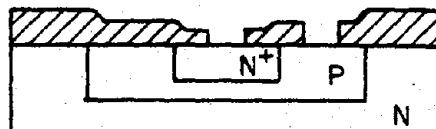
f. Regrowth of the  $\text{SiO}_2$  Layer



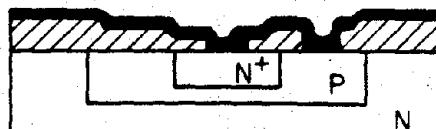
b. Removal of  $\text{SiO}_2$  by Photoetching



c. Diffusion of P-Type Dopant



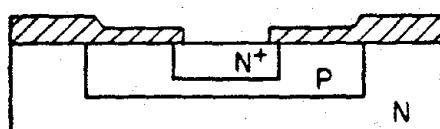
g. Photoetch of Emitter and Base Contacts  
Photoetch



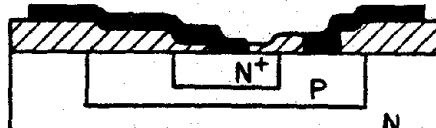
h. Vapor Deposition of  $\text{Al}$



i. Selective Etch of  $\text{Al}$  to Produce Desired Current Paths

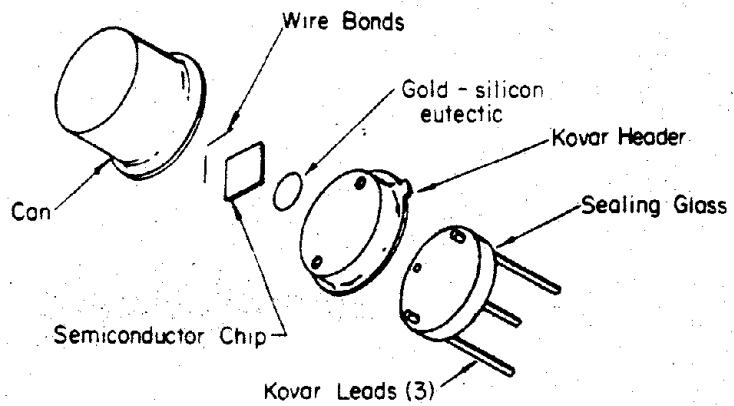


e. Photoetch Followed by Diffusion of N Type Dopant to form  $\text{N}^+$  Emitter Region

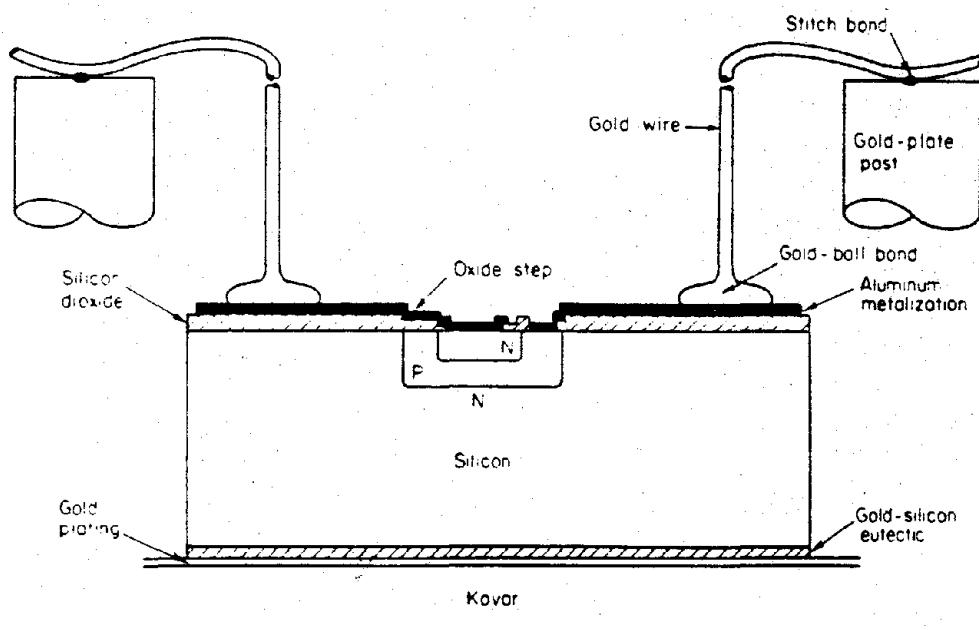


j. Mounting of the Die or Die Bonding

Figure 9-57. [REDACTED] Steps in the Fabrication of an NPN Silicon Planar Transistor [REDACTED]



a) Transistor Package



b) Cross-Sectional View of NPN Silicon Planar Transistor

Figure 9-58. Transistor Cross Section and Package

The three Kovar leadout wires are electrically insulated from each other by glass feed-throughs in the Kovar header. Since Kovar oxidizes easily, the external leads, and often the internal leads, on the transistor usually are plated to facilitate subsequent soldering or welding.

The processed semiconductor chip is attached to the header by a fabrication step known as die bonding. Die bonding involves soldering, brazing, or glazing the die to the header. This attachment serves as a mechanical contact, a thermal path, and in some cases (such as the example being employed) an electrical contact. When the connection is to a metal portion of the header, the attachment usually is accomplished by brazing using a eutectic brazing alloy (generally containing gold). This is superior to a soft solder because the high melting point of the eutectic permits use of higher temperatures in sealing the top on the header and in preconditioning the devices if desired. Some disadvantages in the use of eutectic alloys for die bonding are that they generally are expensive, quite brittle, difficult to form into unusual shapes, and they cannot be vacuum evaporated to form thin films. A preform of the eutectic alloy is placed on the header on a platform directly connected to the collector leadout wire. In many applications, a simple gold plating on the Kovar platform suffices as the preform, since on heating in contact with the silicon chip, a gold-silicon eutectic will form. Heat is applied ( $390^{\circ}$ - $400^{\circ}\text{C}$ ), the transistor chip is placed on the preform, and the eutectic is chilled with a jet of nitrogen. This operation attaches the chip to header and forms the chip-to-header bond (Step j, Figure 9-57).

Wire bonding makes electrical contact to the emitter and base regions. In some devices this connection is made by attaching the bridging wires directly to suitably metallized etched-open areas on the silicon chip. In many devices, however, these areas are much too small to per-

mit forming quality connections, so the connections are made to extended tabs formed in the aluminum metallization on top of the silicon oxide. This latter configuration is illustrated in Figure 9-58b. The bridging wires, 1/2 to 3 mils in diameter, may be composed of any of a number of materials, but generally they are either gold or aluminum. Gold is used because it forms ohmic contact when alloyed with silicon, is available as extremely fine wire with reasonable strength, and may be bonded by thermocompression. Aluminum wire is used because it provides a one metal system when aluminum metallization is employed for extended tabs and avoids the formation of gold/aluminum alloys ("purple" and "white" plagues), it is available as fine wire, and it makes ohmic contact to both P-type and ( $\text{N}^{+}$ )-type silicon.

In thermocompression bonding, the two metals (such as the wire and the bonding pad) are made to seize without a third intermediate phase (such as solder) and without melting. This is accomplished with high pressures and temperatures. The high temperature keeps the metals in the annealing range as they flow into atomic intimacy under the bond. One form of thermocompression bonding (called ball bonding or nail-head bonding) employs gold wire that is heated at the tip with a hydrogen flame to form a ball, which is subsequently driven against the heated chip under pressure to form the bond and concurrently is flattened into a nailhead configuration. In stitch bonding (another form of thermocompression bonding), the wire is bent under pressure from the tool head and forced into the heated pad in such a way that the wire is wedged flat at the point of contact. Either gold or aluminum may be employed in stitch bonding. In ultrasonic bonding, ultrasonic energy is employed to force the two metals into atomic intimacy. The resultant bond resembles a stitch bond. These three bonding techniques are illustrated in Figures 9-59a, b, and c, respectively.

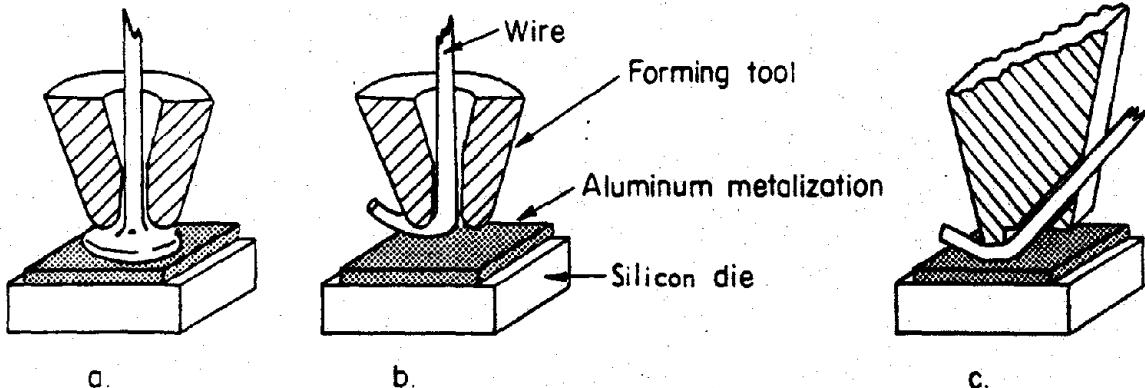
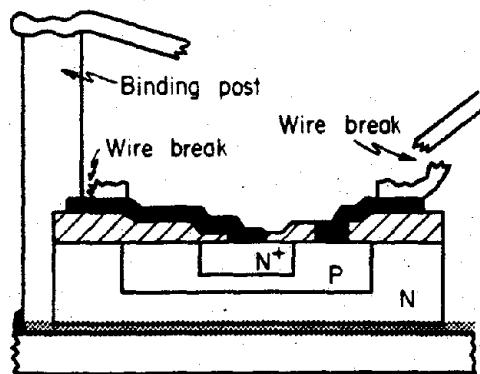


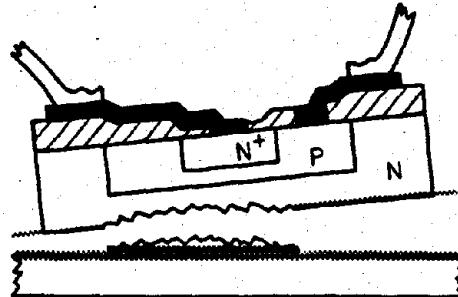
Figure 9-59. Ball Stitch and Ultrasonic Bonding

DNA  
(1)(3)

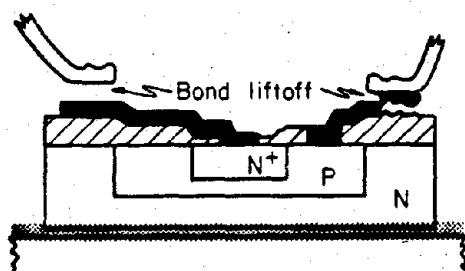
Several general modes of failure (see Figure 9-60) are apparent: (a) the wires may break; (b) the emitter or base bonds may separate from the chip; (c) the silicon chip might fracture; (d) the chip may separate from the header; (e) the aluminum metallization constituting the extended tabs might become discontinuous; and (f) the wire bonds at the post may separate.



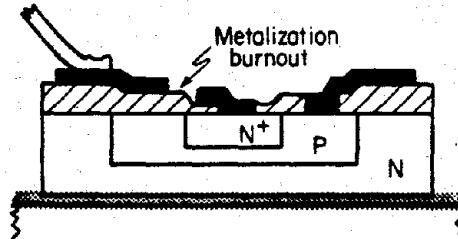
a. Wire Break



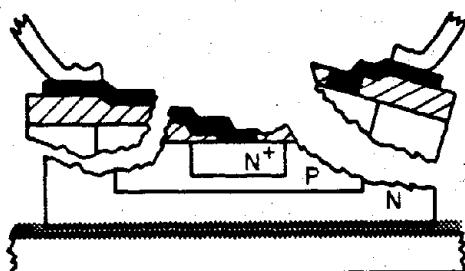
d. Chip Separated From Header



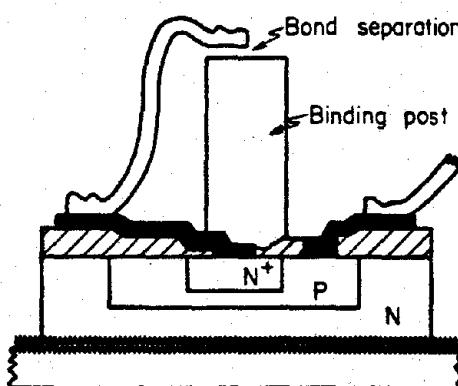
b. Bond Liftoff



e. Metalization Burnout



c. Chip Fracture



f. Bond-Binding Post Separation

Figure 9-60. Semiconductor Failure Modes

TDA

(1)(3)

expected to differ for each category of tube.

Permanent damage to vacuum tubes is associated with thermal and fast neutron exposure. No significant permanent damage has been observed in conventional vacuum tubes or Nuvistors exposed to test radiation pulses or to a thermal neutron fluence of less than  $10^{13}$  n/cm<sup>2</sup> (fission). Moderate damage may occur in standard size glass or metal tubes at thermal neutron fluences from  $10^{13}$  to  $10^{16}$  n/cm<sup>2</sup> (fission), and severe damage may occur at fluences greater than  $10^{16}$  n/cm<sup>2</sup> (fission). "Severe damage" is often the failure of the glass envelope, usually at a glass-to-metal seal; "moderate damage" is generally a permanent change in tube operating characteristics. Miniature, subminiature, and ceramic-type tubes are less subject to both moderate and permanent damage than standard size tubes, largely because of the smaller area and mass of the tube parts. However, thermal-neutron fluences sufficient to cause permanent damage to high-vacuum tubes are greater than neutron fluences expected to be encountered in the nuclear weapon environment, e.g.,  $>10^{16}$  n/cm<sup>2</sup> (fission).

The principal transient effect that results from exposure of vacuum tubes, including the Nuvistor, to nuclear radiation is produced by Compton scattering of electrons from structural members by gamma rays. Leakage currents caused by ionization of air between external electrodes, or reduction of resistance of insulating materials such as glass, ceramics, and mica, caused by electron excitation within the material, may have minor effects on tube performance. There is no appreciable radiation induced liberation of gas from tube parts, or ionization of residual gases within the tube.

Most of the Compton electrons produced in the structural parts of the tube and ejected into the evacuated region are too energetic to be influenced significantly by the electronic fields in the tube. However, the impact of

## OTHER ELECTRONIC COMPONENT PARTS

### 9-47 Electron Tubes

The electron tubes discussed in this subsection are divided into three categories: vacuum tubes, gas-filled tubes, and phototubes. These categories include nearly all types of conventional electron tubes with the exception of microwave tubes. Because of the known differences in interaction of nuclear radiation with metals, gases, and photoemissive materials, as well as with glasses and other ceramics, the observable effects of these interactions might be

high energy electrons on the interior surfaces of the tube assembly produces low energy secondary electrons that can be influenced by the existing electric fields, and thus can alter the normal operating characteristics of the tube. The ejected electrons can be collected by one or more electrodes, depending upon the electrode potential and position. The magnitudes of the resulting transient voltages that appear at the respective electrodes depend on the magnitudes of the transient current and the circuit resistance. The grid circuit is particularly affected by this phenomenon, since it usually suffers a net loss of electrons and therefore may assume a positive charge. The resulting increase in plate current is determined largely by the grid resistance and the gain of the tube.

Gas-filled tubes (thyatrons), under extensive neutron bombardment, most likely will fail by breaking of the glass envelope or glass-to-metal seals. Such damage occurs at thermal neutron fluences exceeding  $10^{16}$  n/cm<sup>2</sup> (fission).

The principal transient effect in a thyatron subjected to a nuclear radiation pulse is spurious firing caused by ionization of the filling gas. The filling gas, in these cases xenon, becomes partially ionized, primarily by gamma rays. Additional ions are created by ion-neutral molecule collisions in the electric field between the plate and the grid. A positive ion sheath can form around the negatively-biased control grid, which will neutralize the grid charge and will permit electrons to be accelerated from the cathode space charge toward the plate. As ion density increases, a sustaining discharge ensues, which can be shut off only by removing the plate voltage.

Phototubes are designed to exhibit peak sensitivities to electromagnetic radiation in the visible and near-infrared regions by choosing photosensitive cathodes with low work functions. The presence of photosensitive material in

a vacuum tube introduces effects other than those found in receiving type electron tubes in a radiation field.

Severe permanent damage to phototubes, as with other vacuum tubes, is attributable to large thermal neutron fluences. Severe damage starts in phototubes at about  $10^{15}$  n/cm<sup>2</sup> (fission). However, moderate permanent damage may occur at thermal neutron fluences two orders of magnitude lower. Moderate damage in some cases is an increase in dark current, or a decrease in anode luminous sensitivity, but in most cases it is a darkening of the glass envelope. This darkening effectively reduces tube sensitivity. The glass discoloration has been observed at fast neutron fluences of  $5.5 \times 10^{12}$  ( $E > 10$  keV, fission), and gamma ray doses of  $6.3 \times 10^6$  rads (C). Thus, both gamma and neutron components of mixed radiation contribute to permanent damage.

The principal transient effect in photomultiplier exposed to pulsed X-ray radiation (and presumably to gamma radiation) is an increase in anode current. The increase can be as much as the space-charge-limiting value for a given tube. Furthermore, the duration of the current increase is much greater than that of the radiation pulse. At first, the current increases as a result of currents initiated by luminescence of those areas of the glass envelope that are optically coupled to the cathode of the photomultiplier. This current increase also has been demonstrated in steady-state gamma fields. Glass luminesces at wavelengths and intensities determined by the glass composition and by the dose rate. Since a great deal of the radiant energy is in the visible portion of the light spectrum, where common photomultipliers are sensitive, it would be expected that the degree of photomultiplier response to X-ray and gamma radiation would depend upon both the type of glass used for the envelope and the spectral sensitivity of the cathode material.

A second mechanism is required to explain the relatively slow decay of anode current after the radiation field is removed, since glass luminescence decays rapidly. It is believed that decay of anode current may be retarded by electric-field changes in the tube when electrical insulators become charged as a result of large initial current pulses.

The excess conductivity induced in a material irradiated with a short pulse of ionizing radiation is generally classified in two components: the prompt component, and the delayed component. The prompt component is primarily the result of excess carrier concentration from direct ionization by the radiation and the concurrent recombination and trapping of these carriers. The delayed component is that component of conductivity that remains after the termination of the ionizing pulse. This does not mean to imply that it does not make a small contribution during the radiation pulse. The delayed component is the result of thermal generation of excess carriers from shallow traps, in which they are caught during the prompt pulse, and their concurrent loss to recombination and retrapping. The rate at which these carriers are thermally regenerated depends on the energy level of the trap site, the concentration of filled traps, and the temperature. As there is usually more than one energy level trap in a material, more than one regeneration rate usually is observed in the delayed component.

#### 9-48 Capacitors

Nuclear radiation affects most of the electronic properties of capacitors to some extent. Changes in the capacitance value, dissipation factor, and leakage resistance have been observed during steady-state reactor experiments. These effects generally are not considered severe for fast neutron fluences less than  $10^{15}$  n/cm<sup>2</sup> ( $E > 10$  keV, fission), and for most capacitors this limit is about  $10^{17}$  n/cm<sup>2</sup> ( $E > 10$  keV, fission).

During a high-intensity pulse of nuclear radiation, the most pronounced effect in a capacitor is a transient change in the conductivity of the dielectric material with a corresponding increase in the leakage currents through the capacitor. The most recent concept of ionization effects in insulating and dielectric materials indicates that the ionizing particles create ionizing tracks in the irradiated material. This means that, microscopically, the material is not uniformly ionized (an exception to this occurs at very high dose rates,  $\approx 10^{12}$  rads (Si)/sec, where there should be sufficient overlap of the ionized tracks for the material to be considered uniformly ionized).

The excess conductivity is proportional to the number of carriers available to drift under the influence of the applied electric field. However, the microscopic nonuniformity of the carrier concentration must be considered for the pulsed irradiation case. For irradiation with ionizing particles with a low specific ionization (the ratio of the number of ion pairs produced per unit path length to the number produced per unit path length by a minimum ionizing particle), the excess prompt conductivity will be the same as if these carriers were generated uniformly throughout the material. However, if the specific ionization is increased (by bombardment with more heavily ionizing particles), a point will be approached where the separation of ionization sites is less than the distance travelled by the electron before it has become thermalized and is able to drift under the influence of

[REDACTED]  
the applied electric field. As this point is approached, the probability that the electron will be captured in the field of a neighboring ion increases, and the contribution to excess conductivity will be reduced. Thus, a plot of prompt conductivity as a function of specific ionization would show the prompt conductivity constant at low specific ionization and decreasing slowly after some threshold values of specific ionization is reached.

[REDACTED] The rate at which carriers are lost concurrent with their generation by the ionizing radiation is proportional to the concentration of recombination centers and unfilled trapping centers. While an insignificant number of the total traps in the material might be filled at low doses, the concentration of filled traps within a track depends only on the specific ionization. Thus, the trapping rate is affected by the specific ionization. The result of this effect is to cause an increase in prompt conductivity with specific ionization, which would serve in part to compensate for the decreasing effect mentioned above. However, this effect on the carrier loss rate should be slight, since most of the carriers are lost to recombination rather than trapping.

[REDACTED] When the radiation is delivered in a time short compared with the regeneration time of carriers from the traps, and the dose delivered in the pulse is large enough that significant numbers of tracks near the end of the pulse overlap tracks generated earlier, the concentration of filled traps in a track late in the pulse is different from that in a track created earlier in the pulse. When this occurs, the observed prompt conductivity becomes a function of the total dose delivered in the pulse, as well as of the specific ionization of the irradiating particle. It should be noted that a sufficient fraction of traps in a track must be filled to significantly affect the response. Hence, it is quite possible that trap densities in many insulators are high enough so that this condition is not realized in most pulse experiments.

[REDACTED] The delayed conductivity component depends on the rates of carrier regeneration and retrapping from trap sites, which depend on the concentration of filled traps and the energy levels of the traps. The concentration of filled traps is a function of the specific ionization of the irradiating particle and, in the case of overlapping tracks, the total dose. As the initial concentration of filled traps within a track is usually a significant fraction of the total concentration of traps, the retrapping probability changes during the time the traps are emptying, thus altering the characteristic time for emptying the remainder of the filled traps. As a result, the decay of the delayed component does not usually follow a simple law. Only in certain cases, where the trapping probability is negligibly perturbed by the radiation, will simple exponential decays be observed.

[REDACTED] Neutrons produce ionization by a number of collision processes that give rise to ionizing secondary particles. These processes include:

- Elastic scattering when the recoil atom receives sufficient energy to produce ionization.
- Inelastic scattering, producing a recoil atom that may or may not ionize but that emits a gamma photon that can produce a secondary ionization.
- Capture, resulting in the emission of a photon and/or an ionizing secondary particle (primarily thermal neutrons).
- Reactions resulting in an ionizing particle, e.g.,  $(n,p)$ , or  $(n,\alpha)$  reactions (high-energy neutrons).

There are, therefore, many possible different specific ionizations associated with ionized tracks in neutron bombarded materials.

[REDACTED] In hydrogenous materials, the principal ionization is caused by recoil protons, which have a high specific ionization. For this reason, neutron induced conductivity in hydrogenous dielectrics has been found to be approximately

one-fifth to one-half that of gamma ray induced conductivity for equal ionization energy deposition rates. For nonhydrogenous dielectrics, the most important contribution to neutron induced ionization is by the interactions of very high-energy neutrons ( $E > 2$  MeV).

A "polarization effect" that is attributed to space charge buildup within the dielectric material due to nonuniform trapping has been observed with some capacitors, particularly with Mylar, mica, polycarbonate, tantalum oxide and Vitamin Q devices. This effect is manifested in several ways. One is an apparent decrease in the induced conductance with sequential radiation pulsing. Charge transfer across the dielectric during a radiation pulse builds up a space charge field opposing the applied electric field. If the applied electric field is then removed, subsequent radiation pulses result in a current in the external circuit opposite in direction to that observed with the field applied. This is caused by the discharge of the space charge field. Similarly, if the electric field is reversed rather than removed after the space charge has been built up, the space charge field enhances the applied field, and a larger current results than would be observed normally.

Saturation of the polarization effect, where no further decrease in the charge transfer is observed with subsequent radiation pulses, occurs after one or more pulses, depending on the capacitor and on the dose delivered in each pulse. Decreases of 50 to 70 percent for mica, 10 to 20 percent for tantalum oxide, and 30 percent for Mylar have been observed due to this space charge buildup during radiation pulsing.

#### 9-49 Resistors

Radiation effects in resistors are generally small compared with effects in semiconductors and capacitors and are usually neglected. However, in circuits requiring high precision resistors transient effects may be significant at dose rates of as low as  $10^7$  rads (C)/sec and at neutron fluences of  $10^{14}$  n/cm<sup>2</sup> ( $E > 10$  keV, fission).

The transient effects are generally attributed to gamma rays that interact with materials to produce electrons, primarily by the Compton process; however, energetic neutrons can also produce significant ionization. Transient effects include (1) a change in the effective resistance due to radiation induced leakage in the insulating material and the surrounding medium, (2) induced current that is the result of the difference between the emission and absorption of secondary electrons by the resistor materials, and (3) change in the conductivity in the bulk material of the resistor. There is no substantial evidence, however, that the third effect is a first-order transient effect.

The permanent effects are generally caused by the displacement of atoms by neutrons, causing a change in the resistivity of the material.

#### 9-50 Batteries and Cables

Batteries are affected much less by radiation than other component parts. The effects of radiation on nickel-cadmium batteries appear to be insignificant at dose rates up to  $10^7$  rads (air)/sec. No radiation damage was apparent in a number of batteries and standard cells that were subjected to  $10^{13}$  n/cm<sup>2</sup> ( $E > 10$  keV, fission). Transient radiation effects on an ammonia fuze indicated that pulsed gamma ray irradiation of  $10^8$  rads (air)/sec had no effect on the operation of the battery.

[REDACTED] It has been recognized for some time that intense pulses of radiation produce significant perturbations in electrical cables and wiring, including coaxial and triaxial signal cables. Even with no voltage applied to a cable, a signal is seen when the cable is exposed to a pulsed radiation environment. The current associated with this signal is defined as a replacement current, since it is most likely a current in an external circuit that is necessary to replace electrons or other charged particles that are knocked out of their usual positions by the radiation. The replacement current definition also applies to the effect of charged carriers associated with the incident radiation embedded in a test sample.

[REDACTED] The magnitude of the radiation induced signal varies with the voltage applied to the cable. This voltage-dependent portion of the signal, i.e., the total signal exclusive of the replacement current, is called conduction current, thus it is ascribed to the conductivity induced in the insulating dielectric by the radiation. However, it may also contain major contributions from polarization or depolarization processes in the dielectric. These can usually be identified by their gradual disappearance (saturation) after repetitive exposures and by their reappearance in additional "shots" in which the applied voltage is changed greatly, e.g., removed or reversed.

[REDACTED] Ionizing radiation of any type produces free electrons that contribute to the conductivity of the material. Hence, insulators are expected to have a transient enhanced conductivity in an ionizing radiation environment. Conduction in the insulator is frequently characterized by two components: for very short radiation pulses, a prompt component whose magnitude is a function of only the instantaneous exposure rate, and frequently at the end of the short radiation exposure, a delayed component having approximately exponential decay.

[REDACTED] Although the replacement, conduction, and polarization currents are fairly well under-

stood in terms of the interactions between the ionizing radiation and the metal-dielectric target system, it is not yet possible to predict quantitatively the response for a given cable in a specified environment. In a mixed neutron-gamma environment, the induced replacement current usually contains positive and negative components, and may therefore assume either polarity. The conduction current sometimes exhibits a rather complicated time dependence consisting of prompt- and delayed-conductivity contributions. The polarization current appears to be greatly affected by the properties of the metal-dielectric interface.

[REDACTED] Permanent damage effects in cables and wiring are manifested as changes in the physical and electrical properties of the insulating materials. When such damage becomes appreciable, e.g., when the insulation resistance is reduced severely, electrical characteristics may be affected. The extent of the damage to insulating materials is an increasing function of neutron fluence, exposure or dose, humidity, and irradiation temperature. Certain types of wire insulation are quite susceptible to permanent damage. For example, silicon rubber becomes severely cracked and powdered after approximately  $2 \times 10^{15} \text{ n/cm}^2$  ( $E > 10 \text{ keV}$ , fission). The approximate damage thresholds for three common types of cable insulation are: polyethylene,  $1 \times 10^7$  rads (C); Teflon TFE,  $1 \times 10^4$  rads (C); and Teflon FEP,  $2 \times 10^6$  rads (C). On the other hand, some irradiated polyolefins are capable of withstanding up to  $5 \times 10^9$  rads (C). A considerable degree of annealing has been observed with respect to insulation resistance, which implies the possibility of adequate electrical serviceability after moderate physical damage.

[REDACTED] It is not expected that radiation effects on wiring with thin insulation will exhibit the strange behavior observed in coaxial cables. In particular, the very limited measurements that have been performed indicate that the replace-

ment current is primarily a function of the gamma environment. To a good approximation, it can be assumed that the replacement current for a wire or most other objects placed in the radiation environment will amount to the emission of a number of electrons between 1 and  $5 \times 10^{-3}$  times the number of gamma photons traversing the object.

The conduction current is a very sensitive function of the amount of insulation around the wire and its immediate environment. For a bare wire in air with a ground plane nearby, conduction is due predominantly to the ionization produced in the air. Placing insulation around the wire reduces this conduction, but at the price of increasing the area of the wire and hence the effective replacement current.

### 9-51 Quartz Crystals

The radiation response of a quartz crystal oscillator is primarily a function of radiation dose. The type of material from which the oscillator is fabricated, e.g., natural quartz, Z-growth synthetic, Z-growth swept synthetic, etc., and to a lesser extent the type of cut, e.g., AT, BT, etc., and the frequency and mode of operation determine the sensitivity of the oscillator to the radiation. The primary effect of the radiation is a shift in the frequency of the oscillator. Both transient and steady-state shifts have been observed.

The steady-state frequency offsets are a result of changes in the elastic stiffness constants of the crystal. For example, perturbations in the crystal bonds due to charge trapping at defects or to formation of new defect complexes will result in steady-state frequency offsets. Of materials tested to date, Z-growth swept-synthetic quartz has been the most radiation tolerant to steady-state frequency offsets. Swept natural quartz is slightly more sensitive and unswept natural quartz and unswept synthetic quartz, respectively, are even more sensitive. The

response of a particular crystal also varies with the manner in which the crystal is mounted, the material used for the electrodes, and to a lesser extent differs for each quartz bar grown, even among bars grown under similar conditions. Both swept synthetic and natural quartz crystals can recover 80 percent to 90 percent of their original frequency change after annealing at 500°C for times on the order of 100 to 160 hours.

Transient shifts in the frequency of an oscillator and reduction or cessation of the output result from energy deposition and any subsequent temperature rise in the crystal. Temperature gradients in the crystal due to faster removal of heat near the support wires and due to the electrodes absorbing more energy than the crystal, can give rise to frequency shifts induced by the resulting strain.

Irradiation of general purpose crystal units has shown that they do not suffer significant permanent effects, within the limits of their stability, at a neutron fluence of  $10^{13} \text{ n/cm}^2$  ( $E > 10 \text{ keV}$ , fission) and a gamma dose of  $4.4 \times 10^3 \text{ rads}$  (air). Transient phase and amplitude changes resulting from this environment are not of sufficient magnitude to cause concern about their operation under such conditions.

Moderate precision crystal units display negligible frequency and amplitude changes when subjected to a reactor pulse. Weapon tests as well as steady-state gamma source tests indicate that a gamma dose greater than  $10^4 \text{ rads}$  (air) is required to induce significant permanent frequency changes in these devices. Frequency changes up to almost one part in  $10^5$  were observed after exposure to  $7.5 \times 10^4 \text{ rads}$  (air) and  $10^{12} \text{ n/cm}^2$  at a weapon test. The possibility that causes other than radiation contributed to the changes observed at this test cannot be excluded.

High precision natural quartz-crystal units either stop oscillating or exhibit appreci-

able decreases in the amplitude of the output signal during nuclear pulses of approximately  $10^{12}$  n/cm<sup>2</sup> ( $E > 3$  MeV, fission), and  $3 \times 10^3$  rads (H<sub>2</sub>O). If oscillation stops, its cessation persists for minutes. The cessation of oscillation is apparently independent of the voltage, current, or power at which the units are being driven. Resumption of oscillation occurs at a reduced drive current and lower frequency. The drive current is tens of microamperes below the specified rated drive when oscillation resumes. Frequency changes as high as 1 part in  $10^7$  have been observed when this type of crystal was exposed to  $7.9 \times 10^{11}$  n/cm<sup>2</sup> ( $E > 3$  MeV, fission), and  $2.9 \times 10^3$  rads (H<sub>2</sub>O).

DNA  
(1)(1)

#### 9-52 Solder Joints

DNA  
(6)(1)

#### 9-53 Infrared Detectors

The infrared detectors that exhibit the greatest sensitivity to infrared radiation are also the most sensitive to nuclear radiation. For radiation pulses that are short compared to the

relaxation time, the response of a photoconductive type of infrared detector cell is an excess conductance that is proportional to the radiation exposure. For long pulses the excess conductance is proportional to the radiation intensity and the carrier recombination time. Neutron bombardment causes permanent degradation of output-signal level and signal-to-noise ratio.

Irradiation of a lead sulfide device to  $1.3 \times 10^{14}$  n/cm<sup>2</sup> ( $E > 0.48$  eV, fission) at 134°F revealed a 67 percent reduction of output signal level and greater than 40 percent reduction in the signal-to-noise ratio. Damage was essentially catastrophic after  $6.9 \times 10^{15}$  n/cm<sup>2</sup> ( $E > 0.48$  eV, fission).

Lead selenide devices appear to be somewhat more tolerant to neutron irradiation than lead sulfide detectors. After a neutron fluence of  $1.2 \times 10^{14}$  n/cm<sup>2</sup> ( $E > 0.48$  eV, fission) at 135°F, the output signal level of a lead selenide cell was reduced by 36 percent, and the signal-to-noise ratio was down more than 46 percent. The output level was down by 96 percent after  $1.8 \times 10^{16}$  n/cm<sup>2</sup> ( $E > 0.48$  eV, fission). Lead selenide cells that are designed to operate at low temperatures are more sensitive to radiation than those that are not designed for low temperatures.

Indium antimode photovoltaic cells that operate at liquid nitrogen temperature showed significant voltage signals at doses less than 0.88 rads (air). The cells exhibited radiation induced voltages roughly proportional to the logarithm of the dose when the radiation was delivered in short pulses. Recovery to within 2 percent of the maximum voltage occurred within 175  $\mu$ sec after the highest intensity radiation pulses. A complete loss of output from these cells has been observed after a neutron fluence of  $2 \times 10^{16}$  n/cm<sup>2</sup> ( $E > 0.48$  eV, fission).

Thermistor-bolometer infrared detectors are the most neutron tolerant of the devices that have been tested. After  $9.6 \times 10^{13}$  n/cm<sup>2</sup> ( $E >$

0.48 eV, fission), the output signal level was down by 28 percent, and the signal-to-noise ratio was down about 11 percent. After  $1.6 \times 10^{16} \text{ n/cm}^2$  ( $E > 0.48 \text{ eV}$ , fission), the output level was down 57 percent, and the signal-to-noise ratio was down 66 percent. The detector may be usable for some applications under these conditions.

Thermomechanical shock effects in infrared detectors will be similar to those discussed for semiconductor devices, and will occur at about the same levels.

## ELECTRONIC CIRCUITS

### 9-54 Radiation Response of Discrete-Component-Part Circuits

Determination of the response of a circuit is complex because of the large variations in circuit configuration and in the component parts that can be used within a circuit configuration. Therefore, determining circuit response becomes a problem of detailed circuit analysis and/or testing. The radiation effects material necessary for this kind of analysis and testing are beyond the scope of this manual. Guidance may be obtained from the *TREE Handbook* and the *TREE Preferred Procedures* (see bibliography). General circuit effects and typical analysis techniques are discussed in this manual.

The transient effects that can cause a system to malfunction can result in circuit responses that, like component-part responses, can be both dose and dose rate dependent. If the radiation pulses are short with respect to component-part recovery times the circuit time constants, the circuits will integrate the effects and will be sensitive to the total dose rather than the dose rate. However, when the pulse widths are wide, the circuits are dose rate sensitive. This can be illustrated by reference to Figure 9-61. Assume that for the circuit response plotted, the malfunction threshold is 1.5 volts. Therefore, a

0.15  $\mu\text{s}$  pulse at  $1 \times 10^9 \text{ rad (Si)}/\text{sec}$  will cause a malfunction. It is obvious from the curve that the malfunction dose rate is much lower for wider pulses.

Discrete digital circuits and circuits that contain silicon controlled rectifiers (SCR's) have displayed failure at doses as low as 0.1 to 1.0 rad (Si) for short pulse widths. It is difficult to design a circuit specially that will not malfunction above a prompt dose of 100 rads (Si).

Another effect that can result from the ionizing radiation is the initiation of a catastrophic action or catastrophic failure. An example would be the firing of a pyrotechnic device or the premature initiation of a firing signal. A second type of catastrophic action occurs if a circuit destroys itself as a result of the effects caused by ionization (burnout). Figure 9-62 shows an output stage of a power supply inverter. In normal operation, Q1 and Q2 are turned on alternately. The output at the transformer secondary is a square wave. Ionizing radiation may cause Q1 and Q2 to turn on simultaneously. After the radiation pulse, the transistors will recover to normal operation, and one of the transistors will attempt to turn off. At this time a large voltage will be induced across the transistor that is attempting to turn off. If this voltage exceeds the breakdown voltage, the transistor may be damaged.

General statements applicable to both permanent and transient effects include:

- Circuits that use low frequency, thick base semiconductors usually are more susceptible to radiation effects than those circuits that contain high frequency, thin base devices
- Germanium devices generally will show larger photocurrents and leakage currents than comparable silicon devices
- High impedance circuitry generally will be more susceptible to radiation effects than low impedance circuitry

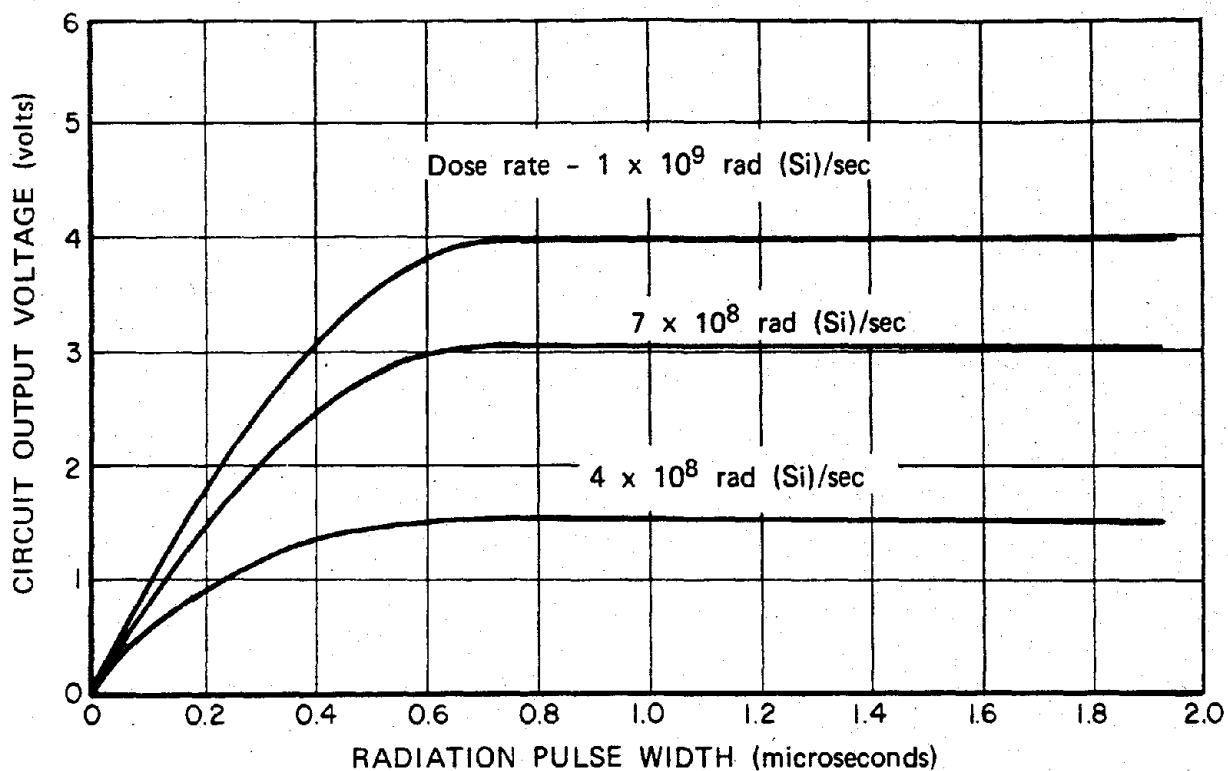


Figure 9-61. [REDACTED] Circuit Response as a Function of  
Radiation-Pulse Width [REDACTED]

- Magnetic memory devices will not be sensitive to the neutron and gamma environments typically specified as the environment in which an electronic system must survive.

[REDACTED] The primary permanent effects on circuits will be the degradation of semiconductor devices. The solid-state power supplies and regulators with their low frequency transistors will fail to perform their required function when exposed to fluence between  $10^{11}$  and  $10^{13}$  n/cm<sup>2</sup> ( $E > 10$  keV, fission) depending on the circuit configuration, component parts, and design margins in the system. Circuits that use MOSFET can fail at gamma doses between  $10^3$  and  $10^5$  rads (Si).

[REDACTED] The failure threshold for thermo-

mechanical shock will be established by the threshold of the component parts.

[REDACTED] It is desirable to have a method of analysis that can be used to predict the response of components, circuits, and systems. The analysis methods that are used consist of established techniques to calculate circuit and system responses by replacing radiation effects by their corresponding electrical effects. Thus, the problem that is solved eventually is wholly electrical in character. A major advantage of analysis as a simulation tool is that it is not necessary for a circuit or system to exist in a physical state before it can be analyzed. In addition, the analyst has control over the "environment," and it is theoretically possible to simulate the total

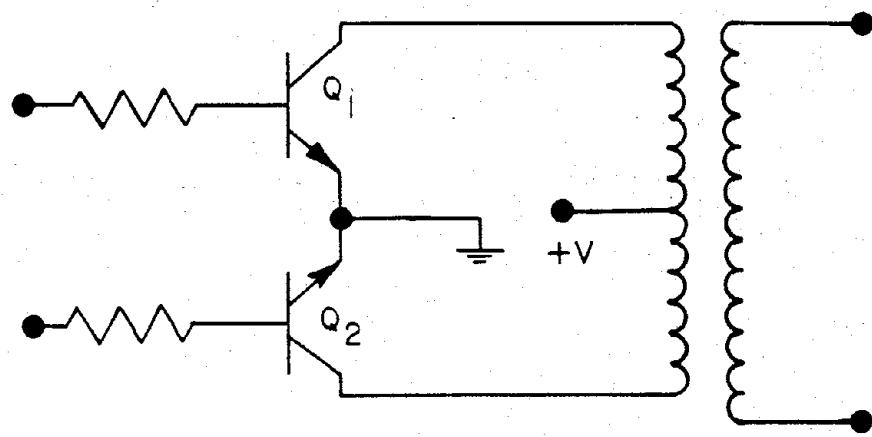


Figure 9-62. [REDACTED] Circuit in Which Burnout Could Occur [REDACTED]

environment during a single (but complicated) analysis. Perhaps the major disadvantage of analysis (for TREE) is the relatively low confidence in the results. This low confidence level usually arises from the simplifying assumptions that are often made to expedite the analysis and which, themselves, are subject to verification, typically by environmental testing.

[REDACTED] Certain requirements or inputs are needed for any circuit or system analysis. First, an accurate mathematical description of the electrical characteristics must be obtained. Such a description usually is checked by comparing the computed electrical response to the measured electrical response of a circuit or system. Second, the radiation effects on electronic materials and devices must be represented, or modeled, by electrical effects. For example, displacement effects may be modeled by making transistor current gain a function of time. This step generally requires environmental testing and/or sound analytical procedures to obtain the required radiation effects data. Third, an analysis method must be employed to make an accurate calculation of the steady-state and transient responses of the electronic network of

interest. This may be done by hand or with the aid of a computer.\*

[REDACTED] Hand analysis techniques are useful for a quick qualitative and, to a limited degree, quantitative appraisal of the sensitivity of linear circuits and logic circuits to radiation environments. Manual techniques are valuable in the prediction of permanent effects of transient radiation, particularly when the relevant electrical parameters assume constant, degraded values after irradiation. The hand analysis techniques are often quite adequate to establish the initial estimate of radiation induced voltage and current transients and of the steady-state performance degradation. This type of analysis is suitable for a rough estimate of the peak-amplitude radiation response. In practice, only small, simple circuits can be handled.

[REDACTED] In doing analysis, there is an inevitable choice between time (man-hours) and accuracy. If great confidence in the results is not required (e.g., when the analysis results are to be used to

\* [REDACTED] A more detailed discussion of hand and computer analysis techniques is contained in the "TREE Handbook" (see bibliography).

plan further environmental tests), a large number of simplifying assumptions can be made, and the analysis can be carried out quickly by hand.

If the results of an analysis are to be used directly in a survivability assessment, high accuracy is desirable. This implies that few simplifying assumptions may be made. If a circuit contains more than one or two active devices (e.g., transistors), the circuit model will be complex, and the speed and accuracy of a digital computer should be used. Both hand analysis and computer aided analysis require an equivalent-circuit model that represents electrical and radiation induced phenomena. A notable difference is that the computer can handle an equivalent circuit model in its entirety and can generate the desired response function without making engineering approximations.

Both analog and digital computers have been used for response predictions, and each has advantages and disadvantages; however, recently developed mathematical techniques and programming capabilities make the digital computer preferable for most problems. Several digital programs are available for circuit analysis. These are described in some detail in the "TREE Handbook" (see bibliography). These codes do not do the analysis. They do perform the tedious, error-prone calculations. The individual who uses them must provide the accurate description of the equivalent circuit model and must interpret the results.

Two factors control the accuracy of the results of any TREE analysis method. The first factor is the accuracy and completeness of the description of the response of individual components to a particular radiation environment. This information is basic to the success of any analysis technique and frequently has been the major stumbling block for analysis attempts.

The second factor that affects the accuracy of the analysis results is the assumptions that are made to simplify the analysis problem.

Certain aspects of the radiation response of individual components generally are neglected by assuming that they will contribute only a small or negligible portion to the radiation response of the circuit. These assumptions are made on the basis of general experience with the radiation response of circuits and with knowledge of the limits over which they might be valid. Although these assumptions are generally correct, there are specific instances and specific circuit configurations for which they may not hold, and care must be taken in making such assumptions.

In practice most of the analysis approaches result in a fairly reasonable correlation with experimental results. However, it is common knowledge that any experimental result can be explained by a theory, but the theory will not always predict the correct result in a new situation. Therefore, caution should be exercised when accepting a component representation or an analysis technique that predicts the results for a pulsed reactor environment reasonably accurately, if these results are to be applied to a nuclear weapon environment. It is also possible that techniques applicable to switching circuits or nonlinear circuits will not apply to all linear circuit analysis.

### 9-55 Radiation Response of Integrated Circuits

Integrated circuits include many circuit types differing in construction materials and methods. The four construction types are the monolithic semiconductor, thin film, multichip, and hybrid integrated circuits. The scope of this section will be limited to monolithic and thin film circuits since the radiation response of both multichip and hybrid circuits can be inferred from the discussion of monolithic and film circuits or discrete devices. The discussion includes junction isolated, dielectrically isolated, and air isolated integrated circuits.

In junction isolated circuits, the components are defined within a single crystalline substrate by regions of alternate doping that are electrically isolated by reverse biased PN-junction boundaries. The doped regions are formed by the geometrically controlled diffusion of appropriate impurities into the substrate. One or more uniformly doped, epitaxial layers may be grown upon the substrate prior to diffusion (planar epitaxial). The dielectric-isolated circuit is distinguished by the use of a dielectric (silicon dioxide or ceramic) instead of a PN-junction isolation between critical components. A single component or a small number of components are formed within individual single crystalline islands (called tubs) that are imbedded in a polycrystalline substrate. The active elements in both the junction and dielectric isolated circuits can be bipolar transistors, junction FET's, or insulated gate (MOS) FET's. The air isolated circuit usually employs aggregates of unipolar (i.e., field effect) transistors of metal-oxide-silicon construction.\* Since this type of transistor may be used as a bias-dependent resistor, complete designs usually are constructed without the use of other circuit elements. Air isolated MOS integrated circuits are fabricated by growing silicon on sapphire (SOS). Portions of the silicon are etched away, leaving isolated islands of silicon upon which transistors are fabricated.

Thin-film integrated circuits employ geometrically controlled surface films of conductive and dielectric materials upon a glass or ceramic substrate to define passive circuit elements and interconnections. The active elements may be formed as an integral part of the process (thin film, insulated gate, field effect transistors) or welded to the circuit (conventional, discrete transistors). Circuits of the latter type are referred to as hybrid thin film circuits.

The categorization of circuit types given above is somewhat arbitrary. It is based on the

present developments in the integrated circuit industry, rather than on strict lines of variance between the types. The categorization is used for convenience of discussion with respect to the effects of transient radiation, where distinctly different effects may occur. For example, the PN junction used for isolation is a source of photocurrents during an ionizing radiation pulse, and may result in large substrate (and hence, power-supply) currents in junction isolated monolithic circuits. This effect is absent in either the air or dielectric-isolated monolithic circuit or the thin film, hybrid circuit.

Transient radiation may cause both transient, permanent and thermomechanical shock effects. On a qualitative basis, the primary electrical effects introduced in integrated circuits by transient radiation are similar to the effects described for conventional solid-state circuitry. The magnitude, duration, and electrical consequences of these effects, however, do not follow directly from conventional circuit experience.

The effects of radiation on an integrated circuit are more closely related to its geometrical and physical characteristics than to its electrical function or circuit configuration. The proximity of circuit elements within the device, and in some cases its integral structure, make several modes of secondary interaction possible. This is especially important in the case of junction isolated integrated circuits.

The transient effects observed in integrated circuits result from the generation of excess charge carriers that cause photocurrents and voltage changes. As previously described for transistors, the motion of excess carriers is governed by the response of carriers to electric fields and concentration gradients. The charge carriers will cause currents to occur until they

Air-isolated bipolar integrated circuits have also been constructed.

are swept out by external fields and electron-hole recombination. The peak photocurrents can be a function of either dose rate or dose depending on the duration of the radiation pulse. As a result, if the radiation pulse is long compared to the circuit radiation response time, the microcircuit response is dose rate dependent. However, for radiation pulses that are short compared to the circuit radiation response time, microcircuit response will be dose dependent. Thus, the width of the radiation pulse can be of considerable significance, since the peak photocurrent generated can be a function of the duration of the pulse as well as its amplitude.

In a transient-radiation environment, the semiconductor integrated circuit reacts to several mechanisms that have been discussed in connection with conventional circuitry. One point of departure that is made necessary by the monolithic nature of the circuit, is the significant and often predominant interelement effects that occur in addition to the intraelement effects. It is important to consider current paths between as well as within component parts of the microcircuit.

Quite generally, the transient effects in any integrated electronic device are a consequence of a sequence of events that may be described as follows:

- The radiation interacts with the circuit material and surrounding encapsulant to introduce charge carriers and to establish a nonequilibrium charge distribution.
- Acting under nonequilibrium electric fields and concentration gradients, mobile carriers flow in the direction that restores equilibrium and thereby produce primary electrical currents. These electrical currents may be semiconductor-junction photocurrents, replacement currents, dielectric-leakage currents, gas-ionization currents, etc.
- The nonequilibrium charge distribution and

the primary electrical currents may interact with the electrical circuit to produce secondary effects, e.g., secondary photocurrents. Under certain circumstances, the secondary effects may be sufficiently regenerative to be self-sustaining, and a new stable circuit state will result. In addition, localized electrical stresses may introduce permanent damage.

- The cumulative effects of the radiation induced currents and circuit action are voltage, current, and impedance changes of variable duration at the terminals of the integrated circuit.

In junction isolated circuits, the predominant effect is PN-junction photocurrents resulting from ionization in the semiconductor material. Important secondary effects include secondary photocurrents produced by transistor action in any three adjacent doped regions, potentially large substrate currents, and "latchup."

The predominant effect in dielectric isolated circuits is also PN-junction photocurrents. The major difference from other monolithic structures is the absence of the extra PN-junction between the components and the substrate and its associated photocurrent. Also, current paths are more restrictive.

In air isolated integrated circuits, the important primary transient effects are PN-junction photocurrents, replacement currents resulting from charge scattered from device lead wires and the case, and ionization currents through the surrounding encapsulant. The predominant secondary effect is a secondary photocurrent resulting from the radiation induced gate current and transistor action. In addition, photocurrent is generated in the Zener diode employed for protection in the gate lead of MOS circuits.

In MOS integrated circuits, the important primary transient effects are drain-substrate and source-substrate PN-junction photocurrents,

[REDACTED] replacement currents resulting from charge scattered from device lead wires and the case, and ionization currents through the surrounding encapsulant. The predominant secondary effect is a secondary drain current resulting from the radiation induced gate current. In addition, photocurrent is generated in the Zener diode employed for protection in the gate load.

[REDACTED] For the most part, thin film circuits may be treated as conventional circuits with extremely small geometries. Ionization currents within and between elements have specific importance, especially in the high-impedance circuitry associated with thin film circuits that employ field effect transistors. Nevertheless, in most cases of interest, the transistor is the predominant element that determines the transient radiation response of the circuit.

[REDACTED] Semiconductor integrated circuits of the planar-diffused (or planar epitaxial) type experience transient effects that may be attributed to the interaction of the circuit elements through the active substrate. Two predominant interelement effects that must be considered are the presence of large substrate currents and the occurrence of latchup.

[REDACTED] In practice, the high packing density of elements on a substrate chip results in the presence of isolation diodes over most of the area of the chip. Thus, a chip 40 x 40-mils may have 1,500 mils<sup>2</sup> of effective isolation-diode area. The total substrate photocurrent may be 100 times that of a typical diode in the circuit. Since the substrate is connected to the power supply system, the substrate currents will be reflected in large currents appearing in the power supply leads. Radiation induced power supply currents of the order of 1 ampere, with durations of a few microseconds have been observed at prompt doses of approximately 10 rads (Si). The potential hazards to the power supply system, which must supply many such circuits, are evident.

[REDACTED] Present evidence indicates that the very large power supply currents occur primarily in those circuits where transistor action through the substrate is possible. In circuits of this type, radiation thresholds above which the current increases suddenly have been observed. The thresholds have been attributed to the turning on of an equivalent four layer device. Other possibilities include second breakdown and sustaining voltage breakdown.

[REDACTED] Transients induced in integrated circuits by pulsed ionizing radiation last from less than a microsecond in high speed digital circuits to several tens of microseconds in slower circuits. Occasionally, pulsed-radiation effects with considerably longer recovery times can be explained by circuit time constants. In the extreme case, the abnormal state persists until the dc power is interrupted. When this occurs, normal circuit operation is inhibited and latchup has occurred. In some cases, which are referred to as incipient latchup, the condition lasts only for periods that are long with respect to normal recovery times of the circuits. Latchup can be induced in three ways: by exposure to ionizing radiation; by particular sequences of applying voltage to circuits employing more than one power supply; and other electrical stimulations such as high voltage pulses. Only radiation induced latchup is considered here. Radiation induced latchup has been observed in only a small percentage of the device types that have been irradiated with pulsed ionizing radiation, and of these device types usually only a small percentage of the samples exhibit latchup. In a few cases, a majority of the samples of a certain part from a manufacturer of integrated circuit part types have exhibited latchup.

[REDACTED] Integrated circuit latchup is always caused by one or more normally reverse biased PN junctions becoming conductive, either by the initiation of a breakdown mechanism or by becoming forward biased. In either case, a sustain-

ing mechanism must act to maintain the breakdown or forward bias condition, once it has been initiated. Three latchup mechanisms have been postulated and observed in junction isolated integrated circuits. These are: PNPN action, second breakdown, and transistor sustaining voltage breakdown. No other mechanisms for sustaining latchup are known, although several others have been postulated.

Latchup is normally associated with junction isolation since it usually involves some type of interaction with the silicon substrate through an isolating PN junction. Dielectric isolation is effective in isolating elements from one another and from the silicon substrate and, thus, is an important step in reducing the latchup vulnerability of integrated circuits. However, analyses of the structural characteristics of certain dielectric-isolated circuit types have indicated that the possibility of latchup cannot be ruled out in dielectric-isolated circuits. It is possible that some of the same mechanisms that are responsible for latchup in junction-isolated circuits also can exist in a dielectric-isolated circuit. These mechanisms include second breakdown, sustaining voltage breakdown of transistors and PNPN action if 4 layer structures are included within a dielectrically-isolated region.

No latchup mechanisms have been found that are peculiar to dielectric isolation. While photocurrents can be generated in dielectric isolation, there are no sustaining mechanisms for these currents unless the isolation is defective or is subjected to destructively high voltages.

Hybrid thin film circuits may be expected to be as tolerant of radiation as their conventional circuit counterparts. The radiation response is determined primarily by the active elements in the circuits.

Undoubtedly, dielectric isolated circuits are much less vulnerable to latchup than are their junction isolated counterparts. However, dielectric isolated circuits probably are more

latchup-prone than discrete component circuits because: dielectric isolated process limitations occasionally permit four layer structures; diffused resistors are present in some dielectric isolated circuits; and protective surface coatings occasionally are used in special purpose potting compounds or encapsulants, which might compromise the isolation. Component isolation in a dielectric isolated circuit, while much superior to that in a junction-isolated circuit, is still somewhat less complete than that in a discrete component circuit because of photocurrents through the dielectric.

A large number of integrated circuits have been irradiated, but the testing has been concentrated on specific microcircuit types, and a broad base of experimental data on the response of microcircuits to radiation is not available. This lack of data is especially true for linear circuits. Representative radiation failure levels for some common digital junction-isolated types are shown in Table 9-23. The levels are listed either in terms of gamma dose or of dose rate, depending upon whether the circuit is normally dose or dose rate dependent. Design and production changes in integrated circuits are common in the industry. The broad ranges given reflect highly variable experimental results and indicate the necessity of considering each circuit as a separate problem.

The proximity and intercoupling of elements do not assume importance in the production of permanent effects by nuclear radiation. Integrated circuits may be treated as conventional circuits of small dimensions. The primary factor that determines the tolerance of the circuits to radiation induced permanent effects is the degradation of the active elements with accumulated radiation exposure.

Changes in the electrical parameters of diodes and transistors that result from radiation have been discussed. Experiments have shown that the circuits will experience failure when the

Table 9-23. Representative Radiation-Failure Levels for Digital Junction-Isolated Semiconductor Integrated Circuits

Type†	Radiation-Failure Level
Large area, slow speed	5 - 20 rads (Si)
Large area, moderate speed	$10^6$ - $10^7$ rads (Si)/sec 20 - 60 rads (Si)
Small area, moderate or high speed	$10^7$ - $10^9$ rads (Si)/sec

Here, the "failure" level corresponds to exceeding the circuit's noise margin.

† Type designations defined as follows: Large area - chip area  $> 5,000$  mil<sup>2</sup>, Small area - chip area  $< 5,000$  mil<sup>2</sup>, Slow speed - propagation delay  $> 100$  nsec, Moderate speed - propagation delay between 25 and 100 nsec, High speed - propagation delay  $< 25$  nsec.

gain of the transistors has dropped to the point that they will no longer support proper circuit action. The radiation resistance of the circuits is determined by the stability of the gain of the transistor elements with respect to radiation exposure and the tolerance of the circuit design with respect to gain degradation. Although no class of integrated circuits has been shown to be inherently superior to another, those circuits employing faster transistors usually can withstand a greater neutron fluence. Epitaxial transistors usually, but not exclusively, represent the faster transistor types. Radiation failure levels have been shown to vary from  $10^{12}$  to  $10^{15}$  n/cm<sup>2</sup> ( $E > 10$  keV, fission), with the faster circuit types at the high end. The normally conservative design and digital function of most integrated circuits accounts for the circuit

longevity beyond what would be considered the minimum useful transistor gain point.

The radiation induced circuit response of microcircuits is manifested by changes in both the dc and switching characteristics. The effect on the integrated circuit parameters of changes in components after irradiation will, of course, depend on the specific circuit configuration involved. Frequently, the radiation sensitivity of the circuit is determined by the tolerance of the circuit design with respect to gain degradation.

The most radiation sensitive circuit parameter of digital gates and flip-flop circuits is the output low voltage. Circuit failures result when normally ON transistors leave saturation. The amount of current that an output transistor can sink is directly proportional to the current gain. The changes in the output transistor current gain are reflected directly in the current-drive capability (fan-out) of both digital gates and flip-flops.

Changes resulting from radiation are observed for other digital-circuit parameters. The saturation voltage of transistors,  $V_{SAT}$ , increases with neutron fluence, even though sufficient base drive is supplied to maintain the transistor in saturation, as a result of an increase in the saturation resistance. These changes in saturation resistance usually are negligible at threshold fluences applicable for maximum fan-out. The input threshold voltage of gate circuits normally will increase with radiation exposure as a result of changes in the base-emitter voltage of the output transistor and increased diode forward voltage. Changes in this parameter, however, are not considered significant. Increases in leakage currents also have been observed with radiation exposure, but the changes in this parameter usually will not affect circuit performance.

The switching characteristics of typical digital circuits also are affected by radiation.

The rise and fall times of the transistor elements of the microcircuit are increased and its storage time is decreased after neutron exposure. These effects combine, and usually a small net increase of switching time is observed.

A good estimate of the radiation tolerance (at different fan-out conditions) of digital circuits can be made by measuring the output current-voltage characteristics. The gain degradation can be calculated, and the degraded characteristics can be plotted with the measured characteristic. An example prediction with experimental results is shown in Figure 9-63 for the RD 308 flip-flop.\*

Failure in MOS logic circuits results from changes in the threshold voltage of the transistors caused by ionizing radiation. Since a large, negative supply voltage permits greater degradation in threshold voltage before circuit failure occurs, the radiation failure threshold of MOS circuits depends on the maximum supply voltage rating. Experiments indicate that MOS digital microcircuits fail at radiation levels from  $10^5$  to  $6 \times 10^7$  rads (Si) at manufacturer's rated supply voltages. Such an exposure can be associated with a neutron fluence of 1 to  $2 \times 10^{14}$  n/cm<sup>2</sup> ( $E > 10$  keV, fission) for the mixed neutron-gamma flux of a typical fast-burst reactor. The characteristics of a particular MOS integrated circuit must be established with reasonable confidence before meaningful predictions can be made.

As with digital circuits, the primary cause of linear-microcircuit failure is transistor gain degradation. The degradation of performance of a linear circuit is characterized by radiation induced changes in the transfer characteristics. In linear circuits, the functional dependence of the overall circuit performance on individual transistor elements can be determined only by a detailed circuit analysis. This analysis usually is frustrated by circuit complexity and the inability to measure individual

microcircuit elements as a result of the lack of accessible terminals. Therefore, prediction of the performance of linear circuits under irradiation is difficult. The large variety of linear circuits precludes a discussion of each type; however, some general comments can be made concerning the performance of some devices.

The radiation responses of both differential and operational amplifiers have been studied. A typical transfer characteristic of a differential amplifier is shown in Figure 9-64. The gain of the circuit began to decrease at a fluence of  $3 \times 10^{13}$  n/cm<sup>2</sup> ( $E > 10$  keV, fission) and was degraded to roughly 50 percent of its initial value after an order-of-magnitude-larger fluence. These amplifiers were found to maintain their balance during irradiation significantly better than amplifiers made from discrete devices.

The largest changes in operational amplifiers induced by radiation were observed in the open loop voltage gain and input bias current. The reduction in the open loop gain is a direct consequence of degradation of transistor gain. The use of lateral and substrate PNP transistors results in a relatively low radiation tolerance of these amplifiers compared to logic circuits. These PNP transistors are widebase units that are degraded at lower fluences than vertical NPN transistors. Changes in voltage gain begin to be observed (5 percent changes) at fluence levels near  $10^3$  n/cm<sup>2</sup> ( $E > 0.1$  MeV, fission) for 709-type operational amplifiers. The neutron fluence where the voltage gain has decreased by 50 percent is about  $8 \times 10^{13}$  n/cm<sup>2</sup> ( $E > 10$  keV, fission) for units with lateral and substrate transistors. Amplifiers that have eliminated lateral and substrate transistors show improved performance in the presence of radiation. The degradation in gain that is induced by radiation in operational amplifiers depends on the elec-

\* More details are given in the "TREE Handbook" (see bibliography).

Legend

- Load-terminal I-V characteristic, experimental
- - - Load-terminal I-V characteristic, predicted
- Load line at  $R_L = 360\Omega$

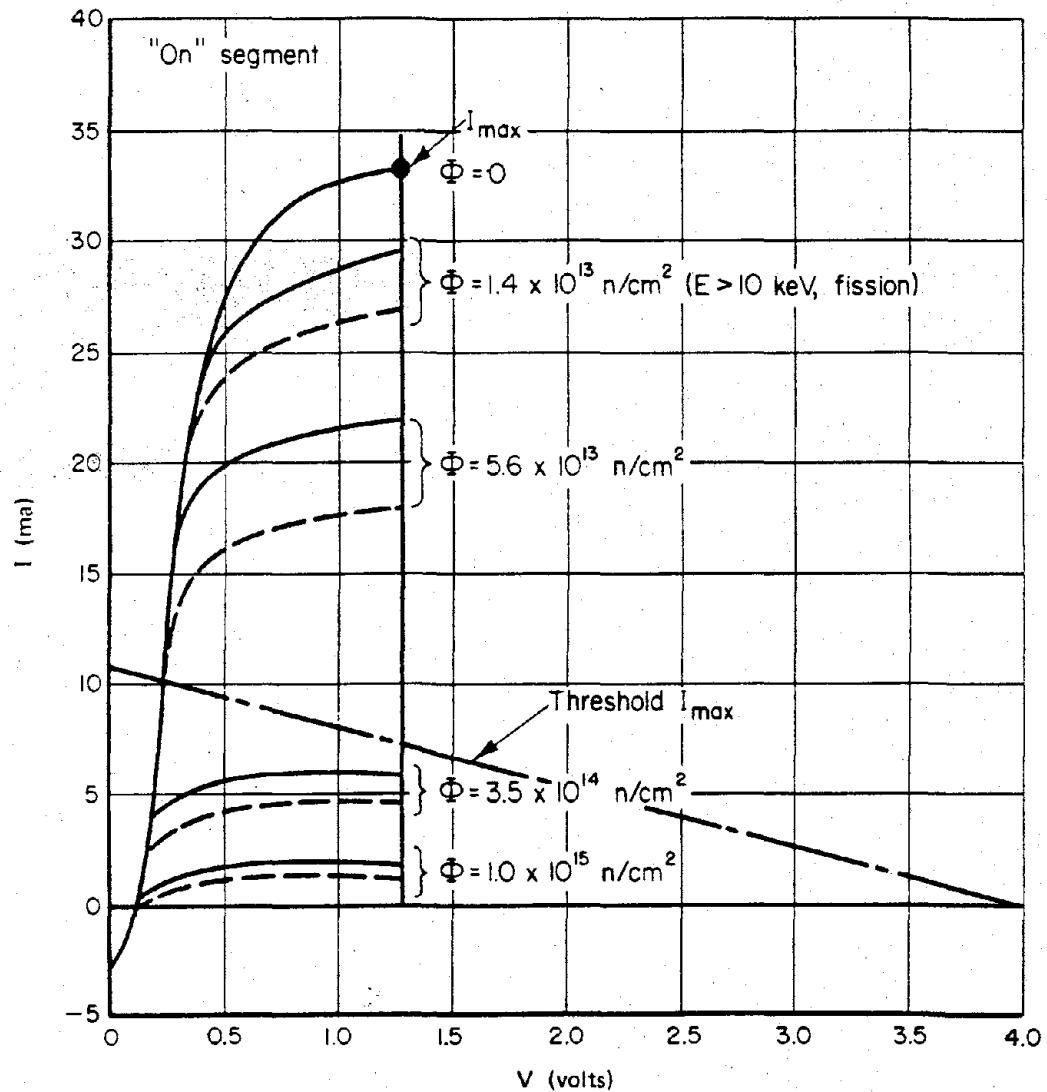


Figure 9-63. Load-Terminal I-V Characteristic ("On" Segment)  
of RD 308 in Neutron Environment

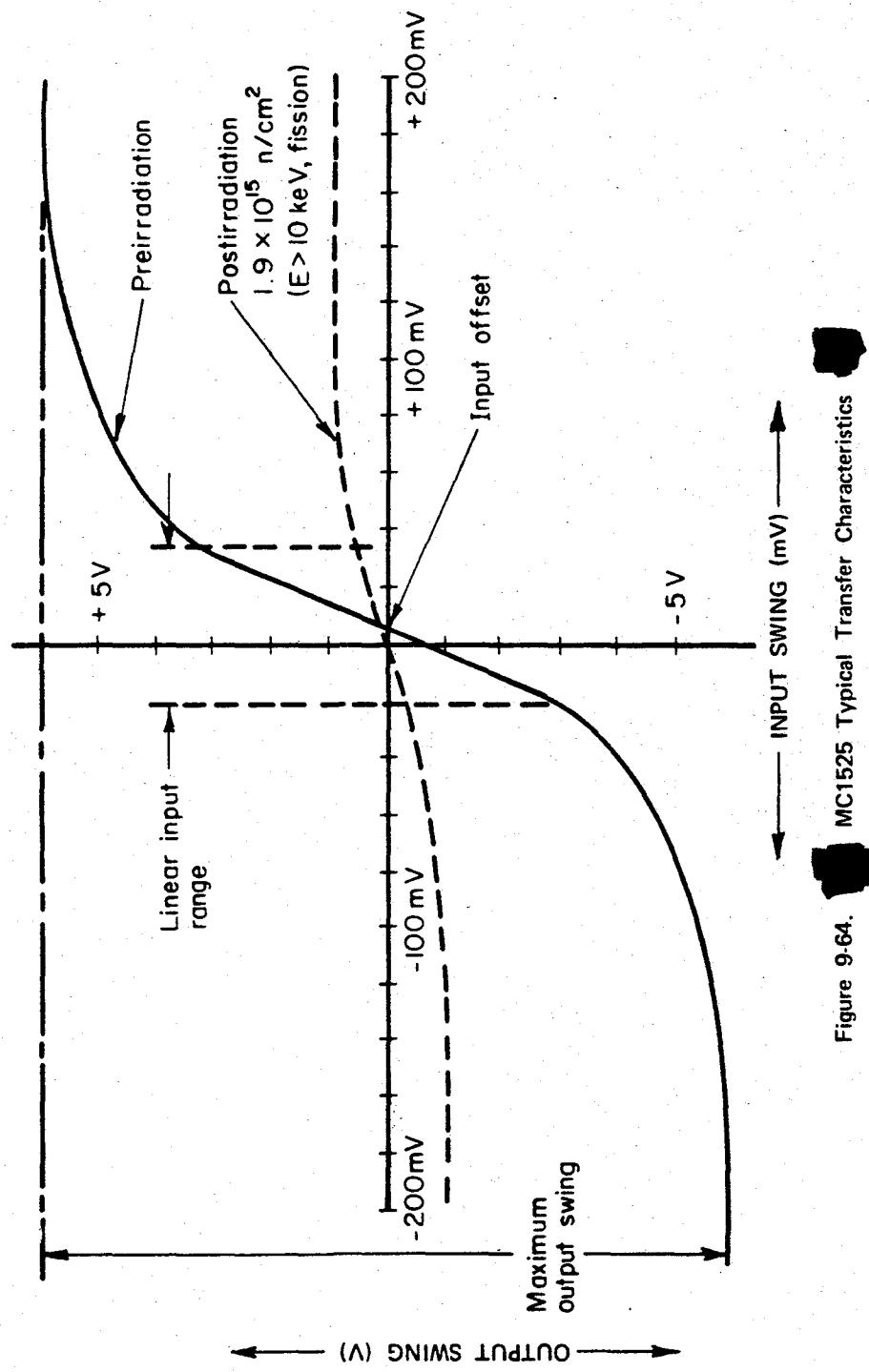


Figure 9-64. MC1525 Typical Transfer Characteristics

trical design. For example, it is important to determine whether the open-loop gain is determined by resistor ratios or by transistor gains. The changes in the input bias current can be correlated directly with changes in the common base current gain of the input transistors. It should be noted that the input transistors of operational amplifiers operate at very low currents (high input impedance), thus degradation of the base-transport factor is accompanied by degradation of the emitter efficiency as well. Factor-of-two increases in bias current have been observed for 709 amplifiers after  $3 \times 10^{13}$  n/cm<sup>2</sup> ( $E > 10$  keV, fission). Offset voltage and offset current were found to increase after irradiation. These changes result from emitter-base-voltage and current-gain mismatches after irradiation. The changes in both current and voltage offsets were small at fluences where the gain and the bias current were degraded appreci-

ably, which indicates the uniformity of active elements on the same chip.

Even though a large number of integrated microcircuits have been tested, data on the effects of neutron irradiation on microcircuits are still sparse. This is especially true for the linear types of integrated circuits. Radiation experiments indicate that the failure threshold of digital microcircuits is fairly independent of the construction technique. For buffered circuits the failure threshold, at unity fan-out, is near  $10^{15}$  n/cm<sup>2</sup> ( $E > 10$  keV, fission), while it is somewhat lower for the nonbuffered circuit types; however, the failure level at rated fan-out ( $\sim 10$ ) usually occurs over an order of magnitude lower in fluence than the failure level at unity fan-out. Representative radiation failure levels for some common digital microcircuits are shown in Table 9-24. The failure level is specified when the output voltage of the test circuit

Table 9-24. Failure Thresholds for Typical Digital Microcircuits

Designation	Function	Construction	Failure Level, (n/cm <sup>2</sup> )	
MC 201	DTL Gate	Junction Isolation	$1.5 \times 10^{15}$ *	$1.2 \times 10^{14}$ †
DT $\mu$ L 932	DTL Gate	Junction Isolation	$3.0 \times 10^{15}$	$1.5 \times 10^{14}$
RD 209	DTL Gate	Oxide Isolation	$3.0 \times 10^{15}$	$1.5 \times 10^{14}$
MC 507	TTL Gate	Junction Isolation	$0.8 \times 10^{15}$	$0.8 \times 10^{14}$
SN 54932	TTL Gate	Junction Isolation	$1.5 \times 10^{15}$	$1.2 \times 10^{14}$
DT $\mu$ L 945	DTL Flip-Flop	Junction Isolation	$1.5 \times 10^{15}$	$1.2 \times 10^{14}$
SE 124	DTL Flip-Flop	Junction Isolation	$0.85 \times 10^{15}$	$0.8 \times 10^{14}$
RD 208	DTL Flip-Flop	Oxide Isolation	$0.85 \times 10^{15}$	$0.8 \times 10^{14}$

\* Failure level at fan-out of 1; neutron fluence specified as ( $E > 10$  keV, fission).

† Failure level at fan-out of 10; neutron fluence specified as ( $E > 10$  keV, fission).

exceeds the noise margin of the following circuit. Typical radiation failure levels for some linear circuits are shown in Table 9-25. Table 9-26 contains irradiation test results for some representative MOS integrated circuits. The failure level is specified as the point when the circuit would not operate or when the threshold voltage exceeded the supply voltage.

The test results presented are only intended to provide a broad range of failure levels for order-of-magnitude reference purposes and

should be treated with appropriate caution. It should be borne in mind that design and production changes in integrated circuits are common in industry. For this reason, each circuit should be considered a separate problem.

The thermomechanical shock effects for all integrated circuit types are the same as those effects on discrete semiconductor parts. The only difference to consider is the increased number of bonds used in each device package, which increases the chance of bond failure.

Table 9-25. Failure Thresholds for Typical Linear Microcircuits

Designation	Function	Construction	Failure Level* (n/cm <sup>2</sup> )†
$\mu$ A 709	Operational Amplifier	Junction Isolation	$0.8 \times 10^{14}$
RA 909	Operational Amplifier	Oxide Isolation	$0.8 \times 10^{14}$
Ph 709	Operational Amplifier	Oxide Isolation	$3.0 \times 10^{14}$
MC 1709	Operational Amplifier	Oxide Isolation	$3.0 \times 10^{14}$
MC 1525	Differential Amplifier	Junction Isolation	$3.0 \times 10^{14}$
NM 1024	Differential Amplifier	Oxide Isolation	$3.0 \times 10^{14}$
NM 1006	Differential Amplifier	Junction Isolation	$4.0 \times 10^{14}$
RA 138	Amplifier	Oxide Isolation	$1.5 \times 10^{14}$

\* Failure level - gain degradation 50 percent.

† Neutron fluence specified as ( $E > 10$  keV, fission).

Table 9-26. Failure Thresholds for Typical MOS Digital Microcircuits

Designation	Function	Failure Level	
		Gamma, (rads (Si))	Neutron.* (n/cm <sup>2</sup> )
SC 1171	NAND gate	$2 \times 10^5$ †	—
MEM 529	Binary element	$1.4 \times 10^5$ ‡	—
SC 1171	Binary element	$1.1 \times 10^5$ ‡	—
MEM 501	Shift register	$1.1 \times 10^5$ §	—
MEM 590	Chopper	Not measured**	$3 \times 10^{14}$
SC 1149	Flip-Flop	Not measured**	$8 \times 10^{14}$
MC 1155	AND/OR gate	$2 \times 10^5$ (Cobalt-60)††	—
3300	25-bit static shift register	$>5 \times 10^3$ (FXR)‡‡ $>8 \times 10^4$ (TRIGA)‡‡	—
3003	100-bit shift register	$>2 \times 10^4$ (FXR)‡‡ $>5 \times 10^4$ (TRIGA)‡‡	—
1406	100-bit shift register	$>10^5$ (FXR)‡‡ $<2.5 \times 10^4$ (TRIGA)	—
1101	256-random access memory	$4 \times 10^4$ (FXR) $2 \times 10^4$ (TRIGA)	$3 \times 10^{11}$

\* Neutron fluence specified as ( $E > 10$  keV, fission).

† Supply voltage - 20 volts.

‡ Supply voltage - 15 volts.

§ Clock voltage - 10 volts.

\*\* Supply voltage - 10 volts.

†† Type of facility in which test was performed.

‡‡ No failures at these levels.

## SECTION VIII

### ELECTROMAGNETIC PULSE (EMP) DAMAGE MECHANISMS

As described in Chapter 7, the nuclear electromagnetic pulse (EMP) is part of a complex environment produced by a nuclear environment. The EMP contains only a very small part of the total energy produced by a nuclear explosion; however, under the proper circumstances, EMP is capable of causing severe disruption and sometimes damage to electrical and electronic systems at distances where all other effects are absent.

As with the EMP generation described in Chapter 7, the complexity of the calculation of EMP damage mechanisms requires that heavy reliance be placed on computer code calculations for specific problems, and even these calculations must be supplemented by testing in most cases. Consequently, the information presented herein is largely qualitative and will only serve as an introduction to the subject. More complete treatments of EMP damage mechanisms may be found in the "DNA EMP (Electromagnetic Pulse) Handbook" (see bibliography).

Figure 7-18, Chapter 7, provides a matrix that provides some indication of whether EMP constitutes a threat in a given situation relative to the hardness of a system to blast overpressure. This section provides a brief description of EMP energy coupling, component damage, EMP hardening, and testing.

#### ENERGY COUPLING

##### 9-56 Basic Coupling Modes

There are three basic modes of coupling the energy contained in an electromagnetic wave into the conductors that make up an electric or electronic system: electric induction, magnetic induction, and resistive coupling.

Electric induction arises as the charges in

a conductor move under the influence of the tangential component of an impinging electric field. The overall result is that of a voltage source distribution along the conductor. One such point-voltage source is shown in Figure 9-65 for a simple conducting wire, where the current  $I$  is produced as a result of the tangential component  $E_{i \tan}$  of the incident electric field  $\bar{E}_i$ .

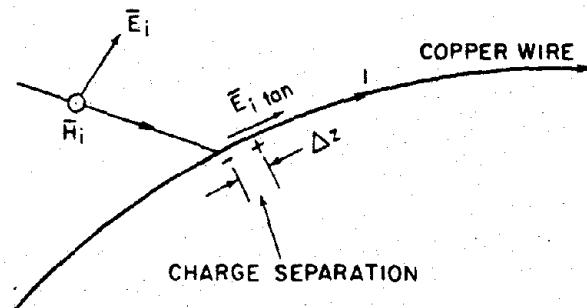


Figure 9-65. Electric Induction in a Copper Wire

Magnetic induction occurs in conductors shaped to form a closed loop when the component of the impinging magnetic field perpendicular to the plane of the loop varies in time, causing charges to flow in the loop. This effect is illustrated in Figure 9-66 for a simple wire loop. Here the magnetic field is shown coming out of the plane of the loop. The loop need not be circular, and magnetic induction may occur with any set of conducting components assembled so as to form a loop.

Resistive coupling comes about indirectly as a conductor that is immersed in a conducting medium, such as ionized air or the ground, is influenced by the currents induced in the medium by the other coupling modes. In effect the conductor shares part of the current as an alternate conducting path. This effect is illustrated in Figure 9-67 for the simple case of a

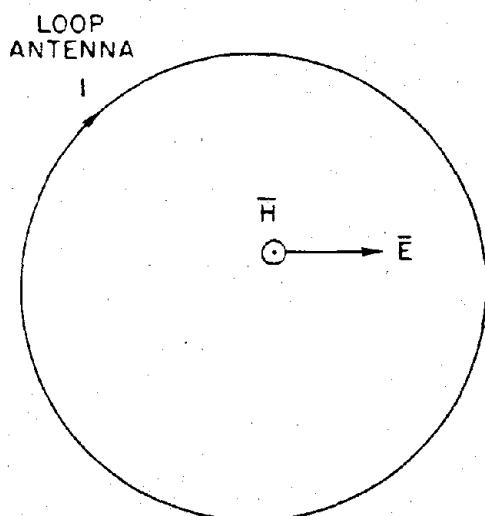


Figure 9-66. [REDACTED] Magnetic Induction in a Simple Loop [REDACTED]

conductor immersed in the ground. The tangential component of the incident electric field  $\bar{E}_i$  induces a current density  $J$  in the ground. A distributed voltage drop appears along the wire as a result of the current flow in the ground, and this incremental voltage causes current flow  $I$  in the wire. Current also may be induced in the wire directly by the tangential component of the refracted electric field, shown as  $\bar{E}_g$ . The reflected EMP,  $\bar{E}_r$ ,  $\bar{H}_r$ , is also shown in Figure 9-67. The potential importance of these reflected fields is discussed below.

### 9-57 Resonant Configurations [REDACTED]

[REDACTED] The coupling of energy to a conductor is particularly efficient when the maximum dimension of the conductor configuration is about the same size as the wavelength of the radiation. In this event the voltages that are induced along the conductor at various points are all approximately in phase, so the total voltage induced on the conductor is a maximum. The conductor is said to be resonant, or to behave as an antenna, for

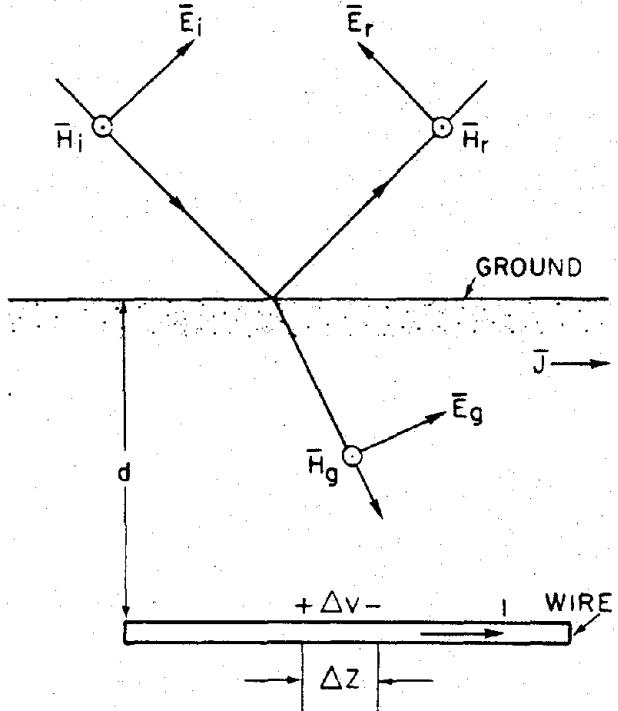


Figure 9-67. [REDACTED] Resistive Coupling as a Result of Currents in the Ground [REDACTED]

frequencies corresponding to near this wavelength. Since EMP has a broad spectrum of frequencies (see Chapter 7), only a portion of this spectrum will couple most efficiently into a specific conductor configuration. Thus, a particular system of interest must be examined with regard to its overall configuration as well as its component configuration. Each aspect will have characteristic dimensions that determine what part of the pulse (strength and frequencies) constitutes the principal threat.

[REDACTED] Gross system features that are not normally considered antennas, such as structural features, beams, girders, buried cable, overhead conduit or ducting, wings, fuselage, missile skins, and any wall apertures, must be considered to be potential collectors and conductors of energy into the system. In particular, radiation that

enters through an aperture is analogous to radiation that originates from a plate of the same size and shape as the aperture. Thus, it is resonant, and the aperture is resonant, and it admits a maximum of energy from the pulse for those frequencies near its resonance.

When the EMP strikes the ground, a portion of the pulse will be transmitted through the interface, inducing currents in the ground or any system components buried there, and a portion normally will be reflected as shown in Figure 9-68. Thus, a system that is above the ground will receive the reflected pulse as well as the direct pulse. These may cancel one another partially, but in the worst case they may reinforce and may constitute a greater threat level.

It can be seen that most practical systems in their operational environment present exceedingly complex coupling problems for an arbitrary explosion. The solution for any combination of system and environment is probably unique and will be very sensitive to even minor

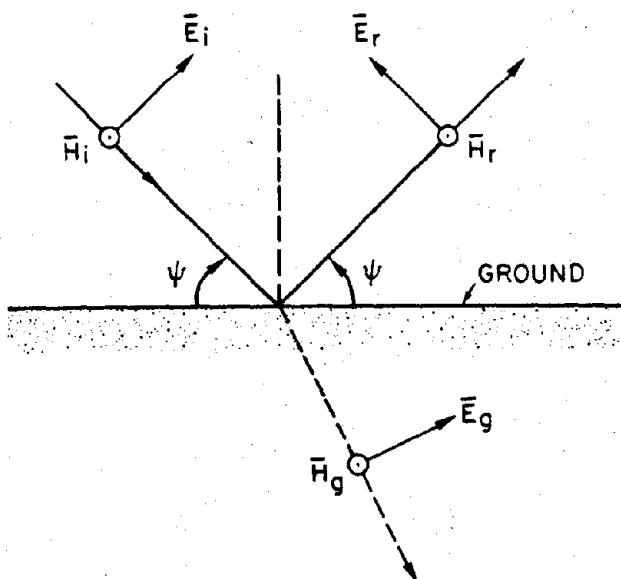


Figure 9-68. [REDACTED] Reflected and Refracted Waves at the Air-Ground Interface [REDACTED]

changes in the parameters. Two approximate approaches have been tried: computer studies as mentioned in Chapter 7, and threat simulation, which will be discussed in succeeding paragraphs.

## [REDACTED] COMPONENT DAMAGE [REDACTED]

### 9-58 Types of Damage [REDACTED]

[REDACTED] Degradation of system performance may occur as a result of functional damage or operational upset. A system will suffer damage if it is damaged permanently as a result of a large electrical transient. For example, a catastrophic failure of a device or component will render its operation unsatisfactory in any circuit. A parametric failure of a device occurs when degradation of some parameter has proceeded to a point where the circuit will continue to operate but at reduced efficiency. These latter failures are classed as functional damage. On the other hand, a system suffering operational upset is only impaired temporarily.

[REDACTED] Electronic components that are sensitive to functional damage or burnout are listed below in the order of decreasing sensitivity to damage effects:

microwave semiconductor diodes,  
field-effect transistors,  
radio-frequency transistors,  
audio transistors,  
silicon-controlled rectifiers,  
power rectifier semiconductor diodes,  
vacuum tubes.

Thus, on the basis of components alone, vacuum tubes are less susceptible to EMP damage effects than transistors.

[REDACTED] Electronic or electrical systems that are subject to malfunction include:

#### *Most susceptible:*

- Low power, high speed digital computer

- (upset) either transistorized or vacuum tube
- Systems employing transistors or semiconductor rectifiers (either silicon or selenium), such as
  - computers
  - computer power supplies
  - transistorized components terminating long cable runs, especially between sites
  - alarm systems
  - intercom systems
  - life-support system controls
  - some telephone equipment which is partially transistorized
  - transistorized receivers
  - transistorized transmitters
  - transistorized 60 to 400 cps converters
  - transistorized process control systems
  - power system controls; communication links

*Less susceptible:*

- Vacuum tube equipment (does not include high speed digital equipment and equipment with semiconductor or selenium rectifiers)
  - transmitters
  - receivers
  - alarm systems
- Equipment employing low current switches, relays, meters
  - alarms
  - life-support systems
  - power system control panels

- Hazardous equipment containing
  - detonators
  - squibs
  - pyrotechnical devices
- Other
  - Long power cable runs employing dielectric insulation, equipment associated with high energy storage capacitors or inductors

*Least susceptible:*

- High-voltage 60 cps equipment
  - transformers
  - motors
  - lamps, filament
  - heaters
- rotary converters
- heavy duty relays, circuit breakers
- air-insulated power cable runs

[REDACTED] The less susceptible equipment or components would be made more susceptible if they are connected to long exposed cable runs, such as intersite wiring or overhead exposed power or telephone cables. The equipment can be made less vulnerable if it is protected.

#### 9-59 Damage Levels [REDACTED]

[REDACTED] The nature of a circuit has a strong bearing on the transients that cause damage; however, in general pulse lengths of microsecond and submicrosecond duration are required to cause problems. Table 9-27 shows a list of common active devices and the approximate energy required to cause functional damage. The wide range of energies should be noted.

[REDACTED] The minimum energy required to damage meters or to ignite fuel vapors is about the same as that required to damage semiconductors as shown in Table 9-28. Good composition resistors can withstand pulse powers more than 10,000 times their power rating for micro-

Table 9-27. Minimum Observed Joule Energy to Cause Burnout

Type	Minimum Joule Energy	Material	Other Data
2N36	$4.0 \times 10^{-2}$	Ge	PNP Audio Transistor
2N327A	$1.6 \times 10^{-2}$	Si	PNP Audio Transistor
2N1041	$2.0 \times 10^{-2}$	Ge	PNP Audio Transistor
2N1308	$5.0 \times 10^{-5}$	Ge	NPN Switching Transistors
2N706	$6.0 \times 10^{-5}$	Si	NPN Switching Transistors
2N594	$6.0 \times 10^{-3}$	Ge	NPN Switching Transistors
2N398	$8.0 \times 10^{-4}$	Ge	PNP Switching Transistors
2N240	$1.0 \times 10^{-2}$	Ge	PNP Switching Transistors
MC715	$8.0 \times 10^{-5}$	Si	Data Input Gate Integrated Circuit
2N4220	$1.0 \times 10^{-5}$	Si	RF General Purpose FET
2N4224	$3.0 \times 10^{-5}$	Si	VHF Amp and Mixer FET
1N3659	$8.0 \times 10^{-3}$	Si	Automotive Rectifier Diode
1N277	$2.0 \times 10^{-5}$	Ge	High Speed Switching Diode
1N3720	$5.0 \times 10^{-4}$		Tunnel Diode
1N238	$1.0 \times 10^{-7}$	Si	Microwave Diode
2N3528	$3.0 \times 10^{-3}$	Si	Silicon Controlled Rectifier
67D-5010	$1.0 \times 10^{-4}$		G.E. Varistar (30-joule Rating)
6AF4	$1.0 \times 10^0$		UHF Oscillator Vacuum Tube
66N8	$2.0 \times 10^0$		General Purpose Triode Vacuum Tube

Table 9-28. [REDACTED] Minimum Joule Energy to Cause Permanent Degradation Indicated [REDACTED]

Designation	Minimum Joule Energy	Malfunction	Other Data
Relay	$2 \times 10^{-3}$	Welded Contact	Potter-Brumfield (539) low-current relay
Relay	$1 \times 10^{-1}$	Welded Contact	Sigma (IIF) one-ampere relay
Microammeter	$3 \times 10^{-3}$	Slammed Meter	Simpson Microammeter (Model 1212C)
Explosive Bolt	$6 \times 10^{-4}$	Ignition	EBW 8 amp for 10 $\mu$ sec detonator, MK1
Squib	$2 \times 10^{-5}$	Ignition	Electric Squib, N8 3.5 watts for 5 $\mu$ sec detonator
Fuel Vapors	$3 \times 10^{-3}$	Ignition	Propane-air mixture 1.75 mm ignition gap

[REDACTED] second pulses. Capacitors are also fairly hard components. The approximate energies required for degradation of several common components are shown in Table 9-28.

[REDACTED] The minimum energy necessary for operational upset is a factor of 10 to 100 less than that which is required to damage the most sensitive semiconductor component. Table 9-29 shows the levels required to cause operational upset to some common components to illustrate this factor.

[REDACTED] A gross comparison of the energy required to damage several classes of electrical equipment is provided in Figure 9-69.

[REDACTED] The large range of damage levels emphasizes the fact that it is important to consider EMP damage criteria early during the design stage of any piece of equipment that might be

susceptible. It is also important to realize that energy collected in one part of a system may be transmitted to other parts of the system as a result of the currents that are induced. Thus, it is not necessary that the EMP couple directly to a sensitive component; energy coupled to various parts of a system may ultimately reach a particular component in sufficient quantity to cause malfunction. With the current state of the art in EMP vulnerability evaluation, the design and hardening of complicated systems requires the joint efforts of systems engineers and professional EMP effects personnel.

### EMP HARDENING

#### 9-60 System Analysis

[REDACTED] A general approach to the examination

Table 9-29. [REDACTED] Minimum Joule Energy to Cause Circuit Upset or Interference [REDACTED]

Designation	Minimum Joule Energy	Malfunction	Other Data
Logic Card	$3 \times 10^{-9}$	Circuit Upset	Typical logic transistor inverter gate
Logic Card	$1 \times 10^{-9}$	Circuit Upset	Typical flip-flop transistor assembly
Integrated Circuit	$4 \times 10^{-10}$	Circuit Upset	Sylvania J-K flip-flop monolithic integrated circuit (SF50)
Memory Core	$2 \times 10^{-9}$	Core Erasure Via Wiring	Burroughs fast computer core memory (FC2001)
Memory Core	$5 \times 10^{-8}$	Core Erasure Via Wiring	Burroughs medium speed computer core memory (FC8001)
Memory Core	$3 \times 10^{-9}$	Core Erasure Via Wiring	RCA medium speed, core memory (269M1)
Memory Core	$2 \times 10^{-8}$		Minimum observable energy in a typical high-gain subsystem
Amplifier	$4 \times 10^{-21}$	Interference	Minimum observable energy in a typical high-gain amplifier

of a system with regard to its EMP vulnerability could include the following steps. First information concerning the system components and devices is collected. The information is categorized methodically into physical zones based on the susceptibility and worst case exposure for these items. Using objective criteria, problem areas are identified, analyzed, and tested. Suitable changes are made as necessary to correct deficiencies, and the modified system is examined and tested. The approach may be followed on proposed systems or those already in place, al-

though experience indicates that the cost of retrofitting EMP protection is usually overwhelming.

#### 9-61 Recommended Practices [REDACTED]

[REDACTED] Within the scope of this manual it is only possible to mention a few of the practices that may be employed in hardening a system to EMP. The following discussion is intended to convey some impression of the extra effort involved in hardening a system to the EMP rather than to provide a comprehensive treat-

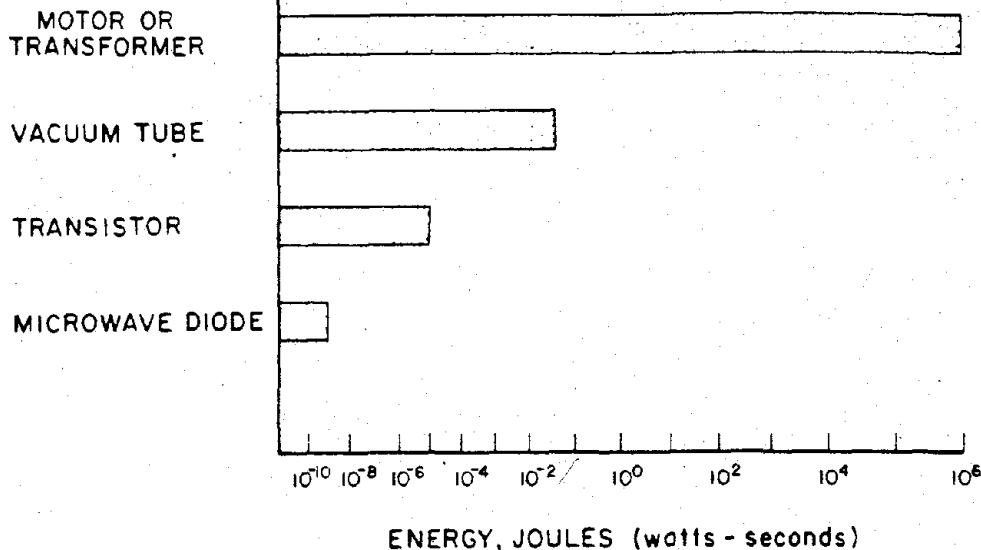


Figure 9-69. Energy Required to Damage Various Classes of Equipment

ment of what is a highly technical and specialized field.

Some general methods for reduction of the EMP environment include geometric arrangement of the equipment, shielding, geographic relocation, and proper grounding.

Circuit layout recommendations include the use of common ground points, twisted cable pairs, system and intrasystem wiring in "tree" format (radial spikes) avoiding loop layouts and circuit routes coupling to other circuits, use of conduit or cope trays, and shielded isolated transformers. Avoiding ground return in cable shields is also recommended. Many specific practices carry over from communications and power engineering while many do not. Each must be examined carefully.

Good shielding practices include the use of independent zone shields, several thin shields

to replace a thick one, continuous shield joints, and keeping sensitive equipment away from shield corners. Avoiding shield apertures, and avoiding the use of the shield as a ground or return conductor is also recommended. The shielding effectiveness of many enclosures frequently is defeated by energy carried by cables or pipes (including water pipes, sewage lines, etc.) into the enclosure.

Cabling recommendations include the use of deeply buried intersystem cables (more than 3 feet), shield layer continuity at splices, and good junction box contact. Ordinary braid shielding should be avoided. Cable design represents an extension of shielding and circuit practices from the viewpoint of EMP protection. It is an area where compromises frequently are made in the interests of economy, and thus is an area where professional EMP effects personnel can be

of considerable assistance.

Good grounding practices must be employed. In general, a "ground" is thought of as a part of a circuit that has a relatively low impedance to the local earth surface. A particular ground arrangement that satisfies such a definition may not be optimum, and may be worse than no ground from the EMP viewpoint. A ground can be identified as: the chassis of an electronic circuit, the "low" side of an antenna system, a common bus, or a metal rod driven into the earth. The last depends critically on local soil conditions, and it may result in resistive induced currents in the ground circuit. A good starting point is to provide a single point ground for a circuit cluster, usually at the lowest impedance element — the biggest piece of the system that is electrically immersed in the earth, e.g., the water supply system. It is beyond the scope of this manual even to list all of the grounding recommendations. Once again, this is an area where professional EMP effects personnel can be of considerable assistance.

Finally, various protective devices represent a means to counter other protective shortcomings indirectly. Filters, absorbers, limiters, decouplers, switching devices, arc arresters, fuses, etc., are part of this class of components. When other design practices cannot be used or are not adequate, such devices must be added. Typically they are found in an "EMP room" at the cable entrance to underground installations, in aircraft antenna feeds, in telephone lines, at power entry panels to shielded rooms, etc. On a smaller scale, diodes, nonlinear resistors, SCR clamps, and other such items are built into circuit boards or cabinet entry panels. Few of these devices by themselves are sufficient as a complete solution to a specific problem area, because each has some limitation in speed of response, voltage rating, power dissipation capacity or reset time. Thus, most protective devices are hybrids. A few prepackaged hybrids

are available for the protection of audio and power lines from lightning strokes and power surges and, if modified, may be used for EMP protection. No such packages are readily available for high frequency lines, multiple wire cables, antennas, etc., and usually must be custom designed for each application.

## TESTING

### 9-62 Importance of Testing

Even with present day sophistication in analytic techniques, it is clear from the complexities described above that sole reliance cannot be placed in analysis and prediction alone. Testing has a number of important functions.

Testing is essential to verify prior analysis of devices, components, and complete systems early in the design stage. Testing also is the only known method that can be used to identify surprises. Surprises can be unexpected coupling or interaction modes or weaknesses that were overlooked during the design. Nonlinear effects in interaction are a form of surprise that only can be found by testing. After the test, many of the original approximations made in analysis can be refined and improved for future analysis, and the data can improve the analytic capability for more complex problems.

Testing quickly locates weak or susceptible points in components or systems early enough for economic improvement. After the improvements, testing quickly verifies that the improvements bring the performance up to standards.

Testing provides assurance and confidence that the complete system is actually hardened to EMP to the specified threat level. Actual certification can only be obtained by providing the actual nuclear threat environment. Further, periodic testing insures that system hardness is not degraded as a result of environmental or human factors.

## 9-63 Simulation Facilities

[REDACTED] As a result of the limited test ban treaty, heavy reliance must be placed on simulation to test the EMP hardness of systems. A brief description of generic simulation techniques is given below. A more thorough description of these techniques is contained in the "DNA EMP (Electromagnetic Pulse) Handbook, Volume 2, Analysis and Testing" (see bibliography).

[REDACTED] The classes of EMP tests are:

- Low level current mapping.
- High level current mapping.
- High level fields.

Low level current mapping is a good test for the beginning of any program. With the system power turned off and a low-level field, the magnitudes and signatures on internal cables are determined. This provides an insight on the work that must follow. After this test and the indicated improvements are made, a high-level current can be injected directly into the system with the system power on to explore for nonlinearities, and to uncover initial indications of system effects. If subsystems malfunction, it may be desirable to conduct extensive subsystem tests in the laboratory. Finally, a high level field test is essential.

[REDACTED] The type of excitation must be defined in any type of test. The two principle choices are:

- Waveform simulations (time-domain data),
- Continuous wave signals (frequency-domain data).

If the intent is to match a system analysis in the frequency domain to measured system response, continuous wave (CW) signals may be more suitable. If the desire is to compare the test results to known electronic thresholds, it is frequently necessary to test in the time domain. For a complete analysis, it is advisable to consider both types of tests.

[REDACTED] Large-scale simulators are required for

the final test of large systems. The two principal kinds of large simulators are:

- Metallic structures that guide an EM wave past a test object,
- Antennas that radiate an EM field to a test object.

Guided wave simulators use pulse generators that simulate EMP waveforms and operate in the time domain. Radiating antennas use either pulse generators (time domain) or continuous wave (CW) signal generators (frequency domain). Pulse generators themselves can be either high level single shot or low level repetitive.

(U) The essential elements of a guided wave or transmission line simulator include:

- Pulser
- Transition section
- Working volume
- Termination.

An electromagnetic wave of suitable amplitude and waveshape is generated by the pulser. This wave is guided by a tapered section of transmission line (the transition section) from the small cross sectional dimension of the pulser output to the working volume. The working volume, where the test object is located, should be large enough to provide a certain degree of field uniformity over the test object. A test object dimension one-fifth that of the working volume satisfies this condition. The termination region prevents the reflection of the guided wave back into the test volume, and consists of a transition section that guides the incident wave to a geometrically small resistive load whose impedance is equal to the characteristic impedance of the transmission line structure.

[REDACTED] The basic types of radiating simulators are:

- Long wire
- Biconic dipole or conical monopole.

The long wire is usually a long dipole oriented

parallel to the earth's surface. It is supported above the ground by nonconducting poles with high-voltage insulators. The two arms of the dipole are symmetric about the center and constructed from sections of light weight cylindrical conductor, such as irrigation pipe. Pipe sections decrease in diameter with increasing distance from the center, and resistors are placed between the pipe sections to shape the current wave and reduce resonances. The two arms of the dipole are oppositely charged, and when the voltage across the spark gap at the dipole center reaches the breakdown voltage, the gap begins conducting and a current wave front propagates away from the gap.

Conical and biconical antennas use pulsers, such as Marx generators, or CW transmitters instead of relying on the discharge of static surface charges. The antennas are fabricated out of lightweight conducting surfaces or wire grids.

Differences between guided wave and radiating simulators are listed in Table 9-30.

Electromagnetic scale modeling is an important alternative to full scale testing under the following conditions:

- Test facilities or available equipment are at a premium,
- The system to be tested is very large,
- The system dedication cost for full scale testing is high.

In addition to the advantages of modeling under these conditions, benefits can be derived as follows:

- Perhaps sensors can be placed better during full scale testing as a result of model experiments,
- Design modifications or cable reroutes can be made prior to full scale testing,
- EM angles-of-arrival can be determined for worst- and best-case conditions,
- Effects of changes in the conductivity of

the surrounding media can be explored to an extent,

- Estimates can be made of some of the responses of a complex system prior to full scale testing,
- Design confirmation of costly systems can be made prior to system fabrication and costs can be reduced,
- Quantitative data can be obtained to validate analysis.

It should be pointed out that because of the difficulty in introducing minute openings or poor bonds into models, and since these often control interior fields, the usefulness of modeling ordinarily is limited to the measurement of external fields, voltages, and currents. Once the exterior fields, voltages, and currents are known for a complex structure, perhaps having cable runs, analysis can often provide internal field quantities of interest.

In actually setting up a scale model test, the following should be kept in mind:

- Broadband pulse response determination involves much more than a steady-state, single-frequency response test does.
- Special EM illumination sources that are coherent, have uniform time delay, and use antennas with constant effective height are required.
- Special modeling techniques are required to study exposed conductors that pass over or within a lossy dielectric, such as earth.

A pulse-type waveform theoretically can be replaced by a continuous wave (CW) source with a sensing system which references the sensed CW signal to a reference phase from the source. Complex Fourier transfer functions can be developed by processing the recorded data on a computer. However, long sweep times are required to ensure that all narrow band responses are explored adequately, and the actual physical implementation of such an approach in the

Table 9-30. Comparison of Guided Wave and Radiating Simulators

	Guided Wave	Radiating
Energy use	Efficient — mostly directed toward test object	Energy radiated symmetrically about axis — only fraction directed toward test object
Test volume	Limited by size of simulator — difficult to construct large enough for sizable test objects	Limited by desired field intensity
Polarization	Fixed (or bipolar, e.g., ARES)	Variable*
Angle of incidence	Fixed†	Variable*
Earth reflection effects	No	Yes
Geometric attenuation of EM wave amplitude	No — relatively uniform within test volume	Yes (1/R)
Planar wave capability	Yes	Only at distance
Interference with nearby electronics	Limited	Yes

\* These are, however, limited by the height of the antenna unless it is airborne.

† Polarization is fixed relative to earth coordinates; however, a range of polarizations and angles of incidence can be provided in some facilities by changing the position and orientation of the object that is being tested. For example, a missile can be rotated on several axes in ARES to change these to items relative to the missile.

[REDACTED]

microwave band poses additional difficulties. On the other hand, the use of scaled real time waveforms allows quick development of actual responses, from which complex Fourier transfer functions also can be developed with the aid of computers.

[REDACTED] Several variations of each type of simulation technique described above are currently

operational. Each has some advantages and disadvantages when compared to others. As mentioned previously, it is beyond the scope of this manual to describe individual facilities. The interested user should consult the "DNA EMP (Electromagnetic Pulse) Handbook, Volume 2, Analysis and Testing," (see bibliography), and the references listed therein.

[REDACTED] BIBLIOGRAPHY [REDACTED]

Abbott, L. S., H. C. Claiborne, and C. E. Clifford, Eds., *Weapons Radiation Shielding Handbook*, DASA 1892-1, through 1892-6, Oak Ridge National Laboratory, Oak Ridge, Tennessee, December 1966 through March 1972 (Vols. I, II, III, V, Vol. VI, Vol. IV)

Barash, R. M., and J. A. Goertner, *Refraction of Underwater Explosion Shock Waves: Pressure Histories Measured at Caustics in a Flooded Quarry*, NOLTR-67-9, U.S. Naval Ordnance Laboratory, White Oak, Silver Spring, Maryland, 19 April 1967

Batter, J. F., *Transient Effects of a Time Varying Thermal Pulse*, Part II, AFSWP1058, TOI Report No. 58-7, Technical Operations Incorporated, Burlington, Massachusetts, March 1958

Bell, J. F., *Single Temperature-Dependent Stress-Strain Law for Dynamic Plastic Deformation of Annealed Face-Centered Cubic Metals*, Journal of Applied Physics, Vol. 34, No. 1, January 1963

Bergman, P., and N. Griff, *A Method for Evaluation of the Response of Coatings to Thermal Radiation from a Nuclear Weapon*, Naval Applied Science Laboratory Project 940-105, Progress Report 9, November 12, 1968

Bergman, P., et al., *Temperature Response Charts for Opaque Plates Exposed to the Thermal Radiation Pulse from a Nuclear Detonation*, Naval Applied Science Laboratory Project 940-105, Progress Report 10, July 10, 1969

Bethe, H. A., and W. L. Bade, *Theory of X-Ray Effects of High Altitude Nuclear Bursts and Proposed Vehicle Hardening Method*, RAD-TR-9(7)-60-2, AVCO Corporation, Wilmington, Massachusetts, 8 April 1960

Bothell, L. E., *PUFF IV-EP Code Comparisons to Test Results*, KN-664-67-2, Kaman Nuclear, Colorado Springs, Colorado, 16 January 1967

Bothell, L. E., and C. E. Archuleta, *PUFF V-EP Code*, Parts I and II, KN-703-67-101(R), Kaman Nuclear, Colorado Springs, Colorado, December 1967 (Part I, Part II)

Bridges, J. E., *DNA EMP Awareness Course Notes*, DNA 2772T, Illinois Institute of Technology Research Institute, Chicago, Illinois, August 1971

Chandler, C. C., et al., *Prediction of Fire Spread Following Nuclear Explosions*, U.S. Forest Service Research Paper PSW-5, Pacific Southwest Forest and Range Experiment Station, Berkeley, California, 1963

Clarke, T. C., *Interaction Study, Vol. IV, Structural Degradation by Short Time Heating*,  
AFWL TR-70-157, Boeing Company, Seattle, Washington, December 1970

Cohen, M. L., *A Numerical Technique to Determine the Thermal Histories of Two-Dimensional Solids in the Nuclear Environments*, Naval Applied Science Laboratory Project 940-105, Progress Report 5, June 1958

Cole, R. H., *Underwater Explosions*, Dover Publications, Inc., New York, N.Y., 1965

Davis, G. T., et al., *Project TROIKA, Re-Entry Vehicle Vulnerability Assessment for Advanced Planning for Underground Tests*, DASA 2230, AVCO Corporation, Wilmington, Massachusetts, January 1969

Derkesen, W. L., *Ship Vulnerability to Nuclear Attack-Thermal Radiation Effects*, Technical Briefing to the Chief of Naval Material, 2 March 1967.

DNA EMP (Electromagnetic Pulse) Handbook, DNA 2114H1-2114H4, DASIAC, General Electric TEMPO, Santa Barbara, California, Volume 1, Design Principles, November 1971, Volume 2, Analysis and Testing, November 1971, Volume 3, Environment and Applications, to be distributed during early calendar year 1973, Volume 4, Resources, November 1971 (Volumes 1, 2, and 4, Volume 3,

*Electromagnetic Pulse Sensor and Simulation Notes, Volumes 1-10*, AFWL EMP 1-1 through EMP 1-10, Air Force Weapons Laboratory, Kirtland Air Force Laboratory, New Mexico, April 1967 through 1972

Goodwin, L. K., et al., *An Equation of State for Metals*, DASA 2286, Aeroneutronics Division of Philco-Ford, Newport Beach, California, April 1969

Hall, W. J., and N. M. Newmark, *Interpretation of Event Pile Driver Tunnel Liner Results*, DASA 2374, University of Illinois, Urbana, Illinois, February 1970

Hall, W. J., and N. M. Newmark, *Supplemental Studies of Event Pile Driver Backpacked Tunnel Liner Results*, DASA 2374-1, University of Illinois, Urbana, Illinois, October 1970

Harrison, G., *A Plan for the Development and Evaluation of an Advanced Re-Entry Vehicle*, DASA 2208-I, General Electric Corporation, Philadelphia, Pennsylvania, June 1969

Hillendahl, R. W., *Theoretical Models for Nuclear Fireball*, DASA 1589-1 through 1589-39, Lockheed Missiles and Space Company, Sunnyvale, California, 1965-68

Julian, A., and C. E. Eves, *Thermal Effects on Strength of Aircraft Structural Sandwich-Type Panels*, WT 1341, Project 8.4, Operation REDWING, Cook Research Laboratories, Skokie, Illinois, 30 April 1958 [REDACTED]

Julian, A. N., *In-Flight Structural Response of FJ-4 Aircraft to Nuclear Detonations*, WT 1432, Project 5.3, Operation PLUMBOB, Bureau of Aeronautics, Washington, D.C., 10 February 1960 [REDACTED]

Kalinowski, J. J., *A Management Guide to Transient-Radiation Effects on Electronics (TREE)* [REDACTED] DNA 2051H, Battelle's Columbus Laboratories, Columbus, Ohio, February 1972 [REDACTED]

Kaplan, K., and C. Wiegle, *Air Blast Loading in the High Shock Strength Region* [REDACTED] Part II, Prediction Methods and Examples, URS 633-3, DASA 1460-1, URS Corporation, Burlingame, California, February 1965 [REDACTED]

Kaufmann, R., and R. J. Heilferty, *Equations and Computer Program to Calculate the Temperature Distribution and History in a Cylinder Subject to Thermal Radiation from a Nuclear Weapon*, NASL Project 940-105, PR-8, U.S. Naval Applied Science Laboratory, Brooklyn, New York, 18 July 1968 [REDACTED]

Kaufmann, R., and R. J. Heilferty, *Equations and Computer Program to Calculate the Temperature Distribution and History in a Tee Beam Subject to Thermal Radiation from a Nuclear Weapon*, NASL Project 940-105, PR-6, U.S. Naval Applied Science Laboratory, Brooklyn, New York, 20 February 1968 [REDACTED]

Larin, F., *Radiation Effects in Semiconductor Devices*, John Wiley and Sons, Inc., New York, 1968 [REDACTED]

Martin, S. B., and S. Holton, *Preliminary Computer Program for Estimating Primary Ignition Ranges for Nuclear Weapons*, USNRDL-TR-866, U.S. Naval Radiological Defense Laboratory, San Francisco, California, 3 June 1965 [REDACTED]

Melin, J. W., and S. Sutcliff, *Development of Procedures for Rapid Computation of Dynamic Structural Response*, University of Illinois Final Report on Contract AF33(600)-24994 for Physical Vulnerability Division of Intelligence, USAF [REDACTED]

Moon, D. P., and W. F. Simmons, *Methods for Conducting Short-Time Tensile, Creep, and Creep-Rupture Tests under Conditions of Rapid Heating*, Defense Metals Information Center Report 121, December 28, 1959 [REDACTED]

Moon, D. P., and W. F. Simmons, *Selected Short-Time Tensile and Creep Data Obtained under Conditions of Rapid Heating*, Defense Metals Information Report 130, June 17, 1960 [REDACTED]

Morris, P. J., *Proposed Addition to Chapter 7, DASA EM-1, Section 7.6, Thermal Radiation Degradation of Structural Resistance to Air Blast*, URS 7029-6, URS Research Company, San Mateo, California, December 1971 [REDACTED]

Newmark, N. M., et al., *Analysis of Design of Flexible Underground Structures*, DA-22-079-eng-255, University of Illinois; Urbana, Illinois, 31 October 1962 [REDACTED]

Newmark, N. M., *An Engineering Approach to Blast Resistant Design*, Paper No. 2786, Transactions, ASCF, 121, 45-64, 1956 [REDACTED]

*Nuclear Weapons Blast Phenomena*, DASA 1200-I, -II, -III, -IV, Defense Atomic Support Agency, Washington, D.C., Vol. I, March 1971, Vol. II, December 1970, Vol. III, March 1970, Vol. IV to be issued during calendar year 1972 (Vol. I, [REDACTED] Vol. II, [REDACTED] Vol. III, [REDACTED])

Old, C. C., et al., *TROIKA Study Final Report*, DASA 2191-I, -II, -III, and -IV, Lockheed Missiles and Space Company, Sunnyvale, California, August 1968 (Vols. I and II, [REDACTED] Vols. III and IV, [REDACTED])

Reaugh, J., *Equation-of-State Evaluation Predix Topical Report*, PITR-239-1, DASA 2596, Physics International Co., San Leandro, California, April 1972 [REDACTED]

Seaman, L., et al., *Dynamic Fracture Criteria of Homogeneous Materials*, AFWL-TR-71-156, Stanford Research Institute, Menlo Park, California, February 1972 [REDACTED]

Seaman, L., *Spall and Fracture Phenomena in the Response of Materials to Nuclear Effects*, Third Annual Meeting of Nuclear Survivability Working Group on Propulsion and Ordnance, Stanford Research Institute, Menlo Park, California, 29-30 August 1971 [REDACTED]

Shelton, F., *Nuclear Weapons as X-Ray Sources, the Environments They Produce, and Some Effects on Aerospace Systems*, Volume II, *Some Effects on Aerospace Systems*, DASA 2397-2, KN-770-69-30, Kaman Nuclear, Colorado Springs, Colorado, September 1969 [REDACTED]

Snay, H. G., *Underwater Explosion Phenomena: The Parameters of Migrating Bubbles*, NAVORD Report 4185, U.S. Naval Ordnance Laboratory, White Oak, Silver Spring, Maryland, 12 October 1962 [REDACTED]

Snay, H. G., *Hydrodynamic Concepts Selected Topics for Underwater Nuclear Explosions*, NOLTR 65-52, DASA 1240-1(2), U.S. Naval Ordnance Laboratory, White Oak, Silver Spring, Maryland, 15 September 1966 [REDACTED]

Staff of Kaman Avidyne, *Handbook for Analysis of Nuclear Weapon Effects on Aircraft*  
KA-TR-50A, DASA-2048, Kaman Avidyne, Burlington, Massachusetts, April 1970  
[REDACTED]

Staff of Kaman Avidyne, *Handbook of Computer Programs for Analysis of Nuclear Weapon Effects on Aircraft* [REDACTED] KA-TR-50S, DASA-2048S, Kaman Avidyne, Burlington, Massachusetts, April 1970 [REDACTED]

Timoshenko, S., and S. Woinowsky-Krieger, *Theory of Plates and Shells*, McGraw-Hill Book Company, 1959 [REDACTED]

TREE (*Transient-Radiation Effects on Electronics*) Handbook [REDACTED] DNA 1420H-1, Vol. 1, Edition 3, Battelle's Columbus Laboratories, Columbus, Ohio, December 1971 [REDACTED]

TREE (*Transient-Radiation Effects on Electronics*) Handbook [REDACTED]  
DASA 1420-1, Edition 2, Revision 2, Battelle Memorial Institute, Columbus, Ohio, September 1970 [REDACTED] (to be replaced by DNA 1420H-2 during early calendar year 1973).

TREE Preferred Procedures (*Selected Electronic Parts*), DNA-2028H, Battelle's Columbus Laboratories, Columbus, Ohio, June 1972 [REDACTED]

TREE Simulation Facilities, DASA 2432, Edition 1, Battelle Memorial Institute, Columbus, Ohio, September 1970 [REDACTED]

Veigle, W. J., et al., *X-Ray Cross Section Compilation from 0.1 keV to 1 MeV*, DNA 2433F Vols. 1 and 2, Revision 1, KN-71-431(R), Kaman Nuclear, Colorado Springs, Colorado, 31 July 1971 [REDACTED]

Whitaker, W. A., and R. A. Deliberis, *Aircraft Thermal Vulnerability to Large High-Altitude Detonations* [REDACTED] AFWL-TR 67-85, Air Force Weapons Laboratory, Kirtland Air Force Base, New Mexico, August 1967 [REDACTED]

Whitener, J. E., *Deflection of Ballistic Missiles by Nuclear Weapons* [REDACTED] RM-2345, RAND Corporation, Santa Monica, California, April 1959 [REDACTED]

## Chapter 10

# PERSONNEL CASUALTIES

### INTRODUCTION

The three principal phenomena associated with nuclear explosions that result in casualties to personnel are blast and shock, thermal radiation, and nuclear radiation. Blast injuries may be direct or indirect; the former are caused by the high air pressure (overpressure), while the latter may be caused by missiles or by displacement of the body.

The frequency of burn injuries resulting from a nuclear explosion is exceptionally high. Most of these are flash burns caused by direct exposure to the thermal radiation, although personnel trapped by spreading fires may be subjected to flame burns. In addition, personnel in buildings or tunnels close to ground zero may be burned by hot gases and dust entering the structure even though they are shielded adequately from direct or scattered radiation.

The harmful effects of the nuclear radiations appear to be caused by ionization and excitation (see paragraph 6-4, Chapter 6) produced in the cells composing living tissue. As a result of ionization, some of the constituents, which are essential to the normal functioning of the cells, are altered or destroyed. As described in Section III, these changes may result in sickness that may terminate with death in some cases.

The effects of these three phenomena on personnel are described in the succeeding three sections. A brief discussion of the effects of combinations of the phenomena is provided in Section IV.

### SECTION I

#### AIR BLAST

#### MECHANISMS AND CRITERIA FOR INJURY

Injury that results from exposure of per-

sonnel to air blast may occur from sudden changes in environmental pressure acting directly on the exposed subject, from displacement of personnel involving decelerative tumbling or impact against a rigid object, from blast-energized debris striking the individual, and from a variety of miscellaneous changes in the immediate environment. Individuals who are injured to such an extent that they are unable to perform assigned tasks are designated casualties. Such a condition typically starts almost immediately following air-blast trauma and it can be expected to last from hours to several days, depending on the nature and severity of the injury. The biological effects which may result from exposure to a blast wave are divided into four categories: (1) direct overpressure effects, (2) effects from translational forces and impact, (3) effects of blast energized debris, and (4) miscellaneous effects. These effects are discussed separately in the following paragraphs.

#### 10-1 Direct Overpressure Effects

Casualties that result from direct overpressure effects are those that result from man's inability to withstand rapid changes in his environmental pressure. The body is relatively resistant to the crushing forces from air blast loading; however, large sudden pressure differences resulting from blast wave overpressure may cause serious injury. Anatomic localization of such injury occurs predominantly in air-bearing organ systems such as the lungs, gastroenteric tract, ears and perinasal sinuses. At high overpressures both early (less than 30 minutes) and delayed (30 minutes to several days) lethality will occur as a result of disruption of lung tissue. Early lethality is generally caused by interruption in the blood supply to the heart or brain as a result of air emboli entering the circulatory system.

from the damaged lung. Delayed lethality occurs as a result of suffocation caused by continuing hemorrhage within the lung or the development of pulmonary edema. Delayed appearance of casualties also may occur at high overpressures as a result of internal hemorrhage from ruptured organs or as a result of infection due to perforation of the intestine.

Experiments conducted with animals indicate that direct overpressure effects depend upon the peak overpressure, duration and shape of the incident blast wave, and the orientation of the subject. Both the peak overpressure and the duration appear to be important for fast-rising blast waves that have durations less than 50 msec, whereas peak overpressure predominates for positive phase air-blast durations greater than 50 msec. If the time to peak overpressure is greater than a few milliseconds, there is a lower probability of injury because the anatomic structures will be subjected to pressure differences that occur less rapidly. This effect can take place in a structure where the pressure rises gradually due to a long fill time or it may occur near a reflecting surface where the pressure rises in "steps" as a result of a separation in the arrival times of the incident and reflected waves. In general, personnel who are oriented with the feet or head toward the oncoming blast wave will be injured less than those who are oriented with the long axis perpendicular to the blast wave. This is apparently caused by the action of the dynamic pressure to increase the load on the thorax in the latter case. A potentially more hazardous exposure condition occurs when personnel are situated against a flat surface, since normal reflection of a blast wave results in pressures two or more times the magnitude of the incident wave.

Current criteria for direct overpressure effects, based on extrapolations from animal data, predict 50-percent casualties and one percent mortality for randomly oriented, prone personnel exposed to a long-duration fast-rising

blast wave of 41 psi and one percent casualties for those exposed to 12 psi. Animal experiments and human accident cases have shown that a 50-percent incidence of eardrum rupture may be expected to occur at 16 psi, whereas one percent might be anticipated at 3.4 psi. Although in certain situations auditory acuity is imperative, eardrum rupture currently is not considered to be a disabling injury in terms of overall effectiveness to individuals in military units.

## 10-2 Translational Forces and Impact

Injuries caused by translational impact occur as a result of whole body displacement of personnel by blast winds. Anatomic localization of such injuries is not as readily definable as the case for direct overpressure effects. In instances where head impact occurs, concussion, skull fractures, and intracranial hemorrhage may result in rapid loss of consciousness and, in many cases, early lethality. By contrast, impact in which the head is not involved results in a variety of traumatic injuries such as skeletal fractures, ruptured internal organs, blood loss and, in more serious cases, the development of shock. Recovery following such injuries may be more delayed than recovery from direct overpressure effects.

The translational and rotational velocities that are attained by personnel during the accelerative phase of blast-induced displacement depend upon the geometry of exposure and the shape and magnitude of the dynamic-pressure wave. In general, a longer duration of the positive phase of the blast wave will result in a lower peak overpressure being required to produce a given translational velocity. Therefore, larger yields will produce injuries at lower pressures (see Section I, Chapter 2). The severity of the injuries caused by displacement depends to a large extent on the nature of the decelerative phase of the motion. If deceleration occurs by an "impact" with a rigid object, resulting in a stopping distance of less than a few inches, the



UNARMED UNARMED

[REDACTED]  
probability of a serious injury is much greater than if deceleration occurs by "tumbling" over open terrain, which will result in much longer stopping distances.

[REDACTED] Because of the limited data available, casualty criteria for translational impact are far less certain than those for direct overpressure effects. In addition, there are marked differences in impact velocities that are associated with serious injury following head trauma compared with those for noncranial impact. Human cadaver studies indicate that 50 percent mortality may occur following head impact at velocities of 18 ft/sec, whereas large animal studies and human free-fall experience suggest that 54 ft/sec is required for 50 percent mortality when head impact is minimized. Decelerative tumbling experiments involving a limited number of animals suggest that significant mortality does not occur at translational velocities below 88 ft/sec.

[REDACTED] Although tentative in nature, estimates based on human accidents and animal experiments predict that a peak translational velocity of 70 ft/sec will result in 50 percent casualties for personnel when deceleration occurs by tumbling over open terrain. If translation occurs where 50 percent of the personnel impact against structures (buildings, vehicles, trees or other rigid objects) the peak translational velocity for 50 percent casualties is expected to be near 35 ft/sec. Similar figures for one percent casualties are 13 ft/sec for decelerative tumbling and 8.5 ft/sec for translation near structures.

### 10-3 Blast-Energized Debris [REDACTED]

[REDACTED] The effects of blast-energized debris include injuries that result from the impact of penetrating or nonpenetrating missiles energized by winds, blast overpressures, ground shock, and, in some cases, gravity. The wounding potential of blast-energized debris depends upon the nature and velocity of the moving object and the portion of the body where impact occurs. The types of

[REDACTED] injuries range from simple contusions and lacerations to more serious penetrations, fractures, crushing injuries, and critical damage to vital organs. The physical factors that determine the velocity attained by debris and thereby determine the severity of potential injury, are similar to those described for translation of personnel. When small light objects are displaced by a blast wave, they reach their maximum velocity quite rapidly, often after only a small portion of the wave has passed; therefore, the maximum velocity is not as dependent on duration as it is for large heavy objects. There are too many variables to establish definitive criteria for injury from debris.

[REDACTED] In the specific instance of personnel in forests, tentative casualty criteria are available based on the probability of being struck by falling trees. These criteria are related to the amount of forest damage. Fifty percent casualties are predicted at ranges where the forest damage is moderate to severe, and one percent casualties are anticipated where the damage is light (see Forest Damage Data, Chapter 15).

### 10-4 Miscellaneous Effects [REDACTED]

[REDACTED] Miscellaneous blast injuries are those that result from non-line-of-sight thermal phenomena, ground shock, blast-induced fires and high concentrations of dust,

- Non-line-of-sight thermal burns have been observed on animals located in open underground shelters in close proximity to nuclear explosions. Although this phenomenon is not well understood, it has been suggested that the burns resulted from contact with hot dust-laden air that was carried into the structures by the blast wave.
- Ground shock may be a serious problem for personnel in blast-hardened underground structures at close ranges. The magnitude of this hazard may be estimated from the horizontal and vertical motions of the structure, which in turn may be estimated from

[REDACTED]  
the predicted ground motions discussed in Chapter 2.

- Blast-induced fires are primarily a problem for urban areas. The likelihood of such fires depends on the amount of burning and combustible materials in the vicinity of an explosion.
- The evidence indicates that a high concentration of dust represents more of a discomfort than a serious hazard to personnel.

[REDACTED] With the possible exception of ground shock, currently there is inadequate information to predict the hazards associated with these miscellaneous effects reliably.

## CASUALTY PREDICTION

### 10-5 Personnel in the Open

[REDACTED] For most burst conditions casualties from whole body translation of personnel in the open will extend farther than those from direct overpressure hazards, excluding eardrum rupture. This is especially true for larger yield weapons because of the increased duration of the blast wave. The translation hazard will be less for personnel located in relatively open terrain than for personnel located where they may be blown against buildings, vehicles, trees or other structures. Warned personnel can reduce the translation risks by assuming a prone position, and in the case of larger yields there will be sufficient time for the fireball flash to serve as a warning. It should be noted, however, that for overhead bursts, the direct overpressure effects would be less severe for a standing man than for a prone man because of the "step" loading of the thorax in the former case.

[REDACTED] Unless the target area is cluttered with materials subject to fragmentation with displacement, blast-energized debris is not expected to be an overriding hazard for personnel in the open. For small yield surface bursts, however, crater ejecta may extend beyond the other blast effects,

although nuclear or thermal radiation may produce casualties at greater distance. In general, the probability of being struck by flying missiles can be reduced by lying down; however crater ejecta, which is likely to be falling nearly vertically at the greater distances may strike more prone personnel than those who are standing. As in the case of blast-energized debris, the miscellaneous air blast effects are not generally expected to represent major hazards for personnel in the open.

[REDACTED] If a precursor form of blast wave should develop, personnel located in its proximity would probably be subjected to greater translation and debris hazards than would be expected otherwise because of the increased dynamic pressures. Burst conditions associated with precursor development are discussed in Section 1 of Chapter 2.

[REDACTED] Figures 10-1 and 10-2 show the ground distances for 50 percent and one percent casualties, respectively, from the indicated air blast effects as a function of height of burst for randomly oriented, prone personnel exposed in the open to a one kt burst. These figures were derived on the basis of the criteria and assumptions discussed earlier in this section, with the added conditions that crater ejecta was not present and no precursor formed. Since a man with a ruptured eardrum may or may not be considered a casualty depending on the tasks he is expected to perform, this effect has been removed from the other direct overpressure effects, and separate curves are provided. Two translation curves are shown in each figure and the one that is more appropriate to the existing conditions should be used. The figures show the effects for one kt, but they may be scaled to other yields by the scaling rules provided in Problem 10-1.

### 10-6 Personnel in a Forest

[REDACTED] For personnel in a relatively dense forest, the hazard of being struck by falling and translating trees generally will override that resulting from any other air-blast effect. In addition, for

most burst conditions a forest will provide significant protection from thermal radiation and will provide some shielding from nuclear radiation. Therefore, casualties resulting from forest blowdown generally will extend to greater ranges than those from any other weapon effect (direct overpressure, translation, thermal radiation, nuclear radiation, etc.). Exceptions to this general rule are casualties resulting from initial nuclear radiation associated with low yield weapons, and casualties resulting from forest fires ignited by the thermal radiation pulse.

Casualty prediction curves for forest blowdown are given in Figures 10-1 and 10-2 as a function of height of burst and ground range for randomly oriented, prone personnel exposed to a one kt burst. These curves may be scaled to other yields by multiplying both the burst heights and the ground ranges by the four-tenths power of the yield. In general, a forest does not greatly reduce or otherwise modify a blast wave. For this reason the other curves in Figures 10-1 and 10-2, which were developed to predict air-blast casualties for personnel in the open, also may be used for personnel in a forest. A description of the particulars concerning these curves has been given in the above discussion for personnel in the open.

#### 10-7 Personnel in Structures

In addition to providing shielding against thermal and nuclear radiations, blast-resistant structures such as bomb shelters, permanent gun emplacements and, to a certain extent, foxholes usually reduce the blast hazards unless personnel are located directly in the entryway of the structure. The design of these structures may, however, permit the buildup of blast overpressures to a value in excess of the overpressures outside the structure as a result of multiple reflections. Nevertheless, there is generally a lower probability of injury from direct overpressure effects inside a structure than at equivalent distances on the outside, particularly if personnel do not lean against the walls of the structure or sit or lie on

the floor. This results from alterations in the pattern of the overpressure wave upon entering the structure.

Structural collapse and damage are the major causes of casualties for personnel located in buildings subjected to air blast; for this reason, the number of such casualties can be estimated from the extent of the structural damage. Table 10-1 shows estimates of casualties in two types of buildings for three damage levels. Data from Chapter 11 may be used to predict the ground distances at which specified structural damage will occur for various yields. Collapse of a brick house is expected to result in approximately 25 percent mortality, 20 percent serious injury and 10 percent light injury to the occupants. Reinforced concrete structures, though much more resistant to blast forces, will produce almost 100 percent mortality on collapse. Casualty percentages in Table 10-1 for brick homes are based on data from British World War II experience. They may be assumed to be reasonably reliable for cases where the population expects bombing and most personnel have selected the safest places in the buildings. If there were no warning or preparation, the number of casualties would be expected to be considerably higher. To estimate casualties in structures other than those listed in Table 10-1, the type of structural damage that occurs, and the characteristics of the resultant flying objects must be considered. Broken glass may produce large numbers of casualties, particularly to an unwarned population, at overpressures where personnel would be relatively safe from other effects. Overpressures as low as one or two psi may result in penetrating wounds to bare skin.

#### 10-8 Personnel in Vehicles

Personnel in vehicles may be injured as a result of the response of the vehicle to blast forces. Padding, where applicable, and the use of safety belts, helmets and harnesses can reduce

Table 10-1 [REDACTED] Estimated Casualty Production in Buildings  
for Three Degrees of Structural Damage [REDACTED]

Structural Damage	Percent of Personnel*		
	Killed Outright	Serious Injury (hospitalization)	Light Injury (no hospitalization)
1-2 story brick homes (high-explosive data from England):			
Severe damage	25	20	10
Moderate damage	<5	10	5
Light damage	—	<5	<5
Reinforced-concrete buildings (nuclear data from Japan):			
Severe damage	100	—	—
Moderate damage	10	15	20
Light damage	<5	<5	15

\*These percentages do not include the casualties that may result from fires, asphyxiation, and other causes from failure to extricate trapped personnel. The numbers represent the estimated percentages of casualties expected at the maximum range where a specified structural damage occurs. See Chapter 11 for the distances at which these degrees of damage occur for various yields.

this source of casualties significantly, at least within armored vehicles that are strong enough to resist collapse. Serious injury may result to personnel in ordinary wheeled vehicles from fly-

ing glass as well as from impact with the vehicle's interior. Comparative numbers of casualties are almost impossible to assess because of the many variables involved.

### Problem 10-1 Calculation of Casualties for Personnel in the Open or in a Forest

Figures 10-1 and 10-2 are families of curves that show 50 percent and 1 percent casualties, respectively, from the indicated air-blast effects, as a function of height of burst and distance from ground zero. The curves apply to randomly oriented, prone personnel exposed in the open to a 1 kt burst.

**Scaling.** For yields other than 1 kt, scale as follows:

1. For the direct overpressure and ear-drum rupture curves

$$\frac{d}{d_1} = \frac{h}{h_1} = W^{1/3}$$

where  $d_1$  and  $h_1$  are the distance from ground zero and height of burst respectively, for 1 kt; and  $d$  and  $h$  are the corresponding distance and height of burst for a yield of  $W$  kt.

2. For the translation and forest blow-down curves

$$\frac{d}{d_1} = \frac{h}{h_1} = W^{0.4}$$

where  $d_1$  and  $h_1$  are the distance from ground zero and height of burst, respectively, for 1 kt; and  $d$  and  $h$  are the corresponding distance and height of burst for a yield of  $W$  kt.

#### Example

**Given:** A 50 kt weapon burst at an altitude of 860 feet over open terrain.

**Find:** The distance from ground zero at which translational effects would produce 50 percent casualties among prone personnel.

**Solution:** The corresponding height of burst for 1 kt is

$$h_1 = \frac{h}{W^{0.4}} = \frac{860}{(50)^{0.4}} = 180 \text{ ft.}$$

From Figure 10-1, at a height of burst of 180 feet, the distance from ground zero at which 50 percent casualties among personnel in the open will occur for a 1 kt burst is 660 feet.

**Answer:** The corresponding distance for a 50 kt weapon is

$$d = d_1 \times W^{0.4} = 660 \times (50)^{0.4} = 3150 \text{ ft.}$$

**Reliability:** The distances obtained from Figures 10-1 and 10-2 are estimated to be reliable to within  $\pm 15$  percent for the indicated effects; however, in view of the uncertainties discussed in paragraphs 10-5 and 10-6 (e.g., the presence of debris, crater ejecta, etc.) no precise estimate of the reliability can be made for a specific situation.

**Related Material:** See paragraphs 10-1 through 10-6.

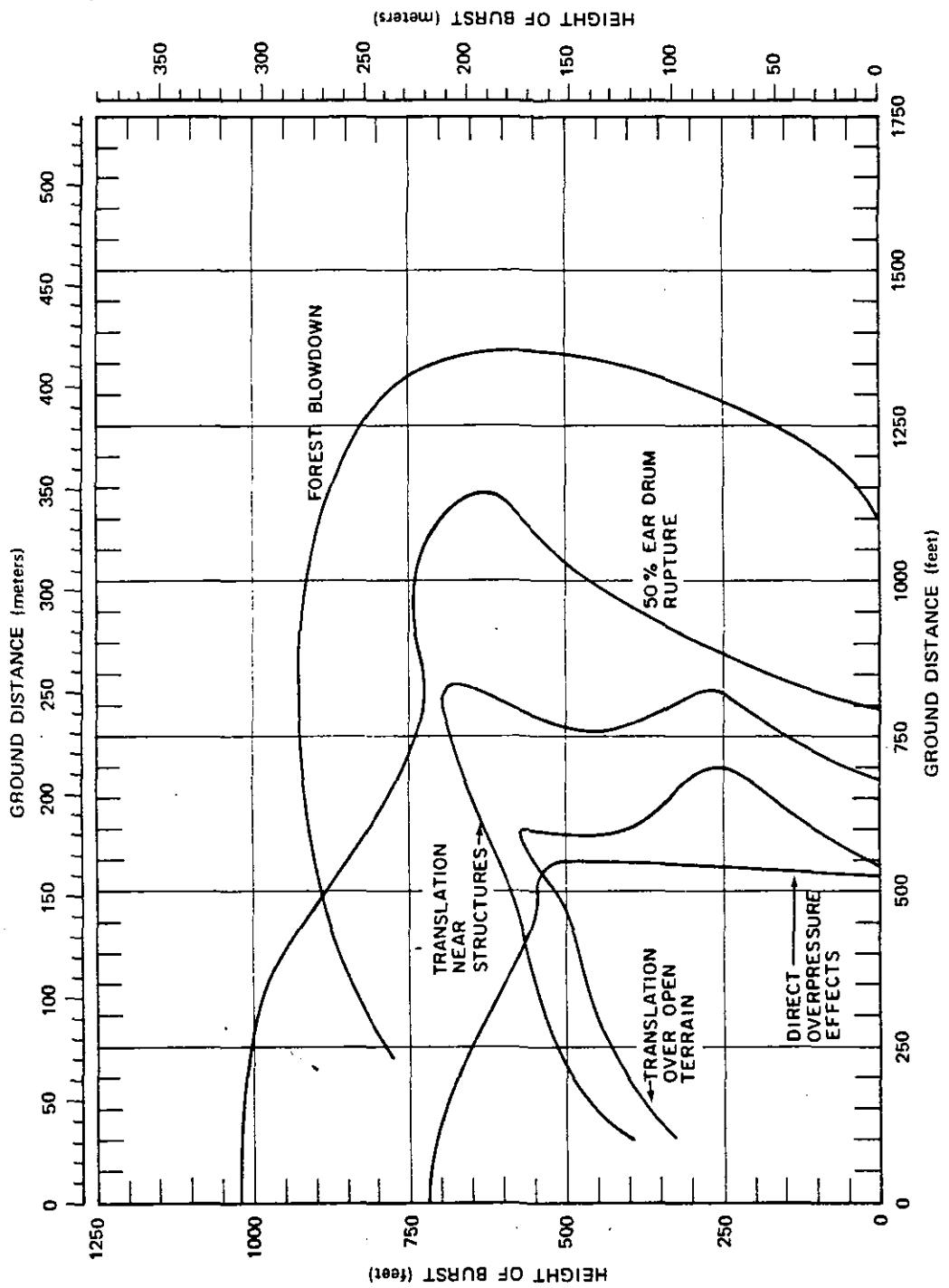


Figure 10-1. [REDACTED] Fifty Percent Casualties for the Indicated Blast Effects for Prone Personnel Exposed in the Open or in a Forest to a 1 kt Burst [REDACTED]

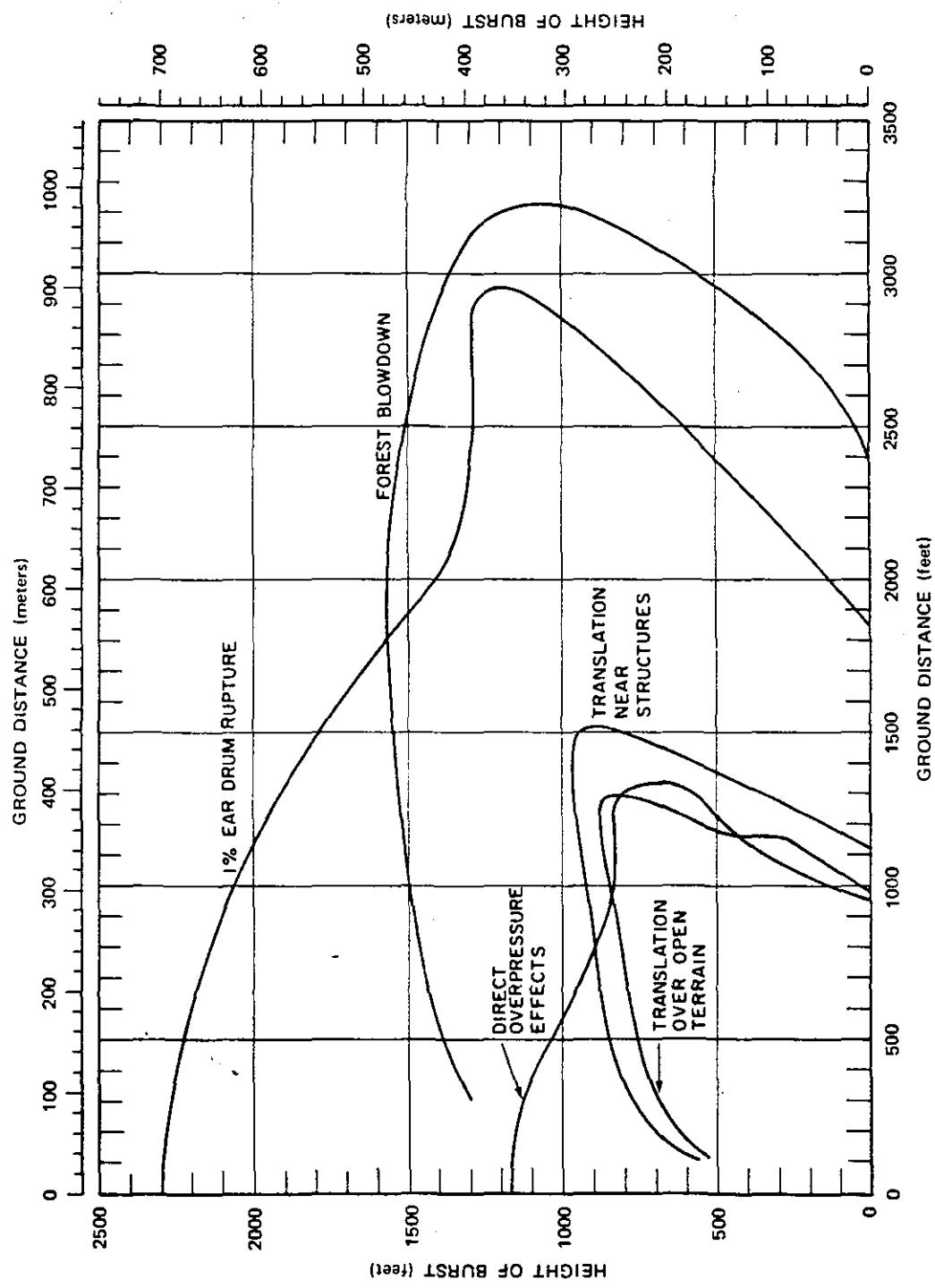


Figure 10-2. [REDACTED] One Percent Casualties for the Indicated Blast Effects for Prone Personnel Exposed in the Open or in a Forest to a '1 kt Burst' [REDACTED]

## SECTION II

### THERMAL RADIATION

#### SKIN BURNS

When a nuclear weapon detonates, personnel will sustain skin burns at distances that may be larger than those distances at which injury occurs as a result of blast or nuclear radiation. These burns may be produced directly by the absorption of radiant energy by the skin, or indirectly by heat transference through clothing or by ignition of the clothing. Thermal radiation is composed of light in the ultraviolet, visible and infrared regions of the spectrum and travels in a straight line at the speed of light. It is emitted within periods of a few milliseconds to several tens of seconds.

If there is substantial material between the individual and the nuclear burst, the thermal radiation will be absorbed and no burns will be produced. Thus, persons in or behind buildings, vehicles, etc., will be shielded from the thermal pulse either partially or completely. In some instances, burns may be avoided or reduced if evasive action is taken during the delivery of the thermal pulse, since heating takes place only during direct exposure. These and other protective measures will be discussed later.

#### CLASSIFICATION OF BURNS

Burn severity is related to the degree of elevation of skin temperature and the length of time of this elevation. Pain, a familiar warning sensation, occurs when the temperature of certain nerve cells near the surface of the skin is raised to  $43^{\circ}\text{C}$  ( $109^{\circ}\text{F}$ ) or more. If the temperature is not elevated to a high enough degree or for a sufficient period of time, pain will cease and no injury will occur. The amount of pain is not related to burn severity as is the classification of first degree ( $1^{\circ}$ ), second degree ( $2^{\circ}$ ) or third degree ( $3^{\circ}$ ) burns but it is a useful tool in warning an individual to evade the thermal pulse.

#### 10-9 First Degree Burns

A skin burn is an injury to skin caused by temperature elevation following application of heat by absorption of direct thermal radiation or by transference through cloth. First degree burns are characterized by immediate pain which continues after exposure and by ensuing redness of the exposed area. The first degree burn is a reversible tissue injury; the classic example is sunburn.

#### 10-10 Second Degree Burns

Second degree burns are caused by temperatures that are higher and/or of longer duration than those necessary for first degree skin burns. The injury is characterized by pain and may be accompanied by either no immediate visible effect or by a variety of skin changes including blanching, redness, loss of elasticity, swelling and blisters. After 6 to 24 hours, a scab will form over the injured area. The scab may be flexible, tan or brown, if the injury is moderate, or it may be thick, stiff and dark, if the injury is more severe. Second degree burn wounds will heal within one to two weeks unless they are complicated by infection. Second degree burns do not involve the full thickness of the skin, and the remaining uninjured cells may be able to regenerate normal skin without scar formation.

#### 10-11 Third Degree Burns

Third degree burns are caused by temperatures of a higher magnitude and/or longer duration than second degree burns. The injury is characterized by pain at the peripheral, less injured areas only, since the nerve endings in the centrally burned areas are damaged to the extent that they are unable to transmit pain impulses. Immediately after exposure, the skin may appear normal, scalded, or charred, and it may lose its elasticity. The healing of third degree burns takes several weeks and always results in scar formation unless new skin is grafted over the

[REDACTED]  
burned area. The scar results from the fact that the full thickness of the skin is injured, and the skin cells are unable to regenerate normal tissue.

#### 10-12 Reduction in Effectiveness by Burns [REDACTED]

[REDACTED] The distribution of burns into three groups obviously has certain limitations since it is not possible to draw a sharp line of demarcation between first- and second-degree, or between second- and third-degree burns. Within each class the burn may be mild, moderate, or severe, so that upon preliminary examination it may be difficult to distinguish between a severe burn of the second degree and a mild third-degree burn. Subsequent pathology of the injury, however, will usually make a distinction possible. In the following discussion, reference to a particular degree of burn should be taken to imply a moderate burn of that type.

[REDACTED] The depth of the burn is not the only factor in determining its effect on the individual. The extent of the area of the skin which has been affected is also important. Thus, a first-degree burn over the entire body may be more serious than a third-degree burn at one spot. The larger the area burned, the more likely is the appearance of symptoms involving the whole body. Furthermore: there are certain critical, local regions, such as the hands, where almost any degree of burn will incapacitate the individual.

[REDACTED] Persons exposed to a low or intermediate yield nuclear weapon burst may sustain very severe burns on their faces and hands or other exposed areas of the body as a result of the short pulse of directly absorbed thermal radiation. These burns may cause severe superficial damage similar to a third degree burn, but the deeper layers of the skin may be uninjured. This would result in rapid healing similar to a mild second degree burn. Thermal radiation burns occurring under clothing or from ignited clothing or other tinder will be similar to those ordinarily seen in

burn injuries of nonnuclear origin. Because of the longer duration of the thermal pulse, the differences between flash burns on exposed skin from air burst high yield weapons and burns of nonnuclear origin may be less apparent.

#### BURN INJURY ENERGIES AND RANGES [REDACTED]

[REDACTED] The critical radiant exposure for a skin burn changes as the thermal radiation pulse duration and spectrum change; therefore, the critical distance cannot be determined simply from the calculated radiant exposure. The effective spectrum shifts with yield and altitude; the thermal radiation pulse is shorter for smaller yields or higher burst altitudes (see Chapter 3).

#### 10-13 Personnel Parameters [REDACTED]

[REDACTED] The probability and severity of an individual being burned will depend upon many factors including: pigmentation, absorptive properties, thickness, conductivity and initial temperature of the skin; distance from the detonation and the amount of shielding; clothing, orientation with respect to the burst, and voluntary evasive action.

[REDACTED] Severity of the burn cannot be determined by temperature elevation and pulse duration alone. The energy absorbed by the skin in a normal population may vary by as much as 50 percent because of the variance in skin pigmentation. It is known that depths in skin of 0.001 to 0.002 centimeter are the sites of the initial damage that results in a burn from thermal radiation pulses and that skin temperatures of 70°C (158°F) for a fraction of a second or temperatures of 48°C (118°F) for minutes can result in burns. Skin temperatures for first degree and third degree burns are roughly 25 percent lower and higher, respectively, than those for second degree burns.

[REDACTED] For pulses of 0.5 second duration and longer, the amount of energy absorbed is an im-

portant factor. Figure 10-3 shows the effect of absorptive differences of human skin as calculated from measurements of the spectral absorptance and the spectral distribution of the peak power of nuclear weapons bursts in the lower atmosphere. As shown in Figure 10-3, very dark skinned people will receive burns from approximately two-thirds the energy required to produce the same degree of burns on very light skinned people.

#### 10-14 Burn Exposures for Unprotected Skin

Figure 10-4 shows ranges of radiant exposures for the probabilities of burn occurrence. The solid lines represent 50 percent probability for an average population taking no evasive action to receive the indicated type of burns. The dotted lines divide the burn probability distributions into ranges for the three burn levels with average burn probabilities of 18 percent and 82 percent assigned within these exposure ranges.

For example, from Figure 10-4, it can be predicted that, if a normal population is exposed to the thermal pulse at distances producing between 4.5 and 6.0 calories per square centimeter from a 1 megaton weapon, 18 percent of the population will receive second degree burns and 82 percent will receive first degree burns.

A radius from ground zero that produces areas of equal burn probability may be obtained by employing the radiant exposures for skin burn probability from Figure 10-5 and the weapon yield-distance relationship for radiant exposures from Chapter 3.

#### 10-15 Burns Under Clothing

Skin burns under clothing are produced several ways: by direct transmittance through the cloth if the cloth is thin and merely acts as an attenuating screen; by heating the cloth and causing steam or volatile products to impinge on the skin; by conduction from the hot fabric to

the skin; or the fabric may ignite, and consequent volatiles and flames will cause burns where they impinge on the skin.

Heat transfer mechanisms cause burns beneath clothing as a result of heat transfer for some time after the thermal pulse ends. These burns generally involve deeper tissues than those that result from the direct thermal pulse on bare skin. Burns caused by ignited clothing also result from longer heat application, and thus will be more like burns occurring in nonnuclear weapon situations.

#### 10-16 Body Areas Involved

The pattern of body area involved in thermal radiation burns from nuclear weapons will differ from the areas injured from conventional means. For weapons of 100 kt or less, where effective evasive action cannot be taken, burns would occur primarily on the directly exposed parts of the body unless the clothing ignites. First and second degree burns of the uncovered skin, and burns through thin clothing occur at lower radiant exposures than those which ignite clothing. Because of these factors, first and second degree burns for this low yield range would involve limited body area and would occur only on one side of the body. For closer distances where the direct thermal pulse produces burns and clothing ignition takes place, persons wearing thin clothing would have third degree burns over that area of the body facing the burst. This phenomenon is typically seen in persons whose clothing catches fire by conventional means.

For the yield range 100 kt and less, persons wearing heavy clothing (in the third degree bare skin burn and clothing ignition zone) will have third degree burns on one exposed body surface and third degree burns on other areas resulting from the burning clothes prior to its removal, or full body third degree burns if the clothing cannot be removed.

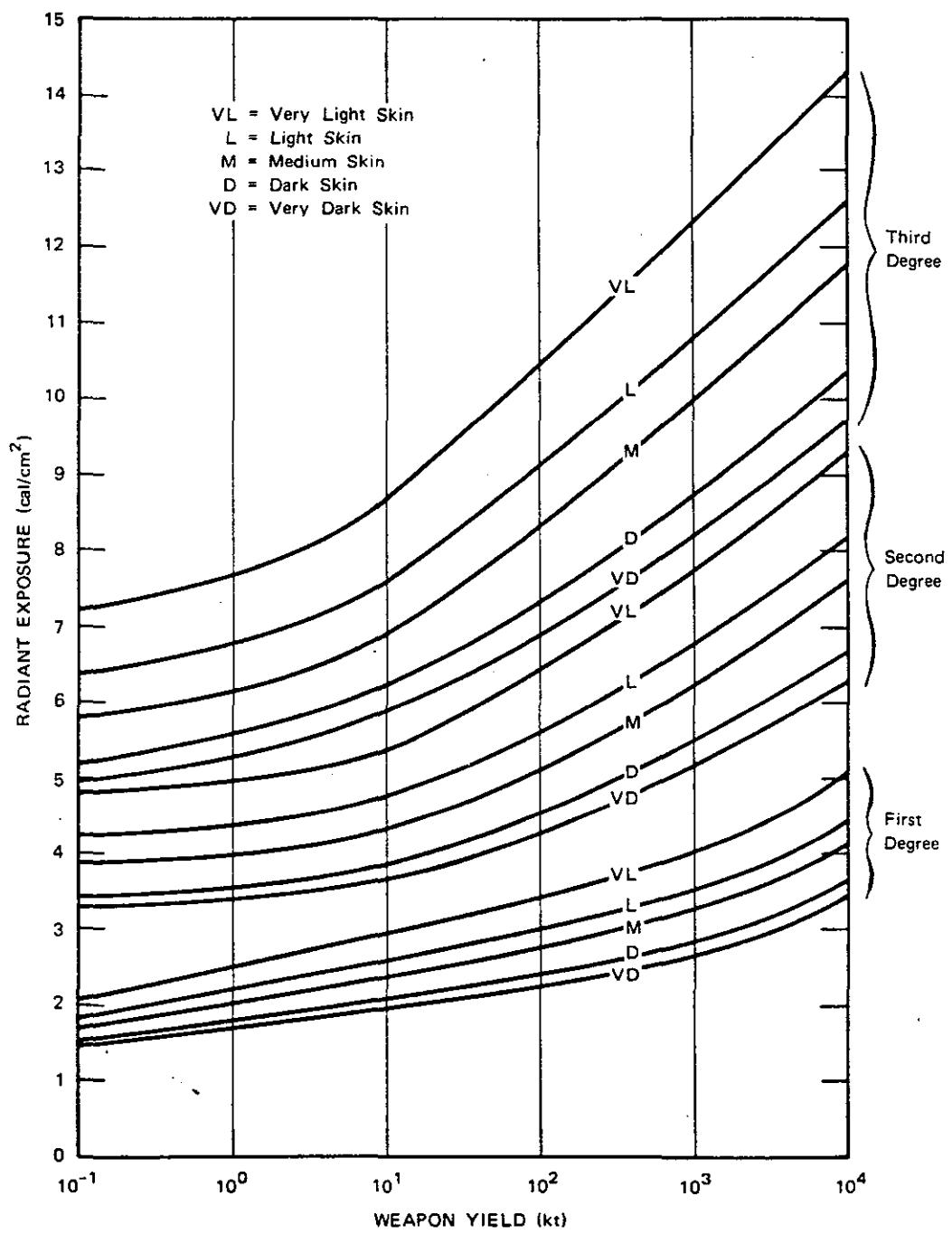


Figure 10-3. Radiant Exposure Required to Produce Skin Burns for Different Skin Pigmentation

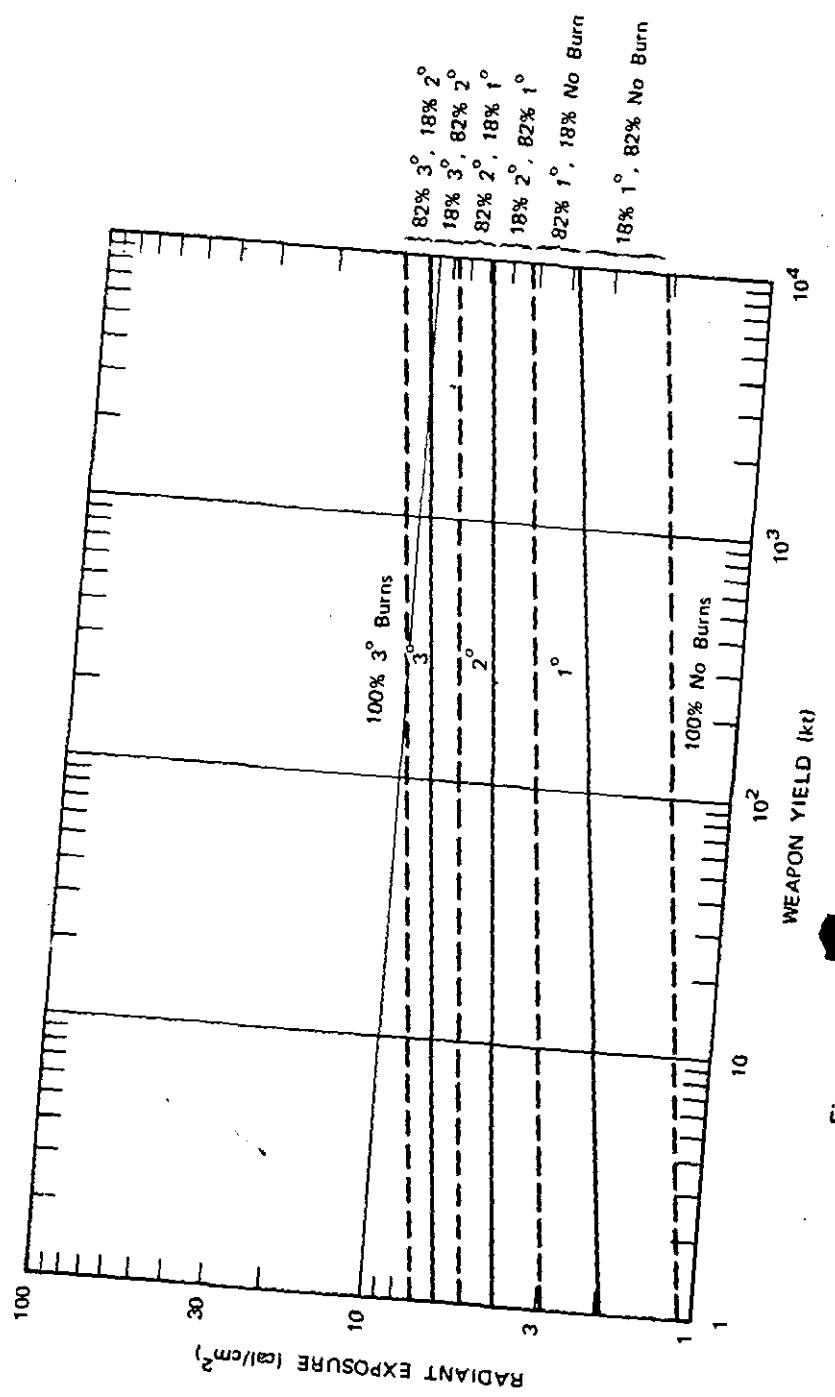


Figure 10-4. Skin Burn Probabilities for an Average Population  
Taking No Evasive Action [REDACTED]

### **10-17 Incapacitation from Burns**

Burns to certain anatomical sites of the body, even if only first degree, will frequently cause ineffectiveness because of their critical location. Any burn surrounding the eyes that causes occluded vision because of the resultant swelling of the eyelids, will be incapacitating. Burns of the elbows, knees, hands and feet produce immobility or limitation of motion as the result of swelling, pain or scab formation, and will cause ineffectiveness in most cases. Burns of the face and upper extremity areas are most likely to occur because these areas will more frequently be unprotected. Second or third degree burns in excess of 20 percent of the surface area of the body should be considered a major burn and will require special medical care in a hospital.

Shock is a term denoting a generalized state of severe circulatory inadequacy. It will result in ineffectiveness and if untreated may cause death. Third degree burns of 25 percent of the body and second degree burns of 30 percent of the body will generally produce shock within 30 minutes to 12 hours and require prompt medical treatment. Such medical treatment is complicated and causes a heavy drain on medical personnel and supply resources.

### **10-18 Modification of Injury**

Timely evasion can be effective in reducing burns with weapons yields of 100 kt and greater. The length of time between the burst and the point at which critical radiant exposure occurs increases with increasing yields, permitting personnel to react prior to receiving severe burns. With yields of less than about 100 kt, or for high altitude bursts of larger yields, the thermal pulse is too short for personnel to react and take cover. Since pain occurs at low radiant exposures and at lower temperatures than those that cause first degree burns, it is the initial sensation that occurs, and involuntary action due to pain can be expected instinctively. More effective action can

be expected with proper training. Figure 10-5 illustrates the effect of evasion on the production of burns.

Personnel in the shadow of buildings, vehicles, or other objects at the time of detonation will be shielded from the pulse and will not be burned.

### **EFFECTS OF THERMAL RADIATION ON THE EYES**

Exposure of the eye to a bright flash of a nuclear detonation produces two possible effects; flashblindness and/or retinal burns.

#### **10-19 Flashblindness**

Flashblindness (dazzle) is a temporary impairment of vision caused by the saturation of the light sensitive elements (rods and cones) in the retina of the eye. It is an entirely reversible phenomena which will normally blank out the entire visual field of view with a bright after-image. Flashblindness normally will be brief, and recovery is complete.

During the period of flashblindness (several seconds to minutes) useful vision is lost. This loss of vision may preclude effective performance of activities requiring constant, precise visual function. The severity and time required for recovery of vision are determined by the intensity and duration of the flash, the viewing angle from the burst, the pupil size, brightness necessary to perform a task and the background, and the visual complexity of the task. Flashblindness will be more severe at night since the pupil is larger and the object being viewed and the background are usually dimly illuminated.

Flashblindness may be produced by scattered light and does not necessarily require eye focusing on the fireball.

#### **10-20 Retinal Burns**

A retinal burn is a permanent eye injury that occurs whenever the retinal tissue is heated.

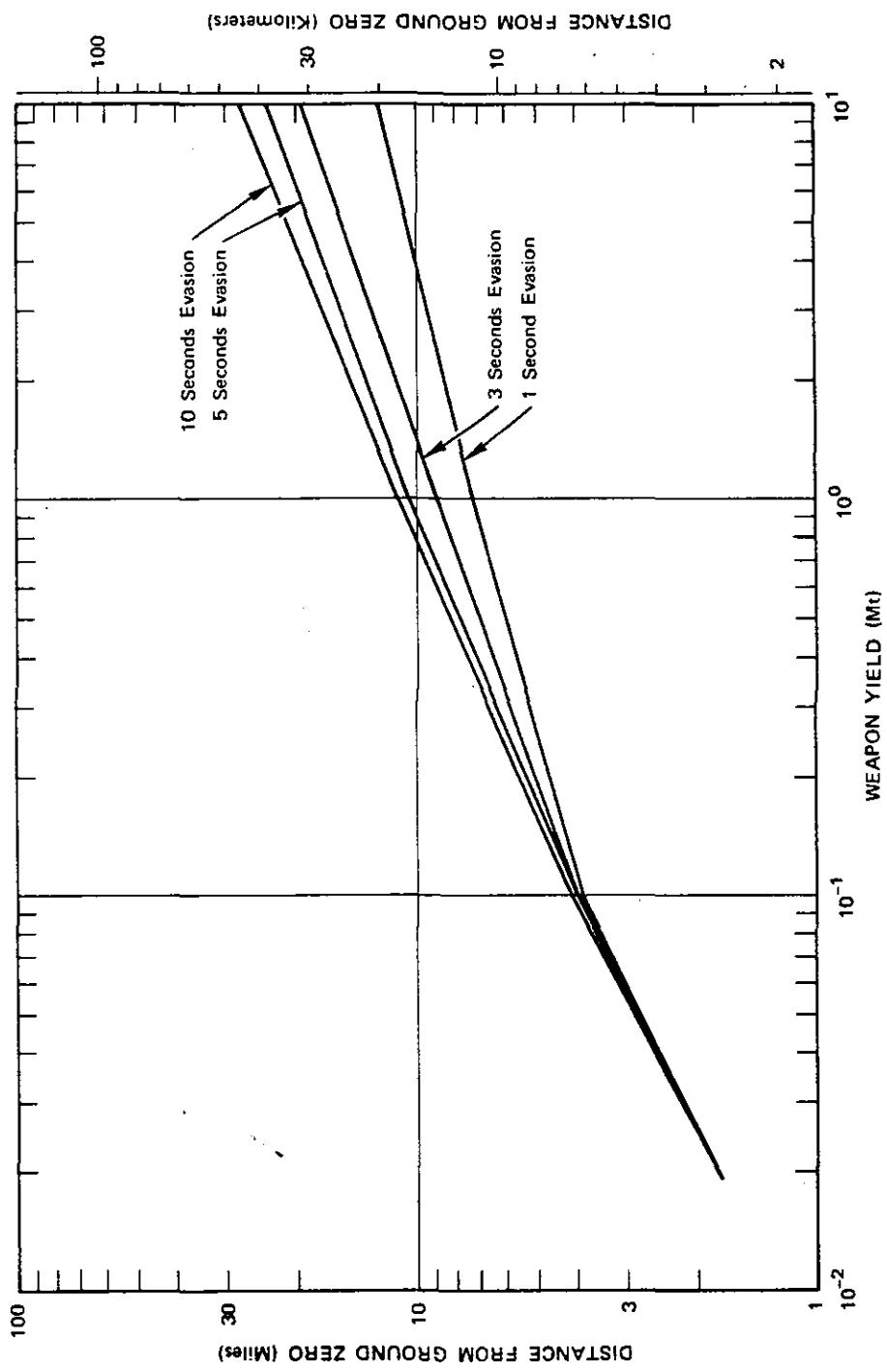


Figure 10-5. [REDACTED] Distance Thresholds for Second Degree Burns for Various Evasion Times [REDACTED]

[REDACTED]  
[REDACTED]  
excessively by the focused image of the fireball within the eye. The underlying pigmented cells absorb much of the light and raise the temperature in that area. A temperature elevation of 12-20°C (22-36°F) in the eye produces a thermal injury which involves both the pigmented layer and the adjacent rods and cones, so the visual capacity is permanently lost in the burned area. The natural tendency of personnel to look directly at the fireball tends to increase the incidence of retinal burns.

[REDACTED] Retinal burns can be produced at great distances from nuclear detonations, because the probability of eye burns does not decrease as the square of the distance from the detonation as is true of many other nuclear weapons effects. Theoretically, the optical process of image formation within the eye negates the inverse square law and keeps the intensity per unit area on the retina a constant, regardless of the distance. However, meteorological conditions and the fact that the human eye is not a perfect lens, all contribute toward reducing the retinal burn hazard as the distance is increased between the observer and the detonation.

[REDACTED] Explosion yields greater than one megaton, and at heights of burst greater than about 130 kilofeet may produce retinal burns as far out as the horizon on clear nights. Bursts above 490 kilofeet probably will not produce any retinal burns in personnel on the ground unless the weapon yield is greater than 10 Mt.

(U) A retinal burn normally will not be noticed by the individual concerned if it is off the central axis of vision; however, very small burned areas may be noticeable if they are centrally located. Personnel generally will be able to compensate for a small retinal burn by learning to scan around the burned area.

#### 10-21 Modification of Thermal Effects on the Eye [REDACTED]

[REDACTED] The thermal pulse from a nuclear weapon is emitted at such a rapid rate that any device de-

signed to protect the eye must close extremely fast (<100  $\mu$ sec) to afford a sure degree of protection for all situations. During the daytime, when the pupil is smaller and objects are illuminated brightly, the 2 percent transmission gold goggle/visor will reduce flashblindness recovery times to acceptable levels. At present, this goggle is unsatisfactory for use at night, and there is no protective device that is adequate for night use.

[REDACTED] The blink reflexes of the eye are sufficiently fast (~0.2 second) to provide some protection against weapons greater than 100 kt detonated below about 130 kilofeet. The blink time is too slow to provide any appreciable protection for smaller weapon yields or higher burst altitudes.

[REDACTED] When personnel have adequate warning of an impending nuclear burst, evasive action including closing or shielding the eyes will prevent flashblindness and retinal burns.

#### 10-22 Safe Separation Distance Curves [REDACTED]

[REDACTED] Figures 10-6 through 10-10 present flashblindness and retinal burn curves for a number of burst heights as a function of weapon yields and safe separation distance, e.g., that distance where personnel will not receive incapacitating eye injuries. The retinal burn curves show distances that current data show to be safe. The curves for flashblindness were specifically designed for pilots of strategic bombers, where a pilot can effectively read his instruments and complete his mission after a temporary 10 second complete loss of vision. These curves are also applicable to any task where the same criteria of dim task lighting, visual demands, and the 10 second visual loss can be applied. Data are not available for specific distances at which flashblindness will not occur.

[REDACTED] It should be noted that the flashblindness and the retinal burn safe separation distances do not bear the same relationship to one another as the yield changes. In circumstances that require determination of complete eye safety (realizing

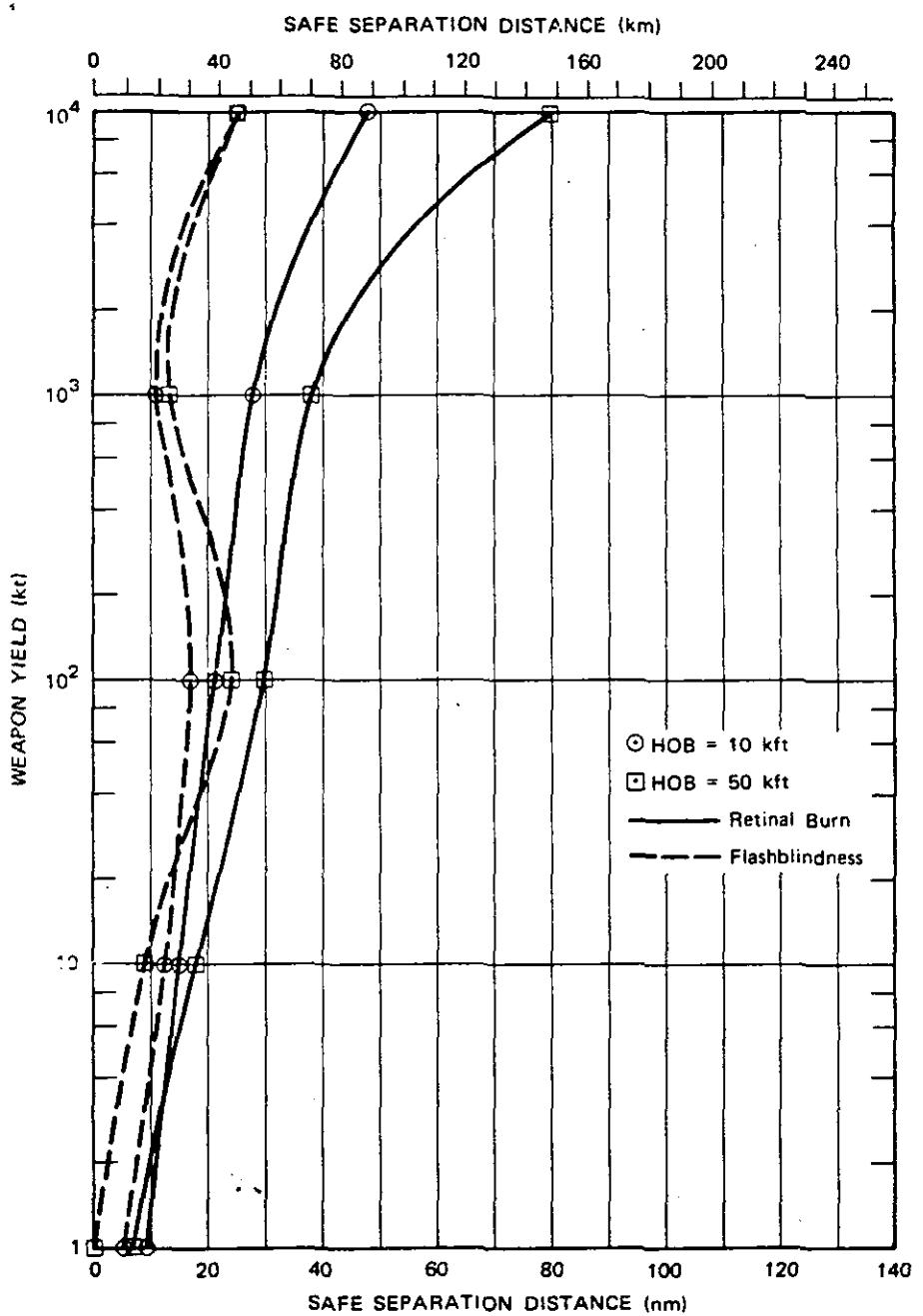


Figure 10-6. [REDACTED] Safe Separation Distances, for an Observer on the Ground, from Bursts at 10 kft and 50 kft During the Day [REDACTED]

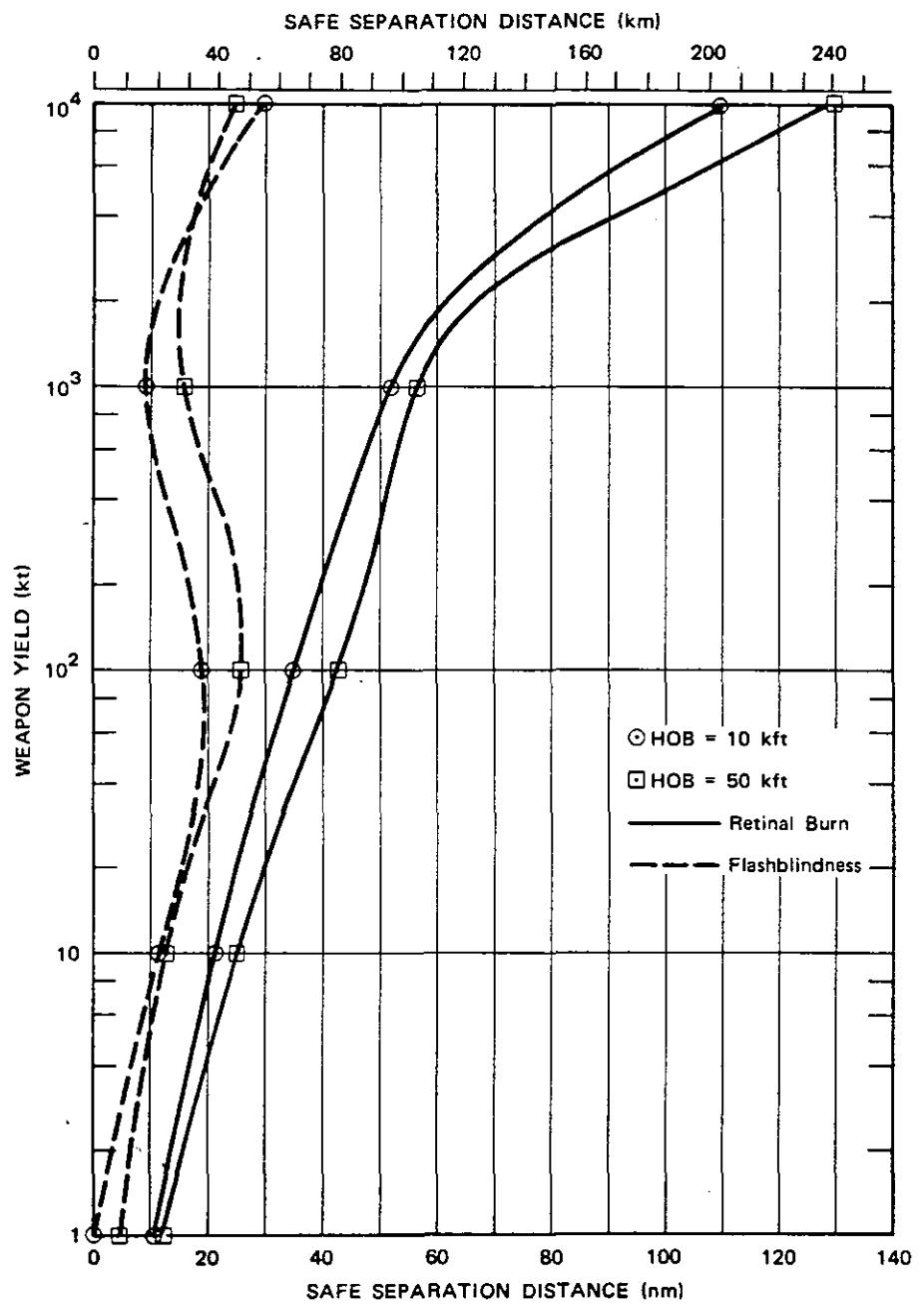


Figure 10-7. [REDACTED] Safe Separation Distance, for an Observer at 50 kft, from Bursts at 10 kft and 50 kft During the Day [REDACTED]

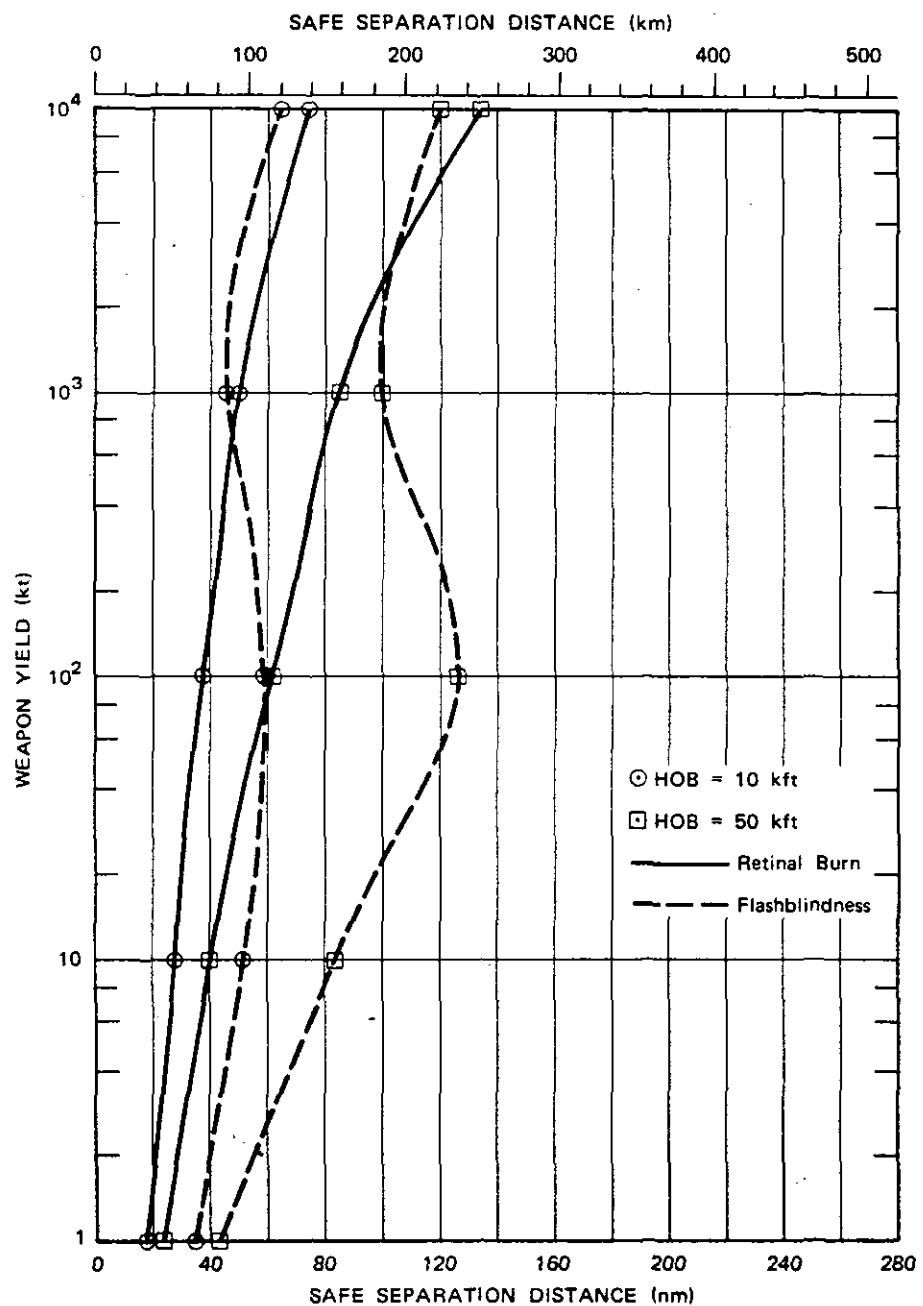


Figure 10-8. Safe Separation Distance, for an Observer on the Ground, from Bursts at 10 kft and 50 kft, During the Night

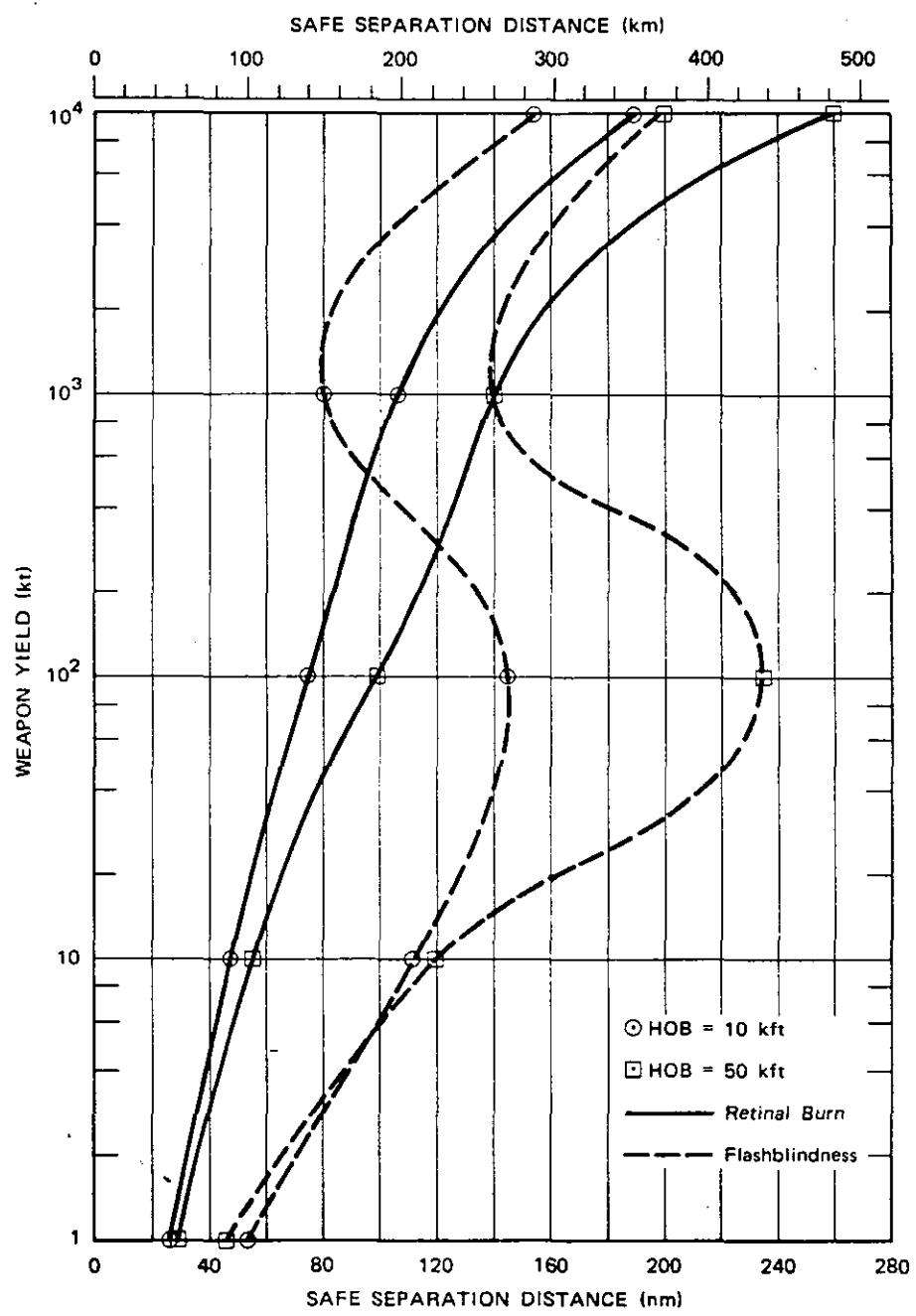


Figure 10-9. Safe Separation Distance, for an Observer at 50 kft, from Bursts at 10 kft and 50 kft, During the Night

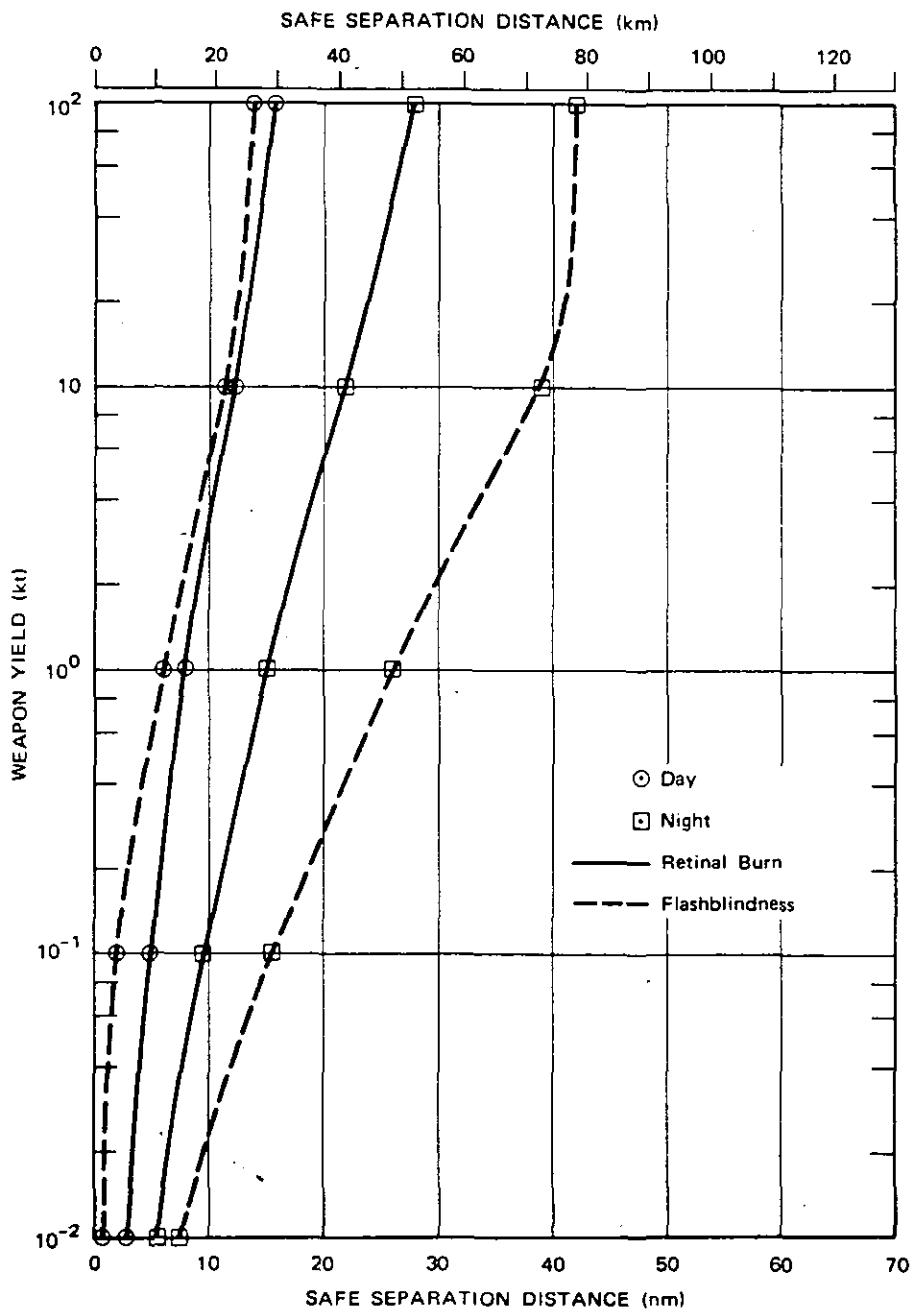


Figure 10-10. Safe Separation Distance, for an Observer on the Ground, from Low Yield Weapons Exploded at 1,000 ft Height of Burst

the 10 second loss of vision criterion in the flashblindness curves), the retinal burn or flashblindness curve that shows the effect that occurs at the greatest distance from the burst should be used. For example, using Figure 10-8 and a 50 kilofeet height of burst, to determine the distance from a nuclear detonation where there will be no incapacitating eye effects, the flashblindness curve is the limiting factor up to about 3 megatons, then the retinal burn curve becomes the limiting factor.

In instances where only permanent eye damage is of interest, and the temporary loss of vision from flashblindness is not of concern, only the retinal burn curves should be used.

The retinal burn curves show distances at which a nuclear burst will not produce retinal burns provided the eye can blink within 250 milliseconds. A faster blink time would not change the distances appreciably. The curves are based on a very clear day (60 mile visual range). For a cloudy day with a 5 mile visual range, the safe separation distances would be reduced by about 50 percent.

### SECTION III

#### NUCLEAR RADIATION

The injurious effects of nuclear radiations (gamma rays, neutrons, beta particles and alpha particles) on the human target represent a phenomenon that is completely absent from conventional explosives. Since there has not been sufficient experience with humans in the exposure ranges of military interest, the material presented below is based largely on animal experimentation that has been extrapolated to the area of human response. Even if sufficient human data were available, they would be expected to show similar responses and the same wide range of biological variability within species as is seen in animals. Data are presented in terms of absorbed dose at or near the body surface in order to relate to source and transport factors given in Chapter 5. Current radiobiological research re-

sults are frequently reported as *midline tissue dose* in rad, a dose significantly lower than doses measured by radiac instruments and absorbed within those volumes near the surface of the body that faces toward the source. For nuclear weapon radiation, the midline tissue doses would be approximately 70 percent of the body surface doses presented in the following paragraphs.

#### INITIAL RADIATION

Neutrons and gamma rays in various proportions are responsible for biological injury from initial radiation. For military purposes, and until further animal experimentation provides evidence to the contrary, it must be assumed that damage to tissue is directly proportional to the absorbed dose regardless of whether it is delivered by neutrons or gamma rays. For effects of military interest, it is assumed that injury from a neutron rad is equal to that from a gamma rad, and that one rad absorbed dose results from exposure to one roentgen.

#### 10-23 Radiation Sickness

Individuals exposed to whole body ionizing radiation may show certain signs and symptoms of illness. The time interval to onset of these symptoms, their severity, and their duration generally depend on the amount of radiation absorbed, although there will be significant variations among individuals. Within any given dose range, the effects that are manifested can be divided conveniently into three time phases: initial, latent, and final.

During the initial phase, individuals may experience nausea, vomiting, headache, dizziness and a generalized feeling of illness. The onset time decreases and the severity of these symptoms increases with increasing doses. During the latent phase, exposed individuals will experience few, if any, symptoms and most likely will be able to perform operational duties. The final phase is characterized by frank illness that re-

quires hospitalization after exposure to the higher doses. In addition to the recurrence of the symptoms noted during the initial phase, skin hemorrhages, diarrhea and loss of hair may appear, and, at high doses, seizures and prostration may occur. The final phase is consummated by recovery or death. At doses above 1000 rad, death may be expected in all cases. Maximum recovery of survivors exposed to lower doses may require as much as three to six months time. With the foregoing in mind, Table 10-2 is presented as the best available summary of the effects of various whole-body dose ranges of ionizing radiation in human beings.

#### 10-24 Incapacitation

Direct effects of high doses of external radiation administered over a short time period

may result in loss of ability to perform purposeful actions. At doses greater than 2,000 rads, an acute collapse may occur in a short time. The collapse may persist from several minutes to a few hours. A period of relatively normal performance capability will then occur; however, after some time permanent incapacitation and death will result. This early incapacitation, followed by a temporary period of recovery, is defined as early transient incapacitation (ETI). Following this transient incapacitation, exposed personnel *may* be reasonably well oriented, lucid, and able to perform tasks requiring coordination of visual and auditory sensory input. The duration of early transient incapacitation is believed to be dose dependent, i.e., the greater the dose, the longer the transient incapacitation phase. The duration of the temporary period of effec-

Table 10-2 Response to Single Whole-Body Exposures

	100-200 Rad	200-400 Rad	400-600 Rad	600-1000 Rad	1000-2500 Rad
<u>Initial Phase</u>					
1. Onset of symptoms after irradiation	3-6 hrs	1-6 hrs	1/2 to 6 hrs	1/4 to 4 hrs	5-30 min
2. Duration of phase	≤1 day	1-2 days	1-2 days	≤2 days	≤1 day
<u>Latent Phase</u>					
1. Onset after irradiation	≤1 day	1-2 days	1-2 days	≤2 days	≤1 day
2. Duration of phase	≤2 weeks	2-4 weeks	1-2 weeks	5-10 days	0-7 days*
<u>Final Phase</u>					
1. Onset of symptoms after irradiation	10-14 days	2-4 weeks	7-14 days	5-10 days	4-8 days
2. Duration of phase	4 weeks	2-8 weeks	1-8 weeks	1-4 weeks	2-10 days
3. Time from irradiation to death	—	4-12 weeks	2-10 weeks	1-6 weeks	4-14 days
4. Deaths (% of those exposed)	No deaths	0-30%	30-90%	90-100%	100%

\*At the higher doses within this range there may be no latent period.

tiveness is inversely related to the dose. At doses in excess of 15,000 rads, most individuals will experience permanent complete incapacitation within a few minutes post-irradiation, followed by death within 2 to 24 hours.

[REDACTED] Figures 10-11 through 10-15 list estimated personnel effectiveness at various times following acute radiation doses of 1,400 rads and greater. It should be noted that incapacitation, or performance decrement, and not death, is the endpoint of interest in these figures.

#### **10-25 Modification of Injury**

[REDACTED] When only a portion of the body is exposed to radiation, the effects are significantly less than those described in the preceding two sections. The reduction of the effects depends on the magnitude of exposure and the particular portion of the body that is exposed. Thus, partial shielding afforded by natural or man-made structures can be expected to decrease the severity of radiation injury.

[REDACTED] Considerable effort has been expended in searching for compounds that will reduce the extent and seriousness of radiation injury when they are administered prior to exposure. At present, there is no satisfactory compound available for issue, although research continues in this area.

[REDACTED] Treatment of radiation injury is supportive in nature. The treatment is based primarily on symptomology rather than measured or estimated dose received by the individual.

#### **10-26 Military Assumptions**

[REDACTED] In order to apply the material above to other than single exposures, it may be assumed that multiple exposures within any 24-hour period are arithmetically additive. This assumption is necessary because the information concerning the results of multiple exposures is limited.

[REDACTED] Although there is reason to believe that recovery from radiation exposure(s) is never really complete (i.e., some residual injury not

necessarily affecting effectiveness remains), it may be assumed for military planning purposes that recovery is complete in approximately 30 days following a single sublethal exposure. Table 10-2 lists more specific information regarding durations of ineffectiveness under varying exposure conditions.

#### **RESIDUAL RADIATION**

[REDACTED] The importance of residual radiation as a source of injury to personnel depends upon the necessity for military operations in or near areas of local fallout. Time of arrival, weathering, and decay of the deposited fallout all result in a constantly changing rate of external protracted exposure to personnel in contrast to the almost instantaneous exposure to initial radiation. An added hazard results from the presence of small, finely divided, radioactive particulate sources that can contribute to injury by both external and internal irradiation.

#### **10-27 External Hazards**

[REDACTED] Gamma rays present the major militarily significant external hazard from residual radiation. Effects on personnel will range from those described previously for initial radiation exposures (in new, high dose-rate, fallout fields) to lesser effects for the same total exposure in low dose-rate fields.

[REDACTED] Beta burns can occur if fallout particles remain on the skin for periods of hours or more. They will occur most frequently when the fallout particles are deposited on moist skin areas, body crevices, in the hair, or when the particles are held in contact by clothing. While minor skin symptoms may occur during the first 48 hours following exposure, the appearance of burns will be delayed two weeks or more after exposure. Severity of the burns is a function of the radioactivity of the fallout particles and the time period during which they adhere to the body. Personnel ineffectiveness will depend on the severity of the burn and its location on the body.

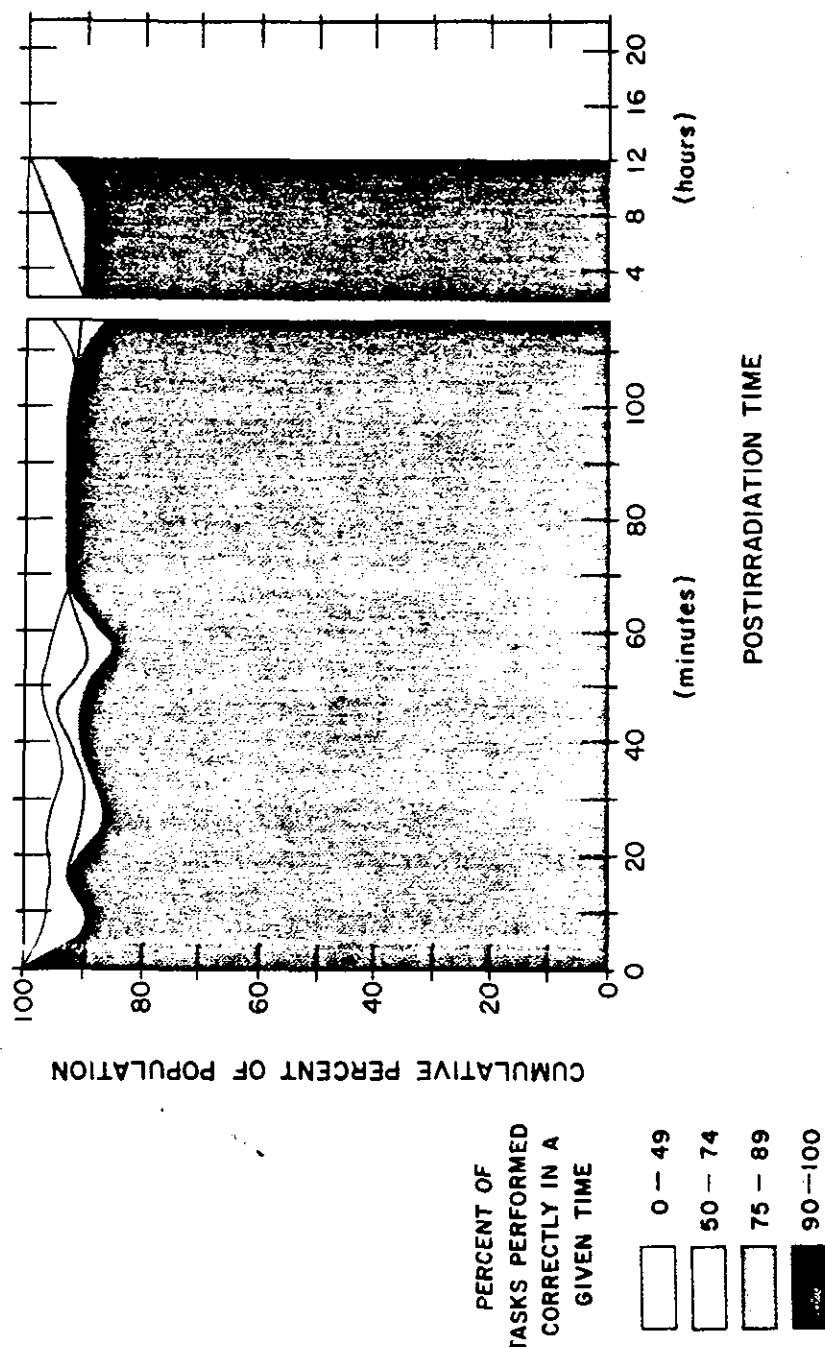


Figure 10-11. Personnel Effectiveness After Exposure to 1,400 rads

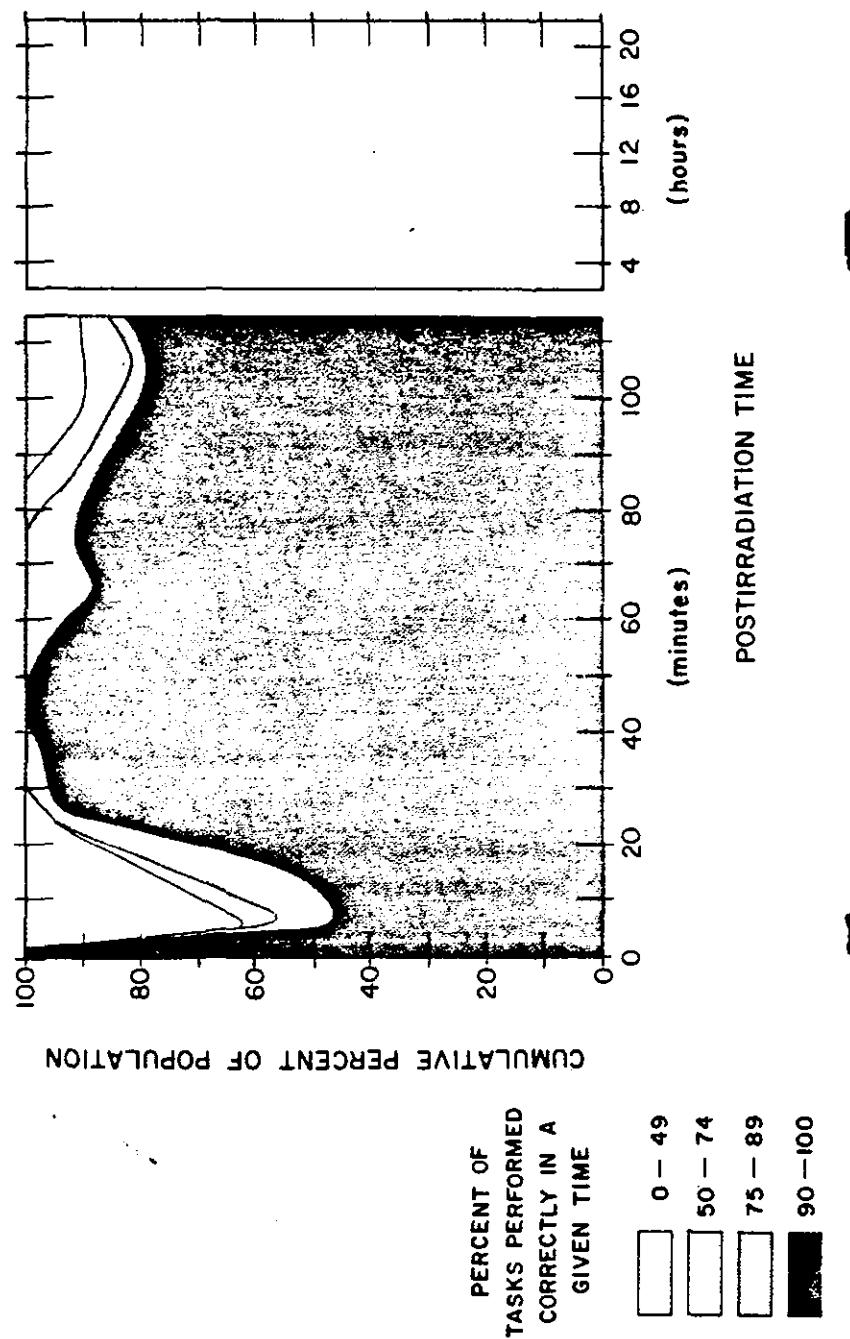


Figure 10-12. Personnel Effectiveness After Exposure to 2,800 rads

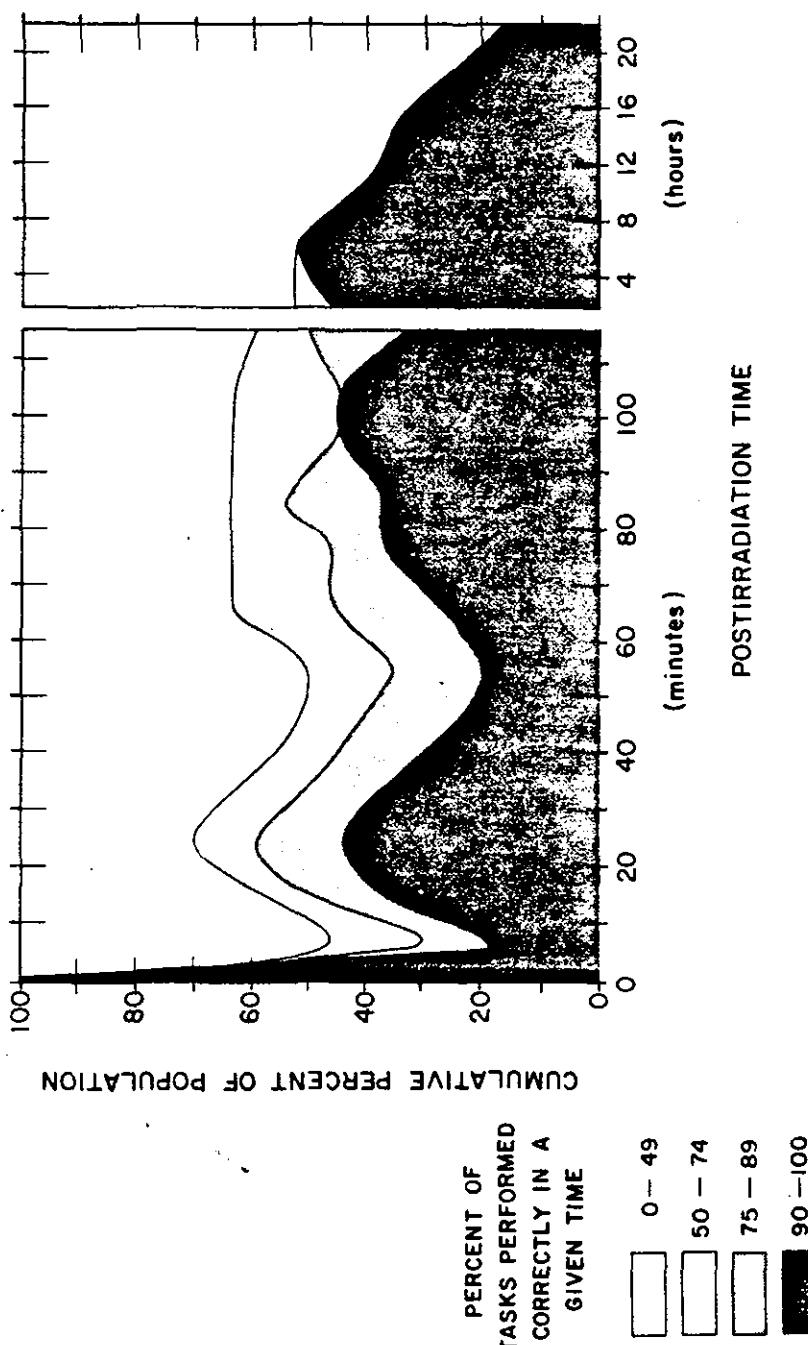


Figure 10-13. Personnel Effectiveness After Exposure to 7,000 rads

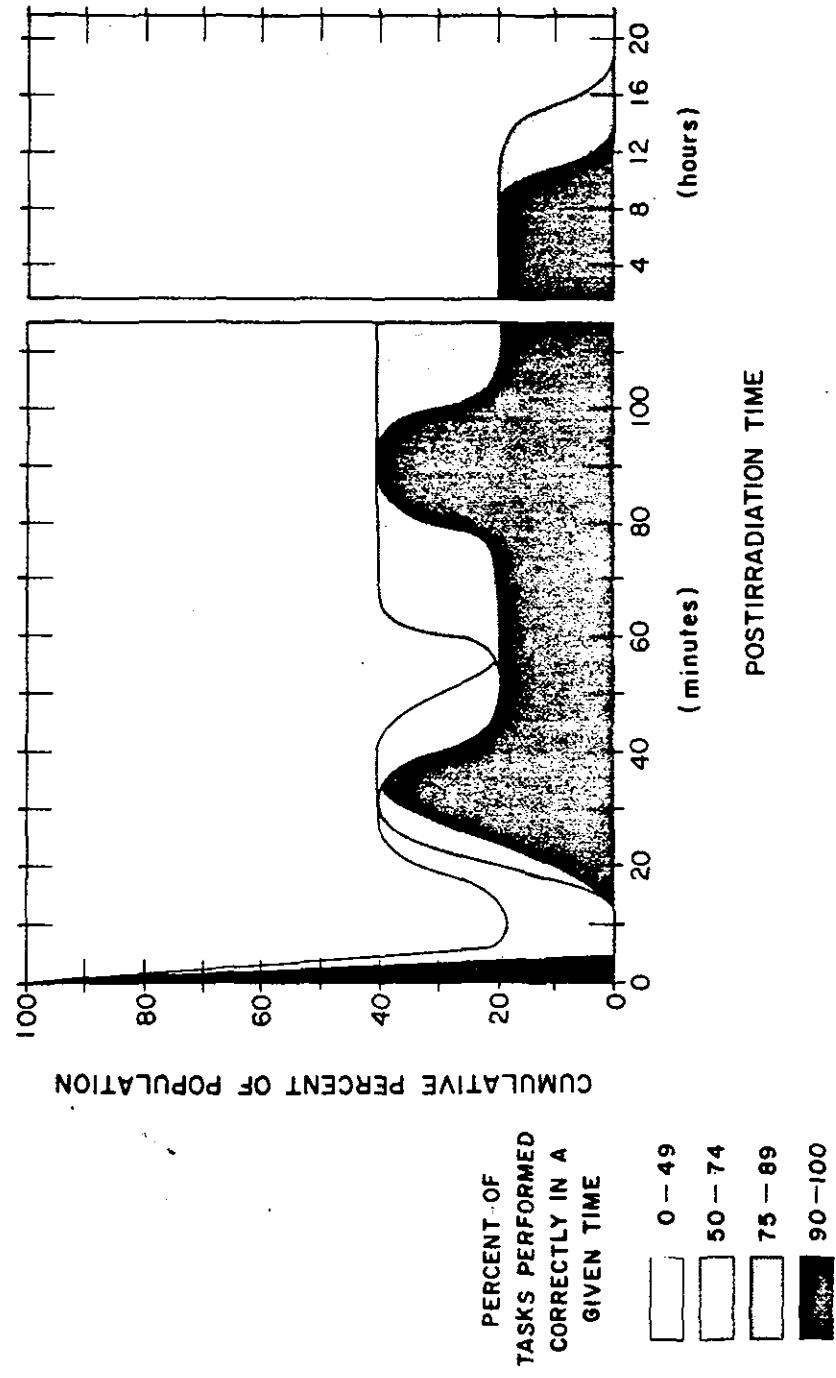


Figure 10-14. Personnel Effectiveness After Exposure to 13,000 rads

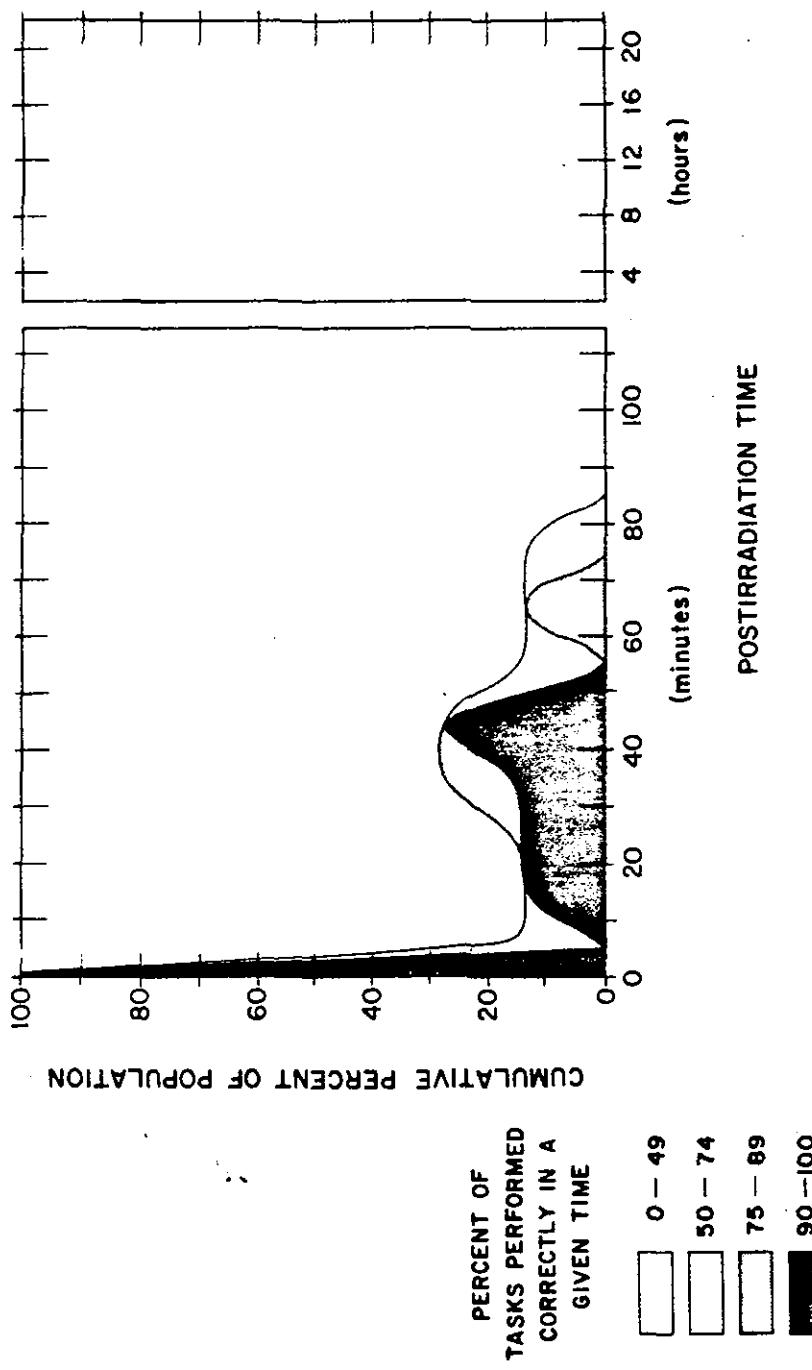


Figure 10-15. Personnel Effectiveness After Exposure to 22,000 rads

#### 10-28 Internal Hazards

Radioactive materials entering the body by inhalation, eating, or through wounds or breaks in the skin may be deposited in the body where alpha particles, beta particles or gamma rays continue to bombard adjacent tissues. Once fixed within the body, removal is almost impossible, except through natural processes. Effects of internal emitters usually become apparent after a period of years, so, while of not immediate concern insofar as personnel effectiveness is concerned, this deposition may eventually be of great concern to the individual.

Inhalation as a route of entry can be expected as the result of resuspension of radioactive materials from dust-producing activities, such as the operations of helicopter and fast-moving vehicles. Handling of contaminated equipment, supplies, and clothing may result in the hands becoming contaminated. The contamination then may enter the body while eating. Ingestion of contaminated foodstuffs and water supplies is another source of internal emitters.

#### 10-29 Modification of Injury

External residual radiation can be reduced by shielding, i.e., interposition of dense material between personnel and the source of radiation, as described previously for initial radiation. Protection is afforded to varying degrees by armored vehicles, foxholes, buildings and underground shelters. However, in a residual radiation environment, it is probable that radioactive materials will be brought into the protected areas as a result of their adherence to clothing, skin, hair, and equipment. Thus, to reduce exposure, it is necessary to decontaminate both the individual and his equipment. Additionally, as much time as is militarily feasible should be spent in protected environments while the residual radiation is decaying to lower levels. Decontamination of the outer surfaces of structures also will reduce the total dose to personnel.

If the outer packaging of foodstuffs is undamaged, they may be consumed without hazard, provided care is taken to insure that the food is not contaminated during removal of the protective covering. Cans should be washed before opening. Normal water filtration procedures will remove a majority of the fallout radioactive materials.

Treatment of individuals showing radiation sickness symptoms from exposure to residual radiation is similar to the treatment of sickness caused by initial radiation. Burns caused by prolonged contact of beta emitters with the skin can be reduced in severity, or prevented, by early removal of the fallout material. Burns which do occur respond to conventional methods of treatment for similar burns resulting from other causes.

Medical management of conditions arising at later times as a result of fixed internal emitters depends on the organ(s) in which the material is fixed, the number of demonstrated lesions, and the threat of this damage to life.

### SECTION IV

#### COMBINED INJURY

Thus far in this chapter little has been said about the possibility of personnel receiving multiple types of injury; however, such injuries probably would be a common occurrence in the advent of a nuclear war. Multiple injuries might be received nearly simultaneously (e.g., from exposure to a single detonation without fallout radiation) or separated in time by minutes to days (e.g., from exposure to a single detonation followed by fallout radiation, or exposure to multiple detonations). These injuries may consist of any combination of radiation, blast and thermal injuries from nuclear weapons as well as wounds from conventional weapons. Furthermore, such injuries may be influenced by other conditions that might be expected during or after a nuclear attack, such as malnutrition, poor

[REDACTED]  
sanitation, fatigue, and various other environmental factors. Since there are insufficient quantitative data to indicate the manner in which casualty production might be influenced by these latter factors, only combinations of pairs of the following three categories will be discussed in this section: (1) ionizing radiation injuries, (2) thermal injuries, and (3) mechanical injuries (e.g., injuries that result from blast effects).

[REDACTED] Most of our current knowledge concerning combined injuries is derived from studies of Japanese bomb victims in Hiroshima and Nagasaki and from laboratory and field test experiments involving a variety of animals. In Hiroshima and Nagasaki, 50 percent of the injured 20-day survivors within about 2,200 yards of ground zero received combined injuries whereas an incidence of 25 percent was observed in those located between 2,200 and 5,500 yards. The contribution of such injuries to overall mortality and morbidity has never been determined adequately, but two general impressions have emerged: the combination of mechanical and thermal injury was responsible for the majority of deaths that occurred within the first 48 hours; delayed mortality was higher and complications were more numerous among burned people who had received radiation than what would be anticipated in a burned population where no radiation exposure had occurred. It should be recognized that the stated incidences of combined injuries apply only to the conditions existing in the two Japanese cities at the time of attack and that the number and types of combined injuries are sensitive to yield, burst height, and conditions of exposure. Yields smaller than 10 kilotons probably would result in a significant number of casualties with combinations of prompt-radiation, thermal, and mechanical injuries. On the other hand, larger yields would be expected to result in a marked increase in the number of people with burns associated with mechanical injuries, and prompt-radiation injuries would be relatively insignificant in the

surviving population. A weapon detonated at a burst height where fallout is minimized would result in a large number of thermal and mechanical injuries, and, depending upon yield, might also produce a significant number of prompt-radiation injuries. A weapon detonated near (above or below) the surface would maximize the number of injuries due to fallout and would produce a large number of casualties where such injuries would be combined with mechanical and thermal trauma. Personnel outside and unshielded would have a greater likelihood of sustaining prompt and/or fallout radiation in combination with thermal burns than would be the case for personnel inside of any form of structure. In the latter case, thermal burns would be minimized, whereas combinations of mechanical and radiation injury might dominate.

[REDACTED] Combined injuries may result in synergistic effects, additive effects, or antienergistic effects. That is, the resultant response, whether measured as percent combat ineffectiveness (CI) or mortality, may be greater than, equal to, or less than what would be predicted based on the assumption that the various injuries act independently of one another in producing casualties. Quantitative data from laboratory experiments suggests that, in situations where a combined effect has been observed, the interaction of the various forms of trauma has resulted in enhanced delayed mortality, with little apparent effect on early mortality.

#### 10-30 Radiation and Thermal Injuries [REDACTED]

[REDACTED] Depending upon the radiation dose and the severity of burn, mortality has been found to increase by as much as a factor of six above that which might be expected from the two injuries administered singly. Thus, burns which serve as a portal of entry for infection may be considerably more hazardous to a person whose resistance to infection has been lowered by ioniz-

ing radiation. However, enhanced mortality has not been observed when low radiation doses have been administered in combination with minimal burn injuries. Very little information is available on fallout radiation in combination with thermal or any other form of injury.

#### 10-31 Mechanical and Radiation Injuries

Mechanical and radiation injuries can be expected to be frequent, particularly if fallout is present. Studies indicate that a delay in wound healing is observed with doses in excess of 300 rads, and that wounds in irradiated subjects are considerably more serious if treatment is delayed for more than 24 hours. In addition, missile and impact injuries that result in disruption of the skin and damage to the soft tissues would provide a portal of entry for infection, and thus may be extremely hazardous to irradiated people. Injuries that are associated with significant blood loss would be more serious in personnel who have received a radiation dose large enough to interfere with normal blood clotting mechanisms.

#### 10-32 Thermal and Mechanical Injuries

Burns and mechanical injuries in combination are often encountered in victims of conventional explosions and increased delayed complications, shorter times-to-death and enhanced mortality are frequent occurrences. However, little quantitative data are available on this form of combined injury.

#### CASUALTY CRITERIA

No reliable criteria for combat ineffectives are known for personnel receiving combined injuries. The available data do indicate, however, that individuals receiving combined injuries that occur nearly simultaneously are unlikely to become casualties within a few hours, provided the individual injuries would not produce casualties

if administered separately. Consequently, it is not unreasonable to make early casualty predictions for a single nuclear detonation on the basis of the most far-reaching effect. In regard to troop-casualty predictions, combined effects can be considered as a bonus, helping to assure the attainment of predicted CI levels, especially since there is a reasonable amount of uncertainty in the predictions for individual effects. If exposure exceeds any "minimal" risk level, that effect could contribute to combined injury and could result in increased casualties at later times. This becomes an important factor in terms of troop safety.

#### PERSONNEL IN THE OPEN

Figure 10-16 indicates expected burn levels, prompt ionizing-radiation doses, and peak translational velocities as functions of yield and ground distance for randomly-oriented, prone personnel exposed in the open. The curves were derived, assuming a visual range of 16 miles and a burst height such that the fireball would just touch the surface. This is the minimum height of burst which would result in negligible early, or local, fallout. The curves, which are presented for illustrative purposes only, form the limits of a band for each effect. These limits correspond to 50 percent early casualties and "minimal" early risk. The ionizing-radiation dose required to produce 50 percent CI within one hour, e.g., approximately 5,000 rads, is so large that it will result in 100 percent mortality within several days. For this reason, a 500-rad curve, which would correspond to approximately 50 percent mortality within 60 days, is included in Figure 10-16. Direct overpressure effects are not included in the figure since, except for eardrum rupture, which is not normally considered to produce CI, translational effects extend to greater ranges for all of the yields considered.

In the case of troop-casualty predictions, prompt-radiation predominates for yields less

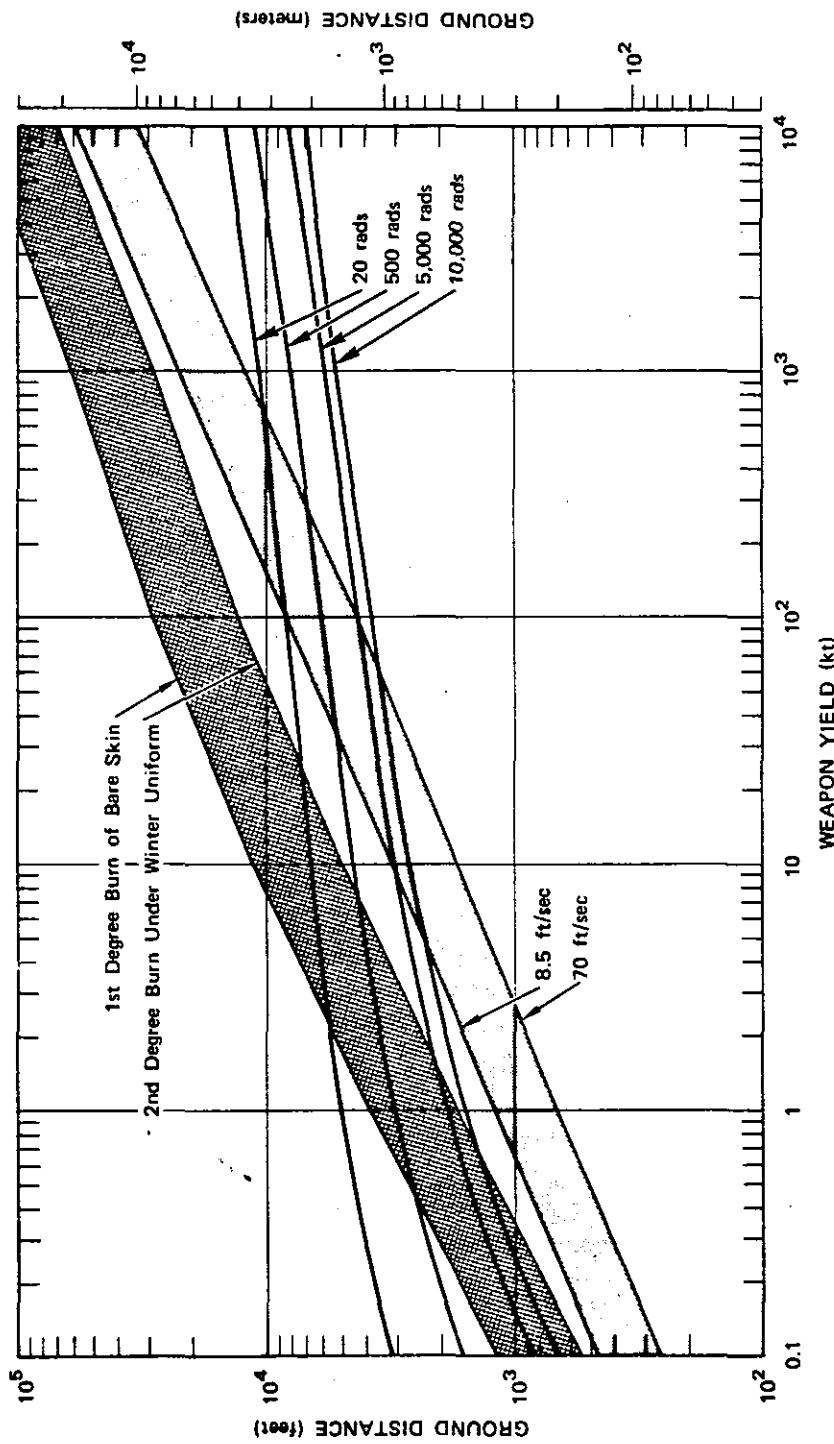


Figure 10-16. Comparison of Effects from Low Altitude Bursts

than 2 kt whereas thermal radiation is the most far-reaching hazard for yields greater than 2 kt. In situations where thermal exposure is neglected as a casualty-producing factor, ionizing radiation is the major effect in producing a 50 percent CI level for yields below 100 kt, while for larger yields, blast effects (translation) predominate.

With regard to troop safety, ionizing radiation is the major hazard below 1 kt, while thermal radiation predominates for larger yields. If the troops can be shielded adequately from the thermal pulse, ionizing radiation is the major hazard for yields up to 100 kt, above which blast effects are the most far-reaching hazard.

#### PERSONNEL IN STRUCTURES

In order to predict casualty levels for troops in situations other than open terrain, for example, inside armoured vehicles or field fortifications, the amount of nuclear radiation, thermal radiation, and blast shielding, as well as the degree of blast hardness of the surrounding materials must be taken into account for each geometry of exposure. As was the case for personnel in the open, casualty predictions must be made on the basis of the most far-reaching single effect rather than on the basis of combined effects. In general, for troops in structures, the major effect producing early casualties is likely to be ionizing radiation for small yields and blast effects for larger yields, with the cross-over point depending on the degree of hardness of the structure. While the hazards from thermal and ionizing radiation levels are reduced in a structure, the hazards from air blast may be magnified as a result of structural collapse, whole-body impact, and falling debris. This is particularly true for relatively soft structures at greater distances.

In the case of personnel in field fortifications, severe damage to the structure (Section VI, Chapter 9) should be taken as representative of 50 percent early CI from blast. Shielding fac-

tors (Section IV, Chapter 9) must be considered when estimating nuclear radiation responses of personnel in such structures.

#### TREATMENT

The triage and treatment of combined injuries present special problems, particularly if significant radiation exposure has occurred. Certain modifications in accepted medical and surgical practices must be considered since radiation exposure, depending upon dose, is known to increase susceptibility to infection, to decrease the efficiency of wound and fracture healing, to increase the likelihood of hemorrhage, to decrease tolerance to anesthetic agents, and to decrease the immune response.

It is imperative that primary closure of wounds be accomplished at the earliest possible time and that patients be treated with a broad spectrum antibiotic throughout the period of maximum bone marrow depression. Secondary closure of small soft-tissue wounds should be accomplished by the second or third day. Reparative surgery of an extensive nature should not be performed later than four to five days after injury since skin and soft-tissue healing should have occurred before the effects of ionizing radiation occur. If reparative surgery is not performed within this limited period of time, it must be postponed until the bone marrow has recovered (one to two months post-exposure). Wounds of injuries that require longer than three weeks for healing, such as severe burns and most fractures, should not be definitively treated until radiation recovery is evident. Although reconstructive surgery in the absence of radiation exposure might be performed within the second month or earlier after conventional trauma, it must be postponed for at least three months in instances where radiation exposure is a significant contributory factor. In all instances, extra precaution must be taken to avoid infection and blood loss.

[REDACTED] BIBLIOGRAPHY [REDACTED]

Allen, R. G., et al., *The Calculation of Retinal Burn and Flashblindness Safe Separation Distances*, U.S. Air Force School of Aerospace Medicine, Brooks Air Force Base, Texas, September 1968, SAM-TR-68-106 [REDACTED]

Anderson, R. S., F. W. Stemler, and E. B. Rogers, *Air Blast Studies with Animals*, Chemical Research and Development Laboratories, Army Chemical Center, Maryland, April 1961, DASA 1193 [REDACTED]

Behrens, C. F., *Atomic Medicine*, Williams & Wilkins, Baltimore, 1959. *Biological and Environmental Effects of Nuclear War*, Hearings before the Special Subcommittee on Radiation of the Joint Committee on Atomic Energy, Congress of the United States, June 1959. U.S. Government Printing Office, Washington, D.C. [REDACTED]

Blatz, H., *Radiation Hygiene Handbook*, McGraw-Hill Book Co., Inc., New York, 1959 [REDACTED]

Bowen, I. G., A. F. Strehler, and M. B. Wetherbe, *Distribution of Missiles from Nuclear Explosions*, Lovelace Foundation for Medical Education and Research, Albuquerque, New Mexico, December 1956, WT-1168 [REDACTED]

Bowen, I. G., et al., *Biophysical Mechanisms and Scaling Procedures Applicable in Assessing Responses of the Thorax Energized by Air-Blast Overpressures or Non-Penetrating Missiles*, Lovelace Foundation for Medical Education and Research, Albuquerque, New Mexico, November 1966, DASA 1857 [REDACTED]

Bowen, I. G., F. R. Fletcher, and D. R. Richmond, *Estimate of Man's Tolerance to the Direct Effects of Air Blast*, Lovelace Foundation for Medical Education and Research, Albuquerque, New Mexico, October 1968, DASA 2113 [REDACTED]

Bruce, M., *The Acute Radiation Syndrome: Y-12 Accident*, Oak Ridge Institute of Nuclear Studies, April 1959, ORINS-25 [REDACTED]

Bryant, F. J., et al., U.K. Atomic Energy Authority Report AERE HP/R 2353 (1957); *Sr90 in Diet*, Brit. Medical Journal, 1, 1371 (1958) [REDACTED]

Claus, W. D. (Ed.), *Radiation Biology and Medicine*, Addison-Wesley Publishing Co. Inc., Reading, Mass., 1958 [REDACTED]

Conard, R. A., et al., *Medical Survey of Rongelap People Five and Six Years After Exposure to Fallout*, Brookhaven National Laboratory, September 1960, BNL-609 [REDACTED]

Fletcher, E. R., et al., *Determination of Aerodynamic-Drag Parameters of Small Irregular Objects by Means of Drop Tests*, Lovelace Foundation for Medical Education and Research, Albuquerque, New Mexico, October 1961, CEX-59.14 [REDACTED]

Fletcher, E. R., and I. G. Bowen, *Blast Induced Translational Effects*, Lovelace Foundation for Medical Education and Research, Albuquerque, New Mexico, November 1966, DASA 1859 [REDACTED]

Gerstner, H. B., *Acute Radiation Syndrome in Man*, U.S. Armed Forces Medical Journal, 9, 313 (1958) [REDACTED]

Hayes, D. F., *A Summary of Accidents and Incidents Involving Radiation in Atomic Energy Activities*, TID-5360, August 1956; Supplement No. 1, August 1957; Supplement No. 2, September 1959. U.S. Atomic Energy Commission, Washington, D.C. [REDACTED]

Hirsch, F. G., *Effects of Overpressure on the Ear - A Review*, Lovelace Foundation for Medical Education and Research, Albuquerque, New Mexico, November 1966, DASA 1858 [REDACTED]

Kulp, J. L., A. R. Schulert, and E. J. Hodges, *Strontium-90 in Man IV*, Science, 132, 448 (1960) [REDACTED]

Lappin, P. W., and C. F. Adams, *Analysis of the First Thermal Pulse and Associated Eye Effects*, Aerospace Medical Research Laboratories, Wright Patterson Air Force Base, Ohio, December 1968, AM RL-TR-67-214 [REDACTED]

Loutit, J. F., and R. S. Russell, (Eds.), *The Entry of Fission Products into Food Chains*, Progress in Nuclear Energy, Series VI, Vol. 3, Pergamon Press, Inc., New York, 1961 [REDACTED]

Miller, R. W., *Delayed Radiation Effects in Atomic Bomb Survivors*, Science, 166, 569 (1969) [REDACTED]

National Academy of Sciences-National Research Council, *The Biological Effects of Atomic Radiation*, 1956; *Pathological Effects of Atomic Radiation*, Publication No. 452, 1961; *Long-Term Effects of Ionizing Radiations from External Sources*, Publication No. 849, 1961; *Effects of Ionizing Radiation on the Human Hematopoietic System*, Publication No. 875, 1961; *Effects of Inhaled Radioactive Particles*, Publication No. 848, 1961, Washington, D.C. [REDACTED]

National Council on Radiation Protection and Measurements, *Basic Radiation Protection Criteria*, NCRP Report No. 39, 1971, Washington, D.C. [REDACTED]

Oughterson, A. W., and S. Warren, *Medical Effects of the Atomic Bomb in Japan*, National Nuclear Energy Series VIII, McGraw-Hill Book Co., Inc., New York, 1956 [REDACTED]

Proceedings of the International Conferences on the Peaceful Uses of Atomic Energy, Geneva, *Biological Effects of Radiation*, Volume 11, 1956; Vol. 22, 1958; United Nations, New York [REDACTED]

[REDACTED]  
Richmond, D. R., I. G. Bowen, and C. S. White, *Tertiary Blast Effects: The Effects of Impact on Mice, etc.* Aerospace Medicine, 32, 789 (1961) [REDACTED]

Richmond, D. R., and C. S. White, *Biological Effects of Blast and Shock*, Lovelace Foundation and Research, Albuquerque, New Mexico, April 1966, DASA 1777 [REDACTED]

Richmond, D. R., et al., *The Relationship Between Selected Blast Wave Parameters and the Response of Mammals Exposed to Air Blast*, Lovelace Foundation for Medical Education and Research, Albuquerque, New Mexico, November 1966, DASA 1860 [REDACTED]

Symposium on Radioactive Fallout in Foods, *Agricultural and Food Chemistry*, 9, 90 (1961)  
[REDACTED]

United Nations General Assembly, *Report of the United Nations Scientific Committee on the Effects of Atomic Radiation*, UN A/3838 Suppl. 17, (13th Sess.) w/Annexes A through I, 1958, United Nations, New York [REDACTED]

Wald, N., and G. E. Toma, Jr., *Radiation Accidents through December 1958*, Oak Ridge National Laboratory, March 1961, ORNL-2748, Part B [REDACTED]

White, C. S., et al., *Comparative Nuclear Effects of Biomedical Interest*, Civil Effects Study, January 1961, CEX-58.8 [REDACTED]

White, C. S., and D. R. Richmond, *Blast Biology*, Lovelace Foundation for Medical Education and Research, September 1959, TID-5764 [REDACTED]

White, C. S., I. G. Bowen, and D. R. Richmond, *A Comparative Analysis of Some of the Immediate Environmental Effects at Hiroshima and Nagasaki*, Health Physics, Pergamon Press, 10, 89 (1964) [REDACTED]

White, C. S., *Tentative Biological Criteria for Assessing Potential Hazards from Nuclear Explosions*, Lovelace Foundation for Medical Education and Research, Albuquerque, New Mexico, December 1963, DASA 1462 [REDACTED]

White, C. S., *The Scope of Blast and Shock Biology and Problem Areas in Relating Physical and Biological Parameters*, Lovelace Foundation for Medical Education and Research, Albuquerque, New Mexico, November 1966, DASA 1856 [REDACTED]

White, C. S., *The Nature of Problems Involved in Estimating Immediate Casualties from Nuclear Explosions*, Lovelace Foundation for Medical Education and Research, Albuquerque, New Mexico, November 1968 [REDACTED]

White, C. S., I. G. Bowen, and D. R. Richmond, *The Environmental Medical Aspects of Nuclear Blast*, Lovelace Foundation for Medical Education and Research, Albuquerque, New Mexico, November 1962, DASA 1341 [REDACTED]

White, C. S., et al., *The Biodynamics of Air Blast*, Lovelace Foundation for Medical Education and Research, Albuquerque, New Mexico, July 1971, DNA 2738T [REDACTED]

Table C-2. [REDACTED] Median Vulnerability to Overpressures Corresponding to Severe  
Damage of Diffraction Sensitive Structures [REDACTED]

Weapon Yield	Type of Structure				
	11-2	11-3	11-4	11-5	11-6
(Median Vulnerability Overpressure, psi)					
30 mt	28	10	5.0	9.0	3.4
10 mt	29	10	5.0	9.0	3.4
3 mt	30	10	5.0	9.0	3.4
1 mt	30	11	5.0	9.0	3.5
300 kt	30	11	5.0	9.0	3.5
100 kt	32	11	5.0	9.5	3.5
30 kt	34	12	5.0	9.5	3.6
10 kt	34	13	5.5	10.0	3.6
3 kt	36	15	5.5	10.0	3.8
1 kt	48	17	5.5	11.0	4.0
0.1 kt	—	20	6.0	12.0	4.4
0.03 kt	—	22	6.5	12.0	4.8
0.01 kt	—	24	7.0	13.0	5.2
	—	28	7.5	14.0	5.8

**Table C-3. Median Vulnerability to Dynamic Pressures Corresponding to Severe Damage of Drag Sensitive Structures**

Weapon Yield	Type of Structure																
	11-7	11-8	11-9	11-10	11-11	11-12	11-13	11-14	11-15	11-16	11-17	11-18	11-19	11-20	11-21	11-22	11-23
(Median Vulnerability of Dynamic Pressure, psf)																	
30 mt	0.8	1.6	2.6	5.0	2.4	5.0	2.6	2.4	2.0	0.6	5.0	2.8	3.3	2.0	1.4	0.6	
10 mt	0.8	1.6	2.6	6.0	2.6	5.0	2.8	2.4	2.0	10.0	5.0	2.8	3.3	2.0	1.4	0.6	
3 mt	0.9	1.8	2.8	7.0	3.0	6.0	3.0	2.6	2.0	13.0	5.2	2.8	3.3	2.0	1.4	1.0	
1 mt	1.0	2.0	3.2	8.5	3.6	7.0	3.4	3.0	2.0	20.0	6.0	2.8	3.4	2.0	1.4	1.6	
300 kt	1.2	2.2	3.6	12.0	4.8	9.0	4.2	3.8	2.5	2.0	48.0	8.0	3.0	4.0	2.0	1.4	2.8
100 kt	1.4	2.6	4.4	18.0	6.0	11.0	5.2	5.0	3.0	2.2	12.0	3.4	5.2	2.2	1.4	4.5	
30 kt	2.0	3.6	5.8	34.0	10.0	16.0	7.0	10.0	4.0	2.6	—	20.0	4.0	10.0	2.6	1.4	7.5
10 kt	3.2	5.2	7.5	—	16.0	26.0	10.0	24.0	7.0	3.5	—	40.0	5.2	24.0	3.4	1.6	12.0
3 kt	5.4	7.5	12.0	—	36.0	—	18.0	—	15.0	5.0	—	—	7.0	—	4.6	2.0	20.0
1 kt	9.5	13.0	20.0	—	60.0	—	28.0	—	35.0	12.0	—	—	12.0	—	8.0	2.2	32.0
0.3 kt	18.0	26.0	38.0	—	—	—	—	—	—	—	—	22.0	—	18.0	—	3.0	55.0
0.1 kt	—	—	—	—	—	—	—	—	—	—	—	—	—	—	—	4.0	85.0
0.03 kt	—	—	—	—	—	—	—	—	—	—	—	—	—	—	—	6.0	—
0.01 kt	—	—	—	—	—	—	—	—	—	—	—	—	—	—	—	9.0	—

Table C-4. Median Vulnerability to Overpressures Corresponding to Moderate Damage of Diffraction Sensitive Structures

Weapon Yield	Type of Structure				
	11-2	11-3	11-4	11-5	11-6
(Median Vulnerability Overpressure, psi)					
30 mt	20	6.5	3.4	6.5	2.2
10 mt	20	6.5	3.4	6.5	2.2
3 mt	20	6.5	3.4	6.5	2.2
1 mt	20	6.5	3.4	6.5	2.2
300 kt	20	6.5	3.4	6.5	2.2
100 kt	20	7.0	3.4	6.5	2.2
30 kt	20	7.0	3.4	6.5	2.2
10 kt	20	7.0	3.6	6.5	2.2
3 kt	22	7.5	3.6	6.5	2.2
1 kt	24	8.0	3.6	6.5	2.2
0.3 kt	28	9.0	3.8	7.0	2.4
0.1 kt	-	10.0	4.0	7.5	2.6
0.03 kt	-	11.0	4.2	7.5	2.8
0.01 kt	-	12.0	4.4	8.0	3.0

**Table C-5. Median Vulnerability to Dynamic Pressures Corresponding to Moderate Damage of Drag Sensitive Structures**

Weapon Yield	Type of Structure																
	11-7	11-8	11-9	11-10	11-11	11-12	11-13	11-14	11-15	11-16	11-17	11-18	11-19	11-20	11-21	11-22	11-23
30 mt	0.6	1.2	2.0	3.4	1.6	3.6	2.0	2.4	2.0	2.0	9.6	5.0	2.8	3.2	2.0	1.4	0.2
10 mt	0.6	1.2	2.0	3.4	1.6	3.6	2.0	2.4	2.0	2.0	10.6	5.0	2.8	3.2	2.0	1.4	0.2
3 mt	0.6	1.2	2.0	3.4	1.6	3.6	2.0	2.4	2.0	2.0	12.0	5.2	2.8	3.2	2.0	1.4	0.4
1 mt	0.6	1.2	2.0	3.6	1.8	3.8	2.0	2.6	2.0	2.0	16.0	5.8	2.8	3.2	2.0	1.4	0.6
300 kt	0.6	1.2	2.0	4.0	2.0	4.0	2.2	2.8	2.0	2.0	26.0	7.4	2.8	3.4	2.0	1.4	1.0
100 kt	0.6	1.2	2.2	4.4	2.0	4.4	2.4	3.2	2.2	2.0	46.0	9.0	3.0	4.0	2.0	1.4	2.0
30 kt	0.6	1.4	2.4	5.4	2.4	5.2	2.6	4.0	2.8	2.2	88.0	14.0	3.4	5.0	2.2	1.4	3.0
10 kt	0.8	1.4	2.6	7.5	3.0	6.0	3.0	6.0	3.6	2.8	-	22.0	4.0	8.4	2.4	1.4	5.0
3 kt	0.8	1.6	3.2	12.0	4.4	9.0	3.6	12.0	6.4	4.2	-	40.0	5.4	18.0	3.4	1.6	8.0
1 kt	1.0	2.0	4.0	20.0	7.5	12.0	5.0	30.0	12.0	6.2	-	-	7.4	36.0	4.6	13.0	
0.3 kt	1.2	3.0	6.0	40.0	13.0	22.0	9.0	-	-	16.0	-	-	10.0	-	6.4	2.2	22.0
0.1 kt	2.2	5.0	10.0	-	20.0	-	-	-	-	-	-	-	15.0	-	14.0	2.6	60.0
0.03 kt	-	-	-	-	-	-	-	-	-	-	-	-	-	-	-	3.4	100.0
0.01 kt	-	-	-	-	-	-	-	-	-	-	-	-	-	-	-	4.2	-

## LIST OF ILLUSTRATIONS (Continued)

<i>Figure</i>	<i>Title</i>	<i>Page</i>
10-5	Distance Thresholds for Second Degree Burns for Various Evasion Times	10-16
10-6	Safe Separation Distances, for an Observer on the Ground, from Bursts at 10 kft and 50 kft During the Day	10-18
10-7	Safe Separation Distance, for an Observer at 50 kft, from Bursts at 10 kft and 50 kft During the Day	10-19
10-8	Safe Separation Distance, for an Observer on the Ground, from Bursts at 10 kft and 50 kft, During the Night	10-20
10-9	Safe Separation Distance, for an Observer at 50 kft, from Bursts at 10 kft and 50 kft, During the Night	10-21
10-10	Safe Separation Distance, for an Observer on the Ground, from Low Yield Weapons Exploded at 1,000 ft Height of Burst	10-22
10-11	Personnel Effectiveness After Exposure to 1,400 rads	10-26
10-12	Personnel Effectiveness After Exposure to 2,800 rads	10-27
10-13	Personnel Effectiveness After Exposure to 7,000 rads	10-28
10-14	Personnel Effectiveness After Exposure to 13,000 rads	10-29
10-15	Personnel Effectiveness After Exposure to 22,000 rads	10-30
10-16	Comparison of Effects from Low Altitude Bursts	10-34
11-1	Idealized Loading Functions	11-4
11-2	Isodamage Curves for Fifty Percent Probability of Severe Damage to Multistory Blast-Resistant Reinforced Concrete Buildings	11-16
11-3	Isodamage Curves for Fifty Percent Probability of Severe Damage to Multistory Reinforced Concrete Buildings with Concrete Walls, Small Window Area, Three to Eight Stories	11-17
11-4	Isodamage Curves for Fifty Percent Probability of Severe Damage to Multistory Wall Bearing Buildings, Brick Apartment House Type, up to Three Stories	11-18
11-5	Isodamage Curves for Fifty Percent Probability of Severe Damage to Multistory Wall Bearing Building, Monumental Type, up to Four Stories	11-19
11-6	Isodamage Curves for Fifty Percent Probability of Severe Damage to Wood Frame Buildings, House Type, One or Two Stories	11-20
11-7	Isodamage Curves for Fifty Percent Probability of Severe Damage to Light Steel Frame Industrial Buildings, Single Story, Frangible Walls, up to 5 Ton Crane Capacity	11-21
11-8	Isodamage Curves for Fifty Percent Probability of Severe Damage to Heavy Steel Frame Industrial Buildings, Single Story, Frangible Walls, 25 to 50 Ton Crane Capacity	11-22

## LIST OF ILLUSTRATIONS (Continued)

Figure	Title	Page
11-9	Isodamage Curves for Fifty Percent Probability of Severe Damage to Heavy Steel Frame Industrial Buildings, Single Story, Frangible Walls, 60 to 100 Ton Crane Capacity	11-23
11-10	Isodamage Curves for Fifty Percent Probability of Severe Damage to Multistory Steel Frame Office Type Buildings, 3- to 10-Stories, Frangible Walls, Earthquake Resistant Construction	11-24
11-11	Isodamage Curves for Fifty Percent Probability of Severe Damage to Multistory Steel Frame Office Type Buildings, 3- to 10-Stories, Frangible Walls, Non-Earthquake Resistant Construction	11-25
11-12	Isodamage Curves for Fifty Percent Probability of Severe Damage to Multistory Reinforced Concrete Frame Office Type Buildings, 3- to 10-Stories, Frangible Walls, Earthquake Resistant Construction	11-26
11-13	Isodamage Curves for Fifty Percent Probability of Severe Damage to Multistory Reinforced Concrete Frame Office Type Buildings, 3- to 10-Stories, Frangible Walls, Non-Earthquake Resistant Construction	11-27
11-14	Isodamage Curves for Fifty Percent Probability of Severe Damage to Four-Lane Highway Truss Bridges and Double Track Ballast Floor Railroad Truss Bridges, Span 200 ft to 400 ft	11-28
11-15	Isodamage Curves for Fifty Percent Probability of Severe Damage to Two-Lane Highway Truss Bridges, Spans 200 ft to 400 ft; Single Track Ballast Floors and Double Track Open Floor Railroad Truss Bridges, Spans 200 ft to 400 ft; and Single Track Open Floor Railroad Truss Bridges, Span 400 ft	11-29
11-16	Isodamage Curves for Fifty Percent Probability of Severe Damage to Single Track Open Floor Railroad Truss Bridges, Span 200 ft	11-30
11-17	Isodamage Curves for Fifty Percent Probability of Severe Damage to Four-Lane Through Highway Girder Bridges, Spans 75 ft	11-31
11-18	Isodamage Curves for Fifty Percent Probability of Severe Damage to Two-Lane Deck, Two-Lane Through, and Four-Lane Deck Highway Bridges, Spans 75 ft; Double Track Deck, Open or Ballast Floor Railroad Girder Bridges, Span 75 ft; Single or Double Track Through, Ballast Floor Railroad Girder Bridges, Spans 75 ft	11-32
11-19	Isodamage Curves for Fifty Percent Probability of Severe Damage to Single Track Deck, Open or Ballast Floor, and Single or Double Track Through, Open Floor Railroad Girder Bridges, Spans 75 ft	11-33
11-20	Isodamage Curves for Fifty Percent Probability of Severe Damage to Two-Lane Through and Four-Lane Deck or Through Highway Girder	

## LIST OF ILLUSTRATIONS (Continued)

<i>Figure</i>	<i>Title</i>	<i>Page</i>
	Bridges, Spans 200 ft; Double Track Deck or Through, Ballast Floor	
11-21	Railroad Girder Bridges, Spans 200 ft [REDACTED] .....	11-34
	[REDACTED] Isodamage Curves for Fifty Percent Probability of Severe Damage	
	to Two-Lane Deck Highway Girder Bridges, Spans 200 ft; Single Track	
	Deck or Through, Ballast Floor, and Double Track Deck or Through,	
11-22	Open Floor Railroad Girder Bridges, Spans 200 ft [REDACTED] .....	11-35
	[REDACTED] Isodamage Curves for Fifty Percent Probability of Severe Damage	
	to Single Track Deck or Through, Open Floor,	
11-23	Railroad Girder Bridges, Spans 200 ft [REDACTED] .....	11-36
	[REDACTED] Isodamage Curves for Fifty Percent Probability of Severe Damage	
	to Floating Bridges, U.S. Army Standard	
11-24	M-2 and M-4, Random Orientation [REDACTED] .....	11-37
	[REDACTED] Damage-Distance Reduction for Surface Structures	
	from 1 kt Bursts in Soil [REDACTED] .....	11-39
11-25	Depth of Cover Classification for Arches [REDACTED] .....	11-42
11-26	Buried Arches, Average Depth of Earth Cover [REDACTED] .....	11-43
11-27	Average Depth of Earth Cover for Buried Domes [REDACTED] .....	11-44
11-28	Configuration of Mounded Arches [REDACTED] .....	11-45
11-29	Correction for Attenuation with Depth [REDACTED] .....	11-71
11-30	Damage Pressure Level [REDACTED] .....	11-72
11-31	Correction for Arching [REDACTED] .....	11-73
11-32	Definition of Effective Pulse Duration [REDACTED] .....	11-74
11-33	Approximate Values of $J$ and $r_g$ for Common Shapes [REDACTED] .....	11-77
11-34a	Conditions for Moderate Damage by Impulsive Loading [REDACTED] .....	11-78
11-34b	Conditions for Heavy Damage by Impulsive Loading [REDACTED] .....	11-79
11-35	Resistance of Deeply Buried Horizontal Reinforced Concrete Arches [REDACTED] .....	11-80
11-35a	Arch Radius Versus Rise-Span Ratio [REDACTED] .....	11-81
11-35b	Correction Factor for Material Properties for Deeply Buried	
	Horizontal Reinforced Concrete Arches [REDACTED] .....	11-82
11-36	Resistance of Deeply Buried Horizontal Steel Arches [REDACTED] .....	11-83
11-37	Resistance of Deeply Buried Reinforced Concrete Domes [REDACTED] .....	11-84
11-37a	Dome Radius Versus Rise-Span Ratio [REDACTED] .....	11-85
11-37b	Correction Factor for Material Properties for Deeply Buried	
	Reinforced Concrete Domes [REDACTED] .....	11-86
11-38	Resistance of Horizontal One-Way Slabs [REDACTED] .....	11-87
11-39	Resistance of Horizontal Square Two-Way Slabs —	
	Restraint Edges [REDACTED] .....	11-88

## LIST OF ILLUSTRATIONS (Continued)

<i>Figure</i>	<i>Title</i>	<i>Page</i>
11-40	Resistance of Horizontal Square Two-Way Slabs — Two Adjacent Edges Supported	11-89
11-41	Aspect Ratio Correction Factor for Strength of Two-Way Slabs	11-90
11-42	Resistance of Horizontal Square Flat Slabs	11-91
11-42a	Aspect Ratio Correction Factor for Strength of Rectangular Flat Slabs	11-92
11-43	Radial Dead Load Soil Pressure on Vertical Cylinder	11-93
11-44	Interaction Diagram for Reinforced Concrete Beam — Columns	11-94
11-45	Basic Chart for Vulnerability of Tunnels in Rock	11-96
11-46	Vulnerability Criteria — Class A Equipment	11-101
11-47	Vulnerability Criteria for Personnel	11-102
11-48	Vulnerability Plot for Seismic Velocity ( $c_p$ ) of 1500 fps — Vertical Motion	11-105
11-49	Vulnerability Plot for Seismic Velocity ( $c_p$ ) of 5000 fps — Vertical Motion	11-106
11-50	Vulnerability Plot for Seismic Velocity ( $c_p$ ) of 15,000 fps — Vertical Motion	11-107
11-51	Shock Response Spectra and Vulnerability Calculation	11-108
11-52	Blast Resistance of Unprotected Floating and Conical-roof Tanks for 20 kt	11-114
11-53	Blast Resistance of Protected Floating and Conical-roof Tanks for 20 kt	11-115
11-54	Blast Resistance of Unprotected Floating and Conical-roof Tanks for 500 kt	11-116
11-55	Blast Resistance of Protected Floating and Conical-roof Tanks for 500 kt	11-117
11-56	Command Posts and Personnel Shelters (reference Table 11-13) — Damage by 1 kt as Function of Height of Burst and Ground Distance	11-126
11-57	Machine-gun Emplacements — Damage by 1 kt as a Function of Height of Burst and Ground Distance (reference Table 11-13)	11-124
11-58	Damage Levels to Foxholes and Trenches in Selected Soils Versus Overpressure Impulse	11-126
11-59	Ignition Thresholds for Newspaper	11-133
11-60	Graphical Summary of San Jose Study	11-135
11-61	Graphical Summary of New Orleans Study	11-137
11-62	Graphical Analysis of the Thermal and Blast Effects of Two Nuclear Bursts	11-142

## LIST OF ILLUSTRATIONS (Continued)

<i>Figure</i>	<i>Title</i>	<i>Page</i>
14-2	Target Response Modes [REDACTED] .....	14-5
14-3	Illustration of the Damage vs Distance Curve [REDACTED] .....	14-7
14-4	Damage to 1/4 Ton and 2-1/2 Ton Trucks, Side-On Orientation, as a Function of Ground Distance from a 1 kt Surface Burst [REDACTED] .....	14-8
14-5	Damage to U.S. 57-mm and U.K. 25-Pounder, Side-On Orientation, as a Function of Ground Distance from a 1 kt Surface Burst [REDACTED] .....	14-9
14-6	Damage to World War II and M38 1/4-Ton Trucks as a Function of Distance from a 1 kt Surface Burst [REDACTED] .....	14-10
14-7	[REDACTED] Illustration of the Effect of Target Orientation: Damage to World War II 1/4-Ton Trucks Oriented Side-On and End-On as a Function of Distance from a 1 kt Surface Burst [REDACTED] .....	14-11
14-8	The Effect of Shielding [REDACTED] .....	14-12
14-9	Effect of Weapon Yield on World War II 1/4-Ton Trucks Exposed Side-On in Shielded and Unshielded Conditions to Surface Explosions [REDACTED] .....	14-13
14-10	[REDACTED] Effect of Surface Condition on Damage Category Illustrated by Damage to 1/4-Ton Trucks Oriented Side-On to the Blast Wave from a 1 kt Surface Burst on Two Surfaces [REDACTED] .....	14-15
14-11	[REDACTED] Effect of Vehicle Status on the Distance for a Specified Damage Level from a 1 kt Surface Burst to U.S. 1/4-Ton Trucks (Brakes On, In Gear) and U.K. 1/4-Ton Trucks (Brakes Off, Out-of-Gear) Exposed in an End-On Orientation [REDACTED] .....	14-16
14-12	Peak Dynamic Pressure as a Function of Peak Overpressure [REDACTED] .....	14-26
14-13	[REDACTED] Damage to Wheeled Vehicles as a Function of Height of Burst (HOB) and Ground Distance (GD) for a 1 kt Explosion Over Nonideal and Near-Ideal Surfaces. The curves show HOB and GD at which there is a 50 percent probability that the item of equipment will experience at least the level of damage shown. NOTE: HOB scales as $W^{1/3}$ ; GD scales as $W^{0.4}$ [REDACTED] .....	14-37
14-14	[REDACTED] Damage to Artillery as a Function of Height of Burst (HOB) and Ground Distance (GD) for a 1 kt Explosion Over Nonideal and Near-Ideal Surfaces. The curves show HOB and GD at which there is a 50 percent probability that the item of equipment will experience at least the level of damage shown. NOTE: HOB scales as $W^{1/3}$ ; GD scales as $W^{0.4}$ [REDACTED] .....	14-38
14-15	[REDACTED] Damage to Tracked Vehicles (Except Tanks) and Engineer Heavy Equipment as a Function of Height of Burst (HOB) and Ground Distance	

## LIST OF ILLUSTRATIONS (Continued)

<i>Figure</i>	<i>Title</i>	<i>Page</i>
	(GD) for a 1 kt Explosion Over Nonideal and Near-Ideal Surfaces. The curves show HOB and GD at which there is a 50 percent probability that the item of equipment will experience at least the level of damage shown. NOTE: HOB scales as $W^{1/3}$ ; GD scales as $W^{0.4}$	14-39
14-16	Damage to <i>Tanks (Light and Heavy)</i> as a Function of Height of Burst (HOB) and Ground Distance (GD) for a 1 kt Explosion Over Nonideal and Near-Ideal Surfaces. The curves show HOB and GD at which there is a 50 percent probability that the item of equipment will experience at least the level of damage shown. NOTE: HOB scales as $W^{1/3}$ ; GD scales as $W^{0.4}$	14-40
14-17	Damage to <i>Small Arms</i> as a Function of Height of Burst (HOB) and Ground Distance (GD) for a 1 kt Explosion Over Nonideal and Near-Ideal Surfaces. The curves show HOB and GD at which there is a 50 percent probability that the item of equipment will experience at least the level of damage shown. NOTE: HOB scales as $W^{1/3}$ ; GD scales as $W^{0.4}$	14-41
14-18	Damage to <i>Generators</i> as a Function of Height of Burst (HOB) and Ground Distance (GD) for a 1 kt Explosion Over Nonideal and Near-Ideal Surfaces. The curves show HOB and GD at which there is a 50 percent probability that the item of equipment will experience at least the level of damage shown. NOTE: HOB scales as $W^{1/3}$ ; GD scales as $W^{0.4}$	14-42
14-19	Damage to <i>Locomotives</i> as a Function of Height of Burst (HOB) and Ground Distance (GD) for a 1 kt Explosion Over both Nonideal and Near-Ideal Surfaces. The curves show HOB and GD at which there is a 50 percent probability that the item of equipment will experience at least the level of damage shown. NOTE: HOB scales as $W^{1/3}$ ; GD scales as $W^{0.4}$	14-43
14-20	Damage to <i>Box Cars</i> as a Function of Height of Burst (HOB) and Ground Distance (GD) for a 1 kt Explosion Over both Nonideal and Near-Ideal Surfaces. The curves show HOB and GD at which there is a 50 percent probability that the item of equipment will experience at least the level of damage shown. NOTE: HOB scales as $W^{1/3}$ ; GD scales as $W^{0.4}$	14-44
14-21	Damage to <i>Supply Dumps</i> as a Function of Height of Burst (HOB) and Ground Distance (GD) for a 1 kt Explosion Over both Nonideal and Near-Ideal Surfaces. The curves show HOB and GD at which there is the indicated probability that the dump will experience at least the level of damage shown. NOTE: HOB scales as $W^{1/3}$ ; GD scales as $W^{0.4}$	14-45
14-22	Damage to <i>Telephone Poles</i> as a Function of Height of Burst (HOB) and Ground Distance (GD) for a 1 kt Explosion Over both Nonideal and	

## LIST OF ILLUSTRATIONS (Continued)

<i>Figure</i>	<i>Title</i>	<i>Page</i>
	Near-Ideal Surfaces. The curves show HOB and GD at which there is a 50 percent probability that the item of equipment will experience at least the level of damage shown. NOTE: HOB scales as $W^{1/3}$ ; GD scales as $W^{1/3}$ [REDACTED]	14-46
14-23	[REDACTED] Damage to Water Storage Equipment as a Function of Height of Burst (HOB) and Ground Distance (GD) for a 1 kt Explosion Over Nonideal and Near-Ideal Surfaces. The curves show HOB and GD at which there is a 50 percent probability that the item of equipment will experience at least the level of damage shown. NOTE: HOB scales as $W^{1/3}$ ; GD scales as $W^{1/3}$ [REDACTED]	14-47
14-24	[REDACTED] Damage to Shielded Wheeled Vehicles as a Function of Height of Burst (HOB) and Ground Distance (GD) for a 1 kt Explosion Over both Nonideal and Near-Ideal Surfaces. The curves show HOB and GD at which there is a 50 percent probability that the item of equipment will experience at least the level of damage shown. NOTE: HOB scales as $W^{1/3}$ ; GD scales as $W^{1/3}$ [REDACTED]	14-48
14-25	[REDACTED] Damage to Shielded Engineer Heavy Equipment as a Function of Height of Burst (HOB) and Ground Distance (GD) for a 1 kt Explosion Over both Nonideal and Near-Ideal Surfaces. The curves show HOB and GD at which there is a 50 percent probability that the item of equipment will experience at least the level of damage shown. NOTE: HOB scales as $W^{1/3}$ ; GD scales as $W^{1/3}$ [REDACTED]	14-49
14-26	[REDACTED] Damage to Signal, Electronic Fire Control Equipment, Antennas and Rigid Radomes as a Function of Height of Burst (HOB) and Ground Distance (GD) for a 1 kt Explosion Over Nonideal and Near-Ideal Surfaces. The curves show HOB and GD at which there is the indicated probability that the item of equipment will experience at least the level of damage shown. NOTE: HOB scales as $W^{1/3}$ ; GD scales as $W^{0.4}$ except for Radomes. For Radomes use $W^{1/3}$ [REDACTED]	14-50
14-27	[REDACTED] Damage to Wire Entanglements as a Function of Height of Burst (HOB) and Ground Distance (GD) for a 1 kt Explosion Over Nonideal and Near-Ideal Surfaces. The curves show HOB and GD at which there is a 50 percent probability that the item of equipment will experience at least the level of damage shown. NOTE: HOB scales as $W^{1/3}$ for yields < 1 kt, $W^{0.4}$ for yields > 1 kt [REDACTED]	14-51
15-1	[REDACTED] Light Damage to Various Broadleaf Forest Types [REDACTED]	15-7
15-2	[REDACTED] Moderate Damage to a Type I Forest [REDACTED]	15-8
15-3	[REDACTED] Severe Damage to a Type I Forest [REDACTED]	15-9
15-4	[REDACTED] Total Damage to a Type I Forest [REDACTED]	15-10
15-5	[REDACTED] Moderate Damage to a Type II Forest [REDACTED]	15-11

DTIC  
SELECTED  
S 2 MAR 1989 D

## Chapter 12

# MECHANICAL DAMAGE DISTANCES FOR SURFACE SHIPS AND SUBMARINES SUBJECTED TO NUCLEAR EXPLOSIONS

### INTRODUCTION

#### 12-1 Damage Mechanisms

An air burst nuclear weapon may cause mechanical damage to surface ships by air burst, thermal radiation, ionizing radiation, and the electromagnetic pulse. Ship operations may also be affected by personnel casualties; however, only mechanical damage is considered in this chapter.

An underwater burst may cause damage to surface ships by the shock wave in the water, by the water column or plumes thrown up by the burst, by the surface gravity waves produced, or by the ionizing radiation from the base surge, fallout, or contaminated water pool. As for an air burst, the ship status may be affected by personnel casualties; however, only mechanical damage is considered in this chapter.

An underwater burst may cause damage to submerged submarines by the shock wave in the water, and, in special shallow water cases, by collision with the ocean bottom induced by the waves.

#### 12-2 Damage Classification

Damage to surface ships and submarines is described by the degree of impairment of three major ship capabilities: seaworthiness, mobility, and weapon delivery. Complete loss of a capability is characterized as 100-percent impairment; no impairment is considered 0 percent. Levels of impairment of 90 percent and 10 percent are intended to signify nearly complete and slight impairment, respectively. These degrees of impairment should be interpreted as being the midpoints of a band of percent impairments.

The concept of degree of capability im-

pairment is closely related to the fact that, for any given burst condition, a continuous spectrum of degrees of damage would be inflicted on ships of the same type located over a continuous spread of ranges from the burst. A ship is so complex a system that it is not possible to predict damage precisely for any given attack situation. Another consideration is that the crew of a damaged ship will attempt to repair damage; i.e., to decrease the degree of impairment of capability as quickly as possible. The time consumed by such repair is a vital aspect of the total damage assessment, but available knowledge does not justify an attempt to consider it in detail.

Damage ranges are given in this chapter in terms of zones within which varying degrees of impairment of each capability are to be expected. The outer boundary of a given zone corresponds to slight, and possibly temporary, impairment of the indicated capability; the inner boundary corresponds to nearly complete impairment that would require shipyard facilities for repair. The locations of the boundaries are determined by damage criteria derived from experimental data. There are, however, uncertainties involved as a result of a lack of sufficient experimental data. It is estimated that uncertainties concerning damage criteria cause uncertainties in the boundary locations on the order of 15 to 30 percent.

#### 12-3 Seaworthiness Impairment

The degrees of seaworthiness impairment are defined as follows:

- 100 percent: The ship or submarine is sunk.
- 90 percent: The ship is in danger of sinking,

capsizing, or breaking up as a result of widespread, uncontrollable flooding or the loss of girder strength. Danger is present even in normal weather, but there is some chance of saving the ship. As a result of damage to its structure or to its buoyancy-control gear, a submarine will be in danger of settling to the bottom.

- 10 percent: Slight plastic deformation of the structure that may cause minor leakage. Hogging or sagging, or topside structural damage can occur, but not to an extent sufficient to endanger the ship in stormy weather. For submarines, this degree of impairment includes that damage that can at worst reduce the maximum safe diving depth slightly, but otherwise allows the submarine to submerge in a controlled manner.
- 0 percent: No plastic deformation of structure and no leakage.

#### 12-4 Mobility Impairment

The degrees of mobility impairment are defined as follows:

- 100 percent: The ship or submarine lacks any ability to operate its propulsion devices.
- 90 percent: The ship can at best just barely maintain steerageway in a desired direction, either as a result of damage to main propulsion machinery and control gear, or as a result of personnel casualties.
- 10 percent: Slight loss of ability to achieve top speed and/or to maneuver normally, as a result of damage or personnel casualties.
- 0 percent: No impairment of mobility.

#### 12-5 Weapon Delivery Impairment

The degrees of weapon delivery impairment are defined as follows:

- 100 percent: The ship or submarine cannot release its weapons.
- 90 percent: Weapons can be released, but it

is almost impossible to deliver them effectively because the ship's target-acquisition and communication equipment are inoperative, either as a result of damage to equipment or to topside structure, or as a result of personnel casualties.

- 10 percent: Slight reduction in weapon-delivery efficiency as a result of damage to equipment or topside-structure or as a result of personnel casualties.
- 0 percent: No loss.

### SECTION I

#### DAMAGE TO SURFACE SHIPS FROM AIR BURSTS

##### BLAST DAMAGE

###### 12-6 General

Air blast damage may be significant for surface ships when the burst is at or above the water surface. The following general description of air blast effects on ships is applicable to existing Navy ships.

At close ranges, air blast can cause hull rupture that can result in flooding and sinking. Hull rupture appears likely to begin near the waterline on the side facing the blast. The main hull of existing Navy ships is, however, stronger than the superstructure and equipment. At ranges beyond those at which hull rupture is likely to occur the main effect of air blast is to distort, rupture, or carry away light structures and equipment vulnerably exposed above the waterline, and to cause casualties among topside personnel. Such damage can cause complete impairment of the weapon delivery capability. Blast pressures penetrating through weather openings of ventilation systems and stack-uptake systems can cause damage to interior equipment and compartments, and also to boilers; the latter may result in immobilization. The distortion of weather bulkheads may cause fracture or render interior equip-

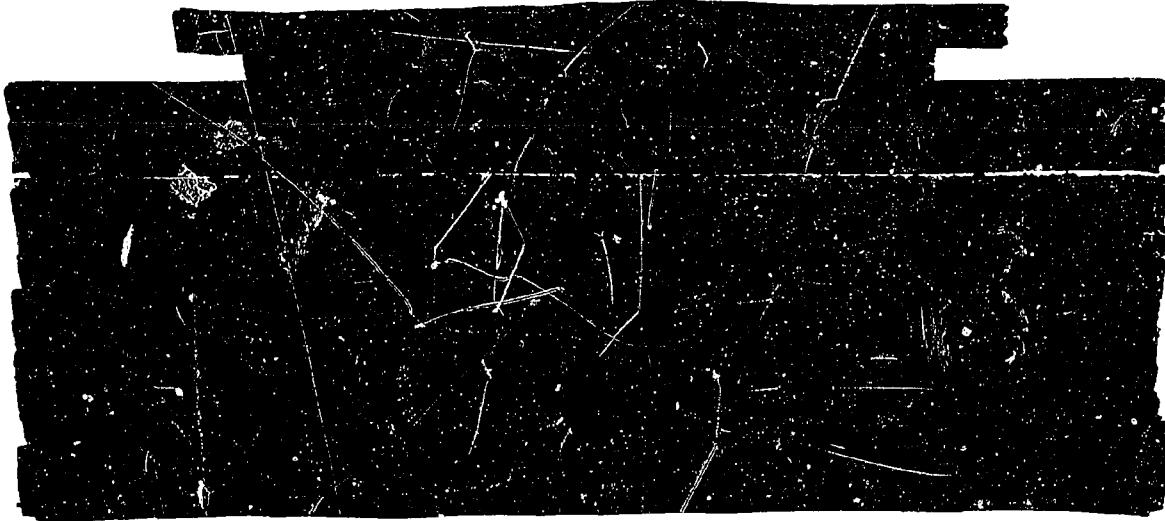
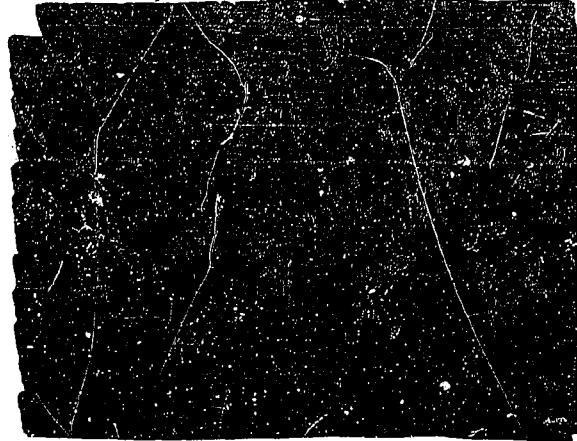
ment mounted on or near them useless. Similarly, the suddenly applied blast loading induces rapid motion of the structures that in turn may cause shock damage to interior equipment. Equipment in the superstructure is most vulnerable to these types of damage, although shock motions may be felt throughout the ship. Air blast also may cause the ship to roll and possibly capsize; this effect is most pronounced for broadside attack by large weapons (multimegaton).

#### 12-7 Damage Criteria

Peak overpressure is used as the sole parameter to describe attack severity, except for the capsizing effect. This criterion is acceptable for most existing surface ship structures, since the effects of the blast wave are practically independent (within predictive accuracies) of the blast wave duration, i.e., weapon yield, for weapons larger than a certain size. Mechanical damage criteria in terms of peak overpressure for some existing Navy ships are given in Table 12-1. The estimates shown in Table 12-1 are derived from CROSSROADS ABLE and SAILOR HAT data, as well as from some structural analyses.

#### 12-8 Damage Distances

Distances at which damage is expected to occur from a 1-Mt air burst are shown in Figure 12-1. The curves define zones in which impairment of a stated capability occurs. The outer boundary of the zone indicates slight (10 percent) impairment; the inner boundary indicates almost complete (90 percent) impairment. At distances beyond the outer boundary of a zone there is essentially no impairment of the stated capability. At ranges within the inner boundary of a zone the impairment is essentially complete.



## 12-9 Capsizing from Blast

Figure 12-2 shows estimates of ranges for capsizing various types of ships as a result of air blast from surface bursts. The distances are shown as functions of weapon yield, since cube-root scaling does not apply. The estimates are based on theoretical calculations alone, since experimental data are not available on capsizing. The width of the bands in Figure 12-2 corresponds to the difference between two sets of theoretical calculations. The ranges are valid for broadside attack only. Air blast will not capsize a ship in a fore-and-aft attack direction. For an attack direction of 45 degrees off the bow or stern, it is roughly estimated that capsizing ranges are 5 to 10 percent smaller. The capsizing distances from an air burst may be greater than those shown for a surface burst in Figure 12-2. For a given yield the increase in range can be determined approximately by assuming that the capsizing overpressure is independent of burst height (within the Mach region), and then by referring to curves of range versus height of burst for constant overpressures (see Section I, Chapter 2).

## DAMAGE FROM OTHER AIR BURST PHENOMENA

### 12-10 Thermal Radiation

Material exposed to thermal radiation may be charred, scorched, ignited, melted, or otherwise changed. In addition, the heat may affect the mechanical properties of structural metals by annealing (reduction of strength). The rapid rate of delivery of thermal energy may induce large temperature gradients, and the resulting thermal stresses may produce effects such as surface spalling or cracking, and/or permanent distortions of structures or structural elements. Weakening of structural elements may cause weapon system and superstructure components to be more vulnerable to the air blast, which

arrives after most of the thermal exposure has been received. Distortion of radar antennas and other superstructure components may cause functional impairment.

Thermal radiation can affect only the exposed topside personnel and material of a surface ship. Any opaque object along the fireball-to-target line of sight will furnish protection from thermal radiation. Topside personnel or material in the shadow or the ship's structural or topside gear would be shielded from thermal radiation.

Fires are not likely to originate except perhaps when severe, and probably overriding, blast damage is also sustained. Normally there is insufficient combustible material topside on combatant ships to sustain fire. Possible exceptions may be vessels carrying inflammable liquids, which may spill as a result of the blast (aircraft carriers), and vessels carrying combustible deck loads (cargo ships). Water washdown systems, installed primarily for protection against deposited radioactive debris, should reduce fire hazards and thermal radiation damage, provided they are turned on prior to the burst.

The main steel hulls of naval ships are not likely to be weakened by thermal radiation, except when severe, and probably overriding, blast damage is also sustained. Of the metallic components in use on present ships, those made of aluminum may be most susceptible to thermal radiation effects (annealing, melting). The effect will be greatest on thin aluminum components. Aluminum plates of alloy 5456-H321 less than 5/16 inch in thicknesses may suffer more than 50-percent loss of strength prior to the arrival of the blast at the 10-psi range from a 1-Mt burst. Lightweight aluminum-alloy components, which have been used extensively in radar antennas as support members, reflector elements, and wave guides, appear to be susceptible to melting, sagging, and buckling when exposed to free-field thermal radiation at the 10 psi overpressure

## BIBLIOGRAPHY

Hansen, I. S., *Handbook of Underwater Nuclear Explosions, Part II - Effects, Chapter 2 - Surface Ship Structural Response and Damage Development - Section 2.2 - The Effects of Air Blast* [REDACTED] DASA 1240 (2.2), David Taylor Model Basin Report C-2023, August 1965 [REDACTED]

Hansen, I. S., *Handbook of Underwater Nuclear Explosions, Part II - Effects, Chapter 3 - Surface Ship Equipment, Section 3.2 - The Effects of Air Blast on Surface Ship Equipment* [REDACTED] DASA 1240 II (3.2), David Taylor Model Basin Report C-2096, October 1965 [REDACTED]

Hansen, I. S., *Weapon Delivery Impairment Ranges for DLG-16 and DDG-2 Class Ships Subjected to Air Blast - Preliminary SAILOR HAT Results* [REDACTED] Proceedings, DASA Conference on SAILOR HAT, DASA 1775, p. 190, May 1966 [REDACTED]

Hirsch, A. E., *Handbook of Underwater Nuclear Explosions, Part II - Effects, Chapter 8 - Marine Personnel Casualties, Section 8.1 - Underwater Shock Effects* [REDACTED] DASA-1240 II (8.1), David Taylor Model Basin Report C-2148, January 1966 [REDACTED]

Irick, J. T., S. Silverman, and W. E. Baker, *The Rigid-Body Response of Naval Surface Vessels to Air Blast* [REDACTED] Final Report, Southwest Research Institute, prepared for Naval Ship Research and Development Center, September 1967 [REDACTED]

Manny, P. A., *Damage Criteria for Naval Ships and Submarines Subjected to Nuclear Explosions* [REDACTED] Naval Ship Research and Development Center (in preparation) [REDACTED]

Murray, W. W., *Engineering Predictions of the Early Bodily Response of Submarines to Underwater Explosion Attacks*, Underwater Explosions Research Division, Norfolk Naval Shipyard, Portsmouth, Va., UERD Report 7-58, October 1958.

Murray, W. W., *Ship Damage Classification and Prediction Methods* [REDACTED] David Taylor Model Basin Report C-1230, September 1961 [REDACTED]

Murray, W. W., *Loading and Response of Surface-Ship Hull Structures from Underwater Bursts* [REDACTED] Project 3.4, Operation HARDTACK, WT-1628, December 1961 [REDACTED]

Murray, W. W., and R. M. Santamaria, *Handbook of Underwater Nuclear Explosions, Part II - Effects, Chapter 2 - Surface Ship Structural Response and Damage Development, Section 2.1 - The Effects of Underwater Phenomena* [REDACTED] DASA 1240-II (2.1), David Taylor Model Basin Report C-2261, December 1966 [REDACTED]

Parnell, U. C., and H. M. Schauer, *Handbook of Underwater Nuclear Explosions, Part II - Effects, Chapter 6 - Submarine Hull Response and Damage Development*, DASA 1240 II (6), David Taylor Model Basin Report C-2188, June 1966

Rich, H. L., et al., *Shock Loading in Ships from Underwater Bursts and Response of Shipboard Equipment*, Project 3.3, Operation HARDTACK, WT-1627, September 1959

Shridar, P. W., *The Interaction of Surface Ships with the Thermal and Radiological Environment*, Chapter IV of DASA Handbook of Underwater Nuclear Explosions, Part II, Effects, DASA 1240-II (4), U.S. Naval Radiological Defense Laboratory Report USNRDL-475, January 1964

Weinberger, F., and R. M. Santamaria, *Mechanical Damage Ranges for Surface Ships and Submarines Subjected to Nuclear Underwater and Air Bursts*, David Taylor Model Basin, Report C-1323, November 1961

Zagorites, H. A., and R. L. Hopton, *Survey of the EMP in Shipboard Systems*, U.S. Naval Radiological Defense Laboratory Report USNRDL-LR-190, July 1966

PAGE 12-32 INTENTIONALLY  
LEFT BLANK

## Chapter 13

### DAMAGE TO AIRCRAFT

#### INTRODUCTION

This chapter treats the damage to aircraft that results from the environment produced by the air blast wave and the thermal radiation from a nuclear explosion. The effects of nuclear radiation on electronic components and circuits are discussed in Section VII, Chapter 9, and some general vulnerability estimates for electronic systems in aircraft are given in Section IV, Chapter 14.

Section I of this chapter describes the blast and thermal effects on aircraft in general terms. Section II describes the response of the aircraft to the various categories of effects, largely in the form of illustrative problems, most of which contain numerical examples. Both in-flight and parked aircraft are considered.

A wide range of test data and a variety of analytical methods have been accumulated over the years to predict both the safe delivery of nuclear weapons and aircraft kill. Criteria for safety and for kill also have been developed; however, all of the aspects of the problems have not been treated in equal depth. The range of available methods that have been developed vary from relatively simple techniques to complex analyses requiring large, high-speed digital computers to obtain the solution. Unfortunately, there is very little information available concerning the relative accuracy and reliability of the various methods.

The discussion provided herein attempts to provide a clear description of the overall problem of aircraft exposed to blast and thermal effects of nuclear explosions. This description provides a means for those who are concerned

with, but who do not have an extensive technical background in this area, to obtain an appreciation of the effects and to obtain first order approximations for the problems of aircraft safety and kill. A comprehensive review of a large body of data pertinent to vulnerability and safety analyses of aircraft subjected to the effects of nuclear explosions is contained in "Handbook for Analysis of Nuclear Effects on Aircraft (U)," DASA 2048 (see bibliography). As shown in DASA 2048, assessment of damage to aircraft is a strong function of the detailed characteristics of the specific aircraft of interest. Thus, it is impossible to provide a simple, short method to determine vulnerability in a general manner. DASA 2048 provides several methods for analyzing various classes of aircraft, arranged in order of increasing complexity. The simplest method described in DASA 2048 for each class of aircraft was selected to illustrate the analysis of that class of aircraft in Section II of this chapter. A brief abstract of DASA 2048, including a methodology matrix, is contained in Appendix D of this manual.

The term aircraft, as used in this chapter, applies to both airplanes and helicopters. Where differentiation between the two types of aircraft is intentional, the terms airplane and helicopter are used.

#### SECTION I

#### BLAST AND THERMAL EFFECTS ON AIRCRAFT

The problem of determining the effects of nuclear weapon explosions on aircraft has been recognized since the development of the

first nuclear weapons during the mid 1940s. For many years, aircraft represented the only means of delivering nuclear weapons to their targets; hence, it was natural to investigate the capabilities of aircraft with respect to delivering nuclear weapons. Nuclear weapons posed new and vital questions to military planners. Previously, when considering the delivery of conventional bombs by aircraft, the limitations on the capabilities of the aircraft were imposed by factors such as the range and payload of the aircraft and enemy defensive actions. With the emergence of nuclear weapons, a new factor was imposed. The energy output of these new weapons was so great that the delivery aircraft was in danger of being damaged by the explosion of the weapon it had delivered.

Subsequently, military planners became interested in the effects of a nuclear explosion on parked aircraft. Early efforts to understand this problem were largely experimental.

Finally, the possibility of nuclear anti-aircraft weapons prompted analysis of the conditions under which an aircraft could be killed by the effects of nuclear weapons. Thus, the complete gamut of nuclear weapon effects on aircraft is of interest, from sure-safe conditions to sure-kill conditions, for both in-flight and parked aircraft.

This section provides background concerning nuclear weapon blast and thermal effects on aircraft, discusses the type, scope and format of the methods of weapon effects analysis presented in Section II, and explains how the results of the analyses may be used together with prescribed criteria to obtain either sure-safe or sure-kill regions for aircraft exposed to blast and thermal effects.

### 13-1 Sure-Safe and Sure-Kill Envelopes

The terms "sure-safe" and "sure-kill" are self explanatory with respect to their general meaning; however, the terms must be examined

more explicitly to provide a basis for understanding the analyses that are described in succeeding paragraphs. If the response of an aircraft to one of the effects of nuclear weapons is known, this response must be compared to some criterion to determine whether the aircraft is "safe" or "killed." For example, the aircraft may be termed safe with respect to that weapon effect as long as the particular weapon effect does not degrade the performance of the aircraft or crew in any way. The specification of a sure-kill, or lethal, criterion is more complex, because it is difficult to define the amount of response that will result in a sure-kill. The response must be sufficient to produce some kind of damage to the aircraft or crew. It could be stated that a sure-kill manifests itself by virtually "immediate loss" of the aircraft, but the relation of immediate loss to an amount of damage is difficult. Although some effort has been devoted to this problem, it still remains a major source of error in determining sure-kill conditions. The best available lethal criteria, with the sample response prediction methods, are presented in Section II.

If both response prediction methods and criteria that relate response to sure-safe and sure-kill conditions are available, the particular geometry that defines the relative positions of the nuclear explosion and the aircraft must be defined. The direction and flight path of the aircraft is an important part of the geometry. Two terms, "orientation" and "range," must be defined. For example, if the aircraft were directly above the burst and in straight and level flight, the orientation would be completely defined; however, the distance between the burst and the aircraft, which is range, would not be defined. The complete geometry of the problem, at the time of burst, is described by giving the range and the orientation.

For a specified orientation and range, the aircraft response to some nuclear effect can be determined. This response can be compared



to the maximum response to that effect that can be tolerated without degradation of the performance of the aircraft or crew, i.e., the criterion for sure-safe response. If the calculated response is less than the sure-safe criterion, the aircraft is safe for that range and orientation. Since weapon effects, and hence aircraft response to weapon effects, decrease with increasing range, a shorter range at the same orientation must be considered to find the range at which the calculated response matches the sure-safe criterion. When this range, which is called the sure-safe range, is determined, this range and the orientation assumed define a point on a sure-safe envelope.

If the sure-safe range is determined for all orientations, a surface in space is defined. If the aircraft is placed at the origin of that surface, any nuclear burst, of the specified yield, which takes place on that surface will produce an aircraft response that matches the sure-safe criterion. Any burst outside of that surface will produce a lesser response; the aircraft will be safe for any burst outside of the surface. Conversely, the aircraft may be unsafe for any burst inside the surface.

The surface described above is sometimes referred to as the "sure-safe volume," since it describes the volume in space outside of which a nuclear burst will produce a level of response that is safe for the aircraft and crew. If a plane is passed through this surface, the intersection of the plane and the surface defines a closed line called an "envelope." A sure-safe envelope is simply a plane section of a sure-safe volume.

The sure-kill surface or volume may be defined in a similar manner. The sure-kill volume, often called the lethal volume, defines the volume in space inside of which a nuclear burst will produce a level of response that will result in an aircraft kill. A sure-kill envelope is a plane section of a sure-kill volume.

For in-flight aircraft, the range and orientation with respect to a given burst point are functions of time as a result of the motion of the aircraft. The time must be specified to specify the geometry completely. In defining the time, it is important to distinguish between types of weapon effects: those effects that take place or at least begin to take place immediately after the burst; and those that do not take place until some time after the burst. Nuclear and thermal radiation, whose effects begin to be felt virtually immediately fall into the first category. Gust and overpressure effects, which are not felt by the aircraft until the arrival of the blast wave are in the second category. Two times of significance are associated with the problem. The first is the burst time and the second is the intercept time, or the time at which the blast wave reaches, or intercepts, the aircraft. For effects in the first category, only the burst time is significant; hence, the orientations and ranges are those corresponding to the burst-time position of the aircraft. For effects in the second category, both the burst time and the intercept time are significant.

In calculating response, it is convenient to use the intercept time, because it is at intercept time that the response begins. Hence, application of the response methods results directly in intercept-time volumes and envelopes. The military planner, however, is generally interested in burst-time envelopes, since he wants to know what the effects of a nuclear burst occurring at some point relative to the aircraft will be on an aircraft. He generally is not interested in where the aircraft will be when it is intercepted by the blast wave, but only that some given response will be achieved when it is intercepted. Thus, it becomes necessary to transform intercept-time envelopes into burst-time envelopes. This transformation can be accomplished rather easily. Each range on an intercept-time envelope represents the distance which the blast wave must

travel in order to reach the aircraft. For a given yield and altitude, a time of arrival of the blast wave may be associated with any distance traveled. Hence, the time, measured from burst time, corresponding to any point on the intercept-time envelope may be calculated from weapon characteristics. Using this time, and knowing the aircraft velocity and maneuver condition, a position occupied by the aircraft at burst time may be calculated for each point on an intercept-time envelope. These positions define the burst-time envelopes.

In determining the burst-time envelopes, the assumption is made implicitly that the aircraft maintains a constant speed and maneuver between the time of burst and the time of interception by the blast wave. Within the scope of this manual, the assumption has been made that the airplane velocity does not exceed Mach 2. For an airplane velocity exceeding Mach 2, certain effects that have been ignored in transforming intercept-time envelopes into burst-time envelopes become important. This assumption is valid for low yield weapons, because of the small distances and times involved. For large yield weapons, however, when the blast wave arrival time may be on the order of several seconds, there is time for a pilot to change his course. It would be impossible to guess the course changes; hence, assumption of an unaltered flight path cannot be avoided reasonably. At the same time, this assumption must be considered as a source of error in the case of large yield weapons.

## **NUCLEAR WEAPON EFFECTS ANALYSIS**

A basic description of nuclear weapon blast and thermal phenomena is contained in Chapters 2 and 3 of this manual. The effects of these weapon phenomena on an aircraft are described in the following paragraphs. These effects include material velocity (gust) effects,

overpressure effects, thermal radiation effects, and combinations of these effects.

### **13-2 Gust Effects**

The blast wave and the associated material velocity and overdensity are described in Section I of Chapter 2. As the blast wave engulfs an aircraft, the angle of attack of the aircraft is changed by the material velocity. The effect is similar to that produced by atmospheric gusts, and the term gust has become associated with this effect.

Another parameter that is important in determining aerodynamic loads is the dynamic pressure. The dynamic pressure is the product of the air density and the square of the velocity of the aircraft relative to the surrounding air. Since both the density and the relative velocity are changed by the blast wave, the dynamic pressure is changed.

The changes in angle of attack and dynamic pressure produce changes in the aerodynamic loads on the aircraft. Several methods may be used to predict the resulting aerodynamic loads. The simplest is the so-called quasi-steady state method. In this method, the angle of attack and dynamic pressure existing at each instant of time are considered to have existed for a time that is sufficiently long that a steady-state condition has been attained. The aerodynamic forces are then the steady-state forces corresponding to the instantaneously-existing conditions. Since the instantaneously-existing conditions actually are changing rapidly as the blast wave engulfs the aircraft and subsequently decays, the method is called quasi-steady. More sophisticated methods account for the truly transient nature of the response to the aerodynamic loads under the rapidly changing conditions. Such methods are called unsteady aerodynamic methods.

One more complication arises in predicting aerodynamic loads. Aerodynamic loads gen-

erally are assumed to be proportional to the angle of attack, i.e., the loads are assumed to be linear with angle of attack. In the sure-kill case, however, severe loadings are required to produce damage corresponding to a sure-kill condition. These severe loadings generally can occur only if the gust induced angle of attack is large, often well beyond the angle of attack range for which linearity can be assumed reasonably, and nonlinear aerodynamics are of interest. The coupling of unsteady and nonlinear aerodynamics is an extremely complex problem that has been solved only semi-empirically.

The aerodynamic loads described above produce rigid-body accelerations of the aircraft, both in translation and rotation. These accelerations result in translational and rotational velocities and displacements. The translational velocity and the rotational displacement are particularly important in the production of additional aerodynamic loads. If an aircraft is intercepted by a blast wave from directly below, the material velocity is upward. This increases the angle of attack of the aircraft and causes an upward translational velocity, so the aircraft tends to "ride" with the gust. The tendency to ride with the gust causes a reduction in the angle of attack of the aircraft and alleviates the aerodynamic loads. The alleviation that results from riding with the gust is a function of the wing loading for an airplane. The wing loading is the ratio of the airplane weight to the airplane wing area. An airplane with a high wing loading is heavy with respect to its aerodynamic loading; it rides very little with the gust and produces very little load alleviation. Conversely, an airplane with a low wing loading will produce considerable load alleviation by riding with the gust.

The rotational displacement that results from rotational acceleration also alleviates the loading, although the effect is more complex. Roughly, a stable aircraft will rotate into the gust, which reduces the angle of attack and alle-

viates the loads. Generally, the translational load alleviation is more important than the rotational load alleviation during the time period of interest.

The aerodynamic loads also produce accelerations and displacements in the elastic modes of the aircraft, e.g., the fuselage bends. The elastic displacements and velocities also change the angle of attack and hence the aerodynamic loads. There is thus an interaction between the elastic motion and the aerodynamic loads; this interaction is called the aeroelastic effect. The aeroelastic effect is generally of secondary importance, but there are cases in which it can be of considerable importance.

One more type of motion interacts with the aerodynamic loading. If the sure-kill problem for an in-flight aircraft is considered, the inelastic response often must be considered. A major component, such as the fuselage, ordinarily will fail in an instability, or buckling, type of mode; however, a buckling failure does not necessarily produce a catastrophic failure of the aircraft, i.e., a sure-kill condition. A structure that has undergone a major buckling failure will be weaker than it was prior to the failure; however, it may maintain the capability of carrying a substantial load. The load carrying capability may be sufficient to permit the aircraft to complete its mission. This situation has been demonstrated analytically, in simulation experiments, and in a full-scale test during Operation TEAPOT, a nuclear test in Nevada in 1955.

As the inelastic deformation of the structure increases, its load carrying capability decreases. At some point, the load carrying capability becomes sufficiently low that a sure-kill condition exists. Inelastic deformations required to produce a sure-kill condition may be very large when compared to elastic deformations; the aerodynamic loads induced by inelastic motions may be much larger than the aeroelastic effect described previously.

The final influence on the aerodynamic loadings for in-flight aircraft is pilot or autopilot action upon interception of the aircraft by the blast wave. Pilot action would be too slow to influence the situation substantially during the time period of interest. Autopilot response has been ignored in all known approaches to the problem, presumably because of the low probability that the aircraft would be on autopilot for realistic engagement conditions. It might be noted, however, that an autopilot that is maintaining constant barometric altitude could react violently to the change in pressure accompanying the blast wave.

The concepts of rigid-body, elastic, and inelastic motion have been introduced in outlining the various influences on the aerodynamic loads. Each of these types of motion is important for some type of sure-safe or sure-kill envelope. For example, parked aircraft may be lifted from the ground. This is a rigid-body mode, which must be considered for both sure-safe and sure-kill conditions for parked aircraft.

Parked aircraft also may be damaged by bending of the fuselage or vertical tail as a result of aerodynamic loading of the vertical tail. For sure-safe conditions, this bending will be elastic; for sure-kill conditions, inelastic response also may be important.

Rigid-body motions generally are not important for in-flight aircraft. These motions enter the problem in two ways: (1) their influence on the aerodynamic loads is significant; (2) rigid-body translational accelerations are rough indices of the amount of elastic or inelastic deformation of the major aircraft components, and they may be used in crude methods instead of such deformations, which are the quantities of real interest. More realistic analyses should consider elastic response for sure-safe conditions and inelastic response for sure-kill conditions.

Most of the preceding remarks apply both to airplanes and to helicopters. The only

new facets added by helicopters are the rotors. There are three types of helicopter main rotor blades: hinged, rigid (hingeless), and teetering. Each type must be considered separately, because each has its own characteristics.

The important characteristic of a hinged rotor is the hinge, which is offset somewhat from the center of rotation. This permits free rotation of the blade outboard of the hinge in an up-and-down, or flapping, direction. Analysis of this type of blade has shown that bending of the blade is not an important mechanism for either sure-safe or sure-kill conditions. Flapping of the blade about the hinge seems to be more important. Extreme flapping could result in a collision between the blade and the fuselage and/or the flapping stops. Even blade flapping appears to be less important than overpressure damage to the overall system, so gust effects are not considered for hinged blade helicopters in this chapter.

Rigid, or hingeless blades, do not use a flapping hinge. Bending may be important for these blades, and it is considered in this chapter.

Finally, a teetering blade roughly combines the characteristics of the hinged and hingeless blades. A teetering blade is essentially a seesaw about a hinge at the center of rotation. The two blades on the two sides of the hinge are connected rigidly. If there is a loading on the two blades, this loading can always be divided into a symmetrical and an anti-symmetrical component. The loadings on the two blades are identical for the symmetrical component; the loadings on the two blades are exactly opposite for the anti-symmetrical component. The response to the anti-symmetrical component is exactly the same as if each blade were separately hinged at the center of rotation, rather than being connected rigidly. The anti-symmetrical gust loading component on teetering blades can therefore be ignored for the same reasons that gust loading on hinged blades was ignored.

The teetering blade responds to sym-

metric loading as if there were no hinge at the center of rotation, i.e., the teetering blade responds to a symmetric loading as if it were a hingeless blade, and the symmetric component of the gust loading must be considered.

In general, gust effects are only of minor importance for parked aircraft, but they are of primary importance for in-flight aircraft.

### 13-3 Overpressure Effects

The gust effects influence the major components of the aircraft, such as the wings and/or the blades, the fuselage, the horizontal tail, and the vertical tail. The overpressure, on the other hand, influences smaller elements of the structure, i.e., the skin, the stringers, and the frames, particularly on the fuselage.

When an aircraft is struck by a blast wave, the pressure on the side of the fuselage facing the burst point is increased above the incident value by reflection, and a local loading of short duration is generated (see Figure 9-3). As the blast wave continues to engulf the aircraft, the pressure on the side of the fuselage facing the burst point decays to the pressure behind the blast wave. The characteristic loading is a high reflected pressure (from two to eight times the overpressure associated with the blast wave), which decays very rapidly, in a few milliseconds, to the value of pressure behind the blast wave. This high pressure, short duration pulse is followed by the much longer duration, but lower pressure, pulse that is characteristic of the blast wave.

It is primarily the high reflected pressure, short duration pulse that is responsible for damage to skin panels, stringers, and frames. These structural elements are vulnerable to such short duration loadings because of their high frequencies. For the converse reason, the much lower frequency major components are not influenced to a great extent by the short duration loading.

The short duration pulse produces dishing-in of skin panels and buckling of stringers and frames or portions of stringers and frames. As in the case of analysis of response to gust effects, analysis of overpressure response only requires consideration of the elastic response for the sure-safe case, but inelastic response should be included for sure-kill conditions.

Early efforts to determine overpressure damage relied virtually entirely on experimental results. Simple approaches were advanced later, which analyze the response of skin panels, stringers, and frames to static loadings, and then modify the results by some dynamic factor to account for the true dynamic character of the loading.

With regard to overpressure damage, airplanes and helicopters may be analyzed in the same way. The distinguishing feature of the helicopter, the rotor blade, is virtually invulnerable to overpressure effects, so the helicopter is no different from an airplane in this regard.

Overpressure damage is generally the predominant effect for parked aircraft; however, overpressure damage is usually of minor importance in comparison with gust effects for in-flight aircraft. Overpressure only becomes important for in-flight aircraft in those regions where gust effects are small, i.e., for bursts almost directly in front of or directly behind the aircraft.

### 13-4 Thermal Radiation Effects

In considering the effects of the thermal radiation from a nuclear explosion, two distinct problems must be addressed: (1) the portion of the thermal radiation emitted by the explosion that reaches the aircraft; and (2) the effect on the aircraft that is produced by the incident radiation.

The radiant exposure of an aircraft in flight varies widely with atmospheric conditions,

orientation of the aircraft with respect to the burst, aircraft velocity, the ground reflecting surfaces, and the location of clouds (see Chapter 3). Scatter and reflection add to the direct radiation, and, under some circumstances, the thermal energy incident on an aircraft in space may be two to three times as great as would be computed at a given slant range for direct radiation only. Conversely, when a heavy cloud layer is between the burst and the aircraft, the radiant exposure may be only a fraction of the predicted value of direct radiation for a given range. In other situations, reflected radiation from clouds may contribute significant thermal energy to areas of the aircraft shaded from direct radiation. During weapon effects tests of an aircraft flying in a cloud above the burst, the radiant exposure at the top of the aircraft and its cockpit area was observed to be as much as one-fourth of the direct radiation on the lower surfaces. This experiment demonstrated the need for protection of weapon delivery aircraft from radiant exposure from any direction.

The motion of the aircraft during the time in which significant thermal radiation is being emitted by the fireball can exert an important influence on the thermal radiation incident upon the aircraft. Obviously, this is particularly true for high-speed aircraft. "Fly-away factors" have been devised which are first order corrections for aircraft motion.

The absorptivity of the aircraft skin and the angle of incidence of the thermal radiation affect the amount of energy that will be absorbed by the structure; the boundary layer in the air flow adjacent to the structure leads to convective cooling. Very thin skins are heated to damaging temperatures rapidly, because the energy is absorbed by the skin much more rapidly than it can be dissipated by conduction and convective cooling. In recent years, designers of military aircraft have reduced aircraft vulnerability to thermal effects by coating ma-

terials with low absorptivity paints, by eliminating ignitable materials from exposed surfaces, and by substitution of thicker skins for very thin skins.

An aircraft thin skin panel, supported by internal structure, which is usually much cooler, can be heated sufficiently that it may be buckled by thermal stresses in the sure-safe case, or it may melt in the case of sure-kill. In either case, there will be essentially no change in temperature through the thickness of a thin skin. The thick skin case is a step higher in complexity. The temperature distribution across the thickness of the skin must be considered in determining thermal stresses. A still more complex temperature distribution occurs in built-up structures, with air gaps acting as insulators between spars, stringers, and skin. For all but the simplest configurations, computer programs are necessary to define these temperature distributions accurately.

Analyses of thermal radiation effects on aircraft generally only concern themselves with temperature rather than with stresses, since buckling of thin skin is generally of little or no consequence. Sure-safe envelopes usually are based upon a rather arbitrary temperature, or temperature rise, in the thinnest skin. The temperature chosen is based roughly upon some percentage reduction in strength or stiffness that results from the increased temperature. Sure-kill envelopes are based upon melting of the skin.

Biological injury to the crew from intense thermal radiation, and damage to non-structural elements that would affect mission performance adversely also must be considered when dealing with thermal criteria. In many cases, these problems can be minimized by adequate protective measures such as cockpit curtains.

A military weapon delivery aircraft properly prepared for its delivery mission with reflective paint and with the crew and all vulner-

able materials shielded from direct thermal radiation will not be damaged by thermal radiation at distances where damage from air blast would be severe. Other aircraft not so prepared may sustain serious damage at very low thermal levels as a result of ignition of items such as rubber and/or fabric seals, fixed landing gear tires, cushions, and headrest covers. Aircraft painted with dark paint are especially vulnerable to thermal radiation damage, because the dark painted surfaces absorb three to four times the thermal energy that is absorbed by polished aluminum surfaces or surfaces protected with reflective paint.

As in the case of overpressure effects, there is no difference between helicopters and airplanes with regard to the analysis of thermal radiation effects. The importance of thermal radiation effects relative to the other effects depends upon the yield of the weapon being considered. Relative to other effects, the importance of thermal radiation increase with increasing yield. For small yields, thermal radiation is generally of secondary importance for both parked and in-flight aircraft; thermal radiation from high yield weapons may be dominant for both.

### 13-5 Combined Effects

The effects of combinations of various weapon phenomena have been examined, but relatively little has been accomplished in the generation of methods for analyzing combined effects. One reason for this is the difficulty in analyzing each effect individually with adequate accuracy. In general, only qualitative comments may be made concerning combined effects.

The first possibility is the interaction between gust and overpressure effects. For in-flight aircraft, the levels of overpressure required to produce a given response are well above the levels associated with significant response to gust effects, and little coupling is expected. For

parked aircraft, the gust effects of most importance are lift-off and crushing of the landing gear; overpressure damage will not influence these phenomena significantly. Thus, gust-overpressure coupling appears to be of secondary importance.

In considering the thermal interactions with either overpressure or gust, it should be recalled that the usual thermal analyses are concerned with temperatures and not with stresses. To examine the interaction between thermal stresses and gust or overpressure effects would require a combined analysis of a higher level of sophistication than is usually employed for the individual effect. Moreover, the few exploratory investigations indicate that transient thermal stresses seem to be less important as a coupling factor than degradation in material properties that result from elevated temperature. Degradation of material properties generally will be of minor importance at ranges associated with significant gust effects for in-flight aircraft, except in the case of high yield weapons. For high yield weapons, the time period between heating of the structure and interception of the aircraft by the blast wave may permit considerable cooling to take place, and thus minimize interaction effects even in this case.

For parked aircraft, the interaction between thermal and overpressure effects could be significant. The state of the art in overpressure effects analysis, however, is such that inclusion of anything more than the effect of degraded material properties (see Section IV, Chapter 9) would be unreasonable.

In summary, the only interactions between effects that seem to be of much importance are those between thermal effects and gust or overpressure effects. In those cases, any consideration of interactions should be restricted to use of material properties in the gust or overpressure analyses corresponding to the elevated temperatures produced by the thermal radiation.

Furthermore, consideration of even this interaction should be restricted to the most sophisticated methods of gust and overpressure analysis, and is not recommended for users of this manual.

## SECTION II

### AIRCRAFT RESPONSE TO BLAST AND THERMAL EFFECTS

#### AIRCRAFT RESPONSE TO GUST EFFECTS

##### 13-6 Aerodynamic Coefficients for Aircraft

When the blast wave arrives and commences to envelop the aircraft, a complicated pattern of shocks passes over the surfaces of the aircraft very quickly. During this period, frequently called the "diffraction period" (see Section II, Chapter 9), the transient airloads are difficult to predict, and sophisticated methods are required even for the simplest combination of aircraft configuration and blast orientation. However, for many cases of blast loading, such as a supersonic airplane enveloped by a blast from below, the lift and normal force during the diffraction period are nearly the same as during the early post-diffraction period. In other cases, the duration of the diffraction loading is so short that the influence on the response of major aircraft components is very small. Hence, it is reasonable to make first estimates of the transient airloads on a quasi-steady basis by using instantaneous quantities (angle of attack, density, etc.) and steady-state coefficients to compute steady state forces. This simplification is adopted in the aerodynamics methods presented in this chapter.

Methods for calculating gust loadings are presented for two orientations: symmetric loading, with the gust velocity from directly above or below the aircraft; and lateral loading, with the gust velocity directly from the side.

When a wing (tail) is added to a fuselage, certain mutual interference effects may arise between the components. For example, a body induces high upwash velocities near the wing-body (tail-body) juncture, which is commonly termed body-induced wing (tail) interference. The local body flow properties such as Mach number and dynamic pressure also affect the wing (tail) loading. The wing (tail) in turn affects the loads on the body.

Another interference effect, normally considered in stability and control, is that on the tail that results from a wing set at an angle of attack. The downwash that is caused by the trailing vortices from the wing generally reduces the lift on the horizontal tail surfaces during straight and level flight. The magnitude of the reduction depends on the span of the wing relative to the span of the tail, the lift distribution on the wing, and a number of other factors. A blast wave changes the loading in the wing, which alters the strength of the vortex sheet behind the wing, but the change in the strength of the vortex sheet that results from the blast wave does not affect the lift on the tail at early times after blast arrival to any great extent. The blast wave also deflects the vortex sheet away from the plane of the wing. The effect of the vortex sheet on the lift on the tail depends strongly upon the position of the sheet relative to the tail surface. Methods to predict the transient location of the vortex sheet have not been demonstrated for strong blasts; therefore, the interference of the wing on the tail is not included in transient load estimates.

The airloads on the vertical tail produced by lateral blasts are more difficult to predict than the airloads on the wing, because, in addition to the body and the wing, the horizontal tail influences the flow field at the vertical tail. At an angle of attack, the downwash from the wing could influence the vertical tail. The lateral flow over the body has a maximum

velocity at the top where the vertical tail is located. Also, at large angles of attack or sideslip, there are vortices shed from the body that could affect the loads on the vertical tail; presumably the effect of the vortices would be most severe at combined angles of attack and sideslip, a combination which is outside the cases considered here. The horizontal tail interacts with the flow field about the vertical tail,

serving to some extent as a reflection plane, so that aerodynamically the vertical tail appears to have an aspect ratio that is larger than the geometric aspect ratio (this is the so-called "end-plating" effect). At supersonic speeds, shocks emanate from the wing and horizontal tail and provide further influence on the vertical tail loads.

### Problem 13-1. Calculation of the Aerodynamic Coefficient for Wing and Horizontal Tail

The transient airloads may be obtained on a quasi-steady basis using the instantaneous quantities (angle of attack, density, etc.) and steady-state coefficients. Typically, the theoretical methods predict a lift for a swept wing-body combination which is about 10 percent greater than for an isolated wing without a body, provided that the wing and body are at the same incidence. In wind tunnel tests, however, the lift on a swept wing-body combination was found to be the same as on an isolated wing. In these cases, the area of the isolated wing includes the area submerged within the body. Other methods indicate that the lift on a delta wing-body combination with a typical ratio of body diameter to wing span and traveling at supersonic speeds is within 2 percent of the lift for the same delta wing alone. In view of these results, the lift on the wing (tail)-body combinations is computed for an isolated wing (tail) having the same wing area, including the wing (tail) area submerged within the fuselage.

The calculation of the aerodynamic coefficient for wings and/or horizontal tails,  $C_{L\alpha}$ , is presented in the following series of steps.

1. Using the silhouette profile of the aircraft (for example, see Figures 13-1 and 13-2), from which lengths and surfaces may be found, determine the following:

$S$  = wing/horizontal tail area (sq ft), defined as the extension of the leading and trailing edges of both wings/horizontal tail to the aircraft centerline.

$c_t$  = wing/horizontal tail root chord, i.e., the length along the fuselage centerline (ft) subtended by extensions of the leading and trailing edges.

$c_t$  = wing/horizontal tail tip chord (ft), defined as the length along the fuselage centerline subtended by the wing tip.

$b$  = wing/horizontal tail span, tip to tip (ft).

$\Lambda_{LE}$  = sweepback angle at wing/horizontal tail leading edge, measured from a line perpendicular to the fuselage centerline (deg).

$M$  = Mach Number =  $V/c$ , where  $V$  is the aircraft velocity and  $c$  is the ambient speed of sound.

2. Calculate the taper ratio  $\lambda$ :

$$\lambda = \frac{c_t}{c_r}$$

and the aspect ratio  $AR$ :

$$AR = \frac{b^2}{S}.$$

3. Calculation of the slope of the lift coefficient depends on the value of the Mach number,  $M$ . Three regions are defined as follows:

Region 1:  $M \leq 0.85$ ,

Region 2:  $M \geq 1.2$ ,

Region 3:  $0.85 < M < 1.2$ .

*Region 1.* Steps a through d present the calculation of the slope  $C_{L\alpha}$  for  $M \leq 0.85$ .

a. Calculate the value of  $\beta^2$ :

$$\beta^2 = 1 - M^2.$$

b. Determine the tangent of the sweep angle of the mid-chord line,  $\tan \Lambda_{c/2}$ :

$$\tan \Lambda_{c/2} = \tan \Lambda_{LE} - \frac{2}{AR} \left[ \frac{1 - \lambda}{1 + \lambda} \right].$$

c. Compute the parameter,

$$AR \left[ \beta^2 + \tan^2 \Lambda_{c/2} \right]^{1/2},$$

and enter Figure 13-3, with the value of the parameter to obtain the corresponding value of  $C_{L\alpha}/AR$ .

d. Calculate the slope of the lift coefficient curve as follows:

$$C_{L\alpha} = \left[ \frac{C_{L\alpha}}{AR} \right] AR.$$

*Region 2.* Calculation of  $C_{L\alpha}$  for  $M \geq 1.2$  is performed by the following steps.

a. Calculate the value of  $\beta$ :

$$\beta = (M^2 - 1)^{1/2}.$$

b. Calculate the values of the parameters:

$$\frac{\beta}{\tan \Lambda_{LE}},$$

and

$$(AR) \tan \Lambda_{LE}.$$

c. Enter Figure 13-4 and select the figure corresponding to the taper ratio  $\lambda$ . Select the curve corresponding to the value of the parameter  $(AR) \tan \Lambda_{LE}$ . If

$$\frac{\beta}{\tan \Lambda_{LE}} < 1,$$

use the left side of the figure to obtain the value of  $\tan \Lambda_{LE} C_{N\alpha}$ . Calculate  $C_{L\alpha}$  as follows:

$$C_{L\alpha} = \frac{\tan \Lambda_{LE} C_{N\alpha}}{\tan \Lambda_{LE}},$$

where the normal force coefficient  $C_{N\alpha}$  and  $C_{L\alpha}$  are taken to be equal within the scope of this method.

If

$$\frac{\beta}{\tan \Lambda_{LE}} > 1,$$

determine its reciprocal,

$$\frac{\tan \Lambda_{LE}}{\beta},$$

and use the right side of the figure to obtain the value of  $\beta C_{N\alpha}$ .

The slope is calculated by:

$$C_{L\alpha} = \frac{\beta C_{N\alpha}}{\beta},$$

where  $C_N$  is represented as  $C_L$  within the scope of this method.

*Region 3.* The following steps a through c, are used to calculate  $C_{L\alpha}$  for  $0.85 < M < 1.2$ .

a. Calculate  $C_{L\alpha}$  at  $M = 0.85$  following the method in Region 1.

b. Calculate  $C_{L\alpha}$  at  $M = 1.2$  following the method in Region 2.

c. Interpolate linearly for the slope at the actual Mach number:

$$C_{L\alpha} = C_{L\alpha} (\text{at } M = 0.85)$$

$$+ \frac{M - 0.85}{0.35} [C_{L\alpha} (\text{at } M = 1.2) - C_{L\alpha} (\text{at } M = 0.85)].$$

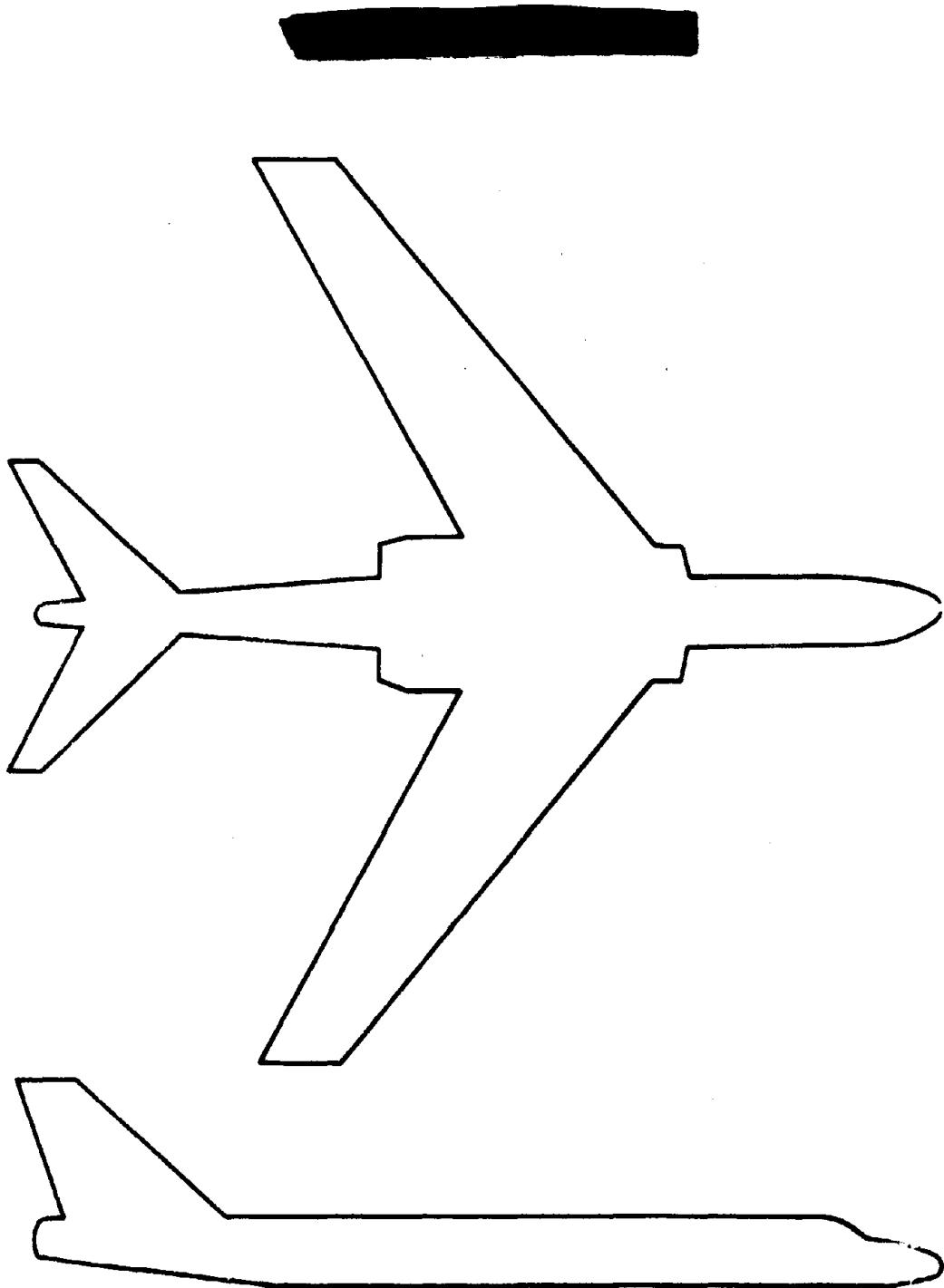
Table 13-1. Selected Data Based on U.S. Standard Atmosphere,  
1962 English Units

Altitude feet	Temperature °F	Pressure psi	Density Ratio <sup>a</sup> $\rho/\rho_0$	Temperature Ratio $T/T_0$	Sound Speed ft/sec
0	59.0	14.696	1.0000	1.000	1116
1 000	55.4	14.17	.9711	.993	1113
2 000	51.9	13.66	.9428	.986	1109
3 000	48.3	13.17	.9151	.979	1105
4 000	44.7	12.69	.8881	.973	1101
5 000	41.2	12.23	.8617	.966	1097
10 000	23.4	10.11	.7386	.931	1077
15 000	5.5	8.297	.6295	.897	1057
20 000	-12.3	6.759	.5332	.863	1037
25 000	-30.0	5.461	.4486	.828	1016
30 000	-47.8	4.373	.3747	.794	995
35 000	-65.6	3.468	.3106	.760	973
40 000	-69.7	2.730	.2471	.752	968
45 000	-69.7	2.149	.1945	.752	968
50 000	-69.7	1.692	.1531	.752	968
55 000	-69.7	1.332	.1206	.752	968
60 000	-69.7	1.049	.09492	.752	968
65 000	-69.7	.826	.07475	.752	968
70 000	-67.4	.651	.05857	.756	971
75 000	-64.7	.514	.04591	.762	974
80 000	-62.0	.406	.03606	.767	978
85 000	-59.3	.322	.02837	.772	981
90 000	-56.5	.255	.02236	.777	984
95 000	-53.8	.203	.01765	.782	988
100 000	-51.1	.162	.01396	.788	991
110 000	-41.3	.103	8.692-3	.807	1003
120 000	-26.1	.0667	5.428	.836	1021
130 000	-10.9	.0438	3.446	.865	1038
140 000	4.3	.0292	2.222	.894	1056
150 000	19.4	.0197	1.454	.924	1073
160 000	27.5	.0135	9.770-4	.939	1082
170 000	27.5	9.23-3	6.690	.939	1082
180 000	18.9	6.31	4.652	.923	1072
190 000	8.1	4.27	3.225	.902	1060
200 000	-2.7	2.87	2.217	.881	1048

NOTE: 7.011-3 means  $7.011 \times 10^{-3}$

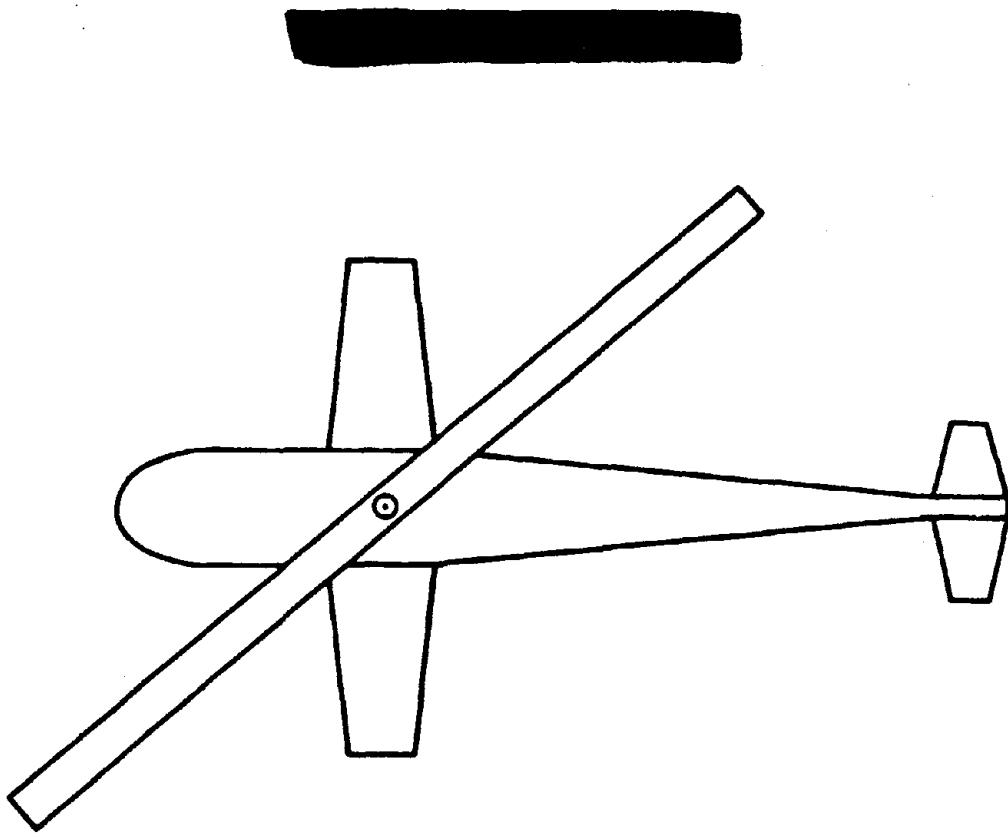
$$\rho_0 = 2.38 \times 10^{-3} \text{ slugs/ft}^3$$

$$= 7.65 \times 10^{-2} \text{ lbs/ft}^3$$



SCALE: 1" = 30'

Figure 13-1. Example Airplane (American)



**SCALE: 1" = 10'**

Figure 13-2. Example Helicopter

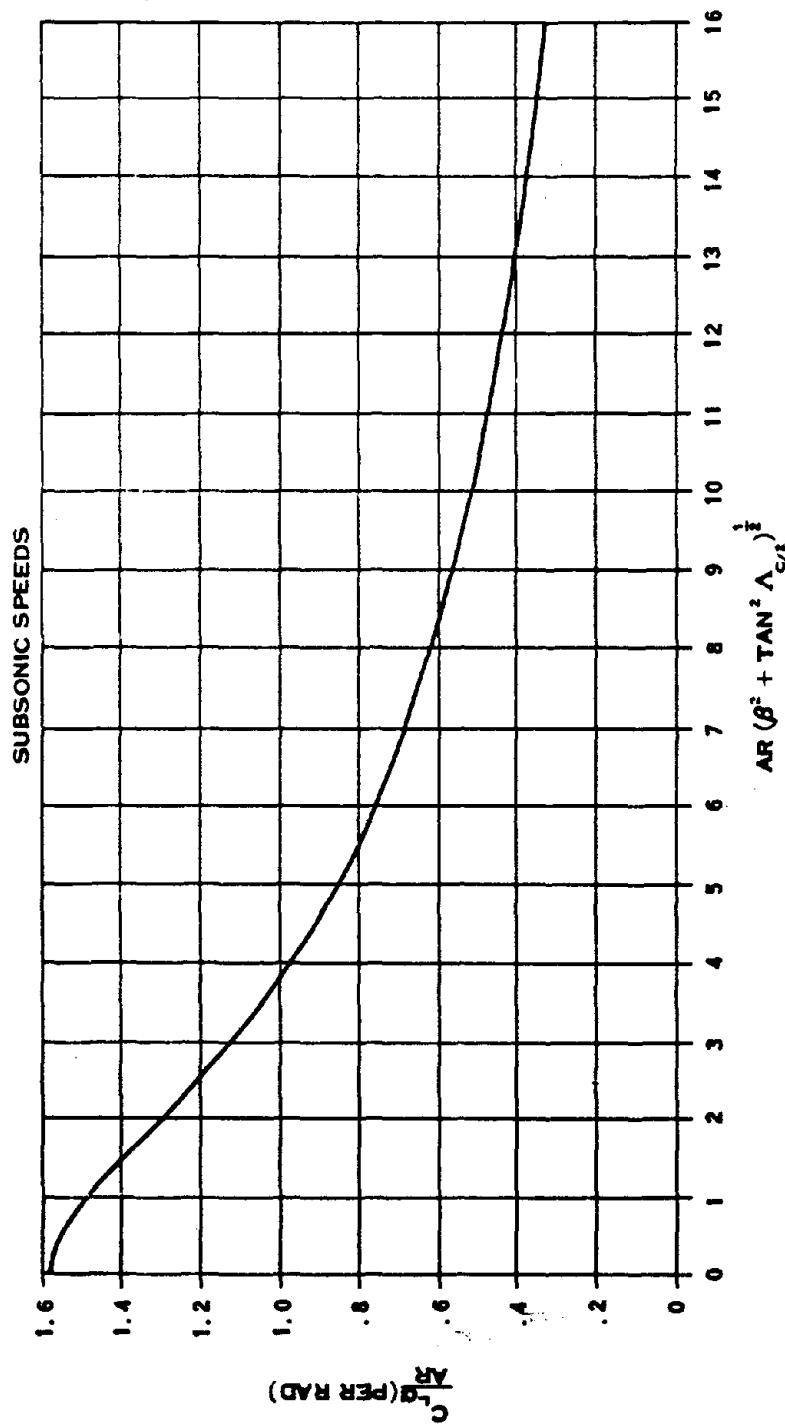


Figure 13-3. Subsonic Wing Lift Curve Slope

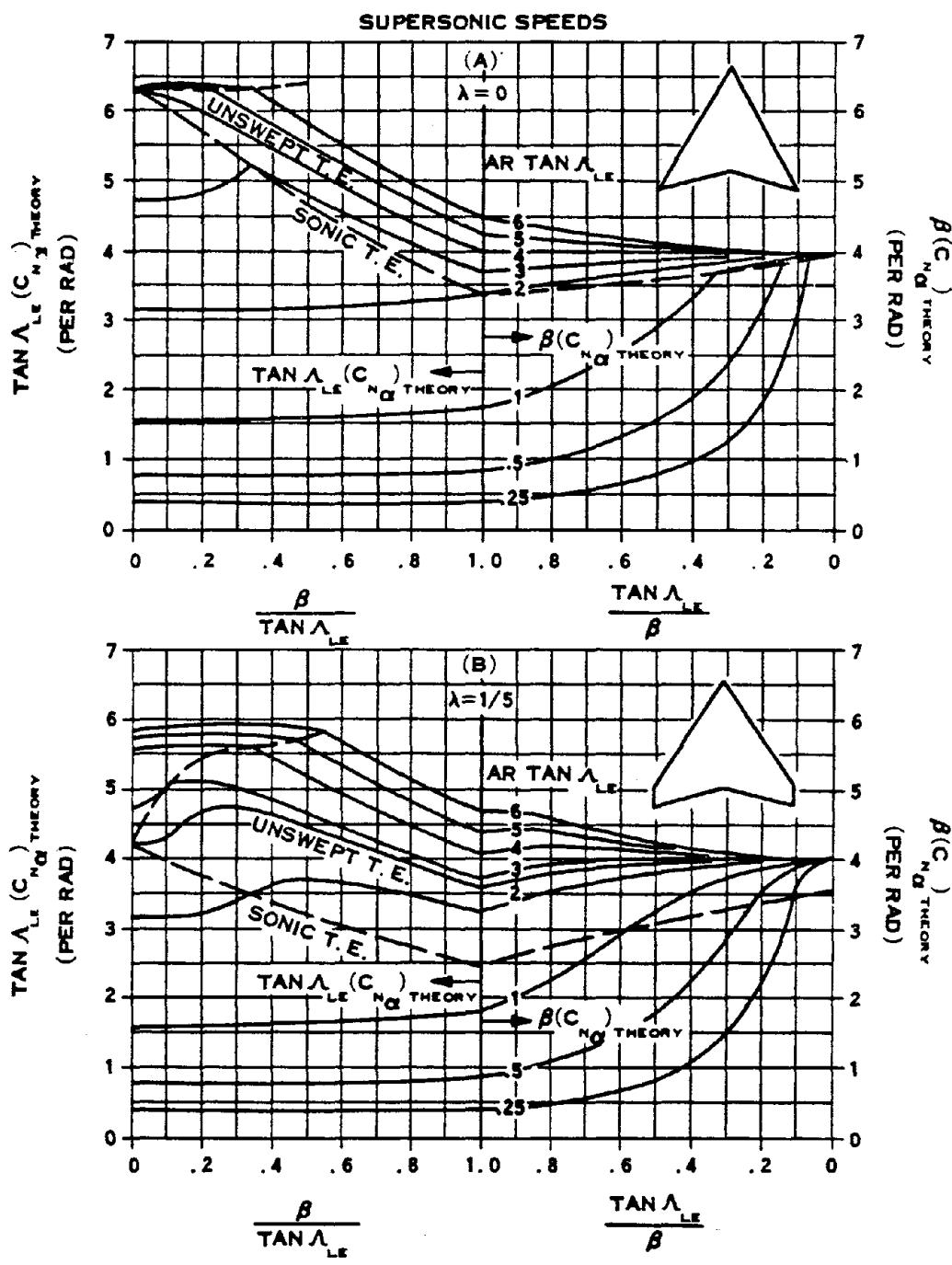


Figure 13-4a. Wing Supersonic Normal Force Curve Slope

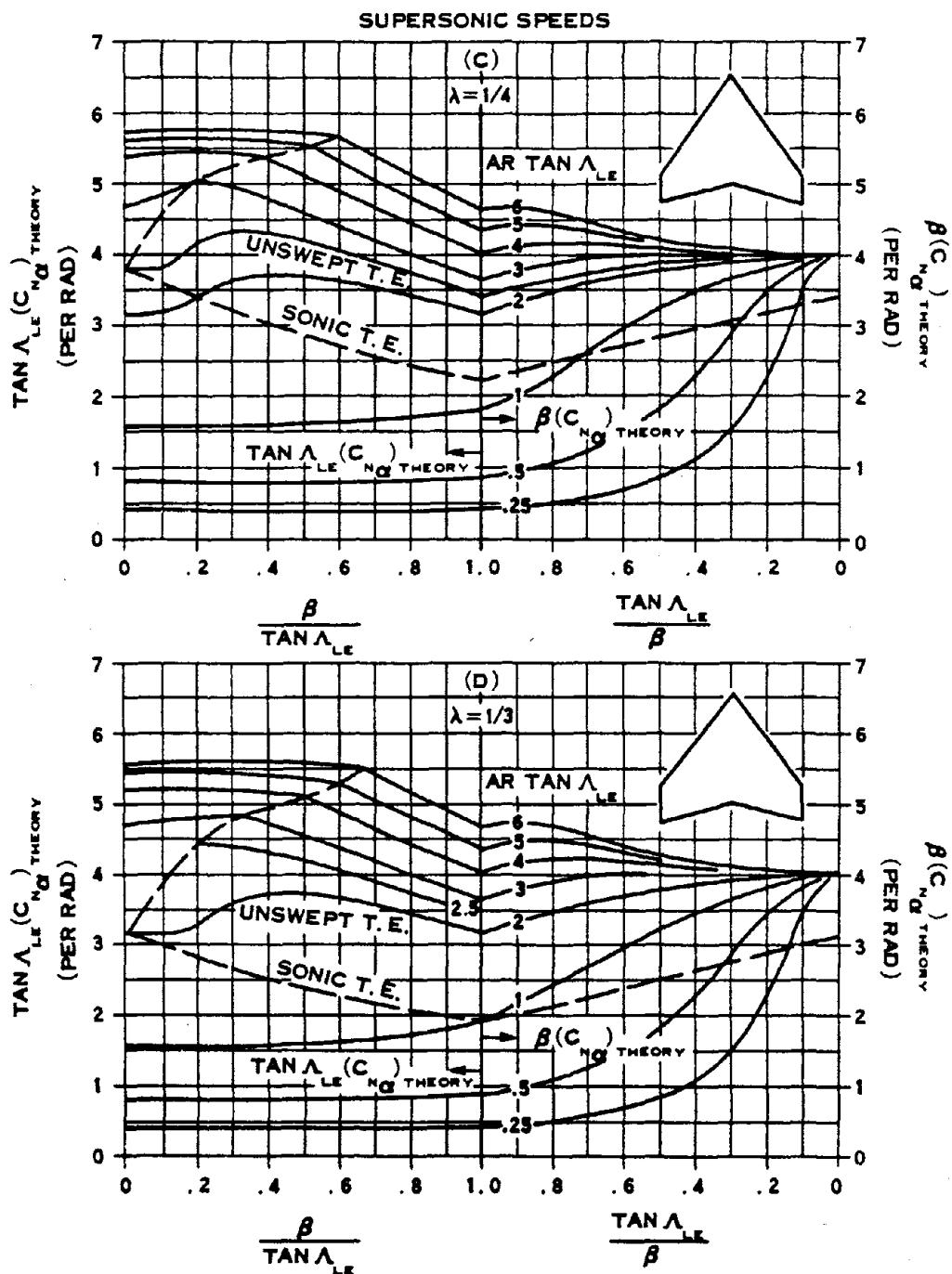


Figure 13-4b. Wing Supersonic Normal Force Curve Slope

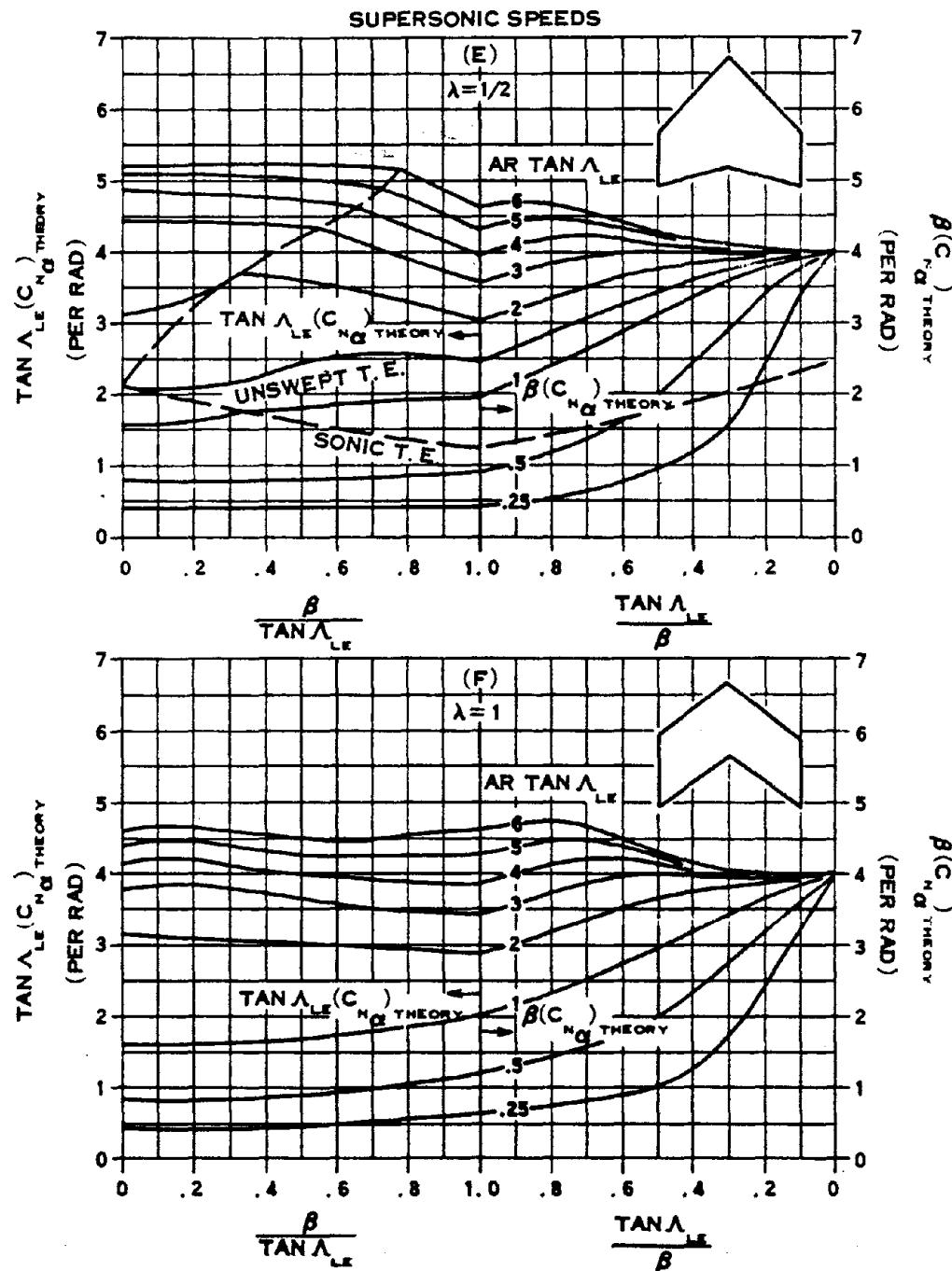


Figure 13-4c. Wing Supersonic Normal Force Curve Slope

### Problem 13-2. Calculation of the Aerodynamic Coefficient for the Vertical Tail

An effective aspect ratio is derived to account for interference effects from the body and the horizontal tail to predict the lateral force on the vertical tail at subsonic speed:

$$AR_{\text{eff}} = \left\{ \frac{(AR)_B}{AR} \right\} \left\{ 1 + K_H \left[ \frac{(AR)_{HB}}{(AR)_B} - 1 \right] \right\} (AR),$$

where  $AR$  is the aspect ratio of the isolated vertical tail, with the span and area of the vertical tail measured to the fuselage centerline; the factor  $(AR)_B/AR$  is the ratio of the aspect ratio of the vertical tail in the presence of the fuselage to the aspect ratio of the isolated tail (this ratio is shown in Figure 13-5); the factor  $K_H$  accounts for the relative size of the horizontal and vertical tails, and it varies from 0 to about 1.1; and the factor  $(AR)_{HB}/(AR)_B$  is the ratio of the vertical tail aspect ratio in the presence of *both* the horizontal tail and body to that of the vertical tail in the presence of the body alone, which varies from 0.9 to 1.2 for typical configurations. Within the accuracy goals of the present calculations, it is reasonable to take this ratio as unity, which gives

$$(AR)_{\text{eff}} = \left( \frac{(AR)_B}{AR} \right) AR.$$

A first approximation for the lift coefficient for the vertical tail,  $\bar{C}_{L\alpha}$ , is determined from the wing lift curve slopes shown in Figures 13-3 and 13-4, using the effective aspect ratio  $(AR)_{\text{eff}}$ . The value of  $C_{L\alpha}$  should be corrected by an empirical factor  $k$ , which is a function of the vertical tail span and the body diameter:

$$C_{L\alpha} = k \bar{C}_{L\alpha}.$$

The diameter  $k$  may be obtained from Figure 13-6. All coefficients are based on the dynamic pressure and the elevation area of the isolated vertical tail.

For *direct* side-on blast orientation cases for parked aircraft, the normal force coefficient is obtained from drag data for flat plates in streams normal to the plates. Data indicate that a drag coefficient of 1.2 would apply to plates having an aspect ratio from unity to about 10, which essentially encompasses the range of aspect ratios for vertical tails of current aircraft. Therefore, for analysis of effects on side-on gusts on parked aircraft, a coefficient of 1.2 has been used.

The drag force on the fuselage also becomes important for parked aircraft subjected to side-on gusts. Values of the steady-state drag coefficient vary from about 0.35 to 1.2, depending upon the Reynolds number, which dictates whether the flow is laminar or turbulent. In the case of unsteady drag, a drag coefficient slightly below the laminar value of 1.2 appears to be applicable at early times. Therefore, a drag coefficient of 1.2 has been used for the fuselage for the analysis of the effects of side-on gusts on parked aircrafts.

For supersonic speeds, the slope of the lift coefficient curve  $C_{L\alpha}$  is estimated by the normal force slope for similar wings. In this calculation,  $C_{L\alpha}$  is computed for a wing having a planform of the isolated vertical tail plus its image about the fuselage centerline, using the method given in Problem 13-1, e.g.,  $C_{L\alpha}$  is computed for the isolated vertical tail with its image as if it were a wing. The isolated vertical tail which extends from the tip to the fuselage centerline is considered; its area includes, in addition to the exposed part, that area within

the fuselage bounded by the extensions of the leading and trailing edges and the fuselage centerline.

The calculation of the aerodynamic coefficient for vertical tails is presented in the following steps. Several of the lengths and areas that are required already will have been determined in the particular response method being followed, which requires the calculation of  $C_{L\alpha}$  (see Problem 13-1).

1. Using the silhouette profile of the aircraft (for example, see Figures 13-1 and 13-2), from which lengths and surfaces may be found, determine the following:

$S$  = vertical tail area (sq ft), defined by the extensions of the leading and trailing edges to the fuselage centerline.

$c_r$  = vertical tail root chord (ft), i.e., the length along the fuselage centerline subtended by the leading and trailing edges.

$c_t$  = vertical tail tip chord (ft), defined as the length along the fuselage centerline subtended by the vertical tail tip.

$b$  = vertical tail span, fuselage centerline to tip (ft).

$\lambda$  = sweepback angle of vertical tail leading edge, measured from the vertical (deg).

$d$  = fuselage depth at the intersection of the vertical tail leading edge and the fuselage (ft).

$M$  = Mach Number =  $V/c$ , where  $V$  is the velocity of the aircraft, and  $c$  is the ambient speed of sound.

2. Calculate the taper ratio  $\lambda$ :

$$\lambda = \frac{c_t}{c_r}$$

and the aspect ratio  $AR$ :

$$AR = \frac{b^2}{S}.$$

3. Calculation of the aerodynamic coefficient for the vertical tail depends on the value of the Mach number,  $M$ . Three regions are defined as follows:

Region 1:  $M \leq 0.85$ ,

Region 2:  $M \geq 1.2$ ,

Region 3:  $0.85 < M < 1.2$ .

*Region 1.* Steps a through g present the calculation of the aerodynamic coefficient for the vertical tail  $C_{L\alpha}$  for  $M \leq 0.85$ .

a. Calculate the value of  $\beta^2$ :

$$\beta^2 = 1 - M^2.$$

b. Determine the tangent of the sweep angle of the mid-chord line,  $\tan \Lambda_{c/2}$ :

$$\tan \Lambda_{c/2} = \tan \Lambda_{LE} - \frac{2}{AR} \left[ \frac{1 - \lambda}{1 + \lambda} \right].$$

c. Calculate the parameter  $b/d$ . With the value of this parameter and the value of  $\lambda$  from step 2, enter Figure 13-5 to obtain the value of  $AR_B/AR$ .

d. Calculate the effective aspect ratio

$$(AR)_{eff} = \left( \frac{(AR)_B}{AR} \right) AR.$$

e. Compute the parameter

$$(AR)_{eff} \left[ \beta^2 + \tan^2 \Lambda_{c/2} \right]^{1/2},$$

and enter Figure 13-3 with this parameter to obtain the value of  $C_{L\alpha}/AR$ .

f. With the value of  $b/d$  from step c, enter Figure 13-6 to obtain the value of  $k$ , an empirical factor, which is a function of the vertical tail span and the body diameter.

g. Calculate the aerodynamic coefficient for the vertical tail  $C_{L\alpha}$ :

$$C_{L\alpha} = k \left( \frac{C_{L\alpha}}{AR} \right) (AR)_{\text{eff}}$$

*Region 2.* The calculation of  $C_{L\alpha}$  is the same as that given for Region 2, in Problem 13-1, except that  $AR$  is twice that calculated in step two of Problem 13-1, i.e.,

$$AR = 2 \left( \frac{b^2}{S} \right)$$

The remaining steps are described once again below.

a. Calculate the value of  $\beta$ :

$$\beta = (M^2 - 1)^{1/2}$$

b. Calculate the values of the parameters:

$$\frac{\beta}{\tan \Lambda_{LE}}$$

$$(AR) \tan \Lambda_{LE}$$

c. Enter Figure 13-4 and select the figure corresponding to the taper ratio  $\lambda$ . Select the curve corresponding to the value of the parameter  $(AR) \tan \Lambda_{LE}$ . If

$$\frac{\beta}{\tan \Lambda_{LE}} < 1,$$

use the left side of the figure to obtain the value of  $\tan \Lambda_{LE} C_{N\alpha}$ . Calculate  $C_{L\alpha}$  as follows:

$$C_{L\alpha} = \frac{\tan \Lambda_{LE} C_{N\alpha}}{\tan \Lambda_{LE}},$$

where the normal force coefficient  $C_{N\alpha}$  and  $C_{L\alpha}$  are taken to be equal within the scope of this method.

If

$$\frac{\beta}{\tan \Lambda_{LE}} > 1,$$

determine its reciprocal,

$$\frac{\tan \Lambda_{LE}}{\beta},$$

and use the right side of the figure to obtain the value of  $\beta C_{N\alpha}$ . The slope is calculated by:

$$C_{L\alpha} = \frac{\beta C_{N\alpha}}{\beta},$$

where  $C_N$  is represented as  $C_L$  within the scope of this method.

*Region 3.* The following steps, a through c, are used to calculate  $C_{L\alpha}$  for  $0.85 < M < 1.2$ .

a. Calculate  $C_{L\alpha}$  at  $M = 0.85$  following the method in Region 1.

b. Calculate  $C_{L\alpha}$  at  $M = 1.2$  following the method in Region 2.

c. Interpolate linearly for the slope at the actual Mach number:

$$C_{L\alpha} = C_{L\alpha} (\text{at } M = 0.85)$$

$$+ \frac{M - 0.85}{0.35} [C_{L\alpha} (\text{at } M = 1.2) - C_{L\alpha} (\text{at } M = 0.85)].$$

No numerical example is provided with this problem since the procedures are so similar to those of Problem 13-1, and since the calculation of the aerodynamic coefficient for the vertical tail is not required for the calculation of the simplified gust loading sure-safe and sure-kill envelopes described in succeeding problems.

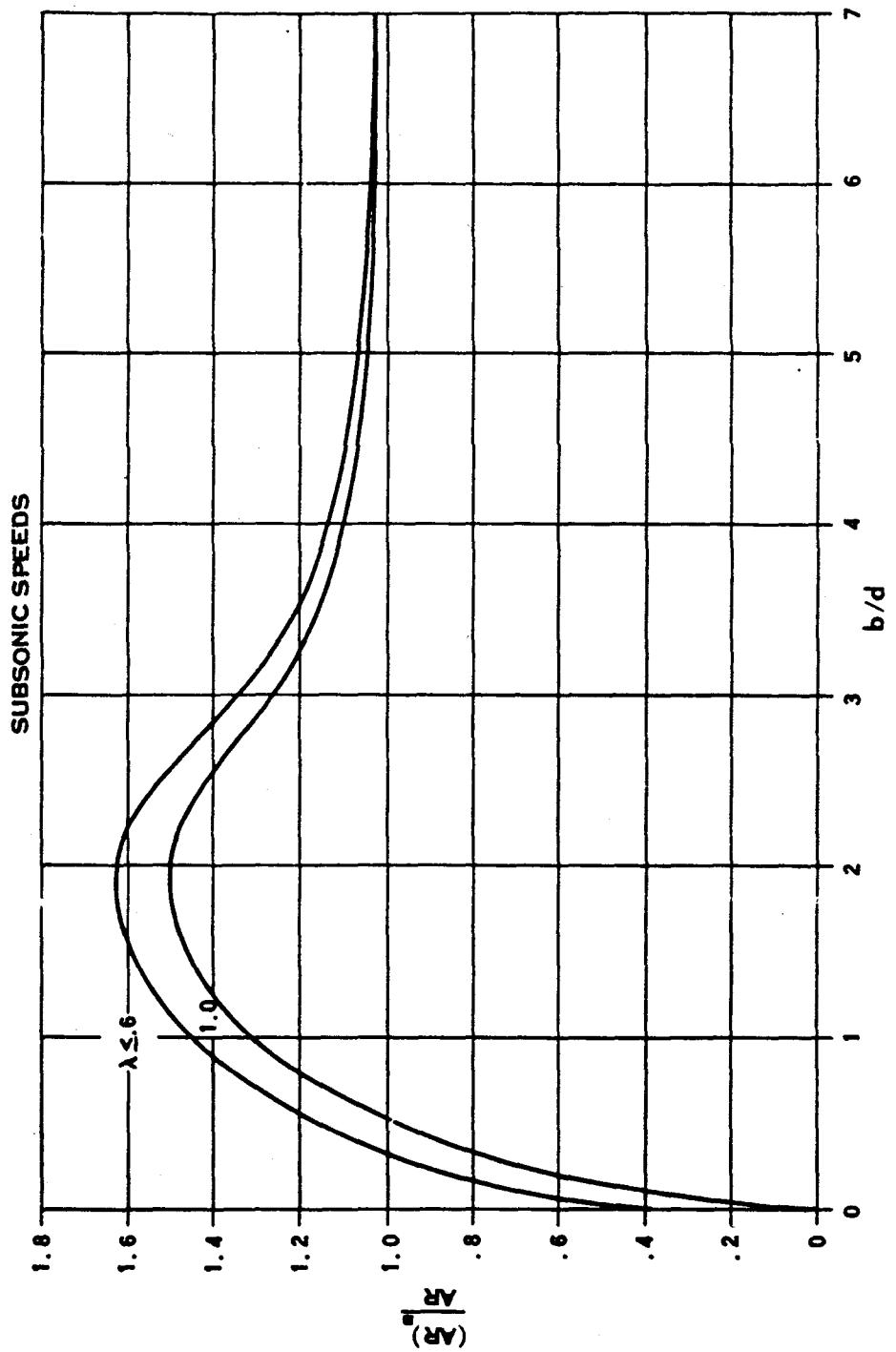


Figure 13-5. [REDACTED] Ratio of the Aspect Ratio of the Vertical Tail in the Presence of the Body to That of the Isolated Vertical Tail at Subsonic Speeds [REDACTED]

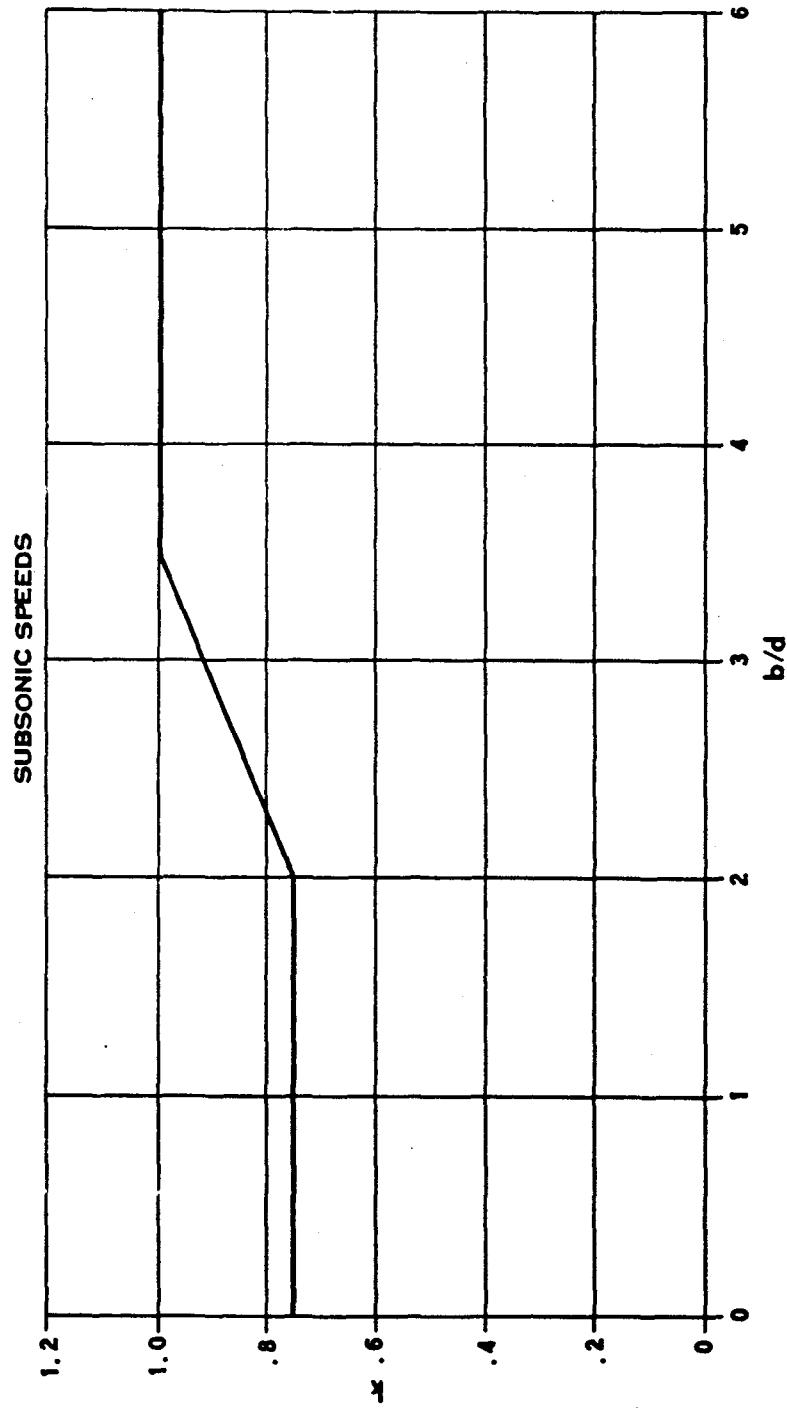


Figure 13-6. Empirical Factor for Estimating  $C_{L\alpha}$  for Vertical Tails

### 13-7 Gust Effects on In-Flight Aircraft

A nuclear explosion produces a blast wave that travels outward from the explosion, decaying in strength as it travels. The blast wave induces a flow velocity in the material (in this case, air), through which it passes. This material velocity, or gust, produces changes in the dynamic pressure and the angle of attack of an airplane that is intercepted by the blast wave. An increase in air density also is associated with the blast wave, and this increase in density also contributes to changing the dynamic pressure. The changes in angle of attack and dynamic pressure result in changes in the aerodynamic forces acting on the airplane. These changes in aerodynamic forces produce rigid-body and elastic motions of the airplane. In the sure-kill case, inelastic motions also are important. These motions produce additional aerodynamic forces. The aerodynamic forces and inertia forces may be summed to determine structural loads (such as bending moments) acting on the structure. Comparison of these structural loads with the allowable loads determines the safety of the airplane.

Gust effects on helicopters must be considered in two categories; first, the effects on the main rotor blades, and second, the effects on major components other than the main rotor blades. The second category of effects is very similar to the gust effects on airplanes. The only difference lies in the introduction of rotors as lift-producing devices. Helicopters have fuselages, horizontal tails, vertical tails, and, in some cases, even wings. These components may be analyzed in substantially the same way that the corresponding airplane components are analyzed.

The main rotor blades on the other hand, are unique to helicopters, and thus require special techniques. Three different types of blades must be considered: hinged, rigid (hingeless), and teetering. In the hinged version, a

hinge somewhat offset from the center of rotation permits free rotation of the blade outboard of the hinge in an up-and-down, or flapping, direction. The rigid, or hingeless, blade does not use a flapping hinge. The teetering blade roughly combines the characteristics of the hinged and hingeless blades. A teetering blade is essentially a seesaw about a hinge at the center of rotation. The blades on each side of the hinge are rigidly connected.

Problems 13-3 and 13-4 describe the calculation of intercept-time envelopes for sure-safe and sure-kill regions for airplanes and helicopters, respectively.

### 13-8 Gust Effects on Parked Aircraft

The material velocity and the increased density behind the blast wave give rise to a dynamic pressure that may be sufficiently high to impose large aerodynamic forces on a parked vehicle. For purposes of damage analysis, dynamic pressure effects are classified in two categories:

1. Direct damage to structural components that result from aerodynamic loading.
2. Gross aircraft motions that might produce indirect damage to structural components as a result of lifting the aircraft from the ground and the subsequent impact, or as a result of overturning the aircraft or crushing the landing gear.

The possibility of lifting the aircraft exists whenever the vehicle is subjected to lift forces that are comparable to the vehicle weight, even if tie-downs are employed. An aircraft with a low wing loading (gross weight divided by the wing area,  $GW/S$ ) is particularly susceptible to this type of damage since, in the parked position, the wing is set at a large angle of attack relative to the ground. Head-on encounter presents the most severe loading condition for this case.

[REDACTED] Skidding is possible whenever the drag, coupled with the lift, can overcome the frictional forces between the ground and the vehicle tires. With a large lift force, the normal force between ground and tire is reduced. The side force required to cause the vehicle to skid may thus be quite small compared with the weight of the vehicle. Vehicle orientations somewhere between head-on and side-on to the gust are expected to present the worst situation for this type of motion. No definitive criteria can be given for damage from skidding, because the damage criteria depend upon the distance of the aircraft from other objects.

[REDACTED] In some cases, the vehicle will overturn before skidding. Overturning will occur whenever the aerodynamic moments (about an axis joining appropriate wheel contact points) are of sufficient magnitude to overcome the stabilizing gravity moment and the frictional forces are sufficiently large to prevent skidding. A gust orientation somewhere between head-on and side-on is expected to provide the most severe condition. Other effects will almost always be predominant compared to overturning, and it is exceedingly difficult to devise a meaningful overturning solution that does not involve a sub-

stantial computer program.

[REDACTED] Negative lift results from tail-on encounters (blast approaching from the rear). The negative lift produces downward forces on the wheels, which, if sufficiently large, will damage the landing gear and perhaps the main supporting structure.

[REDACTED] Tie-downs would be expected to reduce the likelihood of lift-off, skidding, and overturning; however, tests have indicated that tie-downs are not very effective in reducing damage induced by motion when aircraft encounter high strength blast waves.

[REDACTED] Since helicopters do not have the large lifting surfaces that are present on airplanes, the problems of lift-off and crushing of the landing gear are much less severe for helicopters than for airplanes.

[REDACTED] Overpressure usually dictates the largest envelopes among all of the damage modes for parked aircraft. No calculation methodology is presented for gust effects on parked aircraft. The sure-safe and sure-kill overpressure envelopes may be accepted as the complete envelopes (see paragraph 13-9 and Problem 13-5).

**Problem 13-3. Calculation of Intercept-Time Envelopes that Determine Sure-Safe and Sure-Kill Regions with Respect to Material Velocity on Airplanes in Flight**

The analysis of gust effects on airplanes in flight is based upon determining the load factor produced on the airplane during the blast encounter, accounting roughly for the fact that this load factor is dynamically applied, and comparing the resultant effective load factor with the critical load factor. For sure-safe conditions, the critical load factor is based upon design limit conditions. For sure-kill conditions, the critical load factor is based upon design ultimate conditions and a lethal ratio factor. The lethal ratio factor is determined from a simple representation of post-failure response by a single degree of freedom system.

Standard shapes for the gust envelopes at intercept time are assumed applicable for all airplanes, weapon yields, and altitudes. Each point on the envelope shows the critical position of the airplane relative to the burst point at the time when the airplane is intercepted by the blast wave. The size of the envelopes is determined by evaluating the critical slant ranges, or distances from the burst point, associated with intercepts of the airplane from directly above, below and to the side.

The three slant ranges  $R_a$ ,  $R_b$ , and  $R_s$  that represent critical distances from above, below and to the side of the airplane, respectively, from which intercept-time envelopes are determined, must be calculated. The data required for the calculations include:

$h$  = airplane altitude (ft),

$W$  = weapon yield (kt),

$GW$  = airplane gross weight at time of interest (lbs),

$V$  = preblast airplane velocity (ft/sec),

$n$  = airplane preblast load factor (for a level flight,  $n = 1$ ) (dimensionless),

$N^+$  = up-loading airplane limit load factor corresponding to gross weight condition being considered (dimensionless),

$N^-$  = down-loading airplane limit load factor corresponding to gross weight condition being considered ( $N^-$  should be used as a negative number) (dimensionless),

Wing planform (see Figure 13-1).

Calculation of the three slant ranges for sure-safe conditions is performed by the following series of steps.

1. Enter Table 13-1 with the airplane altitude,  $h$ , to obtain  $P$ , the ambient pressure (psi),  $\rho$ , the ambient density (slugs/ft<sup>3</sup>), and  $c$ , the ambient speed of sound (ft/sec).

2. Calculate the Mach number,  $M$ :

$$M = \frac{V}{c}.$$

With  $M$ , and data defining wing planform, calculate the slope of the lift coefficient curve for the wing,  $C_{L\alpha}$ , using the method described in Problem 13-1.

3. Enter Figure 13-7 and select the curve corresponding to GW, airplane gross weight. Obtain the value of DF, the dynamic factor corresponding to the weapon yield,  $W$ .

4. To determine the slant range,  $R_a$ , for a burst from above

$$N = N^+,$$

where  $N$  is the critical load factor.

5. If

$$n < 0 \text{ and } N < 0,$$

or

$$n < 0 \text{ and } N > 0,$$

reverse the signs of both  $n$  and  $N$ . Otherwise, leave the signs as they were calculated. If

$$n < 0.01,$$

set

$$n = 0.01.$$

Thus,  $n$  will become positive in this step, regardless of its original sign.

6. Calculate  $\Delta L/L$ , ratio of the incremental lift due to blast to the preblast value of lift as follows:

$$\frac{\Delta L}{L} = \left[ \frac{N}{n} - 1 \right] \left[ \frac{1}{(DF)} \right].$$

7. Calculate  $w/c$ , the ratio of the component of the airplane velocity normal to the wing ( $w$ ) to the speed of sound:

$$\frac{w}{c} = \frac{2n (GW)}{\rho V S C_{L_\alpha} c},$$

where  $S$  is the airplane wing area, and the other symbols have been defined.

8. Calculate the product of  $\Delta L/L$  and  $w/c$ .

9. Select the curve in Figure 13-8 corresponding to the value of  $w/c$  obtained in step 7. Enter the graph with the value of  $(w/c)(\Delta L/L)$  obtained in step 8, and read the corresponding value of the range parameter  $\bar{R}$ . If  $N$  is positive, use Figure 13-8a. If  $N$  is negative, use Figure 13-8b.

10. Compute  $R_a$ , the range (ft), which defines the distance at which a nuclear explosion would produce critical effects, as follows:

$$R_a = \bar{R} \left[ \frac{14.7 W}{P} \right]^{1/3}.$$

11. Repeat steps 4 through 10 to calculate  $R_b$ . In step 4, set

$$N = N^+$$

for bursts from below, and replace  $R_a$  with  $R_b$  in the equation of step 10.

12. Set

$$N = N^+,$$

and  $n = 1$  (corresponding to straight on level flight). Repeat steps 6 through 10 to calculate  $R_s$  ( $R_s$  replaces  $R_a$  in the equation of step 10). A burst from the side is taken to be equivalent to a burst from below with the airplane in straight and level flight.

13. The ranges  $R_a$ ,  $R_b$ , and  $R_s$  define the size of the standard sure-safe envelopes as illustrated in Figure 13-9.  $R_a$  represents the diameter of a sphere above the airplane;  $R_b$  is the diameter of a sphere below; and  $R_s$  is the diameter of a sphere to the side of the airplane. The X-Y plane is the plane of symmetry of the airplane, with the preblast velocity vector pointing in the direction of the positive X-axis; the Y-axis points in the direction of the right wing; the Z-axis is directed upward, thus determining an orthogonal, left-handed system. The envelopes are symmetric with respect to the X-Z plane.

Calculation of the slant ranges  $R_a$ ,  $R_b$ , and  $R_s$ , that define the size of the standard envelopes at intercept time for sure-kill conditions is performed by the following series of steps.

1. Follow steps 1 through 3 in the calculation of the ranges for sure-safe conditions.

2. Enter Figure 13-10 and select the curve corresponding to GW, airplane gross weight. With weapon yield, W, obtain the value of LR, the lethal ratio.

3. To determine  $R_a$ , the slant range for burst from above, calculate N, the critical load factor:

$$N = (1.5)(N^*)(LR),$$

where the factor 1.5 is the usual factor between limit load and ultimate load. Follow steps 5 through 10 in the calculation for sure-safe conditions.

4. To determine  $R_b$  for burst from below, calculate N:

$$N = (1.5)(N^*)(LR),$$

and follow steps 5 through 10 in the calculation for sure-safe conditions.

5. To determine  $R_s$ , the slant range for burst from the side, calculate N:

$$N = (1.5)(N^*)(LR)$$

and let  $n = 1$  since burst from the side is taken as burst from below corresponding to a straight and level flight. Repeat steps 6 through 10 in the calculation for sure-safe conditions.

6. Construct the sure-kill envelopes as described in step 13 in the calculation for sure-safe conditions.

DNA  
(L)(1)

DNA  
L(X1)

The resulting intercept time envelopes are illustrated in Figure 13-9.

**Reliability:** A typical airplane is used to represent each airplane class for purposes of defining a dynamic factor and a lethal ratio factor.

The airplane is in a symmetric flight prior to blast intercept. This definition includes a straight and level flight. All degrees of freedom are ignored except for the two previously mentioned. The atmosphere is assumed homogeneous, having characteristics associated with the altitude at which the airplane is flying. The standard shapes for the gust envelopes at intercept time are assumed to be applicable for all airplanes, weapon yields, and altitudes. The maximum error in the calculation is estimated to be a factor of 2.

**Related Material:** See paragraphs 13-1, 13-2, 13-6, and 13-7. See also Table 13-1.

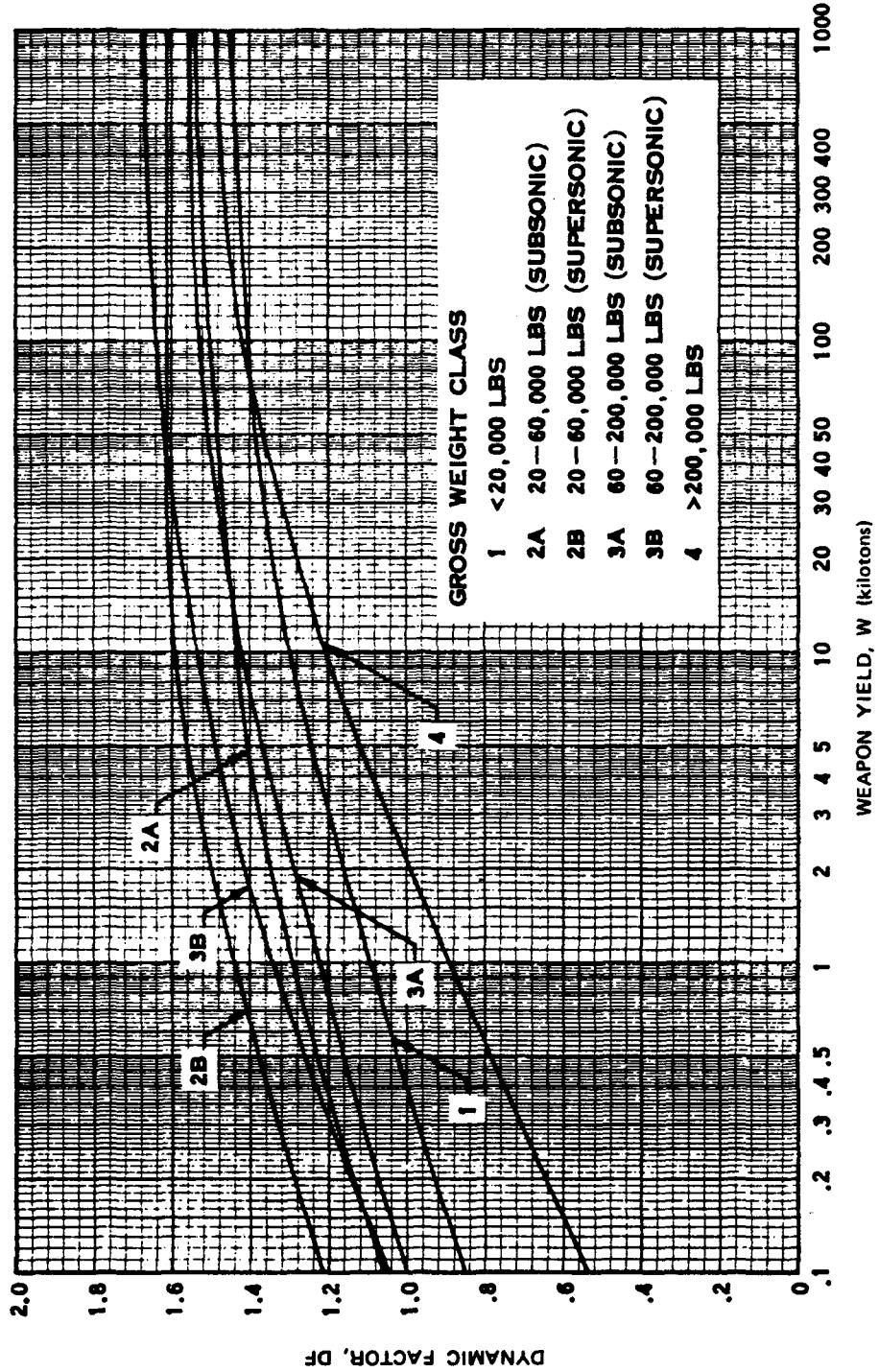


Figure 13-7. [REDACTED] Dynamic Factor vs Weapon Yield [REDACTED]

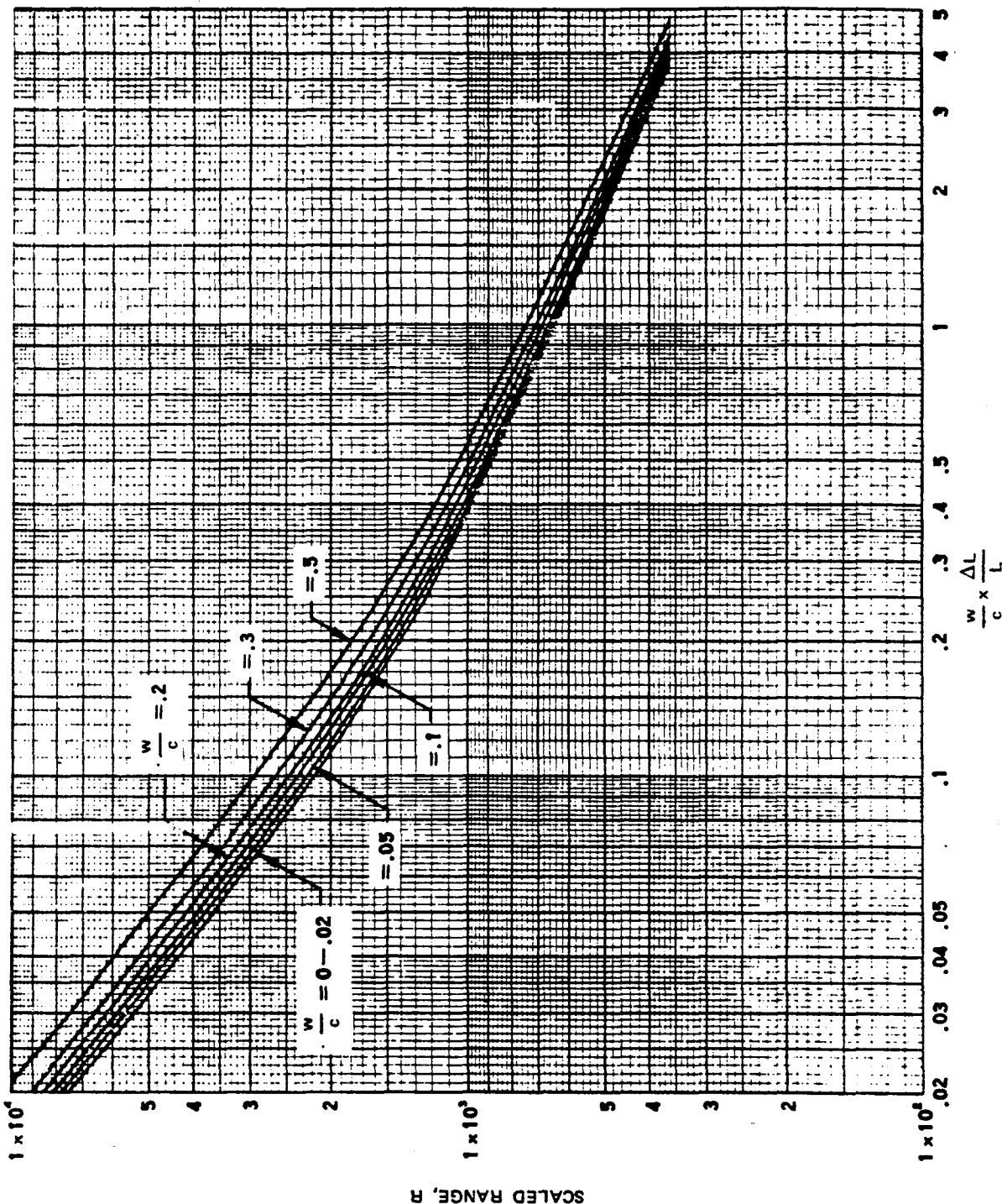


Figure 13-8a.  $\frac{w}{c} \times \frac{\Delta L}{L}$  as a Function of Scaled Range ( $N > 0$ )

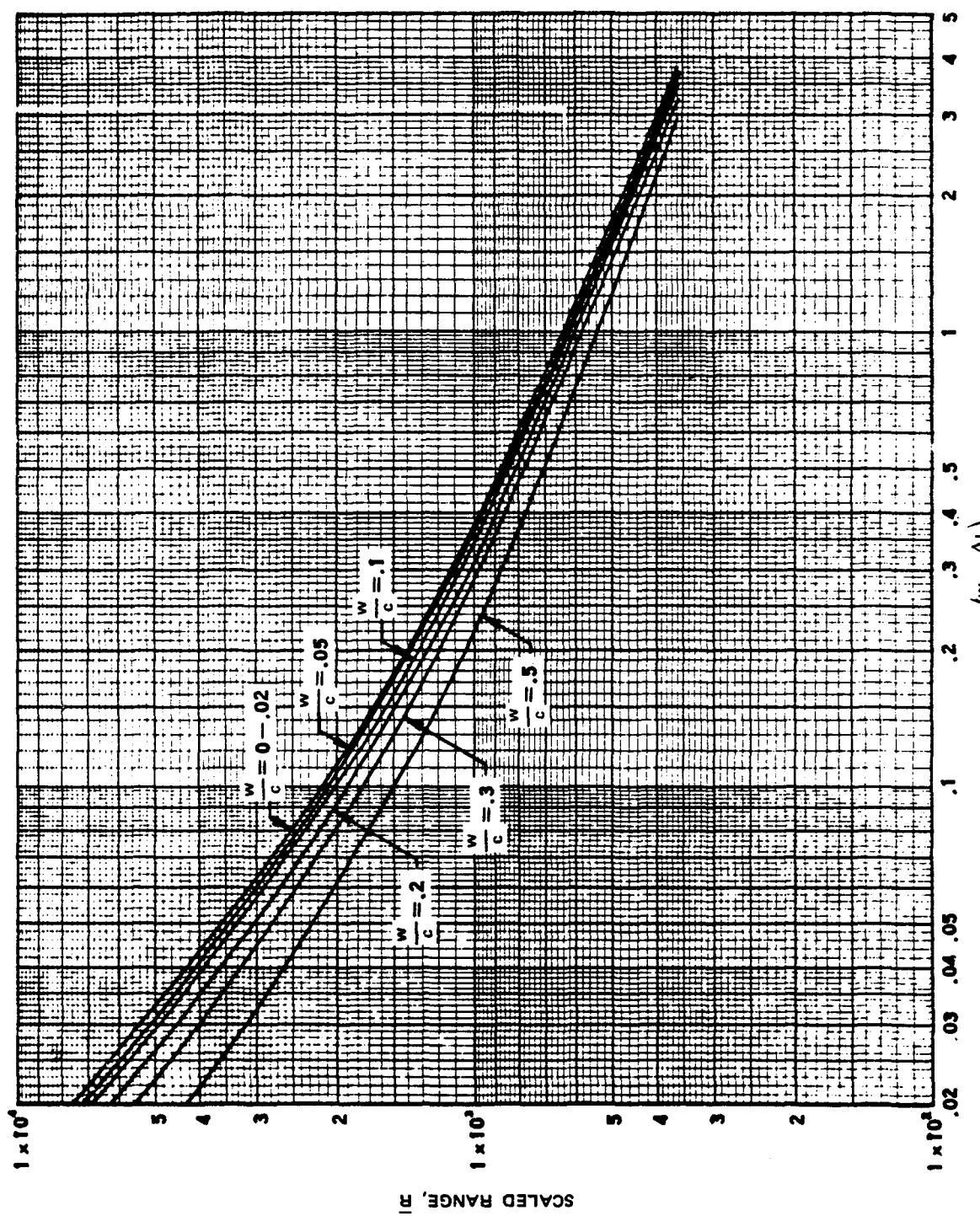
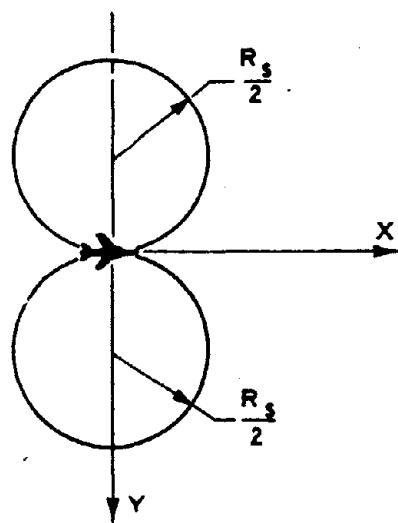
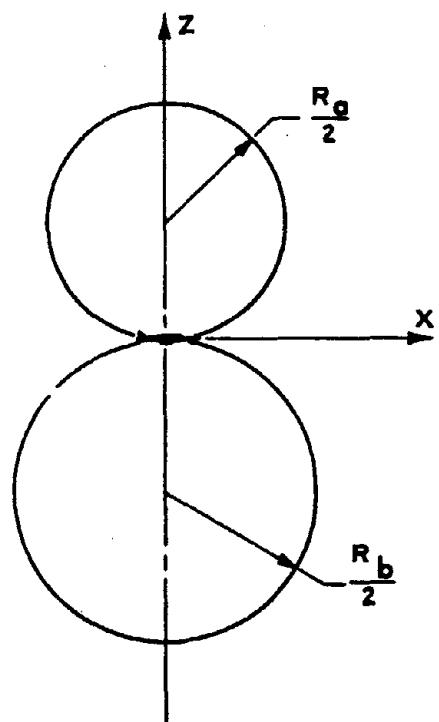


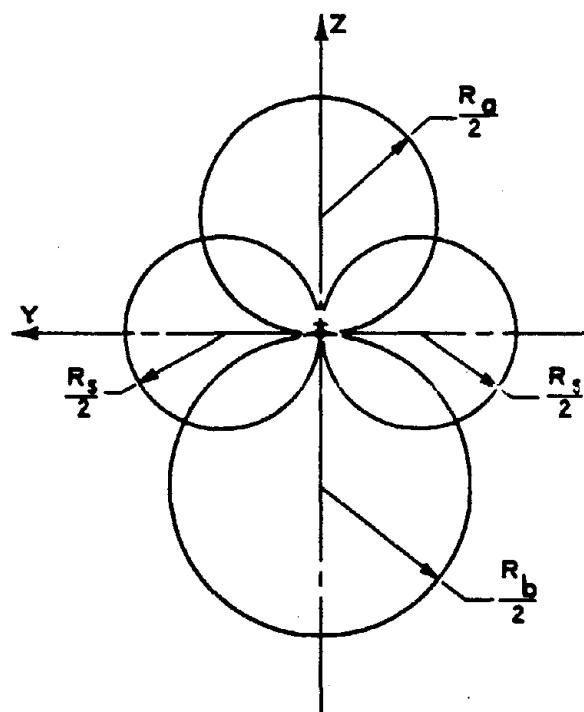
Figure 13-8b.  $\frac{w}{c} \times \frac{\Delta L}{L}$  as a Function of Scale I Range ( $N < 0$ )



TOP VIEW (SECTION IN X-Y PLANE)



SIDE VIEW (SECTION IN X-Z PLANE)



FRONT VIEW (SECTION IN Y-Z PLANE)

Figure 13-9. Standard Shapes for Gust Envelopes at Intercept Time

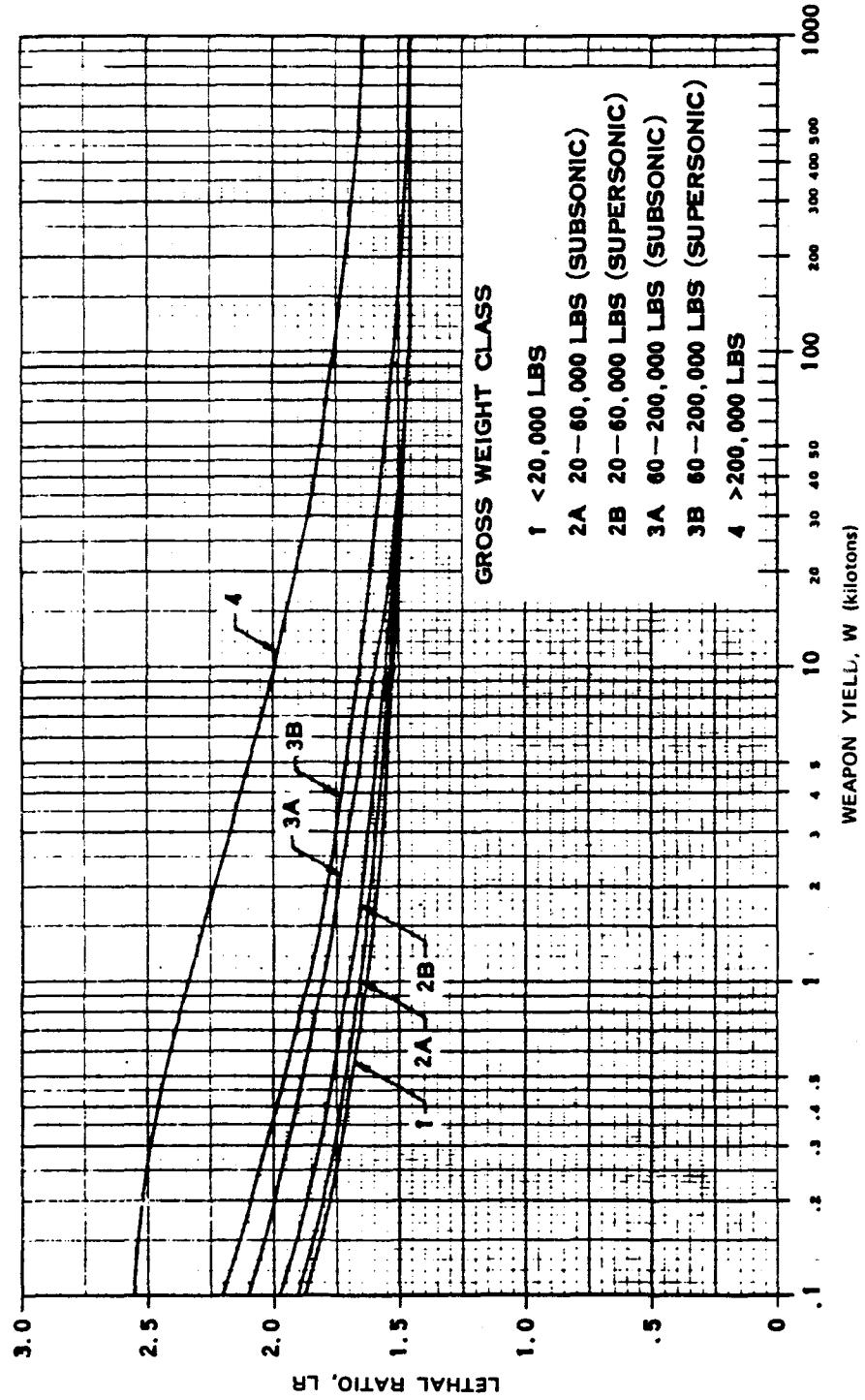


Figure 13-10. [REDACTED] Lethal Ratio vs Weapon Yield [REDACTED]

**Problem 13-4. Calculation of Intercept-Time Envelopes Determining Sure-Safe and Sure-Kill Regions with Respect to Gust Effects of the Material Velocity Behind the Blast Wave on Helicopters in Flight**

The analysis of gust effects on helicopters is based upon determining the load factor produced during the blast encounter, accounting roughly the fact that this incremental load factor is dynamically applied, and comparing the resultant effective load factor with the critical load factor. For sure-safe conditions, the critical load factor is based upon design limit conditions. For sure-kill conditions, the critical load factor is based upon design ultimate conditions and a lethal ratio factor.

Gust effects on helicopters must be considered in two categories: first, the effects on the main rotor blades (hinged, rigid and teetering); and second, the effects on major components other than the main rotor blades, which are very similar to the gust effects on airplanes.

The constraints in the calculation are as follows:

- Representative values of helicopter parameters can be used in defining a dynamic factor and a lethal ratio factor. All other calculations involve the actual helicopter characteristics.
- The helicopter is in a symmetric maneuver prior to blast intercept. This definition includes straight and level forward or hovering flight.
- For a hinged blade, blade response to gust is not considered in this problem; the flapping of a teetering rotor is not considered in the calculation.
- The lift distribution along the blade is linear, starting at zero at the hub and fitted to the actual running lift at the 3/4 blade span position.

- Rigid-body motions of the helicopter are neglected, and the rotor tilt angle is ignored.
- Inflow resulting from the gust is considered to occur too late to influence the response. The effect of the preblast inflow on dynamic pressure is ignored.
- The preblast atmosphere is homogeneous, having characteristics associated with the altitude at which the helicopter is flying.
- Standard shapes for the gust envelopes at intercept time are applicable for all helicopters, weapon yields, and altitudes.

The envelopes calculated in this problem are intercept-time envelopes. The size of the envelopes is determined by evaluating the critical slant ranges, or distances from the burst point, associated with intercepts of the helicopter from directly above, below and to the side.

The three slant ranges  $R_a$ ,  $R_b$ , and  $R_s$  representing the critical distances from above, below and to the side, respectively, are calculated first for sure-safe conditions in the following series of steps. The data that are required for the calculations include:

$h$  = helicopter altitude (ft)

$W$  = weapon yield (kt)

$GW$  = helicopter gross weight at time of interest (lbs)

$V$  = preblast helicopter velocity (ft/sec)

$\Omega_{MR}$  = main rotor angular velocity (rad/sec)

$R_{MR}$  = main rotor blade radius (ft)

$c_{MR}$  = main rotor blade chord (ft)

$b_{MR}$  = number of blades in main rotor (dimensionless)

$n$  = helicopter preblast load factor; for straight and level flight,  $n = 1$  (dimensionless)

$N^+$  = up-loading helicopter limit load factor corresponding to gross weight condition being considered (dimensionless)

$N^-$  = down-loading helicopter limit load factor corresponding to gross weight condition being considered. Note:  $N^-$  should be used as a negative number (dimensionless)

Wing planform (if helicopter has wings).

1. Determine the ambient atmospheric conditions at helicopter altitude  $h$  from Table 13-1;  $P$ , the ambient pressure (psi);  $\rho$ , the ambient density (slugs/ft<sup>3</sup>); and  $c$ , ambient speed of sound (ft/sec).

2. If the helicopter has no wings, or if a helicopter having wings is hovering, i.e.,  $V = 0$ , go to step 4. Otherwise, calculate the total wing area,  $S_W$ , which is defined as the extension of the leading and trailing edges of both wings to the helicopter centerline (ft<sup>2</sup>).

3. Using the wing planform (Figure 13-2), with the Mach Number,  $M$ , equal to zero, calculate the slope of the lift coefficient curve for the wing,  $C_{L\alpha}^W$ , using the method described in Problem 13-1. Let  $C_{L\alpha}^{MR} = 5.7$ , where  $C_{L\alpha}^{MR}$  is the lift curve slope for the main rotor.

4. Enter Figure 13-11 with the weapon yield,  $W$ , and obtain the corresponding value of  $DF$ , the dynamic coefficient.

5. To determine the slant range,  $R_s$ , for a burst from above

$$N = N^-$$

where  $N$  is the critical load factor.

6. If

$$n < 0 \text{ and } N < 0,$$

or

$$n < 0 \text{ and } N > 0,$$

reverse the signs of both  $n$  and  $N$ . Otherwise, leave the signs as they were calculated. If

$$n < 0.01,$$

set

$$n = 0.01.$$

Thus,  $n$  will become positive in this step, regardless of its original sign.

7. Calculate  $\Delta L/L$ , the ratio of the incremental lift due to blast to the preblast value of lift as follows:

$$\frac{\Delta L}{L} = \left[ \frac{N}{n} - 1 \right] \left[ \frac{1}{(DF)} \right].$$

8. Calculate the parameter  $\eta$ :

a. If the helicopter has wings,

$$\eta = \frac{2n(GW)}{\rho c \left[ \frac{1}{2} C_{L\alpha}^{MR} (b_{MR} R_{MR} c_{MR}) \Omega_{MR} R_{MR} + C_{L\alpha}^W V S_W \right]}.$$

b. If the helicopter has no wings,

$$\eta = \frac{2nGW}{\rho c \left[ \frac{1}{2} C_{L\alpha}^{MR} (b_{MR} R_{MR} c_{MR}) \Omega_{MR} R_{MR} \right]}.$$

9. Obtain the product

$$\left[ \frac{\Delta L}{L} \right] \eta.$$

10. Enter Figure 13-12a if  $N > 0$  or 13-12b if  $N < 0$ , and select the curve corresponding to the value of  $\eta$  from step 8. With the value of

$$\left[ \frac{\Delta L}{L} \right] \eta$$

from step 9, obtain the range parameter  $\bar{R}$ .

11. Compute  $R_a$ , the range (ft), which defines the distance at which a nuclear explosion would produce critical effects, as follows:

$$R_a = \bar{R} \left[ \frac{14.7 W}{P} \right]^{1/3}$$

12. Repeat steps 5 through 11 to calculate  $R_b$ . In step 5, set

$$N = N^+$$

for bursts from below, and replace  $R_a$  with  $R_b$  in the equation of step 10.

13. Set

$$N = N^+,$$

and  $n = 1$  (corresponding to straight on level flight). Repeat steps 7 through 11 to calculate  $R_s$  ( $R_s$  replaces  $R_a$  in the equation of step 10). A burst from the side is taken to be equivalent to a burst from below with the helicopter in straight and level flight.

14. The ranges  $R_a$ ,  $R_b$ , and  $R_s$  define the size of the standard sure-safe envelopes as illustrated in Figure 13-13.  $R_a$  represents the diameter of a sphere above the helicopter;  $R_b$  is the diameter of a sphere below; and  $R_s$  is the diameter of a sphere to the side of the helicopter. The X-Y plane is the plane of symmetry of the helicopter with the preblast velocity vector pointing in the direction of the positive X-axis; the Y-axis points to the right side of the helicopter; the Z-axis is directed upward, thus determining an orthogonal, left-handed system. The envelopes are symmetric with respect to the X-Z plane.

(U) Calculation of the slant ranges  $R_a$ ,  $R_b$ , and  $R_s$ , that define the size of the standard envelopes at intercept time for sure-kill conditions is performed by the following series of steps.

1. Follow steps 1 through 4 in the calculation of the ranges for sure-safe conditions.

2. Enter Figure 13-14 with weapon yield, W, and obtain the value of LR, the lethal ratio.

3. To determine  $R_a$ , the slant range for burst from above, calculate  $N$ , the critical load factor:

$$N = (1.5)(N^+)(LR),$$

where the factor 1.5 is the usual factor between limit load and ultimate load. Follow steps 6 through 11 in the calculation for sure-safe conditions.

4. To determine  $R_b$  for burst from below, calculate  $N$ :

$$N = (1.5)(N^+)(LR),$$

and follow steps 6 through 11 in the calculation for sure-safe conditions.

5. To determine  $R_s$ , the slant range for burst from the side, calculate  $N$ :

$$N = (1.5)(N^+)(LR)$$

and let  $n = 1$  since burst from the side is taken as burst from below corresponding to a straight and level flight. Repeat steps 7 through 11 in the calculation for sure-safe conditions.

6. Construct the sure-kill envelopes as described in step 14 in the calculation for sure-safe conditions.

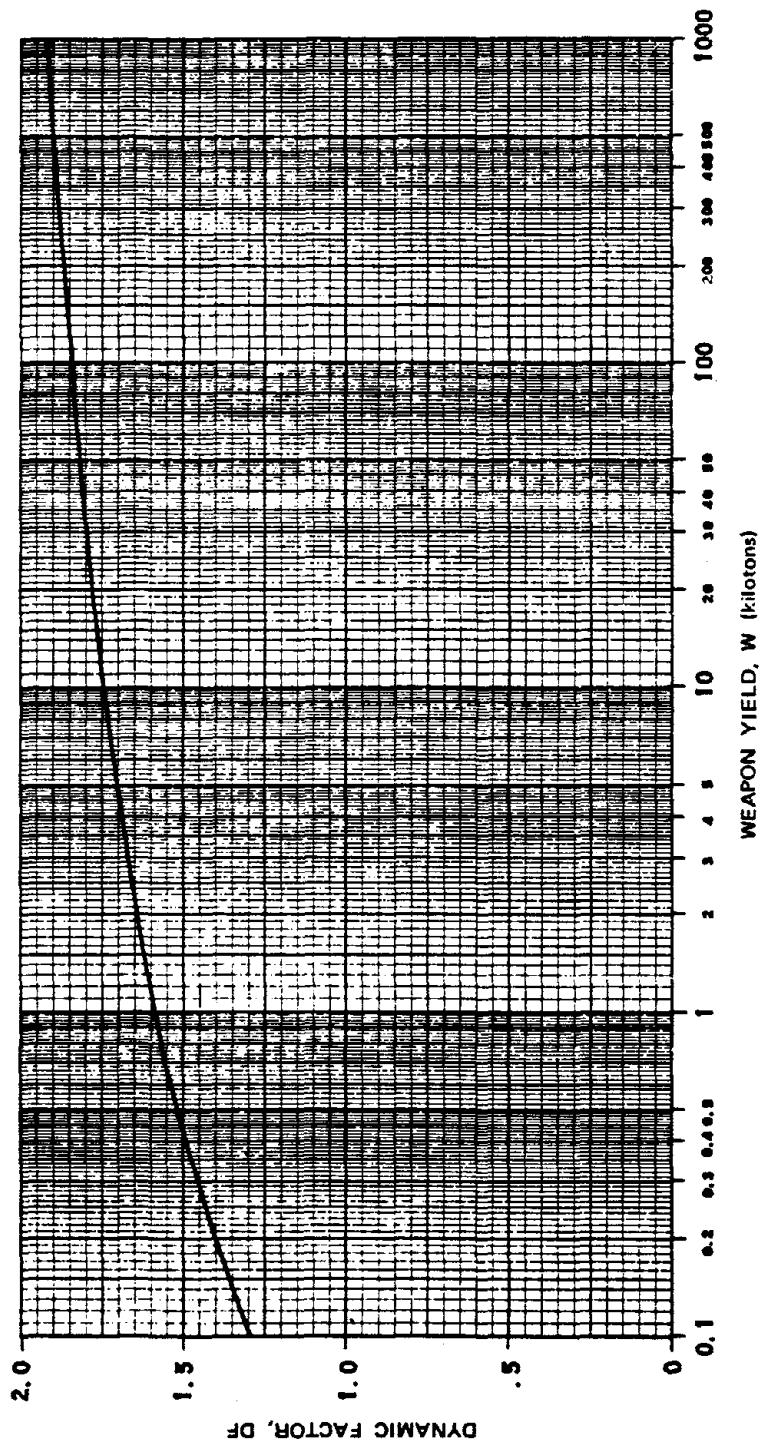


Figure 13-11. [REDACTED] Dynamic Factor vs Weapon Yield [REDACTED]

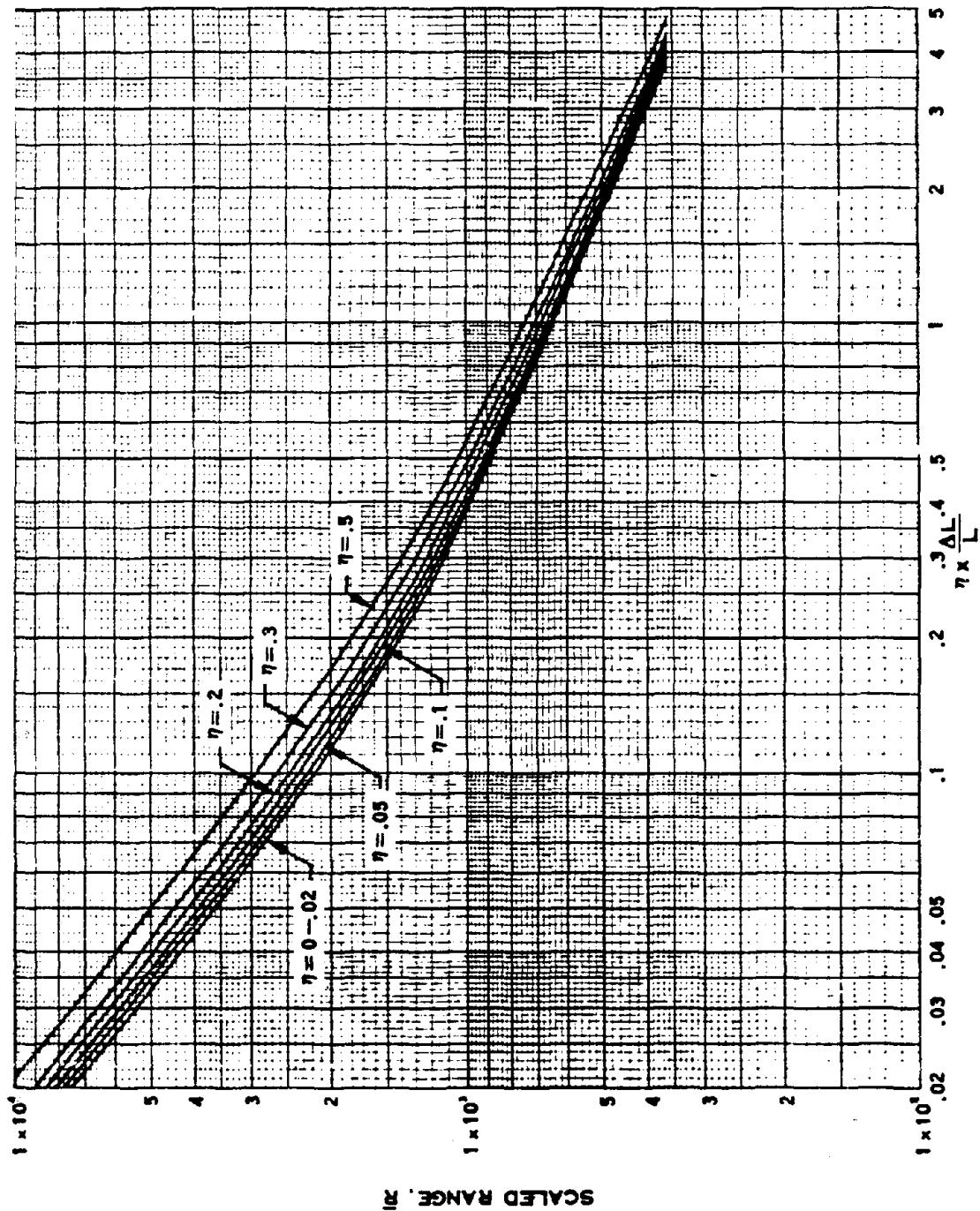


Figure 13-12a.  $\eta \times \frac{\Delta L}{L}$  as a Function of Scaled Range ( $N > 0$ )

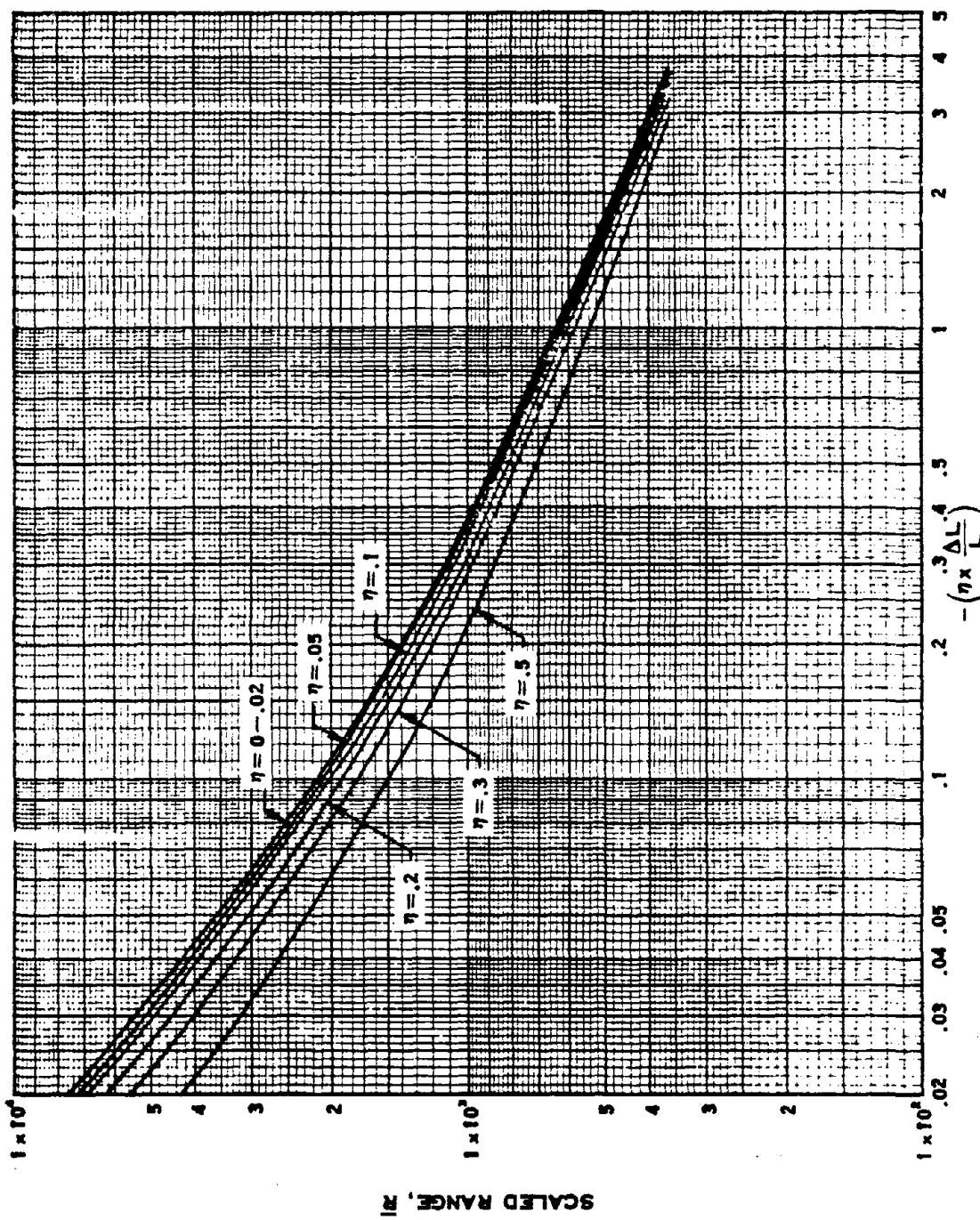
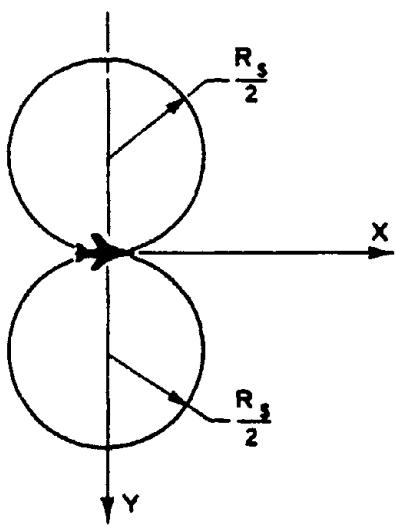
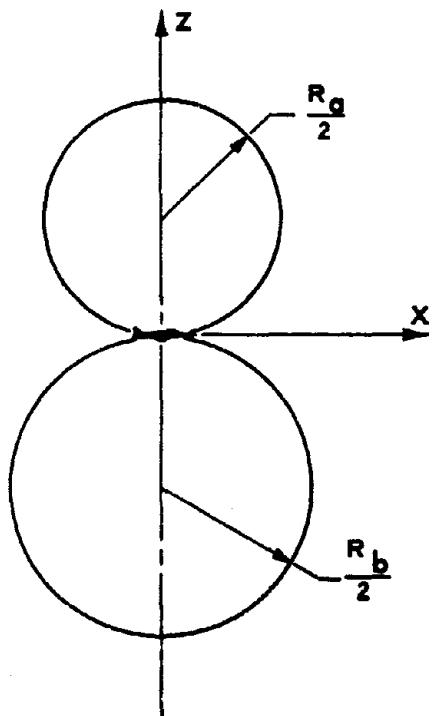


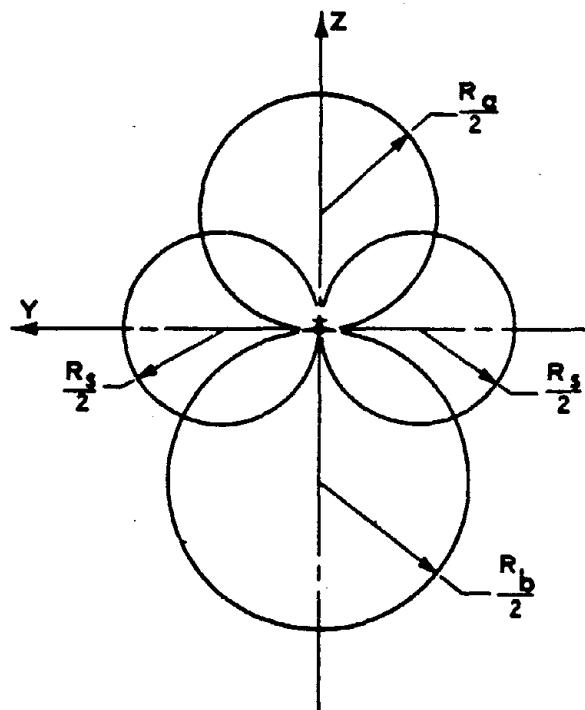
Figure 13-12b.  $\eta \times \frac{\Delta L}{L}$  as a Function of Scaled Range ( $N < 0$ )



**TOP VIEW (SECTION IN X-Y PLANE)**



**SIDE VIEW (SECTION IN X-Z PLANE)**



**FRONT VIEW (SECTION IN Y-Z PLANE)**

Figure 13-13. Standard Shapes for Gust Envelopes  
at Intercept Time

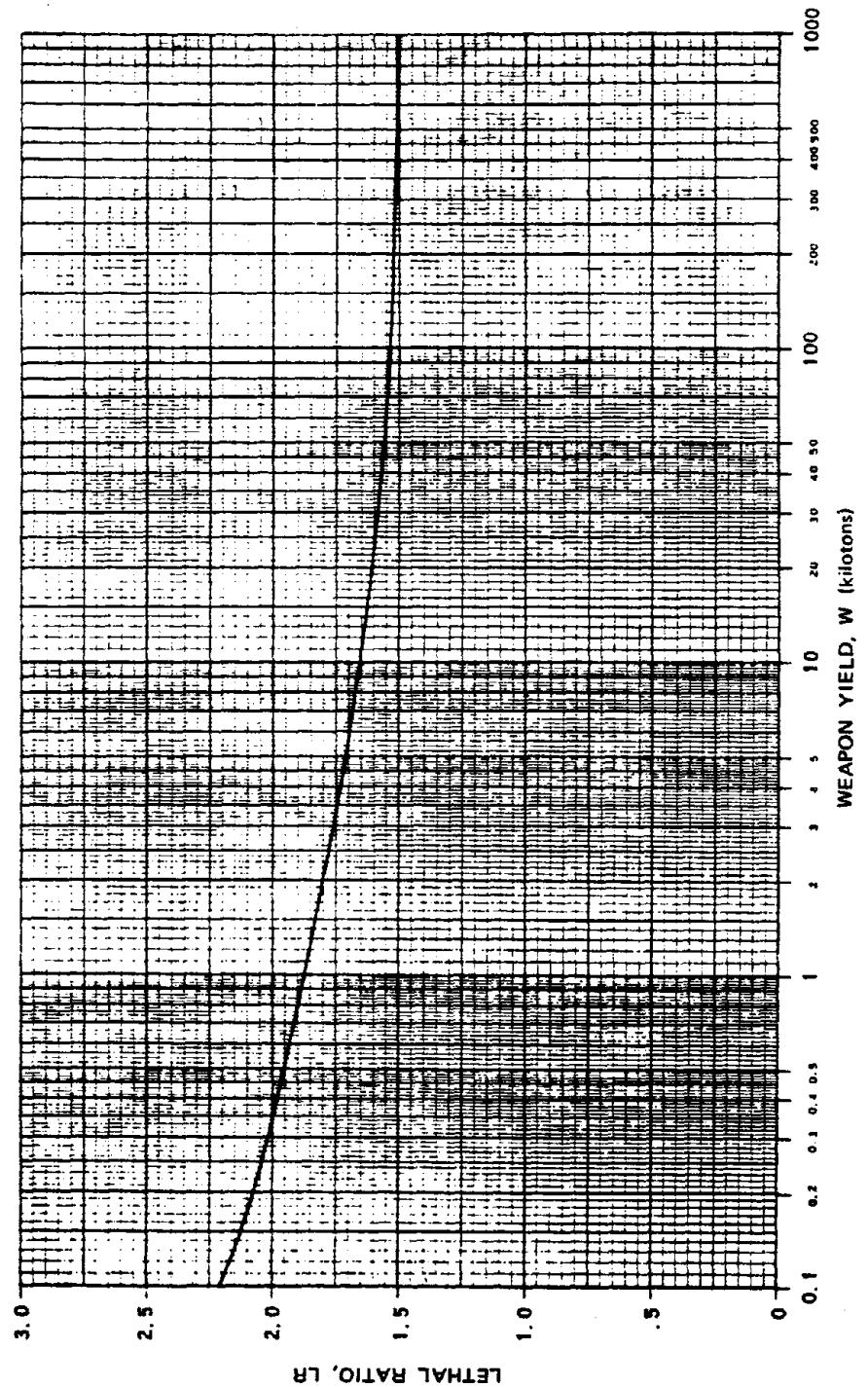


Figure 13-14. [REDACTED] Lethal Ratio vs Weapon Yield [REDACTED]

## AIRCRAFT RESPONSE TO OVERPRESSURE EFFECTS

### 13-9 Overpressure Effects on In-Flight and Parked Aircraft

If an aircraft is located in the vicinity of the nuclear explosion, the expanding blast wave eventually engulfs the aircraft. Depending on the distance of the aircraft from the burst, the pressure rise, or overpressure, experienced by an aircraft can be of a sufficient magnitude to damage the structural components.

An aircraft subjected to an overpressure loading can experience structural damage in several ways. Skin panels may yield or rupture; longerons, stringers, and frames may fail by compressive yielding or local buckling. The fuselage generally is the most susceptible to these types of damage; hence, *only the fuselage is examined for overpressure effects*. The method presented in this section for analyzing overpressure damage is applicable to all types of aircraft and helicopters both in-flight and parked. Methods for performing the analysis are given in Problem 13-5.

**Problem 13-5. Calculation of the Boundaries in Space that Define the Sure-Safe and Sure-Kill Regions with Respect to the Effects of Overpressure Behind the Blast Wave on Aircraft In-Flight or Parked**

As discussed in paragraph 13-9, overpressure loading can produce structural damage in several ways; however, since the fuselage generally is the most susceptible item, only fuselage damage is considered in the following analysis.

The major constraints in the analysis are:

- Overpressure damage to an aircraft is the same for all aircraft in a given class.
- The preblast atmosphere is homogeneous, having characteristics associated with the aircraft altitude.

The data required for the analysis are aircraft altitude (ft), weapon yield, and aircraft class. Table 13-2 lists various aircraft classes and corresponding overpressure limits for sure-safe and sure-kill conditions.

2. Knowing the class of aircraft being considered, obtain the critical overpressure level,  $\Delta p$ , for either sure-safe or sure-kill conditions from Table 13-2.

3. Using the value of the critical overpressure, determine the corresponding value of sea level overpressure by the scaling law given in paragraph 2-14, i.e.,

$$\Delta p_0 = \frac{P_0 \Delta p}{P} = \frac{14.7 \Delta p}{P},$$

where the subscript zero indicates sea level values of overpressure and ambient pressure, and the absence of a subscript indicates the corresponding values at altitude  $h$ .

4. Enter Figure 13-15\* with  $\Delta p_0$ , and determine the corresponding slant range,  $R_1$ , from a 1 kt explosion in a sea level atmosphere.

5. Calculate the corresponding slant range,  $R$ , for a yield of  $W$  kt,

$$R = R_1 \left[ \frac{14.7 W}{P} \right]^{1/3}.$$

6. The critical volume is defined by a sphere of radius  $R$  centered on the aircraft. For in-flight aircraft, continue to step 7; for parked aircraft, go to step 8.

7. The volume defined in step 6 is an intercept-time volume; that is, each point on the surface shows the critical position of the aircraft relative to the burst point at the time when the aircraft is intercepted by the blast wave. Ordin-

\* Figure 13-15 is identical to Figure 2-2, Chapter 2. It is reproduced here for convenience of the user.

The overpressure analysis is performed in a series of steps as described below.

1. Determine the ambient pressure  $P$  at the aircraft altitude,  $h$ , from Table 13-1.

narily, burst-time volumes are desired for in-flight aircraft, rather than intercept-time volumes. A point on a burst-time volume defines the critical position of the aircraft relative to the burst point at the time of burst. Thus, a sure-kill burst-time volume shows the regions in space, relative to the airplane, in which the explosion of a given size nuclear weapon will result in the destruction of the aircraft. This is the information that ordinarily is desired. To obtain the burst-time volume, it is necessary to transform the intercept-time volume obtained in step 6 into a burst-time volume. This transformation is demonstrated in Problem 13-7. This concludes the analysis for in-flight aircraft.

8.\* For parked aircraft only, the sphere found in step 6 (more properly, the hemisphere) must be modified for ground reflection effects. Enter Figure 13-16 with sea level overpressure determined in step 3, and read three horizontal range parameters,  $\overline{HR}_i$  ( $i = 1, 2, 3$ ).

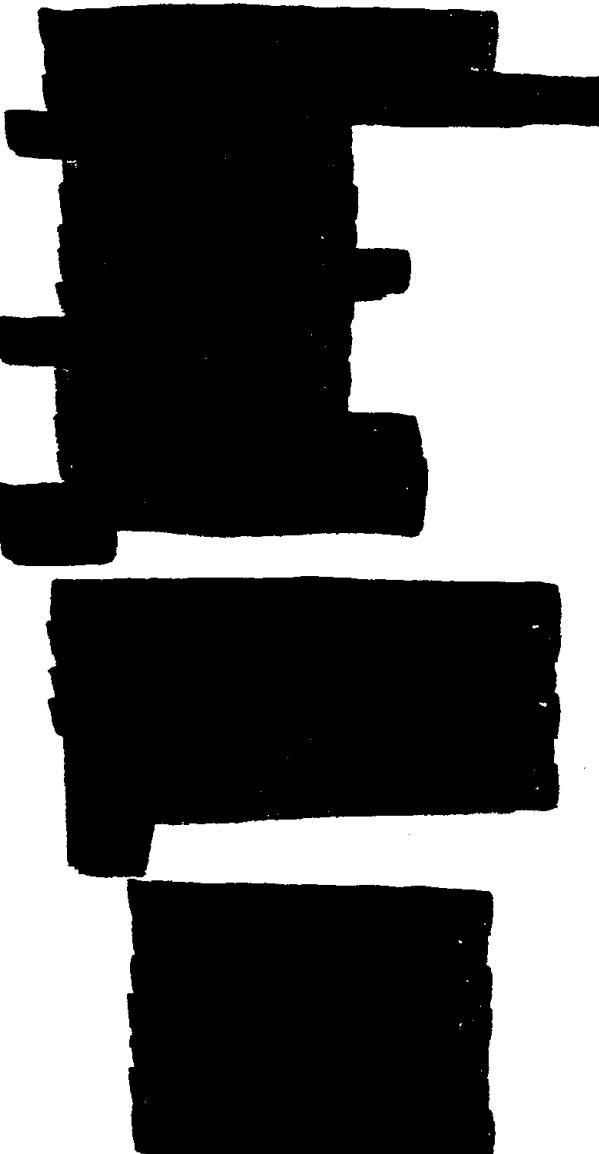
9. Enter Figure 13-17 with  $\overline{HR}_i$  and read three corresponding burst height parameters,  $\overline{BH}_i$  ( $i = 1, 2, 3$ ). (Note  $\overline{BH}_1$  is always zero.)

10. Calculate the burst heights and horizontal ranges, in feet.

$$BH_i = \overline{BH}_i \left[ \frac{14.7 W}{P} \right]^{1/3}$$

$$HR_i = \overline{HR}_i \left[ \frac{14.7 W}{P} \right]^{1/3}$$

11. Plot the burst height versus horizontal range, by connecting the three points determined in step 10. Draw a radial line from the origin to point 3. The volume defined by rotating this envelope about a vertical axis through the aircraft is the ground-effects volume, which is to be combined with the hemisphere already found. Ground reflection effects are seen to add a "collar" around the base of the hemisphere.



DIA  
(LX1)

\* The envelope generated by following steps 8 through 11 could be obtained by using the air blast height of burst curves in Chapter 2; however, these steps (and the accompanying figures) present the information in a more convenient form that is suitable to the accuracy of this analysis.

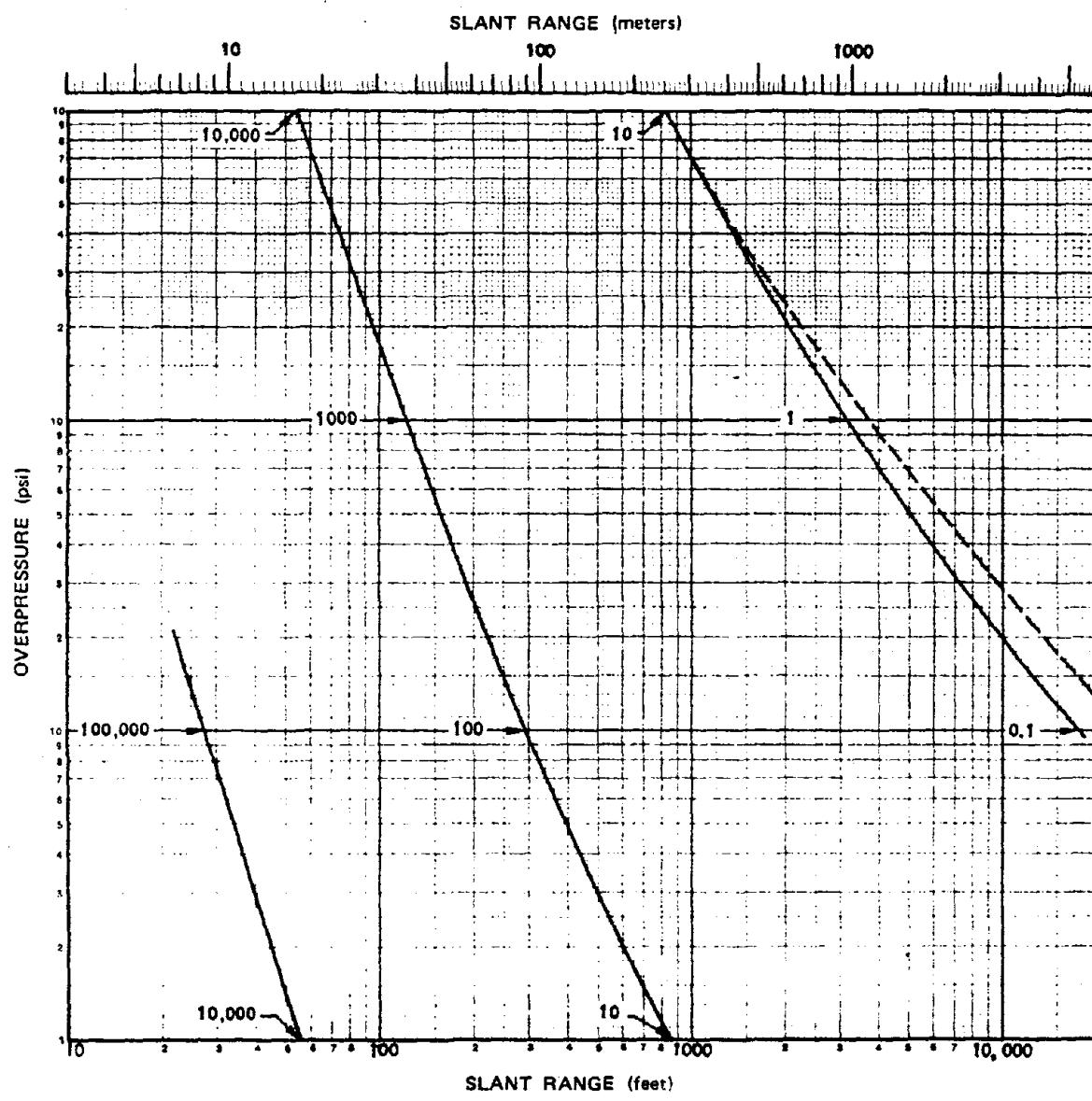


Figure 13-15. Peak Overpressure from a 1 kt Free Air Burst  
in a Standard Sea Level Atmosphere

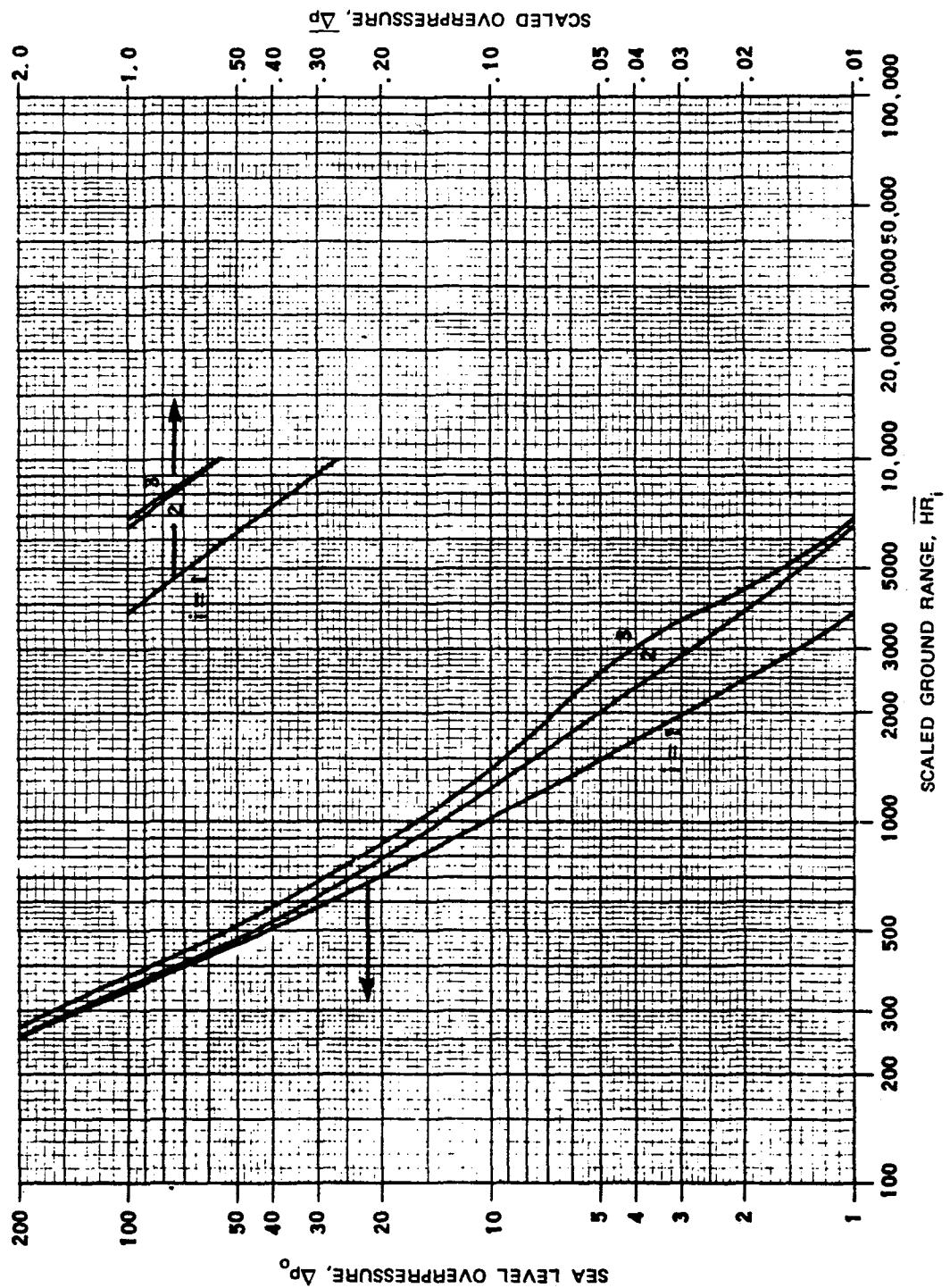


Figure 13-16. The Range Parameter  $\overline{HR}_i$  as a Function of Sea Level Overpressure  $\Delta p_0$

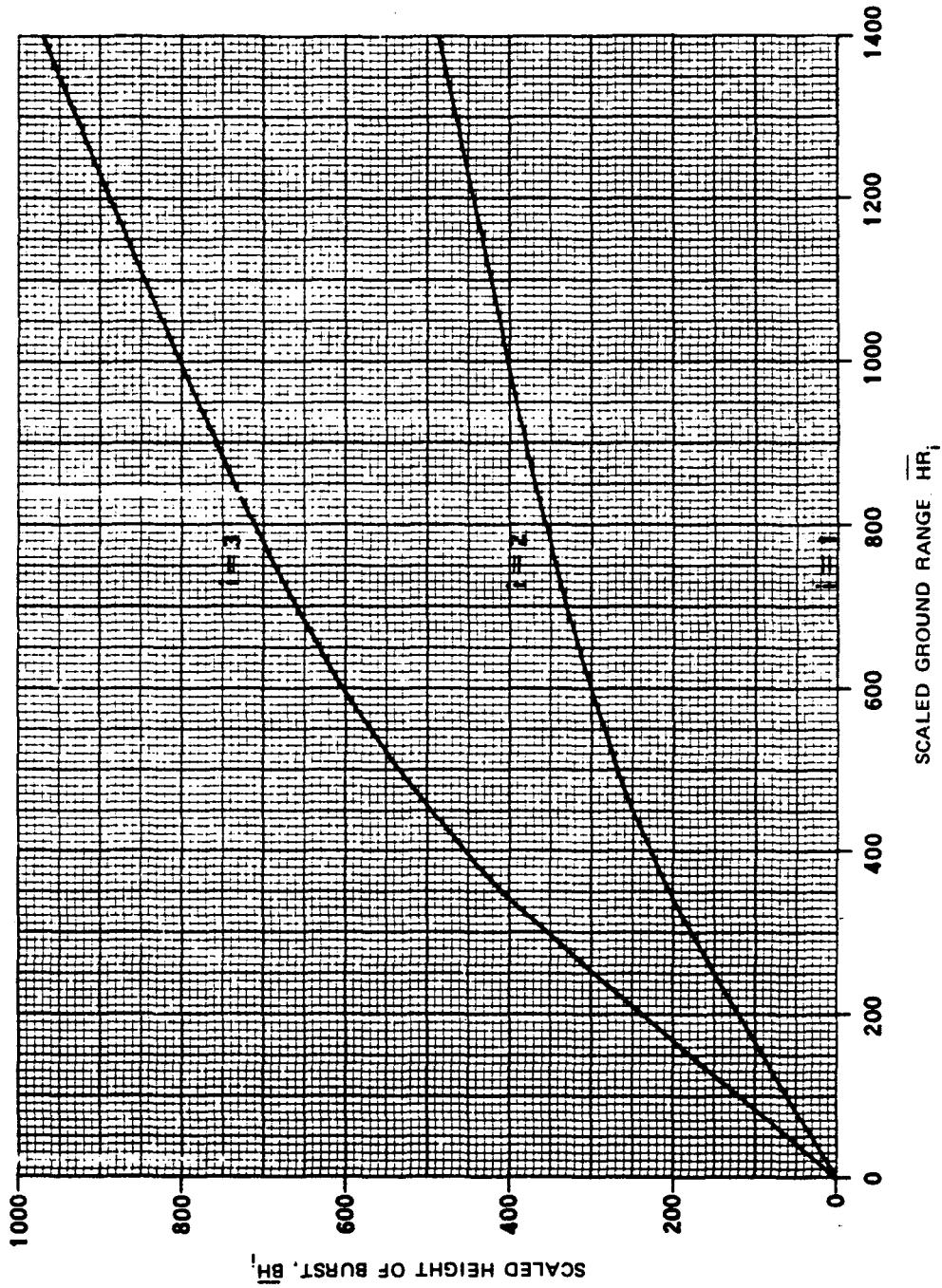


Figure 13-17a.  $\overline{BH}_i$  as a Function of  $\overline{Hf}$ , Short Ranges

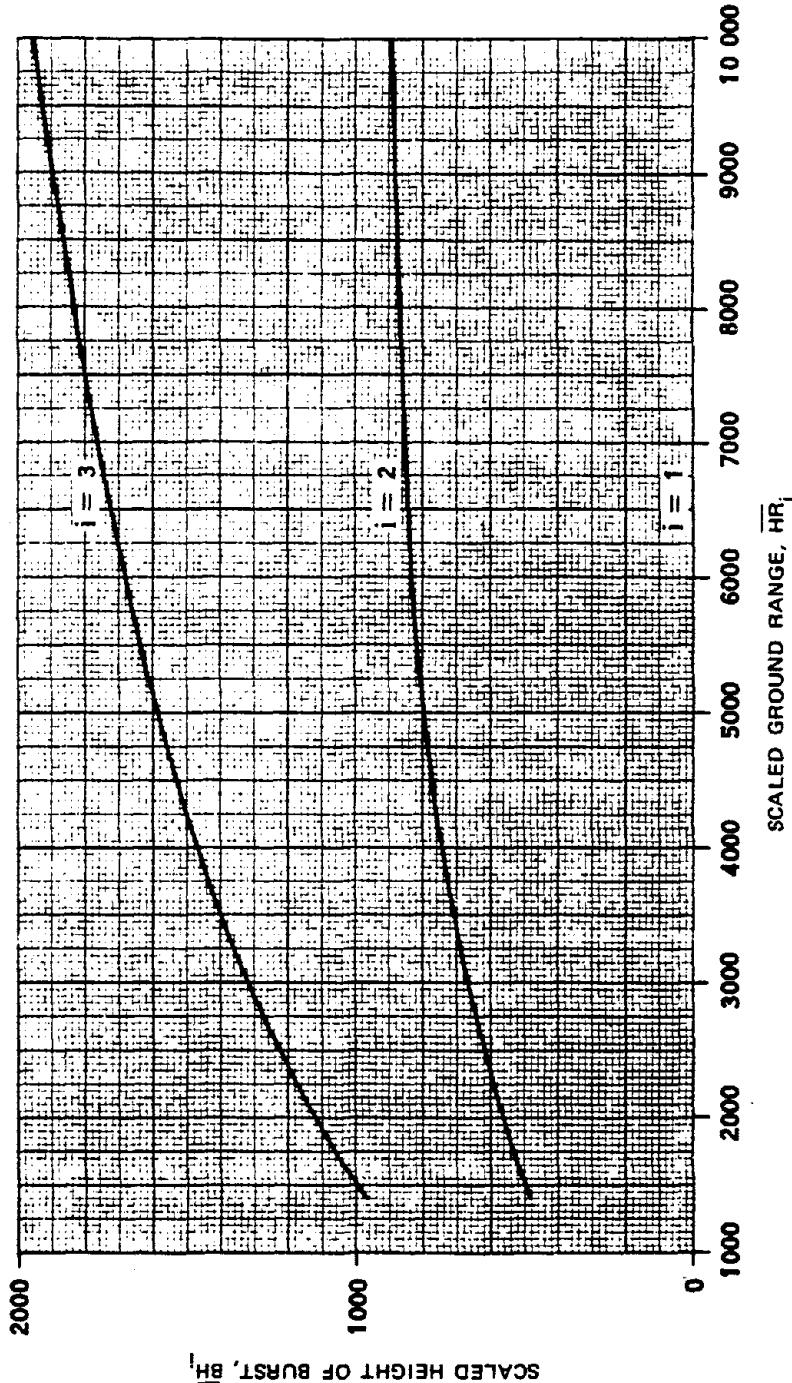


Figure 13-17b.  $\overline{BH}_i$  as a Function of  $\overline{HR}_i$ , Long Ranges

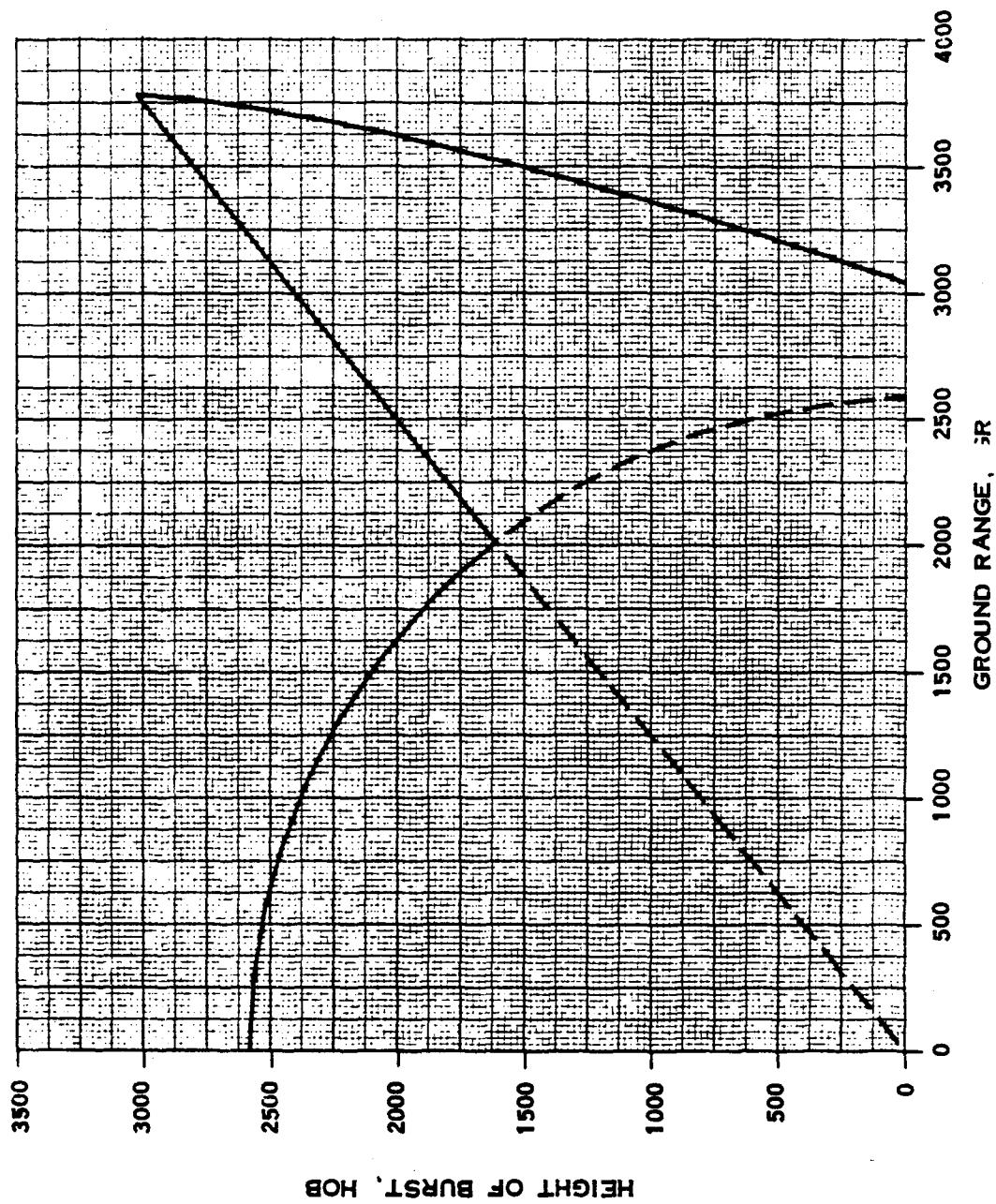


Figure 13-18. Overpressure Envelope for I parked Aircraft

## AIRCRAFT RESPONSE TO THERMAL RADIATION EFFECTS

### 13-10 Thermal Effects on In-Flight and Parked Aircraft

The response of an aircraft to thermal energy is exhibited as a temperature rise in the aircraft skin. Several parameters influence the magnitude of the temperature rise. The most important parameters are skin thickness, skin material, surface condition, cooling effect of the air flowing over the outer surface of the aircraft,

reradiation of thermal energy to the atmosphere, and conduction of the incident energy to the inner layers of the skin and substructure.

Sure-safe conditions are based on an allowable temperature rise of the aircraft skin; however, melting of the skin is required for sure-kill. To produce kill, the temperature must increase to the melt temperature, and further heat must be applied to cause melting. The method for analysis of thermal effects on aircraft that is described in Problem 13-6 applies to both airplanes and helicopters.

**Problem 13-6. Calculation of Boundaries in Space (Envelopes) that Define the Sure-Safe and Sure-Kill Regions with Respect to Thermal Radiation on Aircraft In-Flight or Parked**

The analysis is based on calculating the amount of heat required to produce some specified effect. For sure-safe, this effect is raising the temperature of a skin panel to a value which produces a 20 percent reduction in the modulus of elasticity. This criterion is applied to the thinnest structural skin on the fuselage. For sure-kill, the specified effect is melting of the thickest skin on the fuselage. The critical amount of heat,  $Q_c$ , which is the heat required to produce the specified effect is assumed to be equal to the thermal energy absorbed by the skin,  $Q_a$ . The critical heat,  $Q_c$ , is

$$Q_c = \rho_m C_p t \Delta T,$$

where  $\rho_m$  is the weight density of the material,  $C_p$  is the specific heat of the material,  $t$  is the skin thickness, and  $\Delta T$  is the effective critical temperature rise.

(U) The constraints in the calculation are:

- The aircraft skin is thermally thin, i.e., the incident thermal energy heats the skin uniformly throughout its depth.
- The equilibrium temperature is based on an average set of conditions for turbulent flow.
- At the equilibrium temperature, all degradations of material properties from room temperature values are negligible.
- Cooling effects resulting from airflow over the aircraft are negligible.
- Reradiation is negligible.
- Aircraft motion is neglected.
- Attenuation of the thermal energy by the atmosphere is negligible.

- Reflected radiation from the ground is negligible.

- The fireball is a point source.

(U) Under the constraints

$$Q_a = \alpha Q,$$

where  $Q$  is the radiant exposure, i.e., the energy received per unit area (normal to the direction of propagation under the assumed constraints), and  $\alpha$  is the absorptivity coefficient for the aircraft surface being considered.

(U) From Chapter 3,

$$Q = \frac{10^{12} Wf}{4\pi R^2} \text{ cal/cm}^2,$$

where

$W$  = weapon yield (kt),

$f$  = thermal partition of energy (dimensionless),

$R$  = distance (cm),

Since  $39 \text{ cal/cm}^2 = 1 \text{ Btu/in.}^2$ , and  $929 \text{ cm}^2 = 1 \text{ ft}^2$ ,

$$Q = \frac{10^{12} Wf}{4\pi R^2 (39)(929)} \text{ Btu/in.}^2$$

or

$$Q = \frac{2.19 \times 10^6 Wf}{R^2} \text{ Btu/in.}^2$$

where  $R$  is now expressed in feet. Since

$$Q_a = \alpha Q.$$

$$Q_a = \frac{2.19 \times 10^6 W f \alpha}{R^2},$$

and

$$R = \left[ \frac{2.19 \times 10^6 W f \alpha}{Q_a} \right]^{1/2},$$

or

$$R = 1,480 \sqrt{\frac{W f \alpha}{Q_a}},$$

which can be solved directly for the critical range  $R$ . If  $Q_c$  is taken to be equal to  $Q_a$ ,

$$\begin{aligned} R &= 1,480 \sqrt{\frac{W f \alpha}{Q_c}} \\ &= 1,480 \sqrt{\frac{W f \alpha}{\rho_m C_p t \Delta T}}. \end{aligned}$$

The data required for solution include:

$h$  = aircraft altitude (ft),

$W$  = weapon yield (kt),

$V$  = preblast aircraft velocity (ft/sec),

Detailed layout drawings of the fuselage, showing skin thickness,

Material of the skin, and

Surface condition of the skin.

The analysis is performed in a series of steps.

1. Select the critical skin panels on the fuselage. Three panels should be selected, one each for bursts occurring directly below, directly above, and directly to the side of the aircraft. For each burst orientation, skin panels located in the following regions should be considered:

a. For a burst directly below the aircraft, the lower surface of the fuselage, within  $45^\circ$  of the normal to the bottom of the fuselage.

b. For a burst directly above the aircraft, the upper surface of the fuselage, within  $45^\circ$  of the normal to the top of the fuselage.

c. For a burst directly to the side of the aircraft, the side surface of the fuselage not covered by a and b above.

The selection of the critical skin panel from the locations defined above is based primarily on the thickness of the skin and depends upon whether sure-safe or sure-kill envelopes are sought.

- For sure-safe, select the *thinnest* structural skin. Nonstructural skin, such as access panels, should not be selected. If more than one material is used for the fuselage, investigate the thinnest skin for each material and base the envelopes on the *most* vulnerable.
- For sure-kill, select the *thickest* skin at a fuselage station near the forward end of the tail cone. If more than one material is used for the fuselage, investigate the thickest skin for each material and base the envelopes on the *least* vulnerable.

For a parked aircraft, skip steps 2 and 3 and proceed to step 4. For an in-flight aircraft, proceed to step 2.

2. Determine the ambient speed of sound  $c$  (ft/sec) at altitude  $h$  from Table 13-1.
3. Calculate the Mach Number,

$$M = \frac{V}{c}.$$

4. Determine the equilibrium temperature,  $T_e$ , of the skin.

a. For in-flight aircraft, enter Figure 13-19 with the Mach number,  $M$ , and the altitude,  $h$ , and read  $T_e$ .

b. For parked aircraft, use  $T_e = 60^\circ F$ .

5. Determine the material properties for each of the skin panels selected from Table 13-3.

$T_c$  = critical temperature ( $^{\circ}$ F)

$C_p$  = specific heat (Btu/lb $^{\circ}$ F)

$\rho_m$  = weight density (lb/in. $^3$ )

For sure-kill only, determine

$H$  = heat of fusion (Btu/lb)

6. Calculate the effective critical temperature rise,  $\Delta T$ :

a. For sure-safe,

$$\Delta T = T_c - T_e$$

b. For sure-kill,

$$\Delta T = T_c - T_e + \frac{H}{C_p}$$

7. Determine the effective absorptivity coefficient,  $\alpha$ , from Table 13-4.

8. Determine  $f$  from Figure 13-20\*, and calculate the critical range in feet,

$$R = 1,480 \sqrt{\frac{Wf\alpha}{\rho_m C_p t \Delta T}}$$

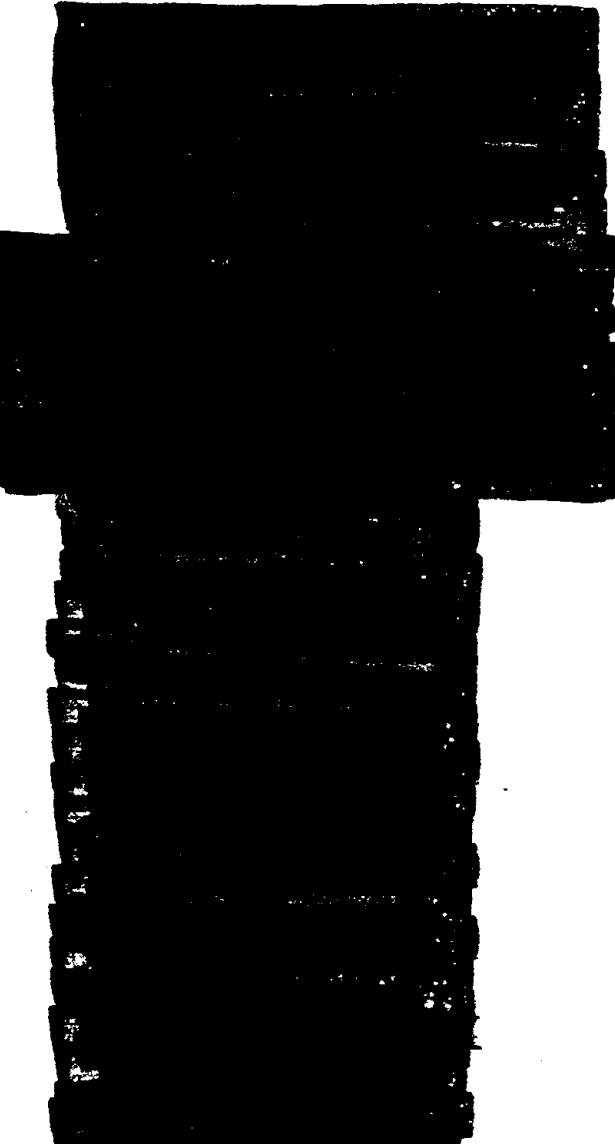
When steps 5 through 8 have been completed for a burst directly below the aircraft, they should be repeated for bursts directly above and directly to the side of the aircraft. Three ranges will have been determined,  $R_b$ ,  $R_a$ , and  $R_s$ , where subscripts "b," "a," and "s" designate below, above, and side, respectively. Note that, if the critical skin panels for  $R_a$  and  $R_s$  are of the same material and have the same surface conditions as the skin panel analyzed for  $R_b$ , only step 8 need be repeated, introducing the proper value of skin thickness,  $t$ .

9. Calculate the average of the three ranges,  $R_b$ ,  $R_a$ , and  $R_s$ ,

$$R_{av} = \frac{1}{3} (R_b + R_a + R_s)$$

10. The critical volume is defined by a sphere of radius  $R$  centered on the aircraft.

DNA  
(X1)



\* Note that Figure 13-20 is identical to Figure 3-1. It is reproduced here for convenience.

DNA  
(ex.)

**Reliability:** The constraints on this analysis are described in the introductory paragraphs of this problem. The maximum error is between a factor of 1.5 and 3.

**Related Material:** See paragraphs 13-1, 13-4, and 13-10. See also Table 13-1.

Table 13-3. Average Properties of Selected Engineering Materials

Material	Critical Temperature, $T_c$ ( $^{\circ}$ F)		Specific Heat, $C_p$ (Btu/lb $^{\circ}$ F)		Weight Density $\rho_m$ (lb/in. $^3$ )	H (Btu/lb)
	Sure-Safe	Sure-Kill	Sure-Safe	Sure-Kill		
Steel	800	2,550	0.13	0.15	0.28	117
Inconel X	1,000	2,550	0.12	0.13	0.30	117
Aluminum	490	1,076	0.22	0.24	0.10	170
Magnesium	200	1,120	0.25	0.26	0.064	160
Titanium	500	2,850	0.13	0.24	0.17	187

Table 13-4. [REDACTED] Average Values of  
Absorptivities,  $\alpha$  [REDACTED]

	Sure-Safe	Sure-Kill
Polished Metals	0.25	0.50
Unpolished metals	0.45	0.55
Painted metals		
Paint color		
White	0.30	0.50
Yellow	0.40	0.55
Olive	0.70	0.60
Black	0.90	0.65

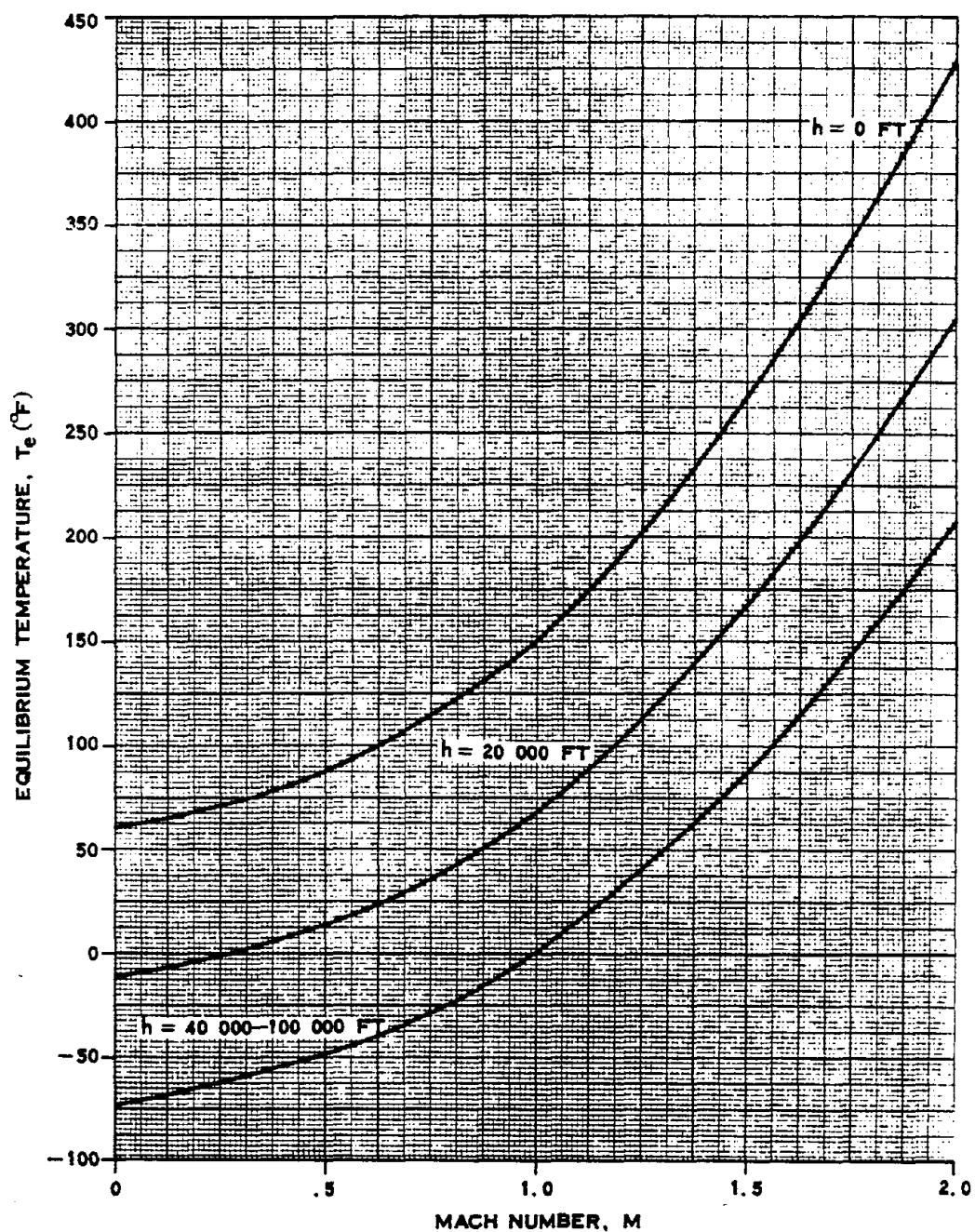


Figure 13-19. Equilibrium Temperature as a Function of Mach Number

## BURST-TIME ENVELOPES

### 13-11 Requirement for Burst-Time Envelopes

The envelopes that are obtained by the methods described in Problems 13-3 through 13-6 define the locus of the center of burst relative to the *position of the aircraft at intercept*, for a specified criterion. It usually is preferable to define the corresponding envelope relative to the *position of the aircraft at burst time*. For parked aircraft and for those envelopes corresponding to thermal radiation, which reaches the aircraft almost instantaneously, the two envelopes are the same, i.e., the methodology presented in Problem 13-5 for overpressure effects

on parked aircraft and that presented in Problem 13-6 for thermal effects on in-flight or parked aircraft apply equally well to intercept-time and to burst-time envelopes. When considering the response of in-flight aircraft to gust or overpressure, however, the relative positions of the aircraft and the burst center are different at the time of burst than at the time of intercept as a result of the distance traveled by the aircraft during the finite time required for the blast wave to propagate to the intercept point. Methods for transforming the intercept-time envelopes obtained by the methods described in Problems 13-3 through 13-5 for in-flight aircraft into burst-time envelopes for the same aircraft are described in Problem 13-7.

**Problem 13-7. Calculation of Burst-Time Envelopes for Gust or Overpressure Effects from Intercept-Time Envelopes**

As discussed in paragraph 13-1, the assumption must be made that the aircraft is following an unaltered flight path when transforming intercept-time envelopes into burst-time envelopes. This assumption is necessary, since it would be impossible to guess the course changes. The assumption is valid for low yield weapons because of the small distances and times between burst and intercept. In the case of high yield weapons, the blast wave arrival time may be of the order of seconds, and the pilot may have time to change his course, so, for these weapons, the assumption must be considered as a source of error.

Two major assumptions, arising from the limitations discussed above, are included in the simplified calculation method described below.

- The aircraft is represented by a point mass traveling at a constant velocity.
- The aircraft is performing a constant symmetric maneuver. As a result of this assumption, the flight path of the aircraft is circular (or straight, for the special case of no maneuver).

Two left-handed, body-centered coordinate systems employed in the analysis are shown in Figure 13-21.

- The intercept reference frame ( $X_I$ ,  $Y_I$ ,  $Z_I$ ), the origin of which is located at the aircraft's center of mass at intercept, with the  $X_I$  axis collinear with the velocity vector, positive forward, and the  $Z_I$  axis in the aircraft plane of symmetry, positive upward.
- The burst reference frame ( $X_B$ ,  $Y_B$ ,  $Z_B$ ), the origin of which is located at the aircraft's center of mass at burst time, with the  $X_B$  axis collinear with the velocity vector, positive forward, and the  $Z_B$  axis in

the aircraft plane of symmetry, positive upward.

The  $X_I - Z_I$  and  $X_B - Z_B$  planes coincide, hence the  $Y_I$  and  $Y_B$  coordinates of any point are the same.

If the center of burst has coordinates ( $X_I$ ,  $Y_I$ ,  $Z_I$ ) in the intercept frame, its position in the burst frame is given by the coordinates ( $X_B$ ,  $Y_B$ ,  $Z_B$ ), where

$$X_B = X_I \cos \Phi + (r - Z_I) \sin \Phi$$

$$Y_B = Y_I,$$

$$Z_B = X_I \sin \Phi - (r - Z_I) \cos \Phi + r,$$

and

$r$  = radius of turn,

$\Phi$  = angular change in flight path between burst and intercept times.

The parameters  $r$  and  $\Phi$  are obtained from the relations

$$r = \frac{V^2}{Ng},$$

$$\dot{\Phi} = \frac{V}{r},$$

where

$V$  = preblast aircraft velocity,

$N$  = maneuver normal load factor,

$g$  = acceleration of gravity,

and a dot indicates differentiation with respect to time. It should be noted that  $N$  is the *maneuver* normal load, and not the load factor,  $n$ , used to calculate the intercept envelopes.  $N$  is related to the load factor  $n$  by

$$N = n - 1.$$

If the equation for  $\Phi$  is integrated from burst time to intercept time, the result is,

$$\Phi = \frac{Vt_a}{r}$$

where

$t_a$  = time of arrival of the blast wave at the intercept point; i.e., the time required for the blast front to propagate to the intercept point.

For the special case when the aircraft is not performing a maneuver ( $N = 0$ ), the equations for the position of the burst point in the burst frame simplify to

$$X_B = X_I + Vt_a$$

$$Y_B = Y_I$$

$$Z_B = Z_I.$$

By means of the above equations, the burst frame coordinates ( $X_B, Y_B, Z_B$ ) may be found for any point on an intercept-time envelope ( $X_I, Y_I, Z_I$ ). Unfortunately, a general planar burst-time envelope cannot be obtained by merely transforming an intercept envelope point by point. For maneuvering aircraft, only those envelopes in the  $X_I - Z_I$  plane (side view) or parallel to the  $X_I - Z_I$  plane, may be resolved directly into corresponding planar envelopes in the  $X_B - Z_B$  plane or parallel to it. All other intercept-time envelopes will transform into three-dimensional surfaces in the burst frame. In the case of no maneuver, any intercept-time envelope parallel to the  $X_I$  axis may be resolved directly into a burst-time envelope in the same plane. This includes envelopes in both the  $X_I - Z_I$  plane (side view), and the  $X_I - Y_I$  plane (top view). However, in neither case can the  $Y_B - Z_B$  plane (front view) envelope be obtained directly. In order to find the burst envelopes for side, front, and top views (or in any arbitrary plane),

it is necessary to adopt an indirect procedure. Since the intercept-time envelopes define a volume in space, this entire volume may be transformed into an equivalent volume in the burst frame. The burst-time envelopes then may be determined as the intersection of this volume with the planes in which burst-time envelopes are desired.

The most convenient way of performing this volume transformation is to take "slices" through the intercept-time volume parallel to the  $X_I - Z_I$  plane, for selected values of  $Y_I$ . Each of these slices may be resolved directly into a slice of the burst-time volume in a plane corresponding to the same value of  $Y_B$ . Definition of the burst-time envelopes in several  $Y_B$  planes is equivalent to defining the burst-time volume.

The data required to perform the analysis include:

$V$  = preblast aircraft velocity (ft/sec)

$h$  = aircraft altitude (ft)

$W$  = weapon yield (kt)

$n$  = aircraft preblast load factor; for straight and level flight,  $n = 1$  (dimensionless)

$X_I, Y_I, Z_I$  = coordinates of points on intercept-time envelopes, as defined in Figure 13-21 (ft).

The analysis is performed in a series of steps, as follows.

1. Determine the ambient atmospheric conditions at altitude  $h$  from Table 13-1.

2. Calculate the maneuver normal load factor,  $N$ ,

$$N = n - 1.$$

3. Calculate the radius of turn,  $r$  (not required if  $N = 0$ ),

$$r = \frac{V^2}{32.2N}.$$

4.\* Select a point on the  $X_I - Z_I$  plane (side view) intercept-time envelope. Its coordinates are  $(X_I, Y_I, Z_I)$ , with  $Y_I = 0$ .

5. Determine the slant range,  $R$ , from the center of burst to the selected intercept point.

$$R = \left( X_I^2 + Y_I^2 + Z_I^2 \right)^{1/2}.$$

6. Calculate the equivalent range for a 1 kt burst in a sea level atmosphere by the scaling procedures described in paragraph 2-14, Chapter 2,

$$R_1 = R \left( \frac{P}{P_o W} \right)^{1/3} = R \left( \frac{P}{14.7 W} \right)^{1/3}.$$

7. Enter Figure 13-22 with  $R_1$ , and read the time of arrival,  $t_1$ , for a 1 kt burst in a sea level atmosphere.<sup>†</sup> Calculate the time of arrival of the blast wave at a range  $R$  from a yield  $W$  at altitude  $h$  by the scaling procedures given in paragraph 2-14,

$$t_a = t_1 \left( \frac{WP_o}{P} \right)^{1/3} \left( \frac{T_o}{T} \right)^{1/2}.$$

A satisfactory expression for the time of arrival within the accuracy of the methodology presented herein is

$$\begin{aligned} t_a &= t_1 \left( \frac{WP_o}{P} \right)^{1/3} \left( \frac{c_o}{c} \right) \\ &= t_1 \left( \frac{14.7 W}{P} \right)^{1/3} \left( \frac{1,116}{c} \right). \end{aligned}$$

8. Calculate the turn angle,  $\Phi$ , in degrees (not required if  $N = 0$ ),

$$\Phi = 57.3 \frac{Vt_a}{r}.$$

9. Calculate the coordinates of the point in the burst frame  $(X_B, Y_B, Z_B)$ .

a. If  $N = 0$ ,

$$X_B = X_I + Vt_a,$$

$$Y_B = Y_I,$$

$$Z_B = Z_I.$$

b. If  $N \neq 0$ ,

$$X_B = X_I \cos \Phi + (r - Z_I) \sin \Phi,$$

$$Y_B = Y_I,$$

$$Z_B = Z_I \sin \Phi - (r - Z_I) \cos \Phi + r.$$

10. Repeat steps 5 through 9 for other points on the intercept-time envelope, until the burst-time envelope has been defined satisfactorily.

11. Determine the intercept-time envelope for a "slice" parallel to the  $X_I - Z_I$  plane, with  $Y_I \neq 0$ . Repeat steps 5 through 10 for points on this envelope.

12. Repeat step 11 for as many "slices" as necessary to define the burst-time volume adequately. Note that only positive values of  $Y_I$  need be used since the envelopes are symmetric about the  $X_I - Z_I$  or  $X_B - Z_B$  plane.

At this point, the problem is essentially solved, since the burst-time volume effectively has been defined. The burst-time envelope in any desired plane may be determined from the burst-time volume. The calculation of the burst-

\* In certain special cases, simpler procedures may be used, although the procedures given above are general and will work in all cases. A description of the special cases is given at the end of the Stepwise Calculation Procedure.

<sup>†</sup> Note that Figure 13-22 is identical to Figure 2-5, Chapter 2. It is reproduced here for convenience.

time envelopes in three planes. The  $X_B - Z_B$  plane (side view), the  $Y_B - Z_B$  plane (front view), and the  $X_B - Y_B$  plane (top view) is described for illustration.

13. The side-view burst-time envelope is the intersection of the  $X_B - Z_B$  plane with the burst-time volume. This is just the transformed side-view intercept-time envelope ( $Y_I = 0$ ), which was the first burst-time envelope defined in the steps given above.

14. The front-view burst-time envelope is the intersection of the  $Y_B - Z_B$  plane with the burst-time volume. For each of the burst-time volume "slices," determine the values of  $Z_B$  corresponding to  $X_B = 0$ , and plot these using the value of  $Y_B$  for the slice being considered.

15. The top-view burst-time envelope is the intersection of the  $X_B - Y_B$  plane with the burst-time volume. For each of the burst-time volume "slices," determine the values of  $X_B$  corresponding to  $Z_B = 0$ , and plot these using the value of  $Y_B$  for the slice being considered.

16. *Special Cases.* In certain cases, simpler procedures may be used. The methodology of Problem 13-5 results in a spherical intercept-time volume for overpressure effects on in-flight aircraft. The sphere is centered at the origin of the intercept frame ( $X_I, Y_I, Z_I$ ). Hence,  $R, R_1, t$ , and  $\Phi$  (steps 5-8) are the same for all points on the intercept-time volume, and the sphere transforms into a sphere of the same radius in the burst frame. The coordinates of the center of the sphere are

a. If  $N = 0$ ,

$$\begin{aligned} X_B &= Vt_a, \\ Y_B &= 0, \\ Z_B &= 0. \end{aligned}$$

b. If  $N \neq 0$ ,

$$\begin{aligned} X_B &= r \sin \Phi, \\ Y_B &= 0, \\ Z_B &= r(1 - \cos \Phi). \end{aligned}$$

Another special case occurs for the gust effects on in-flight aircraft (see Problems 13-3 and 13-4). The complete intercept-time volumes are made up of four spheres. The intersection of any plane with a sphere is a circle. Consider the intersection of a plane parallel to the  $X_I - Z_I$  plane and defined by constant  $Y_I$  with the sphere at the side of the aircraft. The intersection is a circle on the  $Y_I$  axis. All points on this circle are equidistant from the origin; hence, the circle transforms into a circle of the same radius in the burst frame. The coordinates of the center of the circle are

a. If  $N = 0$ ,

$$\begin{aligned} X_B &= Vt_a, \\ Y_B &= Y_I, \\ Z_B &= 0. \end{aligned}$$

b. If  $N \neq 0$ ,

$$\begin{aligned} X_B &= r \sin \Phi, \\ Y_B &= Y_I, \\ Z_B &= r(1 - \cos \Phi). \end{aligned}$$

For the case of  $N = 0$  only, the intersection of a plane parallel to the  $X_I - Y_I$  plane and defined by constant  $Z_I$  with the sphere above or below the aircraft transforms into a circle of the same radius in the burst frame. The coordinates of the center of the circle are

$$X_B = Vt_a$$

$$Y_B = 0$$

$$Z_B = Z_I.$$

In all of the above transformations, it should be emphasized that  $t_a$  corresponds to a point on the intercept-time envelope being considered, *not* to the center of the circle.

DNA  
(6/1)

**[REDACTED]** *Reliability:* The aircraft is assumed to be represented by a point mass traveling at a constant velocity and performing a constant symmetric maneuver. As a result of this assumption, the flight path of the aircraft is circular (or straight for the special case of no maneuver).

The maximum error is estimated to be a factor of 1.1.

**[REDACTED]** *Related Material:* See paragraphs 13-1, 13-2, 13-6, 13-7, and 13-11. See also Problems 13-3 and 13-4, and Table 13-1.

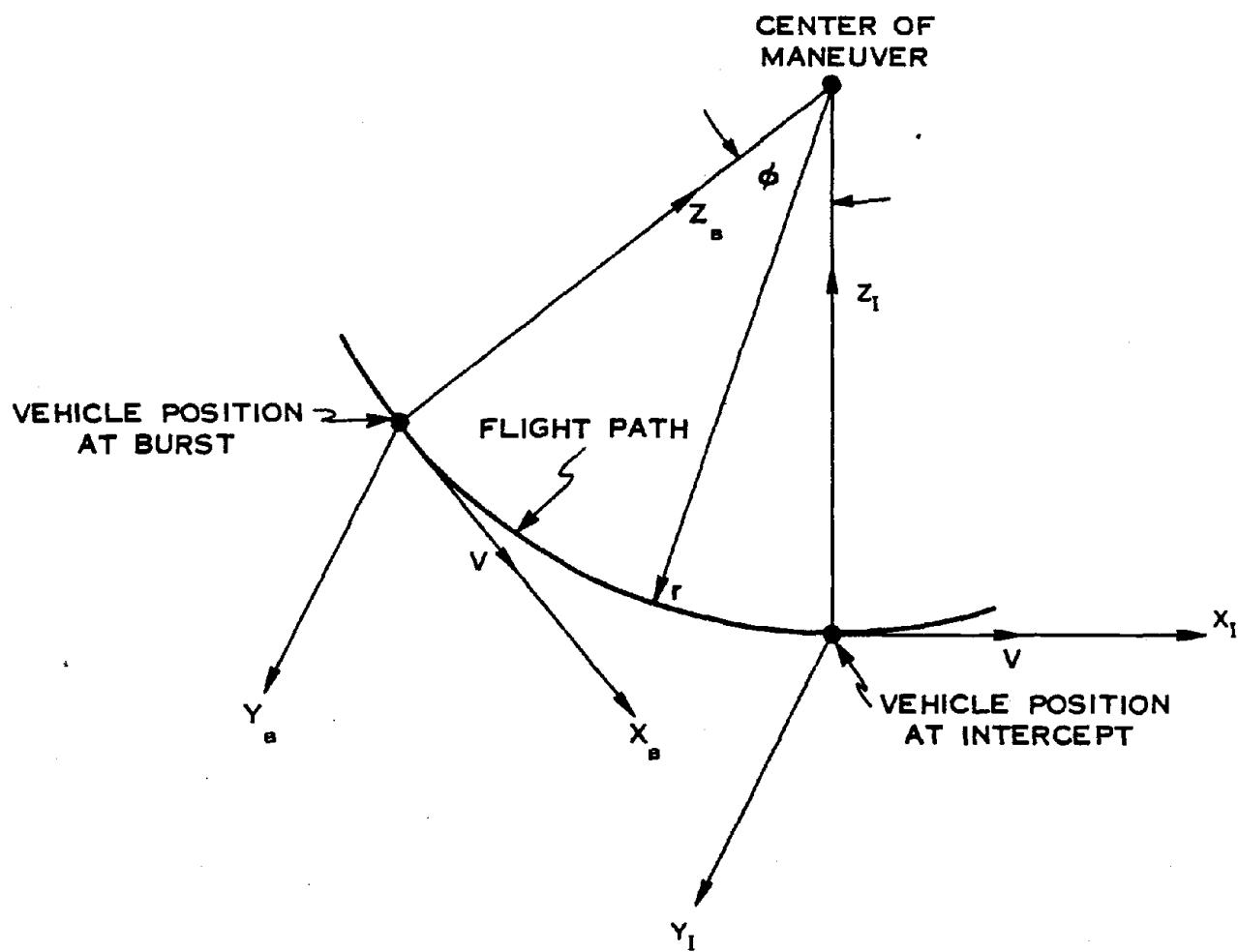


Figure 13-21. ■ Geometry of Burst and Intercept  
Reference Frames ■

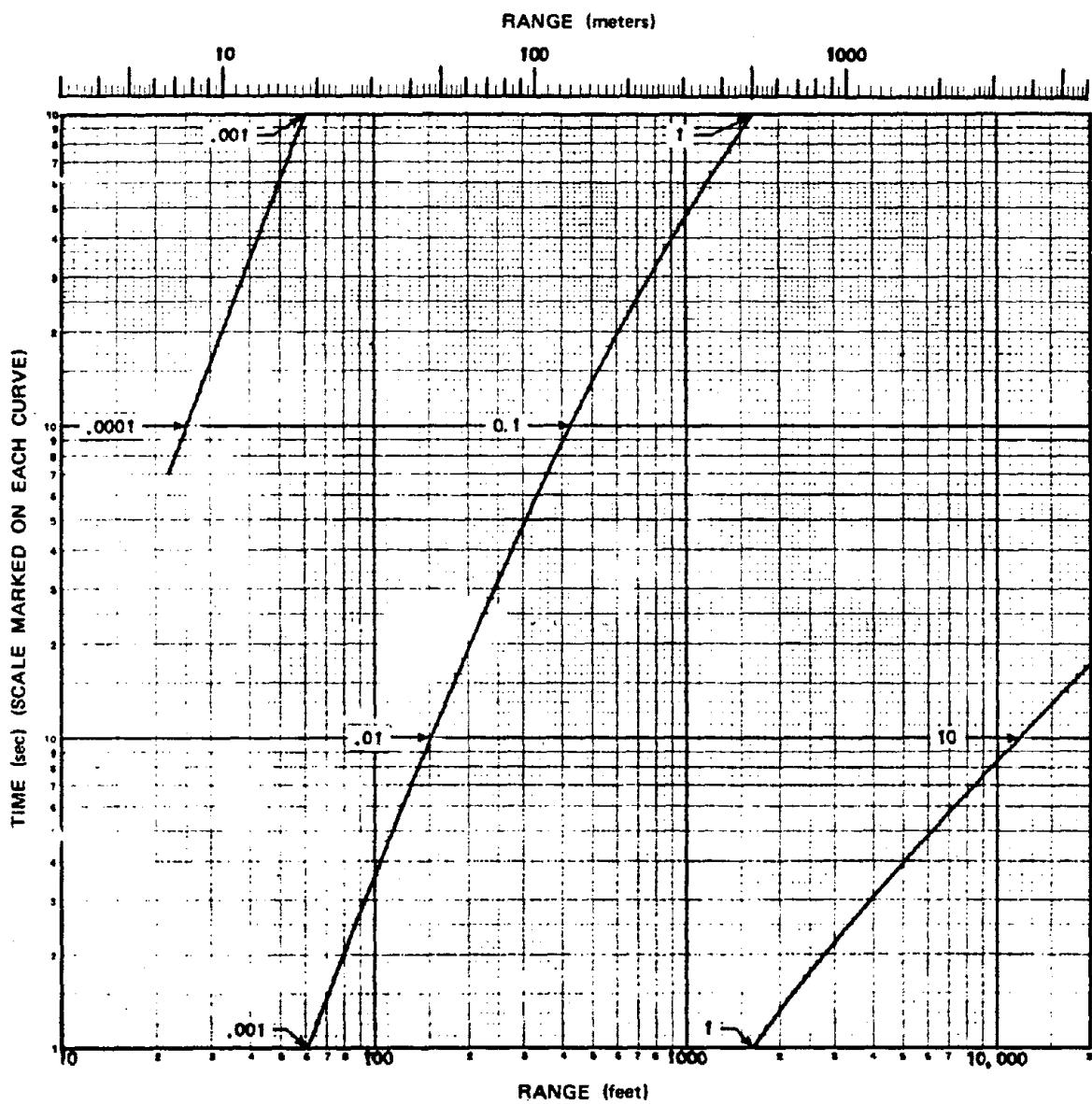


Figure 13-22. Time of Arrival of the Shock Front from a 1 kt Free Air Burst  
in a Standard Sea Level Atmosphere

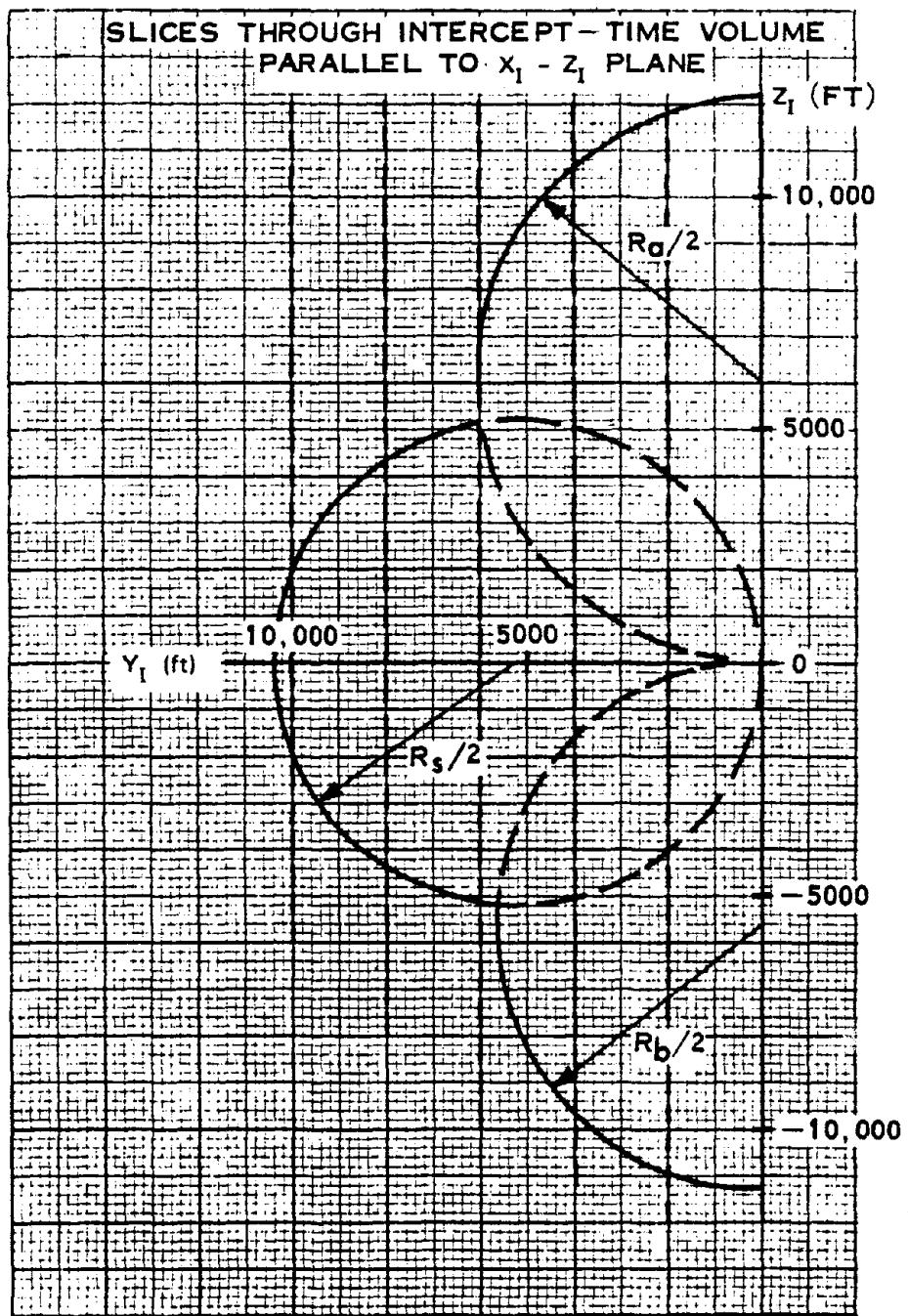


Figure 13-23. Intercept-Time Envelope (Front View)

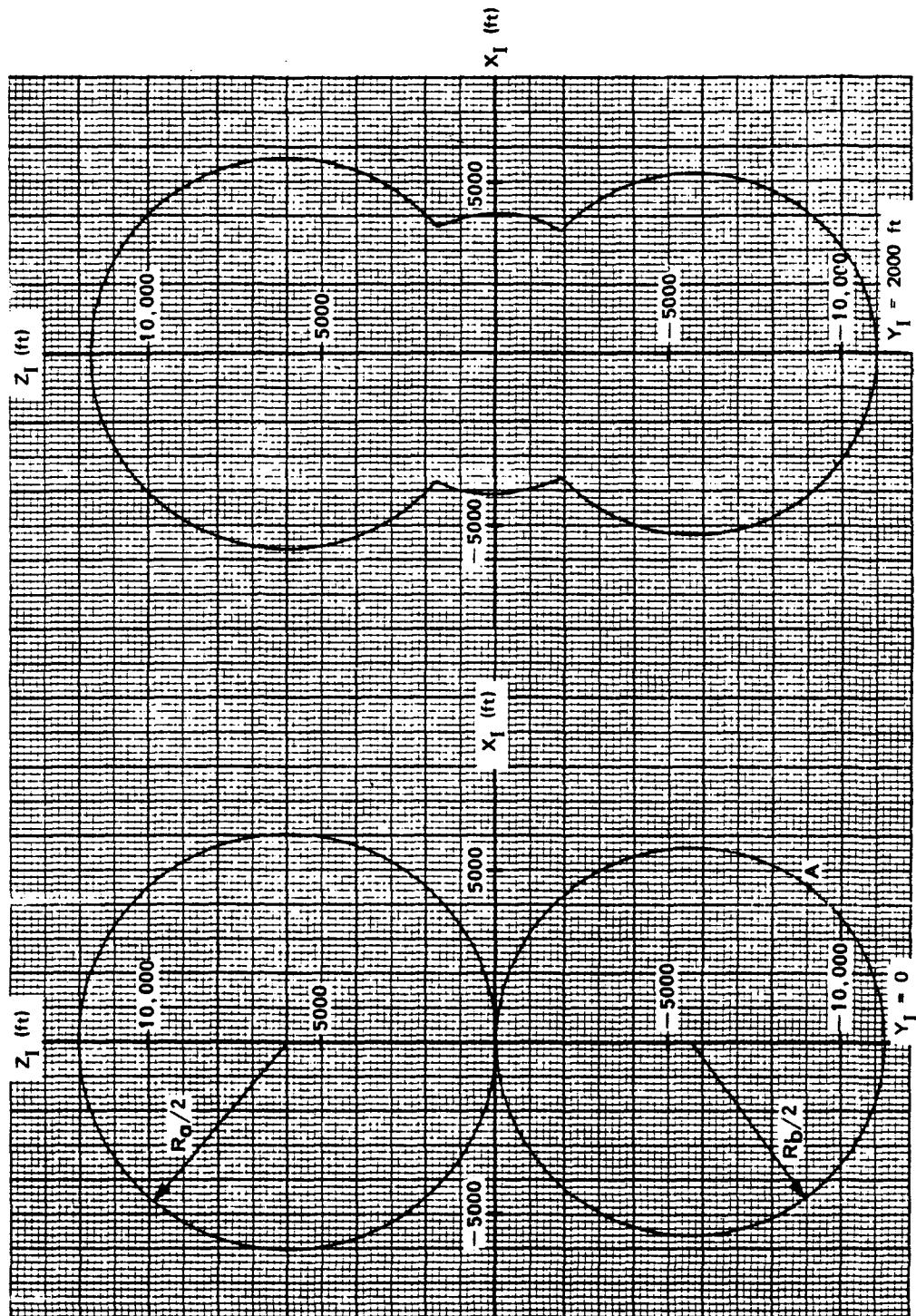


Figure 13-24a. Intercept-Time Envelope  
(Side View)

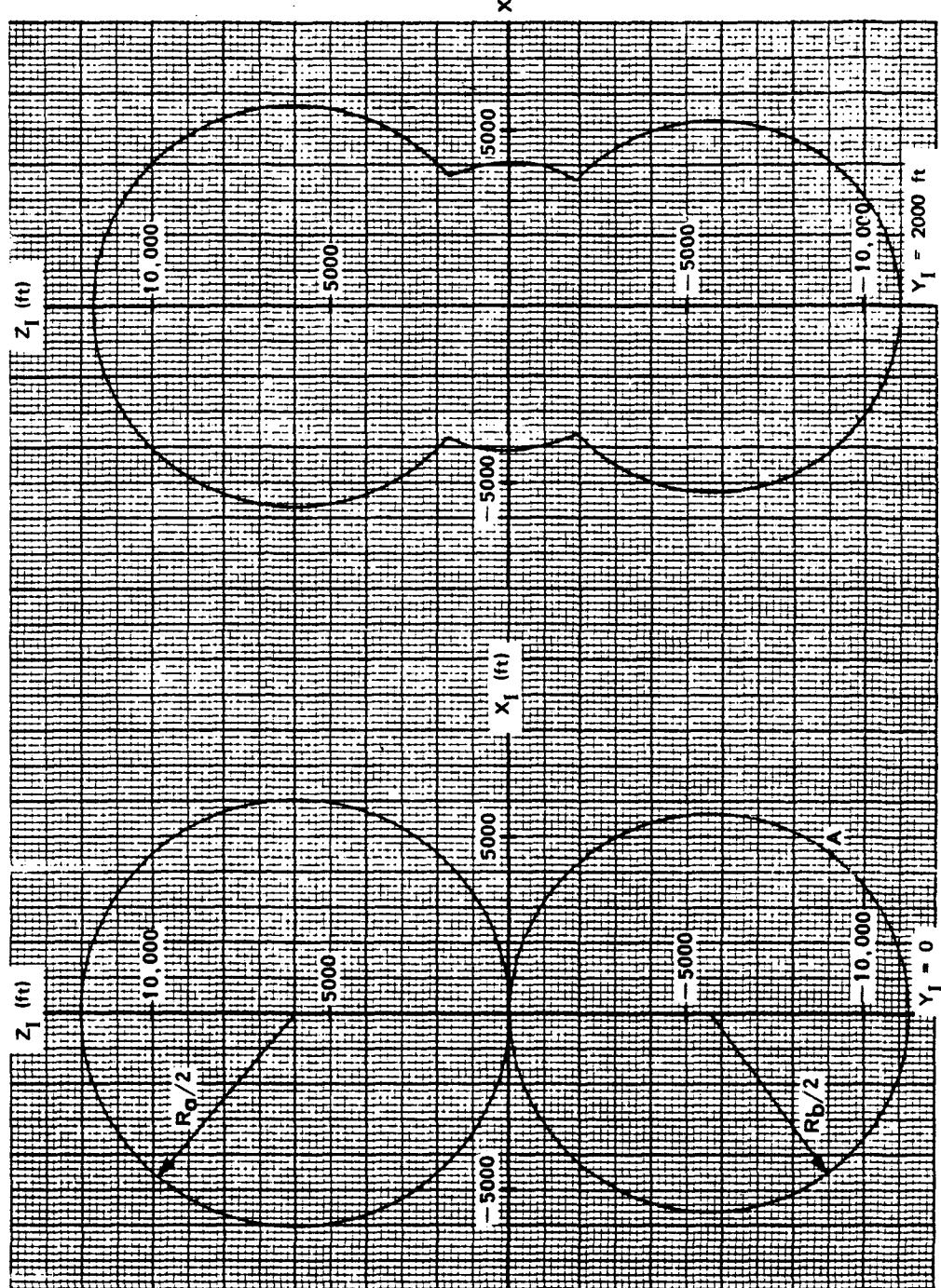


Figure 13-24b. Slice Through Intercept-Time  
Volume at  $Y_1 = 2,000$  Feet

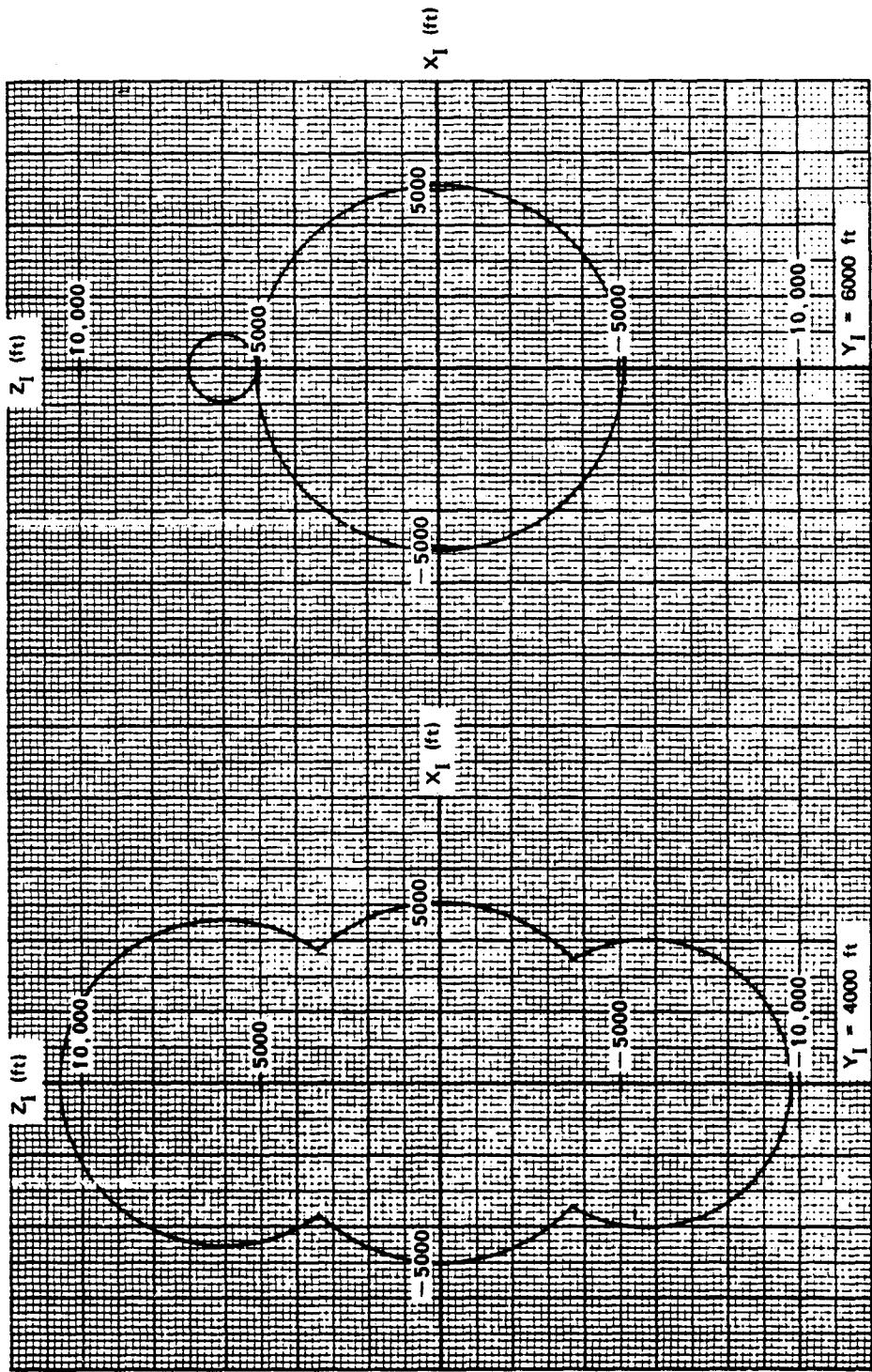


Figure 13-24c. Slice Through Intercept-Time  
Volume at  $Y_1 = 4,000$  Feet

Figure 13-24d. Slice Through Intercept-Time  
Volume at  $Y_1 = 6,000$  Feet

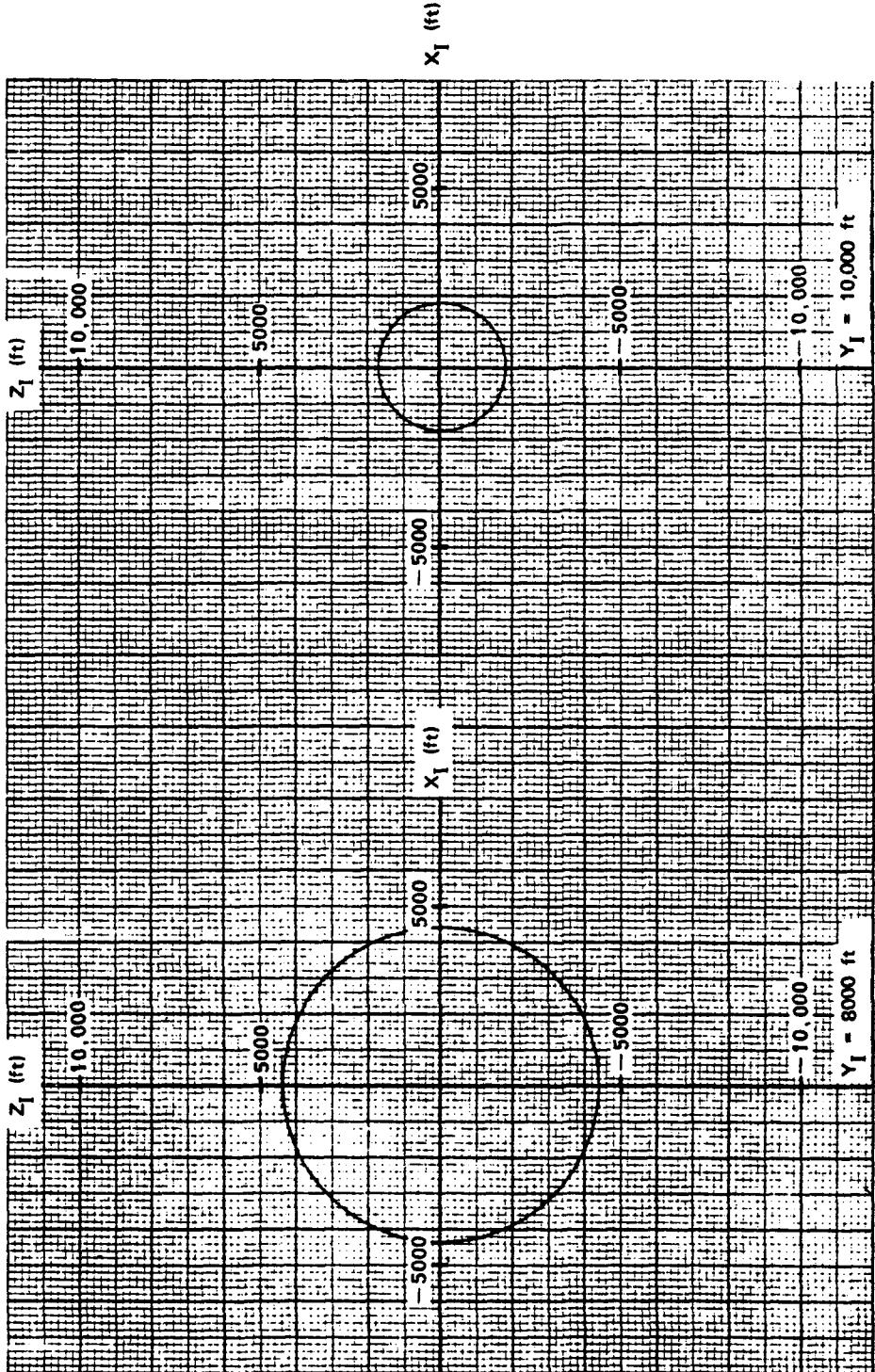


Figure 13-24e. Slice Through Intercept-Time  
Volume at  $Y_1 = 8,000$  Feet

Figure 13-24f. Slice Through Intercept-Time  
Volume at  $Y_1 = 10,000$  Feet

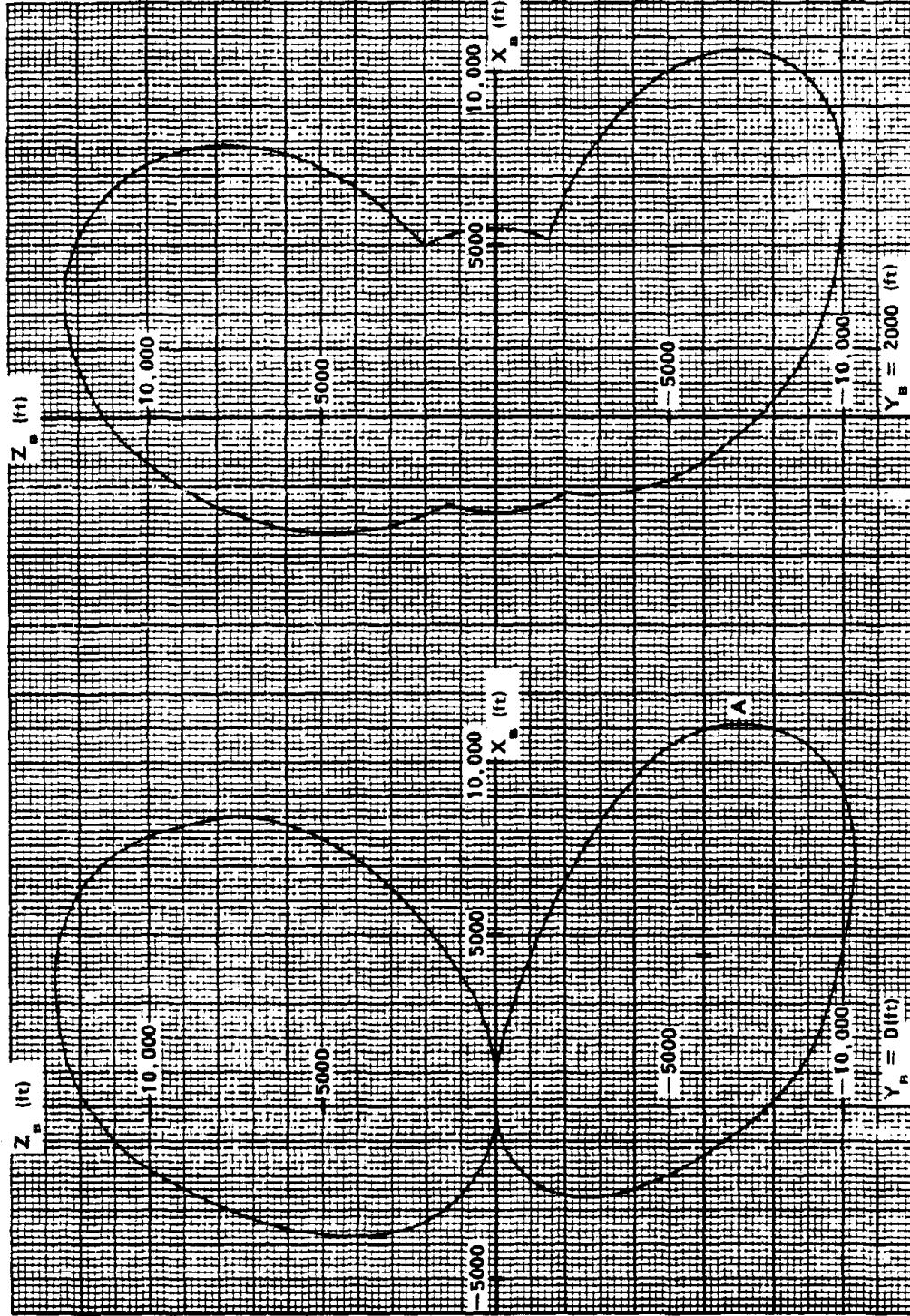


Figure 13-25a. Burst-Time Envelope  
(Side View)

Figure 13-25b. Slice Through Burn Time  
Volume at  $Y_B = 2,000$  Feet

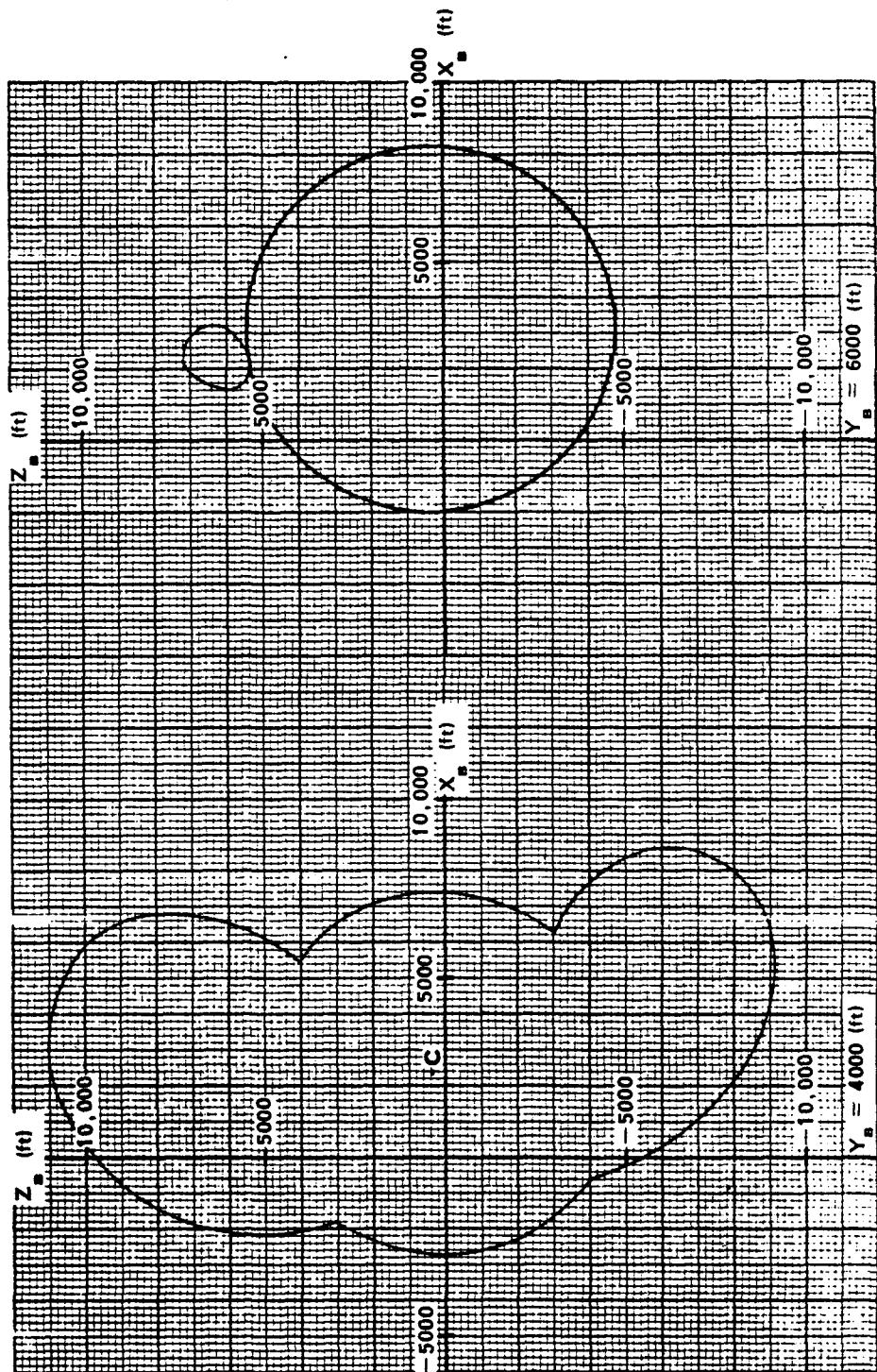


Figure 13-25c. Slice Through Burst-Time Volume at  $Y_B = 4,000$  Feet

Figure 13-25d. Slice Through Burst-Time Volume at  $Y_B = 6,000$  Feet

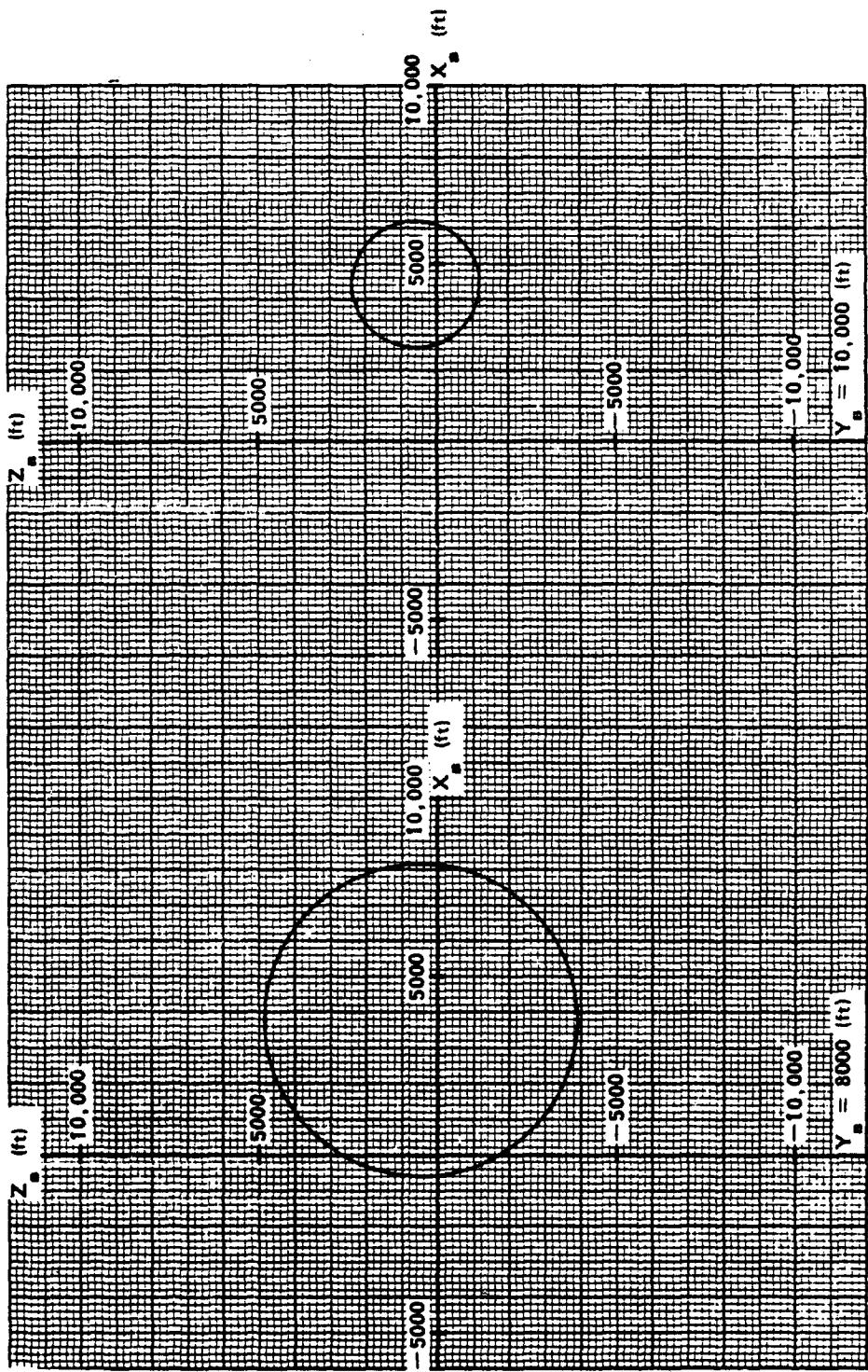


Figure 13-25e. Slice Through Burst-Time Volume at  $Y_B = 8,000$  Feet

Figure 13-25f. Slice Through Burst-Time Volume at  $Y_B = 10,000$  Feet

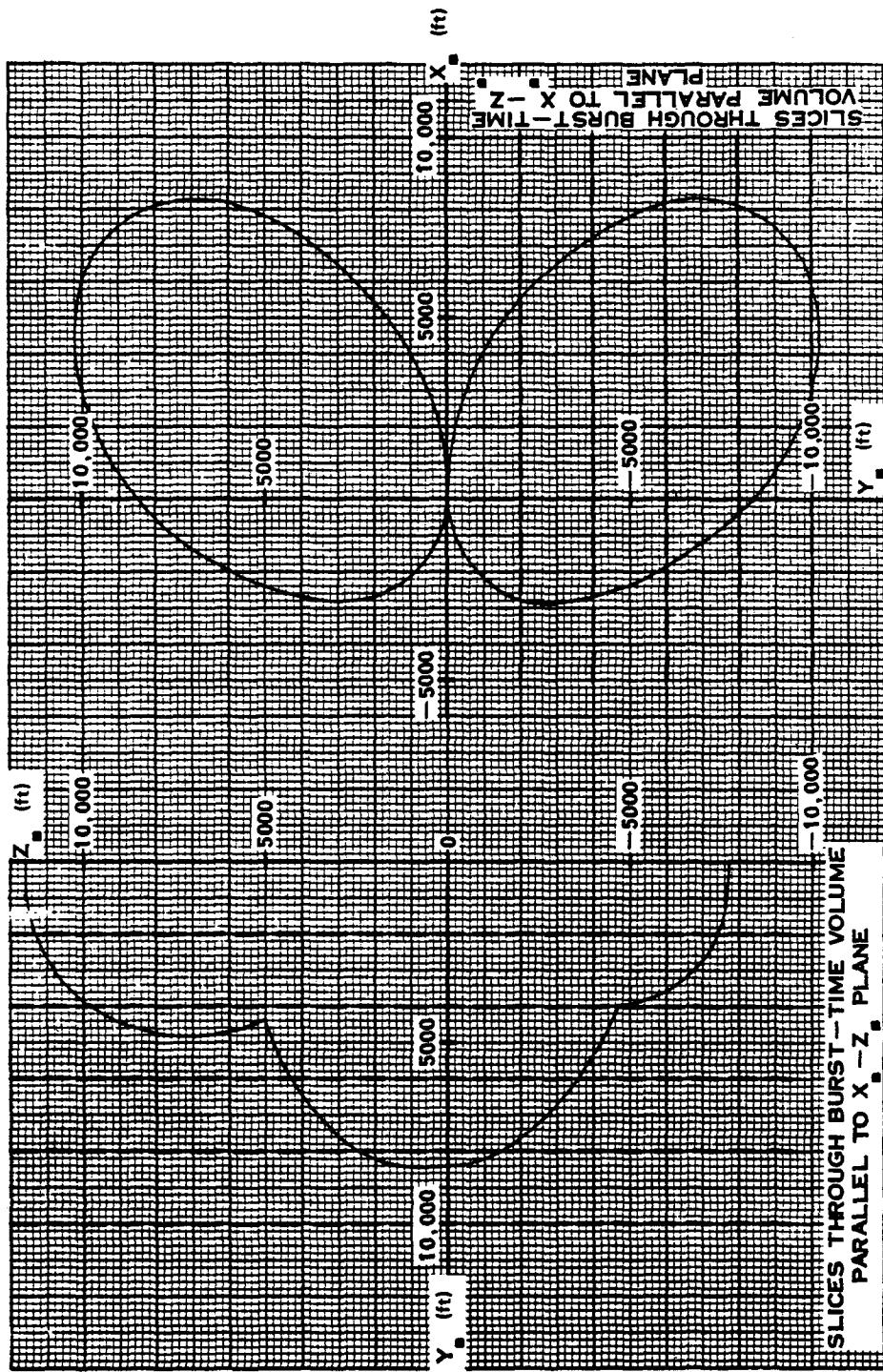


Figure 13-26a. Burst-Time Envelope  
(Front View)

Figure 13-26b. Burst-Time Envelope  
(Top View)

Figure 13-26b. Burst-Time Envelope  
(Top View)

## BIBLIOGRAPHY

Atkinson, G. W., and H. G. Laursen, *Nomographs for Determining the Relationships Between Pressure, Range, Altitude, and Yield in the Shock Front Resulting from a Nuclear Detonation*, NAVWEPS Report 8295, Naval Weapons Evaluation Facility, Albuquerque, New Mexico, 31 January 1965 [REDACTED]

Ayvazian, M., E. S. Criscione, and N. P. Hobbs, *Comparison Between Predicted and Measured Structural Responses of a Supersonic Delta Wing to Blast Loads*, AFFDL-TR-65-212, Kaman AviDyne, Burlington, Massachusetts, March 1966 [REDACTED]

Criscione, E., and J. Putukian, *Preliminary Estimates of the Effect of Blast-Thermal Interaction on the Vulnerability of High-Speed Aircraft in the Vicinity of a Nuclear Detonation*, ASD-TR-61-135, AviDyne Research Inc., Burlington, Massachusetts, January 1962 [REDACTED]

Davis, H. T., W. C. Kaufman, *An Experimental Determination of the Maximum Safe Thermal Radiation Loads for a Fighter-Bomber Cockpit*, ASRMDS-TM-63-4, Flight Dynamics Laboratory, Wright-Patterson, Ohio, January 1963 [REDACTED]

De Hart, R. C., N. L. Basdekas, *Response of Aircraft Fuselages and Missile Bodies to Blast Loading*, ASD TDR-62-458, Southwest Research Institute, San Antonio, Texas, January 1963 [REDACTED]

Donovan, A. F., and H. R. Lawrence, eds., *Aerodynamic Components of Aircraft at High Speeds, Volume VII of High Speed Aerodynamics and Jet Propulsion*, Princeton University Press [REDACTED]

Friedman, M. D., and J. R. Ruetenik, *An Analysis of Measured Blast Loads on Swept Wings at High Subsonic Speeds*, AFFDL-TR-65-170, MIT/ASRL TR-102-1, Massachusetts Institute of Technology, Cambridge, Massachusetts, March 1966 [REDACTED]

*Handbook for Analysis of Nuclear Weapon Effects on Aircraft*, DASA 2048, KA-TR-50A, Kaman AviDyne, Burlington, Massachusetts, April 1970 [REDACTED]

Hobbs, N. P., and K. R. Wetmore, *Lethality Criteria for Aircraft Exposed to Nuclear Blasts*, AFFDL-TR-66-221, Kaman AviDyne, Burlington, Massachusetts, April 1967 [REDACTED]

Hobbs, N. P., G. J. Frassinelli, and E. S. Criscione, *Effects of Variations in Aircraft Parameters on Blast Lethality Envelopes*, RTD-TDR-63-4087, AviDyne Research Inc., Burlington, Massachusetts, February 1964 [REDACTED]

*Nuclear Weapons Blast Phenomena, Volume I, Source and Development of Blast Waves in Air*, DASA 1200-I, DASIAC, Santa Barbara, California, 1 March 1971 [REDACTED]

*Nuclear Weapons Blast Phenomena, Volume II, Blast Wave Interaction*, DASA 1200-II, DASIAC, Santa Barbara, California, 1 December 1970 [REDACTED]

[REDACTED]  
[REDACTED]  
*Nuclear Weapons Blast Phenomena, Volume III, Air and Subsurface Burst Explosions* [REDACTED] DASA  
1200-III, DASIAC, Santa Barbara, California, 1 March 1970 [REDACTED]

[REDACTED]  
Pugh, E. J., and G. B. Bennett, *Vulnerability of Aeronautical Systems to Nuclear Effects, Volume I – Methods of Structural Analysis* [REDACTED] RTD-TDR-64-1, January 1965 [REDACTED]

[REDACTED]  
Schlei, E. J., and D. H. Whitford, *The Vulnerability of Parked Army Aircraft to Nuclear Detonations* [REDACTED] WADC-TR-56-354, University of Dayton, Dayton, Ohio, June 1956 [REDACTED]

[REDACTED]  
Sears, W. R., ed., *General Theory of High Speed Aerodynamics, Volume VI of High Speed Aerodynamics and Jet Propulsion*, Princeton University Press [REDACTED]

[REDACTED]  
Witmer, E. A., J. F. Duvivier, and M. Ayvazian, *The Effects of Atomic Explosions on the Main Rotor of Helicopters in Flight* [REDACTED] WADC-TR-58-301, MIT/ASRL, November 1958 [REDACTED]

[REDACTED]  
Whitaker, W. A., and R. A. Deliberis, Jr., *Aircraft Thermal Vulnerability to Large High-Altitude Detonations* [REDACTED] AFWL-TR-67-85, Air Force Weapons Laboratory, Kirtland Air Force Base, New Mexico, August 1967 [REDACTED]

PAGE 13-88 INTENTIONALLY  
LEFT BLANK

# Chapter 14

## DAMAGE TO MILITARY FIELD EQUIPMENT

### INTRODUCTION

One of the primary uses of nuclear weapons would be for the destruction of military field equipment. This chapter describes how a nuclear explosion can damage military field equipment and provides techniques for estimating certain types and categories of damage. Section I provides a description of the mechanisms of air blast damage to military field equipment, and some examples of variations in damage with weapon yield and exposure conditions. Section II provides the techniques for estimating the various categories of air blast damage to military material. Section III provides a brief description of damage that might be caused by missile (objects translated by the blast wave), fire, and other secondary effects. Section IV discusses transient radiation effects on electronic systems (TREES).

### SECTION I

#### AIR BLAST DAMAGE

The military equipment that is included in this section generally can be described as that material that is used by ground forces in the field. The major types include vehicles (wheeled and tracked), artillery, small arms, communications, field radars, mines, railroad rolling stock, generators, and other miscellaneous items. Types of equipment that are specifically excluded are stationary structures, aircraft, and missile systems. The blast and thermal effects on these three types are discussed in Chapters 11, 13, and 16, respectively. This section discusses the causes and categories of blast-induced damage to

the types of equipment listed above, while techniques for predicting the damage are given in Section II.

##### 14-1 Damage Mechanisms

Most damage to military equipment is caused by the deforming action of blast overpressure or by target movement associated with the air in motion within a blast wave, i.e., the dynamic pressure. The sudden application of high pressure to the surface of a target as a blast wave envelops it can cause crushing, distortion, or buckling of components and subsystems. These may be either closed components and subsystems whose strengths are less than the forces imposed by the differential pressure between the outside and the inside of the element (e.g., fuel tanks), or open elements on which differential forces occurring during the time taken for the blast wave to envelop the element are large enough to cause failure. This type of damage predominates for very low yield weapons or for short duration pulses.

If the weapon yield is greater than several hundred tons, however, the predominant type of damage to targets in the open results from the drag force caused by dynamic pressures. These drag forces may be large enough to move properly oriented, unshielded targets great distances. They may slide, roll, or bounce along the ground surface and may be damaged seriously by the violent motions. There have been instances in which heavy equipment has been picked up and thrown dozens of feet, and then has hit the ground with sufficient force to be dismembered. Stresses induced by dynamic pressure on other types of equipment, e.g., radar or

radio antennas, can be large enough to cause failure even though the target is not crushed and no gross movement occurs prior to failure.

The preceding discussion shows that the three most important parameters involved in damage to equipment from air blast are the air blast environment, the characteristics of the target, i.e., those factors that influence its reactions to blast loadings, and the target exposure, i.e., those factors, principally target orientation and shielding, that influence the target loading and the reaction of a target to a particular blast loading.

#### 14-2 Air Blast Environment

The various means by which air blast can damage a target can be developed most simply by considering the idealized case in which a classical, sharp fronted blast wave moving over the ground encounters a rigid, fixed cube, as previously described in Section II of Chapter 9. If the height of burst (HOB) and ground distance are scaled as the cube root of the yield, the overpressure  $\Delta p$  remains constant, but the shock wave duration  $t^+$  (as in Chapter 9, the positive phase overpressure duration  $t_p^+$  and the positive phase dynamic pressure duration  $t_q^+$  are assumed to be equal and are designated  $t^+$ ) varies as the cube root of the yield. Thus, as shown in Chapter 9, the total impulse is represented by

$$I_T = A \left[ B + C (W^{1/3}) \right],$$

where  $A$  is the area of the face of the cube normal to the blast wave,  $B$  is the overpressure contribution to the impulse, and  $C$  is the dynamic pressure contribution to the impulse. Thus, the contribution to total impulse from overpressure remains constant, while that from dynamic pressure increases as the cube root of the yield. For very low fractional kiloton yields, the loading is highly impulsive with most of the load coming from the overpressure contribution. As the yield

increases, at a constant scaled HOB and ground distance, the total impulse also increases, with an increasing portion resulting from the dynamic pressure contribution.

To maintain the same loading on a target as the yield increases (with a constant  $W^{1/3}$  scaled HOB), the actual ground distance must increase at a faster rate than would be necessary to maintain peak overpressure constant, that is, faster than the cube root of the yield. In other words, if HOB is scaled as  $W^n$ , ground distance must be scaled as  $W^n$ , where  $n > 1/3$ , to maintain the same loading on the target.

This fact has been demonstrated by theoretical calculations of the relationships between yield and ground distance for a particular target, and a particular total impulse. Typical of such calculations is that performed for the blast wave from surface burst incident on a 20 foot fixed cube at distances such that the total impulse would be 0.5 psi-sec. The results of the calculation are shown in Figure 14-1.

An excellent fit to the curve shown in Figure 14-1 was achieved with an equation of the form

$$\text{Ground Distance} = (\text{constant})(\text{yield})^n,$$

where  $n = 0.4138$ .

For many years, it has been observed that experimental data concerning damage to military equipment required ground distance scaling of about  $W^{0.4}$ . The closeness of this exponent to that derived above suggests strongly that the reason for the observed scaling is that the damage was related closely to total impulse. This hypothesis was confirmed by curve-fitting analyses of the relationships between damage to various types of equipment and various air blast parameters. Typical of the results of these analyses is one for damage to 1/4-ton trucks whose sides were exposed to blast waves from weapons ranging in yield from 0.01 kt to 10 Mt. Damage

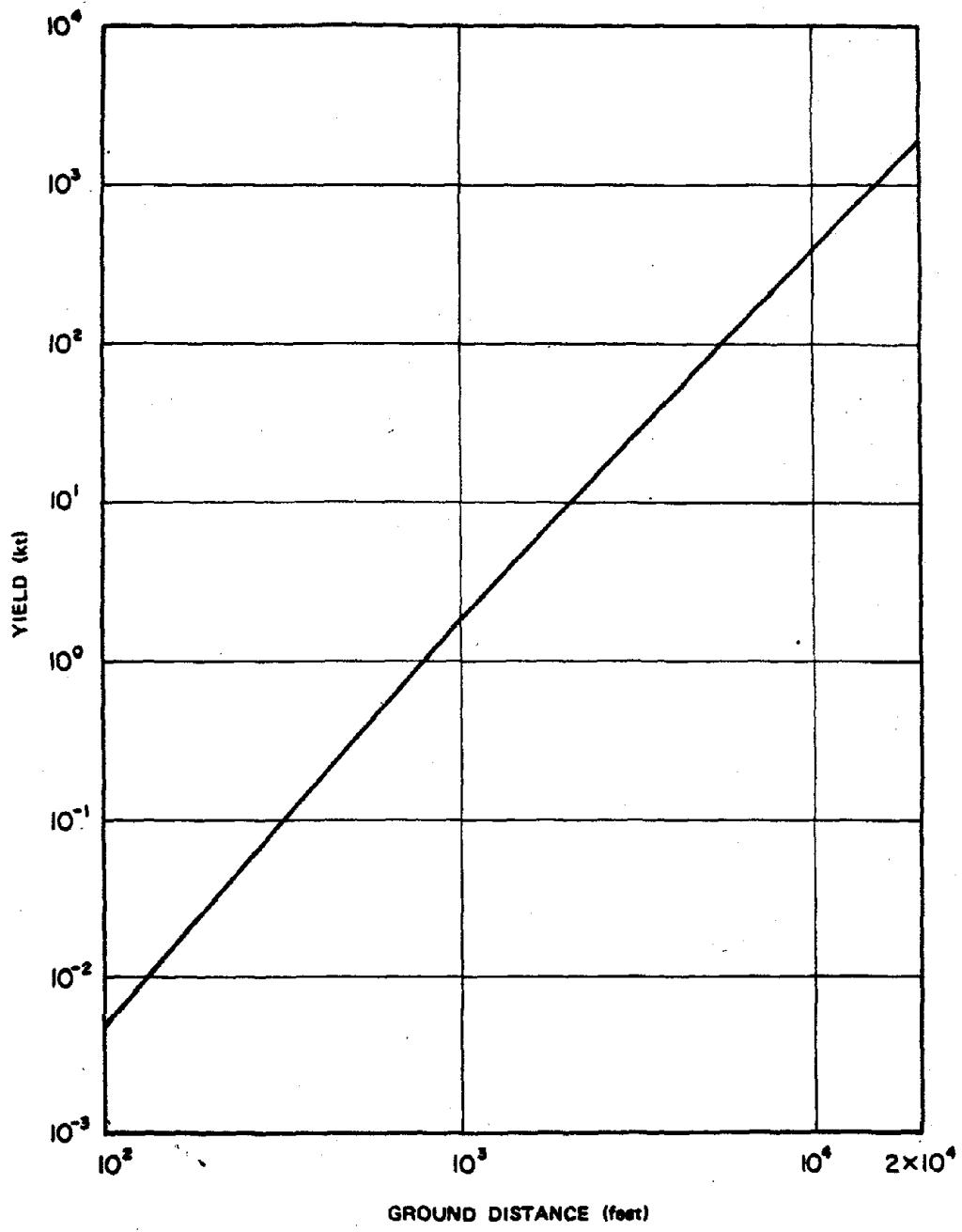


Figure 14-1. Surface Burst Ground Range as a Function of Yield for Constant Total Impulse of 0.50 psi-sec

correlation was best with total impulse (with an index of determination, I.D., of 0.77),\* but the correlation was almost as good with dynamic pressure impulse (I.D. = 0.74). Much poorer correlation was achieved with dynamic pressure, diffraction impulse, and overpressure (with I.D.'s of 0.26, 0.24 and 0.22 respectively).

Most of the foregoing discussion is concerned with air blast phenomena in the Mach reflection region, where the majority of targets usually are found. In the regular reflection region, the overpressure portion of the total impulse usually dominates. This is because the target is exposed to both the incident and reflected air shock, and the horizontal components of dynamic pressure for the two shocks are small, largely because the horizontal component of dynamic pressure is proportional to the square of the sine of the angle  $\theta$  that the shock front makes with the surface. For example, if  $\theta$  is 45-deg, the horizontal component of dynamic pressure would be about one-half as much as the dynamic pressure for a shock making an angle of 90-deg with the surface (which is essentially the case in the Mach region). For 30-deg, the horizontal component would be only about one-fourth as much.

In this review of the discussion of the response of a simple cube to air blast a classical, sharp fronted shock wave was assumed to be incident on the cube. The influence of disturbed or non-classical wave shapes on the impulse delivered to a target can be extensive. If the wave form is not sharp-fronted, a considerable rise time may occur before the peak pressure is observed (see the wave shapes in Figures 2-40 and 2-41 of Chapter 2). If the peak overpressure is not at the front of the wave, the relationships between reflected pressure, shock velocity, sound speed, and overpressure are not valid. Furthermore, such nonideal shock waves usually are associated with precursors, within which peak dynamic pressure is not related to peak overpressure as it is with sharp fronted waves,

and the dynamic pressure impulse contribution to total impulse given in Section II of Chapter 9 for a simple cube is not valid. Damage still can be related to observed air blast parameters (observed overpressures and dynamic pressures) for such wave shapes, but these parameters are not interrelated as they are for ideal waves.

#### 14-3 Target Characteristics

Two types of target characteristics generally are of importance: the overall geometry of the target, on which blast loadings depend; and the distribution of mass in the target, which determines the kind of motions induced by the blast loading. (These can be interrelated in cases when the response of a target during loading changes its geometry and therefore its loading.)

The influence of geometry can be illustrated by considering two targets with the same cross-sectional area, one of which is composed of flat surfaces and sharp edges while the other has curved surfaces and a more streamlined shape. The target with flat surfaces and sharp edges will have a higher load because its shape will result in higher reflected pressures and drag coefficients than will occur on the smoother target. Consequently, the level of air blast required to induce motion in the non-streamlined target will be less than for the streamlined target.

The influence of mass distribution in a target can be seen by noting that for two targets of the same shape, mass, and area, but with different centers of gravity, the one with the higher center of gravity is more likely to sustain damaging motions than the one with the lower center of gravity. Furthermore, a target with a low mass will undergo greater motions than one with a high mass, if the two have the same area, shape, and location of the center of gravity. Figure 14-2 illustrates some of the types of blast-induced motion that may occur, depending

\* The index of determination (ID) is used as a measure of goodness of fit of a curve. The closer the ID is to the number one, the better the fit of the curve.

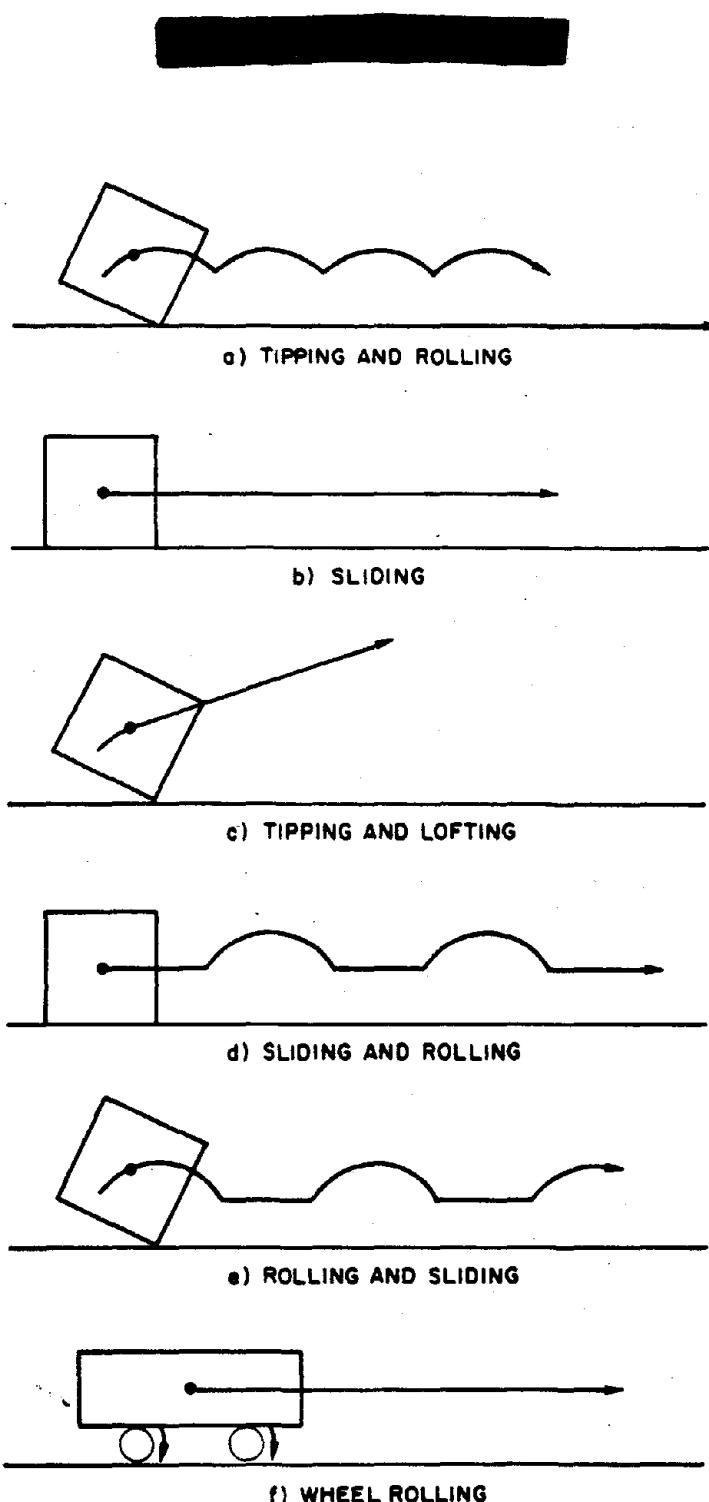


Figure 14-2. ■ Target Response Modes ■

upon geometry and mass distribution.

A detailed assessment of the influences of geometry and mass distribution for each piece of equipment is not presented in this chapter. The damage assessment techniques that are presented in Section II for a variety of equipment types (e.g., wheeled vehicles, artillery pieces, tanks) and for a number of items of equipment within each type, are all based on experimental observations. One purpose of this paragraph is to emphasize the fact that different items of equipment within a single type, and even different production runs of the same item of equipment, can exhibit significant differences in damage from the same blast loadings, but they also can exhibit similarities. These differences and similarities are illustrated by several curves that show damage as a function of distance in a manner similar to Figure 14-3, in which damage on an increasing scale from none to severe is the vertical coordinate (the meanings of the damage categories shown in Figure 14-3 are described in Section II), and distance from a 1 kt surface burst at which the various categories of damage have been observed is the horizontal coordinate.\* Increasing distance implies decreasing values of blast parameters, so the curve indicates that damage decreases with an increase in distance from the burst point. There are infrequent exceptions to this rule, which generally occur in the regular reflection region for large heights of burst.

Figure 14-4 shows a comparison of the damage-distance curves for two types of wheeled vehicles. Although the two vehicles differ markedly in their characteristics, the ground distances at which they sustain moderate and severe damage are not very different; however, the difference in the distances for light damage is large. Figure 14-5 shows larger differences in the damage-distance curves for the similar artillery pieces. Finally, Figure 14-6 shows fairly substantial differences in the distances at which

severe and light damage occurs for two different production runs of the same vehicle.

These comparisons illustrate the difficulties that can be expected to be encountered in making damage predictions for new items of equipment for which little or no information is available.

#### 14-4 Target Exposure

The orientation of the target with respect to the direction of travel of the blast wave, and shielding afforded by nearby terrain features can affect the response of the target significantly. The effects that differences in target exposure can have on damage may be illustrated by curves similar to the schematic presentation in Figure 14-3.

The terminology that is usually used when discussing target orientation describes which side faces the oncoming blast wave, i.e., side-on,<sup>†</sup> front-on, or rear-on to the blast. A flat surface oriented obliquely or normal to the blast will receive substantially different loads than it would if it were parallel to the blast wave. Little difference in damage is observed for front-on and rear-on orientations for many targets; in this chapter the two orientations are grouped into a single category, end-on orientation. Figure 14-7 illustrates the importance of target orientation to the extent of damage.

A target may be shielded from some of the air blast and thermal radiation effects when some substantial object or terrain feature (natural or man-made) is in the vicinity of the

\* Curves were drawn by finding the horizontal scaled distances ( $d_1$ ,  $d_2$ , etc.) at which changeover from each category of damage to the next higher category occurred. The points so derived were connected by smooth curves.

<sup>†</sup> The term "side-on" is also used in an alternate designation for incident pressure in a blast wave, i.e., "side-on overpressure" is the overpressure in an incident blast wave before it interacts with a target or object.

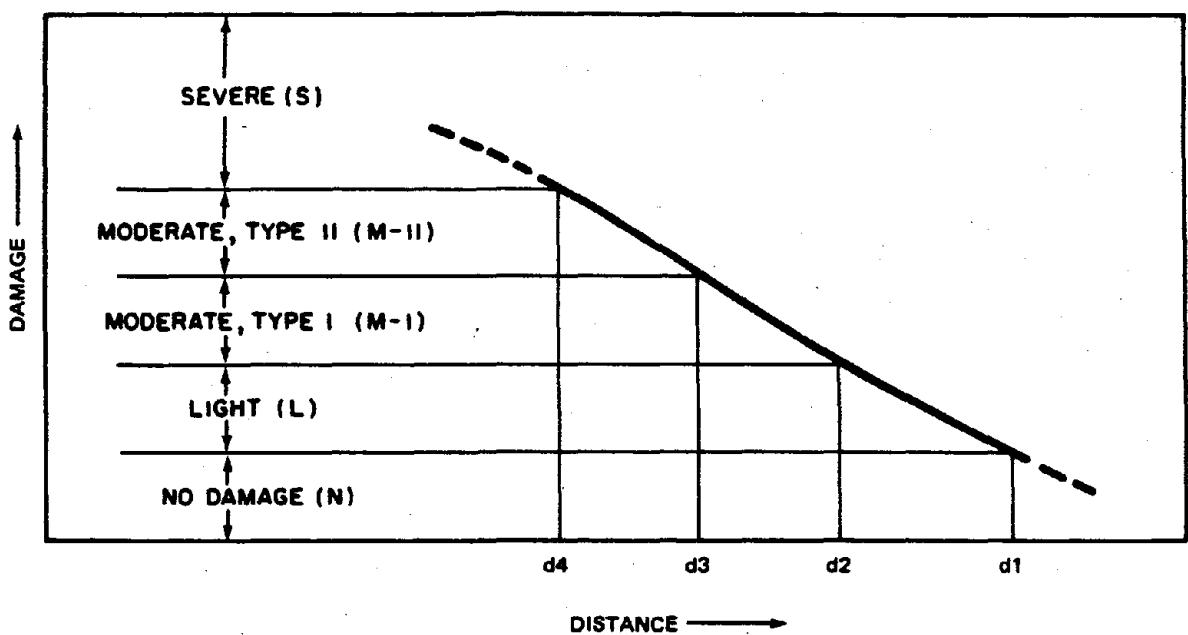


Figure 14-3. Illustration of the Damage vs Distance Curve

Figures 14-5 through 14-7  
 (Pages 14-8 through 14-11)  
 - Detained USANCA 14-7  
 (k)(1)

target. Shielding is most effective when the obstacle is between the target and ground zero.

Obstacles that are considered in the assessment of the effects of shielding from air blast are local obstacles, such as ravines, constructed slots, or revetments (the effects of large terrain features on blast waves are discussed in paragraphs 2-38 through 2-41 of Chapter 2). The importance of shielding is well documented. Comparisons of damage between shielded and unshielded vehicles exposed to blast from both nuclear and chemical explosions are available. The effectiveness of an obstacle in shielding a target generally results as much from its capability to reduce the target movement as from its ability to modify the blast environment. Figure 14-8 illustrates this point. When the obstacle is between the blast wave and the target most of the impulse or translational force that induces motion (drag loading) does not act on the target. When the obstacle is "behind" the target, the translational force initially applied to the target is the same as it would have been without an obstacle, but the obstacle not only can modify later translational forces (as a result of shock wave reflection), but it can restrict movement, the major cause of damage. The overpressure effects of crushing and fracturing still occur in both cases, and these effects provide lower limits for damage ground distances.

Most damage resulting from low yield weapons is caused by overpressure impulse rather than translation, even for unshielded targets, and, since overpressure impulse is not altered drastically by shielding, the effects of shielding are relatively minor for such weapons. However, most damage caused to non-shielded targets by higher yield weapons results from the translational effects of dynamic pressure. Since shielding can reduce translational effects substantially, it can be quite effective as a protection from large yield weapons. Damage to shielded targets results largely from overpressure effects, for which damage distances scale as the cube root of the yield ( $W^{1/3}$ ), while damage to unshielded targets results largely from total impulse effects (including those of dynamic pressure), for which damage distances generally scale as  $W^{0.4}$ . The effects of shielding are illustrated in Figure 14-9, in which damage distances for shielded targets have been scaled as  $W^{1/3}$ , and those for unshielded targets by  $W^{0.4}$ .

#### 14-5 Effects of Ground Surface Conditions

Ground surface conditions affect damage in two ways: by modification of the blast parameters; and by modification of target response. The former is discussed in paragraphs 2-20 through 2-22 and 2-37 through 2-41 of

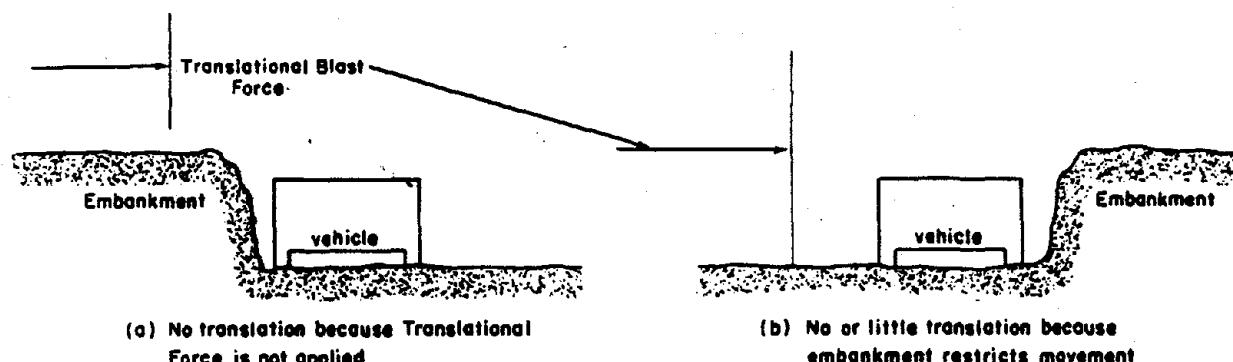


Figure 14-8. The Effect of Shielding

Chapter 2. The latter is discussed here. Information on the effects of ground condition comes from available test data on vehicles exposed on test surfaces constructed to investigate precursor phenomena. These surfaces were desert, asphalt, and desert covered with water. An analysis of these data concluded that there was a significant difference in damage to vehicles on "hard" (non-yielding, non-deforming) and "soft" (yielding, deforming) surfaces. This is illustrated by the curves in Figure 14-10. Blast wave characteristics were different at comparable scaled distances over the two surfaces. Therefore, a scale showing comparable blast wave conditions, dynamic pressure impulse, was substituted for the distance scale shown in previous figures in order to remove the influence of surface conditions on the blast wave from the comparison.

Figure 14-10 shows that surface conditions can influence damage substantially, particularly in the moderate-to-severe categories. This is believed to result from the difference in the target response caused by the difference between the two surfaces shown in Figure 14-10. A soft surface will yield and can be deformed. These surface reactions produce resistive forces against the wheels, which tend to cause the vehicle to tip over. The same vehicle would tend to slide on a hard surface and would not necessarily overturn. The response of a vehicle on a soft surface is likely to resemble the response modes illustrated in Figure 14-2a, c, or e, whereas the same vehicle exposed on a hard surface would be more likely to exhibit the response modes illustrated in Figure 14-2b and d.

Data, such as shown in Figure 14-10, are insufficient to incorporate the effects of surface conditions in the damage prediction techniques given in Section II, except as a source of error that degrades the reliability.

#### 14-6 Vehicle Status

The response of a vehicle to the air blast wave can be influenced by whether or not the brakes are on and/or the transmission is in gear at the time of exposure. Information concerning these influences is available.

DAB  
(6)(1)

Differences in the resulting damage occur primarily for end-on orientation of vehicles. Figure 14-11 illustrates the differences between the damage categories for two comparable [redacted] vehicles. A similar comparison for side-on orientation showed very good agreement, thus the difference shown in Figure 14-11 can be attributed chiefly to differences in vehicle status and not to difference of configuration between [redacted] 1/4-ton trucks.

When a vehicle is exposed end-on with the brakes off and the transmission out of gear, the primary response is rolling on its wheels rather than sliding or overturning. As shown in Figure 14-11, there appears to be an upper limit on the blast forcing function, above which the vehicle will overturn because the forces are too great to be absorbed by rolling or sliding, or because the probability of encountering an obstacle to substantial movement is high. The status of the vehicle at the time of exposure may be as significant in determining the resulting damage as the orientation or even shielding; however, there are insufficient data to include this factor in the damage prediction techniques with any degree of confidence.

## SECTION II

### DAMAGE PREDICTIONS

#### 14-7 Definitions of Damage Categories

The causes of damage to military field equipment by the air blast wave were described in Section I. The description of the various levels of damage (ranging from none to total) must be defined before damage predictions can be made. Various descriptors have been employed over the years by informed and experienced appraisers of damage to describe what they considered to be the degradation of the military effectiveness of various items of equipment. These descriptors, while useful, tend to be somewhat subjective, and they could result in different appraisals of the importance of damage to various items of equipment by different people.

An attempt has been made throughout this manual to describe the damage categories in sufficient detail to indicate the specific damage that applies to a given descriptor (e.g., Tables 11-1 and 11-2, Chapter 11, and Table 12-1, Chapter 12). In this chapter, an attempt has also been made to make the definitions of the damage descriptors less subjective in terms of the availability of a target to perform its intended military functions than descriptor definitions that have been used previously. The definitions that will be presented below include descriptions of the type and level of effort that would be required to restore a target to a condition in which it could perform its intended function, i.e., the definitions provide some insight into the time that would be required to perform essential repairs, although they do not include a measure of any effects that might arise as a result of a time lag before repair (see paragraph 14-13).

To arrive at less subjective definitions, the various items of equipment, which have been examined subsequent to exposure to nuclear and

H.E. tests, were divided into functional subsystems. This was done for two reasons: (1) more precise descriptions of damage could be obtained by considering subsystems than could be obtained by considering the item as a whole; (2) different subsystems can have different degrees of impact on the ability of a particular item of equipment to perform its basic function. Four damage levels were defined for each subsystem: no damage; damaged, but functional; damaged, nonfunctional, but repairable; damaged, non-functional, and not repairable.

Damage categories for the entire piece of equipment were then defined *in terms of damage sustained by the subsystem*. The damage categories that were adopted are defined in Table 14-1.

The subsystems that were identified for wheeled vehicles are shown in Table 14-2 to illustrate the type of system divisions that were employed.

Of the subsystems listed in Table 14-2, the engine, power train, wheels, and chassis were designated critical subsystems which, if they sustain any damage — even easily repairable damage — so as to render them nonfunctional, would render the entire piece of equipment nonfunctional. Operator appliances and parts of the body generally can sustain some degree of damage that might make the individual element nonfunctional (a windshield may be broken, for example, or the hood could be torn off) but would not prevent the vehicle from performing its basic function.

Although the system for identifying damage categories described above reduces the chances of differences in making damage appraisals, some subjectivity is unavoidable, especially in the determination of whether an element of a subsystem can be repaired. A bent steering column, for example, (part of a non-critical subsystem — operator appliances) is deemed to be non-repairable, i.e., normal prac-

Table 14-1. Definitions of Damage Categories

Damage Category	Explanation
Light	Damaged, functional (no critical subsystems – and less than half of all subsystems – are nonfunctional)
Moderate Type I	Damaged, nonfunctional, repairable with little or no special tools, parts or skills (at least one <i>critical</i> subsystem is nonfunctional, but repairable)
Moderate Type II	Damaged, nonfunctional, repairable with special tools, skills, and parts (at least half of all subsystems are nonfunctional but repairable)
Severe	Damaged, nonfunctional, very difficult to repair (at least one subsystem is nonfunctional and not repairable)*

\* An exception to this rule could occur if an otherwise not repairable subsystem could be made functional by replacing it with an immediately available spare.

tice would be to replace it although with difficulty, and with appropriate tools, it could be repaired.

Some typical descriptions of damage to various subsystems of a variety of items of equipment that have been assigned to the four damage categories are shown in Table 14-3. For obvious reasons this table is by no means complete (many equipment items have five or more subsystems). It is included to make the meanings of the damage categories clearer.

#### 14-8 Prediction Techniques

Two types of prediction techniques are presented in this section. For individual pieces of equipment, tables are used to relate (directly or indirectly) the damage categories described in the previous paragraphs to the air blast parameter that results in a particular level of damage.

To determine ground distance for a particular level of damage, the tables are consulted first, then air blast height of burst curves in

Chapter 2 are used to find the scaled (1 kt) ground distance associated with the particular air blast parameter. Finally, appropriate scaling

Table 14-2. Wheeled Vehicle Subsystems

Subsystem	Name and Description
A	Operator Appliances – such as instruments, driving controls, windshield
B	Body – sheet metal work such as fenders, hood, etc.
C	Engine – including fuel, electrical, and cooling systems
D	Power Train – transmission, drive shaft, axles
E	Wheels – tires, suspension, brakes
F	Chassis – basic frame of vehicle

Table 14-3. Typical Subsystem Damage for Various Damage Categories

Type of Equipment	Damage Category							
	Light		Moderate Type I		Moderate Type II		Severe	
	Subsystem	Damage Description	Subsystem	Damage Description	Subsystem	Damage Description	Subsystem	Damage Description
Wheeled vehicles	Body	Glass breakage, bent fenders.	Engine	Air cleaner blown off.	Power train	Transmission broken.	Chassis	Gross frame distortion.
Artillery	Sighting	Glass breakage in optics.	Aiming	Traversing mechanism jammed.	Tube	Recoil mechanism inoperable.	Aiming	Elevating mechanism destroyed.
Tanks	External fittings Gun tube	Bent fenders. Some dirt in tube.	Aiming	Elevating mechanism jammed.	Tracks	Idlers broken, tracks bent and twisted.	Hull	Turret torn off.
Small arms	Stock/Grip	Cracked stock.			Stock/Grip	Broken stock.	Receiver-barrel	Dismembered.
Supply dumps*	Packaging	Packaging not ruptured, items may be scattered.					Packaging	Packaging ruptured.

\*POL in 5 and 55 gal. drums; ammunition and rations in standard packages; other items in small containers.

factors are applied to the scaled ground distance to find the actual ground distance. For broader classes of equipment, "Damage-HOB" curves are presented. These are curves that give scaled distances for particular damage categories as a function of scaled height of burst.

The first technique, though it incorporates one additional step to find damage ranges, provides the user with some knowledge of the air blast parameters that cause damage and, by inference for certain pieces of equipment, some insight into how the equipment is damaged. For shielded equipment, for example, where, as has been discussed, the principle agents of damage are overpressure effects, the tables show this

dependence as well as the need for  $W^{1/3}$  scaling. Similarly, some items of equipment (antenna masts, wire entanglements subjected to bursts from medium or large weapons) are particularly susceptible to wind loading (dynamic pressure) damage, with little or no damage due to overpressure effects. Again the tables show this as well as the required  $W^{1/3}$  scaling which is appropriate for dynamic pressures.

The largest variety of equipment should be sensitive (for reasons given in Section I) to total impulse delivered to the target. Unfortunately, actual total impulse is very difficult to determine. The overpressures portion of total impulse is sensitive to the particular geometry of

the item of equipment being examined. It was demonstrated in paragraph 14-2 that, at least for 1/4-ton trucks oriented side-on to the blast, dynamic pressure impulse ranked second only to total impulse as an air blast parameter to which damage could be related. Thus, with a relatively small loss in accuracy (which would be largest for low yield weapons, for which overpressure effects tend to dominate), dynamic pressure impulse could be employed as an air blast parameter to correlate damage levels.

Unfortunately, height of burst curves are not readily available for dynamic pressure impulse (which would be employed in the second step in the analysis). Therefore, the tables give values of "equivalent overpressure" ( $\Delta p_{eq}$ ) or "equivalent dynamic pressure" ( $q_{eq}$ ), defined as that overpressure under near-ideal conditions, or that dynamic pressure under nonideal conditions (see paragraph 2-20 for a discussion of near-ideal and nonideal surfaces) for a particular yield and height of burst at which the dynamic pressure impulse that would cause a particular level of damage would be experienced. While  $\Delta p_{eq}$  or  $q_{eq}$  are listed as damage causing parameters, ground distance scaling of  $W^{0.4}$  should be used.

The damage prediction technique for individual items of equipment uses three tables and a single graph. Table 14-4 lists the equipment and identifies the appropriate table (14-5, 14-6, or 14-7) from which damage information may be obtained. Table 14-5 is for equipment that is damaged principally by total impulse (as measured by  $\Delta p_{eq}$  or  $q_{eq}$ ), with which  $W^{0.4}$  scaling should be used; Table 14-6 is for equipment that is sensitive to overpressure ( $\Delta p$ ), with which  $W^{1/3}$  scaling should be used; and Table 14-7 is for equipment that is sensitive to dynamic pressure ( $q$ ), with which  $W^{1/3}$  scaling should be used. Tables 14-5 and 14-6 are for use in the Mach shock region only. Table 14-7 can be used in both the Mach and regular reflection region

(see paragraph 2-18 for a discussion of Mach and regular reflection regions).

The graph used in the prediction technique, Figure 14-12, relates peak dynamic pressure  $q$  to peak overpressure  $\Delta p$  for sharp fronted shock waves. It is useful for determining ground distances for damage to equipment that is sensitive to either equivalent dynamic pressure ( $q_{eq}$ ) or actual dynamic pressure ( $q$ ) for values of  $q$  below those shown in the dynamic pressure height of burst curves in Chapter 2 (distances beyond about 1,200 to 1,400 feet for a 1 kt burst). Beyond these distances, the shock waves generally are of classical form, and dynamic pressure at the wave front can be related to peak overpressure (see paragraph 2-17). The peak overpressure height of burst curves of Chapter 2 extend to about 12,000 ft from a 1 kt surface burst, and to about 25,000 feet for a 1 kt air burst (where overpressure is as low as 0.25 psi and dynamic pressure as low as 0.0015 psi).

Tables 14-5 through 14-7 generally show the value of the air blast parameter at which there is a 50 percent probability that the item of equipment will experience the indicated damage or greater. In those cases where sufficient information is available to determine the effect of orientation, values are shown for side-on (SO), end-on (EO), and random orientation. If sufficient information is not available, values are only shown for random orientation.

Figures 14-13 through 14-27 show isodamage — height of burst curves for broad classes of equipment as listed below:

<u>Figure</u>	<u>Equipment</u>
14-13	Wheeled Vehicles,
14-14	Artillery,
14-15	Tracked Vehicles (Except Tanks and Engineer Heavy Equipment),
14-16	Tanks (Light and Heavy),
14-17	Small Arms,

- 14-18 Generators,
- 14-19 Locomotives,
- 14-20 Box Cars,
- 14-21 Supply Dumps,
- 14-22 Telephone Poles,
- 14-23 Water Storage Equipment,
- 14-24 Shielded Wheeled Vehicles,
- 14-25 Shielded Engineer Heavy Equipment,
- 14-26 Signal, Electronic Fire Control  
Equipment, Antennas, and Rigid  
Radomes
- 14-27 Wire Entanglements.

A discussion of damage to untested equipment that is not included in Tables 14-5 through 14-7 or in Figures 14-13 through 14-27 is provided in

paragraph 14-9 together with estimates of some damage levels.

Scaling procedures for use with Figures 14-13 through 14-27 are described in Problems 14-4 and 14-5 as well as on each figure. Strictly speaking, the damage-distance relationship does not scale as a simple power of yield for the classes of equipment included in this family of figures. The yield dependence of the scaling should be reflected by the curves in a manner similar to the presentations of damage to structures in Figures 11-2 through 11-23. Such a family of curves is in preparation; however, they are not available for inclusion in this manual. It is anticipated that such curves will be incorporated in a future change.

Table 14-4. List of Equipment and Corresponding Prediction Tables

Equipment Item	Air Blast Parameter		Table
	Near-Ideal	Nonideal	
<u>Unshielded Equipment</u>			
Wheeled Vehicles			
U.S. WW II 1/4-ton truck	$\Delta p_{eq}$	$q_{eq}$	14-5
U.S. M-38 1/4-ton truck	"	"	"
U.S. 2-1/2-ton truck	"	"	"
U.K. scout car	"	"	"
U.K. 1/4-ton truck	"	"	"
Artillery			
Towed U.S. 57-mm anti-tank gun	"	"	"
Towed U.K. 25-pounder gun	"	"	"
Self-propelled guns	q	q	14-7
Landing Vehicle, Tracked	$\Delta p_{eq}$	$q_{eq}$	14-5
Armored Personnel Carrier, M-59	"	"	"
Construction Equipment			
Crawler tractor	"	"	"
Road grader	"	"	"
Tanks	$\Delta p_{eq}$	$q_{eq}$	14-5
Generators	"	"	"
Railroad Cars	"	"	"
Radio Sets	"	"	"
Radio Aerials			
Antenna masts	q	q	14-7
Whip antennas	"	"	"
Wire Entanglements			
Yields < 1 kt	$\Delta p$	$\Delta p$	14-6
Yields > 1 kt	q	q	14-7
Small Arms	$\Delta p_{eq}$	$q_{eq}$	14-5
Water Storage Equipment			
Lyster bag, 36 gal	$\Delta p$	$\Delta p$	14-6
Tank, cylindrical, open top	"	"	"
<u>Shielded Equipment</u>			
1/4-ton Trucks	$\Delta p$	$\Delta p$	14-6
Crawler Tractors	"	"	"
Road Graders	"	"	"
Lightweight Radios	"	"	"

Tables 14-5 through 14-7  
 Pages 14-23 through 14-25  
 Deleted. USAWDCSA (b)(1)

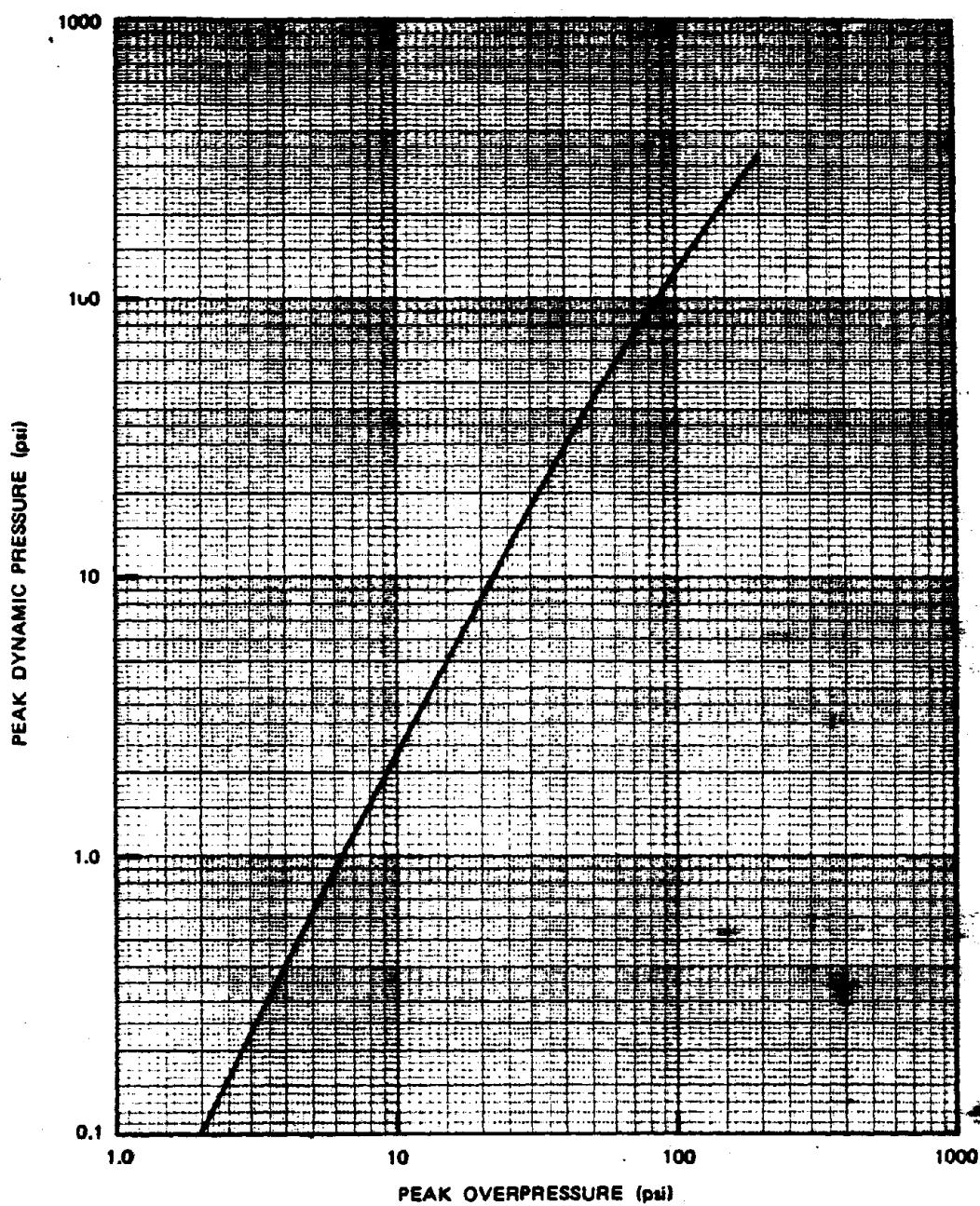


Figure 14-12. Peak Dynamic Pressure as a Function of Peak Overpressure

### Problem 14-1. Calculation of Damage to Wheeled Vehicles

Tables 14-5 through 14-7 show values of equivalent overpressure ( $\Delta p_{eq}$ ) and dynamic pressure ( $q_{eq}$ ) necessary to produce a 50 percent probability of at least the damage category indicated to items of equipment listed in Table 14-4. Ground distances must be obtained from Figures 2-18 or 2-19 for  $\Delta p_{eq}$ , and from Figure 2-25 for  $q_{eq}$ . In those cases where  $q_{eq}$  is lower than shown in Figure 2-25, the corresponding overpressure may be obtained from Figure 14-12. The ground distance corresponding to this overpressure may then be obtained from Figure 2-19 or Figure 2-20.

**Scaling.** The height of burst curves of Chapter 2 must be entered with the height of burst or ground distance for a 1 kt explosion. For yields other than 1 kt, the height of burst and ground distance scale as follows:

For equipment listed in Table 14-5,

$$\frac{h}{h_1} = W^{1/3},$$

$$\frac{d}{d_1} = W^{0.4},$$

For equipment listed in Tables 14-6 and 14-7,

$$\frac{h}{h_1} = \frac{d}{d_1} = W^{1/3},$$

where  $d_1$  and  $h_1$  are the distance from ground zero and height of burst, respectively, for 1 kt, and  $d$  and  $h$  are the corresponding distance and height of burst for a yield of  $W$  kt.

**Example**

Given: A 10 kt explosion at a height of burst of 200 feet.

**Find:** The ground distances for each damage category for randomly oriented 2-1/2 ton trucks for both near-ideal and nonideal (light dust) surface conditions.

**Solution:** From Table 14-4, the equipment is sensitive to total impulse and Table 14-5 is the appropriate table from which to obtain the damage category blast parameters. From Table 14-5, the equivalent overpressures and dynamic pressures for a 1 kt explosion over near-ideal and nonideal surfaces are:

454  
E

**Reliability:** Two factors affect the reliability of damage predictions: the accuracy with which the air blast environment can be predicted; and the accuracy of the damage values or comparable data. The accuracy of the predictions of the overpressure and dynamic pressure environments is discussed in Chapter 2. The values shown in Tables 14-5 through 14-7 are for 50 percent probability with an accuracy of  $\pm 25$  percent, i.e., the value for a change in damage level is for a 50 percent probability that the greater damage will occur, and the value shown in the table is accurate to within  $\pm 25$  percent. These reliability and accuracy values are estimates because there are rarely sufficient data to justify a statistical analysis. The damage values with asterisks, signifying limited data, are estimated to be accurate to within  $\pm 50$  percent. The loss in accuracy resulting from modifications for random orientation and shielding are believed to be small and would have little effect on the overall reliability of the damage prediction.

**Related Material:** See paragraphs 14-7 and 14-8, Tables 14-4 through 14-7, and Figure 14-12. See also paragraphs 2-20 through 2-22, Figures 2-18 through 2-20, and Figure 2-25.

45000CA  
(EX1)

### Problem 14-2. Calculation of Damage to Shielded Wheeled Vehicles

Tables 14-5 through 14-7 show values of equivalent overpressure ( $\Delta p_{eq}$ ) and dynamic pressure ( $q_{eq}$ ) necessary to produce a 50 percent probability of at least the damage category indicated to items of equipment listed in Table 14-4. Ground distances must be obtained from Figures 2-18 or 2-19 for  $\Delta p_{eq}$ , and from Figure 2-25 for  $q_{eq}$ . In those cases where  $q_{eq}$  is lower than shown in Figure 2-25, the corresponding overpressure may be obtained from Figure 14-12. The ground distance corresponding to this overpressure may then be obtained from Figure 2-19 or Figure 2-20.

**Scaling.** The height of burst curves of Chapter 2 must be entered with the height of burst or ground distance for a 1 kt explosion. For yields other than 1 kt, the height of burst and ground distance scale as follows:

For equipment listed in Table 14-5,

$$\frac{h}{h_1} = W^{1/3},$$

$$\frac{d}{d_1} = W^{0.4},$$

For equipment listed in Tables 14-6 and 14-7,

$$\frac{h}{h_1} = \frac{d}{d_1} = W^{1/3},$$

where  $d_1$  and  $h_1$  are the distance from ground zero and height of burst, respectively, for 1 kt, and  $d$  and  $h$  are the corresponding distance and height of burst for a yield of  $W$  kt.

**Example**

**Given:** A 20 kt explosion at a height of burst of 500 feet.

**Find:** The ground distances for each damage category for 1/4-ton trucks within revetments, i.e., shielded on two sides.

**Solution:** From Table 14-4, shielded vehicles are overpressure sensitive and Table 14-6 is the appropriate table from which to obtain the damage category blast parameters. Since no particular orientation was specified, random orientation is assumed. From Table 14-6, overpressures for a 1 kt burst over a near-ideal surface are:

USANCA  
14-29

comparable data. The accuracy of the predictions of the overpressure and dynamic pressure environments is discussed in Chapter 2. The values shown in Table 14-5 through 14-7 are for 50 percent probability with an accuracy of  $\pm 25$  percent, i.e., the value for a change in damage level is for a 50 percent probability that the greater damage will occur, and the value shown in the table is accurate to within  $\pm 25$  percent. These reliability and accuracy values are estimates because there are rarely sufficient data to justify a statistical analysis. The damage values with asterisks, signifying limited data, are estimated to be accurate to within  $\pm 50$  percent. The loss in accuracy resulting from modifications for random orientation and shielding are believed to be small and would have little effect on the overall reliability of the damage prediction.

*Related Material:* See paragraphs 14-7 and 14-8, Tables 14-4 through 14-7, and Figure 14-12. See also paragraphs 2-20 through 2-22, Figures 2-18 through 2-20, and Figure 2-25.

*Reliability:* Two factors affect the reliability of damage predictions: the accuracy with which the air blast environment can be predicted; and the accuracy of the damage values or

**Problem 14-3. Calculation of Damage to  
Wire Entanglement**

Tables 14-5 through 14-7 show values of equivalent overpressure ( $\Delta p_{eq}$ ) and dynamic pressure ( $q_{eq}$ ) necessary to produce a 50 percent probability of at least the damage category indicated to items of equipment listed in Table 14-4. Ground distances must be obtained from Figures 2-18 or 2-19 for  $\Delta p_{eq}$ , and from Figure 2-25 for  $q_{eq}$ . In those cases where  $q_{eq}$  is lower than shown in Figure 2-25, the corresponding overpressure may be obtained from Figure 14-12. The ground distance corresponding to this overpressure may then be obtained from Figure 2-19 or Figure 2-20.

**Scaling.** The height of burst curves of Chapter 2 must be entered with the height of burst or ground distance for a 1 kt explosion. For yields other than 1 kt, the height of burst and ground distance scale as follows:

For equipment listed in Table 14-5,

$$\frac{h}{h_1} = W^{1/3},$$

$$\frac{d}{d_1} = W^{0.4},$$

For equipment listed in Tables 14-6 and 14-7,

$$\frac{h}{h_1} = \frac{d}{d_1} = W^{1/3},$$

where  $d_1$  and  $h_1$  are the distance from ground zero and height of burst, respectively, for 1 kt, and  $d$  and  $h$  are the corresponding distance and height of burst for a yield of  $W$  kt.

**Example**

**Given:** A 15 kt explosion at a height of burst of 400 feet.

**Find:** The damage-distance relations for a concertina wire entanglement.

**Solution:** Table 14-4 indicates that wire entanglements are sensitive to dynamic pressure for yields greater than 1 kt, and that Table 14-7 is the appropriate table from which to obtain the damage category blast parameters.

The equivalent height of burst for a 1 kt explosion is

$$h_1 = \frac{h}{W^{1/3}} = \frac{400}{(15)^{1/3}} = 162 \text{ ft.}$$

**Reliability:** Two factors affect the reliability of damage predictions: the accuracy with which the air blast environment can be predicted; and the accuracy of the damage values or comparable data. The accuracy of the predic-

tions of the overpressure and dynamic pressure environments is discussed in Chapter 2. The values shown in Tables 14-5 through 14-7 are for 50 percent probability with an accuracy of  $\pm 25$  percent, i.e., the value for a change in damage level is for a 50 percent probability that the greater damage will occur, and the value shown in the table is accurate to within  $\pm 25$  percent. These reliability and accuracy values are estimates because there are rarely sufficient data to justify a statistical analysis. The damage values

with asterisks, signifying limited data, are estimated to be accurate to within  $\pm 50$  percent. The loss in accuracy resulting from modifications for random orientation and shielding are believed to be small and would have little effect on the overall reliability of the damage prediction.

**Related Material:** See paragraphs 14-7 and 14-8, Tables 14-4 through 14-7, and Figure 14-12. See also paragraphs 2-20 through 2-22, Figures 2-18 through 2-20, and Figure 2-25.

### Problem 14-4. Calculation of Damage to Artillery

Figures 14-13 through 14-27 show families of curves that define the damage categories as functions of height of burst and ground distance from a 1 kt explosion for the several classes of equipment listed in paragraph 14-8. Separate curves are shown for near-ideal and nonideal surface conditions.

*Scaling.* For yields other than 1 kt the height of burst and ground distance scale as follows:

For Figures 14-13 through 14-21,

$$\frac{h}{h_1} = W^{1/3},$$

$$\frac{d}{d_1} = W^{0.4},$$

For Figures 14-22 through 14-25, and 14-27,

$$\frac{h}{h_1} = \frac{d}{d_1} = W^{1/3},$$

For Figure 14-26,

$$\frac{h}{h_1} = W^{1/3},$$

$$\frac{d}{d_1} = W^{0.4}, \text{ except Radomes, for}$$

which distance scales as,

$$\frac{d}{d_1} = W^{1/3},$$

where  $h_1$  and  $d_1$  are the height of burst and ground distance for 1 kt, and  $h$  and  $d$  are the

corresponding height and distance for a yield of  $W$  kt. For convenience, the proper scaling is indicated on each figure.

*Example*

*Given:* A 250 kt explosion at a height of burst of 1,250 feet.

*Find:* The distance to which severe damage occurs to artillery located on a nonideal surface.

*Solution:* The corresponding height of burst for 1 kt is

$$h_1 = \frac{h}{W^{1/3}} = \frac{1,250}{(250)^{1/3}} = 198 \text{ ft.}$$

The listing given in paragraph 14-8 shows that Figure 14-14 is the appropriate figure to determine damage relationships for artillery.

*Reliability:* The ground distances for the various damage categories shown in Figures 14-13 through 14-18 and 14-22 through 14-27 are estimated to be accurate generally within  $\pm 25$  percent, although wide variations might occur for individual items within a class (see paragraph 14-3). These reliability values are estimates because there are rarely sufficient data to justify a statistical analysis. The ground distances obtained from Figure 14-19 through 14-21 are estimated to be accurate within  $\pm 50$  percent.

percent because of the even more limited data and because of the difficulty in aggregating all supply dumps into one class. As described in paragraph 14-8, curves that reflect the yield dependence of the scaling might be expected to provide somewhat more reliable predictions;

however, such curves are not available at present.

**Related Material:** See paragraphs 14-3, 14-7, and 14-8. See also paragraphs 2-20 through 2-22.

**Problem 14-5. Calculation of the Advantage in Shielding  
Engineer Heavy Equipment**

Figures 14-13 through 14-27 show families of curves that define the damage categories as functions of height of burst and ground distance from a 1 kt explosion for the several classes of equipment listed in paragraph 14-8. Separate curves are shown for near-ideal and nonideal surface conditions.

**Scaling.** For yields other than 1 kt the height of burst and ground distance scale as follows:

For Figures 14-13 through 14-21,

$$\frac{h}{h_1} = W^{1/3},$$

$$\frac{d}{d_1} = W^{0.4},$$

For Figures 14-22 through 14-25, and 14-27,

$$\frac{h}{h_1} = \frac{d}{d_1} = W^{1/3},$$

For Figure 14-26,

$$\frac{h}{h_1} = W^{1/3},$$

$$\frac{d}{d_1} = W^{0.4}, \text{ except Radomes, for}$$

which distance scales as,

$$\frac{d}{d_1} = W^{1/3},$$

where  $h_1$  and  $d_1$  are the height of burst and ground distance for 1 kt, and  $h$  and  $d$  are the

corresponding height and distance for a yield of  $W$  kt. For convenience, the proper scaling is indicated on each figure.

**Example**

**Given:** A 250 kt explosion at a height of burst of 1,000 feet over a nonideal surface.

**Find:** The advantage in shielding engineer heavy equipment at a distance of one mile from the expected ground zero.

**Solution:** The corresponding height of burst for 1 kt is

$$h_1 = \frac{h}{W^{1/3}} = \frac{1,000}{(250)^{1/3}} = 159 \text{ ft.}$$

The listing given in paragraph 14-8 shows that Figure 14-15 is the appropriate figure to determine damage relationships for unshielded engineer heavy equipment, and Figure 14-25 is appropriate for shielded engineer heavy equipment. The corresponding ground distance from a 1 kt explosion for use with Figure 14-15 is (see *Scaling* above)

$$d_1 = \frac{d}{W^{0.4}}$$

$$d_1 = \frac{5,280}{(250)^{0.4}} = 580 \text{ ft.}$$

The corresponding ground distance from a 1 kt explosion for use with Figure 14-25 is (see *Scaling* above)

$$d_1 = \frac{d}{W^{1/3}}$$

$$d_1 = \frac{5,280}{(250)^{1/3}} = 838 \text{ ft.}$$

*USA NCA  
(k)(1)*

**Reliability:** The ground distances for the various damage categories shown in Figures 14-13 through 14-18 and 14-22 through 14-27

are estimated to be accurate generally within  $\pm 25$  percent, although wide variations might occur for individual items within a class (see paragraph 14-3). These reliability values are estimates because there are rarely sufficient data to justify a statistical analysis. The ground distances obtained from Figure 14-19 through 14-21 are estimated to be accurate within  $\pm 50$  percent because of the even more limited data and because of the difficulty in aggregating all supply dumps into one class. As described in paragraph 14-8, curves that reflect the yield dependence of the scaling might be expected to provide somewhat more reliable predictions; however, such curves are not available at present.

**Related Material:** See paragraphs 14-3, 14-7 and 14-8. See also paragraphs 2-20 through 2-22.

*Figures 14-13 through 14-27 on  
Pages 14-37 through 14-51  
are deleted.*

*USA NCA  
(k)(1)*

#### 14-9 Untested Equipment

Although a wide variety of equipment is included in Tables 14-5 through 14-7, many items are not listed, principally because they were never subjected to the air blast environment of nuclear or large HE tests. In some cases it is possible to deduce an approximate set of damage criteria, either because the untested equipment is comparable in some degree to some item that was tested, or because subsystems of the new equipment are similar to subsystems on tested equipment. The principles and the damage agents described in paragraphs 14-1 through 14-6 should aid in predicting damage to untested equipment, although familiarity with subsystem response (a subject beyond the scope of this chapter) would be more satisfactory.\*

Table 14-8 lists a number of items of equipment for which approximate levels of damage were deduced from the principles outlined previously. The response information shown in Table 14-8 is generally considered to be accurate to within  $\pm 50$  percent, unless otherwise stated. This is caused by the inherent inaccuracies associated with the use of the comparability principle, which is primarily useful for obtaining estimates. The remainder of this section describes how the damage levels were determined.

*Bridges, Mobile Assault:* A specific example of this equipment is the "Bridge, Floating: Mobile Assault, 36-ft." This item should be examined for its response when on the road, and when in the water. Unfortunately no information about its response in the water exists.

When on the road and side-on, the critical angle† for overturning is about 45 degrees, which is comparable with a 2-1/2-ton truck. The area of the side-on vehicle is at least twice that of a 2-1/2-ton truck, and the weight is about four times as much. Because the moment of inertia about an overturning axis would be large, the primary response mode is expected to be sliding. However, because of the box-like config-

uration and the large, flat-topped surface, a large lifting force is quite possible. In addition, the large weight force on each of four wheels is likely to cause a buildup of resistive force during sliding. It therefore appears reasonable to assume that overturning occurs shortly after sliding begins.

In the end-on configuration, the sloping surface of the vehicle will cause a significant vertical force. However, the extremely large moment of inertia in this orientation should provide resistance to overturning. The construction of the item, in addition to the flotation gear, may make it vulnerable to low overpressures. A rupture of the hull or flotation gear would make the item useless until repairs are made. In this instance, whether the item was made of steel or aluminum, the thickness of hull, and whether of riveted or welded construction, would be significant. Thermal effects on flotation gear are not expected to cause rupture or burning except at high yields, although the flotation gear may be torn loose in the end-on configuration.

Additional information concerning this item would increase the reliability of damage predictions. Until such time as more information becomes available, the following values are recommended.

\* P. J. Morris, *Study of Military Field Equipment Response to Air Blast and Prediction of Damage (U)* describes predictions based on subsystem response (see bibliography).

† Angle through which the item must rotate for the center of mass to be placed over the center of rotation.

‡ Use  $W^{0.4}$  scaling for ground range.

**Camouflage Nets.** These items are rarely considered in damage predictions. They are included in Table 14-8 primarily as a possible source of fires. Very low dynamic pressures, on the order of 2 psi, are sufficient to destroy their effectiveness for concealment. Cloth netting generally is destroyed by a thermal exposure of 15 cal/cm<sup>2</sup>. Cloth nets can be a considerable fire hazard if this amount of thermal energy is received prior to the arrival of a low overpressure blast of about 5 psi, which may be insufficient to extinguish pre-blast flames. Plastic netting is not as susceptible to burning, but it will melt and char at a thermal exposure of approximately 10 cal/cm<sup>2</sup>.

**Carriers, Full Tracked.** Some data are available on equipment that predates present equipment, e.g., the Armored Infantry Vehicle, M59. So few data are available on similar current equipment, however, that any attempt to apply M59 information to current equipment could be misleading. Present vehicles are significantly different from the M59 since they are constructed of aluminum, whereas the M59 was constructed of steel. The response of carriers is believed to be similar to that of wheeled vehicles in that a boxlike construction and large areas make it susceptible to overturning. It appears that the damage values for 1/4-ton trucks may be appropriate until actual response information becomes available.

**Engineer Construction Equipment.** Tabulated values for road grader and tracked tractors are probably appropriate for the present equipment; however, these response tables are based on very few data points, which undoubtedly affects their reliability. The characteristics of the equipment exposed in nuclear tests are not known, and comparisons with present items cannot be made. It is believed, however, that differences will be relatively small.

No test information is available for wheeled scoop loader type equipment. Since it is

a four-wheeled, rubber-tired vehicle, comparison with other wheeled vehicles is inevitable.

**Howitzers, Self-Propelled.** The M108 105-mm, M109 155-mm, and M110 8-in. self-propelled howitzers are examples of this equipment type. The M108 and M109 howitzers are more similar in mass distribution and geometry to tanks than to the howitzers exposed during nuclear tests. Their somewhat higher profile and more "bulky" construction of the turret indicate they would be more susceptible to overturning than tanks. Nevertheless, the damage values for tanks should provide a good estimate until a closer examination of these items is made. The 8-in. howitzer on the other hand has a configuration similar to howitzers that were exposed at tests; thus, the damage values for the T97 self-propelled howitzer should provide a good estimate.

Damage values for self-propelled howitzers are based on very little data, and care should be exercised in using the tank damage values for the M108 and M109. One major consideration not previously mentioned with regard to these items is the lack of data or analysis for howitzers exposed with their gun tubes in a firing position. Such a configuration could change the response of these items materially as a result of a change in the dispositions of blast forces and resisting moments.

**Howitzer, Towed.** Three examples of this category of equipment are the M101A1 105-mm light howitzer, M114A1 155-mm medium howitzer, and M115 8-in. heavy howitzer. Damage values are available for the 57-mm antitank gun and the U.K. 25 pounder. The damage values for the 57-mm AT gun probably can be used for the M101A1 105-mm how-

[REDACTED] itzer, but insufficient information is available for the M114A1 155-mm medium howitzer, and M115 8-in. heavy howitzer.

[REDACTED] *Radar Sets.* The AN/MPQ-4A radar set is used primarily to locate hostile mortars and to adjust low-velocity artillery fire. When this equipment is in transit, the antenna group and power supply are each mounted on two-wheeled trailers. The antenna trailer has outriggers for stability. The control unit for the radar and power supply can be removed for remote operation from the power supply trailer, which contains a gasoline generator. When in remote operation the control unit is mounted on a tripod-type stand and weighs about 575 pounds. The only response tables which deal with items that resemble any of this equipment are the ones for skid- and trailer-mounted generating sets. The vulnerability of the power supply trailer might be correlated with a trailer-mounted generator, and the antenna group with a skid-mounted generator. The antenna group is difficult to analyze because of its uniqueness, plus the fact that the trailer outriggers should significantly reduce its vulnerability to overturning. The antenna reflector should be the most vulnerable subsystem of this group, and damage to it would probably determine the overall damage category of the radar system. Thus the damage values for generators may be used as an estimate if the antenna reflector is added as another subsystem, which results in the following approximate damage values for both near-ideal and non-ideal blast conditions.

[REDACTED] Another radar set that may be used as an example is the AN/TPS-25. This is a combat surveillance, night vision, target acquisition radar. There are three major groupings of components in the system. The antenna, antenna mast, radar modulator, and receiver-transmitter are grouped together and connected by cable to the shelter that contains the radar controls and plot board, and houses operating personnel. The system is powered by a remotely located gasoline generator. The shelter may be located either on the ground or on its transporting vehicle, a 2-1/2-ton cargo truck or 3/4-ton or 1-1/2-ton two-wheeled trailer. All components are packed in the shelter during transit or when not in use. The antenna mast comes in three 6-1/2 foot tubular sections, one, two, or three of which may be used. The antenna mounted on the mast weighs about 150 pounds. The modulator rests on the ground next to the antenna mast.

[REDACTED]

W.P.  
[REDACTED]

*Radio Sets and Terminal Telegraph.* The radio sets AN/GRC-26D, AN/GRC-50, AN/MRC-80, and terminal telegraph-telephone

[REDACTED] \* Use  $W^{0.4}$  scaling for ground range.

AN/MCC-6 are normally located in electrical shelters mounted on a 2-1/2-ton cargo truck. These shelters have sheet metal walls, metal frames, and wooden interior walls, ceiling and floor.

USARCA  
(Ex-1)

The last example of radio sets is the AN/VRC-12. This is the basic means of communication for vehicles and crew-served weapons upon or within which it is mounted. Its power comes from the vehicle or weapon electrical system. These radios use a whip antenna; they are transistorized except for two tubes in the transmitter driver and power-output stages. The VRC-12 is constructed with printed circuit boards. Therefore, vulnerability should differ considerably from the damage values given for lightweight radios in Table 14-5. Printed circuit boards generally are more vulnerable to shock and vibration than wired circuits. Since these radios are located on or in vehicles and crew-served weapons, the response of the carrier controls the response of the radios to some degree.

For low yields and shielded vehicles, the following values apply for damage to radios from overpressure.

*USARCA*  
*(Ex-1)*

**Wheeled Vehicles.** An example of how untested wheeled vehicles might be analyzed is given by this analysis of the M51A2 5-ton dump truck. Few data exist for a 5-ton dump truck (no vehicles exposed at nuclear tests were loaded). The response of a loaded vehicle could be significantly different because the overturning forces would have to be increased. In fact, the possibility of a sliding response would have to be closely examined. The gross unloaded weight of this vehicle is quite large, about 23,000 lb with a center of gravity that is undoubtedly below the center of pressure, so the vehicle probably would overturn were it not for the high overturning moment and angle required. It is not possible to state categorically how this vehicle will respond. Test data do indicate that when it does overturn, the dump body is separated from the chassis, resulting in serious damage. Therefore, the application of the Table 14-5 damage values for 2-1/2-ton trucks will quite likely result in an overestimation of the low-damage-category ground ranges and an underestimation of the high-damage-category ground ranges.

A truck-mounted water purification set is an example of a special-purpose wheeled vehicle. This item is quite likely to have different responses, depending on whether the water purification set is in operation or the equipment is closed down for transport. In operation, side

\* Use  $W^{1/3}$  scaling for ground range.

panels of the truck body are opened, exposing the purification equipment directly to blast. In addition, the open compartment would increase the clearing times for the reflected pressure and increase the drag coefficient for dynamic pressure. The weight of this item is not known, but it is obvious that the center of gravity would be relatively high. Coupled with the high surface areas, this virtually assures overturning at relatively low blast values. The response of the purification equipment mounted on the truck chassis cannot be estimated without detailed analysis. However, the response of the item as a whole is believed to be quite similar to a 1/4-ton truck.

*Supply Dumps.* Damage to supply dumps should be considered in a functional sense. The purpose of a supply dump is to serve as a collection, storage, and dispensing point for materiel. Available information indicates the effect of a blast wave is to scatter containers, at times rupturing the containers and spilling the contents. If the contents are not in bulk form, such as fuel, the contents generally are not damaged. Thus the collection and storage of materiel is not significantly affected. However, the scattering of supplies and blocking of access aisles can degrade the effectiveness of the dump in issuing supplies. The size of the stacks of supplies appears to influence the amount of scattering through some type of volume-vs-area ratio. The blast winds remove boxes, etc., from outer layers in an unravelling process. Since, for a given volume, the area exposed to blast winds depends upon the number of stacks, shielding of supply dumps, such as placing them below ground level, is quite effective in that dynamic pressures have much less area to act on. Overpressure then becomes the dominant factor causing damage. Since contents of supply dumps generally are resistant to crushing forces, an overpressure level of 30 psi is recommended for shielded supply dumps. A dynamic pressure of 5

psi is recommended for unshielded supply dumps. These values are expected to cause major disruption of the supply dump either through damage to or loss of contents or scattering and mixing of containers.

### SECTION III

#### DAMAGE FROM CAUSES OTHER THAN BLAST AND NUCLEAR RADIATION

##### 14-10 Fire Damage

Damage to equipment by fire is referred to in some damage reports. Although some 20 occurrences have been noted, they involved only a very small percentage of the equipment exposed. Most fires appeared to be secondary in nature, that is, they were not started by direct thermal radiation ignition. Two equipment items were burned during nuclear tests under exposure conditions in which they could have received virtually no thermal radiation. In addition, a 1/4-ton truck exposed at a 100-ton high explosive test (in which thermal radiation was negligible) also burned.

The damage to a 6-kVA generator exposed on a U.K. test is particularly interesting. In the damage report the notation is made, "Fire may have started from fuel from broken carburetor spilling on hot muffler." U.K. practice at nuclear tests was to expose running equipment, that is, the engines were running at the time of the explosion. The six recorded occurrences of fires on U.K. tests represents a considerably larger percentage (about 10 percent) of all U.K. equipment exposed than does the number of fires recorded on U.S. tests. Since this may be due to the U.K. practice of running engines during a test, the incidence of secondary fires in an operational situation may be higher than the U.S. test data indicate.

Although it is believed that most fires in the U.S. tests were from secondary rather than

primary thermal ignitions, the source of some of these secondary ignitions is not clear. The two 1/4-ton trucks that burned on one U.S. test were believed to have been ignited by burning asphalt. In one case of a tank exposed to a very low yield burst, personnel reentered the area of the burst shortly after detonation, approaching within 2,000 ft of ground zero at  $H + 1$  hour. No smoke or open flames were observed. However, approximately 1/2 hour later some smoke was observed, although its cause is not known.

Shielding from direct thermal radiation occurs when the target is below a line from the burst point to the top of any obstacle, that is when the target is in the shadow cast by the obstacle. The obstacle blocks essentially all thermal radiation. Some thermal radiation will still reach the target via the scattering of radiation by the atmosphere. This scattered radiation can be substantial for large yields because the long distances traveled by the radiation increase the opportunities for scattering. Considerable radiation can also be backscattered from clouds. There is not, however, enough information on scattering to be able to predict damage resulting from thermal radiation to shielded targets.

Because the incidence of fires was so low in the U.S. tests (though limited British experience suggests that fires could more frequently occur in operational situations), fire damage is not normally considered in assessing damage to military equipment.

#### 14-11 Obscuration of Optical Devices

Obscuration of optical devices can be an important type of damage. Evidently, the thermal radiation impinging on coated or painted surfaces near an optical surface, together with blast winds, results in the deposit of sufficient sooty material that the optical surface would have to be cleaned prior to use. Most of the information on this phenomenon was obtained from U.S. and U.K. damage reports on exposed

tanks, and some scattered data are available on the artillery optics. Although there is no physical damage to the optics, the obscuration is sufficient to preclude their use, and some remedial action must be taken to make them useful.

45AACA  
(Ex-1)

Little is discernible in the data about the effect that orientation has on which surfaces become sooted, but it seems wise to develop criteria for sooting of all surfaces. Since most nuclear tests were conducted under nearly ideal atmospheric conditions, and there probably was little scattering of thermal radiation, sootting was probably limited to those surfaces more directly facing GZ.

45AACA  
(Ex-1)

The data from the exposure of tanks at nuclear tests are sufficiently extensive that obscuration of optics is included in damage estimates for tanks; however, there is insufficient information to apply this process to other optical systems with any reliability.

#### 14-12 Damage by Missiles

Missiles are objects that are picked up and translated by the blast wave with sufficient velocity that, upon impact with an item of equipment, the stem may be damaged. Examples of such objects are rocks, gravel, sticks, structural debris, battlefield debris, etc. Instances of missile damage are scattered throughout the damage reports of nuclear tests. Some examples are the puncturing of a tire, fuel tank, or radiator by a stick or stone.

Missile damage usually has not been included in damage analysis and prediction tech-

niques because its frequency of occurrence is quite low, and it is rarely possible to predict when an item of equipment would be damaged by a missile. Missile damage, therefore, generally is not considered in damage analysis. (An exception for sand and gravel missiles is the chipping and cracking of glass surfaces by blast-wind-transported material. This phenomenon is mentioned in damage reports with sufficient regularity to include it as a damage mechanism even though it rarely makes optical systems completely inoperable.)

Another possible agent of damage that falls under the general category of missile damage is the deposit of dirt, sand, and gravel in gun tubes and in some cases machine-gun barrels. Although there are several specific references to this problem in the test reports, there are no references for dynamic pressures above 10 psi. The more spectacular physical damage that occurred at high dynamic pressures may have caused this effect to be neglected in the examination of the equipment. There are rare references to sand and dirt getting into the breech mechanism, making it difficult to operate.

Deposition of foreign matter in gun tubes does not seem to depend upon orientation of the tubes, which may be explained by the fact that material is transported by both the positive and negative phase of dynamic pressure. In actual combat, there might not be as much sand and gravel as on the desert where nuclear tests were conducted, but there could be other sources of particulate matter available. A little dirt in a gun tube may only mean an increased rate of wear if the gun is fired before cleaning, but it could also lead to more catastrophic damage. Consequently, the possible effects of material deposition within gun tubes should be considered in assessing damage to equipment with such tubes.

#### 14-13 The Effects of Time

Time itself is not a damage mechanism.

However, the time lag between occurrence of damage and efforts to repair the damage may alter the damage level of one or more subsystems of military equipment significantly. For example, hydrostatic lock may develop in overturned engines; fuel, water, and oil may leak, and require replacement before the equipment is functional; the corrosive action of spilled battery acid or solvents can render subsystems inoperable; soft systems, such as electronics, may be exposed to weather, making them inoperable. Such events can not only increase damage levels but also can increase the amount and nature of effort necessary to repair the damage.

The damage reported on nuclear tests frequently included some effects of time, although damage reports attempted to compensate for time delays. Test areas often were not reentered nor damage assessments made until many days after the explosion. In an operational situation, particularly if personnel are in a warned protected status at detonation time, recovery efforts would probably start in a matter of hours rather than days. Since the significance of time after damage is extremely difficult to assess quantitatively (because of unknowns in the disposition and capability of repair or recovery efforts soon after detonation) damage assessments included herein do not include the effects of time before repairs can be made.

## SECTION IV

### TREE DAMAGE CRITERIA

The phenomena associated with transient radiation effects on electronics (TREE) are discussed in Chapter 6. Section VII of Chapter 9 discusses component part and circuit response to nuclear radiation. This section provides estimates of nuclear radiation levels sufficient to cause moderate to severe effects in military equipment. The discussion in this section is limited to electronics, without regard to the system structure or the operator.

## SYSTEMS ANALYSIS

### 14-14 Types of Systems Analysis Used in TREE

Two approaches may be used in systems analysis with respect to TREE, and each leads to a different result. The first approach to survivability analysis addresses the question of whether the system will malfunction during or after exposure to a specifically defined threat or a given set of radiation hardness criteria. The end result is that a system can be classified as vulnerable, questionable, or hard to that specified radiation threat. The survivability of the system can then be improved by redesign of the more vulnerable circuits or subsystems. Although the system may be classified as hard to the specified radiation threat, there is no certainty that the vulnerability levels of the system will have been identified. This approach to survivability analysis may be adequate in some instances, but changes in threat environment, system mission or tactics will require another complete analysis.

The second approach to survivability analysis differs from the analysis described above in two major respects. First, it includes a detailed vulnerability assessment which defines the susceptibility level of each circuit or subsystem to all types of radiation threats, not just a particular one. Second, it is concerned with the statistics of failure for any component or subsystem variations in failure level for all radiation threats. With these data, the system may be evaluated for a specifically defined threat and any variations in the threat resulting from changes in system employment or tactics. In this section interest centers on the expanded survivability analysis approach.

### 14-15 The Complexity of Performing System Analysis for TREE

The complexity of circuit and system analysis is increased when it becomes necessary

to understand the system response during and after exposure to nuclear radiation. This environmental constraint can change or modify the characteristics of the electronics in a very time dependent manner. The level of understanding and the accuracy in prediction of individual component part response often is not sufficient to allow accurate analysis. Therefore testing (in many cases extensive testing) is necessary to establish component part response and to verify circuit analysis. This, however, is not the complete answer to the additional complexity. The radiation response of component parts can vary widely. For example, samples of a certain transistor type can sustain significant variations in percentage of gain degradation for a given neutron exposure. Component part response can also depend on the particular bias conditions under which the part is being operated. That is, the component part could be most vulnerable to a particular radiation component (e.g., gamma rays) in one bias condition while in another bias condition it may be most vulnerable to a different radiation component (e.g., neutrons). The degree of susceptibility can change with bias conditions. As stated in Section VII of Chapter 9, the response of component parts can depend on prompt dose or dose rate. In survivability analysis, both cases must be considered. This possibility of double dependence also applies at the circuit and subsystem levels of response.

The circuit and subsystem design also are critical with respect to radiation susceptibility. The fact that a component has a significant response to a certain level of radiation does not mean that the circuit that uses that component will be susceptible to the same level of radiation. The radiation susceptibility level of the circuit could be higher or lower than the levels of any of the component parts used in the circuit. The tolerances within which each component part and circuit has to perform in order for the system to achieve its function is a factor

in establishing the susceptibility of the circuit. Information of this nature, however, usually is only available during the design phase and frequently must be obtained through a detailed circuit analysis. The tolerances of the critical component parts and circuits, once obtained, are typically so narrow that another complete analysis of the component response and circuit interactions is required to establish the survivability of the system.

For similar reasons a problem occurs in the analysis of generic functions, such as an amplifier, flip-flop, or clock circuit. Circuit functions can be performed by a large number of circuit configurations using a very large variety of component part types. Thus, it would be necessary to review all pertinent configurations and component part types that would accomplish the desired function in order to determine the survivability of the generic function. Also, the level of confidence associated with a specific vulnerability level for a generic function would be much lower than that for a specific circuit with specific component parts.

The last factor that affects the accuracy of the system analysis is the determination of the environment. That is, the environment that is used to generate the TREE response data (for use in the analysis) has to be correlated to the actual use environment. This correlation may be in error by as much as an order of magnitude unless care is taken to include all factors that may affect the correlation.

All these influences are in addition to the normal circuit and systems analysis problems. The resultant analysis becomes a complex manipulation of many interactions. Hence this type of analysis requires skill and understanding in order to approach a reasonably good characterization of the system response to a nuclear weapon threat.

#### 14-16 Characteristics of the Analysis Used in This Section

A primary concern of this section is to provide an appreciation for the survivability levels of military electronic equipment exposed to radiation from nuclear weapons. For the purposes of this section, only two levels of survival are used — a "sure safe" level and a "sure kill" level. The term "sure safe" implies a zero percent probability of failure while the "sure kill" implies a 100 percent probability of failure. A great deal of generalizing has taken place in this section (i.e., the discussion is by generic term, and each generic term, such as radio, has hundreds of variations). As a result very low confidence levels are necessarily placed on the "sure safe" and "sure kill" terms. Even with a particular system it is difficult to establish a particular probability of failure with a high degree of confidence because of the problems involved in evaluation of circuit and system responses.

These levels of "sure safe" and "sure kill" were established without regard as to whether the system was operating or not operating at the time of the explosion. The levels were established on the basis of system analyses that have been performed on systems in each of the categories. Where analysis information was lacking, estimates were made on the basis of the component parts typically used in that particular generic class and worst-case circuit conditions were assumed. No consideration was given to the aging of the equipment.

Utilization of the estimates presented in the latter portion of this section requires that the system be considered to be divided into subsystems according to function. The relative vulnerability of each subsystem can then be estimated on the basis of the subsystem levels presented in the text of this section. If by chance a subsystem does not fit the generic functions listed, the best estimate would have to be based on

[REDACTED]  
the susceptibility of the component parts used in that system. Component part susceptibility is reviewed in the following subsection and is discussed in more detail in Section VII of Chapter 9.

[REDACTED] THE SURVIVABILITY LEVELS PROVIDED IN LATER PARTS OF THIS SECTION ARE MEANT TO BE USED ONLY AS GUIDES. THEY *SHOULD NOT* BE USED TO FULFILL A REQUIREMENT OR TO ESTABLISH THE VULNERABILITY OR SURVIVABILITY OF A PARTICULAR SYSTEM. More detailed information may be obtained from the TREE (Transient-Radiation Effects on Electronics) Handbook (see bibliography) as well as other references listed in the bibliography.

## REVIEW OF ELECTRONIC SUSCEPTIBILITY TO NUCLEAR RADIATION [REDACTED]

### 14-17 Component Part Vulnerability [REDACTED]

[REDACTED] Any discussion of vulnerability or survivability is ultimately based on some definition of failure. In keeping with the scope of this manual, two cases of failure are considered. First, any condition which renders the electronic equipment inoperable following exposure to a nuclear burst constitutes a system failure. The second definition of failure involves those cases where it is critical that the equipment function during the radiation exposure in order to complete a critical mission. In the latter case, a system malfunction initiated during the exposure that causes loss of the mission objective is classified as a failure.

[REDACTED] Under the first definition of failure, consideration is given primarily to permanent damage in the electronics. The loss of one or more bits of information within a computer as a result of transient effects would not constitute a failure by this definition, if, after reinitialization, the computer functioned satisfactorily, and if

[REDACTED] the system operation was not critical during the time of the weapon burst.

[REDACTED] Permanent damage to electronics can result from (see Section VII, Chapter 9):

[REDACTED]

[REDACTED] Collectively speaking, burnout problems from voltage and current transients normally are not a problem with [REDACTED]

[REDACTED] infrequent exceptions may occur by gate breakdown in MOS transistors, or in poorly designed circuitry. Since gamma rays are not attenuated appreciably in their passage through the electronics package,

[REDACTED] The internal and external X-ray environments can differ considerably, depending on packaging, and other shielding, and the X-ray spectrum (hot or cold, see Chapter 4).

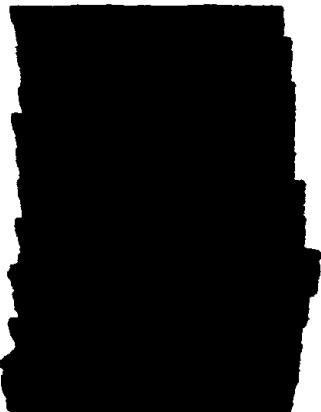
[REDACTED] This assumes roughly 98 percent attenuation of X-rays in transit through packaging, which implies a relatively cold source or effective shielding.

[REDACTED] Neutrons normally affect semiconductor component parts long before they affect other component parts such as capacitors, resistors, and transformers. Among the semiconductor types, unijunction transistors, silicon-controlled

rectifiers, low-frequency and power-type transistors are notably poor performers. The maximum tolerable neutron fluence (or range of fluences) for various semiconductor types are listed below.

These levels are the values at the component part. Because of the variation in X-ray spectra for various conditions, it is not possible to suggest general X-ray levels external to the systems that will result in these effects.

1150NCA  
(L)(1)



Thus, in analyzing systems for hardness, the subsystems containing sensitive semiconductors are likely to be the most vulnerable.

The third type of permanent damage, likely to occur during a nuclear burst is X-ray induced thermomechanical shock. Thermomechanical-shock effects are such that, for a specific device type, there is no unique radiation level that will cause a specific effect.

The second type of failures (failures during exposure) typically are caused by the ionization (gamma and X-ray) dose rate. In component parts, the typical effect is the introduction of potentially large photocurrents that result in a temporary malfunction of the component. This effect could result in a system malfunction if, for example, the extraneous current pulse fired a pyrotechnic device prematurely, or changed a bit of data in a logic circuit required for critical guidance functions. Devices particularly susceptible to large photocurrents are large-area, and/or high-gain devices. Typically the photocurrents generated below  $10^6$  rads (Si)/s are not sufficient to cause malfunction. Failures resulting from prompt dose effects are closely associated with the dose rate effects. Prompt dose is that dose accumulated during the initial gamma pulse ( $\sim 0.1$  microseconds, see Chapter 5) whereas the total dose is that accumulated over seconds or up to a minute (or longer, if the equipment is in a residual radiation field). Prompt doses as low as 0.1 rad (Si) can

To a first approximation,  $n/cm^2$  ( $E > 10$  keV, fission)  $\approx n/cm^2$  (1 MeV silicon damage equivalent).

Some quartz resonator crystals and MOS field-effect transistors are very sensitive to gamma radiation.

1150NCA  
(L)(1)

cause silicon control rectifiers to malfunction, and, normally, prompt doses over 100 rads (Si) will perturb most component parts sufficiently to cause all unhardened circuits to malfunction.

#### 14-18 Subsystem Vulnerability

Generally it is those subsystems that use the more vulnerable semiconductor component parts that will limit the hardness of a system to radiation. The relative sensitivity of semiconductor devices to radiation was outlined in paragraph 14-3. Some of the more common circuits that are likely to use these component parts, and the attendant approximate hardness levels will now be described.\*

Unijunction transistors commonly are employed in time-delay circuits, pulse generators, clocks, pulse-shaping circuits, and as a trigger device driving SCR's.

Power transistors generally are of two types: low-frequency types, such as those used in power supply dc-dc convertors or series regulators; and radio frequency (rf) power-amplifier types.

Linear integrated circuits (amplifiers, etc.) are more susceptible to permanent damage than digital types, but the former are not used widely in military equipment.

Possibly the most critical part of a system is its power source. Power supplied from a motor-generator, dynamotor or battery is least likely to fail in a radiation environment.

Failure levels are typical of those listed for power transistors.

Circuits that must retain information are susceptible to transient damage. That is, transient photocurrents can introduce erroneous information into the memory system or even change the information in the memory system.

Integrated circuits can be triggered into a malfunction called "latchup" by the prompt ionizing dose at levels from 10 to 100 rads (Si). Latchup can be important because this particular condition may burn out the circuit or just simply not allow recovery to proper operation for periods long compared to the normal circuit-recovery times.

Section VII, Chapter 9 provides more detailed information concerning circuit response to radiation.

#### TREE-DAMAGE ESTIMATES

Estimates of system damage from nuclear-burst radiation are based on two factors. First is the likelihood that a given system type contains a susceptible circuit or subsystem as described in paragraph 14-18. Second is the probable environment in which the equipment will be used. Differences in shielding afforded by aircraft, missile, ship, or jeep installations could be significant for some components of nuclear burst radiations.

The estimates that are given in succeeding paragraphs are not all inclusive in the types

\* Estimates are based on the assumption that the equipment was not designed with radiation hardness as a parameter, i.e., they are unhardened.

[REDACTED]  
of systems or installations covered. The cross section of systems should provide some basis for estimating the radiation damage threshold of other similar equipment.

[REDACTED] Radiation levels given in the following paragraphs are considered to be external ambient levels. The gamma environment assumes monoenergetic photons having an energy of approximately 1 to 1.5 MeV. A slightly degraded fission spectrum is assumed for neutrons. The X-ray sources postulated for these estimates are blackbody spectra [REDACTED]

DATA  
(L)(3)

#### 14-19 Ground Equipment

[REDACTED] Estimates of radiation levels sufficient to cause failures as previously discussed are shown in Table 14-9 for typical ground installations or ground support equipment under the heading "sure kill." A lower threshold for failure, below which the equipment in question may be considered operable is referred to as "sure safe." All radiation levels are external ambient values that have meaning only for *unhardened* systems. For hardened systems, the hardening specifications should be consulted. It should be borne in mind that the fact that a system has been hardened does *not* mean that it will survive all radiation environments. It should, however, survive at least those to which it was hardened. It is further assumed that for most reasonable surface encounters,

USANCA  
(L)(1)

[REDACTED] No ambient exposures are given for X-rays ( $\text{cal}/\text{cm}^2$ ), since these depend strongly on the X-ray spectrum, which in turn, is extremely dependent on the weapon type and the degradation of the spectrum through the intervening space.

USADCS  
(L)(1)

Except

under unusual circumstances, X-rays probably do not pose a significant threat for ground equipment.

#### 14-20 An Example of Ground Equipment Survivability Estimation

[REDACTED] The Lance support system provides an illustration of the use of Table 14-9. The missile itself is found under the heading "Ground and Sea Support Equipment"; however, the levels listed for the Lance are associated only with the missile and not with the launch support equipment or the communications equipment necessary to direct the launch. The associated critical electronic equipment for launch can be listed as follows:

1. Radio receiver and transmitter, or transceiver
2. Batteries to fire the missile and to operate the launch vehicle
3. Fire control system for the missile.

[REDACTED] The survivability levels for most of these subsystems can also be found in Table 14-9 and are listed on page 14-67. The firing system, not being listed in the table, must be estimated. A basic description of this system implies that it is a box of electrical toggle switches and lights; which apply power and indicate operation. These component parts are not particularly susceptible to radiation. Therefore, they should be at least as hard as the systems with semiconductor devices. Therefore, they will be considered as part of the communication electronics without affecting the analysis.

[REDACTED] With this summarized information any of three possible situations can be visualized for analysis:

[REDACTED] USANCA (L)(1)  
The critical factors affecting mission completion in the first case are:

Page 14-66 with Table 14-65  
14-9 Deleted. USANCA (L)(1)

USA/NCA  
(b)(1)

USA/NCA  
(b)(1)

USA/NCA  
(b)(1)

For this case the gamma rate would not be critical, since the missile is not in operation and the other equipment does not have to function during the burst.

Either the neutrons or gamma rays specified for the sure-kill level could cause significant problems, and both should be considered:

The second case.

The sure-safe and sure-kill levels for this situation appear to be the same as the previous case. However, the gamma dose rate could cause problems and should be considered in the sure-safe level.

For the third case the missile is dependent solely on itself for control and the levels of survivability are the same as those shown for the missile alone.

#### 14-21 Aircraft Systems

Estimates of sure safe and sure kill radiation levels in aircraft systems are shown in Table 14-10. These levels are considered to represent external ambient conditions. As was the case for ground equipment, the total dose is not considered to be a problem, and thermomechanical shock from X-rays is not considered important. However, the ionization rate includes both the X-ray and gamma-ray rates.

The functional breakdown for aircraft systems is more complex than that for ground systems, since many mission functions require several generic functions within the subsystems. As an example, penetration aids, such as terrain clearance radars, include power sources, radars, computers, flight control links and crew station data display consoles. A brief listing of subsystems that are considered to be part of a mission function are shown in the table. Depending on the type and mission of the aircraft of interest, some of these functions may not be critical or may not even be present in the system. For specific equipment it may be necessary to refer to the levels presented in the previous Table 14-9.

#### 14-22 An Example of Aircraft Survivability Estimation

To clarify the process of analysis, two cases are considered. The first case is a single-engine spotter plane and the second is a jet fighter similar to the F-111A.

Considering first, the spotter aircraft, the generic functions are:

14-67

Pages 14-68 and 14-29  
with Table 14-10 deleted.

USA/NCA (b)(1)

1. Flight control.  
2. Crew station  
3. Propulsion system  
4. Mission and traffic control.

Of these, one function that might be critical to the mission is the Mission and Traffic Control. The crew may not be able to communicate their observations at a critical time, even though they may be able to escape if other generic functions failed.

If all functions except the crew station were considered, the survivability levels would still be the same.

Considering the modern fighter aircraft, it would appear that all generic functions listed in Table 14-10 might be associated with the aircraft. Depending on the mission of the plane, various combinations of these generic functions might be critical. For example, if the fighter was used for battlefield support, penetration aids would not be critical. The worst-case survivability levels would occur if both penetration aids and either the air-to-air or air-to-surface missiles were critical for mission completion.

#### 14-23 Missile Systems

The missile systems included in Table 14-11 are categorized according to mission and guidance type. Thus, the damage criteria, in general, are not representative of a specific system, but reflect the mean susceptibility of systems within each category. Furthermore, unless otherwise specified, all systems are assumed to be

unhardened. The categories are not all-encompassing. Where no information was available, estimates were made as noted. Sure-safe and sure-kill levels are given in terms of radiation levels external to the system. Although not a great problem for ground or aircraft systems, X-rays represent a much more formidable threat to missile systems operating at altitudes above 20 kilometers, hence, this information is included. The sources of X-rays postulated for these estimates are blackbody spectra.

No problems are anticipated with the total gamma dose effects unless the dose exceeds  $10^5$  rads (Si). The prompt dose effects are taken into consideration in the dose rate terms. The dose rate estimates include both the X-ray and gamma ray rates. The dose-rate estimates are based on the damage caused by ionization effects, whereas the column head the "X-ray Exposure" includes estimates based on the damage caused by the thermomechanical effects. No example is provided since it is only necessary to select the correct classification for the missile to establish its survivability levels. There are basically three phases critical to the flight of missiles:

1. Storage
2. Powered flight
3. Reentry.

A prime factor that would influence the survivability of a missile in storage is not necessarily the electronics vulnerability associated with the missile but, rather, the shielding effectiveness provided by the storage area (e.g., missile silo). The activation and ground-control electronics would be evaluated by using Table 14-9. The powered flight would be concerned with both the missile and the reentry vehicle. And, last, the reentry would be concerned only with the reentry vehicles.

[REDACTED]

[REDACTED]

[REDACTED]

BIBLIOGRAPHY

[REDACTED]

*Analysis of Atomic Weapons Effects Upon Army Ground Operations Equipment* [REDACTED] Project Attack, Third Phase Report, ORO-S-200, Armour Research Foundation, Chicago, Illinois, 18 June 1951 [REDACTED]

*Analysis of Atomic Weapons Effects Upon Army Ground Operations Equipment* [REDACTED] Project Attack, Fourth Phase Report, Vol. I, ORO-S-208, Armour Research Foundation, Chicago, Illinois, 9 October 1951 [REDACTED]

*Analysis of Atomic Weapons Effects Upon Army Ground Operations Equipment* [REDACTED] Technical Memo ORO-T-223, Vol. I, Blast Effects, Armour Research Foundation, Chicago, Illinois, 16 March 1953 [REDACTED]

Berning, W. W., *Predicted Effects of Atomic Weapons Upon Ordnance Equipment* [REDACTED] BRL 847, U.S. Army Ballistic Research Laboratories, Aberdeen Proving Ground, Maryland, January 1953 [REDACTED]

Berning, W. W. and N. W. Arnold, *Combat Vehicle Exposure* [REDACTED] Operation Greenhouse, Annex 6.3, WT 90, U.S. Army Ballistic Research Laboratories, Aberdeen Proving Ground, Maryland, August 1952 [REDACTED]

Bowen, I. G., et al., *A Model Designed to Predict the Motion of Objects Translated by Classical Blast Waves* [REDACTED] Civil Effects Study CEX-58-9, Lovelace Foundation for Medical Research, Albuquerque, New Mexico, 29 June 1961 [REDACTED]

Brode, H. L., *Point Source Explosion in Air*, RM-1824-AEC, The RAND Corporation, Santa Monica, California, 3 December 1956 [REDACTED]

Bryant, E. J. and F. E. Grubbs, *Statistical Estimation of Damage to Ordnance Equipment Exposed to Nuclear Blast* [REDACTED] BRL 657-RD, U.S. Army Ballistic Research Laboratories, Aberdeen Proving Ground, Maryland, April 1953 [REDACTED]

Bryant, E. J., N. H. Ethridge, and J. L. McCoy, *Statistical Estimation of Damage to Ordnance Equipment Exposed to Nuclear Blasts* [REDACTED] Operation UPSHOT-KNOTHOLE, Project 3.21, WT-733, U.S. Army Ballistic Research Laboratories, Aberdeen Proving Ground, Maryland, February 1955 [REDACTED]

Bryant, E. J., and J. D. Day, *Effects of Rough Terrain on Drag-Sensitive Targets* [REDACTED] Operation PLUMBOB, Project 1.8b Final Report, WT-1408, U.S. Army Ballistic Research Laboratories, Aberdeen Proving Ground, Maryland, 9 November 1959 [REDACTED]

Bryant, E. J., N. H. Ethridge, and M. R. Johnson, *Response of Drag-Type Equipment Targets in the Precursor Zone* [REDACTED] Operation TEAPOT, Project 3.1 Final Report, WT-1123, U.S. Army Ballistic Research Laboratories, Aberdeen Proving Ground, Maryland, 28 October 1959 [REDACTED]

Burden, H. S. and J. D. Day, *Transient Drag Loading of Actual and Idealized Shapes from High-Yield Detonations* [REDACTED] Operation REDWING, Project 1.5, WT-1305, U.S. Army Ballistic Research Laboratories, Aberdeen Proving Ground, Maryland, 15 March 1960

Calvin, R. L. et al., *The Effects of Atomic Blast on Military Field Equipment* [REDACTED] Armour Research Foundation Report M041, Armour Research Foundation, Chicago, Illinois, 28 February 1955

Deeds, F. E., et al., *Mine Field Clearance by Nuclear Weapons* [REDACTED] Operation PLUMBOB, Project 6.1 Final Report, WT-1435, Midwest Research Institute, Kansas City, Missouri, and U.S. Army Engineer Research and Development Laboratories, Fort Belvoir, Virginia, 16 August 1960

*Effects of the Atomic Bomb on Nagasaki, Japan*, U.S. Strategic Bombing Survey, Physical Damage Division, Vol. I, II, III, June 1947

*Effects of the Atomic Bomb on Hiroshima, Japan*, U.S. Strategic Bombing Survey, Physical Damage Division, Vol. I, II, III, May 1947

Ethridge, N. H., *Blast Effects on Simple Objects and Military Vehicles* [REDACTED] Operation SUN BEAM, Project 1.3, POR-2261, U.S. Army Ballistic Research Laboratories, Aberdeen Proving Ground, Maryland, 18 September 1964

Gwyn, C. W., D. L. Scharfetter, and J. L. Wirth, *The Analysis of Radiation Effects in Semiconductor Junction Devices*, SC-R-67-1158, Sandia Corporation, Albuquerque, New Mexico, July 1967

Hearn, J. N. W., Lt. Col., *Operation BUFFALO: Interim Report of the Target Response Ordnance Group* [REDACTED] FWE-142, AWRE Report T25/57, Atomic Weapons Research Establishment, Aldermaston, Berks, England, June 1957

Henderson, J. E., *Vulnerability of Radar to Nuclear Explosions* [REDACTED] AWE/P(57)44, FWE-136, Air Ministry, Ministry of Defence, U.K., August 1957

Heyman, R. J. and H. G. Myer, *Transient Drag and Its Effects on Structures* [REDACTED] AFSWC-TR-56-46, American Machine and Foundry, Chicago, Illinois, November 1956

Kalionowski, J. J., *A Management Guide to Transient-Radiation Effects on Electronics (TREE)* [REDACTED] DNA 2051H, Battelle Columbus Laboratories, Columbus, Ohio, February 1972

Kaplan, K., and C. Wiegle, *Air Blast Loading in the High Shock Strength Region* [REDACTED] Part I – Analysis and Correlation, Part II – Prediction Methods and Examples, URS 633-3, DASA 1460, URS Corporation, Burlingame, California, February 1965,

Larin, F., *Radiation Effects in Semiconductor Devices*, John Wiley and Sons, Inc., New York, 1968 [REDACTED]

Martin, A. R. F., *The Effects of Blast on Dummies and Scout Cars* [REDACTED] Operation ANTLER, Target Response Group, AWRE Report T6/59, FWE 238, Atomic Weapons Research Establishment, Aldermaston, Berks, England, August 1959 [REDACTED]

McCoy, J. L., *Damage Reports on Exposed Ordnance Equipment* [REDACTED] Operation UPSHOT-KNOTHOLE, Supplement to Project 3.21, WT-821, U.S. Army Ballistic Research Laboratories, Aberdeen Proving Ground, Maryland, December 1954 [REDACTED]

Morris, P. J., *Study of Military Field Equipment Response to Air Blast and Prediction of Damage* [REDACTED] DASA 2005-1 and 2005-2, URS 660-9, URS Research Company, San Mateo, California, 2005-1, October 1971 [REDACTED]  
2005-2, January 1972 [REDACTED]

Morris, W. E., et al., *Air Blast Measurements* [REDACTED] Operation UPSHOT-KNOTHOLE, Projects 1.1a and 1.2, WT-710, U.S. Naval Ordnance Laboratory, White Oak, Silver Spring, Maryland, August 1955 [REDACTED]

Nelson, R. C., Capt., *The Effects of Atomic Weapons on Engineer Heavy Equipment* [REDACTED] ERDL Report 1443, U.S. Army Engineer Research and Development Laboratories, Fort Belvoir, Virginia, 25 April 1956 [REDACTED]

*Nuclear Weapons Blast Phenomena: Volume I, Source and Development of Blast Waves in Air* [REDACTED] DASA 1200-I, Defense Atomic Support Agency, Washington, D.C., 1 March 1971 [REDACTED]

*Nuclear Weapons Blast Phenomena: Volume II, Blast Wave Interaction* [REDACTED], DASA 1200-II, Defense Atomic Support Agency, Washington, D.C., 1 December 1970 [REDACTED]

*Nuclear Weapons Blast Phenomena: Volume III, Air and Subsurface Explosions* [REDACTED] DASA 1200-III, Defense Atomic Support Agency, Washington, D.C., 1 March 1970 [REDACTED]

Olesen, H. L., *Radiation Effects on Electronic Systems* [REDACTED] General Electric Systems, General Electric Company, Missile and Space Division, Philadelphia, Pennsylvania, Plenum Press, New York, 1966 [REDACTED]

*Operation CROSSROADS Atomic Bomb Tests* [REDACTED] Army Ground Group (Task Group 1.4), Report Number XRD-149, Volume I, 27 January 1946 to 27 September 1946 [REDACTED]

*Operation CROSSROADS Atomic Bomb Tests* [REDACTED] Report of Commander, Task Unit 1.4.3 (Ordnance), Report Number XRD-152, Volume IV, Appendix VII, January 27 to September 30, 1946 [REDACTED]

Seager, E. R. Drake, R. F. C. Butler, *Operation TOTEM Group 12 Report: Effects on a Landrover (car, 5 CWT, 4x4) and Generating Sets* [REDACTED] AWRE Report T 79/54(x), FWE-131, Atomic Weapons Research Establishment, Aldermaston, Berks, England, September 1956 [REDACTED]

TREE (*Transient-Radiation Effects on Electronics*) Handbook [REDACTED] Volume 1, Edition Number 3, DNA 1420 H-1, Battelle Columbus Laboratories, Columbus, Ohio, December 1971 [REDACTED]

TREE (*Transient-Radiation Effects on Electronics*) Handbook [REDACTED]  
Edition 2, Revision 2, DASA 1420-1, Battelle Memorial Institute, Columbus, Ohio, September 1970 [REDACTED], (to be replaced by DNA 1420 H-2 during calendar year 1972).

TREE Preferred Procedures (*Selected Electronic Parts*), DASA 2028, Battelle Memorial Institute, Columbus, Ohio, May 1968 [REDACTED] (to be replaced by DNA 2028H during calendar year 1972).

Vook, F. L., Editor, *Radiation Effects in Semiconductors* [REDACTED] Proceedings of the Santa Fe Conference on Radiation Effects in Semiconductors, Plenum Press, New York, 1968 [REDACTED]

Willoughby, A. B., K. Kaplan, and R. I. Condit, *Effects of Topography on Shock Waves in Air* [REDACTED] AFSWC TR-57-9, Broadview Research and Development, Burlingame, California, March 1956 [REDACTED]

[REDACTED]

DTIC  
SELECTED  
2 MAR 1989  
**S E D**

## Chapter 15

### DAMAGE TO FOREST STANDS

•

#### INTRODUCTION

Forest stands may protect personnel from some effects of nuclear weapon explosions, for example, the direct effects of thermal radiation; however, the trees themselves are quite vulnerable to breaking, uprooting, and ignition. Falling limbs and trees may be a hazard, and the debris on the forest floor may impede troop and vehicle movement. In dry, windy weather a nuclear explosion may ignite forest fires, and the smoke and flame may extend the range of hazardous effects many times. The vulnerability of forests depends upon recent local weather history, and upon the type of tree stand involved.

This chapter is divided into three sections. Section I provides data concerning air blast damage to various types of forest stands. Section II contains a discussion of the effects of tree blowdown on troop and vehicle movement and provides methods to predict the degree to which movement might be impaired as a result of tree blowdown. Section III provides information concerning the effects of thermal radiation on forests and the fire hazards that might arise therefrom.

#### SECTION I

##### AIR BLAST

###### 15-1 Forest Stand Types

Forest stands may be divided into four general types for the purpose of discussing air blast effects. Types I through IV as well as the subtypes of Type IV are described in the following discussion.

**TYPE I: IMPROVED NATURAL OR PLANTED CONIFER FORESTS OF EUROPEAN TYPE.** Stands of this type generally

occur in Western Europe. They either have been planted or are natural stands that have been cultivated. Characteristics of this type of forest include uniform tree spacing, uniform height and diameter, and a dense crown canopy. Low stumps usually will be found within the stand as a result of thinning. Lower limbs will be clear as a result of pruning, and there will be little or no underbrush. All of these characteristics combine to provide good visibility and easy passage through the forest. Damage to these stands generally is caused by breaking the trunks rather than by uprooting.

**TYPE II. UNIMPROVED NATURAL CONIFER FORESTS THAT HAVE DEVELOPED UNDER UNFAVORABLE GROWING CONDITIONS.** This type of forest is found in Western Europe and Southeast Asia. Random tree spacing, height, and diameter together with irregular crown canopy characterize this type of stand. The forest floor is partially covered with dead fallen trees, and where clearings occur there is usually heavy underbrush. Visibility is generally poor and passage through the forest is difficult. Damage usually results from uprooting rather than breaking.

**TYPE III. UNIMPROVED NATURAL CONIFER FORESTS THAT HAVE DEVELOPED UNDER FAVORABLE GROWING CONDITIONS.** This type of forest occurs in Western Europe and Southeast Asia. These forests are characterized by random tree spacing and diameter, uneven crown canopy, and irregular clearings. Visibility and passage through these stands are difficult in Western Europe, although the underbrush generally is light, since dead fallen trees clutter the forest floor.

In Southeast Asia, dense shrub undergrowths usually cover the forest floor. Damage to this type of forest usually results from uprooting.

**TYPE IV. ALL TYPES OF DECIDUOUS FORESTS.** The trees in these stands are similar to the deciduous trees of Western Europe and Southeast Asia. Since damage to these trees depends on the condition of the foliage, two categories must be considered: IV (f) is category type IV with foliation, and IV (d) is type IV without foliation. In both cases extensive crown damage and breakage of limbs will occur. In most ground, trunk damage will be caused mainly by uprooting. This class of forests is broken down into four subtypes:

**TYPE IVa.** This subtype includes two further subtypes that have different characteristics but produce similar blowdown obstacles equidistant from a particular nuclear burst. Two categories are required as a result of the difference in time required to clear away blowdown obstacles.

**TYPE IVa-1.** This subtype occurs in Western Europe and Southeast Asia. It includes most temperate zone deciduous forests, such as the shorter, more open parts of the dry season deciduous forests of Northern Southeast Asia and the evergreen oak forests at elevations of 3,000 to 7,000 feet in Southeast Asia. The trees

Table 15-1 Average Height of Trees, Diameter, Tree Density, and Length of Tree Stem

Forest Stand Type	Tree Diameter	Average Height of Trees* (feet)	Average Tree Density per Acre*	Average Total Tree Stem-feet per Acre*
I	up to 24 in.	130	75	9,750
II	up to 20 in.	50	260	13,000
III	up to 40 in.	80	200	16,000
IVa†	up to 40 in.	80	200	16,000
IVa‡	24-in. average	100	140	14,000
IVb‡	40-in. average	100	850	85,000
IVc§	up to 18 in.	35	40	1,400
IVd	up to 18 in.	40	100	4,000

\* Stem-feet per acre is determined by multiplying average tree height by tree density.

† Considers only trees 6 in. or larger in diameter.

‡ Height varies up to 200 ft in rain forest and up to 150 ft in dry season deciduous forest for about 10 percent of trees. Diameter varies up to 80 in. for 10 percent of rain forest trees and up to 60 in. for 10 percent of dry season deciduous forests.

§ Height varies from 10-50 ft.

of this subtype are defoliated in the winter in the temperate zone with the exceptions of the evergreen oak (not defoliated) and the dry season forests of Northern Southeast Asia, which are defoliated in the summer.

**TYPE IVa-2.** Teak plantations and the denser, taller cloud forests that occur at lower elevations are included in this type. The teak plantation trees are planted 15 to 20 feet apart and produce a continuous canopy when foliated. No foliation is present during the dry season. The cloud forests start at an elevation of about 3,500 feet on the mountain slopes of Southeast Asia. The canopy of these forests gives a matted appearance from the air.

**TYPE IVb.** This subtype includes rain forests of Southeast Asia and the majority of the dry season deciduous forests of Northern Southeast Asia. Although no data are available concerning attenuation of the air blast wave, it is probable that these forests are sufficiently dense to decrease the radius of blast effect, thereby reducing the damage distance of a nuclear explosion.

**TYPE IVc.** This type includes cloud forests at high elevations, savannas, and low open forests that are made up of small scattered trees. This type of forest, when defoliated, is a good approximation for open deciduous wooded areas, such as orchards, in temperate zones.

**TYPE IVd.** This type consists of rubber plantation trees that occur mainly in Southeast Asia. The characteristics include little underbrush and dense, overlapping crowns.

Table 15-1 shows the characteristic dimensions, tree densities, and tree stem-feet per acre for the forest stand types described above.

Table 15-2 Index of Isodamage Curves  
Showing Forest Stand Type and Applicable Figure  
Number for Indicated Degree of Damage

Forest Stand Type	Light Damage	Moderate Damage	Severe Damage	Total Damage
I	NA	15- 2	15- 3	15- 4
II	NA	15- 5	15- 6	15- 7
III	NA	15- 8	15- 9	15-10
IVa-1(f)	*	15-11	15-12	15-13
IVa-1(d)	15-1	15-14	15-15	15-16
IVa-2(f)	*	15-17	15-18	15-19
IVa-2(d)	15-1	15-20	15-21	15-22
IVb(f)	*	15-23	15-24	15-25
IVb(d)	*	15-26	15-27	15-28
IVc(f)	*	15-29	†	15-30
IVc(d)	15-1	15-31	†	15-32
IVd	*	15-33	†	15-34

\* The ground range for Light Damage, 50% branch breakage, is less than the ground range for Moderate Damage, 750 stem-feet down per acre.

† Forest is of insufficient density and/or height to produce 7,500 stem-feet down per acre.

## 15-2 Damage-Distance Relations

Isodamage curves that are functions of weapon yield, distance, and height-of-burst are shown in Figures 15-1 through 15-34 for the forest stand types described in paragraph 15-1. Table 15-2 provides an index of the figures as a function of forest stand type and degree of damage. The degrees of damage shown in Table 15-2 are defined as follows:

**TOTAL DAMAGE:** 90 percent or more of trees are uprooted.

**SEVERE DAMAGE:** 9,000 feet of tree stem down per acre for coniferous forests and 7,000 feet of tree stem down per acre for deciduous forests.

**MODERATE DAMAGE:** 1,500 feet of tree

stem down per acre for coniferous forests and 750 feet of tree stem down per acre for deciduous forests.

**LIGHT DAMAGE:** 50 percent breakage of crowns and branches for deciduous forests. Does not exist for coniferous forests.

<b>Accession For</b>	
NTIS GRA&I	
DTIC TAB	
Unannounced	
Justification <i>bases doc</i>	
By _____	
Distribution/	
<b>Availability Codes</b>	
Dist	Avail and/or Special
A-1	



**UNANNOUNCED**

### Problem 15-1 Calculation of Air Blast Damage to Forest Stands

Figures 15-1 through 15-34 show total, severe, moderate, and light isodamage curves for different types of forest stands. Definitions of the degrees of damage are provided in paragraph 15-2. Decreases in the damage distances for shallow subsurface bursts may be estimated from Figure 11-24 by the methods described in Problem 11-2.

**Scaling.** For yields between those for which isodamage curves are provided, scale as follows:

$$\frac{d}{d_i} = \frac{h}{h_i} = \left(\frac{W}{W_i}\right)^{1/3}$$

where  $d_i$  and  $h_i$  are the distance from ground zero and the height of burst, respectively, for yield  $W_i$ , which is the nearest yield to the desired yield for which a curve is provided; and  $d$  and  $h$  are the corresponding distance and height of burst for a (desired) yield of  $W$  kt or Mt ( $W$  and  $W_i$  must be in the same units).

For yields greater than 10 Mt this scaling becomes

$$\frac{d}{d_{10}} = \frac{h}{h_{10}} = \frac{(W/Mt)^{1/3}}{(10)^{1/3}} = \frac{(W/Mt)^{1/3}}{2.15}$$

where  $d_{10}$  and  $h_{10}$  are the distance from ground zero and height of burst, respectively, for 10 Mt; and  $d$  and  $h$  are the corresponding distance and height of burst for a yield of  $W$  Mt.

**Example**

*Given:*

- a. A 5 kt weapon burst at a height of 400 feet above a Type IVa-1(f) forest stand.
- b. A 20 Mt weapon burst at a height of 1,000 feet above a Type I forest stand.

**Find:**

- a. The distance to which severe damage

extends for the Type IVa-1(f) forest stand.

- b. The distance to which moderate damage extends for the Type I forest stand.

**Solution:**

a. Table 15-2 shows that Figure 15-12 contains the isodamage curves appropriate for a Type IVa-1(f) forest stand. Examination of Figure 15-12 shows that the yield nearest 5 kt for which an isodamage curve is provided is 3 kt. The corresponding height of burst for a 3 kt weapon is

$$h_3 = h \left( \frac{3}{W} \right)^{1/3} = 400 \times \left( \frac{3}{5} \right)^{1/3} = 340 \text{ ft.}$$

From Figure 15-12, at a height of burst of 340 feet, the distance from ground zero to which severe damage will occur to a Type IVa-1(f) forest stand is 3,000 feet.

b. Table 15-2 shows that Figure 15-2 contains isodamage curves appropriate for moderate damage to a Type I forest stand. The corresponding height of burst for a 10 Mt weapon is

$$h_{10} = \frac{2.15 h}{(W)^{1/3}} = \frac{2.15 \times 1,000}{(20)^{1/3}} = 790 \text{ ft.}$$

From Figure 15-2, at a height of burst of 790 feet, the distance from ground zero to which moderate damage to a Type I forest stand occurs from a 10 Mt weapon is 42,000 feet.

**Answer:**

- a. The corresponding distance for severe damage to a Type IVa-1(f) forest stand from a 5 kt weapon burst at a height of 400 feet is

$$d = d_3 \left( \frac{W}{3} \right)^{1/3} = 3,000 \times \left( \frac{5}{3} \right)^{1/3} = 3,560 \text{ ft.}$$

- b. The corresponding distance for moderate damage to a Type I forest stand from a 20 Mt

weapon at a height of 1,000 feet is

$$d = \frac{d_{10}/W(Mt)^{1/3}}{2.15} = \frac{42,000 \times (20)^{1/3}}{2.15}$$
$$= 53,000 \text{ ft.}$$

*Reliability:* The curves of Figures 15-1

through 15-34 are based on observed results of limited full scale tests, limited high explosive field tests, and extensive laboratory experiments. No definite estimate of the reliability of the scaling for yields above about 30 Mt can be made.

*Related Material:* See paragraphs 15-1 and 15-2. See also Figure 11-24 and Problem 11-2.

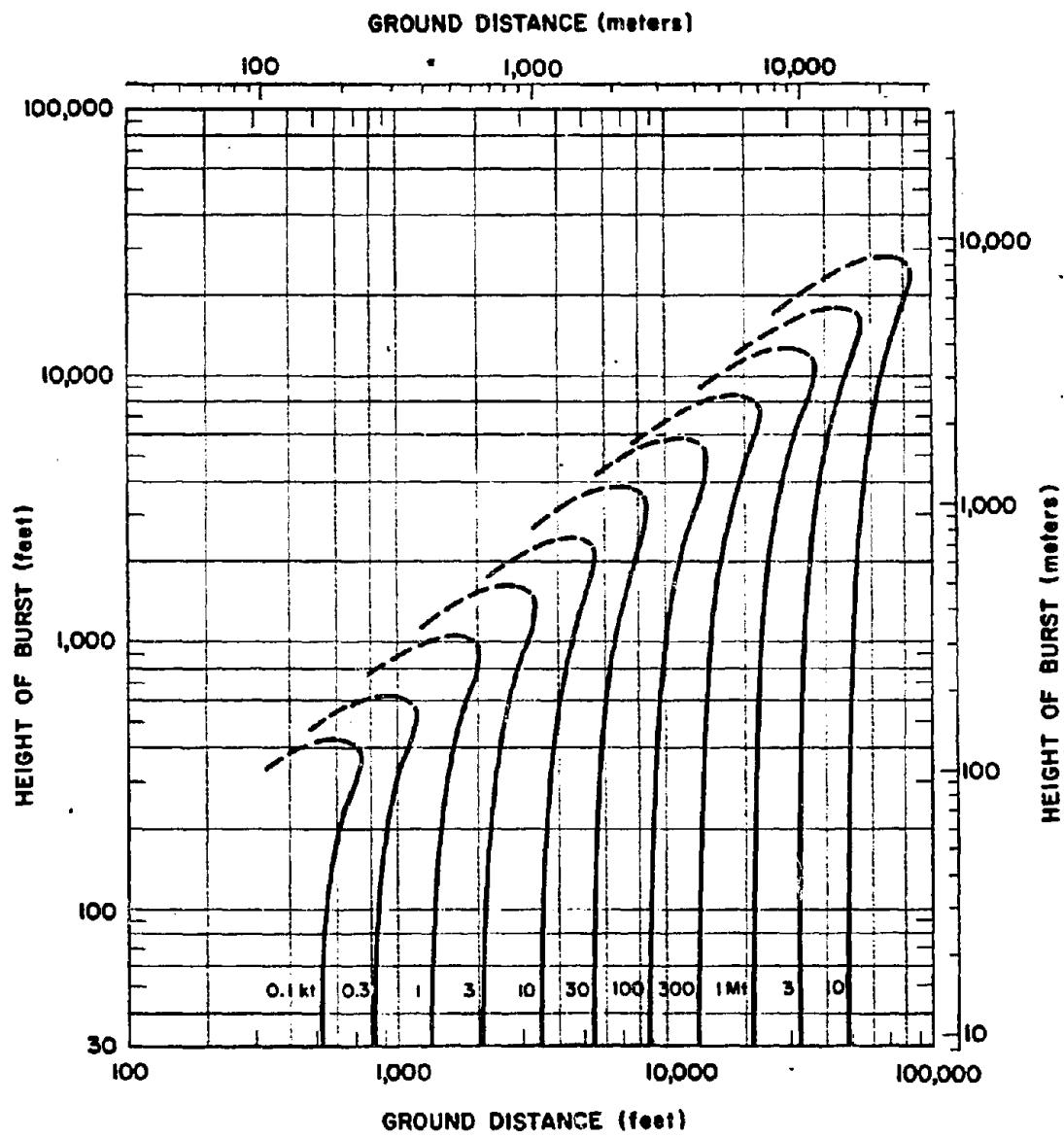


Figure 15-1. Light Damage to Various Broadleaf Forest Types (see Table 15-2)

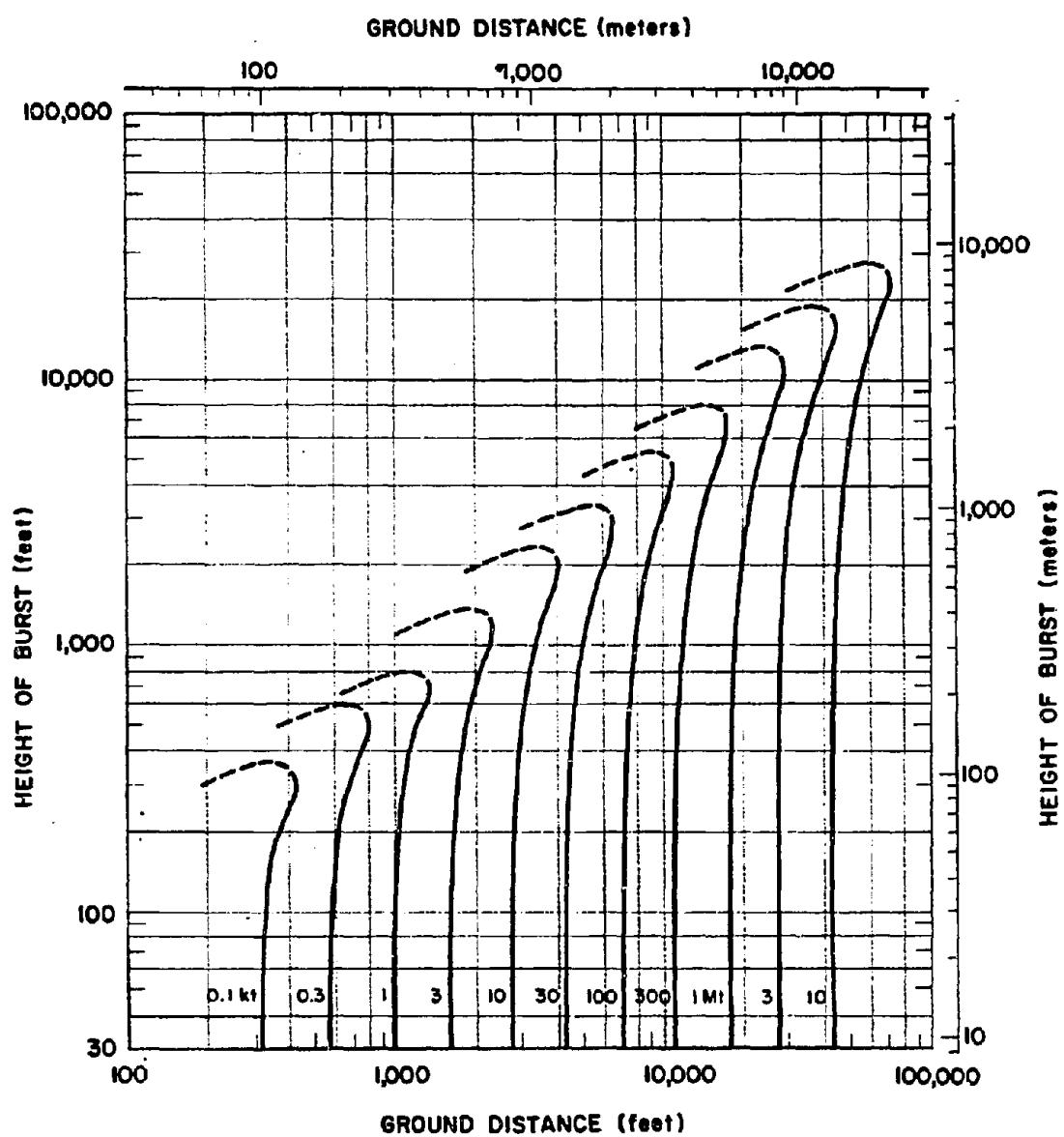


Figure 15-2. [REDACTED] Moderate Damage to a Type I Forest [REDACTED]

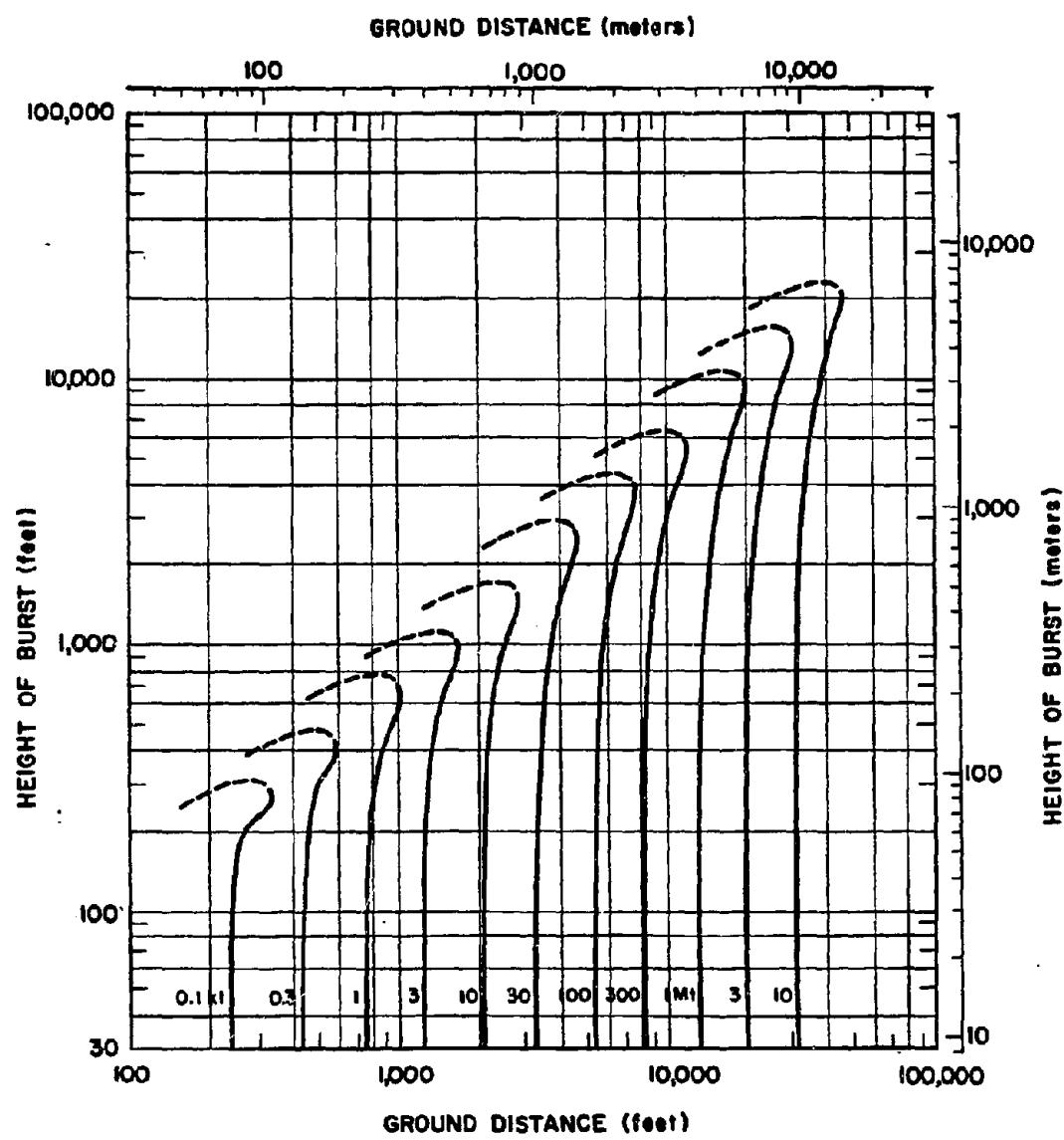


Figure 15-3. [REDACTED] Severe Damage to a Type I Forest [REDACTED]

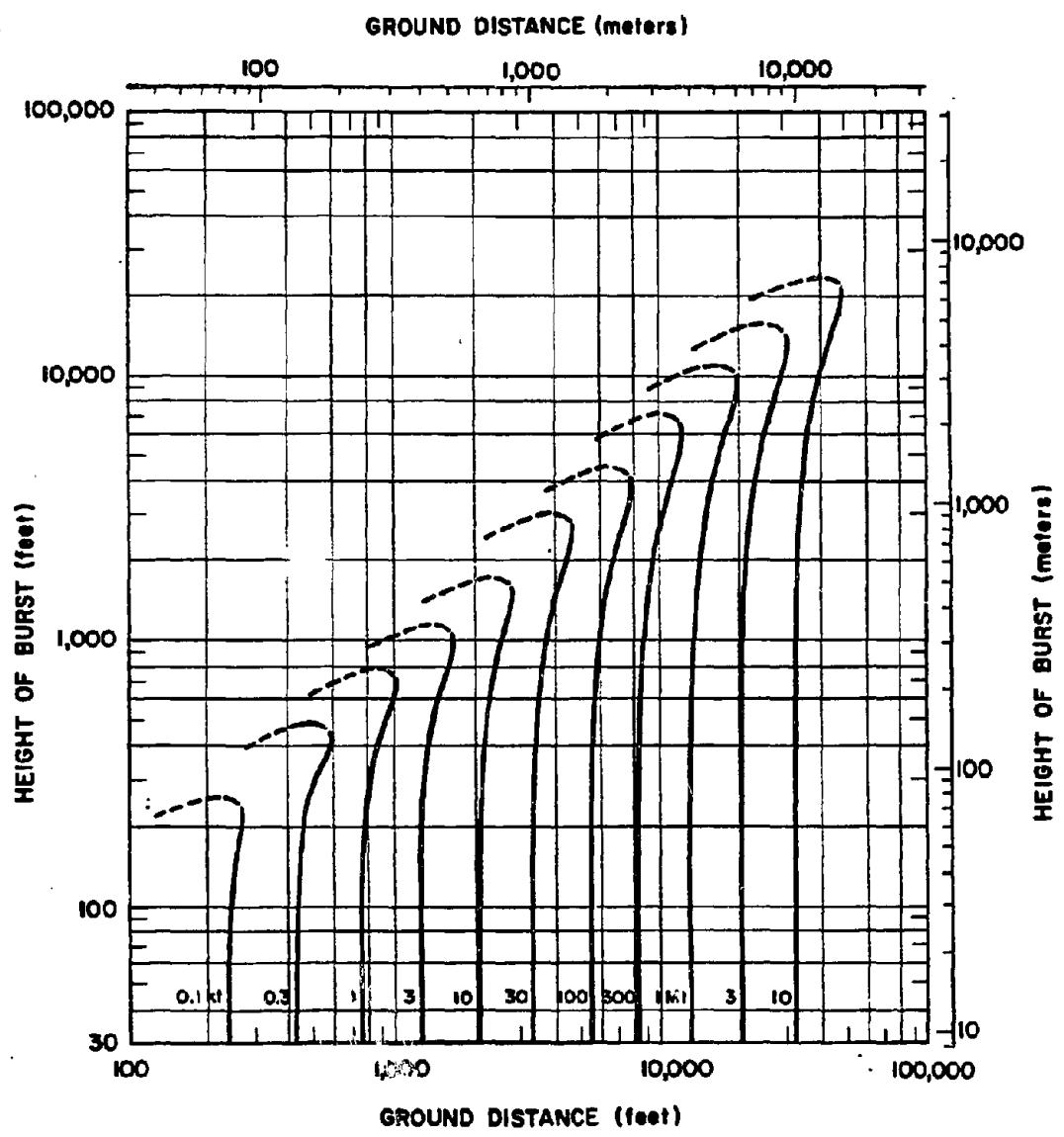


Figure 15-4. Total Damage to a Type I Forest

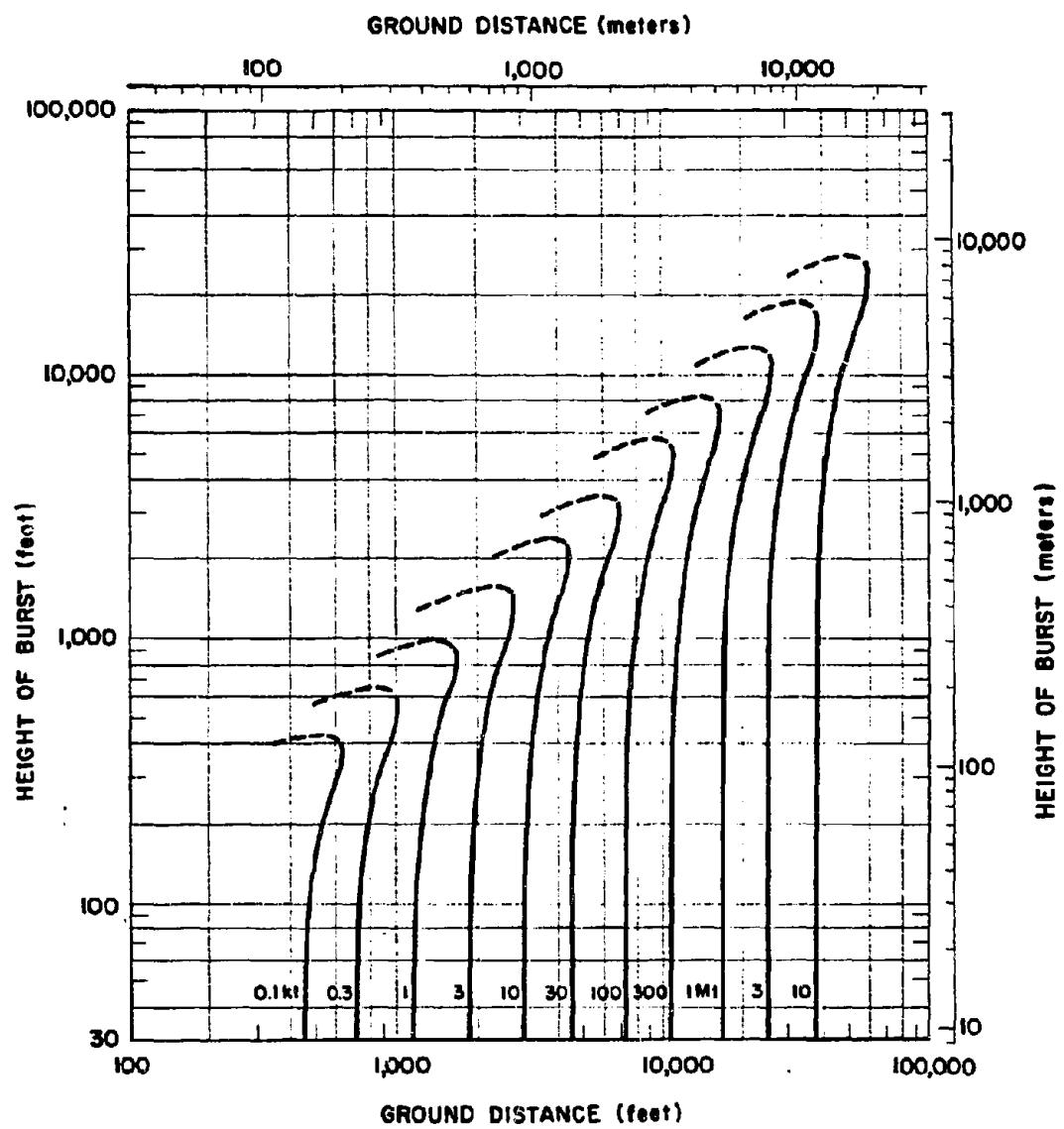


Figure 15-5. [REDACTED] Moderate Damage to a Type II Forest [REDACTED]

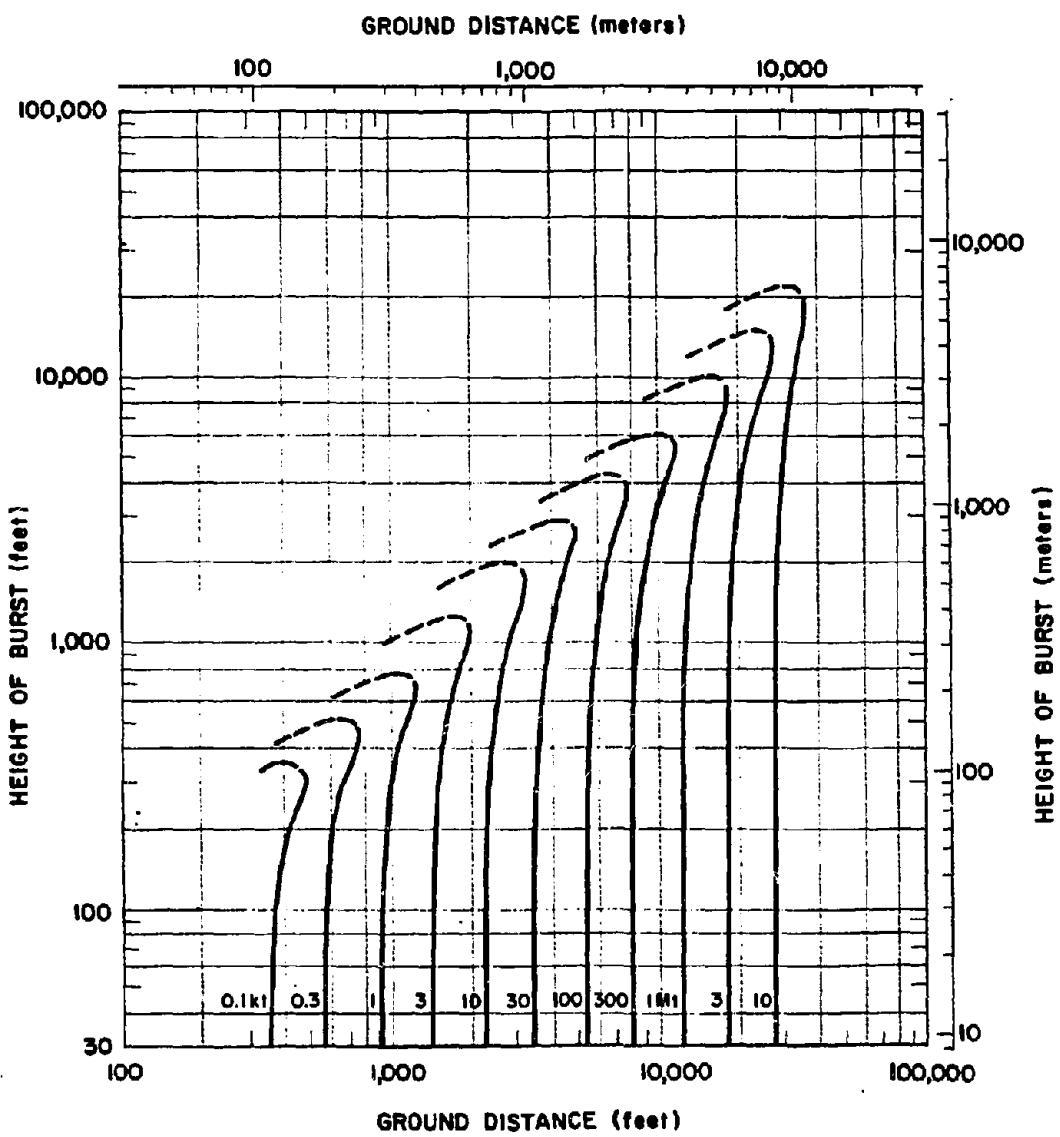


Figure 15-6. [REDACTED] Severe Damage to a Type II Forest [REDACTED]

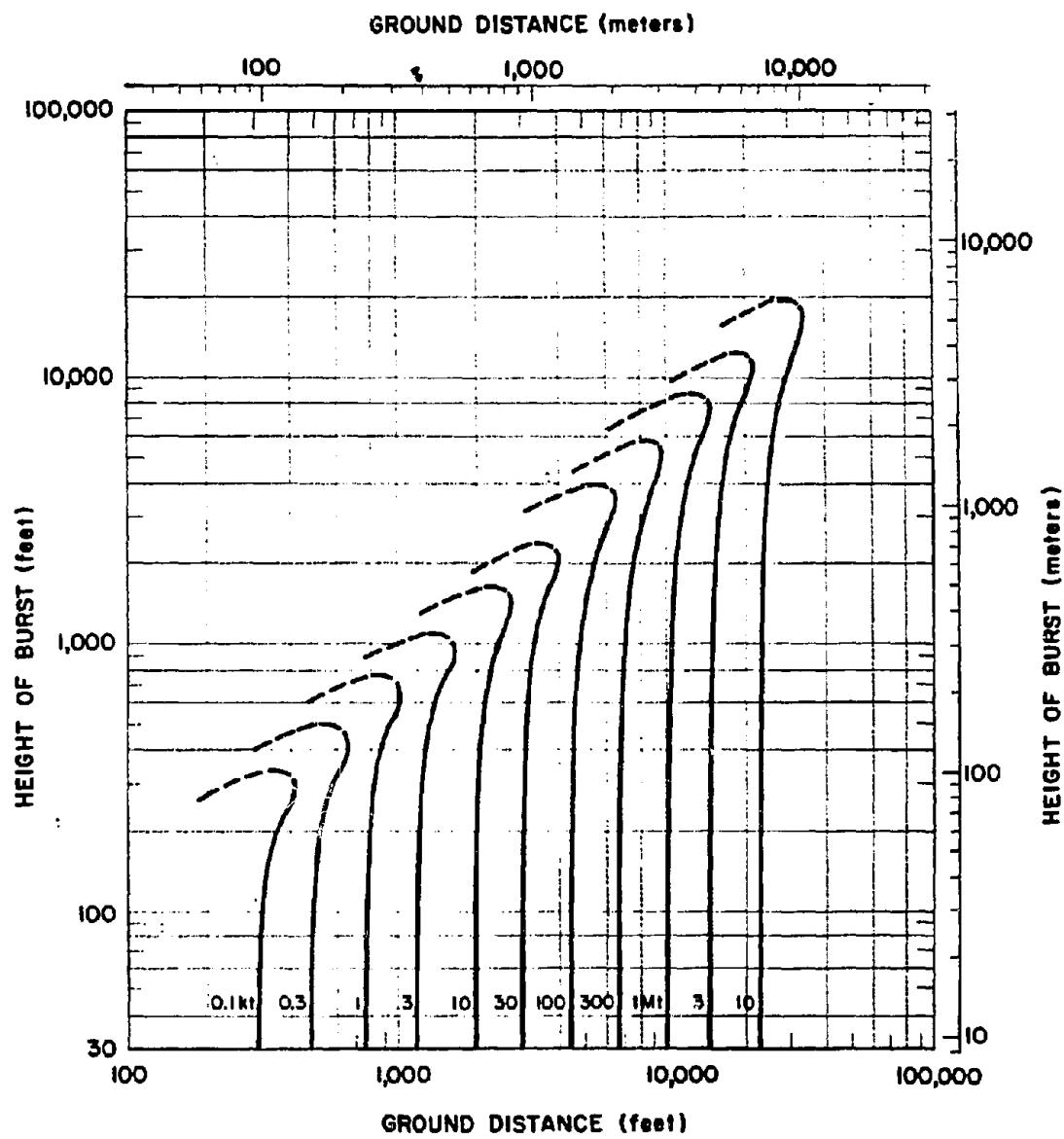


Figure 15-7. Total Damage to a Type II Forest

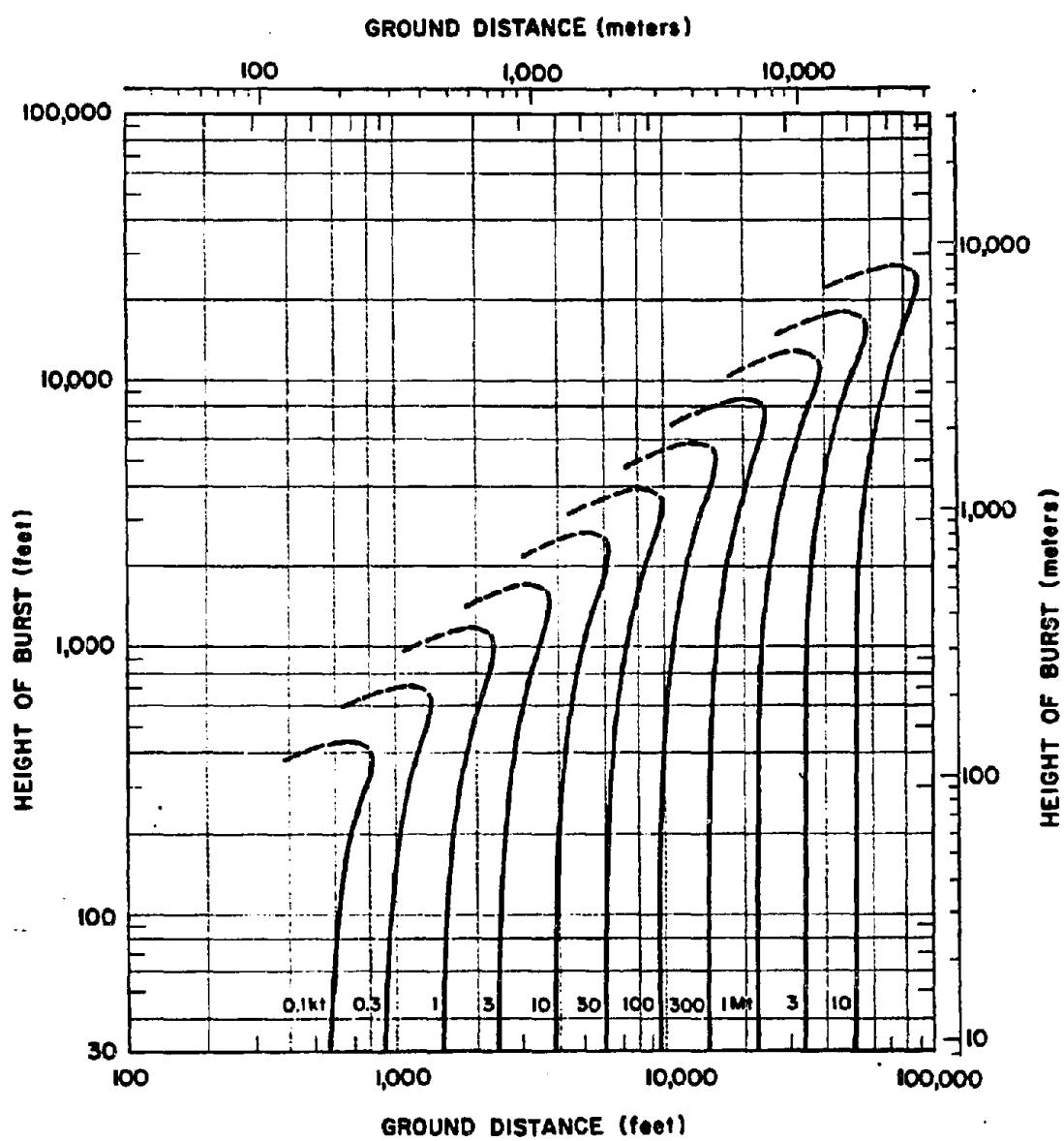


Figure 15-8. Moderate Damage to a Type III Forest

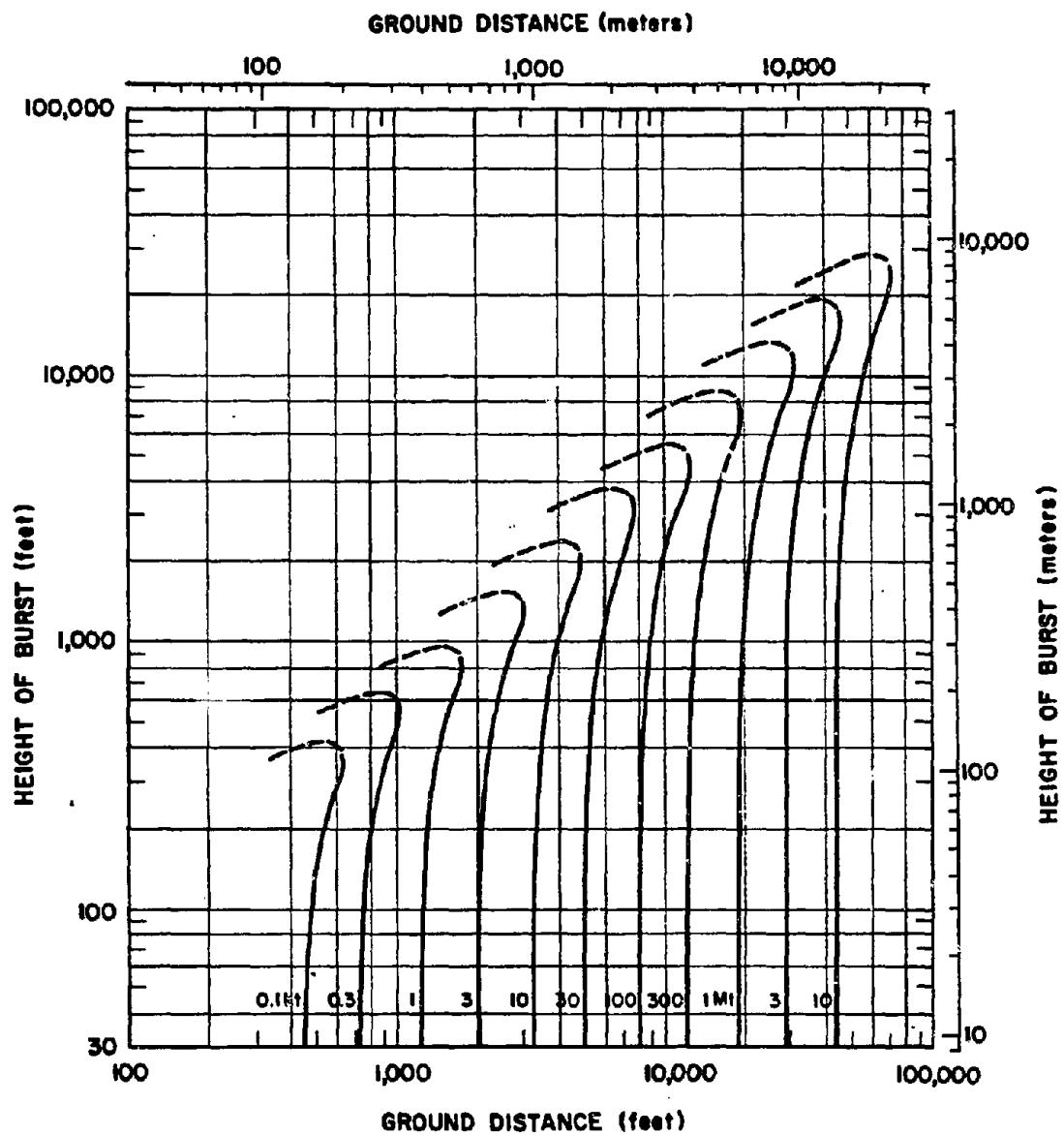


Figure 15-9. Severe Damage to a Type III Forest

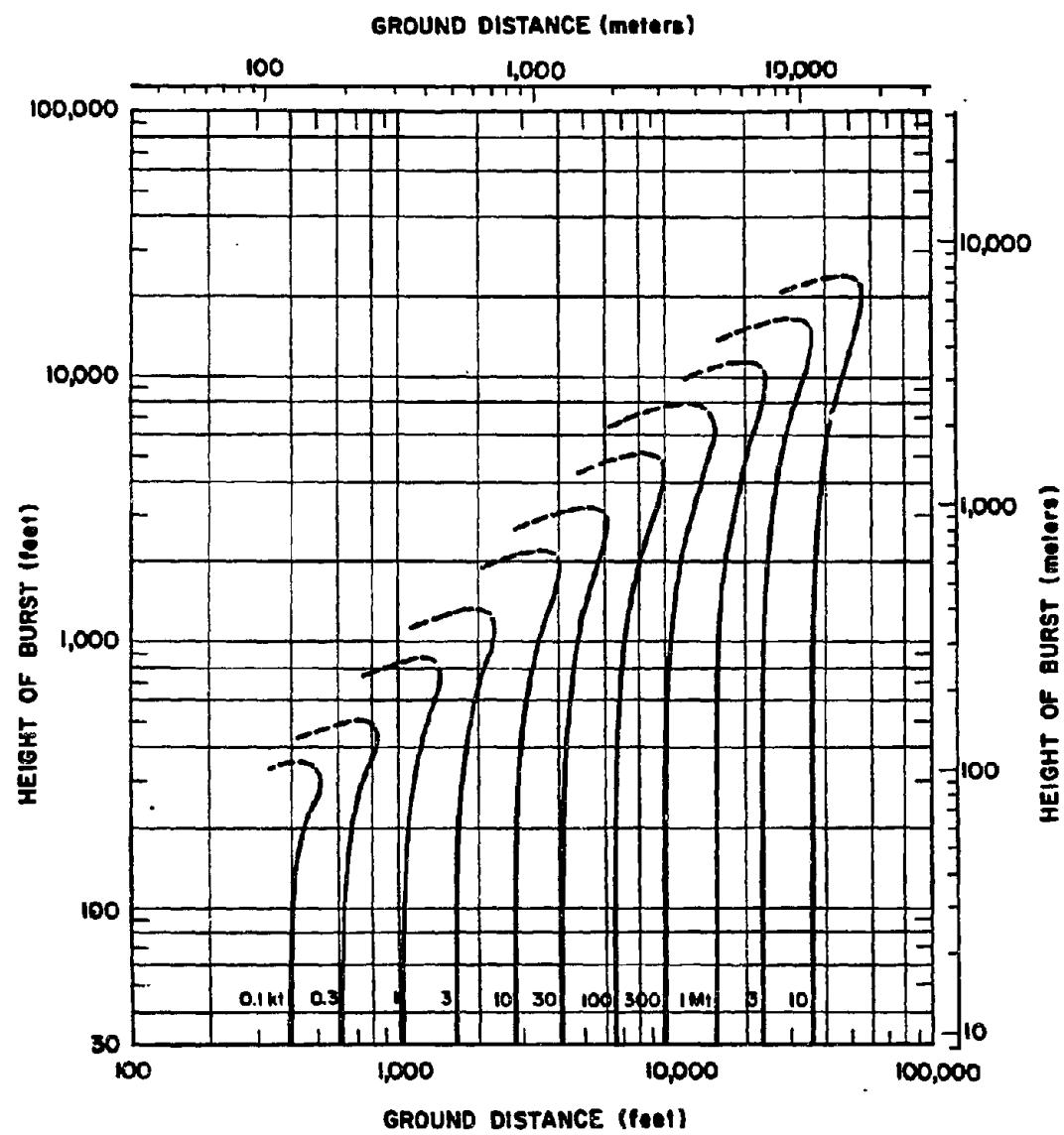


Figure 15-10. Total Damage to a Type III Forest

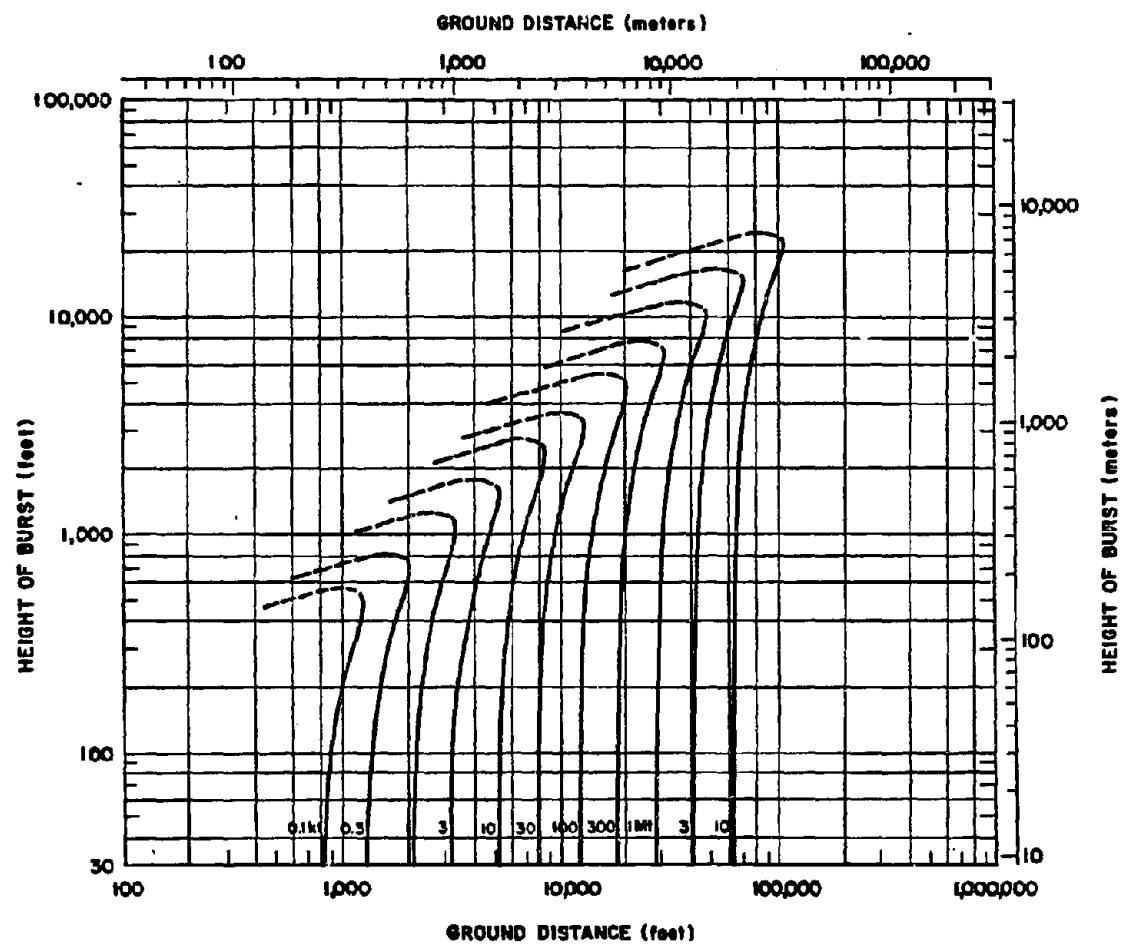
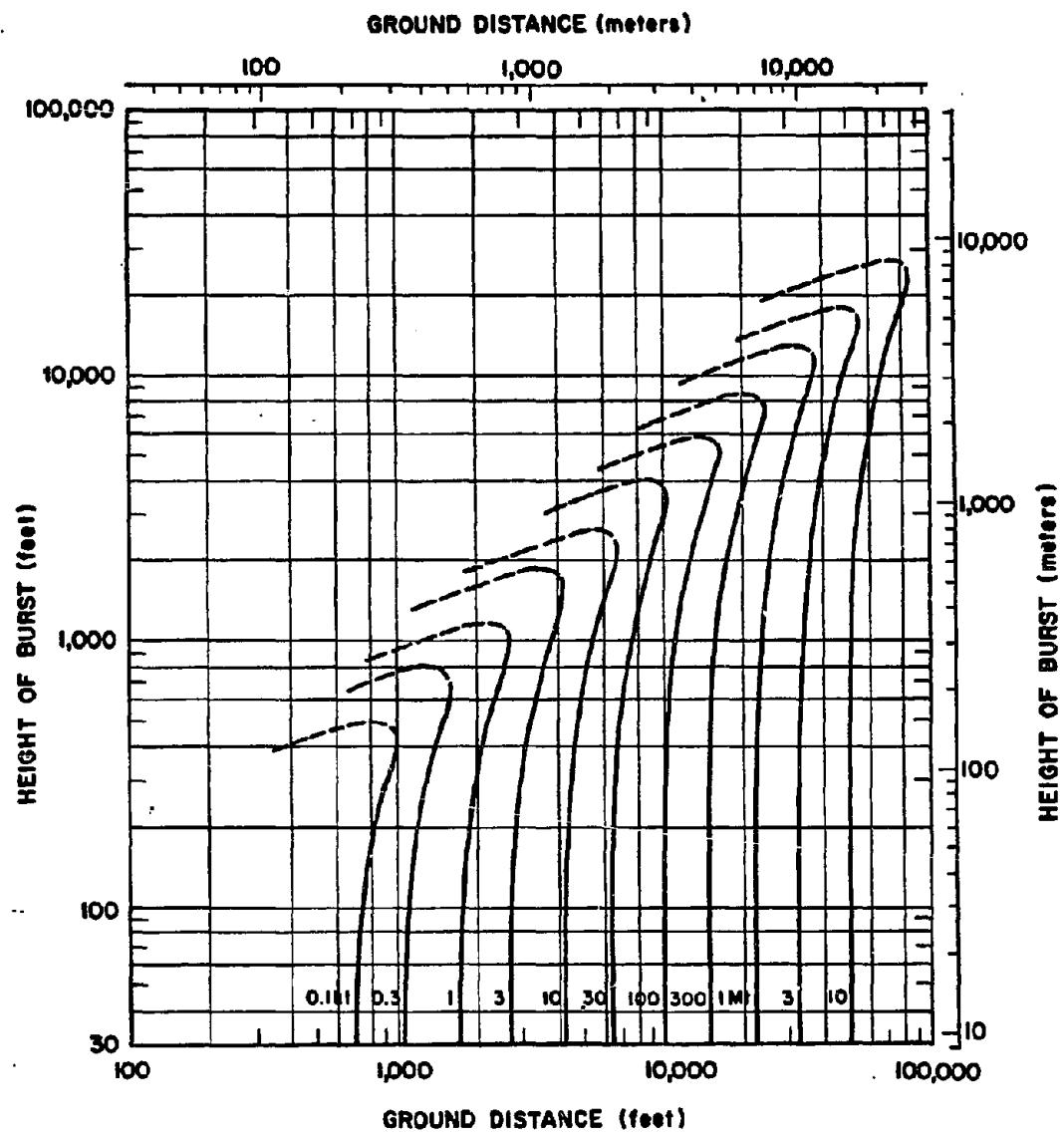


Figure 15-11. Moderate Damage to a Type IVs-1(f) Forest



**Figure 15-12. Severe Damage to a Type IVa-1(f) Forest**

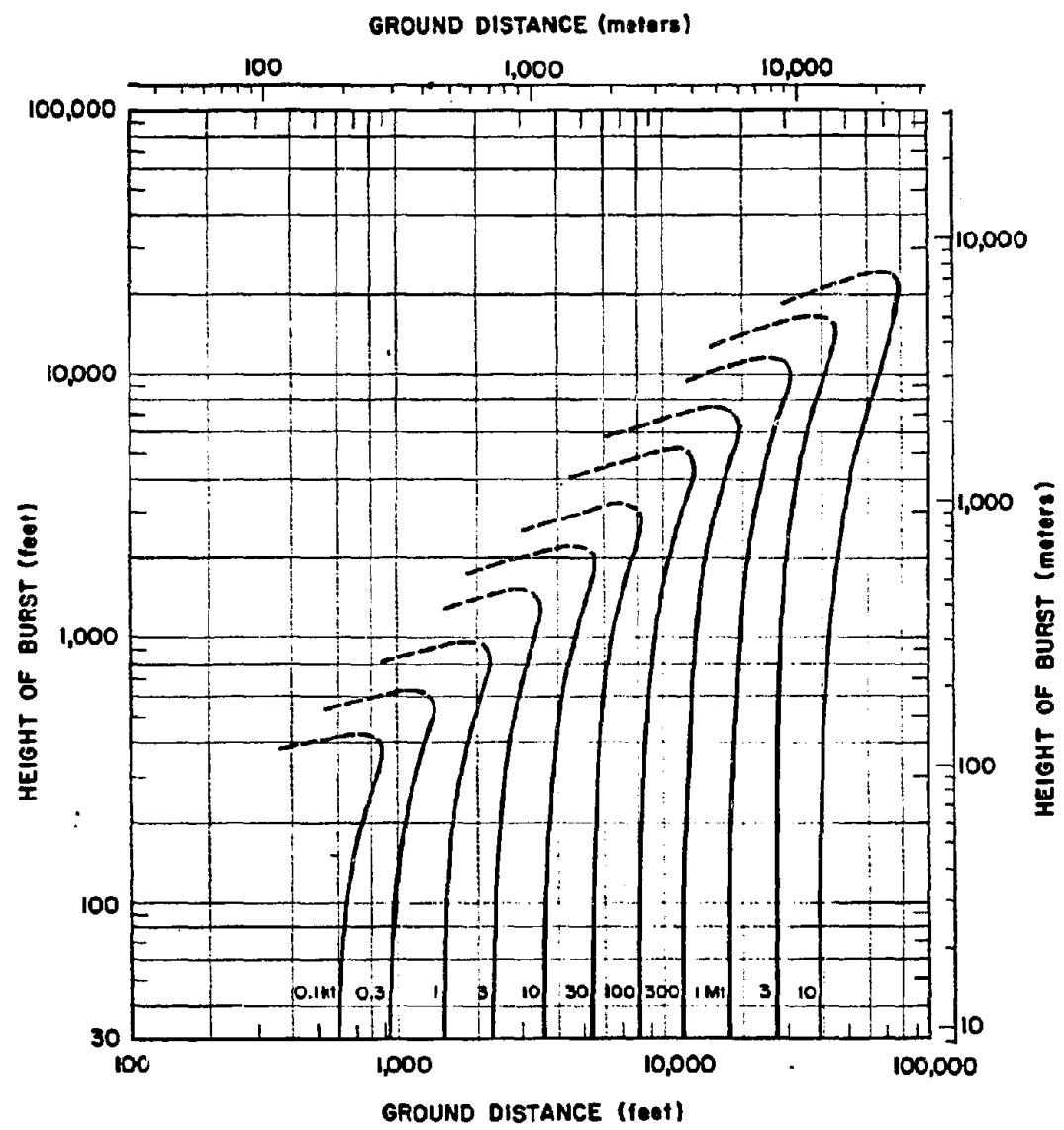


Figure 15-13. Total Damage to a Type IVa-1(f) Forest

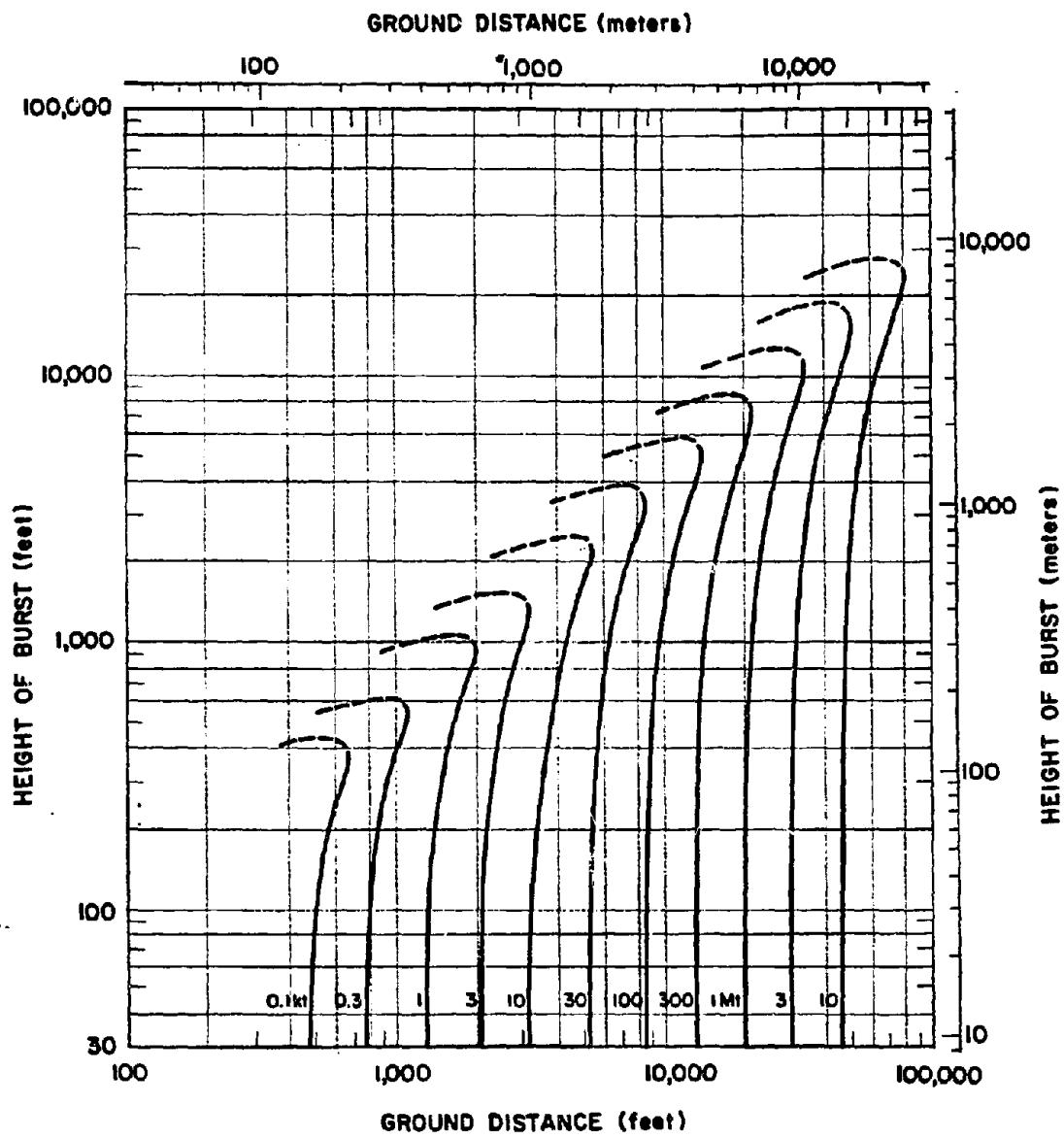


Figure 15-14. [REDACTED] Moderate Damage to a Type IVa-1(d) Forest [REDACTED]

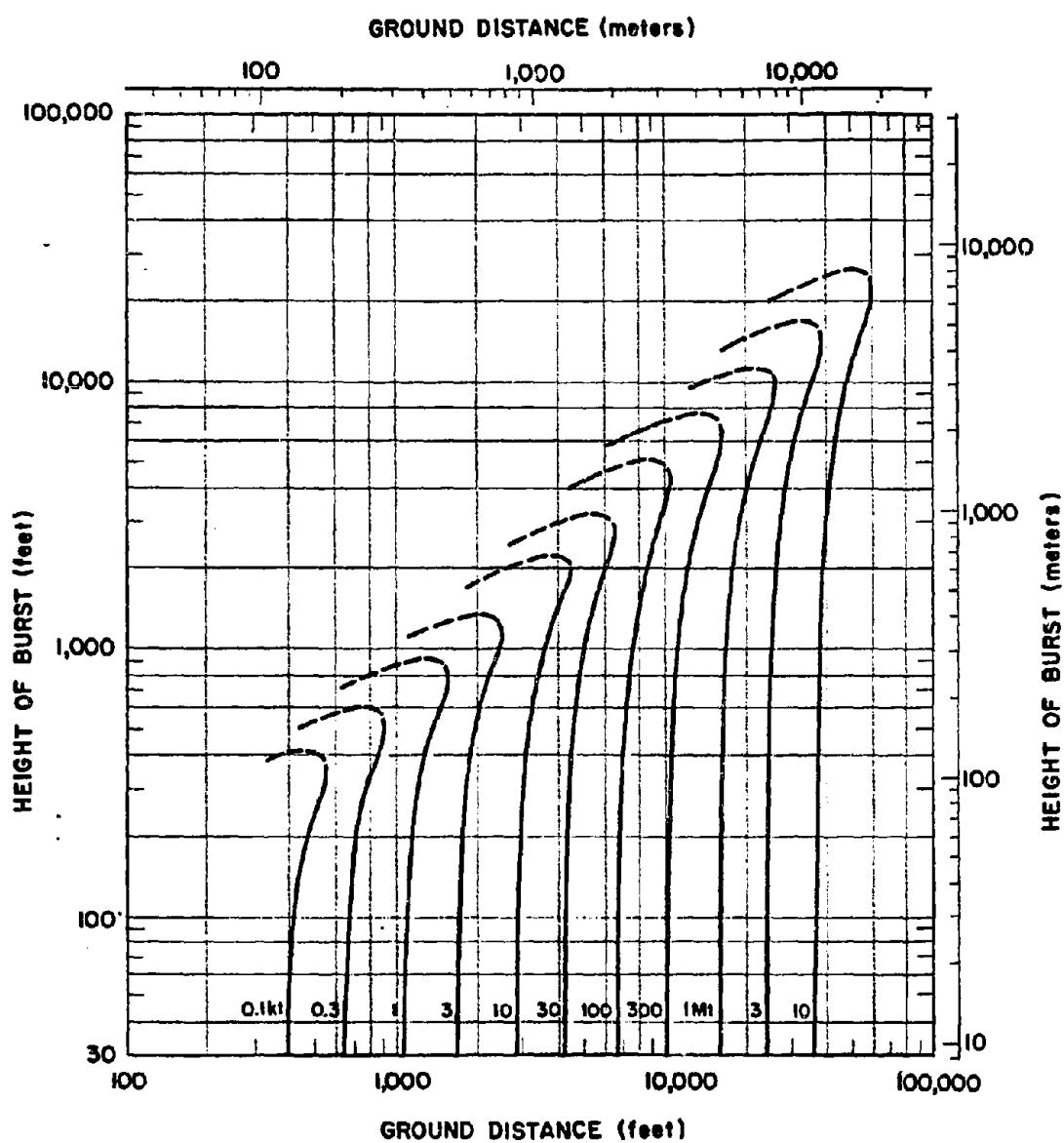


Figure 15-15. Severe Damage to a Type IVa-1(d) Forest

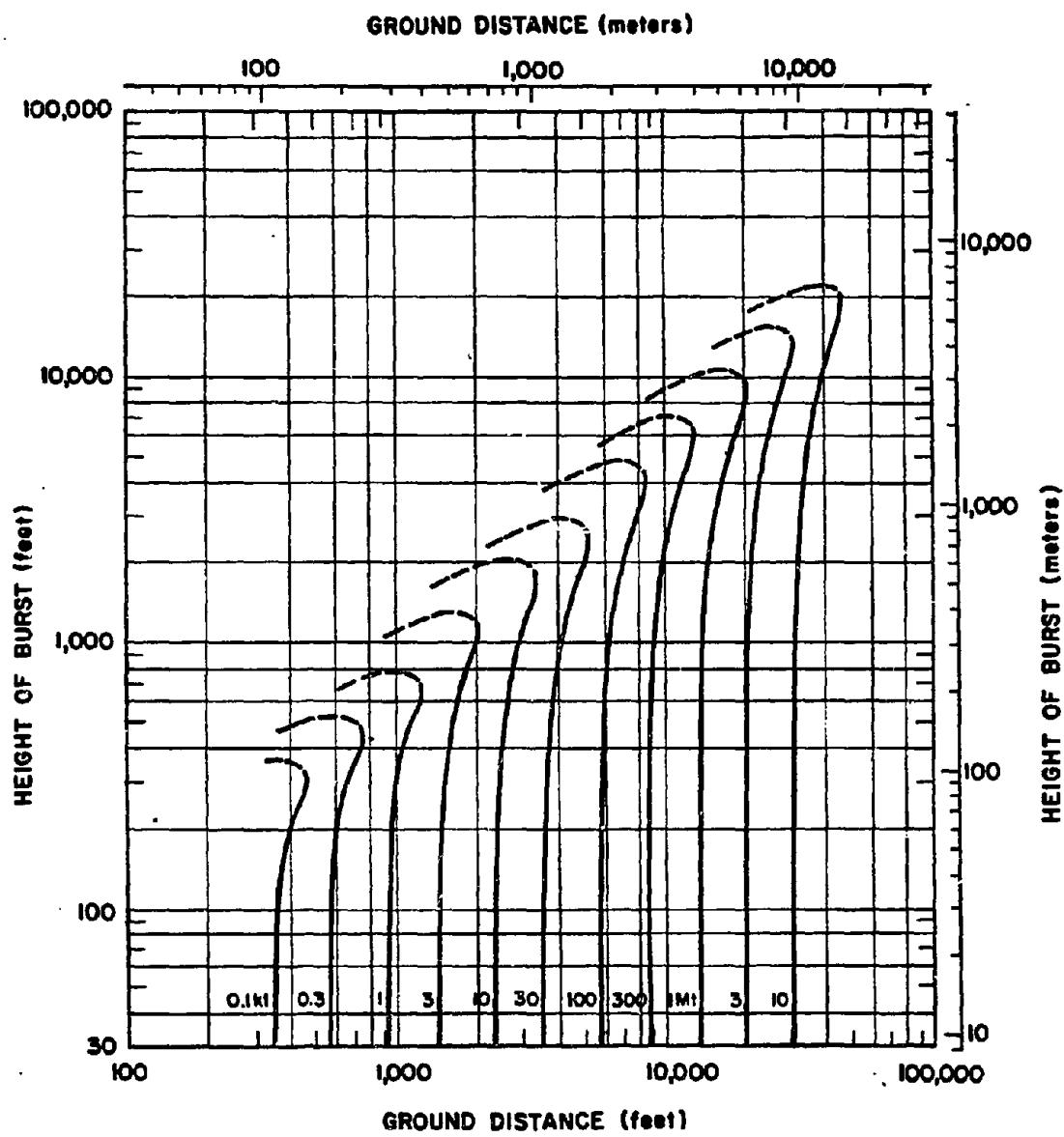


Figure 16-16. Total Damage to a Type IVa-1(d) Forest

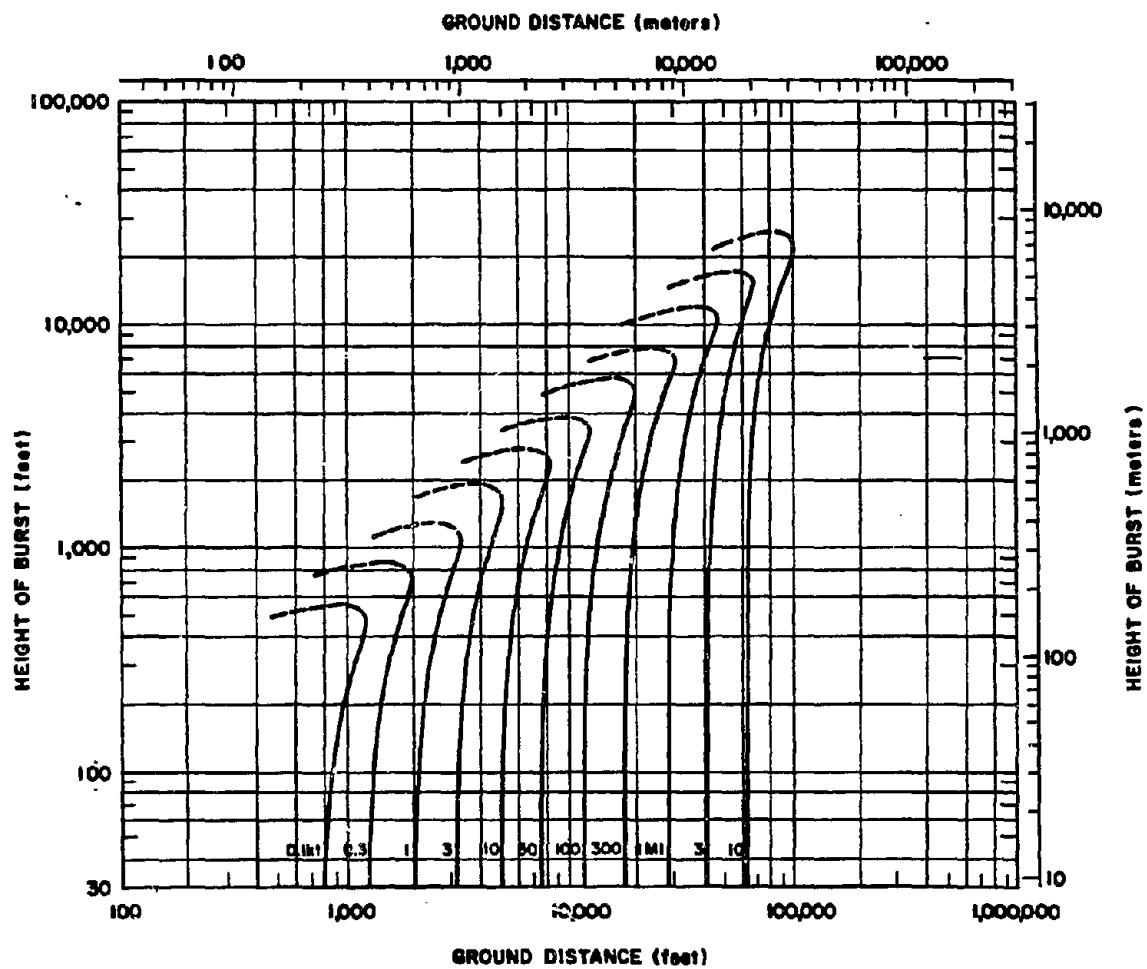


Figure 15-17. [REDACTED] Moderate Damage to a Type IVa-2(f) Forest [REDACTED]

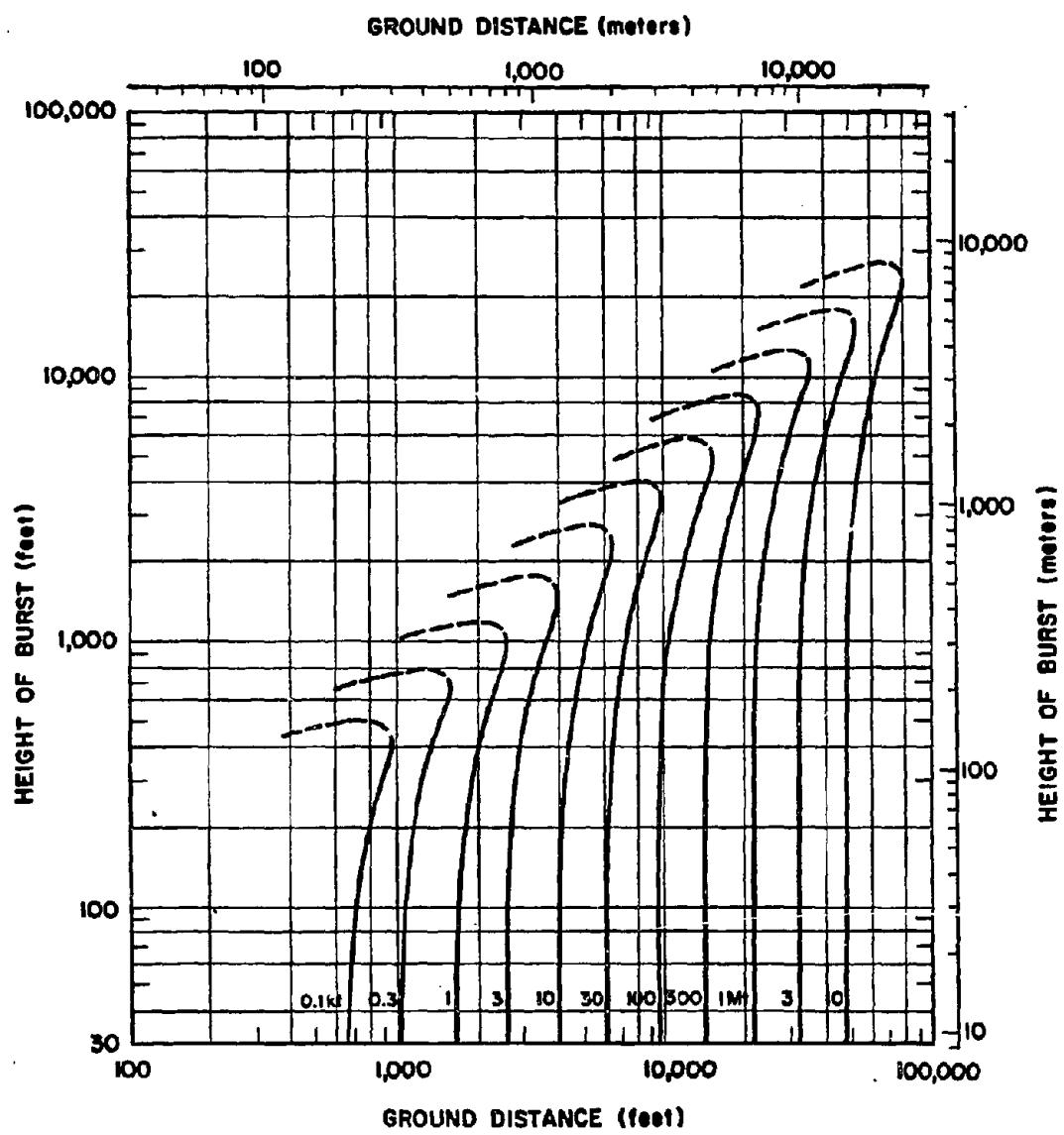


Figure 15-18. [REDACTED] Severe Damage to a Type IVa-2(f) Forest [REDACTED]

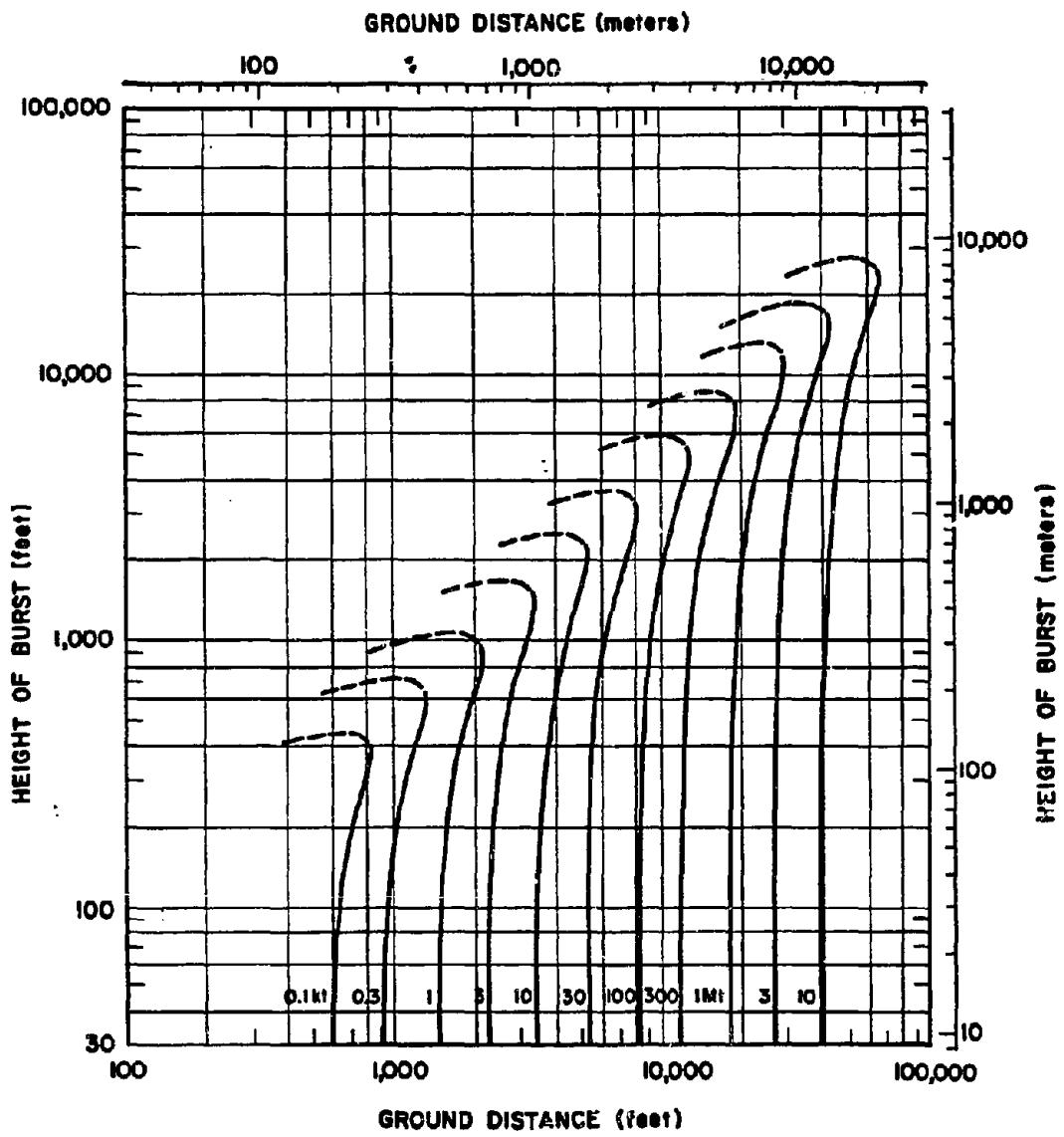


Figure 15-19. Total Damage to a Type IVa-2(f) Forest

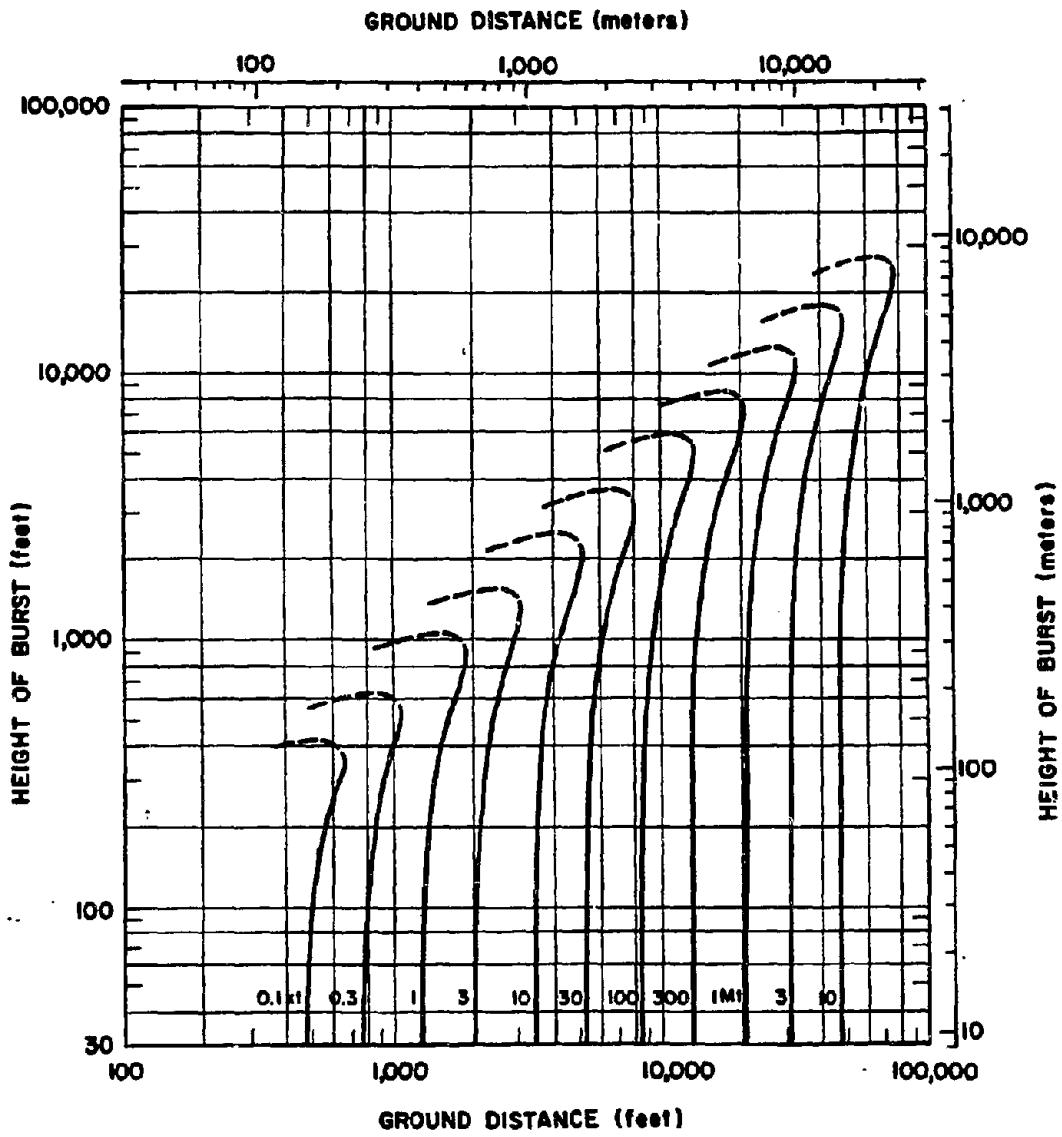


Figure 15-20 [REDACTED] Moderate Damage to a Type IVa-2(d) Forest [REDACTED]

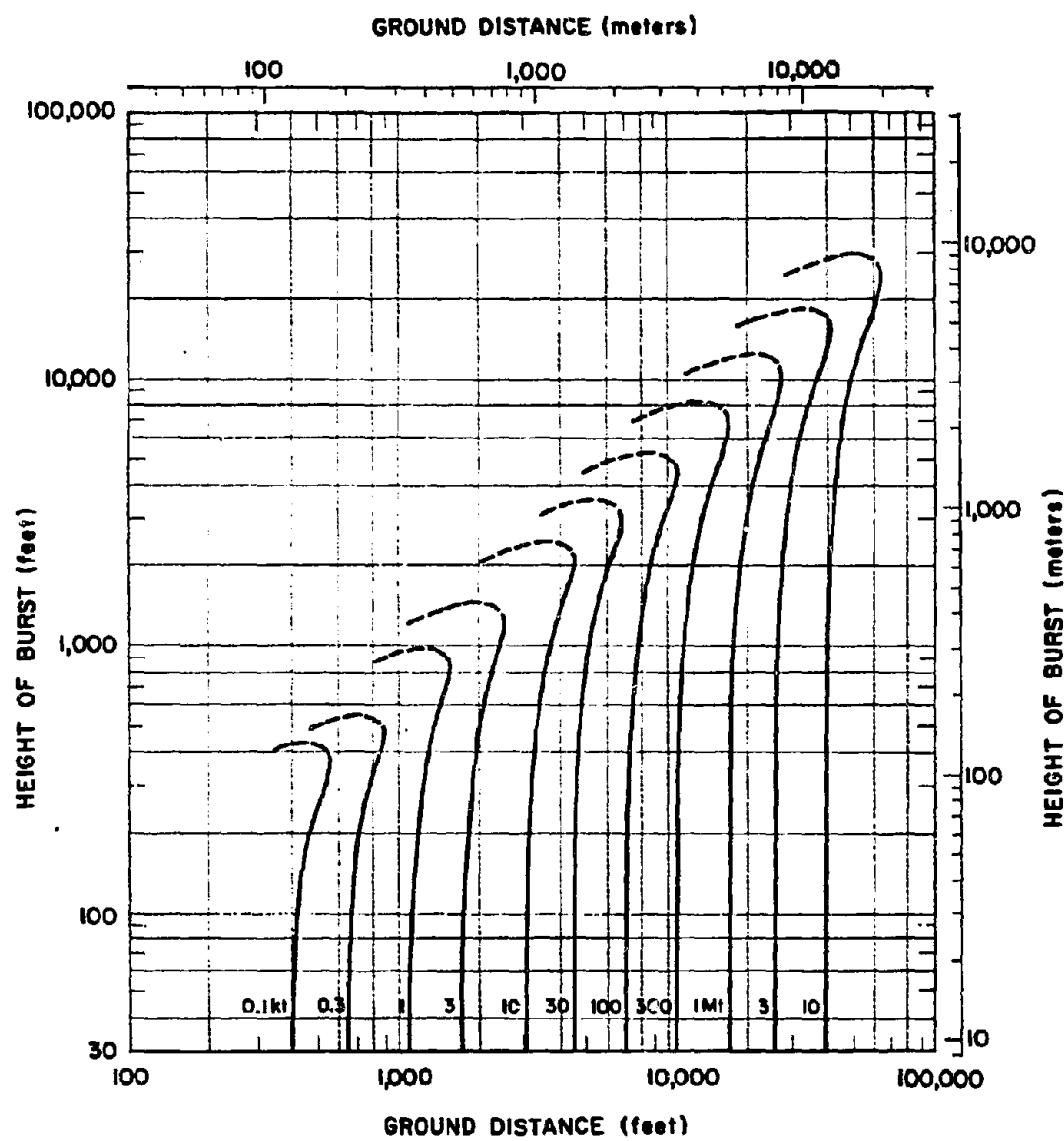


Figure 15-21. Severe Damage to a Type IVa-2(d) Forest

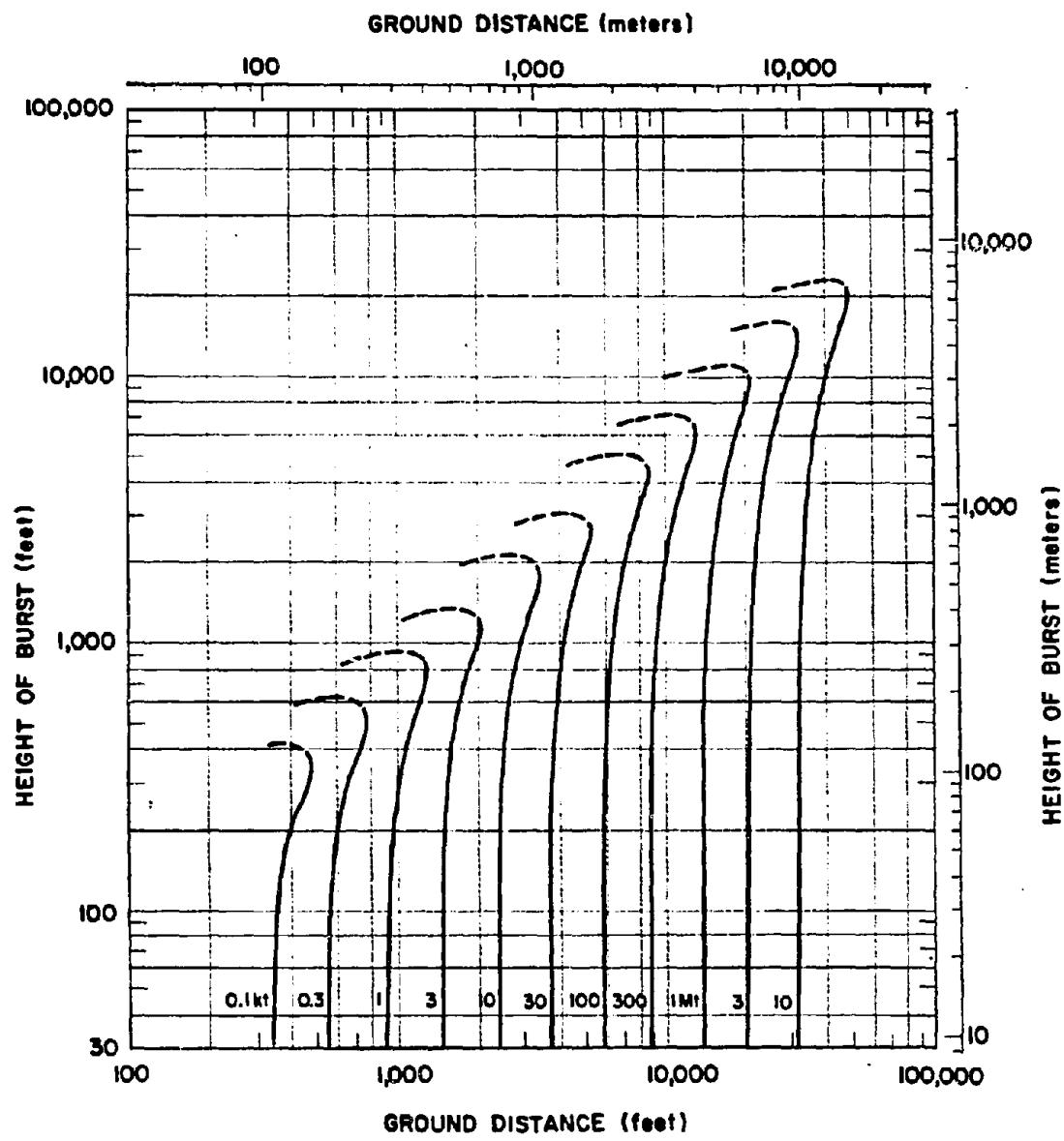


Figure 15-22. [REDACTED] Total Damage to a Type IVa-2(d) Forest [REDACTED]

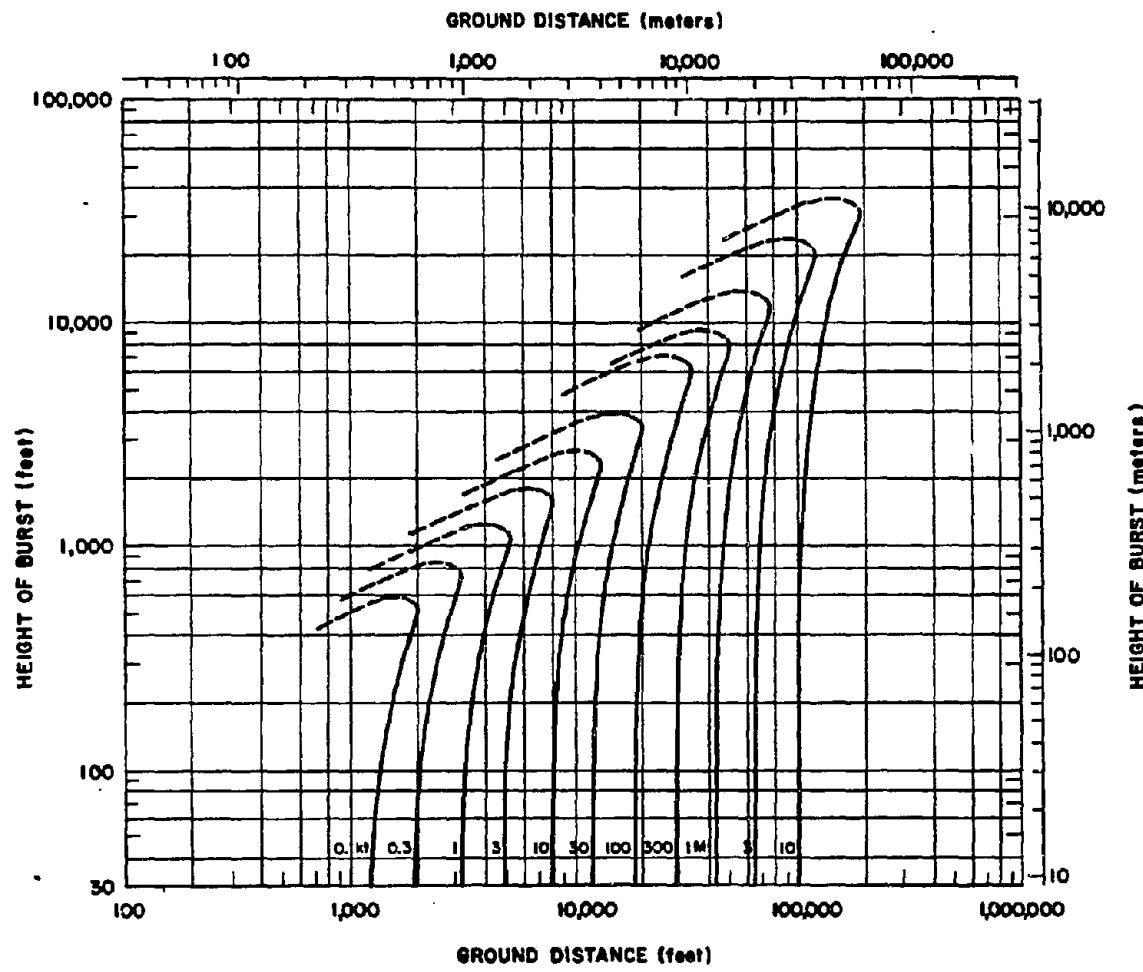


Figure 15-23. [REDACTED] Moderate Damage to a Type IVb(f) Forest [REDACTED]

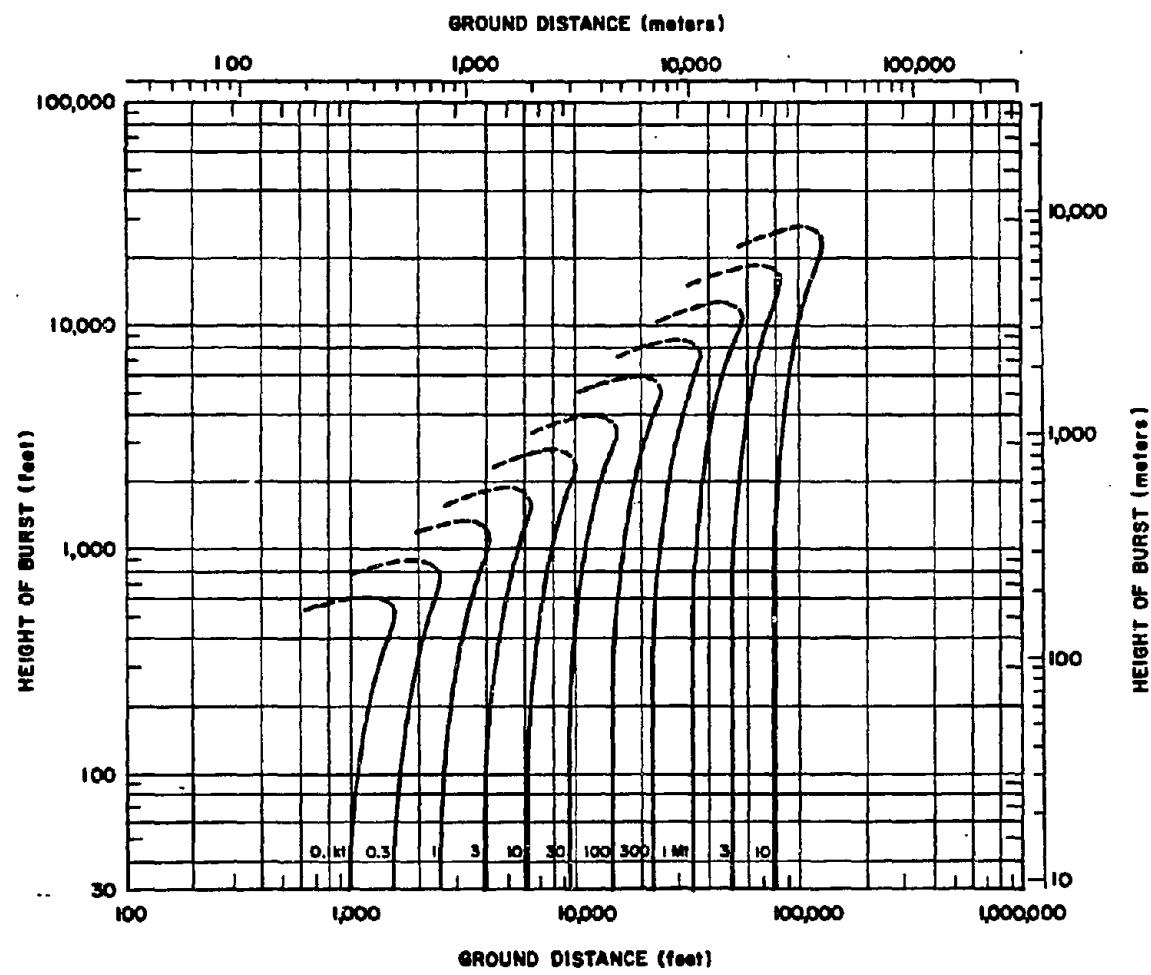


Figure 15-24. Severe Damage to a Type IVb(f) Forest

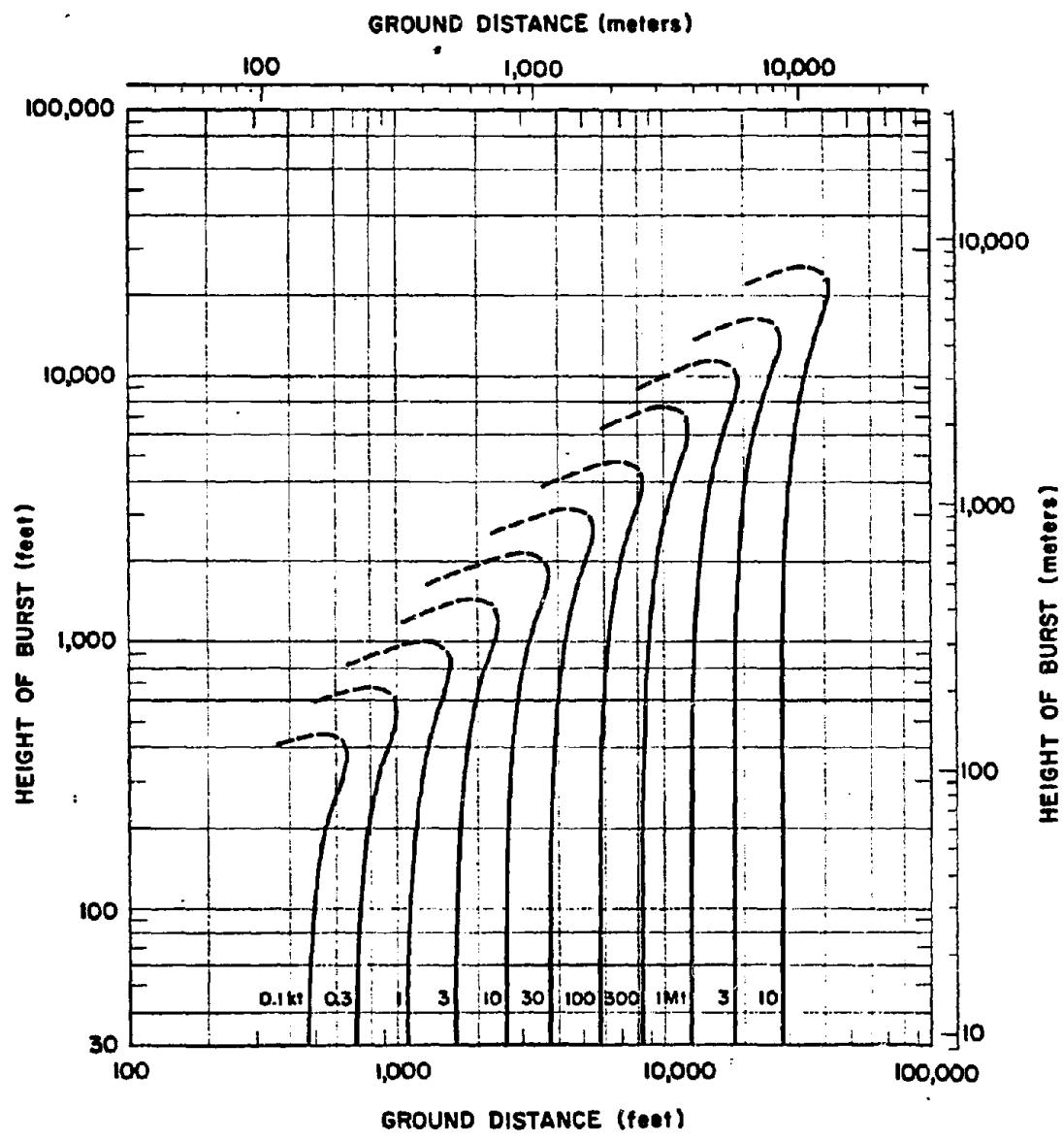


Figure 15-25. Total Damage to a Type IVb(f) Forest

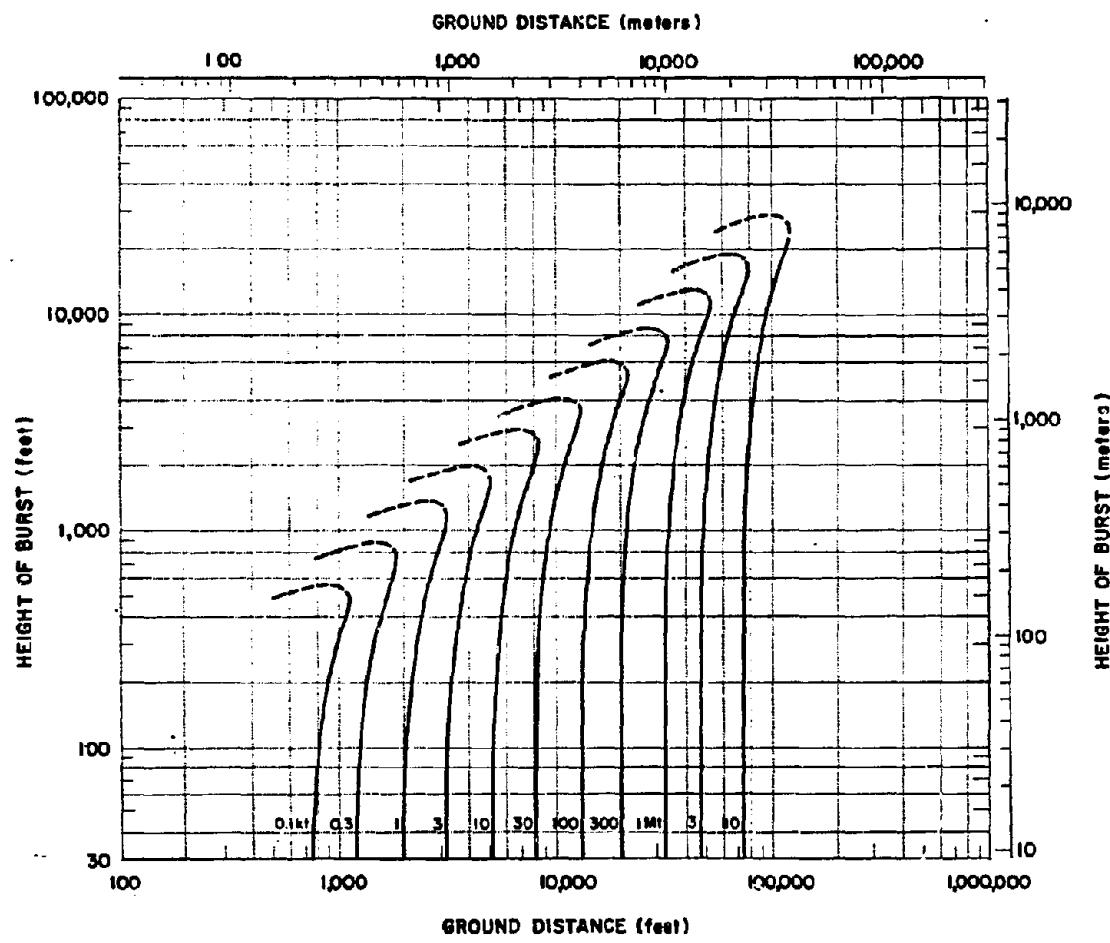
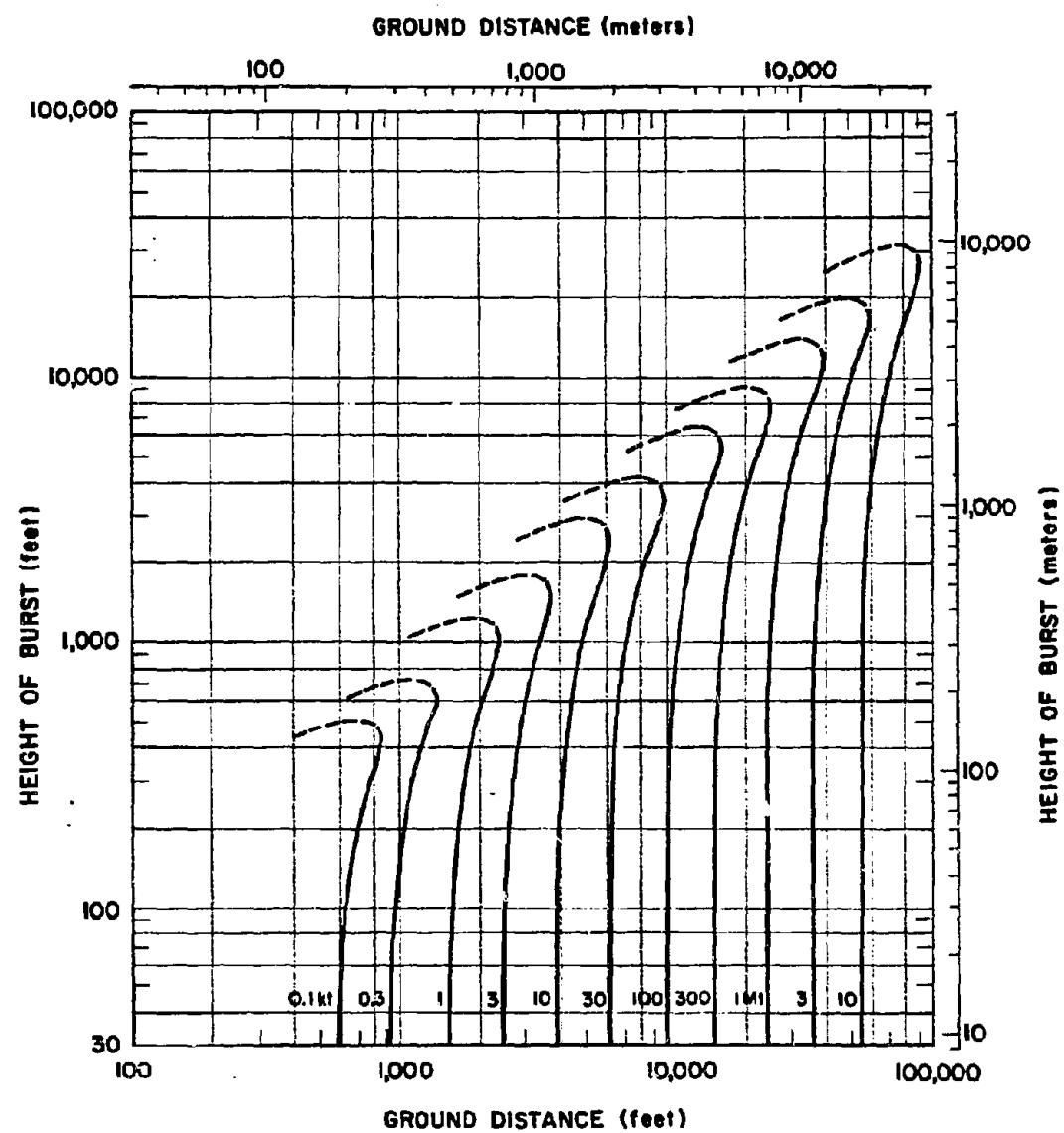


Figure 15-26. Moderate Damage to a Type IVb(d) Forest



**Figure 15-27.** Severe Damage to a Type IVb(d) Forest

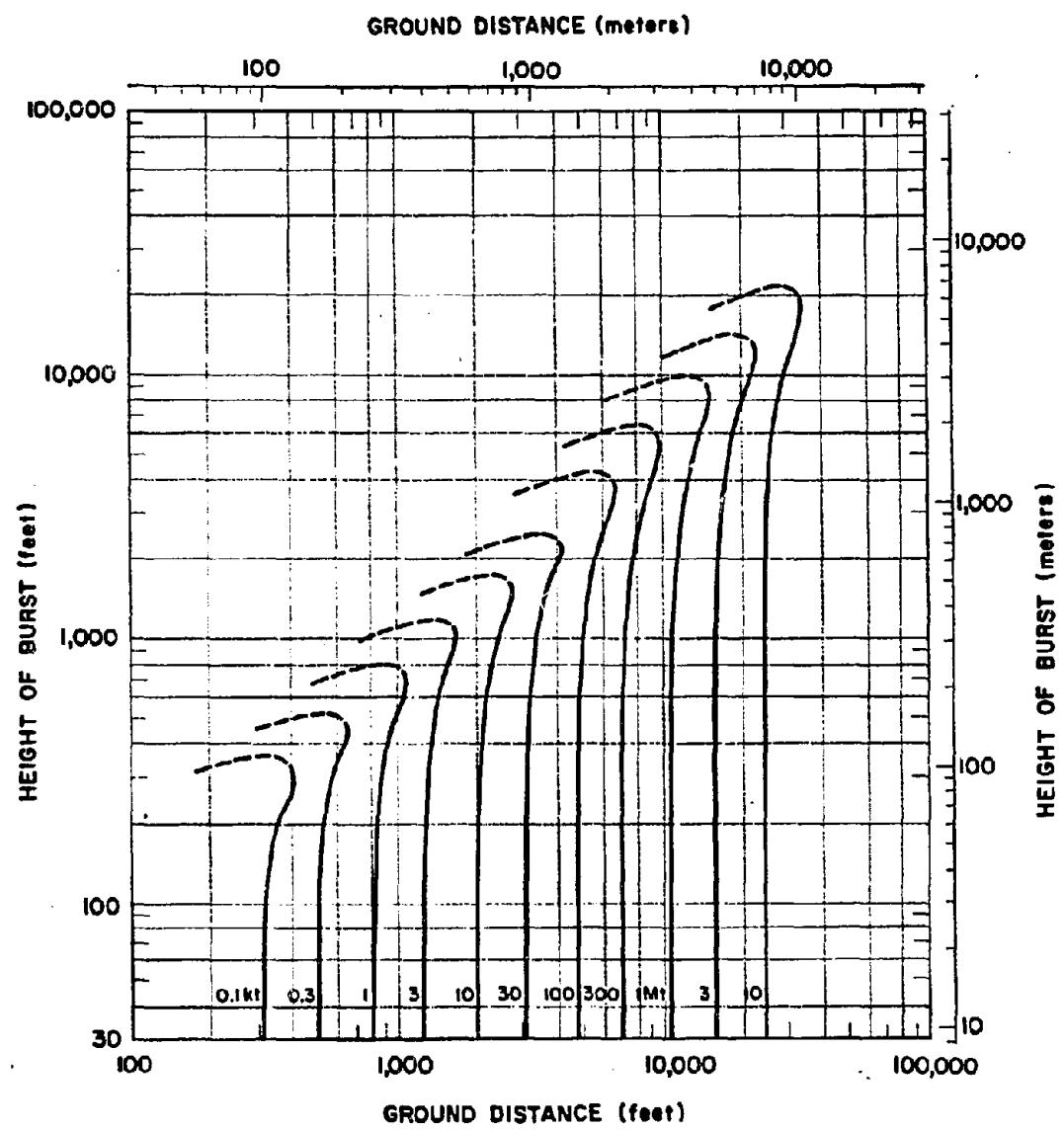
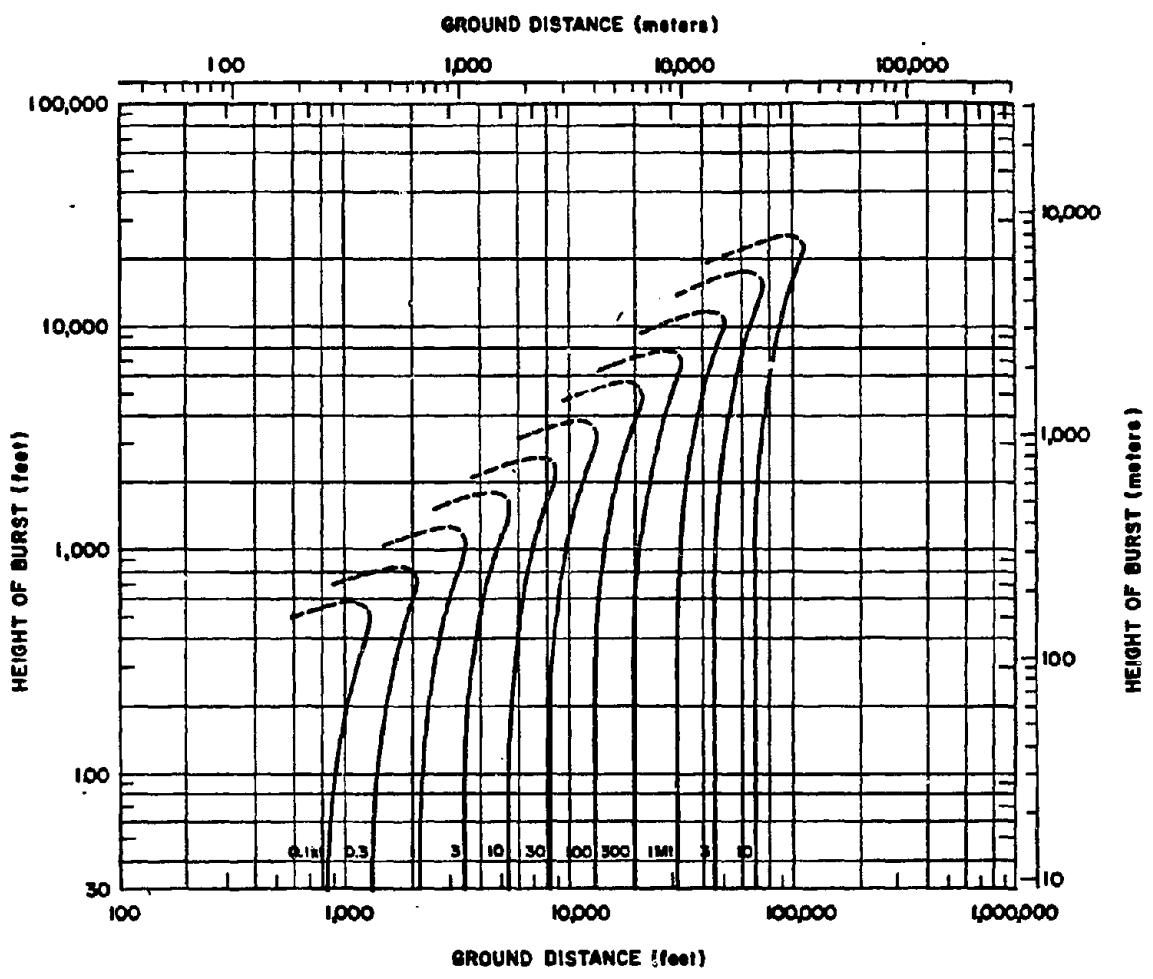


Figure 15-28. [REDACTED] Total Damage to a Type IVb(d) Forest [REDACTED]



**Figure 15-29.** Moderate Damage to a Type IVc(f) Forest

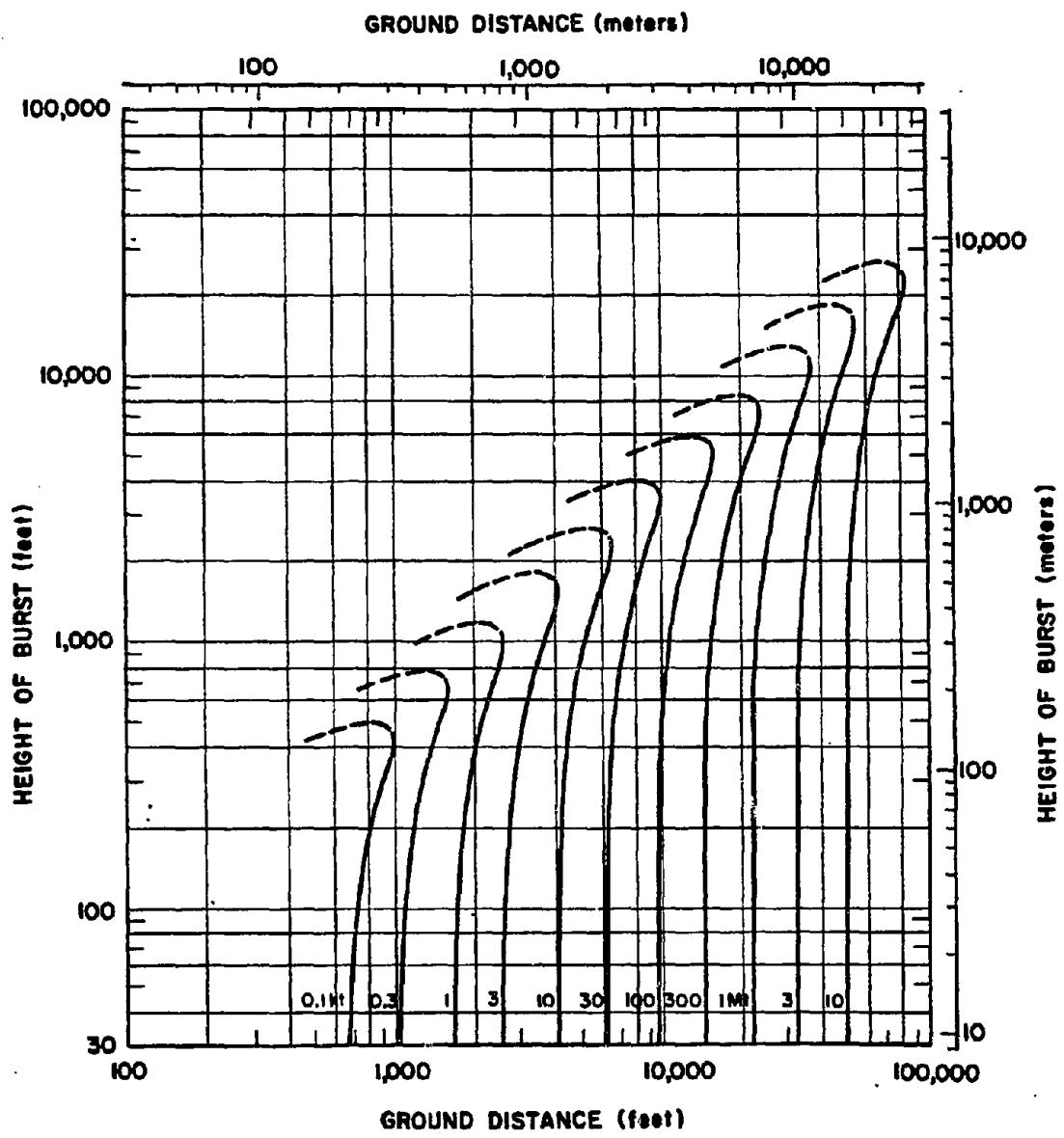


Figure 15-30. Total Damage to a Type IVc(f) Forest

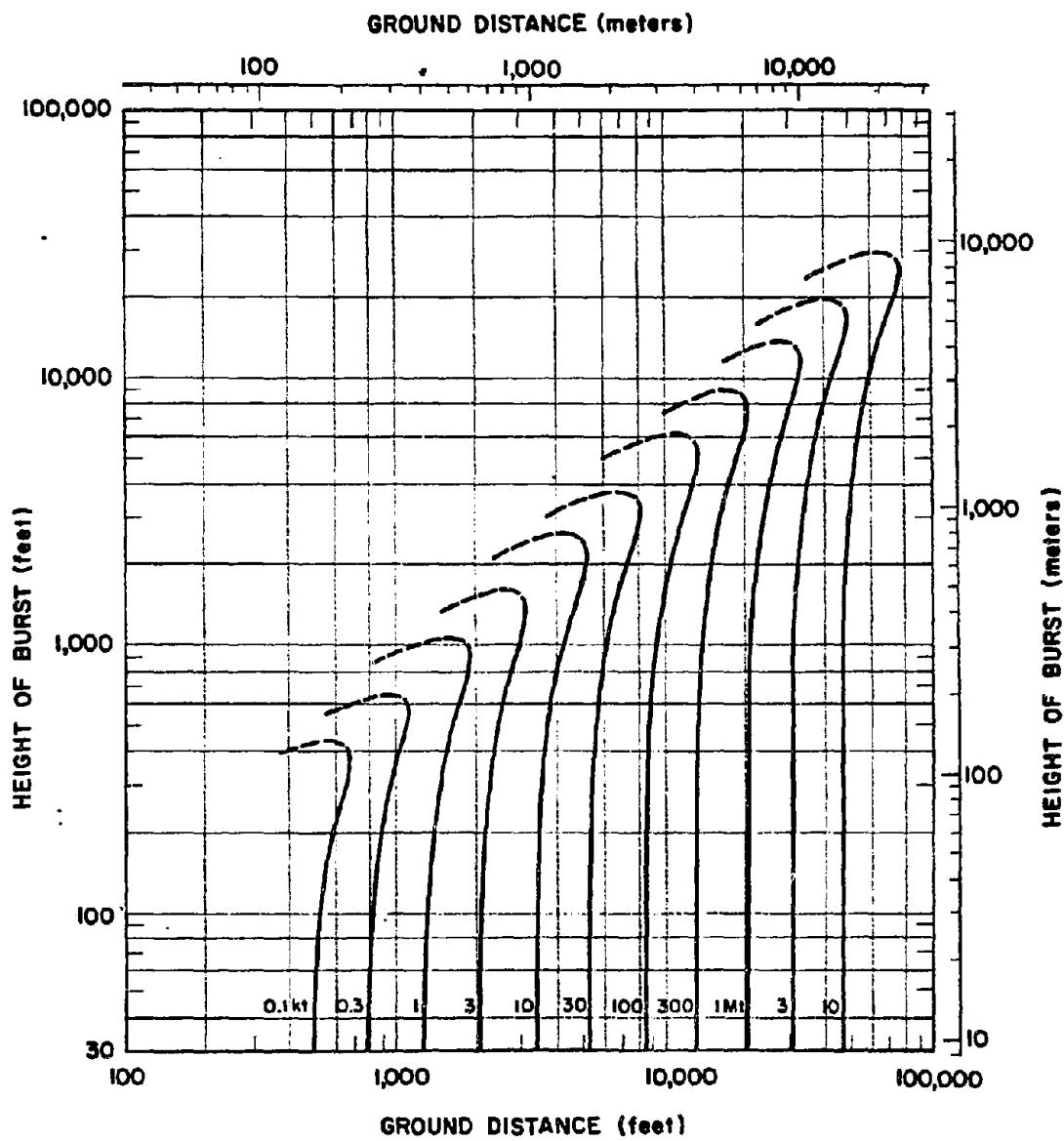
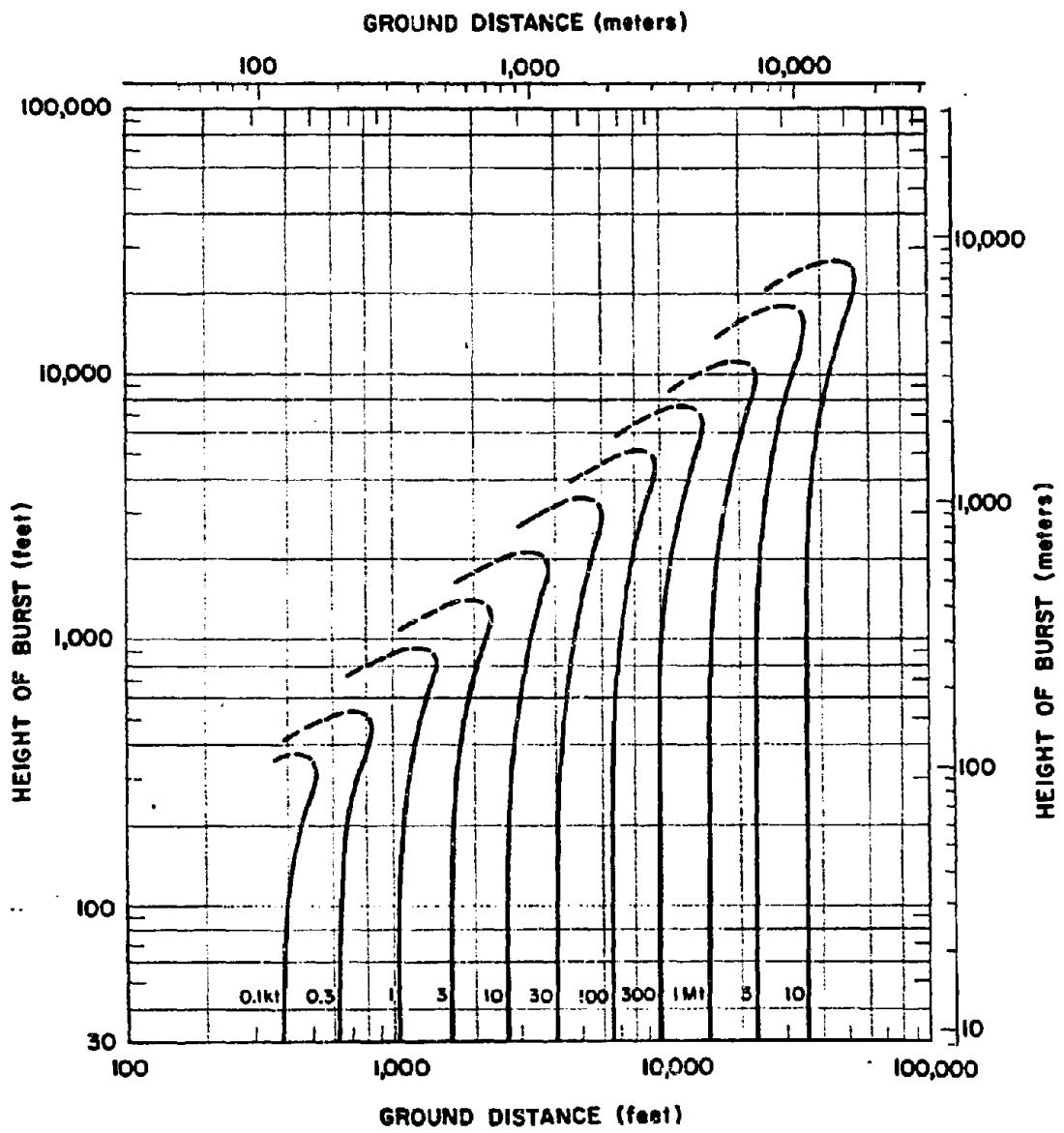
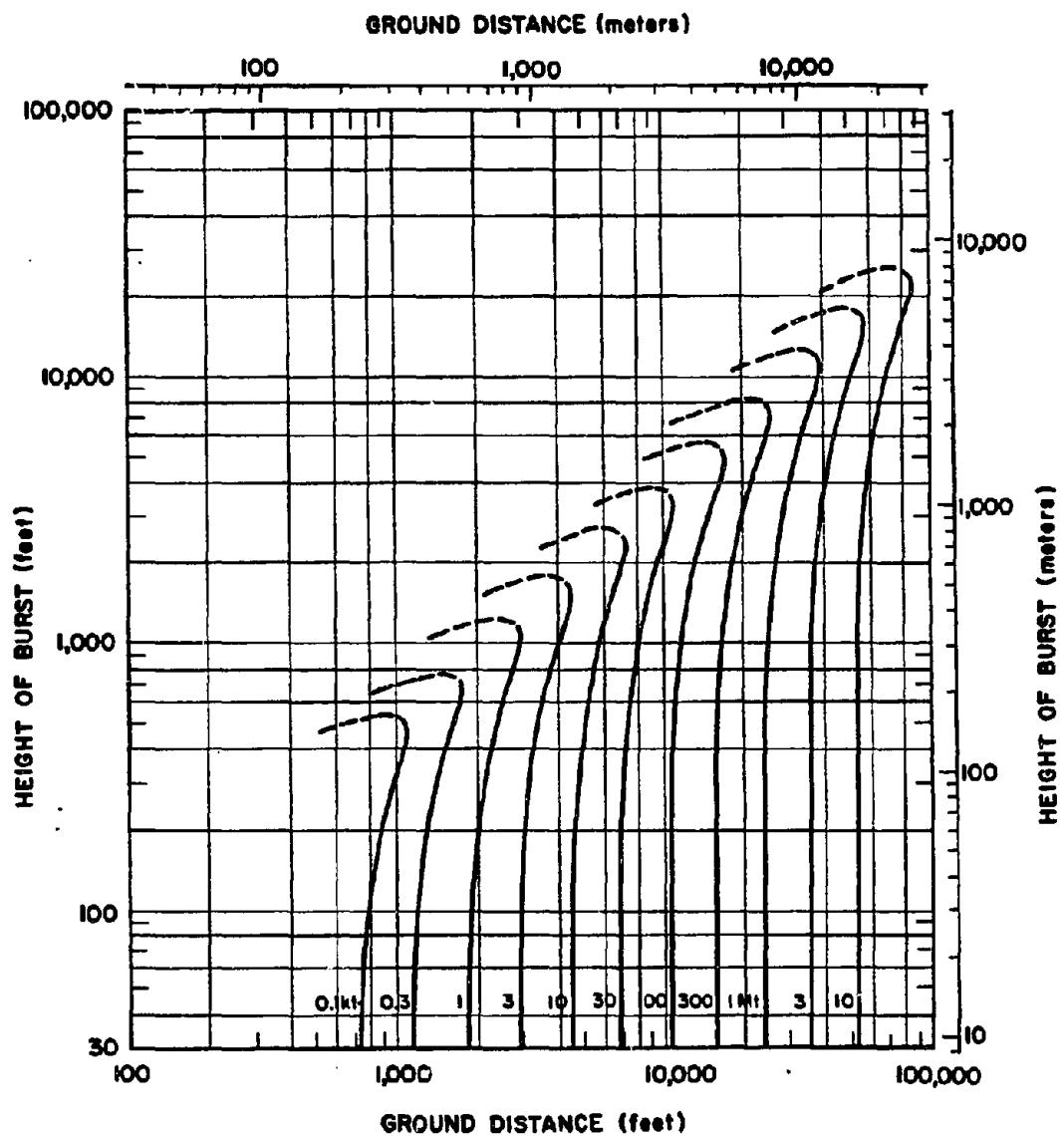


Figure 15-31. [REDACTED] Moderate Damage to a Type IVc(d) Forest [REDACTED]



**Figure 15-32.** Total Damage to a Type IVc(d) Forest



**Figure 15-33.** Moderate Damage to a Type IVd Forest

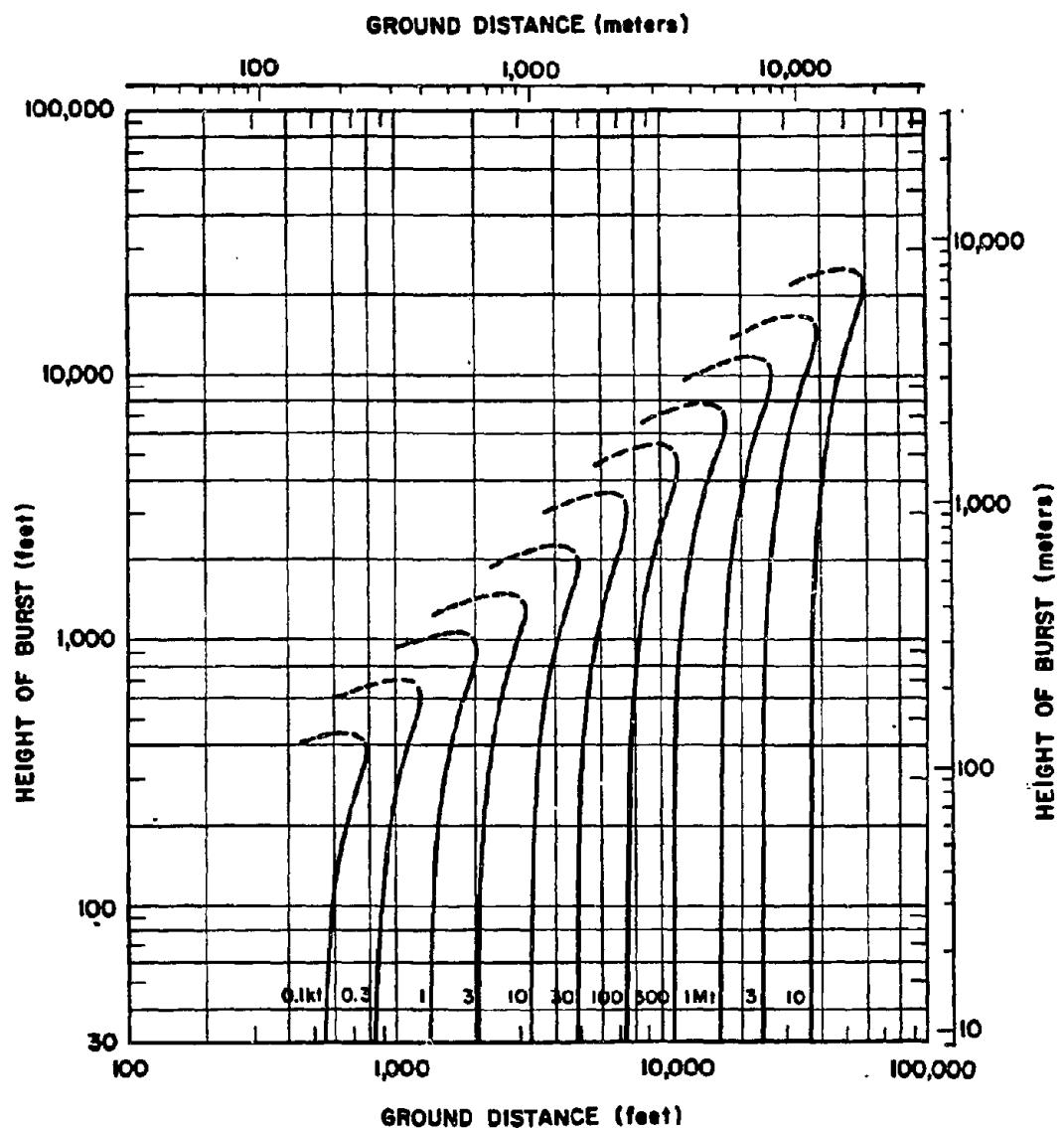


Figure 15-34. Total Damage to a Type IVd Forest

**SECTION II**  
**TROOP AND VEHICLE**  
**MOVEMENT**

The effects of a nuclear explosion on a forest may have a significant influence on military operations within the region of the forest that is affected by the burst.

Two H.E. tests have provided information concerning the character of the region that is damaged and the effect on vehicular and troop movement that the damage will cause.

DNA  
- (b)(1)

An important difference between the ef-

The information in these tables may be used for yields of 20 kt by determining the ground ranges for equivalent dynamic pressure impulses.

Table 15-3 Effects of a 1 kt Weapon Burst at a Height of 270 Feet Over a Rain Forest

Distance from Burst (feet)	Ground Range (feet)	Dynamic Pressure Impulse (psi)	Effect
100	100	0.000	None
200	200	0.000	None
300	300	0.000	None
400	400	0.000	None
500	500	0.000	None
600	600	0.000	None
700	700	0.000	None
800	800	0.000	None
900	900	0.000	None
1000	1000	0.000	None
1100	1100	0.000	None
1200	1200	0.000	None
1300	1300	0.000	None
1400	1400	0.000	None
1500	1500	0.000	None
1600	1600	0.000	None
1700	1700	0.000	None
1800	1800	0.000	None
1900	1900	0.000	None
2000	2000	0.000	None
2100	2100	0.000	None
2200	2200	0.000	None
2300	2300	0.000	None
2400	2400	0.000	None
2500	2500	0.000	None
2600	2600	0.000	None
2700	2700	0.000	None
2800	2800	0.000	None
2900	2900	0.000	None
3000	3000	0.000	None
3100	3100	0.000	None
3200	3200	0.000	None
3300	3300	0.000	None
3400	3400	0.000	None
3500	3500	0.000	None
3600	3600	0.000	None
3700	3700	0.000	None
3800	3800	0.000	None
3900	3900	0.000	None
4000	4000	0.000	None
4100	4100	0.000	None
4200	4200	0.000	None
4300	4300	0.000	None
4400	4400	0.000	None
4500	4500	0.000	None
4600	4600	0.000	None
4700	4700	0.000	None
4800	4800	0.000	None
4900	4900	0.000	None
5000	5000	0.000	None
5100	5100	0.000	None
5200	5200	0.000	None
5300	5300	0.000	None
5400	5400	0.000	None
5500	5500	0.000	None
5600	5600	0.000	None
5700	5700	0.000	None
5800	5800	0.000	None
5900	5900	0.000	None
6000	6000	0.000	None
6100	6100	0.000	None
6200	6200	0.000	None
6300	6300	0.000	None
6400	6400	0.000	None
6500	6500	0.000	None
6600	6600	0.000	None
6700	6700	0.000	None
6800	6800	0.000	None
6900	6900	0.000	None
7000	7000	0.000	None
7100	7100	0.000	None
7200	7200	0.000	None
7300	7300	0.000	None
7400	7400	0.000	None
7500	7500	0.000	None
7600	7600	0.000	None
7700	7700	0.000	None
7800	7800	0.000	None
7900	7900	0.000	None
8000	8000	0.000	None
8100	8100	0.000	None
8200	8200	0.000	None
8300	8300	0.000	None
8400	8400	0.000	None
8500	8500	0.000	None
8600	8600	0.000	None
8700	8700	0.000	None
8800	8800	0.000	None
8900	8900	0.000	None
9000	9000	0.000	None
9100	9100	0.000	None
9200	9200	0.000	None
9300	9300	0.000	None
9400	9400	0.000	None
9500	9500	0.000	None
9600	9600	0.000	None
9700	9700	0.000	None
9800	9800	0.000	None
9900	9900	0.000	None
10000	10000	0.000	None

fects on broadleaf and coniferous forests is the nature of the debris.

(6)

ber and diameter of stems in the path of the vehicles or troops. The variation in these parameters throughout various regions of damage are discussed in the following paragraphs.

Data from the two TNT detonations that were mentioned previously are presented in Figures 15-35 and 15-36. Figure 15-35 shows the relation between stem-feet per acre\* and ground range for a rain forest and for a coniferous forest.

The difference in maximum stem-feet per acre between the two forests results from the difference in average tree density and tree height of the

DN.7  
(b) (i)

### **15-3 Blowdown Debris Characteristics**

The impact of the damaged region of a forest on movement is determined by the num-

See footnote to Table 15-1.

**Table 15-4 Effects of a 1 kt Surface Burst on a Coniferous Forest**

The image consists of a central vertical stack of approximately 15 thick, horizontal bars. These bars have a distinct, slightly irregular texture and are set against a plain white background. At the very top and bottom of the image frame, there are two prominent, solid black rectangular blocks. The overall composition is minimalist and abstract.

DNA  
(b)(1)



Figure 15-35. Stem-ft per Acre Comparison Between a Rain Forest and a Coniferous Forest

forests. The curve for the rain forest is based on data gathered by observation, while the curve for the coniferous forest is based on calculations, using preshot and postshot tree surveys. Figure 15-36 shows the relation between ground range and average diameter of the debris.

DNA  
(b)(1)

DNA  
(b)

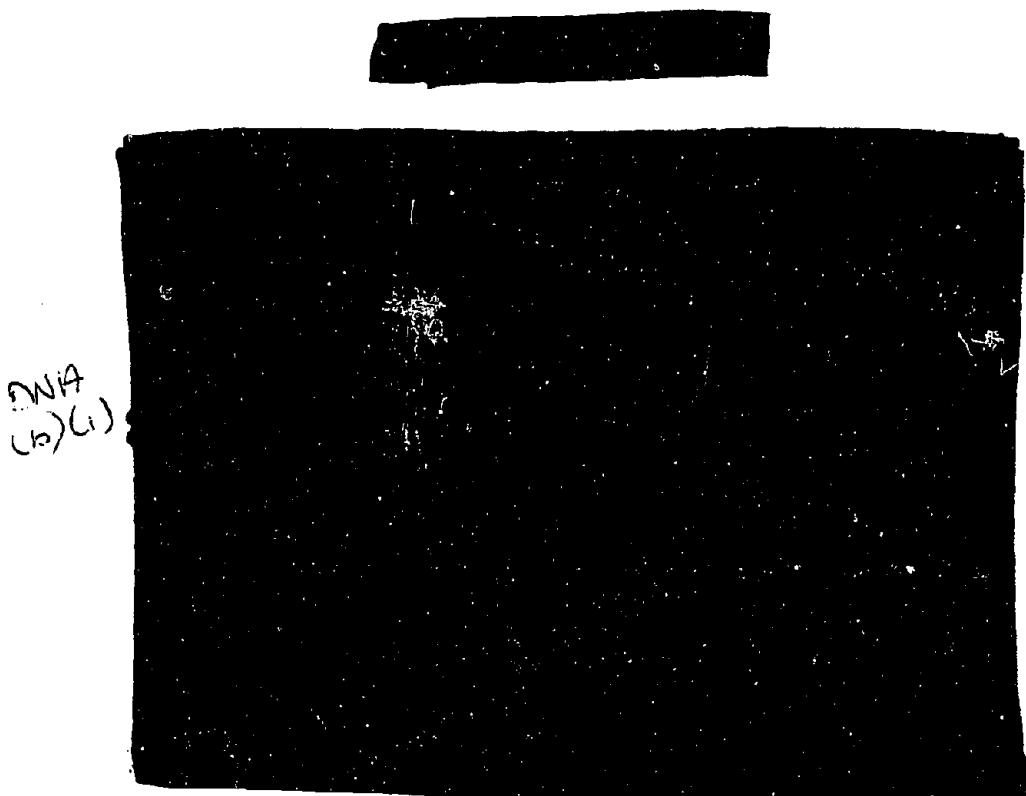


Figure 15-36. [REDACTED] Average Diameter of Stems Down, Comparison Between  
a Rain Forest and a Coniferous Forest, 1 kt

DNA  
(b) (1) [REDACTED]  
This distance is determined easily from photo reconnaissance, as are the debris zones described in Tables 15-3 and 15-4.

#### 15-4 Vehicle Movement

[REDACTED] The movement rates of various wheeled and tracked vehicles have been measured for both radial and circumferential traverses of various debris zones. Although quantitative data were obtained and can be used, correlations between vehicle movement and debris characteristics are incomplete and are not refined to the point of high reliability. Nevertheless, curves have been constructed that indicate in terms of the debris parameters (number of stem-feet per acre and diameter of debris) when a vehicle will not be able to move. These curves are presented in Fig-

ure 15-37 and 15-38 for radial movement from ground zero and circumferential movement, respectively. The general radial orientation of tree stems is significant in terms of movement, because selection of easier routes between stems is possible in some cases of radial movement, while all stems must be crossed in circumferential movement. The shaded areas on the graphs indicate debris characteristics where movement is difficult. The solid line indicates that movement is not possible. For example, from Figure 15-37, for debris characteristics of 10,000 stem-feet per acre with average diameters of 4, 6, and 8 inches, radial movement of wheeled vehicles would be possible, difficult, and not possible, respectively. Curves for wheeled vehicles are fairly well documented with data; however, the curves for the M113 and tank are not, because

DNA  
(b)(1)

Deleted

Figure 15-37. [REDACTED] Debris Characteristics Preventing Radial Movement of Vehicles [REDACTED]

2A.P.  
(b)(1)

Deleled

Figure 15-38. Debris Characteristics Preventing Circumferential Movement of Vehicles

these vehicles were slowed but not stopped by the debris zones in which they were tested. Tracked vehicles can climb onto the debris and mat it down after a number of passes, with the result that wheeled vehicles might pass, although this technique was not tested.

#### 15-5 Troop Movement

The effect of blowdown debris on the movement of troops is difficult to present quantitatively. Many factors other than the physical obstacle itself, such as visibility, leadership, size of force, mission, and what the troops are carrying are also influenced by the debris and indirectly affect movement. Movement of troops through a debris zone can be compared with moving through a thick jungle, although radial movement is generally easier than circumferential

movement. Branch debris in a broadleaf forest blowdown area adds difficulties, particularly in visibility, that are not as severe in coniferous forest debris. Troop trials were conducted on both TNT detonations previously described.

The troop tests conducted in conjunction with the rain forest detonation involved comparisons between preshot and postshot tests of day and night patrols, platoon exercises with a mortar squad, and tests with stretcher parties.

DNA  
(b)(1)

Deleled

[REDACTED]

Deleted

DNA  
(b)(6)

Deleted

Tests with a loaded two-man stretcher indicated that passage through blowdown debris was very difficult. The stretcher bearers' attention was diverted from the patient as a result of the need to concentrate on locating suitable footing. Consequently, the simulated casualty had a very rough trip and was frequently struck by debris. The conclusion drawn from this trial was that the probability for survival of a casualty with a severe wound would be significantly reduced by transit through blowdown debris. If the casualty survived the carriage, it is almost certain that he would experience a marked degree of secondary shock.

Troop trials conducted in the coniferous forest blowdown consisted of radial and circumferential platoon exercises, including a mortar squad, and a simulated casualty-moving test. Some movement rate data that were obtained are shown in Table 15-6.

Deleted

DNA  
(b)  
(c)

In the platoon attack trials, control problems were considerably eased in the blowdown area compared to the virgin forest, as a result of increased visibility.

Deleted

DNA  
(b)(1)

Deleted

DRA  
(b)(1)

Table 15-5 Comparison of Radial and Circumferential Movement Rates for Troops in a Rain Forest Blowdown Area, Scaled to a 1 kt Nuclear Explosion

Deleted

An administrative march also was conducted over a radial-circumferential-radial route. The circumferential portion was in the area of maximum blowdown debris.

A platoon night attack similar to the first circumferential trial described but in the opposite direction was performed. The platoon was organized as three attacking squad columns in line, except for the last 100 yards, where they de-

ployed as a skirmish line. The 2-to-1 ratio in time was observed once again.

The moving of a simulated casualty by two- and four-man stretcher bearer teams trav-

Table 15-6 Comparison of Circumferential Movement Rates for Troops in a Coniferous Forest Blowdown Area, Scaled to a 1 kt Nuclear Explosion

Deleted

DRA  
(b)(1)

eling circumferentially also was tested. Results were essentially the same as those from the rain forest trials.

#### 15-6 Predicting Effects on Movement

The results of the tests conducted after the two TNT detonations, together with the forest descriptions in Section I and Table 15-1, and the forest damage definitions in paragraph 15-2, have been combined in Table 15-7 for use

with Table 15-2 and Figures 15-1 through 15-34 to predict the ground distances at which movement will be affected to various degrees. The forest damage levels in Table 15-7 are restricted to Severe and Total, because Light and Moderate damage to forests have little influence on movement, except as a result of changes in visibility. Example problems will illustrate the use of Table 15-7 and will outline the limitations of the information presented.

Table 15-7 Influence of Forest Damage on the Movement of Troops and Vehicles

Deleted

DNP  
(b) (1)

**Problem 15-2 Calculation of the Distance at Which Movement Will Be Impaired**

Table 15-7 together with Table 15-2 and Figures 15-1 through 15-34 provide the information necessary to estimate the area within which movement will be affected to various degrees as a result of tree blowdown. The information contained in these tables and figures allows determination of the affected area for movement of troops or vehicles as a function of weapon yield and forest stand type.

**Example**

**Given:** A 2-Mt burst at 1,640 feet above a Type III forest stand.

**Find:** Will wheeled vehicles be stopped by the forest damage and at what maximum range?

DNA (b)(i)

**Problem 15-3 Estimation of Movement Difficulty**

DNA  
(b)(1)

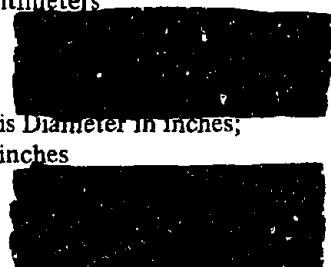


Therefore, it is possible to perform some evaluation of a forest using Figures 15-37 and 15-38 together with the forest characteristics. The forest characteristics required are tree density in trees per acre, average forest height in feet, average girth at breast height of the forest trees in either inches or centimeters, and tree type. The following parameters can then be determined:

Maximum Debris = (Forest density)  
(average height)

Average Debris Diameter in inches; girth, g,  
given in centimeters

DNA  
(b)(1)



Average Debris Diameter in inches;  
girth, g, in inches

DNA  
(b)(1)

With these two parameters, the potential obstacle of a forest can be estimated.

*Example*

*Given:* A coniferous forest with a density of 200 trees per acre and average height of 50 feet. Girth at breast height averages 33 inches.

*Find:* What obstacle could be formed if the forest were damaged by a nuclear burst.



DNA  
(b)(1)

### SECTION III THERMAL RADIATION

Under certain conditions, a nuclear weapon that is exploded over a forest or wildland area may cause fires. During the fire season, even when the burning potential (a measure of probable fire aggressiveness) is low, fires may spread. If fires are started in regions of sufficient fuel density when the burning potential is dangerously high, complete evacuation of personnel and equipment may be necessary. Organized control of the spread of the fire is virtually impossible until changes in weather or fuel availability reduce the burning potential.

#### 15-7 Ignitions

Wildland fuels are typically a mixture of thin and heavy fuel components. Often, the thinner fuels will establish the limiting radiant exposure that will be required to start fires in the mixture.

When fuels are dry, ignitions that have a reasonable chance of surviving the subsequent blast effects and of initiating fires that can represent a hazard to military personnel in the forest can be expected at quite low levels of radiant exposure. For example, broadleaf and coniferous litter (mixtures of fine grass, broken leaves and duff, and thin translucent broadleaf leaves) can be ignited by exposures of 2 to 3 cal/cm<sup>2</sup> from 1 kt low-altitude air burst, and heavier leaves (dead grass, conifer needles, and fallen, nearly opaque broadleaf leaves) can be ignited by exposures between 3 and 4 cal/cm<sup>2</sup>, which correspond to distances at which 2 to 3 psi peak overpressures might occur, provided the full free-field radiant exposure falls on these fuels. As will be discussed subsequently, the likelihood of the full free-field exposure reaching these fuels in a forest area is quite low. Radiant exposure values required to ignite materials increase with moisture content and will be larger for the longer dura-

tion pulses of larger-yield weapons. The increase caused by moisture being absorbed from the air at high relative humidities ordinarily will not be more than a factor of 2 to 3. Wet or green leaves, however, may be impossible to ignite and, if ignited, they will not participate in the development of a persistent fire. The live foliage of conifers and many shrubs ignited by fire in associated dead fuel, however, burn vigorously and would add significantly to the intensity of spreading fire. This foliage is often the significant factor determining whether or not a crown fire develops.

#### 15-8 Kindling Fuels

The majority of thin wildland fuels that serve as kindling material are typed into four classes as shown in Table 15-8. These classes correspond to different minimum exposures required for ignition. Since ignition generally occurs on surfaces that are most exposed to the atmosphere, ignition exposures are a function of relative humidity as shown in Figure 15-39. Fires may be blown out by the blast wave, depending on the time interval between ignition and arrival of the shock. Blowout is not expected to occur

Table 15-8 Classes of Thin Wildland Kindling Fuels (Arranged in Order of Decreasing Flammability)

Class	Description
I	Broadleaf and coniferous litter—mixture of fine grass, broken leaves and duff, and thin translucent broadleaf leaves.
II	Hardwood and softwood punk in various stages of decay.
III	Cured or dead grass.
IV	Conifer needles and thick, nearly opaque broadleaf leaves.

in overpressure regions below 5 psi or when the fuels are fully exposed. When fires are not blown

out, they generally increase in intensity as a result of the blast wind.

#### Problem 15-4 Calculation of the Requirements for Wildland Kindling Fuel Ignition

The curves of Figure 15-39 show the maximum radiant exposure as a function of relative humidity for ignition of wildland kindling fuels described in Table 15-8. The radiant exposures shown in Figure 15-39 apply to a 1 kiloton nuclear explosion.

**Scaling.** For yields other than 1 kt, scale as follows:

$$\frac{Q}{Q_1} = W^{1/6}$$

where  $Q_1$  is the radiant exposure for ignition of a particular class of wildland kindling fuel for 1 kt, and  $Q$  is the corresponding exposure for a yield of  $W$  kt.

##### **Example**

**Given:** A 40 kt weapon burst over a Class III wildland fuel when the relative humidity is 75 percent.

**Find:** The minimum radiant exposure required to ignite the fuel.

**Solution:** From Figure 15-39, the minimum radiant exposure for ignition of a Class III wildland fuel by a 1 kt explosion when the relative humidity is 75 percent is 4 cal/cm<sup>2</sup>.

**Answer:** The corresponding exposure for 40 kt is

$$Q = Q_1 W^{1/6} = 4 \times (40)^{1/6} = 6.3 \text{ cal/cm}^2$$

**Reliability:** Based upon observed results of limited full-scale tests and extensive laboratory experiments. The results are not considered reliable in the megaton range.

**Related Material:** See paragraphs 15-7, 15-8. For forest areas, see paragraphs 15-9 through 15-10. For determination of distances corresponding to a particular radiant exposure, see Chapter 3.

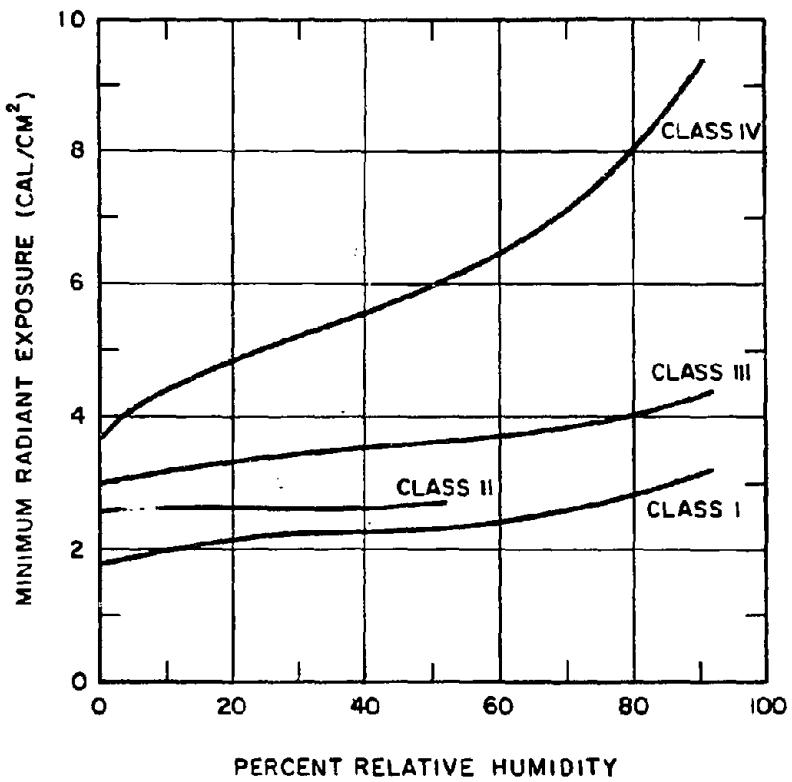


Figure 15-39. Minimum Radiant Exposures of Wildland Kindling Fuels by a 1 Kiloton Explosion

### 15-9 Thermal Radiation on Forests

Probably the largest uncertainty associated with thermal radiation on forested areas arises from a lack of information about the transmission of the radiation through the foliage and other obscuring features of forest stands for high-yield air bursts.

Methods for approximating the fraction of the free-field thermal radiation exposure that is transmitted by the forest environment will be considered here. The methods for calculating the free-field exposure are discussed in Chapter 3.

Both from the point of view of causing injury to exposed personnel and of starting fires, the primary interest is in assessing the exposure of the forest floor to thermal radiation from the nuclear fireball. The foliage making up the crowns of the trees, while it has a high probability of being exposed to the full free-field radiation environment from air bursts and may be severely dessicated, thermally (even explosively) decomposed, and, at high enough flux levels, flash ignited, is not likely to contribute to subsequent sustained fires. It may, however, materially reduce the exposure of the forest floor by generating quantities of smoke and steam as well as by direct shading.

Neglecting these thermally-induced, self-protective screening effects (noting that "scattering in" may effectively offset "scattering out"), an approximation to attenuation by trees and associated vegetation may be obtained by assuming that the attenuation is proportional to the extent of coverage of the field of view of the fireball by the elements of the forest canopy, i.e., that the exposure of any spot on the ground is roughly proportional to the apparent area of the fireball seen by that spot. Hence, height of burst and yield are important geometrical parameters that must be considered.\*

Size of openings and tree height are other important determinants of the susceptibility of a forest to ignition from an air burst. This indicates the need for on-the-ground or from-the-air appraisal of forests and presumed explosion situations. This can be done with reasonable accuracy and much more rapidly from aerial observation or photographs than from surface measurements.

DNA  
(b)(1)

DNA  
(b)(1)

)

Note that this assumes the source of thermal radiation to be above the tree tops. It will be seen in the subsequent discussion that thermal transmission is negligibly small for the low line-of-sight angles corresponding to burst heights less than tree heights, except perhaps for the short transmission paths that accompany bursts in the extreme low-end of the range of yields. Significant thermal exposures will never occur from these weapons, even in a sparsely vegetated forest environment, at distances corresponding to peak overpressures of 10 psi and less, because free-field exposure at these distances are only about  $4 \text{ cal/cm}^2$  and less.

DNA  
(b)(1)

DNA  
(b)(1)

DNA  
(b)(1)

Table 15-9 "Standard Northern European Forest" Data<sup>†</sup>



The "standard Northern European forest" represents a composite of the characteristics of the forests of northern Europe obtained by averaging the features of 10 different forest stands chosen as representative of type (pine woods, spruce and deciduous forests, and mixtures of these) and tree density (range of about 200 to 1,000 trees/acre).

Sites were chosen on flat terrain in Northern Europe having uniform density distributions and generally uniform tree height (not more than 15% variation for not less than 90% of the trees in the stand). This uniformity is typical of the managed forests of Europe along with a general absence of undergrowth. These characteristics are not common to unmanaged (natural) forests. There is no reason to expect that information derived from these studies are in any way applicable to tropical hardwood forests.

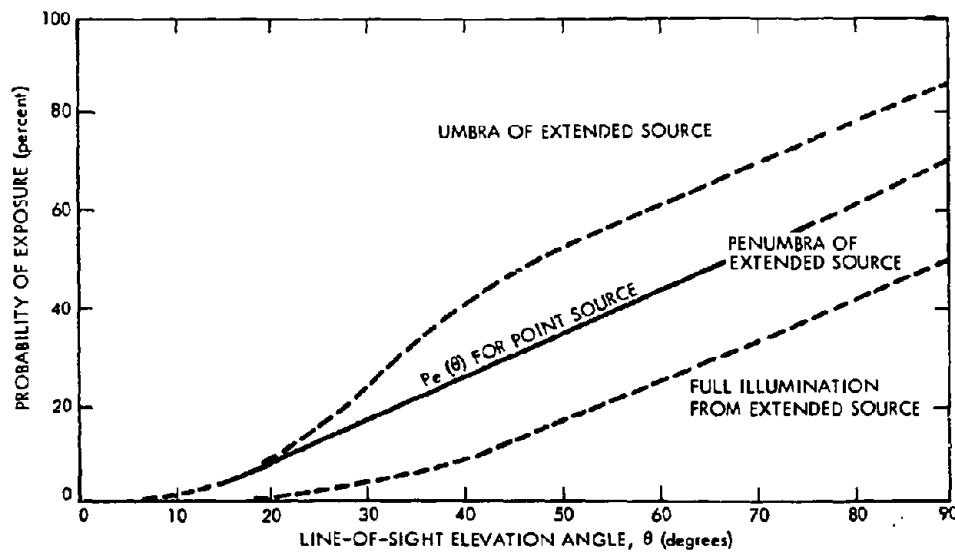


Figure 15-40. Probability of Exposure of the Forest Floor ("Standard Northern European Forest") as a Function of Elevation Angle; Examples of a Point Source and a Spherical Source Subtending an Angle of 10 Degrees

DNA(b)(1)

[REDACTED]

Obviously  $P_{ef}(\theta)$  functions, as illustrated by the "standard Northern European forest" in Figure 15-40, must depend on forest characteristics, notably tree density, with increased dispersion expected toward the larger angles of elevation. The data presently available do not reflect the degree of dispersion nor its dependence on forest characteristics adequately. Some idea of dispersion with tree density can be obtained from Figure 15-41, which displays the range of available results.

Deleted

Although the current data base is quite poor, particularly as it applies to unmanaged forests and tropical or temperate-broad-leaf forests, it can be inferred that direct thermal effects in the forest environment do not contribute substantially to damage and casualties at distances where blast effects are not extreme, except, perhaps, in the least densely populated stands (less than 50 to 100 trees per acre). For most tactical situations where survival of blast effects can be expected, radiant exposures would be much less than half the free field over most of the floor of forests having densities of a few hundred or more trees per acre, and probabilities of exposure to the full free-field level would be negligibly small.

#### 15-10 Forest Fire Ignition and Spread

Under certain conditions, the explosion of a nuclear weapon over a forest or wildland area may cause fires. During the fire season, even when the burning potential is low, fires may spread. If fires are started in regions of high-fuel density when the fire potential is high, complete evacuation of personnel and equipment may be necessary. Organized control may be impossible until changes occur in the weather or the fire runs out of fuel.

An important exception to kindling fuel exposure to the full free-field radiant environment occurs in unmanaged forests of the temperate and cold regions. Many of these forests contain an abundance of dead and frequently punky

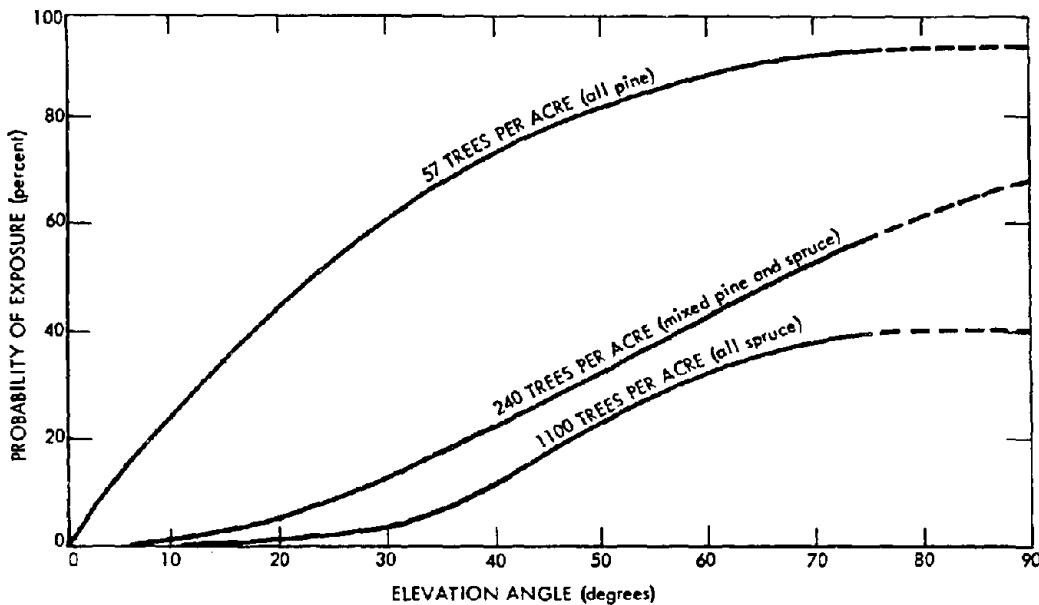


Figure 15-41. Probability of Exposure of Forest Floor for Different Levels of Tree Density

wood exposed at or above the general canopy level. Of the common forest fuels, wood punk is probably the most susceptible to ignition by the thermal pulse. Moreover, since ignition is by charring or glowing combustion, these fuels are less susceptible to extinction by the blast wave than those that ignite with flame. These punky fuels, often easily detached from the parent tree, may be carried downwind for considerable distances and dropped to the forest floor as live embers. More rapid decomposition of dead wood makes this a less likely phenomenon in the moist tropics.

As mentioned previously, the blast wave may extinguish fires at substantial overpressures, but the current state of the art does not permit quantitative evaluation of this phenomenon. On the other hand, at close-in distances where the blast wave arrives early during the thermal pulse (at times less than about  $8 t_{\max}$ ) sufficient radiant exposure may follow the blast wave to re-ignite

fuels and/or to ignite blast-created tinder.

Current interpretations of the qualitative effects of blast on the persistence of incipient fires are based largely on experiments where kindling fuels were anchored in place. Had these fuels been free to move with the blast, many of them would have been translated for considerable distances as effective firebrands. Fire spread following ignitions by these brands would be influenced significantly by the return flow through the negative blast phase of the blast wave.

The high degree of shading by tree crowns and stems for detonations at or below the canopy level often may be offset by scattering of burning debris ignited within the fireball. Many forest types contain large quantities of dead and rotten wood on and above the ground surface. If these materials are in flammable condition they may be expected to travel outward to the approximate limits of tree blowdown and provide plentiful ignition sources. Initial spread of fire from these

Table 15-10 Condition of Wildland Fuels During Fire Season

Fuel Type	Amount and Density of Fuel Required to Constitute a Fire Hazard	Condition During Fire Season
Grass or heath: Grassland; dry bracken ferns and other seasonal plants; dry regrowth in previously burned areas.	Uniform grass cover one-half ton or more per acre.	Vegetation nearly cured or dead.
Evergreen brush: Perennial evergreen shrubs and brush; chapparal; young evergreen growth.	75 percent or more covered.	15-25 percent by weight of leaves and associated twigs dead.
Deciduous broadleaf forest: Forest predominantly of trees such as oak, birch, maple, leaves of which die and fall every year.	Ground covered with more or less continuous layer of dead leaves.	Leaves off trees; ground vegetation dead or nonexistent.
Coniferous forest: Forest of evergreen pines, firs, spruces, etc.; generally the family of needle bearing trees.	Ground covered with more or less continuous layer of dead needles and twigs.	Needles and twigs dry enough to break easily when bent. Grass and other ground vegetation, if present, curing or dead.

sources would also respond to the inflow during the negative phase of the blast wave. Later behavior would depend on the degree of involvement of blowdown debris and the ambient weather.

Times of the year during which the fire hazard is apt to be high are referred to as fire seasons. These are determined principally by the annual rainfall-temperature pattern and the amount and kinds of vegetation associated with it. Fire seasons vary widely from place to place throughout the world. Conditions associated with fire seasons in some typical wildland fuels are shown in Table 15-10. The more difficult problem is that of obtaining and systematically appraising local forest flammability data within a fire season on a day-to-day basis for fire spread predictions. No one formula will fit all situations.

The main factors, aside from the fuels, that determine the fire hazard are: the nature of the terrain; the wind speed close to the ground; the relative humidity; and the precipitation history. Fuels seldom burn vigorously, regardless of wind conditions, when fuel moisture content exceeds about 16 percent. This corresponds to an equilibrium moisture content for a condition of 80 percent relative humidity. Rainfall of only a fraction of an inch will render most fuels temporarily nonflammable and may extinguish fires in thin fuels. The time required to restore the fire-danger condition may vary from hours to days depending on weather and soil conditions. Surface fuels in the interior of timber stands are exposed to reduced wind velocities; generally, these fuels retain their moisture as a result of

Table 15-11 Criteria of "No-Spread" of Fires

Fuel Type	Criteria
All forest fuels	Over 1 inch of snow on the ground at the nearest weather stations.
Grass	Relative humidity above 80 percent.
Brush or hardwoods	0.1 inch of precipitation or more within the past 7 days and: Wind 0-3 mph; relative humidity 60 percent or higher, or Wind 4-10 mph; relative humidity 75 percent or higher, or Wind 11-25 mph; relative humidity 85 percent or higher.
Conifer timber	1. One day or less since at least 0.25 inch of precipitation and: Wind 0-3 mph; relative humidity 50 percent higher, or Wind 4-10 mph; relative humidity 75 percent higher, or Wind 11-25 mph; relative humidity 85 percent or higher.  2. Two to three days since at least 0.25 inch of precipitation and: Wind 0-3 mph; relative humidity 60 percent or higher, or Wind 4-10 mph; relative humidity 80 percent or higher, or Wind 11-25 mph; relative humidity 90 percent or higher.  3. Four to five days since at least 0.25 inch of precipitation and wind 0-3 mph; relative humidity 80 percent or higher.  4. Six to seven days since at least 0.25 inch of precipitation and wind 0-3 mph; relative humidity 90 percent or higher.

shielding from the wind and shading from sunlight by the canopy. The spread or no-spread criteria are summarized in Table 15-11. This table lists the conditions under which fire would not be expected to spread.

The criteria of Table 15-11 have been compared to the records of 4,378 wildland fires. Of the fires for which "no spread" would be predicted, 97.8 percent did not spread; only 40 percent of the fires that were predicted to spread actually did spread (at a rate of 0.005 mph or

faster). This failure to spread often may be attributable to lack of fuel continuity around the point of origin.

The criteria of Table 15-11 are considered to be reliable for American forests and suitably conservative to assure a low level of hazard to friendly forces. On the other hand, the criteria are probably not overly conservative to predict conditions for which enemy forces may be denied forested areas because of fire whenever the local weather history and conditions at the time of

Table 15-12 [REDACTED] Fire-Out Criteria [REDACTED]

Fuel Type	Criteria
Grass	"No-spread" conditions, or measurable precipitation.
Brush or hardwoods	0.1 inch of precipitation or more, or "no-spread" conditions for the next 12-hour period.
Conifer timber	1. 0.5 inch of precipitation or more; 2. 0.25 to 0.5 inch of precipitation and "no-spread" conditions for the following two 12-hour periods; 3. "No-spread" conditions for eight consecutive 12-hour periods and measurable precipitation during any two 12-hour periods; 4. "No-spread" conditions for 14 consecutive 12-hour periods.

[REDACTED] detonation are known reliably, or whenever the initial fire is expected to be of substantial size.

[REDACTED] Weather conditions are subject to change, sometimes unpredictably, and fires that have been spreading may stop or go out. Conversely, fires that have not been spreading (other than on the microscale necessary to keep them dormant alive) may flare up quite suddenly and spread rapidly as a result of a change in the weather. Whenever this threat of weather change cannot be tolerated, it is necessary to choose conditions for the employment of nuclear weapons so that dormant fires will not persist for times that are long compared to reliable weather-forecast periods. The "fire-out" criteria in Table 15-12 provide guidelines for this purpose. These criteria are derived from opinions of experienced fire personnel and should not, therefore, be considered to be as reliable as the "no-spread" criteria.

[REDACTED] Under identical weather conditions, concentrations of heavy fuels are more hazardous than thin fuels, even though they tend to reduce wind speeds locally and do not respond as rapidly to changes in relative humidity. This results from the fact that trees and heavy limbs on the forest

floor may be ignited by an otherwise non-hazardous surface fire, and when heavy fuels are present near the borders of standing timber, the fire may travel into the tree crowns and spread from top to top even though ground fuel concentrations are low. Coniferous trees are most susceptible to crown fires. Hardwoods (deciduous trees) rarely, if ever, exhibit a true crown fire.

[REDACTED] Considerable information exists concerning rates of fire spread in American forests from historical records of major forest fires. Rates of spread rarely exceed 1 mile per hour except for brief periods of time during extreme burning conditions. Crown fires are capable of spreading at rapid rates, exceeding the rates of progress by men on foot attempting to out-run them. The high rate of progress of fire through crowns of trees probably results from the unimpeded wind-flow velocities above the forest canopy.

[REDACTED] Because of their potentially rapid rates of spread, crown fires represent a much higher level of hazard to personnel in forests than surface fires. Accordingly, it is desirable to be able to predict the occurrence of crown fires. Unfortunately, only qualitative criteria are available.

Table 15-13 [REDACTED] Burning Durations by Fuel Type [REDACTED]

Fuel Type	Violent Burning		Residual Burning		Total Burning Time
	Time (min)	Energy Release (percent)	Time (min)	Energy Release (percent)	
Grass	1.5	90	0.5	10	30 min
Light Brush (12 tons/acre)	2.	60	6.	40	16 hr
Medium Brush (25 tons/acre)	6.	50	24.	50	36 hr
Heavy Brush (40 tons/acre)	10.	40	70.	60	72 hr
Timber	24.	17	157.	83	7 days

[REDACTED] Surface fires exhibit brief "runs" at high speeds (a few miles per hour for several minutes, and a large fraction of a mile per hour for up to an hour or more), but average speeds over long periods of time range generally from 0.01 mile per hour to 0.5 mile per hour, with the most frequently noted values in the range of 0.1 to 0.5 mile per hour for 6- to 11-hour periods and in the range of 0.01 to 0.1 mile per hour for durations of 12 hours and more. These values are for American forests and should not be expected for managed forests (such as those of Europe) or tropical hardwood forests (such as those of some areas of Southeast Asia).

[REDACTED] An additional factor that affects the hazard of fire to military personnel and equip-

ment is the burning duration of forest fuels. Examples of burning durations for fuels that are typical of American wildlands are summarized in Table 15-13.

[REDACTED] Table 15-13 refers to natural fuels in their undisturbed states. Experience shows that the highest fire intensities and fuel consumptions occur in the areas of greatest fuel accumulation. This fact has two implications with respect to nuclear detonations: if burning conditions are favorable, incipient fires from the thermal pulse falling on areas covered with a large amount of blast debris may build up rapidly; the blast debris accumulation may subsequently desiccate sufficiently to be a prime target for ignition by any means, either friendly or enemy.

## BIBLIOGRAPHY

Bowe, T. W., et al., *Operation Blowdown, Scientific Observations and Analysis*, Commonwealth of Australia, July 1964, Report No. DSL 273 (3 volumes).

Chandler, C. C., et al., *Prediction of Fire Spread Following Nuclear Explosions*, Pacific Southwest Forest and Range Experiment Station, Berkeley, California, 1963, U.S. Forest Service Research Paper PSW-5.

Fons, W. L., F. M. Sauer, and W. Y. Pong, *Blast Effects on Forest Stands by Nuclear Weapons*, U.S. Department of Agriculture Forest Services, December 1957, AFSWP 971.

Kerr, J. W., et al., *Nuclear Weapons Effects in a Forest Environment—Thermal and Fire Panel N-2*, TTCP, N2:TR 2-70, DASIAC Special Report No. 112, March 1971

Martin, S. and S. Holton, *Preliminary Computer Program for Calculating Ignition Ranges*, U.S. Naval Radiological Defense Laboratory, San Francisco, California, June 1965, USNRDL TR 866.

*Nuclear Weapons Effects in a Forest Environment—Blowdown*, Panel N-2, TTCP, August 1969, N2:TR 1-69, DASIAC Special Report No. 73.

Sauer, F. M., *Forest Blowdown in Comparison of the Results of High Explosive Experiments and Prediction Experiments*, Poulter Laboratory, Stanford Research Institute, Menlo Park, California, July 1969, DASA 2300.

Zacor, J., et al., *Prediction and Significance of Forest Damage from a 50-Ton HE Surface Burst*, Project 7.01 Operation Distant Plane, Event 4, URS Research Company, June 1967, DASA 2065.

**AD-A955 400**

**Chapter 16  
DAMAGE TO MISSILES**

**DTIC  
ELECTE  
F 2 MAR 1989  
S E D**

Missile systems are subject to damage by essentially all of the phenomena described separately in Chapters 2 through 8. Part I, of this manual, i.e., all or part of the system may be damaged by blast and shock (Chapter 2), by thermal radiation (Chapter 3), by X-ray radiation (Chapter 4), by nuclear radiation (Chapter 5) mainly in the form of transient radiation effects on electronics (TREE) phenomena (Chapter 6), or by the electromagnetic pulse (EMP (Chapter 7)). Communications and/or radar subsystems are also subject to degradation of their propagation characteristics as described in Chapter 8.

The damage that might result from several of the phenomena listed above is so dependent on specific system design that general methods for predicting specific missile system response cannot be provided. These phenomena include X-ray radiation, TREE, and EMP. Consequently, general descriptions of the damage mechanisms associated with these phenomena, applicable to missiles as well as other systems, are provided in Sections V, VII, and VIII, respectively, of Chapter 9. Additionally, some ambient nuclear radiation levels for "sure safe" and "sure kill" of missiles are given in Table 14-11, Chapter 14. Chapter 17 discusses the signal degradation of communications and radar systems. No further discussion of the damage or degradation from these phenomena is included herein.

This chapter is divided into two sections. Section I describes blast damage to tactical missiles. Section II describes the response of strategic systems to blast and thermal phenomena. Where appropriate, separate discussions are pro-

vided in Section II for antimissile systems (commonly called ABM) and reentry vehicles (RV's).

**SECTION I**

**BLAST DAMAGE TO  
TACTICAL MISSILE SYSTEMS**

The effects of air blast on three specific sample systems, the SERGEANT, the LANCE, and the HAWK, are described in this section. The vulnerability analysis of these missiles and their support equipment is intended to provide information from which the probable effects of air blast on other tactical missile systems may be estimated. An example of such an estimation for the HONEST JOHN missile is also provided. Outline drawings of the sample systems are shown in Figure 16-1 for comparison purposes.

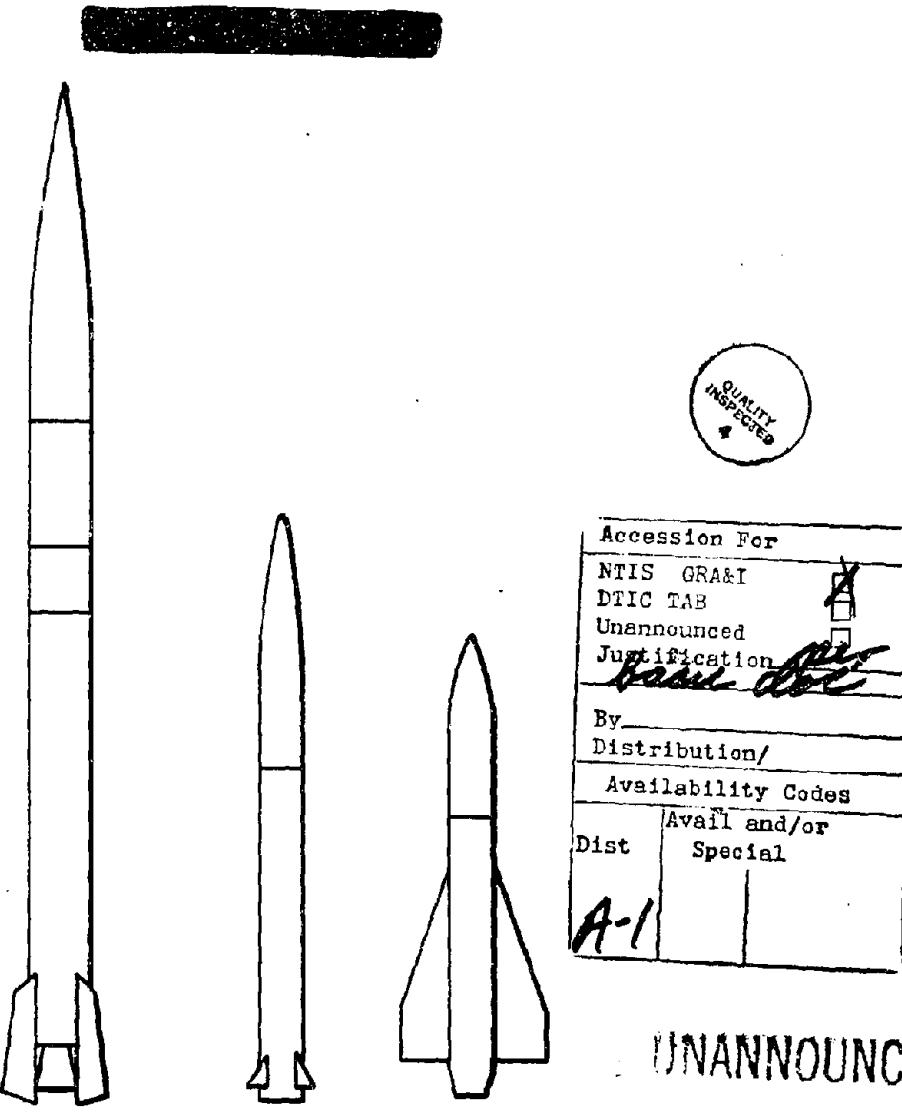
In the case of each system, it is assumed that the system may be attacked from the time that the missiles are in stockpile until the missile warhead is detonated over the target. During any phase of this stockpile-to-target sequence, the system vulnerability is determined by the most susceptible component that is essential to completion of the mission. The vulnerability of all critical components is tabulated for each system. Vulnerability is expressed in terms of peak overpressure, assuming that the blast wave is from a contact surface burst with a yield between 1 kt and 300 kt. A range of values is given for the overpressure vulnerabilities, e.g., 12 to 19 psi. These numbers mean that either 12 psi from a 300 kt burst or 19 psi from a 1 kt burst is estimated to be sufficient to render the system component incapable of performing its necessary functions to complete the mission. Each vulnera-

**DISTRIBUTION STATEMENT A**

Approved for public release  
Distribution Unlimited

**16-1**

**89 3 02 034**



UNANNOUNCED

Missile	SERGEANT	LANCE	HAWK
Length ~ Ft.	34½	20	16
Diameter ~ In.	31	22	14
Weight ~ Lbs.	10,000	3100	1300
Application	Surface to Surface	Surface to Surface	Surface to Air
Range	46 to 137 NM.	5 to 75 NM.	to [REDACTED] Altitude with Horizontal Range
Warhead Section	1500 Lbs Nuclear	1000 Lbs Nuclear	73 Lbs. H.E.

AMC  
 (U-X)  
 (A)(1)

Figure 16-1. [REDACTED] Missile Configurations, SERGEANT, LANCE, and HAWK [REDACTED]

ability level is also shown in the form of a number curve, which allows critical values of range and overpressure to be determined as a function of weapon yield.

Many circumstances alter the vulnerability threshold of specific system components. For example, a truck that is carrying a missile to the launch site is less likely to be overturned by a blast wave if it is facing the burst than if it is hit from the side (see Table 14-5, Chapter 14). The velocity and orientation of a missile in flight both are important. If the terrain is conducive to the formation of a precursor, the truck may be subjected to a greatly enhanced dynamic pressure impulse, capable of overturning it much more easily than if it were exposed to the same burst at the same range under near-ideal conditions (paragraph 14-2, Chapter 14). The overpressure and dynamic pressure at the target depend on height of burst as well as distance. In order to reduce vulnerability data to a manageable set of numbers, the following conditions are assumed for the analysis in this section.

- The orientation of the system component with respect to the blast wave is such that the probability of serious damage is a maximum.
- Near-ideal surface conditions exist (no precursor).
- The blast wave is produced by a contact surface burst.

If radically different conditions are expected, appropriate changes in vulnerability levels must be made. In the case of a burst that produces a precursor, the dynamic pressure would be enhanced, and drag sensitive targets, i.e., those susceptible to toppling or overturning, probably would be damaged at an overpressure lower than predicted. Also, an air burst could produce a double shock on a target located in the regular reflection region; again this could lead to significant target damage at an overpressure lower than

predicted. Thus, the numbers given should only be used as guides to the assessment of system blast damage.

Damage to targets that are primarily drag sensitive is determined by the dynamic pressure level. However, for near-ideal surface conditions, there is a known correspondence between peak overpressure and peak dynamic pressure (although the pulse durations can be somewhat different). Therefore, for the purpose of this chapter, all damage levels are expressed as overpressure levels, including the damage levels that apply to drag sensitive targets.

SERGEANT WEAPON  
SYSTEM

## 16-1 Description of the SERGEANT Weapon System

The SERGEANT weapon system is a second generation surface-to-surface missile system capable of being used under all terrain and weather conditions. Major items of the system are:

- **SERGEANT** missile M15 and containers. The SERGEANT missile body consists of four major assemblies:  
(1) rocket motor M53; (2) guidance section M38; (3) warhead section M65; and (4) control surface assemblies M58. Figure 16-1 shows a drawing of the missile. Figure 16-2 shows the missile parts in containers and ready for transport.
- **Four-wheel, semitrailer mounted guided missile launching station M504.** Figure 16-3 shows this unit in firing position. One component, the launching station firing set, is shown in more detail in Figure 16-4.
- **Four-wheel, 6 ton, low-bed semitrailer M527.**
- **Organizational Maintenance Test Station (OMTS) AN/MSM-35.** This trailer housed

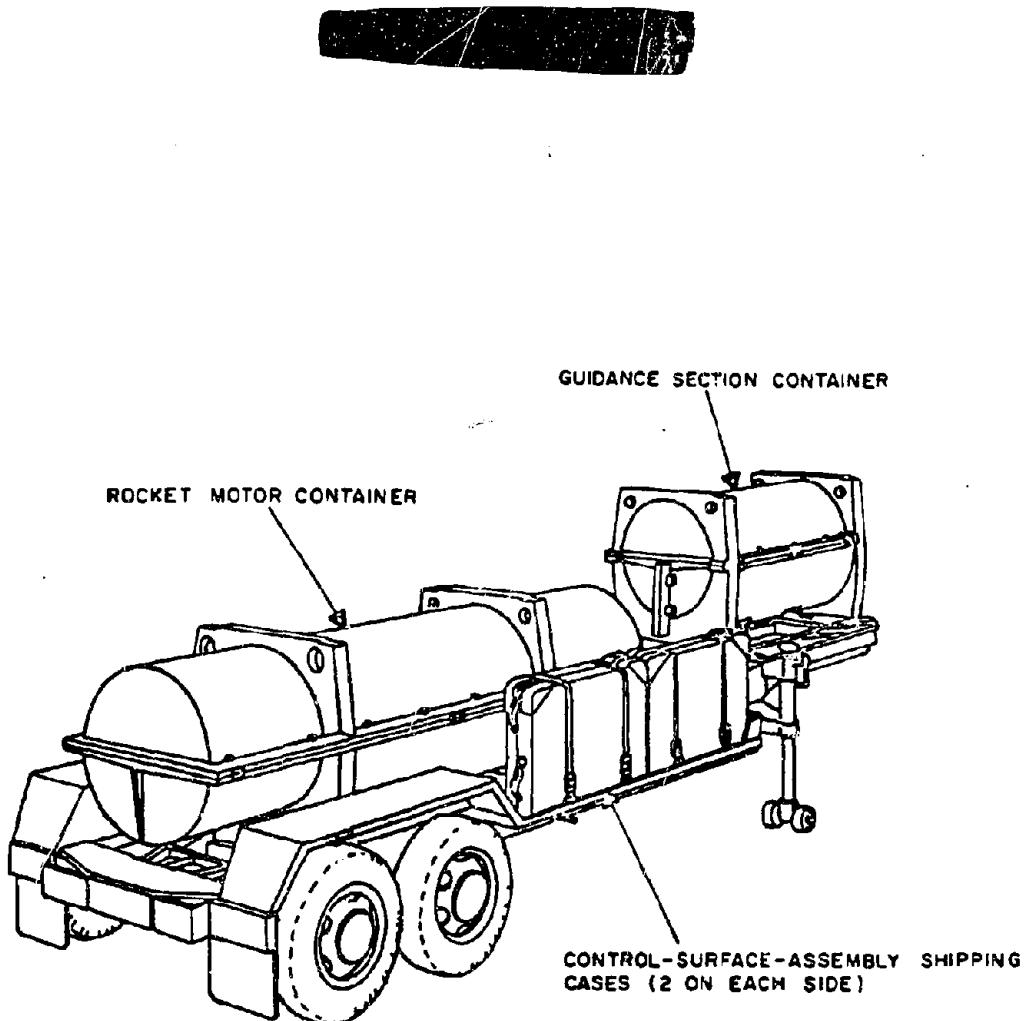


Figure 16-2. █ SERGEANT System, Semicar Transporter  
with Missile Section Containers █

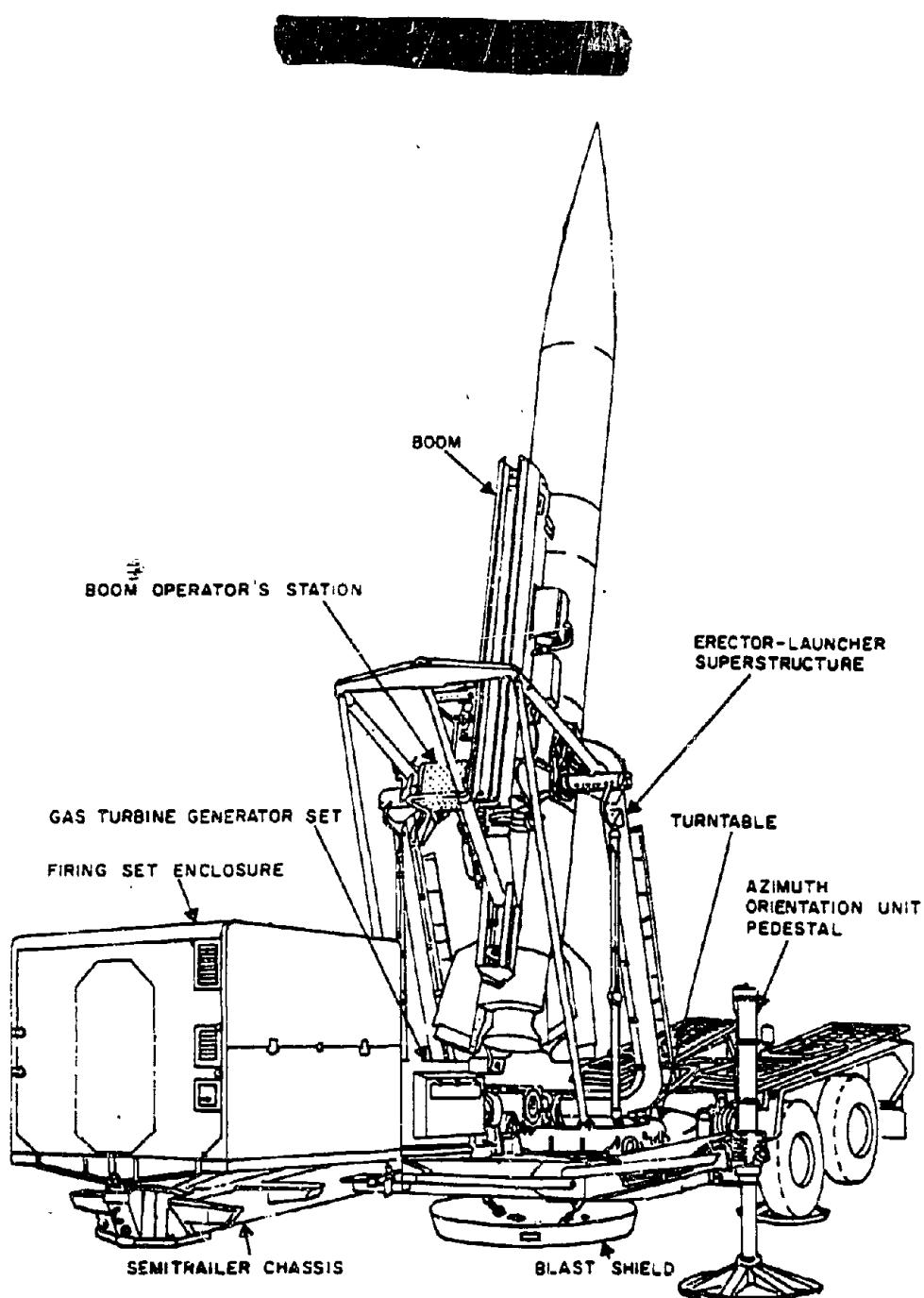


Figure 16-3. SERGEANT System, Launching Station  
with Missile in Firing Position

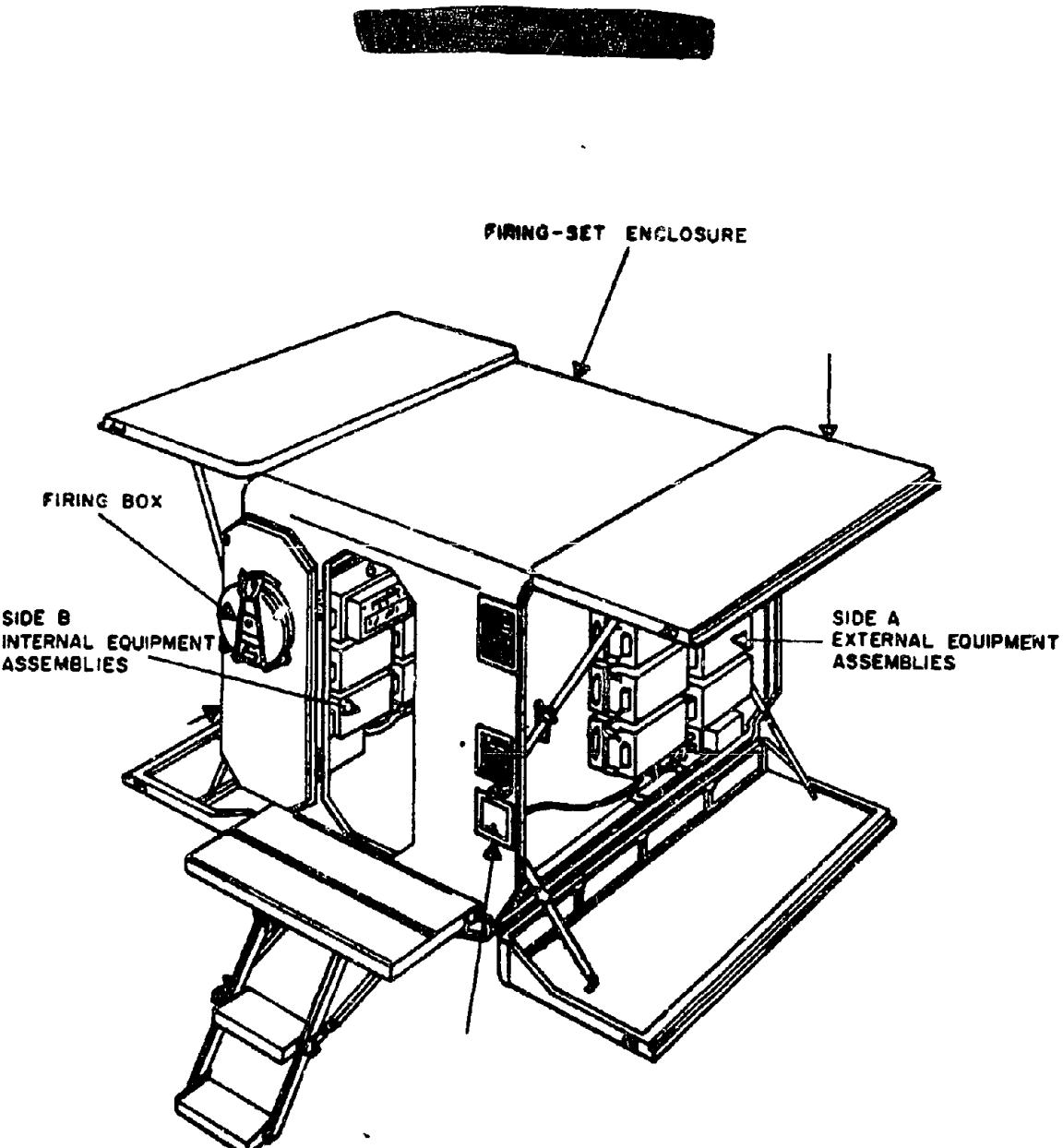


Figure 16-4. SERGEANT System, Launching  
Station Firing Set

[REDACTED]  
[REDACTED]  
unit, shown in Figure 16-5, is used for pre-launch testing and replacement of defective assemblies.

- *Field Maintenance Test Station (FMTS) AN/MSM-36.* This unit is similar to the OMTS. It can be used to perform many of the functions of the OMTS, and it is also used in situations that require more extensive testing and repair work than normally is done by the OMTS.

- *Warhead Section Container*
- *Truck, M35*

In addition to the equipment listed above, an M55 cargo truck is used to transport the rocket motor when the M527 is not available.

## 16-2 Vulnerability Levels of the SERGEANT Missile System

[REDACTED] The vulnerability levels of the various components of the SERGEANT missile system are shown in Table 16-1.

[REDACTED] The estimated vulnerability levels of the system in its various operational phases are described below. The most likely damage modes are also described.

- *Missiles in Containers at Storage Site (SERGEANT).* Figure 16-2 shows the type of containers used to store missile parts. The warhead section container, which is slightly longer than the guidance section container, is not shown.

DNA  
(A)(1)

[REDACTED]

- *Missiles in Containers in Transit (SERGEANT).* Since the transport vehicles afford partial protection for the containers, the vulnerability estimates were based on the pressure levels required to overturn the more vulnerable vehicle.

DNA  
(A)(1)

[REDACTED]

- *Equipment and Missile at the Firing Site (SERGEANT).*

DNA  
(A)(1)

[REDACTED]

- *Missile in Flight (SERGEANT).*

DNA  
(A)(1)

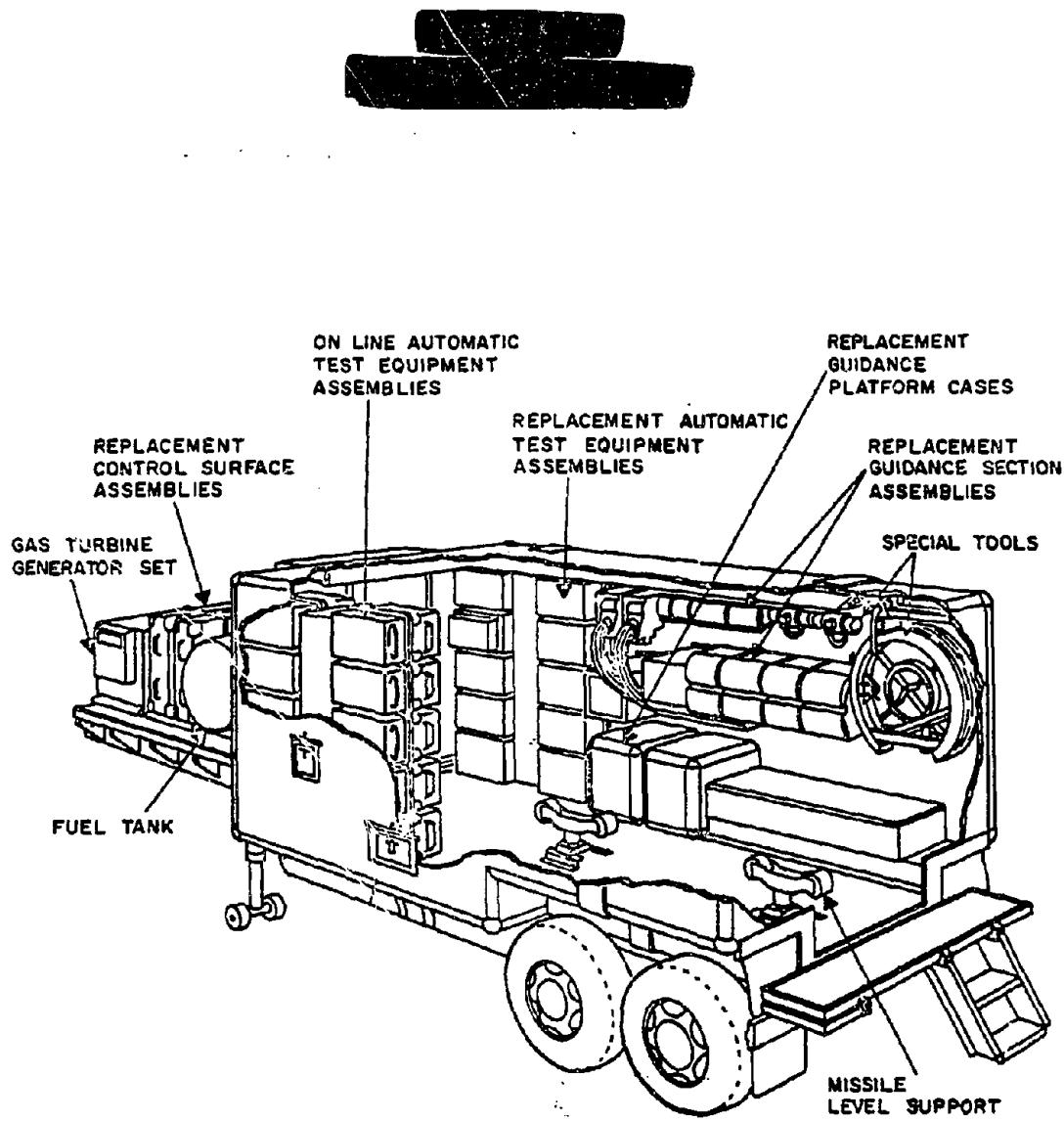


Figure 16-5. SERGEANT System, Organizational Maintenance Test Station (OMTS)

Table 16-1. [REDACTED] SERGEANT, Characteristics and Damage Levels for System Components [REDACTED]

USANC  
(4)(1)

Deletions

DNA  
(4)(3)  
(4)(1)

USANCA  
(G)(1)

DNA  
(G)(3)

The blast vulnerability of the principal components of the SERGEANT missile system can be determined by reference to Table 16-1 and Figure 16-6; the figure provides curves that allow the determination of pressure levels and distances for damage corresponding to various weapon yields. Table 16-2 shows a summary of the blast vulnerability of the susceptible subsystems in the various configurations of the SERGEANT missile system.

### 16-3 Reliability of SERGEANT Vulnerability Estimates

DNA  
(G)(1)

Table 16-2. Blast Vulnerability Summary, SERGEANT Missile System

Deleted

DNA  
(G)(1)  
(A)†(3)

USANCA  
(G)(1)

[REDACTED]  
[REDACTED]

[REDACTED]

Figure 16-6. [REDACTED] SERGEANT, Major Item Blast Vulnerability [REDACTED]

16-11

[REDACTED]

[REDACTED]

DNA  
(4)(1)

DNA  
(4)(3)

The sources of SERGEANT system damage data for the major items considered are:

DNA  
(4)(1)

## LANCE WEAPON SYSTEM

### 16-4 Description of the LANCE Weapon System

The LANCE is a surface-to-surface missile for general field artillery fire support of Army Divisions. The five major items of the LANCE system are:

- LANCE Missile Body, shown in Figure 16-1.
- Self-propelled Launcher (SPL), shown in Figure 16-7.
- Transporter Loader (TL), shown in Figure 16-7.
- Lightweight Launcher (LWL), shown in Figure 16-7.
- Other Ground Support Equipment, shown in Figure 16-8 (contact Support Test Set is not shown).

DNA  
(4)(1)

### 16-5 Vulnerability Levels for the LANCE Missile System

Blast vulnerability levels for the components of the LANCE missile system are shown in Table 16-3. Based on these values, the

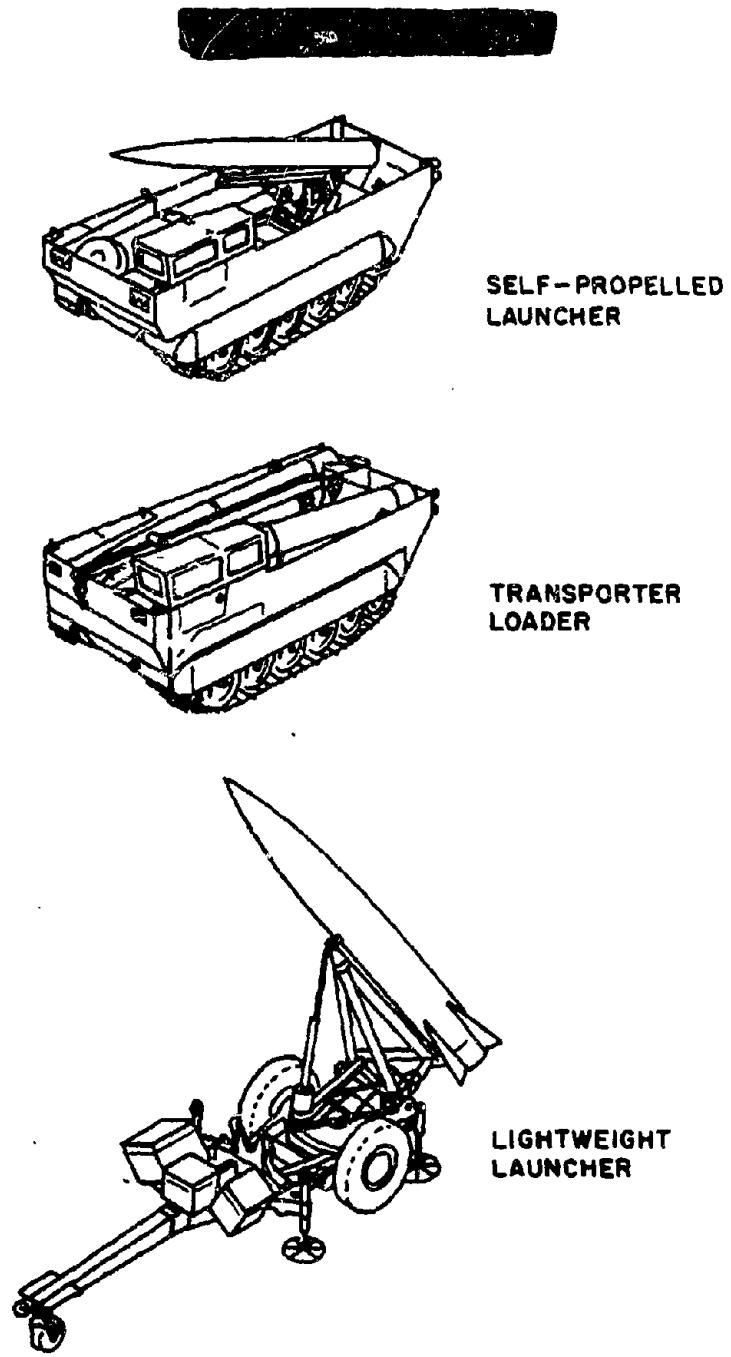
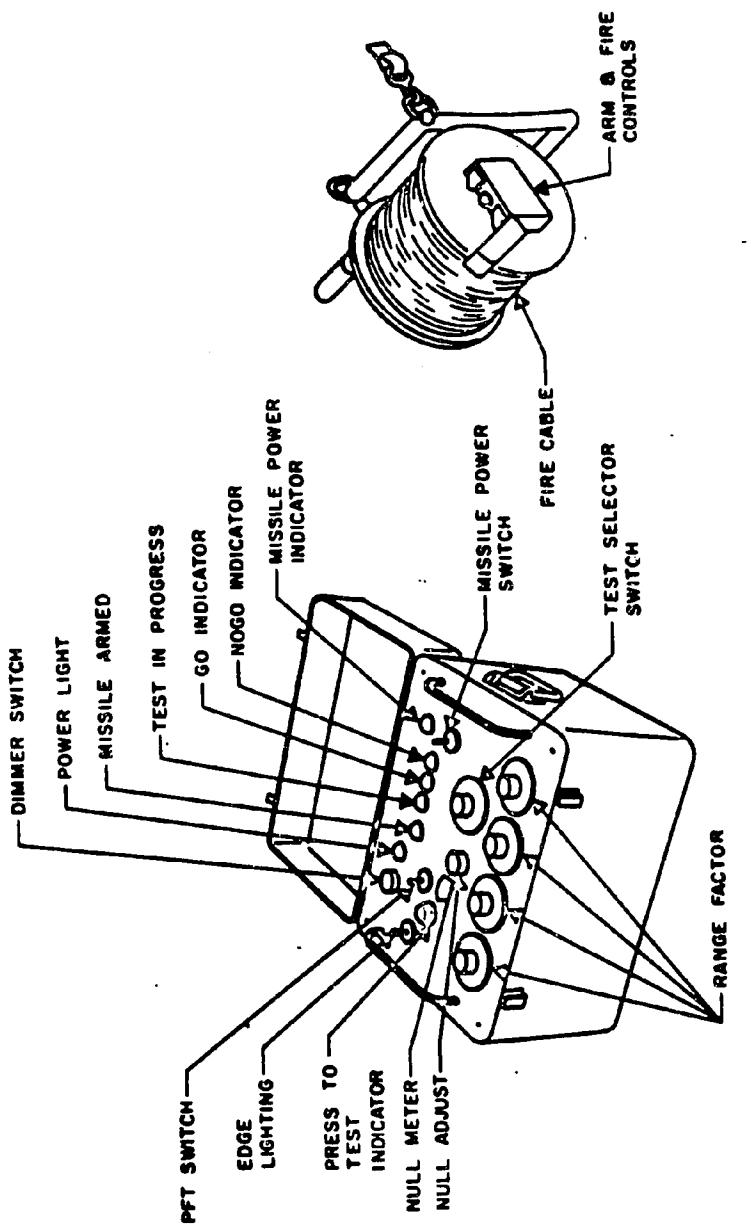


Figure 16-7. [REDACTED] LANCE System, Primary Units of  
the Missile System [REDACTED]



Firing Device (FD)

Missile Test Set (MTS)

Figure 16-8. [REDACTED] LANCE System, Prefire Tester and Fire Pack [REDACTED]

Table 18-3. [REDACTED] LANCE, Characteristics and Damage Levels for System Components [REDACTED]

DNA  
(f)(1);  
+  
(f)(3),

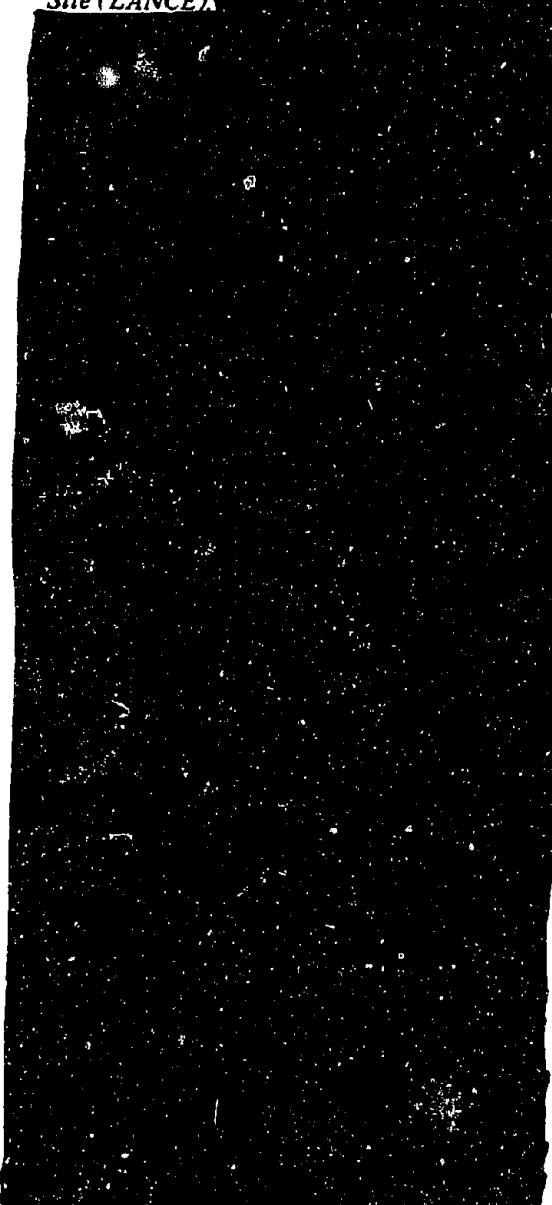
459  
NC  
(f)(1)

Deleted

susceptibility levels of the LANCE missile system during its various operational phases are estimated to be as follows:

- Missile Parts in Containers at the Storage Site (LANCE).

DNA  
(U)(1)



USANCA  
(U)(1)

AMC  
USAMICOM  
(U)(1)

DNA  
(U)(1)

USANCA  
(U)(1)

- Missiles in Containers in Transit (LANCE).

DNA  
(U)(1)

USANCA  
(U)(1)



AMC/IDA  
(~~U~~)(1)

DNA  
(~~U~~)(1)

USA/DOA  
(~~U~~X1)

- *Missile System During Checkout, Prelaunch Phase, and Launching (LANCE).*

DNA  
(~~U~~)(1)

- *Missile in Flight (LANCE).*

DNA  
(~~U~~)(3)

AMC/IDA  
(~~U~~X1)

USA/DOA  
(~~U~~X1)

The blast vulnerability of the principal configurations of the LANCE missile system can

be obtained from Table 16-3 and Figure 16-9; the figure includes curves from which the pressure levels for damage corresponding to various weapon yields and ranges may be obtained. Table 16-4 shows a summary of the blast vulnerability of the susceptible subsystems in the various configurations of the LANCE missile system.

#### 16-6 Reliability of LANCE Vulnerability Estimates

The source of the LANCE system damage data for the major items considered are:

DNA  
(~~U~~)

AMC/  
(~~U~~X1)

DNA  
(f)(3)

**Deleted**

Figure 16-9. [REDACTED] DANCE, Major Item Blast Vulnerability [REDACTED]

16-18

DNA (L-X3)  
DNA (L-Y1)  
DNA (L-Z1)

Table 16-4. Blast Vulnerability Summary, LANCE Missile System

Deleted

LANCE  
(L-X1)

AMC/LDA  
DNA (L-Y1)  
(L)(1)

These data were used for the missile structure vulnerability.

DNA  
(L)(1)

### HAWK WEAPON SYSTEM

#### 16-7 Description of the HAWK Weapon System

The HAWK is a surface-to-air, supersonic air defense system, designed to detect and identify airborne targets by means of radar, and to intercept and destroy those designated as hostile

with homing guidance missiles.

DNA (L-X)  
The major items of the HAWK system are:

- HAWK Missile Body, shown in Figure 16-1.
- Missile Loader, shown in Figure 16-10.
- Missile Launcher, shown in Figure 16-10.
- Assault Fire Command Console (AFCC) or Battery Control Central (BCC), shown in Figure 16-10.
- Radar Units, including
  - (1) Range-only Radar (ROR), shown in Figure 16-11.
  - (2) Pulse Acquisition Radar (PAR), shown in Figure 16-11.
  - (3) CW Acquisition Radar (CWAR), shown in Figure 16-11.

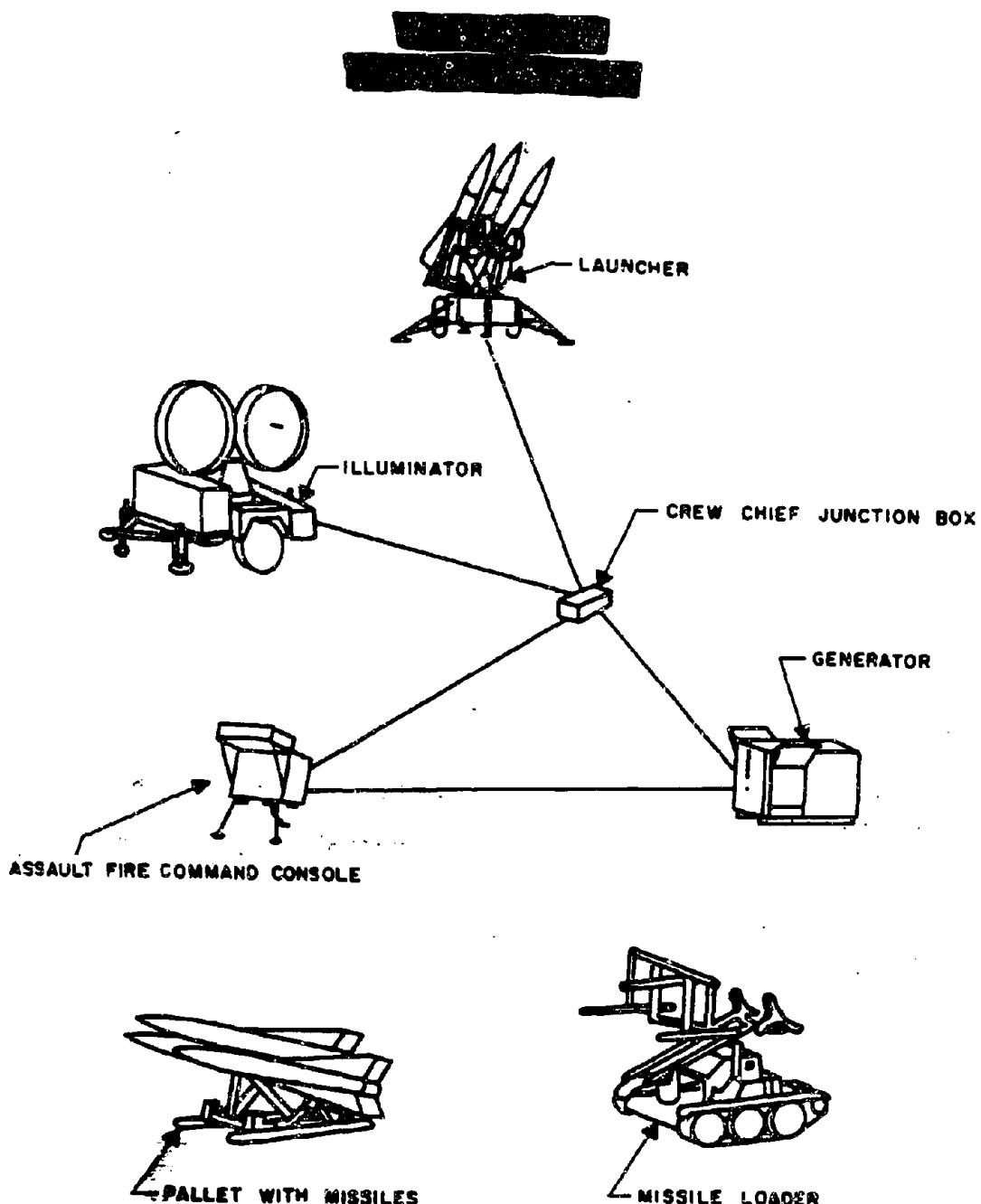


Figure 16-10. HAWK System, Basic Assault  
 Firing Unit

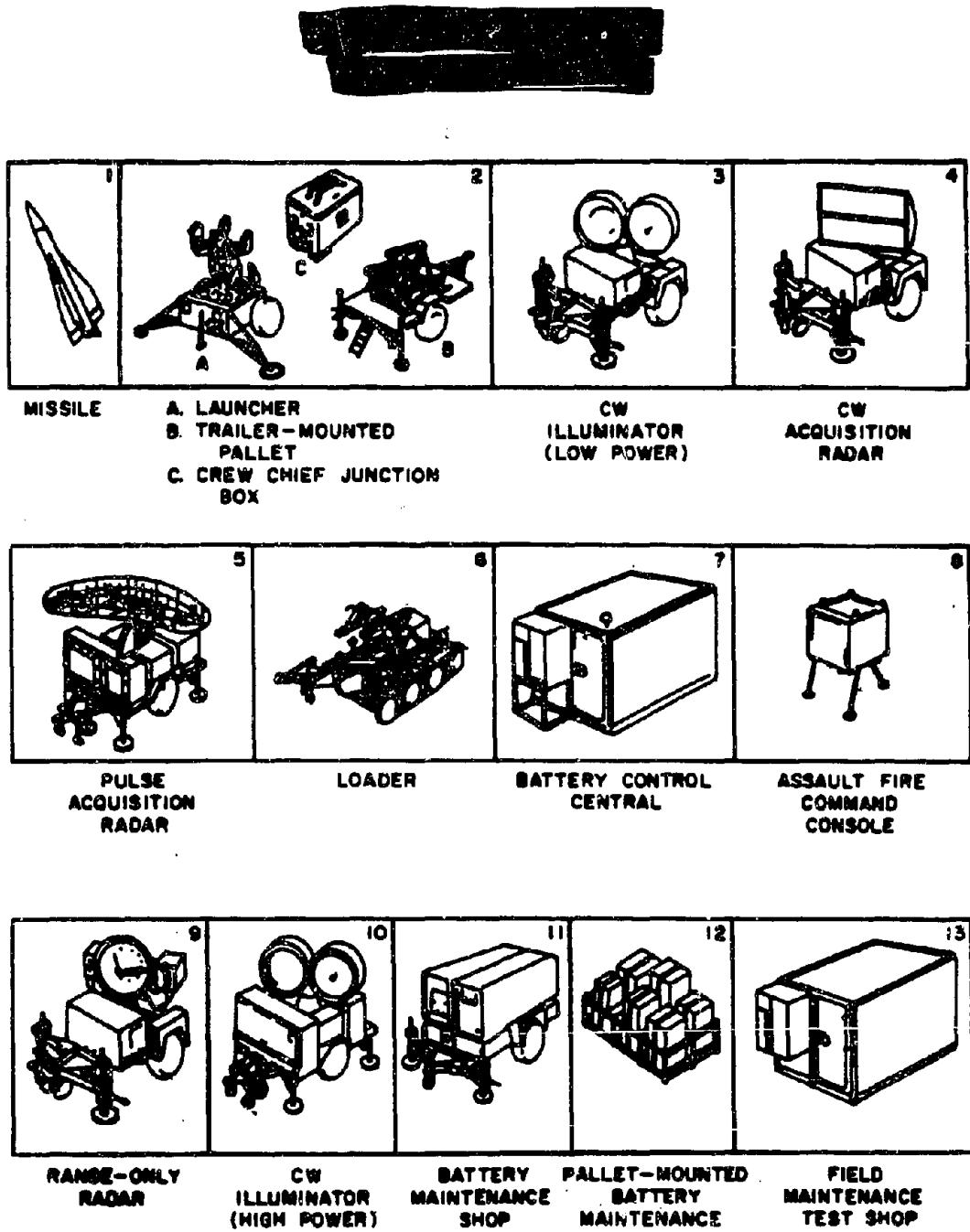


Figure 16-11. HAWK System, Auxiliary Components

Table 16-5. [REDACTED] HAWK, Characteristics and Damage Levels for System Components [REDACTED]

DND  
(X)(1)

USANCA  
(X)(1)

**Deleted**

(4) CW Illumination Radar (CWIR), shown in Figure 16-10.

Structurally, the missile body consists of four major sections: the warhead section; guidance components; rocket motor; and surface controls.

#### 16-8 Vulnerability Levels for the HAWK Missile System

Blast vulnerability levels for the components of the HAWK missile system are shown in Table 16-5. Based on these values, the susceptibility levels of the HAWK missile system during its various operational phases are estimated to be as follows:

- *Missile Parts in Containers at Storage Site (HAWK).*

DNA  
(4)(i)

USANCA  
(b)(1)

DNA  
(b)(1)

- *Missile System During Checkout, Pre-launch, and Launch (HAWK).*

DNA  
(b)(1)

WARC  
(b)(1)

DNA  
(b)(1)

WARC  
(b)(1)

DNA  
(G)(1)

USA/NSA  
(G)(1)

• *Missile in Flight (HAWK).*

DNA  
(G)(1)  
USA/NSA  
(G)(1)

The blast vulnerability of the principal configurations of the HAWK missile system can be obtained from Table 16-5 and Figure 16-12; the figure includes curves from which pressure levels for damage corresponding to various weapon yields and ranges may be obtained. Table 16-6 shows a summary of the blast vulnerability

of the susceptible subsystems in the various configurations of the HAWK missile system.

16-9 Reliability of HAWK  
Vulnerability Estimates

The sources of the HAWK system damage data for the major items considered are:

DNA  
(G)(1)

Table 16-6. Blast Vulnerability Summary, HAWK Missile System

Deleted

[REDACTED]

DNA  
K-YI

4 SANCH  
(GYN)

**Deleted**

Figure 16-12. [REDACTED] HAWK, Major Item Blast Vulnerability [REDACTED]

DNA  
(X1)



#### SAMPLE PROBLEM: AIR BLAST DAMAGE TO A TACTICAL MISSILE SYSTEM

The material presented above concerning the SERGEANT, LANCE, and HAWK weapon systems is used to estimate the blast vulnerability of the HONEST JOHN weapon system as an illustration of the methods by which the vulnerability data may be applied.

#### 16-10 Description of the HONEST JOHN System

The HONEST JOHN is a 762 mm, surface-to-surface, field artillery rocket designed to deliver warheads, weighing between 1,000

and 1,500 pounds, at horizontal ranges up to about 26 miles. It uses solid propellant, and it follows a ballistic trajectory after firing (no guidance).

The HONEST JOHN system is mobile by both ground and air transport. The principal units of the system are the following:

- *Complete rocket.* The rocket includes a warhead section, motor assembly, and fins, for which containers are provided (see Figure 16-13).
- *Launcher, truck-or trailer-mounted.* The launcher includes the launching beam assembly, elevating and traverse mechanisms, and electrical controls (see Figures 16-14 and 16-15).
- *Other ground support equipment.* A wrecker, transporter trailer, generator, motor and warhead cradles, and handling beam make up the ground support equipment (see Figure 16-16).

Table 16-7 lists the weight and size of the various HONEST JOHN components. The principal operational phases can be listed as follows:

- Storage at Storage Site,

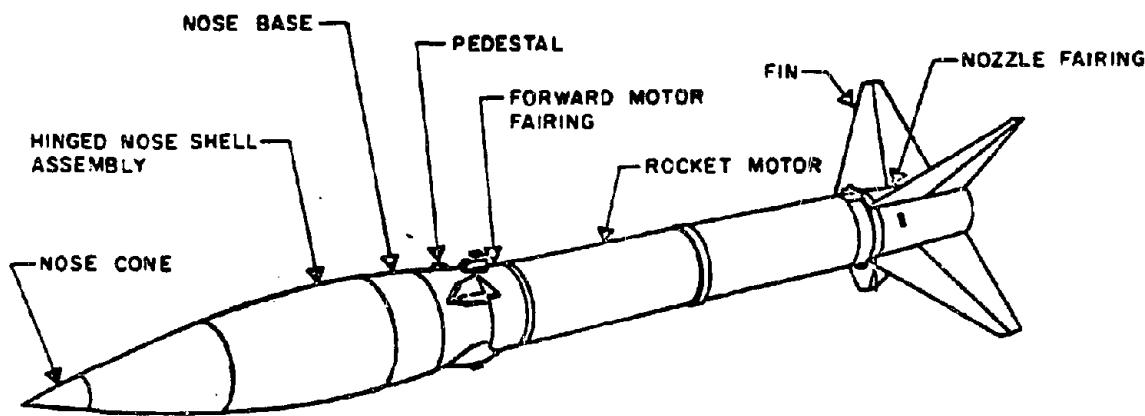


Figure 16-13. HONEST JOHN, Major Components of Rocket

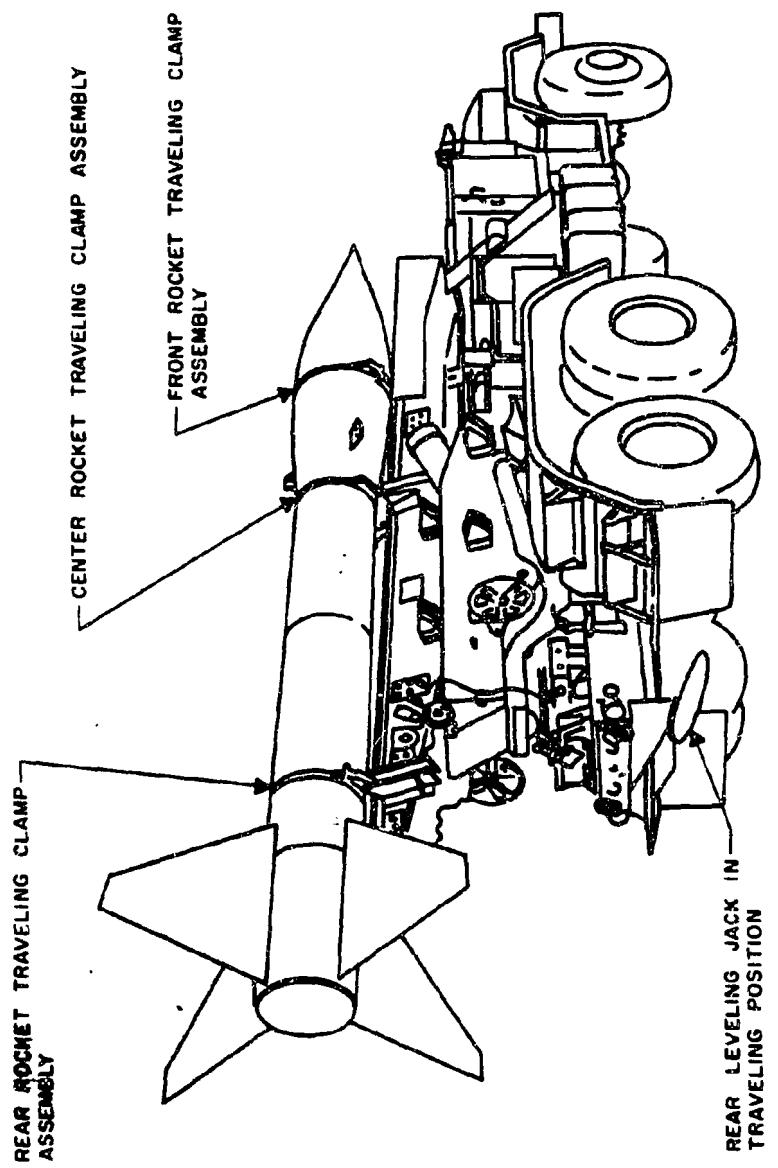


Figure 16-14. HONEST JOHN, Truck-Mounted Rocket Launcher  
in Traveling Position

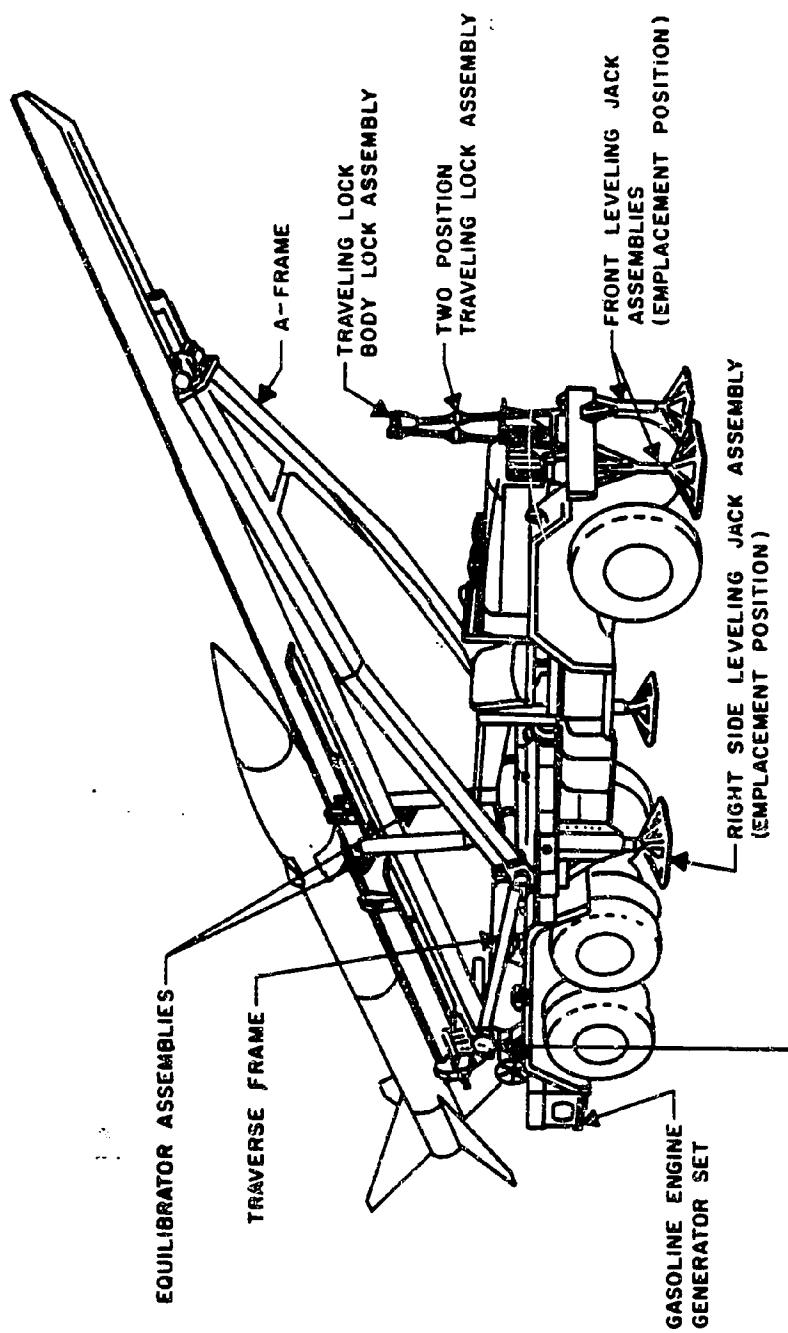


Figure 16-15. ■ HONEST JOHN Rocket Launcher in Firing Position ■

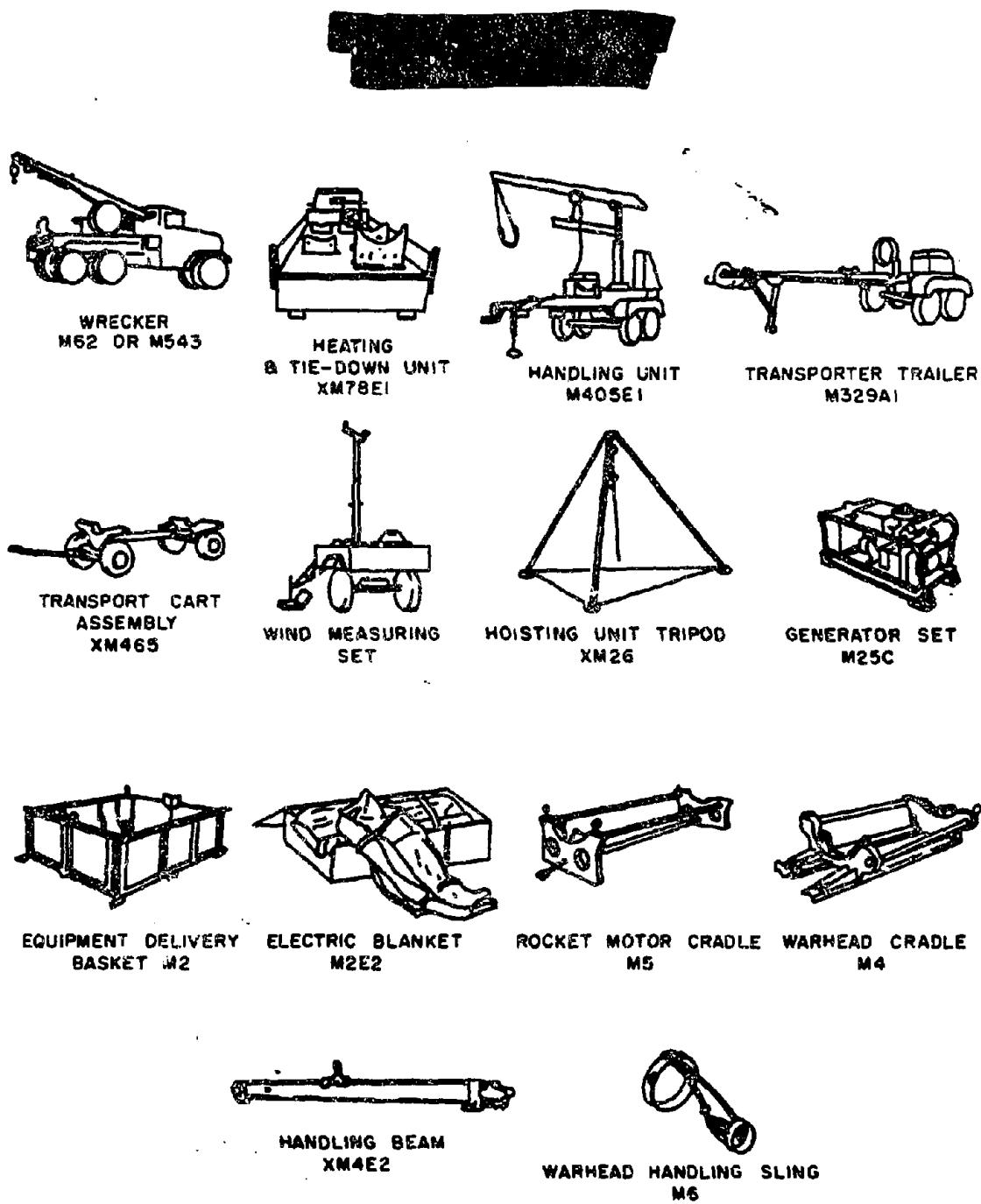


Figure 16-16. HONEST JOHN, Auxiliary Equipment

**Table 16-7. Missile System Components — HONEST JOHN**

Item	Refer to Figure	Dimensions (in.) (Weight (lbs))	Remarks
<b>1. Missile Components (in containers)</b>			
(a) Warhead sections	—	144 x 50 x 45 (2,500)	Plywood containers
(b) Guidance sections	None	—	
(c) Rocket motor sections	—	235 x 44 x 38	
(d) Fins	{	(3,500)	Plywood containers
<b>2. Missile Body (assembled)</b>			
(a) Ready for launch	13	327 x 28 (3,750)	
(b) In-flight (near target)	13	327 x 28 (2,000)	Propellant burned
<b>3. Transport Equipment</b>			
(a) Semitrailers	16	315 x 97 x 48 (3,500)	w/o missile
(b) Trucks (M543 or M62)	16	310 x 97 x 103 (34,000)	
<b>4. Launch Equipment</b>			
(a) Lightweight launchers	—	346 x 83 x 61 (4,375)	w/o missile
(b) Self-propelled launchers	14, 15	508 x 121 x 151 (42,000)	w/o missile
(c) Loaders (handling unit on M62 truck)	16	310 x 97 x 210 (40,000)	w/o missile
<b>5. Auxiliary Ground Equipment</b>			
(a) Firing unit assembly	—	36 x 24 x 24 (300)	
(b) Sighting equipment	—	36 x 20 (175)	
(c) Generator set	16	60 x 30 x 30 (1,800)	On truck chassis

- Battalion Area Test and Repair,
- Transportation to Firing Site,
- Emplacement and Prefire Preparations,
- Flight.

#### 16-11 Vulnerability Levels for HONEST JOHN Missile System

Blast vulnerability levels for the principal system configurations of the HONEST JOHN missile system are given in Table 16-8.

- Missiles in Containers at Storage Site (HONEST JOHN).

- Missiles in Transit to Firing Site (HONEST JOHN).

Table 16-8. Summary - HONEST JOHN

Deleted

DNA  
(b)(1)  
USA/NUCA  
(b)(1)

- Missile System During Checkout and Launch Operations (HONEST JOHN).

DNA  
(b)(1)

USA/NUCA  
(b)(1)

- Missile in Flight (HONEST JOHN).

DNA  
(b)(3)  
+  
(b)(1)

The blast vulnerability of the principal configurations of the sample missile system (HONEST JOHN) are described in Table 16-8 and Figure 16-17; the figure includes curves that allow the determination of pressure levels for damage corresponding to other weapon yields.



DA  
U-X

**Deleted**

Figure 16-17. [REDACTED] HONEST JOHN, Major Item Blast Vulnerability [REDACTED]

16-33



## SECTION II BLAST AND THERMAL VULNERABILITY OF IN-FLIGHT STRATEGIC SYSTEMS

### INTRODUCTION

The blast and thermal damage to strategic systems are considered together since blast and thermal effects are closely associated in the physics of a nuclear explosion and also because the damage mechanisms of these two effects tend to interact and, at times, complement each other. It should be noted that this section only treats damage to in-flight aerospace systems; blast and thermal damage to surface and underground installations characteristic of the ground support portions of a strategic system are treated separately in Chapter 11.

Blast effects are important to in-flight strategic systems from sea level to altitudes of approximately 100,000 feet (about 30 kilometers). When a nuclear explosion occurs in this altitude region, the blast wave is formed by conventional hydrodynamic processes as the fireball expands. The details of these processes depend on the yield of the weapon, the altitude of burst, and the weapon design (see Chapter 2). The latter consideration (weapon design) is becoming increasingly important as warheads are tailored to [redacted] or to enhance specific elements of the output. The mechanisms of blast wave formation are reasonably well understood from a theoretical viewpoint for nuclear bursts up to altitudes as high as 50 kilometers but experimental verification is lacking (see paragraphs 2-42 through 2-44).

(U) Blast is important to in-flight strategic systems operating below about 100,000 feet, in terms of the following effects:

- Overpressure (static or dynamic) crushing or bending of the primary structure.

- Gust (or deceleration) loading on primary and/or secondary (internal) structures.
- Trajectory deviation (CEP degradation).
- Alteration of aerodynamic stability.

[redacted] The thermal radiation (excluding X-ray effects\*) associated with a nuclear burst must be considered from two main aspects:

- "Early" time thermal radiation emitted from a distant source that is incident on the missile surface; this radiation comes from the fireball and from the high-pressure shock front.
- Missile "fly-through" of the fireball region at "later" times, with the associated thermal radiation imposed on the body surface while it is inside the fireball region.

[redacted] In addition to considering the effects of blast and thermal radiation on in-flight strategic systems separately, the possible coupling of these two effects in producing damage to the system should be considered. The magnitude of possible coupling effects probably will depend on the details of the system design; general statements are not valid.

[redacted] The two major strategic systems of concern are defensive antimissile missiles (AMM), more commonly known as ABM, and offensive reentry vehicles (RV). Both systems respond to exposures to the environment produced by nuclear explosions in similar manners, despite significant differences in their configurations (Figure 16-18). The degree to which any system will respond depends on the flight characteristics of the specific vehicle involved, but, in general, there is considerable overlap between RV's and ABM's with respect to their velocity at different altitudes within the atmosphere. A comparison of operational regimes is shown in Figure 16-19.

[redacted] See Section V, Chapter 9 for a discussion of X-ray effects on aerospace vehicles.

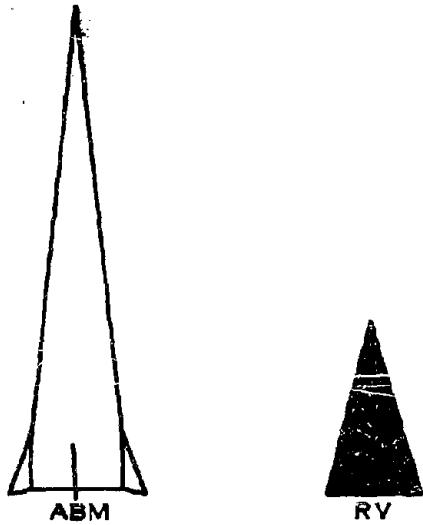


Figure 16-18. ABM and RV Configuration Comparison

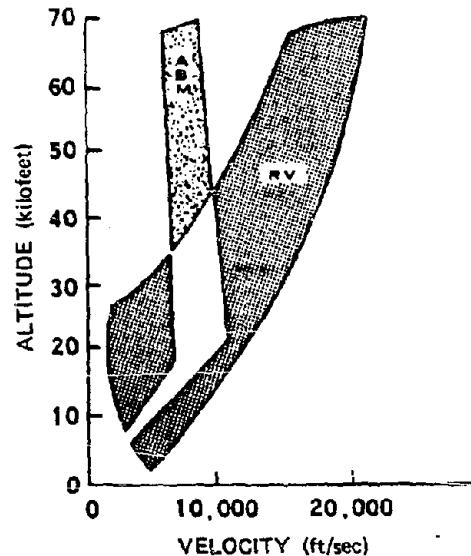


Figure 16-19. ABM and RV Operating Envelope Comparison

The first two categories of blast effects listed above, static and dynamic overpressure crushing (or bending) and gust (acceleration) loading can damage the system physically, i.e., the blast wave from a nuclear explosion at altitudes up to 100,000 feet can cause permanent structural deformation to reentry vehicles, interceptor missiles, boosters, and aircraft. As the structure crosses the shock front, it is suddenly immersed in a "new," transient pressure field, hence, the term "pressure crushing." There is, of course, a complicated shock interaction when the bow shock surrounding a supersonic vehicle intersects the shock front of the blast wave. This interaction results in a high pressure transient ("shock-on-shock" load) that decays quickly to a quasi-steady loading behind the front. The duration of this transient or "spike" can be quite short (tens of microseconds) compared to the response time of the vehicle. At the same time, the vehicle structure is suddenly subjected

to a gust loading or an additional aerodynamic loading that results from the particle velocity and the over-density behind the shock front that causes a jump in the dynamic pressure, which causes an abrupt deceleration of the whole vehicle body.

The extent of physical damage or structural response from either pressure crushing or gust loading depends on the distance from the target to the burst point, the orientation of the target, the strength and duration of the blast wave, and the preblast flight loads imposed on the vehicle. These last loads depend on the speed, trajectory, and physical design characteristics of the vehicle. For an incoming reentry vehicle, the altitude of maximum deceleration from atmospheric drag depends on the ballistic coefficient,  $\beta$ . The ballistic coefficient is defined as  $\beta = W/C_d A$ , where  $W$  is the vehicle mass,  $C_d$  is the drag coefficient, and  $A$  is the body reference area. As the ballistic coefficient is increased, the

altitude at which the vehicle experiences maximum deceleration is decreased. The high performance, thin, cone-shaped vehicles have very high ballistic coefficients. Figure 16-20 shows the various response regimes for an interceptor missile including structural, e.g., shell buckling and beam bending, rigid body, and thermal response.

Rigid body response describes the gross whole body motion of an in-flight strategic vehicle that results from passing through the blast sphere and the fireball interior. It includes trajectory deviation (CEP degradation), aerodynamic stability changes, and the drag forces exerted on the overall vehicle; it should be noted that the deceleration forces imposed on the whole body also are transmitted, in a complex manner, to the internal components of the missile system. Trajectory deviation occurs when the blast wave deflects or displaces an in-flight vehicle from its preassigned (or benign) environment.

Passing through the hot fireball results in a thermal load on the system in addition to the thermal loads caused by the benign reentry heating or the supersonic flight of an ABM. Consequently, the impact of the total environment of a high altitude nuclear burst must be examined. Figure 16-21 shows the nuclear encounter sequence for RV and ABM systems. The loading and response of the vehicle at each point from 1 through 6 is a function of the local environment, the physical characteristics of the vehicle, and its flight profile.

After the vehicle enters the blast sphere, it may traverse a region of density lower than

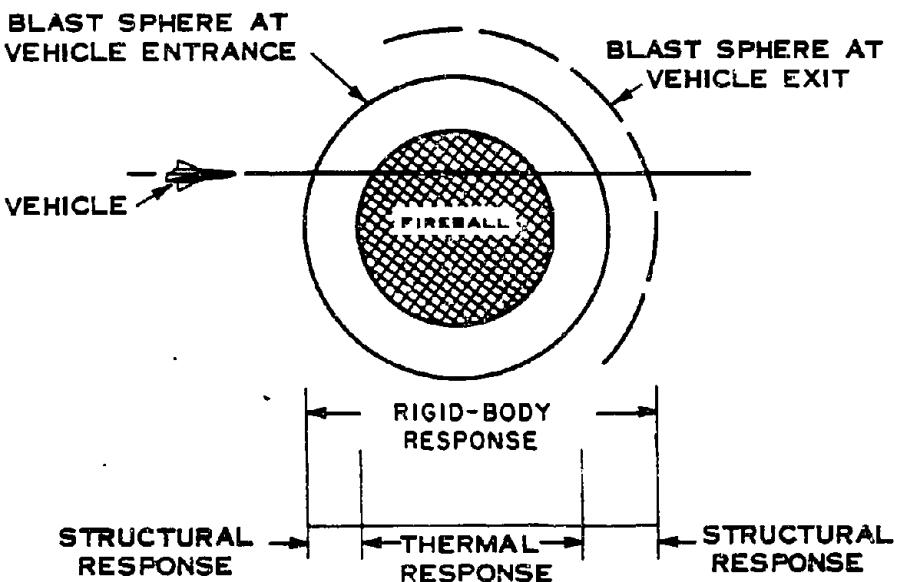


Figure 16-20. Response Regimes for Interceptor Missile

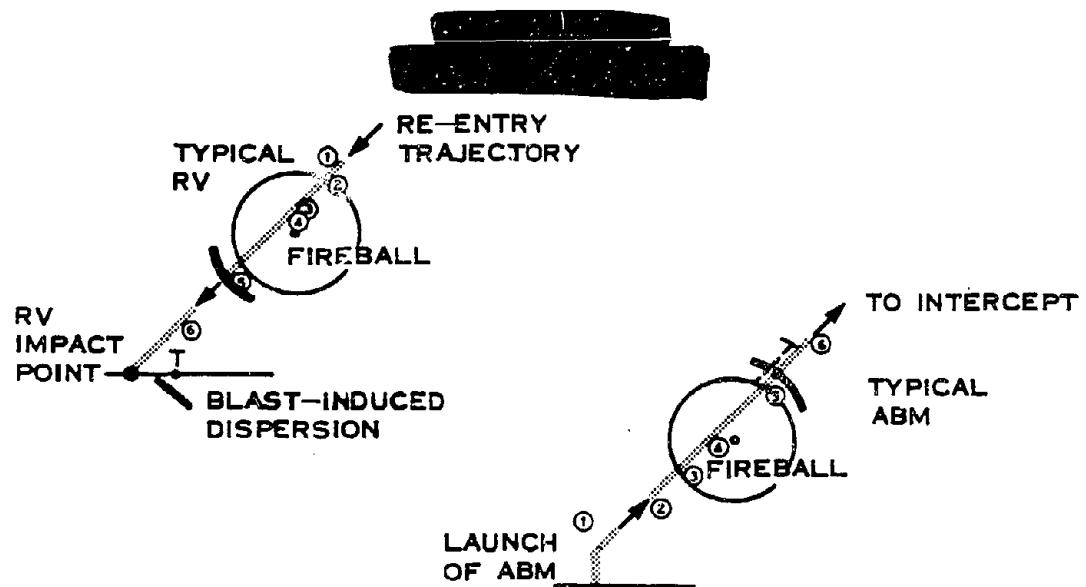


Figure 16-21. Nuclear Encounter and Event Sequence for RV and ABM

ambient before it exits the blast sphere. This may affect its flight stability, depending on the design characteristics, i.e., static margin and rate of damping. Under some conditions, a reentry vehicle on a ballistic trajectory may tumble in this region and/or subsequently emerge from the blast sphere with a large flight angle of attack, which may cause severe structural loading and may result in serious damage. Even if tumbling does not occur, exit loads imposed on a vehicle at a large angle of attack sometimes could be greater than initial entrance loads. Also, since the RV may exit the blast sphere at a large angle of attack, loss of accuracy and increased dispersion are likely. This is particularly true for advanced systems that use slender body configurations whose drag coefficients are very sensitive to changes in angle of attack.

Maneuvering reentry vehicles are being considered with a view toward avoiding a nuclear encounter or reducing the exposure time by altering the usual ballistic trajectory on reentry. However, while the maneuverability of

the reentry vehicle could increase its survivability, it could, under some circumstances, also increase its vulnerability to blast. The maneuvering vehicle would experience more severe aerodynamic preloads, to which the air blast induced loads would be added.

These maneuver load effects also can be important for ABM systems. Since ABM's are required to maneuver within the atmosphere, control surfaces, which also are susceptible to damage from gust loading, are involved. For many situations, assuming a range of yields and warhead designs, spacing between interceptors is governed by blast fratricide. In a saturation attack, the stepdown firing doctrine for defense tactics depends directly on the hardness of the interceptor to all nuclear effects. Consequently, a complete description of the nuclear environment is necessary to predict the effects of a nuclear burst on in-flight strategic systems. With respect to the blast wave, the parameters of interest include overpressure, particle velocity, density and temperature, as a function of both time and distance.

The propagation of the blast wave from the point of burst downward through a non-homogeneous atmosphere must be considered. Atmospheric inhomogeneity is not a serious problem for small yields at moderate heights, although it does distort the blast sphere somewhat. Blast wave inhomogeneity becomes more severe as the altitude of burst is raised above about 100,000 feet; however, it is significant that at these higher altitudes, blast begins to be less severe as a damage mechanism than other competing effects.

#### 16-12 Sources of Data

The blast effects on early RV's were expressed in terms of rigid body gust loading or "g" levels of deceleration. When these g loads were added to the normal "peaceful" reentry loads and then compared to design safety factors, it was found that the early RV designs were relatively soft and had large radii of blast vulnerability that outreached over nuclear effects. At these "vulnerable" ranges, overpressure levels were so low that local crushing or beam bending was not a problem.

As better theoretical models of the nuclear environment have been developed, blast loading and structural response calculations have become more sophisticated. Progress has been made, from the early engineering analysis of simple spring-mass models subjected to idealized loading, to more complex computer codes that handle rings and shells subjected to loads more representative of the nuclear engagement, including local body pressures. Through the use of 6-degree-of-freedom trajectory codes, the trajectory dispersions induced by the blast wave can be computed and the tumbling within the blast sphere can be predicted using approximate values of environment levels. Theoretical analyses have been developed to treat the shock-on-shock interaction and these analyses have been confirmed at normal incidence by experiments.

Test techniques have been developed to determine properties of materials at high strain rates.

Early programs to determine blast and thermal vulnerability of in-flight strategic vehicles include HARTS, SPINE, and ABM Vulnerability and Hardening. These research programs were closely coordinated with the research requirements of systems designers. This coordination is shown by the following list of the various configurations of research vehicles that have been studied and their counterparts in terms of military systems.

Program	Research Vehicle	System Application
Air Force	HARTS A	Mark 12 (RV)
Air Force	HARTS B	Mark 11A (RV)
Army	AIRS I	SPRINT (ABM)
Army	AIRS II	SPARTAN (ABM)

This correlation permits use of physical data and the aerodynamic coefficients obtained during the development of the specific systems.

#### 16-13 Limitations in Application of the Data

Since vulnerability (or damage) assessment of an in-flight strategic vehicle is such a strong function of the detailed characteristics of the specific vehicle, it is virtually impossible to devise a general method of vulnerability determination that could be applied to any vehicle. Some of the parameters that enter the problem are the details of the design of the primary structure of the vehicle (including all materials used, internal supports, field joint fixtures, etc.), the design features of the internal components and how they are supported on the primary structure, the detailed aerodynamic characteristics of the body and how it may fly (including the possible requirements for maneuvers). Therefore, it is obvious that an accurate definition of

the blast and thermal vulnerability of a particular in-flight strategic vehicle requires a great deal of analysis and the use of specialized computational models as well as experiments. Such analyses are beyond the scope of this manual.

The following discussion will attempt to explain, in general terms, the technical aspects of the problem that appear to have the most important influence on the determination of nuclear weapon blast and thermal damage to in-flight strategic vehicles. The technical discussion will be presented under two main sections, one devoted to RV bodies and the other to ABM vehicles; some of the material appearing under the RV section will be applicable to the ABM and, where this is the case, it will be noted.

#### BLAST LOADING ON REENTRY (RV) SYSTEMS

The general approach used herein to describe the important factors related to the determination of blast and thermal vulnerability of reentry vehicles was generated primarily under the Hardening Technology Study (HARTS). The HARTS vehicles that were studied are shown in Figure 16-22. Configuration A is a blunted cone and Configuration B is a sphere-cone-cylinder-flare. The dimensions and the ballistic coefficients are shown in the figure. Table 16-9 lists the range of parameters that were used in the HARTS studies. The term "hardness level" will be explained below.

#### 16-14 Environment Scaling

The nomenclature used to describe RV/blast intercept conditions is shown schematically in Figure 16-23. The conditions pictured correspond to those where the RV does not traverse the center of the burst fireball ( $\varphi \neq 0^\circ$ ). As described in Chapter 2, blast scaling has been used extensively to predict air blast environments. Since RV intercept loads and traversal phenomena depend on the blast parameters, it is

Table 16-3. Range of Basic Parameters for HARTS II

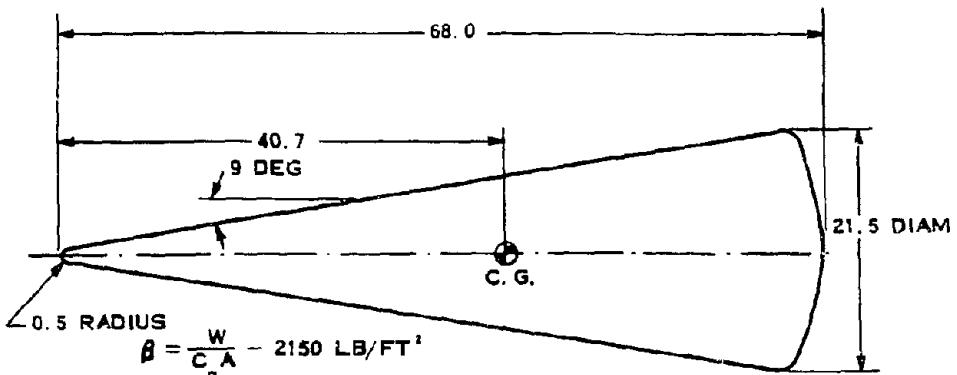
Blast yield	30, 200, and 440 kt – blast environment from Hillendahl FIREBALL code
Intercept altitude	30,000 to 100,000 ft
Intercept angle ( $\varphi$ )	0 to 90 deg
Trajectory	Minimum energy trajectories for 2,000, 5,500, and 7,000 nm ranges
Hardness levels (axial acceleration for head-on intercept)	200 to 1,000 g
Configurations (see Figure 16-22)	A: $\beta = 2,150 \text{ lb}/\text{ft}^2$ B: $\beta = 680 \text{ lb}/\text{ft}^2$

possible to scale RV intercept loads and traversal phenomena in a manner similar to the blast parameters.

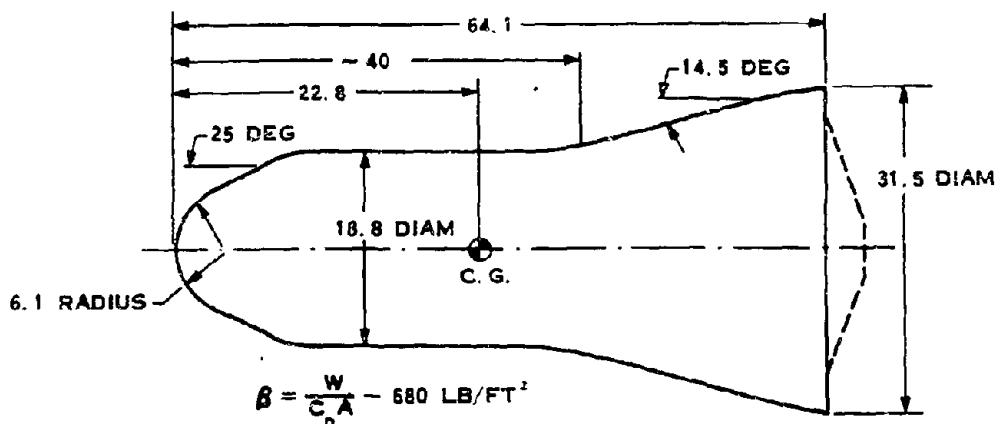
Figure 16-23 indicates that there are two important radii. First, the distance between the burst center and the vehicle at the time of detonation, denoted by RD, is significant for the comparison of *prompt* effects (e.g., neutrons, X-rays, etc.) as well as blast effects. Consideration of these RD values for various vehicle paths and orientations results in vulnerability envelopes referred to as *burst time* envelopes. Second, the distance between the burst center and the vehicle when the blast wave intercepts the vehicle, denoted by RB, results in envelopes referred to as *intercept time* envelopes. The reference time for which the envelope is constructed must be specified for each envelope.

"Hardness Level" is a useful parameter to hold constant when studying blast phenomena. Hardness level is defined as that *axial* load

NOTE: ALL DIMENSIONS  
IN INCHES



CONFIGURATION A



CONFIGURATION B

Figure 16-22. HARTS Configuration

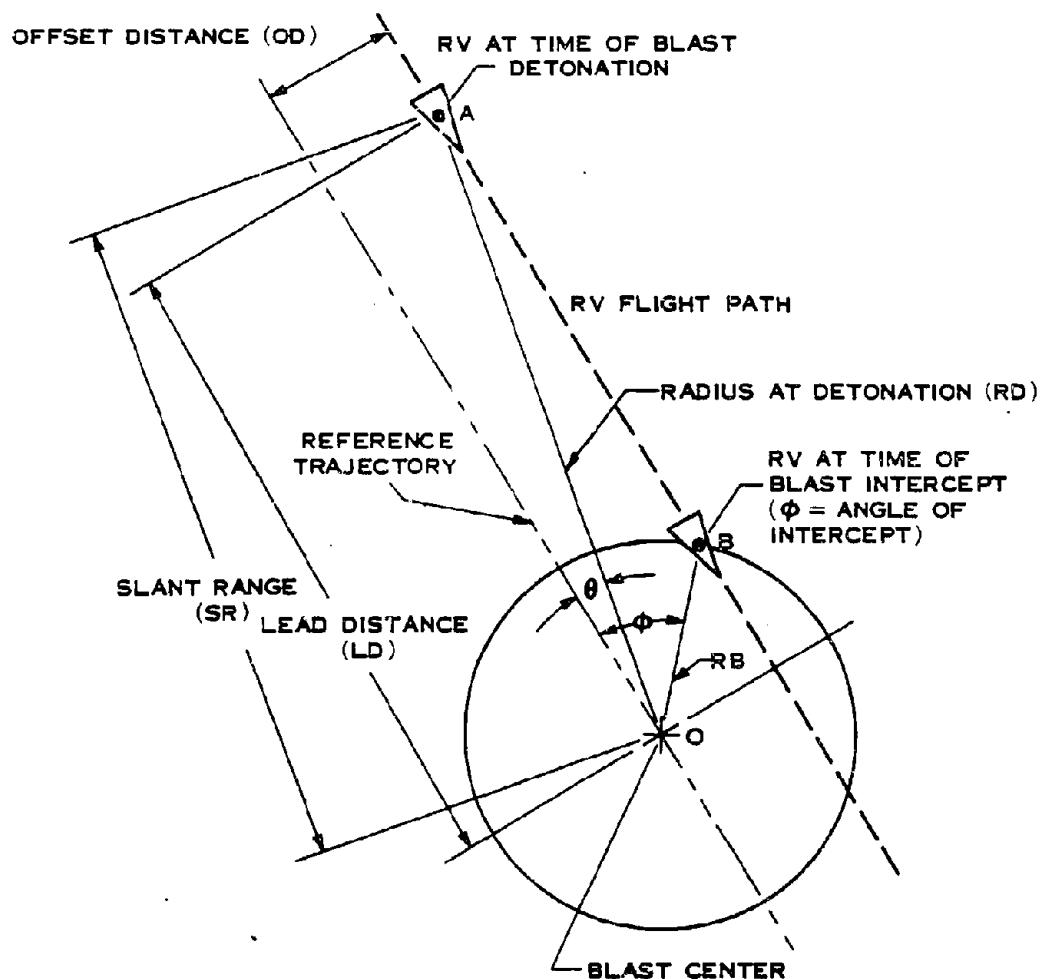


Figure 16-23. Blast Intercept Conditions Nomenclature

acceleration experienced by a vehicle intercepting a blast wave head on ( $\varphi = 0^\circ$ ) at zero angle-of-attack ( $\alpha = 0$ ). For a given yield, burst altitude, and configuration combination, the specification of a blast intercept hardness level determines the blast wave radius. This in turn determines the blast front environment. Blast scaling laws indicate that these blast front conditions are identical to those at a different yield and radius where the new radius is equal to the old radius multiplied by the cube root of the ratio of the yields. For example:

$$RB_2 = RB_1 (W_2/W_1)^{1/3} \text{ (ft)},$$

where  $RB_2$  and  $RB_1$  are the blast intercept radii for yields of  $W_2$  and  $W_1$ , respectively, and in general,

$$RS = RB/W^{1/3} \text{ (ft/kt}^{1/3}\text{),}$$

where  $RS$  is known as the scaled intercept radius. Values of scale radius,  $RS$ , at constant hardness level for varying altitude are shown in Figure 16-24. A similar presentation of scale time of blast intercept can be made, since time and radius are proportional. Thus, in general,

$$\tau_1 = t_1 W^{1/3} \text{ (sec/kt}^{1/3}\text{),}$$

where  $t_1$  is the time after burst to intercept and  $\tau_1$  is the scaled time. Values of scaled time,  $\tau_1$ , for

constant hardness levels for varying altitude are shown in Figure 16-25.

The hardness level, position-time relationships are defined in a manner that data for any yield can be derived over the given range of hardness levels and burst altitudes. System analysis parameters such as slant range  $SR$ , lead distance  $LD$ , and offset distance  $OD$ , from the burst at time of explosion also can be derived simply. For a given hardness level and burst altitude one  $RS$  and  $\tau_1$  combination exists. For specified yield,

$$RB = RS W^{1/3} \text{ (ft)}$$

$$t_1 = \tau_1 W^{1/3} \text{ (sec).}$$

Referring to Figure 16-23, the following spacing relationships are apparent.

$$OD = RB \sin \varphi,$$

$$LD \approx RB \cos \varphi + Vt_1,$$

$$SR = (LD^2 + OD^2)^{1/2},$$

where  $V$  is the  $RV$  velocity, and the other symbols are defined in Figure 16-23.

Determination of lead distance is illustrated in Problem 16-1. The variation of hardness level with altitude and slant range is shown in Figure 16-26.

DNA  
(1)(3)

[REDACTED]

Problem 16-1. Calculation of Hardness Level

[REDACTED] Figures 16-24 and 16-25 show the scaled blast radius and scaled time of blast intercept, respectively, for a Configuration A vehicle on a 5,500 nautical mile flight path as a function of burst altitude for various hardness levels. Various system parameters may be determined from Figures 16-24 and 16-25 as discussed in paragraph 16-14.

[REDACTED] Example [REDACTED]

[REDACTED] Given: A HARTS Configuration A vehicle (Figure 16-22) is on a 5,500 nm trajectory. The RV hardness level is 500 g.

[REDACTED] Find: The slant range at which the RV would experience a head on ( $\phi = 0^\circ$ ) load equal to its hardness level if it were exposed to the blast wave.

DNA  
(L)(3)

[REDACTED]

DNA  
(L)(3)

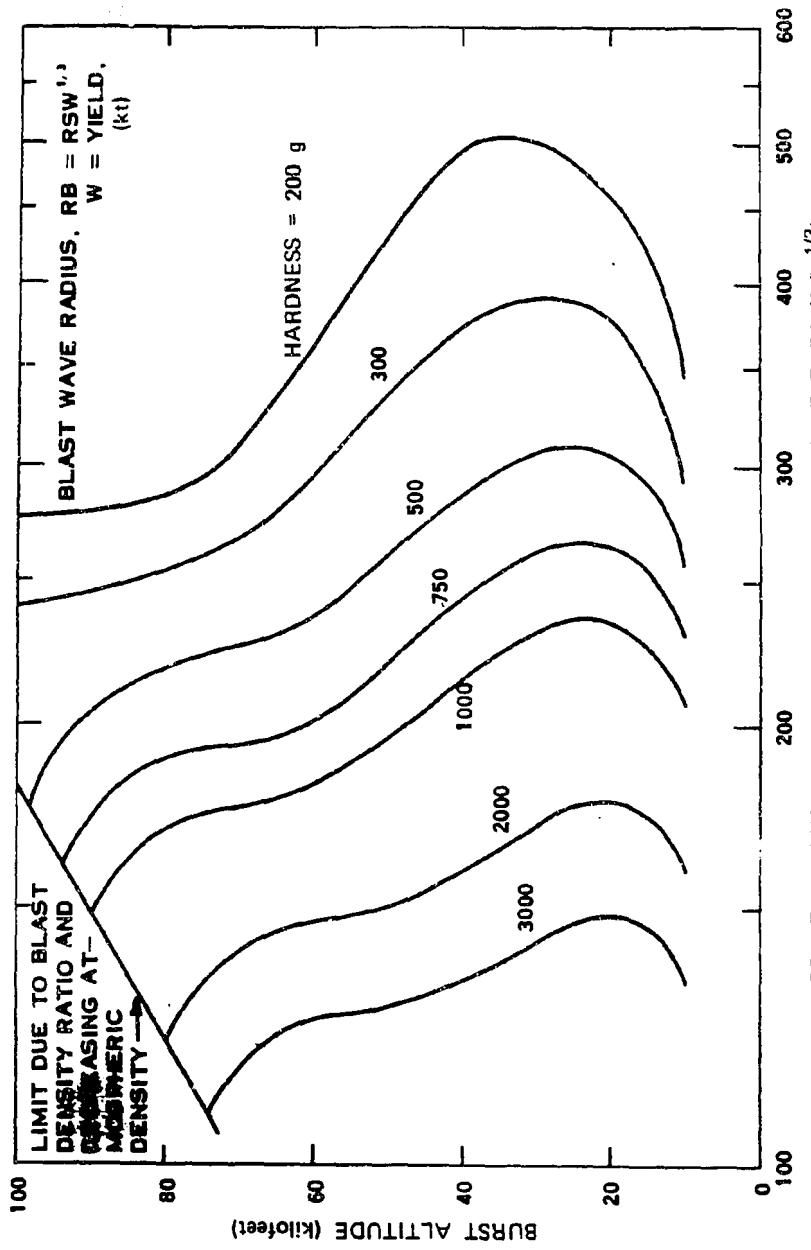


Figure 16-24. Scaled Blast Wave Radius at Blast Intercept,  $RS$  (ft/ $kt^{1/3}$ ) for Configuration A, 5,500 nm Range

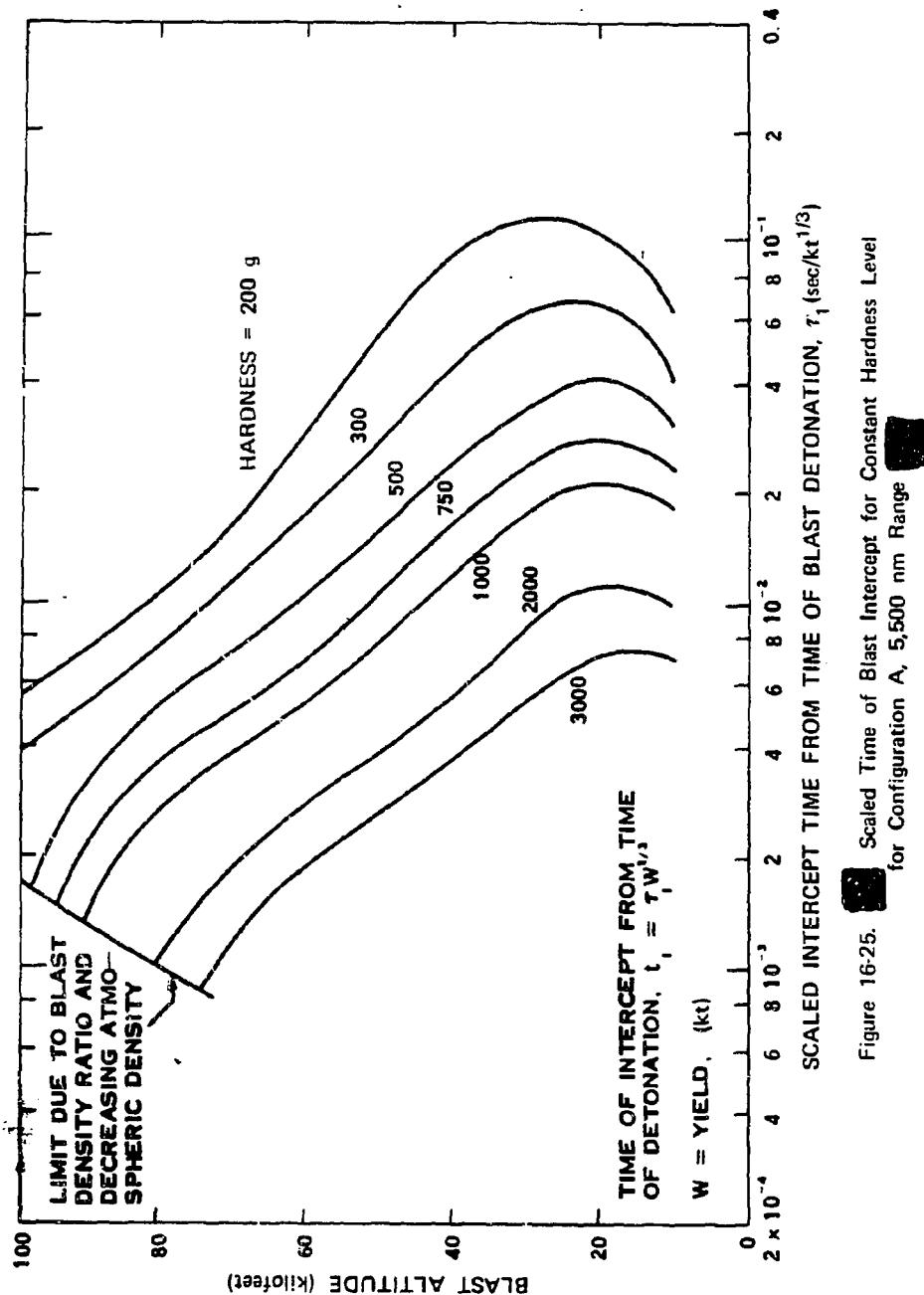


Figure 16-26. Variation of Hardness Level with Altitude and Slant Range  
for [REDACTED] Configuration A [REDACTED]  
[REDACTED]

Deleted

DIA  
 $\lambda(z)$

### 16-15 General Intercept Loads and Load Duration

The aerodynamic loading on hypersonic reentry vehicles can be divided into two general categories: steady state loading and transient loading. Steady state loading occurs when the pressure, density, particle velocity, and temperature do not change with time. Transient loading occurs when there is a time change in the environment surrounding the reentry body.

The vehicle experiences a continuing change in environment during normal reentry. However, since this change is relatively slow, steady state drag loading provides a good approximation for normal reentry conditions. For any type of flow over a body, the local pressure at any point on the surface can be found from the relation:

$$P_b = P_f + qc_p,$$

where

$P_b$  = pressure at some point on the body surface,

$P_f$  = free stream ambient pressure,

$q$  = free stream dynamic pressure.

$c_p$  = local pressure coefficient.

Classic Newtonian impact theory provides a simple closed-form solution for the local pressure coefficient,  $c_p$ . For steady state, hypersonic flow (above Mach 5) this theory provides adequate loading predictions. For any body of revolution the Newtonian theory predicts:

$$c_p = 2(\cos \alpha \sin \delta - \sin \alpha \cos \delta \sin \beta_r)^2,$$

where

$\alpha$  = angle between the vehicle longitudinal axis and the relative wind vector,

$\delta$  = vehicle semivertex angle,

$\beta_r$  = rotational angle about axis of reentry vehicle.

A vehicle experiences axial and lateral decelerations and local pressure loading during normal reentry. The amount of deceleration and local pressure depends on the vehicle reentry angle, velocity, shape, weight, and altitude. Figures 16-27 through 16-29 show some nominal reentry trajectories. These graphs only include the combinations of reentry velocity and reentry angle that correspond to a ballistic missile having a nominal range of 5,500 nm. The reentry vehicle is characterized by the ballistic coefficient, which is varied over a range of values typical for reentry vehicle designs. Calculations for the parameters (velocity, altitude, and time) of the reentry trajectories were begun at an altitude of 400,000 feet, since this altitude is well above that of appreciable aerodynamic forces for the reentry vehicles considered. The reentry angles measured from the local horizontal at 400,000 feet were chosen arbitrarily as 20 and 30 degrees. The corresponding reentry velocities at 400,000 feet were determined from the basic equation for vacuum ballistic trajectories. The ballistic coefficients vary from 800 to 2,500 lb/ft<sup>2</sup>. Below 100,000 feet the angle of attack is largely damped out, and the lateral force is very small.

The hardness level curves in Figure 16-24 represent one value on the intercept/load matrix of axial rigid body loads,  $G_A$ , for zero blast intercept angle ( $\varphi = 0^\circ$ ). It was determined that, at constant hardness level, the blast front environments for varying yields are essentially identical. The last variable to be accounted for in intercept loads is blast intercept angle. At constant hardness level and altitude, the intercept angle is the only factor that can affect intercept loads by changing the angle between the blast wind vector and the vehicle velocity vector, thereby causing a blast induced angle of attack at blast intercept.

(U) Blast yield scaling also can be applied to the scaling of intercept load duration, fireball

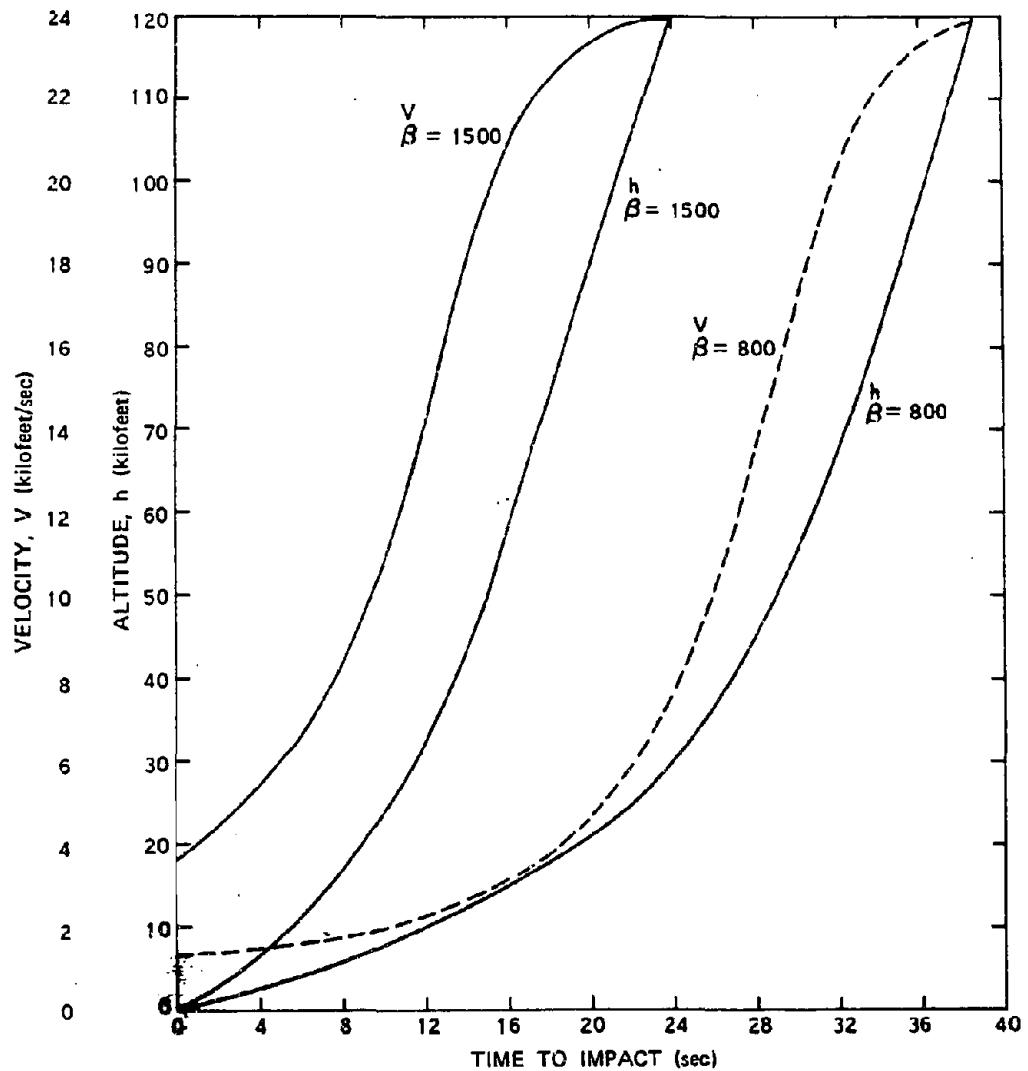


Figure 16-27. [REDACTED] Normal Reentry Trajectory; Initial Altitude = 400,000 ft, Initial Velocity ( $V_0$ ) = 23,900 ft/sec, Initial Flight-Path Angle =  $20^\circ$ , Ballistic Coefficient  $\beta = W/C_d A$  lb/ft $^2$  [REDACTED]

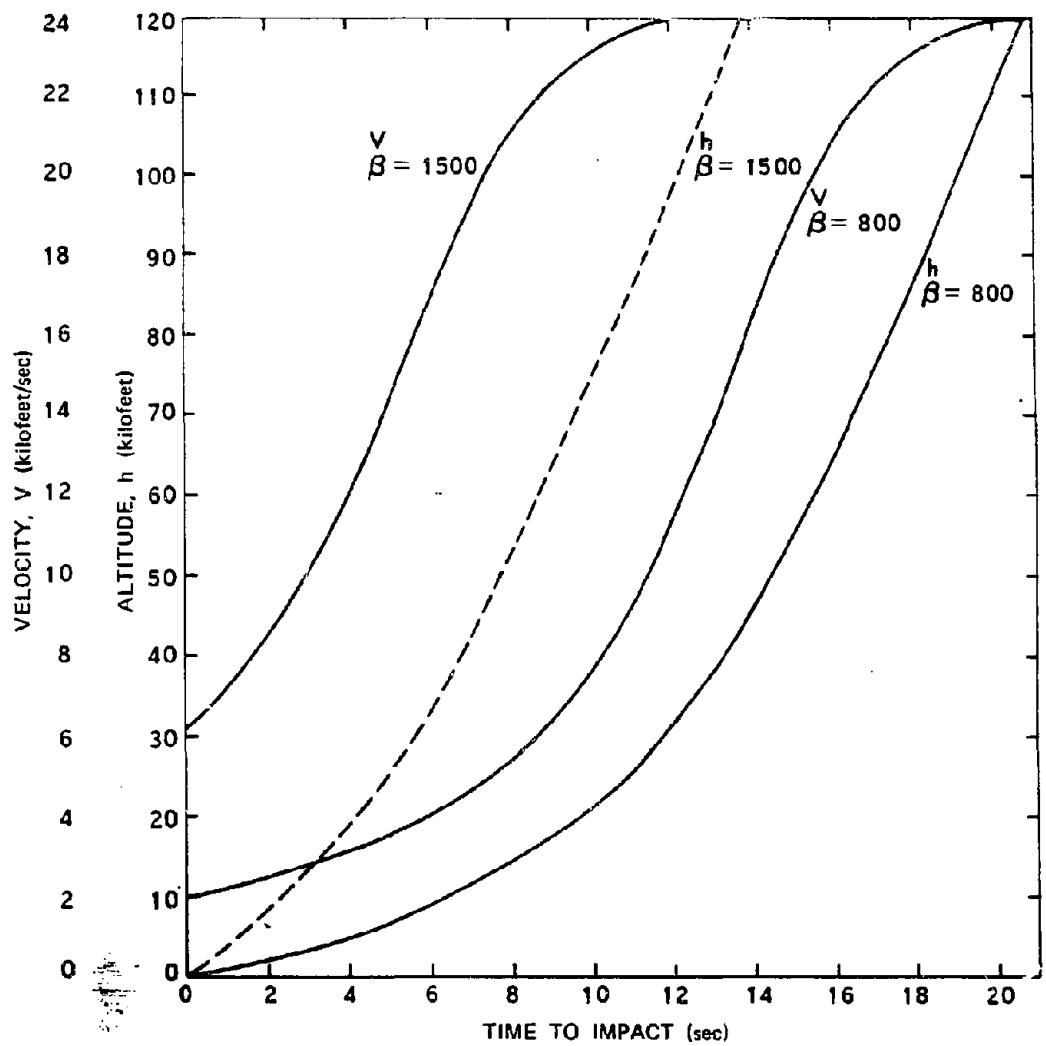


Figure 16-28. Normal Reentry Trajectory; Initial Altitude = 400,000 ft,  
 Initial Velocity ( $V_i$ ) = 24,000 ft/sec, Initial Flight-Path Angle =  $30^\circ$ ,  
 Ballistic Coefficient  $\beta = W/C_d A$  lb/ft<sup>2</sup>

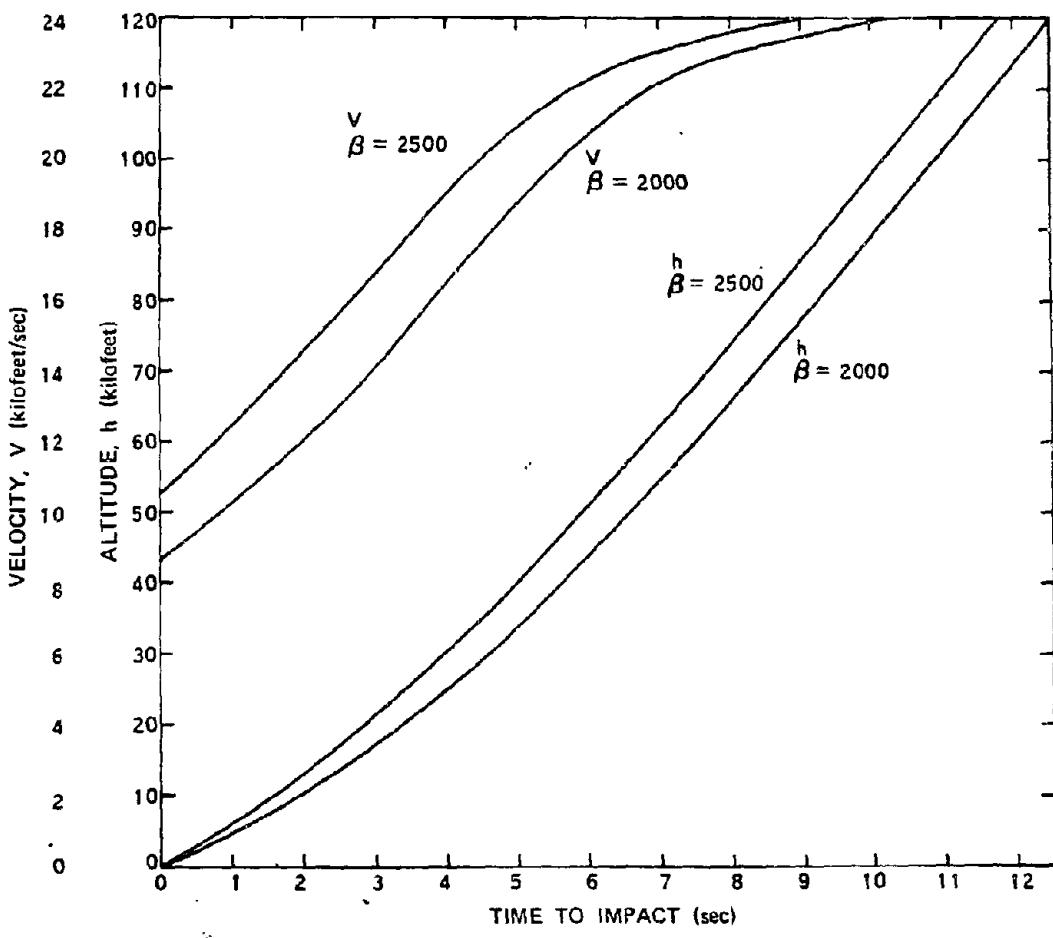


Figure 16-29. Normal Reentry Trajectory; Initial Altitude = 400,000 ft,  
 Initial Velocity ( $V_i$ ) = 24,000 ft/sec, Initial Flight-Path Angle =  $30^\circ$ ,  
 Ballistic Coefficient  $\beta = W/C_d A$  lb/ft<sup>2</sup>

traversal time, and total traversal time. Time and radial distance are scaled with the cube root of the yield. Interior blast phenomena can be assumed to scale with the cube root of the yield to obtain reduced radius or time. At any point in time the blast can be imagined to have a size of unity for 1 kt. The blast size for larger yields is unity times the cube root of yield in kilotons, on a relative basis. Since blast loading duration depends on the blast size, which can be scaled, the loading duration also can be scaled.

#### 16-16 Intercept Load Duration

Intercept loads are a function of hardness level, blast intercept angle, and blast altitude. The duration of the load is necessary to describe the intercept loading phase adequately. Under most conditions, the intercept loading history can be approximated by a triangular shaped pulse, i.e., intercept impulse is essentially one-half the maximum load multiplied by the duration time.

$$I_1 = \frac{G_1 \Delta t_{ILP}}{2} \text{ g-sec.}$$

The intercept load time constant,  $\Delta t_{ILP}$ , is

$$\Delta t_{ILP} = t_1 - t_{10\%} \text{ sec.}$$

where  $t_{10\%}$  is the point at which the intercept load decays to 10 percent of its maximum value. The scaled intercept load duration time,  $\tau_{ILP}$ , is

$$\tau_{ILP} = \frac{\Delta t_{ILP}}{W^{1/3}} \text{ sec/kt}^{1/3}.$$

Scaled intercept load duration times for a hardness level of 500 g are shown in Figure 16-30 for various intercept angles and altitudes. The intercept load duration times and intercept loads provide a usable set of data for estimating

the intercept load impulse. The duration times apply to axial, normal, or total resultant loads. In general,

$$\Delta t_{ILP} = \tau_{ILP} W^{1/3} \text{ sec.}$$

and any load impulse is

$$I_1 = \frac{1}{2} \Delta t_{ILP} G_1 \text{ g-sec}$$

where  $I_1$  and  $G_1$  represent any intercept load impulse and maximum load, respectively.

#### 16-17 Fireball Traversal Time

The time at which the intercept load has decayed to 10 percent of its maximum value (end of the intercept load pulse) corresponds approximately to the time when the vehicle enters the fireball (temperature  $\approx 10,000$  to  $15,000^\circ R$ ). For practical considerations, the end of the intercept load pulse and initial fireball immersion can be considered as the same time. The time of fireball traversal is

$$\Delta t_{FB} = t_{EFB} - t_{10\%} \text{ sec.}$$

where  $t_{EFB}$  is the time of exiting the fireball, and the scaled time of fireball traversal is

$$\tau_{FB} = \Delta t_{FB} / W^{1/3} \text{ sec/kt}^{1/3}.$$

Scaled fireball traversal time for a hardness level of 500 g is shown in Figure 16-31 for various intercept angles and altitudes. The time of exiting the fireball,  $t_{EFB}$ , is that time during the exit phase when increasing dynamic pressure reaches the ambient level at the blast altitude. This time also is approximately when the temperature level drops below 10,000 to  $15,000^\circ R$ . It should be noted that the point during entry at which the decreasing dynamic pressure reaches

ambient level is about the same as the point of 10 percent load.

#### 16-18 Total Traversal Time

Total blast traversal time is

$$\Delta t_t = t_E - t_i \text{ sec},$$

where  $t_E$  is the time of exit from the blast wave

shell, and as before,  $t_i$  is the time of intercept. The scaled time of blast traversal is

$$\tau_t = \Delta t_t / W^{1/3} \text{ sec}/kt^{1/3}.$$

Scaled total blast traversal time for a hardness level of 500 g is shown in Figure 16-32 for various intercept angles and altitudes.

**Problem 16-2. Calculation of Load Characteristics, Fireball  
Traversal Time and Total Traversal Time**

[REDACTED] Figures 16-30 through 16-32 provide the information necessary to calculate the load characteristics, the fireball traversal time, and the total blast traversal time for a vehicle similar to Configuration A with a hardness level of 500 g that enters the blast front at various intercept angles.

**Example**

**Given:** An RV similar in design to HARTS Configuration A (see Figure 16-22) with a hardness level of 500 g that is traveling on a 5,500 nm trajectory.

**Find:** The intercept load characteristics, and traversal times if the RV is exposed

DNA  
(1)(3)

DNC  
R-X?

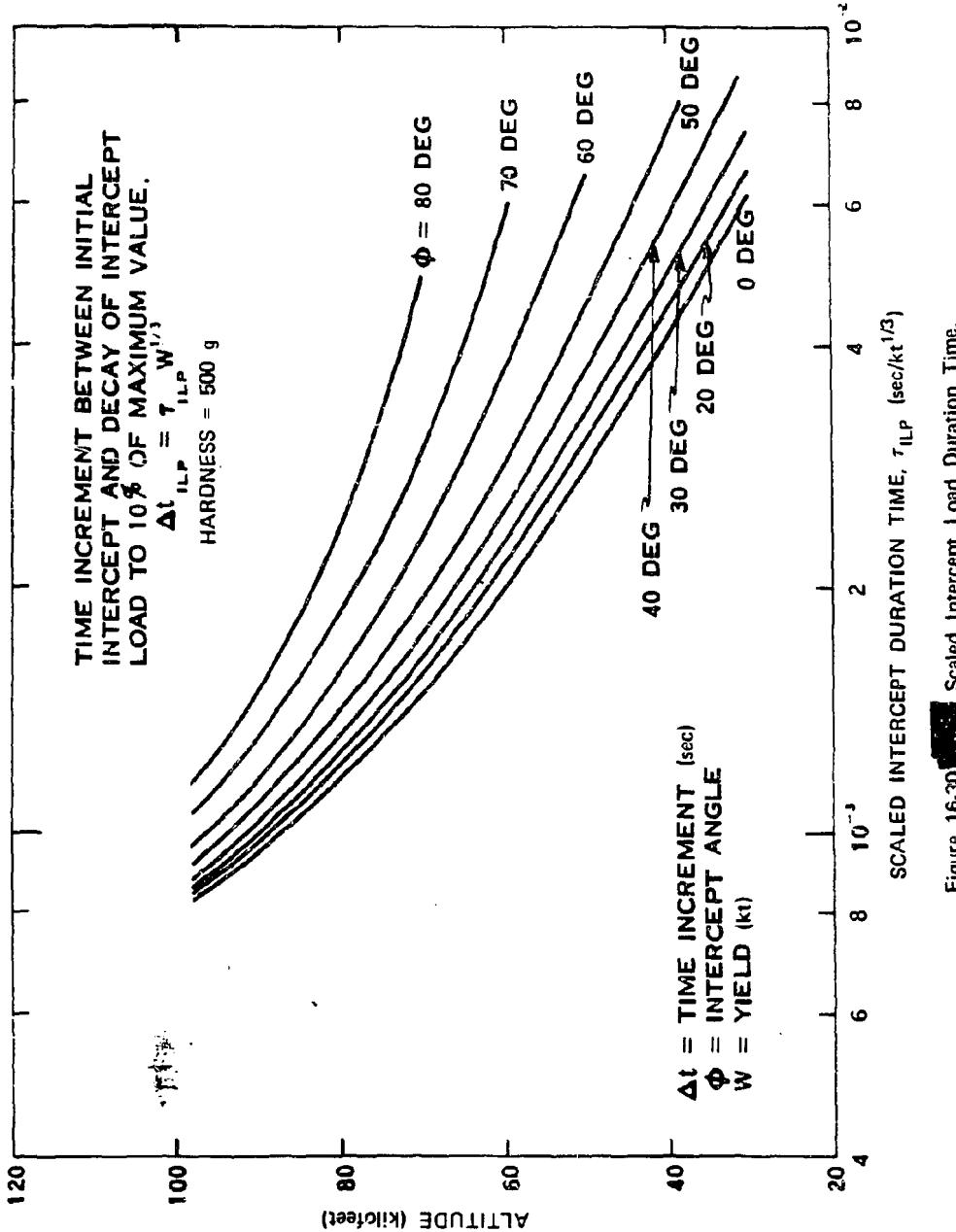


Figure 16-30 [REDACTED] Scaled Intercept Load Duration Time.  
500 g Hardness, Configuration A [REDACTED]

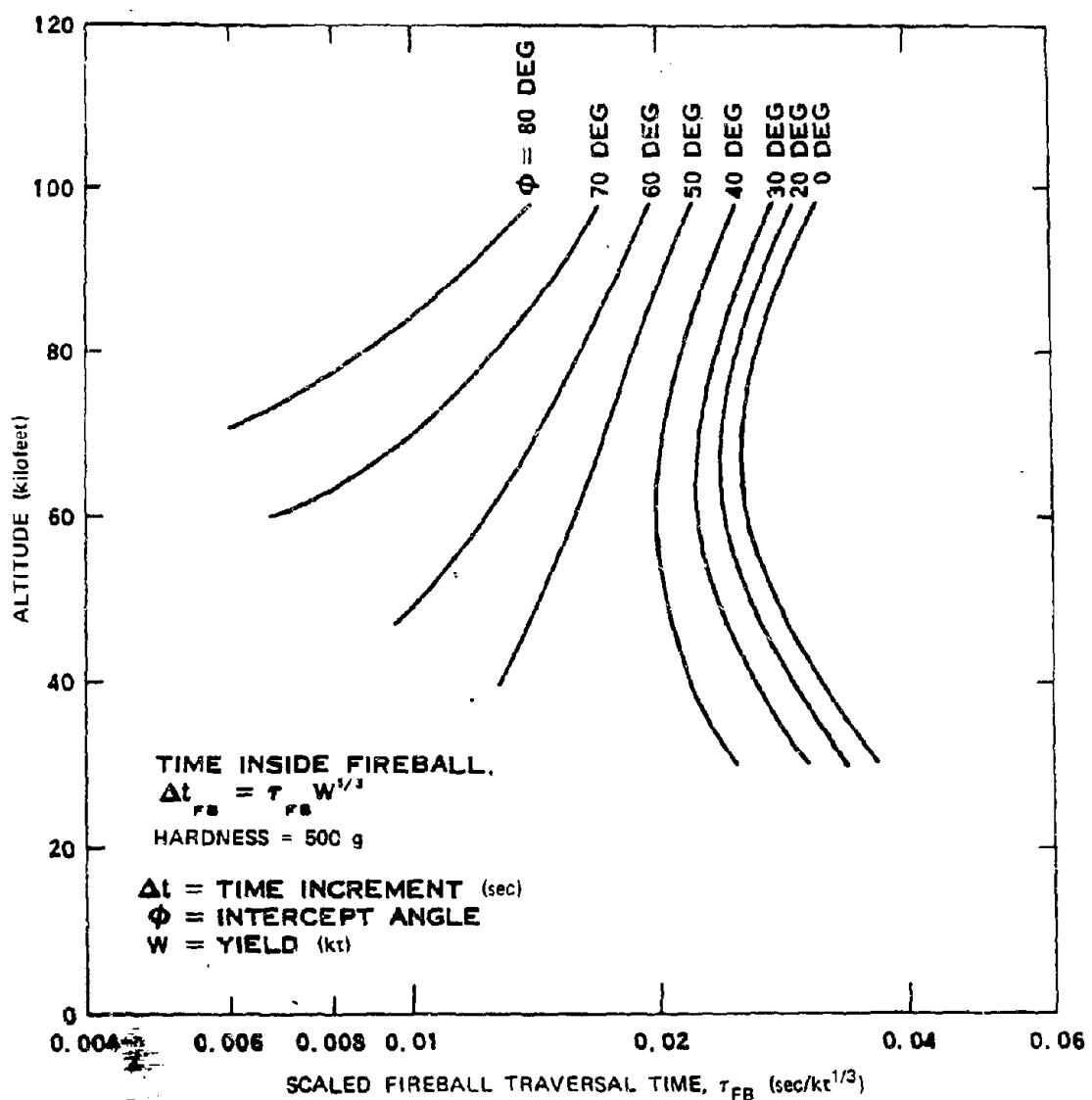


Figure 16-31. Scaled Fireball Traversal Time,  
500 g Hardness, Configuration A

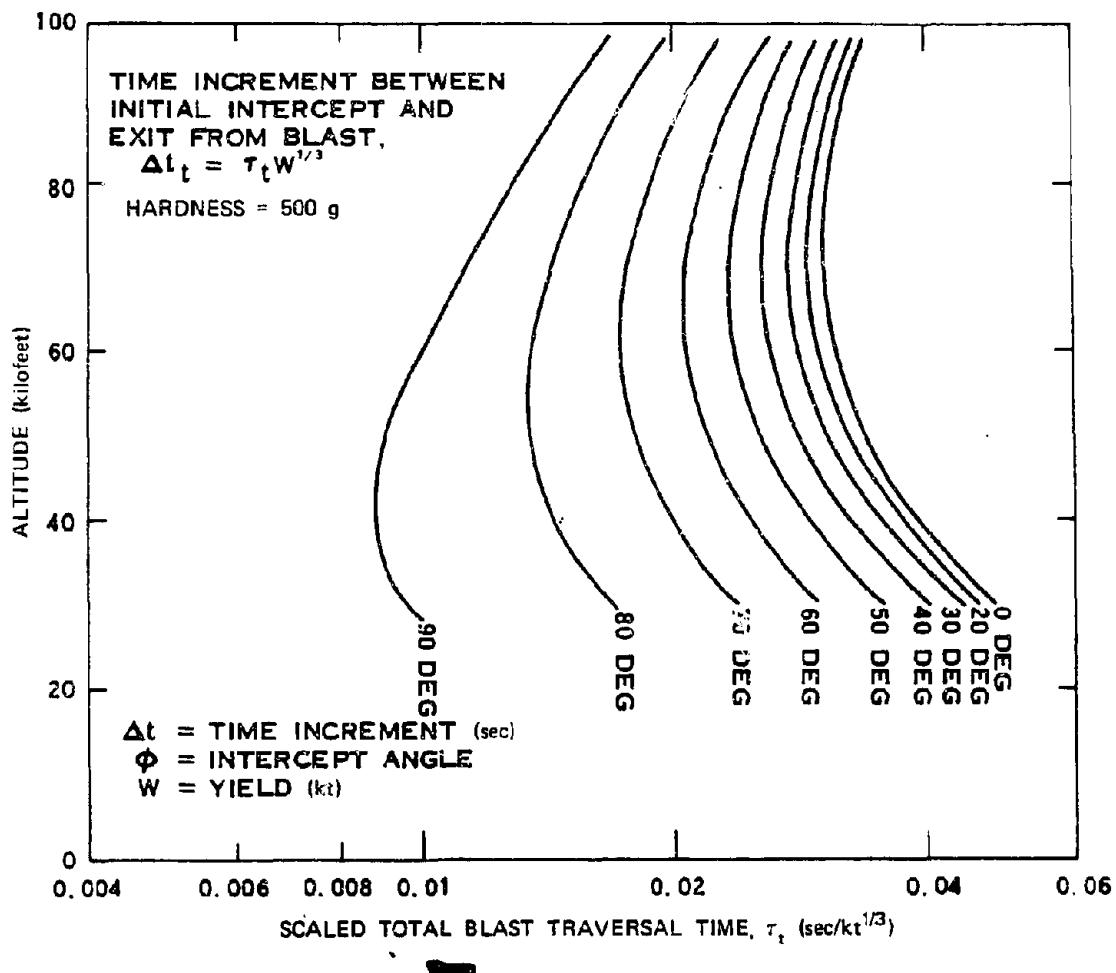


Figure 16-32. Scaled Total Blast Traversal Time,  
500 g Hardness, Configuration A

### 16-19 Exit Loads

Intercept load, intercept load duration, fireball traversal time, and total traversal time are functions of hardness level, blast intercept angle, and blast altitude (on a scaled basis). Exit loads also depend on blast yield as well as the functions listed above. This precludes any universal scaling of exit loading; however, the following are generally true of exit loading conditions:

- The probability of obtaining higher exit than intercept loads is very low for vehicles similar to Configuration A.
- Exit loads decrease with decreasing intercept hardness level.

### 16-20 Blast Data Generalization

The data summarized in the preceding paragraphs were generated for Configuration A with a 5,500 nautical mile range minimum energy trajectory. Loading and duration scaling procedures applicable to the blast problem were demonstrated for this case. These specific data are *not* directly applicable to *any* configuration-range combination. However, by some simple relationships and approximations, the data can be applied to different configurations and ranges, or combinations of both, within limits.

*Configuration Variations.* For other configurations, assume that the velocity, flight path

angle, and intercept conditions at the same blast altitude are identical. With these constraints, the intercept loads become a function of ballistic coefficient and lift characteristics. For axial loads,

$$\frac{G_{AI_1}}{G_{AI_2}} \approx \frac{\beta_2}{\beta_1}$$

and for normal loads,

$$\frac{G_{NI_1}}{G_{NI_2}} \approx \frac{\beta_{\alpha_2}}{\beta_{\alpha_1}}$$

where

$$\beta = \frac{W}{C_D A} \text{ lb/ft}^2$$

$$\beta_{\alpha} = \frac{W}{C_{N\alpha} A} \frac{\text{lb-deg}}{\text{ft}^2}$$

The term  $\beta_{\alpha}$  is defined as the normal force ballistic coefficient.

### 16-21 Typical RV Aerodynamics

A body that is moving along a reentry trajectory at hypersonic velocities has a flow field associated with it. The flow field is composed of the following main regions or characteristics (see Figure 16-33): stagnation point,

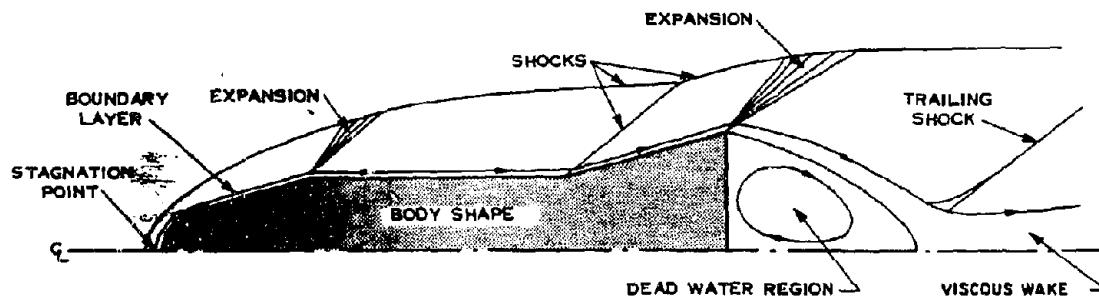


Figure 16-33. Flow Pattern Around an Axisymmetric Blunt-Nosed Body

shock layer, boundary layer, expansion shocks, pressure and density contours, wake, etc. The details of these flow regions are a strong function of the body shape, its velocity, and the properties of the air (i.e., altitude) through which the body is moving. Consequently, the flow field associated with even a single body is constantly changing during the reentry process.

Figure 16-34 shows the pressure distribution (in terms of pressure ratio) over the surface of a body similar to a HARTS Configuration B vehicle as a function of vehicle velocity. The pressure ratio is  $(P_b - P)/P$ , where  $P_b$  is the local pressure at any point along the surface and  $P$  is the ambient pressure. The overpressure ( $P_b - P_0$ ) are shown for sea level conditions ( $P_0$  is the ambient pressure at sea level) to provide some idea of the overpressures involved. It is evident that the overpressures near the stagnation region exceed all other pressures by a wide margin for this blunt body. It should be pointed out that these pressures do not take account of boundary layer perturbations, but the calculated pressures are indicative of actual flow field conditions; the overpressures associated with the flow field shock front are slightly higher than pressures on the surface. The curves in Figure 16-34 may be used to interpret the flow fields at altitude. For instance, the ambient pressure at 50 kilofeet is about one-tenth that at sea level. Thus, a vehicle at 50 kilofeet traveling at Mach 10 would have an overpressure on the flare of about 12 psi (i.e., 120/10) and stagnation value in excess of 150 psi. If the vehicle were traveling at Mach 20, the flare overpressure would be about 41 psi (410/10).

Another typical reentry flow field, which gives the pressure ratio distribution over a body similar to the HARTS Configuration A (i.e., cone-sphere shape), is shown in Figure 16-35. Figures 16-34 and 16-35 emphasize the differences caused by body shape. Depending on the bluntness of the nose section, there is a very

small region over which high stagnation pressures exist. The pressures are virtually constant over the conical section. Figure 16-36 also shows sea level overpressure values for reference; the overpressures shown indicate that at altitudes near 50 kilofeet with the body traveling at Mach 20, the overpressure at the surface of the cone section is about 32 psi.

### 16-22 Initial Interaction of Vehicle Flow-Field and Blast Wave (Shock-Shock)

When the reentry vehicle bow wave and the blast wave contact each other a region of high pressure is generated. This region is characterized by a value of pressure that is larger than the value of pressure associated with either shock wave before the interaction. The HARTS results can be summarized by referring to a representative figure. Figure 16-36 shows the variation of maximum overpressure ratio (shock-shock maximum overpressure divided by quasi-steady maximum overpressure, *after interaction*) and duration with the nose surface angle for a hemispherical nose at typical intercept conditions ( $M_\infty = 15$  to 22 and  $M_B = 5$  to 8) assuming  $\gamma = 1.4$ . The general conclusion to be drawn from the upper curve of Figures 16-36 is that the shock-shock interaction peak overpressure will not exceed a factor of two larger than the quasi-steady overpressure (after interaction). Also, the lower curve on Figure 16-36 indicates that the duration of the shock-shock interaction is extremely short; as an example, if  $\tau V_v/R$  is 0.2, then  $\tau = 1 \mu\text{sec}$  ( $10^{-6}$  sec) for  $V_v = 20,000$  ft/sec and  $R = 0.1$  ft. However, it is evident that for the same nose radius ( $R$ ), the value of  $\tau$  increases as the vehicle speed ( $V_v$ ) decreases.

### 16-23 Damage Envelopes

The culmination or end result of loading and response calculations is the damage envelope. The damage envelope defines a volume

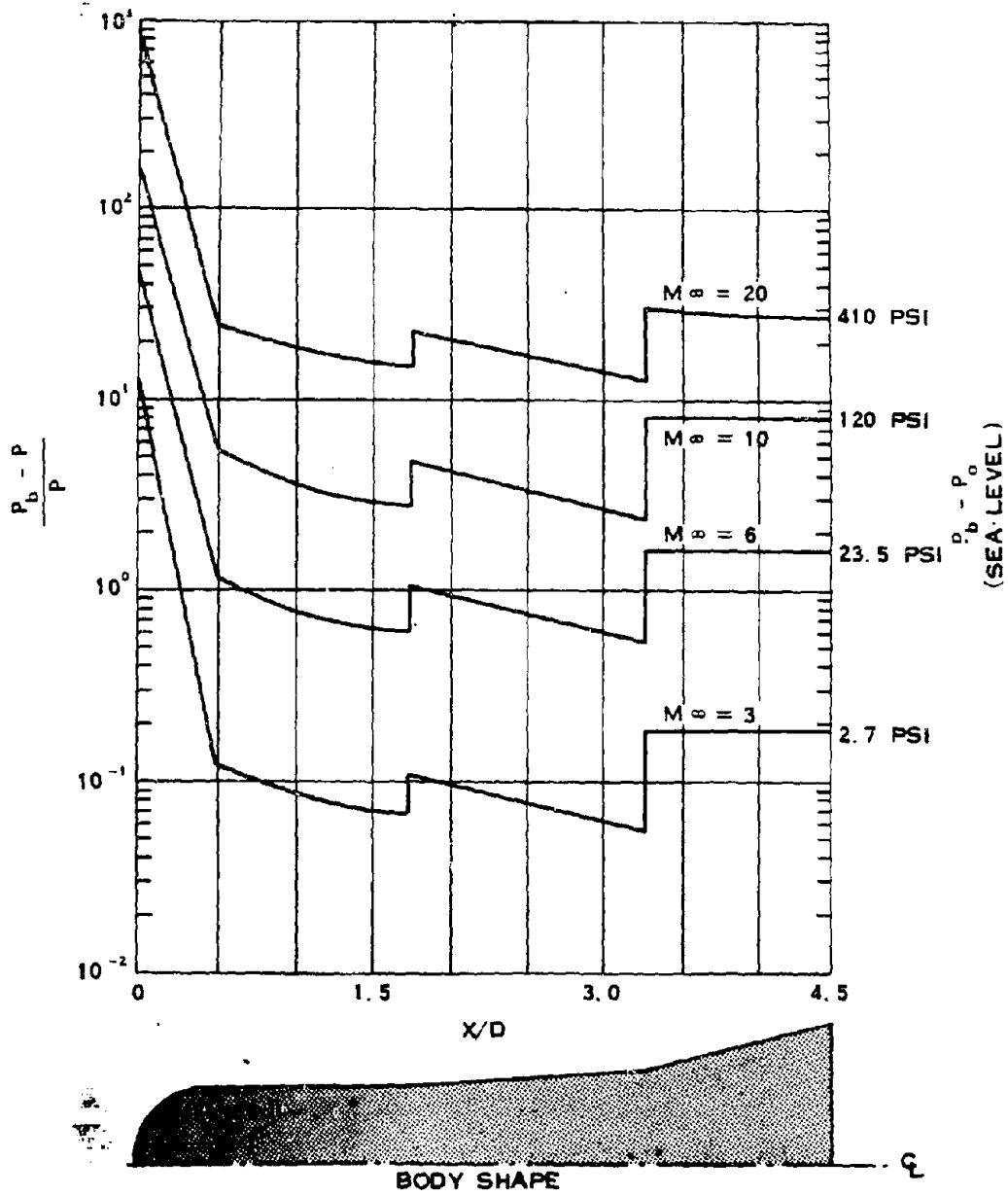


Figure 16-34. Steady State Flow Field Surface Pressures,  
Sphere-Cone-Flare Body

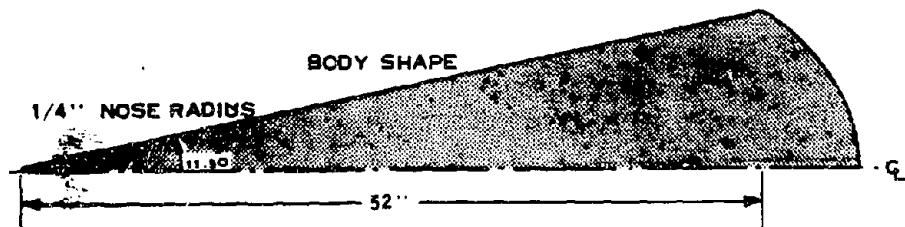
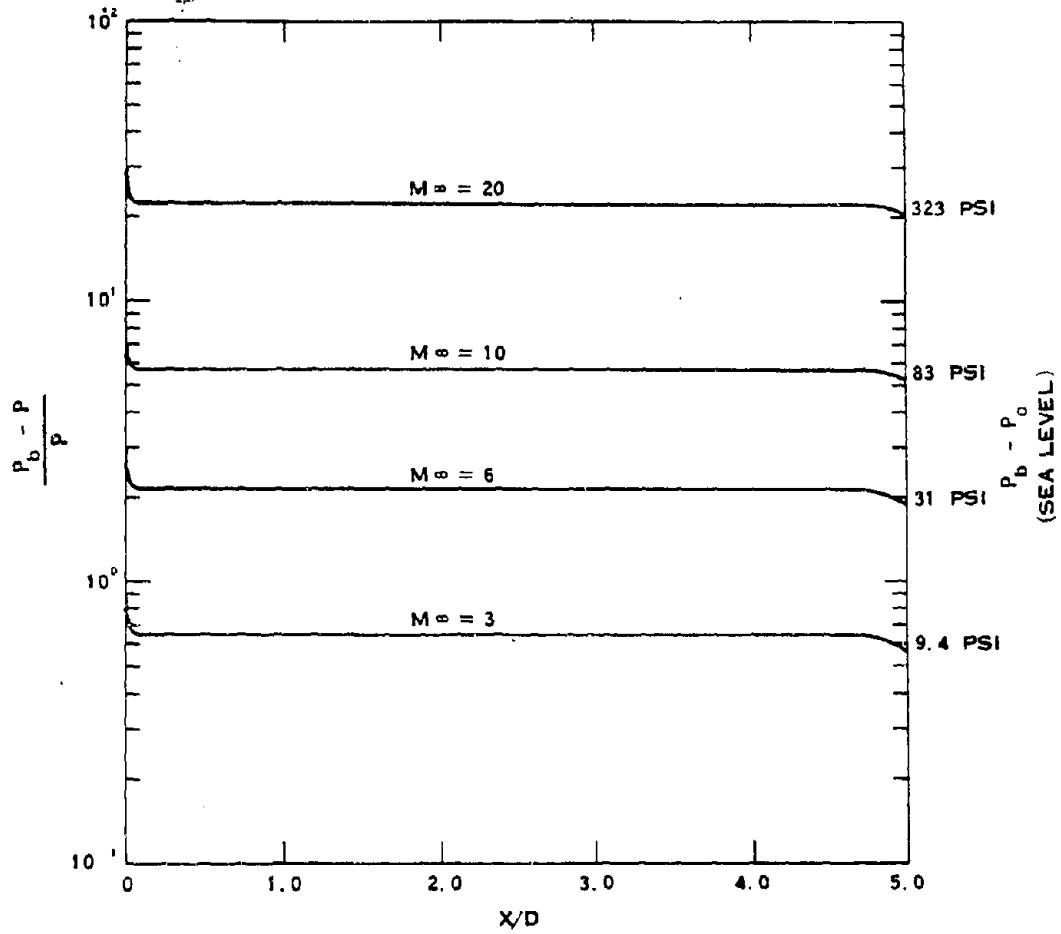


Figure 16-35. Steady State Flow Field Surface Pressures,  
Cone Sphere Body

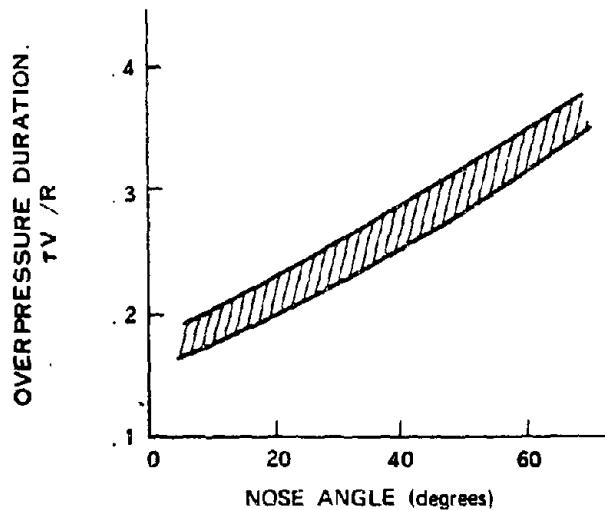
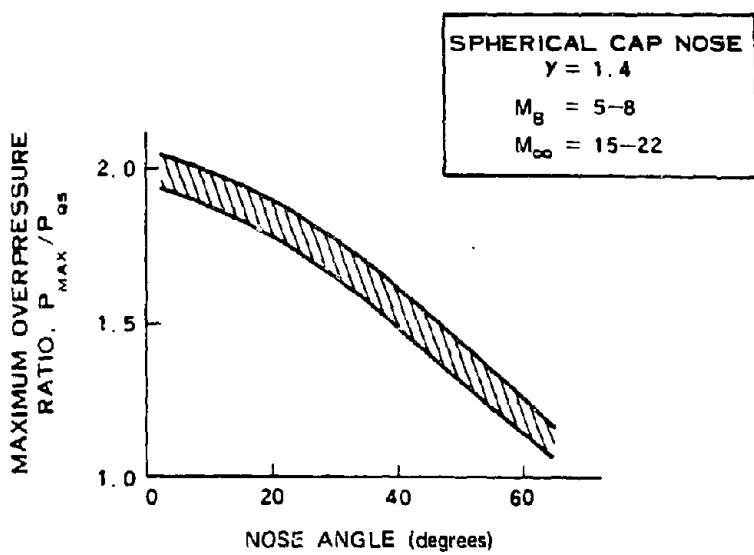


Figure 16-36. Maximum Overpressure and Overpressure Duration for Typical Shock-Shock Interactions

within which a burst of specific yield will cause axial or lateral forces greater than those for which the vehicle was designed. This envelope is required as part of the iterative processes in which tradeoffs involving weight penalties, yields, target damage criteria, defense capabilities, dispersion and booster capabilities must be considered. Two basic steps in determining the damage envelopes for an *RV* are: construction of the Locus of Escape (*LOE*); and location of points, relative to burst point, where the *RV* is subjected to forces equal to design loads.

The nomenclature defined by Figure 16-23 will be used for simplicity and clarity. In this blast-intercept configuration, point A is the position of the *RV* at time of detonation; B is the point of intercept of the *RV* and the blast sphere; OD is the distance of closest approach of the *RV* to the burst center. The distance LD is called the lead distance, and RB is the radius of intercept.

A reference trajectory is introduced to define a new coordinate system. This trajectory, which is one axis of the new coordinate system, is parallel to the *RV* trajectory and intersects the burst point (O) (see Figure 16-23). With the center of this coordinate system at O, the other axis is perpendicular to the reference trajectory. This coordinate system locates the position of the vehicle at the time of detonation relative to the reference trajectory.

The following procedure is used to construct the locus of escape (*LOE*). The *LOE* defines a volume, outside of which the reentry vehicle will not intercept the blast shock wave. Figure 16-37 illustrates a situation from which one point on the *LOE* is defined. During the time interval  $(t_c' - t_x')$  the shock front expands to point C. During the time interval  $(t_c' - t_o')$  the vehicle travels from point X to point C where it intersects the shock front. If  $(t_c' - t_x') = (t_c' - t_o')$ , X is a point on the *LOE*. The distance XC is the lead distance, while OC is the cross range. To

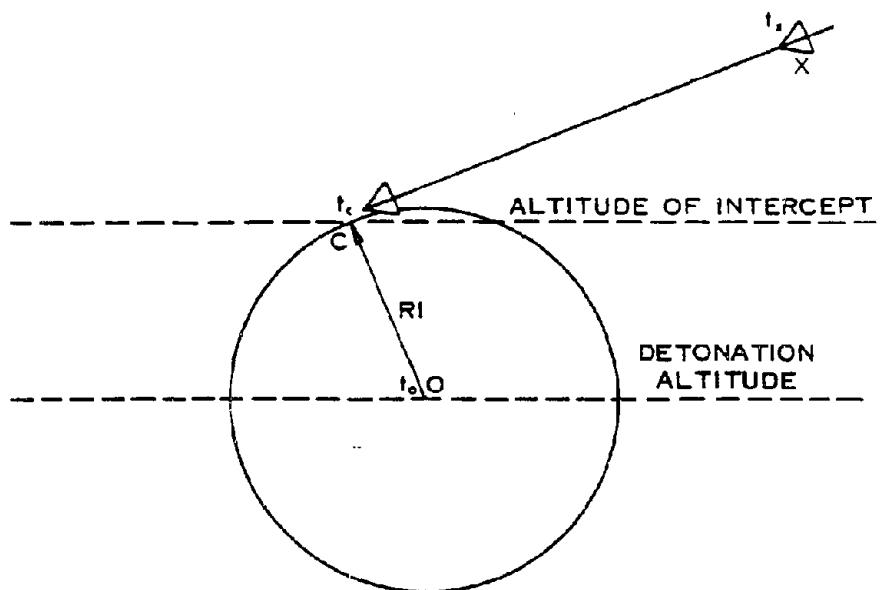
determine another point on the *LOE*, pick another radius of intercept and find a distance  $X'C$  such that  $(t_c' - t_x') = (t_c' - t_o')$ . Determination of several points, both above and below the reference trajectory, will define the *LOE*.

The next step in defining the damage envelope is to determine locations, with relation to the burst, at which the reentry vehicle would suffer lateral and axial forces equal to the design loads. Sufficient locations must be selected and g loads calculated for each point so that iso-g contours can be constructed. Correlation of design loads with these iso-g contours defines the damage envelope. In this case, a g level is specified as the damage criterion.

(U) Figure 16-38 is a qualitative example that shows the *LOE* and the lateral and axial iso-g contours. This figure is oriented with respect to a reference trajectory. Figure 16-39 shows the relation between Figure 16-38 and a real situation.

It must be realized that the g loadings described in the above examples are those experienced by a rigid body vehicle. Since the forces are applied dynamically, dynamic amplification factors must be considered. Displacements that result from dynamic loading can be greater than those that result from static loading. Thus, the effective force experienced by the warhead or other internal components may be more than the rigid body g's.

It should also be noted that the response of reentry vehicles depends not only on peak values of the force, but also on the rate of application and the rate of decay of the force. Having sustained the peak value of the force, which occurs at the shock front, the reentry vehicle suffers lesser forces and pressures as it penetrates the blast sphere. Complete and accurate definition of the damage envelope must include responses during the entire force-pressure time history. This will be discussed further in connection with the structural response analyses of



$t_0$  = TIME OF DETONATION

$t_c$  = TIME SHOCK FRONT AND RV ARE AT POINT C

$t_s$  = TIME RV IS AT POINT X

Figure 16-37. Determination of Locus of Escape

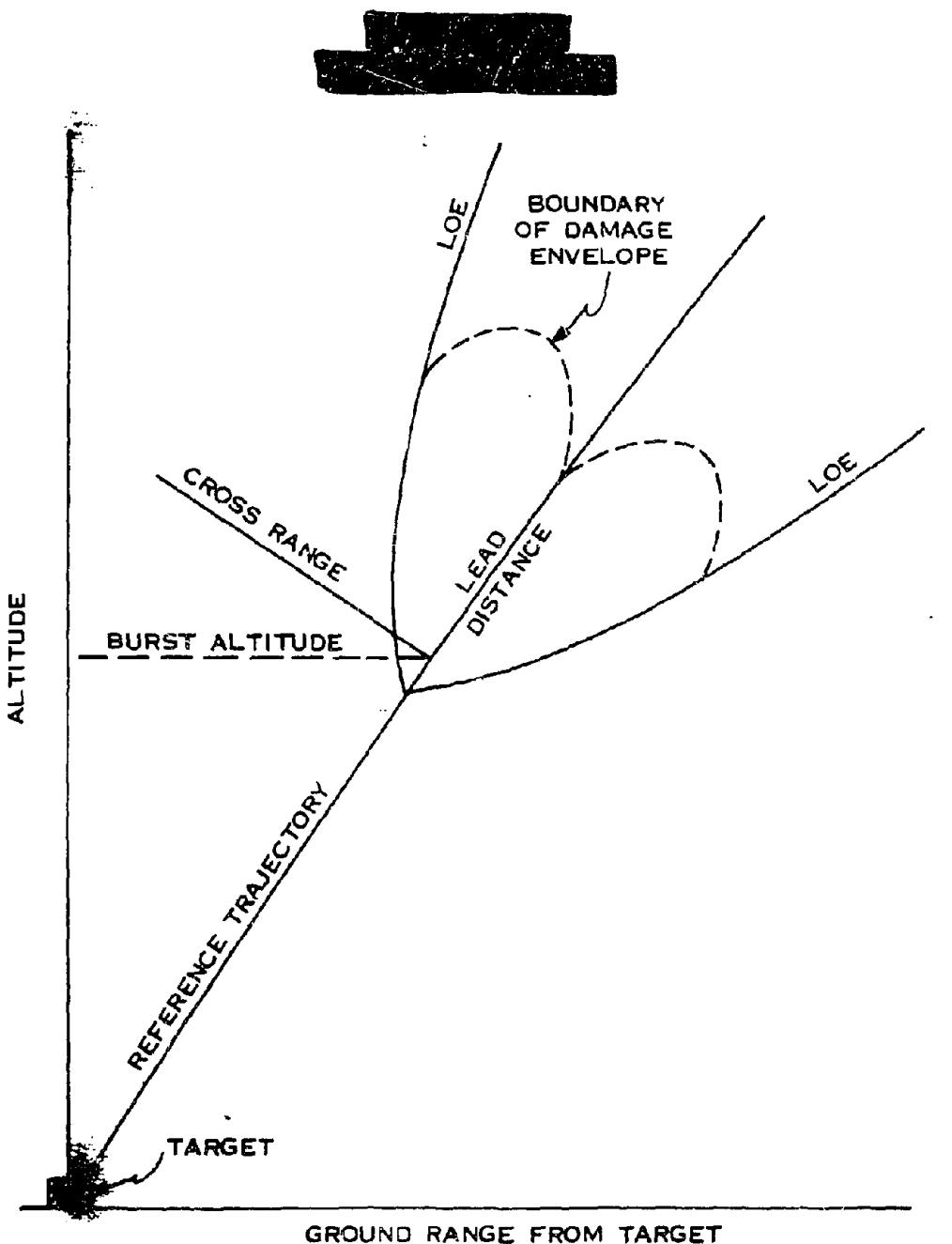


Figure 16-39. In-Flight Intercept

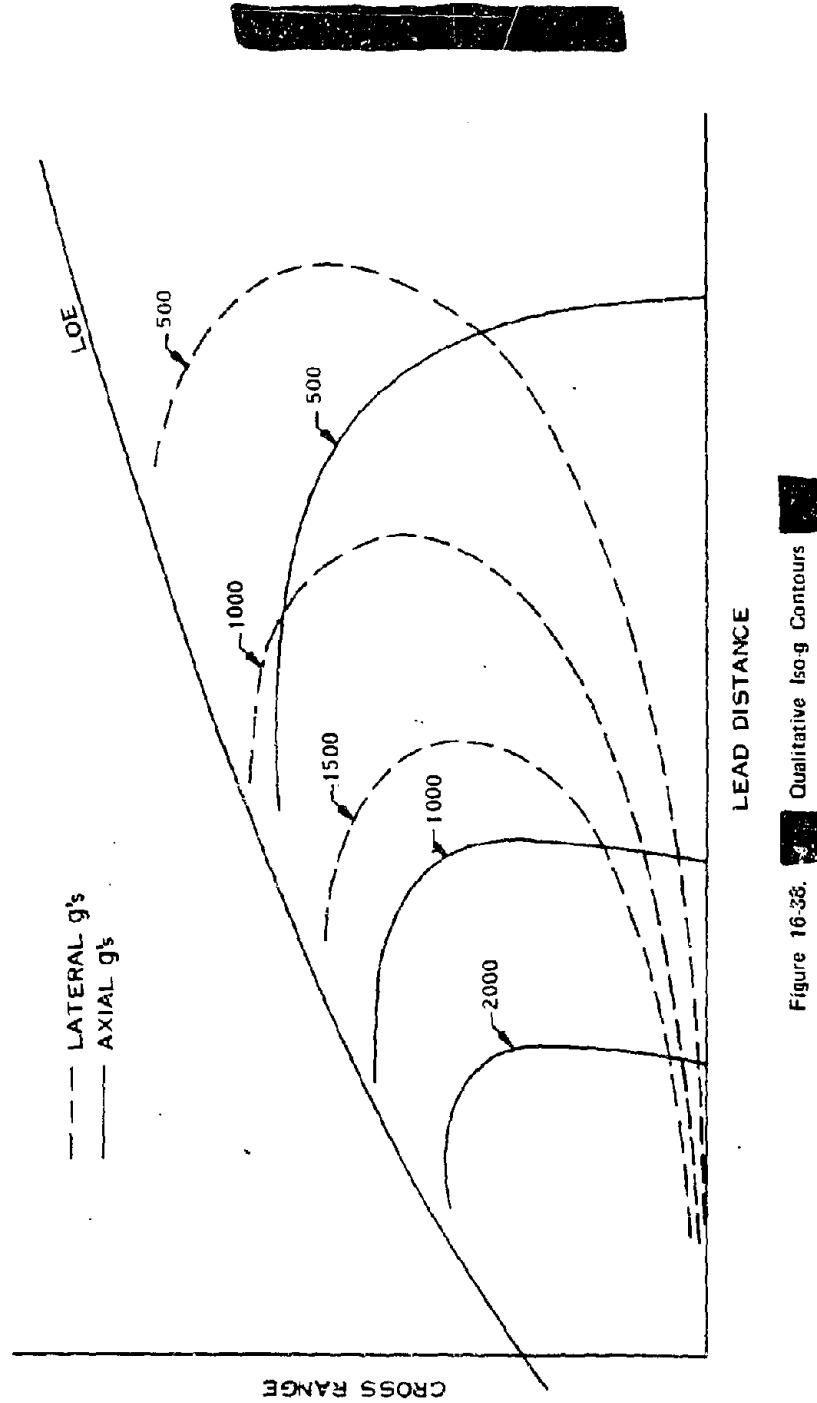


Figure 16-38. Qualitative Iso-g Contours

ABM vehicles (paragraph 16-32). It is evident that damage criteria other than rigid body g levels can be specified to define the damage envelope for a vehicle.

### RESULTS OF SOME RV BLAST AND THERMAL LOAD AND VULNERABILITY CALCULATIONS

As pointed out in paragraph 16-13, it is impossible to condense the determination of blast and thermal vulnerability into a generalized methodology suitable for hand computation. The computations are associated too intimately with the design details of the particular *RV* of interest. In order to provide the users of this manual with some understanding of the procedures involved in such computations, some typical calculations are described in the following paragraphs.

#### 16-24 Blast Loads on the RV

Assume that a reentry vehicle is hardened to survive 200 cal/cm<sup>2</sup> incident X-ray environment. The information desired is whether or not the *RV* will be vulnerable to blast and/or thermal effects at any point along the trajectory. The sample vehicle is assumed to have the following parameters.

- It is a 6° sphere cone configuration.
- The ballistic coefficient is  $\beta = 1,000 \text{ lb/ft}^2$ .
- Reentry altitude = 400,000 feet.
- Reentry angle = -35°.
- Reentry velocity = 17,000 ft/sec.

Two questions are examined separately to obtain the desired information.

- What blast load (axial and lateral accelerations) accompanies 200 cal/cm<sup>2</sup> incident X-ray exposure at the altitudes of interest from the standpoint of blast?
- What are the minimum axial and lateral rigid body accelerations that will allow

blast survival through all altitudes for separation distances equal to the vacuum separation distance for 200 cal/cm<sup>2</sup> incident X-rays (the minimum separation during exoatmospheric flight)?

Figure 16-40 shows the results of calculation of the axial and lateral rigid body g loads as a function of intercept altitude that would result when the *RV* is initially separated from [REDACTED] burst so as not to receive more than 200 cal/cm<sup>2</sup> X-ray energy incident on the vehicle. The vacuum separation distance for this X-ray level is about 11,000 feet (Chapter 4), and if the vehicle maintains that separation between altitudes of 40 and 100 kilofeet it will attain maximum g loads at an altitude of 40 kilofeet. The axial load at this altitude is 230 g's and the lateral load is 280 g's. At intercept altitudes less than 40 kilofeet, the rigid body loads will be less for the same separation distance.

The axial and lateral loads that would be sustained if the separation distance is such that 200 cal/cm<sup>2</sup> X-ray energy were deposited from [REDACTED] weapon are also shown in Figure 16-40. The approximate distances are shown as a function of intercept altitude in Figure 16-41.

Figure 16-41 shows near maximum separation distance as a function of intercept altitude for the 230 g axial load and the 280 g lateral load. The approximate 200 cal/cm<sup>2</sup> separation distances also are shown as a function of intercept altitude for the [REDACTED] weapon.

The maximum separation distances for the axial loads were obtained for the near head on interception of the *RV* by the blast wave. The maximum distances for the lateral loads were obtained from the near side on interception, i.e., 65 to 70° measured from the nose of the vehicle.

The incident blast overpressures required to induce the g loads are shown in Figure 16-42 for the 230 g axial and 280 g lateral loads of

Figure 16-41. At 40 kilofeet intercept altitude, a minimum overpressure of 22 psi is required to attain the 230 g axial load. The overpressure required to attain 280 g's laterally is 18.5 psi at 40 kilofeet, and a minimum of 13.5 psi is required above 90 kilofeet altitude.

Figure 16-43 shows the curves of g load as a function of maximum separation distance for a 40 kilofeet altitude intercept by a blast wave from [redacted] weapon. It should be noted, from this figure, that extremely large separation distances are indicated if the lateral hardening of an RV is less than 100 g's. For yields less than or greater than [redacted] this separation range changes approximately as [redacted]. The approximate nature of this ratio results from the change in the velocity of the vehicle between the points of initial separation and interception.

Based on this brief examination of the results of calculation of blast vulnerability, the main conclusion is that rigid body loads of 280 g's axially and 230 g's laterally are compatible with the 200 cal/cm<sup>2</sup> X-ray hardening of the RV. Moreover, if the RV rigid body response hardness level falls short of these g levels, the blast effects may predominate as a damage mechanism. More specific trajectory/blast cases must be studied to determine the required g loading criteria for balance with a 200 cal/cm<sup>2</sup> X-ray criterion.

#### 16-25 Thermal Radiation Loads on the RV [redacted]

A sample investigation has been made of the free field thermal radiation incident on the same RV described in paragraph 16-24 as it flies through a nuclear burst in the lower atmosphere. The basic trajectory considered in this study had a reentry velocity 17,000 ft/sec and a flight path angle of -35°. In addition, a limited study was performed for a 19,200 ft/sec/-75° trajectory. Thermal radiation heat loads

were computed for head on intercepts of [redacted] burst at 40-, 60-, 80-, and 100-kilofeet burst altitudes. Burst yields of [redacted] and [redacted] were also considered at the 60 kilofeet altitude.

[redacted] The thermal radiation heat flux produced by a nuclear burst can be obtained as a function of distance, direction and time from the radiation/hydrodynamic calculations of Hillendahl that were used to describe the thermal source in Chapter 3 together with the appropriate form factors. These are free field thermal radiation data and do not include any interaction between the vehicle and the radiation field, i.e., the possible attenuation of radiation resulting from an opaque layer of vaporized heat shield material in the flow field surrounding the vehicle was not included (see paragraph 16-31 for a discussion of these "blocking" effects). The total free field heat load to the stagnation point, cone, and base region of the RV was determined by integrating the heat flux as a function of time after detonation, assuming a straight line, constant velocity trajectory in the vicinity of the burst.

[redacted] The total radiation heat load for this example is shown in Figures 16-44 through 16-46 as a function of the initial slant range of the vehicle, burst altitude, burst yield, and trajectory. For initial slant ranges less than about 3 to 5 kilofeet, the heat load is very large (35,000 Btu/ft<sup>2</sup>) and is essentially independent of location on the vehicle. For a fixed burst yield and initial slant range, the heat load decreases with increasing altitude; conversely, for a fixed burst altitude and initial slant range, the heat load increases with increasing yield. Finally, a higher velocity trajectory increases the heat load for a fixed yield and altitude.

[redacted] The thermal data shown in Figures 16-44 through 16-46 could be used in conjunction with the blast data of paragraph 16-24 to determine the total radiation heat loading as a function of blast loading (rigid body axial load

$\Sigma Q_R$   
 $Q_R(z)$

Deleted

Figure 16-44. [REDACTED] Thermal Radiation Heat Load on the Cone as  
a Function of Initial Slant Range for  
Several Burst Altitudes [REDACTED]

DNA  
W(?)

Deleted

Figure 16-45. [REDACTED] Thermal Radiation Heat Load on the Cone as  
a Function of Initial Slant Range for  
Several Burst Yields [REDACTED]

DIA  
(e)(3)

Deleted

Figure 16-46. [REDACTED] Thermal Radiation Heat Load on the Cone as  
a Function of Initial Slant Range for  
Several Trajectories [REDACTED]

factors). As a particular example, these data show that, for a 350 kt burst at 40 kilofeet and the 17,000 ft/sec/-35° trajectory, the radiation heat load on the cone associated with a 200 g, head on intercept condition is only 530 Btu/ft<sup>2</sup>, whereas for a 300 g intercept condition it is 5,400 Btu/ft<sup>2</sup>. This particular example indicates that a 50 percent increase in blast hardness (as measured by the rigid body g criteria) produces an order of magnitude larger thermal environment.

#### 16-26 Description of a Blast/Thermal Vulnerability Determination

This paragraph continues the description of the sample computations that were described in paragraphs 16-24 and 16-25. The determination of the sample RV to blast and thermal effects produced by a nuclear weapon burst is described below.

The blast vulnerability analysis of the RV is made under the following assumptions:

- 6° sphere cone vehicle with a ballistic coefficient of 1,000 lb/ft<sup>2</sup> (assumed constant for normal reentry).
- Point mass-zero lift trajectories were used in the computations.
- Reentry altitude = 400,000 ft.

The blast model used in the computations is considered to be an upper bound to a conventional weapon blast output. Modified Sachs' scaling (see paragraph 2-14) was used in conjunction with curve fits to radius-time-overpressure data. The other peak blast parameters, such as density and particle velocity, are Rankine-Hugoniot values consistent with the scaled overpressures. The environment to which the vehicle is exposed in the interior of the shock front was simulated by assuming constant vehicle velocity during fly through and Sach's scaling curve fits to the interior profiles. It should be noted that, in actual practice, vehicle fly through loading calculations are performed

on an electronic computer using the results of detailed radiation/hydrodynamic calculations corresponding to the nuclear device and burst altitude of interest.

The vehicle reentry conditions used for this calculation are as follows:

- Case 1
  - a. Reentry velocity = 17,000 ft/sec
  - b. Reentry angle = -35°
- Case 2
  - a. Reentry velocity = 19,300 ft/sec
  - b. Reentry angle = -75°

The temperature of the heat shield can be an important factor in determining the structural response of the RV to blast induced loading because of the possible temperature dependence of some of the structural properties, e.g., elastic modulus and yield stress, at elevated temperatures. For the study discussed here, predictions of the heat shield bulk temperature accounted for ascent heating, normal reentry heating to the burst altitude, and thermal radiation heating from the nuclear burst. The bulk temperature is symbolically related to the heat loads by

$$Q_{\text{ascent}} + Q_{\text{reentry}} + \alpha Q_{\text{radiation}} = \rho t \int_{T_{\text{launch}}}^{T_{\text{bulk}}} C_p dT \text{ (Btu/ft}^2\text{)},$$

where it has been assumed that the temperature is uniform across the thin ablator skin and that heat losses are negligible compared to heat inputs. In general, considerable caution must be exercised in employing the thin skin-bulk temperature method.

The thermal radiation heat flux produced by the nuclear burst was obtained as described in paragraph 16-25. The thermal radiation heat load incident on the vehicle was deter-

mined by numerically integrating the flux, as a function of time after detonation, assuming constant vehicle velocity at that altitude and no vehicle spin. It should be noted that, aside from the inherent uncertainties in the free field thermal radiation data, there are additional uncertainties in determining what fraction of the incident thermal radiation is actually absorbed by the ablative surface during the fireball fly through. This is due to a lack of knowledge of the spectral absorptivity of the vehicle surface under these conditions and of the possible attenuation of radiation as a result of an opaque layer of vaporized heat shield material in the flow field surrounding the vehicle.

Two basic methods of structural analysis were employed for this sample calculation. The first method involves the application of a finite length, elastic cylinder response solution to determine the dynamic shell stresses resulting from head on intercept loadings. The second method, which was applied to the side on intercept, involved the evaluation of the dynamic response of a lumped parameter, free free beam model subjected to transient blast loadings. In actual practice, the analysis of the structural response of *RV* configurations should employ much more sophisticated and complex methods. The description of these relatively simple methods is included to indicate to the user the general analytical methods that could be used.

The results of these two methods of structural analysis depend on assumptions made concerning the blast and thermal environment that the *RV* encounters. In this calculation, the transient aerodynamic loading was developed by using Newtonian theory for pressure magnitudes and distributions (see paragraphs 16-21 and 16-22) combined with a curve-fit exponential time decay obtained by flying an unperturbed trajectory through the blast model. To simplify the calculation, instantaneous engulfment was assumed and shock-on-shock interaction effects

were ignored. In addition, the structural response was only examined for blast entrance and for normal reentry conditions. Blast traversal and exit of the vehicle from the blast region were not examined. Thermal loading from normal reentry and nuclear burst thermal radiation were considered for structural response through the bulk skin temperature rise. No attempt was made to evaluate resulting thermal stresses from this high temperature environment; however, the bulk temperature effect was accounted for when choosing material elastic properties and allowables.

Three separate bays or ring-stiffened sections of the *RV* were investigated for the head on intercepts. After a few dynamic response calculations were made, it became apparent that Bay L-I (Station 37.5 to Station 49) was the most vulnerable to head on blast loadings; therefore, the results presented are for Bay L-I. The cylinder solution used is a closed form, elastic response code that computes all stresses at both the inside and outside shell fibers at any desired point on the shell.

The side on intercept conditions were examined with a lump-parameter, free-free, "Timoshenko" beam model. The bending rigidity was supplied completely by the ablator shell, whereas the mass distribution was made up of both the main shell structure and all internal components. As in the head on studies, the thermal effects were included only in the evaluations of material elastic properties and allowables. Using this lumped-parameter mode, a normal mode solution was employed to determine the complete time history of bending stresses that developed at a number of stations along the missile length from the transient pressure loading that resulted from blast intercept. In all cases, the peak beam bending stresses occurred in a region bounded by Stations 20 and 25.

In addition to these two basic tools of structural analysis, i.e., cylinder solution and

beam model, a check of shell buckling was made by using the semi-empirical results from the HARTS Program. This check calculation revealed that, if buckling did occur during blast intercept, it probably would be elastic; however, since rather thick walled shells were involved, the calculated critical buckling pressures are very high compared to pressures necessary to cause conditions leading to plastic deformation and rupture.

#### 16-27 Results of the RV Vulnerability Determination

The results of the structural response study are shown in Figure 16-47 for head on intercept and Figure 16-48 for side on intercept. Figures 16-47 and 16-48 show the allowable stresses and the peak stresses developed from blast entrance loads (characterized by the plotted loads) as a function of initial slant range from a 350 kt burst at an altitude of 40 kilofeet. For the side on intercept cases (i.e., interception by the blast wave normal to the longitudinal axis of the vehicle), the loads are the total g's obtained by vectorially combining the axial and lateral values. For the head on intercept cases, the total loads are the same as the axial loads.

The incipient structural damage is indicated in the figures by the intersection of the curve showing peak stress developed with the allowable stress curve. The curve labeled "Developed Stress" indicates the variation with slant range of the peak dynamic stresses developed in the vehicle during blast wave intercept. These curves are shown for both the nominal RV and the 1.2 nominal vehicle, which is the same vehicle with the skin thickness increased by 20 percent. The slant range, stress, and loads are tabulated for each of the points of incipient structural damage.

It is apparent that the addition of 20 percent to the skin thickness reduces the vulnerability of the RV by decreasing the slant range

for incipient structural damage markedly. It should be recognized that these values of slant range probably are minimum values for the onset of incipient structural damage as a result of the assumptions used in the stress calculations.

The thermal response data are shown in Figure 16-49 in terms of the temperature at the aft end of the cone ( $X/R_N = 19.4$ ) after burst exit as a function of the initial slant range of the vehicle from the burst. These data are the temperatures developed during normal reentry (including ascent heating) to the burst altitude plus the temperature rise caused by the fireball thermal radiation. Beyond initial slant ranges of 16 to 18 kilofeet, the temperatures shown are the normal reentry temperatures at the burst altitude, since the thermal radiation heat load is quite small at these large ranges. The 40-kilofeet burst altitude induces higher temperatures than the 60-kilofeet altitude because of increases in both reentry heating and thermal radiation heating.

Two specific temperatures, 2,340°F and 1,750°F, are shown in Figure 16-49. The former is the ablator melt temperature, while the latter is the temperature at which the ablator has low structural strength. Since the bulk temperature generally lies somewhere in between the surface and backface temperatures, surface melting will commence before the bulk temperature reaches 2,340°F, but probably only in small amounts. Of more importance is the fact that if the vehicle emerges from the burst with a bulk temperature greater than 1,750°F at critical structural locations, it probably will not be able to survive the exit blast loads and/or the subsequent reentry loads as it descends through maximum dynamic pressure to impact, i.e., if the thermal radiation heat loads are sufficiently great to result in temperatures of 1,750°F at burst exit, "delayed" structural damage may occur subsequent to the blast entrance, even if the entrance loads are not sufficient to cause damage.

Pages 16-78 and 16-79

Deleted.  
DNA (b)(3)

~~DAE~~  
~~(L)(z)~~

Deleted

Figure 16-49 Cone Bulk Temperature after Fly Through  
as a Function of Initial Slant Range from Burst  
(Head On Intercept)

### 16-28 Summary and Conclusions Concerning RV Vulnerability Calculations

There are many different ways to summarize the blast/thermal vulnerability of an RV; this subsection employs a bar graph method, whereas the damage envelope method is used in the succeeding subsection to portray ABM Blast/Thermal Vulnerability. The minimum initial slant ranges for structural and thermal damage are summarized in Figure 16-50 for the 17,000 ft/sec/-35° trajectory and 40 kilofeet burst altitude. These data show that the RV is more vulnerable to the side on intercept/structural damage condition than any other condition. The 20 percent increase in ablator thickness reduces the initial slant ranges for damage considerably. The total "g" loading at the slant range for structural damage and the total free field radiation heat load at the slant range for thermal damage also are shown in the figure. It can be seen that there is no unique mechanical "g" load or thermal "Q" load that determines when damage occurs. This points out the requirement for more definitive information concerning damage criteria associated with actual RV designs.

The separation distance at the burst altitude between two vehicles that were originally at the 130 and 200 cal/cm<sup>2</sup> X-ray separation distances apart in the exoatmosphere

also are shown in Figure 16-50. It can be seen that if two vehicles were spaced for these X-ray loadings from a 350 kt weapon in the exoatmosphere, and the lead vehicle encountered a direct hit from 350 kt at 40 kilofeet, the trailing vehicle definitely would incur damage if it encountered the blast wave.

(S) The foregoing description of the method and results of an RV blast/thermal vulnerability sample calculation was presented to give the user an indication of the important technical aspects that must be included in this type of analysis. Based upon the results, a few rather general conclusions can be drawn:

- It is apparent that the blast/thermal vulnerability of an RV cannot be uniquely expressed in terms of either rigid body "g" load levels or thermal radiation heat loads, but rather is a function of the particular reentry trajectory, intercept geometry, yield of the attacking weapon, and the specific damage mechanism considered.
- Vulnerability loads or damage criteria assigned to a particular RV corresponding to blast or thermal effects may not be compatible with the loads or criteria assigned for other nuclear weapon effects (e.g., X-rays).
- Thermal loads on the RV, resulting from a combination of reentry heating and radiation from the nuclear weapon, can have an important deleterious effect on the material properties (and in turn upon the structural response) of the RV ablator/substructure combination.
- The accurate assessment of RV vulnerability to nuclear weapon effects requires detailed analyses using advanced analytical tools and high-speed electronic computer facilities.

### ANTIMISSILE (ABM) SYSTEMS

The assessment of blast and thermal vulnerability of an antimissile (ABM) system presents many of the same problems that were discussed for reentry vehicles; however, ABM systems have some important characteristics that are unique, and these will form the basis for a large portion of the following discussion.

There are fundamental differences between the views of the designers of RV's and ABM concerning blast and thermal vulnerability. The designer of an RV may be willing to have his vehicle sustain limited damage if the damage would not degrade the probability of mission success significantly. This willingness to sustain

DATA  
(4)(3)

DAN  
(4)(3)

Deleted

Figure 16-50. [REDACTED] Minimum Initial Slant Range for Structural/Thermal Damage at 40 km Burst Altitude,  $V_E / \gamma_E = 17,000$  ft/sec/35° [REDACTED]

some level of damage results from the fact that the RV designer usually deals with large numbers of vehicles directed against an array of targets with the objective of insuring that a fraction of the RV's penetrate the defense and reach the targets. The defense, on the other hand, attempts to deny all "leakage" of enemy RV's. Therefore, when considering blast and thermal fratricide damage, the ABM designer usually will not tolerate any degree of damage to the vehicle (i.e., it is designed to be "sure safe"). When assessing the ability of an ABM to defend a target and to kill an enemy RV, however, the objective dictates that the ABM designer achieve a "sure kill" miss distance relative to the incoming RV.

Most of the following discussion results from a study to determine the probable damage modes and damage envelopes for the AIRS I and II vehicles (paragraph 16-12) when exposed to blast waves and thermal radiation from nuclear explosions.

The scope of the discussion can be summarized as follows:

- Two vehicles are considered, AIRS I and AIRS II. These vehicles nominally represent interceptor vehicles of the SPRINT and SPARTAN class, respectively. Inboard profiles of these vehicles are shown in Figures 16-51 and 16-52.
- Four response modes are considered:
  - (1) Shell breathing response to the blast wave.
  - (2) Vehicle bending response to the blast wave.
  - (3) Internal component damage due to rigid body acceleration produced by the blast wave.
  - (4) Material damage produced by the thermal radiation.
- Coupling effects among the damage modes are neglected, except for the inclusion of degradation of material properties that results from heating the material.

- Control surface damage is not considered.
- Each vehicle is assumed to be in a steady state " $n$ "-g maneuver (where  $n$  can be zero).

The aerodynamic loads initiated by the blast wave must be defined to perform a blast vulnerability analysis. In the definition of the aerodynamic loads imposed on a vehicle traveling at hypersonic speeds when subjected to a strong blast wave, the initial shock-on-shock interactions during the vehicle engulfment by the blast wave present the most difficulty. Recent studies of the response of missile structures to blast loads indicate that the response to the shock-on-shock loads does not contribute significantly to the total response experienced by the missile structure.

The response of the structure to blast is separated into shell breathing, vehicle bending, and rigid body acceleration responses. The separation of the total response into uncoupled breathing and bending responses is required since current methods cannot perform the coupled problem; however, this separation is justified to some extent by consideration of the types of damage associated with each response. In shell breathing response, segments of the shell between bulkheads are excited, and the damage is associated with high frequency local shell deformation. In vehicle bending, the damage results from relatively low frequency excitations of the overall structure.

Criteria for the yielding and buckling response have been generated primarily from data generated in tests of simple cylindrical and conical bodies subjected to air blast from HE detonations. Studies of damage to the vehicle by bending have neglected the short-duration diffractive loading, which is of little consequence in exciting the long period oscillations associated with bending deformations (except possibly for very low yield weapons). The damage criteria for bending deformations, and the response analysis

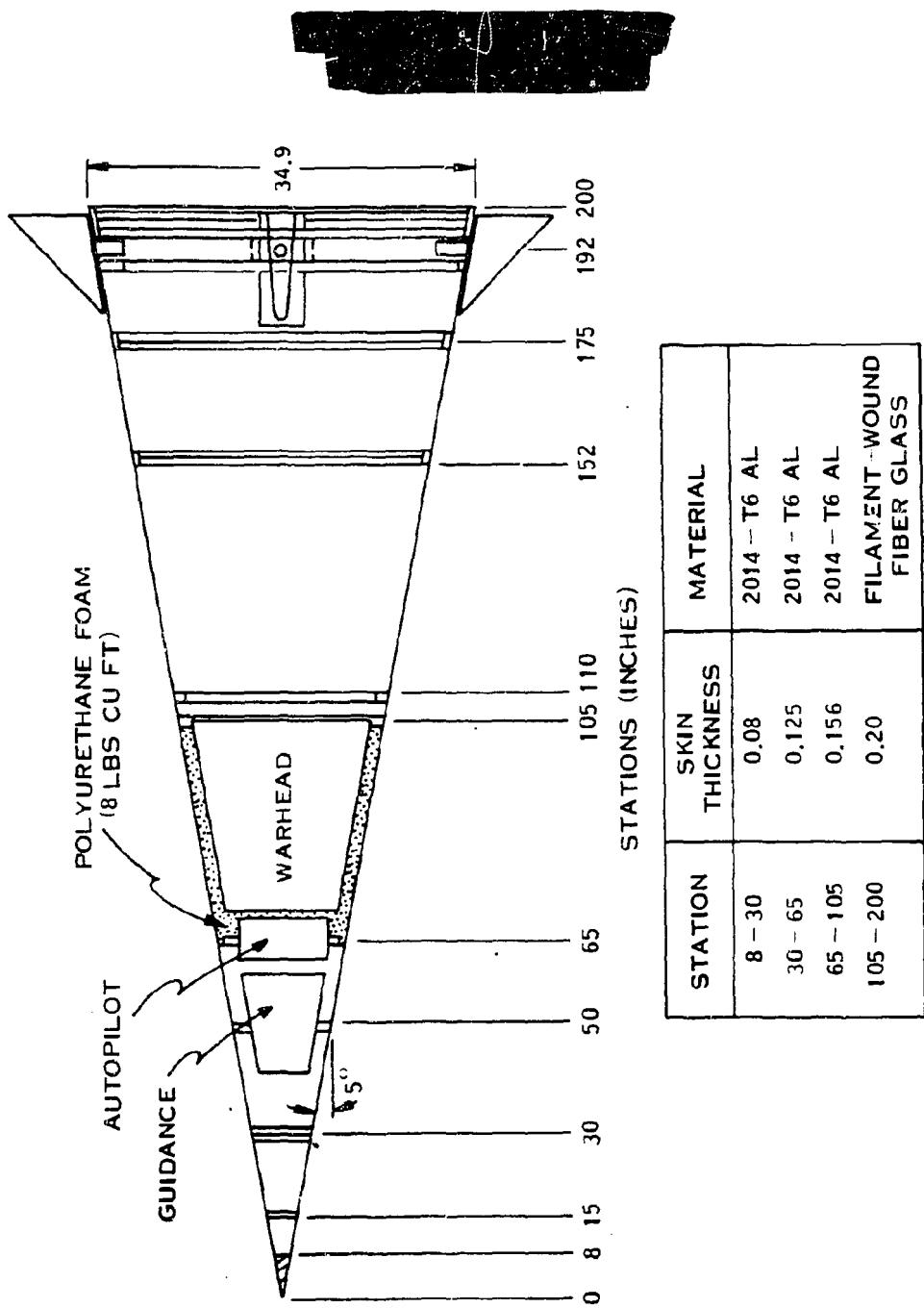


Figure 16-51. Inboard Profile of AIRS I Vehicle

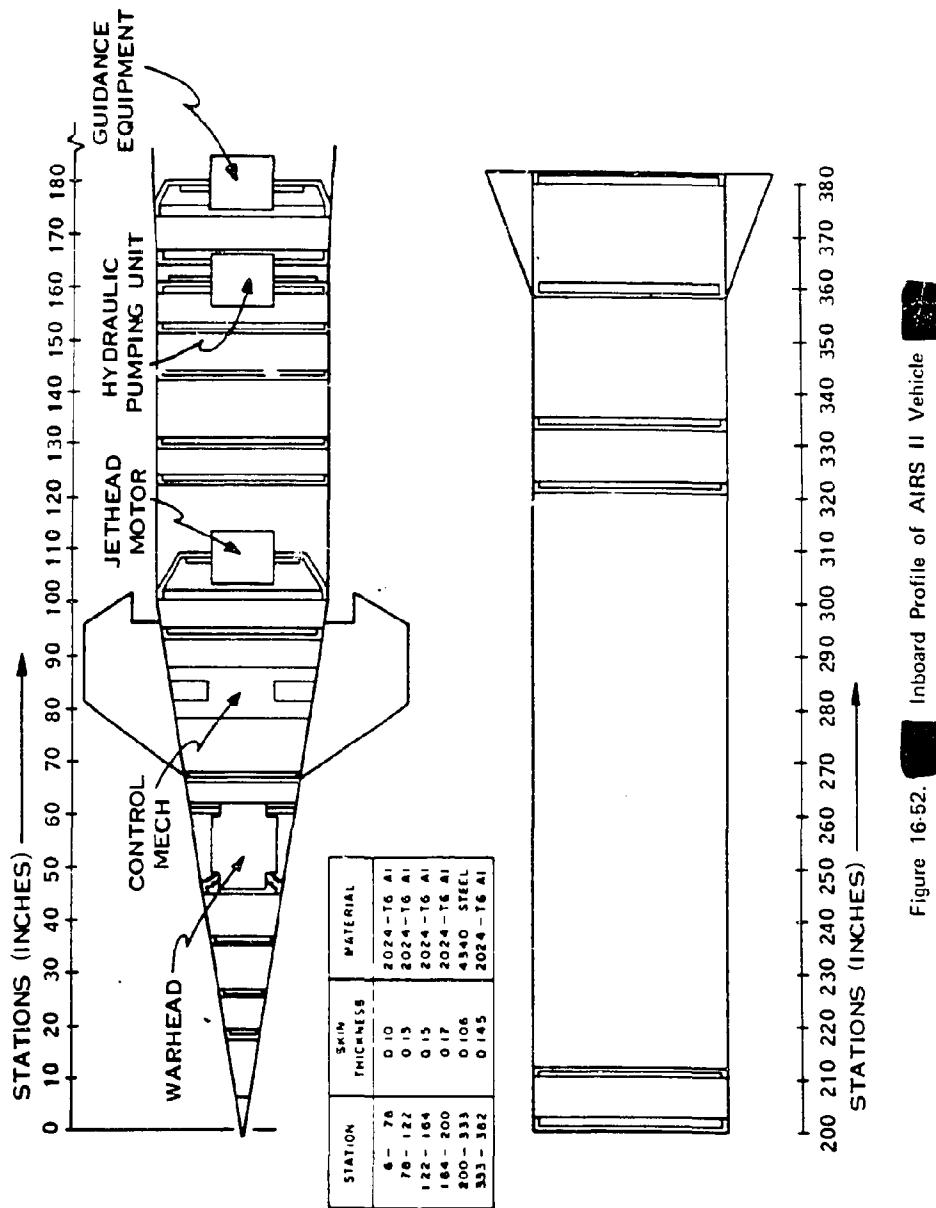


Figure 16-52. [REDACTED] Inboard Profile of AIRS II Vehicle [REDACTED]

techniques, rely on knowledge developed in similar studies performed for aircraft and launch vehicles in the boost phase.

Analysis of response to thermal radiation effects define the mechanisms by which heat is absorbed and distributed throughout the structure, both when the vehicle is outside and inside the fireball. Damage criteria from thermal radiation effects are selected on the basis of the loss of the insulative coverings over the substructure.

Blast and thermal radiation effects damage envelopes for both AIRS I and II are presented below. The relative sizes of these envelopes for the various effects on the two representative vehicles and for the encounter condition variations (in yield and altitude) are discussed briefly.

#### 16-29 Shell Breathing Response

Blast induced pressure loading causes the shell segments of the vehicle between the ring reinforcements to respond in what is usually termed the "breathing mode." Damage occurs in the form of permanent deformation of the skin through the formation of a dented area in the surface of the shell. The primary damage mechanism for the shells is an instability (buckling) of the shell that can occur either when the shell is all elastic or after portions of the shell have become plastic. This damage mechanism can be complicated by the presence of the ablator over the structural shell and by other states of stress and deformation imposed by bending of the vehicle as a result of blast and normal flight loads, or the thermal condition of the vehicle at blast intercept. These interaction problems are not considered.

A complete determination of the blast damage to a shell segment that would be required to prevent the AIRS vehicles from performing a specified maneuver requires two separate analyses. The first analysis predicts response

levels from threshold to severe post buckling damage, and a second analysis predicts the post damage response; the latter is the response of the "damaged" vehicle to the loads imposed by maneuver. Thus, it is not sufficient to calculate the shell response resulting from the blast loading. A sure-safe criterion also must be established for the actual in-flight conditions in the fratricide mode. The amount of damage that constitutes an "unsafe" level under a known set of environmental conditions must be determined eventually if vulnerability studies are to be considered useful to the military planner.

The analyses of the response of critical shell segments of the AIRS I and II vehicles to blast that were selected for this example can only predict the threshold damage level caused by elastic buckling or initial material yielding. Analyses that calculate elastic-plastic response in the post buckling region have only been developed recently for shell response to blast, but experimental data are not sufficiently comprehensive to apply the results to various loading conditions and to different materials. Thus, rather arbitrary criteria must be postulated to relate computed damage levels to "unsafe" conditions for the ABM.

The analyses discussed thus far primarily calculate the response of the shell up to threshold damage, i.e., sure-safe levels. These analyses are elastic in nature and cannot be used directly to determine response that includes severe damage. There are three additional elements required before lethality predictions can be made:

- Selection of the applicable analysis; that is, inelastic buckling or yielding (or possibly fracture).
- Definition of damage criteria, i.e., definition of the amount of damage that must occur in the selected damage mode to negate the intended mission of the vehicle.
- Selection of a means to apply the inelastic analysis to the determination of the load

[REDACTED]  
[REDACTED]  
level required to produce the amount of damage specified.

#### 16-30 Vehicle Bending Response (U)

[REDACTED] Discussions of prediction techniques for the response of the AIRS I and AIRS II vehicles to blast in their rigid body and bending degrees of freedom are separated into two parts. First, a formulation of *damage criteria* for these vehicles in bending is discussed for damage to the primary structure and to the internal components. In the second part, analysis that predicts the *structural response* is discussed. The inclusion of critical damage criteria in a computer program for the response analysis results in the capability to determine sure safe envelopes for bending response to blast.

[REDACTED] A most difficult, but necessary, part of defining damage contours for interceptor missiles in a blast environment is the definition of the amount of damage that must be produced in the primary structure in bending or to internal components to constitute a positive failure of the mission. The approach adopted is to use a simple damage criterion available for interceptor vehicles.

[REDACTED] Selection of simple damage criteria for an interceptor vehicle undergoing bending deformations requires an understanding of the damage modes involved. The primary bending damage modes possible to the primary structure of a vehicle may be:

- Damage to the joints resulting from tensile stresses in excess of the stresses allowable for the joints.
- Buckling damage to the overall shell structure resulting from combined axial and bending induced normal stresses in the shell.

For this discussion, a damage condition in which the vehicle damage cannot support the loads associated with a specific "n"-g maneuver after buckling was selected tentatively as sufficient.

[REDACTED] Damage criteria for internal components should involve detailed investigations of the acceleration-time history environment that a component can withstand. In addition, the supports of internal components and the load-carrying ability of the supports must be considered in a comprehensive vulnerability analysis. It is the usual practice to consider an acceleration time-history and to assign a certain peak acceleration value to be critical.

[REDACTED] In view of a lack of fragility data for the internal components of the AIRS I and II, representative allowable peak acceleration values were selected from information available for design requirements for SPRINT and SPARTAN. These acceleration values are used to demonstrate the procedures involved in determining damage envelopes for internal component damage, but they are not necessarily representative of what the internal equipment mounted inside the vehicles can actually withstand.

[REDACTED] It is necessary to perform a comprehensive analysis of the blast loading and response of the entire missile structure (including primary and secondary structures) to determine the details of the blast loads imposed upon (and the response of) specific internal components when a missile body is exposed to a nuclear weapon environment. This analysis includes development of a detailed mathematical lumped-mass/spring model of the missile to determine the proper "transfer functions" between the primary structure and the internal component of interest. Calculations that use the mathematical model and the definition of the blast loads imposed on the missile structure during a real encounter lead to the determination of the loads imposed on the internal structures.

#### 16-31 Thermal Radiation Effects [REDACTED]

[REDACTED] The establishment of thermal radiation damage criteria for AIRS I and AIRS II required an examination of the individual structures involved.

In general, data concerning thermal radiation effects consists of a description of the temperature distribution through the ablator (and substructure material) and the mass ablation rate, both as a function of time and position on the missile. This fundamental information provides the thermal portion of the inputs for a realistic assessment of the overall vehicle performance during and after an encounter with a nuclear burst. The temperature distribution data can be used in a structural analysis to determine the magnitude of the allowable stresses (or strains), thermal stresses, etc. Furthermore, there are usually internal components in the guidance section, fuzing, arming and firing section (FAF), or warhead section that have a fairly low temperature tolerance. The ablation rates also affect the mass distribution and can affect the aerodynamic characteristics of the missile, which can affect its flight characteristics; however, the following discussion is limited to an examination of thermal effects in the ablator and substructure. No concurrent structural and/or trajectory analyses were performed.

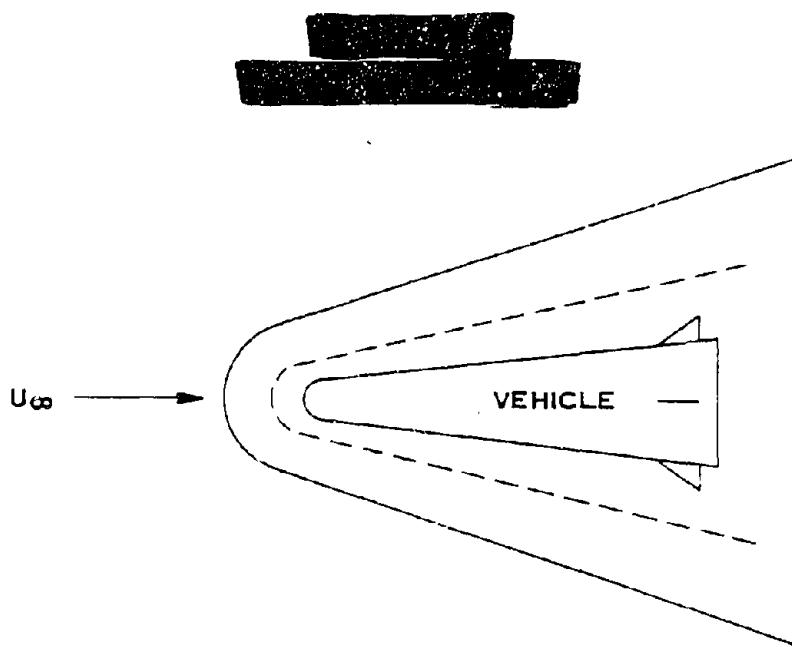
The principal type of ablation material used on the AIRS I missile is tape-wrapped silica phenolic, which is a silica cloth impregnated with phenolic resin. A detailed theoretical prediction of the thermal response of a charring, melting and vaporizing ablator such as silica phenolic on a high-speed missile that flies through (or near) a nuclear fireball during some portion of its mission involves simultaneous consideration of complex physical and chemical phenomena. The general situation is illustrated in a simplified fashion in Figure 16-53. During normal flight (i.e., preburst or post traversal), the vehicle is heated by forced convection ( $\dot{q}_c$ ) caused by friction forces in the boundary layer on the vehicle (aerodynamic heating). During the fireball traversal phase, the predominant mode of heating is thermal radiation ( $\dot{q}_R$ ) from the high temperature fireball air. In this case, the

ablation rates generally are so high that the boundary layer is blown off, and the local flow field (which may be subsonic) is dominated by the ablation vapors. In either case, the heat transfer to the surface causes the ablator to heat, pyrolyze internally, and melt and vaporize at the surface.

A realistic thermal analysis for a silica phenolic coated vehicle should consider the following effects:

- Internal heat conduction in the ablator and substructure.
- Pyrolysis of the phenolic resin in the ablator, with the attendant endothermic chemical reactions and pyrolysis gas flow through the char.
- Convective and radiative heat transfer at the ablator outer surface, and the accompanying surface recession that results from melting and vaporization of the silica cloth.
- The interaction of the injected ablation vapors with the local vehicle flow field, especially the absorption of thermal radiation by the vapors (radiation blocking).
- The time dependent nature of the fireball environment, as well as the transient nature of the temperature response of the ablator.
- Variation of all of the effects listed above with location on the body that result in differences in environment, type and/or thickness of ablator, etc.
- Variation of all of the effects with burst encounter conditions.

It is convenient to separate the thermal analysis into several basic parts, each of which uses somewhat different techniques of analysis according to the most important physical processes that are treated. This concept can be visualized with the aid of Figure 16-53 and an energy balance at the outer surface of the ablator (denoted by a subscript  $w$ ).



#### DEFINITION OF TERMS

FREE STREAM AIR



SHOCK LAYER AIR

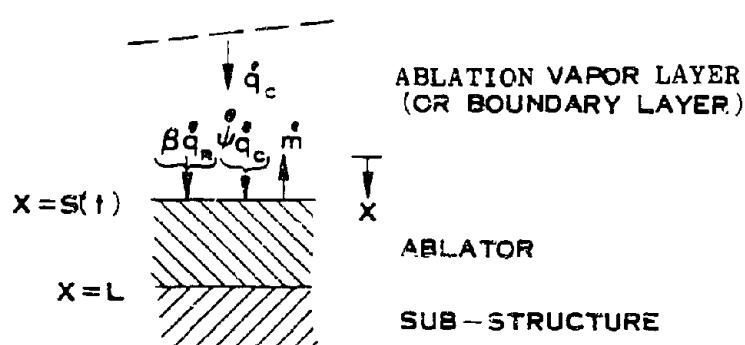


Figure 16-53. Illustration of Ablation Phenomena

$$\psi \dot{q}_c + \beta \dot{q}_R - \epsilon \sigma T_w^4 - \dot{m} \Delta H = \left( -K \frac{\partial T}{\partial x} \right)_w$$

where  $\dot{q}_c$  and  $\dot{q}_R$  are the free field convective and radiant heating rates, respectively. The term "free field" heating rate denotes that the quantity is computed without regard to ablation effects. Thus, the free field convective heating is computed on the basis of nonblowing boundary layer solutions, while the free field radiative heating is computed on the basis of the fireball flow field being unperturbed by the presence of the vehicle. Therefore, by definition, the free field thermal environment depends only on time and body position for a particular trajectory and encounter condition, and not on the type of ablation material used.

The quantities  $\psi$  and  $\beta$  are the convective and radiative blocking functions, respectively. They denote the fraction of the free field heating rate that exists at the ablator surface during the actual ablation process. The blocking functions must be obtained from a solution for the local vehicle flow field that accounts for the effects of the injected ablation vapors on the flow field. In general, their values will depend on the level of the free field environment and on the particular ablation material. The quantity  $\epsilon \sigma T_w^4$  represents the energy reradiated from the surface, while the term  $\dot{m} \Delta H$  represents the energy absorbed in surface melting and vaporization. Finally,

$$\left( -K \frac{\partial T}{\partial x} \right)_w$$

is the heat conducted into the surface of the solid ablator, which in general must be obtained from a solution of the temperature profile in the ablator.

The equation simply states that the net convective and radiative heating at the surface,

less the energy reradiated and absorbed in melting and vaporization, equals the energy conducted into the ablator. When the net heating rate is sufficiently high to produce surface melting and vaporization, the equation relates the mass ablation rate ( $\dot{m}$ ) to the free field environment and the temperature distribution in the ablator.

For the purpose of the present discussion, which is primarily concerned with the thermal effects of a nuclear environment, the overall analysis is separated into two basic parts: fireball radiation and ablation, and the internal temperature and ablation response. The former is essentially multidimensional (around the body) and quasi-steady in nature, since it deals with high temperature flow about a high speed missile, whereas the latter is primarily one dimensional (through-the-thickness) and transient in nature since it deals with heat conduction. The coupling condition (boundary condition) that relates the free field environment and local flow field to the internal response is the energy balance at the surface, i.e., the equation given above.

When the results of various theoretical methods are compared there is about a  $\pm 50$  percent uncertainty in the predictions of the total silica phenolic mass ablated during a nuclear fireball traversal, even among theoretical models that assume full vaporization. If only melting is assumed, the results are at least a factor of five higher, and typically a factor of ten.

The condition for thermal damage to the AIRS vehicles was taken to be the time at which 50 percent of the ablator mass was gone; this condition is probably on the conservative side, leading to an upper limit in the size of the vulnerability envelopes.

### 16-32 ABM Blast/Thermal Vulnerability Envelopes

The previous paragraphs described techniques of analysis that can be employed to de-

[REDACTED]  
fine vulnerability envelopes for the AIRS I and AIRS II vehicles exposed to blast and thermal radiation from nuclear explosions. The vulnerability envelopes for the AIRS vehicles and for two typical encounter conditions are shown in Figures 16-54 through 16-57. In each figure, the vehicle under attack is at the origin (0, 0) flying from left to right. If the attacking weapon is burst inside the envelope, the load on the vehicle will exceed the critical level. Thus, the largest envelope on the graph identifies the "most" critical damage mechanism for the vehicle and the burst condition considered.

[REDACTED] Figures 16-54 and 16-55 correspond to the AIRS I vehicle in a typical fratricide situation; it is obvious that the size of the critical damage envelopes are very sensitive to the maneuver (or nonmaneuver) condition of the AIRS I. The AIRS II curves in Figures 16-56 and 16-57, indicate envelopes of somewhat different shapes, but the general behavior is similar to AIRS I.

### 16-33 Conclusions

[REDACTED] The AIRS I and AIRS II vulnerability study produced the following main conclusions:

- The internal component acceleration envelopes are the largest for both AIRS I and AIRS II, but this predominance must be regarded cautiously as a result of the arbitrary nature by which acceleration damage

levels were selected for the AIRS internal components.

- Thermal radiation effects appear to be more important for AIRS I than for AIRS II; however, blast effects produce the larger envelopes for both vehicles.
- Thermal radiation effects tend to increase in relative importance for the larger yields and lower intercept altitudes.
- Shell response and bending response damage are of comparable importance for the nonmaneuver condition for both vehicles. For the maneuver condition, however, the shell damage mode is more important than the bending damage mode in defining vulnerability envelopes for both vehicles.
- The maneuver condition modifies the acceleration, bending and shell damage vulnerability envelopes appreciably. In general, the overall areas (or volumes) of these envelopes increase significantly for the maneuver condition.

[REDACTED] It should be emphasized that the conclusions only apply to the AIRS I and AIRS II vehicles. The foregoing discussion was presented to indicate the types of analyses that must be performed to assess the vulnerability of ABM vehicles to blast and thermal effects. The conclusions could well be significantly different for vehicles of different design.

Pages 16-92 through 16-95

DELETED.

DNA (b)(3)

## **BLAST AND THERMAL LETHALITY**

Previous subsections of this section have concentrated on concerns relative to the blast and thermal vulnerability of friendly RV's and ABM's. This subsection will discuss the concern of the defense in the effectiveness of ABM in "killing" an RV. The emphasis shifts from "sure safe" criteria to "sure kill" criteria.

The definition of the threat RV vehicles and the details of the free field blast and thermal environments of the ABM are the two primary factors that influence the determination of the kill effectiveness of an ABM system. Calculations of blast kill radii have been performed by various groups for the SPRINT ABM against some representative RV threats. The results of these calculations are described in the following paragraphs.

### **16-34 Blast and Thermal Free Field Environments**

DNA (1)(3)

Some of the results of these calculations are shown in Figures 16-58 through 16-61 in the form of blast wave parameters at one altitude, e.g., temperature and flow field profile data, at one typical time. These data are essentially self explanatory. They are useful to provide an overview of the environments; however, for detailed vehicle response studies, the principal output of a radiation-hydrodynamics code calculation consists of the radiation-hydrodynamic and field data as a function of radius at a large number of times after burst. These basic data are stored on magnetic tapes (called Usertapes), which allows dissemination of the principal results for use in many studies. This is necessary since blast/thermal effects studies often require that the vehicle be flown through the environment as a function of time, and it is impossible to present environmental data at the vehicle position as a function of time graphically for all possible combinations of vehicles, trajectories, and intercept conditions.

### **16-35 ABM Blast Loads on Threat Vehicles (Point Mass)**

The study of ABM blast loads on threat vehicles consisted of computer analyses using a generalized trajectory code, with capabilities of including the free field blast environment provided by the radiation-hydrodynamics Usertapes. A nonrotating spherical earth model with a 1962 atmosphere was used for this calculation. The aerodynamics were computed by Newtonian mechanics, based on the input size and shape data defining a sphere-cone for each vehicle. The reentry conditions for the RV nominal-trajectories were defined in terms of altitude, flight path angle, and reentry velocity. Having computed a flight profile with the specified reentry conditions, the blast fly through runs included trajectory computations that started

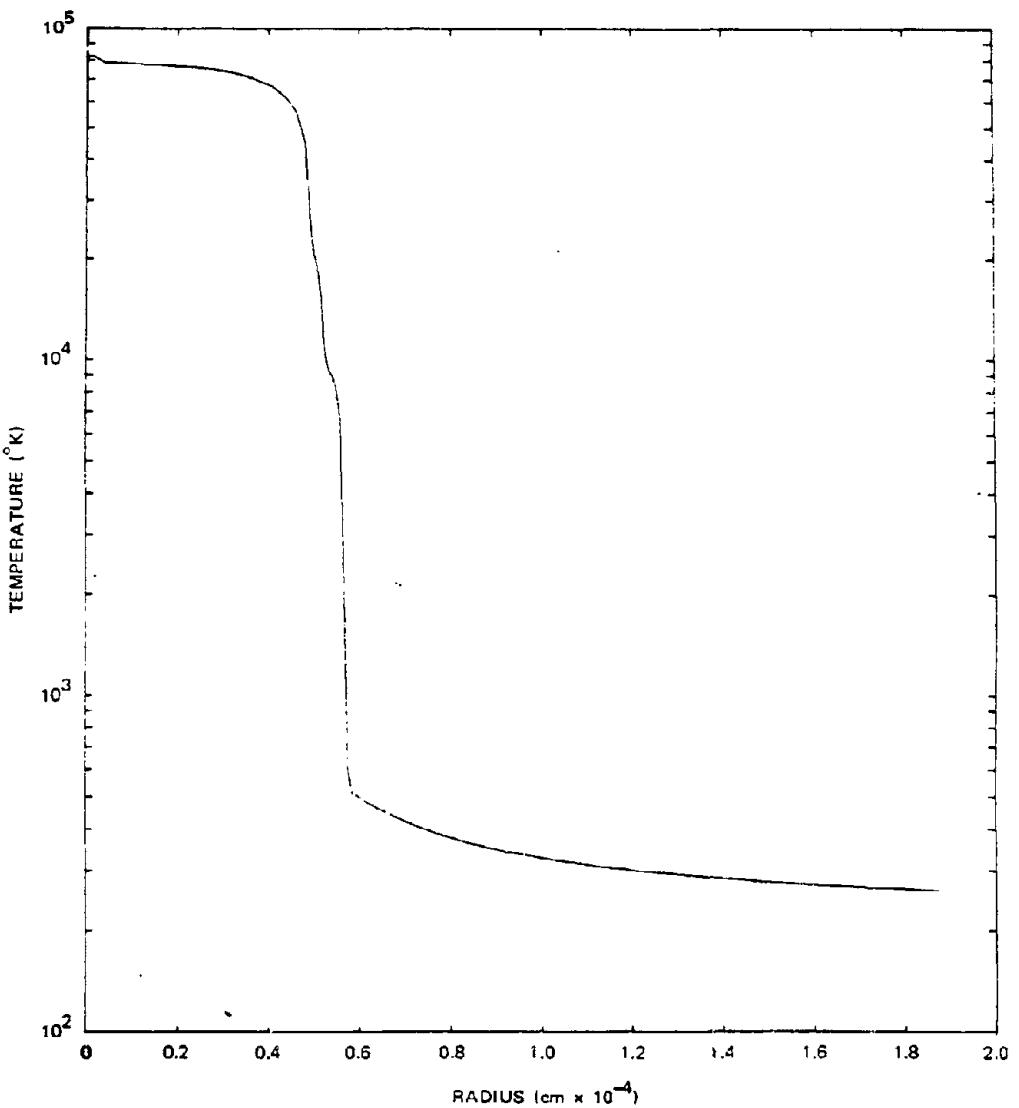


Figure 16-58. [REDACTED] Computed Temperature Profile,  
t = 4.64 msec, 30 kilofeet Altitude [REDACTED]

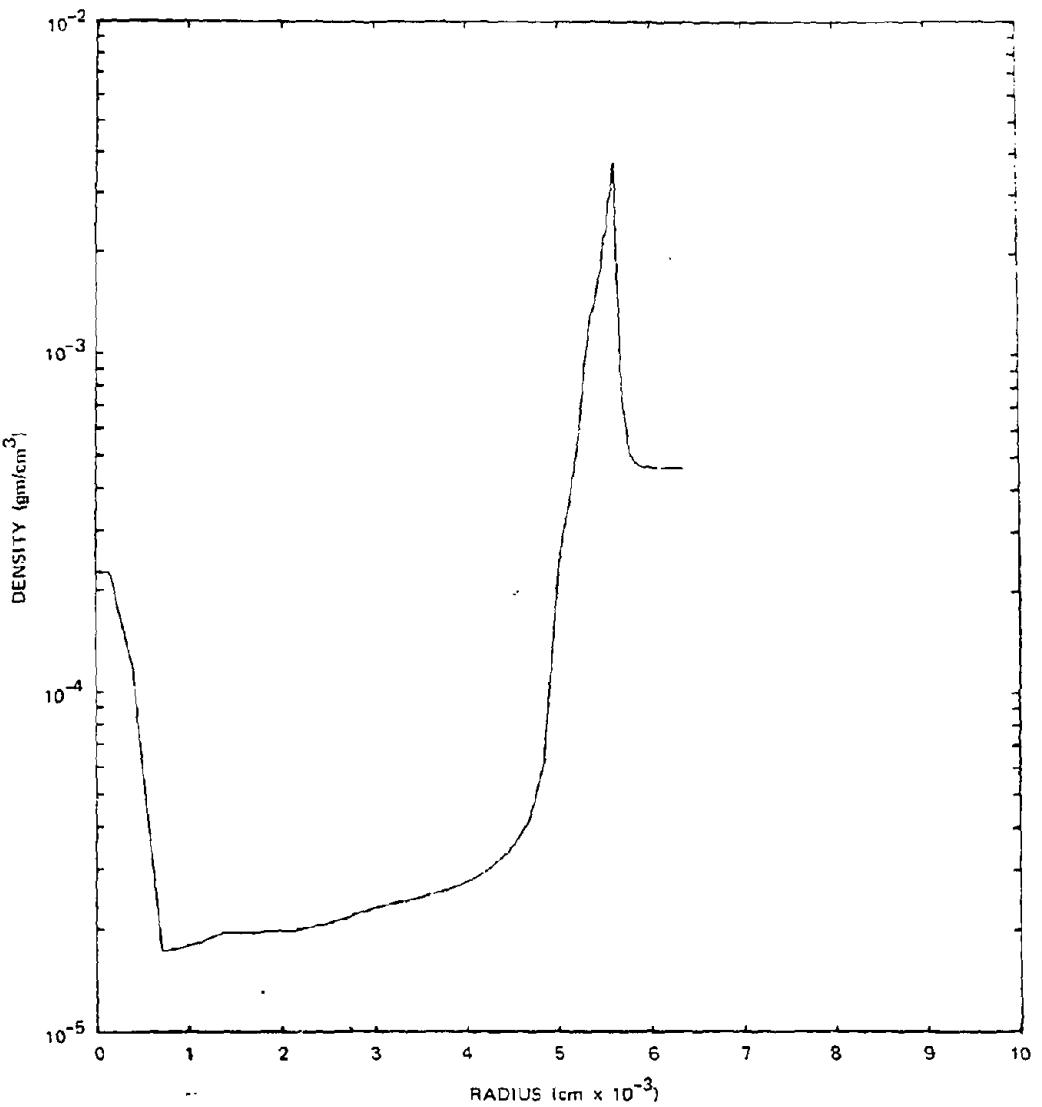


Figure 16-59. [REDACTED] Computed Density Profile,  
t = 4.64 msec, 30 kilofeet Altitude [REDACTED]

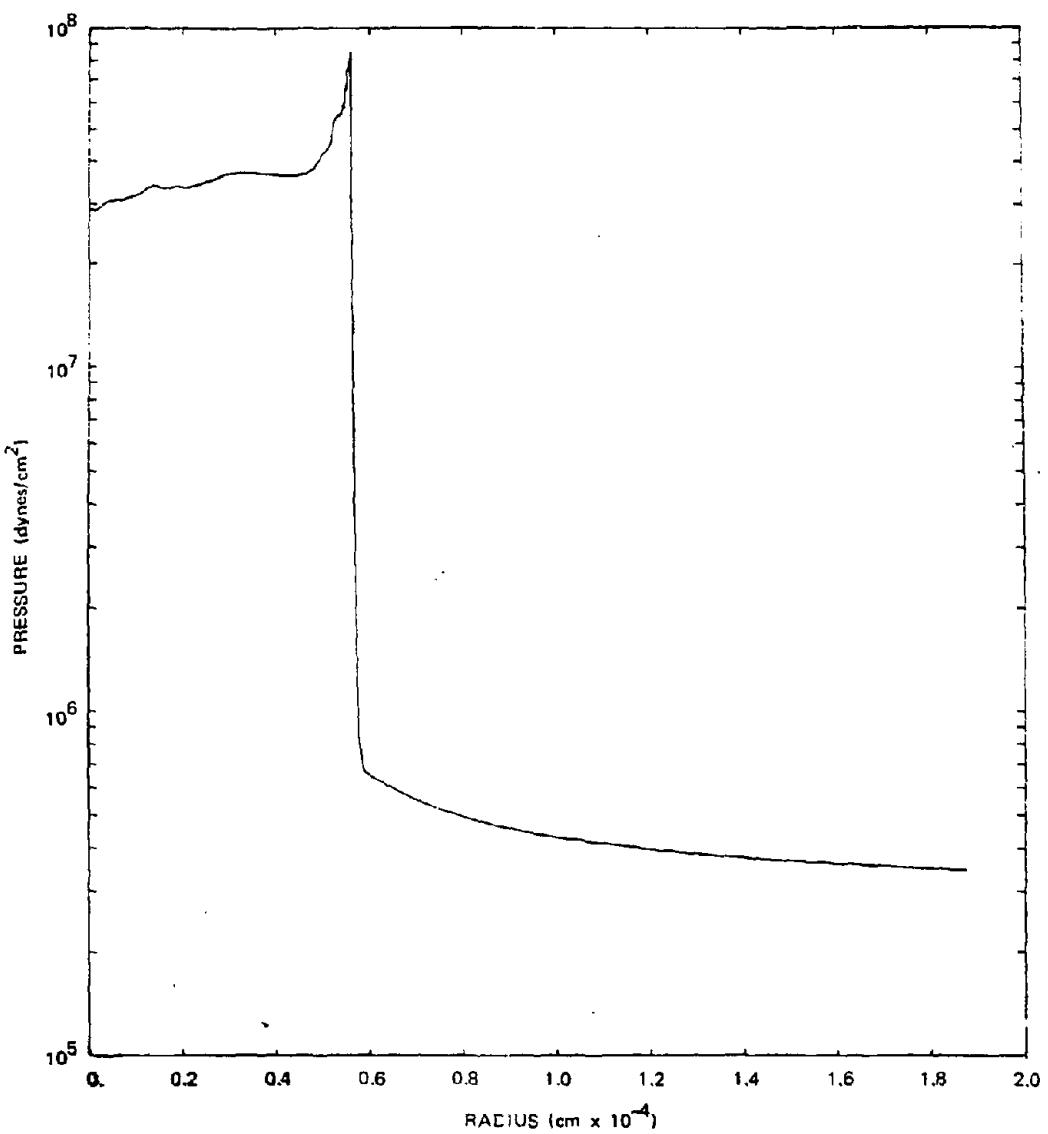


Figure 16-60. Computed Static Pressure Profile,  
 $t = 4.64$  msec, 30 kilofeet Altitude

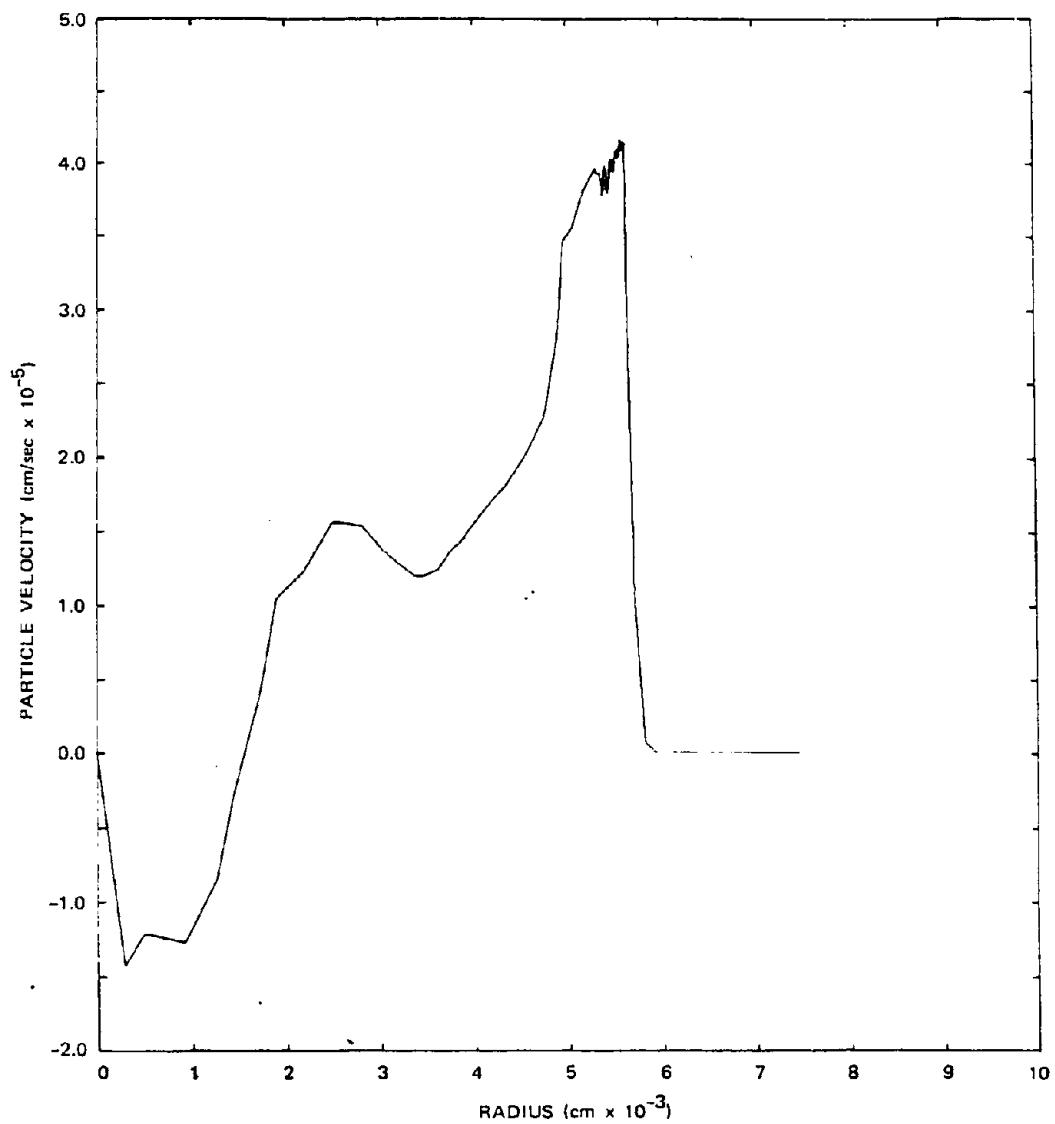


Figure 16-61. [REDACTED] Computed Particle Velocity Profile,  
t = 4.64 msec, 30 kilofeet Altitude [REDACTED]

just prior to shock front intercept and terminated within one second. In the dynamic simulation involving interaction between the rapidly changing blast environment and the vehicle trajectory, the environment changes rapidly; changes are measured in microseconds and in inches. The computed dynamic response, nevertheless, is considered to be a valid model.

Figures 16-62 through 16-65 provide a graphic portrayal of a sample blast intercept condition. For this one intercept case, four curves are shown: static overpressure, dynamic pressure, static overpressure impulse, and dynamic pressure impulse. All times indicated are measured from the time of blast wave intercept. Twenty-five milliseconds of data are shown in Figure 16-62 while only the first millisecond is shown in Figures 16-63 through 16-65. The values of dynamic pressure impulse are the results of continuous summation from prior trajectory restart conditions, and the measurements must be read relative to a baseline value at time of intercept.

The two impulse curves (Figures 16-64 and 16-65) show the relative importance of the dynamic pressure impulse compared to overpressure impulse at early times. The former builds up and levels off extremely quickly while the latter continues to increase. This characteristic is due to the rapid drop in dynamic pressure, whereas the overpressure, plotted for 25 msec, illustrates a considerably slower decay rate.

### 16-36 Blast Loads on the RV Threat Vehicle

The time history of surface loading on a threat reentry vehicles were computed from knowledge of the fly through environments (overpressure, dynamic pressure, relative wind angle of attack) and local vehicle aerodynamics. The time history of loading on any part of the RV is found to be the sum of a very short

duration dynamic pressure or drag loading, superimposed on a longer duration overpressure loading. (See Figures 16-62 through 16-65 for typical pressure-time histories.)

The spatial distributions of these two types of loads on the vehicle surface generally will differ considerably. Blast overpressure results in uniform pressure being applied over the complete vehicle surface, whereas dynamic pressure loadings vary over the vehicle surface, depending on the structural configuration and intercept geometry. These various relationships can be expressed in the following functional form.

$$P(t) = q(t, \alpha, \theta, \psi, \beta) + \Delta p(t)$$

where

$q$  = dynamic pressure

$\Delta p$  = static overpressure

$\alpha$  = relative wind intercept angle

$\psi, \theta$  = local angles defining structural geometry

$\beta$  = circumferential angle on structure measured from windward ray of intercept.

Newtonian aerodynamics were used to determine the peak values of surface pressure resulting from the dynamic pressure environment for all the reentry vehicles that were studied. The structural configurations all were made up of some combination of a sphere nose cap and a conical body. Most of the early structural lethality studies were concentrated on the aft (or weakest) conical shell bay. Shock-on-shock loads were neglected in the analysis.

The surface pressure loading on the conical shell elements is computed from the equation on page 16-106.

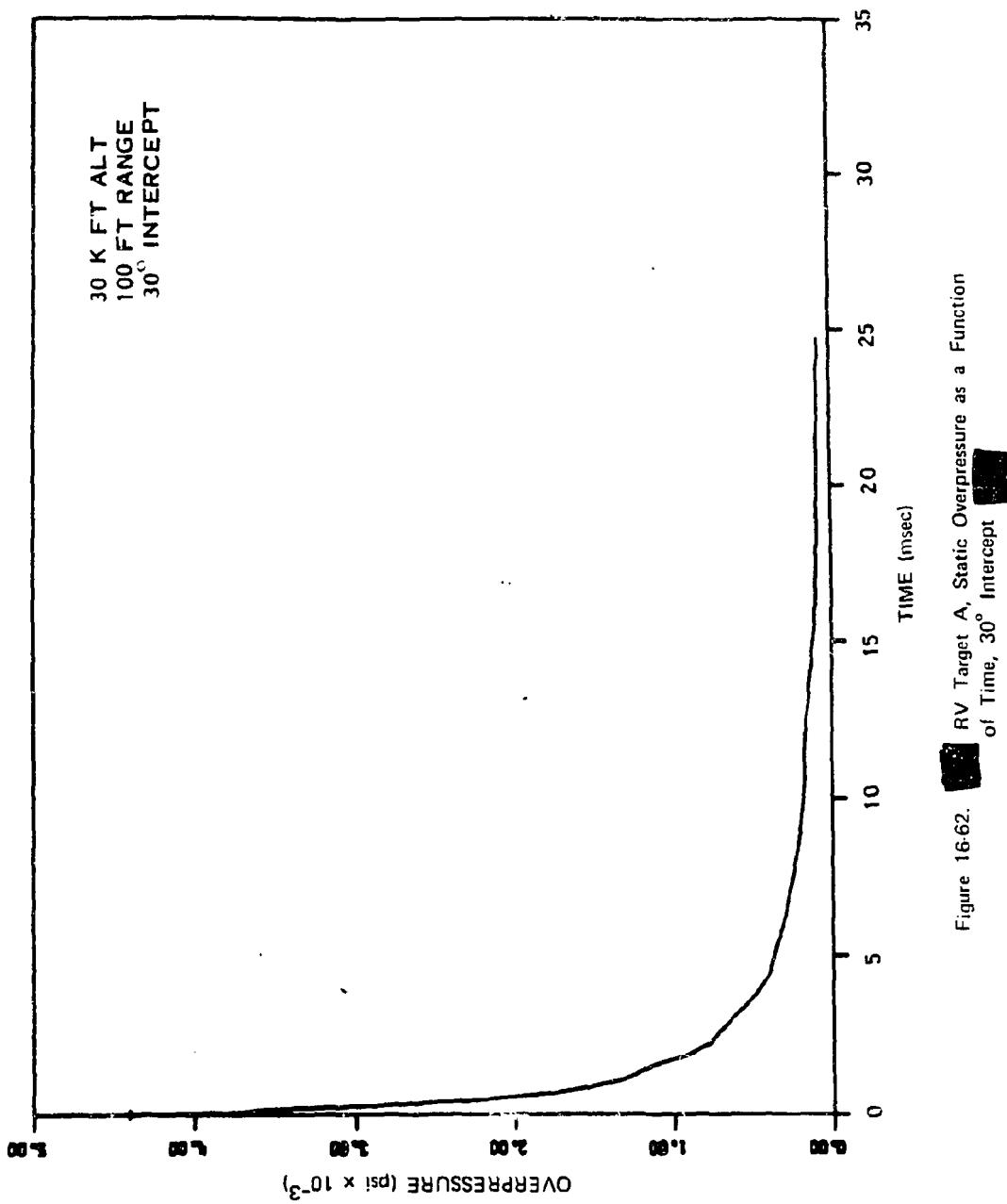


Figure 16-62. RV Target A, Static Overpressure as a Function of Time,  $30^\circ$  Intercept

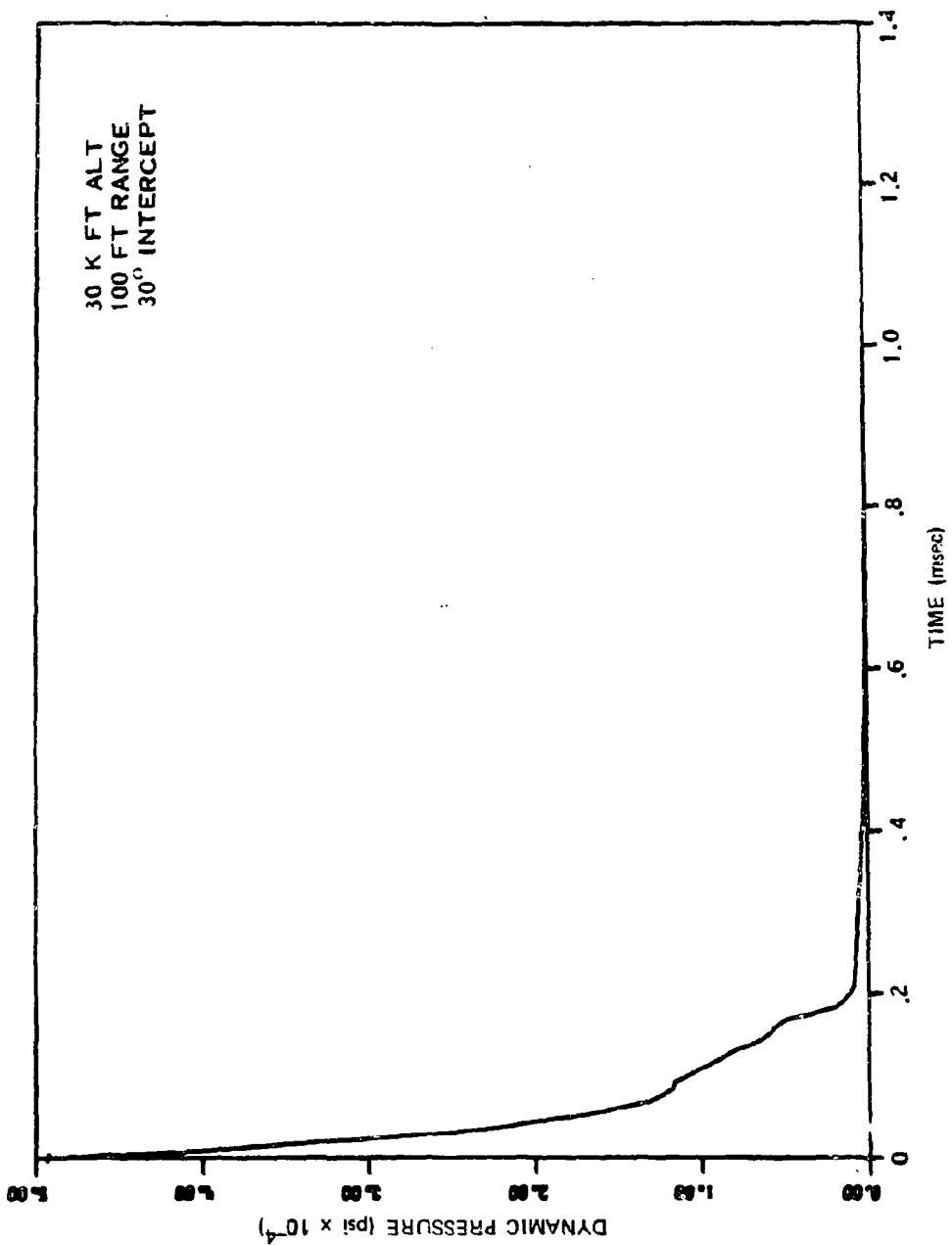


Figure 16-63. RV Target A, Dynamic Pressure as a Function of Time, 30° Intercept

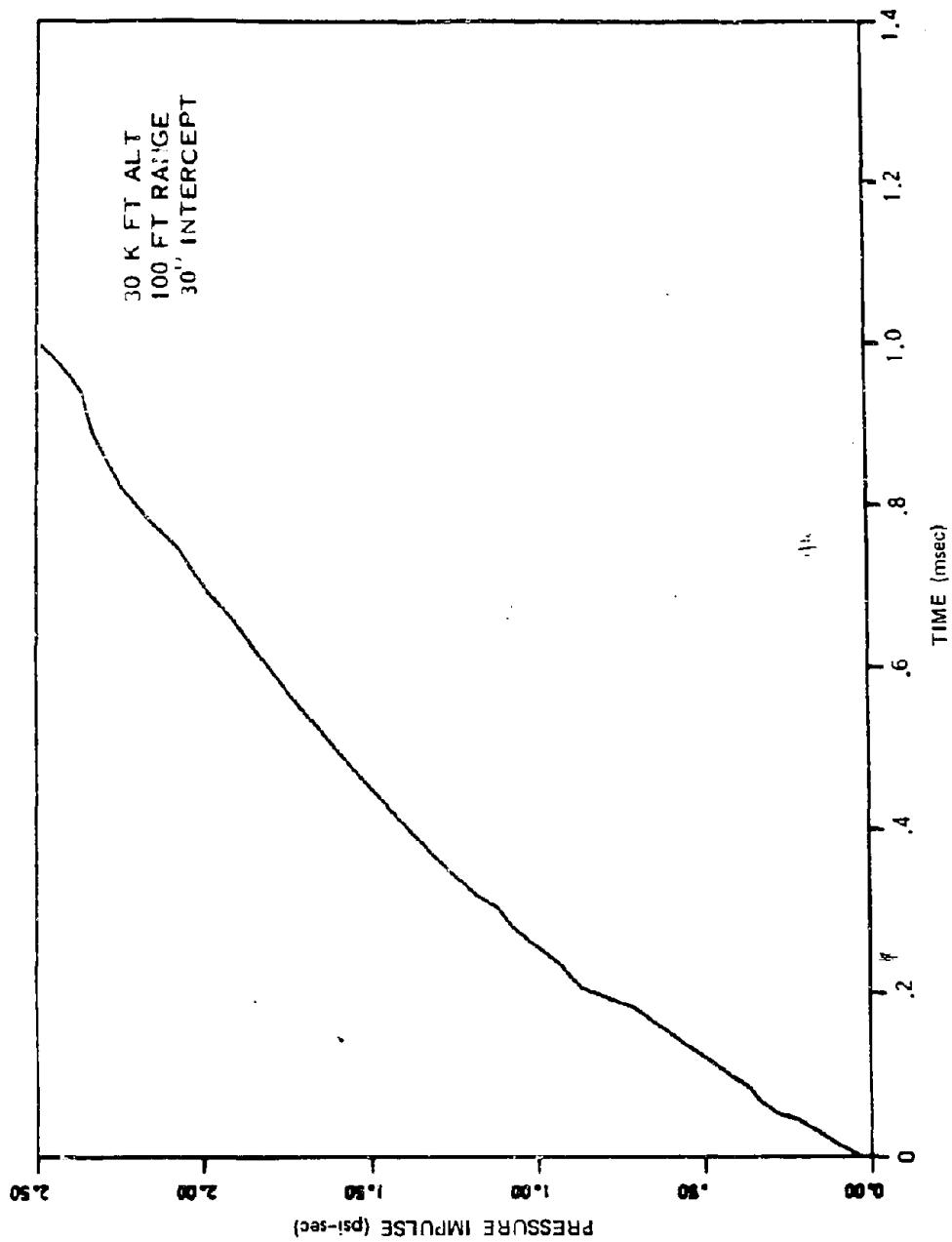


Figure 16-64. RV Target [REDACTED] Static Overpressure Impulse as a Function of Time, 30° Intercept [REDACTED]

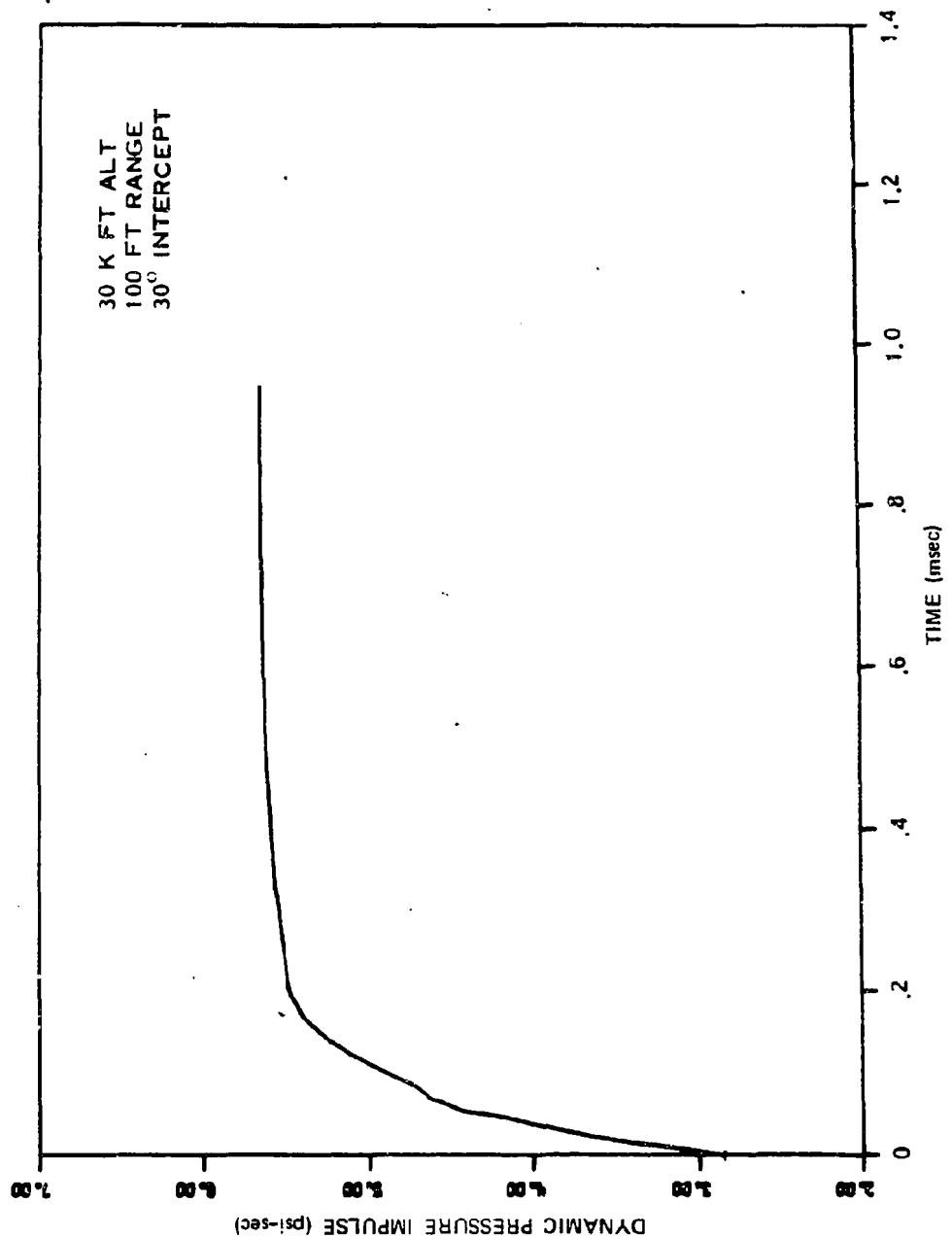


Figure 16-65. RV Target Dynamic Pressure Impulse as a Function of Time, 30° Intercept

$$P(t) = 2q(t) (\cos \alpha \sin \theta + \sin \alpha \cos \theta \cos \beta)^2 + \Delta p(t);$$

$$-\beta_{\max} \leq \beta \leq \beta_{\max}$$

$$P(t) = \Delta p(t) \quad \beta_{\max} \leq \beta \leq -\beta_{\max}$$

where

$$\beta_{\max} = \cos^{-1} \left\{ 1 - \left( \frac{\tan \theta}{\tan \alpha} \right)^2 \right\}^{1/2}$$

$\theta$  = cone half angle

at the windward ray  $\beta = 0$ , therefore maximum surface pressure is

$$P(t) = 2q(t) \sin^2(\theta + \alpha) + \Delta p(t),$$

and the impulse at any time,  $T$ , at  $\beta = 0$  on the cone is

$$I(t) = \int_0^T \left\{ 2q(t) \sin^2(\theta + \alpha) + \Delta p(t) \right\} dt,$$

where it is noted that  $q(t)$  and  $\Delta p(t)$  will not, in general, have the same time dependency.

### 16-37 ABM Blast Kill Radii

Structural lethality levels of the threat reentry vehicles are evaluated in terms of the blast loadings on the primary structure of the vehicle. In the calculations described here, two categories of lethal loadings were evaluated: (1) Immediate kill, Category 6\* and (2) Delayed kill, Category 4. Immediate kill corresponds to load levels sufficient to cause some degree of structural breakup of the metallic subshell. This

usually will be accompanied by removal of the ablative covering and severe structural deformation of the remaining subshell. Delayed kill refers to removal of the ablative covering over large portions of the loaded side of the vehicle. In general, this load level also will be sufficient to cause considerable plastic deformation in the vehicle subshell. These definitions of damage are consistent with those recommended by Stanford Research Institute following participation in the HARTS and SPINE experimental programs.

One approach used to relate these damage levels to the computed applied loading involves the establishment of a given damage level in terms of the pressure and impulse of the applied surface loading. The equation for a given damage level in the  $P$ - $I$  plane is then defined by the following hyperbolic form:

$$\left( \frac{I}{I_o} - 1 \right) \left( \frac{P}{P_o} - 1 \right) = 1.0.$$

In this equation  $I_o$  and  $P_o$  are asymptotes corresponding to values of impulsive loading and static pressure loading necessary to induce the specified damage level. Thus,  $I_o$  and  $P_o$  must be determined for each structure to be studied and for both damage categories, i.e., immediate kill and delayed kill. Although much of the data are consistent with the value 1.0 on the right-hand side of the equation, some data indicate that a value near 3.0 would be more appropriate.

For a given structural element, the  $I_o$  and  $P_o$  asymptotes for a given damage level can be related to computed values of impulse and pressure based on some very simplistic structural analysis techniques. For example, modeling the two layered aft bay shell element as a rigid, perfectly plastic cylinder, the uniform externally applied impulse necessary to cause a permanent

\* Sometimes referred to as "catastrophic damage."

strain,  $\epsilon$ , in the shell wall is found to be:

$$I = \left\{ 2\epsilon(\rho_s h_s + \rho_c h_c)(\sigma_{ys} h_s + \sigma_{yc} h_c) \right\}^{1/2},$$

where

$\rho_s, \rho_c$  = mass densities of shell and ablative cover materials.

$\sigma_{ys}, \sigma_{yc}$  = yield stress values of shell and ablative cover materials.

$h_s$  = shell thickness.

$h_c$  = ablator thickness.

Under similar assumptions, the value of uniform static pressure necessary to cause material yielding in the shell wall is

$$P_y = \frac{1}{a} \left\{ \sigma_{ys} h_s + \sigma_{yc} h_c \right\}$$

where  $a$  = average radius of cylinder. The well-known  $I_{05}$  parameter for impulsively loaded shells can be obtained by setting  $\epsilon = 0.05$ .

$$I_{05} = \left\{ 0.1(\rho_s h_s + \rho_c h_c)(\sigma_{ys} h_s + \sigma_{yc} h_c) \right\}^{1/2}.$$

The next step in lethality evaluation is to relate the  $I_{05}$  and  $P_y$  load levels to load levels corresponding to the Category 6 and Category 4 damage. For the cylindrical or slightly conical shells representative of the aft bay of most threat RV's, these relationships are empirically established based on results obtained from a large number of experimental tests performed during the HARTS, SPINE, and DRIS Programs. Based on the results of these correlations, the following relations were selected to establish the impulsive and quasistatic load level asymptotes for damage Categories 6 and 4.

#### IMPULSE ASYMPTOTE

Category 4:  $I_4 = I_{05}$

Category 6:  $I_6 = 2.5 I_{05}$

#### QUASISTATIC PRESSURE ASYMPTOTE

Category 4:  $P_4 = 0.7 \frac{a}{L} P_{05}$

Category 6:  $P_6 = 1.56 \frac{a}{L} P_{05}$

It should be noted that, in the definition of the quasistatic pressure asymptote, the effect of shell length has been included empirically by including the radius-to-length ratio ( $a/L$ ).

Based on the structural lethality estimates described above and the blast environment loading for the various encounter geometries, lethality estimates of the threat RV's can be made. A sample plot is shown in Figure 16-66; the  $I_{05}$  and  $P_{05}$  ( $P_y$ ) asymptotes have been determined, and the curves corresponding to the damage asymptotes  $I_6$ ,  $P_6$  (immediate kill) and  $I_4$ ,  $P_4$  (delayed kill) are shown. The dashed line shows the damage curve for immediate kill corresponding to the constant in the pressure-impulse equation being equal to 3.0 instead of 1.0.

By combining the loads calculated for the various encounters, in terms of pressure and impulse of peak surface loading, with the damage level plot (Figure 16-66), estimates of loads (in terms of slant range and intercept angle) necessary to incur lethal damage can be made for each vehicle. An example of the superposition of the structure load pressures and impulses on the damage definition curves is shown in Figure 16-67. In the figure, different symbols correspond to loads for various intercept angles, and the number adjacent to each symbol defines the value of slant range at burst time to which that particular load calculation corresponds.

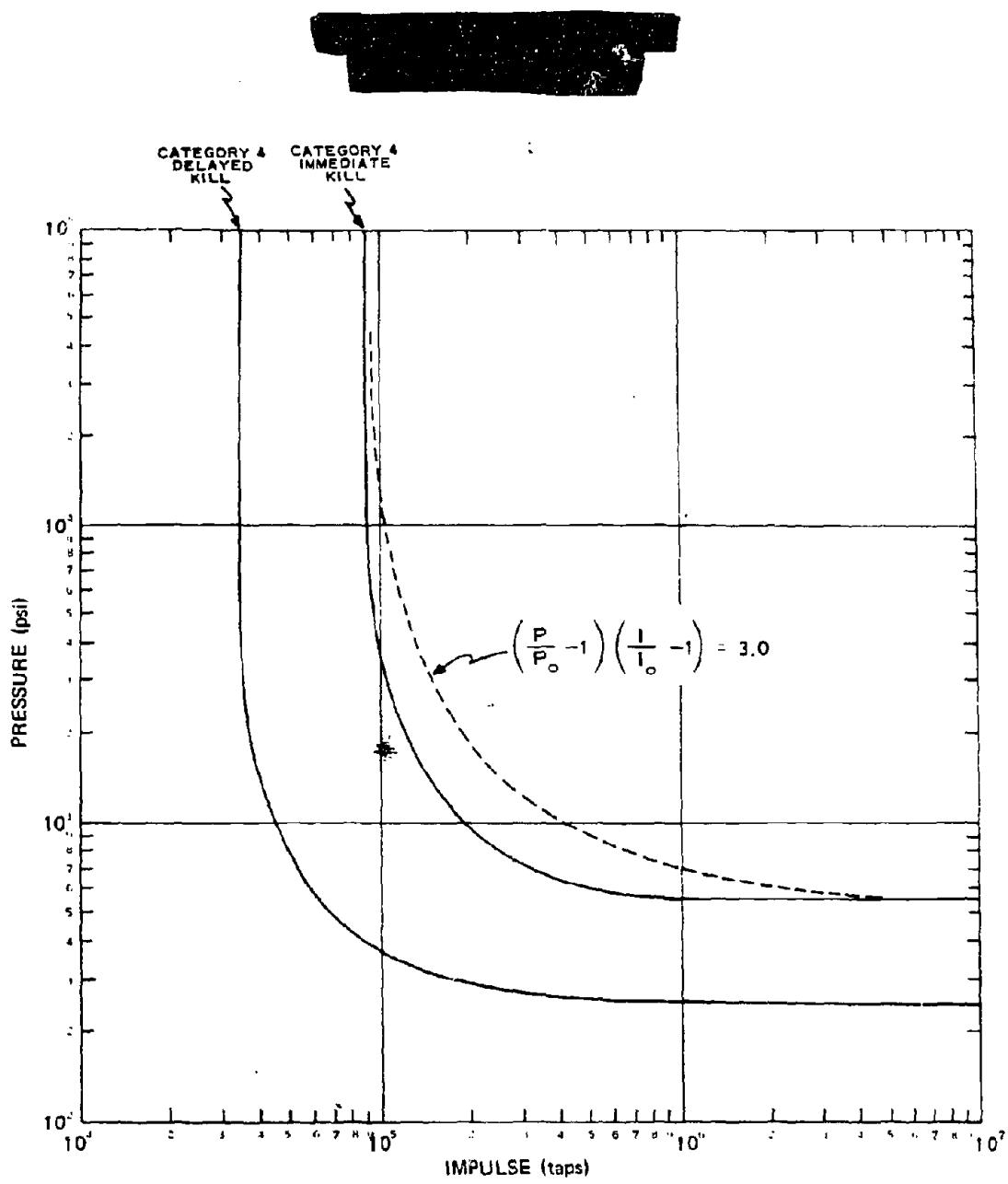
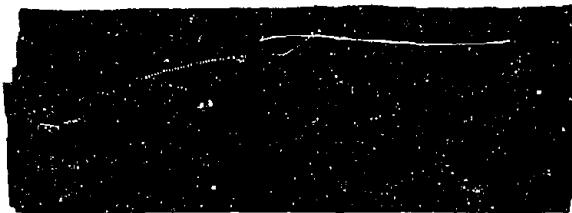


Figure 16-66. Pressure-Impulse Damage Levels, RV Target A Configuration, Aft Bay

DNA (E)(3) By noting where the blast loading points cross the damage level lines in the P-I plane, estimates of burst time slant range can be made, for a given intercept angle, that will result in Category 6 immediate kill and Category 4 delayed kill. The following RV kill slant ranges (at burst time) are obtained from the example (Figure 16-67).

DNA  
(E)(3)



DNA (E)(3) It should not be inferred that the P-I plot method described above is the only method of analysis that is used to determine blast lethality radii. Some investigators have been successful in computing the structural response of RV's to the derived blast load inputs; however, here experimental data must be used to relate the computed response to damage level, e.g., immediate kill.

### 16-38 Fireball Thermal Effects on Threat RV's

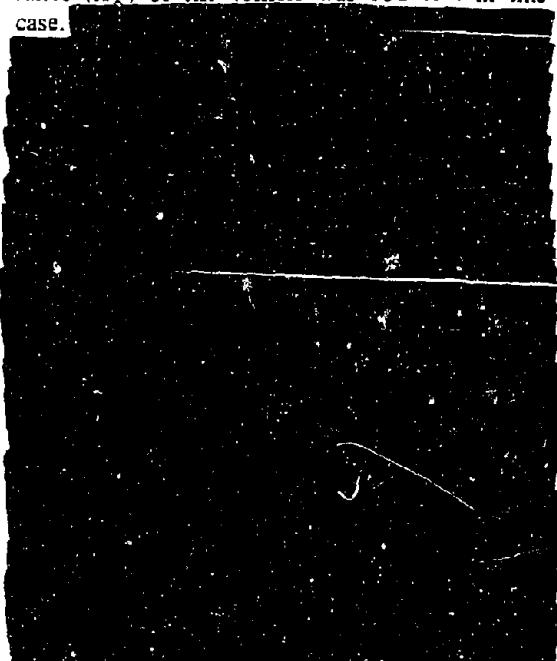
DNA (E)(3) Whenever a vehicle intercepts an early time blast wave, it subsequently traverses through (or very near) a high temperature nuclear fireball. Therefore, as one part of a lethality investigation, the thermal effects that would be expected on a threat RV flying through an ABM nuclear fireball would be examined. The calculations for the following example employed the RAD ABLE code. This code uses the free field fireball thermal environment data as read off of a rad-hydro Usertape. The RAD ABLE code formalism assumes that the vehicle flies a constant velocity-straight line trajectory in the vicinity of the burst point. A simplified method is used that accounts for radiation blocking

effects in an approximate manner based on detailed stagnation point (rad-hydro) flow field solutions.

DNA (E)(3) Figure 16-68 shows a typical history of the ablation rate ( $\dot{m}$ ) and the amount of material ablated

$$(m = \int_0^t \dot{m} dt)$$

DNA (E)(3) for a head on traversal of an ABM explosion at 30 kilofeet altitude. The burst time standoff distance ( $X_0$ ) of the vehicle was 100 feet in this case.



DNA (E)(3) Figure 16-69 summarizes the results of a number of fireball traversal calculations (similar to those illustrated in Figure 16-67) in the form of total mass ablated at fireball exit as a function of initial standoff distance ( $X_0$ ) and burst altitude. All of these results are for head on ( $X_0 > 0$ ) or tail on ( $X_0 < 0$ ) intercepts with

DNA  
(b)(3)

Deleted

Figure 16-67. [REDACTED] SPRINT Blast Loads, RV Target A,  
30 kilofeet Altitude, Aft Bay [REDACTED]

16-110

[REDACTED]

[REDACTED]

DOSR  
( $\Delta X^2$ )

Deleted

Figure 16-68. [REDACTED] Ablation Rate and Mass Ablated as a Function  
of Time for Target A Threat RV [REDACTED]

16-111

D.J.R.  
K.Y.

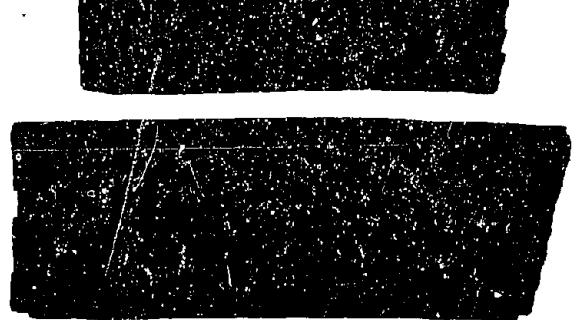
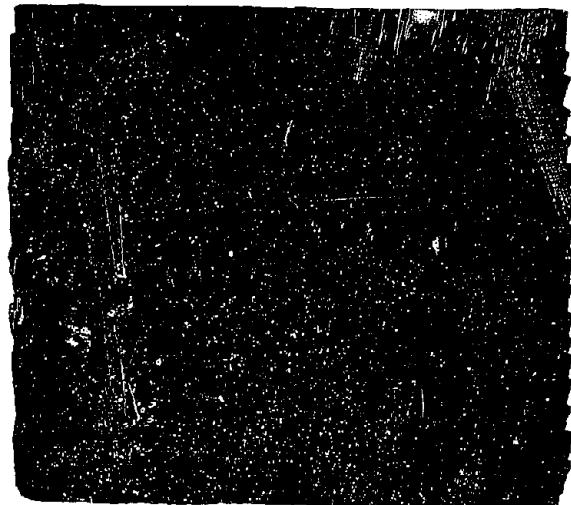
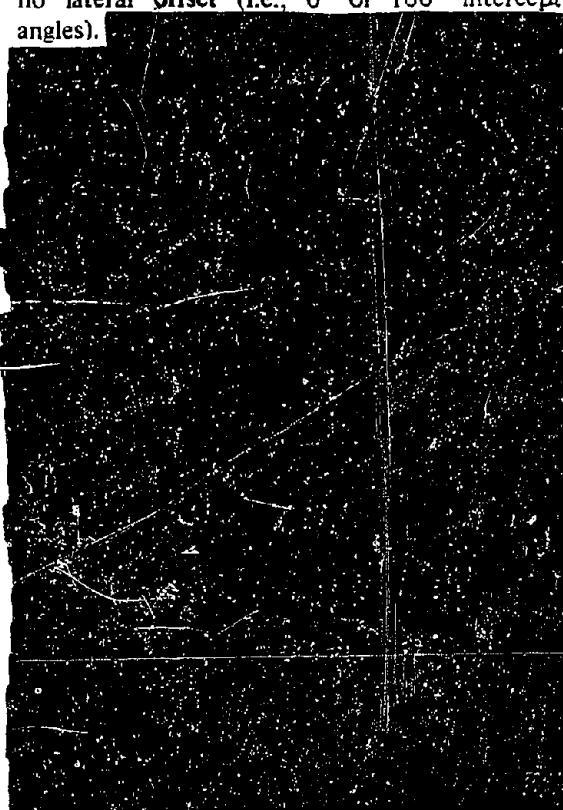
Deleted

Figure 16-69. [REDACTED] Mass Ablated as a Function of Burst Time  
Standoff Distance for Target A Threat RV [REDACTED]

16-112

[REDACTED]  
no lateral offset (i.e., 0° or 180° intercept  
angles).

DNA  
(f)(3)



16-113



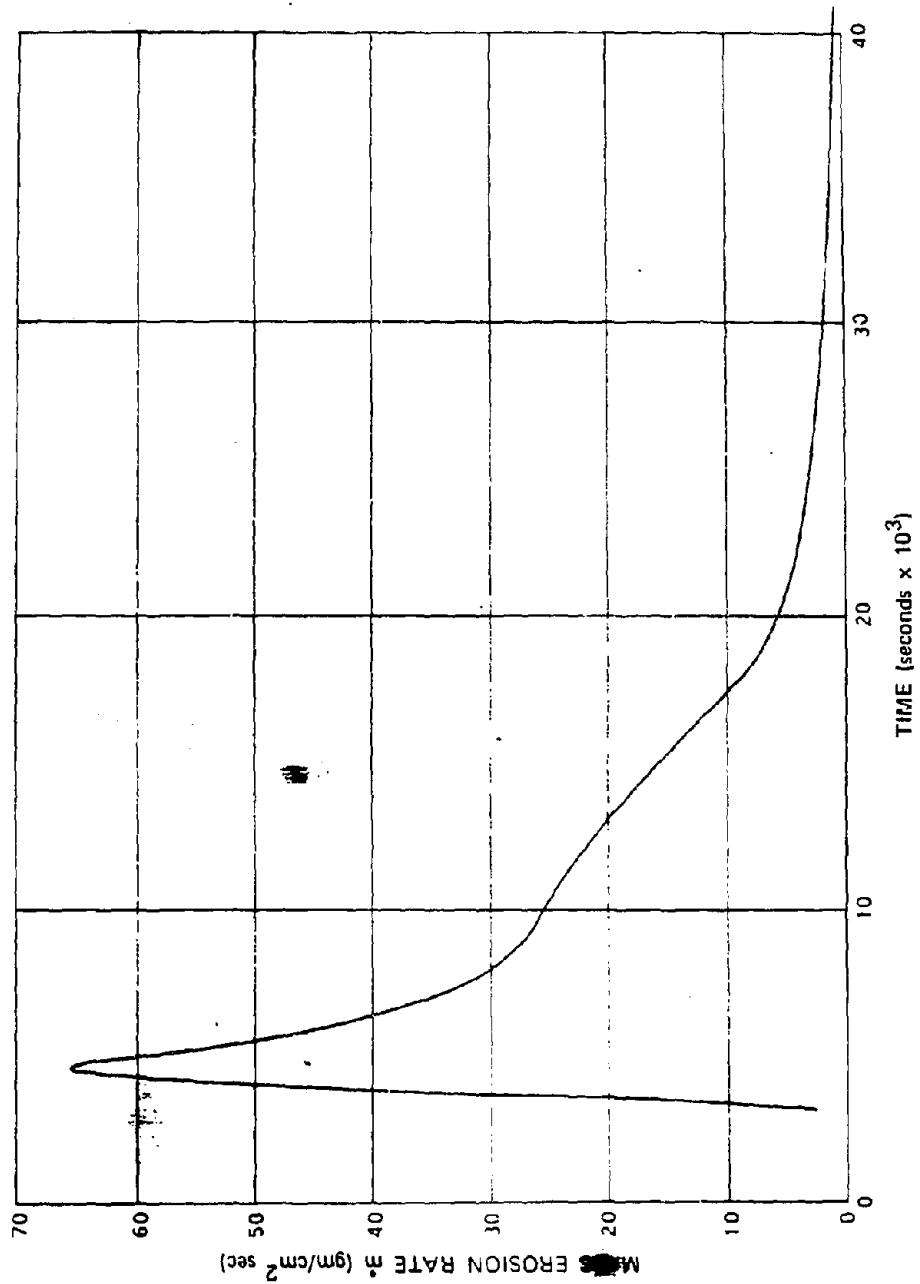


Figure 16-70. Typical Traverse-Mass Erosion Rate History

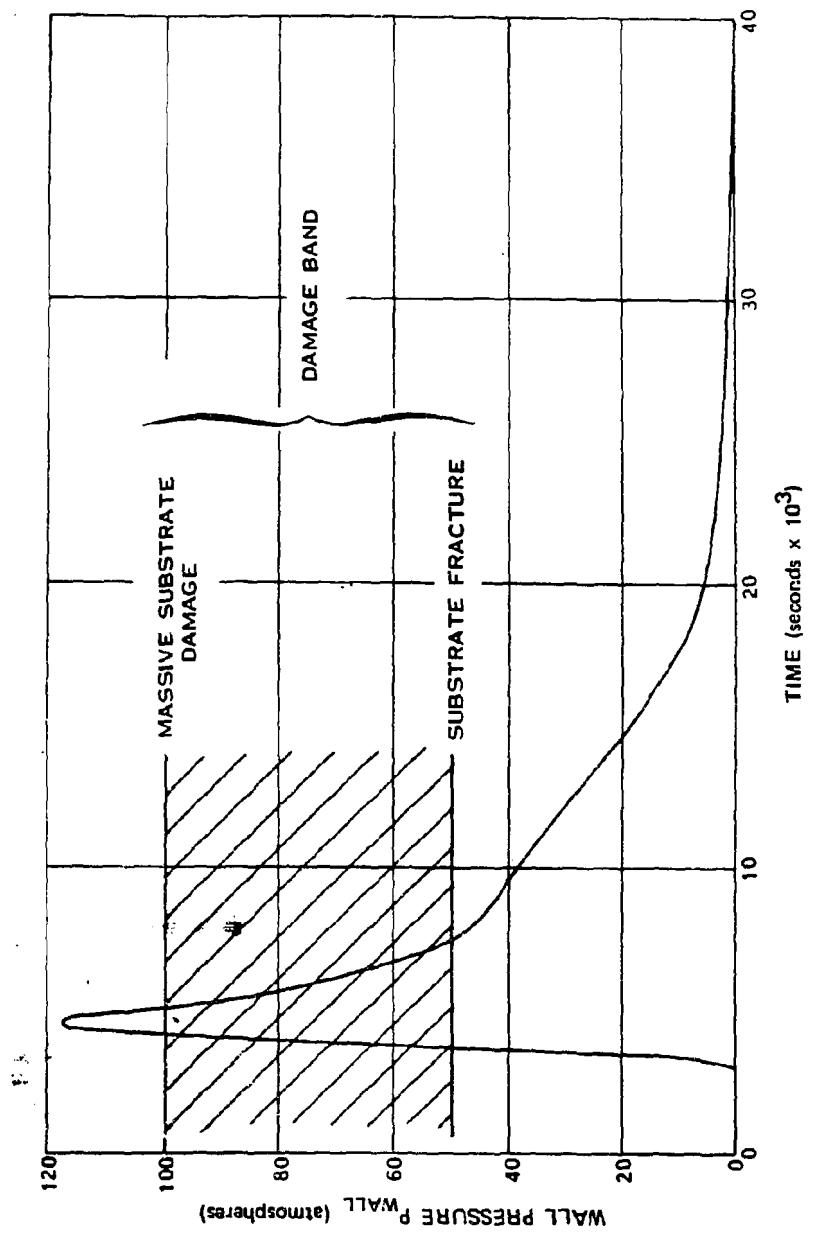


Figure 16-71. Typical Traverse TMI History

[REDACTED]

BIBLIOGRAPHY

[REDACTED]

Baker, W. E., P. A. Westine, and S. Silverman, *Feasibility Study on Simulating the Structural Response of High Altitude Missiles to Blast Loading*, Final Technical Report AMC-66-8, Southwest Research Institute, San Antonio, Texas, 21 January 1966 [REDACTED]

Barry, Jr., J. M., *Supplementary Data for the AIRS-II Vehicle* [REDACTED], Kaman AviDyne TM-25, AMC-66-15, Kaman AviDyne, Burlington, Massachusetts, July 1966 [REDACTED]

Bryant, E. J., N. H. Ethridge, and M. R. Johnson, *Response of Drag Type Equipment Targets in the Precursor Zone* [REDACTED], WT1123, Ballistic Research Laboratories, Aberdeen Proving Ground, Maryland, August 1956 [REDACTED]

Bryant, E. J., and J. D. Day, *Effects of Rough Terrain on Drag-Sensitive Targets* [REDACTED], WT1408, Ballistic Research Laboratories, Aberdeen Proving Ground, Maryland, 9 November 1959 [REDACTED]

Criscione, E. S., L. J. Mente, N. P. Hobbs, *Vulnerability of Standard Army Interceptor Systems (AIRS I and II) to Nuclear Weapon Blast and Thermal Radiation Effects* [REDACTED], AMC-67-18, Kaman AviDyne, Burlington, Massachusetts, April 1967 [REDACTED]

Eppes, R., Jr., *Review of Experimental Programs for Blast Intercept and Traversal, and Feasibility of Using a Large Bore Gun Facility for Launching Vehicles for Blast Intercept* [REDACTED], AMSMI-RS-TR-66-12, AMC-66-8, U.S. Army Missile Command, October 1966 [REDACTED]

*Field and Depot Maintenance Manual: Description and Theory of Air Defense Guided Missile XM3E1* [REDACTED] TM 9-1410-500-35, June 1960 [REDACTED]

*Field and Depot Maintenance Manual: Description and Theory: Guided Missile System Components Organizational Maintenance Test Station AN/MSM-35 (SERGEANT Artillery Guided Missile System)* [REDACTED], Notes on Material NOM 9-4935-303-35/2, November 1961.

*Field and Depot Maintenance Manual: Schematics: SERGEANT Artillery Guided Missile XM 15 (SERGEANT Artillery Guided Missile System)* [REDACTED], TM 9-1410-302-35/1, August 1963.

Fraser, W. A., *A Comparison of Experimentally and Theoretically Determined Pressure Distribution on a Blast-Loaded Missile Body*, AMC-67-30, Kaman Nuclear, Colorado Springs, Colorado, June 1968 [REDACTED]

*Hardening Technology Studies - I* [REDACTED], LMSC-B130200, Volumes I-IV, Lockheed Missiles and Space Company, Sunnyvale, California, 30 September 1965 [REDACTED]

[REDACTED]

*Hardening Technology Studies - II* [REDACTED] LMSC-B130391, Volumes I-IV, Lockheed Missiles and Space Company, Sunnyvale, California, 30 September 1966 [REDACTED]

Hillendahl, R. W., *Theoretical Models for Nuclear Fireballs* [REDACTED] DASA 1589-1 through 1589-39, Lockheed Missiles and Space Company, Sunnyvale, California, 1965-1966 [REDACTED]

*Joint Engineer/Service Test SERGEANT Guided Missile System* [REDACTED] Volume I, U.S. Army Test and Evaluation Command Technical Report 143, November 1963 [REDACTED]

Johnson, O. T., R. D. Mayerhofer, and W. J. Schuman, Jr., *Effect of Blast Upon Simulated and Actual Missiles (Project 1.4 Operation Snow Ball)* [REDACTED] Memorandum Report No. 1655, U.S. Army Ballistic Research Laboratories, Aberdeen Proving Ground, Maryland, May 1965 [REDACTED]

Johnson, O. T., and R. D. Mayerhofer, *Susceptibility and Vulnerability of the Lance Missile System to Nuclear Effects (Blast)* [REDACTED] BRL-MR-1862, U.S. Army Materiel Command, Ballistic Research Laboratories, Aberdeen Proving Ground, Maryland, August 1967 [REDACTED]

Johnson, O. T., R. D. Mayerhofer, *Susceptibility and Vulnerability of the SERGEANT Weapon System to Nuclear Effects (Blast)* [REDACTED] BRL-R-1324, U.S. Army Materiel Command, Ballistic Research Laboratories, Aberdeen Proving Ground, Maryland, June 1966 [REDACTED]

Kelley, B. E., *LANCE Automet Control System* [REDACTED] RG-TR-64-3, U.S. Army Missile Command, Redstone Arsenal, Alabama, 25 June 1964 [REDACTED]

Lindberg, H. E., et al., *Response of Reentry Vehicle-Type Shells to Blast Loads*, LMSC-B130200, Volume IV-C, Stanford Research Institute, Menlo Park, California, for Lockheed Missiles and Space Company, Sunnyvale, California, 30 September 1965 [REDACTED]

Lindberg, H. E., and G. E. Sliter, *Response of Reentry Vehicle-Type Shells to Transient Surface Pressures*, AFWL-TR-68-56, Stanford Research Institute, Menlo Park, California, June 1969 [REDACTED]

*Logistic Support Plan for the LANCE Missile System* [REDACTED] (Second Revision), U.S. Army Missile Command, Redstone Arsenal, Alabama [REDACTED]

Mente, K. J., *Standard Research Systems for Army Interceptors* [REDACTED] TR-35, Kaman AviDyne, Burlington, Massachusetts, July 1965 [REDACTED]

Mente, K. J., *Supplementary Data for the AIRS-I Vehicle* [REDACTED] TM-24, Kaman AviDyne, Burlington, Massachusetts, June 1966 [REDACTED]

Mikami, K., R. D'Amato, *Criteria for the Effect of Damage on the Operational Capabilities of U.S. Army Missile Systems Volume 2, Lance Missile System* [REDACTED] TR-38, Kaman AviDyne, Burlington, Massachusetts, February 1966 [REDACTED]

Mikami, K., L. J. Mente, R. D'Amato, *Criteria for the Effect of Damage on the Operational Capabilities of U.S. Army Missile Systems Volume 5, Hawk Missile System* [REDACTED] TR-38, Kaman AviDyne, Burlington, Massachusetts, July 1966 [REDACTED]

Muller, J. and D. L. Blank, *SLEDGE Program: Phase I, Feasibility Study* [REDACTED] DASA-1988, Martin Marietta Corporation (Orlando Division), Orlando, Florida, September 1967 [REDACTED]

Nicholson, J. E., and J. J. Rossi, *Pressure-Time Histories of Blast Wave Interactions with a Re-Entry Body*, MC-65-163-R1, Mithras, Inc., February 1966 [REDACTED]

Nicholson, J. E., E. F. Kent, N. Zessoules, and P. H. McIngvale, *A Ballistic Wind Tunnel Test Technique for Measuring Shock-on-Shock Interactions*. MC-66-142-R31, Mithras, Inc., 4 October 1966 [REDACTED]

*Nuclear Radiation Effects Study on LANCE Directional Control Electronics* [REDACTED] RG-TR-64-14, U.S. Army Missile Command, Redstone Arsenal, Alabama, September 1964 [REDACTED]

*Nuclear Weapons Blast Phenomena, Volume I, Source and Development of Blast Waves in Air* [REDACTED], DASA 1200-I, DASIAC, Santa Barbara, California, 1 March 1971 [REDACTED]

*Nuclear Weapons Blast Phenomena, Volume II, Blast Wave Interaction* [REDACTED] DASA 1200-II, DASIAC, Santa Barbara, California, 1 December 1970 [REDACTED]

*Nuclear Weapons Blast Phenomena, Volume III, Air and Subsurface Explosions* [REDACTED] DASA 1200-III, DASIAC, Santa Barbara, California, 1 March 1970 [REDACTED]

*Organizational Maintenance Manual: SERGEANT Artillery Missile XM 15 (SERGEANT Artillery Guided Missile System)* [REDACTED] Notes on Material NOM 9-1410-302-20, May 1962.

*Operation and Field Maintenance Manual: General Support Shop Set (GSSS) (SERGEANT Field Artillery Guided Missile System)* [REDACTED], Technical Manual TM 9-4935-305-40/1, July 1963.

*Operator and Organizational Maintenance Manual: Guided Missile System Components Organizational Maintenance Test Station AN/MSM-35 (SERGEANT Artillery Guided Missile System)* [REDACTED], Notes on Material NOM 9-4935-303-12, October 1961.

*Operator's Manual: Guided Missile System Components Field Maintenance Test Station AN/MSM-36 (SERGEANT Artillery Guided Missile System)* [REDACTED]. Notes on Material NOM 9-4935-304-10, October 1963.

*Operator's Manual, SERGEANT Artillery Guided Missile System* [REDACTED]. Notes on Material NOM 9-1400-300-10, December 1960 [REDACTED]

*Operator and Organizational Maintenance Manual: Air Defense Guided Missile XM3E1* [REDACTED]. TM 9-1410-500-12, July 1962 [REDACTED]

*Operator and Organizational Maintenance Manual: Emplacement of Hawk Air Defense Guided Missile System* [REDACTED], TM 9-1400-500-12/1, August 1961 [REDACTED]

*Operator's Manual: Description for Hawk Air Defense Guided Missile System* [REDACTED]. TM 9-1400-500-10, June 1960 [REDACTED]

*Operator and Organizational Maintenance Manual: SERGEANT Missile Trainer, Device 3G52 (SERGEANT Artillery Guided Missile System)* [REDACTED]. Technical Manual TM 9-6920-130-12, January 1963.

*Operator and Organizational Maintenance Manual: Four-Wheel Semicrailer-Mounted Guided Missile Launching Station XM 504 (SERGEANT Artillery Guided Missile System)* [REDACTED]. Notes on Material NOM 9-1440-301-12, October 1961.

Parechanian, H. S., et al., *Dynamic Response Investigation of Simulated R/V Structure - Volume II Impulse and Blast Tests* [REDACTED]. SAMSO TR-69-144, Volume II, McDonnell Douglas Astronautics Company, Santa Monica, California, September 1969 [REDACTED]

*Proceedings: DASA/RAND Hydrodynamic Code Conference* [REDACTED]. DASA-1553, DASA Data Central, General Electric Company, Tempo, Santa Barbara, California, September 1964 [REDACTED]

*Proceedings: DASA Conference on Nuclear Weapons Effects on Re-Entry Vehicles and Interceptor Missiles* [REDACTED]. DASA-1651, DASA Data Center, General Electric Company, Tempo, Santa Barbara, California, September 1965 [REDACTED]

*Proceedings: DASA/AFFDL Shock-on-Shock Interaction Conference* [REDACTED]. DASA-1674, DASA Data Center, General Electric Company, Tempo, Santa Barbara, California, May 1966 [REDACTED]

*Proceedings: DASA Anti-Ballistic Missile Blast Vulnerability Conference* [REDACTED]. DASA-1744, DASA Data Center, General Electric Company, Tempo, Santa Barbara, California, April 1966 [REDACTED]

Reck, R. J., and H. E. Lindberg, *Structural Response of the SPINE Reentry Vehicle Models to Blast and Impulsive Loads* [REDACTED]. AFWL-TR-67-118, Stanford Research Institute, Menlo Park, California and Douglas Aircraft Company, Santa Monica, California, January 1968

Sachs, D. C. and R. E. Keeffe, *An Investigation of Static Blast/Vehicle Intercept Simulation Methods* [REDACTED]. AMC-67-30, Kaman Nuclear, Colorado Springs, Colorado, November 1967

Sachs, D. C., et al., *An Investigation of Dynamic Blast/Vehicle Intercept Simulation Methods* [REDACTED]. AMC-67-28, Kaman Nuclear, Colorado Springs, Colorado, August 1967

Schuman, W. J., Jr., *The Response of Cylindrical Shells to External Blast Loading*, BRL Memorandum Report No. 1461, U.S. Army Ballistic Research Laboratories, Aberdeen Proving Ground, Maryland, March 1963

Schuman, W. J., Jr., *The Response of Cylindrical Shells to External Blast Loading, Part II*. BRL Memorandum Report No. 1560, U.S. Army Ballistic Research Laboratories, Aberdeen Proving Ground, Maryland, May 1964

*SERGEANT Missile System Operation and Environment Test Program* [REDACTED]. White Sands Missile Range Technical Memorandum 874, White Sands, New Mexico, June 1961

Sieck, D. W., *Stress Analysis of the Hawk I Missile* [REDACTED]. NA 1-55-10, Volumes I & II, Northrop Aircraft, Inc.

Sliter, G. E., et al., *Warhead Optimization for Structural Kill of Re-Entry Vehicles. Lethality Tests of SPINE Vehicles* [REDACTED]. DASA-2215, Stanford Research Institute, Menlo Park, California, July 1969

Sliter, G. E., et al., *Warhead Optimization for Structural Kill of Re-Entry Vehicles* [REDACTED]. DASA-2281, Stanford Research Institute, Menlo Park, California, July 1969

*SPRINT Blast Survivability Program-Interim Report* [REDACTED] AMC-4-69(T), Kaman Sciences Corporation, Colorado Springs, Colorado, June 1969

*Studies of Blast Simulation Techniques on Re-Entry Vehicles* [REDACTED]. AFSWC TDR 62-129, Sandia Corp., Albuquerque, New Mexico, November 1962

*Transportation Data for the U.S. Army Hawk Missile System* [REDACTED] AR-150, Raytheon Company Aero/Weapons Division, Andover Plant, Andover, Massachusetts, June 1961.

[REDACTED]

Wells, P. B. and E. A. Bathke, *Theoretical Methods and Computer Codes for Fireball Ablation Effects*, KN-70-220(R), Kaman Nuclear, Colorado Springs, Colorado, 14 April 1970.

Wells, P. B., E. A. Bathke, and D. C. Sachs, *SPRINT Blast and Thermal Environment Calculations*, KN-70-754(R), Kaman Nuclear, Colorado Springs, Colorado, 2 October 1970.

Whitaker, W. A., et al., *Theoretical Calculations of Early Phenomenology - 200 kt at 32 kilometers*, AFWL-TR-67-68, Air Force Weapons Laboratory, Kirtland Air Force Base, Albuquerque, New Mexico, October 1967.

Zvara, J., R. D'Amato, *Criteria for the Effect of Damage on the Operational Capabilities of U.S. Army Missile Systems, Volume I. SERGEANT Guided Missile System*, TR-38, Kaman AviDyne, Burlington, Massachusetts, February 1966.

(This page intentionally left blank)

DTIC  
SELECTED  
S - 2 MAR 1989 D

AD-A955 401

Chapter 17

RADIO FREQUENCY SIGNAL DEGRADATION RELEVANT  
TO COMMUNICATIONS AND RADAR SYSTEMS

INTRODUCTION

Nuclear detonations can affect the performance of radio communication, radar, and other electronic systems that rely on electromagnetic-wave propagation. Usually, the effects will be deleterious although performance may occasionally be enhanced. Applicable nuclear-weapon-induced phenomena are discussed in Chapters 3, 5, and 8. Generally, each system and environmental situation of interest must be examined to determine whether nuclear weapons effects will be important and to what extent they will be important.

Electromagnetic waves propagating along paths entirely below 25 kilometers are not likely to be affected by nuclear-produced disturbances. When a detonation occurs below 25 kilometers, the major degradation region is the fireball, which is limited in extent. When a detonation occurs above 25 kilometers, very little of the weapon radiation penetrates below 25 kilometers and the effects that are produced are short-lived.

Electromagnetic waves propagating along paths above 25 kilometers can be affected severely by nuclear detonations. If the detonation occurs below 25 kilometers, the effects will be minimal, unless the weapon yield is so large that the fireball debris is carried well above 25 kilometers. As the detonation altitude is raised above 25 kilometers, propagation disturbances can cover a major portion of a hemisphere; they may last for hours, and they may interfere with systems that depend on the natural ionosphere to reflect or scatter energy, such as HF systems,

seriously. The size of the region affected and the duration of the effects on the system decrease with increasing wave frequency for frequencies above a few megahertz. Effects on wave frequencies above a few gigahertz are limited to the fireball region (a few tens to a few hundred kilometers in diameter).

As a result of the very large number of possible interactions between the effects caused by a nuclear burst and the electronic system in its operating environment, problems deriving from the degradation of signals in a nuclear environment are so complex that techniques for calculating signal degradation in nuclear environments are not appropriate for the subject material of this chapter. Such problems are performed most effectively with the aid of computers, using codes such as RANC 4 (see bibliography). Methods for computation of system performance by hand have been devised, but, in general, they are lengthy, even though many simplifications must be included. Some such computations for determining absorption are described in Chapter 8. Analyses of generic systems for selected burst conditions are useful for determining the nature and order of magnitude of effects; however, generalizations from such analyses are not warranted.

Although the English system of units for measuring distance is given priority throughout most chapters of this manual, wavelengths and other dimensions dealing with electromagnetic wave propagation usually are given in the metric system. Therefore, in this chapter and in Chapter 8, the metric system is used for distance dimensions. Conversion factors from the metric system to the English system are provided in Appendix B.

17-1

89 3 02 033

This document has been approved  
for public release and sale.  
Distribution is unlimited.

As discussed in Chapter 8, considerable uncertainty exists in the prediction of the effects of nuclear weapon bursts on electromagnetic propagation, particularly for burst or propagation conditions different from those for which test data have been obtained. While in general the prediction of weapon effects is more difficult in a multiple-burst environment than for a single burst, system performance may be relatively insensitive to burst parameters; for such cases simple models of the disturbed environment can be used for analysis.

## SECTION I

### DEGRADATION MECHANISMS

Nuclear weapon effects on electromagnetic propagation are grouped into three degradation mechanisms in this section: attenuation, which defines the change in the amount of electromagnetic energy reaching a given location; interference, which defines the level of noise competing with a received signal; and distortion, which defines the change in information content of a received signal.

### ATTENUATION

Attenuation of signals in a nuclear environment derives principally from the phenomena of absorption, scattering, and beam spreading (small angle scattering, i.e., differential refraction or defocusing). In some instances, generally at times after detonation in excess of a few minutes, scattering and beam spreading can be the more important phenomena. For most cases, however, attenuation caused by absorption is regarded as one of the most important effects caused by nuclear detonations (see ELECTROMAGNETIC PROPAGATION IN IONIZED REGIONS in Chapter 8), and it is one of the best understood and most predictable of the effects. There are three principal atmospher-

ic absorption regions caused by a nuclear detonation: the fireball, a region around the fireball, and the D-region of the ionosphere (approximately 50 to 80 km altitude). Figure 17-1 illustrates the absorption regions for several burst altitudes and times after burst.

#### 17-1 Fireball Absorption

The fireball is generally the most intensely absorbing region. Significant absorption within the fireball can last tens of seconds for frequencies less than about 10 GHz (see paragraph 8-6). Fireball sizes vary from less than a kilometer for small-yield surface bursts to several hundred kilometers for large-yield, high-altitude bursts. The fireball size and location as a function of burst parameters can be determined from Table 8-2 and Figures 8-16 and 8-38. The amount of signal attenuation caused by absorption of signals propagating through the fireball can be determined from Tables 8-3 through 8-7. For many cases of interest in analyzing a system, the duration of attenuation due to fireball absorption is determined by the rise rate of the rising fireball rather than the length of time the fireball remains absorbing.

#### 17-2 Absorption in the Region Around the Fireball

When the fireball is below the D-region, delayed gamma rays emitted from fission debris in the fireball cause ionization and thus absorption in a small region surrounding the fireball (see paragraph 8-8). The size of the region depends on the burst and propagation parameters; it can extend beyond the fireball for tens of kilometers for frequencies below a few gigahertz. Estimates of signal attenuation can be obtained from Figures 8-42 through 8-48 (Problem 8-6).

When the fireball is above the D-region, most of the absorption outside the fireball occurs in the D-region as discussed below.



For	
Distribution/	
Availability Codes	
Dist	Avail and/or Special
9-1	

UNANNOUNCED

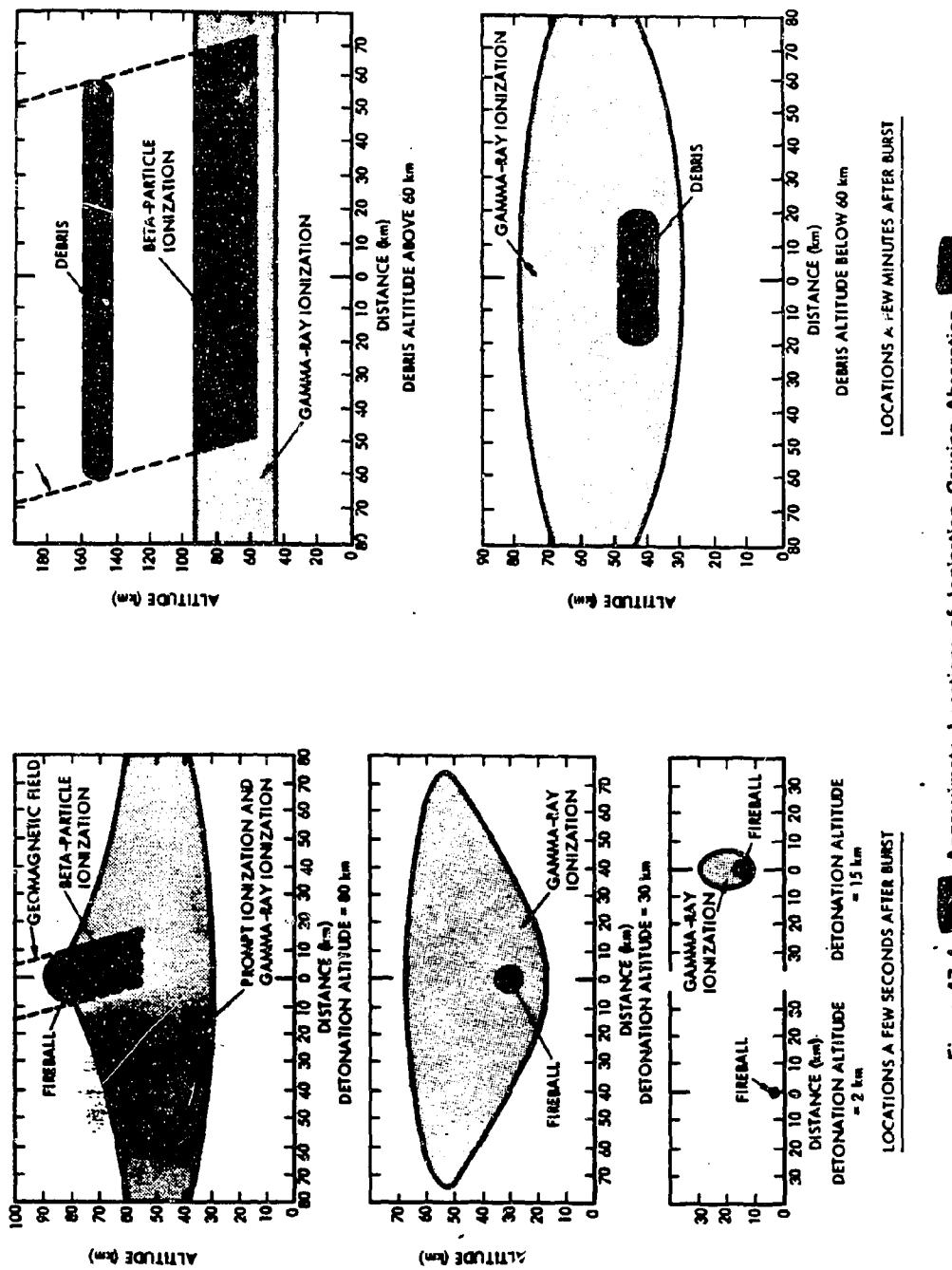


Figure 17-1. Approximate Locations of Ionization Causing Absorption

### 17-3 D-Region Absorption

The largest and most persistent absorption region caused by nuclear detonations generally occurs in the D-region. Depending on detonation altitude and weapon yield, both prompt radiation (X-rays and neutrons) and delayed radiation (beta particles and gamma rays) can ionize the D-region and cause absorption (see paragraphs 8-2 through 8-8). For frequencies above a few megahertz, absorption in the D-region is related inversely to the square of the frequency at which the system operates. The extent of D-region ionization caused by prompt radiation depends on the detonation altitude. The size of the ionized region increases from a few tens of kilometers for detonations below the D-region to thousands of kilometers for detonations above several hundred kilometers. The duration of significant absorption caused by ionization resulting from prompt radiation varies from less than a second for 1 GHz and nighttime conditions to tens of minutes for 10 MHz and daytime conditions.

Delayed gamma rays are an important D-region ionization source when the fission debris is above about 25 kilometers. The extent of the ionization increases with debris altitude. Large regions (thousands of kilometers in diameter) are affected when the debris is above several hundred kilometers in altitude. The larger ionization regions are primarily of importance for frequencies below a few hundred megahertz. Some of the Compton electrons produced in the burst region by gamma rays are guided by the geomagnetic field and produce ionization in the D-region on the opposite side of the magnetic equator (see paragraph 8-3). The resulting absorption is less intense than that due to gamma ray ionization in the burst region, but it can be important for frequencies in and below the HF band.

Beta particles ionize the D-region when the fission debris is above about 60 kilometers.

As illustrated in Figure 17-1 and discussed in paragraph 8-3, the size and location of the region ionized by beta-particles depend on the size and location of the debris region and the direction of the geomagnetic field. For each debris region above 60 kilometers there are two beta-particle absorption regions; one in the burst locale and one on the opposite side of the geomagnetic equator. At early times after burst when the debris region is relatively small (less than a few hundred kilometers in radius), beta-particle ionization can cause significant absorption for frequencies below a few gigahertz. At later times, when the debris is dispersed over large regions, the ionization is primarily important in causing absorption for frequencies below a few hundred megahertz.

Estimates of D-region absorption caused by prompt and delayed radiation can be obtained from Figures 8-40 through 8-51.

### 17-4 Absorption of Noise

Receiving system performance also may be affected if noise normally reaching the system via the ionosphere is absorbed. The noise level of some systems is determined by external sources (atmospheric noise, cosmic noise, or interfering signals from other sources) that propagate energy through the atmosphere. Both the desired signal and the undesired signal may be attenuated. The resulting signal-to-noise ratio depends upon the exact location of terminals, noise source, and weapon-produced ionization.

### 17-5 Attenuation by Scattering and Beam Spreading

Attenuation by absorption results when energy from a radio wave is deposited in the propagation medium in the form of heat. A different class of attenuation is that due to scattering of radio energy from the desired direction to other (possibly widely different) directions. A fundamental requirement for scattering is that

the refractive index of the medium be structured. Thus, regions of high electron-density gradient (e.g., fireball boundaries and various regions containing plasma striations) are of prime concern.

Characteristics of the electron-density structure that are important are its strength (i.e., the magnitude of spatial variation) and its size or scale. Generally, the greater the variation (especially in the integral of electron density along the line of sight), the greater the portion of energy scattered, and, the smaller the structure, the wider the scatter cone. The scale, relative to two parameters of the operating system, the wavelength and the Fresnel-zone radius, determine the nature of the attenuation effects associated with this scattering.

As a practical matter, the environments of concern seem to divide naturally, leading to a useful separation of effects into attenuation by scattering and attenuation by signal reduction through beam spreading. The former, loss by scattering, implies scattering at angles that are substantially larger than the system beamwidth. The latter, beam spreading, implies scattering, defocusing, or diffraction at angles comparable to or less than the system beamwidth.

The simplest effects to visualize are those due to structure that is large compared with both the wavelength and the Fresnel zone. These effects are refractive in nature and can be understood on the basis of ray optics. Simple ray bending may apparently displace a radio source from an antenna beam, resulting in attenuation, unless the beam is made to track the source. A patch of enhanced plasma will cause such ray bending in its border regions. In the mid-region of such a patch, the ray bending is minimum, but the radio energy density is actually decreased by defocusing, even if the source is kept in beam center. In effect, the plasma patch acts as a radio-frequency diverging lens. A region of lower-than-average electron density, on the

other hand, will act as a converging lens.

A region of plasma-density irregularities (e.g., fireball striations) may act as an ensemble of diverging and converging lenses, producing both attenuation and enhancement of signals. If the scale of the irregularities is small enough to be comparable with the system Fresnel zone at the range of the plasma, then they are too small to produce lenslike focuses, and the propagation must be treated by diffraction theory. The result regarding signal strength, however, still is to produce positive and negative fluctuations. This diffractive scatter can occur even if the irregularities are too weak to produce significant focuses or defocuses; the situation may be viewed intuitively as multipath propagation.

As the irregularity scale becomes smaller, the scatter cone becomes wider and can exceed the system beamwidth. In this case, not only will there be fluctuations in signal strength but also a net attenuation on the average. This net attenuation will occur whether the antenna achieves its directivity by employing a reflecting aperture (e.g., a dish antenna) or from phased elements distributed on the aperture (i.e., a phased array).

In the extreme, when the plasma structure becomes comparable in scale to the system wavelength, the radio energy is backscattered and lost to any receiver on the opposite side of the structured plasma, regardless of its antenna beamwidth. In this case, the attenuation effect is virtually indistinguishable from that due to absorption. Usually, the intensity of very small scale size fluctuations is small so that, although backscatter does occur — leading to radar clutter (paragraph 8-12) — such a small fraction of the energy goes into this phenomenon that the resulting attenuation of the primary beam is quite small. The presence of radar clutter does not necessarily imply that targets cannot be seen on the other side of the scattering region.

## **17-6 Effects of Reflection**

In addition to absorption, another important cause of signal attenuation in the HF band is loss of reflection from the E- and F-regions of the ionosphere (see TRAVELING DISTURBANCE in Chapter 8). Signals that normally would be returned to the receiver continue on into space. Conversely, burst-induced ionization in the E- and F-regions of the ionosphere may increase the electron density and allow reflection of signals at higher frequencies than normal.

## **INTERFERENCE**

### **17-7 Noise**

Thermal noise radiated by the hot fireball can produce receiving-antenna noise temperatures of several thousand degrees Kelvin for tens of seconds to several hundred seconds, depending upon the fireball altitude. A system normally will not experience problems from fireball noise unless the fireball is large enough that the antenna beam is essentially filled by the fireball and that absorption outside the fireball is significant at the frequency of interest.

Synchrotron noise may be associated with nuclear bursts that take place at very high altitudes or if the weapon debris rises to very high altitudes. The effect is noticeable only if a large number of electrons are trapped in the geomagnetic field outside the atmosphere. Only very sensitive HF receiving systems with upward-pointing antennas are likely even to detect synchrotron noise, but it may persist for weeks.

### **17-8 Reflection, Refraction, and Scatter**

Reflection and refraction of electromagnetic (EM) waves can cause unwanted signals to reach the receiver. These signals can mask and distort desired signals. Multipath interference occurs when a desired signal travels two or more

paths. The result is severe fading and distortion. HF and VHF systems operating in a nuclear-burst environment may experience unusual multipath conditions due to E- and F-region ionization, causing highly anomalous propagation modes with consequent signal distortion. Reflection from fireball surfaces may, under certain conditions, cause multipath in the UHF band.

Signal scattering can occur as a result of irregularities in electron density. A radar signal scattered back to the receiver may mask desired target returns or may produce a false target. Signals from other transmitters may scatter into a receiver, increase the noise level, and mask desired signals. In general, scatter in and above the HF band is caused by fireballs and by beta-particle ionization regions.

## **SIGNAL DISTORTION**

Propagation media disturbances may change the characteristics of a signal and degrade system performance. Frequency shifts, time delays, angle-of-arrival deflection, and polarization rotation are all possible effects (see PHASE EFFECTS in Chapter 8). The results may include reduction of effective system bandwidth and increased error rates when the signal is processed by the system.

Range and angular errors may be induced in radar systems by time delay and bending of the propagation direction. Generally, D-region ionization sufficient to produce signal distortion also will produce large absorption levels. At altitudes above the D-region, signal distortion (particularly range and angular errors) may occur at low or moderate absorption levels. Irregularities in electron density in and above the upper part of the D-region can change the direction of propagation and cause fluctuations in the angle of arrival of received signals (scintillation).

The significance of a change in signal characteristics depends critically on the signal

processing employed and on the system mission. The effects are most likely to be significant in systems that feature extreme accuracy and sensitivity, and depend upon sophisticated waveform processing.

## SECTION II

### SYSTEM CHARACTERISTICS AND EFFECTS

Nuclear environments related to the various types of military engagements affect the propagation medium and noise production differently. A detailed analysis of nuclear effects depends on specifying all of the nuclear burst and system parameters, and is beyond the scope of this chapter. However, the kinds of effects and their spatial and temporal extent can be illustrated with a limited number of examples. These examples suggest the general nature of the nuclear effects for most practical cases and will assist in identifying critical system parameters.

### VLF AND LF SYSTEMS

#### 17-9 VLF and LF Propagation

Propagation at frequencies below about 1 MHz, i.e., in the VLF, LF, and part of the MF bands, is controlled by the D-region of the ionosphere. Under natural conditions, there is a distinct difference between propagation of VLF (10 to 30 kHz) and LF (30 to 300 kHz). At VLF, the distance between the earth and the ionosphere is only a few wavelengths, and it is natural to think of these two boundaries as the walls of a waveguide. The received field is then the sum of the normal modes that have propagated to the observation point. The quantities of interest are the excitation factor (the relative energy supplied to the mode by the transmitter), the attenuation rate (loss of energy per unit distance), and the phase velocity of each mode. If the ionosphere is less than about three wavelengths from the ground, the modes are almost

equally excited, and the most important mode is always the mode of least attenuation. Lowering the ionosphere (which results from weapon-produced ionization) will usually increase the attenuation rate, and will increase the energy in the propagating modes. The effect on the total field strength depends on the trade off of these two effects. The different modes have different phase velocities, so if two modes are of almost equal strength, their sum will vary as a function of distance. The sum will be large where the two components are in phase and small where they are out of phase.

At frequencies above 30 kHz, the distance between the earth and the ionosphere is many wavelengths, and it is more convenient to think of the total field strength as the sum of the direct (or ground) wave, the first-hop skywave (energy reflected once from the ionosphere), the second-hop skywave (energy reflected twice from the ionosphere), etc. This is the same concept used at HF, but there is an important additional consideration. At LF, the downcoming skywaves diffract significantly around the curvature of the earth, so it is necessary to include them at distances that would be considered geometrically impossible at HF.

In the VLF and LF bands, the noise at the receiver is assumed to have an atmospheric source. It therefore depends upon season, time, and geographic location.

#### 17-10 Effects of Nuclear Bursts on VLF and LF Systems

The effects on propagation of VLF and LF signals caused by nuclear detonations result from ionization produced in and below the D-region (see IONIZATION AND DEIONIZATION, Chapter 8). Usually the effects are caused by free electrons, but significant absorption also may result from ions. Depending on weapon type and burst location, prompt radiation (neutrons and X-rays) can produce D-region ioniza-

tion in the general vicinity of the burst. Significant D-region ionization also can be produced in the burst region by delayed gamma rays from fission debris if the debris is above 25 kilometers altitude and by beta particles if the debris is above 60 kilometers altitude. Beta particles and Compton electrons (produced by gamma rays) can cause significant ionization in the region magnetically conjugate to the debris location. Under certain circumstances, ionization at locations very distant from the burst may result from neutron-decay betas and the dumping of trapped radiation.

Blackout or complete disruption, of VLF and LF communication systems usually requires burst-produced ionization to affect a large portion of the propagation path. Since the propagation paths are typically many thousands of kilometers long, high-altitude detonations or multiple detonations dispersed over the propagation path are required to produce the necessary ionization. Degradation can be caused by reduction of signal amplitude and rapid changes in signal phase. The significance of phase changes to system performance depends critically upon the system characteristics.

Usually the greatest change in signal amplitude and phase from preburst conditions occurs for nighttime conditions; however, there are little day-night differences for large weapon yields. Effects are not uniform over the frequency band. When there is sufficient ionization to cause low reflection altitudes, propagation near the lower end of the LF band appears to suffer the least degradation. When the reflection boundary is near normal height but diffuse, propagation near the lower end of the VLF band appears to be affected least. In some cases the ionization distribution along the propagation path is such that low reflection altitudes occur over part of the path and a diffuse reflection boundary over the remainder.

In general, the longer the path length, the greater the probability of circuit degradation. Although there is a small probability that the signal-to-noise ratio may be increased, it will generally be reduced. Severe signal reductions can persist for hours, depending on the extent and kind of weapon-produced ionization. Equal reduction of signal and atmospheric noise may not influence system performance until the reduction in noise is so great as to render local receiver noise a determining factor.

Phase shifts up to about 1,000 degrees per burst at rates as high as 1 degree per microsecond may occur for each burst. The rate of recovery is usually a few degrees per second. Systems that cannot follow these phase shifts will lose synchronization. Time to reestablish synchronization is very difficult to estimate, but may require tens of minutes or longer.

The general effects of nuclear bursts on VLF and LF systems may be summarized as follows:

1. The most severe signal degradation and system outages of longest duration occur for widespread debris environments. This environment may be caused by a large-yield weapon detonated at high altitudes or by multiple detonations distributed over a large area.
2. An ionization impulse resulting from a very-high-altitude (even though low yield) detonation affects a wide area and may degrade LF system performance for tens of minutes. The propagation effects are greater at night than during the day.
3. Single detonations at altitudes below several hundred kilometers produce less severe signal degradation, unless the burst is close to the propagation path. Detonations near the surface (below about 30 km) have the least effect on VLF and LF propagation.

### 17-11 Spread-Debris Environment

Following nuclear bursts, debris can be spread over a large area if weapons are detonated above about 50 kilometers at dispersed locations. By assuming the debris to be uniformly distributed, a relatively simple model that provides useful estimates of propagation effects resulting from several bursts is obtained. The ionization affecting VLF and LF propagation is caused by beta and gamma radiation from the fission debris. This ionization can be characterized by the fission yield per unit area and the average age of the debris. Assuming the detonations occur within a few minutes of each other, a parameter  $w$  can be defined by

$$w = \frac{W_F}{A} \cdot \frac{1}{t^{1.2}}$$

where  $W_F/A$  is megatons of fission yield per square kilometer, and  $t$  is time after attack in seconds. A value for  $w$  of  $10^{-7}$  represents a very severe attack environment. Values of  $w$  between  $10^{-9}$  and  $10^{-11}$  are representative of a wide range of attack conditions, and can apply over a considerable area even for relatively light attacks.

Figure 17-2 shows the signal attenuation for a 4000 km path. For large values of  $w$ , the reflection altitude is low and propagation near the low end of the LF band is least affected. In the range of the more likely  $w$  value of  $10^{-11}$  to  $10^{-9}$ , the reflection boundary becomes more diffuse and propagation in the VLF band shows minimum effects. For daytime conditions the LF signal attenuations are somewhat smaller than for nighttime conditions when  $w$  is less than about  $10^{-11}$ . Effects similar to those described for propagation beneath the debris occur on the opposite side of the geomagnetic equator as a result of beta-particle and Compton electron ionization (see paragraph 8-3).

While the results shown are for that portion of a path under the debris, it should be noted that degradation effects will not be limited to this region. Gamma radiation will increase the size of the ionization region up to several thousand kilometers from the debris boundary. Propagation effects outside the debris region, while significant, depend on the details of the debris-path geometry.

### 17-12 Effect of a [REDACTED] 6300-km Burst

Prompt radiation from [REDACTED] burst at 6300-km altitude (one earth radius) produces an impulse of ionization over a very large region. The extent of ionization is determined by the X-ray horizon.

Figure 17-3 shows the signal attenuation for nighttime conditions on a 4000-km path. The ionization impulse produces a diffuse reflection boundary, and propagation near the lower end of the VLF band is affected less than at the higher end.

Attenuation caused by prompt radiation is much less in the daytime than at night.

The phase advance caused by the ionization impulse (for times greater than 1 second after burst) is shown in Figure 17-4. At the time of the burst, the phase advance is much larger, on the order of thousands of degrees occurring in a few milliseconds.

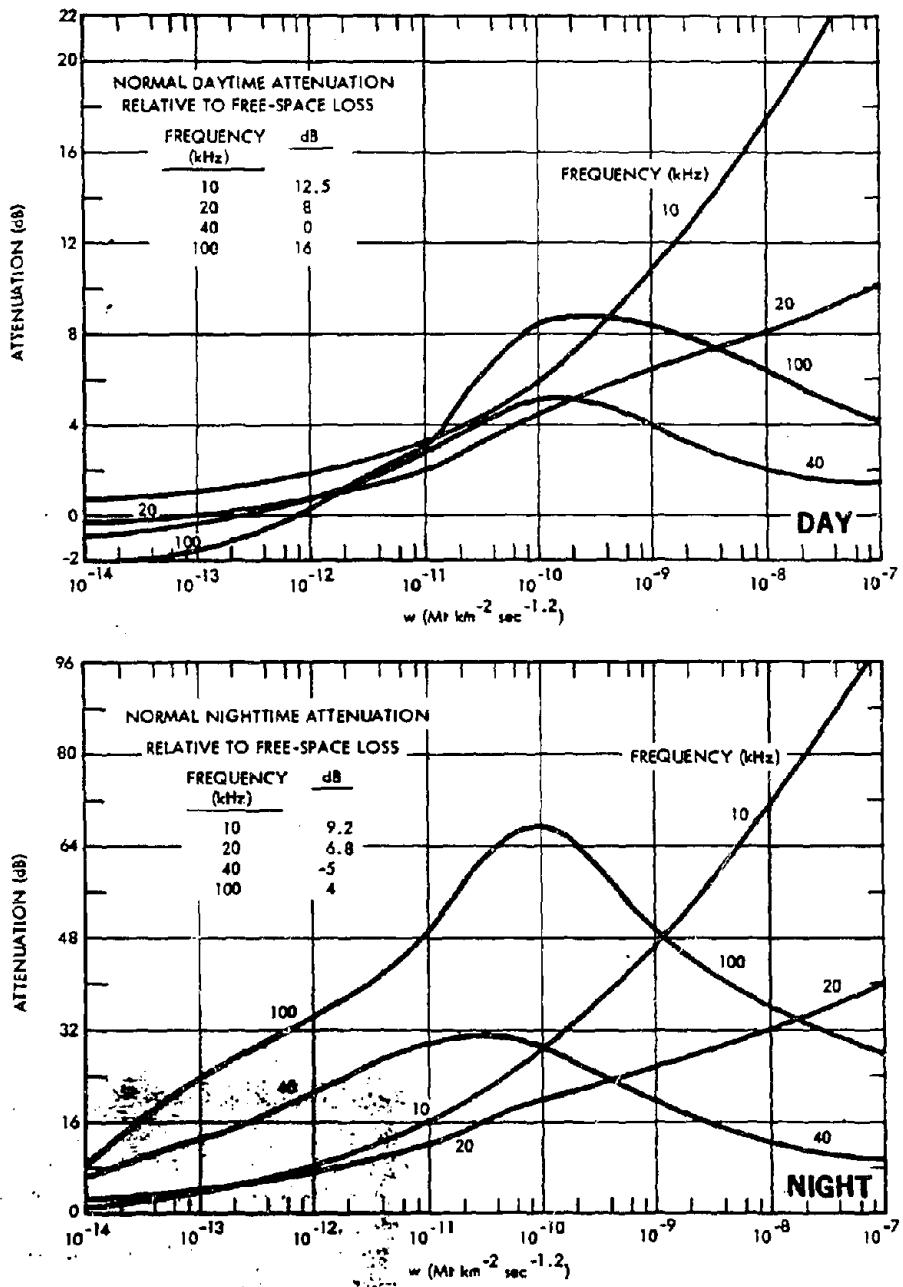


Figure 17-2. Attenuation Related to Normal Loss Due to Spread-Debris Environment, 4000-km Path Length

### **17-13 Effect of Detonations Below About 300 km**

If a nuclear burst occurs below 300 km, the portion of a propagation path that is affected is generally small unless the burst is close to the path. Depending on burst location and detonation altitude, there can be two degradation periods. The first period occurs at or within few minutes of burst time and is caused by prompt radiation and gamma radiation from the fission debris. The second period occurs when the fission debris has spread sufficiently that beta particles produce ionization along the path. In general, degradation is more severe in the LF band than the VLF band. An exception to this rule occurs during the first few minutes after a large-yield burst, which can produce intense ionization along the path that will cause low reflection altitudes.

When a nuclear weapon is burst on the surface, ionization is limited essentially to the fireball region until the debris reaches altitudes above about 25 kilometers, where gamma radiation can penetrate the atmosphere. Even then, the extent of ionization affecting propagation is only a few hundred kilometers, and the effects are minimal. A large number of surface bursts, such as might occur during a nuclear war, could produce widespread ionization. Propagation effects similar to those described above for the case where the fission debris has spread to large distances would be expected for such conditions.

## **HF SYSTEMS**

### **17-14 HF Propagation**

Propagation at frequencies between about 1 and 60 MHz is supported by the F-region of the ionosphere. Generally speaking, the HF signal is a composite of many signals propagated along ray paths with different geometries. Figure 17-5 is an example of the ray-path

geometry of a 4000-km path during the daytime at a single frequency. This multiple ray-path characteristic of HF is very important in any analysis of the susceptibility of a circuit to degradation from nuclear effects. Natural variations in the ionosphere affect the exact ray-path geometry at any specific time.

Noise at HF comes from a variety of sources. Noise power in this frequency range has been conventionally calculated as a combination of propagated noise from thunderstorm centers (concentrated mostly in tropical areas) and man-made local noise. Atmospheric noise tends to be dominant at night when ionospheric absorption is less, whereas man-made noise may set the daytime level. Very often, however, the noise level is determined by other interfering signals because of congestion of the HF band. No means have been devised for quantitatively treating this latter and perhaps most important source of noise.

### **17-15 Effect of Nuclear Bursts on HF Systems**

The most important phenomenon produced by nuclear bursts that affects HF systems is absorption resulting from D-region ionization. The ionization of the D-region is produced by prompt and delayed radiation. The amount of ionization depends on the altitude and the yield of the detonation (see IONIZATION AND DEIONIZATION in Chapter 8). Persistent absorption results from delayed gamma radiation when the debris is above 25 kilometers, and from beta particles when the debris is above 60 kilometers. Beta particles and Compton electrons can produce significant absorption in the region magnetically conjugate to the debris location. D-region absorption can extend over several thousand kilometers and can be important for hours after burst. For detonations above about 100 kilometers, there are often two distinguishable absorption periods: one, which starts at burst time,

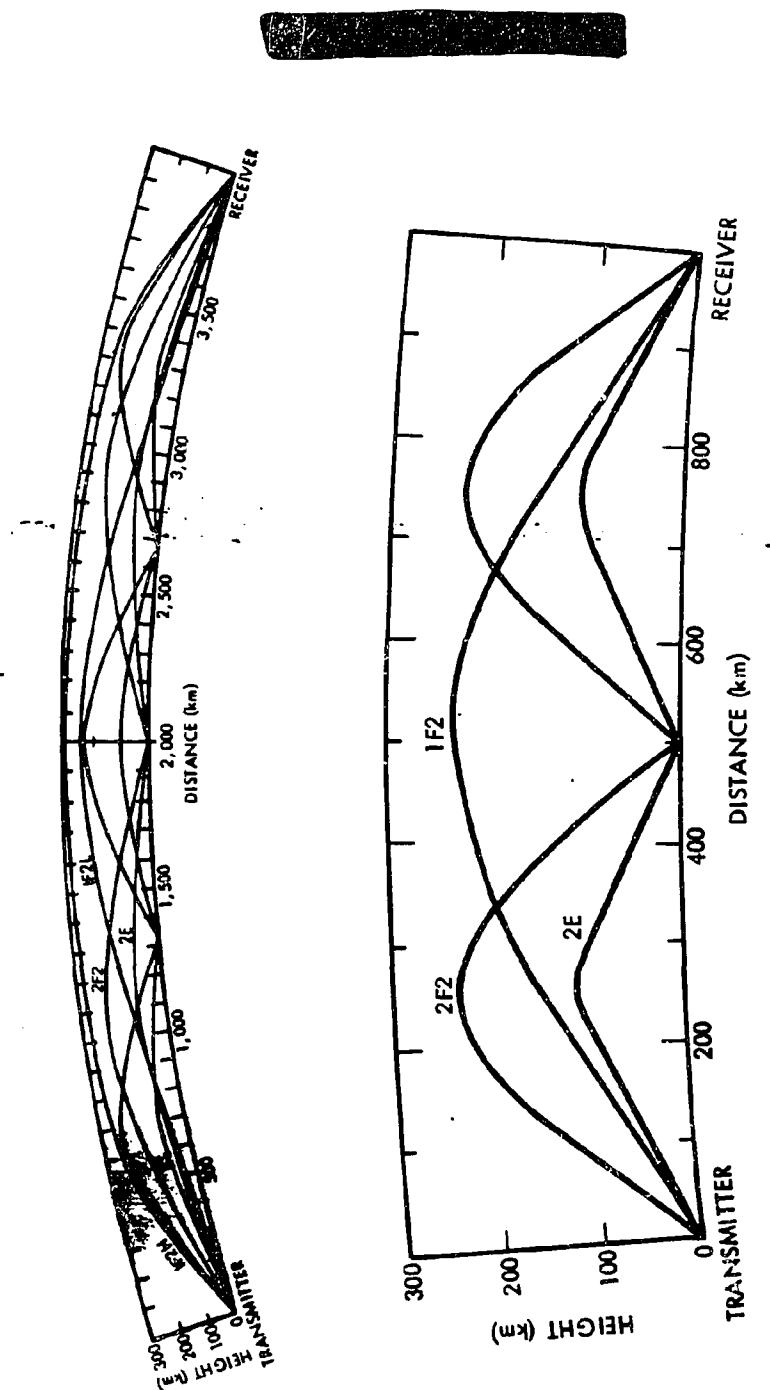


Figure 17-5. Examples of Daytime HF Ray-Path Geometry

results from ionization caused by prompt radiation and delayed gamma rays; a second results from ionization caused by beta particles. This latter starts when the fission debris has spread sufficiently that beta particles can ionize the D-region at the location of the propagation path. The duration of absorption depends on weapon yield and design, frequency, and time of day. The duration may vary from a few minutes for a small-yield weapon burst at night to several hours or more for a large-yield weapon burst during the day.

Detailed calculations of signal attenuation due to D-region absorption require the determination of the absorption for each ray path connecting transmitter and receiver. The procedures given in Chapter 8 (see Problems 8-5 through 8-7) can be used to determine the absorption when the ray path geometries are specified. Since D-region ionization does not alter ray-path geometry appreciably (see paragraph 8-10, Chapter 8), the pre-burst ray-path geometry can often be used in determining absorption. However, as discussed below, changes produced by the burst in the E- and F-region electron density can alter the number and location of ray paths, and thus can affect absorption calculations.

Ionization produced by a nuclear burst and traveling disturbances in the E- and F-regions of the ionosphere can produce significant changes in the E- and F-region electron densities that can last for hours (see TRAVELING DISTURBANCES IN E- AND F-REGIONS OF THE ATMOSPHERE in Chapter 8). Changes in the E- and F-region electron density can result in significant multipath effects by increasing the available ray paths and by introducing off-great-circle propagation paths. The maximum usable frequency (MUF) may be much lower than normal after nighttime detonations for ray paths that pass within several thousand kilometers of the detonation. For certain geometries and burst

conditions the MUF may be higher, perhaps up to 60 MHz. Current theoretical models do not provide reliable prediction of the MUF as a function of burst and system parameters. Oblique, frequency-sweep ionospheric sounders may allow determination of usable frequencies during disturbed conditions.

While HF system performance usually will be degraded by nuclear bursts (often resulting in complete circuit outage for significant periods of time), there may be factors that tend to minimize the degradation. For example, a reduction in noise or interference may accompany a reduction in signal strength, thus tending to preserve the preburst signal-to-noise ratio. Higher frequency propagation may be possible because of increased E- and F-region ionization, and the higher frequency will be less susceptible to absorption.

The general effects of nuclear bursts on HF systems are summarized below:

1. The higher the altitude of detonation, the greater and more widespread are the effects.
2. HF systems can recover from a nuclear attack, with nighttime recovery being much more rapid than daytime.
3. Intermittent propagation may occur even under severe circumstances, but the frequency range is not always predictable.
4. When ionization produced by weapon debris is not widespread (less than about 500 km) and the circuit is longer than a few thousand kilometers, the chances are good that continuous communication can be maintained after recovery from the prompt effects.
5. Multiple bursts occurring at dispersed locations and times can increase the degradation greatly and can reduce the sensitivity of the system to burst location.

The variations in the effects of nuclear bursts on

HF systems are illustrated by the descriptions of several specific examples in the following paragraphs.

#### 17-16 Effect of Surface or Near-Surface Bursts

Single or closely spaced bursts may occur during attacks against ground targets. Weapon radiation initially is confined to a volume of space near the detonation point, and a fireball is produced that subsequently rises (see paragraph 1-12 and 1-20). Ionization produced by the burst is essentially confined to the fireball region until the fireball carries the fission debris above about 25 kilometers, where gamma radiation can penetrate the atmosphere and produce D-region ionization. The extent of this ionization is a sensitive function of debris altitude. Gamma rays produce ionization over about 200 km horizontal extent for a 1-Mt surface burst, and over about 400 km for a 10-Mt surface burst. Because the area of high absorption is small, multiple rays will be affected only if they have a common D-region intersection. In any situation where the signal propagates over multiple ray paths that are sufficiently separated in the vicinity of the absorbing area, there will be little if any effect. Calculations for long and intermediate path lengths show that it is very difficult to eliminate all propagating frequencies. In some cases it would be necessary to switch to lower rather than higher frequencies to avoid outage, but communications could be maintained.

Signal attenuation caused by surface bursts can be severe for short paths since the D-region intersections of the ray paths are close together (see Figure 17-5). Communications on certain frequencies can be disrupted for a period of hours, especially during the day.

#### 17-17 Effect of a 30-km Burst

A [redacted] device detonated near an

altitude of 30 kilometers has potential as a possible penetration aid. The detonation point is sufficiently high that gamma rays will produce moderately widespread ionization even at early times. By 5 minutes after detonation, the debris will have risen [redacted] and beta particles can escape the debris region. Therefore, both gamma rays and beta particles are important ionization sources.

DNA  
(X)

For a typical burst location, there would be two periods of pronounced absorption; the first would occur during the initial debris rise, and the second would occur when the radiation from the spreading debris reaches critical D-region points.

DNA  
(X)

Because the region of increased ionization for this example is comparable to the D-region spacing between ray paths, the sensitivity to exact burst position is less critical than it is for surface bursts. The effects are still relatively limited, however, and the communication degradation does depend upon the burst location and the propagation path length.

DNA  
(X)

*PNA (LX)*

### 17-18 Effects of a [REDACTED] 50-km Burst

The effects of an extremely large yield weapon can be illustrated by describing the effects of [REDACTED] at 50 kilometers. Ionospheric effects are widespread and severe in both the burst and the conjugate regions. The debris rises to approximately 150 kilometers in less than 10 minutes, and it spreads to nearly 600 kilometers radius within 15 minutes. Thereafter, the debris radius continues to increase slowly as a result of winds.

The relatively high altitude and large yield of such a burst produce immediate and severe effects.

*PNA (LX)*

The size of the absorbing region is large enough that nearly all rays along a given propagation path will be affected simultaneously, causing path orientation and path length within the region to be unimportant. Absorption effects of a similar nature also can be expected in a region on the opposite side of the magnetic equator from the burst centered at the conjugate of the burst point.

The shock wave from a nighttime explosion [REDACTED] can be expected to reduce the critical frequency of the reflection region.

*PNA (LX)*

This condition will probably persist until after sunrise.

If the propagation path is offset from the burst, there can be an initial period of ab-

sorption as a result of prompt and delayed gamma radiation. This period might be followed by a period of recovery to near normal conditions, and then a second period of absorption would occur as the debris expands and beta particles affect the path.

*DNA (LX)*

### 17-19 Effect of Multiple Multimegaton 150-km Bursts

Multiple multimegaton high altitude bursts represent conditions that may result from the employment of a ballistic missile defense system. The most significant effects on HF circuits are widespread prompt ionization, widespread and intense delayed radiation, and F-region modifications. The debris will be distributed over a large altitude region, with some debris reaching altitudes above 1000 kilometers. The geomagnetic field plays an important role in determining late-time debris location (see Problem 8-7, Chapter 8).

If multiple multimegaton high altitude bursts occur, HF circuits will be interrupted over a very substantial area, essentially at burst time.

*DNA (LX)*

The duration of the outage for paths at these extreme ranges will be brief.

*DNA (LX)*

The particularly large radius of effects at early times results from the high altitude to

which the debris rises. Gamma radiation from the debris has a horizon of about 4000 kilometers from the burst points. Eventual expansion of the debris results in secondary outages when beta-particle ionization reaches a given path. In the region around the conjugate of the burst points beta-particle ionization is similar to that produced in the burst region. Compton electrons cause ionization which is less intense than that produced by gamma rays in the burst locale (see paragraph 8-3).

The critical frequency of the reflection region probably will be affected out to about 1000 kilometers after many large yield high altitude bursts. Significant electron density enhancement may occur near the detonation points, and electron density depletion may occur at more remote locations.

DNA  
(b)(1)

#### 17-20 Effect of a 1-Mt, 250-km Burst

A 1-Mt weapon burst at an altitude of 250 kilometers will result in significant propagation effects from prompt radiation, delayed radiation, and changes in the F-region. Debris will be distributed over a large altitude region; the geomagnetic field will affect the late-time debris location, with some debris being transported across the geomagnetic equator. Very intense and widespread effects will be produced on the ionosphere; hence there will be degradation of HF communication systems. However, because of the lower yield and somewhat shorter debris rise than in the case discussed in paragraph 17-18, the effects are more dependent on the

location and length of the communication path.

Ionization caused by the betas emitted by the spreading debris from such a burst will result in prolonged outage of HF systems. The lowest frequencies will be out for the longest period of time.

DNA  
(c)(1)

During the nighttime, the rapid decay of D-region ionization results in rapid recovery of all HF communication circuits that are not affected by beta ionization.

DNA  
(c)(1)

Circuits within several thousand kilometers of the conjugate of the burst point will also experience significant degradation. The absorption caused by beta-particle ionization is similar to that described for the burst region.

For this type of high-altitude burst, the E- and F-region electron densities may be increased in the region near the burst.

DNA  
(c)(1)

DNA  
(L)(X)

reduced below the MUF at distances beyond 500 kilometers from the burst.

#### 17-21 Effect of a [REDACTED] 1000-km Burst

[REDACTED] weapon burst at an altitude of 1000 kilometers would be primarily an anticomunication event. In spite of the small yield, the X-ray output is sufficiently large that even from an altitude of 1000 kilometers, significant ionization would be produced in the lower ionosphere.

[REDACTED] The radius of effects from such a burst is much greater than individual mode separation distances; thus, the exact ray path position, path length, and orientation are not important for distances less than approximately 2000 kilometers.

DNA  
(L)(X)

[REDACTED]

### SATELLITE COMMUNICATION SYSTEMS

[REDACTED] The basic elements of a satellite communication system consist of a ground-terminal transmitter, a satellite-borne repeater, and a ground-terminal receiver. Typically, the satellite-borne equipment provides only the functions of frequency translation and amplification; signal processing and demodulation take place at the ground terminals. Gigahertz frequencies and large bandwidths are typical of satellite communication systems, but some systems may operate in the VHF and lower UHF bands.

#### 17-22 Effects of Nuclear Bursts on Satellite Systems

[REDACTED] The nuclear bursts of primary impor-

tance to military satellite communication systems are those that produce an intense ionization region which is intersected by the propagation paths of the relay circuit. One of the principal effects of this ionization is absorption of the propagating signal. The region of significant ray-path absorption for communication satellites operating at several gigahertz is usually confined to the fireball; however, other important absorption regions may exist for some combinations of yield and burst altitude. (See Chapter 8 for a discussion of ionization and absorption regions produced by nuclear detonations.)

DNA  
(L)(X)

[REDACTED]

D-region ionization produced by prompt and delayed radiation (beta particles and gamma rays) produces absorption that [REDACTED]

[REDACTED] depending on propagation frequency, burst altitude, and fission yield. Delayed gamma rays can affect propagation in the VHF band.

[REDACTED] The extent of D-region absorption caused by beta particles is determined by the debris expansion, and this absorption can affect propagation in the VHF and UHF bands.

DNA  
(L)(X)

[REDACTED] In modern low-noise receivers, it is often the noise appearing at the terminals of the receiving antenna that will set the limit on the overall performance of the system. As a result, fireball thermal noise can be significant in degrading the performance of satellite communication systems (see ELECTROMAGNETIC RADIA-

ATIONS in Chapter 8). The amount of electromagnetic thermal radiation reaching the receiver antenna depends on the effective fireball temperature at the frequency of interest (a function of temperature and emissivity) and on the amount of attenuation between the fireball and the antenna. Antenna temperature generally will be less than the effective fireball temperature as a result of absorption that occurs outside the fireball and the effect of antenna gain in the direction of the fireball.

DNA  
K-10

The group time delay associated with signal propagation through a plasma usually is frequency dependent. This causes phase distortion of angle-modulated signals (frequency and phase modulation are forms of angle modulation), resulting in what is termed intermodulation noise. This frequency-dependent time delay, or dispersion, also results in envelope distortion for pulse transmission through a plasma. Hence, another effect of burst-produced ionization that may be of importance to angle-modulated multichannel satellite systems of large channel capacities is the intermodulation distortion noise. The strength of this intermodulation noise is determined largely by the integrated electron density along the ray path and the modulation parameters. Typically, it is the late-time, high-altitude fireball ionization that may give rise to this dispersion effect. Similarly, satellite digital-communication systems may encounter pulse distortion when propagating through burst-produced ionization, which in

turn may result in large decoding error rates. The dispersive medium may affect pulse amplitude systems because of envelope distortion. The magnitude of the pulse distortion is determined by the integrated electron density along the ray path, the carrier frequency, and the pulse width.

Time-variant time delays due to the structured and filament-like behavior of high-altitude fireball striations may be a possible source of degradation to satellite communication systems; no estimate has been made of these effects because of the lack of data from which to scale results. The effects of time-variant time delays would be to introduce channel noise of a nature similar to intermodulation noise or adjacent-channel interference.

### 17-23 Nuclear Effects on Two Typical Satellite Systems

Two hypothetical but typical satellite systems have been selected to illustrate many of the problems of satellite communication in a nuclear warfare environment. System A (see Table 17-1) represents a high-volume military communication system. The mission requires continuous coverage between virtually every pair of points on the earth's surface. The system provides a tactical quality of voice communications.

System B (see Table 17-2) operates in the UHF band at 400 MHz. It employs an 8-hour circular communications orbit. The power requirements, antenna size, channel capacity, and grade of service provided represent a tactical, transportable communication system.

The systems considered employ Frequency Division Multiplex-FM (FDM-FM) as a means of carrier modulation. Voice channels are frequency multiplexed onto a single baseband using subcarriers. This baseband is then applied to a linear frequency modulator to modulate the transmitter RF carrier.

**Table 17-1. Satellite Communications Link Description, System A**

System Parameters	Description
Frequency	4 GHz
Channel capacity	300 duplex channels
Baseband	60 to 1300 kHz
Modulation format	FDM-FM
RMS frequency deviation	0.9 MHz
FM threshold	12 dB
Ground antenna	80-foot dish
Ground transmitter power	10 kw
Ground receiver I-F bandwidth	15 MHz
Ground receiver system noise temperature	100°K
Satellite receiver noise figure	10 dB
Satellite antenna (toroidal pattern)	5 dB gain
Satellite transmitter power	25 watts
Satellite altitude (synchronous)	35,788 km

**Table 17-2. Satellite Communications Link Description, System B**

System Parameters	Description
Frequency	400 MHz
Channel capacity	12 duplex channels
Baseband	0 to 60 kHz
Modulation format	FDM-FM
RMS frequency deviation	27.4 kHz
FM threshold	12 dB
Ground antenna	30-foot dish
Ground transmitter power	10 kw
Ground receiver I-F bandwidth	0.672 MHz
Ground receiver system noise temperature	250°K
Satellite receiver noise figure	10 dB
Satellite I-F bandwidth	1 MHz
Satellite antenna (toroidal pattern)	-3 dB
Satellite transmitter power	20 watts
Satellite altitude (8-hour circular orbit)	13,896 km

Table 17-3 summarizes outage times for the two systems.

TPA  
(5)(1)

DNA  
(4)(1)

Table 17-3. [REDACTED] Estimated Outage Times for Fireball Intersection of the Propagation Path [REDACTED]

Deleted

DNA  
(u)(1)

(u)(1)   
Figures 17-6 and 17-7 illustrate two degradation mechanisms: fireball absorption and fireball noise. Figure 17-6 shows signal-to-noise ratio for Systems A and B.

The fireball is located such that the ray path traverses the fireball when it has stabilized in altitude. Figure 17-6 also shows, for reference, the absorption along the ray path.

Figure 17-7 shows signal-to-noise ratio and received noise for Systems A and B.

#### TROPOSCATTER COMMUNICATION SYSTEMS

Tropospheric forward-scatter communications are used for communications and military purposes in locations where the nature of the terrain makes other means of highly reliable communication difficult.

Figure 17-8 shows the geometry for a troposcatter link. Propagation from transmitter to receiver is via scatter in the common volume in the troposphere.

#### 17-24 Effects of Nuclear Bursts on Troposcatter Systems

Three potential sources of degradation of troposcatter communication systems are signal absorption, fireball thermal noise, and multipath interference via fireball scattering.

Since troposcatter systems typically operate between a few hundred MHz and a few GHz, only the regions of intense ionization will produce appreciable signal absorption. The ionization resulting

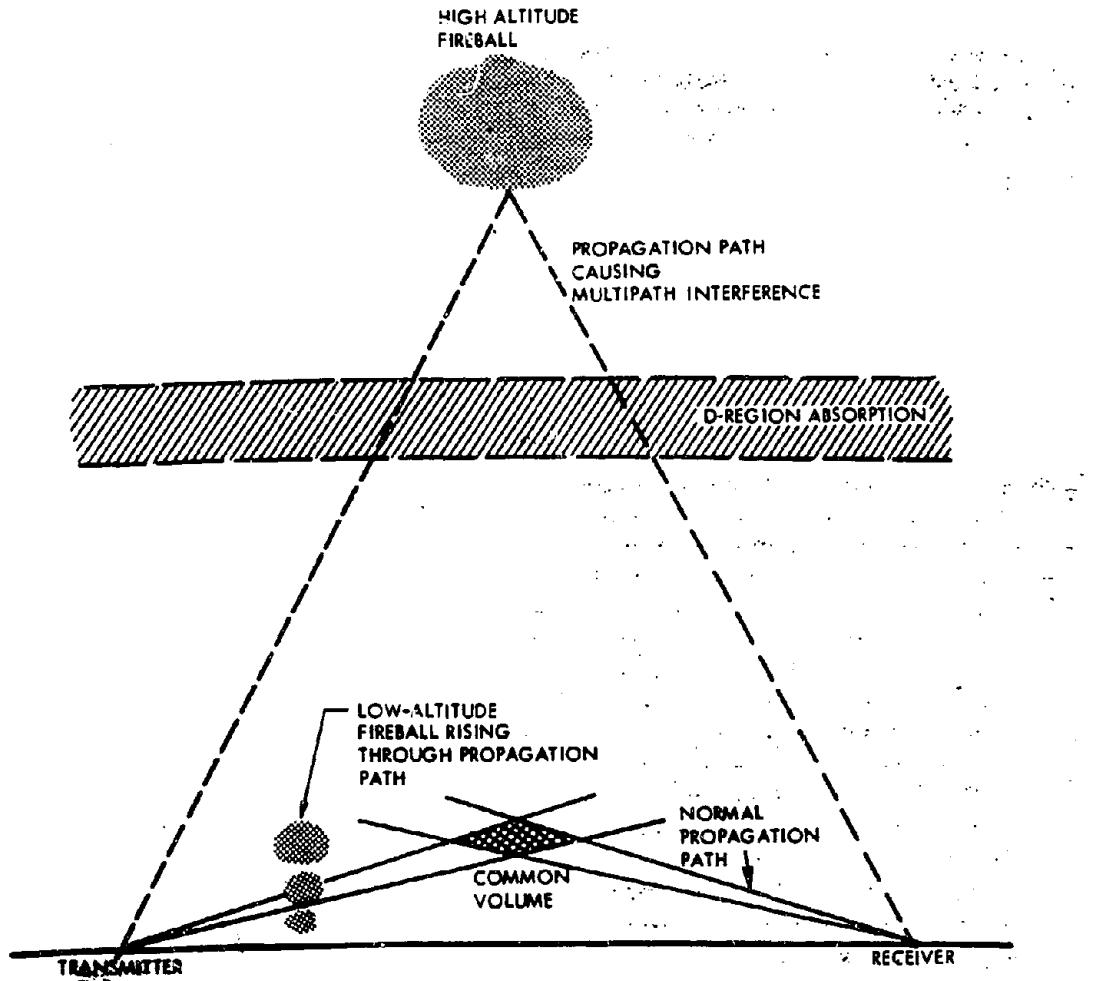


Figure 17-8. Illustration of Troposcatter Geometry

from a low-altitude nuclear burst is largely confined to the immediate vicinity of the fireball; consequently, in order to obstruct troposcatter communications as a result of ray-path absorption, the fireball must be within the scatter path.

In low-noise receivers, fireball thermal noise may degrade the performance of troposcatter communication systems significantly. The amount of electromagnetic thermal radiation reaching the receiver antenna depends on the effective fireball temperature at the frequency of interest (a function of temperature and emissivity) and on the amount of attenuation between the fireball and antenna.

There are no significant differences between day and night effects for troposcatter systems.

#### 17-25 Nuclear Effects on Three Typical Troposcatter Systems

Three typical troposcatter communication systems have been selected to illustrate propagation effects for selected weapon environments. System A is representative of a high-quality commercial scatter system; System B is representative of a tactical system; and System C is representative of a long-distance system. The system characteristics are summarized in Table 17-4.

Table 17-5 summarizes the effects on the typical systems for several burst environments. There are essentially no differences between day and night effects. The amount of degradation depends on the fireball/debris geometry, which is variable with regard to size, shape, and location. The magnitude of multipath attenuation also depends on the antenna pattern (in the examples, the side-lobe gain was taken to be that of an isotropic antenna).

#### IONOSCATTER COMMUNICATION SYSTEMS

Ionoscatter systems provide intermediate-distance radio service of 4 to 16 channels of teleprinter and/or a single voice channel. Figure 17-9 shows the geometry for an ionoscatter link. Propagation between transmitter and receiver occurs via scattering from a common volume in the D-region.

The ionoscatter system considered here transmits at a continuous low data rate via a scatter signal that is always present, although weak and variable. The ionospheric scatter mode is fundamentally most suitable for low-data-rate teleprinter operations. High-quality voice communications via ionospheric scatter cannot be

Table 17-4. Troposcatter Communication Link Description

System Parameter	System A	System B	System C
Frequency	2 GHz	900 MHz	400 MHz
Path length	300 km average per hop, 6 hops	150 km, 1 hop	600 km, 1 hop
Channel capacity	120 channels	24 channels	12 channels
Power	10 kw	1 kw	100 kw
Antennas	80-foot dish	18-foot dish	120-foot dish
Antenna height	30 meters	30 meters	30 meters
Diversity	Quad, space	Dual, space	Quad, space
FM threshold	12 dB	8 dB	12 dB
Receiver noise figure	9 dB	9 dB	2.5 dB
Baseband	60-552 kHz	12-108 kHz	12-60 kHz
Modulation format	FDM-FM	FDM-FM	FDM-FM
RMS frequency deviation	362 kHz	63.5 kHz	35.3 kHz
I-F bandwidth	6 MHz	1.3 MHz	775 kHz

achieved with reasonable transmitter power.

Ionoscatter systems typically operate at frequencies just above the E- and F-layer MUFs to eliminate multipath reflections and HF interference.

#### 17-26 Effects of Nuclear Bursts on Ionoscatter Systems

As a result of their reliance on D-layer scattering mechanisms, ionoscatter systems are very susceptible to low-level residual ionization from a nuclear explosion. In view of the very small margin of operation above receiver threshold, usually limited by galactic noise, such systems are vulnerable to abnormal absorption along the scatter path and/or within the scattering volume. Prediction of effects in a nuclear

environment is very difficult, because the ionospheric scatter phenomena in the natural environment are not well understood.

The low frequencies employed by ionoscatter systems (about 35 to 50 MHz) allow appreciable absorption, even at low levels of residual ionization. Prompt radiation, delayed gammas from fission debris if the debris is above 25 km, and betas particles if the debris is above 60 km can all cause significant D-region ionization. If the debris is above 60 km, the betas will usually be more important than the gammas, and about one-half of the betas will be deposited in the region magnetically conjugate to where the debris is located.

TNF  
(u)

Table 17-6. [REDACTED] Approximate Extent and Duration of Effects on Troposcatter Communications, Assuming Proper Burst Placement [REDACTED]

Deleted

DNA  
(f)(1)

DNA  
(b)(1) [REDACTED]  
Increased E- and F-region ionization caused by prompt radiation and traveling disturbances from a nuclear detonation may result in multipath effects, which decrease the effective bandwidth of ionoscatter circuits.

DNA  
(b)(1) [REDACTED]  
Electromagnetic thermal radiation from fireballs is usually not important to ionoscatter systems because of the high ambient noise environment.

17-27 Nuclear Effects on Typical Ionoscatter Systems [REDACTED]

[REDACTED] The ionoscatter system selected as an example uses two-frequency operation: 35 MHz for low transmission loss, and 60 MHz to avoid multipath interference at times of high solar activity.

[REDACTED] The system parameters are summarized in Table 17-6. For digital communication, the encryption and order of diversity are perhaps the most important parameters that influence system performance. Because of the large variations in system performance with path length, results for 1000-, 1500-, and 2000-km links are considered. The antennas of the system consid-

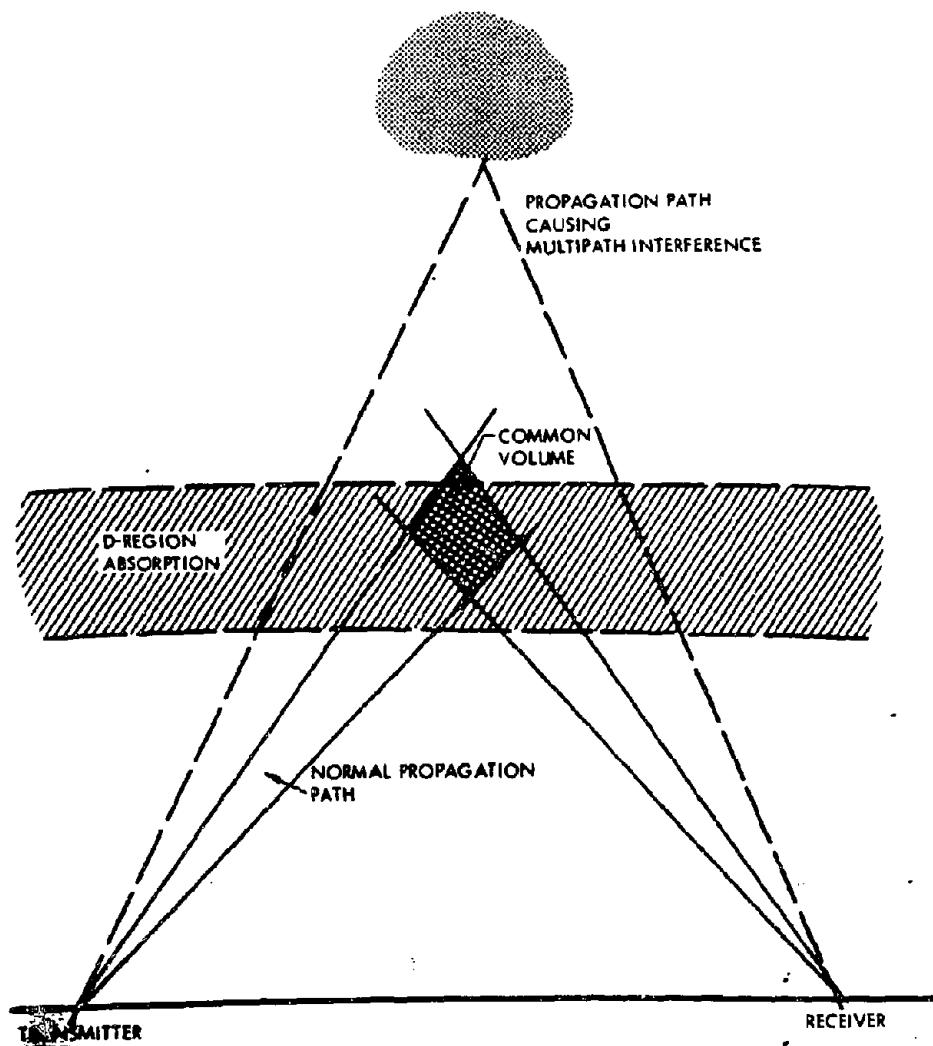


Figure 17-9. Illustration of Ionoscatte Geometry

Table 17-6. Ionoscorer Communications Link Description

System Parameters	Description
Frequency	35 or 60 MHz
Path lengths	1,000, 1,500, 2,000 km (three systems)
Channel capacity	16 channels, teletype
Power	60 kw
Antenna gain	19 dB
Antenna 3-dB beamwidths	45 degrees vertical, 11 degrees horizontal
Polarization	Horizontal
Diversity	Dual, space
Receiver noise temperature	450°K
Receiver noise bandwidth	1.2 kHz
Modulation format	TDM-FSK
Frequency shift	6 kHz mark-space
Demodulator	Dual filter, optimal without Doppler spread
Radiated signal element length	1.7 milliseconds
Transmission rate	600 bauds
Coding and synchronization	Standard 5-unit, start-stop neutral code

ered here are aligned along a great-circle path. Each terminal of an ionoscorer link is capable of duplex transmission.

Table 17-7 summarizes the effects of several burst environments on the system described in Table 17-6. These effects show a strong dependence on the location of the burst with respect to the scatter path and on the scatter path length.

Thermal noise from the fireball has negligible effect on this system because of the high cosmic noise levels. Effects of scattering from high-altitude fireballs, field-aligned ionization, or enhanced E- and F-region electron densities that may produce multipath interference are not in-

cluded in Table 17-7 because the phenomena are not sufficiently understood.

The most serious difficulty in predicting ionoscorer propagation characteristics in a nuclear environment is lack of understanding of the mechanisms involved in normal propagation.

#### RADAR SYSTEMS

Radar are used in a wide variety of missions, including surveillance, target acquisition, navigation, tracking, fire control, discrimination between true targets and decoys, guidance and control, and fuzing. The radars may be ground-based or airborne. Their frequency usually is above the HF band with line-of-sight propaga-

Table 17-7. [REDACTED] Approximate Outage Times 1000-, 1500-, and 2000-km Ionomscatter Links, Assuming Proper Burst Placement [REDACTED]

Deleted

DNA  
(S-X1)

tion paths. An exception is over-the-horizon radar (OTH or OHR), which operates in the HF band and uses E- and F-region refraction to detect objects at long ranges. Nuclear-weapon effects on over-the-horizon radars correspond to effects on [REDACTED] systems, described earlier in this section. OTH radars may be used for early detection of targets before detonation of nuclear weapons, and to provide supplementary information to ballistic missile defense radars at later times.

The choice of parameters to be used (frequency, radiated power, antenna beam shape, pulse waveforms, etc.) depends on the function intended for the system. Acquisition radars are designed to maximize the initial detection range and angular coverage. These radars generally use lower frequencies than tracking systems and have less stringent requirements for measurement accuracy. Tracking and discrimination radars require high measurement accuracy, and they generally use as high a frequency as

possible. Discrimination radars may use complex waveforms and signal processing to estimate the nature of the incoming object. An important parameter related to radar susceptibility to nuclear-weapon effects is the altitude of the region of space (sometimes called the battle space) from which target echoes are to be received.

In view of the different parameters and accuracy requirements for the different types of systems, the significance of weapon effects depends on the radar function. For example, fairly low levels of D-region ionization can cause sufficient absorption to reduce the initial detection range of an acquisition radar without affecting track radars. Levels of clutter, scintillation, and dispersion effects that are too small to affect acquisition radars may degrade discrimination radars seriously.

Radars associated with detection of aircraft or surface targets usually will not experience signal degradation, since the propagation paths are below altitudes where persistent or widespread effects are caused by nuclear weapons (about 25 km). Fireballs from surface or air bursts may interdict the propagation path, but the small size of low-altitude fireballs and the relative motion between the rising fireball and the propagation path will usually limit outage to a few seconds. Blast, thermal, and nuclear radiation damage generally will be more significant for such systems when weapons are detonated close enough to interdict the propagation path.

#### 17-28 Ballistic Missile Defense Systems

Ballistic missile defense (BMD) systems can be categorized conveniently according to the size of the region defended. Area and regional defense systems are designed to protect a large area, such as one or more cities. The functions of detection, tracking, and discrimination of incoming objects are performed at as great a range as possible to allow the area to be defended with a minimum number of radars and interceptor

missile sites, and to minimize the damage to the defended area from detonation of intercept weapons. Initial detection ranges are typically a few thousand kilometers (approximately 10 minutes before impact of the incoming object). Intercept of those objects designed as threatening usually is above about 50 kilometers.

Hardsite defensive systems are designed to protect a small area, usually hardened against direct damage effects (blast, thermal, etc.). Information concerning threatening objects may be transferred to the system from area defense radars. Since the defended site is hardened, intercept altitudes usually are below 30 kilometers, and may be as low as a few kilometers. The system typically is designed to be able to perform acquisition, tracking, and discrimination functions after incoming objects are below 100 kilometers. High-performance interceptor missiles and data handling systems are used.

#### 17-29 Nuclear Effects on Area Defense Systems

Nuclear weapon effects on area-defense radars may be caused by interceptor weapons (self-blackout) or by penetration aid weapons used by the offense. Although interceptor weapons are designed to minimize propagation effects on defensive radars, the use of a number of interceptor weapons in certain locations can cause significant problems. In the cases of area and regional defense systems, where interceptor detonation altitudes are high, the degradation mechanisms include absorption in the fireball and the D-region, scattering in the fireball and the E- and F-regions, noise, and clutter interference. Scattering and beam spreading can produce attenuation even in the absence of absorption; these propagation effects also produce scintillation of various kinds (amplitude, phase, angle, etc.). Receiver response to these effects will be similar to that associated with multipath. Absorption and scattering appear to be the most significant of the effects.

DNA  
(b)(1)

Whether the interceptor fireball will interdict the radar propagation path depends on the spacing of incoming objects, the interceptor weapon yield and detonation altitude, and the geometrical relation between the radar and the threat approach azimuth.

DNA  
(b)(1)

D-region ionization caused by prompt and delayed radiation can be a significant cause of absorption, because for typical geometries the propagation path must traverse the D-region. D-region absorption scales inversely with frequency squared and is essentially negligible for frequencies above a few gigahertz. At a few seconds after burst, the most intense D-region absorption is caused by beta particles. As discussed in paragraph 8-4, the beta-particle ionization region is offset horizontally from the debris region by an amount that is determined by the orientation of the geomagnetic field and the height of the debris above the D-region. Intercept altitudes that place the beta-particle ionization region along the propagation path to successive objects can produce significant signal attenuation as a result of absorption after each intercept burst. Both the location of the ionization region and the propagation path are moving, and the duration of absorption is determined by the length of time the propagation path remains in the beta-particle ionization region. Refraction effects from D-region ionization are generally

negligible, unless the level of ionization is large enough to also cause large signal attenuation.

Prompt radiation from bursts detonated above about 100 kilometers increases the electron density in the E- and F-regions. The horizontal extent of the affected region depends on the burst altitude, weapon yield, and weapon design. While absorption resulting from E- and F-region ionization outside the fireball is small for radar frequencies, refraction or bending of the propagation path will cause angular errors. Even very small elevation and azimuth errors can result in significant interceptor miss distances.

Interference and signal distortion also may be caused by noise (fireball thermal radiation), clutter, dispersion, and scintillation. While noise from fireball thermal radiation does not appear to be a significant problem for military radar systems, the conclusion should be reviewed for specific systems, particularly if low-noise receivers are used. Clutter returns can be orders of magnitude larger than target echoes and may mask the desired echo or appear as false targets. While it appears that antenna side-lobe rejection and doppler discrimination techniques can be used to reject clutter returns, these techniques may increase the data processing required by a substantial amount. Signal distortion caused by dispersion appears to be a secondary effect for acquisition and track radars, but it may degrade the performance of discrimination radars. Scintillation may cause pulse-to-pulse fluctuation in the apparent direction of the target. Computational models for scintillation are currently incomplete.

The computational models given in Chapter 8 can be used to estimate fireball absorption for ray paths traversing the fireball or D-region. While effects other than absorption are discussed in Chapter 8, computational models are not given because of the complexity of the scaling. Analysis of radar performance in a nuclear environment usually is done with computer

*DNA (G)(1)*

codes to facilitate the large number of computations required.

An example of the results of code calculations is provided below to illustrate the types of effects and the sensitivity of the effects to radar and burst parameters. The example is not intended to model an actual engagement, but it provides representative nuclear environments that might be produced by penetration aid or interceptor weapons. The geometry chosen for the example is shown in Figure 17-10. The threat trajectory (path of an incoming object) is in the direction of the geomagnetic field. One radar is located at the defended target and another is offset from the target to view the incoming object from the side.

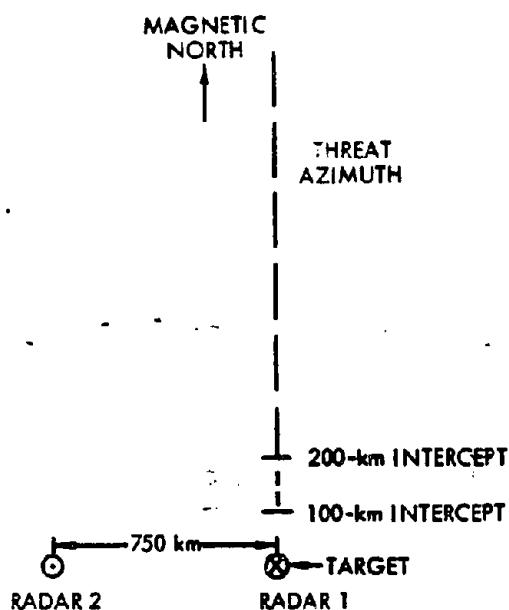


Figure 17-10. (U) Plan View of Radar and Target Geometry (U)

*DNA (G)(1)*

As the incoming object approaches the target a series of nuclear bursts are assumed to occur at a fixed altitude on the trajectory.

*DNA (G)(1)*

Figure 17-11 shows the signal-to-noise ratio and the elevation errors calculated for the radar located at the target. Results are shown for bursts occurring at two detonation altitudes. The propagation path from the radar to the incoming object traverses beta-particle ionization regions.

*DNA (G)(1)*

As previously mentioned, refraction due to E- and F-region ionization can cause angular errors that affect the defense's ability to predict the location of incoming objects and perform intercepts. Figure 17-11 shows the elevation errors computed for the radar located at the target.

DNA  
(4)(1)

Figure 17-12 shows the signal-to-noise ratios and elevation errors calculated for the offset radar. Because of the offset, the propagation path does not traverse beta-particle ionization regions or fireball regions, and signal attenuation is due to ionization caused by prompt radiation and delayed gamma radiation.

DNA  
(4)(1)

The above example does not show the dependence of system performance on the type of burst, the spacing and number of incoming objects, or the location of the threat azimuth with respect to the geomagnetic field, all of which can be significant. Further, the calculations for the example were based on the assumption that the phenomenology for each weapon was independent of previous weapons.

DNA  
(4)(1)

It is expected that modifications of burst phenomenology in a sequential-burst environment will be important. Models for such environment are under development (see Appendix E for code listings).

DNA  
(4)(1)

Some field simulation has been performed by releasing barium in the ionosphere (at altitudes between 100 and 200 km) in order to produce structured plasmas. The resulting plasma does not produce significant absorption, but it does tend to striate along the geomagnetic field to produce structure.

This permits at least qualitative simulation of scattering effects.

17-36

### 17-30 Nuclear Effects on Hardsite Defense Systems

DNA  
(4)(1)

The angular extent of the region obscured by the fireball is shown in Figure 17-13 as a function of detonation altitude for a typical sight line. The solid angle subtended varies as a function of time due to rise and expansion of the fireball (see Problem 8-1, Chapter 8). The magnitude of the variation is not great, however, and the values of solid angle shown in Figure 17-13 are representative of those occurring for the first few tens of seconds after detonation.

DNA  
(4)(1)

PAGE 17-37 DELETED

DNA  
(4)(1)

[REDACTED]

Deleted

DNA  
(b)(1)

Figure 17-13. [REDACTED] Solid Angle Obscured by 10-kt Intercept [REDACTED]

DNA  
(b)(1)

[REDACTED]  
Clutter returns and thermal noise from the fireball are potential degradation mechanisms for area defense systems. The use of narrowbeam antennas and signal processing will generally prevent degradation, but detailed analyses of system performance for specific scenarios and radar geometries are required.

[REDACTED] Penetration-side weapons (precursors) detonated between about 20 and 50 kilometers can interfere with detection, track, and discrimination functions, and can reduce the reaction time available to the defense.

DNA  
(b)(1)

[REDACTED]  
Denial of all information to the defense  
is very difficult.

## BIBLIOGRAPHY

*Atmospheric Ionization and Effects on Radar and Communications, A Bibliography*, DASA 2069, Defense Atomic Support Agency, Washington, D.C., January 1968

*Electromagnetic Blackout Handbook (U)*, Second Edition, Volume I: *Guide to System Effects* DASA 1580, Defense Atomic Support Agency, Washington, D.C., December 1964

*Electromagnetic Blackout Handbook*, Second Edition, Volume II: *Nuclear Weapons Effects* DASA 1580-1, Defense Atomic Support Agency, Washington, D.C., February 1965

Knapp, W. S., and P. G. Fischer, *Aids for the Study of Electromagnetic Blackout*, DASA 2499, General Electric, TEMPO, Santa Barbara, Calif., July 1970

*Nuclear Effects on HF Communications Systems Selected Examples*, DASA 1955-1, October 1967; *General Prediction Techniques*, DASA 1955-2, April 1968; Defense Atomic Support Agency, Washington, D.C.

*Nuclear Effects on VLF and LF Communications Systems Selected Examples*, DASA 1954-1, June 1968; *General Prediction Techniques*, DASA 1954-2, September 1968; Defense Atomic Support Agency, Washington, D.C.

*Nuclear Effects on Satellite and Scatter Communication Systems Selected Examples*, DASA 1956-1, October 1967; *General Prediction Techniques for Satellite Systems*, Vol. 1, DASA 1956-2, July 1968; *General Prediction Techniques for Scatter Systems*, Vol. 2, DASA 1956-2, October 1968; Defense Atomic Support Agency, Washington, D.C.

*RANC IV, Computer Simulation of Radar in a Nuclear Environment*, Volume I, *Computational Models*, DASA 2497-1; Volume II, *Operational Data*, DASA 2497-2; Volume III, *Appendices*, DASA 2497-3; Defense Atomic Support Agency, Washington, D.C., prepared by General Electric Company-TEMPO, Center for Advanced Studies, Santa Barbara, California, July 1970

*Weapon Effects Computer Code Directory*, DASA 1727, Special Report 43, DASI-AC, Santa Barbara, California, April 1969

Younker, E. L., et al., *VLF/LF Communications During a Major Nuclear Attack* SRI 7045, DASA 2369, Stanford Research Institute, Menlo Park, California, September 1969

AD-A955 402

ADA955402



DTIC  
SELECTED  
S 2 MAR 1989 D  
C E

## APPENDIX A

### SUPPLEMENTARY BLAST DATA

This appendix consists of two sections. Section I is a collection of equations and data useful in the study of shock waves. Section II contains a description of certain shock wave properties in a way that is intended to convey an understanding of these topics. None of the information in this appendix is required to solve the problems in Chapter 2 concerning blast phenomena or the blast related problems in the chapters of Part II of this manual. This appendix provides supplementary information, useful for solving special problems or for developing a better physical understanding of the phenomena described in Chapter 2.

The shock wave equations presented in this appendix are those that are most likely to be encountered in the study of air blast phenomena, and the concepts that are discussed are those that are most likely to be troublesome to the person who is studying shock wave theory for the first time.

This appendix presupposes a reasonable familiarity with the laws of mechanics and some understanding of how these laws apply to energy and momentum exchange in gases in motion.

#### SECTION I

##### MATHEMATICAL DESCRIPTION OF THE SHOCK FRONT

Most mathematical descriptions of shock wave phenomena are focused on the shock front itself since shock front conditions are fairly easy to treat mathematically, but the characteristics of the waveforms that follow the front are not. This limitation is not serious for many types of calculations, because the strength of the shock

front is usually the best indicator of the severity of the entire shock wave.

In the absence of direct, simple mathematical techniques, analysis of the shock waveform usually depends on empirical data such as the predetermined shock waveforms shown in paragraph 2-12, Chapter 2. Numerical integration of shock wave problems on a computer provides an alternate method. The computer codes for blast waves from nuclear weapons incorporate the details of weapon configuration, radiation transport, and hydrodynamics; these codes are complex and their characteristics will not be discussed here.

##### A-1 The Rankine-Hugoniot Equations

A set of three equations governing shock front behavior may be derived from the laws of mechanics. These equations (or any set of three independent equations derived from them) are called the Rankine-Hugoniot equations. They do not completely specify shock front behavior; a fourth equation, the equation of state of the material, is necessary to specify the complete behavior of the shock front. However, these equations have the advantage of being valid for all conditions under which a shock front can occur. They apply equally well to shock waves in solids and in gases.

The equations given below outline the conventional derivation of the Rankine-Hugoniot equations. The same set of equations are derived in Section II in a manner that requires less algebra but more physical reasoning. The three conservation equations that lead to the Rankine-Hugoniot equations involve the so-called jump conditions across a shock front. The parameters involved are illustrated in Figure A-1.

A-1

[REDACTED]

QUALITY  
INSPECTED  
4

Accession For	
NTIS GRA&I	
DTIC TAB	
Unannounced	
Justification	<i>[Signature]</i>
By _____	
Distribution/	
Availability Codes	
Dist	Avail and/or Special
A-1	

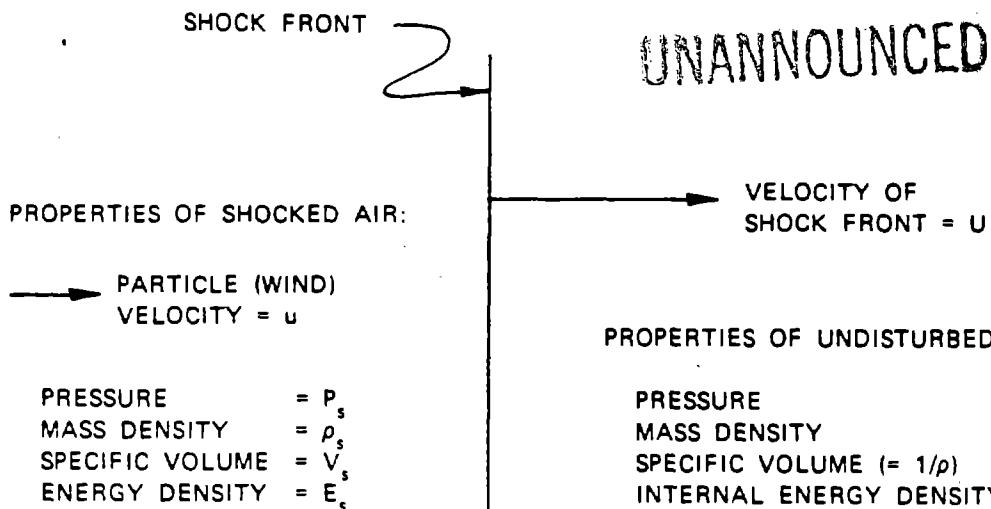


Figure A-1. (U) Change in Air Properties Across a Shock Front [REDACTED]

[REDACTED] An equation for the conservation of mass states that the mass of air per unit time overtaken by a unit area of the shock front is equal to the mass of air per unit area per unit time added behind the shock front.

$$\rho U = \rho_s(U - u),$$

where  $\rho$  is the ambient air density,  $U$  is the shock velocity,  $\rho_s$  is the density of the air behind the shock front, and  $u$  is the peak velocity of the air behind the shock front.

[REDACTED] Newton's second law states that force is equal to the rate of change of momentum. The force per unit area acting to accelerate the air entering the shock front is the overpressure,  $\Delta p = P_s - P$ , where  $P_s$  is the absolute pressure behind the shock front and  $P$  is the ambient pressure. The mass per unit time that enters a unit area of the shock front is  $\rho U$ . The change of velocity of the air is  $u$ . Thus,

$$\Delta p = P_s - P = \rho U u.$$

[REDACTED] Conservation of energy requires that the work done while the shock front moves through

a unit mass of air,  $P_s(V - V_s)$ , must equal the kinetic energy imparted to the unit mass of air,  $u^2/2$ , plus the change in internal energy,  $E_s - E$ , where the various symbols are defined in Figure A-1. Thus,

$$P_s \Delta V = (u^2/2) + (E_s - E),$$

or

$$P_s(V - V_s) = (u^2/2) + (E_s - E).$$

Using the relations  $V = 1/\rho$  and  $V_s = 1/\rho_s$ , a simultaneous solution of these three equations leads to the Rankine-Hugoniot equations in their usual form:

$$E_s - E = \frac{1}{2} (P_s + P)(V - V_s),$$

$$u = ((P_s - P)(V - V_s))^{1/2},$$

$$U = V \left( \frac{P_s - P}{V - V_s} \right)^{1/2}.$$

## A-2 Equation of State of an Ideal Gas

A gas that is heated at constant volume does not do external work; therefore, all of the thermal energy added to the gas is converted to internal energy. This amount of energy is

$$\Delta E = C_V \Delta T$$

where  $\Delta E$  is the change in internal energy per unit mass,  $C_V$  is the specific heat of the gas at constant volume, and  $\Delta T$  is the temperature change. By definition, the specific heats of an ideal gas are constant; and the internal energy per unit mass is

$$E = C_V T,$$

where  $T$  is absolute temperature.

Using the thermodynamic identities  $PV = RT$ , and  $C_p - C_v = R$  (where  $C_p$  is specific heat at constant pressure, and  $R$  is the universal gas constant) the following equation follows:

$$E = \frac{C_V PV}{C_p - C_V} = \frac{PV}{\gamma - 1}$$

where

$$\gamma = \frac{C_p}{C_v}.$$

Eliminating the variables  $E$ , and  $E$  makes it possible to use the Rankine-Hugoniot equations to determine the conditions across a shock front in an ideal gas uniquely.

The significance of the quantity  $\gamma$  as it appears in the shock wave equations deserves some explanation. In thermodynamics,  $\gamma$  appears most frequently in equations that involve isentropic compression. For example,  $\gamma$  appears

in the equation for sound speed because sound wave pressure fluctuations are isentropic. The presence of  $\gamma$  in shock wave equations is sometimes incorrectly interpreted as implying a relationship between shock wave compression and isentropic compression; actually,  $\gamma$  is a convenient constant relating energy content of a gas to pressure and volume. This fact becomes important in paragraph A-6 where strong shock waves are discussed. Variations in the value of  $\gamma$  must then be considered, and the equations

$$\Delta E = C_V \Delta T, \text{ and}$$

$$E = C_V T$$

cannot hold simultaneously. Conveniently,  $\gamma$  is redefined, so the equation

$$\Delta E = C_V \Delta T$$

still may be used. The meaning of  $\gamma$  as a specific heat ratio is lost, and  $\gamma$  becomes simply a constant in the energy equation.

## A-3 Shock Wave Equations for an Ideal Gas (U)

From the relation for the speed of sound in ambient air,

$$c = (\gamma P / \rho)^{1/2}$$

and the equation for overpressure,

$$\Delta p = P_s - P$$

the set of shock wave equations shown in Table A-1 can be derived. The equations in the right hand column were obtained by assigning to  $\gamma$  the value 1.4, the value for air at moderate temperatures and pressures.

These ideal gas equations apply to shock

Table A-1. Shock Wave Equations for an Ideal Gas

Equations in General Form	Equations for $\gamma = 1.4$
<u>Velocity of the Shock Front</u>	
$U = c \left( 1 + \frac{\gamma + 1}{2\gamma} \cdot \frac{\Delta p}{P} \right)^{1/2}$	$U = c \left( 1 + \frac{6\Delta p}{7P} \right)^{1/2}$
<u>Particle Velocity Behind the Shock Front</u>	
$u = \frac{\Delta p}{\gamma P} \cdot \frac{c}{\left( 1 + \frac{\gamma + 1}{2\gamma} \cdot \frac{\Delta p}{P} \right)^{1/2}}$	$u = \frac{5\Delta p}{7P} \cdot \frac{c}{\left( 1 + 6\Delta p/7P \right)^{1/2}}$
<u>Density Ratio Across the Shock Front</u>	
$\frac{\rho_s}{\rho} = \frac{2\gamma + (\gamma + 1)\Delta p/P}{2\gamma + (\gamma - 1)\Delta p/P}$	$\frac{\rho_s}{\rho} = \frac{7 + 6\Delta p/P}{7 + \Delta p/P}$
<u>Dynamic Pressure Behind the Shock Front</u>	
by definition, $q = \frac{1}{2} \rho_s u^2$	
$q_s = \frac{(\Delta p)^2}{2\gamma P + (\gamma - 1)\Delta p}$	$q_s = \frac{5}{2} \cdot \frac{(\Delta p)^2}{7P + \Delta p}$
<u>Temperature Behind the Shock Front</u>	
$T_s = T \left( 1 + \frac{\Delta p}{P} \right) \frac{2\gamma + (\gamma - 1)\Delta p/P}{2\gamma + (\gamma + 1)\Delta p/P}$	$T_s = T \left( 1 + \frac{\Delta p}{P} \right) \frac{7 + \Delta p/P}{7 + 6\Delta p/P}$
<u>Peak Reflected Overpressure at Normal Incidence</u>	
$\Delta p_r = 2\Delta p + (\gamma + 1)q$	$\Delta p_r = 2\Delta p \frac{7 + 4\Delta p/P}{7 + \Delta p/P}$

Table A-2. English and Metric  
Systems of Units

Unit	mks	cgs	English
length	meter	centimeter	foot
mass	kilogram	gram	pound
force	newton	dyne	slug
time	second	second	second
pressure	newtons/m <sup>2</sup>	dynes/cm <sup>2</sup>	pounds/ft <sup>2</sup>
density	kg/m <sup>3</sup>	g/cm <sup>3</sup>	slugs/ft <sup>3</sup>
velocity	m/sec	cm/sec	ft/sec
energy	joule	erg	ft-lb

waves in air provided the shock strength,  $\xi = (\Delta p + P)/P = P_s/P$ , is not too large. Usually these equations are assumed to hold for shock strengths of about 10 (132 psi overpressure at sea level) or less; note that at high altitudes this limit corresponds to relatively low overpressures, e.g., about 25 psi at 40,000 ft. The equations for high pressure shock waves are given in paragraph A-6.

As shown in Figure A-1, the subscript  $s$  denotes conditions behind the shock front; the absence of a subscript denotes ambient conditions (the subscript  $o$  is reserved for ambient conditions at sea level as in Chapter 2). The overpressure is  $\Delta p = P_s - P$ ;  $c$  is the speed of sound in undisturbed air; and  $\gamma$  is the ratio of specific heats  $C_p/C_v$ . Other quantities are defined by subheadings in the table.

#### A-4 Units, Constants, and Conversion Factors

Since the most commonly used shock wave equations are written in terms of dimensionless ratios, the choice of units is purely a matter of convenience; therefore, there is an inclination to ignore the fact that certain equations must be handled more carefully. Examples of these equations are the Rankine-Hugoniot equations and the dynamic pressure equation. Three consistent sets of units in common use are shown in Table A-2. Conversion factors and sea level values of various parameters are given in the various units in Appendix B.

#### A-5 Equation of State of Air

As air is heated by the compression of strong shock waves, the specific heat ratio  $\gamma$  decreases. Therefore, the equation that gives  $\gamma$  in terms of the ratios of the specific heats, which is based on the assumption of a constant  $\gamma$ , is no longer valid. The means of avoiding this problem has already been stated in paragraph A-2:  $\gamma_s$  customarily is *redefined* as that number which gives the correct value for internal energy. Since  $\gamma$

appears frequently in shock wave equations to replace an energy term, the new definition is a convenient one. Note, however, that (except in undisturbed air, where the new and old definitions of  $\gamma$  agree)  $\gamma$  is no longer the specific heat ratio. Therefore,  $\gamma$  should not be used (for example) to calculate sound speed in strongly shocked air.

Figure A-2 shows the equation of state of air for altitudes up to 240,000 feet. The nearly vertical curves are the Hugoniot curves for air at the indicated altitudes. The Hugoniot curve for a given altitude shows the combinations of peak pressure and peak density that are possible behind a shock front moving into undisturbed air, i.e., into air that is initially at the ambient pressure and density corresponding to that altitude. Curves that show the value of  $\gamma$  assigned to the air just behind the shock front cross the graph as nearly horizontal lines. The curves that cut diagonally across the graph show absolute pressure (not overpressure) just behind the shock front. The ordinate of the graph is shock strength, which was defined in paragraph A-3.

#### A-6 Equations for Strong Shock Waves in Air

For shock strengths of 10 or more, accurate calculations must use the nonideal equation

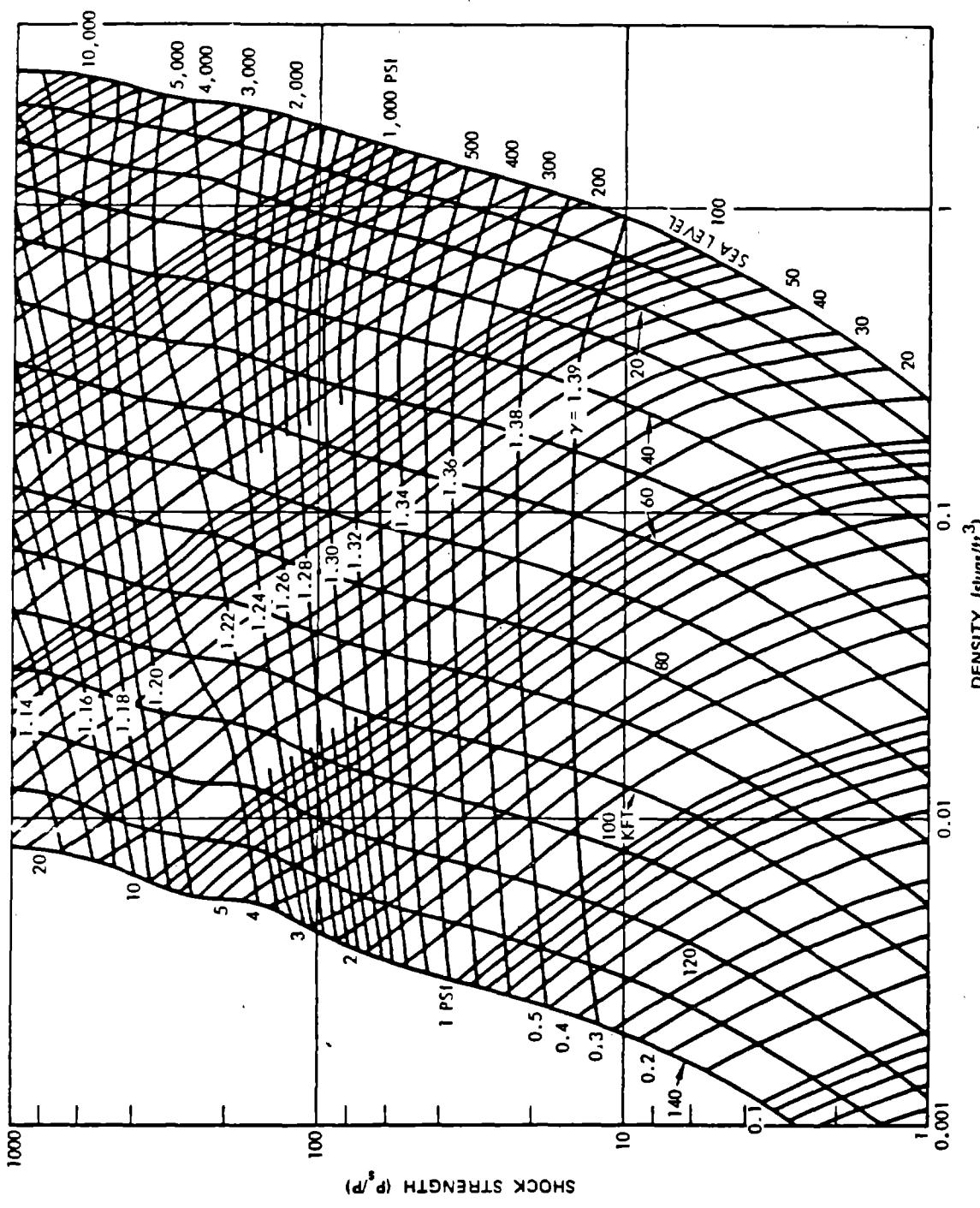


Figure A-2. [REDACTED] Equation of State Data for Air [REDACTED]

of state data from Figure A-2. The appropriate shock wave equations are derived in the same manner as those shown in Table A-1. The principal difference is that two values of  $\gamma$  appear,  $\gamma$  for the air ahead of the shock and  $\gamma_s$  for the air just behind the shock front; the values in general are not equal. The shock wave equations for strong shock waves in air are listed in Table A-3. Two approximate velocity equations, accurate to within about 5 percent for shock strengths greater than 5, are shown on the right. As in Table A-1, the subscript  $s$  refers to parameters behind the shock front, and symbols with no

subscript refer to ambient conditions.

Note that shock strength  $\xi$  is a direct function of the absolute pressure  $P_s$  behind the shock front, rather than of  $\Delta p$ , the overpressure.\* A shock strength of 1 therefore represents a vanishingly weak shock wave; and, at sea level, a shock strength of 2 represents an overpressure of 14.7 psi. Values for  $\gamma_s$  must be obtained from the equation of state data in Figure A-2.

This definition is not universal; shock strength is defined in some reports as  $\Delta p/P$ .

Table A-3. Equations for Strong Shock Waves

Complete Equation:	High-Shock-Strength Approximation:
<u>Velocity of the Shock Front</u>	
$U = c \left( \frac{(\xi - 1)(1 + \mu_s \xi)}{\gamma[\xi(\mu_s - 1) - (\mu - 1)]} \right)^{1/2}$	$U = c \left( \frac{\xi(\gamma_s + 1)}{2\gamma} \right)^{1/2}$
<u>Particle Velocity Behind the Shock Front</u>	
$u = c \left( \frac{(\xi - 1)[\xi(\mu_s - 1) - (\mu - 1)]}{\gamma_0(1 + \mu_s \xi)} \right)^{1/2}$	$u = c \left( \frac{2\xi}{\gamma(\gamma_s + 1)} \right)^{1/2}$
<u>Density Ratio Across the Shock Front</u>	
$\frac{\rho_s}{\rho} = \frac{1 + \mu_s \xi}{\mu + \xi}$	
<u>Dynamic Pressure Behind the Shock Front</u>	
$q_s = \frac{1}{2} P(\xi - 1) \left( \frac{1 + \mu_s \xi}{\mu + \xi} - 1 \right)$	
where	
$\mu_s = \frac{\gamma_s + 1}{\gamma_s - 1}, \quad \mu = \frac{\gamma + 1}{\gamma - 1}, \quad \xi = \frac{P_s}{P} = \left( \frac{\Delta p + P}{P} \right), \quad \gamma = 1.4$	

## SECTION II

### PHYSICAL DESCRIPTION OF SHOCK WAVE BEHAVIOR

Newton's second law, which relates force to the change in momentum that it produces, provides straightforward explanations of many shock wave phenomena. In particular, it explains certain reflection phenomena and the way in which these phenomena determine the forces produced by a blast wave when it strikes a surface or a small object.

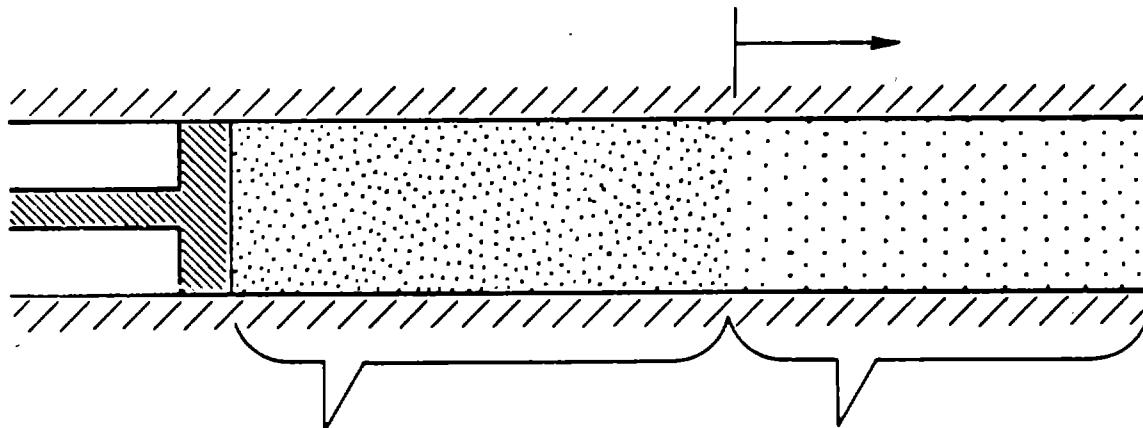
Acoustic theory also provides explanations of blast phenomena. These explanations are important because they appear frequently in discussions of shock wave reflection. The following discussion relates the acoustic theory explanations with those that are based on Newton's second law.

### A-7 Step Function Shock Wave

In most respects, the properties of the shock front are independent of the shape of the pressure waveform that follows the front. Shock wave phenomena, therefore, can be explained in terms of the simplest possible waveform: a region of completely uniform pressure, density, and particle velocity behind a planar shock front. In such a wave, the shock front usually is considered a mathematical discontinuity, in which the pressure, velocity and other parameters are step functions of position and time.

This type of simple shock wave may be generated by the mechanism shown in Figure A-3. A piston moves at constant velocity in a frictionless cylinder (a piston velocity of 431 ft/sec, a number that will be used later for purposes of illustration, produces a shock wave with

VELOCITY OF SHOCK FRONT =  $U$



CONDITIONS BEHIND  
SHOCK FRONT:

PARTICLE (WIND) VELOCITY =  $u$   
DENSITY =  $\rho_s$   
PRESSURE =  $P_s$   
ENERGY PER  
UNIT MASS =  $E_s$

CONDITIONS IN AMBIENT AIR:

PARTICLE VELOCITY = 0  
DENSITY =  $\rho$   
PRESSURE =  $P$   
ENERGY PER  
UNIT MASS =  $E$

Figure A-3. Idealized Shock Wave

[REDACTED]  
[REDACTED]  
an overpressure of 10 psi). The compressed air that constitutes the shock wave is uniform in density, pressure, and velocity.

[REDACTED] The step function shock wave differs from the blast wave from a nuclear burst in that the latter: (1) becomes weaker as it propagates away from the burst; (2) produces a decaying rather than a constant overpressure after the shock front passes a given point; and (3) has a spherical rather than a planar shock front. However, these differences are unimportant in the development of most of the concepts that apply to the shock front. As a result of its long overpressure duration, the blast wave from a high yield nuclear weapon is in many respects comparable to the idealized shock wave of Figure A-3.

#### A-8 Shock-Front Formation [REDACTED]

[REDACTED] The piston shown in Figure A-3 will require an interval of time to reach its final velocity. While it is accelerating, the pressure at the face of the piston will increase steadily. The pressure wave that the piston generates during this time lacks the abrupt pressure rise characteristic of a shock; however, differences in the velocities of different parts of the pressure wave ultimately will cause a shock front to form. Small pressure disturbances travel at the local speed of sound. In the air compressed by the piston, two factors cause this speed to differ from the speed of sound in ambient air; (1) compression of the air raises the air temperature, thereby increasing the speed of sound; (2) in moving air, pressure disturbances move with a velocity that is the vector sum of the air and sound velocities.

[REDACTED] As the piston starts to move, it creates an initial pressure disturbance that propagates ahead of the piston (to the right in Figure A-3) with a velocity equal to the velocity of sound in ambient air. By the time the piston reaches its final velocity, it will have produced a pressure wave that can propagate considerably faster than

the ambient speed of sound. The wave produced by the high pressure just ahead of the piston soon overtakes the lower pressure wave, and a shock front is formed.

[REDACTED] After steady-state conditions are reached, the shock front moves at supersonic velocity with respect to the undisturbed air but at subsonic velocity with respect to the air behind the shock front. Ahead of the shock front, there is no early pressure increase to indicate the impending arrival of the shock wave. If such an early pressure wave were present, the shock front would overtake it. Behind the shock front, whatever pressure irregularities that may form can overtake the front and merge with it. The tendency for all pressure gradients to concentrate at the shock front is so strong that moderately strong shock waves in air generate shock fronts that are only a few atomic mean free paths (mfp) thick (at sea level, 1 mfp is about  $10^{-5}$  cm).

#### A-9 Pressure-Momentum Interaction at a Shock Front [REDACTED]

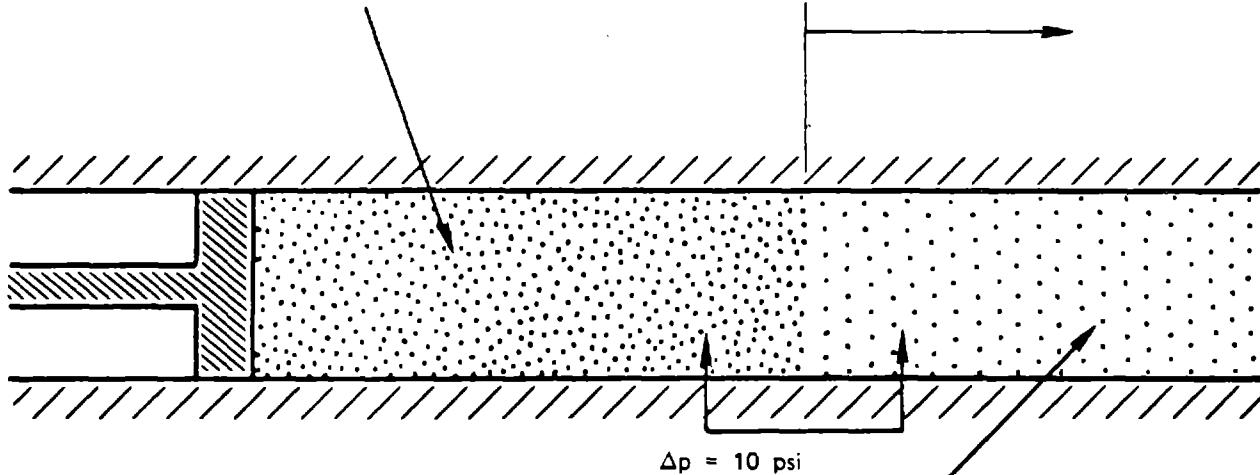
[REDACTED] Before applying Newton's second law to a reflection problem, it will be examined with respect to a step function shock wave shown in Figure A-4. This is a simple problem that requires little more than a sample calculation. It is, however, useful as a preparation for the reflection problem that is discussed below. Numerical values of pressure, density, and velocity, calculated from the equations in Table A-1, appear in the figure.

[REDACTED] To evaluate Newton's second law, it is necessary to determine the momentum change per unit time and the force that produces the change. If a unit area of the shock front is considered, the force is numerically equal to the shock wave overpressure  $\Delta p$ , which in this example is 10 psi. To obtain a consistent set of units, this pressure must be expressed as 1,440 lbs/ft<sup>2</sup>.

CONDITIONS BEHIND  
SHOCK FRONT:

$$\begin{aligned} u &= 431 \text{ ft/sec} \\ c_s &= 1,205 \text{ ft/sec} \\ P_s &= 24.7 \text{ psi} \\ \rho_s &= .00343 \text{ slugs/ft}^3 \end{aligned}$$

VELOCITY OF SHOCK  
FRONT  
 $U = 1,405 \text{ ft/sec}$



AMBIENT CONDITIONS:

$$\begin{aligned} P &= 14.7 \text{ psi} \\ \rho &= .00238 \text{ slugs/ft}^3 \\ c &= 1,116 \text{ ft/sec} \end{aligned}$$

Figure A-4. Parameters of a 10 psi Shock Wave

The mass of air that enters one square foot of shock front area each second is the ambient density, .00238 slugs/ft<sup>3</sup>, times the shock front velocity of 1,405 ft/sec. This air is given a velocity of 431 ft/sec as it enters the shock wave. Thus,

$$\Delta p = \rho U u, \text{ or}$$

$$1,440 = .00238 \times 1,405 \times 431$$

A-10 Normal Reflection at a  
Solid Barrier

Figure A-5 shows a 10-psi shock wave

that has struck the end of the cylinder and has formed a receding shock wave. Behind the receding shock front, the air is stationary. The velocity change at the reflected shock front has the same magnitude (but the opposite direction) as the velocity change of 431 ft/sec at the incident shock front. However, the pressure jump  $\Delta p_1$  across the reflected shock front is greater than  $\Delta p$  because more mass per second is involved (see Figure A-5). The difference results principally from the higher density of the air entering the shock wave, but also results from the greater relative velocity, 1,491 ft/sec, between the shock front and the incoming air.

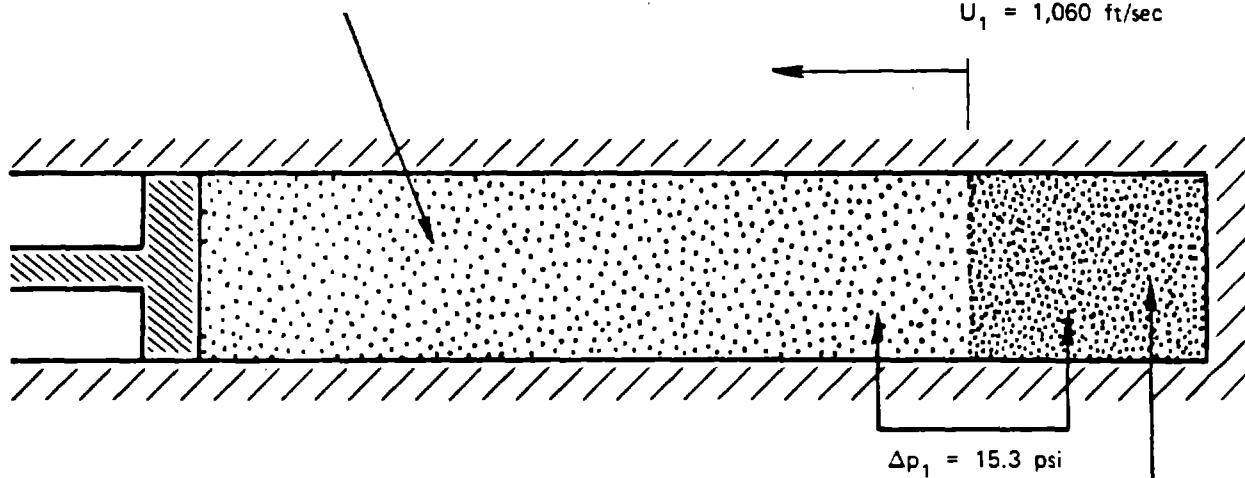
CONDITIONS IN INCIDENT SHOCK WAVE:

$$P_s = 24.7 \text{ psi } (= P + 10)$$

$$u = 431 \text{ ft/sec}$$

$$\rho_s = .00343 \text{ slugs/ft}^3$$

VELOCITY OF  
REFLECTED  
SHOCK FRONT =  
 $U_1 = 1,060 \text{ ft/sec}$



CONDITIONS IN REFLECTED SHOCK WAVE:

$$P_1 = 40.0 \text{ psi } (= P + 25.3)$$

$$u_1 = 0$$

$$\rho_1 = .00482$$

Figure A-5. Reflection of a 10 psi Shock Wave from a Solid Barrier

The equation expressing Newton's second law may be obtained from basic physical principles, or it may be obtained from equations given in Section I by changing the frame of reference to one that is stationary with respect to the air ahead of the reflected shock front.

$$\Delta p = \rho U u,$$

$$15.3 \times 144 = .00343 (1,060 + 431) 431,$$

$$2,220 = .00343 \times 1,491 \times 431$$

The reflected overpressure,  $\Delta p_1$ , is the amount by which the pressure at the reflecting

surface exceeds ambient pressure. It is the sum of the pressure jumps across the incident and the reflected shock fronts, or 25.3 psi.

Acoustic theory often draws on the useful concept of images to explain the shock wave patterns produced at a reflecting surface. The reflecting surface is equivalent to a plane of symmetry. In the foregoing example, the image created by the reflecting surface would be a second piston, moving to the left with a velocity of 431 ft/sec, and located as far to the right of the reflecting surface as the real piston is to the left of it. As the two shock waves of equal strength collide, they produce conditions equivalent to those shown in Figure A-5.

Explanation of the strength of the reflected shock front does not follow as readily from acoustic theory as does the basic shock wave pattern. Acoustic theory began with the study of sound waves, which have such low amplitudes that air acts as a linear medium. In such a medium, pressures are additive, and the wave reflected by a perfect reflector has the same amplitude as the incident wave. Shock wave effects are decidedly nonlinear, as is shown in the preceding example.

Acoustic theory explains that the pressure jump of 15.3 psi instead of 10 psi at the reflected shock front is caused by the effect of dynamic pressure. Mathematically, this is a convenient explanation. For shock strengths less than about 10, the equations

$$\Delta p_1 = \Delta p + 2.4 q$$

and

$$\Delta p_r = 2\Delta p + 2.4 q$$

give correct values for  $\Delta p_1$ , the pressure jump at the reflected shock front and  $\Delta p_r$ , the reflected overpressure. The constant 2.4 is valid for air subjected to low shock strengths. In general, the constant has the value  $\gamma + 1$ .

Physically, however, the explanation is artificial. In the sense that dynamic pressure effects are the effects caused by the momentum of

air in motion,  $\Delta p_1$  is produced entirely by dynamic pressure. The basic acoustic theory fails to predict shock wave phenomena. Predictions are possible only from a modified theory, tailored to fix experimental facts, and experience in using this theory is necessary to use it successfully.

#### A-11 Pressures on Simple Shapes

Two examples will be used to illustrate the phenomena that occur when a blast wave interacts with a target.

The first example is the steady-state pressure pattern around a sphere placed in the path of the shock wave. Figure A-6 shows the nature of this pattern after the shock front has passed, and equilibrium conditions apply.

This problem is more complex than the one discussed in paragraph A-10. The air particles directed exactly toward the center of the sphere reach the stagnation point, a point on the sphere at which the air is brought to rest, and the momentum that these particles give up may be calculated readily. All of the other air particles affected by the sphere behave in a more complicated way. They are slowed down and deflected, but they are not stopped.

An order-of-magnitude equation for force may be obtained by assuming that all of the air directed toward the sphere is stopped. The momentum per unit area per unit time di-

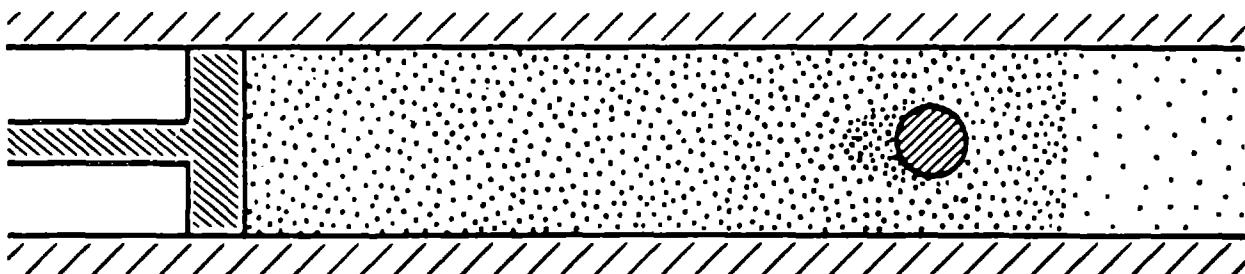


Figure A-6. Reflection of a Shock Wave by a Small Object

rected toward the sphere is  $\rho_s u$  (the mass flow per unit area per unit time). Application of Newton's second law shows that the wind pressure is about

$$F/A = \rho_s u^2.$$

A detailed analysis would show that the pressure produced at the stagnation point of a sphere in a moderately strong wind is more closely approximated by dynamic pressure, which has a value that is just half of that given by the previous equation

$$q = \frac{1}{2} \rho_s u^2.$$

Therefore, the wind pressure at the stagnation point on the sphere is roughly

$$\begin{aligned} q &= \frac{1}{2} \times .00343 \times (431)^2, \\ &= 318.58 \text{ lbs/ft}^2, \\ &= 2.2 \text{ psi.} \end{aligned}$$

Total pressure at the stagnation point is about 12.2 psi, the sum of the static overpressure and the dynamic pressure.

The important point in this example is that the high pressure region around the object is stationary, not moving forward to meet the oncoming air as was the receding shock wave shown in Figure A-5. Consequently, the rate at which air enters the high pressure region is lower. The rate at which momentum is extracted from incoming air is correspondingly lower. By Newton's second law, the pressure developed is smaller.

Acoustically, no reflection is considered to occur in this example. The problem is simply one of an object in an airstream.

The second illustration is the transient interaction between a blast wave and a small cube. This type of interaction is largely a combination of those already discussed. For simplicity, the blast wave is assumed to strike one side of the cube head-on. Shortly after the shock front strikes the cube, the reflection process is much like that produced at the closed end of a piston (Figure A-5). A receding shock wave is formed, the mass flow rate into this shock wave is high, and the front face of the cube is subjected to a high reflected overpressure (25.3 psi for a 10 psi incident shock wave).

At the edges of the front face of the cube, the layer of compressed air in the receding shock wave is unconfined. It flows outward, around the edges of the cube. This outward flow relieves the high pressure behind the receding shock front. As a result of this pressure relief, the receding shock front loses velocity; consequently, the incoming air gives up its momentum at a decreasing rate. A steady-state flow pattern develops, and the pressure at the front surface of the cube drops to roughly the incident overpressure plus the incident dynamic pressure. The situation is now similar to that shown in Figure A-6.

Part of the acoustic explanation is very descriptive. Pressure relief waves form at the edge of the front surface of the cube and propagate inward. Reflections that occur when these relief waves meet increase the rate of flow over the front face and around the edges of the cube. The time required for the steady-state flow pattern to develop is about two or three times that required for a shock wave to travel from the edge of the cube to the center of the front face.

The remainder of the acoustic explanation is evident only to a person familiar with acoustic theory or to a person who has previously encountered this particular explanation. It involves understanding: (1) the reflection coefficient of an object becomes small as the wave-

[REDACTED]  
length of the incident sound wave becomes large compared with the dimensions of the object; and (2) a pressure waveform has an equivalent spectrum of sound waves of different wavelengths (strictly speaking, the equivalent spectrum requires a linear medium and is only an approximation in strongly shocked air).

[REDACTED] These acoustic concepts, applied to the problem of reflection from a small cube, predict that the cube will reflect the shock front strongly, but that the reflection coefficient of the cube will decrease rapidly after the shock front passes. The reflected wave weakens by spherical divergence as it propagates away from the cube, and the pressure on the front face of the cube decreases to its steady-state value.

#### A-12 The Rankine-Hugoniot Equations (Alternate Analysis)

[REDACTED] In the conventional derivation of the Rankine-Hugoniot equations (paragraph A-1), the algebra tends to obscure the physical picture associated with the derivation. The following analysis provides a more intuitive introduction to the subject.

[REDACTED] *The interaction at the shock front is basically an inelastic collision.* The truth of this statement is evident from the definition of an inelastic collision. It is a collision in which the colliding bodies stick together and move with a common velocity after they collide.

[REDACTED] The statement given above provides a method to account for the energy exchanges that occur at the shock front. It may be applied most readily if the collision is considered to occur between a very thin layer of unshocked air and the mass of air behind the shock front. The following statement may then be confirmed readily.

[REDACTED] *The inelastic collision at the shock front is 50 percent efficient in transferring kinetic energy to the incoming air.* A change to the center-of-mass frame of reference is the first step

necessary to demonstrate this fact. Since the mass of air being picked up at any instant is infinitesimal, this frame of reference moves with the air behind the shock front. The initial kinetic energy per unit area of the shock front is, in this frame of reference, that of the thin layer of unshocked air approaching the shock front with a relative velocity of  $u$ . If its mass is  $dm$ , its initial kinetic energy is\*

$$d(KE) = \frac{1}{2} u^2 dm.$$

After a completely inelastic collision, the kinetic energy in the center-of-mass frame of reference is zero.† In other words, the amount of energy that is converted from kinetic energy to internal energy in the collision is equal to  $d(KE)$ .

[REDACTED] In the original frame of reference (stationary with respect to the unshocked air),  $d(KE)$  is equal to the kinetic energy of the thin layer of air after it has become a part of the shock wave. Thus, the kinetic energy imparted to the air and the kinetic energy converted to internal energy by the inelastic collision are equal, i.e., this method of transferring kinetic energy is 50 percent efficient.‡

[REDACTED] Accounting for all of the work done at the shock front is complicated by an energy ex-

[REDACTED] rigorous derivation of the equations governing the inelastic collision of two bodies requires the simultaneous solution of the energy and momentum equations of the system. If a large mass and a very small mass are approaching one another with equal and opposite momenta, the kinetic energy of the larger mass is negligible compared to the kinetic energy of the smaller mass.

[REDACTED] By definition, total momentum in the center-of-mass frame of reference is zero. Since momentum is conserved in the collision of two bodies, the total momentum remains zero after any collision. After a completely inelastic collision, neither of the colliding bodies is moving with respect to the center of mass; therefore, their final kinetic energy in this frame of reference is zero.

[REDACTED] Although kinetic energy changes with changes in the frame of reference, the energy loss in an inelastic collision does not.

change that is independent of the exchange produced by the inelastic collision. The total work done on a unit mass of incoming air results from the pressure  $P_s$  that is behind the shock front moving through the distance required to compress this mass of air from its initial volume  $V$  to its final volume  $V_s$ .

$$W_{\text{total}} = P_s(V - V_s).$$

One portion of this work is done by the ambient pressure  $P$  in displacing the volume  $V - V_s$ . Since the ambient pressure does not produce a force that has directional characteristics, it has no function in setting the air in motion. This portion of the work only contributes to compression.

$$W_{\text{comp}} = P(V - V_s)$$

The remainder of the work is done by the overpressure  $\Delta p = P_s - P$ , displacing the volume  $V_s$ . At the shock front, the effect of overpressure is completely directional, and overpressure creates the force that accelerates the air that is overtaken by the shock front. This is the portion of the work that is required to produce kinetic energy by a collision process,

$$W_{\text{coll}} = (P_s - P)(V - V_s).$$

As already demonstrated, half of this work appears as kinetic energy and half as internal energy of the unit mass of air added to the shock front. Note that the work converted to internal energy by the collision process is closely related to  $W_{\text{comp}}$  in that both contribute to compressing the gas to the volume  $V_s$  and, in this way, both increase the internal energy of the air.

The energy exchange equations for a unit mass of air entering the shock front follow directly from the discussion in the preceding

paragraph. The kinetic energy added to the unit mass of air is

$$\frac{1}{2} u^2 = \frac{1}{2} W_{\text{coll}} \\ = \frac{1}{2} (P_s - P)(V - V_s),$$

and the particle (wind) velocity is

$$u = ((P_s - P)(V - V_s))^{1/2}.$$

The change in internal energy of the unit mass of air is

$$E_s - E = W_{\text{comp}} + \frac{1}{2} W_{\text{coll}} \\ = P(V - V_s) + \frac{1}{2} (P_s - P)(V - V_s) \\ = \frac{1}{2} (P_s + P)(V - V_s).$$

To obtain the equation for shock front velocity, note that while the air in the shock wave moves into a volume  $V - V_s$ , the shock front has advanced through a volume  $V$ . The ratio of shock front velocity to particle velocity is therefore

$$\frac{U}{u} = \frac{V}{V - V_s}$$

$$U = \left( \frac{V}{V - V_s} \right) ((P_s - P)(V - V_s))^{1/2}$$

$$U = V \left( \frac{P_s - P}{V - V_s} \right)^{1/2}.$$

The equations for  $u$ ,  $(E_s - E)$ , and  $U$  are the Rankine-Hugoniot equations given previously in paragraph A-1.

[REDACTED] Note: Although the interaction at the shock front is completely inelastic, the overall reaction of a blast wave in free air is partially elastic. In such a blast wave, the pressure behind the shock front is not constant, but decays with time. The air behind the front expands and returns energy that helps to propagate the shock wave (see footnote to paragraph 2-33, Chapter 2). This fact does not alter the validity of the argument presented above. It simply points out that the inelastic collision at the shock front only describes part of the mechanism of blast wave propagation.

#### A-13 Dynamic Pressure [REDACTED]

[REDACTED] Dynamic pressure is frequently equated to the wind force produced on a target by the high velocity winds in a blast wave, but the relation between force and dynamic pressure is not this simple.

[REDACTED] One source of confusion is the name which implies a meaning that differs from the correct one. In a compressible fluid, the true meaning of dynamic pressure is limited to the mathematical definition

$$q = \frac{1}{2} \rho_s u^2$$

where  $\rho_s$  is mass per unit volume and  $u$  is particle velocity behind the shock front. Strictly speaking,  $q$  is not a pressure. A body moving along with moving air will not feel a force that is attributable to dynamic pressure. Dynamic pressure is kinetic energy per unit volume. Reasons for calling it a pressure are: (1) it has the dimensions of pressure; and (2) this energy can be used to develop a pressure.

[REDACTED] A stationary body exposed to a wind will experience pressures that differ at different points on its surface. The highest pressure on the body is the stagnation pressure, which occurs wherever the air is completely stopped by im-

pact with the body. For example, if the body is a sphere, the stagnation pressure occurs at the point on the surface that faces directly into the wind. For an incompressible fluid, stagnation pressure is simply the sum of the free-stream static pressure and the free-stream dynamic pressure. However, for a compressible fluid, such as air, stagnation pressure is the sum of the free-stream static pressure and a quantity called the free-stream *impact pressure*. At low velocities, impact pressure and dynamic pressure are essentially equal, but at velocities that are appreciable compared with sound speed, impact pressure rises above dynamic pressure. When wind speed is equal to sound speed, impact pressure exceeds dynamic pressure by about 28 percent.

[REDACTED] The forces exerted by strong winds correspond more directly to impact pressures than to dynamic pressure. This suggests that weapons effects calculations should be based on impact pressures rather than on dynamic pressures; but, both in this field and in aerodynamics, dynamic pressures are employed more commonly. The choice is based on conventional practice. In aerodynamic problems, dynamic pressure is used because it may be calculated readily. Wind force on an object is calculated from the equation

$$F_w = C_D q A$$

where  $C_D$  is drag coefficient and  $A$  is an area related to the size of the object. The drag coefficient is not constant. It is a function of velocity, and its variation absorbs not only the discrepancy between dynamic pressure and impact pressure, but also accounts for the net effect of the complex pressure pattern that forms around an object in an airstream. The product  $qA$ , although it has the dimensions of a force, has no direct physical relation to any force exerted by the wind.

[REDACTED] In weapons effects calculations, dynamic pressure often is as convenient as it is in aerody-

[REDACTED]

[REDACTED]

namics: damage criteria for such objects as buildings are established in terms of conventional shock wave parameters, such as overpressure, dynamic pressure, or impulse. Consequently, the stagnation pressure or other actual pressures found at various points on specific structures usually are not calculated unless specific blast loading information is desired. In some cases, the choice of dynamic pressure may not be appropriate for damage criteria. For example,

when the air in the blast wave is dust laden (as it is for certain combinations of yield, burst height, ground range, and surface properties), a measurement with a conventional dynamic pressure gauge often is ambiguous. The dust is not necessarily in velocity equilibrium with the air, and the amount of dust is not known. As a result, it is often difficult to calculate the dynamic pressure of air alone from such experimental measurements.

## APPENDIX B

### USEFUL RELATIONSHIPS

#### B-1 General Equivalents

One kiloton (kt) is defined to be  $10^{12}$  calories of energy release.\* This amount of energy will be released by the complete fission of 0.057 kg (57 grams or 2 ounces) of fissionable material.† Equivalents to this amount of energy in other units are:

- $2.61 \times 10^{25}$  million electron volts (MeV),
- $4.18 \times 10^{19}$  ergs,
- $1.16 \times 10^6$  kilowatt-hours,
- $3.97 \times 10^9$  British thermal units.

Some equivalents of the complete conversion of mass to energy are:

$$\begin{aligned}1 \text{ gram mass} &= 5.61 \times 10^{-6} \text{ MeV} \\&= 8.99 \times 10^{20} \text{ ergs} \\&= 2.15 \times 10^{13} \text{ calories}\end{aligned}$$

The temperature associated with one electron volt is 11,605.9 degrees Kelvin.

#### B-2 Constants

Velocity of light:  $3 \times 10^8$  m/sec =  $3 \times 10^{10}$  cm/sec.

Avagadro's number:  $6.023 \times 10^{23}$  molecules per mole (gram molecular weight).

Planck's constant:  $6.625 \times 10^{-34}$  erg-sec.

Boltzmann constant:  $1.38 \times 10^{-16}$  erg/K.

† Mass of electron:  $9.1085 \times 10^{-31}$  gm.

† Mass of proton:  $1.672 \times 10^{-24}$  gm.

† Mass of neutron:  $1.675 \times 10^{-24}$  gm.

† Mass of alpha particle:  $6.64 \times 10^{-24}$  gm.

Loschmidt number:  $2.687 \times 10^{24}$  molecules of ideal gas per cubic centimeter at  $0^\circ\text{C}$ .

Electron charge:

$$\begin{aligned}4.803 \times 10^{-10} \text{ esu} &= 1.602 \times 10^{-20} \text{ emu} \\&= 1.602 \times 10^{-19} \text{ coulombs.}\end{aligned}$$

#### B-3 Standard Sea Level Atmosphere

Pressure = 14.696 psi

$$\begin{aligned}&= 2,116.22 \text{ lb}/\text{ft}^2 \\&= 1,013.25 \text{ millibars} \\&= 101,325. \text{ newtons}/\text{m}^2 \\&= 1,013,250. \text{ dynes}/\text{cm}^2\end{aligned}$$

Temperature =  $59^\circ\text{F}$

$$\begin{aligned}&= 15^\circ\text{C} \\&= 288.15^\circ\text{K} \\&= 518.4^\circ\text{R}\end{aligned}$$

Density =  $2.38 \times 10^{-3}$  slug/ $\text{ft}^3$

$$\begin{aligned}&= 7.65 \times 10^{-2} \text{ lb}/\text{ft}^3 \\&= 1.225 \times 10^{-3} \text{ gm}/\text{cm}^3 \\&= 1.225 \text{ kg}/\text{m}^3\end{aligned}$$

Speed of sound = 1,116.45 ft/sec

$$\begin{aligned}&= 340.29 \text{ m/sec} \\&= 34,029 \text{ cm/sec}\end{aligned}$$

\* See footnote on page 1-3 for the origin of the definition.

† This is the energy released by the fission of 57 grams of fissionable material. It is *not* the energy that would be released by the conversion of 57 grams mass to energy.

‡ Classical rest mass.

## **APPENDIX D**

### **ABSTRACTS OF DNA HANDBOOKS**

#### **[REDACTED] NUCLEAR WEAPONS BLAST PHENOMENA [REDACTED]**

**[REDACTED] DASA 1200 (Vols. I-IV) (Vol. I, SRD; Vol. II, CRD; Vol. III, SFRD; Vol. IV, to be published; Vol. V, CFRD).**

**[REDACTED] Prepared by: DASIAC, Santa Barbara, California. Major contributors: Defense Atomic Support Agency, Kaman Nuclear, URS Research Company, Bolt, Beranek, and Newman, and Dijkewood Corporation.**

**[REDACTED] Availability: Volumes I through III through Defense Documentation Center on request through Defense Nuclear Agency, Washington, D.C. 20305. Volume V, limited distribution.**

**[REDACTED] DASA 1200 is a source book of air blast data and theory applicable to nuclear explosions occurring in free air, on or near the surface, and beneath the surface. Volume I begins with a detailed description of the nuclear explosion energy source, and presents the theoretical background associated with the formation and propagation of the blast wave in free air. The long range propagation of shock waves is treated in detail. Volume II presents a discussion of blast wave interaction phenomena, including ideal reflection and refraction, ideal diffraction, and nonideal effects. A discussion of topography and shock wave shielding and a section on air blast measurements in the high pressure region also are included. Volume III contains an analysis of and methods for the prediction of the blast phenomena from nuclear weapons burst at moderate altitudes, on the surface, underwater, and underground. Volume IV contains a discussion of the simulation of nuclear air blast phenomena**

**with high explosives. Volume V is a compilation of the measurements of the various blast parameters associated with nuclear weapons at the various nuclear operations. It is planned for limited distribution to scientists and agencies who are working in the field of nuclear weapons blast phenomena.**

#### **[REDACTED] HANDBOOK OF UNDERWATER NUCLEAR EXPLOSIONS [REDACTED]**

**[REDACTED] DASA 1240 [REDACTED]**

**[REDACTED] Prepared by: DASIAC, Santa Barbara, California. Major contributors include NOL, DTMB, Waterways Experiment Station, Naval Civil Engineering Laboratory and the U.S. Naval Radiological Defense Laboratory.**

**[REDACTED] Availability: Qualified requestors may obtain these documents from the Defense Documentation Center. Each transmittal outside the agencies of the U.S. Government must have prior approval of the Defense Nuclear Agency.**

**[REDACTED] The Handbook of Underwater Nuclear Explosions is divided into two parts: Part I, Phenomena, consists of 11 chapters, and Part II, Effects, consists of 13 chapters. Individual chapters and in some cases sections of chapters have been previously published separately.**

**[REDACTED] The entire handbook is undergoing revision and will be published in three volumes. The revised Handbook of Underwater Nuclear Explosions will be an authoritative presentation of current knowledge and a reliable source of useful data concerning the phenomena of underwater nuclear explosions. The presentation will include the phenomena of shock wave propaga-**

tion, surface waves, underwater cratering, and radioactive debris. The effects of underwater explosions on surface ships, submarines, harbors, and structural installations also will be described.

[REDACTED] NUCLEAR GEOPLOSICS (A Sourcebook of Underground Phenomena and Effects of Nuclear Explosions)

DASA 1285 (Volumes I-V)

[REDACTED] Prepared by: Stanford Research Institute, Menlo Park, California.

[REDACTED] Availability: This document is not approved for open publication or distribution to the Office of Technical Services, Department of Commerce. Qualified requestors may obtain copies of this report from Defense Documentation Center. Foreign announcement and dissemination of this report is not authorized.

[REDACTED] The Nuclear Geoplosics Handbook contains five volumes: Part I, Theory of Directly Induced Ground Motions; Part II, Mechanical Properties of Earth Materials; Part III, Test Sites and Instrumentation; Part IV, Empirical Analysis of Ground Motion and Cratering; and Part V, Effects on Underground Structures and Equipment.

[REDACTED] The theory of directly induced ground motion is presented in Part I. The tools and elements required for the study of ground motion effects are discussed. Two analytical solutions of shock propagations are presented. Theoretical predictions (obtained by numerical and analytical methods) are compared with field measurements. The mechanical properties of earth materials are described in Part II. It consists of a preparation of a clear and systematic, but largely qualitative, description of the resistance of earth materials to compression and shear. A summary on stress-strain behavior with very short load durations is included. The basic concepts regarding the mechanical behavior of

soil and experimental methods of determining the mechanical properties of soil are described. The physical characteristics of test sites and instrumentation of nuclear and high explosive detonations on which ground motion has been measured are presented in Part III. The discussion of air blast induced ground motion in Part IV relies primarily on experimental evidence. A knowledge of the effects induced in the free field ground motion, the factors influencing these effects, the structure-medium interaction, and the factors influencing interaction is implicit in the study of behavior of underground structures. Part V summarizes these various phenomena as they apply to understanding structures in general and discusses the behavior of equipment mounted within a structure.

[REDACTED] The book is meant to be an authoritative sourcebook. It is not meant to be a handbook of design specifications.

[REDACTED] Part II and Part IV are currently under revision. Publication is expected during calendar year 1973.

[REDACTED] TREE (Transient-Radiation Effects on Electronics) HANDBOOK

[REDACTED] DNA 1420 H-1 (edition 3), DNA 1420 H-2 (edition 3), (1420 H-1, 1420 H-2)

[REDACTED] Prepared by: Battelle Memorial Institute, Columbus, Ohio

[REDACTED] Availability: Qualified requestors may obtain this document from the Defense Documentation Center. Foreign announcement and dissemination is not authorized.

[REDACTED] The TREE Handbook consists of two volumes which present information that will be useful to a design engineer who is designing electronic systems for survival in a nuclear-burst environment. The information that is presented covers those areas directly related to electronic parts, circuits, and systems. The

nuclear-burst environment that is covered includes both transient and steady state. It also includes all radiation effects except external EMP. Major areas covered in DNA 1420 H-1 are: the simulated versus burst environment, interaction of transient radiation with matter, discrete semiconductor devices, integrated circuits, capacitors, resistors, miscellaneous electronic materials and devices, circuit hardening, and network analysis techniques. DNA 1420 H-2 discusses the nuclear weapon-burst environment, interaction of transient radiation with matter, system hardening, and internal EMP.

The TREE Handbook is updated on a continuing basis.

#### **THEORETICAL MODELS FOR NUCLEAR FIREBALLS**

DASA 1589-A, 1589-B, 1589-1 through 1589-39 (1589-A, 1589-B, 1589-1 through 1589-39)

*Prepared by:* Lockheed Missiles and Space Company, Sunnyvale, California.

The first volume, with parts A and B, describes a radiation hydrodynamic code appropriate for calculation of nuclear fireball phenomenology in the lower atmosphere. Part A describes the code, and part B discusses the results. The FIREBALL code is a one dimensional, spherical, Lagrangian, radiation-hydrodynamics code, which employs a non-grey transport equation to describe the radiation field. The code is used to compute 39 theoretical models for bombs of various explosion yields at various altitudes. These graphical descriptions are the 39 volumes (DASA 1589-1 through 1589-39). Results are compared to experimental measurements made in U.S. field tests.

#### **WEAPONS RADIATION SHIELDING HANDBOOK**

DASA 1892-1 through 1892-6 (DASA 1892-1, -2, -3, and -5, DASA 1892-4)

DASA 1892-6

*Prepared by:* Oak Ridge National Laboratory, Oak Ridge, Tennessee. Major contributors: Radiation Research Associates and the University of Tennessee.

*Availability:* Qualified requestors may obtain these documents from the Defense Documentation Center. Requests for DASA 1892-4 must be on request through Headquarters, Defense Nuclear Agency, Washington, D.C. 20305.

DASA 1892-5 (Chapter 2 of the handbook) describes the basic concepts underlying the methods used for weapon radiation shield analyses. These concepts include the quantities used to describe particle populations and the quantities used to describe radiation interactions with materials. The characteristics of the particular radiations produced by weapons, neutrons and gamma rays, are discussed in detail, including their physical properties and their important interactions. The processes by which neutrons and gamma rays are produced also are described. The chapter also discusses the various response functions that are used to convert a radiation field to a biological effect.

DASA 1892-3 (Chapter 3 of the handbook) surveys the methods used most frequently to calculate the attenuation of neutrons and gamma rays. Summaries of computer codes based on the various methods also are provided. All of the techniques are either approximate solutions to the Boltzmann equation or are based on kernels obtained from solutions to the equation.

DASA 1892-2 (Chapter 4 of the handbook) surveys the work performed to date on

[REDACTED]  
the various types of nuclear radiation albedos, particularly as they relate to penetration of air filled openings through radiation shields (ducts, passageways, etc.). This topic is important in that the primary increase in the radiation that penetrates a shield results from such openings and enters primarily as a result of the successive scattering of the radiation from the walls of the openings. Most of the techniques for estimating the transmission through such openings depend on the use of albedos.

[REDACTED] DASA 1892-1 (Chapter 5 of the handbook) describes effective methods for designing air filled holes in protective structures (access ways, ventilation ducts, other utility pipes, distributed voids resulting from the use of non-homogeneous material in the structure, etc.) to reduce the amount of radiation that enters the structure.

[REDACTED] DASA 1892-4 (Chapter 6 of the handbook) describes the various sources of radiation produced by a nuclear explosion and presents techniques for calculating the transport of the radiations from the point of burst to the surface of a shield, i.e., it presents methods for determining source terms for shield attenuation calculations. The emphasis is on initial radiation, i.e., that produced within the first minute following the explosion.

[REDACTED] DASA 1892-6 (Chapter 7 of the handbook) presents a simplified method for designing (or evaluating) shield covers on single compartment underground structures that will protect against the neutrons and initial gamma rays. Emphasis is given to neutrons. The method is limited to surface or near surface bursts, to weapon yields between 1 kiloton and 20 megatons, and to distances from the burst at which overpressures are between 5 and 100 psi, but no closer than 500 meters.

## THERMAL RADIATION PHENOMENA

[REDACTED] DASA 1917 (Volumes 1-6) (Vols. I-V,

[REDACTED] Vol. VI, [REDACTED]

[REDACTED] Prepared by: Lockheed Missiles and Space Company, Palo Alto Research Laboratory, Palo Alto, California. Major contributor: The Rand Corporation.

[REDACTED] Availability: Qualified requestors may obtain these documents from the Defense Documentation Center. Volumes I through V are approved for open publication. Volume VI is available only by request through Headquarters, Defense Nuclear Agency, Washington, D.C. 20305.

[REDACTED] Volume I of the six volume handbook describes the equilibrium thermodynamic properties of high temperature air. The report contains information on air and a mixture of ideal gases in chemical equilibrium: ideal gas properties for monatomic gases, diatomic gases, and polyatomic gases. The effects of interparticle forces on the thermodynamic properties of air, effects of coulomb forces on the thermodynamic properties of air, and equilibrium calculations and results for air are discussed. Tables and graphs of the composition and properties of the atmosphere are included.

[REDACTED] Volume II presents the theoretical aspects of the equilibrium radiative properties of air. The theory of radiation in hot gases (elementary radiative transfer, theory of radiation, theory of molecular absorption) is described. Spectral and mean absorption coefficients of heated air and spectroscopic properties of six important band systems that contribute to opacity of heated air are included.

[REDACTED] Tables of the equilibrium radiative properties of air and its constituents are presented in Volume III for a wide range of temperatures and densities. The information contained in the tables is a combination of experimental data and theoretical computation.

[REDACTED] Volume IV describes the excitation and nonequilibrium phenomena of air that has been subjected to a large amount of radiation. Topics include: absorption and scattering of X-rays and gamma rays; collisions of ions and electrons with air molecules; secondary processes following this excitation (including the creation of various chemical species); X-ray heating and shock heating of air, with special reference to very high energy densities; the approach to composition equilibrium in low and high temperature air; adiabatic, near equilibrium cooling of air and the formulation of a criterion for local thermodynamic equilibrium; nonequilibrium radiative transport and its effect on the total amount and the spectrum of emitted radiation; radiation in tenuous air at high temperatures; and radiation in tenuous air with contaminants at low temperatures.

[REDACTED] Volume V provides an introduction to radiation hydrodynamics (RH). It contains a discussion of the application of RH to fireballs in the atmosphere. After formulating the basic equations of RH, special attention is given to the radiative transfer problem. Several methods for solving the equations of transfer are touched upon, but special emphasis is placed on the two stream method with a frequency averaging procedure, which is specifically designed for use with finite zone sizes. A version of the fireball code, which uses this approach, is described.

[REDACTED] Volume VI provides data concerning the interaction of nuclear weapon radiation and debris with the atmosphere. The theoretical analysis of fireball development uses computations based on the equations of radiation hydrodynamics (RH). Various models for simplifying these equations are described, and a summary of codes and calculations based on these models is included. The emphasis of the theoretical discussion is on the status of understanding rather than a detailed quantitative treatment. Yield and altitude scaling laws are developed.

## DASA REACTION RATE HANDBOOK

[REDACTED] DASA 1948H [REDACTED]

[REDACTED] Prepared by: General Electric Company, Missile and Space Division, Philadelphia, Pennsylvania. Major contributors: General Electric, TEMPO, University of Pittsburgh, Air Force Cambridge Laboratory, Geophysics Corporation of America, The Rand Corporation, G. C. Dewey Corporation, University of Colorado, General Atomic, Westinghouse Research Laboratories, NASA Ames Research Center, and Air Force Weapons Laboratory.

[REDACTED] Availability: Qualified requestors may obtain this handbook from the Defense Documentation Center.

[REDACTED] This handbook contains useful, accurate, and reliable information on upper atmospheric chemical and physical processes. Such information is required for the solution of various problems involving military radar and communication blackout. Periodic additions to, and revisions of, this handbook are planned to accommodate new information, revisions of older data, corrections, etc. The material is presented in 19 separate chapters covering pertinent aspects of reaction rate science. Appropriate appendices and illustrations are included.

[REDACTED] This handbook was issued in March 1973 and is still in process of being completed according to original plans. Several revisions have been made to update the original contents.

## [REDACTED] NUCLEAR EFFECTS ON VLF AND LF COMMUNICATION SYSTEMS [REDACTED]

[REDACTED] DASA 1954 (Volumes I and II) (Vol. I,

[REDACTED] Vol. II, [REDACTED]

[REDACTED] Prepared by: Institute for Telecommunications Sciences, Boulder, Colorado. Major contributors: General Electric/TEMPO, Illinois Institute of Technology Research Institute.

[REDACTED] Availability: Qualified requestors may obtain these documents from the Defense Documentation Center through Headquarters, Defense Nuclear Agency, Washington, D.C. 20305.

[REDACTED] This handbook is published in two volumes that describe the effects of nuclear bursts on the propagation of LF and VLF communication systems.

[REDACTED] The examples presented in Volume I illustrate the approximate duration and extent over which typical systems may experience difficulty. In addition to specific results, a brief tutorial description of the effects of nuclear bursts on radio wave propagation and VLF and LF propagation in natural environments is given.

[REDACTED] Volume II presents techniques for modeling a relatively wide range of nuclear situations and for predicting how these situations would degrade LF and VLF communications system performance. This volume is intended to be used with Volume I. Together, they provide a basic understanding of nuclear phenomenology and its interrelation with LF and VLF propagation.

## [REDACTED] NUCLEAR EFFECTS ON HF COMMUNICATION SYSTEMS [REDACTED]

DASA 1955 (Volumes I and II)

[REDACTED] Prepared by: Stanford Research Institute, Menlo Park, California. Major contributors: General Electric/TEMPO, Illinois Institute of Technology Research Institute.

[REDACTED] Availability: Qualified requestors may obtain these documents from the Defense Documentation Center through Headquarters, Defense Nuclear Agency, Washington, D.C. 20305.

[REDACTED] This handbook is published in two volumes that describe propagation effects of nuclear bursts on HF communication systems.

[REDACTED] The examples presented in Volume I illustrate the approximate duration and extent over which typical systems may experience difficulty. In addition to specific results, a brief tutorial description of the effects of nuclear bursts on radio wave propagation and HF propagation in natural environments is given.

[REDACTED] Volume II presents techniques for modeling a relatively wide range of nuclear situations and for predicting how these situations would degrade HF communication system performance. This volume is intended to be used with Volume I. Together they provide a basic understanding of nuclear phenomenology and its interrelation with HF propagation.

## [REDACTED] NUCLEAR EFFECTS ON SATELLITE AND SCATTER COMMUNICATION SYSTEMS [REDACTED]

DASA 1956-1, 1956-2 Vol. I, 1956-2  
Vol. II

[REDACTED] Prepared by: Electromagnetic Systems Laboratories, Sunnyvale, California. Major contributors: General Electric/TEMPO, Illinois Institute of Technology Research Institute.

[REDACTED] Availability: Qualified requestors may obtain these documents from the Defense Documentation Center through Headquarters, Defense Nuclear Agency, Washington, D.C. 20305.

[REDACTED] This handbook contains two parts. Part I describes the propagation effects of selected nuclear bursts on satellite and scatter communication systems. The examples presented illustrate the approximate duration and extent over which typical systems may experience difficulty. In addition to specific results, a brief tutorial description of the effects of nuclear bursts on radio wave propagation and satellite and scatter propagation in natural environments is given.

[REDACTED] Part 2, consisting of two volumes, describes the effects of nuclear bursts on the propagation of satellite communication systems

(Vol. I) and troposcatter and ionoscatter communication systems (Vol. II). Techniques to model a relatively wide range of nuclear situations and to predict how these situations would degrade the communication systems performance are presented. These volumes are intended to be used with DASA 1956-1. Together, they provide a basic understanding of nuclear phenomenology and its interrelation with propagation to satellites.

#### **TREE PREFERRED PROCEDURES (Selected Electronic Parts)**

DNA 2028H  
Prepared by: Battelle Columbus Laboratories, Columbus, Ohio.

**Availability:** Qualified requestors may obtain this document from the Defense Documentation Center.

This document provides persons conducting TREE (transient radiation effects on electronics) experiments with recommended procedures which experience has shown to be efficient for determining transient radiation effects on electronic parts. Areas that are covered in detail include: experimental design, experimental documentation, dosimetry and environmental correlation, and preferred measurement procedures for diodes, transistors, capacitors, and microcircuits.

#### **HANDBOOK FOR ANALYSIS OF NUCLEAR WEAPON EFFECTS ON AIRCRAFT**

DNA 2048 (Revised March 1976) (DNA 2048 H-1) DNA 2048 H-2.

Prepared by: Kaman Avidyne, Burlington, Massachusetts

**Availability:** Qualified requestors may obtain this handbook from the Defense Documentation Center.

This handbook and its supplement are designed for use in analyzing conventional nu-

clear weapon effects on aircraft. DNA 2048 contains a comprehensive review of a large body of available literature pertinent to vulnerability and safety analysis of aircraft subjected to the effects of nuclear explosions. The handbook describes methods for analyzing material velocity, overpressure, thermal radiation and nuclear radiation effects on airplanes and helicopters, including the crew. Sure-safe and sure-kill criteria pertinent to the various weapon effects are presented, as well as the methods to be employed in constructing aircraft sure-safe and sure-kill burst-time volumes. The supplement to DNA 2048 is a handbook of computer programs designed to analyze nuclear weapon effects on aircraft. Detailed methodology for analyzing material velocity (gust), overpressure, thermal radiation and nuclear radiation effects on airplanes and helicopters, including crew, are presented. Only the computer programs corresponding to the methods of analyzing of DNA 2048 are included, and a full understanding of the programs will require access to DNA 2048.

#### **A MANAGEMENT GUIDE TO TREE**

DNA 2051H

Prepared by: Batelle Columbus Laboratories, Columbus, Ohio.

**Availability:** Qualified requestors may obtain this document from the Defense Documentation Center through Headquarters, Defense Nuclear Agency, Washington, D.C. 20305.

This guide is intended primarily for management personnel associated with the development of electronic systems that must survive the transient radiation environment generated by a nuclear explosion. The document is intended to be useful to the manager, whether his background and responsibilities are wholly technical, technically oriented, or wholly administrative. The guide is also a satisfactory primer for engineering and scientific personnel.

[REDACTED] SUMMARY OF COMMUNICATION  
SYSTEMS DEGRADATION IN A NUCLEAR  
ENVIRONMENT [REDACTED]

[REDACTED] DASA 2090 [REDACTED]

[REDACTED] Prepared by: General Electric/TEMPO,  
Santa Barbara, California. Major contributor:  
Illinois Institute of Technology Research Institute.

[REDACTED] Availability: Qualified requestors may  
obtain this document from the Defense Docu-  
mentation Center through Headquarters,  
Defense Nuclear Agency, Washington, D.C.  
20305

[REDACTED] This report summarizes the degradation  
of communication systems in a nuclear environ-  
ment. It is based on the results of a three year  
program to determine the effects of nuclear  
detonations on communication systems. The  
report provides information that will aid in  
determining whether sophisticated analyses are  
required to predict degradation.

[REDACTED] DNA EMP (ELECTROMAGNETIC  
PULSE) HANDBOOK [REDACTED]

[REDACTED] DNA 2114H-1 (Volume 1), DNA  
2114H-2 (Volume 2), DNA 2114H-3 (Volume  
3), DNA 2114H-4 (Volume 4). (Volumes 1, 2,  
and 4 [REDACTED]. Volume 3, [REDACTED]

[REDACTED] Volume 3 will be issued  
early in calendar year 1973.

[REDACTED] Prepared by: DASIAC, Santa Barbara,  
California. Major contributors: Illinois Institute  
of Technology Research Institute, Mission  
Research Corporation, American Nucleonics  
Corporation, Lawrence Livermore Laboratory,  
U.S. Army Harry Diamond Laboratories, Brad-  
dock, Dunn and McDonald, Incorporated,  
Hughes Aircraft Corporation, Procedyne Corpo-  
ration, Stanford Research Institute, Sandia Cor-  
poration, Air Force Weapons Laboratory, Massa-  
chusetts Institute of Technology, Defense  
Nuclear Agency, General Electric/TEMPO.

[REDACTED] Availability: Qualified requestors may  
obtain this document from the Defense Docu-  
mentation Center. Volume 3 must be obtained  
on request through Headquarters, Defense Nu-  
clear Agency, Washington, D.C. 20305.

[REDACTED] Volume 1 is designed for the practical  
electrical engineer. It contains information con-  
cerning an overall system evaluation and the  
practices that should be followed in circuit lay-  
out, shielding, grounding, and the use of protec-  
tive devices for systems that are hardened to  
EMP. Volume 2 is designed for the theoretical or  
experimental analyst. It includes an analytic  
treatment of EMP problems in shielding, anten-  
nas, cables, and filters, experimental and ana-  
lytic information on component degradation,  
and survey information on test methods and  
hardware. Volume 3 develops EMP threat cri-  
teria and provides an assessment of real system  
effects. The EMP environment information is  
presented from a system standpoint. Volume IV  
contains bibliographic and computer code infor-  
mation. Over 1,000 citations are given for such  
topics as theoretical calculations and nuclear test  
data related to the EMP environment and detec-  
tion, EMP vulnerability analysis for systems and  
components, EMP protection, internal EMP, test  
direction and planning, and EMP simulators,  
sensors, and instrumentation. Current EMP com-  
puter codes are described and compared for the  
topics of environment, internal EMP, and circuit  
analysis.

[REDACTED] CORRECTIONS FOR DASA COMMUNI-  
CATION HANDBOOK (DASA 1954, 1955,  
1956) [REDACTED]

[REDACTED] DASA 2313 [REDACTED]

[REDACTED] Prepared by: General Electric/TEMPO,  
Santa Barbara, California.

[REDACTED] Availability: Qualified requestors may  
obtain this document from the Defense Docu-  
mentation Center. No foreign dissemination is  
allowed without approval of Headquarters.

Defense Nuclear Agency, Washington, D.C. 20305.

This handbook provides a set of corrections to the DASA Communications Handbooks, DASA 1954, 1955 and 1956 (see abstracts of these handbooks above).

### TREE SIMULATION FACILITIES

DNA 2432H (Edition 1)

Prepared by: Battelle Memorial Institute, Columbus, Ohio

Availability: Qualified requestors may obtain this document from the Defense Documentation Center.

This handbook characterizes individual pulse reactors, flash x-ray and LINAC facilities on a technical basis for those persons working in the area of transient radiation effects on electronics (TREE). DNA 2432H is arranged to provide the persons who perform TREE experiments with the information concerning facilities which they would require in order to perform an experiment at one of the facilities.

### X-RAY CROSS SECTION COMPILATION

DNA 2433F-1 and -2 and DNA 2433F Supplement

Prepared by: Kaman Sciences Corporation, Colorado Springs, Colorado.

Availability: Qualified requestors may obtain this document from the Defense Documentation Center. Requests from other than U.S. government agencies must be made through Headquarters, Defense Nuclear Agency, Washington, D.C. 20305.

The experimental X-ray attenuation cross sections for 94 elements between 0.1 keV and 1 MeV, which were obtained for the period from 1920 through 1970, together with exact photoelectric absorption values for hydrogen, are presented in this compilation.

Scattering cross sections were calculated by relativistic SCF methods. These were subtracted from the total attenuation data, and the resulting photoelectric and measured photoelectric absorption cross sections from 1 keV to 1 MeV were fit by a least squares procedure to obtain best values. Interpolations were made for elements and energy ranges for which there were no experimental data. From 0.1 keV to between 1 keV and 10 keV nonrelativistic, self-consistent, independent electron theory was used to calculate photoelectric absorption cross sections. Scattering values were added to all photoelectric cross sections to obtain a best set of attenuation cross sections.

### NUCLEAR ENVIRONMENT DESCRIPTIONS

DAS.A 2491 (CONFIDENTIAL)

Prepared by: Boeing Company, Seattle, Washington.

Availability: Qualified requestors may obtain this document from the Defense Documentation Center.

The phrase "Nuclear Environment Descriptions" includes: (1) nuclear environment criteria; (2) nuclear effects design specifications; and (3) nuclear effects test specifications. This volume provides an introductory discussion of the three types of nuclear environment descriptions, but it is concerned primarily with the first of these descriptions.

The major considerations and procedures required for the development of nuclear environment criteria within a logical system development process are described and illustrated. A standard, comprehensive, understandable format for expressing this description is specified. The material presented is not predicated on the administrative procedures of any one military service and is, therefore, of general applicability.

[REDACTED] NUCLEAR WEAPON THERMAL RADIATION PHENOMENA [REDACTED]

[REDACTED] DNA 2500H [REDACTED]

[REDACTED] Prepared by: Kaman Sciences Corporation, Colorado Springs, Colorado

[REDACTED] Availability: Volumes 2 and 3 were published in July 1974 and February 1974 respectively. Part of Volume 1 were completed and published separately in February 1974 as DNA 3220Z, "New Thermal Scaling Laws for Low Altitude Nuclear Bursts (U)," and DNA 3223Z, "Atmospheric Transmission of Nuclear Weapon Thermal Radiation (U)." In November 1977, a draft version of Volume 1 was completed. It is expected to be incorporated into one document and published by mid 1978 under the title *New Thermal Scaling Laws for Bursts Below 30 Kilometers*. All published portions are available for qualified users from the Defense Documentation Center.

[REDACTED] The DNA Thermal Sourcebook is being prepared as a comprehensive summary of theoretical and experimental information on the prompt thermal radiation environment produced by atmospheric nuclear weapons. This book is designed to provide the latest and most reliable information on thermal environments, including both fireball source characteristics and the transport of the fireball radiation through great distances in the atmosphere. The book does not include the numerous considerations relating to target response, although a short appendix on thermal damage effects will be provided.

[REDACTED] Volume 1 of this sourcebook will treat the following subjects: nuclear weapon outputs, energy deposition in the atmosphere, the physics of fireballs, radiation-hydrodynamics codes, atmospheric transmission phenomena, weapons test data, comparisons of theory and experiment, and environment prediction methods. Volume 2 provides a complete tabulation of all thermal environment measurements made at all U.S.

atmospheric nuclear tests through Operation DOMINIC in 1962. Volume 3 is an extensive bibliography of reports, papers, etc., on the subject of nuclear weapons thermal radiation phenomena.

[REDACTED] TRAPPED RADIATION HANDBOOK

[REDACTED] DNA 2524H (Unclassified)

[REDACTED] Prepared by: Lockheed Palo Alto Research Laboratory

[REDACTED] Availability: This document has been approved for public release and sale; its distribution is unlimited.

[REDACTED] The Trapped Radiation Handbook provides useful information and design data for scientists and engineers engaged in the design of spacecraft systems that must operate in the trapped radiation environment. It contains a compilation of useful charts and graphs and abbreviated derivations of equations and developments of concepts in a wide range of subject matter pertinent to the radiation belts. The handbook is intended to be helpful to scientists who are beginning studies or research in this field as well as to scientists who are actively engaged in magnetospheric research. The following subjects are discussed: the magnetosphere; features and mathematical models of the earth's magnetic field; the motion of charged particles in the field; the properties of the particles in the natural radiation belts; source and loss mechanisms; the artificial radiation belts that have resulted from tests of nuclear devices conducted at high altitudes; the phenomenology of nuclear detonations and beta injection processes; the effects of trapped particles (both natural and fission betas) on materials and devices; the irradiation of circular orbit satellites by trapped particles of the natural environment as well as the environment produced by weapon tests L-values, and an estimated wartime environment; the synchrotron radiation emitted by the trapped electrons; and the vulnerability of oper-

ational systems in the environments mentioned previously.

This handbook is updated on a periodic basis. As of September 1977, five changes have been issued.

## STATUS OF NEUTRON AND GAMMA OUTPUT FROM NUCLEAR WEAPONS

DASA 2567

Prepared by: Science Applications Incorporated, La Jolla, California.

Availability: Qualified requestors may obtain this document from the Defense Documentation Center on request through Headquarters, Defense Nuclear Agency, Washington, D.C. 20305.

This report presents a review and evaluation of existing experiments and calculations of neutron and gamma output spectra and intensities. Comparisons of calculated and measured results for a number of devices are described together with possible explanations for some deviations between the experiment and numerical results. In addition, detailed gamma output calculations were performed for Tambourine, using up-to-date neutron and gamma production cross section data.

## IMPROVED MODELS FOR PREDICTING NUCLEAR WEAPON INITIAL RADIATION ENVIRONMENTS

DASA 2615

Prepared by: Radiation Research Associates, Inc., Fort Worth, Texas.

Availability: Qualified requestors may obtain this document from the Defense Documentation Center on request through Headquarters, Defense Nuclear Agency, Washington, D.C. 20305.

DASA 2615 presents a review and evaluation of current data and techniques for predict-

ing the initial radiation exposure at or near the ground surface resulting from a nuclear explosion. State-of-art models were then developed for neutron dose, secondary gamma exposure from neutron interactions in the air and ground, and fission product gamma ray exposure occurring during the first minute following a detonation. The neutron and secondary gamma model, based on Straker's discrete ordinates calculations of neutron transport in an air-over-ground geometry and French's first-last collision method for source height effects, yield results for slant ranges up to 4.800 meters from each of 8 different types of weapons. The results may be adjusted for the desired burst height and air density. The fission-product gamma ray model is based on Monte Carlo air transport calculations by Marshall and Wells. It incorporates source spectra, source decay rates, cloud rise approximations, and hydrodynamic enhancement treatments based on the work of a number of previous investigators. The model provides for a wide variety of burst heights and air densities and provides for slant ranges up to 4.800 meters. The models and the incorporated data were validated through extensive comparison with weapon test results and with other calculated and semi-empirical data.

## THE MODELING OF NUCLEAR CLOUDS

DASA 2626

Prepared by: General Research Corporation, Arlington, VA

Availability: This document is available to qualified users from the Defense Documentation Center.

This modeling was performed in response to the need for a systems program to describe the dust particle environment in a nuclear cloud from a detonation on or near the surface. The flowfield during cloud rise was parameterized using a spherical vortex model empirically

[REDACTED]

fit to data from nuclear tests. This work is supplemental to DASA-2304T [REDACTED] Volume I, "Nuclear Surface Burst Debris" [REDACTED] as is also the determination of the lofted mass. The cloud dust loading depends on the height-of-burst in a nonlinear manner which is analyzed and modeled empirically. The particle size distribution of the dust in the cloud is that of the crater ejecta and sweep-up modified by the drag forces exerted by the buoyant and convective air flow. Both during rise and after stabilization, the cloud and dust are translated with the ambient wind. The speed and directional shears cause a time dependent cloud shape, which is important to the systems analyst, for whom the model was developed.

[REDACTED] The spherical model was completed and reported in DNA 2940T [REDACTED] "Vortex Dust Model for Rising Nuclear Cloud." Some modifications of the post stabilization model was reported in DNA 2745T [REDACTED] "New Measurements of Visible Cloud Diameter," and DNA 3158F-1 [REDACTED] "Post-Stabilization Nuclear Dust Cloud," and have been incorporated in the programming of the vortex model.

#### HANDBOOK OF NUCLEAR WEAPONS AS X-RAY SOURCES

DNA 2866H [REDACTED]

[REDACTED] Prepared by: Kaman Sciences Corporation, Colorado Springs, Colorado.

[REDACTED] Availability: Qualified requestors may obtain this document from the Defense Documentation Center.

[REDACTED] This handbook contains a chronological tabulation of most of the X-ray effects tests that have been conducted by the Department of Defense and the Atomic Energy Commission, as well as a general description of the X-ray spectra and the fluence levels available for experiments on each event. Six illustrative X-ray tests are discussed in some detail. Their X-ray spectra are presented as curves and tabulations and some

[REDACTED]

discussion of their radiation times is given. There is some discussion of the outputs from underground X-ray tests simulating tactical ABM environments.

[REDACTED] The handbook is not intended to provide all the information required by a person who is not familiar with X-ray effects testing, nor is it for a person whose full time occupation is analysis of X-ray spectra from nuclear weapons. The information is useful to the large majority of the community associated with military effects of X-rays from nuclear weapons. Whether or not this is a "handbook" depends more on the user's definitions than on the author's.

#### INSTRUMENTS FOR MEASURING NEUTRON AND GAMMA RADIATION FROM NUCLEAR-WEAPON TESTS

DNA 2888F [REDACTED]

[REDACTED] Prepared by: Science Applications Incorporated, La Jolla, California.

[REDACTED] Availability: To be issued during calendar year 1972.

[REDACTED] DNA 2888 reviews the methods to obtain neutron and gamma ray fluence and spectral data in a nuclear test environment. Approximately forty instruments of those surveyed during this study are described. A complete outline of the experimental techniques employed in these types of measurements is provided, with a description of device input and typical radiation environments encountered during a nuclear test.

[REDACTED] With few exceptions, only those instruments that have been used in past tests are con-

sidered in this report. Instruments to provide neutron and gamma ray dose as a function of time, dose or fluence as a function of energy, and integrated dose were considered. A summary of the relative merits of each instrument is included.

## THE EFFECTS OF NUCLEAR WEAPONS

*Prepared and published by:* The U.S. Department of Defense and the U.S. Department of Energy, S. Glasstone and P. J. Dolan, editors.

*Availability:* This document may be obtained by contacting the Superintendent of Documents, U.S. Government Printing Office, Washington, D.C.

This book presents as accurately as possible, within the limits of national security, a comprehensive summary of information concerning nuclear weapons effects in an unclassified form. The phenomena of air blast, ground and water shock, thermal radiation, and nuclear radiations associated with nuclear explosions are very complex, and descriptions of these phenomena and their related effects are somewhat technical in nature. However, this handbook has been arranged in such a manner as to serve the widest possible range of readers. Most of the chapters are presented in two parts, the first consisting of a general treatment of a particular topic in a less technical manner and the second discussing some of the more technical aspects. The material is so arranged that the reader will experience no loss of continuity by the omission of any or all of the more highly technical sections, but the technical material is available for the use of those who may have need of such information.

The third edition of this book was published in December 1977.

## VORTEX DUST MODEL FOR RISING NUCLEAR CLOUDS

DNA 2940T

*Prepared by:* Science Applications, Incorporated, Arlington, VA

*Availability:* Qualified users may obtain this document from the Defense Documentation Center.

The transport of soil particles after a nuclear detonation on or near the surface is modeled by the vortex flowfield which has a simple mathematical form. By including appropriate particle drag relations and empirically fitting the vortex parameters to both experimental and hydrocode data, a simpler hydrodynamic model (VORDUM) was obtained to predict the soil particle environment. The boundary condition of zero vertical flow velocity at the surface is obtained by using an image vortex moving downward. The VORDUM results are similar to those obtained using the SHELL hydrocode (developed at AFWL). The model has been applied to yields from less than 1 MT to greater than 10 MT. The pancake geometry of the post stabilization model, reported in DASA 2304T Volume I, "Nuclear Surface Burst Debris" was superseded by this description.

The post stabilization cloud geometry was improved by the modeling of the late time cloud reported in DNA 3158 F-1 "Post-Stabilization Nuclear Dust Cloud."

## COMMUNICATION SATELLITE SYSTEMS VULNERABILITY TO NUCLEAR EFFECTS – SELECTED EXAMPLES BY FREQUENCY BAND

DNA 3185H-1

*Prepared by:* ESL Incorporated

*Availability:* Qualified requestors may obtain these documents from the Defense Documentation Center. Each transmittal outside the

[REDACTED]  
[REDACTED] agencies of the U.S. Government must have prior approval of the Defense Nuclear Agency.

[REDACTED] This document describes communication satellite system vulnerability to propagation disturbance induced by nuclear explosions. Examples of the effects of selected nuclear burst on communication satellite system performance are given by frequency band. The satellite systems analyzed are representative of existing, planned, or proposed systems in seven bands extending from 150 MHz to 14 GHz. The examples presented illustrate the approximate duration and extent over which typical systems may experience difficulty. In addition to specific results, the nuclear effects from the selected weapon environments have been parameterized so that these results can be extended to other systems.

[REDACTED] Among the effects considered are radio wave absorption, thermal noise, signal dispersion, and propagation time delays. The effect of signal dispersion is considered on systems employing frequency division multiplex-frequency modulation (FDM-FM), and digital systems employing phase shift keying (PSK). While not modeled for the selected examples, the potential effects of phase scintillations on systems employing PSK modulation are shown. Potential effects on systems employing Time Division Multiple Access (TDMA) and Code Division Multiple Access (CDMA) using spread spectrum techniques are discussed.

#### [REDACTED] ELECTROMAGNETIC BLACKOUT HANDBOOK

[REDACTED] DNA 3380 H-1, 2, 3 (DNA 3380 H-1,

[REDACTED] DNA 3380 H-2,

DNA 3380 H-3

[REDACTED] Prepared by: General Electric Company

[REDACTED] DPO.

[REDACTED] Availability: Qualified requestors may obtain these documents from the Defense Documentation Center. Each transmittal outside the

agencies of the U.S. Government must have prior approval of the Defense Nuclear Agency.

[REDACTED] This handbook provides source material on nuclear weapon phenomenology, atmospheric processes, and effects of disturbed atmospheric environments on electromagnetic propagation for use in analysis of radar and communications systems. This edition of the handbook is a revision of DASA 1580 and DASA 1580-1 (same title) and replaces those documents. The handbook is divided into seven chapters plus appendices and is published in three volumes. Chapter 1 provides an introduction to nuclear weapon effects on electromagnetic propagation and a summary of communication and radar system performance in nuclear environments. Chapters 2, 3, and 4 present detailed descriptions of weapon radiations and energy deposition in the atmosphere, the phenomenology of heated regions, and atmospheric processes that affect nuclear weapon-induced atmospheric ionization. Chapters 5, 6, and 7 describe electromagnetic propagation effects and weapon-produced noise sources that can have effect on radar and communication systems. The several appendices include material on the properties of the atmosphere and earth's magnetic field, reference material on electromagnetic propagation and thermal radiation, and parametric scaling for weapon-produced regions and effects.

#### [REDACTED] ELECTROMAGNETIC PULSE HANDBOOK FOR ELECTRIC POWER SYSTEMS

[REDACTED] December 1974

[REDACTED] DNA 3466F

[REDACTED] Prepared by: Stanford Research Institute, Menlo Park, California

[REDACTED] Availability: Qualified users may obtain this handbook from the Defense Documentation Center.

[REDACTED] This handbook has been prepared primarily for the power, communications, and systems engineer who must be concerned with the

[REDACTED]  
[REDACTED]  
effects of the nuclear electromagnetic pulse on his system. The power engineer should be aware of the effects of EMP on his transmission and distribution system, and the power users must protect their equipment from the pulse conducted into their facilities on the power lines. The commercial power system can be a major path for coupling the EMP into ground-based systems. The power distribution system forms a very large, completely exposed antenna system that is hard-wired into the customer's facility. Thus, extremely high voltages may be developed on the power conductors, and even if the commercial power is not relied on for system survival, these voltages may be delivered to the system either before commercial power is lost, or by the ground or neutral system after transferring to auxiliary power.

[REDACTED] Considerable research has been performed on EMP coupling to commercial power systems in an effort to characterize the power distribution lines as EMP collectors, and to determine the effects of major components, such as transformers, lightning arresters, and low-voltage wiring, on the penetration of the received signal into ground-based facilities. This research has entailed development and experimental verification of the theory of coupling to transmission lines. This handbook on the interaction of EMP with commercial power systems has been prepared so that designers and systems engineers can benefit from the results of extensive data already accumulated.

#### [REDACTED] A POCKET MANUAL OF THE PHYSICAL AND CHEMICAL CHARACTERISTICS OF THE EARTH'S ATMOSPHERE [REDACTED]

[REDACTED] DNA 3467H [REDACTED]

[REDACTED] Prepared by: General Electric Co., Space Sciences Laboratory, P. O. Box 8555, Philadelphia, Pa. based upon information provided by the Bell Telephone Laboratory, the Lockheed Palo Alto Research Laboratory, and the Santa Barbara Research Center. Information

was also obtained from "Aid for the Study of Electromagnetic Blackout," DASA 2499 (1970), the DNA "Reaction Rate Handbook, Second Edition," DNA 1948H (1972), and "The Trapped Radiation Handbook" (1971), DNA 2542H.

[REDACTED] Availability: Qualified requestors may obtain the handbook from the Defense Documentation Center or from the National Technical Information Service (NTIS).

[REDACTED] This pocket manual provides a pocket size compendium of current available knowledge concerning the physical and chemical properties of the earth's ionosphere. It is based principally upon data contained in greater detail in DNA Reaction Rate Handbook, Second Edition (1972), DNA 1948H, as well as the other sources mentioned above. A circular slide rule is normally inserted in the flap of the front cover for convenient calculational use.

[REDACTED] It is anticipated that as important changes occur in relevant information they will be issued to recipients for inclusion in this pocket manual.

#### [REDACTED] AID FOR THE STUDY OF ELECTROMAGNETIC BLACKOUT [REDACTED]

[REDACTED] DNA 3499H [REDACTED]

[REDACTED] Prepared by: General Electric Company - TEMPO

[REDACTED] Availability: Qualified requestors may obtain this document from the Defense Documentation Center.

[REDACTED] This report is a revision of DASA 2499 (same title) and replaces that document. The report is a compendium of selected graphs, charts, equations, and relations useful in the analysis of electromagnetic blackout caused by nuclear explosions. Information is provided concerning weapon outputs, ionization source functions, deionization, absorption, phase effects, and noise. The report also contains sections listing atmospheric properties, physical constants, definition of symbols, and a glossary of frequently used terms.